

*Peters*  
~~Aug 20 1980~~  
~~Nov 8 1980~~

NOV 10 1980

AGARD-CP-271

AGARD-CP-271

MAY 1 1983

~~5 20 1991~~

# AGARD

ADVISORY GROUP FOR AEROSPACE RESEARCH & DEVELOPMENT

7 RUE ANCELLE 92200 NEUILLY SUR SEINE FRANCE

AGARD CONFERENCE PROCEEDINGS No. 271

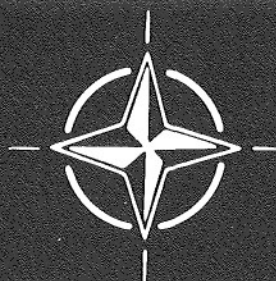
## Turbulent Boundary Layers

### Experiments, Theory and Modelling

~~TECHNICAL REPORTS~~  
~~FILE COPY~~

c.1

NORTH ATLANTIC TREATY ORGANIZATION



DISTRIBUTION AND AVAILABILITY  
ON BACK COVER

Property of U. S. Air Force  
~~Feb 1981~~  
F40600 17 0 0003

## EXECUTIVE SUMMARY

As stated in the theme for the meeting: "Recent experiments have demonstrated the persistence of coherent structures in turbulent shear flows and consequently have cast doubt on the usual local transport relations and even on the usefulness of Reynolds averaging, used in practically all modelling approaches.

It is the purpose of the symposium to take stock of the present situation in turbulence research and to attempt, by bringing together experimentalists and theoreticians, to map out new directions in modelling and experimentation. In order to concentrate on one of the most important applied problems, the symposium deals specifically with turbulent boundary layers, in both incompressible and compressible fluid flow."

The existence of coherent vortex structures has led to renewed interest in Lagrangean descriptions of the flow. Current work thus emphasizes flow-visualization methods together with development of sophisticated conditional sampling methods in hot-wire anemometry. Both the need for such methods and their usefulness are amply demonstrated in the research presented at the symposium. Experimentalists have taken up the challenge presented by the existence of coherent structures, and new results are reported from several laboratories.

Theoreticians interested in these new results face the very difficult task of coming to grips with nonlinear vortex interactions, a subject which has been somewhat neglected in recent times. Development of a physically satisfactory and mathematically tractable theory is a formidable task and progress is very slow. The decomposition of a fluctuating flow field into waves is a traditional and thus familiar approach while decomposition into horseshoe vortices (say) presents conceptual as well as mathematical difficulties.

Computer modelling of turbulent shear flows using Reynolds averaged equations with various closure schemes is the most useful technique presently available. However, sooner or later, modelling will have to recognize the experimental fact of coherent structures. In both theory and modelling, two-level approaches dealing with definite vortex structures on one level and some form of random small-scale turbulence on another level are being studied, and significant progress is reported at the meeting.

Finally, considerable attention is paid in several papers to the early development of turbulence, during or immediately following transition. These papers go some way toward establishing that wave packets and turbulent spots can be viewed as models and perhaps as prototypes for coherent structures in fully developed flow.

All in all the symposium served its purpose. Probably the most significant result is cross-fertilization of ideas among the three groups of researchers. The communication of significant research results, however, is also evident in the papers which follow.

H.W.LIEPMANN  
Chairman, Program Committee



NORTH ATLANTIC TREATY ORGANIZATION  
ADVISORY GROUP FOR AEROSPACE RESEARCH AND DEVELOPMENT  
(ORGANISATION DU TRAITE DE L'ATLANTIQUE NORD)

AGARD Conference Proceedings No.271  
TURBULENT BOUNDARY LAYERS – EXPERIMENTS,  
THEORY AND MODELLING

## THE MISSION OF AGARD

The mission of AGARD is to bring together the leading personalities of the NATO nations in the fields of science and technology relating to aerospace for the following purposes:

- Exchanging of scientific and technical information;
- Continuously stimulating advances in the aerospace sciences relevant to strengthening the common defence posture;
- Improving the co-operation among member nations in aerospace research and development;
- Providing scientific and technical advice and assistance to the North Atlantic Military Committee in the field of aerospace research and development;
- Rendering scientific and technical assistance, as requested, to other NATO bodies and to member nations in connection with research and development problems in the aerospace field;
- Providing assistance to member nations for the purpose of increasing their scientific and technical potential;
- Recommending effective ways for the member nations to use their research and development capabilities for the common benefit of the NATO community.

The highest authority within AGARD is the National Delegates Board consisting of officially appointed senior representatives from each member nation. The mission of AGARD is carried out through the Panels which are composed of experts appointed by the National Delegates, the Consultant and Exchange Programme and the Aerospace Applications Studies Programme. The results of AGARD work are reported to the member nations and the NATO Authorities through the AGARD series of publications of which this is one.

Participation in AGARD activities is by invitation only and is normally limited to citizens of the NATO nations.

The content of this publication has been reproduced directly from material supplied by AGARD or the authors.

Published January 1980

Copyright © AGARD 1980  
All Rights Reserved

ISBN 92-835-0257-4



*Printed by Technical Editing and Reproduction Ltd  
Harford House, 7-9 Charlotte St, London, W1P 1HD*

## AGARD FLUID DYNAMICS PANEL

CHAIRMAN: Mr J.L.Jones  
Special Assistant for Planning & Analysis — MS 200-10  
NASA Ames Research Center  
Moffett Field  
California 94035 — USA

DEPUTY CHAIRMAN: Dr K.J.Orlik-Rückemann  
National Aeronautical Establishment  
National Research Council  
Montreal Road  
Ottawa, Ontario K1A 0R6 — Canada

## PROGRAMME COMMITTEE MEMBERS

Dr H.W.Liepmann (Chairman)  
Director of GALCIT — MS 105-50  
California Institute of Technology  
Pasadena, California 91125 — USA

Professor Dr F.J.Hindelang  
Fachbereich Luft-und Raumfahrttechnik  
Hochschule der Bundeswehr Munchen  
8014 Neubiberg — Germany

Professor S.M.Bogdonoff  
Chairman, Department of Aerospace  
and Mechanical Sciences  
Room 214 — The Engineering Quadrangle  
Princeton University  
Princeton, N.J.08540 — USA

Professor Dr J.L. Van Ingen  
Dept. of Aerospace Engineering  
Delft University of Technology  
Kluyverweg 1  
2629 HS Delft — Netherlands

M. l'Ing. Général P.Carrière  
Senior Scientific Adviser  
ONERA  
29 Avenue de la Division Leclerc  
92320 Châtillon — France

Professor A.D.Young  
Dept. of Aeronautical Engineering  
Queen Mary College  
University of London  
Mile End Road  
London E1 4NS — United Kingdom

## PANEL EXECUTIVE

Robert H.Rollins, II

Mail from US and Canada  
AGARD/NATO  
APO New York 09777

Mail from Europe  
AGARD/NATO  
7 rue Ancelle  
92200 Neuilly sur Seine — France

A TURBULENCE CLOSURE OF THE TRANSPORT EQUATION FOR THE PROBABILITY DENSITY OF VELOCITY by M.M.Ribeiro	15
MODELLING REQUIREMENTS FOR THE CALCULATION OF THE TURBULENT FLOW AROUND AIRFOILS, WINGS AND BODIES OF REVOLUTION by T.Cebeci and H.U.Meier	16
THE TURBULENT BOUNDARY LAYER AND THE CLOSURE PROBLEM by L.N.Persen	17
BOUNDARY LAYER MEASUREMENTS ON A TWO DIMENSIONAL WING WITH FLAP AND A COMPARISON WITH CALCULATIONS by B. van den Berg and B.Oskam	18
COUCHE LIMITE TURBULENTE TRIDIMENSIONNELLE: RESTRUCTURATION D'UN ECOULEMENT AXISYMETRIQUE SOUMIS A UNE DISCONTINUITE DE LA VITESSE DE PAROI par E.Arzoumanian, L.Fulachier, J.Cousteix et B.Aupoix	19
 <u>SESSION III – TRANSITION AND STRUCTURE</u>	
THE ROLE OF WAVE PACKETS IN TRANSITION* by M.Gaster	20
EVIDENCE FOR INSTABILITY-WAVES IN THE VELOCITY-FIELD OF A FULLY DEVELOPED TURBULENT CHANNEL-FLOW by M.Hofbauer	21
RESULTATS EXPERIMENTAUX RELATIFS A L'INFLUENCE DES PROCESSUS DE TRANSITION SUR LA STRUCTURE INITIALE D'UNE COUCHE LIMITE TURBULENTE par D.Arnal et J-C.Juillen	22
SOME MEASUREMENTS IN SYNTHETIC TURBULENT BOUNDARY LAYERS by O.Savaş	23
COHERENT STRUCTURES IN TURBULENT BOUNDARY LAYERS by R.F.Blackwelder	24
FLOW VISUALISATION OF TURBULENT BOUNDARY LAYER STRUCTURE by M.R.Head and P.Bandyopadhyay	25
SOME OBSERVATIONS OF THE STRUCTURE OF THE TURBULENT BOUNDARY LAYER by A.S.W.Thomas	26
ROUND TABLE DISCUSSION	RTD

---

\* Oral presentation only – No Paper available

## CONTENTS

	Page
EXECUTIVE SUMMARY	iii
PANEL AND PROGRAMME OFFICIALS	iv
	Reference
<b><u>SESSION I – EXPERIMENTS IN BOUNDARY LAYERS</u></b>	
EXPERIMENTAL METHODS AND TECHNIQUES IN TURBULENT BOUNDARY LAYER RESEARCH by G.Comte-Bellot	1
ETUDE EXPERIMENTALE DES APPORTS ET DES EJECTIONS DE FLUIDE DANS UNE COUCHE LIMITE TURBULENTE par M.Elena, L.Fulachier et R.Dumas	2
EXPERIMENTAL STUDY OF COHERENT STRUCTURES IN THE TURBULENT BOUNDARY LAYER OF PIPE FLOW USING LASER-DOPPLER ANEMOMETRY by H.R.E. Van Maanen	3
TURBULENT BOUNDARY LAYER STRUCTURE AT LOW AND HIGH SUBSONIC SPEEDS by V.Zakkay, V.Barra and K.Hozumi	4
COHERENT STRUCTURES IN TIME DEPENDENT SHEAR FLOWS by H.Viets	5
AN INVESTIGATION OF THE STRUCTURE OF EQUILIBRIUM TURBULENT BOUNDARY LAYERS by L.F.East and W.G.Sawyer	6
EQUILIBRIUM BOUNDARY LAYERS OVER VERY ROUGH SURFACES by I.S.Gartshore and K.A. de Croos	7
TURBULENCE BEHAVIOUR IN A SHOCK WAVE/BOUNDARY LAYER INTERACTION by P.Ardonceau, D.H.Lee, T.Alziary de Roquefort and R.Goethals	8
LONGITUDINAL VORTICES IN A CONCAVE SURFACE BOUNDARY LAYER by R.I.Crane and S.H.Winoto	9
A DISCUSSION OF PROBE EFFECTS AND IMPROVED MEASURING TECHNIQUES IN THE NEAR-WALL REGION OF AN INCOMPRESSIBLE THREE-DIMENSIONAL BOUNDARY LAYER by J.D.Vagt and H.H.Fernholz	10
<b><u>SESSION II – THEORY AND MODELLING</u></b>	
DEVELOPMENTS IN THE COMPUTATION OF TURBULENT BOUNDARY LAYERS by M.W.Rubesin	11
A NAVIER-STOKES FAST SOLVER FOR TURBULENCE MODELING APPLICATIONS by J.D.Murphy and M.W.Rubesin	12
REYNOLDS STRESS CLOSURES – STATUS AND PROSPECTS by B.E.Launder	13
LARGE EDDY SIMULATION OF TURBULENT CHANNEL FLOW – ILLIAC IV CALCULATION by J.Kim and P.Moin	14



## EXPERIMENTAL METHODS AND TECHNIQUES IN TURBULENT BOUNDARY LAYER RESEARCH

by

Geneviève COMTE-BELLOT  
Ecole Centrale de Lyon  
Laboratoire de Mécanique des Fluides  
36, route de Dardilly - 69130 ECULLY  
France

1. Introduction.

The arsenal of methods and techniques available to investigate turbulent boundary layers is impressive and this is due to at least three reasons :

- (i) the scientific motivations are manifold. For example, for the basic case of an incompressible unheated two-dimensional turbulent boundary layer on plane walls without a pressure gradient, the interest lies at present in the detailed knowledge of all the physical mechanisms involved. Sophisticated multipoint and multicomponent measurements are therefore developed. On the other hand, for boundary layers observed in real situations, i.e. with additional effects due to pressure gradients, rotation, gravity forces, suction or blowing... the goals are less ambitious, but techniques which overcome the inherent difficulties due to the situation encountered in practice are needed. For example, investigation of regions of reverse flow is a matter of concern for the aerodynamics of airfoils. When rotation or buoyancy effects are present the achievement of the kinetic energy balance is a legitimate objective. The data helping to develop the numerical modeling of the flow are also a strong motivation in these practical situations.
- (ii) the transducers can be placed not only inside the flow (or even far from the flow), as for any turbulent flow, but also at the wall. Special transducers have therefore been developed for the measurement of wall pressure fluctuations and velocity gradients at the wall. These wall variables are, of course, relevant to other problems, such as the noise emitted by solid-flow interactions, or the vibratory response of structures excited by turbulent boundary layers.
- (iii) the signal processing technique has gained a great deal of refinement since the 1960's due to the development of compact electronic devices and computers. There is also the need to understand complex unsteady flows through a limited number of probe signals. For example, conditional zone averages are used to take into account the random and convoluted edge of the boundary layer. Pattern recognition techniques help the detection of particular structures making up the turbulent flow.

This lecture is intended to be a survey of the three points which have been listed. The most recent facts will be emphasized as much as possible, and compared with routine techniques such as conventional averages, spectra, or space and time correlations. Because of the limited time available, the survey is, however, limited to incompressible boundary layers. Even in this case, many references could be given and I apologize in advance for any omissions.

2. Actual objectives of boundary layer research

As mentioned in the introduction, the state of motivation is different for the basic case of the boundary layers without a pressure gradient and for the more complex usual boundary layers, so that the objectives have to be listed separately. For the former, a brief historical evolution of the objectives is helpful for the understanding of the present situation, although a highly documented review by WILLMARTH 1975 is available. For the latter, the additional relevant factors have to be pointed out at once.

2.1. Boundary layer without a pressure gradient

As soon as a statistical approach of turbulence became available, after the pioneering work of G.I. TAYLOR for isotropic turbulence, experimental investigations were aimed at the measurement of as many statistical characteristics as possible : r.m.s. values of velocity fluctuations, energy-spectra, space correlation functions... (TAYLOR 1936 ; KLEBANOFF & DIEHL 1952 ; LAUFER 1951 (the fully developed channel or pipe flows are also referred to because of their similarity to boundary layers in the wall region)).

Interest in the balance of the turbulent kinetic energy came in the early fifties (KLEBANOFF 1955, LAUFER 1954), along with the idea of preferred turbulent large structures to convey energy from the mean flow to turbulence (TOWNSEND 1956). The local isotropy expected for fine structures was checked and usually obtained except very close to the wall because of the large mean velocity gradients. The non-Gaussian features of the velocity and its time derivative were also examined in detail (COMTE-BELLOT, 1965).

The idea of considering turbulence as a material with some sort of constitutive law came later (LUMLEY 1970) and assumed different forms. At first, the memory of turbulence was obtained through space-time correlations (FAVRE, GAVIGLIO & DUMAS 1957; SABOT & COMTE-BELLOT 1972, BLACKWELDER & KOVASZNY 1972; SABOT, RENAULT & COMTE-BELLOT 1973).

Integral time scales in the convected frame of reference are, taking the example of the wall region, of the order of  $L_{\parallel}^{(u)}/u_{\parallel}'$  with  $u_{\parallel}'$  rms of the velocity component  $u_{\parallel}'$  and  $L_{\parallel}^{(u)}$  the longitudinal integral length scale of  $u_{\parallel}'$ . A second aspect is the response of the boundary layer to imposed perturbations: introduction of sinusoidal perturbations by HUSSAIN & REYNOLDS 1972; introduction of a turbulent spot into a fully developed turbulent boundary layer (HARITONIDIS, KAPLAN & WYGNANSKI 1978; WYGNANSKI 1979).

Other perturbations of interest are the sudden change in the wall condition, for example from smooth to rough walls (ANTONIA & LUXTON 1971) or the sudden application of a rotation to create 3-D effects (BISSENETTE & MELLOR 1974; LOHMANN 1973; ARZOUMANIAN, FULACHIER & DUMAS 1979).

The need to separate the experimental data issued from the turbulent and non-turbulent zones was pointed out by KAPLAN & LAUFER 1969 and by KOVASZNY, KIBENS & BLACKWELDER 1970, although the existence of a time-varying but sharp interface had been known for a long time in free turbulent flows (CORRSIN & KISTLER 1955). Since then conditional zone averaging have been widely used.

The way entrainment takes place at the boundary layer edge quickly became a main objective for experimental research. The mean entrainment rate is also an important boundary condition for the numerical modelling of turbulent boundary layers (HEAD & PATEL 1970; MARI, JEANDEL & MATHIEU 1976).

From space-time correlations, KOVASZNY, KIBENS & BLACKWELDER (1970) obtained the image and motion of the large bulges limiting the boundary layer edge (upward motion and rotation). Shortly afterwards, measurements of the Reynolds stress at various distances from the front or the back of the bulges (conditional point averages) were made by ANTONIA who concluded that most of the entrainment takes place at the front (downstream part) of the bulges where the Reynolds stress is small and matches the external value.

The search for identifiable structures inside the boundary layer may be important for the downstream growth of the layer (Fig. 1). The problem is, per se, difficult because it requires looking for some kind of hidden structures in respect to the conspicuous large bulges modelling the free edge. However, many elegant methods have been devised:

(i) visual observations (KLINE, REYNOLDS, SCHRAUB & RUNSTADLER 1967; CORINO & BRODKEY 1969; KIM, KLINE & REYNOLDS 1971, GRASS 1971, FALCO 1977), (ii) the four quadrant analysis of the  $u, v$  fluctuations (WILLMARTH & LU 1972, WALLACE, ECKELMANN & BRODKEY 1972, LU & WILLMARTH 1973, SABOT & COMTE-BELLOT 1976), (iii) analysis of cross-correlations between velocity gradients at the wall and velocities across the boundary layer (BROWN & THOMAS 1977), (iv) analysis of the activity periods of filtered velocity signals (RAO, NARASIMHA & BADRI NARAYANAN 1971), (v) detection of characteristic patterns or "signatures" in the velocity signals (WALLACE, BRODKEY & ECKELMANN 1977; COMTE-BELLOT, SABOT & SALEH 1979).

Close to the wall ( $y_{eff}/\nu \leq 40$ ) typical structures have been clearly observed: low-speed streamwise streaks, pairs of contra-rotating vortices aligned in the streamwise direction, occasional lift-up of the streaks with a breaking up into a chaotic small scale motion ("bursting" sequence\*). For a recent account of the numerous investigations, one can refer to the paper which will be given later in this meeting by BLACKWELDER. The essential result is that the mean frequency of occurrence of the bursts scales with the outer flow variables,  $\delta$  and  $U_e$ , and not with the inner variables,  $\nu/u_{\tau}$  and  $u_{\tau}$  (KIM, KLINE & REYNOLDS 1971; RAO, NARASIMHA & BADRI NARAYANAN 1971; LAUFER & BADRI NARAYANAN 1971).

Farther from the wall, several features have been reported: (i) existence of organized large scale structures inclined to a preferred angle in respect to the mean flow (FALCO 1977; BROWN & THOMAS 1977), (ii) correlation between these structures and the behaviour of the viscous sub-layer (BROWN & THOMAS 1977), (iii) intermittency of very large amplitude of  $- \rho u v(t)$  associated with "ejections" ( $v > 0, u < 0$ ) whose longitudinal dimension is small relative to that of the large structures (of the order of  $L_{\parallel}^{(u)}$  and  $L_{\parallel}^{(v)}$  respectively, with  $L_{\parallel}^{(u)} \approx 0.1 L_{\parallel}^{(v)}$ ) (SABOT 1976), a result which holds for rough walls (GRASS 1971; SABOT, SALEH & COMTE-BELLOT 1977), (iv) existence of "typical eddies" (average streamwise length approximately  $200 \nu/u_{\tau}$ ) formed on the upstream side of large scale motions (average length  $1.6 \delta$ ) and associated with significant Reynolds stress contributions (FALCO 1977; cf. Fig. 1).

A plausible dynamic for these structures is still missing. The difficulty is to find the origin and development of the large structures and the link with the wall events. However, interesting suggestions have been proposed using perturbation and instability concepts (COLES & BARKER 1975; BROWN & THOMAS 1977; MOLLO-CHRISTENSEN 1971; LANDHAL 1977) pairing processes (OFFEN & KLINE 1973) and vortex models (THEODORSEN 1954; KLINE, REYNOLDS, SCHRAUB & RUNSTADLER 1967; WILLMARTH & BOGAR 1977). The vorticity dynamic and its relation with the velocity field (stretching, tilting) is probably of great importance. In particular, it has been known for a long time, that the skewness factor of the time derivative of the velocity fluctuations is very large in the wall region,  $S_1 \approx 0.80$  at  $y_{eff}/\nu \approx 15$ , and small near the free edge  $S_1 \approx 0.20$  at  $y/\delta = 1$  (COMTE-BELLOT 1959, 1965; conventional averages). Some of these measurements have been recently repeated by WALLACE, BRODKEY & ECKELMANN 1977 and used in a pattern recognition technique (cf. section 4.2). In this context, multipoint vorticity measurements would probably be useful, but are very difficult to perform (cf. section 3.1.1.). The difference

\* The term "burst" was introduced by CORRSIN as early as 1957 when investigating with RUETENIK the turbulent flow in a 2 D divergent channel, and was related to large  $u > 0$  signals which occur intermittently close to the wall.

in the order of magnitude between the integral length scales related to the longitudinal velocity component and the transverse component ( $L_{22}^{(u)} \approx 0.1 L_{11}^{(u)}$  SABOT 1976) is also an important experimental fact which shows that the spatial coherence is given by different steps in the sequence mechanism which governs the boundary layer growth.

Finally, the detailed knowledge of wall-pressure fluctuations from the turbulent velocity field is a matter of concern. Of course, they are theoretically known since governed by a Poisson equation, but the relative importance of the different flow regions has to be analyzed, after the first speculation of STERNBERG (1962). In most applications (aerodynamic noise, GOLDSTEIN 1976 ; panel vibration, MAESTRELLO 1965 ; cavitation at or near walls for material damages, ARNDT & GEORGES 1979) it is the instantaneous space-time field which is of interest rather than the overall statistical features. Numerical modelling has also been attempted for both (DEARDORFF 1970 ; SCHUMANN 1975 ; GROTZBACH & SCHUMANN 1979, SCHUMANN, GROTZBACH & KLEISER 1979), and all comparisons with experiments are desirable. New developments with more grid points in the wall region, will be presented in the course of this meeting by KIM & MOIN.

## 2.2. More complex boundary layers

Numerous cases of complex turbulent boundary layers, i.e. with extra strain rates, are encountered in technical problems and we shall examine some of the most pertinent situations.

### 2.2.1. Boundary layer with adverse pressure gradient

This is a basic case for flows around airfoils in turbomachinery and aeronautics and it has been a subject of research since the pioneering work of SCHUBAUER & KLEBANOFF 1951. The eventual separation of the boundary layer is the main problem to investigate with the urgent need to know (i) the mean velocity profile, (ii) the entrainment rate, (iii) the fraction of time during which the flow moves upstream (a sort of internal intermittency), (iv) the importance of the additional normal stress terms relative to the usual shear stress term in the equation governing the momentum and the turbulent kinetic energy (cf. Fig. 2) and (v) the possible 3D effects. Up-to-date analyses are given by SIMSON, STRICKLAND & BARR 1977 and by MELINAND & CHARNAY 1979. In the former, a preliminary investigation of the bursting frequency is also reported, but this problem seems far beyond the reach and understanding of such a complex flow, at least in the present state of the art regarding boundary layers without a pressure gradient.

### 2.2.2. Rotating turbulent boundary layer

The incentive for studying rotating boundary layers comes mainly from their occurrence in turbomachines (e.g. on blades of centrifugal compressors) and their implication in secondary losses.

Since the general situation is complex, a basic model has been considered (JOHNSTON, HALLEEN & LEZINS 1972, KOYAMA, MASUDA, ARIGA & WATANABE 1979 (a) and 1979 (b)). It consists of a whole 2D-channel installed on a merry-go-round whose axis of rotation is parallel to the span of the channel. The Coriolis force is responsible for additional terms in the rate of production of  $\overline{u^2}$ ,  $\overline{v^2}$  and  $\overline{uv}$  as indicated in Fig. 3. This implies that the rotation tends to exchange the energy between the  $u$  and  $v$  components, which results in the further change of the production rate of  $\overline{uv}$ . As expected, the rotation rate does not appear explicitly in the equation of the turbulent kinetic energy  $q^2$  since the Coriolis force produces no net work.

The scaling laws imply a new parameter, the rotation number  $Ro_x = \lambda t$  or  $\Omega x / U$  which is positive for the high-pressure side. In this case, when  $Ro_x$  increases, there is at first the occurrence of secondary flows (TAYLOR - GORTLER vortices) and then the development of turbulence due to the dominance of the destabilizing effects, so that  $\overline{v^2}/\overline{u^2}$  and  $-\overline{p'uv}$  and finally  $q^2$  increase with respect to the case of no-rotation. The increasing turbulence also tends to prevent the boundary layer from separating. Numerical predictions have been recently suggested for the evolution of the Reynolds stress tensor. They use the fact that the time during which the turbulence is submitted to the rotation is short with respect to its own characteristic time, so that linear (rapid distortion) concepts can be used (BERTOGLIO, CHARNAY, GENCE & MATHIEU 1978).

### 2.2.3. Boundary layer on curved walls

Boundary layers on concave or convex walls (Fig. 4) are present in many practical situations such as the flow along the casing and the guiding vanes of turbomachines. An exhaustive survey is given by BRADSHAW (1973) and additional experimental work is reported by SO & MELLOR (1973) and HUNT & JOUBERT (1976). The new terms which appear in the kinetic energy budget are due to the centrifugal force. They are listed in Fig. 4 and it can be noted that  $U/R$  has the same role as  $-2\Omega$  except for the equation governing  $\overline{v^2}$  (a factor 2 difference) and hence for the equation giving  $q^2$ . The boundary layer on a concave wall ( $R < 0$ ) has therefore features similar to those which we have just described for the high pressure side of a rotating channel.

### 2.2.4. Boundary layer with thermal stratification

The implication of buoyancy forces in the lower part of the atmospheric boundary layer is well known and has been extensively analyzed by MONIN & YAGLOM (1971). Experiments in situ (WYNGAARD, COTE & IZUMI 1971, KAIMAL, WYNGAARD, HAUGEN, COTE & IZUMI 1976, BUSCH, LARSEN & THOMSON 1979) and simulations in the laboratory (CERMAK 1971 ; MERY, SCHON & SOLAL 1974, SCHON 1974 ; ARYA 1975 ; REY 1977 ; REY, SCHON, MATHIEU 1979) are at first oriented toward a comprehensive view of the turbulence through the determination of the kinetic energy budget (Fig. 5), the velocity and temperature spectra and the turbulent diffusion terms. The general state is however less advanced than for unheated boundary layers with a zero

pressure gradient. For example, no measurements seems to be available for the memory of turbulence nor for the eventual existence of coherent events which could be of a very distinct nature.

However, the large turbulent Reynolds numbers encountered in the atmosphere have suggested very fine measurements such as the probability density functions of velocity and temperature derivatives to check theoretical predictions concerning the fine scale intermittency of turbulent flows (SHEIH, TENNEKES & LUMLEY 1971, GIBSON & MASIELLO 1972).

The main (and practical) objective remains the dispersion of pollutants for which the large and energetic turbulent structures are the most efficient and correctly simulated in laboratory experiments (PASQUILL 1968 ; MALHOTRA & CERMAK 1964 ; SOLAL 1972). The Lagrangian characteristics which are essential are however difficult to determine directly in a way similar to the investigation of SNYDER & LUMLEY (1971) for grid turbulence. A new experimental approach has recently been suggested by SCHON, DANIEL, MELINAND, REY & CHARNAY (1979) which uses combined particle displacements and stroboscopic views of the flow by a rotating laser beam (cf. Section 3.1.4).

Sudden changes in the wall heat flux are also of interest. The case of an inversion (sudden drop of the wall temperature) makes it possible to investigate the relaxation of the previously structured turbulence (CHARNAY, SCHON, ALCARAZ & MATHIEU 1979 ; AWAD, MOREL, SCHON & CHARNAY 1979). In practice it simulates the temperature step between the atmosphere of a city and that of the surrounding country.

#### 2.2.5. Boundary layer with mass transfer

Boundary layers on porous wall are encountered in nuclear engineering (isotope separation) and in turbomachinery (turbine blade cooling). In the laboratory, they are often investigated without a pressure gradient (TENNEKES 1965 ; VEROLLET 1972 ; BAKER & LAUNDER 1974). The main feature is again the change of the Reynolds shear stress ; it increases for blowing, hence makes possible the artificial thickening of normal boundary layers ; conversely it decreases for suction and can become so small that turbulence cannot be maintained (inverse transition). More knowledge on the detailed structure of the flow is again a pending question for a comprehensive view of all the physical mechanisms involved.

### 3. Transducer techniques

In this section, we describe some of the most useful systems, along with the main problems one has to be aware of in order to obtain signals which follow faithfully the physical variables under investigation. We divide the presentation in two parts : (i) the transducer and remote systems which can be used, in principle, in any turbulent field except that the presence of a wall requires special attention, and (ii) the transducers which are embedded in the wall itself.

#### 3.1. Measurements inside the boundary layer

##### 3.1.1. Hot-wire anemometry

Because of their versatility and relatively low cost, hot-wire anemometers are well suited to the measurement of a given physical variable at a large number of points or to that of several physical variables at a given point. Recent surveys of "multichannel" or "multivariant" measurements are given by VAN ATTA (1979) and DEMETRIADES (1979). These hot-wire arrays are usually designed for basic situations in which advanced research is possible (Fig. 6 and 7) :

- arrays of hot-wires (6 to 12) spanning the boundary layer in the transverse direction BLACKWELDER & KAPLAN 1976. They permit investigation of the topology of the large bulges limiting the free edge of turbulent flows. Thermal tagging is often very useful for tracking sharp internal fronts and the investigations on boundary layers (CHEN & BLACKWELDER 1978 ; LAUFER 1975) have been developed following those on jets or mixing layers (SUNYACH 1971). These arrays are also used to investigate the possibility of creating coherent structures by disturbing the flow in a manner which triggers inherent instabilities (WYGNANSKI, 1979) or to follow the downstream development of a turbulent spot artificially introduced into the boundary layer (HARITONIDIS, KAPLAN & WYGNANSKI 1978).
- probe with three hot-wires to obtain the three components of the velocity fluctuations (LARSEN, MATHIASSEN & BUSCH 1979 ; MOFFATT, YAVUZKURT & CRAWFORD 1979).
- probe with an X-wire and a cold wire to obtain two components of the velocity and the fluctuations of temperature (JOHNSON 1959, CHARNAY, SCHON & SUNYACH 1973).
- combination of a hot-wire and three cold wires to obtain the temperature fluctuation and the  $u$  and  $v$  velocity components (FULACHIER 1979). The volume of the probe is very small (around 0.1 mm between each wire). This array in which the  $v$  component is deduced from the lateral flapping of the wake of the upstream wire, is derived from the three-wire probe designed by BEGUIER, REY, DUMAS & ASTIER 1973, which is itself an extension of a three-wire probe first suggested by REICHARDT as early as 1938.
- array of four cold wires to obtain the three components of the temperature gradient (SCREENIVASAN, ANTONIA & DANH 1977). The measuring volume is  $1.2 \times 0.9 \times 0.6 \text{ mm}^3$ .
- combination of interacting sensors to measure the concentration and two velocity components without ambiguity problems for air-helium mixtures (STANFORD & LIBBY 1974 ; LARUE & LIBBY 1977 ; LIBBY & LARUE 1979). The measuring volume is of the order of  $0.7 \text{ mm}^3$  and can be improved by split hot-films.

- pyramidal probe with four identical wires located along the edges of a tetrahedron to get the longitudinal component  $\omega_x$  of the vorticity fluctuations (KOVASZNAY 1950, KISTLER 1952, KASTRINAKIS, ECKELMANN & WILLMARTH 1979). The measuring volume is of the order of  $2 \text{ mm}^3$ .
- combination of an  $X$ -wire and a pair of parallel wires to obtain the transverse vorticity component  $\omega_z$  (FOSS 1979).
- combination of a single probe,  $V$  probe and  $X$  probe to obtain the transverse vorticity components  $\omega_y$  and  $\omega_z$  (ECKELMANN, NYCHAS, BRODKEY & WALLACE 1977). The largest wire separation is of the order of 3 mm.

In all these systems attention has to be paid to various questions in order to get an accurate response :

- a) aerodynamic interference between the elements of the array ;
- b) spatial resolution of the probe ;
- c) time-resolution of the probe ;
- d) calibration of the sensor ; detection and correction of spurious signals ; ambiguity problems ; effect of large fluctuations ; extra cooling due to the wall vicinity ;
- e) development of low-cost and high quality electronics to operate the elements of the sensor ;
- f) acquisition and handling of the large amounts of data provided by the probe.

Since vorticity is important for the dynamics of turbulence, we shall concentrate on the two components  $\omega_x$  and  $\omega_z$  which have been mainly considered so far. For the other aspects, one can consult CORRSIN (1963) and COMTE-BELLOT (1976) or also FREYMUTH (1978) for references.

At first, it is necessary to stress that the spatial resolution of the vorticity probe is a severe limitation to vorticity measurements, at least from the computation of WYNGAARD (1969) for isotropic turbulence. In short, the probe volume has to be of the order of the Kolmogorov scale. More precisely, the relevant parameters are  $\eta/d$  and  $\eta/\ell$ , where  $d$  is the wire separation,  $\ell$  the hot-wire length and  $\eta$  the Kolmogorov length scale. For example,  $\omega_x$  is obtained within 3 % if  $\eta/d \approx 0.32$  and  $d \approx \ell$ .

On the other hand, in the measurements of  $\omega_x$ , the smallest miniature pyramidal probe which has been built has  $d \approx 2 \text{ mm}$ , so that reliable signals can only be expected in flows with large viscous lengths, such as the oil channel at the Max Planck Institut Für Strömungsforschung, originally designed by REICHARDT and described by ECKELMANN (1974), in which  $\nu/u_f \approx \eta \approx 0.63 \text{ mm}$ . Ordinary laboratory flows cannot therefore be investigated for the time being. Moreover, KASTRINAKIS, ECKELMANN & WILLMARTH (1979) pointed out that the transverse velocity fluctuations  $v$  and  $w$  induce on the pyramidal probe a signal which is of the same order of magnitude as the expected vorticity signal (Figs. 8 and 9). Since instantaneous values of  $v$  and  $w$  are unknown, no correction is possible.

For the  $\omega_z$  component, which is probably larger than  $\omega_x$  because of a stronger relationship to the boundary layer field, FOSS (1979) pointed out some of the difficulties. Besides the spatial resolution, which seems to be here again a severe limitation, FOSS has to go through the whole analysis of the hot-wire response to large velocity fluctuations.

Some short-cuts have also been suggested, such as the measurement of  $\partial u / \partial z$ . Although FOSS (1979) thinks that errors are still possible, multipoint measurements would be worth making for boundary layer research by taking advantage of the advanced analysis of KUO & CORRSIN (1972) who were able to detect the shape of the vorticity structures in isotropic turbulence (2 D elongated filaments).

The wall vicinity creates also many difficulties : decrease of the turbulent scales, additional cooling of the sensors by the near-by wall ; occurrence of large fluctuations. In ordinary laboratory situations, boundary layers measurements are wrong for about  $\nu/u_f / \ell \leq 5$  (WILLS 1962 ; see also the accurate comparisons made by ALCARAZ & MATHIEU 1975 for the measurement of wall shear stress by different methods).

To investigate the viscous sublayer it is then necessary : (i) to increase the physical dimensions of this layer by use of high viscous fluid, such as glycerin (BAKEWELL & LUMLEY 1967) or oil (ECKELMANN 1974) and (ii) to use a miniature probe such as a single ended hot split-film (HERZOG & LUMLEY 1979) whose measuring dimensions ( $\approx 0.25$ - $0.15$ - $0.15 \text{ mm}$ ) are down to at least one-half of the viscous length  $\nu/u_f$  ( $\approx 0.56 \text{ mm}$ ). In addition, the high Prandtl number of glycerin ( $Pr = 2340$ ) has the advantage of reducing considerably the thermal boundary layer thickness of the probe and, hence, of suppressing the cooling by the near-by wall.

### 3.1.2. Laser Doppler Anemometry

Many advantages of the L.D.A. technique are appreciated in turbulent boundary layer investigations : the non-intrusiveness of any probe, the extraction of velocity fluctuations from other random variables such as temperature or concentration, the linear dependence of the detected frequency on the velocity, the possible detection of reverse flow simply by the use of an optical frequency shift applied to one of the laser beams (e.g. Bragg cell). The latter is especially useful when investigating separating boundary layers (SIMPSON, STRICKLAND & BARR 1977 ; MELINAND & CHARNAY 1979).



Sources of concern exist, however, and we shall concentrate on some of the most important or recent ones, particularly those which exist because of the vicinity of a solid boundary (for a review of the L.D.A. technique see, for example, BUCHHAVE, GEORGE & LUMLEY 1979).

At first, a practical problem arises from the fixation of the scattering particles on the glass ports which have to be cleaned frequently. A spurious peak can also occur in the velocity histogram at  $U = 0$  and should be deleted.

Concerning the probe volume (volume within the boundary of the optical fringe modulation), improvements are in progress to reduce it by the use of beam expanders which are introduced upstream of the front lens. The beam waist  $d_f$  of the focused laser beam is reduced as expressed by

$$d_f = \frac{4}{\pi} \frac{f \lambda}{d_e}$$

where  $d_e$  is the beam waist diameter of the unfocused laser,  $f$  the focal length of the lens and  $\lambda$  the wave length of the laser light. The smallest probe volume which has been achieved so far (KARPUK & TIEDERMAN 1976) is a  $244 \mu\text{m}$  long cylinder with a diameter of  $61 \mu\text{m}$ . It is, of course, oriented so that the axis of the cylinder is parallel to the wall and normal to the streamwise velocity. Compared to a standard single hot-wire, the diameter of the probe volume is approximately 12 times larger, but the length of the probe volume is approximately 2 times smaller (compared to a  $5 \mu\text{m}$  wire whose aspect ratio is 100). Further reduction is even expected, although the number of fringes has to be kept large enough.

As for the measuring volumes (the region of space from which Doppler signals are received and detected by the optics), it is a priori different from the probe volume since truncated by the detector field of view. ORLOFF (1979) and BUCHHAVE (1979) stressed this point and considered different situations, Fig. 10. For example, for the coaxial backscattering optics often used in boundary layer investigations, the length of the measuring volume is determined by the focal region  $l_f$  of the receiving lens. It can advantageously be made smaller than the probe volume length ( $2c = d_f / \sin \theta/2$ ) by choosing a receiving lens with a very large aperture, since  $l_f$  is given by

$$l_f = 8 F^2 \lambda / D^2 \quad (F \text{ focal length, } D \text{ aperture of the receiving lens}).$$

The spatial resolution of the method, which is critical for boundary layer studies, has been estimated by GEORGE & LUMLEY (1973) for the continuous many-particle L.D.A. The measuring volume is assumed to be the probe volume so that the weighting function describing the signal transmitted by the particles has simply a Gaussian shape. The attenuation affecting the measurements of the one-dimensional spectrum is found to be of the order of 50 % for the Kolmogorov cut off when  $m^* \equiv \sqrt{2} \sigma_z / \eta \approx 0.4$  ( $\sigma_z$  is the standard width of the Gaussian function describing the light intensity in the incident beam). For comparison purposes, the attenuation encountered with a single hot-wire is 20 %, at the same wave-number, when  $\eta / \ell \approx 0.40$  ( $\ell$  hot-wire length,  $\eta$  Kolmogorov scale). For the burst type single particle LDA numerical computations do not seem to have been carried out.

An opposite effect due to the finite size of the measuring volume is the noise generated by the technique itself. For the continuous many-particle LDA there are two spurious signals (i) the so-called "ambiguity noise" which is caused by the random dispersion of particles in the fluid (even in a uniform flow field) and the subsequent random phase composition of the scattered light, and (ii) the "gradient noise" due to the spatial variation of the velocity (mean velocity and fluctuation) within the measuring volume. For the burst type LDA, the first source of noise does not exist since, in principle, there is only one or zero particles in the measuring volume. For the gradient noise, KARPUK & TIEDERMAN 1976 estimated the error for residence time weighted signals, assuming a rectangular probe volume and linear dependence on the distance to the wall for both the mean velocity and the r.m.s. of the streamwise velocity fluctuation. Under these conditions, for the time-weighted signals :

$$u_m'^2 = u_o'^2 + \frac{S^2 b^2}{12} + \frac{S^2 b^2}{12} \mathcal{I}$$

where  $u_o'^2$  is the turbulence intensity at the center of the probe volume,  
 $S$  the velocity gradient  
 $b$  the probe volume width  
 $\mathcal{I}$  the turbulence intensity of the streamwise velocity component

Fig. 11 illustrates the importance of the last two terms for measurements in the viscous layer of a channel flow. More recently, BUCHHAVE, GEORGE & LUMLEY 1979 have shown that these terms are equivalent to those occurring in continuous LDA, so that corrections have definitively to be taken into account. Of course, lessening the probe volume would further reduce the corrections by a substantial amount.

The two sources of error which we have just presented (and which act in opposite directions) affect the turbulence spectra. Fig. 12 illustrates the results usually obtained (BUCHHAVE, GEORGE & LUMLEY 1979 ; MELINAND & CHARNAY 1979). Much too high levels are obtained at high frequencies, even for burst type LDA, which shows that the error due to the velocity gradient within the measuring volume is much greater than the error due to the averaging effect of the measuring volume. Hot-wire anemometry seems therefore, at least so far, to be better suited than laser Doppler anemometry for measurements of turbulence spectra (only a single source of error for which exact corrections are available).

An important shortcoming of the conventional LDA is that it measures the velocity at a single point in the fluid. To obtain the complete flow pattern, the

experiments have to be repeated, which requires either an accurate mechanism to move the LDA or the flow relative to each other, or a scanning optical system (zoom). The latter is very flexible and allows displacements up to several meters (e.g. used to investigate the instantaneous flow around a large model of helicopter rotor in a wind tunnel, BIGGERS & ORLOFF 1974). The spherical aberration, however, has to be analyzed in detail because the system is either over-compensated or under-compensated when used outside its range of design (ORLOFF 1979). The subsequent changes in the measuring volume and in the errors have therefore to be estimated in every set-up, of course in relation to the size of the flow structures to be reached.

In many industrial studies it is not possible to position the necessary window so as to permit direct optical access to the point under investigation. An ingenious "endoscopic" L.D.A. has been therefore designed by DANIEL 1976 with the help of optical fibers, Fig. 13 a. The size of the optics is reduced considerably, even when three different wave lengths are used to obtain the three components of the velocity. Moreover, what is believed to be the first extensive use of optical fibers is presented : a coherent fiber (with an oil immersion joint) from the laser to the optics and an ordinary fiber from the optics to the photo-multiplier.

The use of optical fibers can also improve multi-points measurements (NAKATANI, YORISUE & YAMADA 1979, Fig. 13 b). Two thin beams obtained by expanding laser beams with spherical and cylindrical lenses, are used as the incident beams into the flow field. A two-dimensional intersection is hence formed, and a set of ordinary optical fibers are used to receive the light intensity in the image plane. Instantaneous velocity profiles (both normal and transverse components) have been obtained in a branch tube at 8 points from the wall. The spatial range covered ( $\approx 1$  mm) is small in comparison to that covered with the zoom technique. However one can consider focusing the spatial range over the specific region of interest in an otherwise large flow field ( wall vicinity, inner edge of a separating flow).

Finally, a detailed description of a turbulent boundary layer also includes the analysis of intermittent phenomena such as the directional changes within a separating boundary layer or the alternation of turbulent and non-turbulent regions at the free edge of the layers. If the former case can be dealt with by the LDA technique alone (of course with the use of Bragg cells), the latter requires generally some tagging procedure. SIMPSON, STRICKLAND & BARR (1977) used smoke and an auxiliary concentration probe whereas MELINAND & CHARNAY (1979) seeded only the fluid of the boundary layer. Intermittency coefficients seem to be attainable from the abrupt change which occurs in the distribution function of the time interval between two successive validated LDA signals. In hot-wire anemometry the occurrence of a similar break in the probability curves of the velocity derivatives was sometimes used (SUNYACH 1971).

### 3.1.3. Laser - Two-focus velocimetry

This technique is based on the time of flight of a particle between two foci (Fig. 14). The fringe pattern of the LDA technique is thus replaced by two discrete light spots. Then, a particle which goes through the two foci emits two successive pulses of scattered light. This method, suggested by THOMPSON (1978) and TANNER (1973), was greatly improved by SCHODL (1976, 1977) for use in turbomachines.

The striking advantage of the method lies in the very small dimensions of the probe volume : the diameter of the focus is of the order of  $10\mu\text{m}$  and the distance between the two foci is between 0.3 and 0.5 mm. Measurements can therefore be made in narrow channels (such as the blade channels of centrifugal compressors). Moreover the possibility to set small apertures in the optics reduces the noise due to the background radiation generated by the solid surface even in the backscattering mode of operation (Fig. 14).

To take the presence of turbulence into account, the line between the two foci has to be set at first along the mean flow direction and then at various different angles with this direction, in the range of the velocity angle fluctuations. The histograms of the time of flight correspond therefore to a whole set of conditional probability functions from which the joint probability of the velocity (and hence any moments) can, in principle, be deduced. Various corrections have been developed to take into account the broadening effects due to the particle and the probe volume. To carry out the measurements, fast electronic equipment is used (a few nanoseconds for a fluid velocity of 500 m/s,  $\Delta T \approx 0.85\mu\text{s}$ ). Each measurement, e.g. each setting angle, requires, however, a long time of observation (3-5 minutes depending on the particle concentration).

This method deserves to be used in the future as it provides useful results in a hostile configuration. New research has been initiated in this area (VOUILLARMET 1979).

### 3.1.4. Visualization

Since the pioneering works of HAGEN or REYNOLDS on turbulent flow visualization, techniques have been developed continuously and in many cases they allow quantitative results to be obtained (MERZKIRCH 1974).

Among the well-known techniques there is firstly the hydrogen bubble visualization method which has enabled KLINE and his co-workers (1967) to discover organized structures in the vicinity of the wall. Later, this method made it possible for KIM, KLINE & REYNOLDS 1971 to clarify the chain of events leading to an overall model of bursting. Observations of smoke-filled boundary layer (pyrotechnic smoke or oil vapour), with emphasis on the smoke concentration, have shown various aspects of transition, the development of turbulent spots and the interaction of boundary layer and free stream (FIEDLER & HEAD 1966 ; FALCO 1977). Combined with hot-wire anemometry (although in a manual way),

the technique has allowed some particular large and small scales motions to be identified (FALCO 1977). Observation can also be made with cameras moving at a speed chosen to go along with selected structures (CORINO & BRODKEY 1969).

Thermal tagging is a very convenient way to detect the free edges of turbulent flows (SUNYACH 1971). Although the coincidence between the thermal and kinetic boundaries has not been proved theoretically, it has been supported by many experiments : measurements of the thermal and kinetic intermittency factors or simultaneous recordings of the velocity and temperature signals (DUMAS, FULACHIER & ARZOUMANIAN 1972 ; KOVASZNY & FIRASAT ALI 1974 ; CHEVRAY & TUTU 1978). The method is particularly well suited for the edges of boundary layers evolving with turbulence in the external stream (CHARNAY, COMTE-BELLOT & MATHIEU 1976). When used to detect structures embedded inside the turbulent boundary layer, the mixing of fluid elements issued from various parts of the flow can blur the features of the structures to be tracked. It is therefore expected that the method would be limited to short times of observation following the heating by pulses of a selected region of the flow, (such as in the detection of events coming from the wall FULACHIER, ARZOUMANIAN & DUMAS 1978), or to the visualization and detection of sharp fronts which suddenly affect the whole thickness of the boundary layer (CHEN & BLACKWELDER 1978) as already observed in mixing layers (SUNYACH 1971, Figs. 15 and 16).

To pass on now to more recent techniques, many deserve attention :

- a) the "smoke-wire" technique suggested by CORKE, KOGA, DRUBKA & NAGIB (1977). It consists of a vertical wire onto which regulated drops of oil are allowed to fall, coating the wire along its length in the form of minute droplets. Discrete streaklines are then formed from each droplet by burning off the oil through resistive heating. The method seems to be comparable, in its quality (but perhaps not in its simplicity) to the hydrogen bubble technique used in water. Work is in progress at the University of Notre-Dame to visualize the transition in the mixing layer of separating bubbles on airfoils (MULLER, private communication).
- b) the use of a glass-rod to fan-out a laser beam (BANDYOPADHYAY 1978). Slices of a smoke filled boundary layer can thus be illuminated. Cine films combined with hot wire data give information on the large scale motions (sharpness of the upstream interface, existence of vortices extending throughout the boundary layer with their axis preferentially oriented at about  $40^\circ$  to the wall. Further details will probably be made available during the meeting (HEAD & BANDYOPADHYAY).
- c) the use of fluorescent particles, excited by laser, such as rhodamine 6 G dye or uranin dye, in the case of liquids. DIMOTAKIS, LYE & MORRISON (1978) extended the technique for gases. This method which has been applied to jets, has shown that external unmixed fluid can be found all the way to the jet axis.
- d) the generation of a high speed rotating laser beam to illuminate, at regular time intervals, small particles injected into the flow (SCHON, DANIEL, MELINAND, REY & CHARNAY 1979). The successive positions reached by the same particle moving in the plane swept by the beam can be photographed and analyzed to obtain the velocity component in that plane and the corresponding Lagrangian correlation function (Fig. 17). The trajectories of several particles can also be photographed at once if the flow is seeded accordingly. In the present experiment, the mirror is made up of 16 facets set on a cylindrical support (5 mm in diameter) rotating at 4 000 R.P.M, so that the time interval between two sweeps is 1 ms. The injected particles are droplets of dioctylphthalate (diameter  $\approx 1 \mu\text{m}$ ). Small power lasers are well suited for this experiment since the particles receive all the light of the laser at the instant they are photographed.
- e) the analysis of the light scattered by highly anisotropic particles which get oriented in a preferred way in the flow, depending on the rate of the deformation-tensor. Direct measurements of the velocity gradients  $\partial u_i / \partial x_j$  have been attempted (JOHNSON 1975 with tobacco virus which is 3 000 Å in length and 150 Å in diameter ; PETIT 1979 with thermal spots induced by a high power laser and distorted by the flow).
- f) small mirrors embedded in tiny hollow glass sphere have also been suggested by WEBB (private communication) to obtain the instantaneous and local value of the vorticity tensor. This work is now in progress.
- g) three dimensional high speed movies have also been used in an attempt to locate the large scale structures of flows (PRATURI & BRODKEY 1977), but difficulties arise because the features of the phenomena to track are not sufficiently defined.

### 3.2. Measurements made by means of transducers embedded in the wall

Several physical variables are of interest at the wall such as pressure, wall shear stress and velocity gradient for unheated boundary layers. Elaborate devices have been developed and data obtained in some cases at a large number of points.

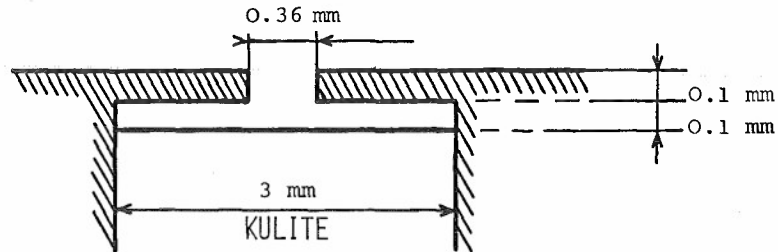
#### 3.2.1. wall pressure measurements

The status of the measuring techniques and the understanding of the pressure field under turbulent boundary layers have been recently presented by WILLMARTH (1975 b). We shall therefore concentrate here on specific points.

At first, there is the attenuation caused in the high frequency range by the finite size of the pressure transducer. Corrections have been made by CORCOS (1963, 1967) in the case of transducers mounted flush with the wall. Their application to real cases is however inaccurate. The first reason is that the measured data from which one starts are far too much attenuated (down to 0.011 for  $\omega d / U_e \approx 10$  with  $d$  diameter of the sensor). The second reason is that a simple similarity shape of the cross-spectral density function  $\Gamma(\omega, \xi_1, \xi_2)$  has to be assumed for both very high frequency  $\omega$  and very small

longitudinal or transverse separation  $\xi_1$  and  $\xi_2$  (experimental results are obtained up to  $\omega \delta^+ / U_e \approx 5$  i.e.  $\omega \nu / u_\tau^2 \approx 0.4$ ).

Pin-hole transducers have therefore been introduced to improve the spatial resolution, the diameter of the probe being 3 to 4 times smaller than the diameter of the transducer itself. They have, of course, to be used below their own resonant frequency which can be estimated by considering the system as a Helmholtz resonator or by using a more elaborate theory for the transient response of the orifice and (or) experimental tests (LIMURA & HATANAKA, 1973). For example, with the dimensions indicated below which are close to the miniature sensors developed by BROOKS & HODGSON 1979.



the resonant frequency is found to be 41 kHz and 31 kHz by the two methods respectively.

The flow disturbance at the pin-hole orifice is however a matter of concern. BULL & THOMAS 1976 took careful measurements with the same measuring surface which is either a wall portion or a pin-hole orifice and found that a definite systematic error exists, the pin-hole data being too large by a factor of about 4 when  $\omega \nu / u_\tau^2 \approx 0.10$  (Fig. 18). A comparison with the scale of turbulence does not seem to have been made. It is however possible, from the parameters which are given, to find that  $\omega \nu / u_\tau^2 \approx 0.10$  corresponds to

$K_1 d \approx 2.2$ . The flow pattern is however not known so far and more information would probably be gained from the recent analysis by ROCKWELL & NAUDASCHER (1979) concerning the self sustained oscillations of impinging free shear layers, in particular in the case of cavities. Anyway, the  $K_1 d$  limit has to be compared with the smallest scales present in the pressure field. This is not an easy question to answer because the pressure at a given point depends on the whole surrounding velocity field. The theoretical prediction made by PANTON & LINEBARGER 1974 (who keep only the linear terms in the velocity fluctuation when resolving the Poisson equation governing the pressure field) leads to a cutoff located at  $K_1 \nu / u_\tau \approx 0.10$  i.e. around  $\omega \nu / u_\tau^2 \approx 0.6$ . On the other hand, a rough estimate can be made, assuming that the smallest velocity scales making up the pressure field at the wall are those located at the edge of the viscous sublayer. In that case  $\eta u_\tau^+ / \nu \approx \eta L / \nu \approx 1$  and  $U_{conv} \approx U \approx 5 u_\tau$ , which leads to a much higher limit,  $\omega \nu / u_\tau^2 \approx 5$ . More information is certainly to be gained from several experimental works now in progress in air (BULL 1979, BROOKS & HODGSON 1979) and in water (BENARROUS 1979).

The obtention of the 1 D wave-number spectra from the frequency spectra presents some difficulties in the lower  $K_1 - \omega$  range. The reason is that the convection velocity strongly depends on the wave-number (WILLS 1970). Microphone arrays acting directly as wave-number filters have therefore been suggested (MAIDANIK & JORGENSEN 1967; BLAKE & CHASE 1971). Non zero values of the  $K_1$ -spectra are then obtained when  $K_1 \rightarrow 0$  and are most useful in the prediction of the noise radiated by turbulent boundary layers.

Concerning the multi-point and multi-time measurements, the spectacular displays offered by EMMERLING, MEIER & DINKELACKER (1973), and DINKELACKER, HESSEL, MEIER & SCHEWE (1977), by means of a Michelson interferometric technique have to be recalled (Fig. 20). The pressure fluctuations cause a deflection of the membrane covering the 650 small holes of the measuring plate (hole diameter  $\phi = 2.5$  mm so that  $\phi u_\tau^+ / \nu \approx 56$ ) and this causes a shift of the fringes which are photographed - 7 000 frames/s - during 30 seconds. For example, positive pressure patterns which are at first intense and roughly circular, then larger in the cross stream direction, have been identified. Connections with the ejection and burst sequence will probably be made in the near future.

Finally, considerable information can be gained from the numerical resolution of the full Navier Stokes equations as developed by SCHUMANN in 1975. Comparisons of the numerical and experimental values of the wall-pressure level can first be made (the numerical value is  $p' / \rho u_\tau^2 \approx 2.4$  and the experimental data give  $p' / \rho u_\tau^2$  in the range 2.4 to 3.6 (Fig. 19)). It would also be interesting to compare the eventual organized structures generated in the model with those observed in real flows. (Figs 20 and 21).

### 3.2.2. Wall shear stress fluctuations

Hot-film embedded in the wall or laid directly on it can be used to obtain the two components of the velocity gradient at the wall,  $\partial u / \partial y$  and  $\partial w / \partial y$  (LUDWEIG 1950, LIEPMANN & SKINNER 1954, BROWN 1967). Two questions, however, have to be considered carefully in order to get correct measurements: (i) the non-linearity of the expression  $q \approx \tau_w^{1/3}$  relating the surface heat transfer  $q$  to the surface shear  $\tau_w$ ; here, corrections are compulsory because the wall shear stress fluctuations are large (the r.m.s. value of  $\partial u / \partial y$  is about 0.30 times that of  $\partial \bar{u} / \partial y$ ); (ii) the spurious heat transfer to the substrate which affects the frequency response of the film (BELLHOUSE & SCHULTZ 1966, BRISON, CHARNAY & COMTE-BELLOT 1979); the film supporting material has therefore to be properly selected and isolated from the wall; fluids with high Prandtl number (water, oil) can also be advantageously used. Calibration of the single film (measurement of  $\partial u / \partial y$ )

is done by reference to data obtained with a Preston tube or to the static pressure gradient in a fully developed pipe or channel flow. For the hot film arranged in a V-configuration to measure  $\partial W / \partial y$ , it is usually assumed that the sum of the two signals is proportional to  $\partial U / \partial y$  and that the difference produces a signal proportional to  $\partial W / \partial y$  at the wall.

Several results have been already obtained. SREENIVASAN & ANTONIA 1977 and also SANDBORN 1979 have described the highly skewed characteristics of the probability density of  $\partial U / \partial y$  (with large positive values) a result which is compatible with the skewness factors of the longitudinal velocity component  $u$  (COMTE-BELLOT 1965, KREPLIN & ECKELMANN 1979 a). The extensive surveys of BLACKWELDER & ECKELMANN 1979, and KREPLIN & ECKELMANN 1979 b, deal with space-time correlations and quadrant probability analysis. The results indicate that the pair of counter-rotating streamwise vortices pointed out by BAKEWELL & LUMLEY 1967, occur frequently in the wall region and that the low speed fluid is pumped away from the wall by the vortex pair.

The electrochemical technique has been also used to measure the limiting values of  $\partial U / \partial y$  and  $\partial W / \partial y$  at the wall (MITCHELL & HANRATTY 1966, MIZUSHINA 1971, SIKKAR & HANRATTY 1970, LEBOUCHE 1968 and PY 1973). This technique is the mass transfer analogue of the constant temperature anemometer when the chemical reaction at the electrode embedded in the wall is working under the diffusion - controlling conditions. This is possible for large Schmidt numbers, with an appropriate choice for the reactors (redox couple) and addition of a large excess of an unreactive electrolyte to the solution. For applications to boundary layers, many refinements have been added to the technique : development of array of electrodes (up to 20 in the spanwise direction) analysis of the frequency response, effect of the setting angle of the electrode relative to the flow direction, detection of reversed flows, analysis of non-linear effects. In particular, HANRATTY and his co-workers were able to measure very accurately the spanwise spacing  $\lambda$  between the streamwise vortices close to the wall,  $\lambda u_f / \mu \approx 105$  (LEE, ECKELMAN & HANRATTY 1974).

#### 4. Signal processing

The conventional averages (i.e. moments, correlations, spectra, probability density functions...) are well known techniques. We shall not describe them, but just emphasize the large amount of information they provide in many technical problems (for example, rotating boundary layers). For more sophisticated problems to analyse in basic cases, they constitute the first step of any investigation (localisation of region with high skewness factor for the time derivative of velocities ; obtention of the space and time coherencies...) In a second step, contributions from various fields or from various events are sought. The use of conditional sampling in combination with ensemble averaging and the introduction of pattern recognition techniques are then compulsory. To illustrate this point, an excerpt from the original story of MOLLO-CHRISTENSEN (1971) can be quoted :

"One has to be careful not to be misled by looking at averages, since averages may hide rather than reveal the physics of a process. An absurd example may serve as an illustration. Say that a blind man using a road bed sensor attempted to find out what motor vehicles looked like. Happening to use a road only traveled by airport limousines and motorcycles, he concludes that the average vehicle is a compact car with 2.4 wheels. He might later attempt to construct a theoretical model of the mechanics of such a vehicle, and may attain fame for a tentative model that looks like a motorcycle with a sidecar whose wheel is only in contact with the ground forty percent of the time. In turbulent shear flow, this kind of a vehicle has been called an "average eddy", and may or may not exist..."

##### 4.1. Conditional averages

###### 4.1.1. Zone conditional averages

In this method separate averages are obtained inside and outside the turbulent bulges occurring at the free edge of the boundary layer. This involves the generation of an intermittency function  $I(t)$  which takes the value unity in the turbulent region and the value zero in the non-turbulent region. Many ways to generate  $I(t)$  have been suggested, based either on the velocity signal alone through the combination of one or more time derivatives (KAPLAN & LAUFER 1969, KOVASZNY, KIBENS & BLACKWELDER 1970, SUNYACH 1971, HEDLEY & KEFFER 1974, KIBENS, KOVASZNY & OSWALD 1974) or on the concentration of a contaminant introduced into the turbulent part of the flow, such as heat (SUNYACH 1971, LARUE 1974, CHEN & BLACKWELDER 1978, ANTONIA, PRABHU & STEPHENSON 1975). The latter solution is the only one possible when turbulence exists in the free stream (CHARNAY, COMTE-BELLOT & MATHIEU 1976). Uncertainties affect the signal  $I(t)$  so that the use of pseudo-turbulent signals has been suggested to improve the settings of the intermittency meter (ANTONIA & ATKINSON 1974, KIBENS, KOVASZNY & OSTWALD 1974). On the other hand, when thermal tagging is used, the temperature in the external "cold" zone rises slightly when  $y/\delta$  decreases (CHEN & BLACKWELDER 1978 ; CHEVRAY & TUTU 1978). This could be due to molecular conduction (FULACHIER, ARZOUMANIAN & DUMAS 1978). It is therefore necessary to estimate the amount of fluid which is mislabelled by the threshold (ANDREWS 1972, HAVERBEKE, WOOD & SMITS 1978 ; BLACKWELDER 1979). Such an attempt to find the correct  $I(t)$  may be considered as similar to the pattern recognition technique (section 4.2).

Many examples of zone averages are now available. In Fig. 22 we have selected the results which deal with the Reynolds stress for a turbulent boundary layer evolving in an external flow with free turbulence (after CHARNAY, COMTE-BELLOT and MATHIEU 1976).

###### 4.1.2. Point conditional averages

In this case samples are taken at a specific point, such as on the turbulent/non-turbulent interface, i.e. when  $I(t)$  jumps from zero to unity or conversely.



Comparisons between the leading and trailing edge characteristics are thus possible. They can be moreover extended to points located near the edge, on either side, by adjustment of the time delay and application of the Taylor hypothesis, using the local mean velocity.

The most interesting examples - Fig. 23 - deal with the Reynolds stress distribution which can be associated with the entrainment of the bulges (ANTONIA 1972, HEDLEY & KEFFER 1974). Large values occur at the trailing edges of the bulges. They do not match the external values so that entrainment is negligible. On the contrary, small values occur at the leading edge where most of the entrainment takes place.

Instead of being triggered by the signal  $I(t)$  the sampling can be driven by a well defined external signal. Ensemble averages then allow us to retain only the deterministic (periodic) components. In that case, the electronic equipment is sometimes called "signal averaging" or "eductor". Then, subtraction of this ensemble average from every sample allows us to obtain the random components exclusively. An example is given in Fig. 25 bis, for the pressure measured on one blade of an industrial rotor. The pulse signal is given by the rotating shaft. Upstream of the rotor there is a rod which creates a wake which strikes the selected blade at each revolution (MICHEL, ARBEY & SUNYACH 1979). This set-up is an extension, for rotating machines, of the wake cutting experiment of FUJITA & KOVASZNY 1974. It allows us to estimate the discrete and large-band noise radiated in the far field, from the periodic and random pressure fields on the blade.

Up to this point, only one condition has been considered to select the samples. It is possible to restrict the choice by several conditions. An example is the four quadrant analysis of the instantaneous  $uv(t)$  product in wall shear flows (LU & WILLMARTH 1973). If one tries to get the signature of the ejection events, three conditions are needed :  $u < 0$ ,  $v > 0$  and  $|uv|/|u'v'| \geq H$ , an adjustable threshold to separate the "weak" from the "violent" ejections (COMTE-BELLOT, SABOT & SALEH 1979 ; Fig. 24).

#### 4.1.3. Conditional averaging with correction for random convection velocity

In the above sections, the detector signal is taken precisely at the point which is selected for the measurements, or in its immediate vicinity. When a large downstream distance separates the location of the condition from the location of the measurements, a phase scrambling affects the received signals with respect to the detector signal because of the random motion of the pattern (e.g. variation in the convection velocity). It is therefore necessary to apply a delay time to the received signal to recover the event of interest (Fig. 26). An iterative process is then developed to select the optimum delay time for every signal (BLACKWELDER 1977 ; WYGNANSKI 1979). The "realigned" signals are then used for the correct ensemble average to be performed. In some cases, the motion and the evolution of the event to track are so large and unpredictable that difficulties subsist. For example, the spanwise buffeting of a turbulent "spot" in a turbulent boundary layer is almost beyond reach (HARITONIDIS, KAPLAN & WYGNANSKI 1978).

#### 4.2. Pattern recognition

This technique has been introduced by WALLACE & BRODKEY & ECKELMANN 1977. A pattern is first devised for a selected physical variable on the basis that it is relevant to a typical event or flow structure. For example, in the wall region, large values of the skewness factors of the time derivative of the longitudinal velocity components  $S_1 = (\partial u / \partial t)^3 / [(\partial^2 u / \partial t^2)]^{3/2}$  are obtained ( $S_1 \approx 0.80$  for  $20 \leq y^+ / \delta \leq 50$  ; Fig. 27). A pattern which allows such a feature is therefore suggested for the velocity component. It consists of a gradual deceleration from a local maximum followed by a strong acceleration (Fig. 28). This pattern is then applied to the measured signal  $u(t)$  as a "filter" to select the parts which meet the criteria. Rather broad thresholds are used for the rate of increase and decrease of  $u(t)$  so that the number of accepted events is large enough to form a significant collection. Comparisons between this technique and the four-quadrant analysis are interesting, but difficult, because of the difference which exists in practice, in the conditions imposed on the signals in the two methods.

In the development of the technique we can expect simultaneous multi-point measurements. The excitation by an external source of the coherent structures themselves would be rewarding both for its experimental advantage (recognition of "evoked" structures, WYGNANSKI 1979) and the comprehension it would bring of the growth of boundary layers.

### 5. Conclusions

The state of the art in the investigation of wall turbulent shear flows is different for the fundamental case of boundary layers without a pressure gradient than for the different cases met in practice (atmospheric boundary layers, boundary layers along curved walls and on rotating blades in turbomachines). In the first case, much information has been obtained not only of the statistical characteristics of the flow but also of the existence of recognizable structures. Interest lies, at present, in the study of the physical mechanisms which control these structures and the growth of the boundary layer. In practical situations, the values of the extra-strains are of primary importance both for a general understanding of the flow and for the satisfactory modelling needed in engineering design.

It follows that some future trends in experimental boundary layer research can be forecast. Attention will probably be paid, at first, to multi-point and multi-time measurements in order to understand more precisely the origin and the evolution of the main events making up the boundary layer. Hot-wires arrays are well suited for this type of investigation. This is especially true when thermal tagging is used, as the hot-wires, which are operated at a low overheat ratio, do not require sophisticated electronics. Aerodynamic perturbations have, however, to be analyzed before accurate measurements can be made. As for

the L.D.A. technique which is ideally suited to separated flow investigations, the introduction of optical fibers will probably bring refinements and adaptability to various configurations (not only for multi-point measurements but also for those made at locations difficult to reach with conventional laser instrumentation). On the other hand, visualization of large parts of the flow (in one or several planes, with one or several colors) and the quantitative processing of this optical data would merit investigation.

Concerning the processing techniques, the use of conditional averages will, no doubt, remain mandatory in all the basic flow configurations. The pattern recognition technique will be a powerful way to trace important events. Of course, intuition is needed to define the specific pattern to be looked for and the normalisation conditions to be introduced for subsequent processing. A simpler use of this technique is the investigation of the response of the flow to known perturbations applied to the boundary layers. Corrections for phase scrambling have to be considered when following Lagrangian events in a Eulerian frame, but they may be beyond reach when large random motions are present.

In conclusion, much can be gained in the understanding of turbulent boundary layers by keeping abreast of similar developments in other flows (jets, mixing layers) and also of the stability studies in both linear and non-linear analyses. Attention should also be paid to the development of direct numerical simulations of turbulent flows. The space-time evolution of the structures which mimic those met in real flows could thus be more easily understood and, perhaps, better controlled in future research.

## 6. Acknowledgements

I am sincerely grateful to Dr. ROLLINS II and Mrs. DUBOIS (AGARD, PARIS), Dr. F.P. RICOU (DELTALAB, GRENOBLE) and my co-workers E. ALCARAZ, J.P. BERTOGLIO, G. JANODET D. JEANDEL, C. REY, J. SABOT, & J.P. SCHON for their helpful comments and assistance in the preparation of this paper, and last but not least Mrs. A.M. MOINEL for her patience in the typing of the manuscript.

## 7. References

- ALCARAZ, E. & MATHIEU, J. 1975, "Mesure des vitesses moyennes près d'une paroi par anémométrie à fil chaud", C.R. Acad. Sc. Paris 280 A, p. 737-740.
- ANDREWS, H.C. 1972 "Introduction to mathematical techniques in pattern recognition", Wiley-Interscience.
- ANTONIA, R.A. 1972 "Conditionally sampled measurements near the outer edge of a turbulent boundary layer", J. Fl. Mech. 56, p. 1-18.
- ANTONIA, R.A. & ATKINSON, J.D. 1974 "Use of a pseudo-turbulent signal to calibrate an intermittency measuring circuit", J. Fl. Mech. 64, p. 679-699.
- ANTONIA, R.A. & LUXTON, R.E. 1971, "The response of a turbulent boundary layer to a step change in surface roughness", part 1. smooth to rough, J. Fl. Mech. 48, p. 721-761.
- ANTONIA, R.A., PRABHU, A. & STEPHENSON, S.E. 1975, "Conditionally sampled measurements in a heated turbulent jet", J. Fl. Mech. 72, p. 455-480.
- ARNDT, R.E.A. & GEORGE, W.K. 1979, "Pressure fields and cavitation in turbulent shear flows" 12th Symp. Naval Hydrodyn. Nat. Acad. Sc. Washington, p. 327-339.
- ARYA, S.P.S. 1975 "Buoyancy effects in a horizontal flat-plate boundary layer", J. Fl. Mech. 68, p. 321-343.
- ARZOUMANIAN, E., FULACHIER, L. & DUMAS, R. 1979, "Experimental investigation of the three-dimensional turbulent boundary layer on an axially rotated cylinder", 2nd Symp. Turb. Shear Flows, London (4) p.28-33.
- AWAD, M., MOREL R., SCHON, J.P. & CHARNAY, G. 1979, "Buoyancy effects on a scalar transport in a boundary layer with an wall heat flux inversion" 2nd Symp. Turb. Shear Flow London (12) p. 22-26.
- BAKER, R.J. & LAUNDER, B.E. 1974 "The turbulent boundary layer with foreign gas injection", Int. J. Heat Mass Transfer, 17, p. 275-291.
- BAKEWELL, H.P. Jr. & LUMLEY, J.L. 1967 "Viscous sublayer and adjacent wall region in turbulent pipe flow", Phys. Fluids, 10, p. 1880-1889.
- BANDYODADHYAY, P., 1978 "Combined smoke-flow visualization and hot-wire anemometry in turbulent boundary layers, structure and mechanisms of turbulence", Berlin 1977, Lecture Notes in Physics Springer-Verlag, Vol. 1, p. 205-216.
- BEGUIER, C., REY, C., DUMAS, R. & ASTIER, M. 1973 "Une nouvelle sonde anémométrique", C.R. Acad. Sc. Paris 277 A, p. 475-478.
- BELLHOUSE, B.J. & SCHULTZ, D.L. 1967 "The determination of fluctuating velocity in air with heated thin film gauges", J. Fl. Mech. 29, p. 289-295.
- BENARROUS, E. 1979 "Contribution à l'étude des fluctuations de pression pariétale sous une couche limite turbulente", Th. 3ème Cycle Univ. Lyon.
- BERTOGLIO, J.P., CHARNAY, G., GENCE, J.N. & MATHIEU, J. 1978 "Calcul d'une turbulence homogène soumise à une rotation en bloc et à un cisaillement", C.R. Acad. Sc. Paris 286, p. 957-959.
- BIGGERS, J.C. & ORLOFF, K.L. 1974 "Laser velocimeter measurements of the helicopter rotor induced flow field" Proc. 30th Ann. Nat. Forum. Am. Helicopter Soc.
- BISSONNETTE, L.R. & MELLOR, G.L. 1974 "Experiments on the behaviour of an axisymmetric turbulent boundary layer with a sudden circumferential strain", J. Fl. Mech. 63, p. 369-413.

- BLACKWELDER, R.F. 1977 "On the role of phase information in conditional sampling", *Phys. Fluids* 20, p. S. 232-S.242.
- BLACKWELDER, R.F. 1979 "Pattern recognition of coherent eddies", *Proc. Dyn. Flow Conf. Marseille-Baltimore 1978*, p. 173-190.
- BLACKWELDER, R.F. & ECKELMANN H. 1979 "Streamwise vortices associated with the bursting phenomenon", *J. Fl. Mech.* 94, p. 577-594.
- BLACKWELDER, R.F. & KAPLAN, R.E. 1976 "On the wall structure of the turbulent boundary layer", *J. Fl. Mech.* 76, p. 89-112.
- BLACKWELDER, R.F. & KOVASZNY, L.S.G. 1972 "Time scales and correlation in a turbulent boundary layer" *Phys. Fluids* 15, p. 1545-1554.
- BLAKE, W.K. & CHASE, D.M. 1971 "Wave number-frequency spectra of turbulent boundary layer pressure measured by microphone arrays", *J. Acoust. Soc. Am.* 49, p. 862-877.
- BRADSHAW, P. 1973 "Effects of streamline curvature on turbulent flow", *AGARDograph* 169.
- BRISON, J.F., CHARNAY, G. & COMTE-BELLOT, G. 1979 "Calcul des transferts thermiques entre film chaud et substrat par un modèle à deux dimensions", *Int. J. Heat Mass Transfer* 22, p. 111-119.
- BROOKS, T.F. & HODGSON, T.H. 1979 "Investigation of airfoil trailing edge noise", *Int. Symp. Mechanics of Sound Generation in Flows, Göttingen* (in print).
- BROWN, G.L. 1967 "Theory and application of heated films for skin friction measurement", *Proc. Heat. Transf., Fl. Mech. Inst. La Jolla, Stanford Press* p. 362-381.
- BROWN, G.L. & THOMAS, A.S.W. 1977 "Large structure in a turbulent boundary layer", *Phys. Fluids* 20, p. S. 243-S. 252.
- BUCHHAVE, P. 1979 "Transducer techniques", *Proc. Dyn. Flow. Conf. Marseille-Baltimore 1978*, p. 427-463.
- BUCHHAVE, P., GEORGE, W.K. Jr & LUMLEY, J.L. 1979 "The measurement of turbulence with the laser-Doppler anemometer", *Ann. Rev. Fl. Mech.* II, p. 443-503.
- BULL, M.K. 1979 "On the form of the wall-pressure spectrum in a turbulent boundary layer in relation to noise generation by boundary layer - surface interactions", *Int. Symp. Mechanics of Sound Generation in Flows Göttingen* (in print).
- BULL, M.K. & THOMAS, A.S.W. 1976 "high frequency wall-pressure fluctuation in turbulent boundary layers" *Phys. Fluids* 19, p. 597-599.
- BUSCH, N.E., LARSEN, S.E. & THOMSON, D.W. 1979 "Data analysis of atmospheric measurements" *Proc. Dyn. Flow Conf. Marseille-Baltimore 1978*, p. 887-908.
- CERMAK, J.E. 1971 "Laboratory simulation of the atmospheric boundary layer" *A.I.A.A. J.* 9, p. 1746-1754.
- CHARNAY, G., COMTE-BELLOT, G. & MATHIEU, J. 1976 "Response of a turbulent boundary layer to random fluctuations in the external stream", *Phys. Fluids*, 19, p. 1261-1272.
- CHARNAY, G., SCHON, J.P., ALCARAZ, E. & MATHIEU, J. 1979 "Thermal characteristics of a turbulent boundary layer with an inversion of wall heat flux", *1st Int. Symp. Turb. Shear Flow, Penn State 1977*, p. 104-118.
- CHARNAY, G., SCHON, J.P. & SUNYACH, M. 1973 "Isolement et échantillonnage de signaux aléatoires transmis par plusieurs anémomètres à fils chauds", *Entropie* 50, p. 24-30.
- CHEN, C.P. & BLACKWELDER, R.F. 1978 "The large scale motion in a turbulent boundary layer : a study using temperature contamination" *J. Fl. Mech.* 89, p. 1-31.
- CHEVRAY, R. & TUTU, N.K. 1978 "Intermittency and preferential transport of heat in a round jet" *J. Fl. Mech.* 88, p. 133-160.
- COLES, D. & BARKER, S.J. 1975 "Some remarks on a synthetic turbulent boundary layer", *Turbulent mixing in non-reactive and reactive flows*, S.N.B.-MURTHY ed. Plenum Press, p. 285-292.
- COMTE-BELLOT, G. 1959 "Coefficients de dissymétrie et d'aplatissement des dérivées par rapport au temps des fluctuations longitudinales de vitesse au voisinage d'une paroi", *C.R. Acad. Sc. Paris* 249, p. 2483-2485.
- COMTE-BELLOT, G. 1965 "Ecoulement turbulent entre deux parois parallèles", *Publ. Sc. Tech. Min Air n° 419* (also thesis Univ. Grenoble 1963 and Translation into English by P. BRADSHAW 1969 *ARC n° 31 609*).
- COMTE-BELLOT, G. 1976 "Hot-wire anemometry" *Ann. Rev. Fl. Mech.* 8, p. 209-231.
- COMTE-BELLOT, G., SABOT, J. & SALEH, I. 1979 "Detection of intermittent events maintaining Reynolds stress" *Proc. Dyn. Flow Conference, Marseille-Baltimore 1978*, p. 213-229.
- CORCOS, G.M. 1963 "Resolution of pressure in turbulence", *J. Acoust. Soc. Am.* 35, p. 192-199.
- CORCOS, G.M. 1967 "The resolution of turbulent pressures at the wall of a boundary layer", *J. Sound Vibr.* 6, p. 59-70.
- CORINO, E.R. & BRODKEY, R.S. 1969 "A visual investigation of the wall region in turbulent flow", *J. Fl. Mech.* 37, p. 1-30.
- CORKE, T., KOGA, D., DRUBKA, R. & NAGIB, H. 1977 "A new technique for introducing controlled sheets of smoke streaklines in wind tunnels", *Illinois Inst. Tech. Rep. ICTASF*.
- CORRSIN, S. 1957 "Some current problems in turbulent shear flow", *Publ. 515, Naval Hydrodyn. Nat. Ac. Sc. Nat. Res. Council*, p. 373-407.
- CORRSIN, S. 1963 "Turbulence : experimental methods, Handbuch Phys., Springer-Berlin, 8/2, p. 523-590.
- CORRSIN, S. & KISTLER, A. 1955 "Free-stream boundaries of turbulent flows" *NACA TR 1244*.
- DANEL, F. 1976 "Fiber optics and endoscopic LDA systems", *Proc. LDA Symp. Copenhagen 1975*, p. 490-497.

- DEARDORFF, J.W. 1970 "A numerical study of three-dimensional turbulent channel flow at large Reynolds numbers", J. Fl. Mech. 41, p. 453-480.
- DEMETRIADES, A. 1979 "Probes for multivariant flow characteristics", Proc. Dyn. Flow Conf. Marseille-Baltimore, 1978 p. 13-44.
- DIMOTAKIS, P.E., LYE, R.C. & MORRISON, R.D. 1978 "Laser induced fluorescence and particle streak measurements in round turbulent jets", Am. Phys. Soc. Meeting Div. Fl. Dyn, Los Angeles, paper BB1.
- DINKELACKER, A., HESSEL, M., MEIER, G.E.A. & SCHEWE, G. 1977 "Investigation of pressure fluctuations beneath a turbulent boundary layer by means of an optical method", Phys. Fluids 20, p. S.216-S.224.
- DUMAS, R., FULACHIER, L. & ARZOUMANIAN, E. 1972 "Facteurs d'intermittence et de dissymétrie des fluctuations de température et de vitesse dans une couche limite turbulente" C.R. Acad. Sc. Paris 274 A, p. 267-270.
- ECKELMANN, H. 1974 "The structure of the viscous sublayer and the adjacent wall region in a turbulent channel flow" J. Fl. Mech. 65, p. 439-459.
- ECKELMANN, H., NYCHAS, S.G., BRODKEY, R.S. & WALLACE, J.M. 1977 "Vorticity and turbulence production in pattern recognized turbulent flow structures", Phys. Fluids 20, p. S.225-S.231.
- EMMERLING, R., MEIER, G.E.A. & DINKELACKER, A. 1973 "Investigation of the instantaneous structure of the wall pressure under a turbulent boundary layer flow" AGARD Conf. Proc. n° 131, Noise Mechanism (24), p. 1-12.
- FALCO, R.E., 1977 "Coherent motions in the outer region of turbulent boundary layers" Phys. Fluids, 20, p. S.124-S.132.
- FAVRE, A., GAVIGLIO, J. & DUMAS, R. 1957 "Space-time double correlation and spectra in a turbulent boundary layer", J. Fl. Mech. 2, p. 313-342.
- FAVRE, A., GAVIGLIO, J. & DUMAS, R. 1958 "Further space-time correlation of velocity in a turbulent boundary layer, J. Fl. Mech. 3, p. 344-356.
- FIEDLER, H. & HEAD, M.R. 1966 "Intermittency measurements on the turbulent boundary layer" J. Fl. Mech. 25, p. 719-735.
- FOSS, J.F. 1979 "Transverse vorticity measurements", Proc. Dyn. Conf Flow. Marseille-Baltimore 1978, p.383-1001
- FREYMUTH, P. 1978 "A bibliography on thermal anemometry", TSI Quarterly 4, p. 3-26.
- FUJITA, H. & KOVASZNAY, L.S.G. 1974 "Unsteady lift and radiated sound from a wake cutting airfoil" AIAA J. 12 p. 1216-1221.
- FULACHIER, L. 1979 "Hot-wire measurements in low speed heated flow" Proc. Dyn. Flow Conf. Marseille-Baltimore 1978, p. 465-487.
- FULACHIER, L., ARZOUMANIAN, E. & DUMAS, R. 1978 "Experimental investigation of a turbulent field from temperature fluctuations, Structure and Mechanisms of Turbulence", Berlin 1977, Lecture Notes in Physics, 2 p. 46-57.
- GEORGE, W.K. Jr & LUMLEY, J.L. 1973 "The laser-Doppler velocimeter and its application to the measurements of turbulence" J. Fl. Mech. 60, p. 321-362.
- GIBSON, C.H. & MASIELLO, P.J. 1972 "Observations of the variability of dissipation rates of turbulent velocity and temperature fields, Statistical Models and Turbulence" Symp. Rolla 1971, Lecture Notes in Physics Springer-Verlag, p. 427-453.
- GOLDSTEIN, M.E. 1976 Aeroacoustics, Mc. Graw Hill Int.
- GRASS, A.J. 1971 "Structural features of turbulent flow over smooth and rough boundaries, J. Fl. Mech. 50, p. 233-255.
- GROTZBACH, G. & SCHUMANN, U. 1979 "Direct numerical simulation of turbulent velocity, pressure and temperature fields in channel flows" 1st Int. Symp. Turb. Shear Flow, Penn State 1977, p. 370-385.
- HARITONIDIS, J.H., KAPLAN, R.E. & WYGANSKI I. 1978 "Interaction of a turbulent spot with a turbulent boundary layer, Structure and Mechanisms of Turbulence", Berlin 1977, Lectures Notes in Physics, Springer-Verlag, 1, p. 234-247.
- HABERBEKE, A., WOOD, D.H. & SMITS, A.J. 1978 "Uncertainties and errors in conditional sampling" 2nd Symp. Turb. Sh. Flow, London, p. 11.1-11.6.
- HEAD, M.R. & PATEL, V.C. 1970 "Improved entrainment method for calculating turbulent boundary layer development, A.R.C. R & M. n° 3643.
- HEDLEY, T.B., KEFFER, J.F. 1974 "Some turbulent/non-turbulent properties of the outer intermittent region of a boundary layer" J. Fl. Mech. 64, p. 645-678.
- HERZOG, S. & LUMLEY, J.L. 1979 "Determination of large eddy structures in the viscous sublayer : a progress report" Proc. Dyn. Flow Conf. Marseille-Baltimore 1978, p. 869-885.
- HUNT, I.A. & JOUBERT, P.N. 1976 "Effects of small streamline curvature on turbulent duct flow" Rep. Dept. Mech. Engng, Univ. Melbourne.
- HUSSAIN, A.K.M.F. & REYNOLDS, W.C. 1972 "The mechanics of an organized wave in turbulent shear flow" (part 2), J. Fl. Mech. 54, p. 241-261.
- JOHNSON, D.H. 1975 "Measurements of the rate of strain tensor in a turbulent flow using light scattering from asymmetric particles" Ph. D. Cornell Univ.
- JOHNSON, D.S. 1959 "Velocity and temperature fluctuation measurements in a turbulent boundary layer downstream of a stepwise discontinuity in wall temperature" J. Appl. Mech. 26 E, p. 325-336.
- JOHNSTON, J.P., HALLEEN, R.M. & LEZINS, D.K. 1972 "Effects of spanwise rotation on the structure of two-dimensional fully developed turbulent channel flow" J. Fl. Mech. 56, p. 533-557.

- KAIMAL, J.C., WYNGAARD, J.C. HAUGEN, D.A., COTE, O.R. & IZUMI, Y. 1976 "Turbulence structure in the convective boundary layer" J. Atmosph. Sc. 33, p. 2152-2169.
- KAPLAN, R.E. & LAUFER, J. 1969 "The intermittent turbulent region of the boundary layer" Proc. 12th Int. Congr. Appl. Mech. Stanford, Springer-Verlag, p. 236-245.
- KARPUK, M.E. & TIEDERMAN, W.G. Jr. 1976 "Effect of finite-size probe volume upon laser Doppler anemometer measurements" AIAA J. 14, p. 1099-1105.
- KASTRINAKIS, E.G., ECKELMANN, H. & WILLMARTH, W.W. 1979 "Influence of the flow velocity on a Kovasznay type vorticity probe" Rev. Sc. Instr. 50, p. 759-767.
- KASTRINAKIS, E.G., WALLACE, J.M., WILLMARTH, W.W., GHORASHI, B. & BRODKEY, R.S. 1978 "On the mechanism of turbulent shear flows" Structure and mechanisms of turbulence I, Symp. Berlin 1977, Lecture Notes in Physics, Springer-Verlag, p. 175-189.
- KIBENS, V., KOVASZNY, L.S.G. & OSWALD, L.J. 1974 "Turbulent-nonturbulent interface detector" Rev. Sc. Instr. 45, p. 1138-1144.
- KIM, H.T., KLINE, S.J. & REYNOLDS, W.C. 1971 "The production of turbulence near a smooth wall in a turbulent boundary layer" J. Fl. Mech. 50, p. 133-160.
- KISTLER, A.L. 1952 "The vorticity meter M.S. Thesis" The Johns Hopkins Univ.
- KLEBANOFF, P.S. 1955 "Characteristics of turbulence in a boundary layer with zero pressure gradient NACA TR 1247.
- KLEBANOFF, P.S. & DIEHL, Z.W. 1952 "Some features of artificially thickened fully developed turbulent boundary layers with zero pressure gradient" NACA TR 1110.
- KLINE, S.J., REYNOLDS, W.C., SCHRAUB, F.A. & RUNSTADLER, P.W. 1967 "The structure of turbulent boundary layers" J. Fl. Mech. 30, p. 741-773.
- KOVASZNY, L.S.G., 1950, Quarterly Progress Report Aeron. Dept. Contract N. Ord. 8036 JHB-3D, The Johns Hopkins Univ.
- KOVASZNY, L.S.G. & FIRASAT ALI, S. 1974 "Structure of the turbulence in the wake of a heated flat plate" Proc. 5th Int. Heat Transf. Conf. Tokyo 2, p. 99-103.
- KOVASZNY, L.S.G., KIBENS, V. & BLACKWELDER, R.E. 1970 "Large-scale motion in the intermittent region of a turbulent boundary layer" J. Fl. Mech. 41, p. 283-325.
- KOYAMA, H., MASUDA, S., ARIGA, I. & WATANABE, I. 1979 a "Stabilizing and destabilizing effects of Coriolis force on two-dimensional laminar and turbulent boundary layers" Trans. ASME, J. Engng. Power, 101, p. 23-31.
- KOYAMA, H., MASUDA, S., ARIGA, I. & WATANABE, I. 1979 b "Turbulence structure and three-dimensionality of a rotating two-dimensional turbulent boundary layer" Proc. 2nd Symp. Turb. Shear Flows, London, Session 4, p. 22-27.
- KREPLIN, H.P. & ECKELMANN, H. 1979 a "Behaviour of the three fluctuating velocity components in the wall region of a turbulent channel flow" Phys. Fluids. 22, p. 1233-1239.
- KREPLIN, H.P. & ECKELMANN, H. 1979 b "Propagation of perturbations in the viscous sublayer and adjacent wall region" J. Fl. Mech. (in print).
- KUO, A.Y. & CORRISIN, S. 1972 "Experiment on the geometry on the fine-structure regions in fully turbulent fluid" J. Fl. Mech. 56, p. 447-479.
- LANDHAL, M.T. 1977 "Dynamics of boundary layer turbulence and the mechanism of drag reduction" Phys. Fluids 20, p. S.55-S.63.
- LARSEN, S.E., MATHIASSEN, O. & BUSCH, N.E. 1979 "Analysis of data from three-dimensional hot-wire probes using comparison with profile instrumentation for calibration" Proc. Dyn. Flow Conf. Marseille-Baltimore 1978, p. 591-597.
- LARUE, J.C. 1974 "Detection of the turbulent-nonturbulent interface in slightly heated turbulent shear flows" Phys. Fluids 17, p. 1513-1517.
- LARUE, J.C. & LIBBY, P.A. 1977 "Measurements in the turbulent boundary layer with slot injection of helium" Phys. Fluids 20, p. 192-202.
- LAUFER, J. 1951 "Investigation of turbulent flow in a two-dimensional channel" NACA TR 1053
- LAUFER, J. 1954 "The structure of turbulence in fully developed pipe flow" NACA TR 1174.
- LAUFER, J. 1975 "New trends in experimental turbulence research" Ann. Rev. Fl. Mech. 7, p. 307-326.
- LAUFER, J. & BADRI NARAYANAN, M.A. 1971 "Mean period of the production mechanism in a boundary layer" Phys. Fluids 14, p. 182-183.
- LEBOUCHE, M. 1968 "Contribution à l'étude des écoulements turbulents par la méthode polarographique" Th. Doct. d'Etat, Nancy.
- LEE, M.K., ECKELMAN, L.D. & HANRATTY, T.J. 1974 "Identification of turbulent wall eddies through the phase relation of the components of the fluctuating velocity gradient" J. Fl. Mech. 66, p. 17-33.
- LIBBY, P.A. & LARUE, J.C. 1979 "Hot-wire anemometry for turbulence measurements in helium-air mixtures" Proc. Dyn. Flow. Conf. Marseille-Baltimore 1978, p. 115-130.
- LIEPMANN, H.W. & SKINNER, G.T. 1954 "Shearing stress measurements by use of a heated element" NACA TN 3268.
- LIMURA, I. & HATANAKA, H. 1973 "The frequency characteristics of cavity mounted pressure measuring systems" Fluidics Quarterly, p. 27-45.
- LOHMANN, R.P. 1973 "The response of developed turbulent boundary layer to local transverse surface motion" Ph. D. Univ. of Connecticut.



- LU, S.S. & WILLMARTH, W.W. 1973 "Measurements of the structure of the Reynolds stress in a turbulent boundary layer" J. Fl. Mech. 60, p. 481-511.
- LUDWEIG, H. 1950 "Investigation of the wall shearing stress in turbulent boundary layers" NACA TM 1284.
- LUMLEY, J.L. 1970 "Toward a turbulent constitutive relation" J. Fl. Mech. 41, p. 413-434.
- MAESTRELLO, L. 1965 "Measurement and analysis of the response field of turbulent boundary layer excited panels" J. Sound Vibr. 2, p. 270-292.
- MAIDANIK, G. & JORGENSEN, D.W. 1967 "Boundary wave-vector filters for the study of the pressure field in a turbulent boundary layer" J. Acoust. Soc. Am. 42, p. 494-501.
- MALHOTRA, R.C. & CERMAK, J.E. 1964 "Mass diffusion in neutral and unstably stratified boundary layer flows" Int. J. Heat Mass Transf. 7, p. 169-186.
- MARI, C., JEANDEL, D. & MATHIEU, J. 1976 "Méthode de calcul de la couche limite turbulente compressible avec transfert de chaleur" Int. J. Heat. Mass Transf. 19, p. 893-899.
- MELINAND, J.P. & CHARNAY, G. 1979 "Digital analysis of LDA counter signals in a separated boundary layer" Proc. Dyn. Flow. Conf. Marseille-Baltimore 1978, p. 909-916.
- MERY, P., SCHON, J.P., & SOLAL, J. 1974 "Comparison of thermally neutral and unstable shear flows in the wind tunnel and the atmosphere" Adv. in Geophysics 18 B, p. 273-287.
- MERZKIRCH, W. 1974 "Flow visualization" Acad. Press.
- MICHEL, B., ARBEY, H. & SUNYACH, M. 1979 "Radiation from subsonic rotor operating in a non-uniform incident flow" Internoise, Varsovie.
- MITCHELL, J.E. & HANRATTY, T.J. 1966 "A study of turbulence at a wall using an electrochemical wall shear-stress meter" J. Fl. Mech. 26, p. 199-221.
- MIZUSHINA, T. 1971 "The electrochemical method in transport phenomena" Adv. Heat Transf, Acad. Press, 7, p. 87-161.
- MOFFATT, R.J., YAVUZKURT, S. & CRAWFORD, M.E. 1979 "Real-time measurements of turbulence quantities with a triple hot-wire system" Proc. Dyn. Flow. Conf. Marseille-Baltimore 1978, p. 1013-1036.
- MOLLO-CHRISTENSEN, E. 1971 "Physics of turbulent flow" AIAA J. 9, p. 1217-1228.
- MONIN, A.S. & YAGLOM, A.M. 1971 "Statistical Fluid Mechanics: Mechanics of Turbulence" MIT Press, Cambridge.
- NAKATANI, N., YORISUE, R. & YAMADA, T. 1979 "Simultaneous measurement of flow velocities in multipoint by the laser Doppler velocimeter" Proc. Dyn. Flow Conf. Marseille-Baltimore 1978, p. 583-590.
- OFFEN, G.R. & KLINE, S.J. 1973 "Experiments on the velocity characteristics of "bursts" and on the interaction between the inner and outer regions of a turbulent boundary layer" Rep. MD.31, Dept. Mech. Engng. Stanford Univ.
- ORLOFF, K.L. 1979 "Laser-Doppler anemometer diagnostics in unsteady flow" Proc. Dyn. Flow Conf. Marseille-Baltimore 1978, p. 511-534.
- PANTON, R.L. & LINEBARGER, J.H. 1974 "Wall pressure spectra calculations for equilibrium boundary layers" J. Fl. Mech. 65, p. 261-287.
- PASQUILL, F. 1968 "Atmospheric diffusion, Van Nostrand.
- PETIT, L. 1979 "Nouvelle méthode d'étude d'écoulements par marquage thermique, thèse 3ème Cycle, Univ. Paris Sud-Orsay.
- PRATURI, A.K. & BRODKEY, R.S. 1977 "A stereoscopic visual study of coherent structures in turbulent shear flow" J. Fl. Mech. 80, p. 251-272.
- PY, B. 1973 "Etude tridimensionnelle de la sous-couche visqueuse dans une veine rectangulaire par des mesures de transfert de matière en paroi" Int. J. Heat Mass transf. 16, p. 129-143.
- RAO, K.N., NARASIMHA, R. & BADRI NARAYANAN, M.A. 1971 The "bursting " phenomenon in a turbulent boundary layer, J. Fl. Mech. 48, p. 339-352.
- REICHARDT, Von H. 1938 "Messungen turbulenter schwankungen" Die Naturwissenschaften 24/25, p. 404-408.
- REY, C. 1977 "Effet du nombre de Prandtl, de la gravité et de la rugosité sur les spectres de turbulence cinématique et scalaire" Thèse Doct. d'Etat, Univ. Lyon.
- REY, C., SCHON, J.P. & MATHIEU, J. 1979 "Buoyancy effects in a wind tunnel simulation of the atmospheric boundary layer" Phys. Fluids 22 p. 1020-1028.
- ROCKWELL, D. & NAUDASCHER, E. 1979 "Self-sustained oscillations of impinging free shear layers" Ann. Rev. Fl. Mech. 11, p. 67-94.
- SABOT, J. 1976 "Etude de la coherence spatiale et temporelle de la turbulence établie en conduite circulaire" Th. Doct. d'Etat. Univ. Lyon.
- SABOT, J. & COMTE-BELLOT, G. 1972 "Mémoires des fluctuations longitudinales de vitesse en conduite lisse circulaire" C.R. Acad. Sc. Paris 274 A, p. 1647-1650.
- SABOT, J. & COMTE-BELLOT, G. 1976 "Intermittency of coherent structures in the core region of fully developed turbulent pipe flow" J. Fl. Mech. 74, p. 767-796.
- SABOT, J., RENAULT, J. & COMTE-BELLOT, G. 1973 "Space-time correlations of the transverse velocity fluctuation in pipe flow" Phys. Fluids 16, p. 1403-1405.
- SABOT, J., SALEH, I. & COMTE-BELLOT, G. 1977 "Effects of roughness on the intermittent maintenance of Reynolds stress in pipe flow" Phys. Fluids, 20, p. S.150-S.155.

- SANDBORN, V.A. 1979 "Surface shear stress fluctuations in turbulent boundary layers" 2nd Symp. Turb. Sh. Flows, London, p. 4.1-4.5.
- SCHODL, R. 1976 "On the extension of the range of applicability of LDA by means of the laser-dual-focus (L-2-F) Technique", Proc. LDA Symp. Copenhagen 1975, p. 480-489.
- SCHODL, R. 1977 "Laser-two-focus velocimetry (L-2-F) for use in aero engines" AGARD-LS n° 90, p. 4/1-34.
- SCHON, J.P. 1974 "Contribution à l'étude des écoulements stratifiés en température" Thèse Doct. d'Etat. Univ. Lyon.
- SCHON, J.P., DANIEL, F., MELINAND, J.P., REY, C. & CHARNAY, G. 1979 "Flow visualization and measurements of Lagrangian velocities by means of a rotating laser beam" 6th Biennial Symp. Turbulence, Univ. Missouri-Rolla.
- SCHUBAUER, G.B. & KLEBANOFF, P.S. 1951 "Investigation of separation of the turbulent boundary layer" NACA TR 1030.
- SCHUMANN, U. 1975 "Numerical investigation of the wall pressure fluctuations in channel flow" Nucl. Eng. Design, 32, p. 37-47.
- SCHUMANN, U., GROTZBACH, G. & KLEISER, L. 1979 "Direct numerical simulation of turbulence" Lecture series Von Karman Institute Bruxelles.
- SHEIH, C.M., TENNEKES, H. & LUMLEY, J.L. 1971 "Airborne hot-wire measurements of the small-scale structure of atmospheric turbulence" Phys. Fluids, 14, p. 201-215.
- SIMPSON, R.L., STRICKLAND, J.H. & BARR, P.W. 1977 "Features of a separating turbulent boundary layer in the vicinity of separation" J. Fl. Mech. 79, p. 553-594.
- SIRKAR, K.K. & HANRATTY, T.J. 1970 "The limiting behaviour of the turbulent transverse velocity component close to a wall" J. Fl. Mech. 44, p. 605-614.
- SNYDER, W.H. & LUMLEY, J.L. 1971 "Some measurements of particle velocity auto-correlations functions in a turbulent flow" J. Fl. Mech. 48, p. 41-71.
- SO, R.M.C. & MELLOR, G.L. 1973 "Experiment on convex curvature effects in turbulent boundary layers" J. Fl. Mech. 60, p. 43-62.
- SOLAL, J. 1972 "Etude experimentale de la diffusion de masse dans une couche limite turbulente en écoulement neutre ou en écoulement stratifié instable, Thèse Dr. Ing. Univ. Lyon.
- SREENIVASAN, K.R. & ANTONIA, R.A. 1977 "Properties of wall shear stress fluctuations in a turbulent duct flow" J. Appl. Mech. Trans. ASME 44 E, p. 389-395.
- SREENIVASAN, K.R., ANTONIA, R.A. & DANH, H.Q. 1977 "Temperature dissipation fluctuations in a turbulent boundary layer" Phys. Fluids. 20, p. 1238-1249.
- STANFORD, R.A. & LIBBY, P.A. 1974 "Further applications of hot-wire anemometry to turbulence measurements in helium - air mixtures" Phys. Fluids, 17, p. 1353-1361.
- STERNBERG, J. 1962 "A theory for the viscous sublayer of a turbulent flow" J. Fl. Mech. 13, p. 241-271.
- SUNYACH, M. 1971 "Contribution à l'étude des frontières d'écoulements turbulents libres" Thèse Dr. d'Etat, Univ. Lyon.
- TANNER, L.H. 1973 "A particle timing laser velocity meter" Optics and Laser Techn., 5, p. 108-110.
- TAYLOR, G.I. 1936 "Correlation measurements in a turbulent flow through a pipe" Proc. Roy. Soc. A 47, p. 537-546.
- TENNEKES, H. 1965 "Similarity laws for turbulent boundary layer with suction or injection" J. Fl. Mech. 21, p. 689-703.
- THEODORSEN, T. 1954 "The structure of turbulence" Techn. Note BN 31 United States Air Force.
- THOMPSON, D.H. 1968 "A tracer particle fluid velocity meter incorporating a laser" J. Sc. Instr. (J. Phys. E), Series 2, 1, p. 929-932.
- TOWNSEND, A.A. 1956 "The structure of turbulent shear flow" Cambridge Univ. Press.
- VAN ATTA, C.W. 1979 "Multi-channel measurements and high-order statistics" Proc. Dyn. Flow Conf. Marseille-Baltimore 1978, p. 919-941.
- VEROLLET, E. 1972 "Etude d'une couche limite turbulente avec chauffage et aspiration à la paroi" Thèse Univ. Provence.
- VOUILLARMET, A. 1972 "Contribution à l'étude et à la compréhension de l'écoulement visqueux dans un compresseur centrifuge" Thèse Dr. Ing. Univ. Lyon.
- WALLACE, J.M., BRODKEY, R.S. & ECKELMANN, H. 1977 "Pattern-recognized structures in bounded turbulent shear flows" J. Fl. Mech. 83, p. 673-693.
- WALLACE, J.M., ECKELMANN, H. & BRODKEY, R.S. 1972 "The wall region in turbulent shear flow" J. Fl. Mech. 54, p. 39-48.
- WILLMARTH, W.W. 1975 a "Structure of turbulence in boundary layers" Adv. Appl. Mech. 15, p. 159-254.
- WILLMARTH, W.W. 1975 b "Pressure fluctuations beneath turbulent boundary layers" Ann. Rev. Fl. Mech. 7, p. 13-38.
- WILLMARTH, W.W. & BOGAR, T.J. 1977 "Survey and new measurements of turbulent structure near the wall" Phys. Fluids, 20 p. S.9-S.21.
- WILLMARTH, W.W. & LU, S.S. 1972 "Structure of the Reynolds stress near a wall" J. Fl. Mech. 55, p. 65-92.
- WILLS, J.A.B. 1962 "The correction of hot-wire readings for proximity to a solid boundary" J. Fl. Mech. 12 p. 388-396.

WILLS, J.A.B. 1970 "Measurements of the wave-number/phase velocity spectrum of wall pressure beneath a turbulent boundary layer" J. Fl. Mech. 45, p. 65-90.

WYGNANSKI, I. 1979 "The recognition of an evoked large scale structure in turbulent shear flow" Proc. Dyn. Flow Conf. Marseille-Baltimore 1978, p. 191-211.

WYNGAARD, J.C. 1969 "Spatial resolution of the vorticity meter and other hot-wire arrays" J. Phys. E : Sci Instr, Serie 2, 2, p. 983-987.

WYNGAARD, J.C., COTE, O.R. & IZUMI, Y. 1971 "Local forced convection similarity and the budgets of shear stress and heat flux" J. Atm. Sci. 28, p. 1171-1182.

## 8. Figures

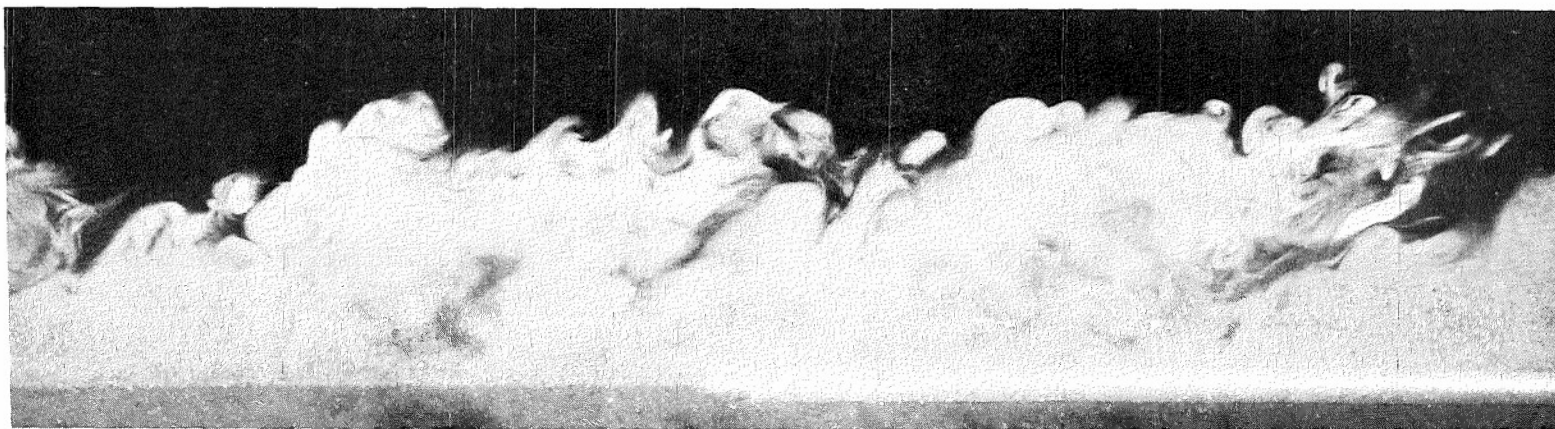
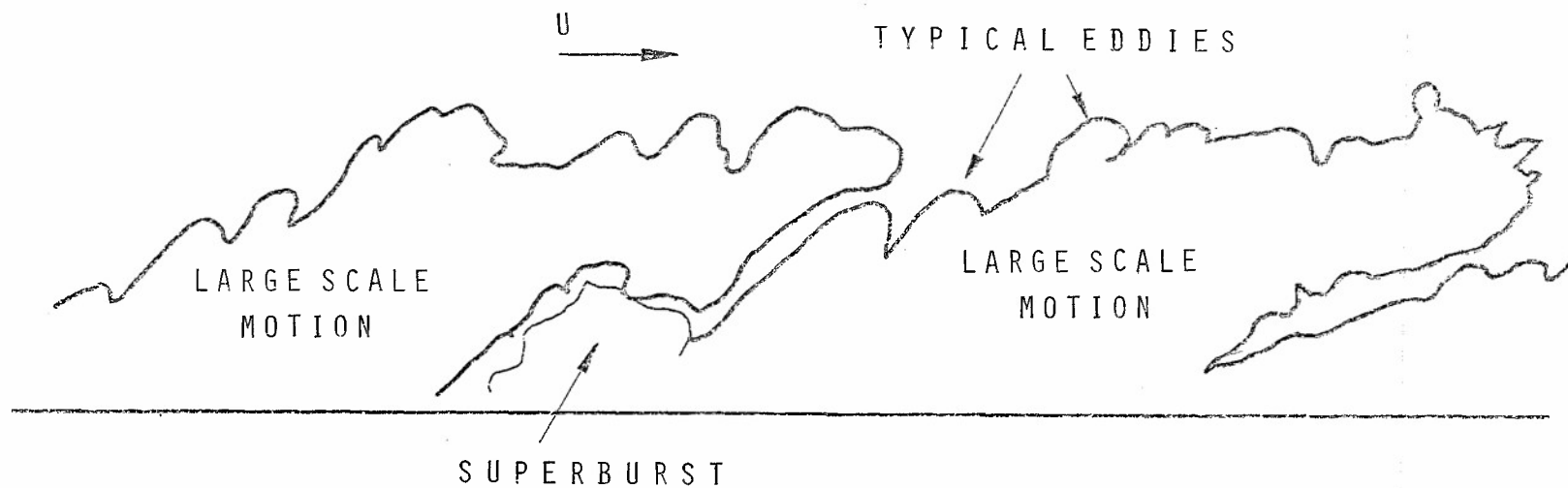
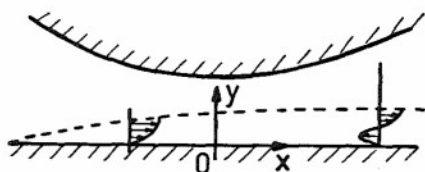
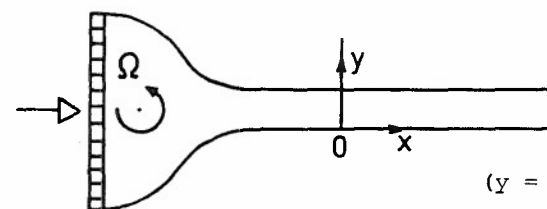


Fig. 1 - Visualization of a turbulent boundary layer without a pressure gradient. Light plane is normal to the wall and parallel to the stream direction,  $Re_\theta \approx 4\,000$  (FALCO 1977)

TURBULENCE QUANTITIESPRODUCTION TERMS

$\frac{1}{2} \overline{u^2}$	$-\overline{uv} \frac{d\overline{U}}{dx}$	$-\overline{v^2} \frac{d\overline{U}}{dx}$
$\frac{1}{2} \overline{v^2}$	0	$-\overline{v^2} \frac{d\overline{V}}{dy}$
$\frac{1}{2} \overline{w^2}$	0	0
$\overline{uv}$	$-\overline{v^2} \frac{d\overline{U}}{dy}$	0
$\overline{q^2}$	$-\overline{uv} \frac{d\overline{U}}{dy}$	$-(\overline{u^2} - \overline{v^2}) \frac{d\overline{U}}{dx}$
	usual terms	terms due to the pressure gradient

Fig. 2 - Reynolds stress tensor for boundary layers with pressure gradient

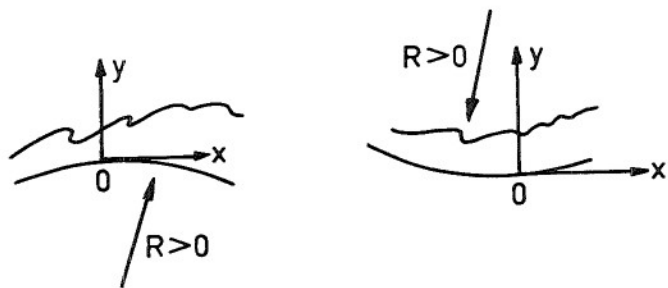


(y = 0, high pressure side)

TURBULENCE QUANTITIESPRODUCTION TERMS

$\frac{1}{2} \overline{u^2}$	$-\overline{uv} \frac{d\overline{U}}{dy}$	$2 \Omega \overline{uv}$
$\frac{1}{2} \overline{v^2}$	0	$-2 \Omega \overline{uv}$
$\frac{1}{2} \overline{w^2}$	0	0
$\overline{uv}$	$-\overline{v^2} \frac{d\overline{U}}{dy}$	$2 \Omega (\overline{v^2} - \overline{u^2})$
$\overline{q^2}$	$-\overline{uv} \frac{d\overline{U}}{dy}$	0
	usual terms	terms due to the Coriolis force

Fig. 3 - Reynolds stress tensor for rotating boundary layer



#### TURBULENCE QUANTITIES

$$\frac{1}{2} \overline{u^2}$$

$$\frac{1}{2} \overline{v^2}$$

$$\frac{1}{2} \overline{w^2}$$

$$\overline{uv}$$

$$\overline{q^2}$$

#### PRODUCTION TERMS

$$-\overline{uv} \frac{d\overline{U}}{dy} \quad -\frac{\overline{U}}{R} \overline{uv}$$

$$0 \quad 2 \frac{\overline{U}}{R} \overline{uv}$$

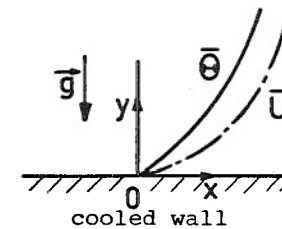
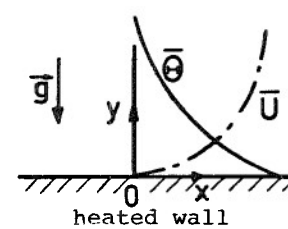
$$0 \quad 0$$

$$-\overline{v^2} \frac{d\overline{U}}{dy} \quad \frac{\overline{U}}{R} (2\overline{u^2} - \overline{v^2})$$

$$-\overline{uv} \frac{d\overline{U}}{dy} \quad \frac{\overline{U}}{R} \overline{uv}$$

usual  
terms

terms due to  
the Centrifugal  
forces



#### TURBULENCE QUANTITIES

$$\frac{1}{2} \overline{u^2}$$

$$\frac{1}{2} \overline{v^2}$$

$$\frac{1}{2} \overline{w^2}$$

$$\overline{uv}$$

$$\overline{u\theta}$$

$$\overline{v\theta}$$

$$-\overline{uv} \frac{d\overline{U}}{dy}$$

$$0$$

$$0$$

$$-\overline{v^2} \frac{d\overline{U}}{dy}$$

$$0$$

$$0$$

$$0$$

$$0$$

$$0$$

$$0$$

$$-\overline{uv} \frac{d\overline{\theta}}{dy}$$

$$-\overline{v^2} \frac{d\overline{\theta}}{dy}$$

usual  
terms

terms due  
to the mean  
temperature  
gradient

$$0$$

$$\frac{g}{T_0} \overline{v\theta}$$

$$0$$

$$\frac{g}{T_0} \overline{u\theta}$$

$$0$$

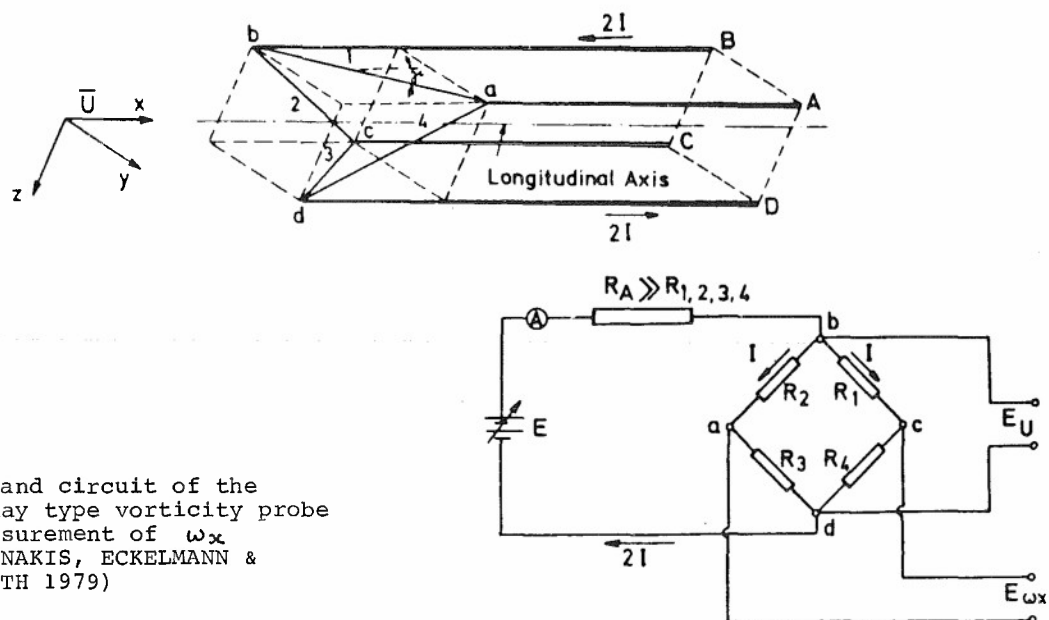
$$g \frac{\overline{\theta^2}}{T_0}$$

terms due  
to the gravity  
forces

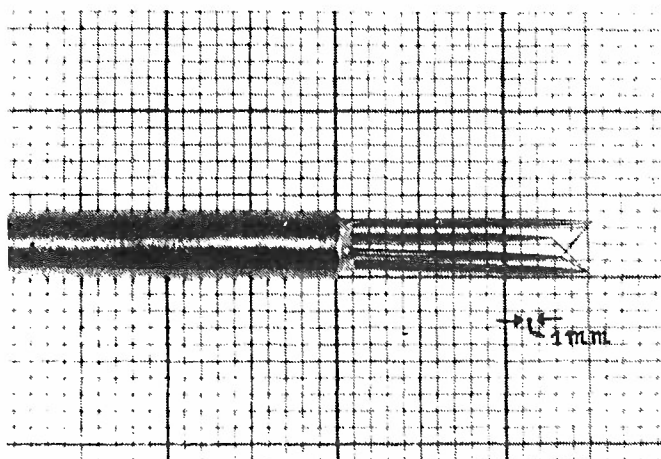
Fig. 4 - Reynolds stress tensor for boundary layer on curved walls

Fig. 5 - Reynolds stress for heated boundary layers with gravity effects

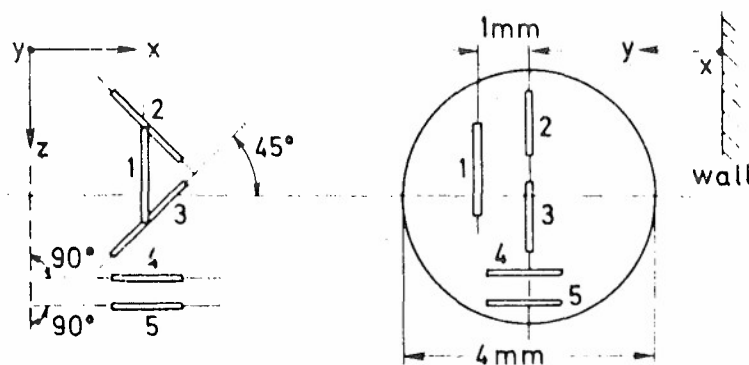




Sketch and circuit of the Kovasznay type vorticity probe for measurement of  $\omega_x$  (KASTRINAKIS, ECKELMANN & WILLMARTH 1979)



View of the Kovasznay type vorticity probe (KASTRINAKIS, WALLACE, WILLMARTH & BRODKEY 1978)



Sketch of five sensor probe (V probe, 2 and 3 ; X probe, 4 and 5) ; U probe, 1) for measurement of two components of vorticity  $\omega_z$  and  $\omega_y$  (ECKELMANN, NYCHAS, BRODKEY & WALLACE 1977)

Fig. 7 - Examples of wire arrays (Cont'd)



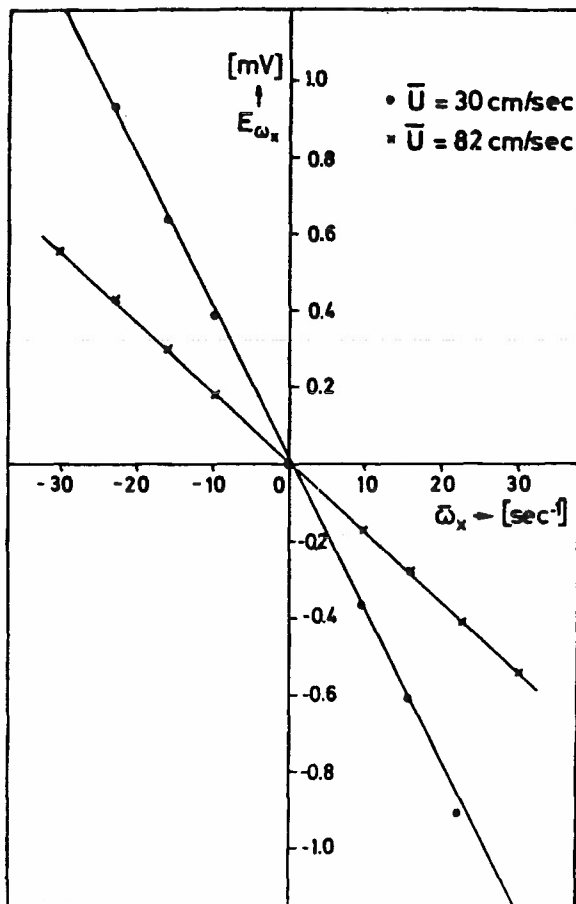


Fig. 8 - Calibration curve of the Kovasznay type vorticity probe with respect to  $\omega_x$ ;  $E_{\omega_x}$  is the voltage across the diagonal points a-c in Fig.7. (KASTRINAKIS, ECKELMANN & WILLMARTH 1979)

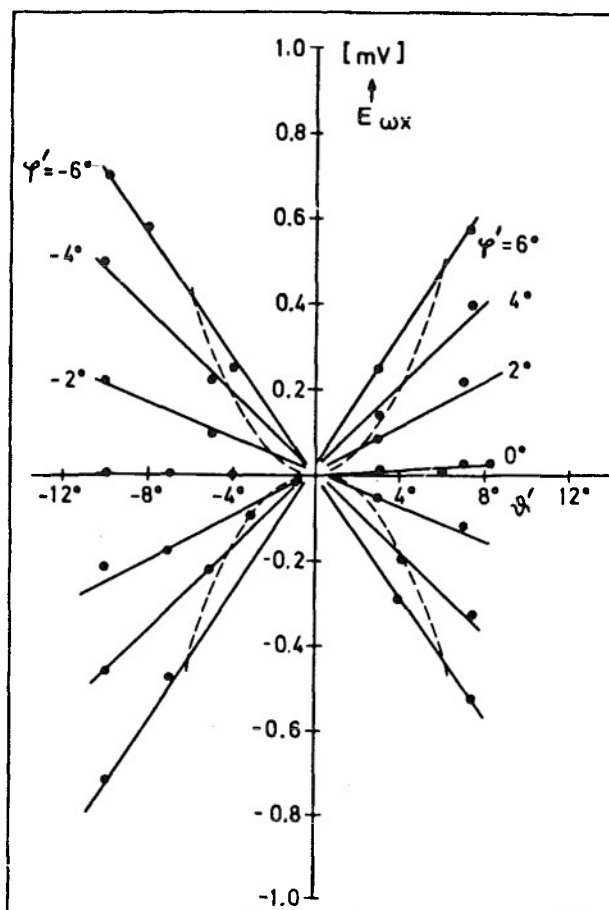


Fig. 9 - Change of the vorticity signal  $E_{\omega_x}$  for various yaw and pitch angles  $\psi'$  and  $\phi'$  (KASTRINAKIS, ECKELMANN & WILLMARTH 1979)

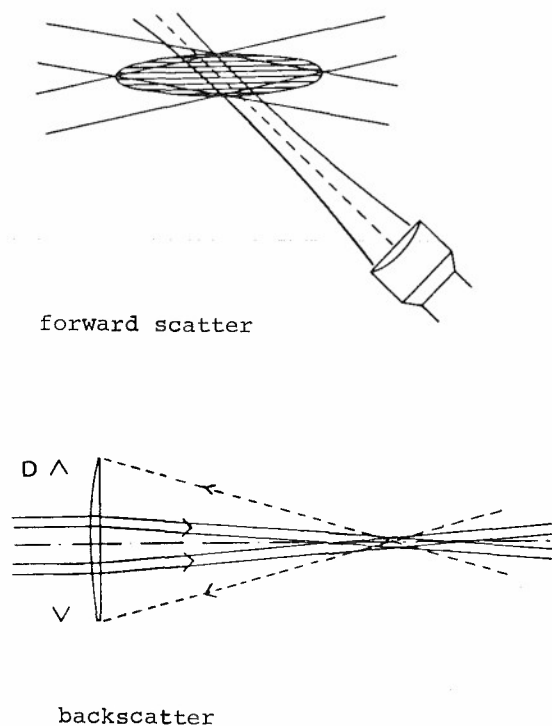


Fig. 10 - Sketch showing the difference between the probe volume and the measuring volume in LDA (BUCHHAVE 1979)

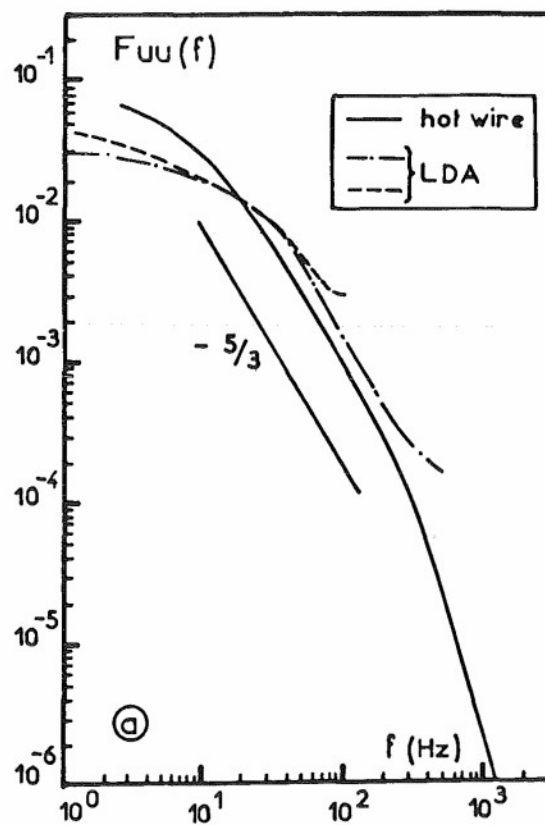


Fig. 12 - Limitation of the LDA for power spectra (MELINAND & CHARNAY 1979)

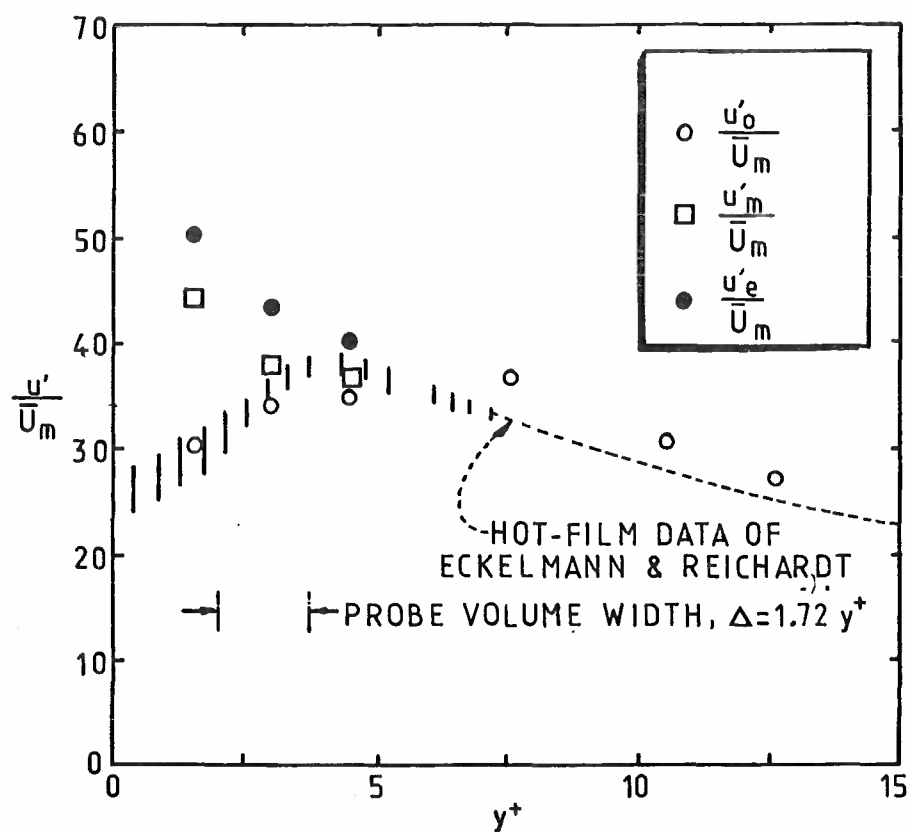
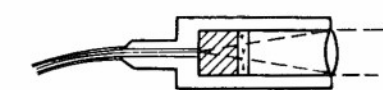
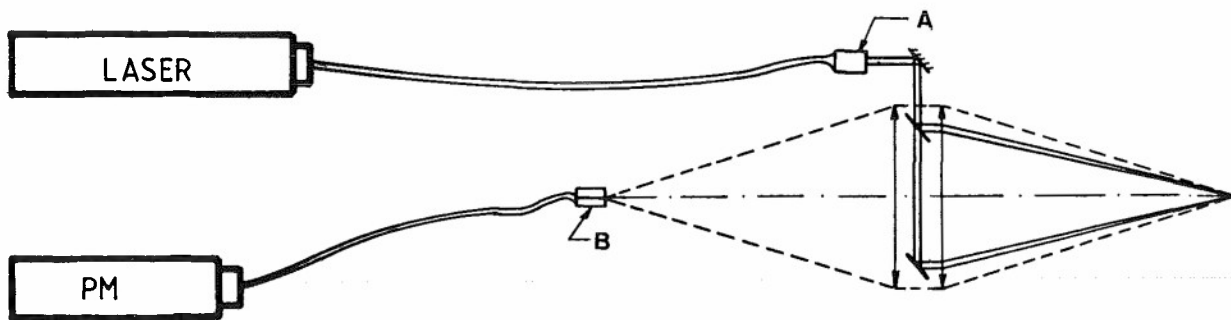
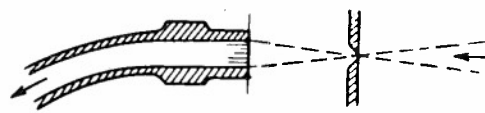


Fig. 11 - Corrections for LDA measurement close to a wall (KARPUK & TIEDERMAN 1976)



A Coherent fiber coupling



B Ordinary light guide coupling

(a) "Endoscopic" LDA system (DANEL 1976)

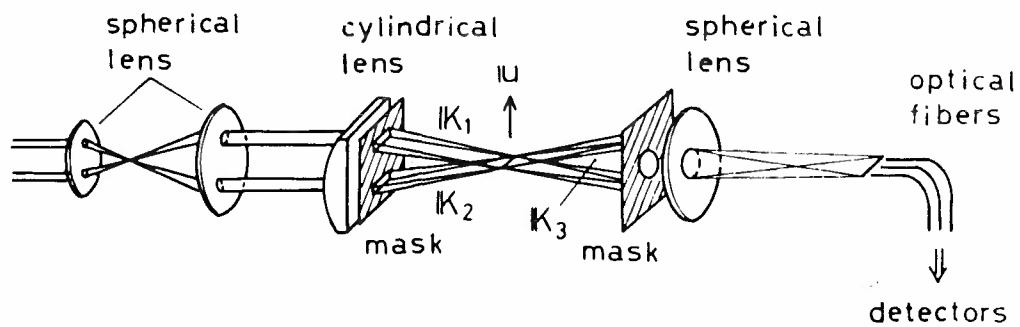
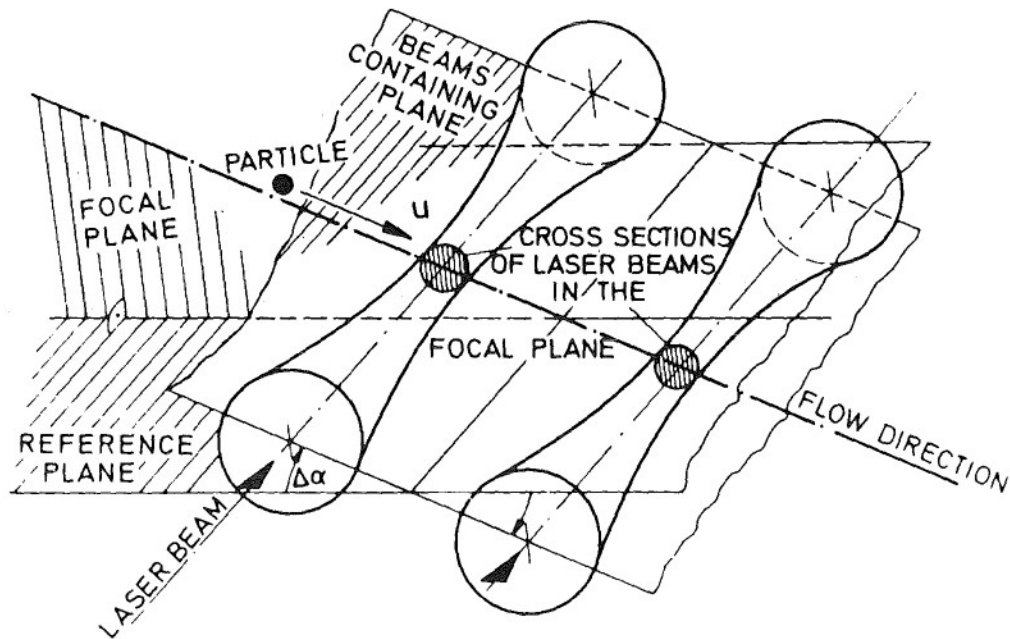
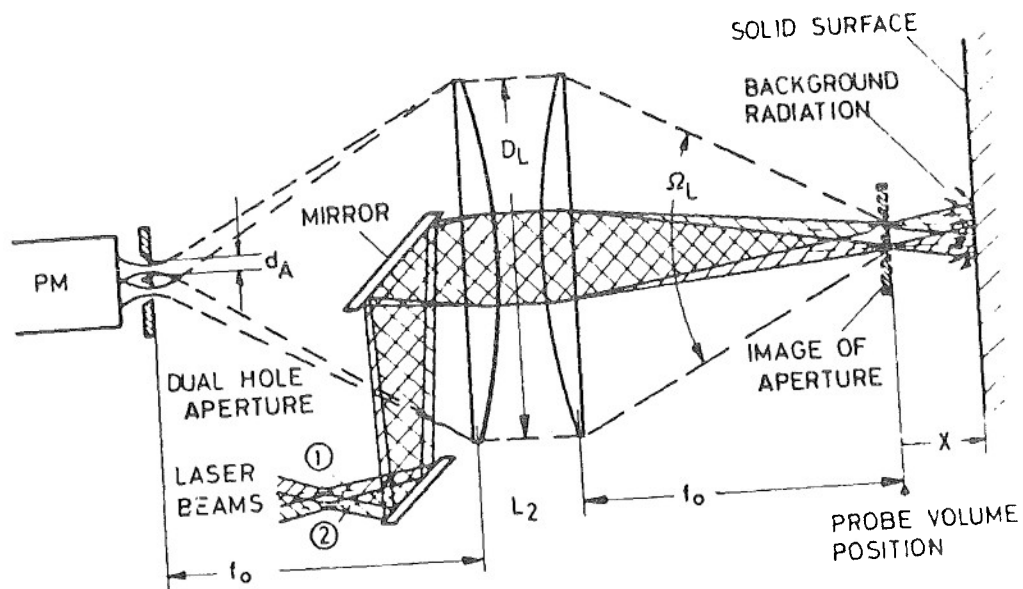
(b) LDA for the measurement of flow velocity profiles  
(NAKATANI, YORISUE & YAMADA 1979)

Fig. 13 - Use of optical fibers in LDA systems



(a) Principle of a time of flight velocimeter (TANNER 1973)



(b) Optical set-up for turbomachinery applications

Fig. 14 - Laser-two-focus velocimetry  
SCHODL 1977

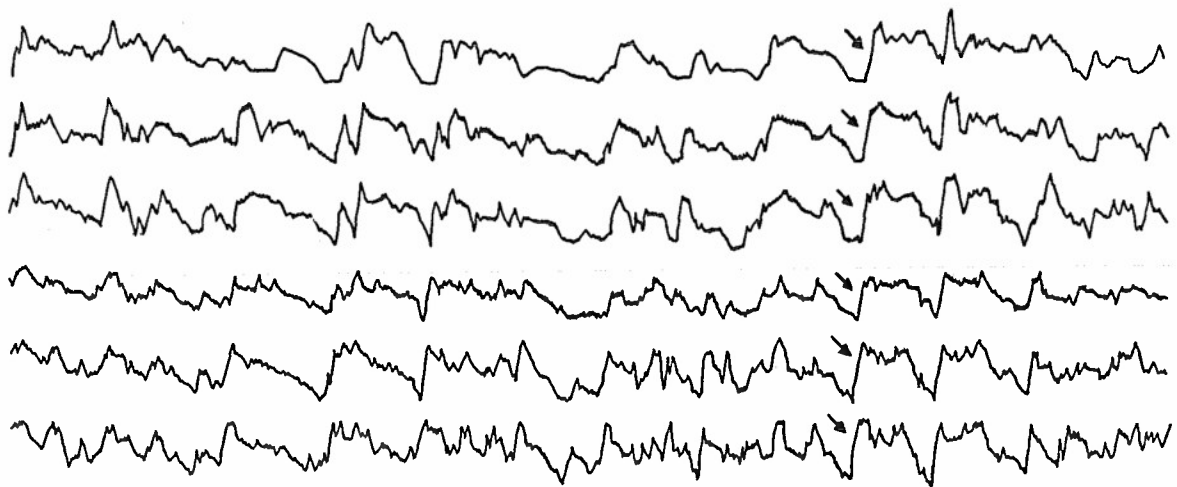


Fig. 15 - Instantaneous temperature fluctuations in of a two-dimensional mixing layer. The six temperature probes are 1.5 mm apart across the layer and are located 8 cm from the origin. Note the sharp temperature gradients existing across the layer, which are believed to be associated with vorticity layers. (Arrows show one such layer). The temperature difference between the two streams is 25°C. The high-velocity side corresponds to the lower traces.  $U_1 = 18$  m/s ;  $U_2 = 0$ . Time increases from left to right. Horizontal scale : 1 cm = 1/150 s ; vertical scale : 0.1 cm = 2.8°C. (SUNYACH 1971 ; LAUFER 1975).

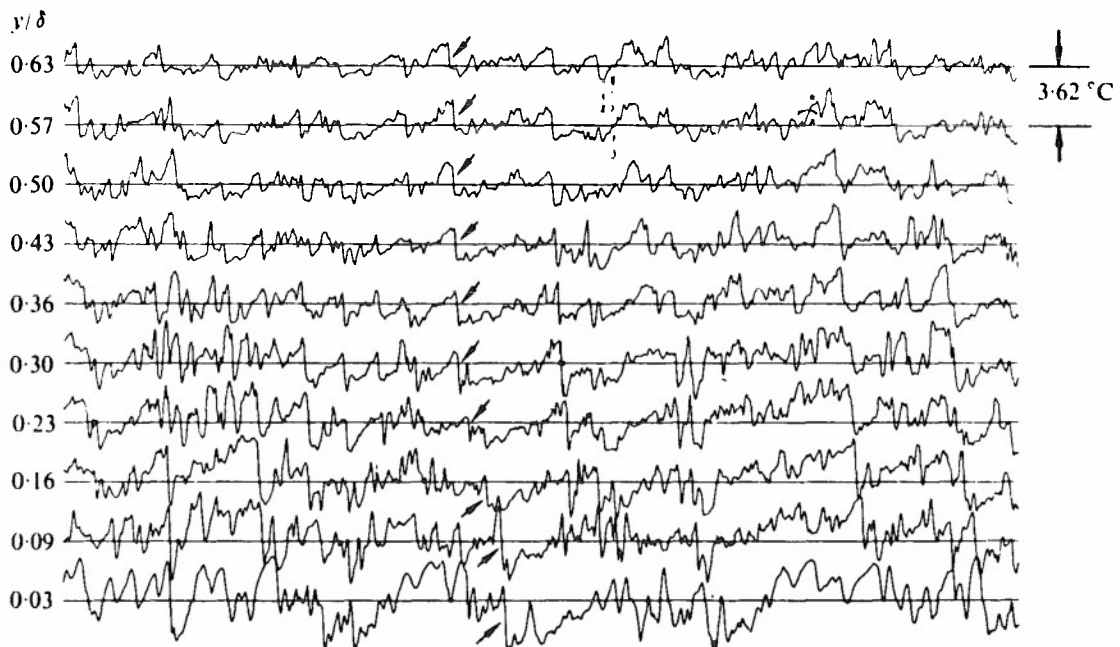


Fig. 16 - Simultaneous temperature signals in a turbulent boundary layer on a slightly heated plate ( $\approx 12^\circ\text{C}$ ). The horizontal time span is  $18.7 U_e \Delta t / \delta$  ( $U_e = 4.57$  m/s,  $\delta = 9.42$  cm). A particular temperature front is denoted by the arrows (CHEN & BLACKWELDER 1978)

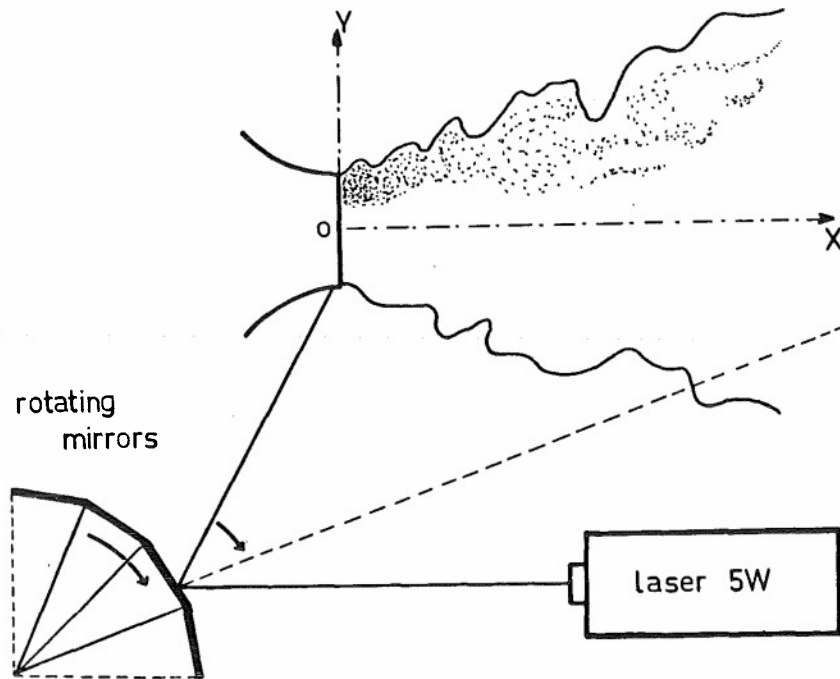


Fig. 17 - Set-up of the rotating laser beam and example of trajectories in a mixing layer  
(SCHON, DANIEL, MELINAND, REY & CHARNAY 1979)

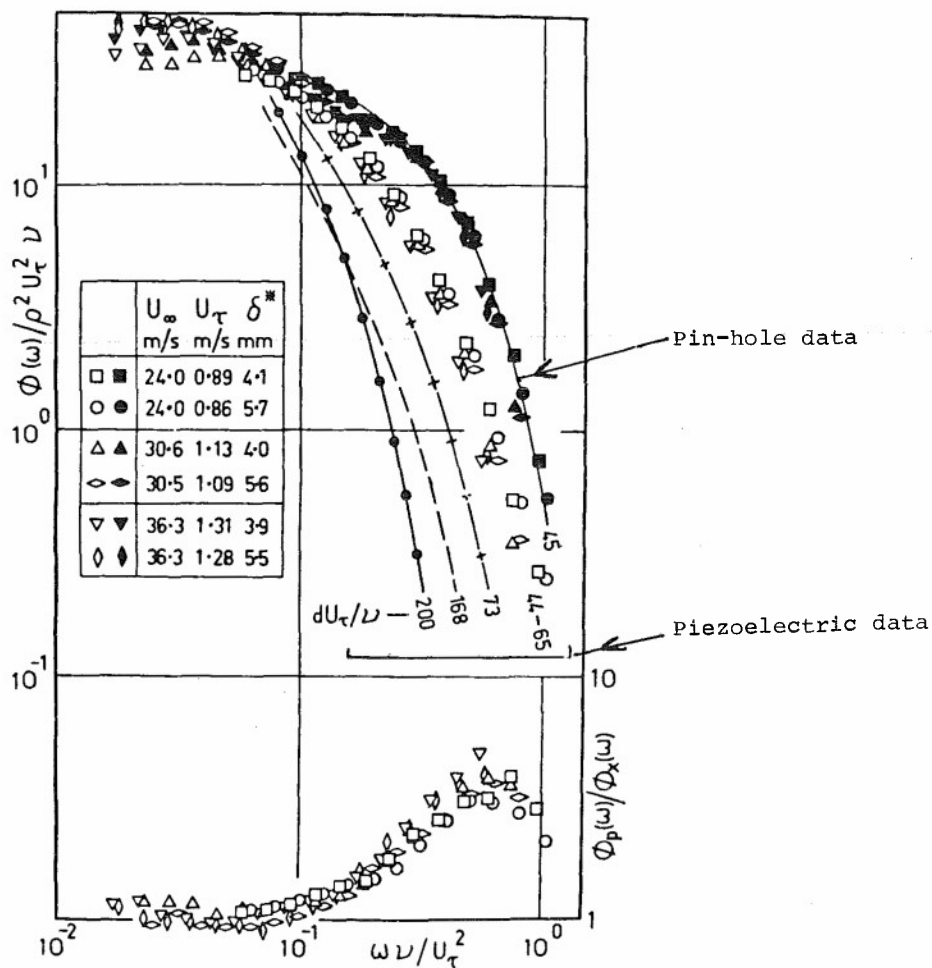


Fig. 18 - Power spectrum of wall-pressure fluctuations : comparison between piezoelectric data and pin-hole data (BULL & THOMAS 1976)

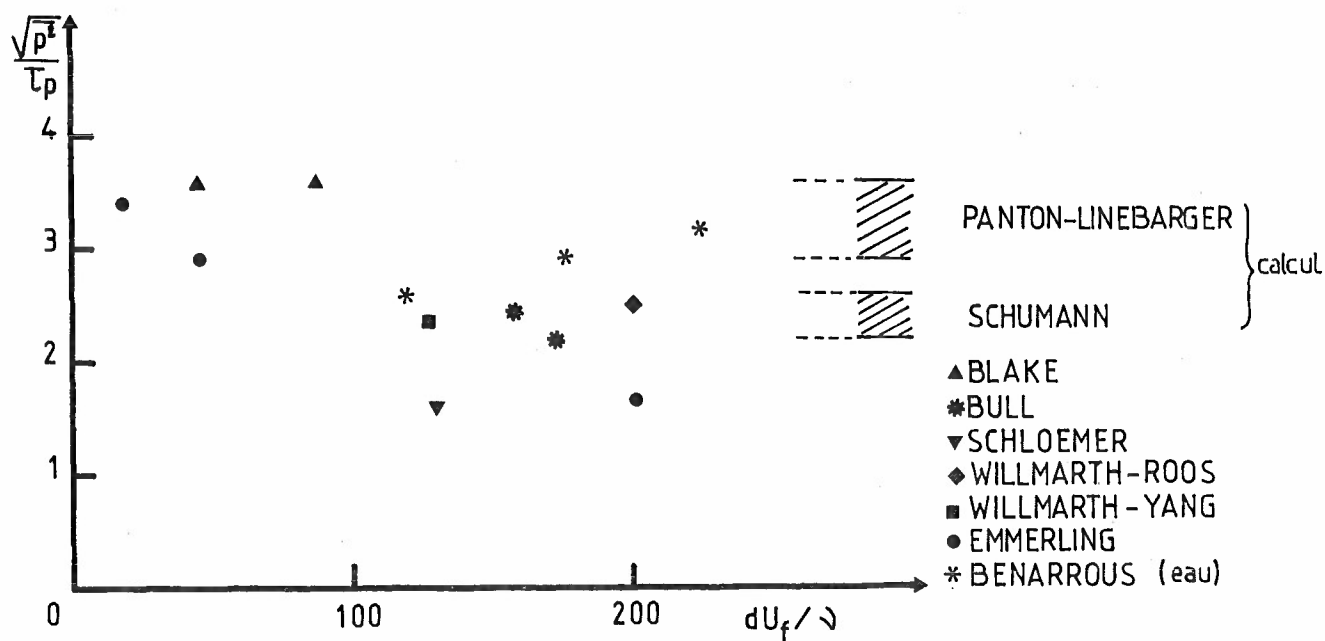


Fig. 19 - RMS value of the wall pressure fluctuation and comparison with numerical prediction (BENARROUS 1979)



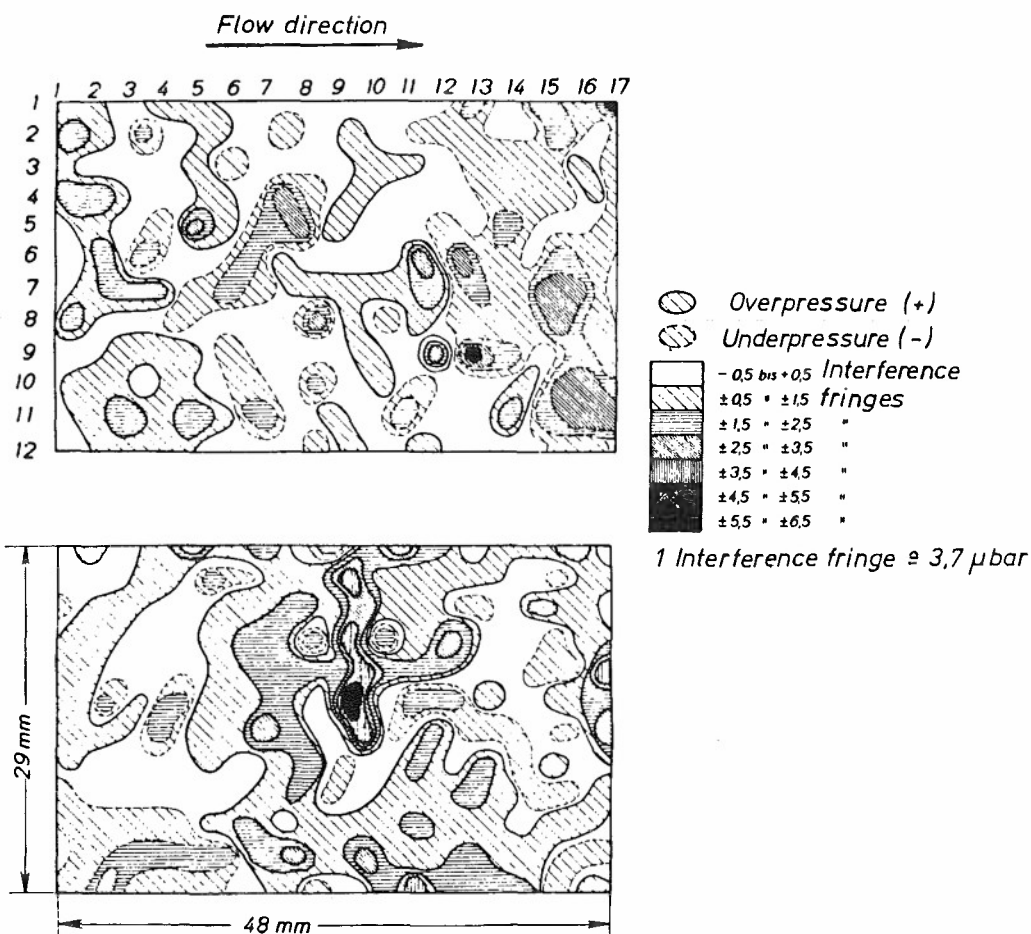


Fig. 20 - Contours of instantaneous pressure fluctuations as measured by EMMERLING, MEIER & DINKELACKER 1973. The time interval between the two maps is 3.6 ms.

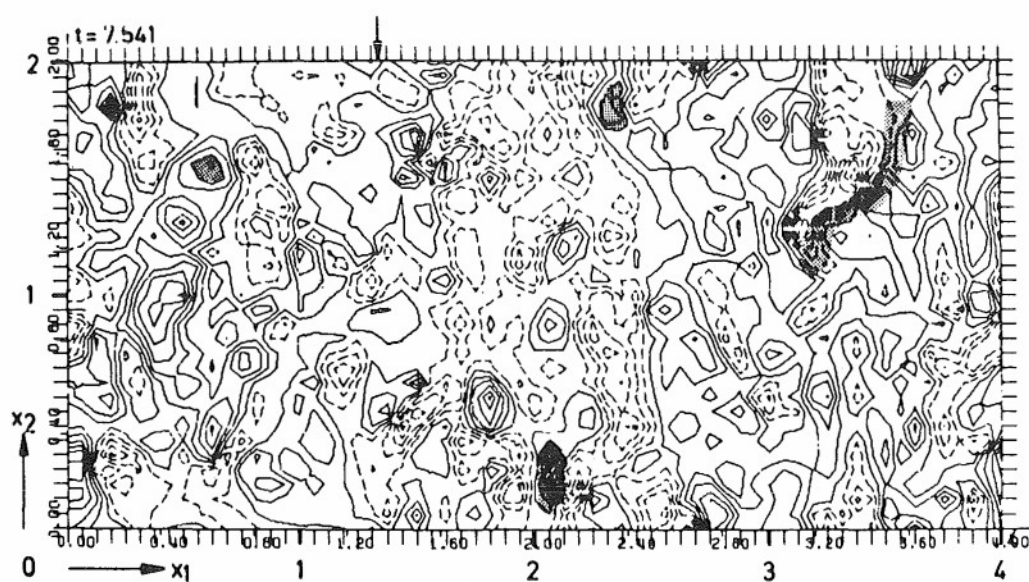


Fig. 21 - Contour-line plots of the wall pressure fluctuations as obtained in numerical simulation of the flow (SCHUMANN 1975)

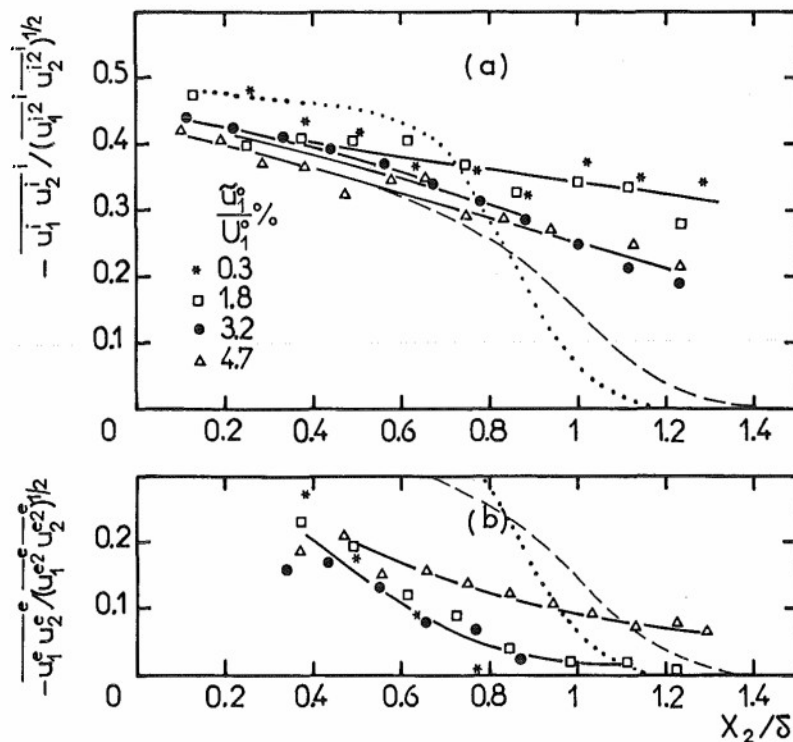


Fig. 22 - Example of zone averaging : values of Reynolds stress inside the bulges (a) and outside the bulges (b) for a turbulent boundary layer with free stream turbulence (CHARNAY, COMTE-BELLOT & MATHIEU 1976)

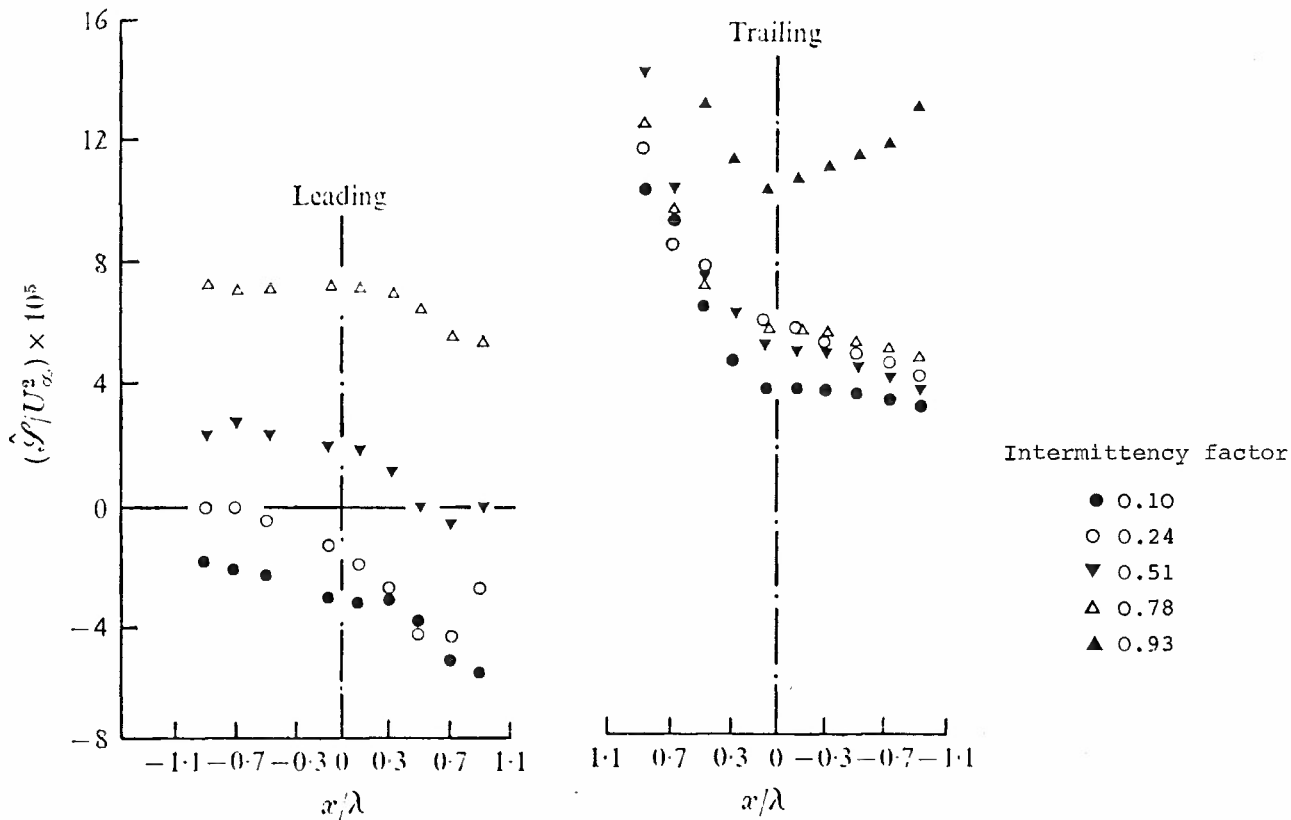


Fig. 23 - Example of point averaging : distribution of Reynolds stress across the interface of a boundary layer without a pressure gradient (HEDLEY & KEFFER 1974)

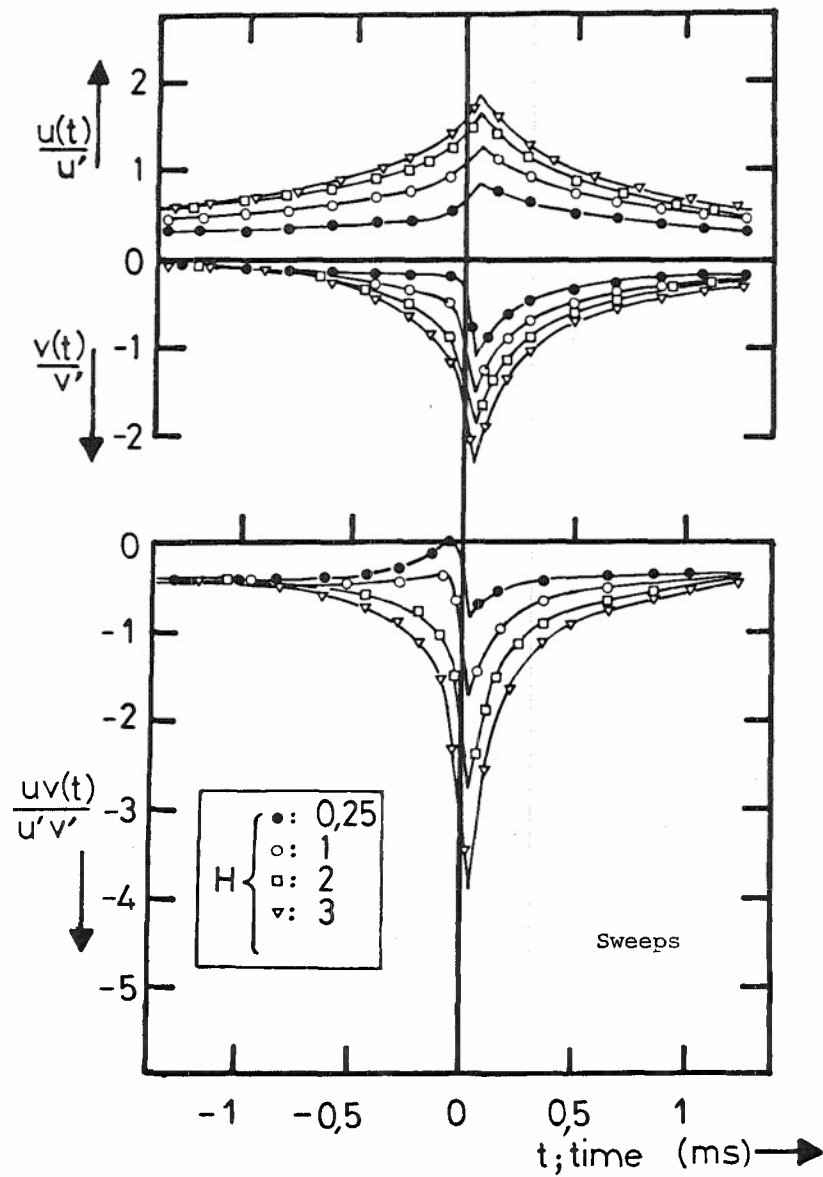
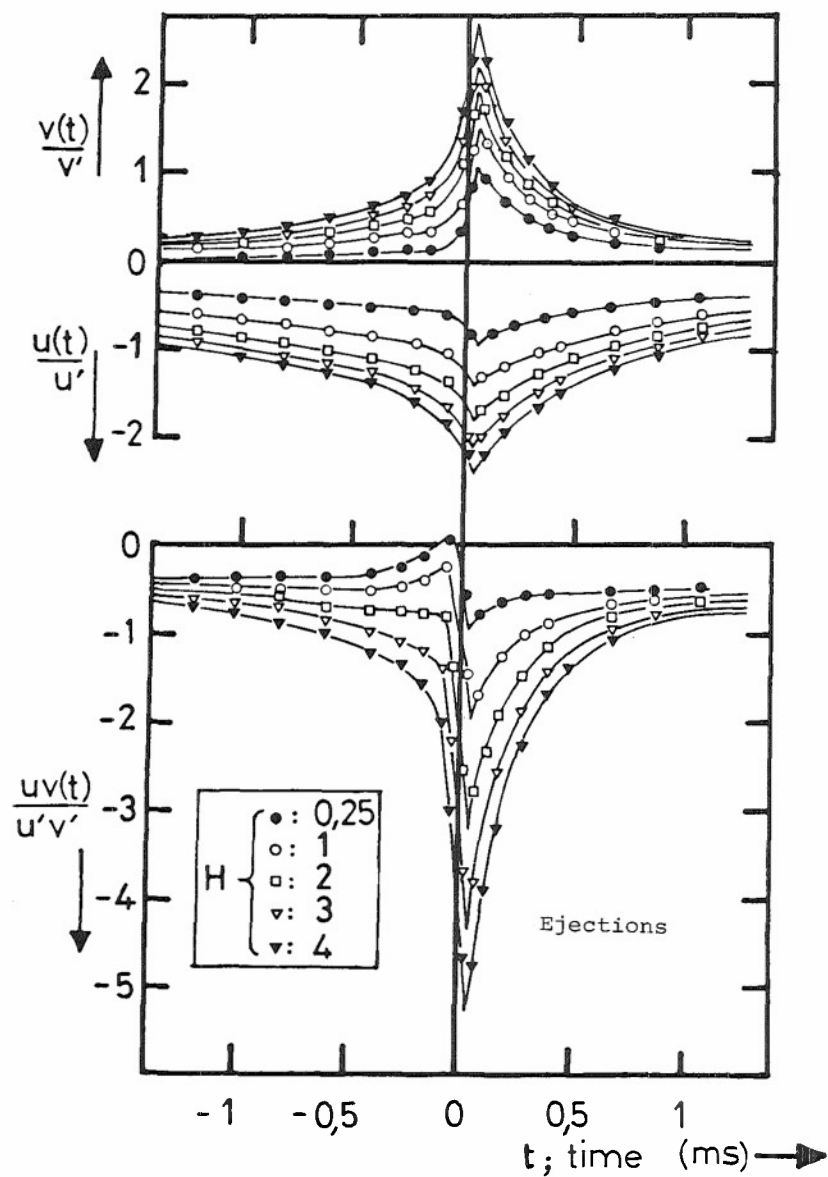


Fig. 24 - Signature of ejections and sweeps : ensemble averages of the  $u$ ,  $v$  and  $uv$  signals around the time of detection,  $t = 0$ , as function of the detection level  $H$  of  $|uv|$ .  
(smooth pipe,  $Re = 135\,000$  -  $y/R = 0.40$  - COMTE-BELLOT, SABOT & SALEH 1979)

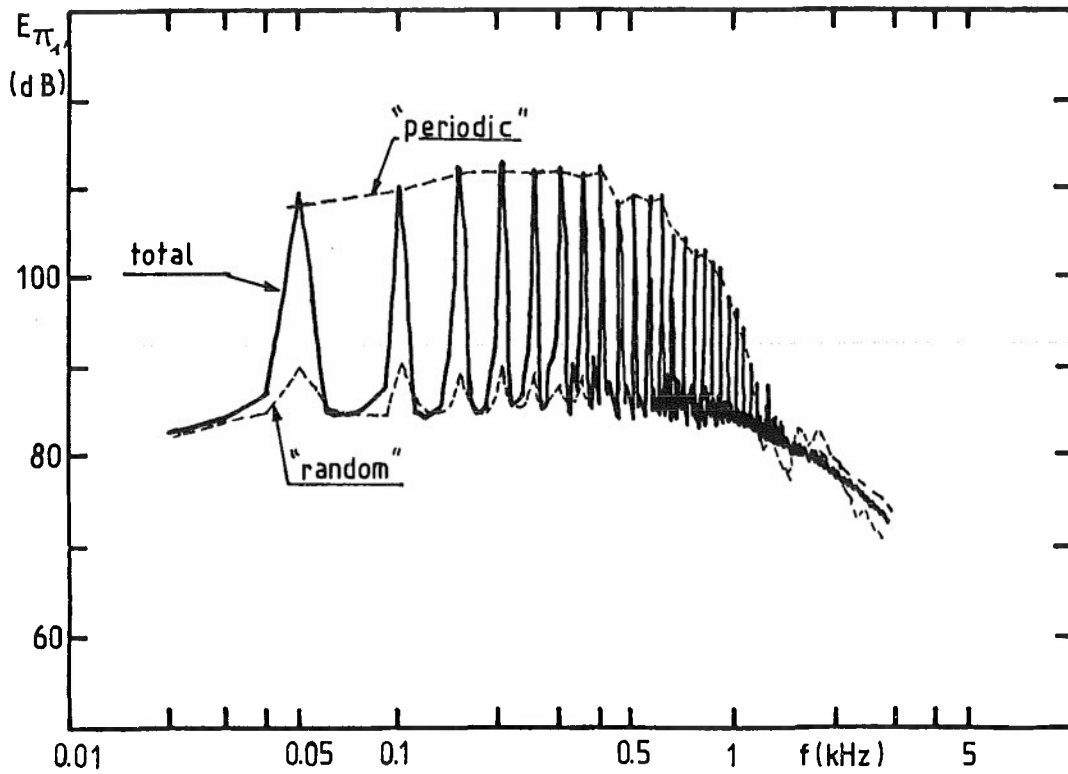


Fig. 25 - Example of periodic averaging : wall pressure spectra on a rotor blade in the case of upstream disturbances (MICHEL, ARBEY & SUNYACH 1979)

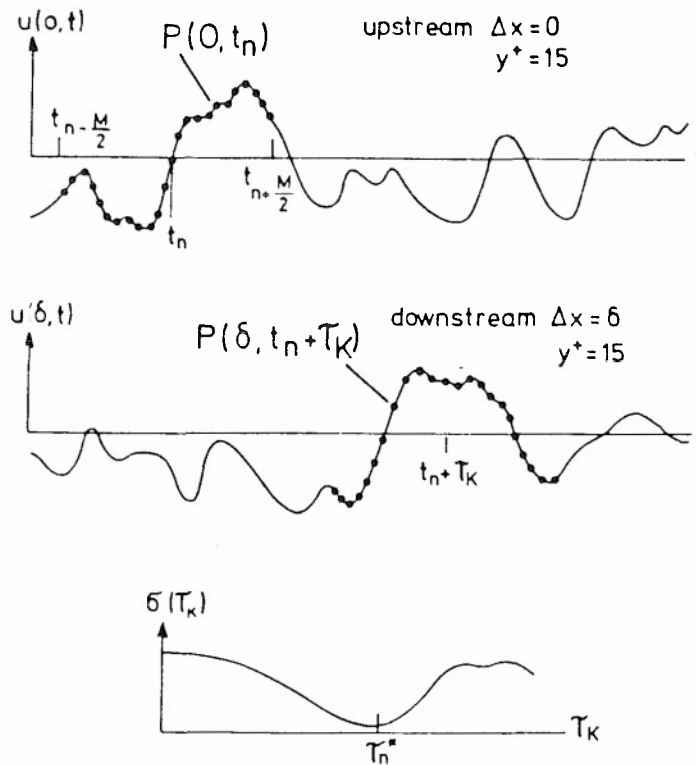


Fig. 26 - Conditional averaging with correction for random convection. The upper curve shows the original pattern  $P(0, t_n)$  obtained from the marked individual time points of the  $u(0, t)$  signal upstream. The indicated time points of the downstream signal in the middle trace are used to form one of the  $P(\delta, t_n + \tau_K)$  patterns. The variance between the patterns as  $\tau_K$  is varied is shown at the bottom. The minimum value at  $\tau_n^*$  corresponds to the "best" match between the patterns. (BLACKWELDER 1977)

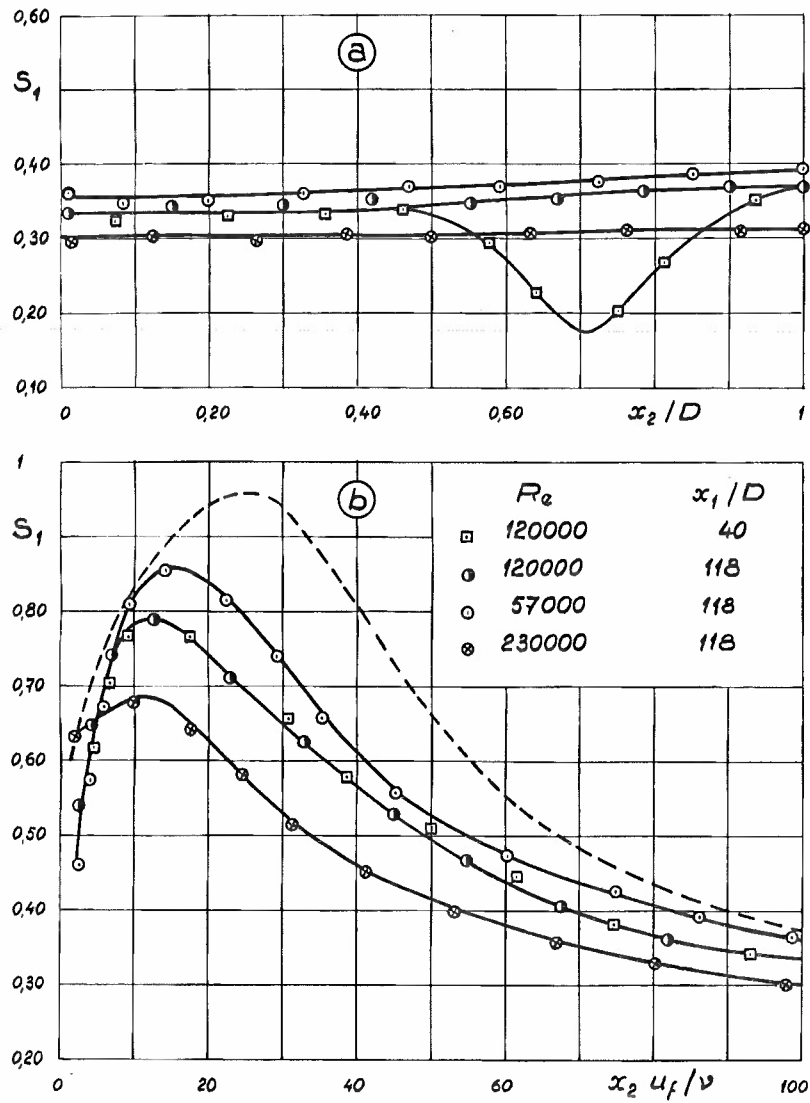


Fig. 27 - Skewness factor of  $\partial u / \partial t$  in the outer region (a) and in the wall region (b) :  
□ ● ○ ⊗ COMTE-BELLOT 1965  
- - - - - WALLACE, BRODKEY & ECKELMANN 1977  
( $Re = 7700$ )

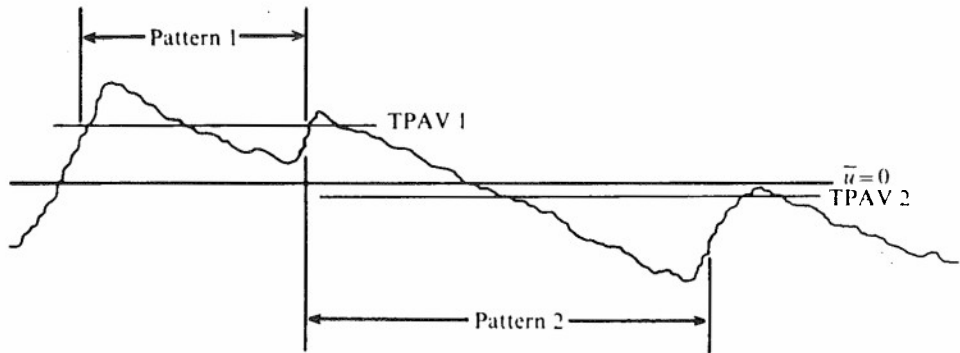


Fig. 28 - Pattern recognition technique : sketch of the signal retained for positive  $\partial u / \partial t$  skewness (WALLACE, BRODKEY & ECKELMANN 1977)

ETUDE EXPERIMENTALE DES APPORTS ET DES EJECTIONS  
DE FLUIDE DANS UNE COUCHE LIMITE TURBULENTE

M. ELENA, L. FULACHIER, R. DUMAS

Institut de Mécanique Statistique de la Turbulence  
L. A. C.N.R.S.

12, Avenue Général Leclerc - 13003 - MARSEILLE

-----

# SOMMAIRE

Les résultats expérimentaux présentés concernent aussi bien la structure de la zone interne qu'externe de la couche limite.

Pour étudier la phénoménologie du champ turbulent, la chaleur est utilisée comme contaminant passif dans de nombreux cas d'expériences.

Dans la sous-couche visqueuse, l'écoulement a un caractère d'intermittence très net; en particulier les apports de fluide en provenance des zones plus éloignées de la paroi l'emportent nettement devant les éjections et pénètrent, par instant, jusqu'au sein de la sous-couche.

Lorsque l'on s'éloigne de la paroi, le nombre d'apports diminue et devient du même ordre que le nombre d'éjections de la zone pleinement turbulente. Les mesures de corrélations spatiotemporelles laissent à penser qu'il existe au moins dans la zone interne une liaison entre les apports et les éjections qui sont prépondérantes.

Des mesures de probabilités conditionnelles montrent que les trajectoires de ces perturbations sont en accord avec celles obtenues par visualisations ou mesures de diffusion thermique à partir d'un point situé à la paroi.

En outre, des mesures de corrélations spatiotemporelles en trois points indiquent que les éjections sont plus cohérentes et plus minces en envergure que les perturbations correspondant aux apports. Ces éjections s'élargissent lorsque l'on s'éloigne de la paroi et diffusent à travers la couche limite.

# SUMMARY

The experimental results which are presented concern the structure of the internal and external zone of the boundary layer.

To study the turbulent field, heat is used as a passive contaminant, in many experiments.

In the viscous sublayer, the flow has obvious intermittent characteristics; particularly the inward flows from regions which are farther from the wall prevail over the outward flows and penetrate the sublayer randomly.

As the number of inward flow decreases with uncreasing distance from the wall, it becomes of the same order as the number of outward flow in the fully turbulent region. The measurements of the space-time correlations reveal that, at least in the internal region, there exists a linkage between the inward and the outward flows, the latter being the more dominating.

Measurements of conditional probabilities show that the trajectories of these disturbances are in agreement with the trajectories obtained through visualizing or measuring thermal diffusion from a point located at the wall.

Additionally measurement of three point space-time correlations indicate that the outward flows are more coherent and spanwise thinner than the disturbances corresponding to the inward flow. These outward flows expend when moving off the wall and diffuse through the boundary layer.

-----

## LISTE DE SYMBOLES

$x, y, z$	Coordonnées rectangulaires
$x, r, \omega$	Coordonnées cylindriques
$t$	Temps
$(\bar{\quad}), (\quad)'$	Valeurs moyennes, fluctuations, avec $(\bar{\quad})' = 0$
$a$	Rayon du tube
$F_{\xi}$	Facteur d'aplatissement de la grandeur $\xi$ ; $F_{\xi} = \overline{\xi'^4} / (\overline{\xi'^2})^2$
$Re$	$= u_e \delta^{**} / \nu$
$S_{\xi}$	Facteur de dissymétrie de la grandeur $\xi$ ; $S_{\xi} = \overline{\xi'^3} / (\overline{\xi'^2})^{3/2}$
$u, v, w$	Composantes du vecteur vitesse instantanée
$u_d$	Vitesse moyenne de débit à travers le tube ; $u_d = (1/\pi a^2) \int_0^a \bar{u} 2\pi r dr$
$u_e$	Vitesse à l'extérieur de la couche limite, ou sur l'axe du tube
$u_*$	Vitesse de frottement
$y^+$	$= y u_* / \nu$
$\delta, \delta_{99}$	Épaisseur de couche limite, à, $u = \bar{u}_e$ , à $\bar{u} = 0.99 u_e$
$\delta^{**}$	Épaisseur de quantité de mouvement: couche limite tube $\delta^{**} = \int_0^{\delta} (\bar{r} \bar{u} / \rho_e u_e) (1 - \bar{u} / u_e) dy$ $\delta^{**} = (\bar{a}^2 / 2) \int_0^1 (\bar{P} \bar{u} / \rho_e u_e) (1 - \bar{u} / u_e) d(\bar{r}/a)^2$
$\theta$	Température instantanée
$\theta_d$	Température de débit $\theta_d = (2 / \rho_d u_d a^2) \int_0^a \bar{P} \bar{u} \bar{\theta} r dr$
$\theta_e$	Température à l'extérieur de la couche limite, ou sur l'axe du tube
$\theta_p$	Température à la paroi
$\nu$	Coefficient de viscosité cinématique
$\rho$	Masse volumique
$\rho_d$	Masse volumique de débit $\rho_d = (2 / a^2 u_d) \int_0^a \bar{P} \bar{u} r dr$
$\tau$	Décalage de temps
$\gamma$	Facteur d'intermittence



## 1. INTRODUCTION

Bien que la couche limite turbulente soit bien connue en ce qui concerne ses propriétés moyennes, le mécanisme profond de création de la turbulence près de la paroi, notamment, et de son interaction avec la turbulence préexistante est encore un sujet de discussions. Des schémas d'ailleurs partiels sont proposés; on peut se reporter aux articles récents de Praturi et Brodkey (1) et de Blackwelder (2). Une vue générale de la couche limite est donnée par Willmarth (3). Cependant tous les auteurs sont d'accord sur un certain nombre de faits : il se forme continuellement près de la paroi ( $y \sim 10$ ) des structures allongées instationnaires de périodicité moyenne en envergure de l'ordre de  $\frac{50 \delta}{u_*}$  (4)

qui sont éjectées dans la zone interne ( $y^+ \leq 100$ ) en donnant lieu à des fortes bouffées de turbulence, conformément aux visualisations de Kline et al. (5). Ce processus semble être lié à celui observé par Corino et Brodkey (6); les bouffées de turbulence sont décrites comme résultant de l'interaction de fluide à vitesse relativement élevée ("sweeps") avec du fluide plus lent en provenance de la paroi ("éjections"). Certaines analogies sont faites avec les instabilités conduisant à la formation des "spots" de turbulence dans la transition laminaire-turbulent sur une paroi lisse; en particulier, le phénomène est essentiellement tridimensionnel. Quant à la périodicité moyenne du phénomène, elle semble plutôt être liée aux paramètres globaux  $u_e$  et  $\delta$  (7). Toutefois, il n'est pas établi que le processus conduisant à une bouffée de turbulence soit sous la dépendance de grands tourbillons préexistants dans la zone pleinement turbulente par exemple. La question est également posée en ce qui concerne la diffusion des bouffées de turbulence en aval à travers la couche limite; en particulier, est-ce que les protubérances de turbulence dans la zone d'intermittence sont en relation directe avec les éjections depuis la paroi? A ce propos, notons que, le volume des protubérances étant beaucoup plus grand que celui des éjections, il ne pourrait s'agir que d'entraînement de fluide, de façon analogue au grossissement d'un tourbillon au cours du temps, ou alors d'un phénomène "d'apairage".

Les résultats expérimentaux qui sont présentés ci-après concernent principalement la fréquence des perturbations, éjections et apports, leurs trajectoires près de la paroi, leurs développements à travers la couche limite et enfin leurs caractères tridimensionnels. Ils sont analysés compte tenu des schémas précités. Notons que nous appellerons éjections, des séquences où le fluide est en provenance d'une région plus près de la paroi que la position de mesure considérée; il n'y a pas nécessairement concordance avec les "éjections" précitées, observées par Corino et Brodkey. Nous appellerons apports, des séquences où le fluide est en provenance d'une région plus éloignée de la paroi que la position considérée; là encore il n'y a pas nécessairement concordance avec les "sweeps" mentionnés précédemment.

Les techniques de mesure utilisent essentiellement les corrélations spatiotemporelles triples (8,9) en deux points et en trois points (10 a et b) ainsi que les contingences spatiotemporelles (11, 12). La paroi étant légèrement chauffée, la chaleur est utilisée comme contaminant presque passif servant d'indicateur (13, 14, 15).

## 2. METHODES DE MESURES ET CONDITIONS EXPERIMENTALES

Les mesures ont été effectuées dans deux types d'écoulements. Les zones à proximité de la paroi, et notamment la sous-couche visqueuse, ont été analysées à partir de mesures effectuées dans un conduit cylindrique de section circulaire; au delà de  $y^+ \approx 20$ , l'analyse a été faite à partir de résultats expérimentaux obtenus dans des couches limites de plaques planes.

Dans ces différentes expériences, les parois pouvaient être légèrement chauffées, les écarts de température maximaux,  $\theta_p - \theta_e$ , étant de l'ordre de 20 K. Avec les vitesses maximales utilisées ( $u \sim 10 \text{ ms}^{-1}$ ), même au voisinage de la paroi, on peut considérer que la chaleur se comporte comme un contaminant pratiquement passif, tout au moins en ce qui concerne les fluctuations (14). Toutefois, on doit signaler que même ce léger chauffage de la paroi entraîne une modification de la composante  $v$  de la vitesse moyenne perpendiculaire à celle-ci (16, 17). Ainsi, l'étude de la structure du champ turbulent a été faite soit à partir des fluctuations des composantes  $u'$  et  $v'$  de vitesse, soit à partir des fluctuations de température. En effet, la distribution de la température instantanée,  $\theta$ , est sous la dépendance du vecteur vitesse instantanée (14, 18). Lorsque la chaleur peut être considérée comme un contaminant passif, comme c'est le cas ici, sa diffusion par la turbulence peut être utilisée pour décrire le champ turbulent et plus spécialement les structures à grandes échelles. En d'autres termes, comme le souligne notamment Bradshaw (19), la chaleur permet de marquer le fluide; de plus, l'utilisation d'échantillonnage conditionnel permet de connaître la provenance des masses fluides considérées.

### 2.1. CONDITIONS EXPERIMENTALES

#### 2.1.1. Conduit Cylindrique

Il s'agit d'une conduite de section circulaire (15) de diamètre  $2a = 76,6 \text{ mm}$ , de longueur  $L = 1116 \text{ mm}$ , dont la paroi peut être chauffée. Elle est précédée d'un tube de 52 diamètres de long environ dans laquelle se développe un écoulement turbulent isotherme. Les mesures sont effectuées dans une section située à 12,8 diamètres du début du chauffage. Les grandeurs caractéristiques de l'écoulement sont les suivantes :  $u_e = 8,27 \text{ ms}^{-1}$ ,  $u_d = 6,7 \text{ ms}^{-1}$ ,  $u_* = 0,37 \text{ ms}^{-1}$ ,  $Re = 1440$

$$\theta_p - \theta_e = 25 \text{ K}, \theta_p - \theta_d = 22 \text{ K}$$

#### 2.1.2. Couche Limite Isotherme

Les mesures concernant les fluctuations de vitesse ont été principalement effectuées dans la couche limite turbulente se développant sous une plaque plane suspendue dans une veine d'expériences  $S_1$  ( $0,8 \times 0,8 \times 4 \text{ m}$ ), à 45 cm en dessus du plancher (20). A la section où les mesures ont été effectuées (position du point  $P_0$  amont, voir paragraphe 2.4), les conditions expérimentales  $S_1$  sont les suivantes :

$$u_e = 16 \text{ ms}^{-1}, \delta = 54 \text{ mm}, u_* = 0,59 \text{ ms}^{-1}, Re = 6120.$$

Le gradient longitudinal de pression statique est négligeable :  $\frac{\delta^{**}}{1/2 \rho u_e^2} \frac{dp}{dx} \approx -0,9 \cdot 10^{-6}$ .

### 2.1.3. Couche Limite Sur Paroi Chauffée

Les mesures concernant les fluctuations de température ont été faites dans la couche limite turbulente se développant sur la plaque plane chauffée constituant le plancher de la veine d'expériences (14) d'une autre soufflerie  $S_2$  ( $0,56 \times 0,56 \times 4,8 \text{ m}$ ). Les caractéristiques expérimentales dans  $S_2$  sont les suivantes, à la section où les mesures ont été effectuées (position du point  $P_0$  amont, voir paragraphe 2.7).

$$u_e = 12,2 \text{ ms}^{-1}, \delta = 59 \text{ mm}, u_* = 0,46 \text{ ms}^{-1}, \\ Re = 4750, \theta_p - \theta_e \approx 22 \text{ K}.$$

Le gradient longitudinal de pression est légèrement négatif :  $\frac{\delta^{**}}{1/2 \rho u_e^2} \frac{dp}{dx} \approx -44 \cdot 10^{-6}$ .

## 2.2. TECHNIQUE DE MESURE DES FLUCTUATIONS DE VITESSE ET DE TEMPÉRATURE

Les signaux relatifs aux fluctuations des composantes  $u'$  et  $v'$  de la vitesse ont été obtenus en écoulement isotherme à l'aide d'anémomètres à fils chauds fonctionnant à résistance constante, avec circuit de linéarisation. Ces fils, en platine rhodiée (10% Rh), ont un diamètre  $d$  de  $5 \mu$ , leur longueur  $l$  est de l'ordre de  $1 \text{ mm}$  ( $l/d \approx 200$ ).

La composante longitudinale  $u'$  est mesurée à l'aide d'un fil droit. Une sonde à fils croisés en X permet d'isoler les composantes longitudinale  $u'$  et transversale  $v'$  instantanément. L'écartement choisi entre les deux fils est de  $0,4 \text{ mm}$ , de telle sorte que l'influence d'un fil sur l'autre soit négligeable sans que pour autant l'effet d'intégration spatiale soit critique (20).

Les fluctuations de température sont détectées à l'aide d'un anémothermomètre à fil "froid" fonctionnant à intensité constante. Les fils utilisés sont en platine et ont un diamètre de  $1 \mu$ . Des précautions nécessaires pour isoler les fluctuations de températures doivent être prises (21). L'intensité  $I$  est de  $0,15 \text{ mA}$ , ce qui correspond à un coefficient de surchauffe de  $3 \cdot 10^{-4}$  et à un rapport de sensibilité vitesse/température de l'ordre de  $10^{-4}$  dans le cas le plus défavorable. Dans les conditions expérimentales précitées, l'erreur relative due à la contamination de  $u'$  sur la variance  $\overline{\theta'^2}$  des fluctuations de température est, dans le cas le plus défavorable, de l'ordre de  $10^{-3}$ . Une compensation par circuit électronique analogique de l'inertie thermique des fils a été faite bien que la valeur de la constante de temps soit faible ( $50 \mu\text{s}$  pour  $\bar{u} = 5 \text{ ms}^{-1}$ , (15)). L'allongement  $l/d$  a été choisi de l'ordre de 600 afin que les effets de bouts jouent un rôle mineur, sans que pour autant l'intégration spatiale soit critique.

## 2.3. UTILISATION DES FLUCTUATIONS INSTANTANÉES

Afin de mettre en évidence les apports et les éjections au voisinage immédiat de la paroi des enregistrements des fluctuations instantanées de la composante longitudinale  $u'$  de vitesse et de température  $\theta'$  ont été effectués. Pour privilégier les fluctuations de grandes amplitudes, tout en conservant leur signe, les cubes instantanés,  $u'^3$  et  $\theta'^3$ , des fluctuations  $u'$  et  $\theta'$  ont été déterminés. Ces fluctuations  $u'$  et  $\theta'$  ont été normées par rapport à leur écart-type; ainsi, toutes les fluctuations d'amplitude inférieure, en valeur absolue, à une fois l'écart type du signal relatif à  $u'$  ou  $\theta'$  sont très atténuées; au contraire, toutes les fluctuations d'amplitude supérieure à cet écart-type sont amplifiées.

Dans le cas d'expérience en conduit cylindrique (Cf 2.1.1.), ces cubes ont été obtenus au calculateur à partir de l'acquisition numérique des signaux relatifs soit à  $u'$  soit à  $\theta'$  (Cf figure 3). La fréquence d'échantillonnage des signaux est de  $12 \text{ KHz}$ ; cette fréquence est suffisante vue l'étendue spectrale des variables (15).

Une méthode analogique a été utilisée (22) dans le cas d'expérience relatif à la couche limite isotherme. Les enregistrements des cubes instantanés  $u'^3$  ont permis de déterminer le nombre d'apports et d'éjections à travers la couche limite (Cf. figure 4). Avec le critère de seuil adopté, seuls les signaux d'amplitude supérieure à l'écart type sont pris en compte.

## 2.4. CORRELATIONS SPATIOTEMPORELLES EN DEUX POINTS

Ces mesures ont été effectuées dans les couches limites précitées (Cf 2.1.2. et 2.1.3.). Le point  $P_0$  situé en amont est fixe et le point situé en aval peut se déplacer, soit perpendiculairement à la paroi (point P figure 1), soit latéralement (point  $P_1$  ou  $P_2$  figure 2).

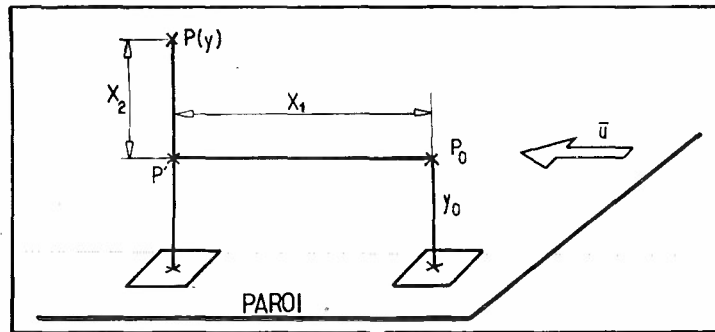


Fig. 1 Mesures spatiotemporelles en deux points P0, P.

L'écart longitudinal  $X_1$  entre  $P_0$  et  $P$  (voir figure 1 ou 2) est quelque peu supérieur à l'épaisseur  $\delta$  ( $X_1 = 1,41\delta$ , cas d'expérience en couche limite isotherme, figure 1;  $X_1 = 1,86\delta$ , cas d'expérience en couche limite sur paroi chauffée, figure 2) afin de privilégier les structures à grande échelle, porteuses d'énergie cinétique, qui jouent un rôle fondamental dans les écoulements cisailés.

D'autre part, pour donner de l'importance aux fluctuations de forte amplitude les corrélations triples ont été souvent utilisées. Elles ont de plus l'avantage de donner le signe des fluctuations dominantes. En fait ce sont les coefficients de corrélations qui ont été mesurés : soit les coefficients de corrélation double

$$r_{\theta\theta} = \overline{\theta'_0(t) \theta'(t+\tau)} / (\overline{\theta_0'^2} \overline{\theta'^2})^{1/2}$$

$$r_{u_0v} = \overline{u'_0(t) v'(t+\tau)} / (\overline{u_0'^2} \overline{v'^2})^{1/2}$$

soit les coefficients de corrélation triple

$$r_{u_0,uu} = \overline{u'_0(t) u'^2(t+\tau)} / (\overline{u_0'^2} (\overline{u'^2 - \overline{u'^2}})^2)^{1/2}$$

$$r_{u_0,uv} = \overline{u'_0(t) (u'v')(t+\tau)} / (\overline{u_0'^2} (\overline{u'v' - \overline{u'v'}})^2)^{1/2}$$

$$r_{u_0,vv} = \overline{u'_0(t) v'^2(t+\tau)} / (\overline{u_0'^2} (\overline{v'^2 - \overline{v'^2}})^2)^{1/2}$$

Ces mesures ont été effectuées avec un corrélateur P.A.R. (20, 23)

L'étude (20), en particulier, des signes des corrélations triples précitées ainsi que celle de leur valeur absolue, permet de mettre en évidence quel est le "mode" de turbulence qui prédomine, apport ou éjection.

## 2.5. CORRELATIONS SPATIOTEMPORELLES CONDITIONNELLES EN DEUX POINTS

Afin de mettre en évidence de façon plus directe les apports et les éjections, nous avons introduit des corrélations spatiotemporelles conditionnelles (10 a et b, 23) la condition portant sur le signe des fluctuations. Par exemple, en ce qui concerne les fluctuations de température  $\theta'$ , si  $\theta'_0 > 0$  cela correspond à de l'air chaud en provenance de régions plus proches de la paroi, si  $\theta'_0 < 0$  cela correspond à de l'air froid en provenance de régions plus éloignées de la paroi.

Les corrélations spatiotemporelles conditionnelles sont définies par :

$$R_{m,n}(\tau) = \overline{J(t) \theta'_0(t) \theta'(t+\tau)} / (\overline{\theta_0'^2} \overline{\theta'^2})^{1/2}$$

où  $m$  et  $n$  sont des signes, + ou -, relatifs à  $\theta'_0(t)$  et  $\theta(t+\tau)$ . Pour un couple choisi de signes  $m$  et  $n$ ,  $J(t) = 1$  lorsque  $\theta'_0(t)$  a le signe  $m$  et  $\theta(t+\tau)$  le signe  $n$ ; dans les trois autres cas  $J(t) = 0$ .

Ces corrélations conditionnelles ne sont pas des coefficients de corrélation, mais chacune représente la contribution d'un couple de fluctuations de signes donnés au coefficient de corrélation total :

$$r_{\theta\theta} = R_{++} + R_{+-} + R_{-+} + R_{--}$$

Notons que cette méthode a aussi été appliquée à la corrélation  $\overline{u'_0 v'}$ , généralisant ainsi aux corrélations spatiotemporelles la décomposition utilisée par Willmarth (3) pour les tensions de Reynolds.

La détermination des corrélations conditionnelles a été effectuée à l'aide d'un système d'acquisition et de traitement numérique de l'I.M.S.T.. L'acquisition des données a été faite sur deux voies par couples de valeurs correspondant aux fluctuations en  $P_0$  et  $P$ . Ce temps, indépendant de la cadence d'échantillonnage qui sépare les deux valeurs, est négligeable. En ce qui concerne la cadence d'échantillonnage, on a vérifié que la corrélation mesurée est correcte quelle que soit cette cadence, à condition que le nombre d'échantillons soit suffisant et que le temps d'intégration correspondant soit très grand par rapport aux échelles de temps du phénomène considéré (25). L'augmentation de la fréquence d'échantillonnage permet simplement une résolution incrémentale plus fine, mais il est alors nécessaire d'augmenter le nombre d'échantillons pour avoir un temps d'intégration suffisant. La cadence adoptée est de 2000 Hz ce qui correspond à un temps incrémental de  $0,5 \cdot 10^{-3}$  s, adapté aux conditions expérimentales. Le nombre de couples généralement traités est de 60 000, correspondant à un temps d'intégration de 30 secondes.

Des tests du programme de calcul numérique du coefficient de corrélation et des corrélations conditionnelles ont été effectués. Il semble que, principalement pour les décalages de temps faibles, la méthode numérique soit plus fiable et précise que la méthode utilisant le corrélateur P.A.R.

Les mesures ont été effectuées soit en couche limite sur paroi chauffée, soit en couche limite isotherme, les points  $P_0$  et  $P \rightleftharpoons P'$  étant à la même distance de la paroi, pratiquement sur une ligne de courant.

## 2.6. PROBABILITES SPATIOTEMPORELLES CONDITIONNELLES EN DEUX POINTS

Les corrélations conditionnelles précédemment introduites ne fournissent pas en fait un critère absolu de liaison statistique.

Certaines propriétés de la turbulence étant liées à des caractères non gaussiens, la nécessité de déterminer un tel critère nous a conduit à utiliser les probabilités conditionnelles spatiotemporelles (11). Ces probabilités sont ici relatives aux fluctuations de température. On considère les probabilités simples et composées telles que, par exemple :

$$\text{Prob} [\theta'_0(t)/\sigma_0 > h_0] ; \text{Prob} [\theta'(t)/\sigma > h]$$

$$\text{Prob} [\theta'_0(t)/\sigma_0 > h_0 \text{ et } \theta'(t+\tau)/\sigma > h]$$

$\sigma_0$  et  $\sigma$  sont les écarts types des fluctuations  $\theta'_0$  et  $\theta'$ ;  $h_0$  et  $h$  sont des seuils quelconques.

Pour caractériser le degré de liaison statistique entre les fluctuations nous introduisons la contingence  $\varphi$ . Par exemple :

$$\varphi^{++} = \text{Prob} [\theta'_0(t)/\sigma_0 > h_0 \text{ et } \theta'(t+\tau)/\sigma > h] - \text{Prob} [\theta'(t)/\sigma > h] \text{ Prob} [\theta'_0(t)/\sigma_0 > h_0]$$

Les signes + rappellent, dans l'exemple donné, que l'on ne considère que les séquences de fluide dont la température est plus élevée que la température moyenne aux points  $P_0$  et  $P$ . Si les événements  $\theta'_0(t) > h_0 \sigma_0$  et  $\theta'(t+\tau) > h \sigma$  sont statistiquement indépendants,  $\varphi^{++} = 0$ ; s'ils sont complètement liés, on a :

$$\varphi^{++} = \text{Prob} [\theta'_0(t)/\sigma_0 > h_0] [1 - \text{Prob} [\theta'(t)/\sigma > h]]$$

On introduit alors une contingence réduite, qui s'écrit, en utilisant la probabilité conditionnelle :

$$\Phi^{++} = \frac{\varphi^{++}}{\varphi^{++}} = \frac{\text{Prob} [\theta'(t+\tau)/\sigma > h \text{ si } \theta'_0(t)/\sigma_0 > h_0] - \text{Prob} [\theta'(t)/\sigma > h]}{1 - \text{Prob} [\theta'(t)/\sigma > h]}$$

Ainsi l'indépendance statistique est équivalente à  $\Phi = 0$  et la liaison complète entraîne  $\Phi = 1$ . Si les événements sont plus ou moins incompatibles,  $\varphi^{++}$  et  $\Phi^{++}$  ont des valeurs négatives. Des considérations similaires s'appliquent aux contingences  $\varphi^{--}$  et  $\Phi^{--}$  relatives aux séquences de fluide plus froid que les températures moyennes en  $P_0$  et  $P$ .

Différents seuils ont été utilisés :  $h = h_0 = 0$ , où l'on considère toutes les séquences où le fluide est chaud ou toutes celles où le fluide est froid, et  $h = h_0 = 1$ , correspondant au fluide très chaud ou bien très froid.

Les contingences conditionnelles spatiotemporelles ont été déterminées avec des méthodes numériques analogues et pour les mêmes conditions expérimentales, que les corrélations conditionnelles spatiotemporelles.

## 2.7. CORRELATIONS SPATIOTEMPORELLES EN TROIS POINTS

Afin de mettre en évidence le caractère tridimensionnel des structures turbulentes à grande échelle des mesures de corrélations spatiotemporelles en envergure ont été effectuées dans la couche limite turbulente sur paroi chauffée. Pour atteindre la largeur statistique du domaine de cohérence de ces structures, des mesures de corrélations spatiotemporelles des fluctuations de température en trois points ont été faites (10 a et b).

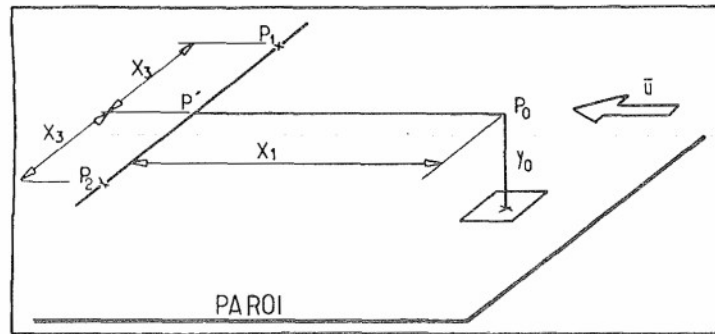


Fig. 2. Mesures spatiotemporelles en trois points  $P_0, P_1, P_2$ .

$P_0, P_1$  et  $P_2$  sont situés dans un plan parallèle à la paroi (figure 2). La distance  $X_1$  séparant le point  $P_0$ , situé en amont, du point  $P'$ , en aval, est de 1,86δ (Cf. 2-4); les deux points  $P_1$  et  $P_2$ , en aval, peuvent être déplacés symétriquement par rapport à  $P_0P'$ . Dans ces conditions, on définit un

coefficient de corrélation triple entre les fluctuations de température en  $P_0, P_1$  et  $P_2$ , avec un temps retard  $\tau$  entre  $P_0$  et  $P_1P_2$  :

$$r_{\theta_0\theta_1\theta_2} = \frac{\overline{\theta_0'(t)\theta_1'(t+\tau)\theta_2'(t+\tau)}}{[\overline{\theta_0'^2}(\overline{\theta_1'\theta_2'} - \overline{\theta_1'\theta_2'})^2]^{1/2}}$$

Si, pour un temps retard  $\tau$ , ce coefficient a une valeur importante ceci signifie que statistiquement des structures, qui sont passées à des instants  $t$  en  $P_0$ , atteignent simultanément les points  $P_1$  et  $P_2$  à des instants correspondants  $t+\tau$ . En d'autres termes, l'envergure statistique du domaine de cohérence est au moins de l'ordre de la distance  $P_1P_2$ . En faisant varier la distance  $P_1P_2$ , c'est à dire  $X_3$ , on obtient la carte des isocoéfficients de corrélation triple en fonction de  $\tau$  et  $X_3$  (Cf. figure 11).

Une interprétation similaire des corrélations spatiotemporelles doubles, par exemple entre  $P_0$  et  $P_1$ , n'est pas possible. En effet, on ne peut pas distinguer alors une structure de petite envergure ayant un parcours très aléatoire d'une structure cohérente de grande envergure. L'aire délimitée par la ligne où la corrélation spatiotemporelle double,  $r_{\theta_0\theta_1}$  ou  $r_{\theta_0\theta_2}$ , s'annule, correspond au domaine d'influence qui est évidemment plus large que le domaine de cohérence.

La considération des signes de  $r_{\theta_0\theta_1\theta_2}$ ,  $r_{\theta_0\theta_1}$  ou  $r_{\theta_0\theta_2}$ ,  $r_{\theta_1\theta_2}$  permet de montrer (Cf. 10 a) qu'il existe trois régions (voir figure 16). Dans la région I, le mode de turbulence statistiquement dominant correspond à la combinaison de signe ( $\theta'_0 > 0, \theta'_1 > 0, \theta'_2 > 0$ ). Il peut être interprété comme étant dû à de l'air chaud passant en  $P_0$  et transféré en aval à la fois en  $P_1$  et  $P_2$ . Les régions II et III correspondent respectivement aux combinaisons de signes ( $\theta'_0 < 0, \theta'_1 < 0, \theta'_2 < 0$ ) et ( $\theta'_0 > 0, \theta'_1\theta'_2 < 0$ ); les modes dominants qui y règnent peuvent être interprétés comme des apports d'air froid.

Les mesures ont été effectuées au corrélateur P.A.R. (23).

## 3. ANALYSE DES RESULTATS EXPERIMENTAUX

### 3.1. ZONES INTERNES

3.1.1. Des enregistrements des fluctuations de vitesse  $u'$  et de température  $\theta'$  ont été effectués jusqu'à une distance de la paroi  $y^+ = 1,7$  dans l'écoulement en conduite cylindrique. La figure 3 donne les cubes normalisés correspondants  $u'^3/(\overline{u'})^3$  et  $\theta'^3/(\overline{\theta'})^3$ ; ceux-ci mettent en relief

les signaux de forte amplitude qui sont déterminants dans le mécanisme non-linéaire de la turbulence. Les ordonnées donnent les pourcentages des fluctuations rapportées aux moyennes  $\bar{u}$  et  $\bar{\theta}$  locales. On constate qu'à la distance  $y^+ = 1,7$  seuls des apports de fluide plus froid, en provenance de zones un peu plus éloignées de la paroi, sont détectées. Les éjections de fluide plus chaud n'apparaissent que peu à peu, à mesure que l'on s'éloigne de la paroi. La figure 4 donne précisément des résultats obtenus dans une couche limite turbulente; ceux-ci concernent la fréquence d'apport  $N_a$  et la fréquence d'éjection  $N_e$  obtenues à partir des cubes  $u'^3/(\overline{u'})^3$ .

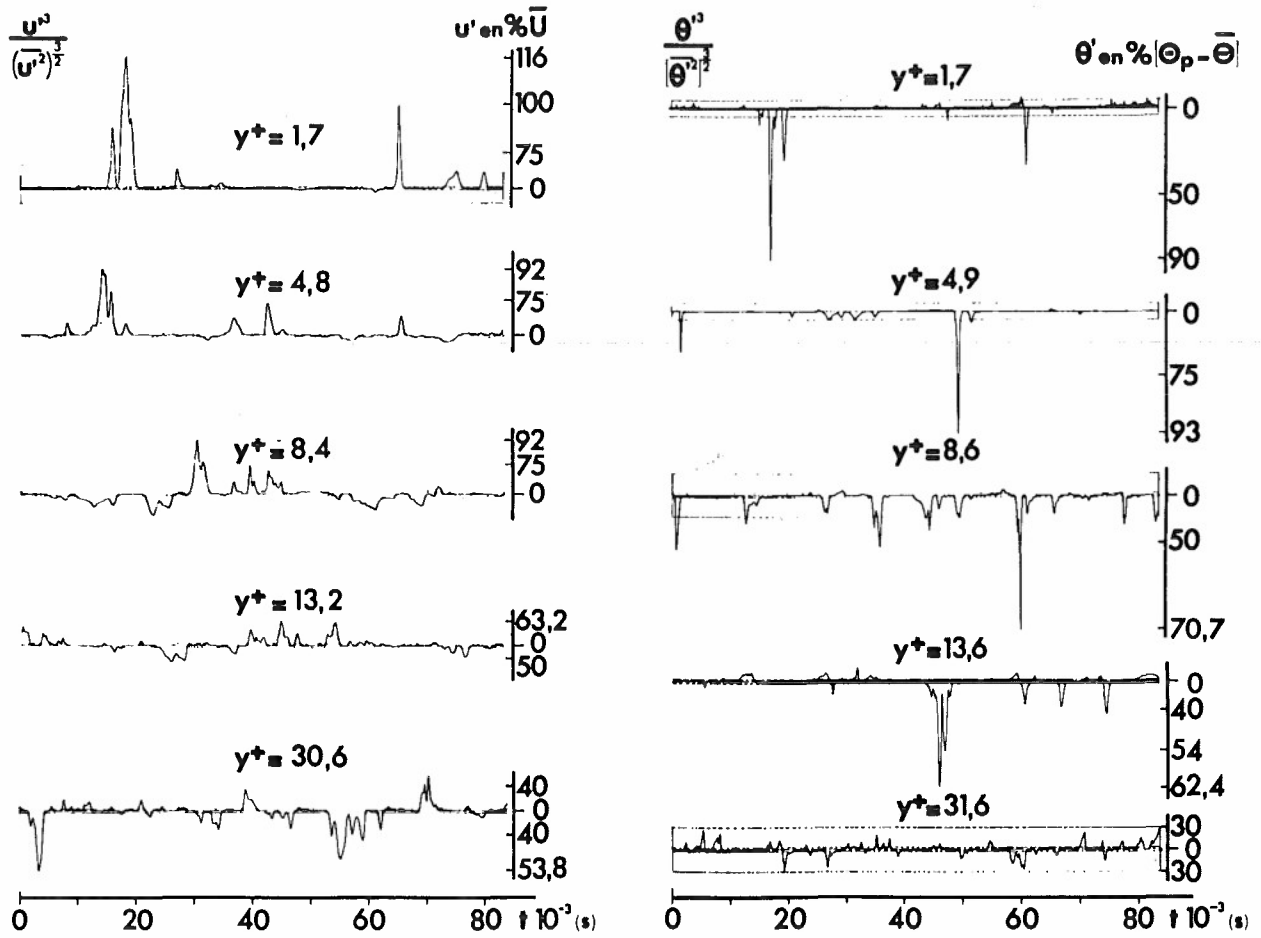


Fig. 3 Enregistrements de cubes normalisés des fluctuations  $u'$  et  $\theta'$ .  
Conduite cylindrique

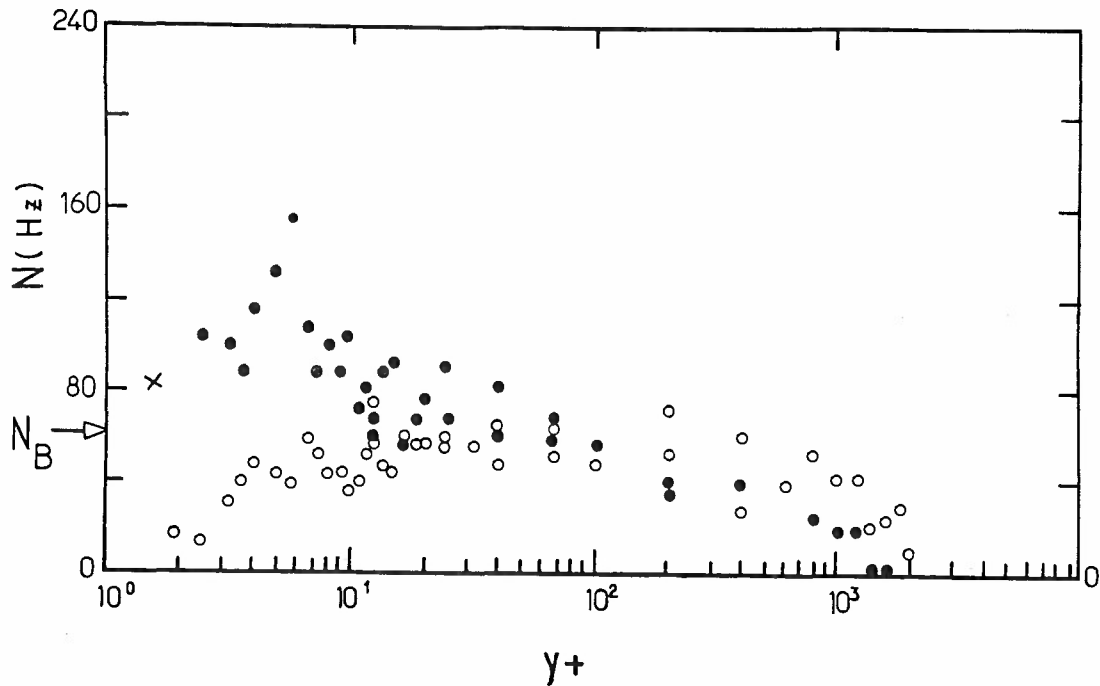


Fig. 4 Fréquence d'apports et d'éjections  
Couche limite  $S_1$ : ● apports, ○ éjections.  
Conduit cylindrique x apports.

$N_B$ : formule de Rao et al.(7).

On vérifie bien que, près de la paroi, seuls les apports subsistent. Un point de mesure de  $N_a$  à  $y^+ = 1,7$ , obtenu dans la conduite cylindrique, est également porté. Pour que la comparaison soit valable la formule de Rao donnée plus loin a été utilisée pour ramener  $N_a$  aux conditions de la couche limite  $S_1$ . Il s'agit surtout, semble-t-il, d'apports de couches très voisines par amincissements locaux de la sous-couche visqueuse ; par exemple, à  $y^+ = 1,7$ , l'apport correspondrait à du fluide venant en moyenne d'une zone située à  $y^+ = 5$  seulement. Par ailleurs cette figure confirme que la fréquence  $N_a$  d'éjections augmente lorsqu'on s'éloigne de la paroi,  $N_e$  étant égale à  $N_a$  à environ  $y^+ = 50$ , au début de la zone turbulente inertielle.

En ce qui concerne les valeurs de  $N_a$  et  $N_e$  il faut les comparer, par exemple, au nombre de bouffées de turbulence ou "bursts" qui serait donné par la formule de Rao (7) :  $N_B = 1,54 Re^{-0,73}$  soit  $N_B^* = 0,0026$ . Cette valeur correspond pratiquement à la fréquence  $N_e$  maximum d'éjections entre  $y^+ = 50$  et 100 environ, dans la zone de maximum des contraintes tangentielles de Reynolds (on définit  $N^* = N\bar{u}/u_*^2$ ).

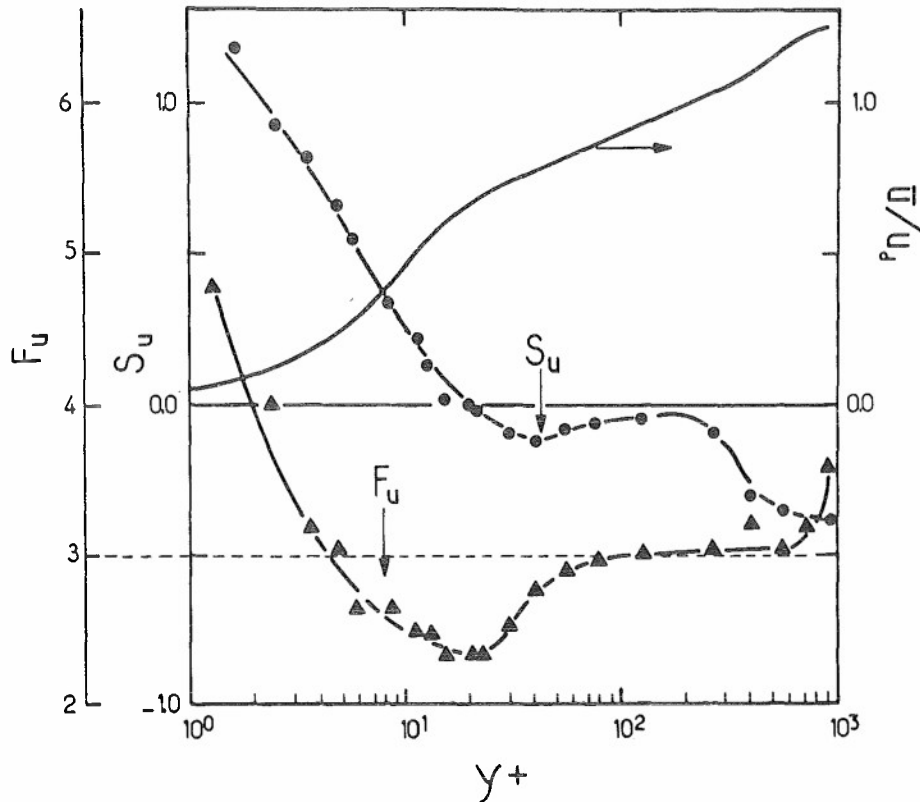


Fig. 5. Facteurs de dissymétrie  $S_u$  et d'aplatissement  $F_u$  relatifs à  $u'$ . Conduit cylindrique.

Les mesures des facteurs de dissymétrie  $S_u$  et  $S_\theta$  relatifs au conduit cylindrique sont présentées sur les figures 5 et 6. Elles confirment les résultats précités, en ce qui concerne la prédominance des survitesses et des refroidissements de grandes amplitudes sur les sousvitesses et les réchauffements près de la paroi. Les facteurs d'aplatissement  $F_u$  et  $F_\theta$  dépassent de beaucoup la valeur gaussienne,  $F = 3$ , très près de la paroi, ce qui indique un caractère intermittent de l'écoulement. Remarquons, par ailleurs, qu'aussi bien pour la vitesse  $u'$  que pour la température  $\theta'$ ,  $F_u$  et  $F_\theta$  passent par des valeurs minimales aux alentours de  $y^+ \approx 20$  (valeur pour laquelle  $S_u$  et  $S_\theta$  sont nuls). Ceci pourrait être dû (26) aux instabilités de type hydrodynamique, dont l'hypothèse est souvent avancée dans cette zone, et qui donnerait lieu à des trains d'ondes harmoniques ( $S = 0$ ,  $F = 1,5$ ).

A partir des mesures d'autocorrélation  $r(\tau)$  de  $u'$  et de  $\theta'$  on a déterminé la fréquence intégrale :

$$N_e = \left[ 2\pi \int_0^{\infty} r(\tau) d\tau \right]^{-1}$$

$\tau$  est un temps toujours relativement grand correspondant à la partie positive de  $r(\tau)$ .  $N_L$  est liée, avec l'hypothèse de Taylor, à l'échelle intégrale classique  $L$  :

$$L = \frac{\bar{u}}{2\pi N_L}$$



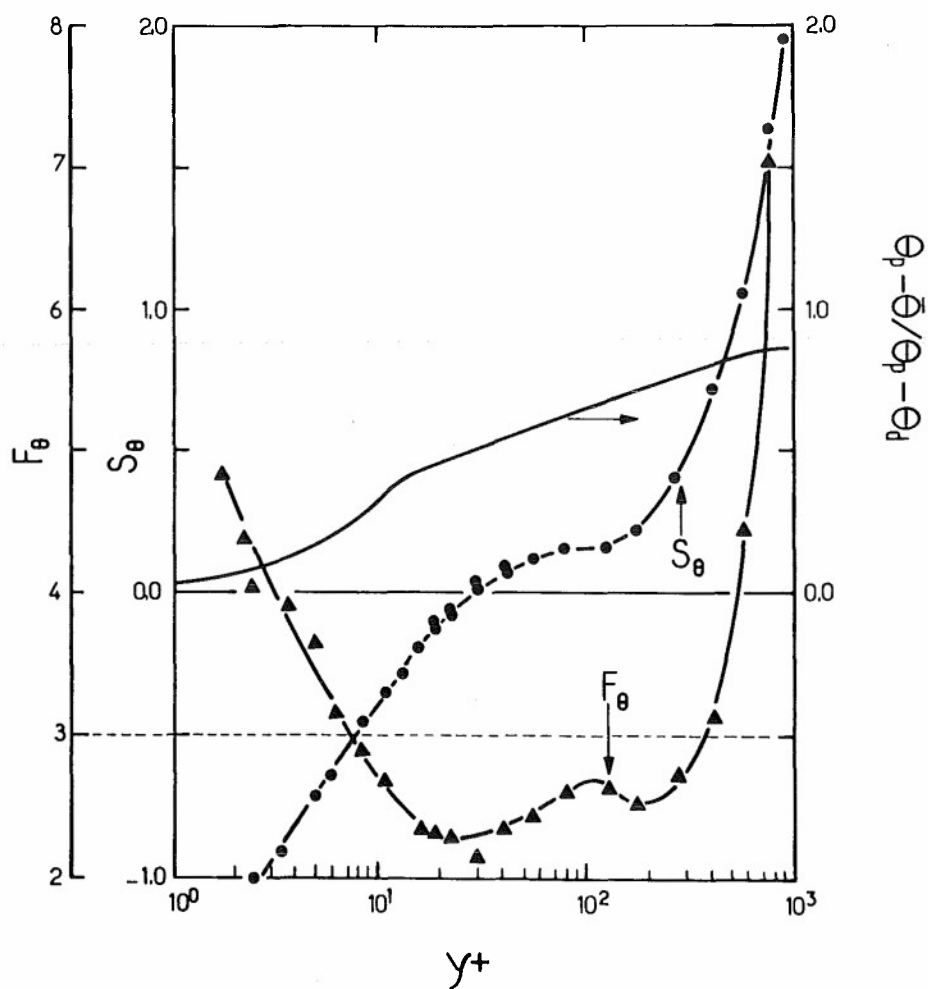


Fig. 6. Facteur de dissymétrie  $S_\theta$  et d'aplatissement  $F_\theta$  relatifs à  $\theta'$ . Conduit cylindrique.

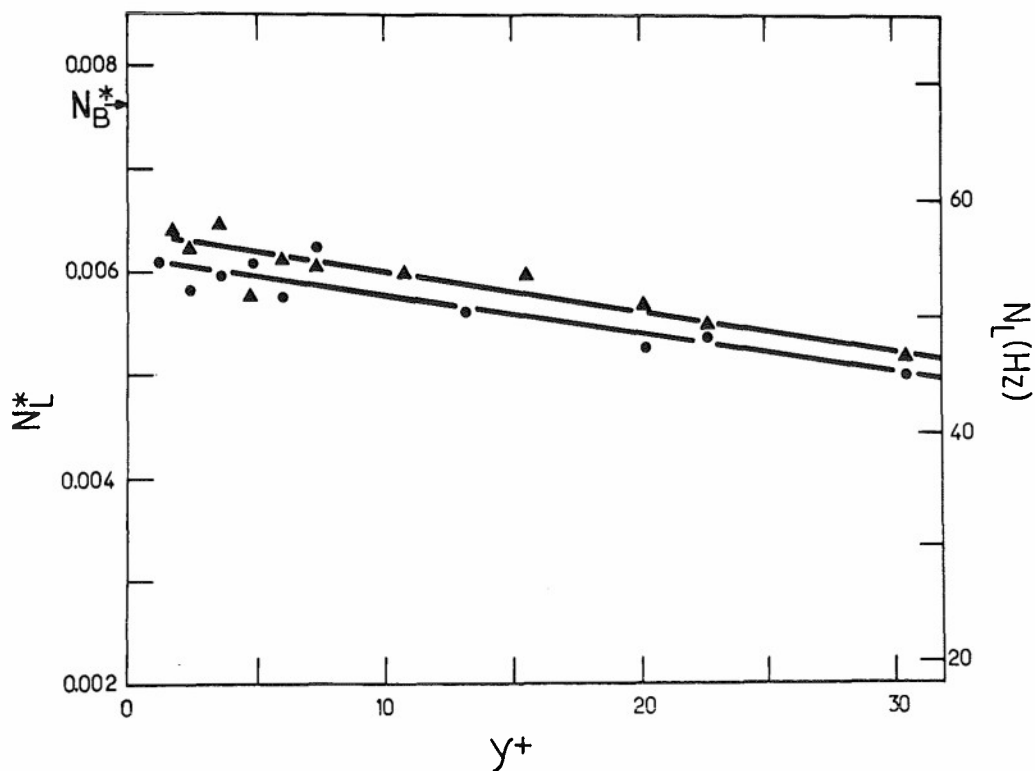


Fig. 7. Fréquences intégrales  $N_L^*$ ;  $\bullet, \blacktriangle$ , relatifs à  $u', \theta'$ . Conduit cylindrique.

Sur la figure 7 on a porté les fréquences adimensionnelles  $N_L^* = \frac{N_L \nu}{u_*}$ . Elles sont inférieures à la

valeur  $N_B^* = 0,0076$  calculée à partir de la formule de Rao précitée, dans l'écoulement considéré. Ceci montre que les échelles intégrales  $L_u$  et  $L_\theta$  sont plus grandes que celles correspondant aux distances moyennes entre les bouffées. L'échelle spatiale entre les bouffées correspondrait plutôt à celle du maximum de contraintes de Reynolds qui est comprise entre la macroéchelle et la microéchelle de Taylor, comme on peut s'en rendre compte en analysant les cospectres de  $\overline{u'v'}$  (14,27).

3.1.2. En ce qui concerne la liaison entre les apports et les éjections, des mesures de corrélation spatiotemporelles conditionnelles tendraient à confirmer qu'elle existe, du point de vue statistique, au moins dans certaines zones, comme on va le voir sur la figure 8 donnant le coefficient de corrélation

$$r(\tau) = \overline{\theta'(t)\theta'(t+\tau)} / (\overline{\theta'^2} \overline{\theta'^2})^{1/2}$$

ainsi que les différentes contributions selon les signes des fluctuations  $\theta'$ . La ligne PoP, parallèle à la paroi, située à  $y_0^+ = 22$ , est pratiquement une ligne de courant moyenne. En abscisse le temps adimensionnel  $\tau^* = \tau u_* / \delta$  est porté.  $\tau_m^*$  correspond au maximum de la corrélation et  $\tau_c^*$  correspond au temps de parcours de la distance  $X_1$  à la vitesse moyenne locale, soit  $\tau_c^* = X_1 / \delta$ . On constate que ,

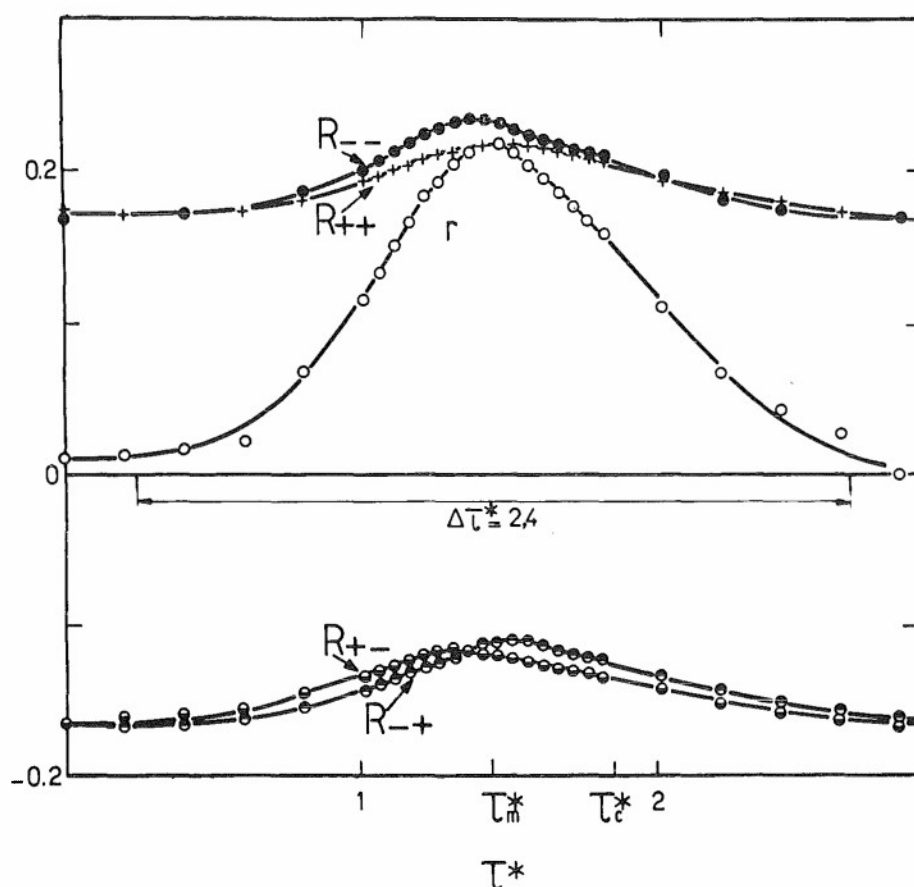


Fig. 8. Corrélations spatiotemporelles de température  $\theta'$ :  $r$  coefficient;  $R_{++}$ ,  $R_{--}$ ,  $R_{+-}$ ,  $R_{-+}$  corrélations conditionnelles.  
Couche limite  $S_2$ :  $y_0^+ = 22$ ,  $\overline{u}/u_e = 0,49$ ,  $X_1 = 1,86\delta$

comme il était attendu, les séquences d'apports  $R--$  (fluide froid) ont une célérité plus forte que la vitesse moyenne ; mais il est plus surprenant de constater que les séquences d'éjections  $R++$  (fluide chaud) ont aussi une célérité qui est plus grande que la vitesse moyenne. D'ailleurs on voit aussi que le temps  $\tau_m^* < \tau_c^*$ , c'est à dire que les fluctuations les plus cohérentes vont plus vite que la vitesse moyenne.

Finalement, dans cette région, il semble qu'il existe des séquences correspondant vraisemblablement aux bouffées de turbulence où les apports et les éjections sont liés. Ce résultat semble être spécifique à cette région, car des mesures similaires de  $r_{\theta\theta}$  montrent que les temps correspondant aux éjections deviennent supérieurs à  $\tau_c^*$  pour  $\gamma \geq 100$  (12).

Remarquons encore que la période moyenne du phénomène de "bursting" serait (7)  $\frac{\tau_{u_e}}{\delta} \approx 5$ ;

soit à la distance considérée ici  $\Delta \tau^* = 2,4$ , ce qui correspond en ordre de grandeur à la durée pendant laquelle la corrélation de  $r_{\theta\theta}$  a une valeur notable, comme on peut le voir sur la figure 8 où l'écart  $\Delta \tau^*$  a été porté. Toutefois, ceci ne signifie pas du tout que le temps de cohérence des bouffées de turbulence soit égal à  $\Delta \tau^* = 2,4$ , car il s'agit là, en raisonnant par analogie avec les corrélations en trois points comparées à celles en deux points (Cf para 2.7), d'un temps "d'influence" et non pas de "cohérence", qui peut lui être très nettement inférieur (voir par exemple Fig. 16a : envergures des corrélations double et triple).

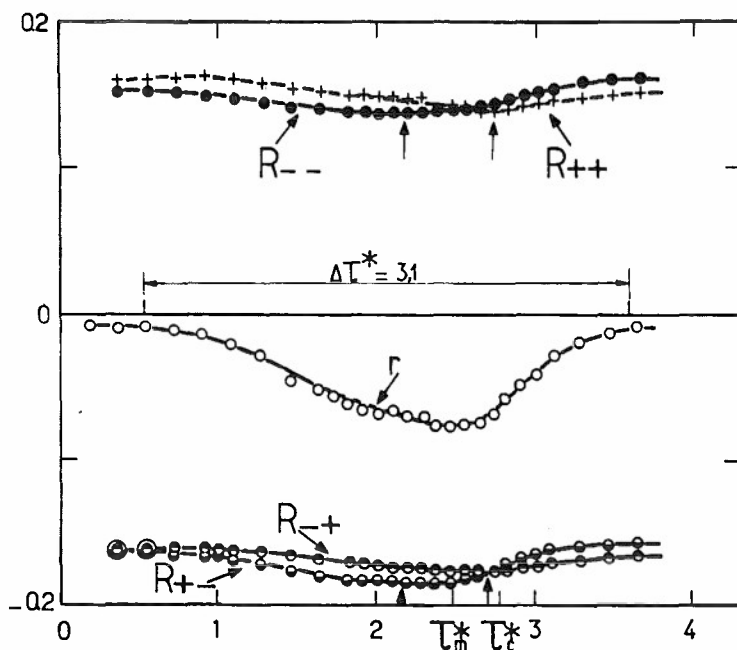


Fig. 9. Corrélations spatiotemporelles de vitesses  $u'_o$ ,  $v'$  :  
 $r$  coefficient;  $R+-$ ,  $R+-$ ,  $R++$ ,  $R--$ ; corrélations conditionnelles. Couche limite  $S_1$  :  $y_0^+ = 117$ ,  
 $u/u_e = 0,62$ ,  $x_1 = 2,78 \delta$ .

Des constatations analogues peuvent être faites à partir de la figure 9 donnant le coefficient de corrélation dans le temps

$$r_{u_o v} = \overline{u'_o(t) v'(t+\tau)} / (\overline{u'^2} \overline{v'^2})^{1/2}$$

Ces corrélations conditionnelles sont notées (Cf. para 2.5)  $R+-$  etc ... signifiant pour l'exemple choisi que  $u'_o(t)$  et  $v'(t+\tau) < 0$ . Les apports correspondent donc à  $R+-$  et les éjections à  $R+$ . On constate que même à cette distance de la paroi les séquences d'éjection ont statistiquement un temps optimum (minimum de  $R+-$ ) pratiquement égal au temps  $\tau_c$  compensateur du mouvement moyen, ce qui signifie que l'on a encore un effet d'entraînement des éjections par des apports.

Le temps  $\Delta \tau^* = 3,1$ , correspondant à la périodicité moyenne des bouffées, a été également porté sur la figure 9. On peut faire les mêmes commentaires que pour la figure 8.

3.1.3. On a aussi effectué une expérience significative du transport des perturbations à l'aide des corrélations spatiotemporelles de température, le point en amont  $P_0$  étant placé à  $\gamma_0^+ = 23$  et le point en aval  $P$  étant déplacé longitudinalement et perpendiculairement à la paroi (Fig. 1). En particulier les lignes de corrélations spatiotemporelles  $r_{\theta\theta}(x, \gamma, \tau)$  maximales, c.à.d. pour la distance  $y_m$  et

le temps  $\tau_m$  optimaux qui donnent la corrélation maximale à un  $X_1$  fixé, ainsi que les lignes de contingences maximales définies de façon analogue, sont à priori significatives de la diffusion des perturbations,

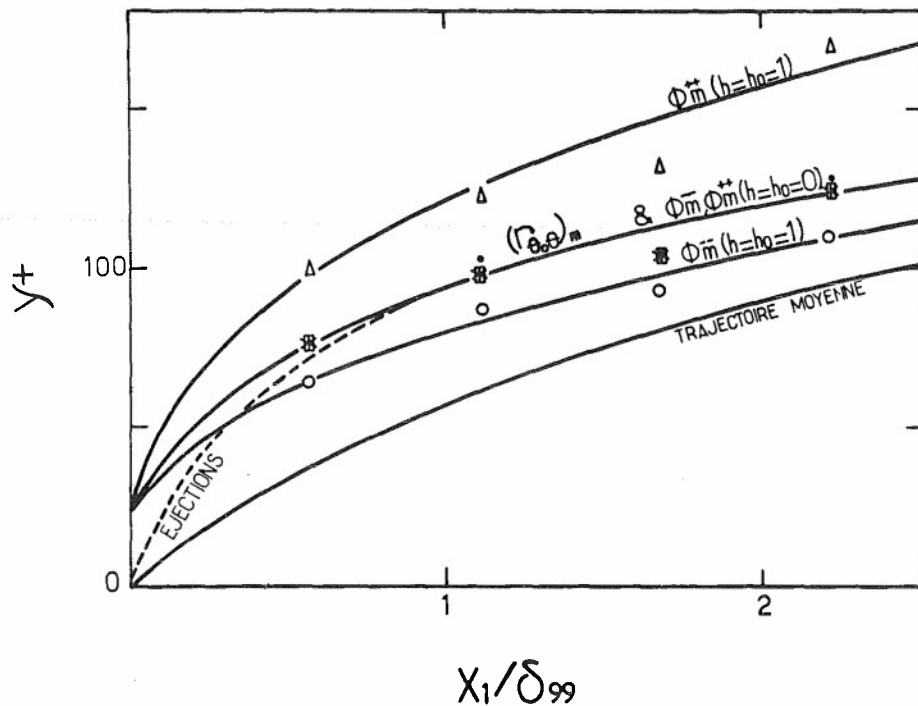


Fig. 10. Couche limite  $S_7$  :  $y^+ = 23$ . Coefficients de corrélations et contingences réduites spatiotemporelles.

•  $(r_{\theta_0\theta})_m$ ,  $\square \Phi_m^{++}(h=h_0=0)$ ,  $\times \Phi_m^{--}(h=h_0=0)$ ,  
 $\Delta \Phi_m^{++}(h=h_0=1)$ ,  $\circ \Phi_m^{--}(h=h_0=1)$ ,  
 --- Ejections, visualisation Rundstadler et al. (35).  
 — Trajectoire moyenne, Shlien et Corrsin (28)

Sur la Figure 10 on a porté le coefficient de corrélation maximal  $(r_{\theta_0\theta})_m$  et les contingences réduites maximales  $\Phi_m$  pour différents seuils  $h$  (Cf. para 2.6.). A titre de comparaison on a également

porté la ligne "ejected eddies" tracée à partir des visualisations par Kline et al. (5), ainsi que la trajectoire moyenne des particules qui auraient été émises à la paroi, obtenue par Shlien et Corrsin (28) en utilisant une source thermique comme émetteur de contaminant. Cette dernière ligne est aussi la trajectoire moyenne en  $y$  au sens lagrangien (28). On constate que les particules fluides très chaudes ( $\Phi_m^{++}(h=h_0=1)$ ) s'écartent plus rapidement de la paroi que les particules très froides ( $\Phi_m^{--}(h=h_0=1)$ ). Ceci, toutefois, n'infirme pas un couplage possible entre les éjections et les apports, car, le phénomène étant tridimensionnel, un apport peut "encadrer" une éjection, comme par exemple dans le modèle donné par Blackwelder (2) et qui sera repris à propos des corrélations en trois points (Para. 3.3.), les noyaux des apports et des éjections se déplaçant sur des lignes différentes. Sauf près de l'origine correspondant à la diffusion initiale, les lignes sont très peu inclinées. A titre indicatif, la pente de la courbe  $(r_{\theta_0\theta})_m$  pour  $X_1/\delta_{99} = 1$  est de l'ordre de  $3^\circ$ , la pente des diverses lignes tendant vraisemblablement vers celles des lignes de courant moyennes considérées, les perturbations étant finalement emportées avec le courant moyen.

3.1.4. La cohérence en envergure des éjections et des apports a été étudiée à partir des corrélations spatiotemporelles en trois points des fluctuations de température comme il a été expliqué au paragraphe 2.7.

Un exemple de résultats est présenté sur la figure 11 relatif à la position  $y^+ = 64$  (Cf. Fig. 2). Il existe essentiellement deux zones de coefficients de corrélation  $r_{\theta_0\theta_1\theta_2}$  respectivement positifs et négatifs, que l'on peut rattacher aux séquences d'éjections et d'apports. Si l'on considère l'échelle  $X_3/\delta$  on voit que du point de vue statistique les éjections sont relativement minces; l'épaisseur au droit du maximum de  $r_{\theta_0\theta_1\theta_2}$  positif est de l'ordre de  $0.07\delta$ . Un autre fait important c'est que les éjections apparaissent être encadrées latéralement par les apports, le système étant fortement tridimensionnel. On peut d'ailleurs, compte tenu des résultats du paragraphe 3.1.1, penser que plus près de la paroi les zones d'éjections s'amincissent, les zones d'apports prenant de plus en plus d'importance. Cette disposition en envergure des éjections et des apports est en faveur du schéma

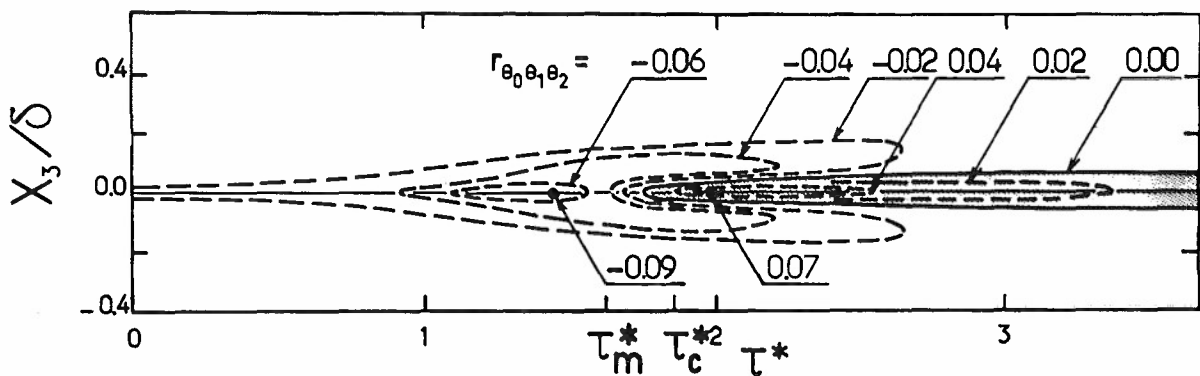


Fig. 11. Coefficients de corrélations spatiotemporelles en trois points. Couche limite  $S_2$   
 $y_0^+ = 64$ ,  $\bar{u}/u_e = 0,594$ ,  $X_1 = 1,865$

précité donné par Blackwelder au voisinage immédiat de la paroi. Notons que l'envergure mesurée entre deux dorsales des coefficients  $r_{\theta_0 \theta_1 \theta_2}$  négatifs, correspondant aux apports, est de l'ordre de  $X_3 \approx \frac{350\nu}{u_*}$  alors que la distance correspondante, dans le modèle de Blackwelder, est de  $\frac{50\nu}{u_*}$ ; cette différence correspond à un grossissement tout à fait plausible depuis  $y^+ \sim 10$  jusqu'à  $y^+ = 64$ .

### 3.2 ZONES EXTERNES

Si l'on admet que la génération de turbulence par bouffées a lieu dans la zone interne, il s'agit surtout dans la zone externe d'étudier les liaisons statistiques qui peuvent exister avec ces bouffées. Nous n'envisageons que le cas de la couche limite. Le cas du conduit est assez différent, car il existe un effet de la paroi opposée (Cf. Sabot et Comte-Bellot (30)).

3.2.1. Du point de vue diffusion, la figure 12 donne l'évolution des courbes d'isocontingences  $\Phi^{++}(h=h_0=1)$ , relatives à des séquences de fluide très chaud, égales à la moitié de la contingence maximale  $\Phi_m^{++}(h=1)$  avec même temps retard optimal. Les conditions expérimentales sont les mêmes que pour la figure 10, ( $\tau_e^* = \tau u_e/\delta$ ).

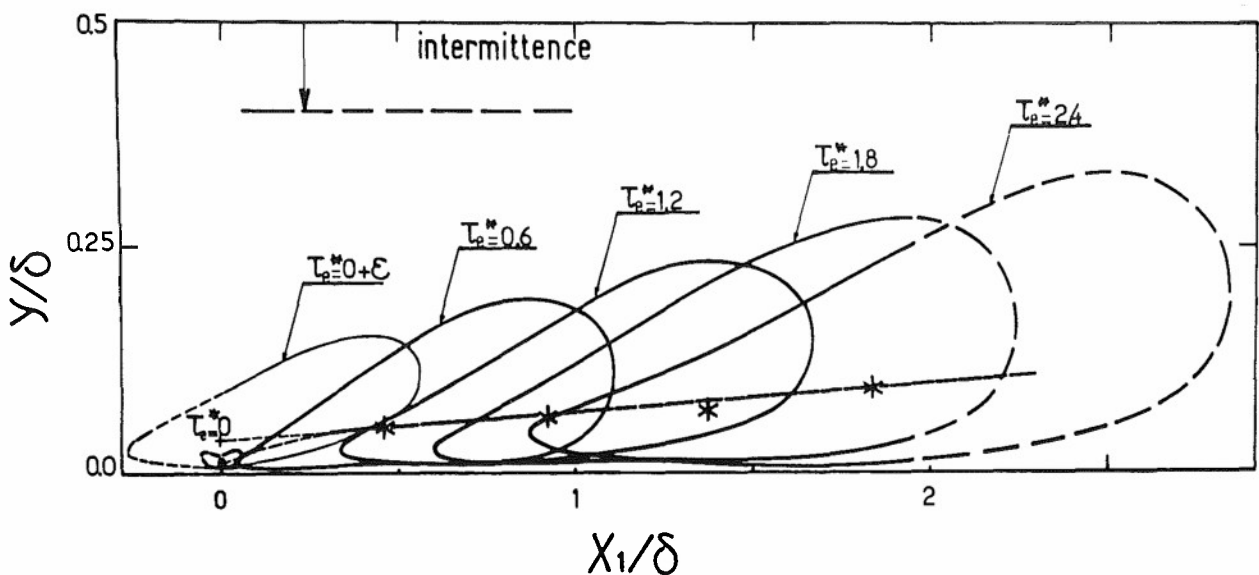


Fig. 12. Isocontingences  $\Phi^{++}(h=h_0=1) = \Phi_m^{++}/2$   
 — \* — ligne de contingences maximales  $\Phi_m^{++}$   
 Couche limite  $S_2$ ,  $y_0^+ = 23$ .

Toutefois, le point en amont  $P_0$  ne peut pas être considéré comme un point source puisque des particules fluides passant près du point en aval  $P$  peuvent ne provenir que du voisinage de  $P_0$  où les fluctuations de température sont fortement corrélées avec celles en  $P_0$ . Aussi nous avons défini une région source initiale, notée  $\tau_e^* = 0 + \epsilon$ , en prenant les points expérimentaux d'isocontingences égales à la moitié d'une valeur limite de la contingence maximale, définie par extrapolation selon une loi exponentielle, ne prenant donc pas en compte la viscosité, pour  $y \rightarrow 0$  (12). On voit que cette région source est en accord de forme avec les autres régions pour des temps différents de zéro. Le point source à la paroi est virtuel, à une distance en amont que l'on a évalué (12) avec une formule de trajectoire lagrangienne donnée par Batchelor (29) à  $X_1 \sim 1,3 \delta$ .

Si l'on excepte les instants initiaux, il apparaît que les éjections sont diffusées à travers la couche limite d'une façon qui n'attire pas de remarques très particulières; notamment l'hypothèse de similitude de Batchelor (29) pour la diffusion dans cette zone paraît être vérifiée en première approximation. On obtient une évolution analogue des isocontingences pour les apports, mais la diffusion est moins inclinée par rapport à la paroi comme on le constate sur la figure 10 pour les contingences maximales  $\phi_m^-(h=h_0=1)$ .

3.2.2. Il existe aussi une liaison statistique à travers la couche limite qui n'est pas due à un transport mais à une liaison structurelle, analogue dans le cas des ondes à celle des plans de phase, qui est bien mise en évidence par les corrélations spatiotemporelles des composantes de la vitesse (Fig. 1). En fait le décalage longitudinal  $X_1$  n'est pas indispensable; son introduction a pour effet de privilégier les structures fortement cohérentes. De plus on a intérêt à considérer les corrélations triples, significatives des fluctuations de fortes amplitudes (Cf. para 2.4)

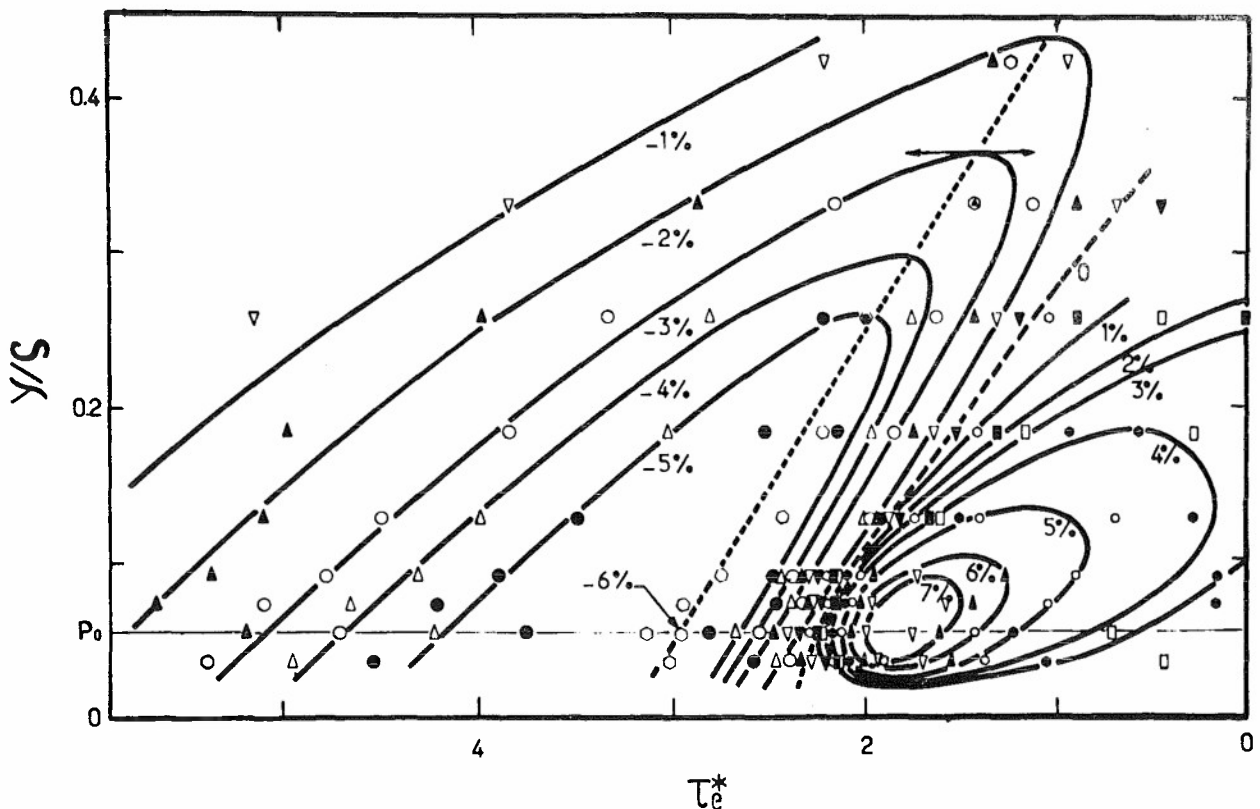


Fig. 13. Isocoefficients de corrélations spatiotemporelles  $r_{u_0, u u}$ .  $\circ$  points de retard optimal. Couche limite  $S_1$ :  $y_0 = 0,056 \delta$ ,  $X_1 = 1,41 \delta$

Les figures 13, 14 a et b donnent respectivement les isocoefficients de corrélations spatiotemporelles triples en deux points (Fig. 1):

$r_{u_0, u u}$ ,  $r_{u_0, u v}$  et  $r_{u_0, v v}$  en fonction des variables  $\tau_e^*$  et  $y/\delta$ . Le point en amont  $P_0$  est situé à  $y_0 = 0,056 \delta$ , soit  $y_0^+ = 119$ , à la limite de la zone interne.

Les lignes en traits tiretés correspondent aux corrélations maximales  $\frac{\partial r}{\partial \tau_e^*} = 0$ , lieu des points de retard optimal.

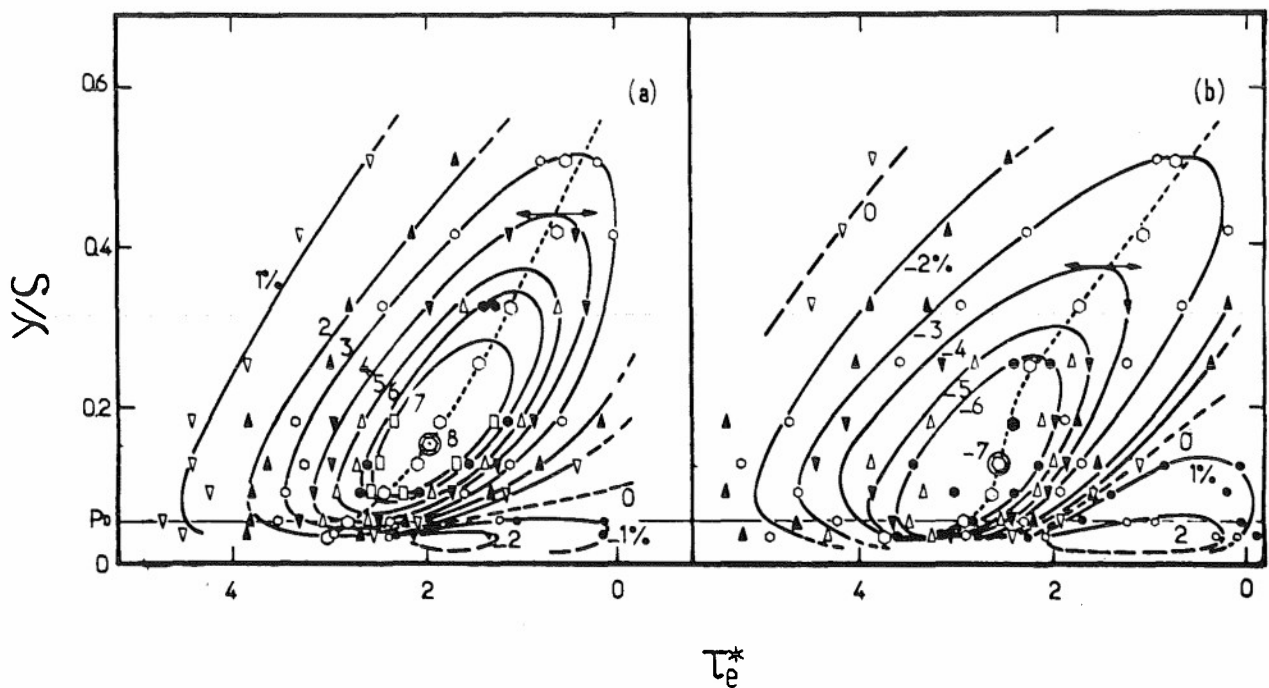


Fig. 14. Isocoefficients de corrélations spatiotemporelles : a,  $r_{u_0, uv}$ , b,  $r_{u_0, vv}$   
Couche limite  $S_1$  :  $y_0 = 0,056\delta$ ,  $X_1 = 1,41\delta$ .

Les isocorrélations ont sur chaque figure deux lobes marqués de signes opposés. On peut vérifier sur les trois figures que les lobes les plus développés et cohérents correspondent à la combinaison ( $u'_0 < 0, u'_0 v'_0 > 0$ ); les autres lobes correspondent à la combinaison ( $u'_0 > 0, u'_0 v'_0 < 0$ ). Ainsi c'est le mode d'éjections qui est le phénomène marquant; la pente du pseudo-plan de phase correspondant aux lignes de corrélations maximales précitées, est de l'ordre de  $18^\circ$  d'après  $r_{u_0, uv}$ , de  $20^\circ$  d'après  $r_{u_0, uv}$ , cette dernière valeur étant la plus significative, puisque liée aux tensions  $\overline{u'v'}$ .

Les visualisations effectuées, en particulier à l'IMST (31), montrent que les grandes structures, issues de la zone interne, qui forment le plus souvent l'intermittence, ont un angle en moyenne plus élevé de l'ordre de  $30^\circ$ , certaines étant même presque à  $90^\circ$ . Toutefois les structures facilement identifiables sont celles qui sont relativement figées et pas nécessairement très actives; de plus les corrélations prennent aussi en compte des structures en voie de disparition, probablement plus couchées au long du mouvement et qui, elles aussi, sont peu visibles.

Les lobes correspondant aux apports apparaissent beaucoup plus allongés au long de l'écoulement, ce qui est en accord avec les schémas actuels (1,2).

Dans une deuxième série d'expériences (9,20) le point en amont  $P_0$  était situé dans la zone d'intermittence ( $y_0 = 0,80\delta$  intermittence 50%,  $X_1 = 1,43\delta$ ). Les figures 15 a, b, c donnent respectivement les isocoefficients de corrélations  $r_{u_0, uv}$ ,  $r_{u_0, uv}$ , et  $r_{u_0, vv}$  en fonction des variables  $y/\delta$  et  $\tau_e^*$ . Lorsque le point P est rapproché de la paroi, le temps compensateur  $\tau_e^*$  diminue du fait de la vitesse moins élevée régnant dans cette région (voir à ce propos les temps  $\tau_i$ , introduits par Favre et al. (32) et (33), dans le cas où  $X_1 = 0$ ).

Sur ces figures seuls les lobes correspondant aux ralentissements de vitesse ( $u'_0 < 0, u'_0 v'_0 > 0$ ) sont bien définis; il s'agit pour l'essentiel du fait que les protubérances d'intermittence ont une vitesse  $u'$  en moyenne plus faibles que dans la zone non-turbulente. Toutefois le fait que  $v'$  soit positif indique une liaison avec des phases d'éjections.

La pente de la ligne de corrélation maximale de  $r_{u_0, uv}$  (Fig 15b traits tiretés) est dans sa partie linéaire de l'ordre de  $21^\circ$ , tout comme dans le cas où  $P_0$  était disposé à la limite de la zone interne. Ceci serait donc plutôt en faveur d'une liaison des protubérances de l'intermittence avec les éjections dans la zone interne pleinement turbulente. Notons cependant que les visualisations précitées montrent plutôt que les bouffées de fluide arrachées depuis la zone de paroi ( $y^+ \sim 20$ ) ne gagnent pas directement la zone d'intermittence, mais seulement la zone centrale pleinement turbulente. Par la suite la diffusion emmène ces bouffées dans la zone d'intermittence.

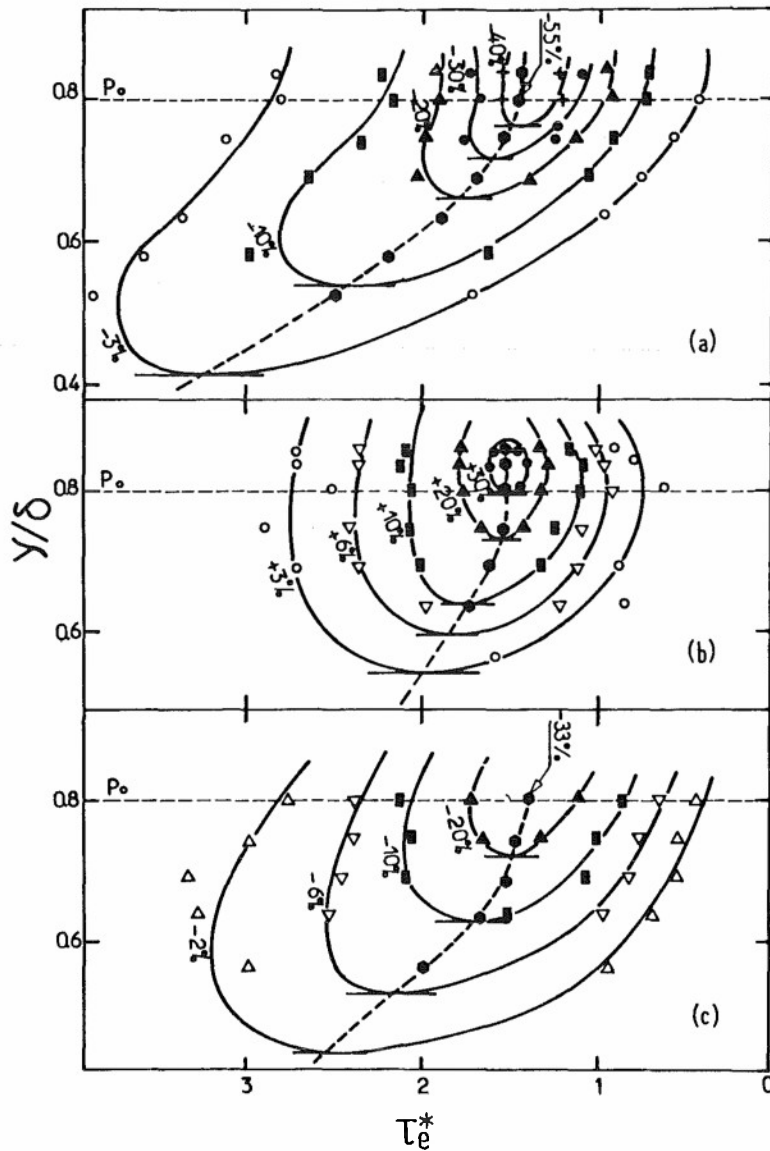


Fig .15. Isocoefficients de corrélations spatiotemporelles

a:  $r_{u_0,uu}$  , b:  $r_{u_0,uv}$  , c:  $r_{u_0,vv}$

○ points de retard optimal

Couche limite  $S_1$  :  $y_0 = 0,808$  ,  $X_1 = 1,436$  .

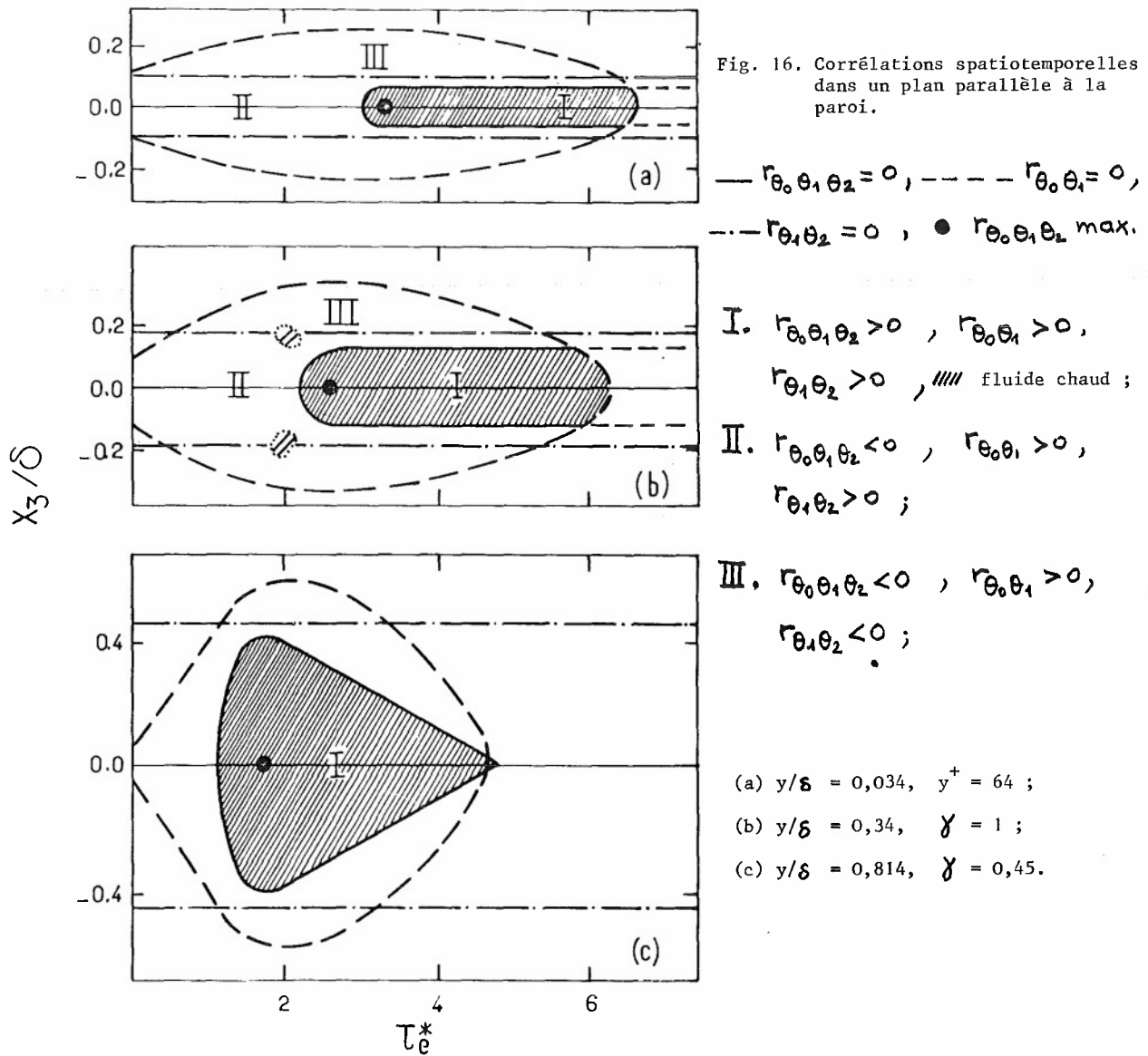
3.2.3. En ce qui concerne le développement en envergure des perturbations, la figure 16 donne une comparaison des diverses zones définies dans un plan parallèle à la paroi selon les signes des corrélations doubles et en trois points (paragraphe 2.7). La figure 16a correspond à la figure 11, soit  $y_0 = 0.034\delta$  ou  $y_0^* = 64$ .

Les figures 16b et c sont relatives à des plans respectivement situés à  $y_0 = 0.34\delta$  et  $y_0 = 0.81\delta$  (intermittence 45%). Les zones hachurées sont celles où le coefficient de corrélation spatiotemporelle en trois points  $r_{\theta_0\theta_1\theta_2}$  est positif, correspondant à des séquences de fluide chaud. On voit que l'envergure des éjections augmente au fur et à mesure que l'on s'éloigne de la paroi. A la position  $y = 0.81\delta$ , l'envergure de la zone hachurée au droit du maximum de corrélation est égale à  $0.8\delta$ , ce qui est pratiquement l'envergure moyenne d'une protubérance d'intermittence à cette distance  $y/\delta$  (10b).

Ceci montre clairement que les protubérances de turbulence sont formées surtout par du fluide en provenance de zones plus intérieures; les visualisations montrent, d'ailleurs, que l'entraînement de fluide extérieur non-turbulent est très faible dans le cas de la couche limite avec gradient longitudinal de pression moyenne nul (31). Mais étant donné que du fluide arrive de l'intérieur dans une protubérance de turbulence, il est nécessaire, d'après ce qui précède, que du fluide reparte en quantité au moins\* égale vers l'intérieur. Ceci n'apparaît pas dans la figure 16c, car dans la région I les valeurs positives de  $r_{\theta_0\theta_1\theta_2}$  signifient seulement que les éjections sont dominantes (10a, 20), du point de vue cohérence, mais non pas qu'il n'existe à certains instants des apports moins cohérents donnant lieu à des produits  $\theta_0'\theta_1'\theta_2' < 0$ .

\* La détransition est pratiquement exclue.





Une autre constatation que l'on peut faire sur la figure 16 est l'aspect fortement tridimensionnel des éjections, ce qui est aussi en accord, dans la zone d'intermittence, avec les résultats de Kovaszny et al. (34).

Enfin, si la figure 16 révèle une unité de mécanisme dans le processus d'éjection depuis la zone interne jusqu'à la zone d'intermittence, ceci ne signifie pas toutefois qu'une même éjection parcourt directement le trajet à travers toute l'épaisseur de couche limite, comme nous l'avons déjà souligné au paragraphe précédent.

#### 4. CONCLUSIONS.

De l'analyse des zones interne et externe qui a été faite se dégage un certain nombre de résultats, dont les plus marquants sont les suivants :

4.1. Très près de la paroi, au moins jusqu'à  $y^+ = 1,7$ , les enregistrements des fluctuations de température et de la vitesse longitudinale, ainsi que les facteurs de dissymétrie correspondants, montrent que les apports constituent le phénomène dominant. Evidemment, du fait de la conservation du débit de masse, il existe nécessairement des éjections, mais celles-ci n'apparaissent pas dans ces mesures parce que, probablement, elles sont plus diffuses, de faibles amplitudes relatives.

Au fur et à mesure que l'on s'éloigne de la paroi, le nombre d'éjections apparentes augmente tandis que celui des apports diminue ; dans la zone,  $50 \leq y^+ \leq 100$ , ces nombres sont pratiquement égaux, à la précision près des mesures, et voisins du nombre de "bursts" donné, par exemple, par la formule de Rao. Par ailleurs, si l'on se réfère aux célérités, mesurées à partir des corrélations spatiotemporelles conditionnelles, les éjections semblent -du moins pour les plus cohérentes- être liées aux apports. Enfin, les mesures de corrélations spatiotemporelles en trois points montrent que, dans une section parallèle à la paroi, les éjections occupent un domaine, relativement mince, entouré par des apports formant, en quelque sorte, les deux doigts d'une main. Ces résultats sont en faveur des schémas tridimensionnels, tels qu'on peut les trouver dans les publications de Praturi-Brodkey, ainsi que de Blackwelder, dans lesquels les bouffées de turbulence ("bursts") sont créées, dans la zone interne, par l'interaction d'éjections ("éjections") et d'apports ("sweep").

4.2. En ce qui concerne le transport des perturbations les plus cohérentes depuis la zone voisine de la paroi, jusque dans la zone pleinement turbulente -mesurée par les probabilités spatiotemporelles conditionnelles à partir de  $y_0^+ = 23$ - il se fait par un processus analogue à la diffusion lagrangienne de particules. Les perturbations liées aux éjections s'éloignent plus de la paroi que celles liées aux apports : si l'on admet qu'au départ les deux perturbations sont liées, ceci signifie que la bouffée se déforme en s'estompant au cours du temps.

4.3. Il existe aussi -comme le montre les corrélations spatiotemporelles de vitesse en deux points, à travers la couche limite- une liaison statistique qui n'est pas due à un transport mais plutôt à une liaison structurelle analogue à celles des plans de phase dans le cas des ondes. Toutefois, de telles liaisons entre les zones interne et intermittente n'ont pas été décelées. Des visualisations effectuées montrent d'ailleurs que l'éclat d'une bouffée, issue de la zone de paroi, ne s'étend pas, en général, au delà de la zone interne pleinement turbulente ; cependant cet éclat est diffusé et peut gagner, comme vu précédemment, une protubérance turbulente de la couche limite.

Dans la zone externe, ce sont les éjections qui semblent jouer -comme le montrent notamment les corrélations spatiotemporelles en deux et trois points- un rôle de plus en plus dominant lorsque l'on s'éloigne de la paroi, les apports étant de moins en moins cohérents. En envergure, le domaine de cohérence des éjections s'élargit progressivement allant jusqu'à intéresser, du point de vue statistique, les protubérances turbulentes. Il existe donc une unicité du processus qui se traduit par une prédominance des éjections, en tant que structure cohérente ; toutefois, cela ne signifie pas du tout que ces éjections sont dues à un même tourbillon intéressant à la fois, par exemple, la zone interne pleinement turbulente et intermittente.

#### REMERCIEMENTS.

Les auteurs remercient Messieurs E. ARZOUMANIAN et M. ASTIER pour leur collaboration scientifique et technologique.

## REFERENCES

- 1.- Praturi A.K., Brodkey R.S.  
A stereoscopic visual study of coherent structures in turbulent shear flow  
J. Fluid Mech. 89, 251,- 1978.
- 2.- Blackwelder R.F.  
The bursting process in turbulent boundary layer  
Workshop on coherent structures in turbulent boundary layers, Lehigh Univ. 1978.
- 3.- Willmarth W.W.  
Structure of turbulence in boundary layers  
Advances in Applied Mech. Vol. 15, Ac. Press, 1975.
- 4.- Gupta A.K., Laufer J., Kaplan R.E.  
Spatial Structure in the viscous sublayer.  
J. Fluid Mech. 50, 493, 1971.
- 5.- Kline S.J., Reynolds W.C., Schraub F.A., and Runstadler P.W.  
The structure of Turbulent boundary layers.  
J. Fluid Mech. 30, 741, 1967.
- 6.- Corino E.R., Brodkey R.S.  
A visual investigation of the wall region in turbulent flow  
J. Fluid Mech. 37, 1, 1969.
- 7.- Laufer J., Badri Narayanan M.A.  
Mean period of the production mechanism in a boundary layer.  
Phys. Fluids 14, 182, 1971
- 8.- Dumas R., Arzoumanian E., Favre A.  
Corrélations spatiotemporelles triples dans une couche limite turbulente  
C.R. Acad. Sc., t 277, A, 759 1973
- 9.- Arzoumanian E., Dumas R., Favre A.  
Corrélations spatiotemporelles doubles et triples dans une couche limite turbulente : zone  
externe. C.R. Acad. Sc. t 286, B, 113 1978
- 10.- Fulachier L., Giovanangeli J.P., Dumas R., Kovasznay L.S.G. et Favre A.  
Structure des perturbations dans une couche limite turbulente.  
a. zone interne C. R. Acad. Sc, t 278, B, 683, 1974  
b. zone d'intermittence C. R Acad. Sc., t 278, B, 999, 1974.
- 11.- Dumas R., Arzoumanian E., Fulachier L.  
Probabilités conditionnelles spatiotemporelles des fluctuations de température dans une couche  
limite turbulente.  
C.R. Acad. Sc., t 284, B, 487, 1977.
- 12.- Dumas R., Arzoumanian E., Fulachier L. et Favre A.  
Conditional correlations and probabilities of temperature fluctuations in a turbulent boundary  
layer.  
Archives of Mech. 30-4-5, 421, Warszawa 1978.
- 13.- Dumas R., Fulachier L., Arzoumanian E.  
Facteurs d'intermittence et de dissymétrie des fluctuations de température et de vitesse dans  
une couche limite turbulente.  
C.R. Acad. Sc. t 274, A, 267, 1972.
- 14.- Fulachier L.  
Contribution à l'étude des analogies des champs dynamique et thermique dans une couche limite  
turbulente. Effets de l'aspiration.  
Thèse Doct. I.M.S.T., 1972.
- 15.- Elena M.  
Structure de la turbulence en conduite cylindrique poreuse et chauffée.  
Thèse Doct., I.M.S.T., 1975.  
Rapport C.E.A., R-4843, 1977.
- 16.- Verollet E.  
Etude d'une couche limite turbulente, avec aspiration et chauffage à la paroi.  
Thèse Doct., I.M.S.T., 1972. Rapport C.E.A., R-4872, 1977.
- 17.- Favre A.  
Equations statistiques fondamentales des fluides turbulents compressibles.  
Comptes Rendus Vè Canad. Congr. Appl. Mech.,  
New Brunswick Univ., Fredericton, Canada, 1975.
- 18.- Fulachier L., Dumas R.  
Spectral analogy between temperature and velocity fluctuations in a turbulent boundary layer.  
J. Fluid Mech., 77, 2, 257, 1976

- 19.- Bradshaw P.  
Complex turbulent flows  
Proc. 14th I.U.T.A.M. Congr. Theor. Appl. Mech., 257-277  
Delft 1976
- 20.- Arzoumanian E.  
Contribution à l'étude de la couche limite turbulente : corrélations spatiotemporelles doubles et triples.  
Th. Doct. Spéc. I.M.S.T. , 1974.
- 21.- Fulachier L.  
Hot Wire measurements in low speed heated flow.  
Proc. Dynamic flow Conference, DISA, 1978
- 22.- Chiapale J.P.  
Contribution à l'étude des caractères statistiques des fluctuations longitudinales de vitesse et de température dans un écoulement turbulent de couche limite.  
Th. Doct. Ing., I.M.S.T., 1974.
- 23.- Giovanangeli J.P.  
Corrélations spatiotemporelles en trois points dans la zone d'intermittence de la couche limite.  
Th. Doct. Spéc. I.M.S.T. 1975.
- 24.- Dumas R., Fulachier L., Arzoumanian E. et A. Favre  
Etude de la structure de la turbulence dans une couche limite par les corrélations spatiotemporelles.  
J. de Phys., suppl. au N° 1, 37, C1 - 181, 1976.
- 25.- Dumas R.  
Corrélations spatiotemporelles d'ordre élevé.  
Proc. Dynamic flow Conference, DISA, 1978
- 26.- Elena M., Chauve M.P., Dumas R.  
Effet de l'aspiration sur les facteurs de dissymétrie et d'aplatissement dans une conduite cylindrique chauffée.  
C.R. Acad. Sc. t. 281, B, 185, 1975
- 27.- Bremhorst K., Walker T.B.  
Spectral measurements of turbulent momentum transfer in fully developed pipe flow  
J. Fluid Mech. 61, 1, 173, 1973
- 28.- Shlien D.J., Corrsin S.  
Dispersion measurements in a turbulent boundary layer  
Int. J. Heat Mass transfer, 19, 285-295, 1976
- 29.- Batchelor G.K.  
Diffusion from sources in a turbulent boundary layer.  
Arch. Mech. Stos. 3 (16), 661, 1964
- 30.- Sabot J., Comte-Bellot G.  
Intermittency of coherent structures in the core region of fully developed turbulent pipe flow.  
J. Fluid Mech. 74, 4, 767, 1976
- 31.- Daïen E., Domptail C., Bonmarin P.  
Visualisations et vélocimétrie laser dans divers écoulements turbulents.  
4ème Congr. Franc. de Mec., Nancy, 1979
- 32.- Favre A., Gaviglio J., Dumas R.  
Further space-time correlation of velocity in a turbulent boundary layer  
J. Fluid Mech. 3, 344, 1958.
- 33.- Favre A., Kovasznay L.S.G., Dumas R., Gaviglio J. et Coantic M.  
La Turbulence en Mécanique des fluides, Gauthier - Villars 1976.
- 34.- Kovasznay L.S.G., Kibens V., Blackwelder R.F.  
Large scale motion in the intermittent region of a turbulent boundary layer.  
J. Fluid Mech. 41, 283, 1970
- 35.- Runstadler P.W., Kline S.J., Reynolds W.C.  
An experimental investigation of the flow structure of the turbulent boundary layer.  
AFOSR, Tech. Note 5241, Stanford, 1963.

EXPERIMENTAL STUDY OF COHERENT STRUCTURES  
IN THE TURBULENT BOUNDARY LAYER OF PIPE FLOW  
USING LASER-DOPPLER ANEMOMETRY

H.R.E. van Maanen

KONINKLIJKE/SHELL-LABORATORIUM, AMSTERDAM

(Shell Research B.V.)

P.O. Box 3003, 1003 AA Amsterdam, The Netherlands

#### SUMMARY

The main objective in this investigation has been the study of the coherent structures in the turbulent boundary layer of a pipe flow. These structures - often called bursts - are thought to be the main mechanism involved in the generation and maintenance of turbulence in flow.

For the purpose of the study we measured the frequency and frequency spread as a function of Reynolds number and tried to resolve the structure of the phenomenon by measuring conditional averages.

The measurements were carried out in a pipe 6 m long and 50 mm in internal diameter, filled with water, using a laser-Doppler velocimeter, down to 0.25 mm from the wall, with the size of the measuring volume in radial direction being 0.1 mm.

The output signal of the laser-Doppler anemometer, which can be regarded as the flow velocity, was fed both into a burst detector as described by Blackwelder and Kaplan and into an electronic delay line. The output signal of the burst detector was used to conditionally average the delayed signal.

The conditional averages close to the pipe wall ( $y^+ \approx 20$ ) are in good agreement with those found by Blackwelder and Kaplan, but further from the wall significant deviations were observed. We found burst phenomena even for  $y^+ = 100$ , so that the structure appears to be bigger than expected.

Results of the measurements of the burst frequency and frequency spread as a function of the Reynolds number, as well as the conditional averages, are presented.

#### 1. INTRODUCTION

In the late sixties detailed flow visualisation studies of turbulent boundary layers (Refs. 1, 2) showed that in these layers more or less periodic phenomena occur, related to "coherent structures" in these layers. These structures - very often referred to as bursts because of the very rapid changes in the velocity during a certain phase of the phenomenon - are thought to be the main mechanism in the generation and maintenance of turbulence in flows. Since then coherent structures have been found and studied in many other flow systems (Ref. 3).

The visualisation studies (Refs. 1, 2) ultimately led to the following schematic picture of the phenomena in the turbulent boundary layer of a pipe flow.

The - always present - laminar sublayer, which has a high velocity gradient, starts to thicken while the velocity gradient is maintained. As the layer reaches a certain thickness, it becomes unstable and trips over its own velocity gradient, probably triggered by turbulent fluctuations in the bulk, and generates a roll-vortex which is quite extensive in the tangential direction. The fluid with a low velocity is thereby transported from the vicinity of the wall and becomes an obstacle for the fluid in the bulk. Pressure begins to build up due to the deceleration of the bulk liquid and shortly after that the vortex is swept away by the bulk liquid, leaving only the laminar sublayer. The vortex decays in the bulk to generate random turbulence and the whole process starts anew. As the laminar sublayer must reach a certain thickness, the process is more or less periodical, although it has a random spread, probably because it is triggered by random fluctuations. A simplified picture is given in Fig. 1, which has been taken from Ref. 1.

One of the major problems in studying these phenomena is to discriminate between bursts and background turbulence. Unambiguous criteria appear to be difficult to define (Refs. 4, 5). This will be discussed in more detail in the section on signal processing.

However, visualisation studies have been of a qualitative nature, and although they reveal much about the mechanisms involved, a need exists for quantitative measurements.

A study of coherent structures in pipe flow was initiated and because of the small dimensions involved we chose a laser-Doppler velocimeter for the measurement of the average burst frequency as a function of the Reynolds number, the frequency spread, the velocity signals and the conditional averages of these. In this paper we present the first results of our experimental work.

## 2. MEASURING EQUIPMENT

### 2.1. The flow system

The flow system consists of a closed pipe loop partly made of stainless steel and partly of Perspex, and is shown in Fig. 2. For stability of the flow centrifugal pumps are used with a maximum capacity of 10 l/s. The measuring liquid is water, which is kept at  $20 \pm 0.2$  °C. The throughput is measured by means of turbine flow transmitters with digital readout. For the sake of accuracy three transmitters are used with overlapping ranges.

The Perspex measuring pipe, internal diameter of 50 mm and located between the two settling chambers, is 6 m long. The actual test section is situated 4.5 m after the entrance of the measuring pipe. The test section itself is of a different design to permit the use of a laser-Doppler velocimeter under optimum conditions. It consists of a rectangular vessel, internal cross-section 80 x 100 mm and 600 mm long. This vessel is filled with the same liquid as the pipe loop (in this case water) and at almost the same static pressure as well. In the vessel a glass pipe is fitted with the same internal diameter as the measuring pipe, but at the measurement location the glass is removed over half the circumference of the pipe and a width of approximately 16 mm. Over the full length of the glass pipe a thin foil is glued on the inside which acts as an inner wall for the flow. As this foil is forced in a cylindrical shape and is supported by the glass tube along its full length, except at the measurement location, it is rigid enough to withstand the pressure fluctuations of the turbulent flow field. In this way a very thin (less than 100  $\mu$ m) wall is obtained without disturbing surface changes close to the measurement location. The test section is shown in Figure 3.

### 2.2. The laser-Doppler velocimeter

Detailed descriptions of laser-Doppler velocimeters and their use for measurements in turbulent flows have been published in many papers. A convenient compilation can be found in Ref. 6. We will therefore confine ourselves to a short review of the main aspects important for this study. As is well known, the system uses small particles carried by the flow that scatter the laser light.

The main advantages of a laser-Doppler velocimeter can be summarised as follows:

- no calibration required
- no interference with the flow
- single component measured
- strict linearity
- using the reference beam mode, easy alignment
- good spatial resolution.

Disadvantages of the laser-Doppler velocimeter are:

- noise in the output signal of the tracker (frequency-to-voltage converter) obscures the signals from the small eddies;
- seeding is necessary in most cases, but in liquid flows the particles will follow the flow without difficulty. In gas flows, however, this requires more attention.

Good spatial resolution can be achieved by a proper choice of the direction of the laser beams, the angle between them and their diameter.

As can be seen from Fig. 4, the measuring volume of a laser-Doppler velocimeter, being as a first approximation the intersection volume of the laser beams, is always long and thin, due to the narrow angle between the beams. During operation all the signals coming from this volume are processed. This means that eddies smaller than the measuring volume are averaged out and hence cannot be measured. This puts an upper limit to the longest dimension of the measuring volume. A reduction of this dimension can be achieved by increasing the beam diameter before focussing it into the flow and increasing the angle between the beams.

On the other hand, a reduction of the measuring volume implies that fewer particles per unit time will contribute to the scattered light to generate the Doppler signal. In order to measure the turbulent fluctuations sufficient particles must traverse the measuring volume per unit time, which puts a lower limit to the size of the measuring volume.

The ratio of the length of the measuring volume to its width is limited by the angle between the beams that can be obtained in practice. As this ratio  $\gg 1$ , the spatial resolution differs in the three perpendicular directions: in the direction of the beams it is smaller than in the directions perpendicular to it.

For this study the highest spatial resolution is required in the radial direction because in the vicinity of the wall the velocity gradients are the largest. In the axial and tangential directions the gradients are a lot smaller or even zero. Consequently, optimum operation of the laser-Doppler velocimeter will be obtained with the shortest dimension in the radial direction and the longest dimension in either the tangential or the axial direction. This is illustrated in Fig. 5. For practical reasons the tangential direction was chosen (Fig. 5B), although the axial direction is theoretically to be preferred.

As can be seen from Fig. 4, the direction of the longest dimension is also the main direction for the laser beams that create the measuring volume. This means that in the case of Fig. 5B the beams hit the pipe wall at a small angle, far from perpendicular, which implies that the pipe acts as a cylinder lens, giving severe distortion of the beams.

To avoid distortion of the laser beams due to the small angle of incidence on the pipe wall, the pipe was mounted in a rectangular vessel also filled with water, and the pipe wall thickness was reduced to 100  $\mu\text{m}$  as described in Section 2.1. In this way the problems caused by the change in refractive index from air into water were eliminated and distortion by the pipe wall reduced so far that measurements down to 0.5 mm from the wall could be made. The influence of the wall thickness on the laser beams is illustrated in Figs. 6 and 7 which show a laser beam traversing a wall of respectively 500  $\mu\text{m}$  and 100  $\mu\text{m}$  with water on both sides of the wall at two different positions from the wall. These pictures show that a wall thickness of 100  $\mu\text{m}$  must be achieved.

The laser-Doppler velocimeter was operated in the reference beam mode for ease of alignment (even the small distortion caused by the remaining wall thickness necessitates realignment for every measurement point (see also Figs. 6 and 7)). It also enabled us to use cross-correlation techniques for noise reduction in turbulence power spectral measurements (Ref. 7). A disadvantage of the use of the reference beam mode is the higher sensitivity to laser noise. However, this noise is confined to the lower frequency range ( $\leq 200$  kHz) and by using a preshift of approximately 400-500 kHz, generated by a rotating grating, the frequency of the Doppler signal was shifted to a band with minimum laser noise.

The output signal of the photodiode is filtered by a Krohn-Hite model 3103 band-pass filter (see Fig. 8) and then fed into a tracker (TPD model 1077, designed and constructed by the Technisch Fysische Dienst, TNO-TH Delft, the Netherlands) where the frequency is converted into a voltage. The output signal was used for further data processing and displayed on the monitoring oscilloscope.

### 2.3. Signal processing

The tracker signal was low-pass filtered to remove the noise (see Fig. 8, filter 1) from the tracker and to act as anti-aliasing filter for the delay line. To be able to change the filtering without affecting the operation of the burst detector, it was separately band-pass filtered for use with the burst detector (see Fig. 8, filter 2). The burst detector used was of the type described by Blackwelder and Kaplan (Ref. 5). A burst detector should discriminate between bursts and background turbulence and should behave neutrally on "pseudo turbulence". This will be discussed in more detail in Section 2.3.4 (Conditional averages).

#### 2.3.1. Average burst frequency

The output of the burst detector was fed into a pulse shaper to yield standard pulses that can be counted. It appeared, however, that the burst detector was not able to discriminate completely between bursts and background turbulence. Therefore, the count had to be corrected for the erroneous triggering of the burst detector on the background turbulence. How this is done will be discussed in Section 3.1.

#### 2.3.2. Time interval distribution

The time lapse between two successive pulses from the burst detector was measured and stored in a 1024-position memory and fed into a computer for further processing. The imperfect discrimination by the burst detector gave rise to erroneous pulses. This could not be avoided, but the average count was so chosen that it corresponded to the average burst count obtained.

#### 2.3.3. The axial fluctuating velocity signals

As the burst detector reacts somewhere during the occurrence of the bursting phenomenon, it is necessary to delay the signal in the measuring system in order to study the beginning of the phenomenon. The degree of coherence between successive bursts is insufficient to use the detection of burst  $n$  to trigger the measuring system for burst  $n + 1$ . Therefore, Blackwelder and Kaplan used two systems: the first (upstream) is used for the detection of the burst and the second, a rack of hot-wires, for study of the burst. This system has several disadvantages:

- The flow field at the location of the measuring system is influenced by the presence of the detection system.
- The time lapse between the detection system and the measuring system is determined by the distance between them and the turbulent convection velocity. As the latter is not constant, the delay time is not constant either but varies from burst to burst.
- The evolution of the burst between the detection point and the measurement point complicates the measurement: the burst may have disappeared on its way from the detection system to the measuring system, for example if it is detected in its final state of evolution. This puts an upper limit to the distance between the detection and measuring systems.

To circumvent these difficulties in the present study both detection and measurement were carried out with the same laser-Doppler velocimeter using an electronic delay line to capture the signal and store it for a time that could be varied from 1 ms to 10 s. In this way the same signal was used for detection and measurement. The delay line employed a 1024-position memory in which the signal was stored after A/D conversion. After a certain time, determined by a continuously variable clock, the store was read out and fed into a D/A converter. The delay time chosen was between 0.5 and 1 times

the average time lapse between two successive bursts. In this way the signal as measured before the actual detection moment was still available to study the onset of the burst phenomenon. The use is illustrated in Fig. 9.

### 2.3.4. Conditional averages

The average value of the turbulent velocity fluctuations is by definition zero. If, however, conditional averaging is used, this is not necessarily the case. The conditional average is defined as

$$F(\tau) = \frac{1}{N} \sum_{n=1}^N f(t_n + \tau - \Delta t)$$

F = conditional average of signal f

$\tau$  = time delay since detection moment  $t_n$  ( $\geq 0$ )

N = number of samples used

f = signal to be averaged conditionally

$t_n$  = detection moment, determined by condition criteria

$\Delta t$  = time delay of electronic delay line

Note again that the position in space at which the measurement is carried out is the same as that at which detection occurs!

Using this technique the "random" background turbulence was averaged out, the distinctive part of the phenomenon remaining. The problem was mainly the generation of the trigger signal. If one induces a flow field, e.g. in a stirred vessel, the trigger moment can be chosen as the passage of a reference marker at the stirrer. In our case, however, the process was spontaneous and not controlled from the outside. Therefore, the trigger signal had to be obtained from the velocity signal itself. A burst detector as described by Blackwelder and Kaplan (Ref. 5) served this purpose.

The criterion for satisfactory performance of the burst detector is that filtered white noise - a completely random signal that resembles turbulence but of course without the coherent structures - must give a conditional average equal to zero for all delay times  $\tau$ . Strictly speaking, the burst detector of Blackwelder and Kaplan does not satisfy this condition, but it comes close to it, as was reported by them (Ref. 5) and confirmed by our own experiments for which we used basically the same burst detector as Blackwelder and Kaplan's.

For this study a Hewlett-Packard 3721A correlator in the signal recovery mode was used as an averager. Either N=1024 or 2048 samples were used to determine the conditional average.

## 3. RESULTS

### 3.1. Average burst frequency

If the reference level on the burst detector is low, it will respond both to bursts and to background turbulence. Increasing the reference level will reduce the number of counts per unit time. Increasing the reference level even further will cause the burst detector to ignore the smaller bursts. In order to determine the optimum threshold level burst count measurements were carried out at various threshold levels. We hoped to find a range where the number of counts per unit time would be (almost) independent of the reference level. However, this did not happen. Only a weak shoulder appeared in the number of counts per unit time as a function of the reference level, as is shown in Figure 10. Although it was reproducible, it is too weak to give an unambiguous result for the burst count. Therefore, a more indirect technique was used. As stated before, the burst detector reacts either to burst or to background turbulence. Just as the conditional average with simulated turbulence is (almost) zero, the contribution from the background turbulence to the final conditional average can be ignored. Hence, the final conditional average will still be of the correct shape, but as the averager divides the contribution of each of the signals by the number of signals to be averaged, its amplitude will be too small, because not all signals give a contribution to the conditional average of the burst. Its shape is therefore independent of the reference level, but not its amplitude.

Assuming now that the conditional average is meaningful, it can be used to study the behaviour of the burst detector by comparing the velocity signal to which the burst detector reacted with the conditional average itself. This enabled us to divide the signals that made the burst detector react into two classes: the signals that resembled the conditional average, which represented bursts, and those that did not, which were due to background turbulence. With this division the count could be corrected to curve b in Figure 10. From this a clear value for the average burst count is obtained. Note that even at high reference levels the count still included erroneous counts from random turbulence. Using this technique, the average burst frequency was measured at three Reynolds numbers. This is illustrated in Figure 11, which shows that the average burst frequency is, as a good approximation, proportional to the Reynolds number.



### 3.2. Measurement of the frequency spread

The results for the frequency spread were obtained by setting the reference level such that the average count corresponded to the average burst count as obtained in Figure 10. The time interval between two successive pulses was measured and fed into a computer. From over 30 000 measurements the time interval distribution was calculated. The result is shown in Figure 12A.

The interval distribution is influenced by the imperfect behaviour of the burst detector, as it also reacts to background turbulence, which can be seen from Figure 10. However, the distribution is very broad, so that we think the effect of the probably random distribution of the background turbulence is not very important. Improvement of the behaviour of the burst detector by implementing more sophisticated detection criteria will improve these results.

The peak for low values of  $\Delta t$  is shown in more detail in Figure 12B. At this moment we do not yet know the cause of this peak, but we tend to believe that it is caused by multiple reaction of the burst detector to bigger bursts and/or to the vortical activity shortly after the burst (see also next section).

The wide distribution may have three causes:

1. Variations in the time intervals can be expected because triggering is more or less random, so that the time that the laminar sublayer is stable is not constant.
2. The burst effect is two-dimensional and two bursts positioned differently in the tangential direction may both be detected. The time interval between two such detections may be not, or not completely, correlated.
3. Coalescence of bursts may occur, and if this happens the two bursts will come close together. We have also found additional evidence for this from the velocity signals.

Plotting of the results shown in Fig. 12A, except for the first two points, which may be erroneous, on a semi-logarithmic scale, as shown in Fig. 13 yields an almost straight line, which indicates that the distribution observed must be due to a more structural phenomenon, which we do not yet know.

### 3.3. Velocity signals

The actual velocity signals of  $u'$  show that the phenomenon is accompanied by vortex motions, as can be seen clearly from the typical signals shown in Figs. 14-19. This has also been found from the visualisation studies (Refs. 1, 2). As will be shown in the next section, some velocity-time traces resemble the conditionally averaged velocity signals, but some are obscured by the "random" background turbulence. It can be seen that the "random" background turbulence mostly has a more or less periodic character, which points at vortices passing by. The most striking phenomenon in the pictures is the very rapid acceleration to which the burst detector reacted roughly 4.5 divisions from the left.

### 3.4. Conditional averages

The conditionally averaged axial velocity fluctuations measured at different  $y^+$  values for  $Re = 9500$  are shown in Figure 20 as a function of time. The detection moment corresponds to  $t=0$ . These traces show that the structure extends quite far from the wall. It is important to note that these conditionally averaged axial velocities differ strongly from those reported by Blackwelder and Kaplan for higher  $y^+$  values, as can be seen from Fig. 21. The following causes may explain this difference:

- The use of the hot-wire technique by Blackwelder and Kaplan has prevented them from distinguishing between the  $u'$  and  $v'$  components. As  $u'v'$  is negative, in particular during bursts, the decrease in  $u'$  as measured by us may be compensated by an increase in  $v'$ .
- The use of the convection velocity to determine the time delay will cause phase fluctuations which will tend to smooth out sharp edges such as those shown here, especially at higher  $y^+$  values. Moreover, the wire used for detection is positioned at a low  $y^+$  value ( $y^+ = 15$ ).
- The evolution of the phenomenon may have strode along so far that the burst had partly disappeared before the authors measured it.
- Our conditionally averaged axial velocity signals are measured at a higher Reynolds number (9500 vs. 2550).

However, study of their velocity signals shows that the bursts can clearly be detected at high  $y^+$  values, while their conditionally averaged velocity signals are then almost zero. This indicates that the last potential cause is not so important.

The influence of the phase fluctuations was later on recognised by Blackwelder, too, and corrected for (Ref. 8), which resulted in conditionally averaged velocity signals that resemble our results, but even then differences remain.

We conclude from this that the conditionally averaged streamwise velocity signals must show some structure for high values of  $y^+$ .

A striking feature of the conditional averages found by Blackwelder and Kaplan and confirmed (except for some details) by our own measurements is the following: Normalising the velocity by dividing it by the reference level results in a conditional average that is (almost) independent of the reference level.

Blackwelder and Kaplan concluded that this was caused by the inclusion of smaller bursts at lower reference levels. Although this seems obvious there are arguments that point in a different direction, such as:

- One does not only measure the bursts at the reference level but also at levels above the reference level. This means that a reduction in reference level would give a less than proportional reduction in amplitude (maximum difference in velocity). If one were able to discriminate completely between bursts and random turbulence the conditional average would not be affected at all.
- The burst detector compares as a first approximation the square of the signal with the reference level (Ref. 5). This gives a less than proportional reduction in amplitude.
- The burst detector will give relatively more erroneous trigger pulses at lower reference levels (Fig. 10), which results in a reduction in amplitude if we assume that the contribution of the erroneous signals to the conditional average is zero.

This phenomenon will only be clarified through a further study of the behaviour of the burst detector and measurement of the size distribution.

The disappearance of the vortex signals from the conditional averages is probably caused by a wide spread in vortex size, which causes phase fluctuations. This is confirmed by the rate of disappearance: the more samples are used for conditional averaging, the less pronounced they are.

#### 4. CONCLUSIONS

The laser-Doppler anemometer is a useful tool for measuring coherent structures in liquid flows. The optical difficulties that arise when measurements are to be made close to the wall can be overcome without costly solutions and without risk of distorting the flow field close to the measurement position. The laser-Doppler anemometer has some very useful properties for studies of this type.

Using this technique and the burst detector described by Blackwelder and Kaplan, the average burst frequency can be measured with sufficient accuracy. The measurement is, however, very laborious. The time interval distribution, on the other hand, cannot be measured so accurately, due to the imperfect behaviour of the burst detector. The accuracy of these measurements can be improved by making the criteria for detection more complex. This would also improve the speed of the measurements of the average burst frequency.

On the basis of our experiments we may say that, as a good approximation, the average number of bursts per unit time was proportional to the Reynolds number. The average burst frequency is in reasonable agreement with the literature.

The measurements of the time interval distribution show a very wide distribution which is close to linear on a semi-logarithmic scale. This suggests a certain underlying mechanism that we do not yet know. But it is too typical to be accidental.

The velocity signals show that the phenomenon is accompanied by strong vortex motions. It is not clear from our experiments whether these are cause or result.

The good result obtained for the average burst frequency due to the use of the conditional average shows that the conditional average is meaningful. This is also illustrated by the ease with which velocity signals are obtained that are a good resemblance of the conditional average.

The disappearance of the vortex motions from the conditional average is probably caused by a wide spread in vortex diameter. As the vortex diameter is probably in some way related to the burst size, which in its turn will probably be related to the time interval between two bursts, this is not surprising because the time interval distribution is very wide. This implies that conditional averages should be used in combination with the velocity signals themselves.

The conditional averages reported here differ significantly from those reported in the literature. This is mainly due to the use of improved measuring and processing equipment.

One of the major problems at this moment is how to combine the results of the visualisation studies with studies like this one, in order to obtain a general model for the bursting phenomena in boundary layers. At this moment the conclusions drawn from the visualisation studies are not yet in agreement with each other. Some investigators conclude that the wall fluid is the cause of bursting, others report that the bulk fluid is the cause. The problem can probably only be solved if theoretical models can be formulated that explain the results found.

REFERENCES

1. S.J. Kline, W.C. Reynolds, F.A. Schraub and P.W. Runstadler, "The structure of turbulent boundary layers", J. Fluid Mech. 30, part 4 (1967), pp. 741-773.
2. E.R. Corino and R. S. Brodkey, "A visual investigation of the wall region in turbulent flow", J. Fluid Mech. 37, part 1 (1969), pp. 1-30.
3. A.E. Perry and T.T. Lim, "Coherent structures in coflowing jets and wakes, J. Fluid Mech. 88, part 3 (1978), pp. 451-463.
4. W.W. Willmarth and S.S. Lu, "Structure of the Reynolds stress near the wall", NATO-AGARD Conference Proceedings No. 93, London, Technical Editing and Reproduction Limited.
5. R.F. Blackwelder and R.E. Kaplan, "On the wall structure of the turbulent boundary layer", J. Fluid Mech. 76, part 1 (1976), pp. 89-112.
6. F. Durst, A. Melling and J.H. Whitelaw, "Principles and practice of laser-Doppler anemometry, London, Academic Press, 1976.
7. H.R.E. van Maanen, K. van der Molen and J. Blom, "Reduction of ambiguity noise in laser-Doppler velocimetry by a cross-correlation technique", Proceedings of the LDA-Symposium, Copenhagen, 1975, pp. 81-88.
8. R.F. Blackwelder, "On the role of phase information in conditional sampling", the Physics of Fluids, Vol. 20, No. 10, Pt. II, October 1977, pp. S232-S242.

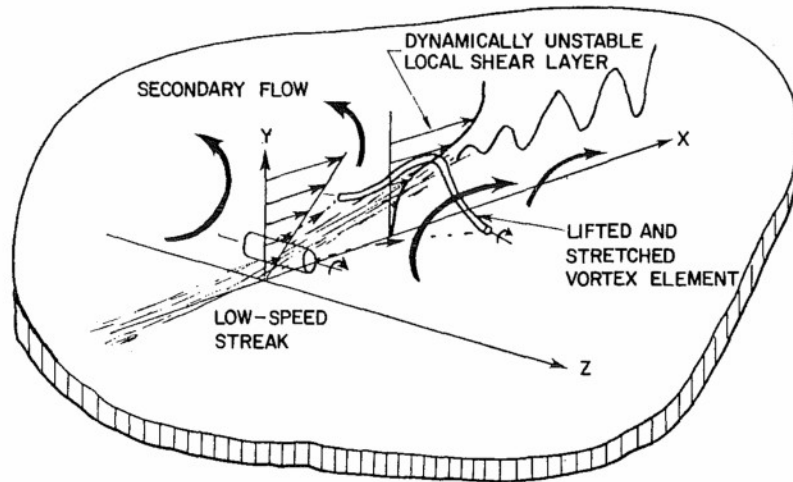


FIG. 1 SCHEMATIC DRAWING OF BURSTING PHENOMENON (TAKEN FROM REF. 1)

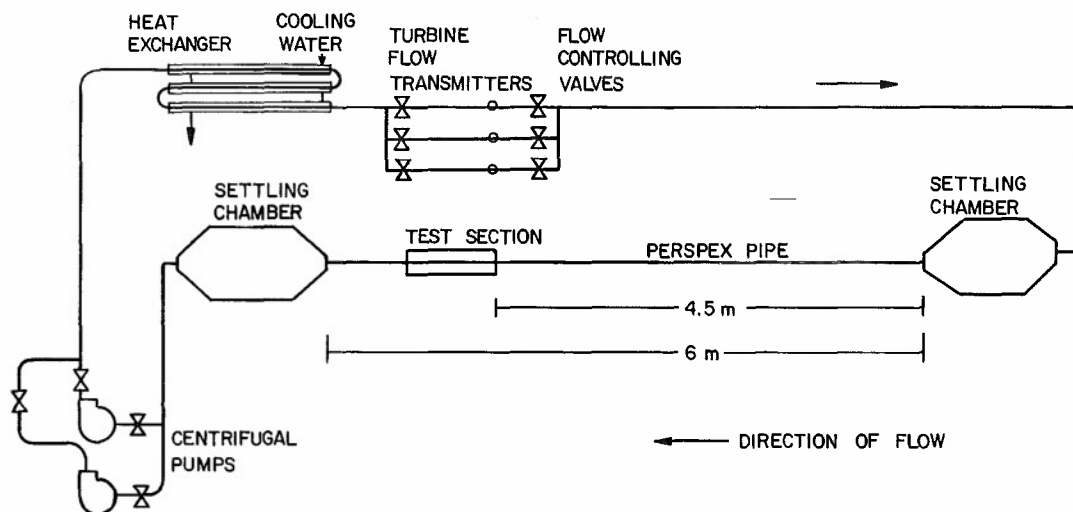


FIG. 2 SCHEMATIC DRAWING OF PIPE LOOP USED FOR EXPERIMENTS

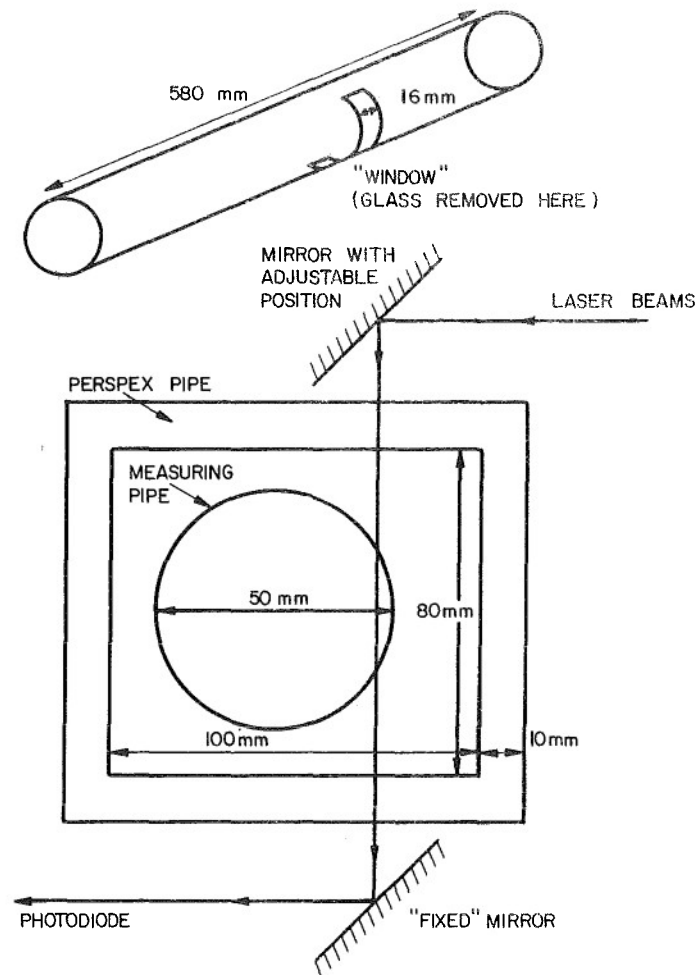


FIG. 3 CONSTRUCTION OF TEST SECTION AND PATHS OF LASER BEAMS

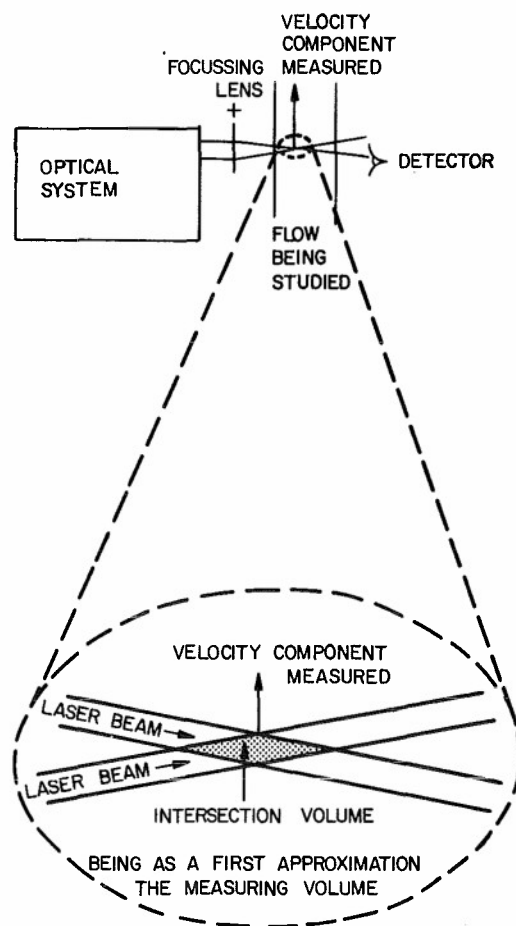


FIG. 4 SCHEMATIC DIAGRAM OF OPTICAL SYSTEM SHOWING POSITION OF MEASURING VOLUME IN FLOW

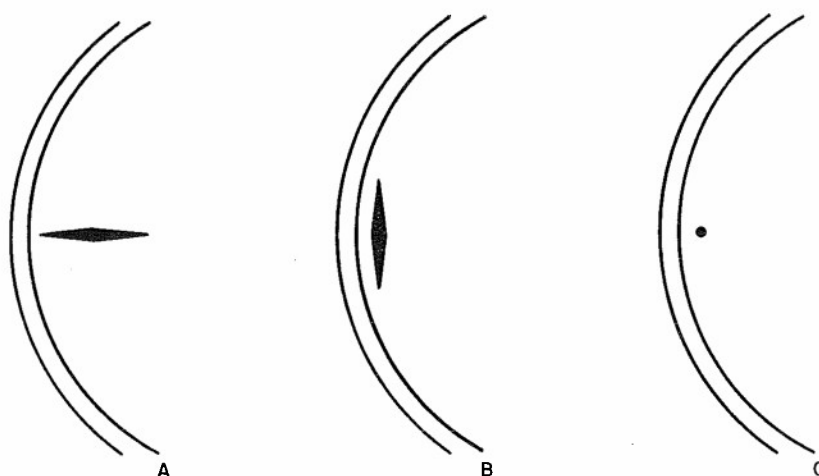


FIG. 5: THREE BASIC ORIENTATIONS OF MEASURING VOLUME

- A. RADIAL. AVERAGING TAKES PLACE OVER A RANGE WITH A STEEP GRADIENT IN THE VELOCITY PROFILE; WORST POSSIBLE ORIENTATION.
- B. TANGENTIAL. HIGH RESOLUTION IN RADIAL DIRECTION; OWING TO THE ROUNDING OF THE WALL THE RANGE OVER WHICH AVERAGING IS DONE IS SLIGHTLY LONGER THAN THE DIAMETER OF THE MEASURING VOLUME.
- C. AXIAL. BEST POSSIBLE ORIENTATION; CANNOT BE REALISED WITHOUT VERY COMPLEX OPTICAL SYSTEMS, AND IS THEREFORE NOT PRACTICAL.

(SIZE OF MEASURING VOLUME EXAGGERATED FOR CLARITY)

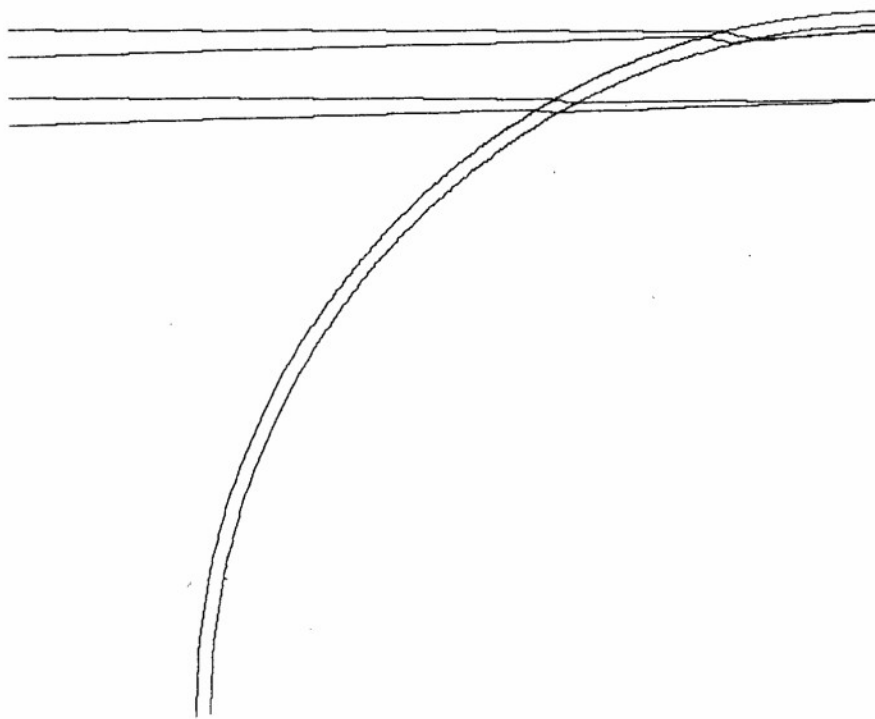


FIG. 6. DISTORTION OF BEAMS DUE TO DIFFERENCE IN REFRACTIVE INDEX OF WALL AND LIQUID AT 0.25 mm AND 2.75 mm FROM WALL  
 $n_{\text{LIQUID}} = 1.33$ ,  $n_{\text{WALL}} = 1.50$ , WALL THICKNESS = 0.5 mm

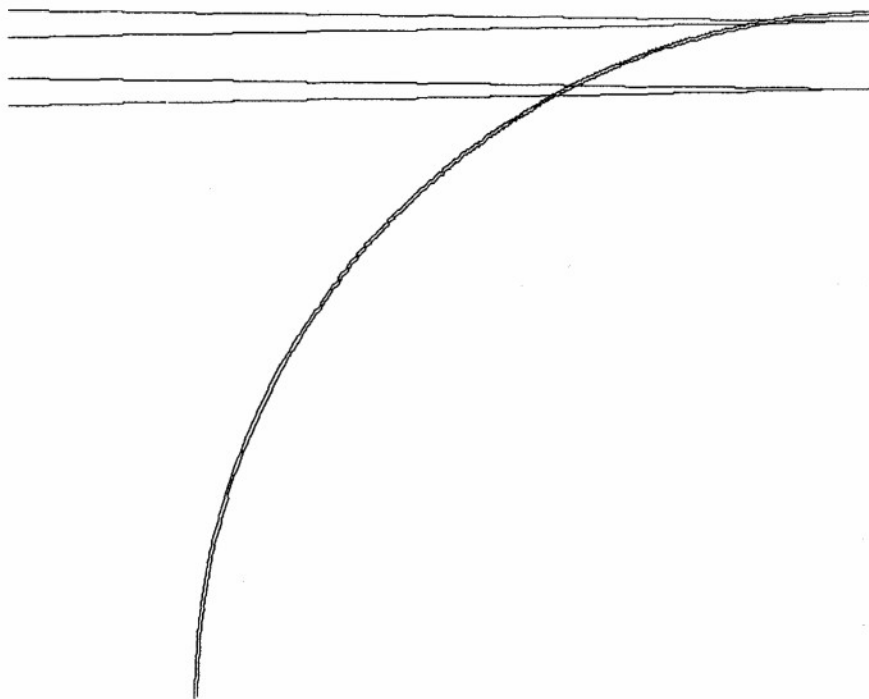


FIG. 7: AS FIG. 6, BUT WITH A WALL THICKNESS OF 0.1 mm

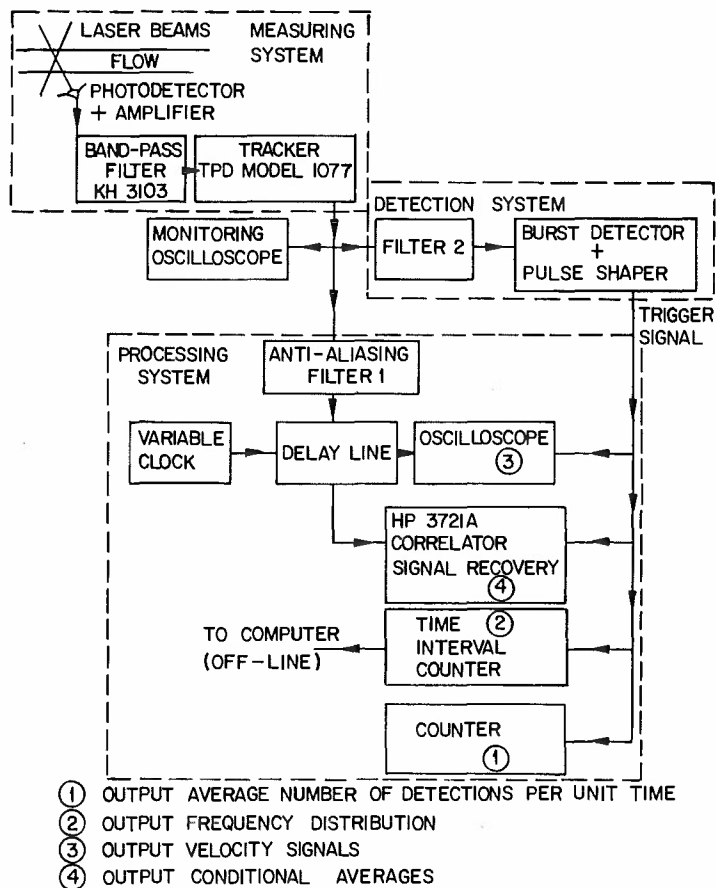


FIG. 8 BLOCK DIAGRAM OF SIGNAL PROCESSING EQUIPMENT



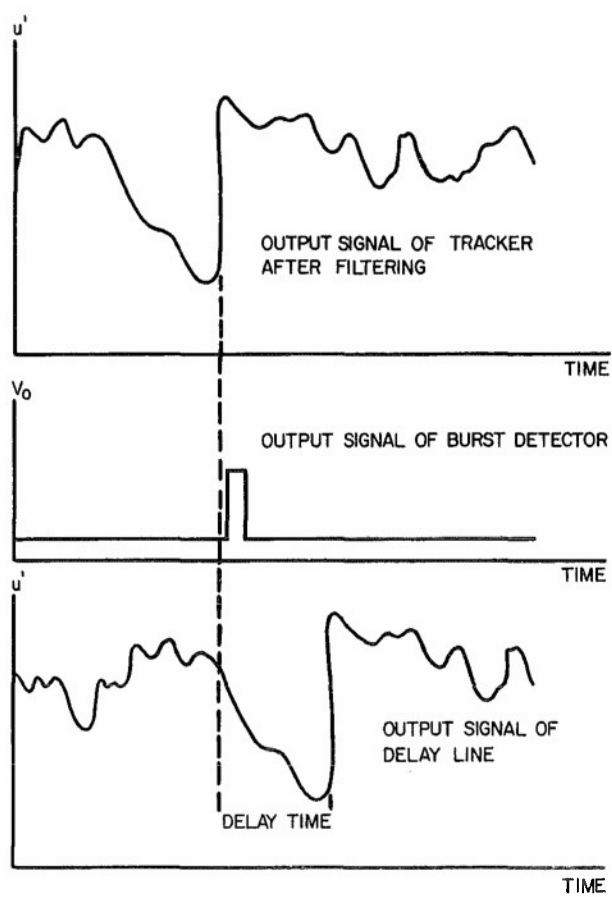


FIG. 9 THE THREE IMPORTANT SIGNALS IN MEASURING, DETECTION AND PROCESSING SYSTEMS IN RELATION TO EACH OTHER, ILLUSTRATING OPERATION OF DELAY LINE

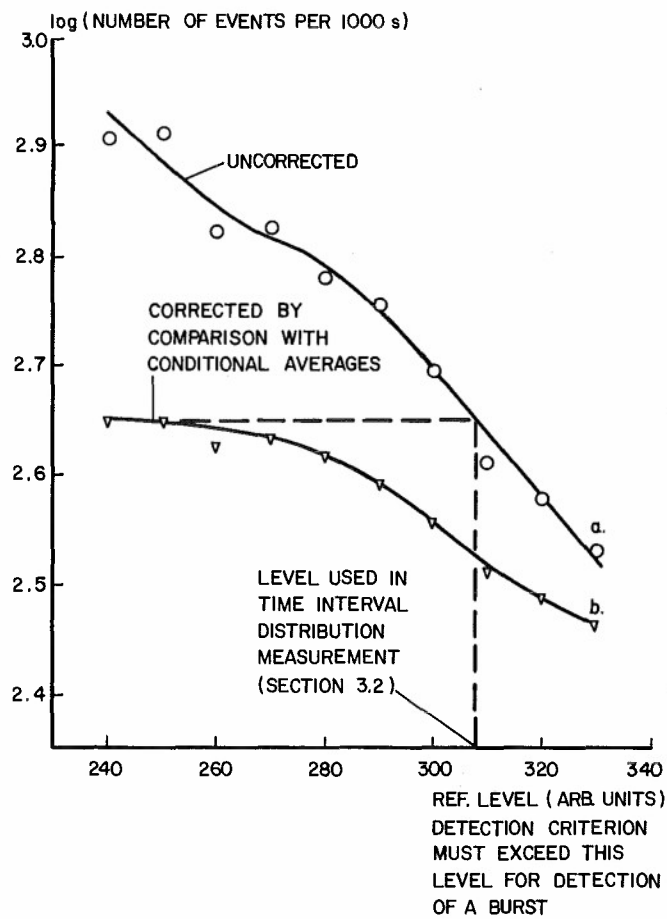


FIG. 10 NUMBER OF COUNTS PER UNIT TIME AS A FUNCTION OF REFERENCE LEVEL WITH AND WITHOUT CORRECTION FOR ERRONEOUS TRIGGERING MEASURED AT  $Re = 9500$  AT  $y^+ = 36$

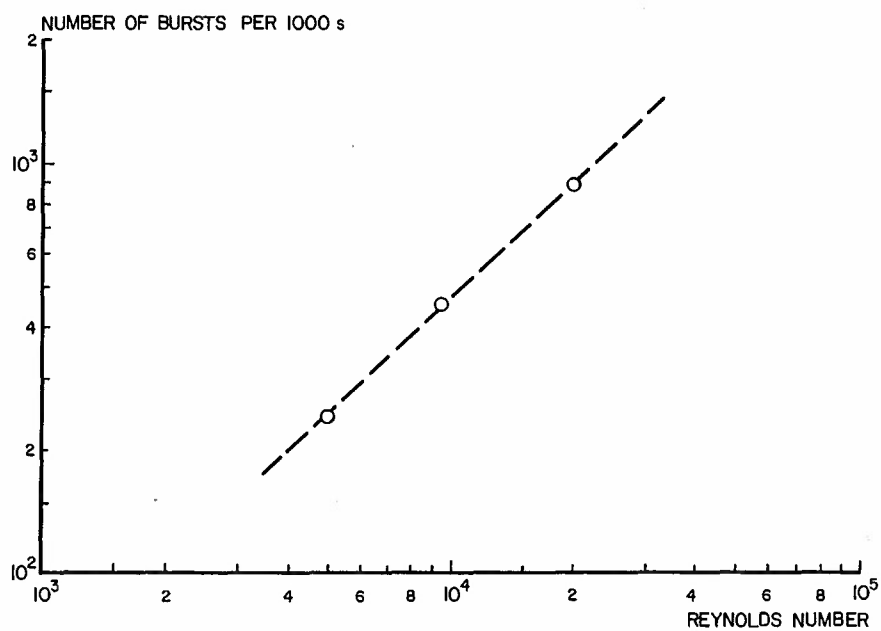


FIG. 11. AVERAGE BURST COUNT PER 1000 s AS A FUNCTION OF REYNOLDS NUMBER

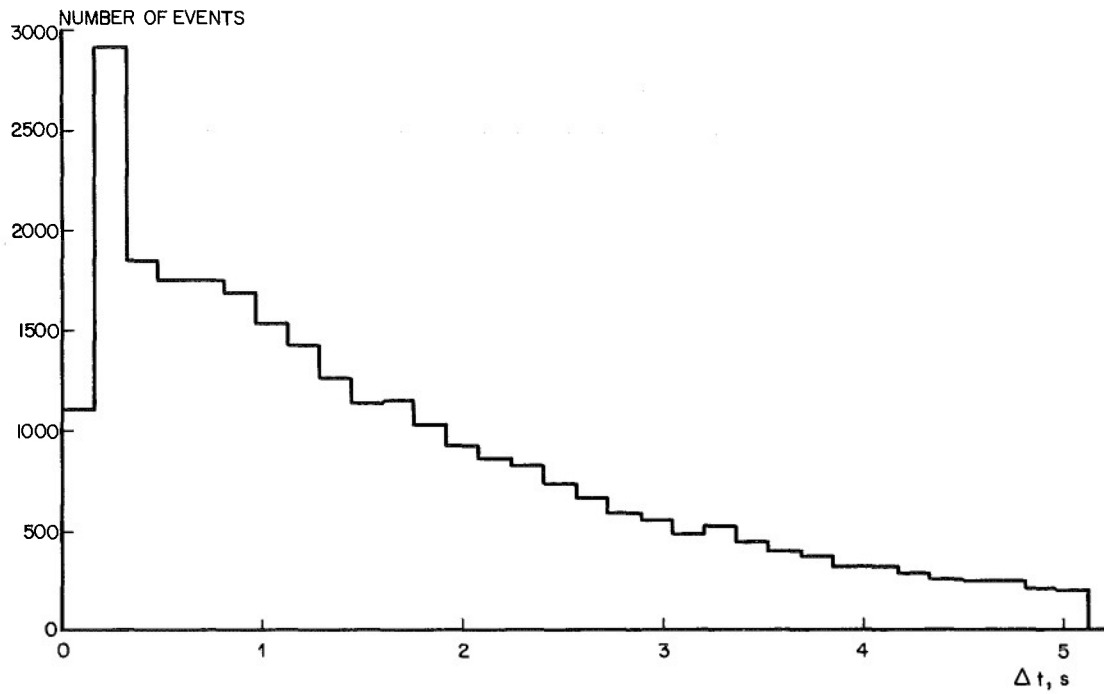


FIG. 12A. MEASURED DISTRIBUTION OF THE TIME BETWEEN TWO SUCCESSIVE DETECTIONS MEASURED AT  $Re = 9500$  AT  $y^+ = 36$   
 NUMBER OF MEASUREMENTS = 30 209; NUMBER OF MEASUREMENTS 5.12 s = 2230; DEAD TIME = 0.12 s

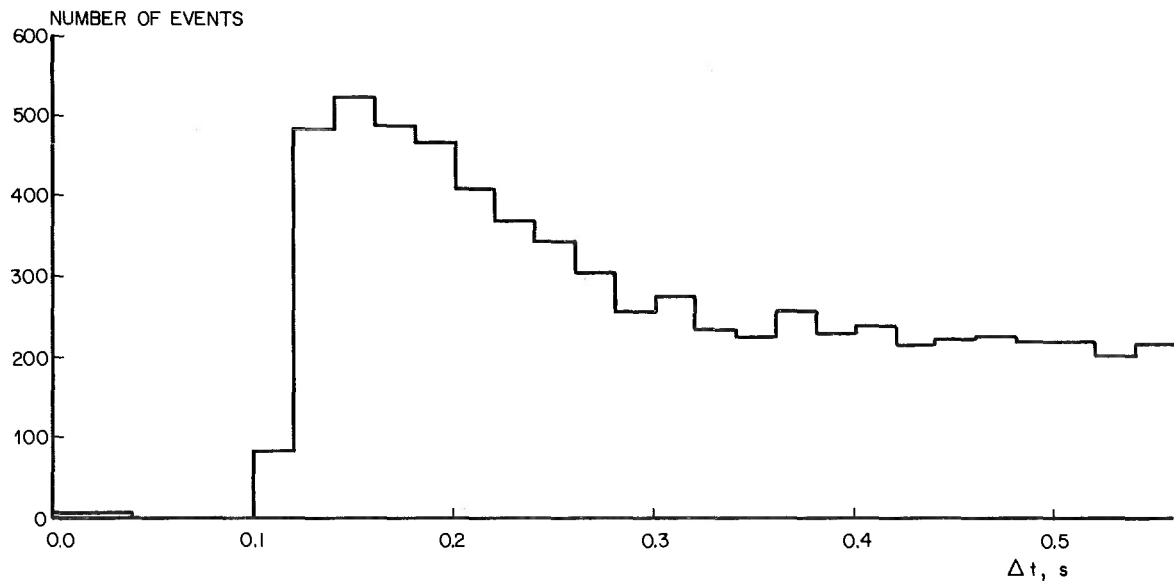


FIG. 12B: AS FIG. 12A, BUT HIGH-RESOLUTION DISTRIBUTION OF THE PEAK FOR SHORT TIME INTERVALS

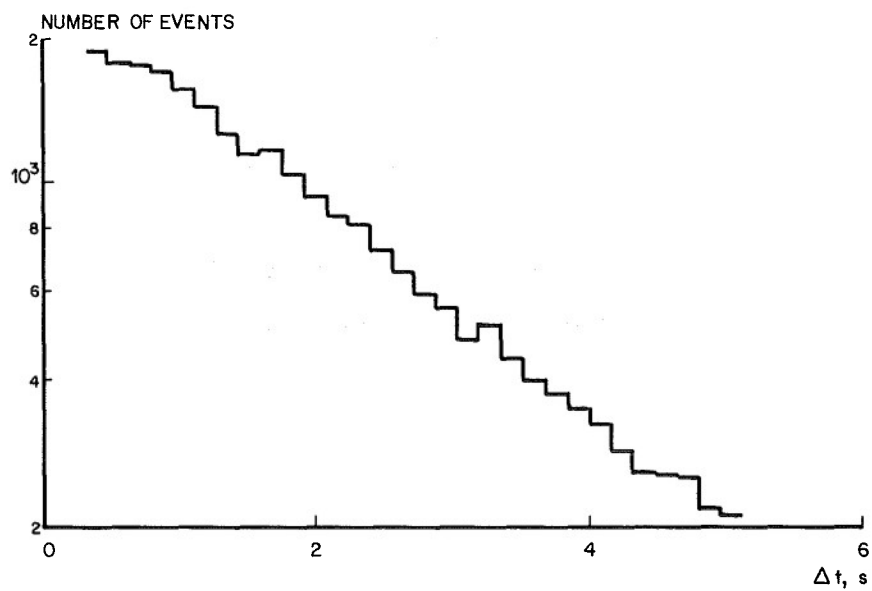
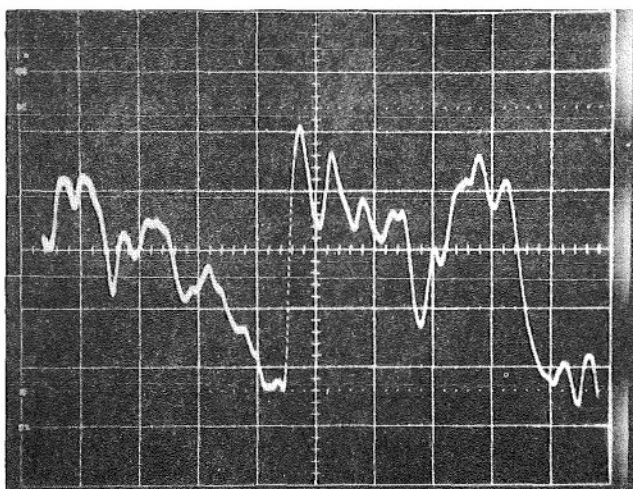
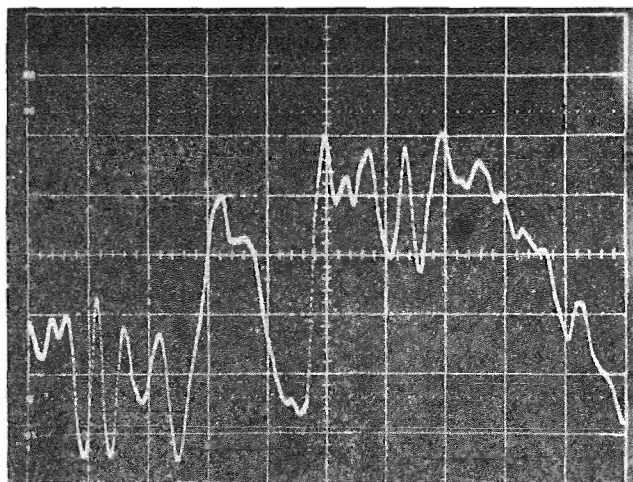
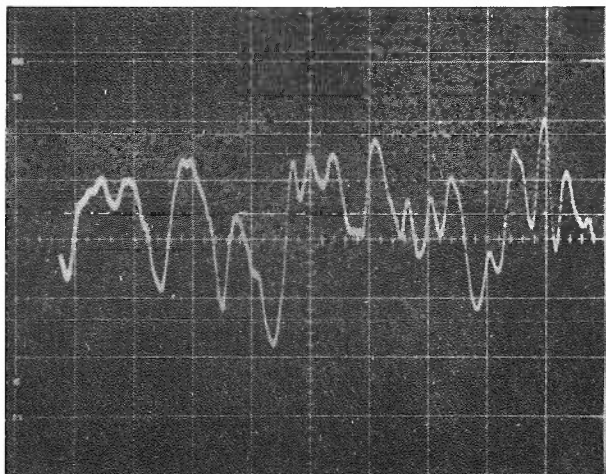
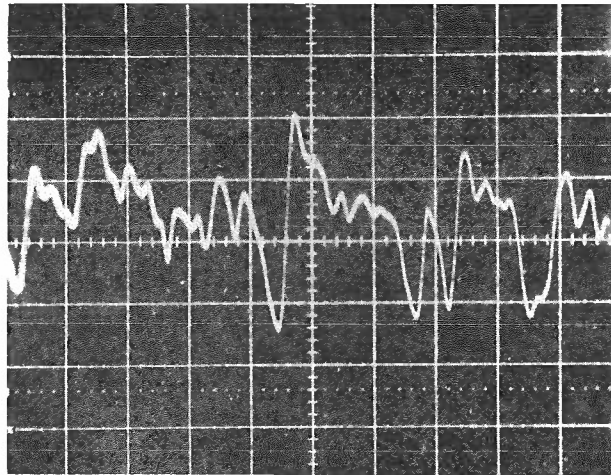


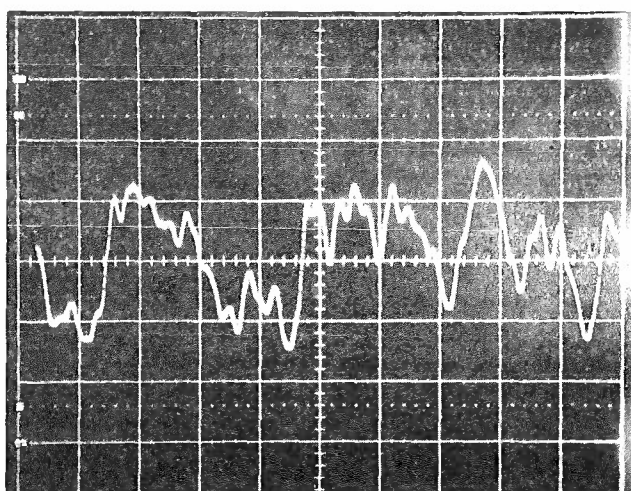
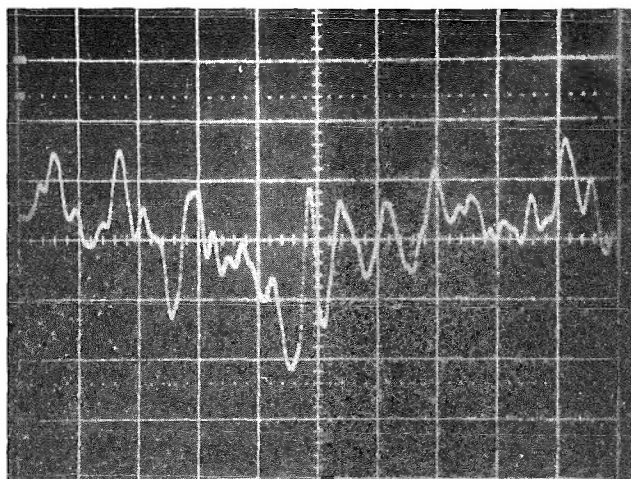
FIG. 13 SAME RESULTS AS SHOWN IN FIG. 12A (AMBIGUOUS FIRST TWO POINTS OMITTED)  
NOTE VERY NEARLY LINEAR BEHAVIOUR



FIGURES 14 AND 15: REPRESENTATIVE VELOCITY SIGNALS AT  $y^+ = 18$  AND  $Re = 9500$   
HORIZONTAL SCALE 0.2 s/div., VERTICAL SCALE 26.7 mm/s/div., AVERAGE VELOCITY OVER THE PIPE=190 mm/s



FIGURES 16 AND 17: AS FIGURES 14 AND 15, AT  $y^+ = 36$



FIGURES 18 AND 19: AS FIGURES 14-17, AT  $y^+ = 72$

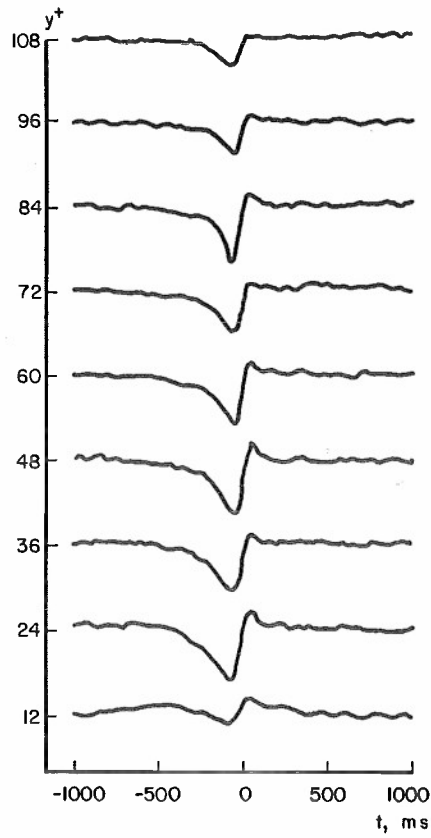


FIG. 20 CONDITIONALLY AVERAGED AXIAL VELOCITIES AT SEVERAL  $y^+$  VALUES MEASURED AT  $Re = 9500$ . COMPARE WITH FIGURES 14-19 (VERTICAL SCALE ARBITRARY)

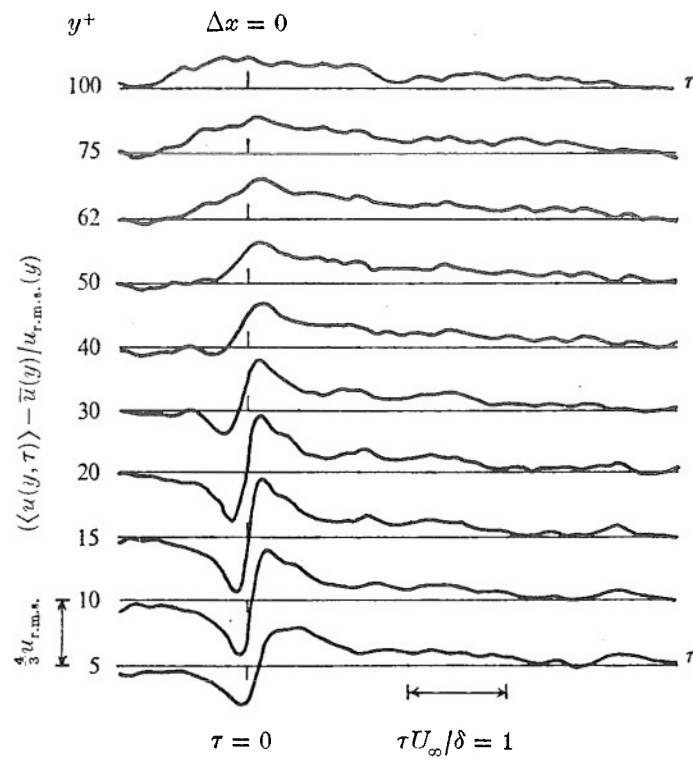


FIG. 21 : AS FIGURE 20;  $Re = 2550$ ; MEASURED IN AIR  
(TAKEN FROM REF. 5)



## TURBULENT BOUNDARY LAYER STRUCTURE AT LOW &amp; HIGH SUBSONIC SPEEDS

V. Zakkay,<sup>†</sup> V. Barra<sup>††</sup> and K. Hozumi<sup>†††</sup>  
 New York University  
 Department of Applied Science  
 26-36 Stuyvesant Street  
 New York, N.Y. 10003

Abstract

Results of simultaneous measurements of velocity, wall pressure, and wall-shear fluctuations in a turbulent boundary layer are presented. The measurements were performed in a range of velocities from 40-700 ft/sec, and a range of  $Re_\theta$  from  $10^4$  to  $10^5$ . The results are analyzed in an attempt to obtain a description of the coherent or quasi-ordered structure of the boundary layer turbulence. On a large scale, the boundary layer is dominated by vortical structures which extend to the viscous-inviscid region. The wall region is dominated by the so called "bursting" process. The relationship or interaction between the large scale outer structure and the turbulent "bursts" is still not clearly defined. The present experiments were particularly performed in order to understand how these processes develop and how their relationship changes with increasing Reynolds number. The results of this investigation at high speed, while confirming some of the previous results with regard to the mean period between coherent events, and their geometrical configuration, did not yet resolve the question as to whether at high subsonic speeds there is, besides the outer flow processes, a distinct inner region. With the limited instrumentation available it was not possible at the high subsonic speed to resolve any inner sublayer region, although it was found that the outer flow structures exert a strong influence on the wall. The experimental results at low subsonic speeds, on the other hand, did indeed identify an inner and outer region, and duplicated some of the results obtained at low subsonic speed by other investigations.

Introduction

The discovery, by means of visual observations (Refs. 1-7) of an organized structure in turbulent shear flows has led to a proliferation of new measurement and data analysis procedures for the investigation of the fluctuating properties of such flows (Ref. 8-19). Questions have been raised concerning the adequacy of measurements which utilize instrumentation and analyses not suited to the coherent, quasi-periodic nature of the flow structures. It has been found that the size of the transducers used in the measurements and the frequency response of the associated electronics is an important consideration in terms of the varied scales of the flow structures; and that single point measurements and conventional time averaged analyses cannot reveal much useful information about coherence or intermittency both of which are important aspects of the flow processes involved.

To overcome these problems, modern research efforts have turned to miniaturized instrumentation and multiple measurements to obtain spatial resolution of the coherent flow structures, and to digitization of the measurements so as to allow various time series analyses to be performed on high speed computers. With respect to the latter, it has become increasingly popular to apply various conditional sampling procedures to the digitized fluctuations in order to isolate temporal sequences associated with the coherent structures. This type of analysis has revealed, among other things, that significant contributions to the long time average Reynolds stress occur during intervals when coherent structures are present in the flow, thus indicating that the modelling of turbulence and the development of drag and noise reduction mechanisms might benefit greatly from a better understanding of these structures.

Visual observations of turbulent boundary layer flows seeded with various tracers have indicated the presence of several different processes involving repetitive flow structures. The wall region ( $y^+ = y u_\tau / \nu < 100$ ) is characterized by streamwise streaks of low speed fluid which lift up from the wall resulting in locally inflexional velocity profiles. The lift-up is followed by some sort of oscillatory motion and then a sudden breakup into small scale turbulence. The ejection of low speed fluid from the wall is accompanied by sweeps of high speed fluid from the outer regions toward the wall. This overall process has been referred to as a "burst" (Refs. 20-21). On a larger scale, the boundary layer is dominated by vortical structures which extend to the viscous-inviscid region (Refs. 6, 14, 16). The relationship or interaction between this large-scale outer structure (LSOS) and the turbulent "bursts" is still not clearly defined. In particular, how these processes and their relationship change with increasing Reynolds number has not been fully explored. On the basis of observations and measurements over a limited range of Reynolds numbers, it has become commonly accepted that the "bursting" process is strictly a sublayer phenomenon that scales with wall variables, while the large-scale outer structure is basically Reynolds number independent. A possible link between the two processes may exist in the fact that the frequency of occurrence of the turbulent "bursts" has been found to scale with outer flow variables and seems to be related to the period of passage of the outer structures (Refs. 22-23).

The primary goal of this investigation has been directed to study these phenomena at a high subsonic speed, and to specifically determine the possible role or influence of pressure fluctuations on the processes involved. Whereas most studies in this area tend to be at relatively low free stream velocities (typically,  $U_\infty < 100$  ft/sec) and Reynolds numbers ( $Re_\theta < 10^4$ ), the present results are for a turbulent boundary layer with  $U_\infty = 675$  ft/sec and  $Re_\theta = 108,000$ . In addition, simultaneous measurements of three properties of the turbulent flow, namely, the streamwise velocity, the wall shear and the wall pressure

<sup>†</sup> Chairman, Department of Applied Science, and Director of the Antonio Ferri Laboratories, New York University.

<sup>††</sup> Research Scientist, Antonio Ferri Laboratories, New York University.

<sup>†††</sup> Research Assistant, Antonio Ferri Laboratories, New York University.

were made. Preliminary results from measurements at  $U_\infty = 675$  ft/sec led to the conclusion that it would be of some value to have comparative measurements at lower velocities. Therefore measurements for boundary layers with  $U_\infty = 73$  ft/sec and  $U_\infty = 32$  ft/sec were also made, and are presented for comparison.

#### Experimental Facilities and Procedures

The New York University one foot diameter induction tunnel was used for this research. The facility has been described in detail in Refs. 19 and 24. The capability of varying the velocity from 30 to 700 ft/sec has since been added to the wind tunnel. In addition the wind tunnel was modified so as to allow the test section to be located at several distances from the inlet of the tunnel. This allowed the measurements to be made at various distances from the inlet depending on the boundary layer thickness required (at the lowest velocity, a boundary layer thickness of 3" was reached within 15 ft of the tunnel inlet).

The development of the data gathering system and the analysis programs has been a major part of the present research program (see Ref. 19). The system has been greatly improved by the acquisition of a PDP-11/34 mini-computer and a 14 channel tape recorder. The mini-computer system includes 64K bytes of memory, two terminals - one of which is an interaction CRT graphics terminal, floppy and cartridge disk mass storage, and most significantly, a 64 channel A/D converter with two programmable clocks. Programs have been developed on this system which are capable of performing the following analysis on a production run basis:

- 1) Long-time average auto and cross correlations.
- 2) Conditional sampling using the variable interval time average (VITA) variance (see Kaplan and Laufer (Ref. 25) or Blackwelder and Kaplan (Ref. 8)).
- 3) Pattern recognition analysis to compensate for random phase "jitter" in conditional samples (see Blackwelder (Ref. 26)).
- 4) Short-time, conditionally sampled auto and cross correlations (see Brown and Thomas (Ref. 14)).

These analyses can be applied directly to the original digitized data or to the data after it has been filtered using the Fast Fourier Transform to include only components within a chosen bandpass. In this way it should be possible to determine the importance or influence of different frequency ranges on particular results. From the use of the different analyses it should also be possible to determine if different approaches to conditional sampling produce comparable results when applied to the same data.

#### Test Conditions

In Ref. 19 experimental results were presented for  $U_\infty = 675$  ft/sec. Since that time the measurements have been repeated for two new sensor arrays and more extensive analyses have been performed. In addition, extensive mean and fluctuating flow measurements at  $U_\infty \approx 75$  ft/sec and  $U_\infty \approx 30$  ft/sec have also been made. The mean flow properties of the boundary layer at several stations along the tunnel for these three flow conditions are summarized in Table I. Simultaneous measurements of the fluctuations have been made primarily with the sensor array shown in Fig. 1 and more recently with that shown in Fig. 2. In the latter, six wall-shear measurements are oriented so as to yield information about the turbulent structure in the lateral directions. The present results are for data from the following test conditions:

- $U_\infty = 675$  ft/sec,  $X/D = 31$ , Both arrays (i.e., Figs. 1 and 2)
- $U_\infty = 73$  ft/sec,  $X/D = 15.5$ , Fig. 1 array only
- $U_\infty = 75$  ft/sec,  $X/D = 20.5$ , Fig. 2 array only
- $U_\infty = 32.6$  ft/sec,  $X/D = 20.5$ , Both arrays

The aim of these tests is to yield data over a wide range of Reynolds numbers (i.e., from approximately 5000 to 100,000) while maintaining the boundary layer thickness in the neighborhood of 3 to 4 inches. The friction velocity, an important parameter in terms of the wall layer, also takes on a wide range of values for these tests, that is, from 1.8 ft/sec to 18 ft/sec.

#### Discussion of Measurements

##### A. Velocity, Wall-Shear and Wall-Pressure (Fig. 1)

Spectral analyses of the measured fluctuations have shown basic agreement with previous measurements except in the case of the pressure fluctuations in the two low speed cases ( $U_\infty = 73$  ft/sec and  $U_\infty = 32.6$  ft/sec). As the result of many previous measurements it is to be expected that the rms level of the wall-pressure fluctuations will fall somewhere between 0.5% and 1% of the dynamic pressure,  $q_\infty$ . In the case of  $U_\infty = 675$  ft/sec a reasonable level of  $0.008 q_\infty$  was measured. But at  $U_\infty = 73$  ft/sec and  $32.6$  ft/sec the measured levels were equivalent to approximately  $0.23 q_\infty$  and  $0.65 q_\infty$ , respectively. The explanation for this is that, for the low speed tests, the wall-pressure fluctuations due to the turbulent boundary layer become so weak that they drop below the noise "floor" of the measuring devices. The noise "floor" is made up primarily of tunnel noise, although other sources such as transducer vibration response and misalignment with the tunnel wall may also contribute to it.

Research performed by other investigators, determined that the level of tunnel noise could be lowered with extensive acoustic treatment of the sonic throat section of the tunnel (where the flow undergoes rapid acceleration) and by improving the suspension system of the tunnel. These modifications were not undertaken for several reasons. First, in the high subsonic regime where the primary interest lies, the wall-pressure fluctuations due to the turbulent boundary layer are found to be sufficiently above the noise "floor" to allow for accurate measurements. Secondly, in the low speed case the main interest is in looking at the wall-shear and fluctuation velocity profiles (for comparison to those obtained at high speed), the measurement of which is not significantly affected by tunnel noise as the spectra of these measurements

seem to indicate. And lastly, the measurement of very low pressure levels would require transducers with much greater sensitivity than the ones that are presently being used.

Sections of the data are digitized for all three free stream velocities and for both of the measurement arrays shown in Figs. 1 and 2. Various combinations of the analyses listed previously are applied to the digitized data in an attempt to obtain results comparable to those found by other investigators and to compare certain properties of the quasi-ordered turbulent structure at the varied flow conditions. It is becoming more evident from continued use of the VITA variance analysis that one must be careful when looking at the mean period between events detected with this scheme. The number of times that the analysis will indicate the occurrence of an event in a fluctuating quantity used as a trigger will depend strongly on the threshold level applied to the VITA variance of that quantity. The results indicate that for all three free-stream velocities a threshold level equal to approximately one-half the long time rms of the fluctuating quantity in most cases yields a mean period between events given by  $TU_\infty/\delta \approx 5$ , although this will vary depending on the measurement used as the trigger. However, this period does not seem to be any more significant than any other that is obtained from this analysis with a different threshold. Some other criteria would have to be used to determine the threshold which has physical meaning in terms of a specific type of organized structure.

Although care must be taken when interpreting the mean period between events obtained in this way, an ensemble average of a set of events detected using the VITA variance can be helpful in depicting average or typical characteristics of coherent structures in the flow. Such a set of ensemble averages of the velocity and wall-shear fluctuations are shown in Figs. 3-5 for the three flow conditions and for the array shown in Fig. 1. They were obtained by applying the VITA variance analysis to the velocity fluctuations at  $y = .075''(O)$  to obtain a set of times where the fluctuations at this point indicate the occurrence of flow processes with certain repetitive characteristics. An ensemble average is then taken of 512 data points centered about these times for each of the six velocity and one wall-shear measurement. It can be seen from Fig. 3, that for  $U_\infty = 675$  ft/sec there is a definite correlation across all seven measurements; that is, the average structure that the analysis triggers on encompasses, or at least has a strong influence on, all seven measurements. That is not the case for the two low speed flows. Figures 4 and 5 show that, for the trigger at  $y = .075''(O)$  (i.e., in the wall region), the average structure extends or correlates only over the three or four measurements nearest the wall. The fact that this correlation seems to extend almost twice as far from the wall (i.e., to  $y = .275''(K)$ ) for  $U_\infty = 32.6$  ft/sec (Fig. 5) than for  $U_\infty = 73$  ft/sec (Fig. 4) may be an indication that this inner region shrinks toward the wall with increasing flow velocity, or alternatively, that it scales with wall variables.

To see whether a similar coherence exists in the outer measurements for the low speed flows, the analysis was repeated using the measurement at  $y = .375''(J)$  as a trigger. The results, shown in Figs. 6 and 7, indicate that there is a correlated structure in the outer region which does not seem to extend further down than  $y = .275''(K)$  from the wall. How far up in the boundary layer this coherence extends cannot be deduced from the present measurements.

An attempt has been made to determine if the loss of coherence with distance is due to noise that enters into the ensemble averages because of random variations in the phase between the events at the trigger and that at the measurement being averaged (see Blackwelder (Ref. 26)). A pattern recognition analysis was applied to adjust the phase, with respect to the trigger at  $y = .075''(O)$ , of each event in the ensemble averages. The results shown in Figs. 8 and 9 are to be compared to Figs. 4 and 5, respectively. Since each event in the ensemble averages has been shifted to zero time delay, the averaged events are centered about  $t = 0$  in all cases. The actual phase relationship of each average to the trigger at  $y = .075''(O)$  is given by the average shift of all the events in the ensemble. This is shown for each measurement position on both figures. It can be seen that for  $U_\infty = 73$  ft/sec (Figs. 4 and 8) this phase correction procedure has little effect in improving the ensemble averages, thus indicating that the loss of coherence in the outer measurements is not due to random phase "jitter" but rather to the fact that the flow structures in the wall region do not, on the average, extend beyond  $y \approx .075'' - .175''$  ( $y^+ \approx 112-261$ ). On the other hand, the phase correction procedure does result in a definite improvement in some of the averages for  $U_\infty = 32.6$  ft/sec (Figs. 5 and 8). This is particularly evident at  $y = .175''(L)$  and to a significantly lesser degree at  $y = .275''(K)$ . Thus, after correction for phase "jitter" it becomes more clear that as the velocity is lowered the coherence of the inner structure extends further from the wall (i.e., to  $y \approx .175'' - .275''$  for  $U_\infty = 32.6$  ft/sec) or perhaps that the inner region scales with wall variables ( $y^+ \approx 160-252$ ). The results of Fig. 3 for  $U_\infty = 675$  ft/sec are not inconsistent with this conclusion since all the measurements except the wall-shear are outside the wall region and the high degree of correlation of this measurement with the outer region may be only in terms of the low frequency components associated with the outer structure. This will be discussed further in the following paragraphs.

The ensemble averaged velocity and wall-shear fluctuations shown in Fig. 3 for  $U_\infty = 675$  ft/sec can be plotted to yield a sequence of fluctuating velocity profiles which are presented in Figure 10. The instantaneous total velocity profiles corresponding to this sequence are shown in Fig. 11. These profiles show a great many similarities to those which have been measured in the wall region of low speed boundary layer flows, in particular, to those obtained by Blackwelder and Kaplan (Ref. 8). Attempts to depict the profiles in the low speed cases is hindered by the limited number of measurements in a given region, but indications are that the flow structures in both the inner and outer regions show the same type of coherence. (A similar conclusion was reached by Chen and Blackwelder (Ref. 16) from measurements of velocity and temperature in a boundary layer over a slightly heated wall). It is not possible to say whether these similarities are a result of the fact that the wall region "bursts" possess the same type of time signatures in terms of the streamwise velocity as the large scale outer structure or that they are a consequence of the detection scheme being used, that is to say, the detection scheme triggers on some "typical" structure which exists in both regions.

On the assumption that the former is the case, the available data will be analyzed further to determine what relationship exists between measurements in the inner and outer regions. From this, some insight may be gained into a possible interaction mechanism between the wall region "bursts" and the large scale outer structure. For the low speed flows, this will involve examining individual events occurring in the inner and outer regions and seeing if any interaction exists between them. In the high speed case this can only be done with the wall measurements. By looking at these fluctuations in various frequency

ranges it may be possible to isolate the components associated with the "bursting" process and to determine what relationship exists between these and the large scale flow structures. The success of such an analysis will depend strongly on the ability to accurately resolve the very small scales associated with turbulent "bursts". In this regard, a commercially available pressure transducer having a diameter of 0.010" will be tested and its output compared to that from the transducers now being used ( $d = 0.040$ ").

Some preliminary results have been obtained concerning the behavior of the wall pressure fluctuations from the measurements and data discussed in Ref. 19 for  $U_\infty = 675$  ft/sec. The measurement grid was similar to that shown in Fig. 1 except that fewer sensors were available at that time and the streamwise velocity was measured at slightly different positions. Figure 12 shows the result of taking the ensemble average of 60 events detected over an interval of  $TU_\infty/\delta^+ = 2000$  using the velocity fluctuations at  $y/\delta^+ = 0.088$  as the trigger. The velocity and shear fluctuations are basically the same as those in Fig. 3 since the trigger is at approximately the same position in both cases. From Fig. 12 the wall pressure fluctuations can be seen to be characterized by a well defined period of overpressure during the passage of the flow structures in the outer region. An examination of the wall pressure fluctuations during individual events consistently shows the superposition of large amplitude high frequency components on the more slowly varying period of overpressure. The fact that these high frequency components do not appear on the average would indicate that they are either a random phenomenon or that they occur at a random phase with respect to the process which triggers the detection scheme. It should be possible to determine which is the case by filtering the pressure fluctuations to obtain some representation of the high frequency components and then applying a detection scheme to see if coherence also exists in this aspect of the data. A dominant phase relationship between the low and high frequency components of the fluctuations could also be determined by cross-correlating the two.

#### B. Wall-Shear Measurements in the Lateral Direction (Fig. 2)

Measurements with the wall-shear array shown in Fig. 2 have been analyzed for  $U_\infty = 675$ , 75, and 32.6 ft/sec. Figures 13-15 show the results of taking ensemble averages at each position using the measurement at C as the trigger for detecting the occurrence of events. It can be seen that except for the high speed case (Fig. 13) there is no discernible correlation in the lateral direction, whereas a definite correlation exists for the measurement (F) oriented directly downstream of the trigger position. This is to be expected since previous measurements as well as visual observations have indicated that both the wall region "bursts" and the large scale outer structures maintain a high degree of coherence for large distances in the streamwise direction. The extent and spread of these structures in the lateral direction is much more limited. In the case of the wall region processes, for example, the separation between the streamwise streaks is estimated to be on the order of  $Z^+ \approx 100$ , while each individual streak is confined to a fraction of this distance.

It is not clear from the results of Figs. 13-15 whether the detection scheme we are using triggers on the wall region structures or on the response of the wall shear to the passage of the large scale outer structures. It can be seen from the non-dimensional distances in Fig. 2 that, at least in the case of  $U_\infty = 32.6$  ft/sec, the size and separation of the wall shear sensors should be adequate for discerning some aspects of the wall region processes. However, several factors would seem to indicate that the typical wall shear response seen in the measurements at C and F in Figs. 13-15 is a result of the large scale outer structure. First, the typical response histories in the low speed cases (Figs. 14 and 15) consistently show that what appears to be an overshoot or superimposed high frequency component at the top of the rapid change in the wall shear. A similar phenomenon was observed by Brown and Thomas (Ref. 14) in their wall shear measurements and led them to speculate that the superimposed high frequency component was a manifestation of the "bursting" process. The high frequency component was seen to occur at a well determined phase with respect to the low frequency component attributable to the large scale outer structure, specifically, it occurred near positive maxima of the fluctuating shear. A similar conclusion concerning the present results would seem to be supported by the fact that this effect appears to be more pronounced in Fig. 15, i.e.,  $U_\infty = 32.6$  ft/sec (where better resolution is possible of the wall region processes) than in Fig. 14 for  $U_\infty = 75$  ft/sec, and does not appear at all in Fig. 13 for  $U_\infty = 675$  ft/sec where the instrumentation is not capable of resolving any processes on the scale of the wall region.

A second indication that the well defined time signatures in Figs. 13-15 are basically the response of the wall shear to the outer structure comes from the results of a phase correction analysis shown in Figs. 16 and 17 for  $U_\infty = 675$  ft/sec, in Figs. 18 and 19 for  $U_\infty = 75$  ft/sec and in Figs. 20 and 21 for  $U_\infty = 32.6$  ft/sec. The set of events which are detected by using  $\tau'(C)$  as a trigger are divided into two groups depending on the phase relationship between each event at C and any similar event found at B by the pattern recognition analysis referred to earlier. The search for a similar event was restricted to time delays approximately in the range  $-5 < t'U_\infty/\delta^+ < 5$ . The ensemble averages obtained for the set of events where a match was found at a later time in  $\tau'(B)$  (positive delay) are shown in Figs. 16, 18, and 20 and at an earlier time (negative delay) in Figs. 17, 19 and 21. The average time delay by which the events in each ensemble average were shifted is also indicated in these figures. The marked improvement, particularly for the two low speed cases, in the ensemble averages (compared to Figs. 13-15) shows that a coherence exists in the lateral direction which was previously obscured by random phase "jitter" and which extends across three or four of the measurements, i.e.,  $Z^+ \approx 500-5000$ . This could not be as a result of wall region processes which have been observed to be confined to lateral distances on the order of  $Z^+ \approx 50$ .

The fact that the events can be separated into two groups with opposite phase relationships across the lateral measurements is thought to be an indication of the "arrowhead" or "horseshow" type shape (see Fig. 2) that has been hypothesized for the large scale outer structure when looked at from above the wall of the boundary layer. It is clear that the phase relationship one would obtain among a set of lateral measurements would depend on which "leg" of the structure crosses the measurements. From the results of Figs. 16-21 it is possible to estimate the angles  $\theta^+$  and  $\theta^-$  in Fig. 2 that each "leg" makes with the X-axis. Taking the average time delay between the measurements at C and F one obtains a streamwise convection velocity of  $U_c/U_\infty = 0.70$  for  $U_\infty = 675$  ft/sec,  $U_c/U_\infty = 0.69$  for  $U_\infty = 75$  ft/sec and  $U_c/U_\infty = 0.64$  for  $U_\infty = 32.6$  ft/sec. Using these convection velocities and the time delay between  $\tau'(C)$  and  $\tau'(B)$  in Fig. 16, the angle  $\theta^+$  is estimated (locally and on the average) to be  $5.8^\circ$  for  $U_\infty = 675$  ft/sec. The time delay in Fig. 19 yields a  $\theta^-$  of  $6.3^\circ$ . Similarly from Figs. 18 and 19 for  $U_\infty = 75$  ft/sec  $\theta^+ \approx 18^\circ$  and

$\theta^- \approx 15^\circ$ , and from Figs. 17 and 18 for  $U_\infty = 32.6$  ft/sec  $\theta^+ = 20^\circ$  and  $\theta^- = 17^\circ$ . The slight differences in  $\theta^+$  and  $\theta^-$  are due to errors in the estimates, since by symmetry they should be equal. The results in the two low speed cases compare favorably with the angle of  $22^\circ$  estimated by Thomas (Ref. 15) from similar measurements at  $U_\infty \approx 100$  ft/sec. The much smaller angle obtained in the high speed case could be an indication that the flow structures become more confined in the lateral direction as the free stream velocity is increased.

### Conclusions

Measurements of the fluctuating properties of a turbulent boundary layer for a wide range of free stream conditions have been analyzed to obtain information concerning coherent or quasi-ordered structures in the flow. The primary interest of the investigation is for free stream velocities in the high subsonic regime (specifically,  $U_\infty = 675$  ft/sec), although comparative measurements have been made at two lower velocities, i.e.  $U_\infty \approx 75$  ft/sec and  $U_\infty \approx 30$  ft/sec. The Reynolds number,  $Re_\theta$ , ranges from  $10^5$  down to approximately  $10^4$ , while the boundary layer thickness is maintained relatively constant at between 3 to 4 inches.

Recordings of the fluctuating streamwise velocity, wall-shear, and wall-pressure in the boundary layer are digitized to obtain simultaneous time histories of the fluctuations. These are analyzed on a mini-computer using various conditional sampling procedures to isolate temporal sequences associated with the coherent structures. From this the mean period between occurrences of the flow structures is estimated and ensemble averages found. These ensemble averages and cross-correlations between measurements at different positions during the occurrence of events are used to deduce information concerning the geometry of the flow structures.

Measurements for two arrays of sensors have been analyzed in this way. In one, wall-shear and wall-pressure sensors are aligned in the streamwise direction upstream of a rake of six streamwise velocity probes. In the other, wall-shear measurements are aligned so as to yield information about the flow structures in the lateral direction. Using a variable-interval time-average (VITA) variance analysis to detect the occurrence of events in the data, the mean period between events ( $\bar{T}$ ) is found to be approximately given by  $TU_\infty/\delta \approx 5$ , although some variation is found depending on the measurement used as the trigger for detection. The number of events detected using this technique, however, is strongly dependent on the threshold chosen in the analysis. The estimate given here was obtained with thresholds in the neighborhood of one-half the overall rms of the fluctuations under consideration. But this choice seems rather arbitrary and the resulting mean period between events should be judged accordingly.

Irregardless of these questions about the number of events detected, a normalized ensemble average of all the events is useful in depicting certain characteristics of the flow structures. In the case of the streamwise velocity measurements normal to the wall for  $U_\infty = 675$  ft/sec, it was found that the average structure correlates well over all the measurements including the wall-shear. This was not the case for the two low speed flows. If a measurement near the wall is used as a trigger the resulting ensemble averages display coherence only up to a certain distance from the wall (i.e., up to  $y^+ \approx 100-200$ ). A similar coherence exists in the outer measurements when one of these is used as a trigger. In addition, the boundary between the inner and outer regions seems to be further from the wall for  $U_\infty = 326$  ft/sec than for  $U_\infty = 73$  ft/sec. This may be an indication that the inner region scales with wall variables.

The similarity of the coherence in the inner and outer regions as well as the similarity between the present measurements in the high speed case (which, except for the wall measurements, are in the outer region) and the results obtained by others in the wall region of low speed flows may be due to one of two reasons. Either the detection scheme being used triggers on some "typical" structure existing in various regions of the boundary layer, or the wall region "burst" process exhibits the same time signature in terms of the streamwise velocity as certain aspects of the large scale outer structure. It is not possible to determine from the present results which of these is actually the case.

Of particular interest in the high speed results is the fact that the coherence seen in the outer measurements extends to the wall. Both the wall-shear and the wall-pressure show a definite correlation to the passage of the outer structure. This is not the case, at least on the average, for the two low speed flows. By looking at individual events in the low speed measurements more carefully it should be possible to determine if there are events which exhibit some correlation between the inner and outer regions. To determine whether the strong correlation seen in the high speed measurements is due to the inability of the sensors to resolve the small scales associated with the wall region processes, a pressure transducer which is  $\frac{1}{4}$  the size of those now being used will be tested. With regards to this question of the interaction between wall region processes and the large scale outer structure, an attempt will also be made to look at the measurements in various frequency ranges and to see what relationship exists between them.

Two important results were obtained from the wall-shear measurements which concentrated on the lateral aspects of these flow structure, or to be more precise, of their "footprint". From two measurements aligned in the streamwise direction, the average convection velocity of the flow structures was found to be in the range  $U_c = 0.6 - 0.7 U_\infty$ . This result, combined with the phase relationship found between the same event as measured at two adjacent lateral position, was used to determine the angle that the sides of the flow structure makes with the streamwise direction. This angle was found to be approximately  $20^\circ$  for  $U_\infty = 32.6$  ft/sec and  $18^\circ$  for  $U_\infty = 75$  ft/sec. In the high speed case ( $U_\infty = 675$  ft/sec) a much smaller angle of about  $6^\circ$  was estimated. This would seem to indicate that the flow structures tend to become more confined in the lateral direction as the flow velocity increases.

### References

1. Kline, S.J., Reynolds, W.C., Schraub, F.A. and Runstadler, P.W., "The Structure of Turbulence," Journal of Fluid Mechanics, 30:741, 1967.
2. Corrinno, E.R. and Brodkey, R.S., "A Visual Investigation of the Wall Region in Turbulent Flow," Journal of Fluid Mechanics, 37:1, 1969.

3. Kim, H.T., Kline, S.J., and Reynolds, W.C., "The Production of Turbulence Near a Smooth Wall in a Turbulent Boundary Layer," *Journal of Fluid Mechanics*, 50:133, 1971.
4. Offen, G.R. and Kline, S.J., "Combined Dye Streak and Hydrogen Bubble Visual Observations of a Turbulent Boundary Layer," *Journal of Fluid Mechanics*, 62:223, 1974.
5. Falco, R.E., "Some Comments on Turbulent Boundary Layer Structure Inferred from the Movements of a Passive Contaminant," *AIAA Paper No. 74-99*, 1974.
6. Falco, R.E., "Coherent Motions in the Outer Region of Turbulent Boundary Layer," *Physics of Fluids*, 20:S124, 1977.
7. Smith, C.A., "Visualization of Turbulent Boundary Layer Structure Using a Moving Hydrogen Bubble-Wire Probe," *Proc. of the Workshop on Coherent Structure of Turbulent Boundary Layers*, p. 48, 1978.
8. Blackwelder, R.F. and Kaplan, R.E., "The Intermittent Structure of the Wall Region of the Turbulent Boundary Layer," *U. Southern California, A.E. Report No. 1-22*, 1972.
9. Wallace, J.M., Eckelman, H., and Brodkey, R.A., "The Wall Region in Turbulent Shear Flow," *Journal of Fluid Mechanics*, 54-39, 1972.
10. Lu, S.S. and Willmarth, W.W., "Measurements of the Structure of the Reynolds Stress in a Turbulent Boundary Layer," *Journal of Fluid Mechanics*, 60:481, 1973.
11. Emmerling, R., "The Instantaneous Structure of the Wall Pressure Under a Turbulent Boundary Layer," *Max-Planck-Institut für Stromungslehre, Rep. No. 9*, 1973.
12. Dinkelacker, A., Hessel, M., Meier, G.E.A., and Schewe, G., "Investigation of Pressure Fluctuations Beneath a Turbulent Boundary Layer by Means of an Optical Method," *Physics of Fluids*, 20:S216, 1977.
13. Zilberman, M., Wygnanski, I., and Kaplan, R., "Transitional Boundary Layer Spot in a Fully Turbulent Environment," *Physics of Fluids*, 20-S258, 1977.
14. Brown, G.L. and Thomas, A.S.W., "Large Structure in a Turbulent Boundary Layer," *Physics of Fluids*, 20:243, 1977.
15. Thomas, A.S.W., "Organized Structure in the Turbulent Boundary Layer," *Lockheed-Georgia Report LG77ER0210*, 1977.
16. Chen, C.P. and Blackwelder, R.F., "Large-scale Motion in a Turbulent Boundary Layer: A Study Using Temperature Contamination," *Journal of Fluid Mechanics*, 89:1, 1978.
17. Eckelmann, H., Wallace, J.M., and Brodkey, R.A., "Pattern Recognition, a Means for Detection of Coherent Structures in Bounded Turbulent Shear Flows," *Proc. of the Dynamic Flow Conference*, p. 161, 1978.
18. Wygnanski, I., "The Recognition of an Evoked Large-Scale Structure in Turbulent Shear Flows," *Proc. of the Dynamic Flow Conference*, p. 191, 1978.
19. Zakkay, V., Barra, V., and Wang, C.R., "The Nature of Boundary Layer Turbulence at a High Subsonic Speed," *AIAA Journal*, 17:356, 1978.
20. Offen, G.R. and Kline, S.J., "A Proposed Model of the Bursting Process in Turbulent Boundary Layers," *Journal of Fluid Mechanics*, 70:209, 1975.
21. Kline, S.J., "The Role of Visualization in the Study of the Structure of the Turbulent Boundary Layer," *Proc. of the Workshop on Coherent Structure of Turbulent Boundary Layers*, p. 1, 1978.
22. Rao, K.N., Narasimha, R., and Badri Narayanan, M.A., "The Bursting Phenomenon in a Turbulent Boundary Layer," *Journal of Fluid Mechanics*, 48:339, 1971.
23. Laufer, J. and Badri Narayanan, M.A., "Mean Period of the Production Mechanism in a Boundary Layer," *Physics of Fluids*, 14:182, 1971.
24. Zakkay, V., Barra, V., and Hozumi, K., "Investigation of the Fluctuation Mechanism in Turbulent Flow," *Final Report prepared under Contract AFOSR-76,2497*, December 1978.
25. Kaplan, R.E. and Laufer, J., "The Intermittently Turbulent Region of the Boundary Layer," *12th Proc. Int. Congr. Mech.*, p. 236, 1969.
26. Blackwelder, R.F., "On the Role of Phase Information in Conditional Sampling," *Phys. Fluids*, 20:S232, 1977.

X/D	15.5	20.5	9.	15,5	31.	31.
$M_{\infty}$	0.0263	0.0296	0.063	0.067	0.072	.64
$U_{\infty}$ (ft/sec)	29.6	32.6	69.0	73.0	79.0	675
$q_{\infty}$ (psi)	0.0068	0.0086	0.039	0.046	0.054	2.9
$\delta$ (in)	2.7	3.5	2.15	3.0	$\approx 5.5$	4.0
$\delta^*$ (in)	0.39	0.497	0.265	0.37	$\approx 0.8$	0.564
$\theta$ (in)	0.31	0.387	0.206	0.29	$\approx 0.6$	0.384
$Re_{\theta}$	$4.62 \times 10^3$	$6.56 \times 10^3$	$8.45 \times 10^3$	$1.25 \times 10^4$	$2.82 \times 10^4$	$1.08 \times 10^5$
$\nu/u_{\tau}$ (in)	$1.66 \times 10^{-3}$	$1.09 \times 10^{-3}$	$.69 \times 10^{-3}$	$.67 \times 10^{-3}$	$.68 \times 10^{-3}$	$1.32 \times 10^{-4}$
$\nu/u_{\tau}^2$ (usec)	120	51.6	24.0	22.5	23.0	0.62
$(u'/u)_{\infty}$	0.005	-	-	0.005	0.021	0.008

TABLE I

Mean Flow Parameters at Several Stations for Three Test Conditions



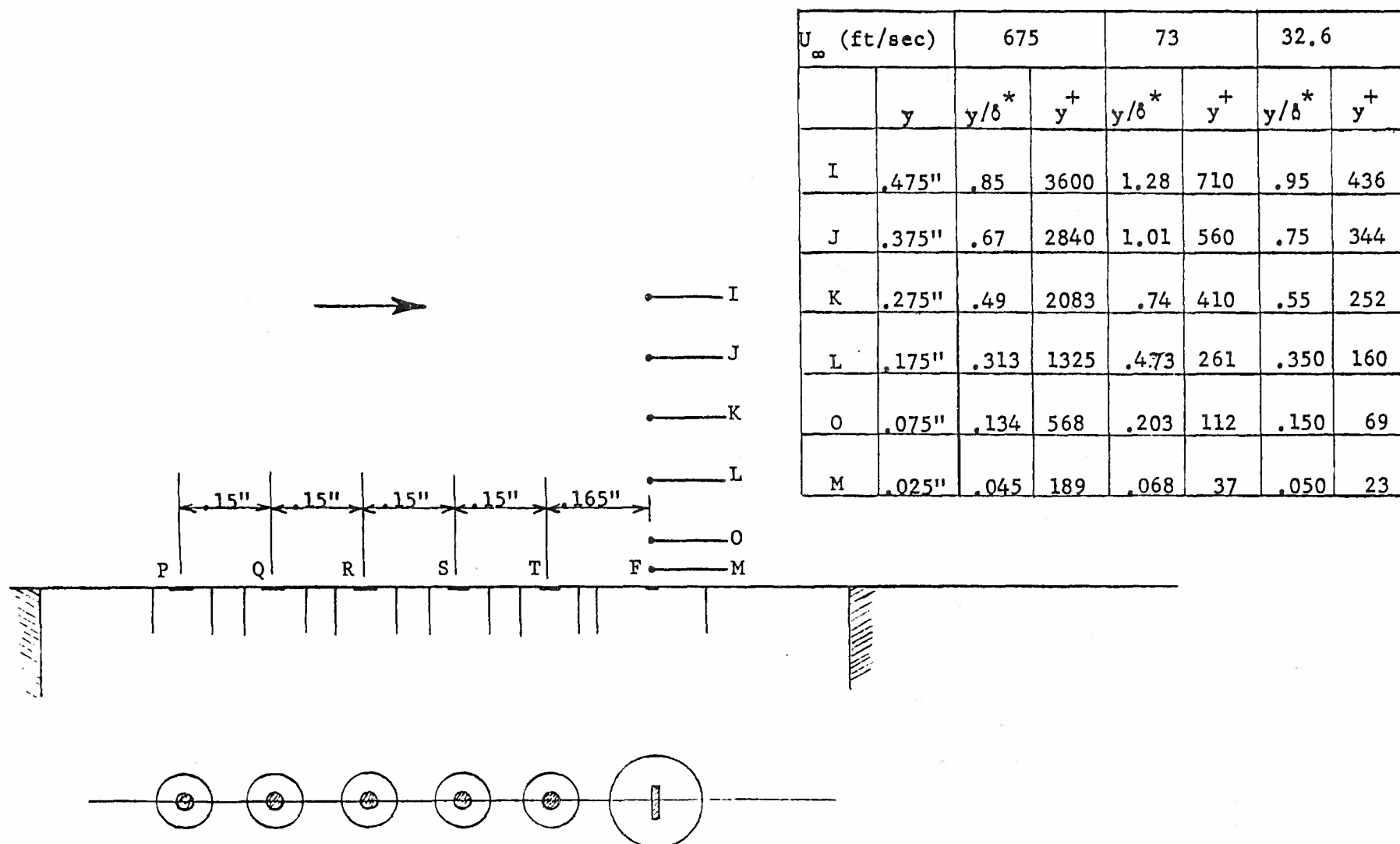
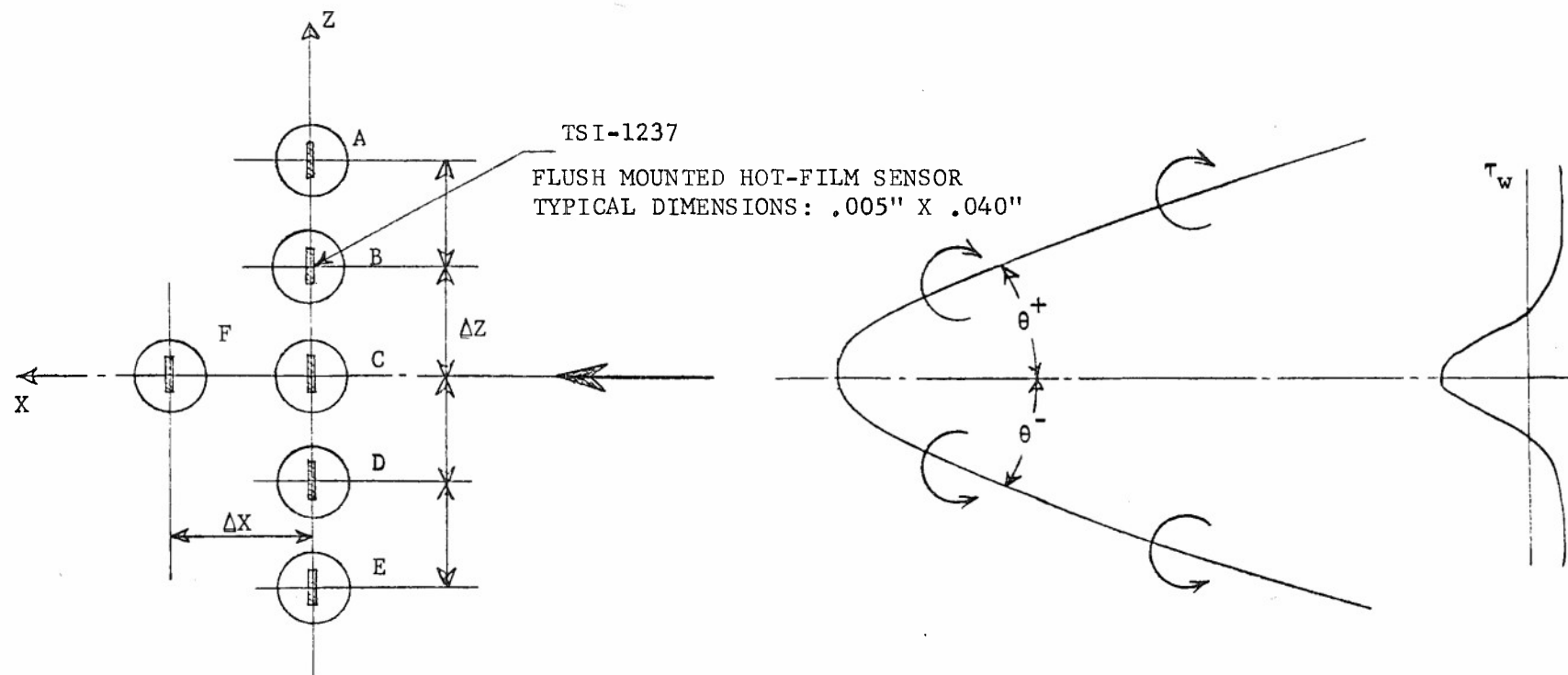


Fig.1 Sketch of instrumentation lay-out including table of non-dimensional distances from wall





$U_\infty$ (ft/sec)		675		75		32.6	
$\Delta X$	$\Delta Z$	$\Delta X^+$	$\Delta Z^+$	$\Delta X^+$	$\Delta Z^+$	$\Delta X^+$	$\Delta Z^+$
0.2"	0.157"	1540	1208	299	234	182	143

Fig.2 Sketch of lateral array of flush-mounted hot-film sensors

(Proposed plan view of large-scale  
outer structure from Thomas, Ref. 15)

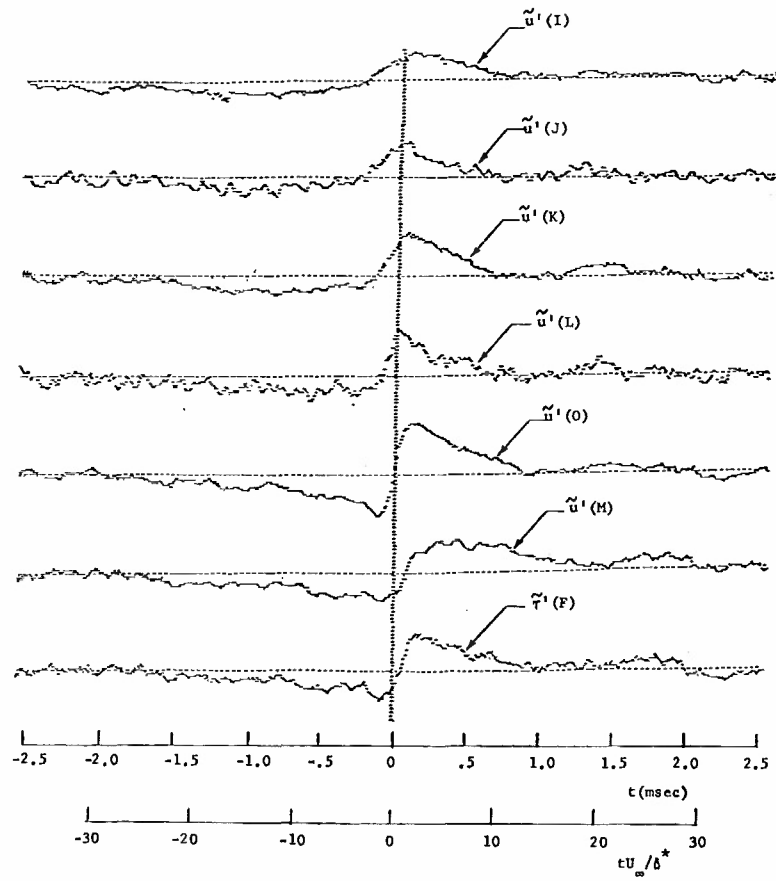


Fig.3 Ensemble averaged velocity and wall-shear fluctuations  $U_\infty = 675$  ft/sec, trigger:  $u'(O)$

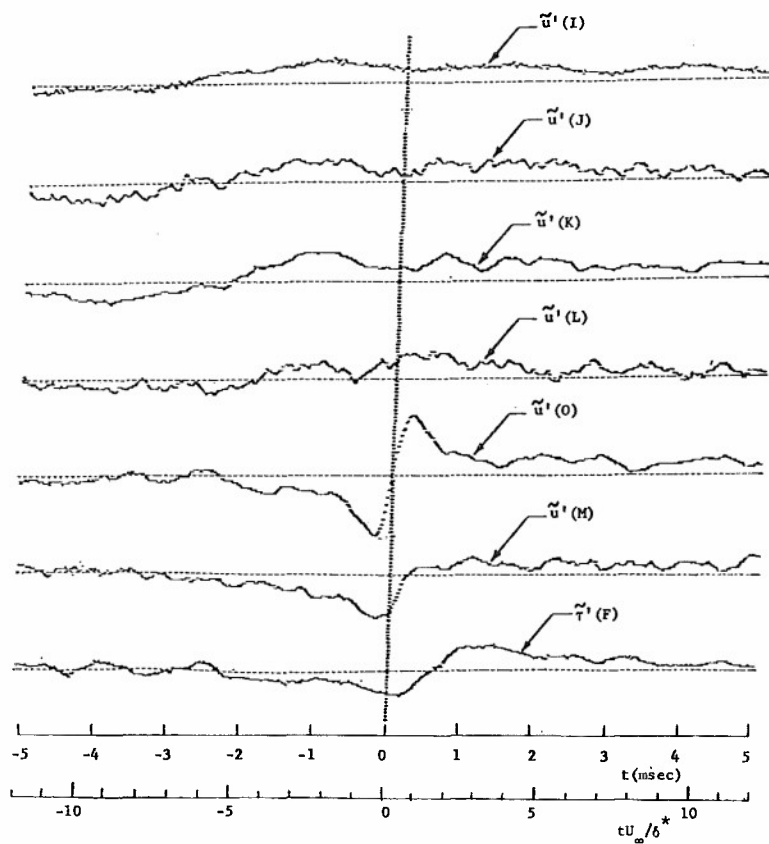


Fig.4 Ensemble averaged velocity and wall-shear fluctuations  $U_\infty = 73$  ft/sec, trigger:  $u'(O)$

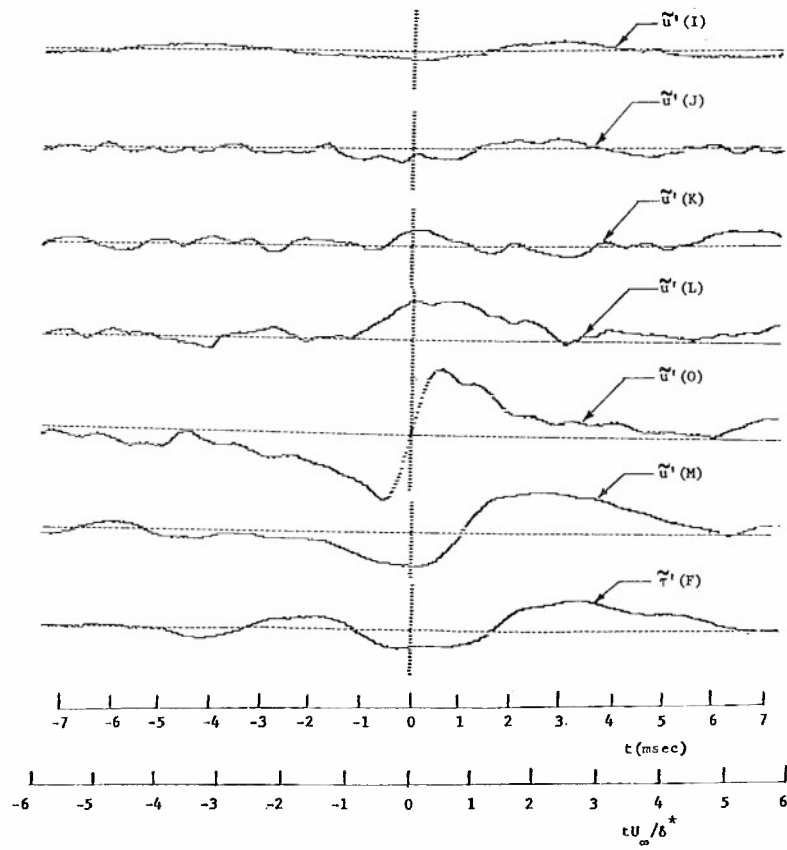


Fig.5 Ensemble averaged velocity and wall-shear fluctuations  $U_\infty = 32.6$  ft/sec, trigger:  $u'(O)$

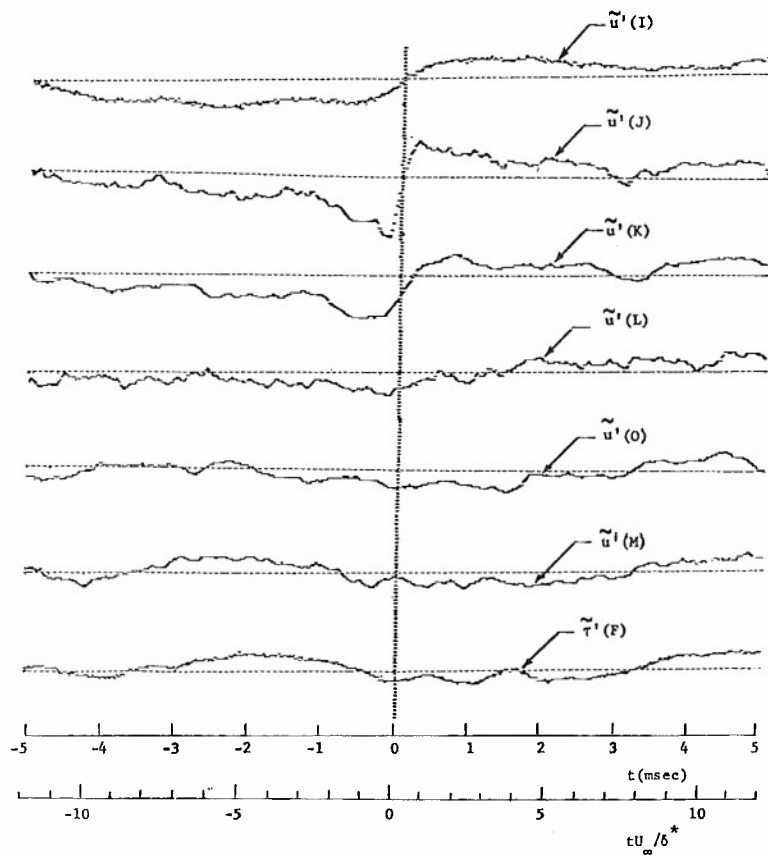


Fig.6 Ensemble averaged velocity and wall-shear fluctuations  $U_\infty = 73$  ft/sec, trigger:  $u'(J)$

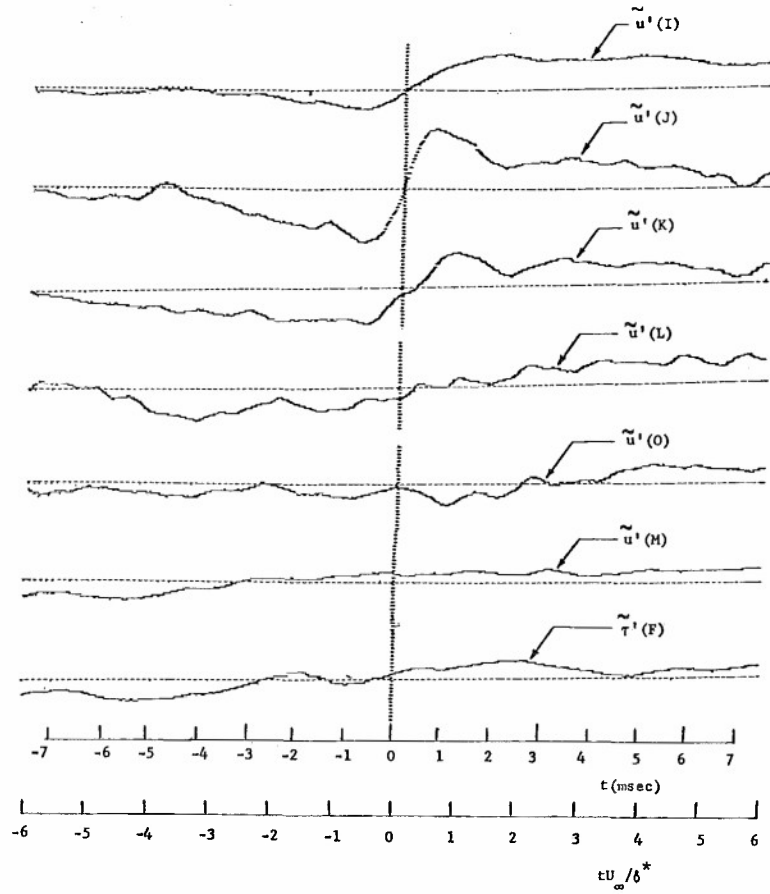


Fig.7 Ensemble averaged velocity and wall-shear fluctuations  $U_\infty = 32.6$  ft/sec, trigger:  $u'(J)$

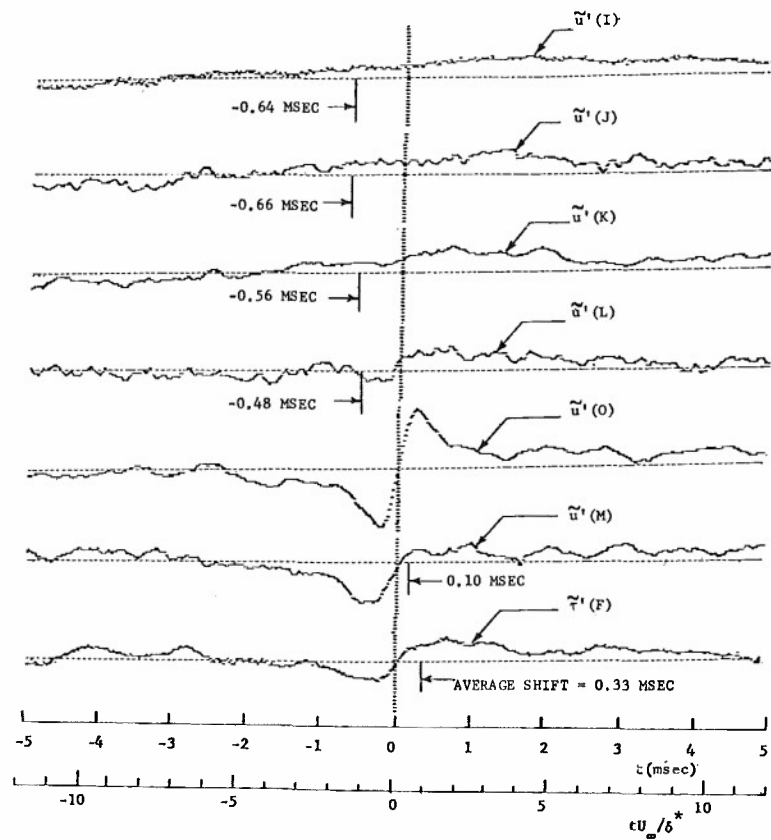


Fig.8 Ensemble averaged velocity and wall shear fluctuations after correction for phase "jitter" —  $U_\infty = 73$  ft/sec, trigger:  $u'(O)$

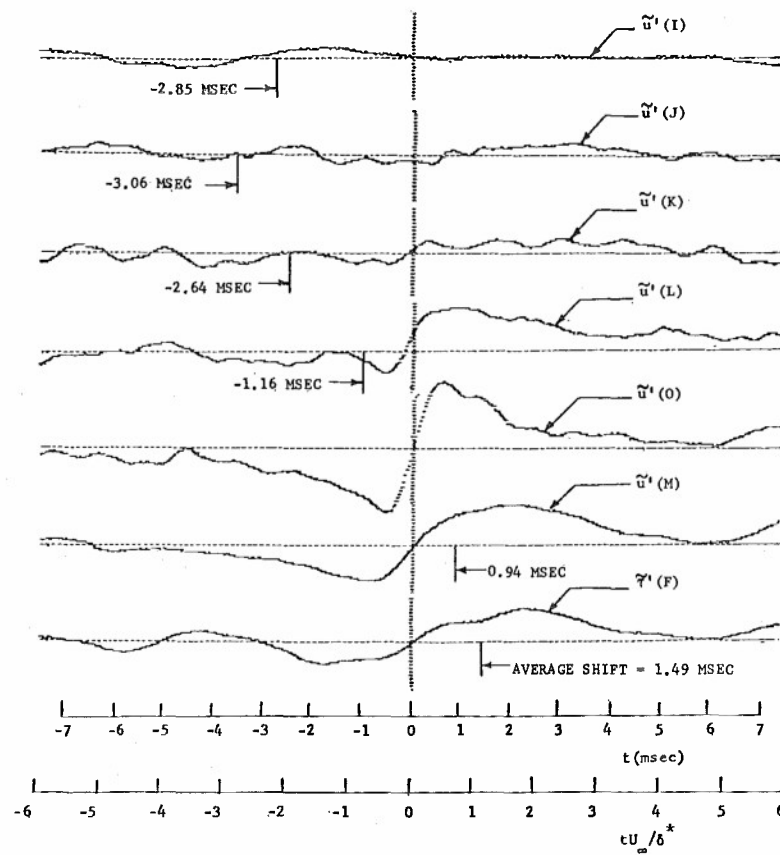


Fig.9 Ensemble averaged velocity and wall-shear fluctuations after correction for phase "jitter" —  $U_{\infty} = 32.6$  ft/sec, trigger:  $u'(O)$

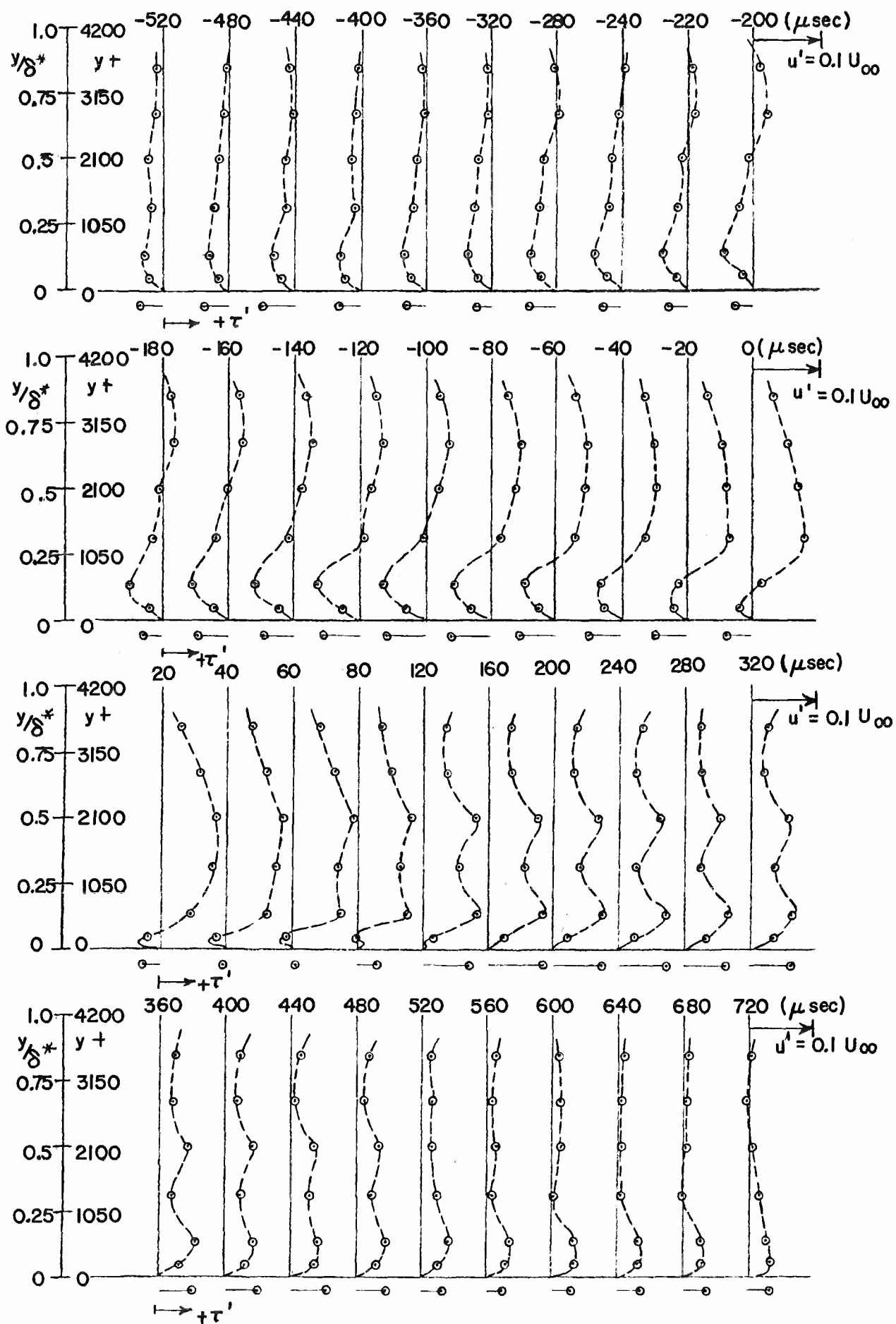


Fig.10 Sequence of velocity fluctuation profiles and fluctuating shear obtained from the ensemble averages in Figure 3 ( $U_\infty = 675$  ft/sec)

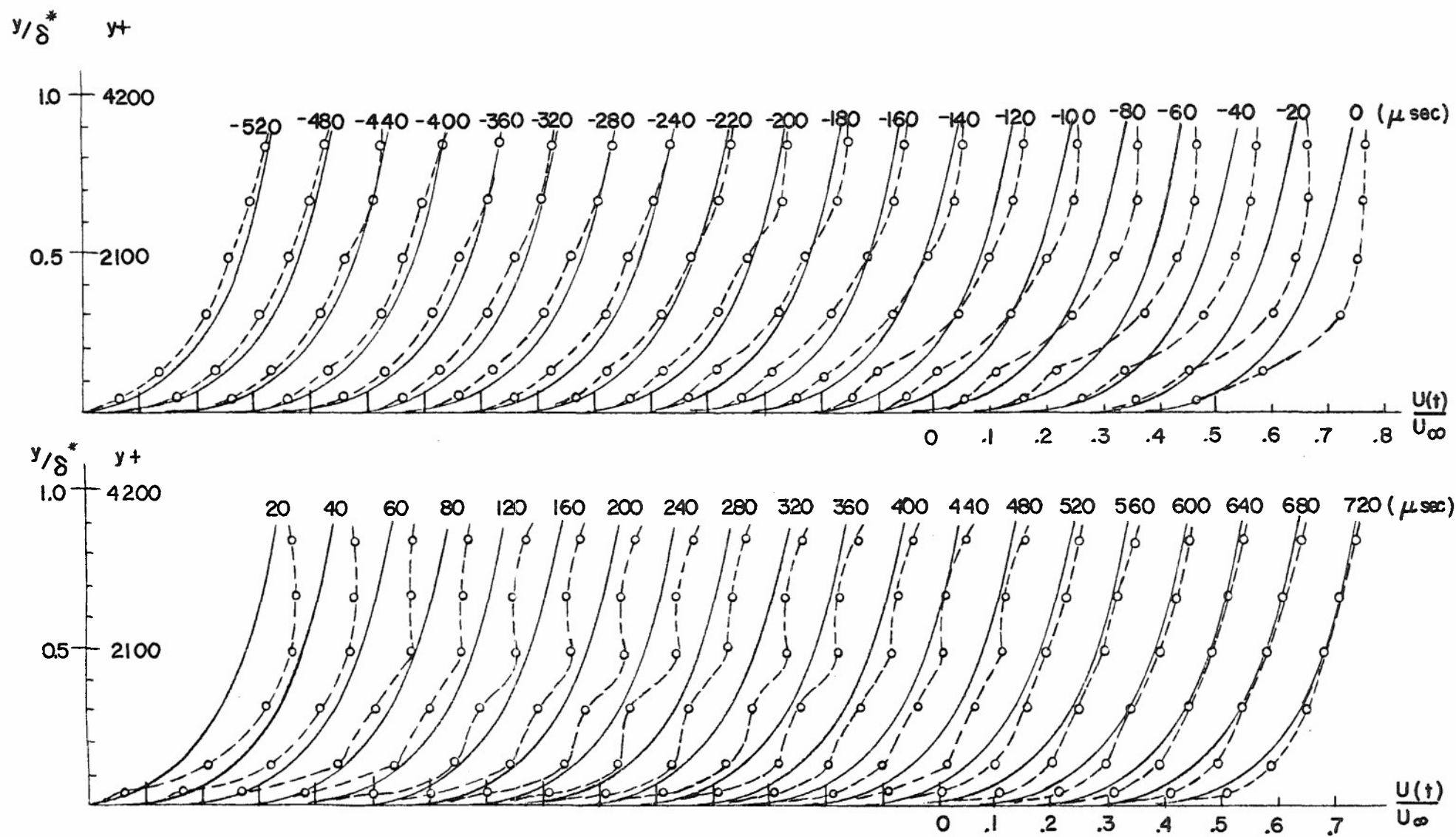


Fig.11 Sequence of total velocity profiles obtained from the ensemble averages in Figure 3 ( $U_\infty = 675$  ft/sec)

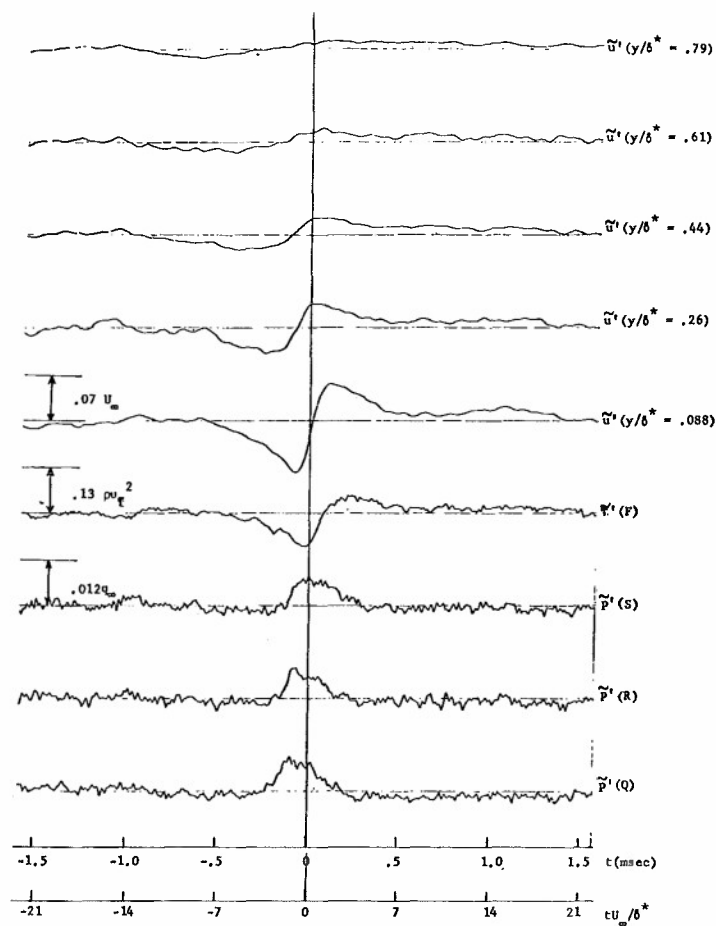


Fig.12 Ensemble averaged velocity shear and pressure fluctuations (from data of Reference 19)  
 $U_\infty = 675$  ft/sec, trigger:  $u'(y/\delta^* = .088)$

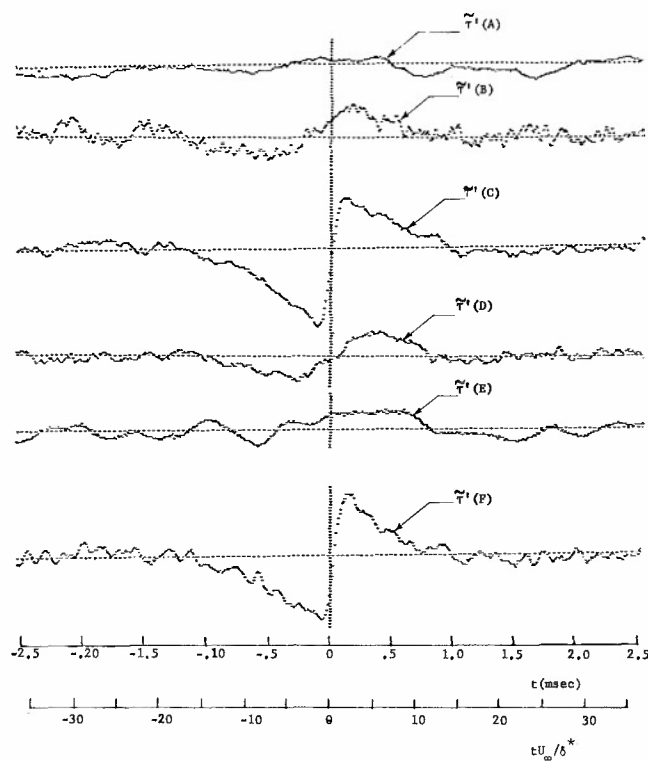


Fig.13 Ensemble averaged wall shear fluctuations for array in Figure 2  
 $U_\infty = 675$  ft/sec, trigger:  $\tau'(C)$



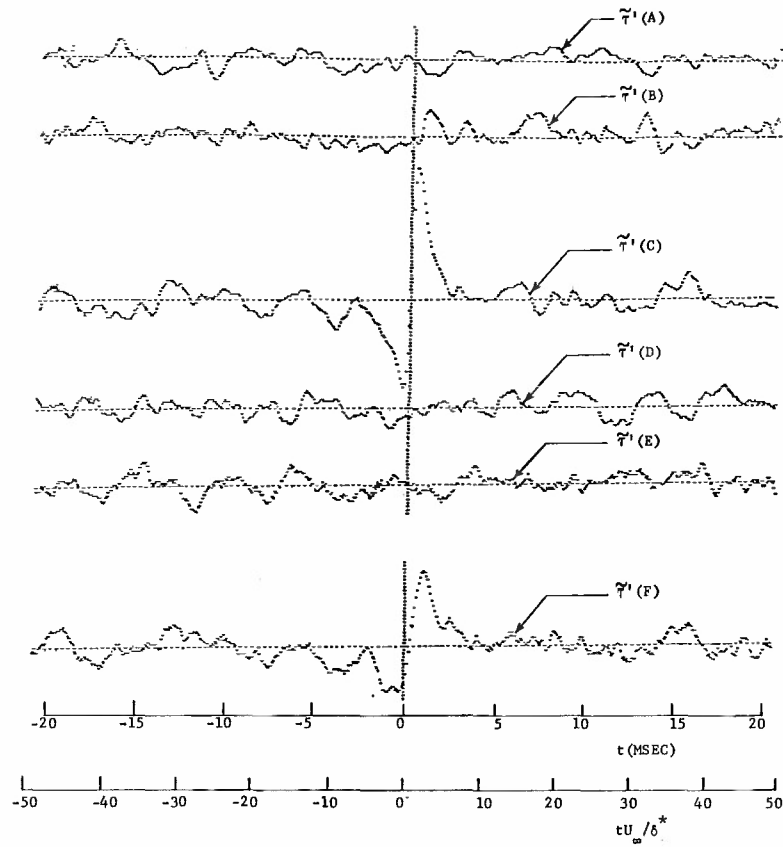


Fig.14 Ensemble averaged wall shear fluctuations for array in Figure 2  
 $U_\infty = 75$  ft/sec, trigger:  $\tau'(C)$

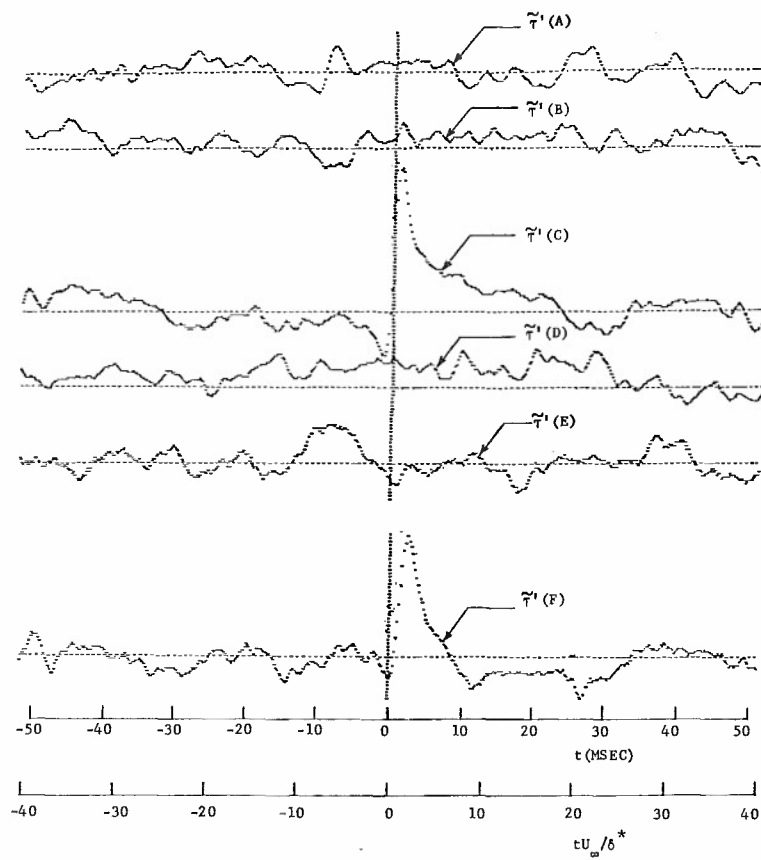


Fig.15 Ensemble averaged wall shear fluctuations for array in Figure 2  
 $U_\infty = 32.6$  ft/sec, trigger:  $\tau'(C)$

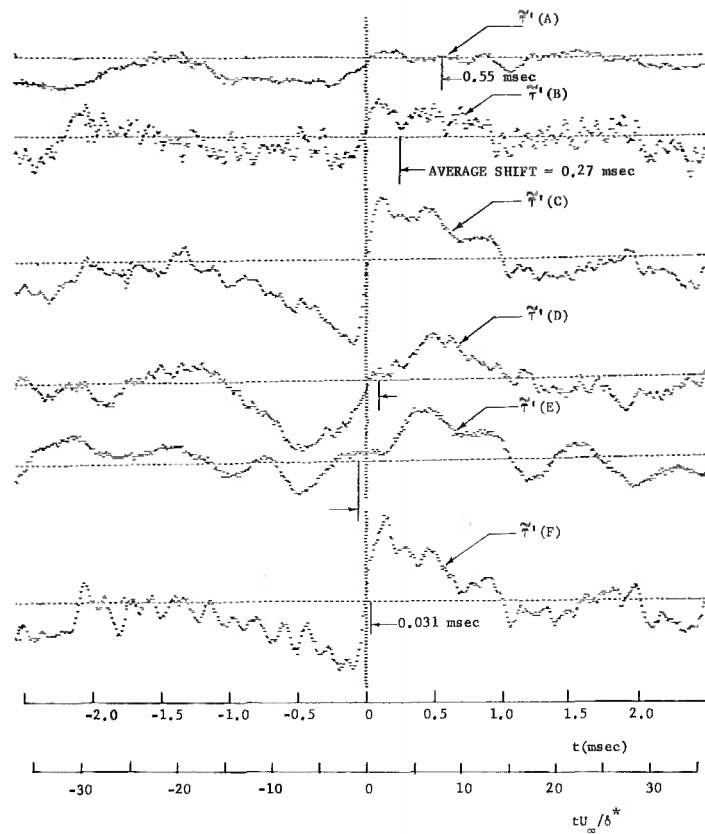


Fig.16 Ensemble averaged wall shear fluctuations for the array of Figure 2 after correction for phase "jitter" (only events with positive shifts between  $\tau'(C)$  and  $\tau'(B)$ )  
 $U_\infty = 675$  ft/sec, trigger:  $\tau'(C)$

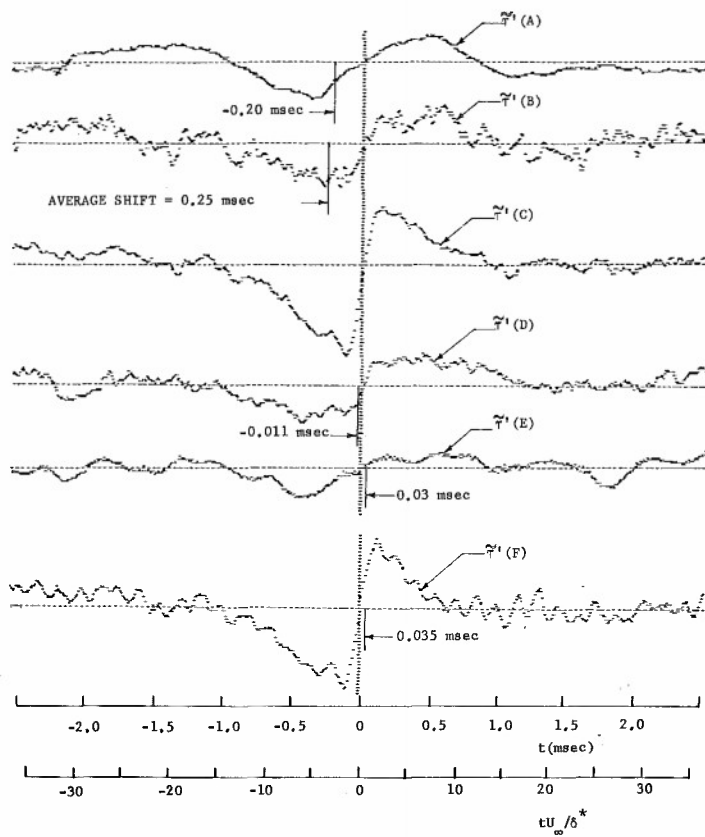


Fig.17 Ensemble averaged wall shear fluctuations for the array of Figure 2 after correction for phase "jitter" (only events with negative shifts between  $\tau'(C)$  and  $\tau'(B)$ )  
 $U_\infty = 675$  ft/sec, trigger:  $\tau'(C)$

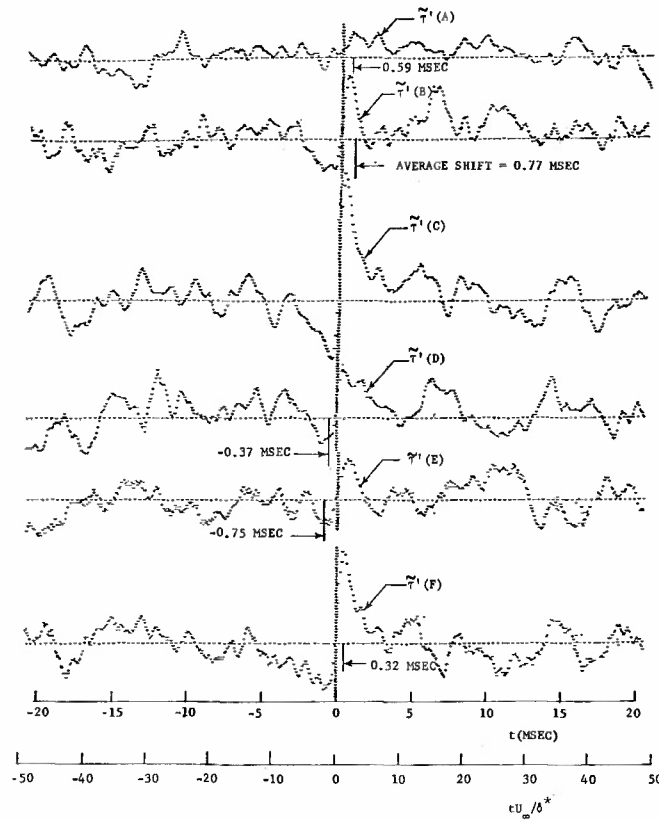


Fig.18 Ensemble averaged wall shear fluctuations for the array of Figure 2 after correction for phase "jitter" (only events with positive shifts between  $\tau'(C)$  and  $\tau'(B)$ )  
 $U_\infty = 75$  ft/sec, trigger:  $\tau'(C)$

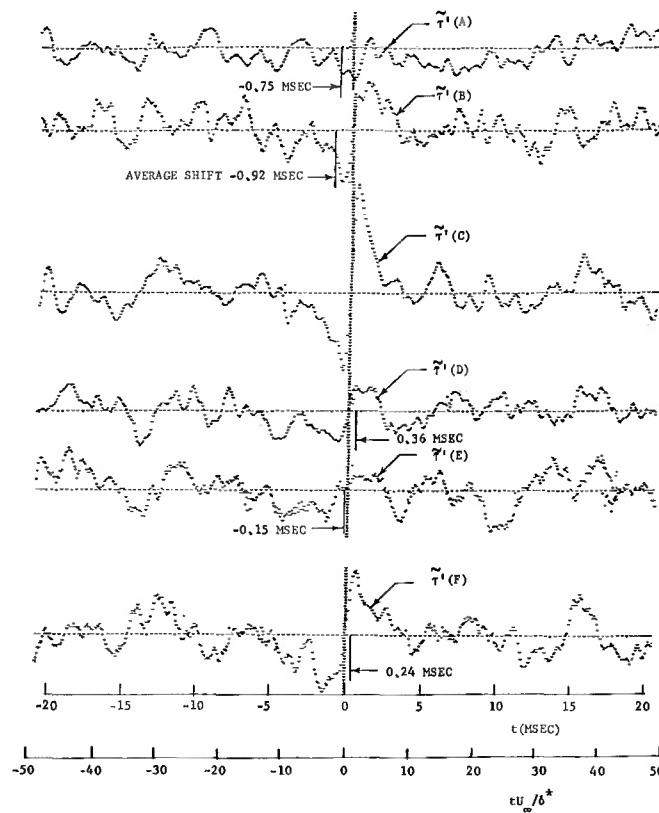


Fig.19 Ensemble averaged wall shear fluctuations for the array of Figure 2 after correction for phase "jitter" (only events with negative shifts between  $\tau'(C)$  and  $\tau'(B)$ )  
 $U_\infty = 75$  ft/sec, trigger:  $\tau'(C)$

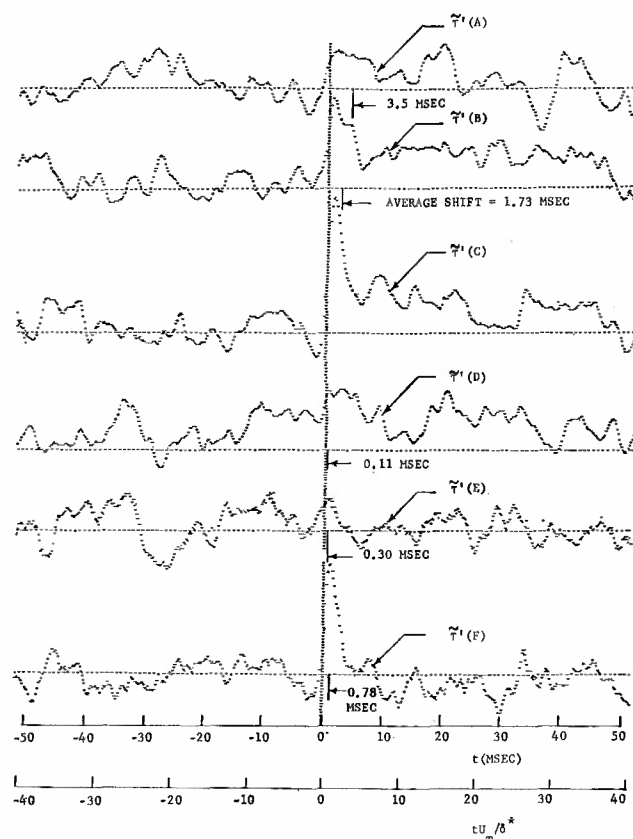


Fig.20 Ensemble averaged wall shear fluctuations for the array of Figure 2 after correction for phase "jitter" (only events with positive shifts between  $\tau'(C)$  and  $\tau'(B)$ )  
 $U_\infty = 32.6$  ft/sec, trigger:  $\tau'(C)$

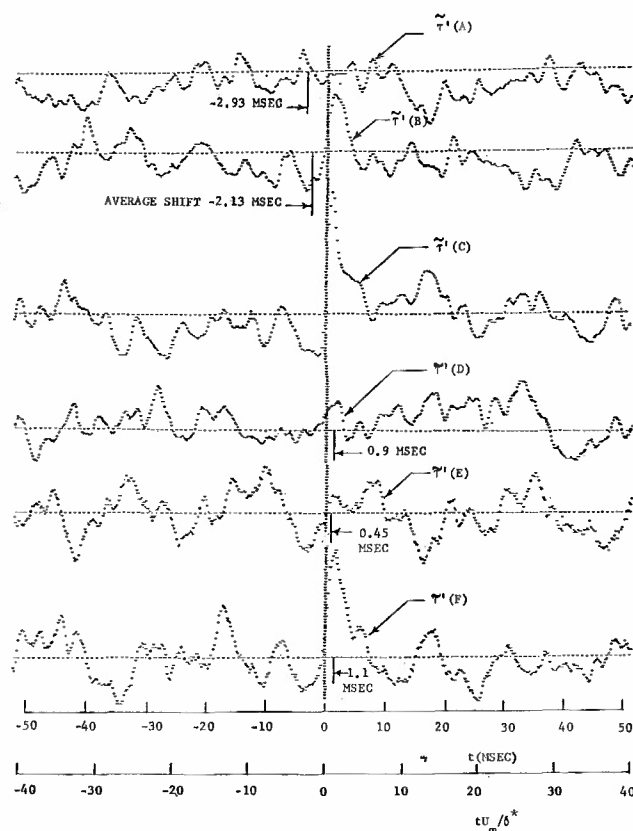


Fig.21 Ensemble averaged wall shear fluctuations for the array of Figure 2 after correction for phase "jitter" (only events with negative shifts between  $\tau'(C)$  and  $\tau'(B)$ )  
 $U_\infty = 32.6$  ft/sec, trigger:  $\tau'(C)$

## COHERENT STRUCTURES IN TIME DEPENDENT SHEAR FLOWS\*

Hermann Viets

Wright State University  
Dayton, Ohio 45435

## SUMMARY

The existence of large scale coherent structures in forced unsteady flows is demonstrated. The time dependency is produced in the free jet case by a fluidically controlled flapping jet and in the wall boundary layer case by a mechanical vortex generator. Advantages of the unsteady flows and similarities to "steady" turbulent shear flow structure are discussed.

## 1. INTRODUCTION

The existence of coherent structures in turbulent shear flows<sup>1</sup> has greatly complicated the task of modelling these flows. Since the use of local transport properties does not appear to be adequate, future descriptions of turbulent flows will probably rely more heavily on phenomenological models. The flow may then be based on some observations of its structure. A very simple example would be to model the coherent large scale structure of a free jet by a number of vortices being convected downstream in a jet without a large scale structure. Of course, other difficulties arise; in particular, the questions of how this structure is initially formed<sup>2</sup> and the geometrical relationships involved<sup>3</sup>.

The motivation, then, for studying unsteady flows is not only due to their own usefulness but also as a guide to the modelling of "steady" flows. In particular, the purpose of the present paper is twofold:

1. Demonstrate some positive aspects of unsteady flow.
2. Produce flows in which the origin of the coherent structure is readily identifiable, thereby perhaps simplifying the modelling task.

## 2. TIME DEPENDENT JET FLOWS

The introduction of a time dependency into free jet flows has been accomplished by various methods including mechanical<sup>4</sup>, acoustic<sup>5</sup> and fluidic<sup>6</sup> means. The fluidic method is considered here and consists of a feedback circuit which produces a jet which flaps from side to side<sup>6</sup>. The main advantage of this system (as with all the unsteady jets) is a more rapid mixing of the jet with the surrounding fluid. The unsteady jet nozzle employed here is shown in Figure 1 and described in detail in Ref. 6. The feedback loop is incorporated into the nozzle body to minimize the interference with the coflowing stream.

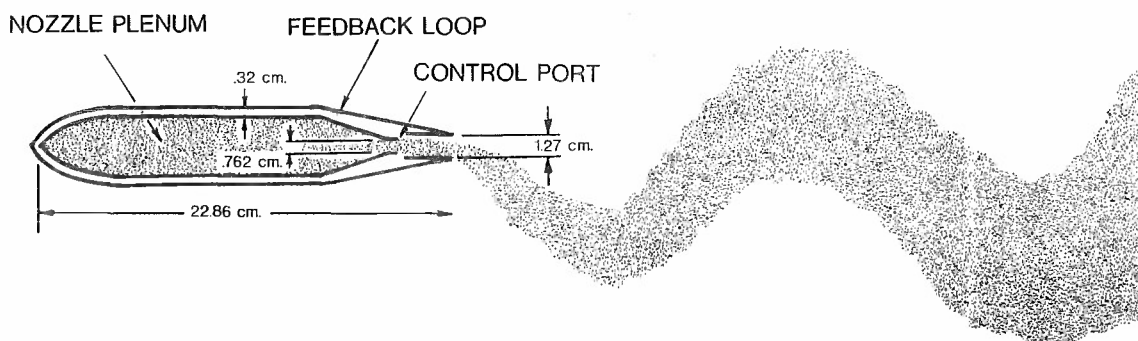


Figure 1. Schematic of the fluidically oscillating jet.

The large scale coherent structure in free shear layers, as demonstrated by Roshko and Brown<sup>7</sup> (See also Ref. 1), is difficult to model due to the lack of detailed understanding of its origin. Although it is clear that the large scale structure is born in the turbulent shear layer, its growth and geometrical spacing have not been predicted analytically. However, it has been shown that the scale must increase with streamwise distance<sup>2</sup> and that the spacing also increases by the amalgamation of adjoining structures<sup>3</sup>. A simpler problem, from the modelling point of view, is the unsteady flow in which the origin of the largest scale structure is more evident.

The large scale structure in the oscillating free turbulent jet is shown in Figure 2. The flow structure is visualized by entraining kerosene smoke into the open circuit low speed wind tunnel. The nozzle exit is at the left and the flow is from left to right. The ratio of the coflowing stream to nozzle exit velocity is .458. Although the jet is highly turbulent, the coflowing stream turbulence is low enough to produce a visible study of the entrainment into a unsteady jet. With such a relatively high coflowing stream, the amplitude of the jet oscillation is not large but the appearance of the large scale structure is evident at various streamwise positions. At position A the large scale structure can only be seen with some difficulty. By position B, the structure is a clearly defined mass of fluid which is rotating in the clockwise sense. The disturbance has grown quite large by streamwise position C.

\* Partially Supported by AFOSR Grant No. 78-3525, monitored by Lt. George Catalano, AFFDL/FXM

Special thanks are due to Michael Piatt and Mont Ball for their assistance in the construction and performance of the experiments.

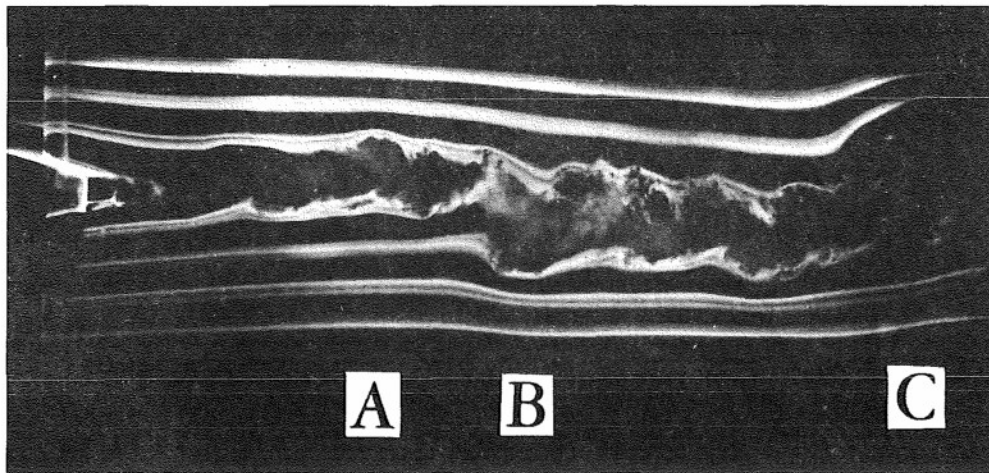


Figure 2. Smoke flow visualization of the oscillating jet in a coflowing stream of 45.8% of the jet velocity.

If the coflowing stream velocity is reduced to 28% of the jet exit velocity, the magnitude of the large scale structure is increased significantly as shown in Figure 3. Now the large scale structure is very evident at position A and the structure at position C has grown to the extent that it dominates the jet flow. Perhaps even more interesting is the structure at position B where the turbulent flow is clearly rotating in a clockwise sense. Since the flow is unsteady, the smoke lines are not streamlines but streaklines so the interpretation is less straight forward. However it appears that of the two streaklines at position B, the lower one is deflected around the large scale structure while the upper streakline is being entrained into the turbulent large scale structure which is the jet. This interpretation is verified by observing the oscillation with a strobe light which is tuned so that there is a small frequency difference between the strobe frequency and the jet oscillation frequency. Then the jet appears to flap in slow motion and the rotational motion may be clearly seen. Thus, the large scale unsteady structure behaves in the same way as the large scale undriven flow structure described by Roshko<sup>6</sup> and entrains fluid on the upstream side. A similar entrainment pattern for the turbulent wake has been found by Bevilaqua and Lykoudis<sup>8</sup>. The effect may be seen for the larger structure at position C in Figure 4 where the turbulent flow is entraining the coflowing stream on the upstream side of the large scale structure.

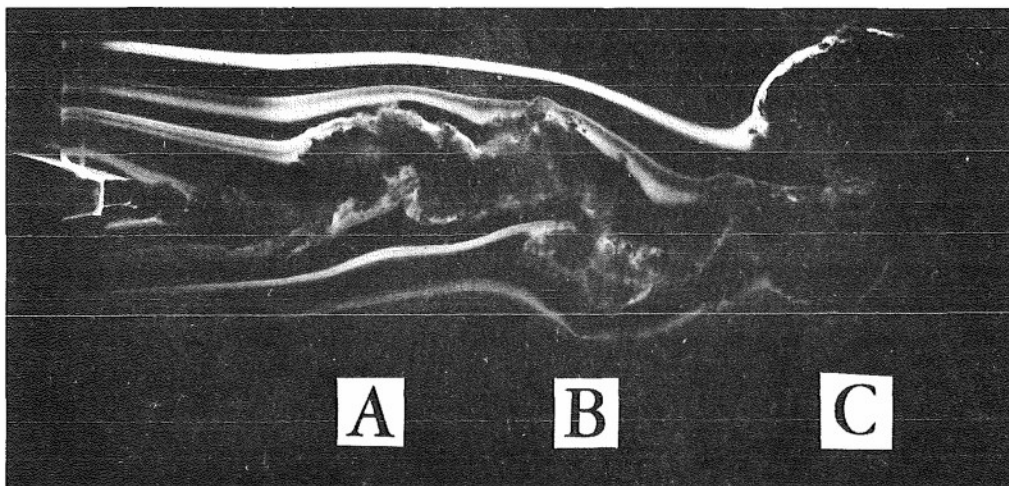


Figure 3. Smoke flow visualization of the oscillating jet in a coflowing stream of 28% of the jet velocity.

Returning now to Figure 2, it may be seen that the turbulent jet produces a large scale structure of its own in addition to that produced by the time dependency. The peaks of smoke on the streaklines closest to the nominal jet centerline all point in a downstream sense, in the same way as those produced by the time dependent structure (position C of Figure 4). Thus, the turbulent unsteady jet produces a "steady" and an unsteady large scale structure but the unsteady portion appears to dominate the flowfield. This may be somewhat analogous to the domination of the large scale structure over the fine scale turbulence in the "steady" jet. Here "steady" is employed to indicate that the jet is steady in the gross view, while there is unsteadiness associated with the turbulence structure.

Both the "steady" and unsteady large scale structures appear to arise through the same, or at least a similar, mechanism. The jet produces a perturbation on its surface. This bulge in the surface grows into a rotating mass of fluid with a vortex-like structure. In the "steady" case the origin and spacing of the structure is not fully understood. In the unsteady case, the bulges are produced at a known position and frequency and therefore may be easier to analyze.

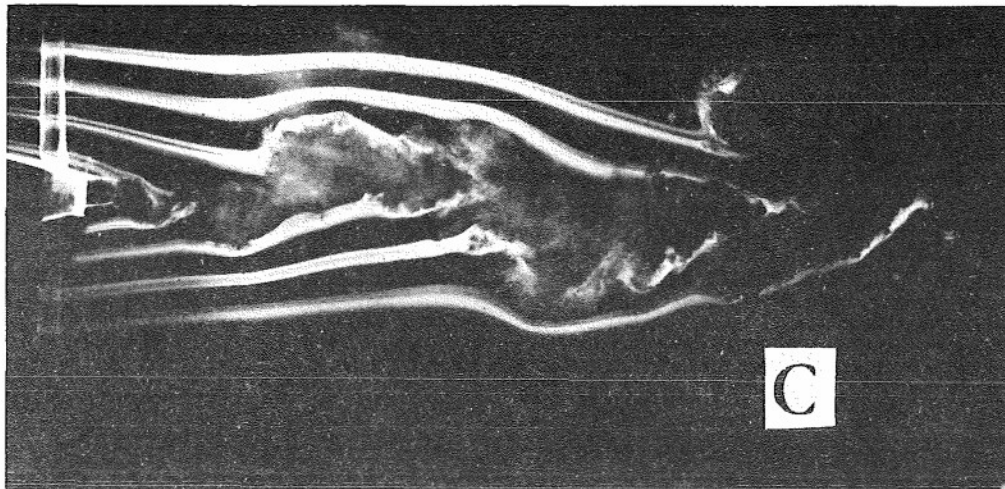


Figure 4. Smoke flow visualization of the oscillating jet in a coflowing stream of 28% of the jet velocity.

### 3. MODELLING THE UNSTEADY JET

To understand the production of the large scale unsteady structure in the unsteady jet, it is useful to construct a very simple phenomenological model of the process. It appears that the growth of the unsteady structure greatly resembles the growth and subsequent breaking of a water wave. This may be seen by examining three positions of the developing large scale structure shown schematically in Figure 5a, where  $u_j(x)$  and  $u_c$  are the jet and coflowing stream velocities, respectively. The original deformation of the free jet surface is a relatively small amplitude wave. This wave travels downstream (left to right) at a velocity  $u_{\text{wave}}$  such that  $u_c < u_{\text{wave}} < u_j$ . Therefore the wave is in a shear flow which causes it to curl in a counter-clockwise direction and entrain fluid into itself. Even without shear, it can be shown that the top of the wave outruns the bottom and curling results<sup>9</sup>. After the curling up is completed, the vortex-like structure continues to entrain fluid. The photographs of Figure 5b are taken from positions A, B & C of Figure 3, where position B has been printed as it would appear on the upper surface of the jet. They clearly verify the schematics of Figure 5a.

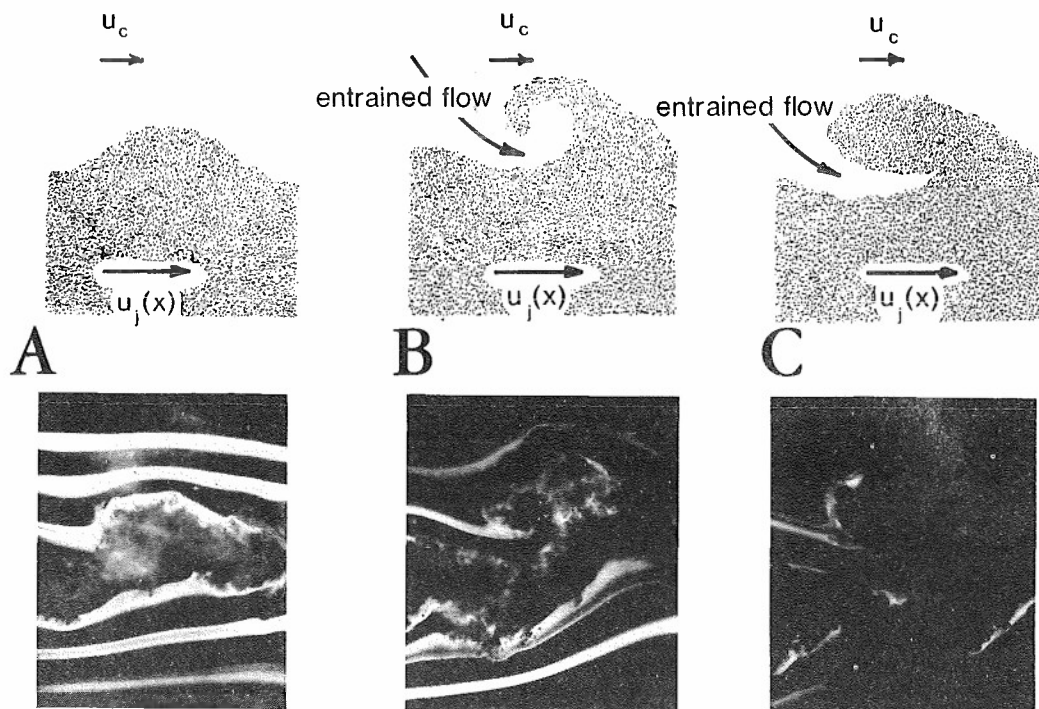


Figure 5. Evolution of the jet surface waves.

If one considers a breaking water wave, the schematic of Figure 5a corresponds to the wave shape at three instants of time, however with the wave traveling from right to left. Position A is the earliest swelling of wave. As the wave travels to the left, its forward face steepens and finally breaks as shown at position B. By position C the wave has broken and resembles a vortex like structure. The energy of the breaking wave is transformed partially into turbulence, which is eventually dissipated as heat, and partially serves to energize the undertow<sup>9</sup> which is the jet velocity itself in the present analogy. The analogy is incomplete, however, because the water wave is driven by gravity and somewhat by viscous effects while the

jet structure is entirely a viscous phenomenon. In spite of this, once the viscosity has created a vortex sheet at the interface, the deformation of this sheet may be modelled inviscidly<sup>2,3</sup> with considerable success.

The main point then is not that the steady and unsteady flow structures are the same but rather that they may have similar origins. As the unsteady structure grows from a large amplitude surface wave, so the steady structure may grow from a small amplitude surface wave.

#### 4. QUANTITATIVE CONFIRMATION

The unsteady fluidically controlled jet was examined in some detail by employing a hot wire anemometer along with conditioned sampling of the data to reveal the time dependent character of the flowfield. The jet was positioned between two Plexiglas sheets to attempt to minimize the three dimensionality of the field, as shown in Figure 6. The hot wire anemometer was driven through the flowfield by a motorized traversing mechanism which also turns a potentiometer, so the probe position is known at any time.

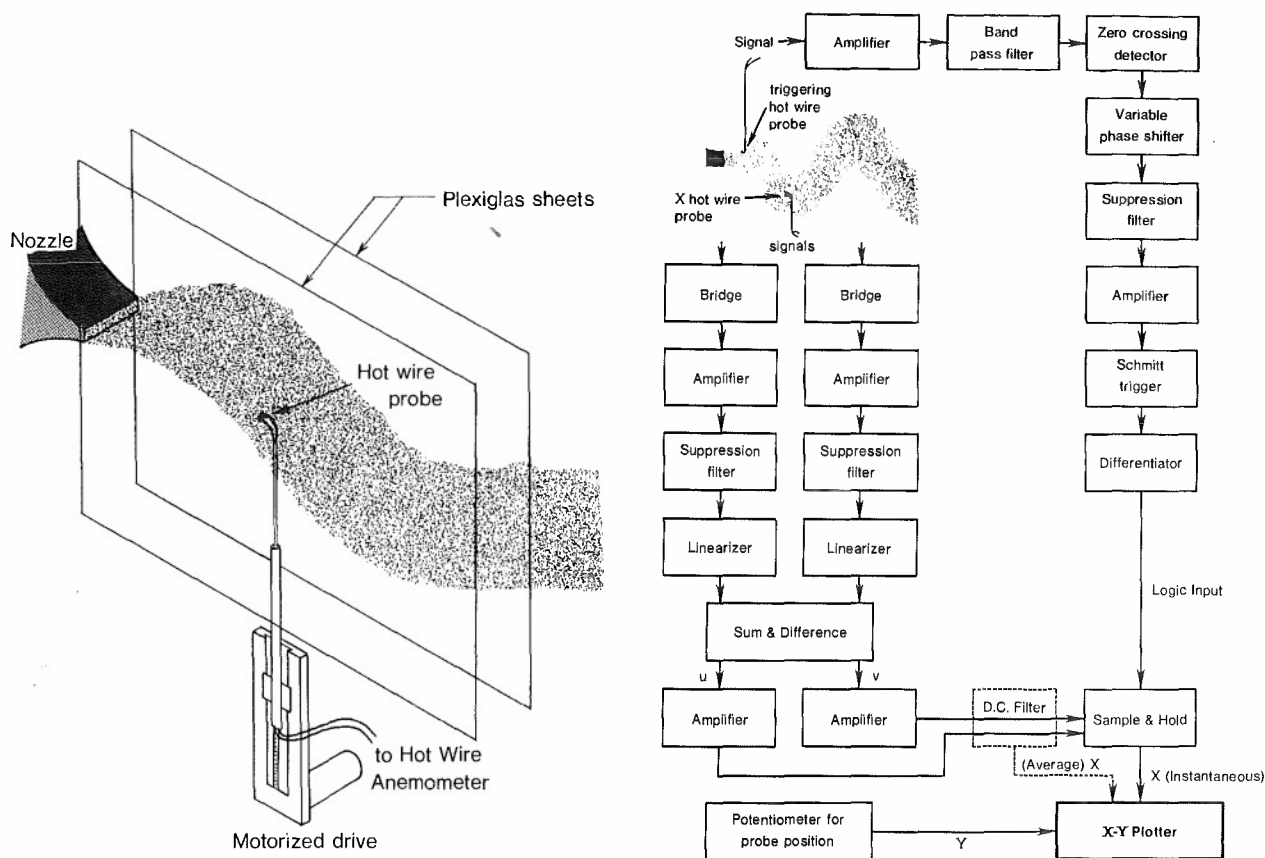


Figure 6. Experimental setup for quantitative tests. Figure 7. Electronic circuitry for conditional sampling with the hot wire anemometer.

The data required are the velocities in the jet at a specific instant of time (or alternately, at a specific point in the oscillation cycle, since the oscillation is repeatable). The conditioned sampling method is shown schematically in Figure 7. A third hot wire anemometer is employed to indicate the position of the jet since its signal is maximized when the jet is in the upward orientation. This signal is electronically manipulated to produce a timing spike which activates a Schmitt trigger circuit and eventually a sample and hold circuit. Thus the sample and hold only accepts a signal from the two channel hot wire probe when the jet is in a predetermined orientation. This orientation may be changed at will due to the presence of a variable phase shifter. The probe can then traverse across the jet and only record the velocities with the jet in a single orientation, neglecting all others.

The data obtained by the above technique have been reported in some detail in Reference 10. The aim here is to investigate quantitatively the existence of large scale coherent structure in the jet as appears to be evident in the flow visualization experiments described above. Looking back at the schematic of the unsteady jet field in Figure 1, a growing sinusoidal wave traveling downstream, where should one look for the existence of the vortex structure observed in the smoke photographs? The question is answered by another look at the model of Figure 5. As the bulge of the jet flow curls up to create a vortex structure, it necessarily does so by breaking toward the upstream direction (as driven by the slower coflowing stream or ambient fluid). Thus the vortex produced would be expected to exist at a position somewhat upstream of the initial jet bulge, which in this case is the extreme off axis position of the instantaneous jet centerline.

A portion of the jet flowfield, for the case of a frequency of 18 Hz and an extreme downward orientation of the jet at the nozzle exit, is shown in Figure 8a. The lengths of the arrows are proportion to the local velocity and the angles are determined from the measured axial and transverse velocities. The instantaneous jet centerline is also shown, from which it may be estimated that if a vortex is present, it should be centered roughly between 16 and 22 jet diameters downstream. No vortex-like structure is evident in this region.



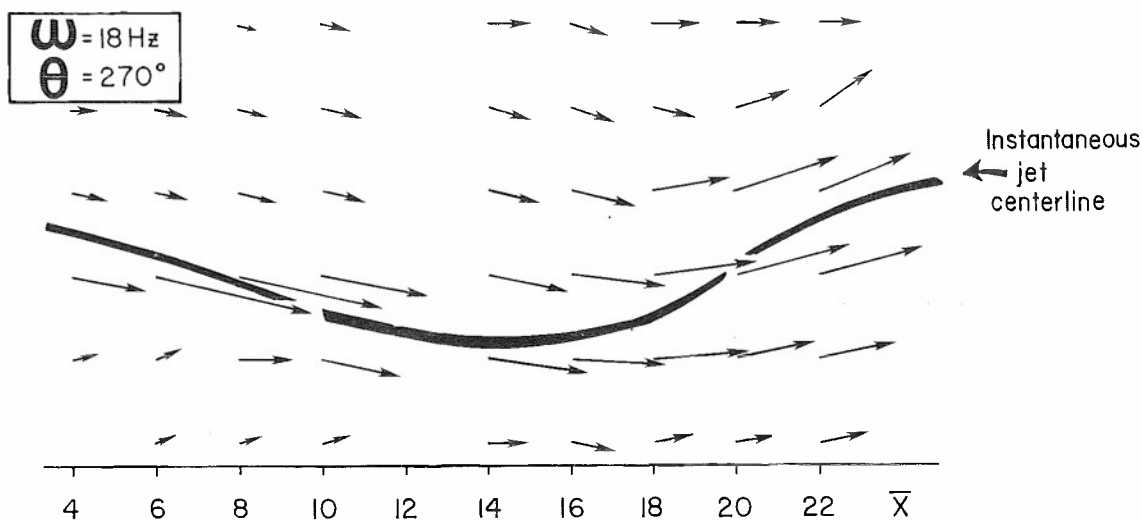


Figure 8a. Jet velocity field at a frequency  $\omega=18$  Hz and phase angle  $\theta=270^\circ$ .

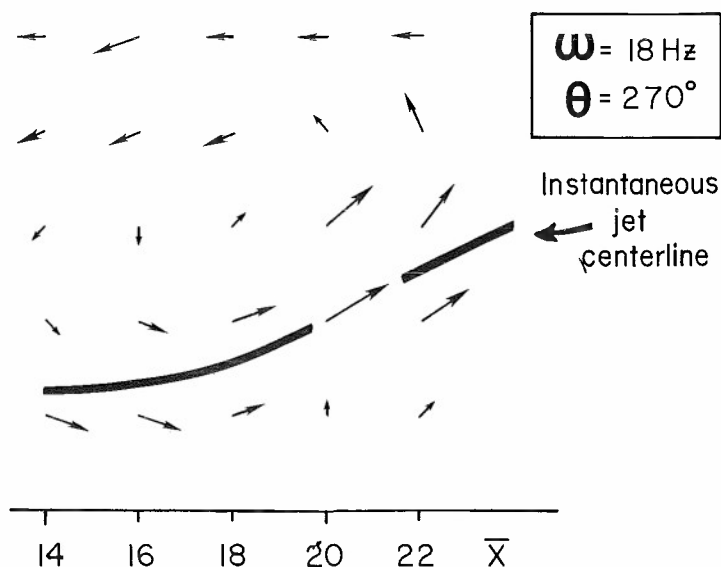


Figure 8b. Coherent structure of the jet seen in a moving coordinate system.

Several investigators have shown, however, that in order to see the coherent motion of a group of particles, the observer must be travelling with the velocity of the center of mass of those particles. Probably the first examination of this effect was made by Prandtl<sup>11</sup> who photographed a boundary layer by travelling at various speeds relative to the flow. Each photograph then revealed a different coherent structure.

In order to see the structure in the flowfield of Figure 8a, a nominal velocity of the vortex center is assumed and that streamwise velocity subtracted from each of the data points in the field. The result is shown in Figure 8b and clearly shows a vortex located in the very region where one would expect it based on the flow visualization results presented above.

Based on the phenomenological model of Figure 5 and the quantitative results of Figure 8 one can then make more predictions of the location of large coherent vortices in a family of instantaneous jets as shown in Figure 9. The 12 Hz frequency jet is shown for three phase angles,  $90^\circ$ ,  $180^\circ$  and  $270^\circ$  or horizontal (sweeping top to bottom), extreme downward or horizontal (sweeping bottom to top) orientation, respectively. The centerline positions of the jets are based on quantitative results. The vortices are drawn in the positions where they might be expected to be found based on the previous results.

Searching at the three positions closest to the nozzle exit, A, C and E leads to the conclusion that coherent vortices do not exist at those positions. This is, however, entirely consistent with the model proposed in Figure 5. It is clear from the flow visualization experiments that it takes some time (or equivalently, distance) for the bulge on the jet to curl up into a coherent structure. The positions near the jet exit have simply not allowed enough time (or distance) for this process to take place.

Looking for the vortex B, the local jet velocity field is shown in Figure 10a. Assuming the vortex center to exist at roughly  $\bar{x} = 22$  and subtracting the streamwise velocity at that point results in the Figure 10b, where the vortex structure is evident. It should be emphasized, of course, that the local structure depends upon the velocity of the observer, so subtracting a somewhat different velocity will result in a somewhat different appearance of the vortex. However, the important fact that the vortex is there is clear in any case.

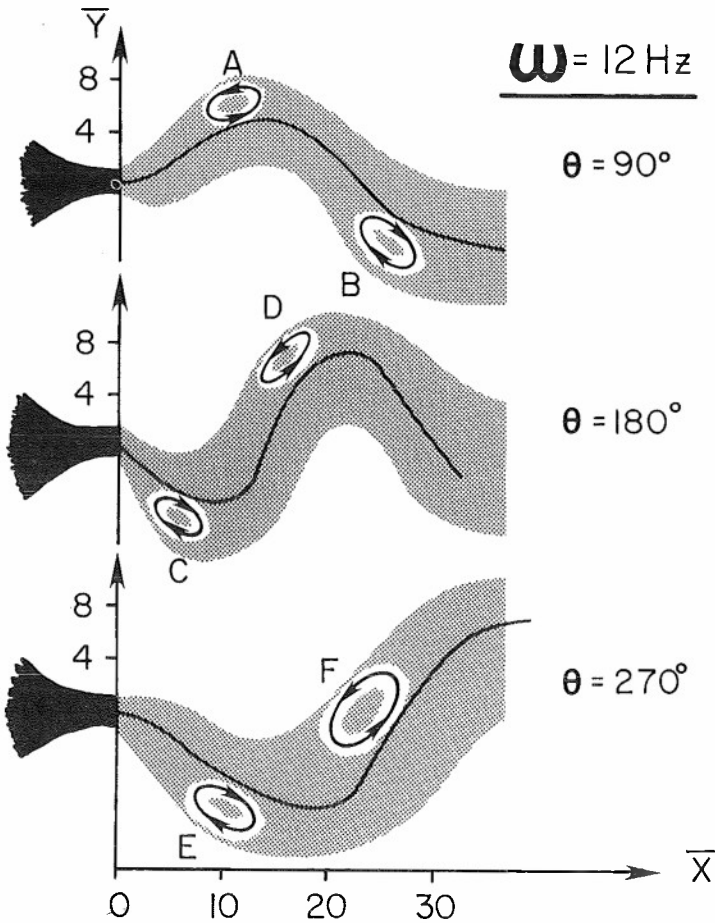


Figure 9. Anticipated vortex locations based on flow visualization results.

Figure 10a. Jet velocity field at a frequency of  $\omega=12 \text{ Hz}$  and phase angle  $\theta=90^\circ$ .

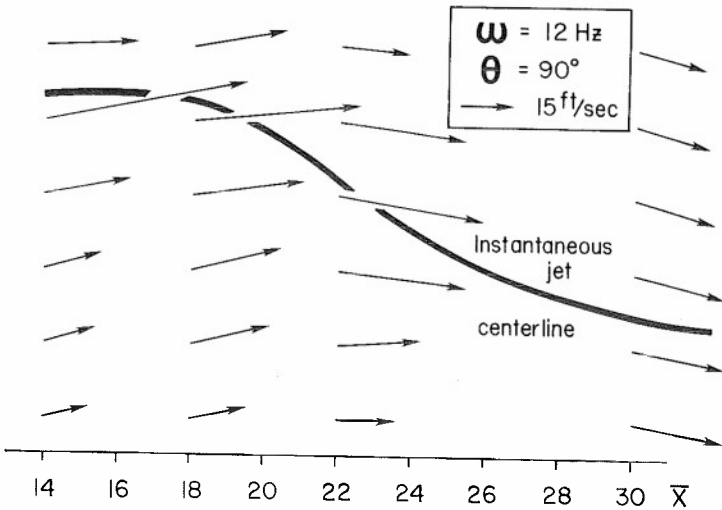
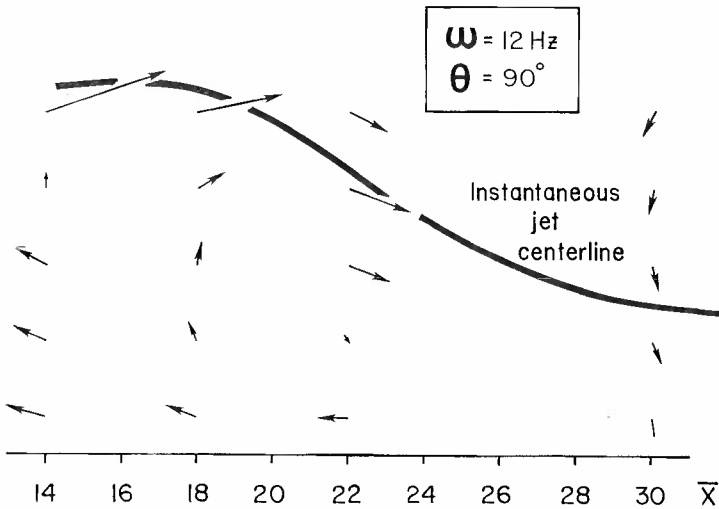


Figure 10b. Coherent structure of Vortex B in a moving coordinate system.



The local velocity field for a phase angle of  $\theta = 180^\circ$  is shown in Figure 11a. Again no vortex structure is seen until the flow is observed from a moving coordinate system as shown in Figure 11b. The vortex appears to be centered approximately at  $\bar{x} = 10$ . Looking back at the schematic of Figure 9, it may be seen that vortices A, D and F are really one and the same vortex at successive times. Thus an indication of the translational speed of the vortex can be obtained by locating the vortex F, having already found vortex D.

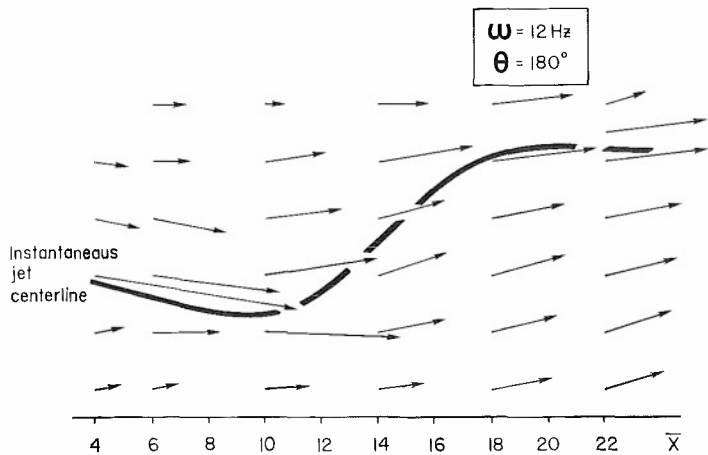


Figure 11a. Jet velocity field at a frequency of  $\omega=12$  Hz and a phase angle  $\theta=180^\circ$ .

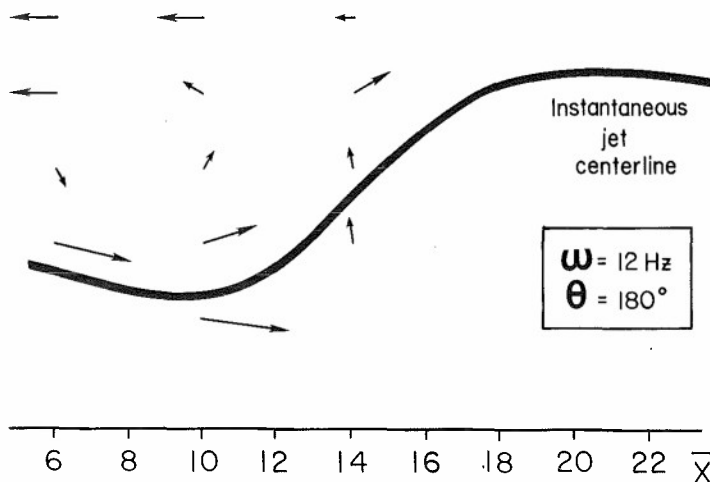


Figure 11b. Coherent structure of Vortex D in a moving coordinate system.

The jet flowfield in the region where vortex F is expected is shown in Figure 12a. In a moving coordinate system, the coherent structure of the jet may be seen in Figure 12b. The vortex center is located at approximately  $\bar{x} = 22$ . Then the translational velocity of the vortex between the positions D and F of Figure 9 is

$$V = \frac{\Delta x}{\text{time}} = \frac{(22-10) \frac{1}{24} \text{ ft}}{(1/12 \text{ sec/cycle}) (1/4 \text{ cycle})} = 24 \text{ ft/sec.} = 7.3 \text{ m/sec}$$

The instantaneous centerline velocities corresponding to the locations of vortices D and F are 11.5 m/sec and 10.8 m/sec, respectively. It should be noted, however, that the vortex translational velocity is only an approximate value because the determination of the vortex locations is not precise. A composite view of the streamwise velocity distribution corresponding to the Jet in Figures 12a and b is shown in Figure 12c.

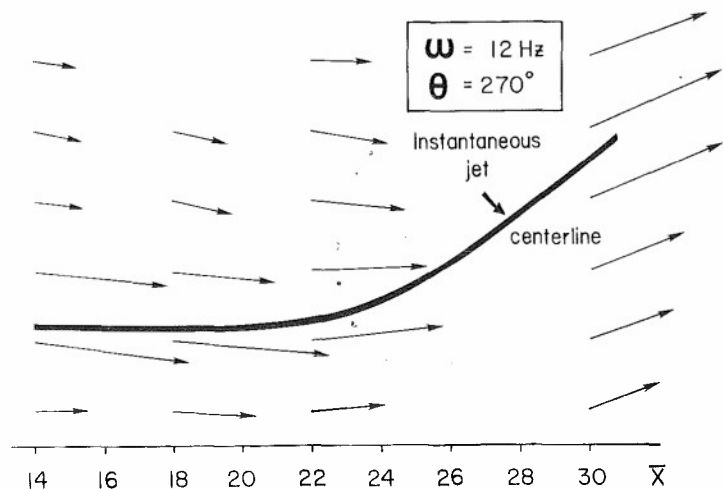


Figure 12a. Jet velocity field at a frequency of  $\omega=12$  Hz and a phase angle of  $\theta=270^\circ$ .

Figure 12b. Coherent structure of Vortex F in a moving coordinate system.

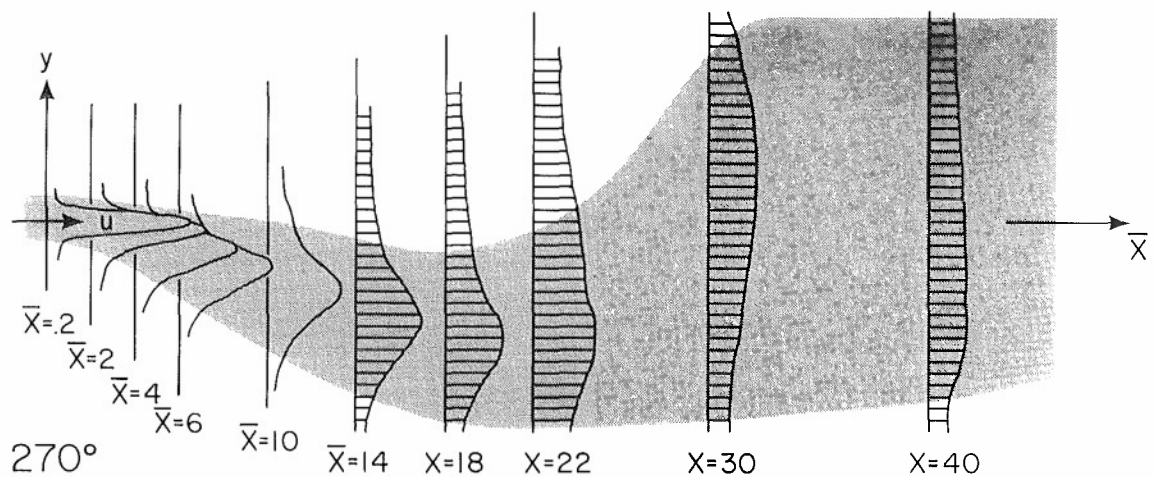
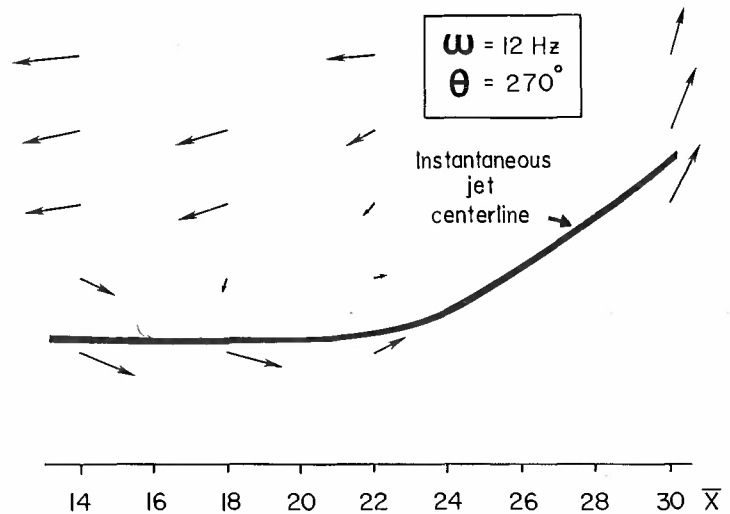


Figure 12c. Composite view of the streamwise velocities in the unsteady jet for  $\omega = 12 \text{ Hz}$  and  $\theta = 270^\circ$

Further evidence of the existence of a large scale vortex structure in the unsteady jet may be found in the instantaneous decay of the jet centerline velocity. In the case of steady jets, the centerline velocity decay is a monotonically decreasing function of streamwise distance. In the unsteady jet case, the centerline velocity decay (where the centerline is a quasi-sinusoidal shape) has a typical behavior<sup>10</sup> shown in Figure 13. The velocity decays with streamwise distance, reaches a local minimum and starts to increase again. A peak is reached, where upon the decay begins anew. The location of the peak corresponds to the existence of a vortex at that position, as illustrated in the inset to Figure 13.

Considering the induced velocity distribution due to the vortex and superimposing that velocity on a monotonically decaying centerline velocity results in the typical distribution of Figure 13. Thus the visual observation of a vortex structure in the unsteady jet is consistent with the quantitative measurements, specifically the instantaneous velocity structure and its centerline decay.

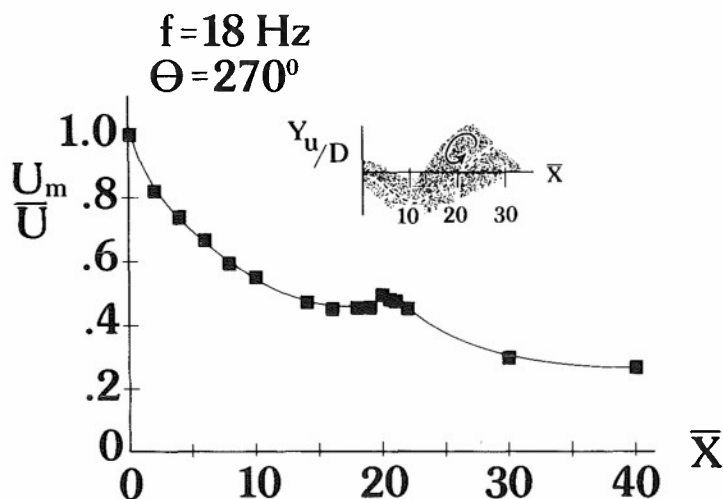


Figure 13. Effect of the vortex structure on the instantaneous jet velocity decay.

## 5. UNSTEADY BOUNDARY LAYER ENERGIZATION

The use of unsteady flow to energize the boundary layer flow has been accomplished implicitly for some time. If one considers the difference between typical laminar and turbulent boundary layer profiles, the turbulent profile is fuller near the wall. That is, the velocity at a given position above the surface is greater in the turbulent case than in the laminar case. The difference was ascribed by Prandtl to the turbulent interchange of momentum between the various layers of flow. This turbulent flow of momentum across streamlines is a time dependent process which can be improved by external stimulation and/or the production of a large scale structure.

The mechanical method employed here to produce a time dependency in the boundary layer is shown in Figure 14. It consists simply of a cam shaped rotor which rotates in a counter clockwise sense and thereby produces a clockwise vortex with each passing of the discontinuity in the rotor surface. The vortices are swept downstream by the flow but their presence causes an increased transfer of momentum from the free stream to the lower reaches of the boundary layer. The flow is capable of overcoming a stronger positive pressure gradient without separation, as has been shown in Reference 12 for the case of a two dimensional rotor. The objective here is to examine the usefulness of a three dimensional rotor geometry and to investigate the effect of rotational direction on that jet.

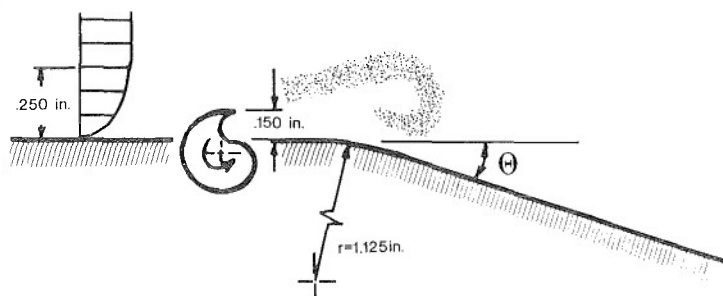


Figure 14. Rotor geometry for boundary layer energization.

The initial motivation for the rotor device was to produce a flowfield similar to the flow above an oscillating airfoil and thereby to improve the life on a stalled airfoil. Positive results on this application are given in Reference 13. The method was subsequently applied to a rearward facing step with potential application to improve mixing in a dump combustor<sup>14</sup>.

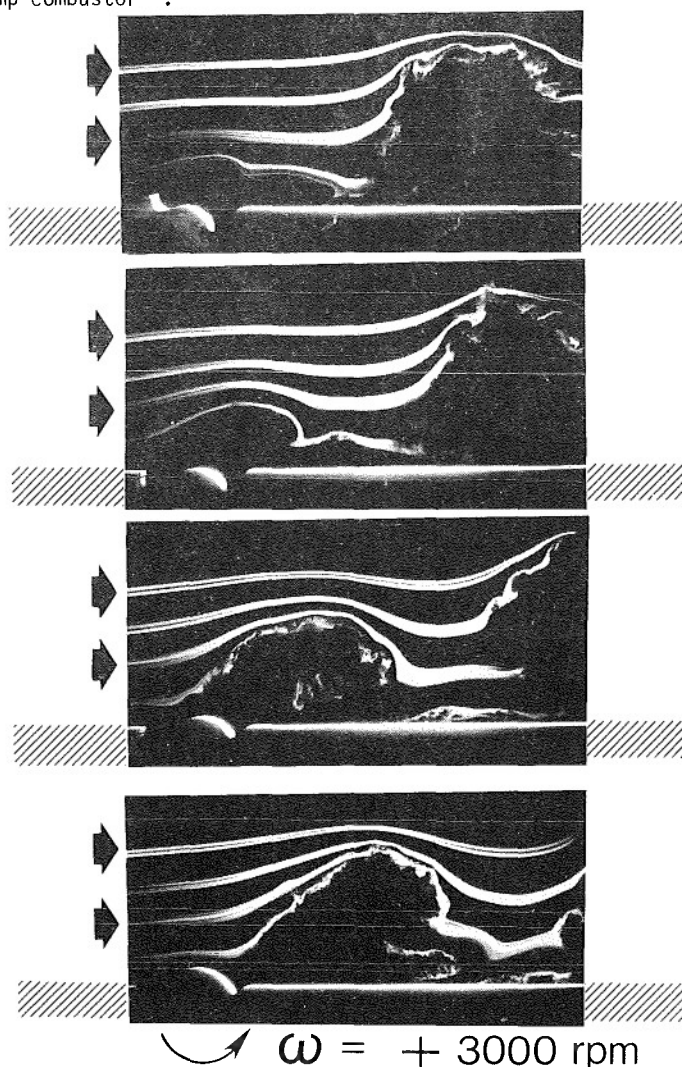


Figure 15. Smoke flow visualization of the vortex generation process,  $\omega=3000$  rpm.

The actual production of a vortex by the rotor geometry is shown in the photographic sequence of Figure 15. In this case the rotor size is 4.76 cm and it is turning in a counter-clockwise direction at 3000 rpm in a flow moving from left to right at 25.0 m/sec. The rotor produces a vortex-like structure which can be seen even more clearly by the use of strobe almost synchronized to the rotor speed so that it produces a slow motion version of the flowfield. The field itself is highly repeatable and can even produce an apparently standing vortex by means of synchronizing the strobe. It is important to note that the rotor does not operate simply as a trip mechanism. The time dependence is important because it concentrates the vorticity and thereby makes it more effective in terms of energizing the boundary layer. Also of importance is the fact that the rotor tip is moving in an upstream direction, so that the rotor is not simply pushing the flow downstream. The rotor apparently supplies only the energy required to bring some high energy external flow down into the boundary layer.

The present experiments are concerned with a three dimensional rotor which is, on the flow centerline, the same dimension as the diagram of Figure 14. However, as one moves away from the centerline (i.e. into or out of Figure 14) the size of the rotor tapers to zero at a transverse position of 3.6 cm from the centerline. Another difference is that there is no undercut in the rotor shape but the discontinuity in the rotor shape is merely a straight step. The subsequent flow visualization results and pressure measurements are all made on the centerline of the flowfield.

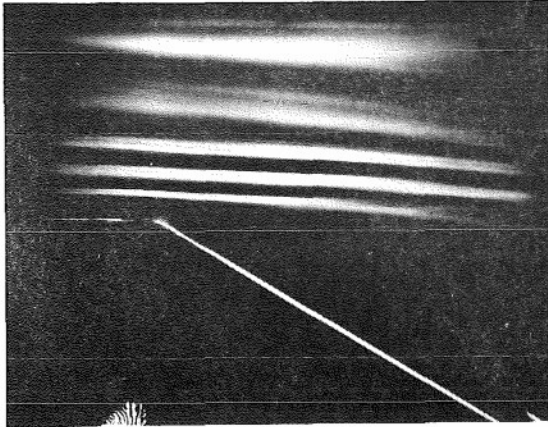
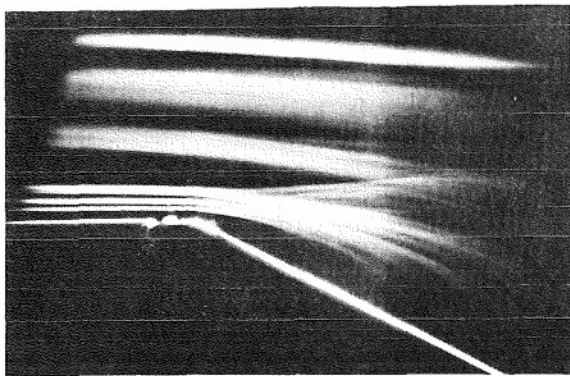
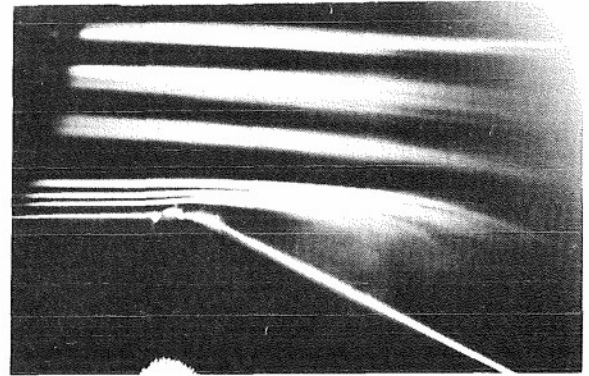


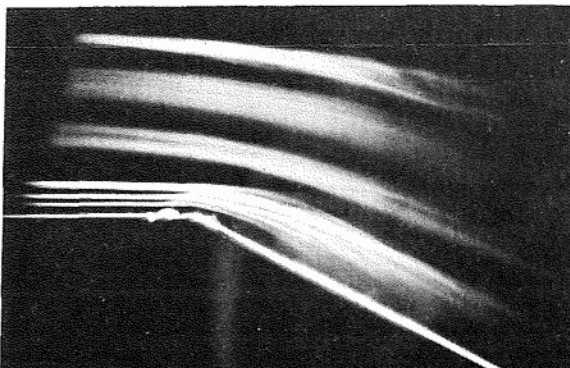
Figure 16. Flow separation at the ramp for no rotor.



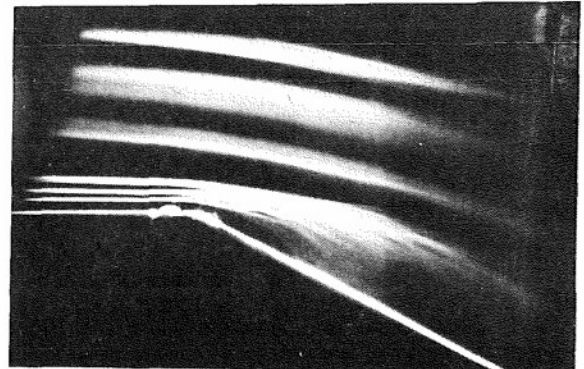
$\omega = 1000 \text{ rpm}$



$\omega = -1000 \text{ rpm}$



$\omega = 2500 \text{ rpm}$



$\omega = -2500 \text{ rpm}$

$\Theta = 28^\circ$   
TAPERED ROTOR

Figure 17. Comparison between rotor motion in the upstream (+) and downstream (-) directions for  $\omega=1000$  and 2500 rpm, and a tapered rotor.

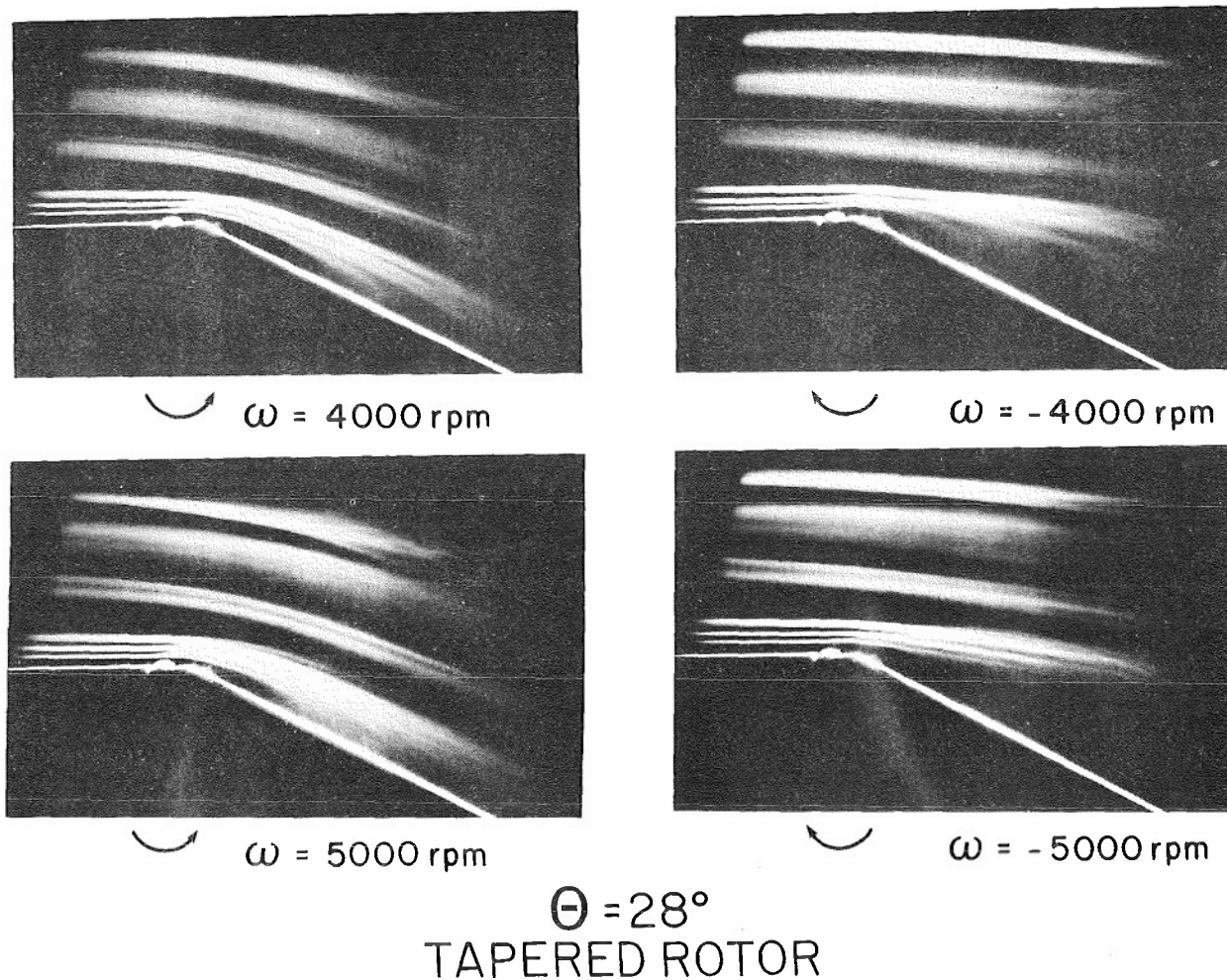


Figure 18. Same as Figure 17 for  $\omega=4000$  and  $5000$  rpm.

The effect of the magnitude and direction of the rotation speed on the ability of the flow to remain attached to a  $28^\circ$  ramp is shown in Figures 16-18. The detached flow for the case of no rotor is shown in Figure 16. The flow separates immediately at the beginning of the ramp. The nominal velocity at the top of the ramp is  $32$  m/sec. The photographs in Figures 16-18 are taken with a sufficiently long time exposure so that the results are essentially a time average of the flowfield and hence are average streamlines.

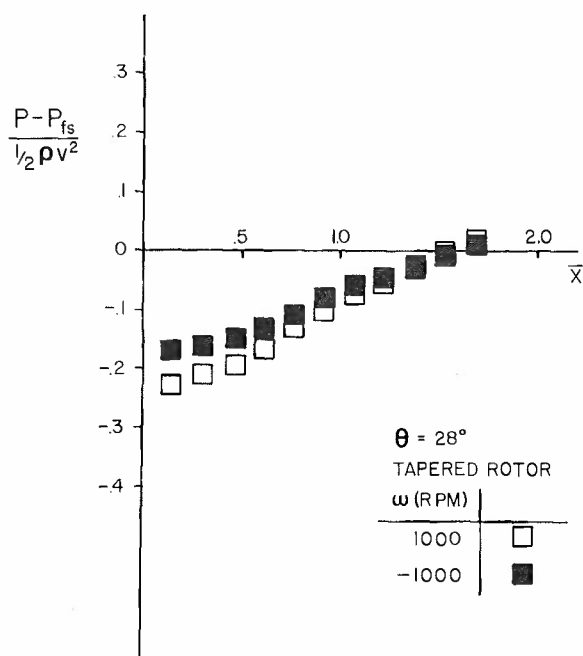


Figure 19. Pressure rise down the ramp for  $\pm 1000$  rpm and a tapered rotor.

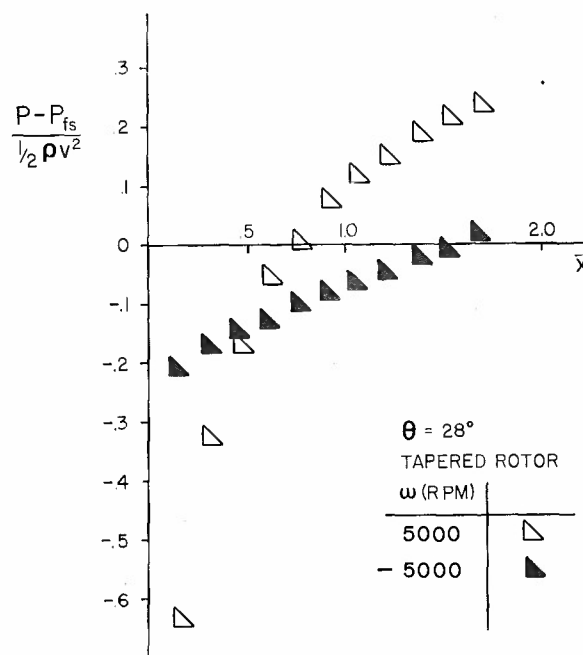


Figure 20. Pressure rise down the ramp for  $\pm 5000$  rpm and a tapered rotor.



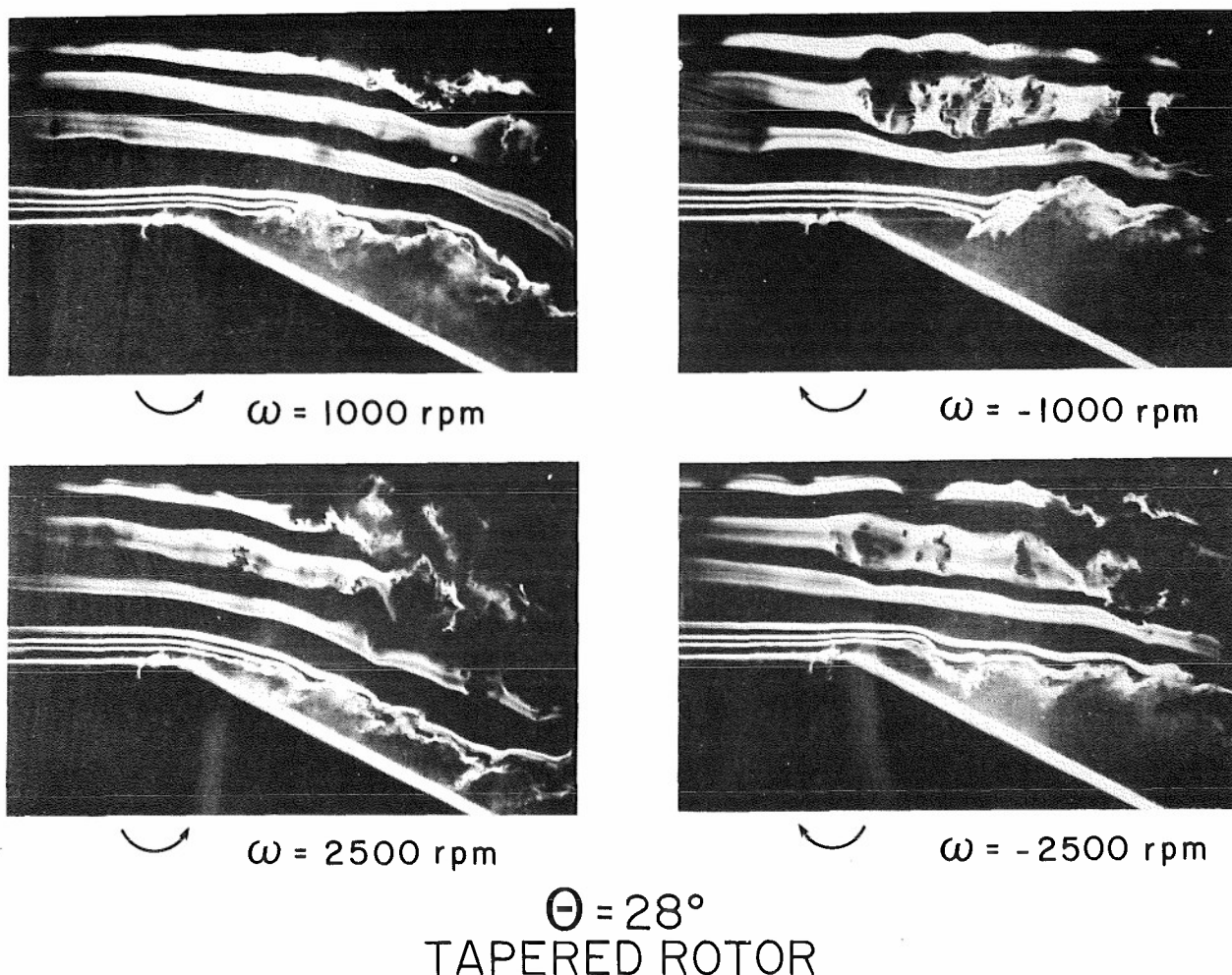


Figure 21. Streaklines in the ramp flowfield for a tapered rotor moving in the counter-clockwise (+) and clockwise (-) directions.

In Figure 17 the comparison is made between rotation in the counter-clockwise (+) direction and the clockwise (-) direction for speed of 1000 and 2500 rpm. The direction of rotation does not appear to be a major effect, but the rotation has not yet caused the flow to turn the corner very effectively. With an increase of rotational speed to 4000 and 5000 rpm, the effect of the rotation direction becomes very pronounced. In particular, at  $\omega = \pm 5000$  rpm the effect is very strong, resulting in a fully attached flow for a counter-clockwise rotation and a fully separated flow for a clockwise rotation.

The time average pressure distribution on the ramp are shown in Figures 19 and 20 for two sets of rotational speeds,  $\pm 1000$  rpm (Figure 19) and  $\pm 5000$  rpm (Figure 20). At the lower rotational speeds, the pressure rise on the ramp is rather small and only weakly affected by the direction of rotation. This is inconsistent with the results of Figure 17 and indicates that the frequency of vortex generation is too low to achieve sufficient boundary layer energization to allow the flow to remain attached. Changing the direction of rotation (at the same  $\omega$ ) keeps the frequency of vortex generation unchanged but changes the strength of each vortex because the relative velocity between the stream and the rotor is changed. However, since the frequency of generation is insufficient for attachment even with the counter-clockwise rotation, the effect is minimal.

At higher rotational speed, however, the effect of rotational direction is very significant as shown in Figure 20 for the case of  $\pm 5000$  rpm. The counter-clockwise rotation (+) produces the stronger vortex and leads to a higher pressure rise on the ramp. This result is a reflection of the improved flow attachment on the ramp and verifies the flow visualization results of Figure 18.

The details of the flow structure may be seen in the streakline photographs of Figures 21 and 22. In this case, the photographs are taken with a single flash strobe and thus yield the instantaneous positions of the entrained smoke or streakline. The interpretation of streakline patterns is more difficult but can be guided by observations of their dynamic behavior as observed with a tunable strobe light. The results at the lower rotational speeds, Figure 21, verify the results of Figure 17 in that the effect of rotation direction is not very strong and indeed, the ability of the unsteady energization to cause the flow to remain attached is rather limited. However, at larger rotational speeds, Figure 22, the effect of rotor direction is very pronounced, leading to a very strong vortex structure and a successful attachment when rotated in the counter-clockwise (+) direction. When rotated in the clockwise (-) direction, the strength of the vortices produced is greatly reduced (since the relative velocity is reduced) and the resulting flow is not well attached to the ramp.



Thus the time dependent method of boundary layer energization appears to show promise from the point of view of application. Rotation in the upstream direction (+) direction is desirable to maximize the relative velocity between the rotor and freestream and thus maximize the vortex strength. Three dimensional rotors show the same promise but additional data is needed on geometrical effects.

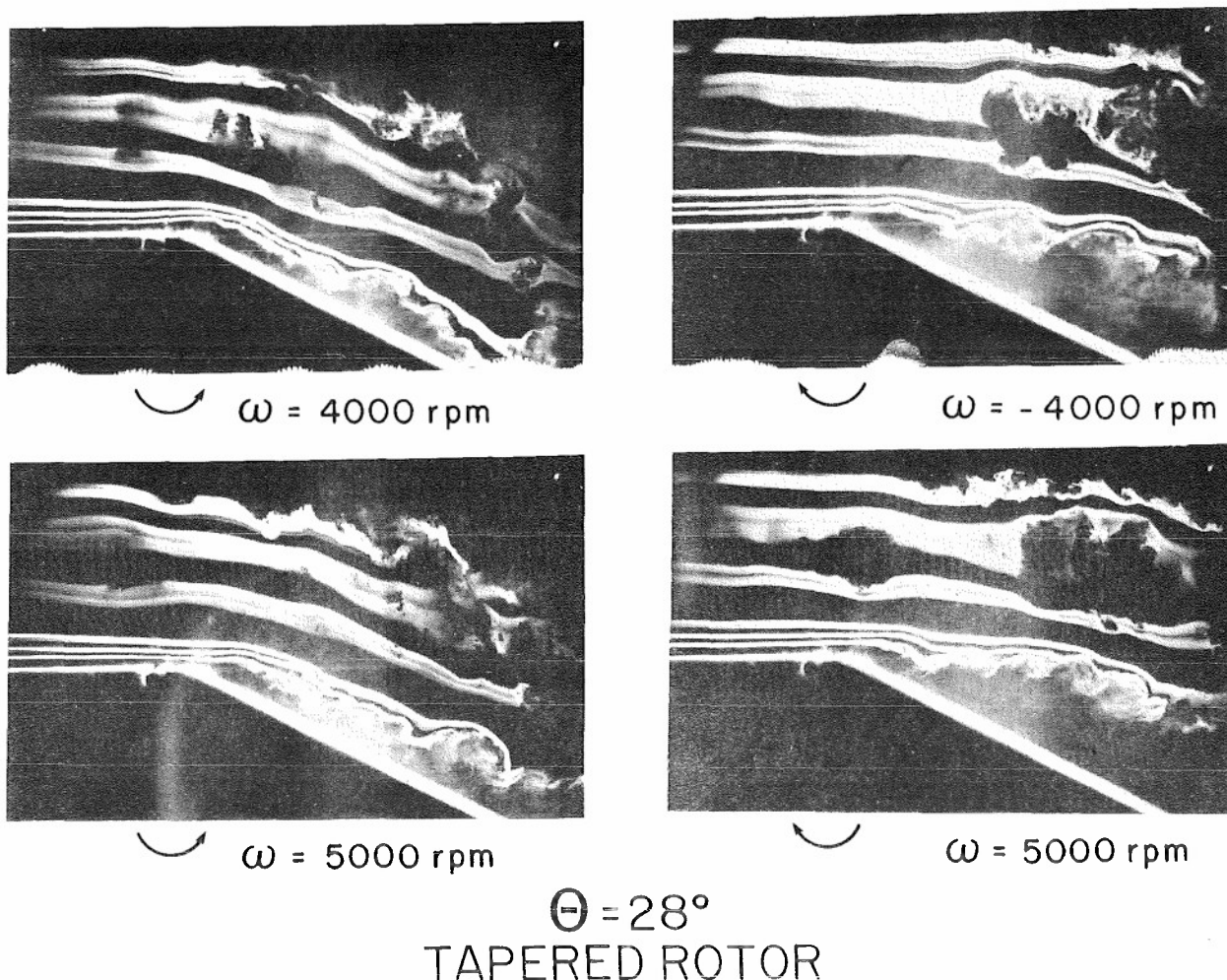


Figure 22. Same as Figure 21 for higher rotor speeds.

## 6. CONCLUSION

The existence of large scale time dependent flow structures in forced time dependent shear flows is demonstrated. These structures dominate the flow and make possible the observed performance improvements of some unsteady devices. Because of the more readily definable structure, unsteady flows could be employed to study the structure of nominally steady flows from a modelling point of view.

## 7. REFERENCES

1. Roshko, A., "Structure of Turbulent Shear Flows: A New Look," AIAA Journal, Vol. 14, No. 10, 1976, pp. 1349-1357.
2. Michalke, A., "On Spatially Growing Disturbances in an Inviscid Shear Layer," J. Fluid Mech., Vol. 23, Part 3, 1965, pp. 521-544.
3. Moore, D.W. and Saffman, P.G., "The Density of Organized vortices in a Turbulent Mixing Layer," J. Fluid Mech., Vol. 69, 1975, pp. 465-473.
4. Binder, G. and Favre-Marinet, M., "Mixing Improvement in Pulsating Turbulent Jets," presented at the ASME Symposium on Fluid Mechanics of Mixing, June 20-22, 1973.
5. Crow, S.C. and Champagne, F.H., "Orderly Structure in Jet Turbulence," J. Fluid Mech., Vol. 48, Part 3, 1971, pp. 547-591.
6. Viets, H., "Flip-Flop Jet Nozzle," AIAA Journal, Vol. 13, No. 10, Oct. 1975, pp. 1375-1379.
7. Brown, G.L. and Roshko, A., "The Effect of Density Difference on the Turbulent Mixing Layer," Turbulent Shear Flows, AGARD-CP-93, 1971, pp. 23 (1-12).
8. Bevilacqua, P.M. and Lykoudis, P.S., "Mechanism of Entrainment in Turbulent Wakes," AIAA Journal, Vol. 9, No. 8, Aug. 1971, pp. 1657-59.

9. Stoker, J.J., "Water Waves," Interscience Publishers, New York, 1957.
10. Piatt, M. and Viets, H., "Conditioned Sampling in an Unsteady Jet," AIAA Paper No. 79-1857, AIAA Aircraft Systems and Technology Meeting, New York City, August 1979.
11. Schlichting, H., Boundary Layer Theory, McGraw-Hill Book Co. Inc., New York, 1960, pg. 400.
12. Viets, H.; Piatt, M. and Ball, M., "Boundary Layer Control by Unsteady Vortex Generation," Proceedings of the Symposium on Aerodynamics of Transportation, published by the ASME, Niagara Falls, N.Y., June 1979.
13. Viets, H.; Piatt, M. and Ball, M., "Unsteady Wing Boundary Layer Energization," AIAA Paper No. 79-1631, AIAA Atmospheric Flight Mechanics Mtg., Boulder, Colorado, Aug. 1979.
14. Viets, H. and Piatt, M., "Induced Unsteady Flow in a Dump Combustor.." Presented at the Seventh International Colloquium on Gas Dynamics of Explosions and Reactive Systems, Göttingen, Germany, Aug. 1979.

## AN INVESTIGATION OF THE STRUCTURE OF EQUILIBRIUM TURBULENT BOUNDARY LAYERS

by

L. F. East

Aerodynamics Department, Royal Aircraft Establishment, Farnborough, Hampshire, England

and

W. G. Sawyer

Aerodynamics Department, Royal Aircraft Establishment, Bedford, Bedfordshire, England

## SUMMARY

The paper presents details of seven low-speed equilibrium boundary layer flows ranging from mildly favourable pressure gradients to adverse pressure gradients almost sufficient to cause incipient separation. The flows are turbulent and second and third order correlations of the turbulence are included in addition to measurements of the mean flow.

The flow parameters are shown to be consistent with existing equilibrium loci. It is also shown that the law of the wall applies to all the flows and that therefore the value of von Kármán's 'constant' in the mixing length formulation of shear stress must vary. The data strongly support the concept of gradient diffusion and it is demonstrated that for flows in strong adverse pressure gradient the shear stress gradient results from the strong diffusion of turbulence towards the wall and not from changes in the dissipation term. Thus although the mixing length is dependent upon pressure gradient the dissipation length is not.

## LIST OF SYMBOLS

$C_f$	skin friction coefficient, $C_f = \tau_w / \frac{1}{2} \rho U_e^2$	$U_{ref}$	reference velocity
$C_\tau$	maximum shear stress coefficient, $C_\tau = \tau_{max} / \frac{1}{2} \rho U_e^2$	$u, v, w$	velocity components of turbulence
$E_f$	equilibrium friction parameter, $E_f = C_f / 2J^2$	$X$	streamwise coordinate measured from the start of the test section
$E_p$	equilibrium pressure gradient parameter, $E_p = -(\delta^* / J^2 U_e) dU_e / dx$	$X_0$	virtual origin of equilibrium flow, $X = X_0$ at $x = 0$
$G$	equilibrium parameter, $G = (H - 1) / (H \sqrt{C_f} / 2)$	$x$	streamwise coordinate of equilibrium flow
$G_{\tau_{max}}$	$G_{\tau_{max}} = (H - 1) / (H \sqrt{C_\tau} / 2)$	$y$	coordinate normal to the surface
$H$	shape parameter, $H = \delta^* / \theta$	$\gamma$	intermittency
$h$	time-dependent mixing length	$\delta$	boundary layer thickness, $y = \delta$ at $U/U_e = 0.995$
$J$	equilibrium shape parameter, $J = (H - 1) / H$	$\delta^*$	displacement thickness $\delta^* = \frac{1}{U_e} \int_0^\delta (U_e - U) dy$
$k$	von Kármán's constant	$\theta$	momentum thickness $\theta = \frac{1}{U_e^2} \int_0^\delta U(U_e - U) dy$
$L$	dissipation length scale	$\pi$	pressure gradient parameter for equilibrium flows, $\pi = - (2\delta^* / C_f U_e) \frac{dU_e}{dx}$
$\ell$	mixing length, $\ell^2 \propto \overline{h^2}$	$\rho$	fluid density
$m$	flow parameter, $m = \frac{x}{U_e} \frac{dU_e}{dx}$	$\tau$	shear stress
$p$	probability	$\tau_{max}$	maximum shear stress
$q$	resultant turbulent velocity, $q^2 = u^2 + v^2 + w^2$	$\tau_w$	shear stress at the wall
$U$	mean velocity in $x$ direction		
$U_e$	mean velocity external to the boundary layer		

## 1 INTRODUCTION

All prediction methods for turbulent flow are dependent on general analytic or numeric representations of the properties of turbulent flow. Ideally these generalised

representations should be obtained by curve-fitting reliable experimental data which cover a sufficiently wide range of conditions to encompass the flows to be predicted. Normally such an ideal is not achieved, particularly with the more sophisticated methods which require empirical information that is more difficult to measure (or even impossible at present) and is consequently neither widely available nor of high accuracy. These prediction methods tend to be based on data correlations obtained in relatively simple flows, for which the most numerous and reliable data are available, and are then applied to more general flows of practical interest.

The flow for which far and away the most data are available is the so-called 'flat-plate flow' both at low and high Mach numbers. Such data can give information on the effect of Reynolds number and Mach number as well as the relationship between turbulence stress and the mean properties of the flow. However the range of conditions covered by flat plate data is very narrow and in particular none of the very important effects of pressure gradient is present. A family of flows which includes some of the effects of pressure gradient is that of the so-called 'equilibrium flows'<sup>1,2,3</sup> in which pressure distributions are selected such that the boundary layers grow with approximately similar profiles of velocity and shear stress. Although equilibrium flows have been used extensively to supply empirical information there is still a shortage of reliable data. Clauser<sup>2</sup> measured two flows in adverse pressure gradients and his work was extended by Bradshaw<sup>3</sup> who studied the turbulence structure in a corresponding pair of flows. There are also the data of Stratford<sup>4</sup> who studied a flow in which conditions were maintained at a point of incipient separation. The present work was undertaken to provide a greater set of equilibrium data than is presently available for attached flows and it is intended that the work should be extended to include equilibrium separated flows.

A general description of the experiment is given in section 2 and the data obtained are presented in section 3. The characteristics of the mean flow and of the turbulence structure are discussed in sections 4 and 5 respectively. Related to the discussion of turbulent diffusion in section 5 is an extended mixing length formulation which is given in the appendix. A more detailed account of this work is given in Ref 5.

## 2 EXPERIMENTAL DETAILS

The general problem of setting up a turbulent equilibrium flow has been discussed at length in the literature (see for instance Refs 1, 2 and 3). Although in theory it is not possible to set up an equilibrium flow without using a surface of varying roughness, in practice flows acceptably close to equilibrium can be obtained without great difficulty. For the present purposes a two-dimensional turbulent boundary layer in incompressible flow is deemed to be in equilibrium if it satisfies the following conditions,

- (a)  $U_e \propto x^m$  where  $U_e$  is the velocity external to the boundary layer,  $x$  is the axis measured along the surface in the streamwise direction and  $m$  is a constant parameter of the flow
- (b)  $\theta \propto x$  where  $\theta$  is the momentum thickness of the boundary layer. It is important to stress that the virtual origin of  $x$  in (a) and (b) must be the same.
- (c) The shape parameter,  $H$ , is constant or dropping slowly as the Reynolds number increases.

The equilibrium flows were set up in the boundary layer tunnel at RAE Bedford which is an open return blower tunnel with a nominal speed range of 0-50 m/s. The test section is 5.4 m long with inlet dimensions of 1.2 m wide by 0.3 m high. The roof of the test section is constructed of ground plates of aluminium alloy and is fitted along its centre line with thirty-three 90 mm diameter removable blank plugs at 150 mm spacing. A row of static tapings is also positioned on the centre line between the removable plugs. The plugs can be replaced by others mounting traverse gears and other forms of instrumentation. The lower surface is constructed of a flexible sheet of fibreglass and its position is maintained by 33 manually operated jacks. The movement of the lower surface is such that the height of the tunnel can be reduced to 150 mm and increased to 750 mm which enables a wide range of pressure distributions to be imposed on the flat upper surface where the boundary layer measurements are made. The flexible floor is not sealed at the junctions with the side walls and there are gaps of up to about 1 mm wide.

Like Clauser<sup>2</sup>, we experienced some difficulty in setting up two-dimensional flow in adverse pressure gradients. The flow was found to break away completely from one or other side wall. To overcome this problem screens were placed at the outlet of the test section of sufficiently high resistance to ensure that the pressure throughout the test section was above the atmospheric pressure. Under these conditions there was outflow at the corners between the flexible floor and the side walls and two-dimensional flow was obtained. It is difficult to be certain about the two-dimensionality of a flow and as an aid tufts were permanently attached to all four surfaces of the test section and provided a ready indication that the flow was running full and approximately parallel with the tunnel axis.

It is a characteristic of equilibrium boundary layer flows that for negative values of  $m$ , corresponding to adverse pressure gradients, two flows having different values of shape parameter and rates of growth are possible<sup>2,6</sup>. If the divergence of the duct is greater than that required to provide maximum adverse pressure gradient (minimum  $m$ ) then two distinct duct flows are possible. Either the symmetry of the flow will be retained, with the top and bottom boundary layers both reaching a value of shape parameter higher than that corresponding to minimum  $m$ , or the flow will become asymmetric with the shape

parameter of one of the boundary layers greater than, and that of the other less than, that for minimum  $m$ . Consideration of the corresponding rates of growth of the boundary layers shows that, for a given duct divergence, the asymmetric flow produces less pressure recovery and is therefore the stable solution. For turbulent flows the maximum adverse pressure gradient corresponds to an attached boundary layer and there is therefore a range of duct divergence in which the flow will be asymmetric but both boundary layers will be attached. In the present tunnel configuration it was found that in this range of conditions the flow with the higher shape parameter always developed on the flexible floor so that the value of the shape parameter of the boundary layer on the test surface was limited to the value corresponding to the maximum adverse pressure gradient. This preferred orientation of the asymmetric flow, which probably resulted from the effect of the curvature of the flexible floor near the inlet to the test section, was reversed by placing delta type vortex generators at the inlet to the test section on the floor and side walls.

Seven equilibrium flows have been studied. In flows 1 and 2 the pressure gradient is favourable and is zero in flow 3. In the remaining four flows the pressure gradient is adverse.

The actual shape of the flexible floor was calculated from a one-dimensional analysis, such that in the absence of boundary layers

$$U_e \propto x^R,$$

by selecting a series of values of  $R$  (actually 0.2 steps from -0.8 to 0.4). The values of  $m$  that were measured differed considerably from the prescribed  $R$  but as will be shown in the next section this method of setting up gave at least 1 m and generally more than 2 m of closely equilibrium flow.

Profile data were obtained with pitot tubes and hot wire probes. The pitot measurements were made with a round probe of 1.13 mm outside diameter and a displacement correction of 0.15 diameters has been applied to all data given in this paper. A limited number of traverses were also made with a static pressure probe and these showed that in all cases the normal pressure gradient was negligible. Turbulence characteristics were measured with an  $X$  hot-wire probe from which mean velocity and second and third order turbulence correlation terms have been deduced. Because of the high turbulence levels in some of the flows the hot-wire signals were first linearised before being processed in analogue form.

### 3 EXPERIMENTAL RESULTS

The characteristics of the seven flows are shown in Figs 1 to 4. In Fig 1 the external velocity distributions are plotted for flow 1, which has the most favourable pressure gradient, and for flows 5 and 7, which are characteristic of the flows with adverse pressure gradients. Also shown in Fig 1 are the fitted curves of the form

$$U_e/U_{ref} \propto x^m \propto (X - X_0)^m \quad (1)$$

where the coordinate  $X$  is measured from the start of the test section and  $X_0$  is the effective start of the equilibrium flow and hence the origin of  $x$ . The curves were obtained by fitting a straight line to plots of  $\ln U$  against  $\ln(X - X_0)$  using the values of  $X_0$  determined from the growth of the momentum thickness  $\theta$  shown in Fig 2. It will be noted that for  $X > 3m$  the growth of  $\theta$  is approximately linear in all cases. The corresponding distributions of shape parameter  $H$  and skin friction coefficient  $C_f$  are shown in Figs 3 and 4. The values of  $C_f$  used in Fig 4 have been deduced by fitting velocity profiles to the law of the wall. These figures show the considerable length of flow required to achieve steady conditions particularly if the shape parameter  $H$  is high. It will also be noted that flow 7 is close to incipient separation.

For each flow the profile at  $X = 3858$  mm has been selected as typical of the equilibrium flow as a whole. The mean velocity profiles deduced from the pitot tube measurements are plotted in Fig 5 and in Fig 6 they are given in log-linear coordinates. The normal coordinate,  $y$ , is plotted in Fig 5 in the non-dimensional form of  $y/x$  as this illustrates very clearly the very great thickness of the layers as  $H$  increases (eg compare 7 with 3 which is flat plate).

The log-linear plots in Fig 6 illustrate that the profiles exhibit a substantial linear region and it will be seen that even flow 7 appears to follow the law of the wall up to  $y/\delta \approx 0.1$  and for most of the flows the law of the wall is closely followed up to at least  $y/\delta \approx 0.2$ . This point will be referred to later in section 5 where the corresponding distributions of shear stress are discussed.

Fig 7 shows that the flow in the outer part of the boundary layers is similar for all the profiles, in the sense of having a common form for the intermittency factor proposed by Sarnecki<sup>7</sup>. The intermittency factor,  $\gamma$ , is defined by

$$U = \gamma U_t + (1 - \gamma) U_e,$$

$U_t$  being the velocity given by the law of the wall, and is plotted in Fig 7 against a normalized coordinate chosen to have a value 0.5 for  $\gamma = 0.5$ .

## 4 EQUILIBRIUM LOCUS

The equilibrium parameters are normally designated  $G$  and  $\pi$ ,

$$\text{where } G = \frac{H-1}{H} \sqrt{\frac{2}{C_f}} \quad (2)$$

and

$$\pi = - \frac{2\delta^*}{C_f U_e} \frac{dU_e}{dx} \quad (3)$$

In the general consideration of laminar and turbulent equilibrium layers given in Ref 6 it is pointed out that these definitions are unsuitable for separated flows and that equivalent, but more general, parameters are an equilibrium friction parameter,  $E_f$ , defined by

$$E_f = G^{-2} = \frac{H^2 C_f}{2(H-1)^2} = \frac{C_f}{2J^2} \quad (4)$$

and an equilibrium pressure gradient parameter,  $E_p$ , defined by

$$E_p = \pi/G^2 = - \left( \frac{H}{H-1} \right)^2 \left( \frac{\delta^*}{U_e} \frac{dU_e}{dx} \right) = - \frac{\delta^*}{J^2 U_e} \frac{dU_e}{dx} \quad (5)$$

where  $J = (H-1)/H$  may be regarded as an equilibrium shape parameter which was introduced in Ref 6 and will also be used in this paper.

Fig 8 gives the equilibrium locus plotted in the form of  $E_f$  against  $E_p$  and in addition to the present data, Bradshaw's<sup>3</sup> data are included together with the calculated locus of Mellor and Gibson<sup>8</sup>. The straight line shown is the empirical equilibrium locus proposed by Green *et al*<sup>9</sup> which takes the simple form in the present coordinates of

$$E_f = 0.024 - 0.8 E_p \quad (6)$$

Clearly the present data are consistent with the existing information and support the simple linear relationships of Green *et al* although the constants could be modified to give a slightly better fit.

## 5 TURBULENCE STRUCTURE

## 5.1 Shear stress profiles

A selection of the turbulence data is reproduced in Fig 9a-c. For each flow Fig 9 gives two graphs, the upper one shows the distribution of  $(\overline{u^2} + \overline{v^2})/U_e^2$  and  $-\overline{uv}/U_e^2$  and the lower one shows the distribution of the turbulence diffusion velocity of these quantities in the  $y$  direction, that is  $(\overline{u^2 v} + \overline{v^3})/(\overline{u^2} + \overline{v^2})U_e$  and  $\overline{uv^2}/\overline{uv}U_e$ . Throughout this section it will be assumed that the terms arising from the  $w$  component of the turbulence, which was not measured, can be approximated by

$$\overline{w^2} \approx \frac{1}{2} (\overline{u^2} + \overline{v^2}) \quad \text{and} \quad \overline{w^2 v} \approx \frac{1}{2} (\overline{u^2 v} + \overline{v^3}) \quad (7)$$

The turbulence kinetic energy  $\frac{1}{2} q^2$  can then be approximated by

$$\frac{1}{2} q^2 = \frac{1}{2} (\overline{u^2} + \overline{v^2} + \overline{w^2}) \approx \frac{3}{4} (\overline{u^2} + \overline{v^2}) \quad (8)$$

and the diffusion of kinetic energy is given by

$$\overline{q^2 v}/q^2 U_e \approx (\overline{u^2 v} + \overline{v^3})/(\overline{u^2} + \overline{v^2}) U_e \quad (9)$$

Also, throughout this section, the density will be omitted and  $(-uv)$  will be referred to as the shear stress and  $\frac{1}{2}q^2$  as the kinetic energy. This shorthand is acceptable as the quantities are always presented in a non-dimensional form and the flow is incompressible. The well-known characteristics of the shear stress profile are clearly evident in Fig 9. As the shape parameter increases the shear stress decreases at the wall and increases further out in the boundary layer. The magnitude of the maximum shear stress is a feature which characterises the shear stress profile and is shown plotted against  $J$  in Fig 10. In Fig 10 it is shown that  $\sqrt{C_\tau}$  varies linearly with  $J$ , where  $C_\tau$  is the maximum stress coefficient defined by  $C_\tau = \tau_{\max}/\frac{1}{2}\rho U_e^2$ . It follows that a function  $G$  based on the maximum stress can be defined which will be constant for all the flows and equal to the flat plate value. Thus

$$G_{\tau_{\max}} = \frac{H-1}{H\sqrt{C_\tau}/2} = \left( \frac{H-1}{H\sqrt{C_{\tau_{\text{flat plate}}}}/2} \right) = 6.55 \quad (10)$$

specifies the straight line in Fig 10.

There is some arbitrariness in the values of  $C_\tau$  for flows 1-3 according to where  $\tau_{\max}$  is evaluated. The actual maximum value of  $\tau$  occurs at  $y = 0$  but as a measure of large-eddy activity in the layer, Bradshaw *et al*<sup>10</sup> take the value of  $\tau$  at  $y/\delta = 0.25$ . As shown in Fig 10 the effect on  $\sqrt{C_\tau}$  is quite small for the flows studied though it may be expected to increase in stronger favourable gradients.

## 5.2 Mixing length representation of shear stress

The most commonly used representations of shear stress in prediction methods are based on eddy viscosity and mixing length formulations. In the mixing length model the shear stress is expressed as,

$$\tau = \rho \ell^2 \left| \frac{dU}{dy} \right| \left( \frac{dU}{dy} \right) \quad (11)$$

where the mixing length,  $\ell$ , is generally assumed to be a function of  $y$  across the layer. The simplest forms of  $\ell$  outside the sublayer region approximate to

$$\ell = 0.4y \quad \text{for } y/\delta < 0.2$$

and

$$\ell = 0.08\delta \quad \text{for } y/\delta > 0.2$$

For flows in which  $\tau$  varies considerably across the inner region it is clearly impossible for both the mixing length model as formulated above and the linear log-law to hold. This is because the linear log-law implies that

$$\tau_w = \rho \ell^2 \left| \frac{dU}{dy} \right| \left( \frac{dU}{dy} \right) \quad (12)$$

which is inconsistent with the mixing length equation unless  $\tau = \tau_w$ .

This point has been extensively studied by Galbraith and Head<sup>11</sup> and by Glowacki and Chil<sup>12</sup>. In Ref 11 it is demonstrated that the linear log-law is the more universally valid and that the mixing length varies from flow to flow. The same result holds for the present data for it has already been shown in Fig 6 that the log-law appears to hold for all the data and Fig 11 shows the consequent trend in the mixing length in the inner region of the boundary layer. Over the outer part of the boundary layer no systematic trend is evident and the curves are shown coalescing onto a single curve. The mixing length has been deduced from the measured shear stress and mean velocity profiles and although there is considerable scatter in the data the trend shown in Fig 11 is unmistakable. Various devices have been proposed in the literature for modifying the mixing length in the wall region so as to recover the law of the wall of which the most direct method is to redefine von Kármán's 'constant',  $k$ , in the inner region as<sup>11</sup>

$$k(y) = 0.4\sqrt{\tau/\tau_w}$$

while retaining an unmodified mixing length in the outer part of the flow. Rather more approximate is the procedure of Ref 12 in which an average value of  $k$  is assumed across the inner layer which is a function of the pressure gradient parameter  $\pi$ .

### 5.3 Turbulence rate equations

To proceed further with the analysis of the turbulence data it is necessary to establish a theoretical framework. The most appropriate framework is provided by the rate equations for turbulence shear stress and kinetic energy which can be deduced from the Navier-Stokes equations and are used in approximate form in the more sophisticated prediction methods.

For a two-dimensional incompressible turbulent boundary layer the rate equation for turbulence shear stress is

$$\frac{D}{Dt}(-\overline{uv}) = \overline{v^2} \frac{dU}{dy} + \frac{\partial}{\partial y}(\overline{uv^2} + \frac{\overline{up'}}{\rho}) - \overline{v(uv^2_v + v^2_v u)} - \frac{\overline{p'}}{\rho} \left( \frac{\partial v}{\partial x} + \frac{\partial u}{\partial y} \right) \quad (13)$$

Advection    Production    Diffusion    Viscous dissipation    Pressure strain

and for turbulence kinetic energy is

$$\frac{D}{Dt} \left( \frac{\overline{q^2}}{2} \right) = (-\overline{uv}) \frac{dU}{dy} - \frac{\partial}{\partial y} \left( \frac{\overline{vq^2}}{2} + \frac{\overline{vp'}}{\rho} \right) + \overline{v(uv^2_u + v^2_v v + w^2_w)} \quad (14)$$

Advection    Production    Diffusion    Viscous dissipation

The production and diffusion terms in these equations have been evaluated from the data and are analysed in sub-sections 5.4 and 5.5 respectively. Although neither the viscous dissipation nor the pressure strain terms can be evaluated from the data some interesting deductions can be made in relation to the turbulence structure in the wall region if the approximate analysis of the rate equations by Bradshaw is followed through.

By an accident of history associated with the fact that the method of Bradshaw *et al*<sup>10</sup> was first derived for two-dimensional flow from the kinetic energy (a scalar quantity) equation and then extended to three dimensions<sup>13</sup> by approximating the rate equations for  $(-\overline{uv})$  and  $(-\overline{vw})$  (vector quantities), Bradshaw<sup>13</sup> had to reconcile his derivations of a useable rate equation for shear stress from both of the above equations. In doing this he assumed that

$$\overline{up'}/\rho \ll \overline{uv^2} \quad \text{and} \quad \overline{vp'}/\rho \ll \overline{vq^2}/2$$

and that

$$\frac{-\overline{uv}}{q^2} = \frac{-\overline{uv^2}}{q^2 v} = a_1 \approx 0.15 \quad (15)$$

throughout the flow. It will be noted that the pressure strain term appears only in the shear stress equation and it was therefore necessary for Bradshaw<sup>13</sup> to reason that the pressure strain term could be regarded as comprising a direct destruction of shear stress, analogous to viscous dissipation, and of a negative production which opposes the generation of shear stress by the term  $\overline{v^2} \frac{dU}{dy}$ . With these assumptions the following equation for shear stress is obtained

$$\frac{D}{Dt} \left( \frac{-\overline{uv}}{2a_1} \right) = (-\overline{uv}) \frac{dU}{dy} - \frac{(-\overline{uv})^2}{L} - \frac{\partial}{\partial y} \left( \frac{-\overline{uv^2}}{2a_1} \right), \quad (16)$$

where  $L$  is the dissipation length scale and was chosen to be very similar to the mixing length  $\lambda$  over most of the boundary layer. Equation (16) forms the basis of the analysis given in section 5.6 of the wall region of the flow.

### 5.4 Turbulence production

The turbulence production terms have been evaluated from the measured mean flow and turbulence profiles and are given in Fig 12 for shear stress; the curves for turbulent kinetic energy are very similar but differ in magnitude. The curves show that as the shape parameter of the boundary layer increases the region of maximum production moves away from the wall to the middle of the boundary layer. This is a well-known fact and correlates with the trend of the maximum shear stress as shown in Fig 9.

However, Fig 12 shows that as  $H$  increases the region of maximum production does not move uniformly away from the surface but rather that there are two regions of high production and the shift is achieved by progressively increasing the production at one region and reducing it at the other. The regions are in the immediate vicinity of the wall, where the velocity shear can be very high, and in the middle of the layer. Thus for flows 1 and 3 very high levels of production are indicated near the wall but these levels rapidly fall and the production over the outer part of the layer is very small. By contrast the production in flow 7 reaches a maximum in the centre of the layer and falls to a low level near the wall. Intermediate flows 4, 5 and 6 combine both the above



distributions (say 3 and 7) in varying amounts and it is noticeable that in flows 5 and 6 the distributions of production do exhibit a pair of maxima.

### 5.5 Turbulence diffusion

The diffusion terms in the rate equations are respectively  $-\frac{\partial}{\partial y}\left(\frac{vq^2}{2} + \frac{vp'}{\rho}\right)$  and  $\frac{\partial}{\partial y}\left(\overline{uv^2} + \frac{up'}{\rho}\right)$  and are important because diffusion is the process by which turbulence is transferred from one mean stream line to another and in particular controls the growth, by entrainment, of boundary layers and shear layers. The pressure diffusion term cannot be measured at present and so the evaluation of the diffusion terms is restricted to the triple correlation terms  $\overline{uv^2}$  and  $\overline{q^2v}$ . The diffusion velocities in the  $y$  direction ( $\overline{uv^2}/\overline{uv}U_e$  and  $\overline{q^2v}/\overline{q^2}U_e$ ) have been given in Fig 9 and clearly show widely varying characteristics over the range of flows studied.

In the Appendix a simple mixing length argument is used to derive forms for the turbulent diffusion terms. Two principal terms are derived for the diffusion, one related to the turbulence itself and the other related to the gradient of the turbulence level, so-called gradient diffusion. The general form of the diffusion shown in Fig 9 is clearly more likely to fit the gradient diffusion concept and as shown in Figs 13 and 14 the data are quite well predicted by the following equations,

$$\overline{uv^2} = 2\ell \frac{d}{dy} \left( -\overline{uv} \right)^{\frac{3}{2}} \quad (17)$$

and

$$\overline{q^2v} = -0.4\ell \frac{d}{dy} \left( \overline{q^2} \right)^{\frac{3}{2}} \quad (18)$$

In these relationships the length scale,  $\ell$ , has been taken as the normal mixing length and, for numerical convenience, is expressed in terms of  $y/\delta$  by the following equation,

$$\ell/\delta = 0.075(5y/\delta) \left[ (5y/\delta)^2 + 1 \right] / \left[ (5y/\delta)^3 + 1 \right] \quad (19)$$

The process of diffusion is important in turbulent flow but should not be thought of as the automatic result of the presence of turbulence or even of the presence of a finite Reynolds stress. It is a statistical property that odd-order correlations are all zero if the joint probability of the velocity components of the turbulence is symmetrical and only the even-order correlations are in general non-zero.

Thus if the joint probability  $p(u,v)$  has the symmetric property that

$$p(u,v) = p(-u, -v) \quad (20)$$

then the general expression for the  $(r+s)$  order correlation,

$$\overline{u^r v^s} = \int_{-\infty}^{\infty} \int_{-\infty}^{\infty} p(u,v) u^r v^s du dv \quad (21)$$

reduces to

$$\overline{u^r v^s} = 2 \int_0^{\infty} \int_{-\infty}^{\infty} p(u,v) u^r v^s du dv$$

if  $(r+s)$  is even

and

$$\overline{u^r v^s} = 0$$

if  $(r+s)$  is odd.

These results show that whereas a finite Reynolds stress ( $r=1, s=1$ ) can be obtained with a correlated but entirely symmetric probability distribution (eg Gaussian) it is essential if diffusion is to occur that the turbulent motion is such as to produce a skewed probability distribution. This makes the prediction of diffusion difficult as it is a function of the fine detail of the turbulence rather than its overall characteristics. On the other hand this general result is entirely consistent with the known characteristics of intermittency and the entrainment of laminar flow which is physically the main process by which diffusion is thought to operate in the outer part of the layer. The phenomena of intermittency may be expected to give rise to a strongly skewed probability distribution.

According to the simple mixing length model given in the Appendix there are two processes that can lead to a skewed probability distribution and hence diffusion. In general terms the fluctuating velocity,  $u$ , is assumed to result from fluid arriving at the measurement point from regions of the flow with different mean velocities. Hence the general form of the fluctuating velocity,  $u$ , is,

$$u(y,t) = u[h(y,t), U(y)]$$

where  $h$  is the instantaneous mixing length and  $U$  is the mean velocity. A skewed distribution can result from either a skewed distribution of the mixing length, that is the distance in the  $y$  direction which the fluid is assumed to have travelled before passing through the measurement point, or from curvature of the mean velocity profile. The present data support the hypothesis that in plane turbulent flow the effects of the curvature of the mean velocity profile are the more important and that consequently the mixing length is assumed to have an effectively symmetric probability distribution. It is reasoned in the Appendix that if the diffusion process is dominated by some directional external influence then the alternative form of diffusion will occur. Smits *et al*<sup>14</sup> have obtained data in a highly curved flow which do not support the gradient diffusion concept and Ramaprian and Shivaprasad<sup>15</sup> have demonstrated that turbulent diffusion is strongly affected by flow curvature. It is possible that centrifugal body forces effectively skew the probability distribution of the mixing length and give rise to turbulence diffusion closer to the general form

$$\overline{u^2 v} \propto (\overline{q^2})^{\frac{3}{2}} \quad \text{and} \quad \overline{uv^2} \propto (-\overline{uv})^{\frac{3}{2}} \quad (22)$$

### 5.6 Turbulence structure in the wall region

Reference has previously been made in section 5.2 to the fact that the 'law of the wall' is not compatible with a constant value of von Kármán's 'constant',  $k$ , in the mixing length formulation of shear stress in flows with shear stress gradients near the wall. It is shown in this section that these two observations can be reconciled to the extent that if the effects of diffusion are included then a constant value of  $k$  in Bradshaw's dissipation length scale is compatible with a law of the wall velocity profile.

As an example of the role of the diffusion term consider flow 7 which exhibits a high shear stress gradient near the wall but a low shear stress at the wall. Fig 12 shows that the direct production of shear stress in the wall region ( $y/\delta < 0.1$ ) is small but Fig 13 shows that there is a large diffusion of shear stress towards the wall from further out in the flow. It is proposed that the shear stress gradient in the wall region of flow 7 results from a balance of dissipation and diffusion, and not from a balance of production and dissipation as has been widely assumed in the past. In this section we seek to provide quantified evidence to support this suggestion and we start from the form of the rate equation for shear stress deduced by Bradshaw and given in equation (16) as,

$$\frac{D}{Dt} \left( -\frac{\overline{uv}}{2a_1} \right) = (-\overline{uv}) \frac{dU}{dy} - \frac{(-\overline{uv})^{\frac{3}{2}}}{L} - \frac{\partial}{\partial y} \left( -\frac{\overline{uv^2}}{2a_1} \right) \quad (23)$$

In the wall region we assume that the convection term is negligible and the diffusion can be represented by equation (17), then

$$(-\overline{uv}) \frac{dU}{dy} - \frac{(-\overline{uv})^{\frac{3}{2}}}{L} + \frac{d}{dy} \left( \frac{\ell}{a_1} \frac{d}{dy} (-\overline{uv})^{\frac{3}{2}} \right) = 0 \quad (24)$$

It is also stipulated that the velocity profile must follow the law of the wall and so outside the sub-layer and blending regions,

$$\tau_w / \rho = \ell^2 \left( \frac{dU}{dy} \right)^2$$

and the velocity gradient can be expressed as,

$$\frac{dU}{dy} = \frac{\sqrt{\tau_w / \rho}}{\ell} \quad (25)$$

We are seeking to show that a constant value of  $k$  can be used and so the mixing length,  $\ell$ , and Bradshaw's dissipation length scale,  $L$ , are expressed in the wall region as,

$$\ell = L = ky \quad (26)$$

With these substitutions equation (24) can be written

$$y \frac{d}{dy} \left\{ y \frac{d}{dy} \left( \frac{\tau}{\rho} \right)^{\frac{3}{2}} \right\} - \left( \frac{a_1}{k^2} \right) \left\{ \left( \frac{\tau}{\rho} \right)^{\frac{3}{2}} - \left( \frac{\tau}{\rho} \right) \left( \frac{\tau_w}{\rho} \right)^{\frac{1}{2}} \right\} = 0 \quad (27)$$

which is an ordinary differential equation for  $\sqrt{\tau/\rho}$  as a function of  $y$ .

Equation (27) requires boundary values of  $(\tau/\rho)$  and  $\frac{d}{dy}(\tau/\rho)$  at a chosen point in the flow. As the convection term has been neglected and the law of the wall has been used to determine the velocity gradient the point must be chosen within the wall region and, in general, should be outside the laminar and blending regions where the equation is not expected to apply. There are two simple analytic solutions which correspond to special flows

$$(i) \quad \tau = \tau_w \quad (28)$$

This is the solution appropriate to flat-plate boundary layers.

$$(ii) \quad \tau \propto y^{\frac{2}{3}} \sqrt{\frac{a_1}{k^2}} \quad \text{for} \quad \tau_w = 0 \quad (29)$$

This is the solution corresponding to incipient separation and will later be shown to be in close agreement with the measured data of flow 7.

A general numerical solution in a closed form can also be obtained as follows: Make the substitutions

$$\eta = (\tau/\tau_w)^{\frac{3}{2}}, \quad s = \ln y \quad \text{and} \quad A = a_1/k^2$$

then equation (27) becomes

$$\frac{d^2 \eta}{ds^2} = A(\eta - \eta^{\frac{2}{3}}) \quad (30)$$

Make the further substitution

$$p = \frac{d\eta}{ds} \quad (31)$$

and equation (30) can then be written

$$\frac{dp}{ds} = p \frac{dp}{d\eta} = A(\eta - \eta^{\frac{2}{3}}) \quad (32)$$

which can be solved for  $p$  as a function of  $\eta$  with the boundary conditions that at  $s = s_1$ ,  $\eta = \eta_1$  and  $p = p_1$ . The following explicit equation for  $p$  is then obtained

$$p = \left[ p_1^2 + 2A \left\{ \left( \frac{1}{2} \eta^2 - \frac{3}{5} \eta^{\frac{5}{3}} \right) - \left( \frac{1}{2} \eta_1^2 - \frac{3}{5} \eta_1^{\frac{5}{3}} \right) \right\} \right]^{\frac{1}{2}}$$

Using the definition of  $p$  as given in equation (31) the above equation is written as

$$\frac{d\eta}{ds} = \left[ p_1^2 + A \left\{ \left( \eta^2 - \frac{6}{5} \eta^{\frac{5}{3}} \right) - \left( \eta_1^2 - \frac{6}{5} \eta_1^{\frac{5}{3}} \right) \right\} \right]^{\frac{1}{2}}$$

This equation can be integrated to give

$$s - s_1 = \int_{\eta_1}^{\eta} \frac{dt}{\left[ p_1^2 + A \left\{ \left( t^2 - \frac{6}{5} t^{\frac{5}{3}} \right) - \left( \eta_1^2 - \frac{6}{5} \eta_1^{\frac{5}{3}} \right) \right\} \right]^{\frac{1}{2}}}$$

which is written in terms of the coordinate  $y$  as

$$y = y_1 \exp \left\{ \int_{\eta_1}^{\eta} \frac{dt}{\left[ p_1^2 + A \left\{ \left( t^2 - \frac{6}{5} t^{\frac{5}{3}} \right) - \left( \eta_1^2 - \frac{6}{5} \eta_1^{\frac{5}{3}} \right) \right\} \right]^{\frac{1}{2}}} \right\} \quad (33)$$

Equation (33) has been evaluated numerically using appropriate values of  $p_1$  and  $\eta_1$  at a starting value of  $y_1 = 0.02\delta$ . The values of  $p_1$  and  $\eta_1$  were selected so that the predicted variation of shear stress with  $y$  matched the measurements over the inner portion of the logarithmic region, using measured values of  $\tau_w$  and  $a_1 = 0.15$ ,  $k = 0.4$ . The results are shown in Fig 15 as solid lines in the region of the law of the wall and dotted elsewhere, where equation (27) should not be expected to apply.

Flow 4 is a little different from the remainder in that  $\tau_{\max}$  occurs only just outside the wall region, as shown in Fig 15, and this probably accounts for the tendency to overestimate the shear stress in this case. For flow 7 the analytic solution (equation (29)) is indistinguishable on Fig 15 from the numerical solution within the wall region, which indicates that the production is indeed negligible and the shear stress results from a simple balance of dissipation and diffusion.

The level of agreement shown in Fig 15 provides strong support for the basic premise of this section that the shear stress gradient results from the strong diffusion of turbulence towards the wall and not from variations in the dissipation term.

## 6 CONCLUSIONS

The seven turbulent boundary layers studied are shown to be good approximations to two-dimensional equilibrium flows. The mean flow parameters are consistent with existing published data and suggest the use of a particular analytic form of the equilibrium locus, which is typical of several that have been proposed in the literature. There is strong evidence that the law of the wall holds for all the flows and that, in consequence, von Kármán's 'constant' in the mixing length model of shear stress must vary appreciably. The evidence supporting the general validity of the law of the wall is that all the flows exhibit an apparent log-linear region of the correct slope and the values of the skin friction at the wall deduced from these curves are consistent with the values of shear stress measured in the flow with hot-wire equipment. In the flow closest to separation the law of the wall appears to hold up to  $y/\delta \approx 0.1$  although by then the shear stress is over ten times its value at the wall.

Consideration of the second and third order correlations of the fluctuating velocity has produced the following relatively simple account of the characteristic behaviour of the turbulence.

The production of shear stress is centred about two distinct regions in the layer. These regions are immediately adjacent to the wall and at approximately the mid point of the layer. Under conditions of favourable or negligible pressure gradient, with corresponding low values of shape parameter, very high levels of production occur near the wall but these levels fall rapidly and the production over the outer part of the layer is very small. Under incipient separation conditions, with high values of shape parameter, the production reaches a maximum in the centre of the layer and falls to a low level near the wall. For intermediate values of shape parameter the above characteristic distributions of production are combined in varying amounts and can lead to double humped distributions across the layer. The corresponding distributions of shear stress and turbulent kinetic energy are similar to the distributions of production except that the double-humped distribution does not occur. Instead, as the shape parameter increases, the position of the maximum stress moves steadily away from the wall region towards the mid point which it reaches under incipient separation conditions.

The diffusion of shear stress and turbulent kinetic energy by the turbulence is shown to relate to the gradient of the shear stress and kinetic energy rather than their magnitudes. Consequently at the higher shape parameters, when the position of the maximum shear stress has moved away from the wall region, shear stress is diffused towards the wall in the inner region and towards the external flow in the outer region of the boundary layer. Finally it is shown that if the diffusion of shear stress towards the wall in the wall region is taken into account, then the dissipation length scale used by Bradshaw in his form of the shear stress rate equation becomes independent of the pressure gradient and compatible with the law of the wall velocity profile. This result is to be contrasted with the mixing length representation in which the length scale must be dependent upon the pressure gradient if the observed law of the wall velocity profile is to be recovered.

## Appendix

## MIXING LENGTH MODEL FOR TURBULENCE DIFFUSION

In this Appendix the mixing length formulation of shear stress is extended to obtain expressions for the turbulence diffusion terms. The derived equations relate the turbulence diffusion to other turbulence quantities and not to the mean velocity field and are not expected therefore to be significantly affected by the absence of any allowance for lag in the simple formulation used.

In the mixing length model of turbulent shear flow the fluid passing through a particular point in the flow at time  $t$  with velocity  $U(y,t)$  is modelled as though it had come from another region of the flow at  $y + h$  with a velocity equal to the time-arranged velocity in that region,  $U(y + h)$ . Thus for all time the identity

$$U(y,t) = U(y + h(t)) \quad (A-1)$$

defines the time history of the length scale  $h$ , which is measured in the  $y$  direction. The turbulence velocity can therefore be expressed as a Taylor series in ascending power of  $h$  as

$$U(y,t) = U(y) + h(t) \left( \frac{dU}{dy} \right)_y + \frac{h^2(t)}{2} \left( \frac{d^2U}{dy^2} \right)_y + \dots \quad (A-2)$$

and the time averaged form of this equation requires that the statistical properties of the length scale  $h$  satisfy the following equation,

$$0 = \bar{h} \left( \frac{dU}{dy} \right)_y + \frac{\overline{h^2}}{2} \left( \frac{d^2U}{dy^2} \right)_y + \dots$$

The fluctuating component of velocity in the  $x$  direction can be deduced from equation (A-2) as

$$u = U(y,t) - U(y) = h \left( \frac{dU}{dy} \right)_y + \frac{h^2}{2} \left( \frac{d^2U}{dy^2} \right)_y + \dots \quad (A-3)$$

where the time-dependence of  $u$  and  $h$  is now understood.

It is usual in the derivation of the mixing length model of shear stress to assume that the  $v$  component of turbulence is proportional in magnitude to  $u$  and negatively correlated with it. The assumption of negative correlation is valid only if the shear stress ( $-\rho \bar{u}v$ ) is positive and furthermore is not invariant with inversion of the coordinate system. In this analysis it is argued that to be compatible with the physical model used to derive equation (A-1),  $v$  should have the same sign as  $(-h)$ . This is because if the flow at  $y$  is modelled as having come from  $y + h$  with  $h > 0$  then it follows that  $v$  may be expected to be negative. It is therefore assumed that  $v$  can be expressed as

$$v \propto -h \left| \frac{u}{h} \right| \quad (A-4)$$

It follows directly from equation (A-4) that the second and third order correlation terms can be written

$$uv \propto -h \left| \frac{u}{h} \right|, \quad v^2 \propto u^2 \quad (A-5)$$

and

$$u^2v \propto v^3 \propto -h^3 \left| \left( \frac{u}{h} \right)^3 \right|, \quad uv^2 \propto u^3 \quad (A-6)$$

Substituting equation (A-3) for  $u$  in equation (A-5) yield the following forms for the second order correlation terms to order  $h^2$ ,

$$uv \propto -h^2 \left| \frac{dU}{dy} \right| \left( \frac{dU}{dy} \right) \quad \text{and} \quad v^2 \propto u^2 \propto h^2 \left( \frac{dU}{dy} \right)^2 \quad (A-7)$$

Taking the time average and introducing the mixing length  $\ell$ ,

where  $\ell^2 \propto \overline{h^2}$ , yields

$$-\overline{uv} = \ell^2 \left| \frac{dU}{dy} \right| \left( \frac{dU}{dy} \right) \quad \text{and} \quad \overline{u^2} \propto \overline{v^2} \propto \ell^2 \left( \frac{dU}{dy} \right)^2. \quad (\text{A-8})$$

The third order correlation terms are all functions of  $(u/h)^3$  which to order  $h$  is given by equation (A-3) as

$$(u/h)^3 \propto \left( \frac{dU}{dy} \right)^3 + \frac{3h}{2} \left( \frac{dU}{dy} \right)^2 \left( \frac{d^2U}{dy^2} \right). \quad (\text{A-9})$$

An approximate form of equation (A-9) expressing  $(u/h)^3$  in terms of second order correlation terms in place of functions of the mean velocity profile can be obtained as follows. The mean velocity profile can be expressed in terms of stresses by taking the square root of equation (A-8) to yield

$$\frac{dU}{dy} = \frac{C\sqrt{|\overline{uv}|}}{\ell} \propto \frac{C\sqrt{\overline{u^2}}}{\ell} \propto \frac{C\sqrt{\overline{v^2}}}{\ell} \quad (\text{A-10})$$

where  $C = 1$  for  $\overline{uv} \leq 0$  and  $C = -1$  for  $\overline{uv} > 0$ .

$C$  has been introduced to remove the ambiguity of sign introduced by taking the square root. The term  $d^2U/dy^2$  in equation (A-9) is then given by differentiating equation (A-10) with respect to  $y$ . For simplicity the mixing length  $\ell$  is assumed to be independent of  $y$ , which is a valid assumption in a boundary layer for  $y/\delta > 0.2$ . Then

$$\frac{d^2U}{dy^2} = \frac{1}{\ell} \frac{dC\sqrt{|\overline{uv}|}}{dy} \propto \frac{1}{\ell} \frac{dC\sqrt{\overline{u^2}}}{dy} \propto \frac{1}{\ell} \frac{dC\sqrt{\overline{v^2}}}{dy}. \quad (\text{A-11})$$

Substituting equations (A-10) and (A-11) into equation (A-9) gives the following expression for  $(u/h)^3$

$$(u/h)^3 \propto \frac{C|\overline{uv}|^{\frac{3}{2}}}{\ell^3} + \frac{h}{\ell^3} \frac{d}{dy} (C|\overline{uv}|^{\frac{3}{2}}) \quad (\text{A-12})$$

where the shear stress can be replaced by either of the normal stresses.

General expressions for the diffusion of shear stress and turbulent kinetic energy can be written by substituting equation (A-12) into the expressions given in equation (A-6). The diffusion of shear stress is given by

$$\overline{uv^2} \propto \overline{u^3} \propto \frac{h^3 C |\overline{uv}|^{\frac{3}{2}}}{\ell^3} + \frac{h^4}{\ell^3} \frac{d}{dy} (C |\overline{uv}|^{\frac{3}{2}}) \quad (\text{A-13})$$

and the diffusion of kinetic energy,  $\overline{q^2}$ , is given approximately by

$$\overline{q^2 v} \propto \overline{u^2 v} + \overline{v^3} \propto -h^3 \left| \left( \frac{u}{h} \right)^3 \right| \propto -h^3 \left| \frac{C \overline{q^2}^{\frac{3}{2}}}{\ell^3} + \frac{h}{\ell^3} \frac{d}{dy} (C \overline{q^2}^{\frac{3}{2}}) \right|. \quad (\text{A-14})$$

Equations (A-13) and (A-14) demonstrate a dependence of the turbulence diffusion both on the magnitude of the turbulence and on its gradient. The significance of the first term depends on the magnitude of  $h^3/\ell^3$  which will be zero if  $h(t)$  has a symmetrical probability distribution. The present data demonstrate that in plane turbulent flow the first term is insignificant and that the second gradient term dominates. Smits *et al*<sup>14</sup> have obtained data in a highly curved flow in which the diffusion is a function of the turbulence level and so in that case the first term in the above equations dominates.

With the assumption that  $\overline{h^4} \propto \ell^4$  it is concluded that in plane turbulent flow

$$\overline{uv^2} \propto \ell \frac{d}{dy} (C |\overline{uv}|^{\frac{3}{2}}) \quad \text{and} \quad \overline{q^2 v} \propto -h^3 \left| \frac{h}{\ell^3} \frac{d}{dy} (C \overline{q^2}^{\frac{3}{2}}) \right| \propto \ell \frac{d}{dy} (C \overline{q^2}^{\frac{3}{2}}) \quad (\text{A-15})$$

which for  $\overline{uv} \leq 0$  reduce to

$$\overline{uv^2} \propto \ell \frac{d}{dy} (-\overline{uv})^{\frac{3}{2}} \quad \text{and} \quad \overline{q^2 v} \propto \ell \frac{d}{dy} (\overline{q^2})^{\frac{3}{2}} \quad (A-16)$$

If some mechanism, such as perhaps centrifugal body forces, is present which leads to a strongly asymmetric probability distribution of the mixing length then

$$\overline{uv^2} \propto C \left| \overline{uv} \right|^{\frac{3}{2}} \quad \text{and} \quad \overline{q^2 v} \propto C q^{\frac{3}{2}} \quad (A-17)$$

#### REFERENCES

1. J.C. Rotta. Turbulent boundary layers in incompressible flow. *Progress in Aeronautical Sciences*, Vol 2, Pergamon Press (1962)
2. F.H. Clauser. Turbulent boundary layers in adverse pressure gradients. *J. Aero. Sci.*, 21, 91 (1954)
3. P. Bradshaw. The turbulence structure of equilibrium boundary layers. NPL Aero Report 1184 (1966)
4. D.S. Stratford. An experimental flow with zero skin friction throughout its region of pressure rise. *JFM*, 5, 17 (1959)
5. L.F. East, W.G. Sawyer, C.R. Nash. An investigation of the structure of equilibrium turbulent boundary layers. RAE Technical Report 79040 (1979)
6. L.F. East, P.D. Smith, P.J. Merryman. Prediction of the development of separated turbulent boundary layers by the lag-entrainment method. RAE Technical Report 77046 (1977)
7. B.G.J. Thompson. A new two-parameter family of mean velocity profiles for incompressible turbulent boundary layers on smooth walls. ARC R & M 3463 (1967)
8. G.L. Mellor, D.M. Gibson. Equilibrium turbulent boundary layers. *JFM*, 24, 225-254 (1966)
9. J.E. Green, D.J. Weeks, J.W.F. Brooman. Prediction of turbulent boundary layers and wakes in compressible flow by a lag-entrainment method. ARC R & M 3791 (1973)
10. P. Bradshaw, D.H. Ferris, N.P. Atwell. Calculation of turbulent boundary layer development using the turbulent energy equation. *JFM*, 28, 593-616 (1967)
11. R.A. McD Galbraith, M.R. Head. Eddy viscosity and mixing length from measured boundary layer developments. *Aero Quart.* 26, 133-154 (1975)
12. W.J. Glowacki, S.W. Chi. Effect of pressure gradient on mixing length for equilibrium turbulent boundary layers. AIAA No. 72-213 (1972)
13. P. Bradshaw. Calculation of boundary layer development using the turbulent energy equation. VII three-dimensional flow. NPL Aero Report 1286 (1969)
14. A.J. Smits, S.T.B. Young, P. Bradshaw. The effect of short regions of high surface curvature on turbulent boundary layers. IC Aero Tech Note 7814 (1978)
15. B.R. Ramaprian, B.G. Shivaprasad. The structure of turbulent boundary layers along mildly curved surfaces. *JFM*, 85, 273-303 (1978)
16. L.F. East. A prediction of the law of the wall in compressible three-dimensional turbulent boundary layers. RAE Technical Report 72178 (1972)

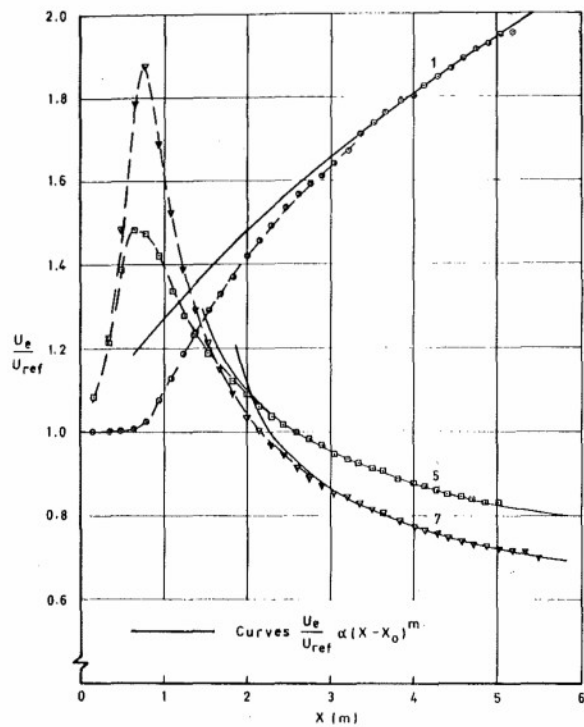


Fig 1 Free stream velocity distribution for flows 1, 5 and 7

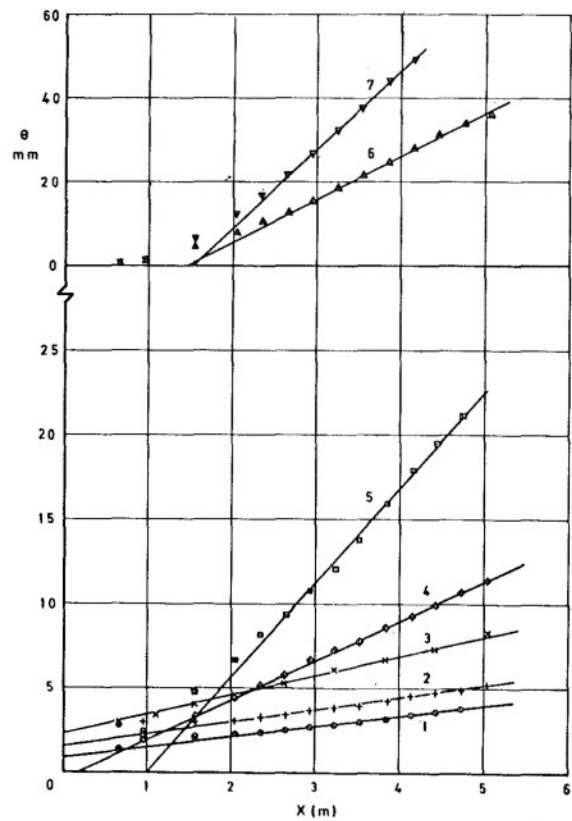


Fig 2 Growth of the momentum thickness for all flows

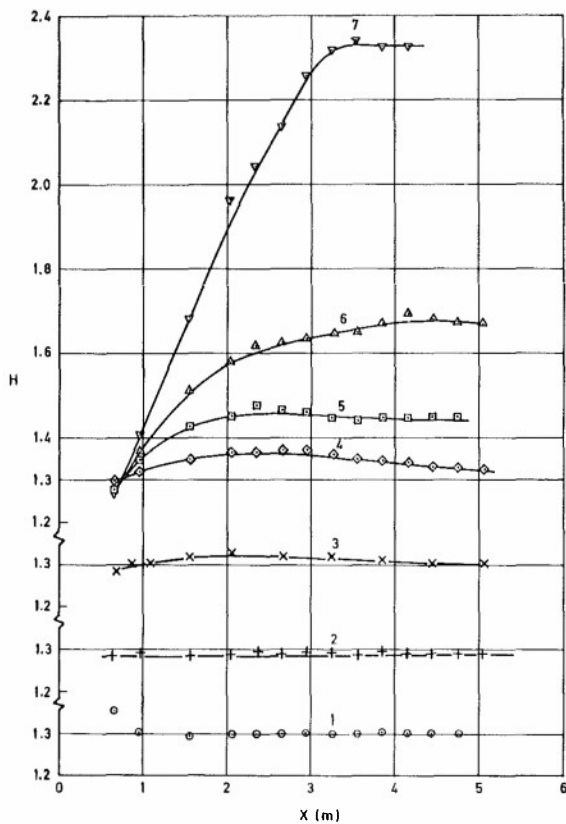


Fig 3 Shape parameter distributions for all flows

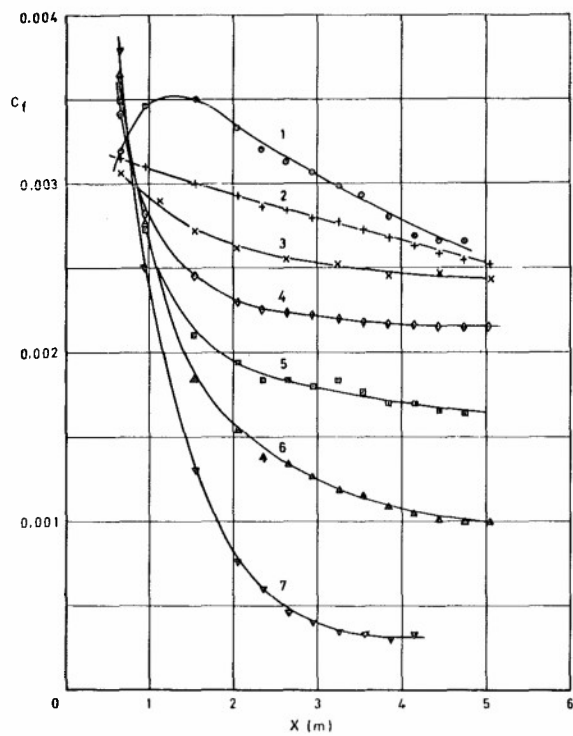


Fig 4 Skin friction distributions for all flows



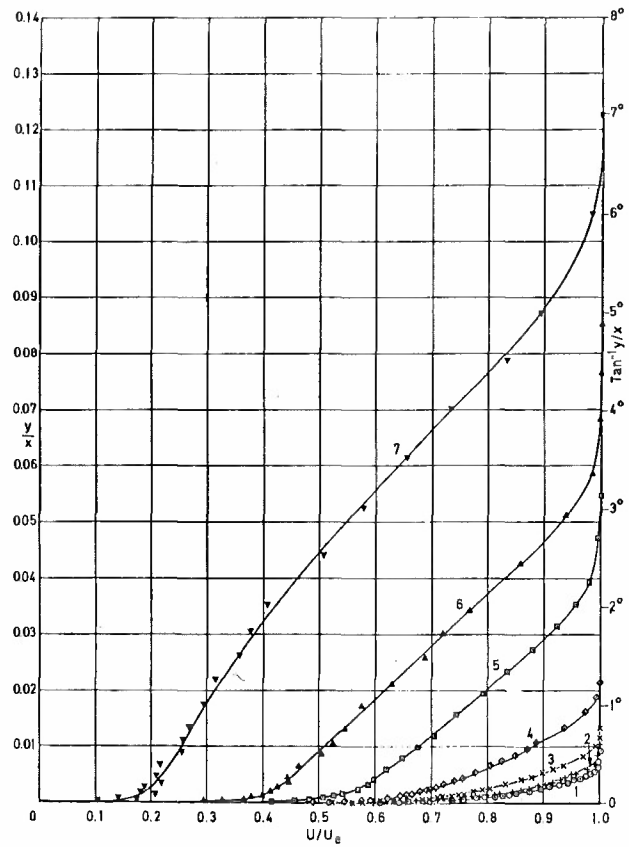


Fig 5 Equilibrium velocity profiles

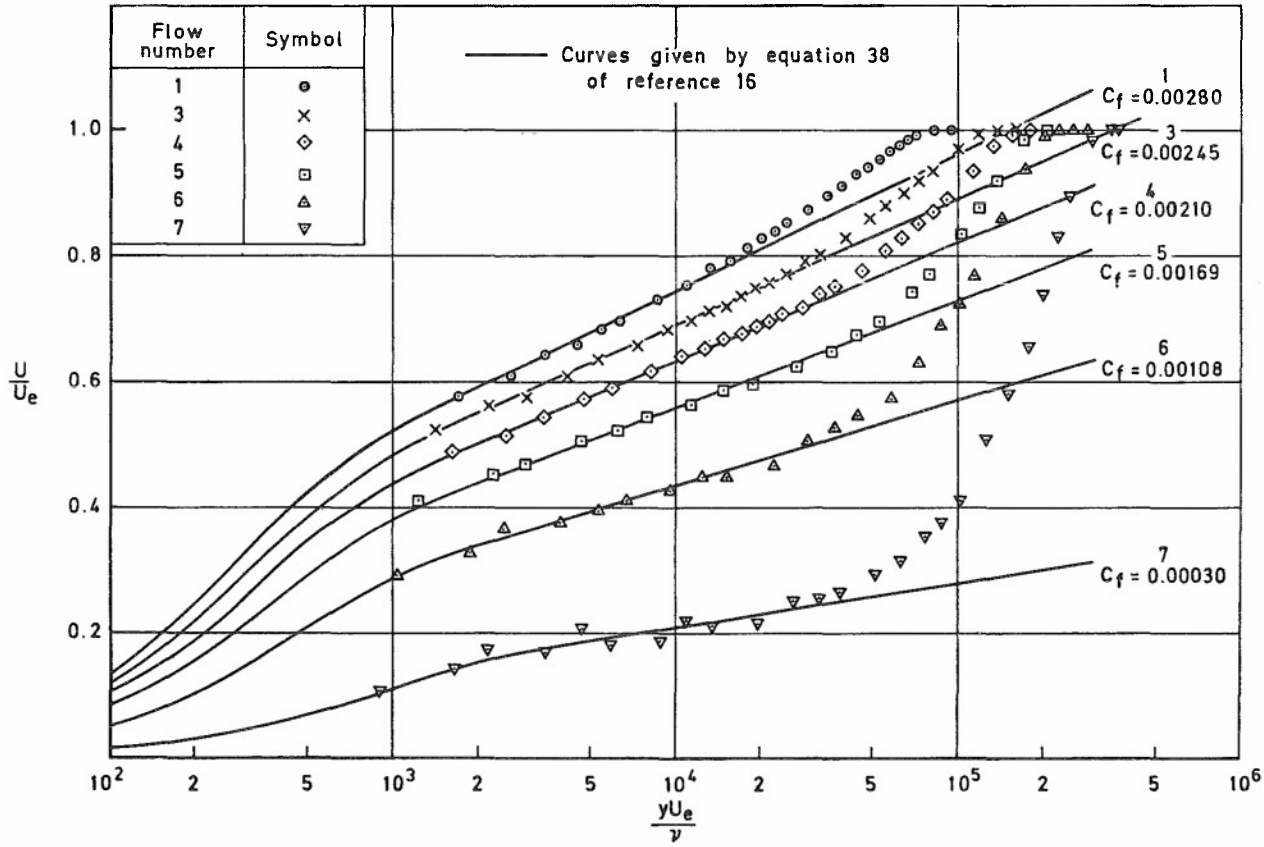


Fig 6 Logarithmic plots of mean velocity profiles

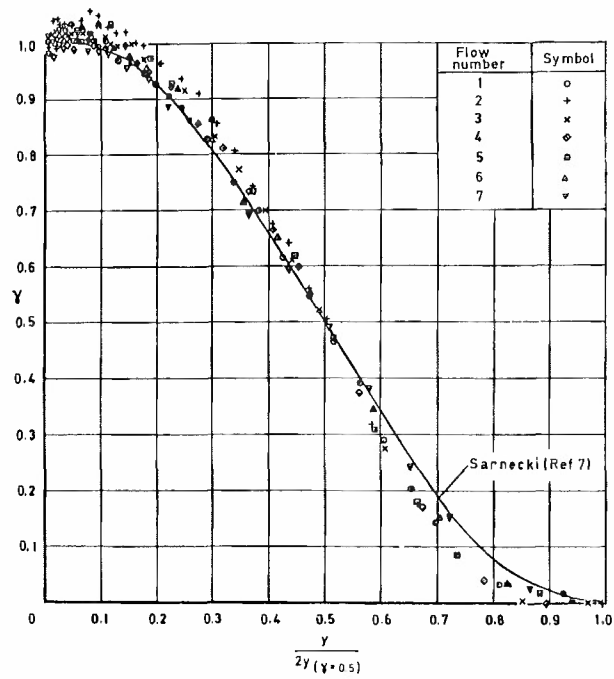


Fig 7 Intermittency distribution derived from mean flow

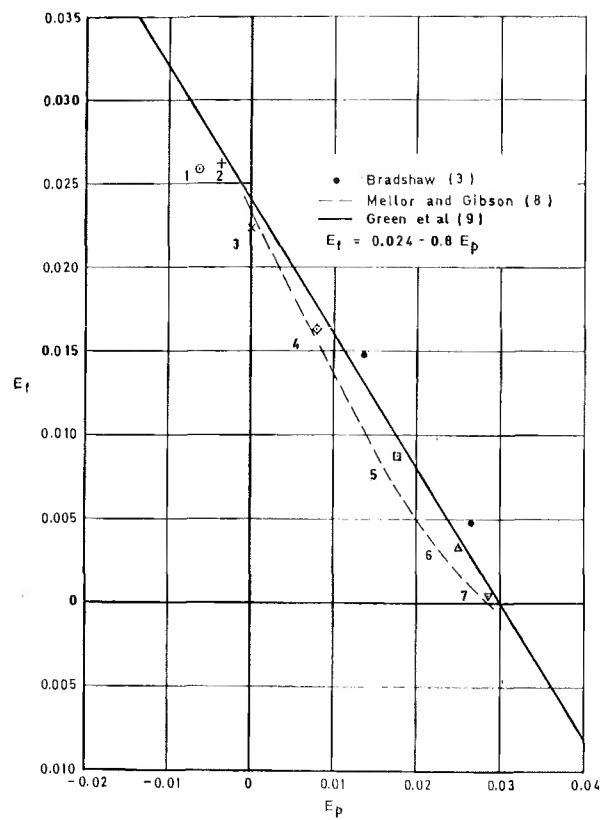


Fig 8 Equilibrium locus in general coordinates

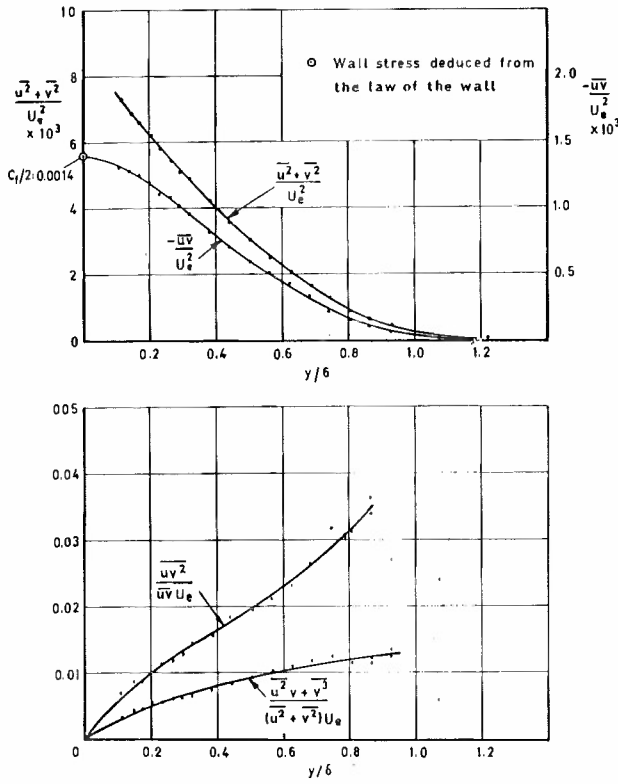


Fig 9a Profiles of shear stress and other turbulence quantities for flow 1

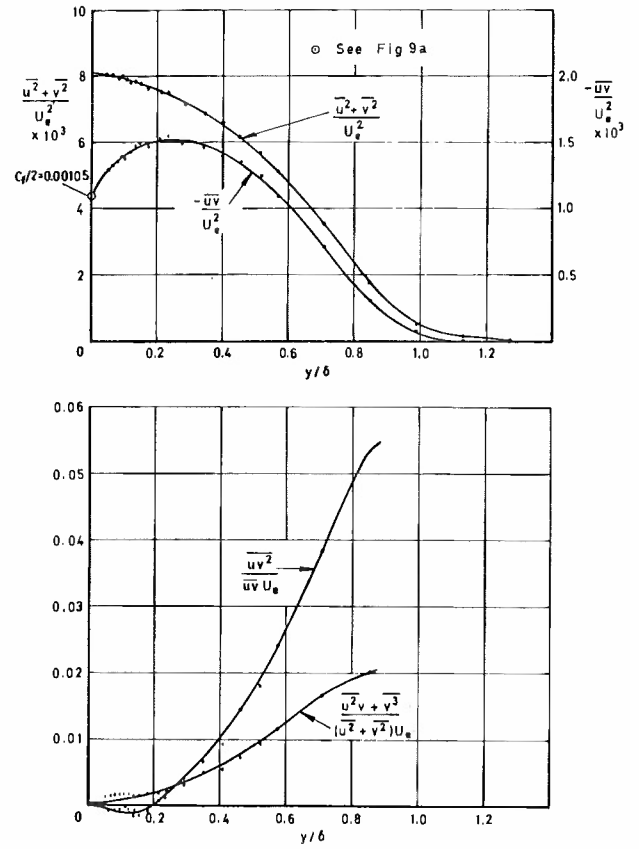


Fig 9b Profiles of shear stress and other turbulence quantities for flow 4

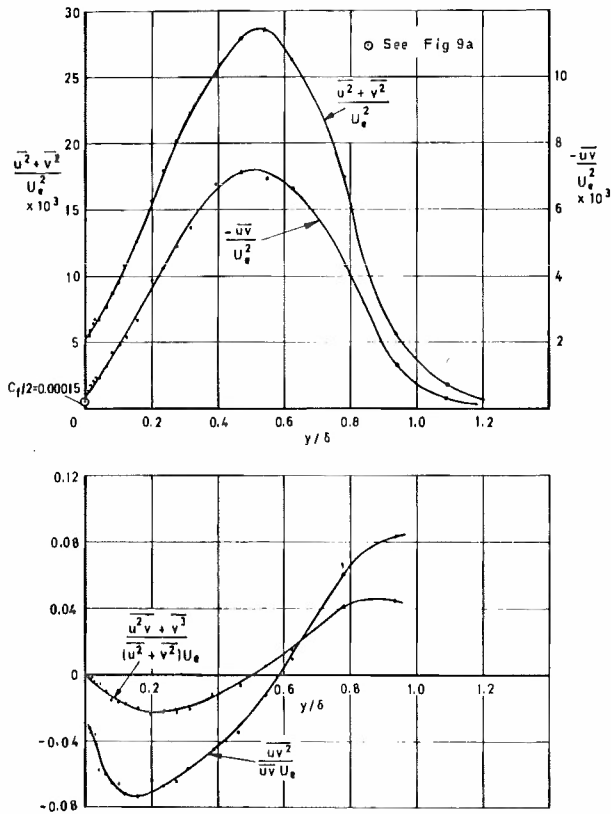


Fig 9c Profiles of shear stress and other turbulence quantities for flow 7

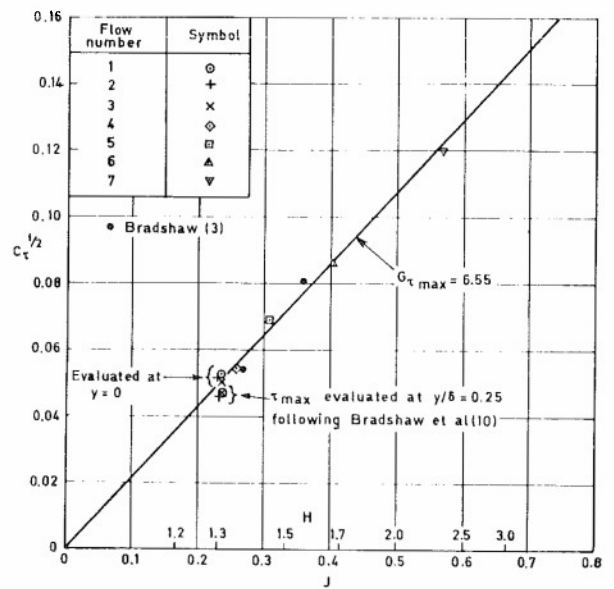


Fig 10 Dependence of the maximum shear stress on the boundary layer shape parameter

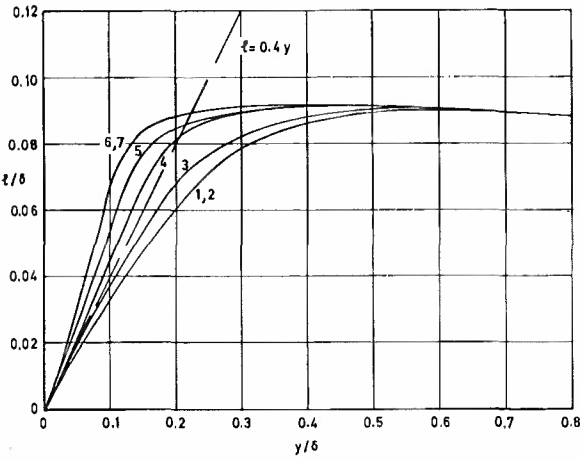


Fig 11 Smoothed curves of mixing length deduced from measured shear stress and mean velocity profiles

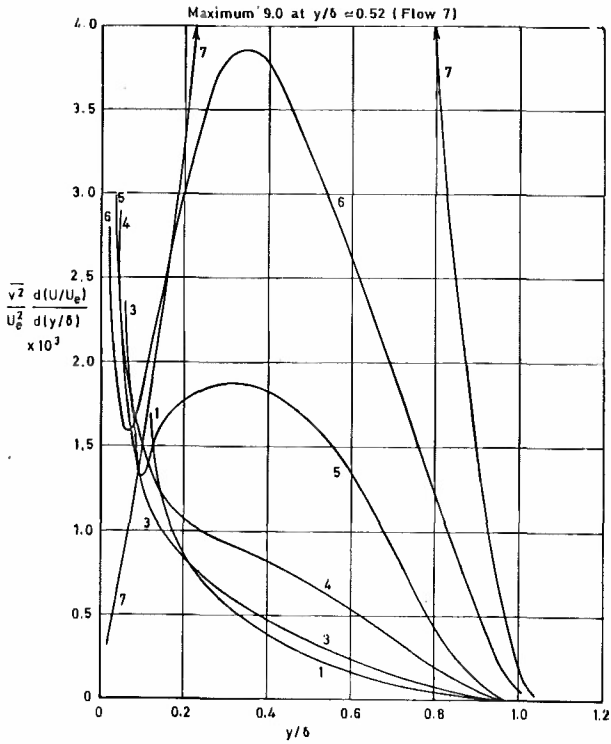


Fig 12 Production of turbulent shear stress

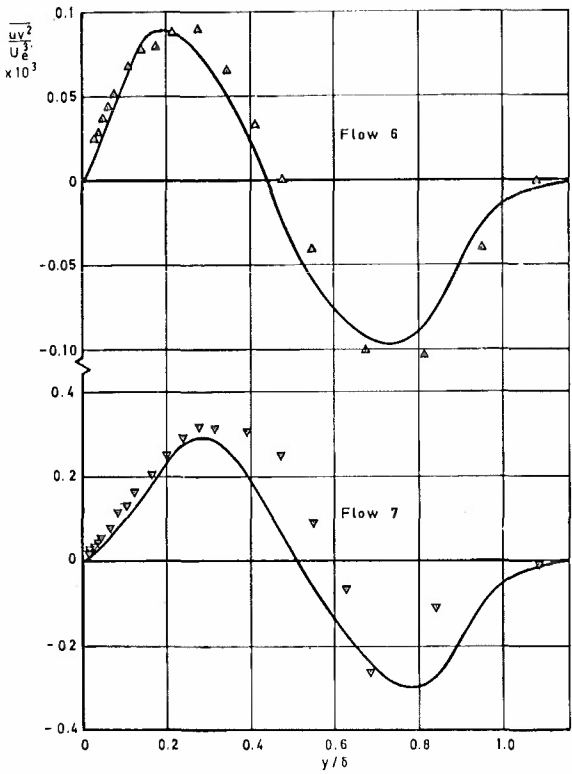
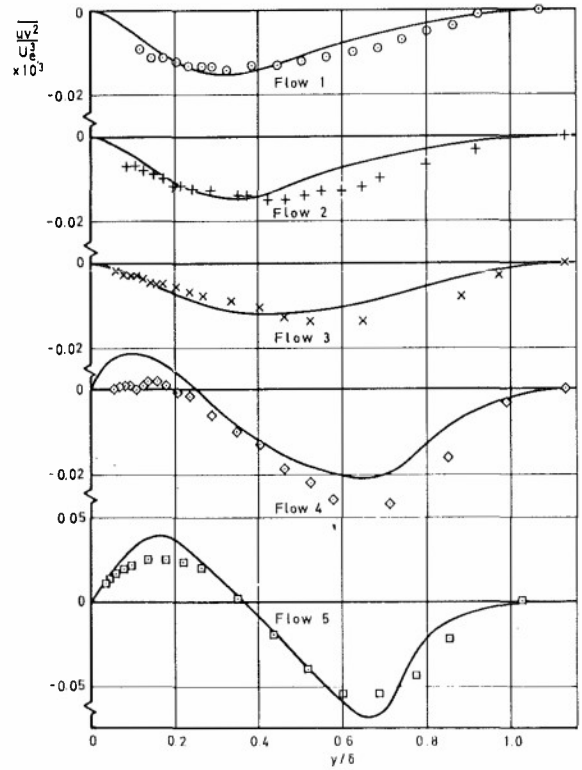


Fig 13 Turbulence diffusion of  $\overline{uv}$ . Flows 1-5.  
Solid time represents  $\overline{uv^2} = 2\ell \frac{d}{dy} (-\overline{uv})^{\frac{2}{3}}$

Fig 13 (concl) Flows 6 and 7

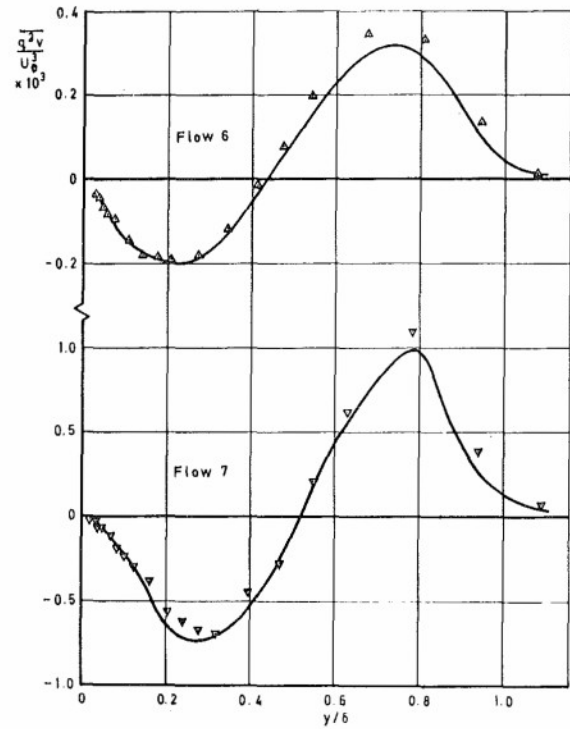
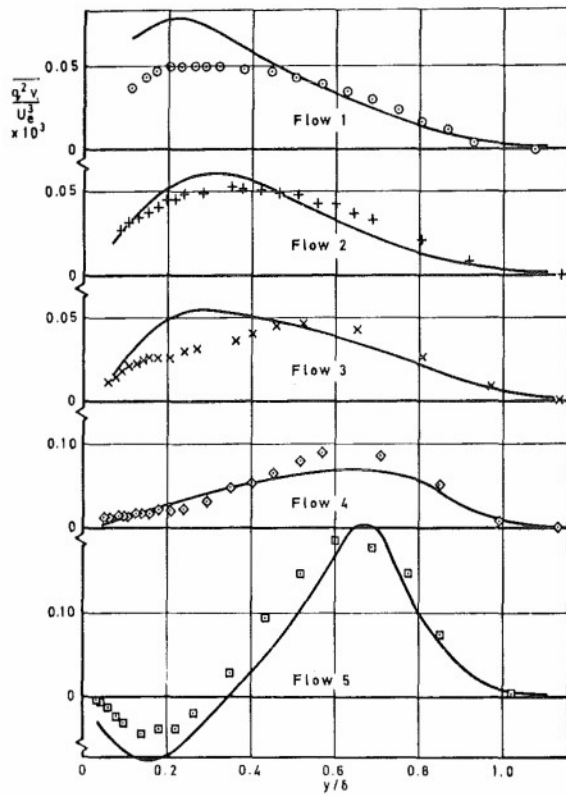


Fig 14 Turbulence diffusion of  $\overline{q^2}$ . Flows 1-5.  
Solid line represents  $\overline{q^2}v = -0.4k \frac{d}{dy}(\overline{q^2})^{3/2}$

Fig 14 (concl) Flows 6 and 7

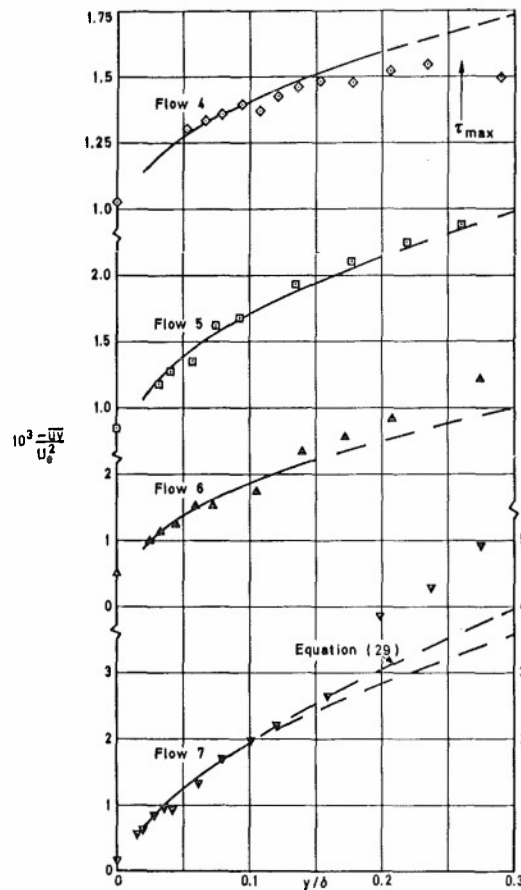


Fig 15 Predictions of shear stress in the wall region of flows 4-7

# Equilibrium Boundary Layers Over Very Rough Surfaces

by I.S. Gartshore and K.A. de Croos\*  
 Department of Mechanical Engineering  
 The University of British Columbia  
 Vancouver, B.C., V6N 2L7, Canada

\* present address: Imperial Oil Co. Ltd.  
 Vancouver, B.C.

## SUMMARY

Commonly-used wall shear stress correlations appropriate for rough walls imply a degree of equilibrium between the boundary layer and the wall. For two roughness geometries examined experimentally in zero pressure gradient, equilibrium in the mean velocity appears to exist beyond 350 times the roughness height from the origin of roughness. For moderately close spacing of simple three-dimensional roughness elements, a correlation due to Dvorak appears accurate; for less dense spacing (but still "fully rough" conditions) the correlation underestimates the wall stress significantly. The equilibrium boundary layer studied experimentally showed unexpectedly large turbulent intensities, constant integral length scales, no region of constant stress and a semi-logarithmic region best described with a von Karman constant of  $0.36 \pm .02$ .

## COMMONLY USED SYMBOLS

d	zero plane displacement height.
k	geometrical roughness height.
n	boundary layer shape factor (equation 17).
V	longitudinal mean velocity.
V <sub>1</sub>	free stream velocity.
V <sub>τ</sub>	shear velocity $\equiv (\tau_o/\rho)^{1/2}$
x, z	longitudinal and cross-stream co-ordinates.
δ	nominal boundary layer thickness (see equation 18).
δ*	displacement thickness.
λ	roughness density; longitudinal spacing of square bars in the two-dimensional case.
λ <sub>e</sub>	density of roughness equivalent to λ.
κ	von Karman's constant (equation 4 and following equations).
θ	momentum thickness.
ρ	fluid density.
τ <sub>o</sub>	total wall shear stress.
ν <sub>o</sub>	kinematic viscosity.

## 1. INTRODUCTION

When estimating wall shear stress created by a fluid flowing over a rough wall, it is neither practical nor desirable to calculate the details of the flow around individual roughness elements by finite difference solutions of the full fluid equations. Semi-empirical relationships are usually constructed which link roughness geometry to some bulk description of the boundary layer which forms on the surface, an integral property of the boundary layer often being used. This practice lends itself to the use of well known integral techniques for the prediction of the boundary layer growth.

Wall stress relationships so formulated imply, for their existence, a degree of dynamic equilibrium between the boundary layer and the surface beneath it. This equilibrium is usually assumed but its limits are seldom identified. Strictly self preserving boundary layers can exist in zero pressure gradient only when wall shear stress co-efficients are exactly constant, the roughness height and spacing growing linearly in the streamwise direction to remain constant fractions of the boundary layer thickness. In the more common case of constant roughness height and spacing, it appears likely that equilibrium would be approached some distance downstream of the origin of roughness. It is the purpose of this work to investigate when this equilibrium is attained in one or two cases, and to measure some of the characteristics of the approximately self-preserving boundary layer so created. A second goal is to check the accuracy of one wall stress relationship, that proposed by Dvorak (ref. 1), when used for three dimensional roughness elements of simple geometry.

The semi-empirical basis for the wall stress relationship is first reviewed, in an attempt to clarify the limitations of the correlation. Experiments are then described which test the correlation and the approach to equilibrium. The results are then discussed, with reference to the original objectives of the work. A well known integral calculation procedure due to Head (ref. 2) is used where necessary to provide quantitative results.

## 2. FORMULATION OF THEORY

In developing an equation for the mean velocity close to a wall, a first step is to form a "law of the wall" by dimensional analysis (Millikan, ref. 3). For smooth walls this takes the form:

$$V = fn[V_\tau, \nu, z] \quad (1)$$

so that  $\frac{V}{V_\tau} = \text{fn} \left[ \frac{Z}{(V_\tau)} \right]$

and the local length <sup>$\tau$</sup>  scale for the flow is  $(v/V_\tau)$ .

For very rough walls, it is usually assumed that viscosity is not important, tacitly implying that the roughness has sharp edges and a sufficiently large height. A common rule is that the viscosity is no longer important when  $(\frac{kV_\tau}{v}) \gtrsim 70$  but this must depend on the form of the roughness and the flow characteristics as well.

If viscosity is not important, a length scale for the roughness must be identified to construct an equation similar to (1). Even when roughness elements project from an otherwise smooth wall, the case considered in this report, the effective height of the roughness may be different from its geometric height so that the origin of  $Z$  and of the roughness height depend on the roughness density.

One formulation consistent with these ideas is described by figure 1, where symbols are defined, and by the equations:

$$V = \text{fn} [V_\tau, Z-d, k-d, \lambda]$$

or

$$\frac{V}{V_\tau} = \text{fn} \left[ \frac{Z-d}{k-d}, \frac{\lambda}{k-d} \right] \quad (2)$$

The effective length scale is now  $(k-d)$  and a density parameter  $\lambda$ , expressing the effective lateral and longitudinal proximity of adjacent roughness elements, is also introduced. Note that expression (2) is not general in the sense that the surface is still assumed to be fully rough; viscous effects are therefore absent.

As roughness elements become more closely spaced, sheltering of neighbouring elements takes place and the effective height of the roughness elements decreases. The magnitude of  $d$ , often called the zero plane displacement, then increases so that  $d$  is dependent on  $\lambda$ , and of course on the roughness geometry. For large enough spacing between discrete elements,  $\lambda/(k-d)$  is large and the effective height of the roughness is then the actual height  $k$ , the displacement parameter  $d$  being zero. It is important to identify cases in which this simplification is permissible, and it is consistent with the foregoing arguments that  $d$  will be zero when the flow separating from any individual roughness element becomes effectively reattached before separating again due to the upstream effect of the next roughness element. The full height of an element ( $k$ ) is then the appropriate physical length on which to base the dimensional analysis of equation (2), not the reduced height  $(k-d)$ .

It appears from studies of flow about individual roughness elements that reattachment distances vary from about 15 times the roughness height, (see ref. 4), for an isolated two-dimensional roughness element such as a fence, to as little as 2.5 times the roughness height for an isolated cube (ref. 5). (In both cases reattachment distances are indicated as measured from the front face of the element).

These reattachment distances and the details of the flow behind the element must depend not only on the geometry of the element but also on the mean velocity and turbulence characteristics of the approaching flow, so that considerable variation can be expected. Indications from other studies by Lee and Soleman (ref. 6) are that a "change of regime, from isolated flow to wake interference flow," occurs at cube spacings (laterally and longitudinally) of about  $3.4 k$ ; the roughness correlation of Dvorak shows a marked change for a spacing of about  $5 k$  for two-dimensional bars; Counihan's studies (ref. 7) show a change in the functional form of his "roughness length" at a spacing which would be equivalent to  $6.7 k$  for two-dimensional elements of height  $k$ . These and other studies confirm that sheltering effects rise rapidly for spacings less than about  $3 k$  between three dimensional elements and for spacings less than  $5$  to  $15 k$  for two-dimensional elements. For greater spacings (lower roughness densities) it appears plausible to assume that  $d = 0$ .

It is worth remarking, in connection with equation (2), that regular and close spacing of uniformly shaped roughness elements can lead to the "D-type" of roughness described by Perry, Schofield and Joubert (ref. 8). For this case  $d$  becomes dependent on parameters describing the flow, such as pipe diameter, for roughened pipes, or boundary layer thickness, for roughened walls. This occurs apparently only for regular and close spacing of two-dimensional elements and is not of concern in this report.

Once a law of the wall has been formulated, the usual assumption for flow farther away from the wall,

$$\frac{\partial V}{\partial Z} = \text{fn} [V_\tau, (Z-d)] \quad (3)$$

leads to the semi-logarithmic law in the form:

$$\frac{V}{V_\tau} = \frac{1}{\kappa} \ln \left( \frac{Z-d}{k-d} \right) + B' \quad (4)$$

where  $B'$  is now a function of  $\lambda/(k-d)$  and  $\kappa$  is either a universal constant, as is usually assumed, or may be a function also of  $\lambda/(k-d)$  for rough walls.

Equation (4) applies away from the immediate vicinity of individual elements  $(Z-d)/(k-d) \gtrsim 2$  but in the "near wall" region  $(Z/\delta \lesssim 0.3$  for zero pressure gradient). Comparable limits exist in the smooth wall case in which the viscous sublayer is excluded. This form of equation has variables more readily identified with the actual flow field than those used in the comparable and fairly common equation:

$$\frac{V}{V_\tau} = \frac{1}{\kappa} \ln \left( \frac{Z}{Z_0} \right) \quad (5)$$

in which  $Z_0$  a "roughness length" has no obvious physical relationship to the actual roughness height.

Another common expression is:

$$\frac{V}{V_\tau} = \frac{1}{\kappa} \ln \frac{Z V_\tau}{\nu} + B' - \frac{\Delta V}{V_\tau}$$

where  $\frac{\Delta V}{V_\tau}$  is the shift in the velocity profile due to the roughness and is therefore a function of roughness density and geometry. The form of  $\frac{\Delta V}{V_\tau}$  is always chosen to be:

$$\frac{\Delta V}{V_\tau} = \frac{1}{\kappa} \ln \left( \frac{k V_\tau}{\nu} \right) + C(\lambda)$$

and  $\frac{\Delta V}{V_\tau}$  is plotted against  $\left( \frac{k V_\tau}{\nu} \right)$  for any one roughness geometry and density as in Dvorak's paper (ref. 1). Although plausible in principle, this formulation is misleading for fully rough surfaces in that it implies that the roughness function  $\frac{\Delta V}{V_\tau}$  depends on viscosity whereas this is not the case for sufficiently rough surfaces.

Provided the roughness density is not sufficiently great to create sheltering effects,  $d$  can be assumed to be zero. This report considers only such cases (equivalent two-dimensional spacing of  $\lambda/(k \gtrsim 32)$ ) and is further concerned only with roughness consisting of identically shaped elements spaced uniformly and projecting from an otherwise smooth surface. No confusion arises about the origin for  $Z$  or the definition of  $k$  for this simple geometry. Thus we assume a semi-logarithmic velocity distribution of the form:

$$\frac{V}{V_\tau} = \frac{1}{\kappa} \ln \frac{Z}{k} + B' \quad (6)$$

where  $B'$  is a function of the roughness geometry and spacing.

Following Millikan (ref. 3) and others, the complete velocity distribution can be described, for zero pressure gradient, by:

$$\frac{V}{V_\tau} = \frac{1}{\kappa} \ln \left( \frac{Z}{k} \right) + B' + h\left(\frac{Z}{\delta}\right) \quad (7)$$

where  $h\left(\frac{Z}{\delta}\right)$  is a universal function describing that part of the velocity profile which deviates from the logarithmic distribution in the centre of the boundary layer. This assumes some kind of equilibrium of the entire flow, a point discussed later. For  $Z=\delta$ ,  $V=V_1$  (the free stream velocity), and equation (7) becomes:

$$\frac{V_1}{V_\tau} = \frac{1}{\kappa} \ln \left( \frac{\delta}{k} \right) + B' + h(1) \quad (8)$$

or, absorbing the constant  $h(1)$  into the function  $B'$ ,

$$\frac{V_1}{V_\tau} = \frac{1}{\kappa} \ln \left( \frac{\delta}{k} \right) + B'' \quad (9)$$

Equation (7) subtracted from equation (8) gives the defect law in the form:

$$\frac{V_1 - V}{V_\tau} = f_n \left( \frac{Z}{\delta} \right) + \text{constant} \quad (10)$$

where the function of  $\left( \frac{Z}{\delta} \right)$  is independent of roughness density or spacing, a conclusion confirmed experimentally by Hama (9) and others.

Equation (9) involves the boundary layer thickness  $\delta$  and it is sometimes more convenient to replace  $\delta$  by  $\delta^*$  the "displacement thickness" defined by:

$$\begin{aligned} \delta^* &\equiv \int_0^\infty \left( \frac{V_1 - V}{V_1} \right) dz \\ &\equiv \int_0^\infty \left( \frac{V_1 - V}{V_\tau} \right) \cdot \left( \frac{V_\tau}{V_1} \right) d\left( \frac{Z}{\delta} \right) \end{aligned}$$

Using equation (10) in the above, it can be seen that

$$\frac{\delta^*}{\delta} \frac{V_1}{V_\tau} = \text{universal constant} \quad (11)$$

provided equation (10) holds for a sufficiently wide range of  $Z/\delta$ . Using (11), equation

(9) becomes:  $\frac{V_1}{V_\tau} = \frac{1}{\kappa} \ln \left( \frac{\delta^* V_\tau}{k V_\tau} \right) + B$  (12)

Dvorak (1) correlated experimental results from various sources to suggest a form for the function  $B$  of equation (12), valid for square two-dimensional bars of height  $k$  and spacing  $\lambda$  and for  $\lambda/k \gtrsim 5$ :

$$B = A + 5.95 \left( 0.48 \ln \frac{\lambda}{k} - 1 \right) \quad (13)$$



where A is a constant with value about 4.8.

Equations (12) and (13) are restricted to cases in which viscosity effects are absent. They allow the shear stress co-efficient  $C_f$ , defined as  $2 \left( \frac{V_\tau}{V_1} \right)^2$ , to be found for any height ratio  $\delta^*/k$  and spacing  $\lambda/k$ .

Equation (7) and those that follow from it, imply an equilibrium in the entire flow, so that properties such as turbulent length scales, spectra and so on when non-dimensionalized by a single length scale and a single velocity scale do not change rapidly enough in the streamwise direction to have their gradients affect the flow in any way. Strictly this is a "self-preservation" of the flow and is possible in zero pressure gradient only when  $C_f = \text{constant}$ , the boundary layer grows linearly and  $\delta^*/k$ ,  $\lambda/k$  are constants. If  $\delta^*$  grows linearly in the streamwise direction  $k$  and  $\lambda$  should also increase linearly. However, over limited streamwise distances far from the origin, it appears that boundary layers growing over roughness with  $k$ ,  $\lambda$  constant can be considered to be in equilibrium, as will be demonstrated later.

The correlation of equation (13) is valid only for square two-dimensional bars normal to the flow, and it is necessary to generalize these results to other roughness element geometries of various shapes. As described in ref. 10, this simply results in the use of the ratio  $\lambda e/k$  in place of  $\lambda/k$ , defining the former as:

$$\frac{\lambda e}{k} \equiv \frac{(C_D)_B}{(C_D)_E} \frac{A_P}{A_F} \quad (14)$$

where  $(C_D)_B$  is the drag co-efficient of a two-dimensional bar of height  $k$  measured with a particular upstream boundary layer;  $(C_D)_E$  is the drag co-efficient of a typical roughness element of height  $k$  measured with the same upstream boundary layer and  $A_P/A_F$  is the ratio of plan area to frontal area for the new roughness element. Since cubes or rectangular plates with a face normal to the flow both have drag co-efficients of about 1.2, as do square bars normal to the flow, equation (14) reduces for these roughness element geometries to:

$$\frac{\lambda e}{k} \approx \frac{A_P}{A_F} \quad (15)$$

The correlation of equations (12) and (13) is plotted as the solid curves of figure 2 for various  $\lambda e/k$  of 10 and above, an approximate limit for the assumption that  $d$  of equations (2) (3) (4) is zero.

These correlations for wall shear stress can be linked with a boundary layer shape if a suitable calculation procedure is adopted. For present purposes, we have adopted Head's integral method (2), used by Dvorak (1) and shown to be fairly accurate for zero pressure gradient cases at least. The method, used with the usual momentum integral equation and the assumption that the non-dimensional shape of the boundary layer does not change in the streamwise direction, result in the following conclusions (see ref. 10 for details):

$$\left( \frac{V_\tau}{V_1} \right) = \text{known arithmetic function of } n \quad (16)$$

where  $n$  is a suitable shape factor describing the boundary layer shape, defined here by:

$$n \equiv \frac{1}{2} \left( \frac{\delta^*}{\theta} - 1 \right) \quad (17)$$

with  $\theta$  as the usual momentum thickness.

This quantity  $n$  is the exponent of a power law if a power law adequately describes the mean velocity profile. If a power law is not an adequate description of the profile,  $n$  can be regarded as a simple shape factor, closely related to the more common shape factor  $\left( \frac{\delta^*}{\theta} \right)$ .

Using equation (16) with equations (12) and (13) allows the shape factor  $n$  to be expressed in terms of  $\frac{\delta^*}{k}$  and  $\frac{\lambda e}{k}$  or, with the use of (11) in terms of  $\frac{\delta}{k}$  and  $\frac{\lambda e}{k}$ . The latter form is shown by solid curves in figure 3, and is of course valid only if the assumption of equilibrium is valid.

Head's method, used with the correlation of Dvorak and the assumption of exact equilibrium ( $dn/dx = d(\delta^*/\theta)/dx = 0$ ) also gives values for the ratio  $\left( \frac{\delta^*}{\delta} \frac{V_1}{V_\tau} \right)$  of equation (11) in the range 3.80 to 4.00, for reasonable values of  $\lambda/k$ .

Experiments are compared to these predictions in the next section. In every case  $\delta^*$  and  $\theta$  were found directly from the measured velocity profiles and  $n$  found from them using equation (17). The nominal boundary layer thickness  $\delta$  was then deduced from the relationship:

$$\frac{\delta}{\delta^*} = \frac{n+1}{n} \quad (18)$$

an equation strictly valid for a power law profile but useful in defining an equivalent or consistent  $\delta$  in any case.

### 3. EXPERIMENTAL ARRANGEMENTS

Three boundary layers have been studied experimentally in the large U.B.C. open-circuit wind tunnel. The tunnel has a test section 24.4 m long, 2.44 m wide and initially 1.5 m in height. The test section roof is adjusted to maintain zero pressure gradient in the entire test section length. Since the tunnel is the blower type, exhausting directly

into the room, the pressure in the entire test section is then zero gauge, a great advantage in some measurements.

Floor roughness was created by fastening thin vertical strips of aluminum to the wall at regular intervals. The ratio of height to width of each strip was always 2:1 and values of  $\lambda e/k$  from equation (15) were 32 for tests I and II and 128 for test III. Roughness heights  $k$  were 38.1 mm in test I and 25.4 mm for tests II and III. The roughness strips were placed in lines across the tunnel, adjacent lines being displaced so that the pattern was staggered.

Wall shear stress was measured directly from a drag plate, a large isolated section of roughened floor fastened to a balance. Velocities were measured with a linearized hot wire anemometer. Details of the measurement techniques and arrangements can be found in ref. 10 or ref. 11.

Experimental set II was conducted as a check on set I; both had the same geometrical arrangements but set II had a roughness size  $2/3$  that of set I. Set III was a study of relatively sparse roughness undertaken to explore the limits to the roughness correlations described in section 2.

#### 4. RESULTS

The measured values of  $\delta^*/k$  and  $\theta/k$  are listed in appendix I together with values of  $n$  and  $\delta/k$  deduced from them, at each streamwise position  $x/k$ . Measured wall shear stress  $\frac{V_\tau}{V_1}$  is also listed, both as a distinct quantity and also in the ratio  $(\frac{V_1}{V_\tau} \frac{\delta^*}{\delta})$ . No evidence of Reynolds number (viscous) effects was found in these tests.

Measured results for  $\frac{V_\tau}{V_1}$ ,  $n$ ,  $\frac{\delta^*}{k}$  and the deduced values of  $\frac{\delta}{k}$  were plotted in figures 2 and 3. The measured values for sets I and II approach the predicted equilibrium conditions for their roughness density ( $\frac{\lambda e}{k} = 32$ ) at distances downstream of the roughness origin greater than about 350 times the roughness height. This appears to be the development length required with this roughness density at least, for the mean velocity to reach a modest degree of equilibrium. It is reassuring that the values from both sets I and II approach equilibrium at about the same  $x/k$ , as they should, and that the results from set I and set II remain on the appropriate equilibrium line for all values of  $x/k$  greater than 350.

The plotted values from set III appear to approach an equilibrium condition with  $\frac{\lambda e}{k}$  between 60 and 80, as indicated by the plots of figures 2 and 3. This is distinctly different from the value of 128 predicted from the roughness geometry and density; the wall shear stress is clearly higher in the measurements than had been predicted from the correlation of measurements on two-dimensional bars.

For the set III data, it is likely that the shear stress associated with the smooth wall between roughness elements is a significant part of the total stress. Roberson and Chen (ref. 12) estimate for a roughness consisting of cubes with a density given by  $\lambda=128$ , that about 40% of the wall stress arises from the smooth wall. In the present model used to generalize Dvorak's collection of square bar measurements to other roughness geometries, it was implicitly assumed that the flow between roughness elements is the same for two and three-dimensional elements, hence giving rise to equal shear stress contributions from the smooth wall sections in equivalent roughness cases. This is not accurate for two reasons: flow separation is greater for two-dimensional bars than for three dimensional strips, as noted in section 2; the reattaching and developing boundary layer behind two-dimensional bars will be very different from that behind three dimensional strips and will probably have greater three dimensionality and larger wall shear stress. For both of these reasons, the smooth wall stress in the three dimensional case will be greater than that for the two-dimensional bars and the total stress will therefore be higher. This effect will be small for concentrated roughness but will become increasingly significant for widely spread elements. Apparently, at  $\lambda/k = 128$ , it leads to differences in total stress of the order of 20%, as shown in figure 2. Until the flow is analyzed in greater detail between two and three-dimensional roughness elements, perhaps along the lines suggested by Roberson and Chen, no quantitative corrections to Dvorak's correlation can be made. We conclude that Dvorak's correlation is useful for a variety of roughness geometries only for  $\lambda e/k$  less than about 50 and that it will underestimate the values of  $\frac{V_\tau}{V_1}$  and  $n$  for surfaces of lower roughness density, for three-dimensional roughness elements.

The equation (6) developed in section (2) from dimensional arguments, is often deduced from the assumptions of a constant stress region and of a Prandtl mixing length proportional to  $Z$ . Neither of these assumptions appears valid from measurements made in the set I series at the farthest downstream location,  $x/k \approx 493$ .

The measured shear stress above the wall is shown in figure 4, together with average value of wall shear stress deduced using the drag plate. No measurements were made above the wall for  $Z/k < 2$  since individual roughness elements create strong spatial non-uniformities in this region. Although the values of shear stress extrapolate smoothly to the measured wall stress, there is no evidence of a constant stress region. In this case the inner tenth of the layer, that usually associated with a constant stress region, is occupied by the inner sublayer ( $Z/k \lesssim 2$ ) so that it is not surprising that a constant stress region is not evident.

Measurements of auto correlation of longitudinal turbulence velocity were made at various  $(\frac{Z}{k})$ , and these were converted to integral length scales  $X_{L_u}$  using the local mean velocity at the same  $\frac{Z}{k}$ . There is no consistent trend in these scales with  $Z$  over the

range investigated, as shown in figure 5. This is in agreement with the common observation that length scales for boundary layers increase with  $Z$  only for the region  $Z/\delta \gtrsim 0.2$ , and are constant thereafter. Apparently in this data for set I, the region in which  $x_{Lu}$  scales with  $Z$  is not evident and only the region in which  $x_{Lu}$  scales with a constant outer length typified by  $\delta$ , is encountered.

It is interesting to note that the ratio of  $(x_{Lu}/\delta)$  found here is about 0.3 which is similar to that reported for the neutrally stable atmosphere for heights above 200 feet, if  $\delta$  is interpreted for the atmosphere as the gradient height of about 1500 feet (see ref. 13).

The longitudinal turbulence intensity for the data of set I is shown in figure 6, non-dimensionalized by  $V_\tau$ . It is easy to presume, from dimensional considerations like those in section 2, that  $\sqrt{u^2}/V_\tau$  will be a universal function of  $Z/\delta$  just as  $\frac{V_1-V}{V_\tau}$  is universal, but this turns out to be incorrect, a fact discussed by Bradshaw (ref. 14). The surprising degree of non-universality is shown in figure 6 where present measurements are compared with those made by Corrsin and Kistler (ref. 15) above a rough wall. Despite the fact that  $\frac{V_1}{V_\tau}$  was about the same in both cases, the differences in the density and geometry of roughness apparently make the turbulence distributions in these two cases very different.

The near universality of the velocity defect law,  $(V_1-V)/V_\tau = f(y/s)$  can be examined rather simply by noting the value of the constant of equation (11). Clauser (ref. 16) found a value of 3.6 from his collection of data; calculated values using Head's method for equilibrium layers of the sort studied here, range from 3.8 to 4.0; measured values of this parameter for the set I, II and III boundary layers (in their apparent equilibrium ranges) run from 4.05 to 3.92 aside from one isolated value at 4.10 in set III: (see Appendix I). This comparison suggests that the expected equilibrium in the mean flow is being approached quite closely.

The velocity measurements for set I have been used to deduce the value of  $\kappa$ , often called von Karman's constant, used in equation (6). These are listed in Appendix I together with the other data and show no trend with  $x/k$ . The average value, 0.36 is considerably lower than the usual value of 0.40 or 0.41 usually assumed. Had the latter value been used to deduce the shear stress from measured velocity profiles, errors of between 16 and 54 per cent would have been made. There is some evidence that  $\kappa$  varies with Reynolds number, being lower at very high Reynolds numbers and in fully rough situations such as those encountered in the atmosphere. Wooding, Bradley and Marshall (ref. 17) report an average value of 0.35 for  $\kappa$  from their own collection of data and Businger et. al. (ref. 18) reports the same value from other full-scale measurements. Thus,  $\kappa$  may vary slowly with Reynolds number, becoming more nearly constant for very high Reynolds number or fully rough wall cases. The present data add support to this argument, but does not rule out the possibility already mentioned in section 2, that  $\kappa$  depends upon the roughness density  $\lambda$ .

## 5. CONCLUSIONS

1. Equilibrium of the mean velocity, implied in simple correlations relating roughness geometry to boundary layer characteristics, is reached about 350 times the roughness height downstream of the origin of the roughness, for constant roughness density and height.
2. For a range of moderate roughness densities, equivalent to square two-dimensional bars placed across the flow with longitudinal spacings between 10 and 50 times their height, the roughness correlation of Dvorak has been generalized to three-dimensional roughness elements and has been found accurate.
3. For low roughness density (few roughness elements) the correlation of Dvorak, when generalized to three-dimensional roughness elements, predicts shear stress and shape factors which are lower than the observed values. This is probably related to the importance of the wall stress associated with the smooth wall between roughness elements in the case of sparse roughness.
4. No region of constant stress was evident in the stress measurements conducted in one case; the height of the roughness elements was large enough in this case to create an inner "sublayer" influenced by individual element geometry and location, which obscured the region usually associated with constant stress.
5. Integral length scales measured in one case were essentially constant through the boundary layer, being about one-third of the boundary layer thickness.
6. The longitudinal turbulence intensity measured in one case was considerably larger than in comparable measurements made elsewhere. It appears that the "inactive" motions generated by the large roughness elements in this case contribute considerable kinetic energy to the turbulence, while not significantly influencing mean velocity or shear stress within the layer.
7. The von Karman's constant, used in the semi-logarithmic mean velocity correlation, has an average value of 0.36 for one of the rough wall boundary layers studied here. This is lower than the value of 0.41 often used and adds support to previous reports listing low values of this "constant" for very rough wall boundary layers.

## REFERENCES

1. Dvorak, F.A.: "Calculation of Turbulent Boundary Layers on Rough Surfaces in Pressure Gradient;" AIAA Journal, 7, pp. 1752-1759 (1969).
2. Head, M.R.: "Entrainment in the Turbulent Boundary Layer;" R & M. 3152 of the ARC (U.K.), (1958).
3. Millikan, C.B.: "A Critical Discussion of Turbulent Flows in Channels and Circular Tubes;" Proc. 5th Int. Congress for Applied Mech. (1938).
4. Bradshaw, P. and Wong, F.Y.F.: "The Reattachment and Relaxation of a Turbulent Shear Layer;" JFM 52, pp. 113-135 (1972).
5. Castro, I.P. and Robbins, A.G.: "The Effect of a Thick Incident Boundary Layer on the Flow Around a Small Surface Mounted Cube;" C.E.G.B. Report No. R/M/N 795, (January, 1975).
6. Lee, B.E. and Soliman, B.F.: "An Investigation of the Forces on Three Dimensional Bluff Bodies in Rough Wall Turbulent Boundary Layers;" Journal Fluids Engrg. (ASME), 99, pp. 503-510 (1977).
7. Counihan, J.: "Wind Tunnel Determination of the Roughness Length as a Function of the Fetch and the Roughness Density of Three-Dimensional Roughness Elements;" Atmospheric Environment, 5, pp. 637-642 (1971).
8. Perry, A.E., Schofield, W.H. and Joubert, P.N.: "Rough Wall Turbulent Boundary Layers;" JFM 37, pp. 383-413 (1969).
9. Hama, F.R.: "Boundary Layer Characteristics for Smooth and Rough Surfaces;" Trans. Naval Arch. and Marine Engrgs, 62 (1954).
10. Gartshore, I.S. and De Croos, K.A.: "Roughness Element Geometry Required for Wind Tunnel Simulations of the Atmospheric Wind;" Journ. Fluids Engineering (ASME) 99, pp. 480-485 (1977).
11. de Croos, K.A.: "Wind Tunnel Simulations of the Atmospheric Boundary Layer," M.A.Sc. Thesis, U.B.C., December 1978.
12. Roberson, J.A. and Chen, C.K.: "Flow in Conduits with Low Roughness Concentration;" Journ. of Hydraulics Division of ASCE, Hy 4, pp. 941-957 (1970).
13. Teunissen, H.W.: "Characteristics of the Mean Wind and Turbulence in the Planetary Boundary Layer;" Univ. of Toronto, UTIAS Review No. 32 (1970).
14. Bradshaw, P.: "'Inactive' Motion and Pressure Fluctuations in Turbulent Boundary Layers;" JFM 30, pp. 241-258 (1967).
15. Corrsin, S. and Kistler, A.L.; see Hinze, J.O.: "Turbulence" (second edition), McGraw Hill; pg. 641.
16. Clauser, F.: "The Turbulent Boundary Layer;" Advances in Applied Mechanics, 4 (1956).
17. Wooding, R.A., Bradley, E.F. and Marshall, J.K.: "Drag Due to Regular Arrays of Roughness Elements of Varying Geometries;" Boundary Layer Meteorology, 5, pp. 285-308 (1973).
18. Businger, J.A., Wyngaard, J.C., Izumi, Y. and Bradley, E.F.: "Flux-profile Relationships in the Atmospheric Surface Layer;" J. Atmos. Sci., 28, pp. 181-189 (1971).

## ACKNOWLEDGEMENTS

This work was supported by the National Research Council of Canada (recently altered to NSERC) under grant A4308.

## APPENDIX I

(a) Data of Set I  $\frac{\lambda_e}{k} = 32$ ,  $k = 38.1$  mm.

$\frac{x}{k}$	$\frac{\delta^*}{k}$	$\frac{\theta}{k}$	n	$\frac{\delta}{k}$	$\frac{V_\tau}{V_1}$	$\frac{V_1 \delta^*}{V_\tau \delta}$	$\frac{x_{Lu}}{\delta}$	$\kappa$
140.8	2.17	1.28	0.35	8.38	0.0607	4.26	0.271	0.33
268.8	2.83	1.75	0.31	11.93	0.0556	4.26	0.317	0.35
332.8	3.25	2.06	0.29	14.44	0.0543	4.14	0.290	0.38
396.8	3.51	2.27	0.27	16.49	0.0534	3.99	0.304	0.38
492.8	4.08	0.67	0.26	19.73	0.0527	3.92	0.289	0.34

(b) Data of Set II  $\frac{\lambda_e}{k} = 32, k = 25.4 \text{ mm}$

$\frac{x}{k}$	$\frac{\delta^*}{k}$	$\frac{\theta}{k}$	n	$\frac{\delta}{k}$	$\frac{V_\tau}{V_1}$	$\frac{V_1 \delta^*}{V_\tau \delta}$
145.5	1.93	1.10	0.380	7	0.0625	4.41
193.5	2.06	1.26	0.320	8.5	0.0600	4.04
253.5	2.54	1.59	0.300	11	0.0570	4.05
349.5	2.85	1.83	0.280	13	0.0560	4.04
445.5	3.61	2.34	0.270	17	0.0530	4.00
541.5	3.92	2.55	0.267	19	0.0525	3.93
637.5	4.54	2.98	0.261	22	0.0520	3.96
685.5	4.54	2.99	0.260	22	0.0520	3.96

(c) Data of Set III  $\frac{\lambda_e}{k} = 128, k = 25.4 \text{ mm}$

$\frac{x}{k}$	$\frac{\delta^*}{k}$	$\frac{\theta}{k}$	n	$\frac{\delta}{k}$	$\frac{V_\tau}{V_1}$	$\frac{V_1 \delta^*}{V_\tau \delta}$
145.5	1.36	0.856	0.294	5.99	0.055	4.12
193.5	1.55	0.993	0.284	7.00	0.0540	4.10
253.5	1.68	1.10	0.265	8.01	0.0530	3.96
349.5	2.06	1.35	0.260	9.97	0.0520	3.96
445.5	2.40	1.55	0.250	12.00	0.0505	3.96
541.5	2.92	1.97	0.242	15.00	0.0490	3.97
637.5	3.26	2.20	0.240	16.98	0.0475	4.04
733.5	3.86	2.61	0.240	19.99	0.0470	4.10

Figure 1  
DESCRIPTION OF SYMBOLS USED IN THE "WALL LAW"

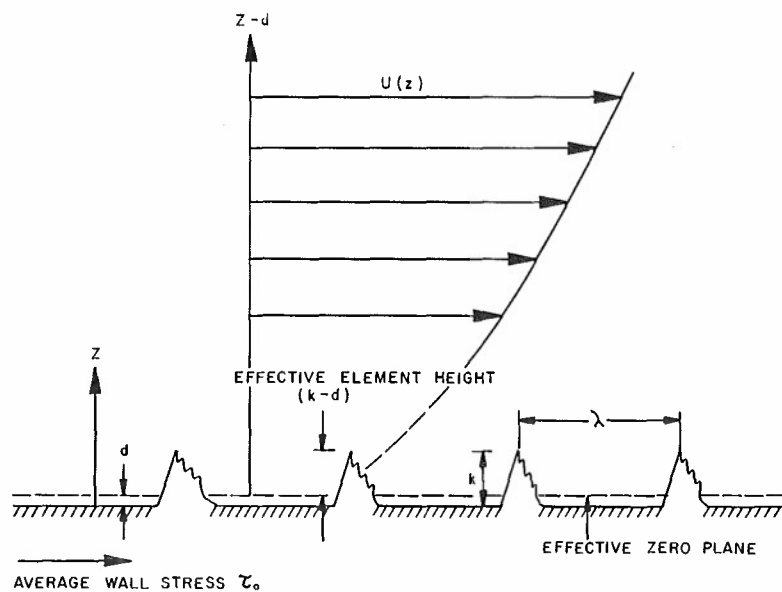


Figure 2  
WALL SHEAR STRESS CORRELATION OF DVORAK

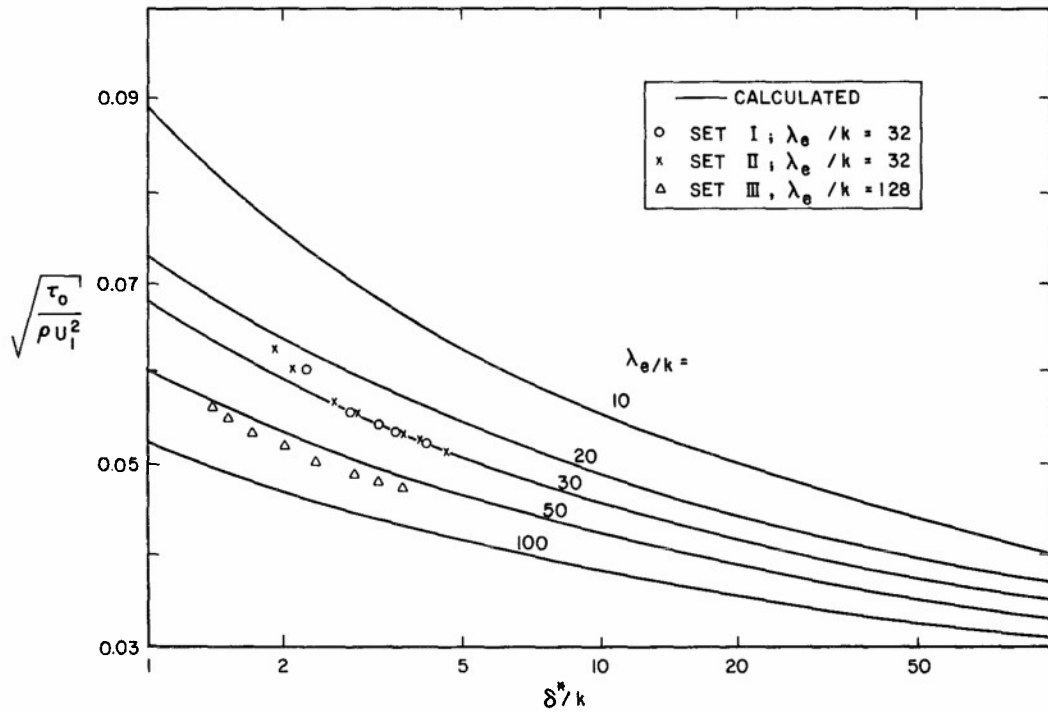


Figure 3  
SHAPE FACTOR  $n$  CORRELATED WITH BOUNDARY LAYER THICKNESS

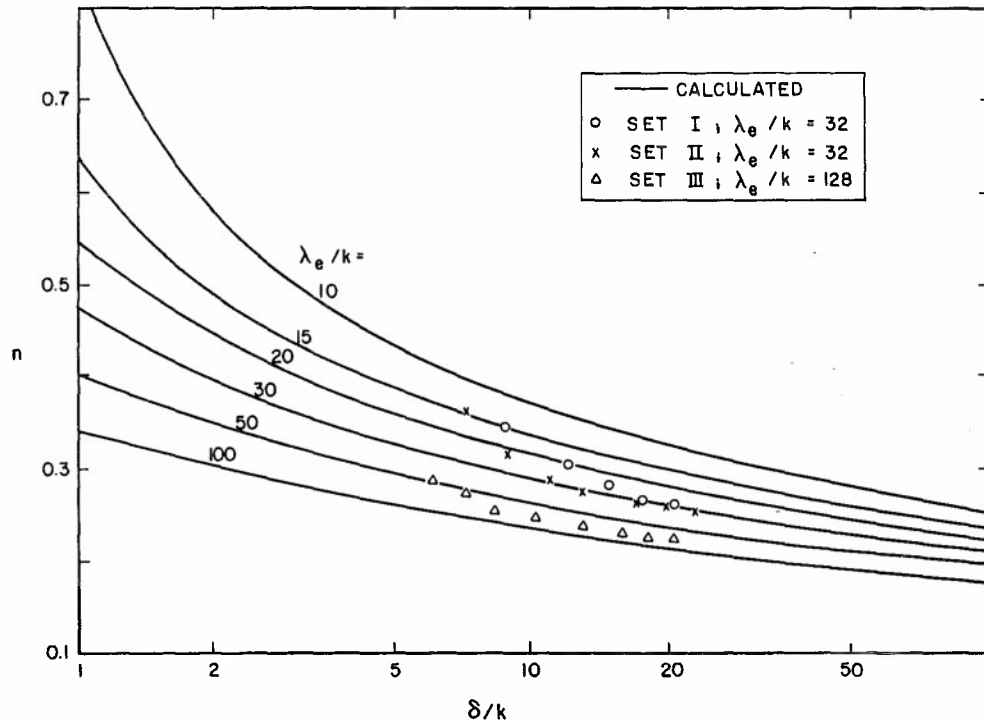


Figure 4  
SHEAR STRESS MEASUREMENTS

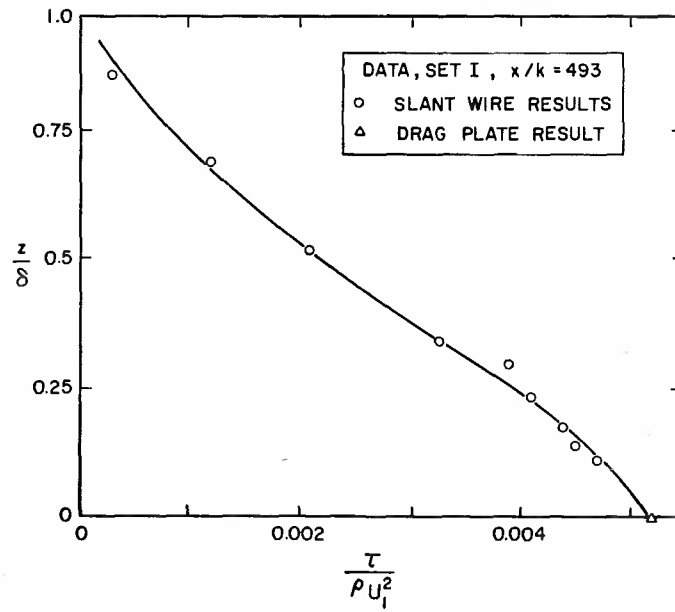


Figure 5  
INTEGRAL LENGTH SCALE  
(SET I,  $x/k = 493$ )

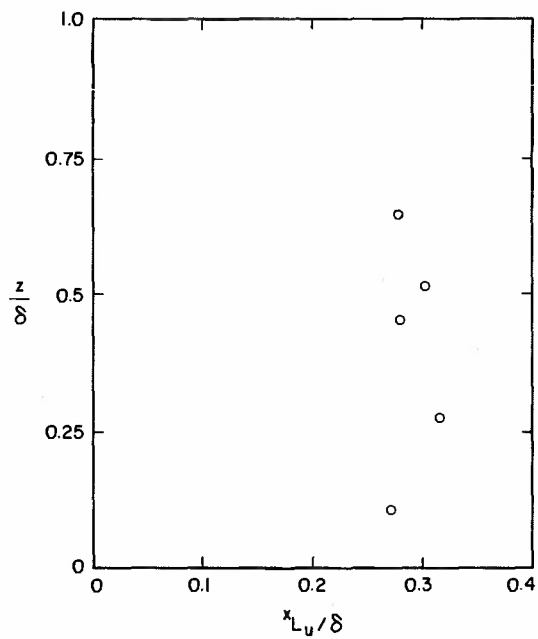
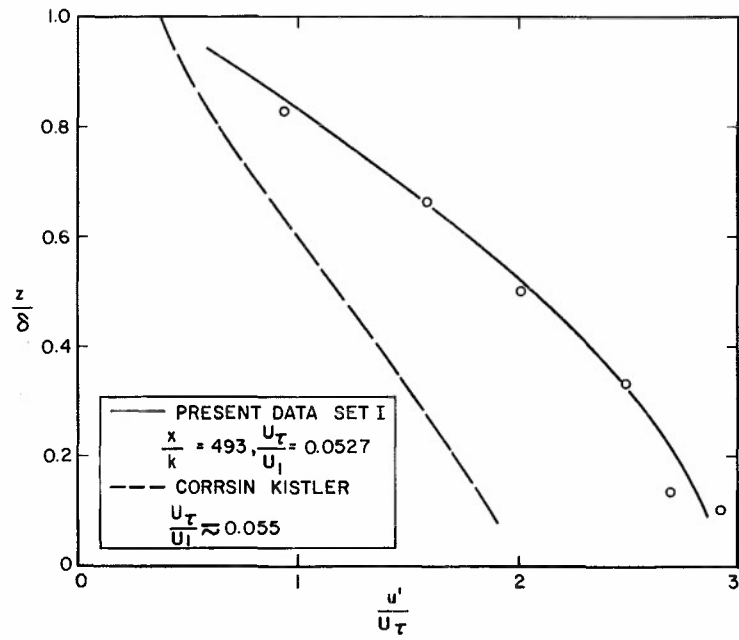


Figure 6  
LONGITUDINAL INTENSITY





## TURBULENCE BEHAVIOUR IN A SHOCK WAVE/BOUNDARY LAYER INTERACTION

by

P. Ardonceau, D.H. Lee, T. Alziary de Roquefort, R. Goethals

C.E.A.T. - E.N.S.M.A.

43 Rue de l'Aerodrome, 86000 Poitiers (France)

## SUMMARY

An experimental study of a two-dimensional shock wave boundary layer interaction is presented. Experiments are carried out at a nominal Mach number of 2.25 for three compression corners of  $8^\circ$ ,  $13^\circ$  and  $18^\circ$  corresponding respectively to attached flow, incipient separation and well separated flow. The Reynolds number based on overall thickness of the undisturbed boundary layer is  $Re \delta_0 = 1.0 \cdot 10^5$ . The measurements involve wall static pressure, static and total pressure profiles, determination of the mean and RMS fluctuations of the  $u$  and  $v$  velocity components with a laser doppler anemometer, hot wire measurements of the mass flow fluctuations and spectrum analysis of the hot wire signal.

## NOMENCLATURE

$C$	correlation coefficient of $(u)'$ and $T_t'$
$E(f)$	spectral density
$M$	Mach number
$R_w$	hot wire imposed resistance
$R_{T_t}$	hot wire resistance at total temperature
$S_{\rho u} = \partial \log E / \partial \log \rho u _{R_w, T_t}$	hot wire sensitivity
$S_{T_t} = -\partial \log E / \partial \log T_t _{R_w, \rho u}$	coefficients
$T_t$	total temperature
$a'_w = (R_w - R_{T_t}) / R_{T_t}$	overheat ratio
$f$	frequency
$p$	static pressure
$r = S_{\rho u} / S_{T_t}$	ratio of the sensitivity coefficients
$u$	longitudinal velocity component
$v$	vertical velocity component
$w$	lateral velocity component
$Re$	Reynolds number
$\alpha$	ramp angle
$\delta$	boundary layer thickness
$\rho$	density
$(\rho u)$	mass flux
$( )'$	instantaneous value
$<( )'>$	RMS value
$(\bar{ })$	mean value

## 1. INTRODUCTION

One of the main difficulties in the numerical prevision of shock wave turbulent boundary layer interaction is the modeling of turbulence in a compressible flow subjected to a very fast evolution. With a suitable turbulence model, the mean flow field may be calculated either by using an interacting boundary layer approach (complete solution {1}, boundary layer only {2, 3} or, more directly, by solving the full compressible Navier Stokes equations {3, 4, 5, 6, 7}). However in each case the agreement with the experimental data is not quite satisfactory for the wall pressure or skin friction coefficient and really poor when the mean velocity profiles or the turbulent quantities are considered. For some computations this unsatisfactory result may be attributed to the use of rather rough turbulence models based on the eddy viscosity concept. But even with more sophisticated models, using for instance several partial differential equations for the transport of turbulent kinetic energy, Reynolds stresses... etc..., the prediction remains unsatisfactory, especially when the boundary layer separates, although the computation becomes time-consuming.

Clearly there is a need for experimental results on the behaviour of turbulence in such flows at first in order to improve the modeling. Recently several experimental studies concerning turbulent quantities have been published {7, 8, 9, 10, 11} and reviewed {3}. The aim of the present work is to furnish reliable data on mean and turbulent RMS quantities and secondly to obtain additional informations on the phenomenological mechanisms involved in the SW/TBL interaction with and without flow separation.

Although many practical situations encountered in external aerodynamics or in turbomachinery involve transonic or weakly supersonic flows, the present work is conducted at a Mach number of 2.25. This value was preferred in order to avoid some experimental difficulties like choking of the wind tunnel or complicated calibration of the hot wire anemometer. It is assumed that the turbulence behaviour is not drastically affected by the Mach number in the transonic-supersonic range.

## 2. EXPERIMENTAL SETUP AND DATA REDUCTION

### 2.1. Wind tunnel and models

Experiments are conducted in a  $M = 2.25$  wind tunnel (section  $150 \times 150 \text{ mm}^2$ ) driven by a  $M = 6$  ejector. Stagnation pressure is 0.9 bars and the resulting Reynolds number is  $1.1 \times 10^7/\text{m}$ . The flow is slightly heated in the plenum chamber ( $\sim 300^\circ\text{K}$ ) in order to obtain a recovery temperature at  $M = 2.25$  equal to the ambient temperature. The wall may be considered to satisfy the adiabatic condition, which is hoped to lead to a very low total temperature fluctuation level according to the strong Reynolds analogy concept. The tunnel may be run up to 2' without any noticeable change in flow conditions. The wall boundary layer used to produce the shock wave/boundary layer interaction is fully turbulent ( $Re \delta_0 = 10^5$ ).

Two types of SW/BL interactions have been considered namely the incident shock wave configuration and the compression corner. The two-dimensionality of the flow has been tested with three models for each configuration, by means of surface oil-flow patterns. The models are respectively a total span type, finite span type and a third type fitted with fences (fig. 1). Very good results are obtained with the "B2" or "B3" ramps, the "B1" ramp or the three "A" shock generators lead to a rather three dimensional flow (fig. 2). The "B2" was finally chosen for its better compatibility with optical methods.

Three angles of the ramp are selected :  $8^\circ$ ,  $13^\circ$  and  $18^\circ$  corresponding to three behaviours of the boundary layer :

- attached
- incipient separation
- separated (fig. 2)

### 2.2. Instrumentation

#### Pressure measurements.

They include, surface, static and pitot pressure measurements. Static and Pitot probes as well as hot wire probe, are mounted on a unique probe support situated downstream of the ramp and automatically actuated along the y axis (fig. 3). A very weak probe interference has been observed on the surface pressure measurements in the separation region ( $\alpha = 18^\circ$ ).

#### Flow visualisation.

Shadowgraph and schlieren pictures have been taken with various exposure times (down to  $2\mu\text{s}$ ) (fig. 4). High speed movies have also been recorded at two speeds : 8000 and 35000 frames/s.

#### Laser Doppler Anemometry.

Mean flow velocity components and RMS velocities (along the x and y axis) are measured with a laser anemometer. A high power, Argon laser (Coherent Radiation CR6) is used in the dual forward scatter mode {12} on the 5145 Å line (approximately 2W). The beam splitter is adjusted to obtain a  $20 \mu\text{m}$  fringe-spacing with a  $f = 600 \text{ mm}$  focusing lens. A Bragg cell (TSI mod.980) is used when measuring the normal velocity component or when the mean longitudinal component becomes too small (relative to the velocity fluctuations). The laser and the other optical components are mounted on the same optical bench which is moved by a computer program along a normal to the wall (fig. 5). The two beams are slightly directed towards the wall and the  $y = 0$  position is defined as the point where the beam crossing occurs on the center of the tunnel wall.

Signal processing is achieved via digital counters (TSI mod.1990 and DELTALAB CEAT ANL 200). The conventional high pass - low pass filter bank is replaced by a special scanning filter which covers the Doppler signal spectrum. The filter (bandwidth  $\Delta f = 5 \text{ MHz}$ ) is swept between two previously defined frequency limits  $f_1, f_2$ . Several advantages may be found :

$$1) \text{ Signal to noise ratio improvement } \approx 10 \log \frac{f_2 - f_1}{\Delta f}$$

2) The filtering may be completely automatized and is thus much faster and reliable than manual tuning

During this work, the frequency limits were defined before the flow probing thus allowing a  $f_1, f_2$  bandwidth much larger than the signal bandwidth. A faster procedure would be to perform first a fast sweep to define the signal spectrum location and the particles/sec ratio and then make a second sweep with a better estimate of :  $f_1, f_2$  and of the sweep time to pick up a significant number of signals.

#### Hot wire anemometry.

A constant temperature hot wire anemometer (CTA DISA M 55) is used to measure the mass flux density fluctuation  $\langle (\rho u)' \rangle$  and the total temperature fluctuations  $\langle T_t' \rangle$ . With the additional hypothesis that the pressure fluctuations are small (ie  $\langle p' \rangle / \bar{p} \ll 1$ ) one may deduce the velocity fluctuation level  $\langle u' \rangle$ .

The probes (DISA 55P11) are modified in two ways

- 1) the gap between the two prongs is reduced to  $\approx 1$  mm to increase spatial resolution and hot wire strength
- 2) the wire ( $\phi = 5 \mu\text{m}$ ) is welded sufficiently "slack" to eliminate some parasitic high frequency components in the signal due to the strain gage effect [13].

A symmetrical bridge (DISA 55M12) is preferred to the conventional 1/20 bridge for its better stability at high overheat ratios when the frequency response of the anemometer is very large ( $\approx 300$  kHz).

The frequency response has been evaluated at several overheat ratios in the flow conditions. The hot wire probe is optically heated by a power modulated laser beam. (The TSI Bragg cell is fed with a 40 MHz sinusoidally modulated wave resulting in a quasi sinusoidal modulation of the first order diffracted beam). The behaviour of the hot wire system is examined at several overheat ratios (fig. 6).

A very good frequency response is obtained for an overheat  $a_w' = 0.75$  with a gain = 10, filter = 4 setting. At the lowest overheat  $a_w' = .26$  the 3dB frequency response does not exceed 100 kHz. The data for the mass flux fluctuation level are obtained with high and medium overheat ratios ( $a_w' \approx 0.8$  and  $a_w' \approx 0.5$ ) (cf. 3.3) resulting in an upper frequency limit greater than 150 kHz which is high enough to take into account the whole spectrum of the fluctuations.

#### Spectrum analysis.

At high overheat ratios the hot wire is mainly sensitive to the mass flux fluctuations, provided that the total temperature fluctuations are small. The spectrum of the hot wire fluctuating signal may be identified to the mass flux fluctuation spectrum. A spectral analysis of the whole flow field is made with a SAICOR 51 A spectrum analyser, regardless to the Mach number influence on the hot wire signal in the transonic and low supersonic range.

#### 2.3. Hot wire data reduction

Following the Morkovin-Kovaszny analysis of the hot wire response in supersonic flow [14, 15] the fluctuations are splitted up in mass flux and total temperature fluctuations. The relations between the instantaneous hot wire voltage  $e'(t)$  and the aerodynamic fluctuations may be written provided that the Mach number is high enough :

$$\frac{e'(t)}{\bar{E}} = S_{\rho u} \frac{(\rho u)'(t)}{\bar{\rho u}} - S_{T_t} \frac{T_t'(t)}{\bar{T}_t}$$

which leads to the mean square relation

$$\overline{\left(\frac{e'}{\bar{E}}\right)^2} = S_{\rho u}^2 \left(\frac{\overline{(\rho u')^2}}{\bar{\rho u}^2}\right) - 2 C S_{\rho u} S_{T_t} \frac{\overline{(\rho u')^2}}{\bar{\rho u}^2} \frac{\overline{T_t'}}{\bar{T}_t} + S_{T_t}^2 \left(\frac{\overline{T_t'^2}}{\bar{T}_t^2}\right)$$

where C is the correlation coefficient between  $\rho u'$  and  $T_t'$  and  $S_{\rho u}$ ,  $S_{T_t}$  are the hot wire sensitivity coefficients.

These coefficients are obtained from a direct calibration of the hot wire system (hot wire + anemometer) in a special  $M = 3.5$ ,  $20 \times 20$  mm<sup>2</sup> wind tunnel. The mass flux variation in the wind tunnel nozzle is used to modify  $\bar{\rho u}$ , the nozzle is designed to give a linear evolution of  $\bar{\rho u}(x)$  with the distance to the  $M = 1$  section.  $\bar{T}_t$  is varied via the generating temperature and the calibration is repeated for several hot wire resistances  $R_w$  (fig. 7) [11]. Strictly speaking  $S_{\rho u}$  and  $S_{T_t}$  are dependent upon  $\bar{\rho u}$ ,  $\bar{T}_t$  and  $R_w$ . However  $S_{\rho u}$  may be considered as a function of  $\bar{\rho u}$  alone (fig. 8). Results for several hot wire resistances and even different probes are grouped together between the dashed lines.  $S_{T_t}$  is mainly a function of the overheat ratio (fig. 8).

It is to be noted that even at  $a_w' = 0.8$  the ratios between the two sensitivities  $S_{\rho u}$  and  $S_{T_t}$  is still small  $\sim 0.5$  which proves that the hot wire remains sensitive to the total temperature fluctuations.

In order to measure  $\langle \rho u' \rangle$ ,  $\langle T_t' \rangle$  and their correlation coefficient C at least three overheat ratios must be used. In fact a higher number is necessary due to the data dispersion. This was done with 7 overheat ratios at several locations in the interacting boundary layer. A very low level of the total temperature fluctuations was found everywhere (fig. 9) and a precise evaluation of  $T_t'$  was very difficult to obtain. However the simplification :

$$\frac{\langle e' \rangle}{\bar{E}} = S_{\rho u} \frac{\langle \rho u' \rangle}{\bar{\rho u}}$$

leads to underestimate the mass flux fluctuations (fig. 10). A precise and a fast method to measure  $\langle (\rho u)' \rangle / \bar{\rho u}$  is to use two overheat ratios. It may be shown that when  $r = S_{\rho u} / S_{T_t}$  is not too small (high overheat) and provided that  $\langle T_t' \rangle / \bar{T}_t$  is not large ( $\sim .01$  in the present study), the relation between  $\langle e' \rangle$ ,  $\langle \rho u' \rangle$  and  $\langle T_t' \rangle$  may be written as

$$\frac{1}{S_{T_t}} \frac{\langle e' \rangle}{\bar{E}} = \frac{r \langle \rho u' \rangle}{\bar{\rho u}} + \frac{C \langle T_t' \rangle}{\bar{T}_t}$$

Then only two relations are necessary to determine  $\langle(\rho u)'\rangle$ .  $C$  and  $\langle T_t' \rangle$  remain unknown but are not neglected. A comparison between the three methods (one, two and seven overheats) is given in fig. 10.

Measurements of  $\langle(\rho u)'\rangle$  shown in the paper are obtained with two overheat ratios.

### 3. RESULTS

#### 3.1. Mean flow-field

The increase of the wall pressure measured at the wall is presented fig. 11 for the three ramp angles. The typical "kink" on the distribution for the  $18^\circ$  angle is an indication of flow separation confirmed by the surface oil flow pattern (fig. 11). A slight overshoot of the wall pressure is observed at  $X/\delta_0 = 5$  distance from the hinge line.

The longitudinal component of the mean velocity is presented fig. 12 as obtained with the laser Doppler anemometer. Velocities are measured along the same axis upstream and downstream of the hinge line regardless of the mean flow turning on the corner.

The slowing of the bottom of the boundary layer is clearly visible especially on the  $\alpha = 18^\circ$  angle. The maximum gradient section of the BL lies farther from the wall as the angle increases. Data obtained inside and near the separation bubble are of questionable quality due to a very pronounced biasing effect of the signal sampling: a very low particles/s rate was found in the vicinity of the bubble where the signals mainly correspond to high speed flow originating from the outer part of the BL. A typical behaviour of the BL velocity profiles is observed downstream of the separated region on the  $\alpha = 18^\circ$  ramp. The flow is highly accelerated near the wall which results in a characteristic profile including two inflexion points [16]. This feature may be attributed to the mixing effect of the turbulence which is very effective (see 3.2.).

The velocity profiles deduced from static and Pitot pressure measurements (the total temperature remains nearly constant) are in fairly good agreement with the LDA data. A 3 % difference was found in the undisturbed flow, probably due to an underestimate of the fringe spacing (fig. 13b). The effect of the large turbulent fluctuations on the pressure measurements is not taken into account. This effect may be very strong in regions where  $\langle u' \rangle / \bar{u} = 0(1)$ .

#### 3.2. Fluctuation measurements

Turbulent quantities measured are  $\langle(\rho u)'\rangle$  (hot wire),  $\langle u' \rangle$  and  $\langle v' \rangle$  (LDA) in the whole flow field. Total temperature fluctuations  $\langle T_t' \rangle$  and the correlation coefficient between  $(\rho u)'$  and  $T_t'$  were obtained for some profiles to test the total temperatures fluctuation level, and then  $\langle u' \rangle$  velocities were deduced from hot wire data with the assumption  $p'/\bar{p} \ll 1$  and compared with LDA measurements.

The effect of the mean flow compression on the  $\langle(\rho u)'\rangle$  fluctuation component is presented in fig. 14. There is a continuous increase of the maximum fluctuation level with the ramp angle which is respectively multiplied by 3, 4, and 5 relative to the initial level. The vertical extent of the turbulent region also increases but more between the  $13/18^\circ$  angles than between the  $8/13^\circ$  angles. This results from the large thickening of the BL in the separated region and also from the formation of large eddy structures originating from the separation bubble.

Measurements have been performed even at locations where the mean Mach number is less than 1.5 and it has been demonstrated that the sensitivity coefficients exhibits large changes in transonic flows with a pronounced non linear character. A  $M = 1.5$  line has been reported and below this line results are certainly under-evaluated ( $S_{pu}$  decreases with the Mach number below  $M = 1.4$ ). Thus an assumed constant value of  $S_{pu}$  leads to under estimate  $(\rho u)'$ .

The laser anemometer is not sensitive to any Mach number influence and the  $\langle u' \rangle$  measurements reveal the existence of a very intense maximum of velocity fluctuations appearing near the wall at  $\alpha = 13^\circ$  and rising up to more than  $\delta_0/2$  when  $\alpha = 18^\circ$  (fig. 15). This result conflicts with the observation made by Mikulla & Horstman [17] that the separation of the BL leads to a lower level away from the wall ( $\delta_0/3$ ).

The  $\langle v' \rangle$  component exhibits an increase similar to that of the  $\langle u' \rangle$  component when  $\alpha = 8^\circ$  but the general level remains moderate on the ramp for  $\alpha = 13$  and  $18^\circ$  (fig. 16). It must be reminded here that the fluctuations are measured along a normal to the wall before turning by the ramp.

The  $\langle v' \rangle$  measured are a combination of  $\langle u_v' \rangle$ ,  $\langle v_v' \rangle$  and  $\overline{u_v' v_v'}$  where \* denotes quantities measured relative to the mean streamline direction. The rather small values of  $\langle v' \rangle$  measured on the  $13^\circ$  and  $18^\circ$  ramps may be attributed to a strong and negative value of  $\overline{u' v'}$ . A third measurement in a  $45^\circ$  direction is to be made which will give informations on the Reynolds stresses.

#### 3.3. Flow visualisation - Spectral analysis

Strioscopic visualisations of the flow have been obtained with long (1/50s) and short exposure times (2 $\mu$ s) (fig. 4). Numerous large scale structures, inclined relative to the flow may be seen in the incoming boundary layer. The visibility of these structures suggests a quite large lateral extension and their longitudinal scale seems to be comparable to the BL thickness. On the back of the shock wave, which penetrates very deeply into the BL, the appearance of the flow indicates a sudden increase of the density fluctuations which is in good agreement with the velocity fluctuations measurements. Pressure waves associated with the intermittent motion of the outer boundary layer in the reattachment region [18] are clearly seen on the  $18^\circ$  ramp. Strong pressure fluctuation levels (10 or 100 times higher than in the undisturbed BL) are currently observed in supersonic separated flows [19].

Films were also recorded at a rate of 8000 frames/s. No instability of the flow was evidenced. The use of a higher speed camera (100000 frames/s) is hoped to reveal more detailed informations on the behaviour of the incoming turbulent structures.

A complete set of spectra of the mass flux fluctuations recorded on the  $18^\circ$  ramp is presented fig. 17. The amplitude of the spectral density  $E(f)$  has been multiplied by the frequency so that the area of a part of the spectrum between two frequencies is equal to the energy contained between these two frequencies.

The vertical scale is arbitrary for each spectrum. In the incoming BL, the energy is located in a 5 to 50 kHz band, with a maximum at 30 kHz which corresponds in the Taylor's sense to a longitudinal scale of about  $2 \delta_0$ .

On the  $x = -12$  mm a general increase of the spectral density is evidenced (the scale is divided by 2 relative to the first profiles). A maximum still remains at the same frequency  $\sim 30$  kHz but in addition an increase of energy in a low frequency range (2 kHz) appears at the bottom of the BL. This feature persists on the next profiles and disappears only at  $x = 60$  mm.

This high level in the low frequency range evidenced near the outer edge of the BL at  $x = -12$ ,  $y = 8$  and  $x = -4$ ,  $y = 14$  may be attributed to a weak instability in the shock position.

The low frequency component of the spectra is not very well explained. It appears very locally on the  $8^\circ$  data and extends on a larger part of the flow for the  $13^\circ$  ramp angle and down to  $x = 36$  on the  $18^\circ$  data.

#### 4. DISCUSSION AND CONCLUSION

Detailed informations on the turbulent structures are uneasy to obtain due to the Mach number limitation of the hot wire anemometer and the sampled nature of the data obtained from LDA. However flow visualisations and spectra of the mass flux fluctuations seem to confirm the existence in the main part of the BL of large turbulent structures similar to those found in incompressible flows {20, 21, 22}.

Downstream of the reattachment point some kind of longitudinal vortices with lateral organization could be expected from previous works. But transverse probing in the  $z$  direction reveals no variation of the  $\bar{v}$  and  $\langle v' \rangle$  components. Moreover the oil flow surface visualisations do not show any evidence of cellular structure organization in the reattachment region.

One of the main features of the SW/TBL interaction is certainly its fast streamwise evolution which occurs within a few boundary layer thicknesses. This scale is of the same order of magnitude as the incoming turbulent structures scale. This may cast some doubt about the suitability of the classical mean value approach and leads to take into account the large scale structures in a more explicit way.

The interaction region is characterized by a large increase of the  $\langle u' \rangle$  fluctuation especially in the shear layer above the separation bubble. This increase is expected on inspection of the transport equation for  $\overline{u'^2}$  and is very likely due to the high value of the production term  $-2\rho(\partial\bar{u}/\partial y)\overline{u'v'}$ .

The ratio  $\langle u' \rangle / \langle v' \rangle$  is plotted on figure 18. It appears that there is a very large increase of anisotropy above the bubble. This situation may be explained by the fact that the turbulent kinetic energy is produced on the  $u'$  component and redistributed on the  $v'$  and  $w'$  components mainly through the pressure strain correlations. Due to the very short  $x$  extent of the phenomena the tendency to isotropy cannot balance the large production and values of  $\langle u' \rangle / \langle v' \rangle$  larger than 4 are obtained in some region. Clearly any modeling of the turbulence behaviour based on an equilibrium concept will fail in this region.

Downstream, on the ramp, the ratio  $\langle u' \rangle / \langle v' \rangle$  decreases and the boundary layer recovers a less anisotropic state. For  $\alpha = 18^\circ$ ,  $x = 60$  the profile has a rather similar shape to the one encountered in the undisturbed boundary layer ( $x = -36$ ). The higher general level for  $x = 60$  may be attributed to the fact that the  $\langle u' \rangle$  and  $\langle v' \rangle$  values are relative to an axis system defined upstream of the hinge line as noted in 3.2. One may conclude that a longitudinal extent of about  $6 \delta_0$  is typical for a return to a more usual ratio of  $\langle u' \rangle / \langle v' \rangle$ . Therefore, any modeling based on a frozen distribution concept is questionable.

The phenomenon may be considered as a relaxation process for the distribution of energy between the  $\overline{u'^2}$ ,  $\overline{v'^2}$ ,  $\overline{w'^2}$  components. In fact many authors {3} solving the complete Navier Stokes equations with some eddy viscosity model, tried to take into account this relaxation process by introducing some empirical relaxation length. The preceding results suggest to use Reynolds stress transport equations and show the dominant importance of the pressure strain terms which unfortunately are very difficult to estimate in a compressible flow subjected to a high mean strain rate.

At last one must notice the appearance of low frequency fluctuations in the vicinity of the bubble. No isolated frequency can be evidenced and the spectra seems to be fully continuous. So, on the present results it is very hard to distinguish between these unidentified low frequency fluctuations and the "proper" turbulence component. Transverse correlation measurements are planned in order to elucidate this point. But even if the origin is an organized motion of the whole bubble one may suspect a strong interaction with the turbulence near the wall where the frequencies are of the same order of magnitude.

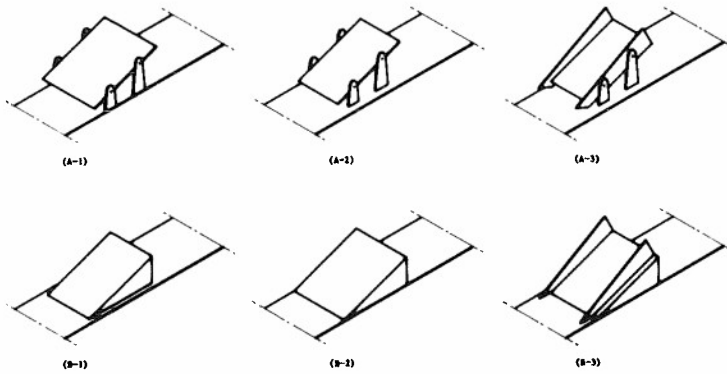
REFERENCES

- {1} WERLE MJ, BERTKE SD  
"Application of an interacting boundary layer model to the supersonic turbulent separation problem"  
Report AFL 76-4-21, 1976
- {2} RUBESIN MW, CRISALLI AJ, HORSTMAN CC  
"A critique of some recent second order closure models for compressible boundary layers"  
AIAA Paper 77-128
- {3} MARVIN JG  
"Turbulence modeling for compressible flows"  
NASA TM X-73, 188
- {4} VIEGAS JR, COAKLEY TJ  
"Numerical investigation of turbulence models for shock separated boundary layer flows"  
AIAA Paper 77-44
- {5} HORSTMAN CC, HUNG CM  
"Reynolds number effects on shock-wave turbulent boundary layer interactions. A comparison of numerical and experimental results"  
AIAA Paper 77-42
- {6} SHANG JS, HANKEY WL  
"Numerical solution of the Navier Stokes equations for supersonic turbulent flow over a compression corner"  
AIAA Paper 75-4
- {7} MATEER GG, BROSH A, VIEGAS JR  
"A normal shock wave turbulent boundary layer interaction at transonic speeds"  
AIAA Paper 76-161
- {8} ROSE WC, JOHNSON DA  
"Turbulence in a shock wave boundary layer interaction"  
AIAA J., V. 13, n° 7, 1975
- {9} KUSSOY MJ, HORSTMAN CC, ACHARYA M  
"An experimental documentation of pressure gradient and Reynolds number effects on compressible turbulent boundary layers"  
NASA TM 78 488
- {10} DELERY J  
"Analyse du décollement resultant d'une interaction choc - couche limite turbulente en transsonique"  
La Recherche Aérospatiale 1978-6, p. 305-320
- {11} LEE DH  
"Etude de l'évolution de la turbulence dans une interaction onde de choc - couche limite"  
These Université de Poitiers, 1979
- {12} TROLINGER JD  
"Laser instrumentation for flow field diagnostics"  
AGARDograph n° 186
- {13} DEMETRIADES A  
"Turbulence measurements in an axisymmetric compressible wake"  
Phico-Ford corporation TR n° UG-4118, 1967
- {14} MORKOVIN MV  
"Fluctuations and hot wire anemometry in compressible flow"  
AGARDograph n° 24, 1956
- {15} KOVASZNY LSG  
"Turbulence in supersonic flow"  
Journal of the Aeronautical Sciences, V. 20, 1953
- {16} SETTLES GS, FITZPATRICK TJ, BOGDONOFF S  
"Detailed study of attached and separated compression corner flow fields in high Reynolds number supersonic flow"  
AIAA J. V. 17, n° 6, 1979
- {18} MIKULLA V, HORSTMAN CC  
"Turbulence measurements in hypersonic shock wave boundary layer interactions flows"  
AIAA J. V. 14, n° 5, 1976
- {19} MONNERIE B  
"Décollement et excitation aérodynamiques aux vitesses transoniques"  
AGARD LS n° 74, 1975
- {20} LAUFER J  
"New trends in experiment turbulence research"  
Annual review of fluid mechanics, V.7, 1975

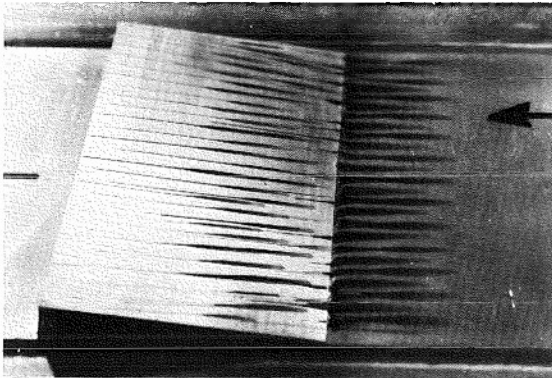
- {21} KIM HJ, KLINE SJ, REYNOLDS WC  
"The production of turbulence near a smooth wall in a turbulent boundary layer"  
JFM V. 50, Part 1, 1971
- {22} WYGNANSKI  
"The recognition of an evoked large scale structure in turbulent shear flows"  
Proceedings of the Dynamic Flow Conference 1978, Marseille, Sept. 1978

#### ACKNOWLEDGMENTS

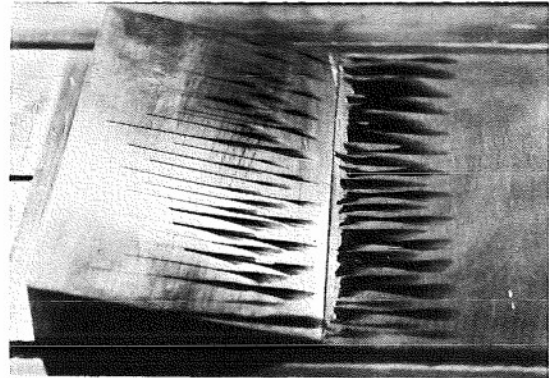
This work was sponsored by the Direction de la Recherche et Etudes Techniques under Grant DRET 78-240 and the Centre National de la Recherche Scientifique.



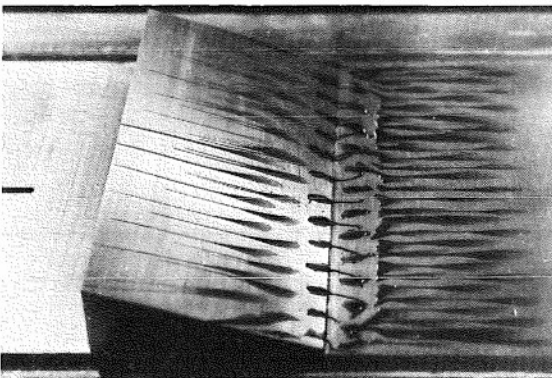
- Fig. 1 - Models used to test the 2D nature of the flow



B2 ramp  $\alpha = 8^\circ$



B2 ramp  $\alpha = 13^\circ$

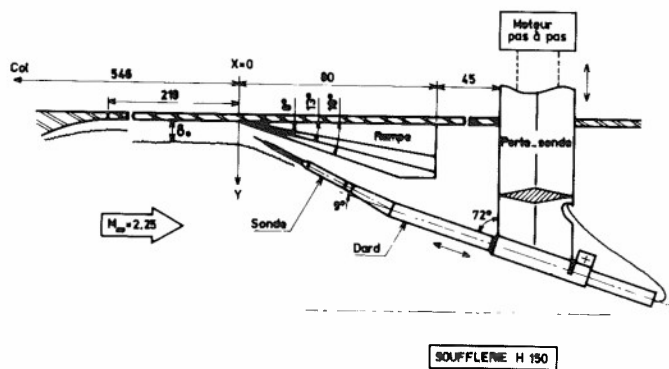


B2 ramp  $\alpha = 18^\circ$



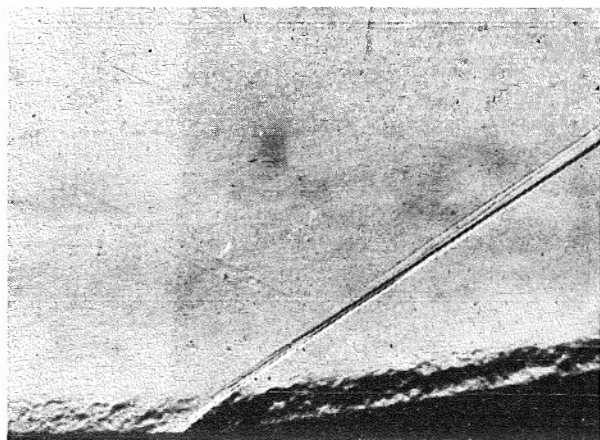
A3 shock generator  $\alpha_G = 8^\circ$

- Fig. 2 - Oil flow patterns

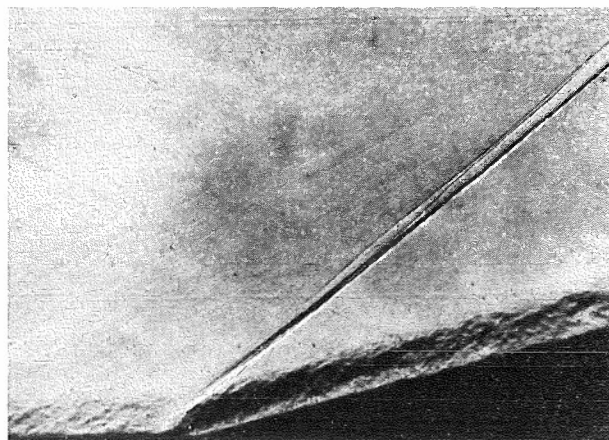


- Fig. 3 - Models and probe support geometry

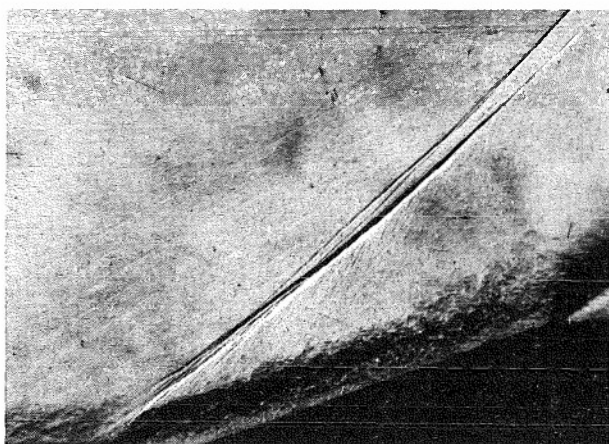




$\alpha = 8^\circ$

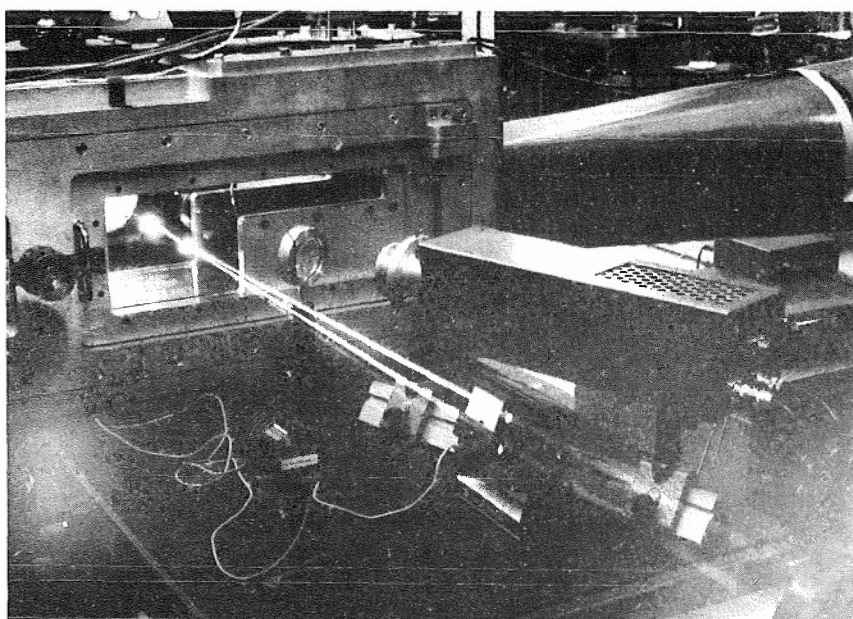


$\alpha = 13^\circ$

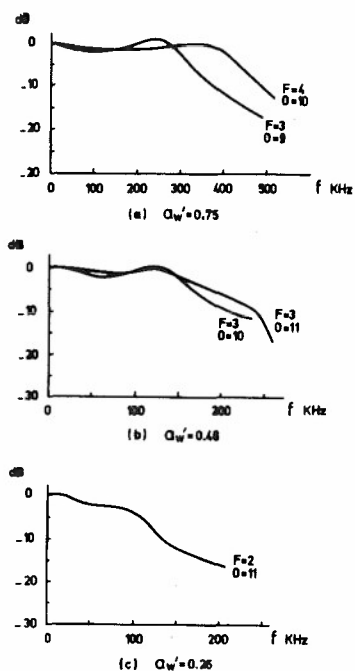


$\alpha = 18^\circ$

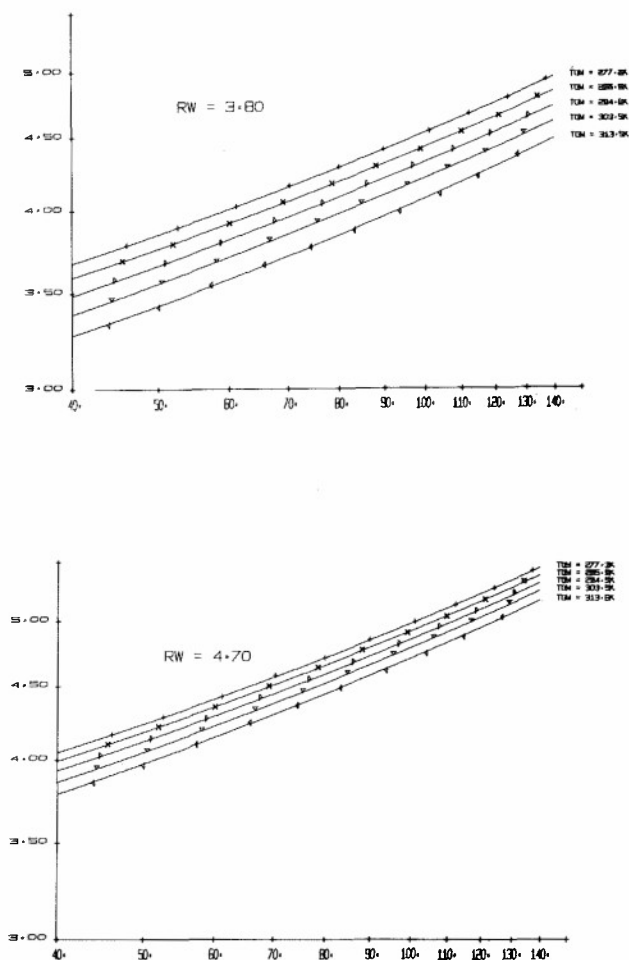
- Fig. 4 - Short exposure time  
strioscopic pictures of the  
flow field



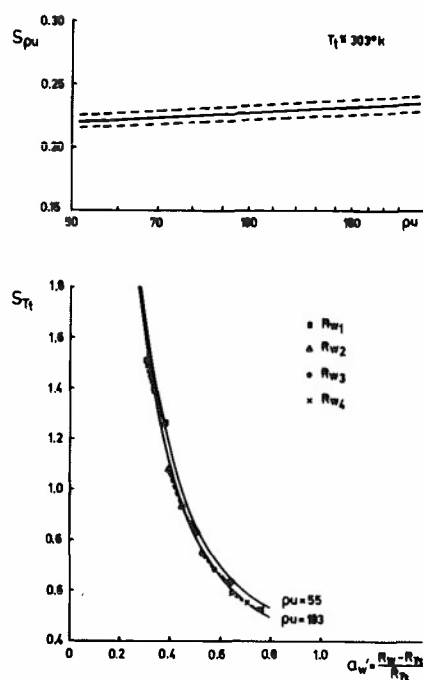
- Fig. 5 - Wind tunnel  
test section and LDA  
receiving optics



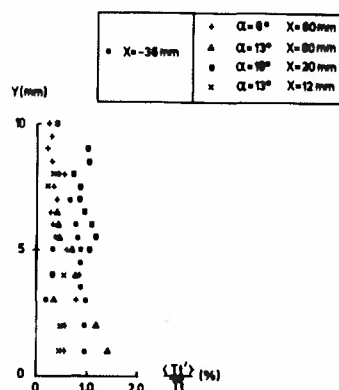
- Fig. 6 - Hot wire frequency response at different overheat ratios (optical excitation)



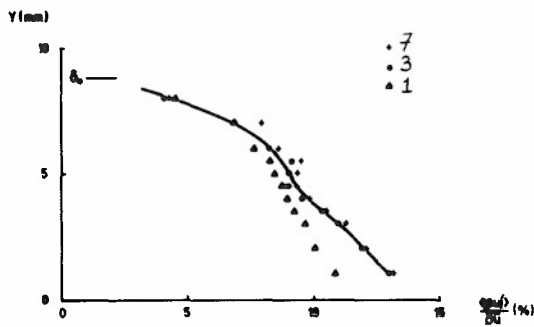
- Fig. 7 - Hot wire calibration  
 $\bar{E}(\rho_u, T_G, R_W)$



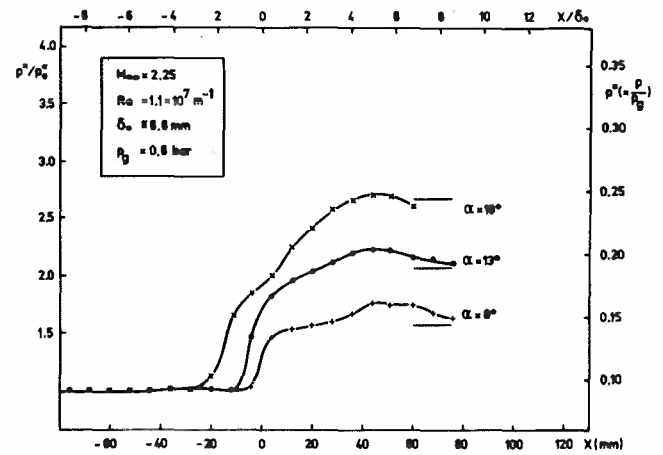
- Fig. 8 - Hot wire sensitivity coefficients



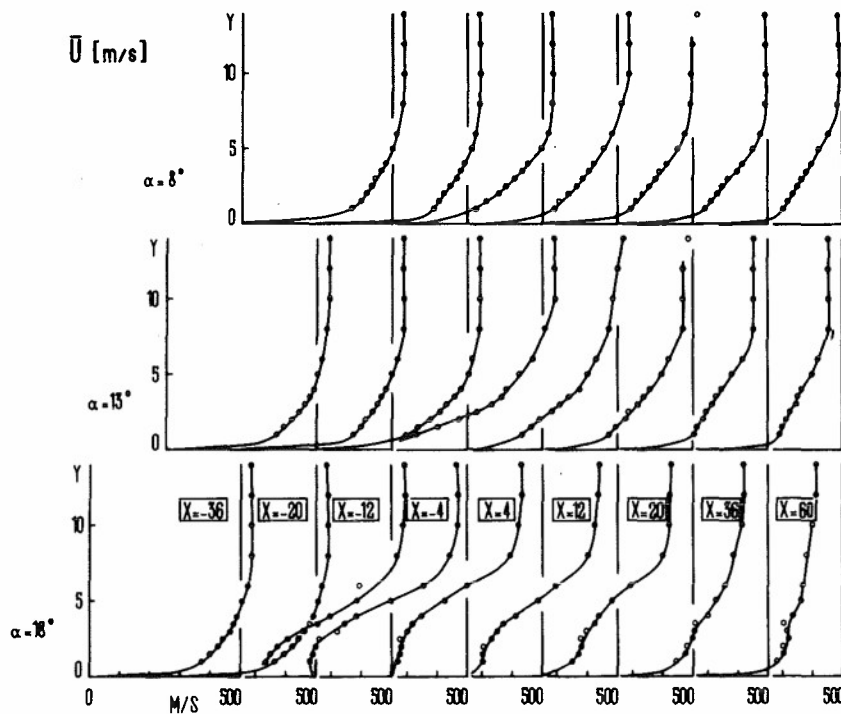
- Fig. 9 - Total temperature fluctuations in the BL at different locations



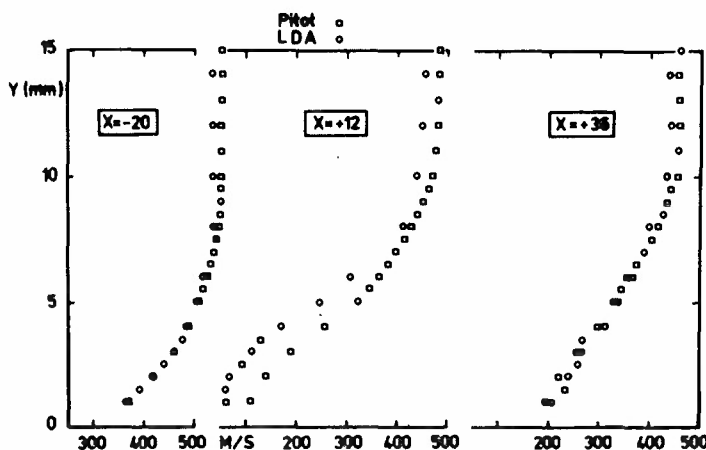
- Fig. 10 - Undisturbed BL mass flux fluctuations measured by different methods (1,2,7 oveheat ratios)



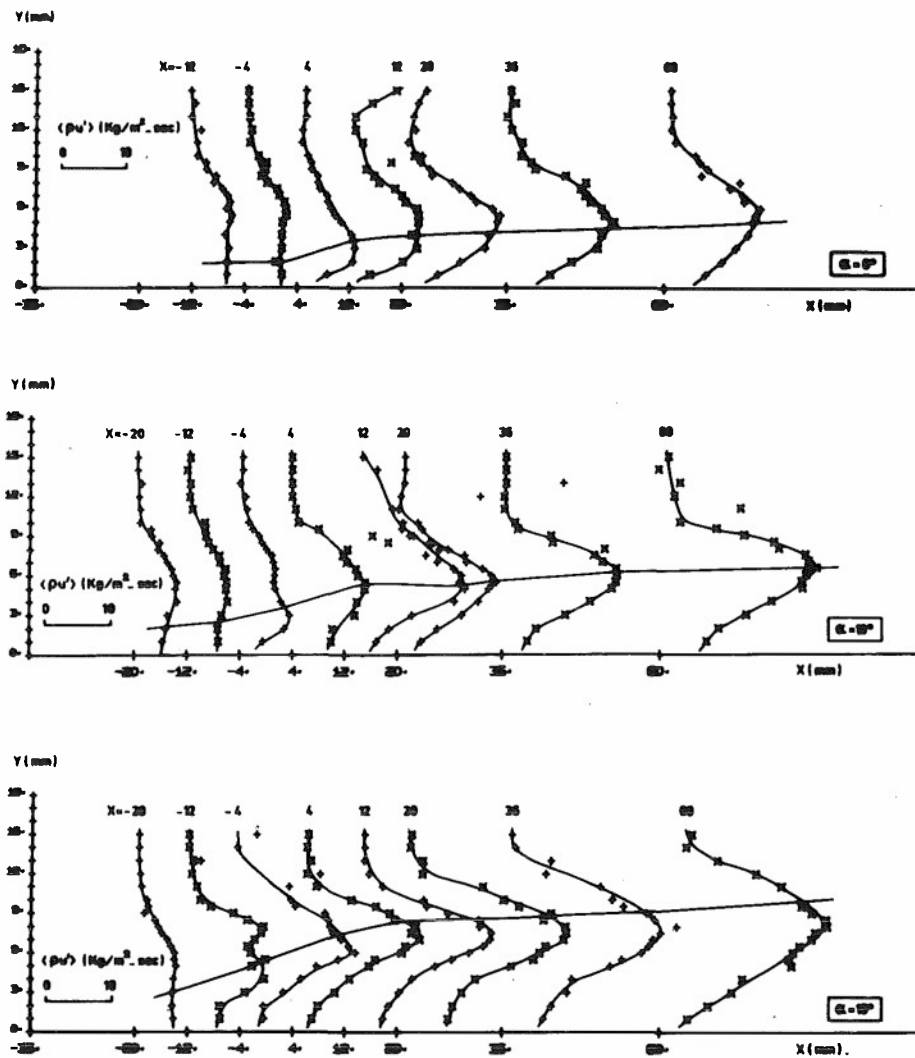
- Fig. 11 - Wall pressure distribution for the three ramp angles



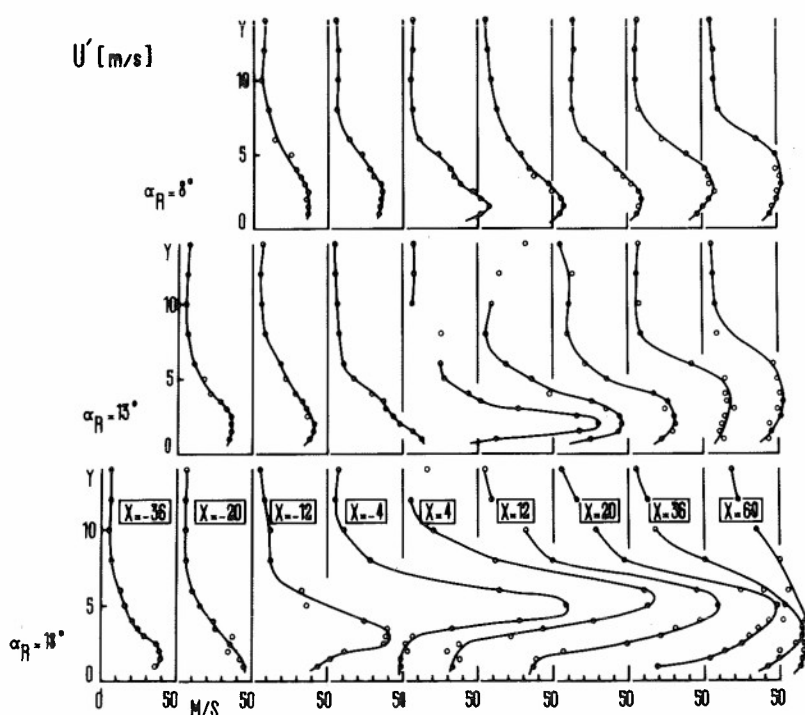
- Fig. 12 - LDA measured longitudinal mean velocity



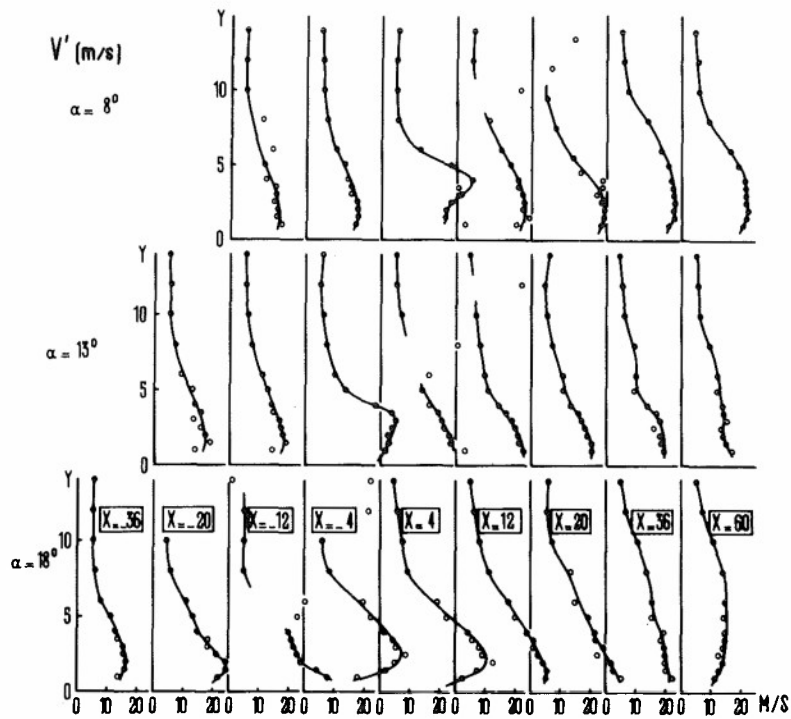
- Fig. 13 (a,b,c) - Comparison of LDA and Pitot velocity profiles ( $\alpha = 18^\circ$ )



- Fig. 14 - RMS mass-flux fluctuations (Hot wire)

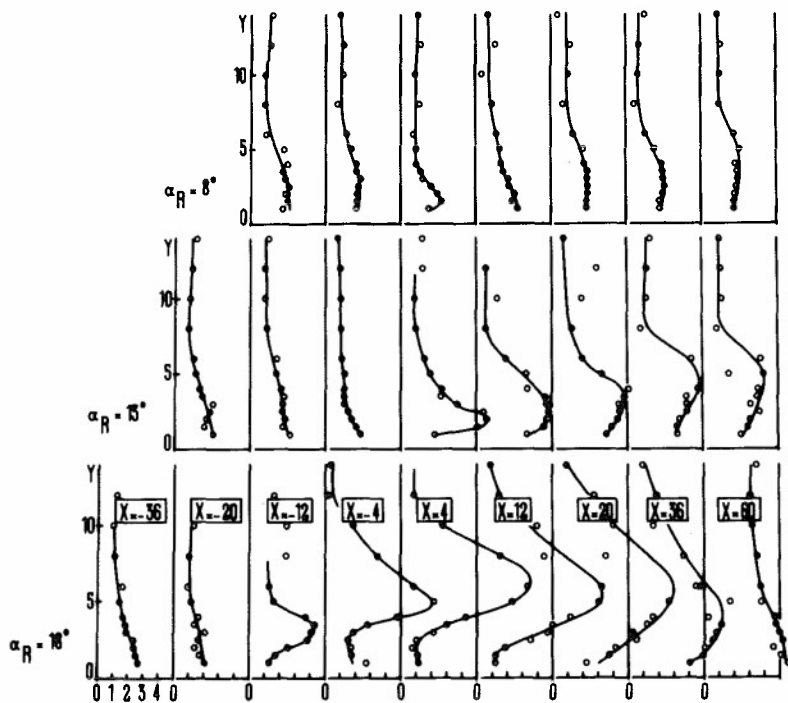


- Fig. 15 - RMS longitudinal velocity fluctuations  $\langle u' \rangle$  (LDA)

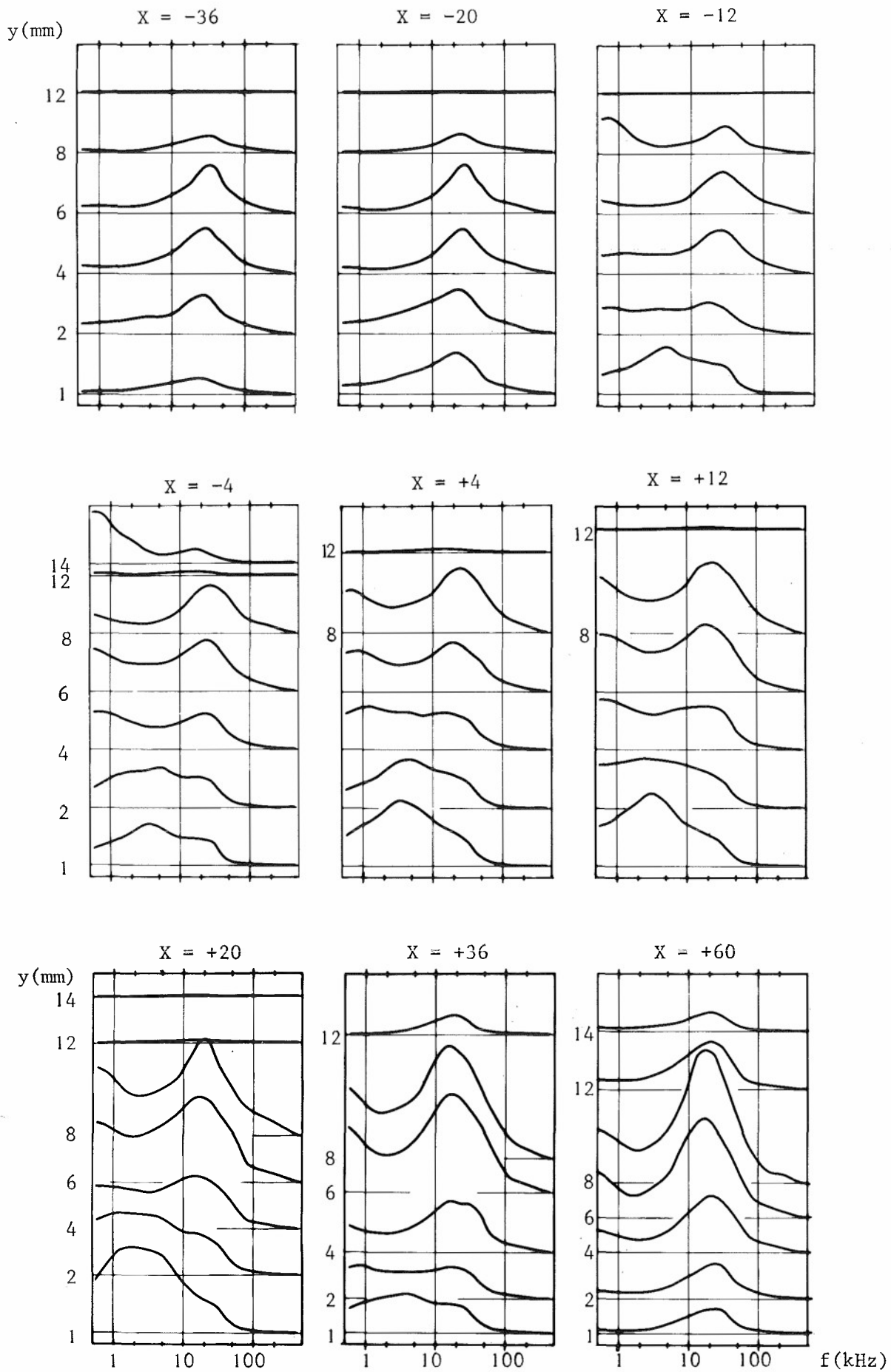


- Fig. 16 - RMS vertical velocity fluctuations  $\langle v' \rangle$  (LDA)

- Fig. 17 - See next page



- Fig. 18 - Ratio between the  $\langle u' \rangle$  and  $\langle v' \rangle$  velocity fluctuations



- Fig. 17 - Spectra of the mass flux fluctuation  $f \times E(f)$   
 $18^\circ$  ramp angle

## LONGITUDINAL VORTICES IN A CONCAVE SURFACE BOUNDARY LAYER

R.I. Crane and S.H. Winoto

Department of Mechanical Engineering,  
Imperial College of Science and Technology,  
Exhibition Road,  
London SW7 2BX,  
U.K.

## SUMMARY

Local measurements of mean and fluctuating velocity, by laser anemometer, have been made inside the the developing concave surface boundary layer in a free-surface water channel at Reynolds numbers  $Re$  (based on channel width) up to 16000. Concave surface radius was 3.5 times channel width and the ratio of spanwise mean boundary layer thickness to surface radius ranged between 0.03 and 0.11.

Systems of longitudinal vortices developed without artificial triggering. Vortex wavelength varied across the span by as much as a factor of 2, but mean wavelength was typically 1.3 times the boundary layer thickness and did not vary significantly in the flow direction. Continuous vortex growth at  $Re = 9800$  contrasted with apparent break-up of the vortices at  $Re = 16000$ . Maximum amplitude of the transverse variation in longitudinal mean velocity did not exceed 10% of potential wall velocity  $u_{pw}$ ; momentum thickness varied across the span by a factor up to 4. Lateral mean velocity parallel to the wall had a maximum amplitude typically 3% of  $u_{pw}$  and lateral fluctuation intensity was generally greater than 40%.

## LIST OF SYMBOLS

$a$	channel width
$b$	water depth
$e$	voltage proportional to Doppler signal frequency representing $u$
$G$	Görtler number $Re_\theta (\theta/r)^{\frac{1}{2}}$
$G_T$	turbulent Görtler number $(u_{pw}\theta/0.018u_l \delta^*) (\theta/r)^{\frac{1}{2}}$
$r$	concave wall radius
$Re_a$	bulk flow Reynolds number $u_b a/\nu$
$Re_\theta$	momentum thickness Reynolds number $u_{pw}\theta/\nu$
$u, v, w$	velocity components in $\phi, y, z$ directions respectively
$u_b$	bulk velocity (volume flow rate $\div ab$ )
$u_p$	value of $u$ in potential core and linear extrapolation into boundary layer
$u_{pw}$	$u_p$ at $y = 0$
$y, z$	coordinates defined in Fig. 1(c)
$\delta$	boundary layer physical thickness
$\delta^*$	boundary layer displacement thickness
$\theta$	boundary layer momentum thickness
$\lambda$	vortex wavelength
$\nu$	kinematic viscosity
$\phi$	angular coordinate defined in Fig. 1(c)

## subscripts

$av$	value averaged between wave crest and trough positions
$l$	value at boundary layer edge

## superscripts

$-$	mean value of fluctuating quantity
$'$	r.m.s. value of fluctuating quantity
$\wedge$	value at crest position in $\bar{u}(z)$ distribution
$\vee$	value at trough position in $\bar{u}(z)$ distribution

## 1. INTRODUCTION

An upsurge of interest in concave surface boundary layers in recent years has arisen from the inability of current calculation methods to make satisfactory predictions of flows with significant curvature. One application of considerable importance is the estimation of heat transfer and skin friction on the pressure surfaces of turbine blading, where curvature, acceleration and high turbulence intensity combine to produce rather complex boundary layer behaviour. In particular, the de-stabilising influence of concave curvature gives rise to strong three-dimensional effects. The occurrence in turbulent layers of systems of longitudinal vortices, analogous to Görtler vortices in laminar layers, is now well established, having been first observed by Tani (1). Subsequent investigations, notably those of So and Mellor (2) and Meroney and Bradshaw (3), have revealed details of the turbulence structure in boundary layers which were well developed before encountering concave curvature, without much emphasis on the vortex pattern itself. With sufficiently strong curvature, the quasi-steady vortices will exert a strong

influence on mass, momentum and heat transfer; their geometry, strength, etc. therefore require more detailed study.

The work reported here is an extension to higher Reynolds numbers of an experimental study of Görtler vortices (4, 5) aimed at determining the distribution of longitudinal and lateral velocity within the vortices. Using a water channel with only a short straight length upstream of a constant-radius  $90^\circ$  bend, curvature parameter  $\delta/r$  (ratio of boundary layer thickness to concave surface radius) was of order 0.1 in a developing duct flow with a potential core. This curvature is similar to that of ref. (2), in contrast to values around 0.01 in ref. (3). The Reynolds number  $Re_a$ , based on channel width  $a$  (40 mm) and bulk velocity  $u_b$ , has so far been limited to 16000, an order of magnitude less than those of ref. (2) and (3). A study of the effects of controlling and systematically varying the vortex wavelength  $\lambda$  is in progress (to complement current work by Bradshaw (6)), but the present results are confined to vortices developing naturally without artificial triggering. The use of laser Doppler anemometry has reduced the possibility that spatial averaging (as with a hot wire) will mask such features as sharp troughs in transverse distributions of velocity, and has also avoided any physical interference which could alter the unstable flow pattern.

## 2. EXPERIMENTAL DETAILS

A block diagram of the flow circuit is shown in Fig. 1(a), the heat exchanger being necessary to maintain a constant water temperature over a period of several hours operation. Water is pumped through multiple hoses into a bank of glass balls at entry to the Perspex channel, to provide a reasonably uniform flow into the settling chamber. Three gauze screens are followed by a 5:1 contraction and a straight channel section of length  $1.4a$ . The  $90^\circ$  bend, with outer wall of radius  $3.5a$ , is constructed from 3 mm thick walls set in machined grooves in a 15 mm thick base, with ties at the top of the walls to maintain their spacing. Downstream of the bend, a  $2.8a$  straight section is followed by a diffuser and a chamber of similar dimensions to the settling chamber. The polished surfaces are hydraulically smooth, with special attention paid to the joint between contraction and concave wall. The channel base is mounted on a milling table, to give two-dimensional motion in the horizontal plane, which in turn is attached to the cantilevered platform of a vertical traversing device.

A free-surface channel was originally chosen to facilitate flow visualization at any desired position, so the effective aspect ratio  $b/a$  is determined by the depth  $b$  of water. In the present work,  $b/a$  was 3.5, a compromise which allowed a reasonable Reynolds number to be obtained with a given pump capacity while avoiding unacceptable secondary flow effects. Guided by hydrogen bubble visualization (in a range of flow rates limited by bubble buoyancy at the lower end and rapid dispersion at the upper end), it was found that the longitudinal vortex system was not noticeably affected by end-wall secondary flow in the central 70% of the span.

Fig. 1(b) shows the fixed laser anemometer system in relation to the test section. The fringe mode of operation was used, with a beam crossing half-angle between  $6.9^\circ$  and  $7.4^\circ$  (depending on the proximity of the curved wall to the integrated optical unit), giving a calibration factor between 504 and 544 kHz per m/s. Dimensions of the beam intersection volume were approximately 1.5 mm and 0.2 mm in the normal ( $y$ ) and longitudinal ( $\phi$ ) directions respectively. Transfer of measurements from the longitudinal ( $\phi$ ) velocity component  $u$  to the transverse ( $z$ ) component  $w$  was effected by rotation of the integrated optical unit and polarised laser. An attempt was made to detect the sign of  $w$  using a rotating diffraction grating, but this requires further development to give a sufficiently steady frequency shift to match the low magnitude of this velocity component. All signal processing was carried out by a frequency tracker, most data points being obtained from five successive integrating periods of ten seconds each.

In view of the problems of measuring the streamwise pressure distribution directly at low flow speeds, and of avoiding too much obstruction of the laser beams by tappings etc., the distribution has been indicated by the variation in potential wall velocity  $u_{pw}$ ; this was obtained by extrapolating to the wall the linear portion of the velocity profile in the inviscid core flow.

Coordinates and dimensions are defined in Fig. 1(c), representing top and side views of the test section.

## 3. MEASUREMENT PROCEDURE

The measurements reported here were made at nominal Reynolds numbers  $Re_a$  of 9800 and 16000. Traverses in the  $z$ -direction were made at several distances from the concave wall, the closest approach possible with the present optical arrangement being  $y = 1$  mm. Having identified crests and troughs in these transverse velocity distributions, profiles in the  $y$ -direction were measured at the corresponding  $z$ -positions. Chosen streamwise stations ranged between a position  $0.68a$  upstream of bend entry, and  $\phi = 76^\circ$ . Checks were made to determine the repeatability of the vortex positions.

## 4. RESULTS AND DISCUSSION

Examples of velocity profiles at bend entry are shown in Fig. 2. The longitudinal pressure gradient on the concave wall is indicated by the distribution of potential wall velocity  $u_{pw}$  in Fig. 3. At  $Re_a = 9800$ , the resulting boundary layer thickness  $\delta$  was



measured as  $0.13a$  at  $\phi = 0$  and  $0.37a$  at  $\phi = 76^\circ$  (defined by the  $y$ -position where  $u/u_p(y) = 0.99$ ). Whereas previous work on this topic has largely dealt with boundary layers developed on long straight surfaces upstream of the bends, the present work is concerned with flows much closer to transition, relying on the curvature and the region of adverse pressure gradient at bend entry to produce a turbulent layer in the downstream part of the bend. A comparison may be made with data on critical values of the Görtler number  $G = Re_\theta (\theta/r)^{1/2}$  at transition; cascade measurements quoted by Kan et al. (7), for example, suggest completion of transition at  $G \approx 7$ , while Liepmann's (8) zero pressure gradient data on constant curvature surfaces, with low turbulence levels, indicated transition at  $G$  values between 6 and 9. Present data for spanwise-averaged momentum thickness  $\theta_{av}$  at  $\phi = 57^\circ$  give  $G \approx 13$  at both  $Re_a = 9800$  and  $16000$  (having earlier exceeded 20 at the higher  $Re_a$ )

Longitudinal vortices developed without artificial triggering, at least three pairs being detected at each station. No evidence of a similar structure was found in the convex wall boundary layer. To aid subsequent discussion, an idealized vortex system is shown diagrammatically in Fig. 4. Vortex wavelength  $\lambda$  was found to vary across the span by as much as a factor of two, but the positions of the crests and troughs in the transverse variation of the mean velocity  $\bar{u}$  did not vary significantly in the  $\phi$ -direction. Mean wavelength  $\lambda_{av}$ , found by averaging the distances between consecutive crests and between consecutive troughs at each station was approximately 21 mm at  $Re_a = 9800$ , 19 mm at  $Re_a = 16000$ , these being around 1.3 to 1.6 times the local average boundary layer thickness  $\delta_{av}$ . An exception occurred at  $Re_a = 16000$ ,  $\phi = 76^\circ$ , where the vortex pattern appeared to be breaking up. At this station, vortex positions were no longer repeatable from run to run and were less clearly defined, some longitudinal velocity distributions giving the impression of a wavelength as low as 11 mm while the variation in lateral component suggested wavelengths similar to those further upstream. The disturbances which are amplified into the observed vortex system are probably related to some physical feature of the channel (as yet unidentified). To determine if this is so, or whether the vortices are amplified selectively from a broad spectrum of initial disturbances (as predicted for laminar flows), vortex generators are now being placed in the contraction, sized so as not to influence the vortex strength. Early results, indicating some suppression of the natural wavelength in favour of that imposed by the generators, suggest only weak selectivity.

By analogy with Smith's (9) calculated stability diagram for laminar flows, Tani (1) indicated the degree of instability in his flows by plotting the data on an equivalent chart, in which Görtler number  $G$  was replaced by the so-called turbulent Görtler number  $G_T$ . This was defined using eddy viscosity  $\nu_e$  in place of molecular kinematic viscosity, with  $\nu_e$  taken as  $0.018 u_1 \delta^*$  where  $u_1$  is the velocity at the boundary layer edge. Fig. 5 shows the present data, using spanwise mean  $\theta$  and  $\delta^*$ , to be well inside the unstable region on such a diagram. (The dashed line indicates the uncertainty in  $\lambda$ .)

Fig. 6 and 7 show examples of the distributions of mean streamwise velocity  $\bar{u}$ , estimated uncertainty being  $\pm 2\%$ . The striking difference between these results and those for Görtler vortices in laminar boundary layers in the same channel (4, 5) is in the amplitude of  $\bar{u}(z)$ ; here, this amplitude did not generally exceed 10% of  $u_{pw}$ , compared with values up to 40% in laminar layers. The only exception was 19% of  $u_{pw}$  at  $Re_a = 9800$ ,  $\phi = 76^\circ$ ,  $y = 1$  mm, where the high mean velocity gradient and greatest possible fractional error in  $y$  could increase considerably the uncertainty in amplitude. Measurements closer to the wall, not feasible with the present optical arrangement, might reveal larger amplitudes, but in laminar layers the peak amplitude occurred in the region of  $y/\delta \sim 0.5$ . At  $Re_a = 9800$ , an increase in the maximum value of amplitude  $\frac{1}{2}(\bar{u} - \bar{u})$  from  $0.045u_{pw}$  to at least  $0.08u_{pw}$  between  $\phi = 57^\circ$  and  $76^\circ$ , indicated continuing vortex growth, whereas at  $Re_a = 16000$ , vortex strength as measured by this maximum amplitude of around  $0.06u_{pw}$  appeared approximately constant over the same distance. The shape of the transverse distributions, with crests and troughs of roughly equal sharpness, is similar to those in laminar flows (5) at  $Re_a = 2300$  and below, but is markedly different from some of those measured at  $Re_a = 3800$  (5) which featured flattened crests and sharp troughs, unsteady in their spanwise positions.

Momentum thickness calculated from the profiles (defined here as  $\int (\bar{u}/u_p)(1 - \bar{u}/u_p) dy$  where  $u_p(y)$  is the potential velocity, extrapolated from the core flow) showed a marked variation across the span. At the lower  $Re_a$  the ratio of  $\theta$  at a trough position to that at a crest was 1.7 at  $\phi = 57^\circ$  and 4.1 at  $76^\circ$ ; corresponding ratios at  $Re_a = 16000$  were 2.2 and 3.6

Profiles of r.m.s. Doppler signal  $e'$ , as a percentage of the local mean signal  $\bar{e}$ , in Fig. 8 shows that fluctuation intensity is generally greater at wave trough positions, where fluid is being swept away from the wall. Except where shown by the scatter band, the scatter in five repeated measurements is contained within the width of the plotted symbol; the uncertainty in each measurement is estimated as  $\pm 2\%$  of  $e'$ . The relationship between  $e'/\bar{e}$  and  $u'/\bar{u}$  may be gauged from estimates of spectral broadening caused by the mean velocity gradient and finite particle transit time in the measuring volume and by instrument noise. Typical values at  $Re_a = 16000$ ,  $\phi = 76^\circ$  are such that  $e'/\bar{e} = 1.8\%$  in the potential core becomes  $u'/\bar{u} = 1.7\%$ , while  $e'/\bar{e} = 8.6\%$  at  $y/a = 0.1$  becomes  $u'/\bar{u} = 8.5\%$ . Measurements of turbulent energy spectra are in progress at the time of writing.

Examples of the limited number of measurements of transverse mean velocity magnitude  $|\bar{w}|$  are presented in Figs 9 & 10. Unlike the case of laminar flows, crests and troughs in the  $\bar{w}(z)$  distributions are not aligned, in general, with "mean" positions in  $\bar{u}(z)$ ,

and vice versa; this indicates a rather distorted vortex pattern. However, profiles normal to the wall, at positions of maxima in  $|\bar{w}|(z)$ , are closer to the idealized pattern. No particular directional meaning is implied in the  $\bar{w}(y)$  plots; however, the change of sign shown near  $y/a = 0.2$  was indicated by a reduction of the Doppler signal below the detectable level in this region. No significant trend in the amplitude of  $\bar{w}(z)$  could be detected, typical values of amplitude being  $0.02u_{pw}$  to  $0.03u_{pw}$  at distances from the wall where peaks in the  $\bar{w}(y)$  profiles were found. In laminar flow at  $Re_a = 2300$ ,  $\bar{w}$  amplitudes (expressed as a fraction of  $u_{pw}$ ) at least twice these values were found.

Measurements of  $w'$ , the r.m.s. value of the fluctuating part of  $w$ , were limited by the fact that, at the low values of  $\bar{w}$  in these flows, intensities  $w'/\bar{w}$  greater than about 40% cannot be handled without frequency shifting. At  $Re_a = 16000$ , intensities less than 40%, but still greater than 30%, were found only for  $0.05 < y/a < 0.15$  at  $\phi = 57^\circ$ ; at  $\phi = 76^\circ$  the limit was exceeded over the whole boundary layer. Almost all data at  $Re_a = 9800$  were in excess of the limit. These results are consistent with unsteadiness in the spanwise positions of the vortices, on a small scale.

## 5. CONCLUSIONS

Details of the longitudinal vortex structure have been revealed by use of a non-disturbing velocity measurement technique. Vortices developing without artificial triggering were found to have a mean wavelength of the order of the boundary layer thickness, as found in other investigations. Their mean lateral positions were repeatable except near the bend exit at the higher flow rate, where signs of break-up appeared, in contrast with continued vortex growth at the lower flow rate.

Amplitudes of the transverse variation in longitudinal and lateral mean velocity, the former reaching 10% of the potential wall velocity, were considerably less than in laminar Görtler vortex flows in the same channel; momentum thickness varied laterally by up to a factor 4. Longitudinal turbulence intensity varied laterally in a manner consistent with the vortex flow pattern, while the lateral intensity was generally in excess of the 40% (approx.) limit of the present instrumentation.

Future work will include an examination of the factors controlling vortex wavelength, and more detailed study of the apparent breakdown of the vortex structure at increased Reynolds numbers.

## 6. REFERENCES

- (1) Tani, I., Production of longitudinal vortices in the boundary layer along a concave wall, *J. Geophys. Res.*, Vol. 67, p. 3075, 1962.
- (2) So, R.M.C. and Mellor, G.L., Experiment on turbulent boundary layers on a concave wall, *Aeronaut. Quart.* Vol. 26, p. 25, 1975.
- (3) Meroney, R.N. and Bradshaw, P., Turbulent boundary-layer growth over a longitudinally curved surface, *AIAA J.*, Vol. 13, p. 1448, 1975.
- (4) Winoto, S.H., Durao, D.F.G. and Crane, R.I., Measurements within Görtler vortices, *Trans. A.S.M.E. Ser. I. (J. Fluids Eng.)*, Vol. 101, 1979 (to be published).
- (5) Winoto, S.H. and Crane, R.I., The vortex structure in laminar boundary layers on a concave wall, Rep. TP/C/7903, Dept. of Mechanical Engineering, Imperial College, London, 1979 (in preparation).
- (6) Bradshaw, P., private communication, 1979.
- (7) Kan, S., Miwa, K. et al., Heat transfer of a turbine blade, Proc. Joint Int. Gas Turbine Conf., Tokyo, Oct. 1971, p. 219.
- (8) Liepmann, H.W., Investigation of boundary layer transition on concave walls, N.A.C.A. Adv. Conf. Rep. 4J28, 1945.
- (9) Smith, A.M.O., On the growth of Taylor-Görtler vortices along highly concave walls, *Quart. Appl. Math.*, Vol. 13, p. 233, 1955.

## ACKNOWLEDGEMENTS

This work was supported by a Science Research Council grant. The authors gratefully acknowledge the advice and assistance of Professor J.H. Whitelaw.

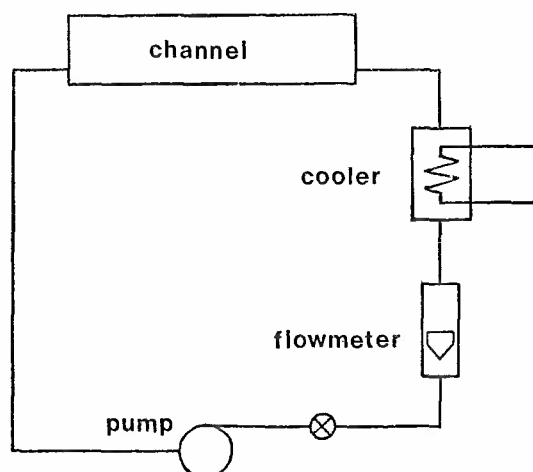


Fig. 1(a) Block diagram of flow circuit

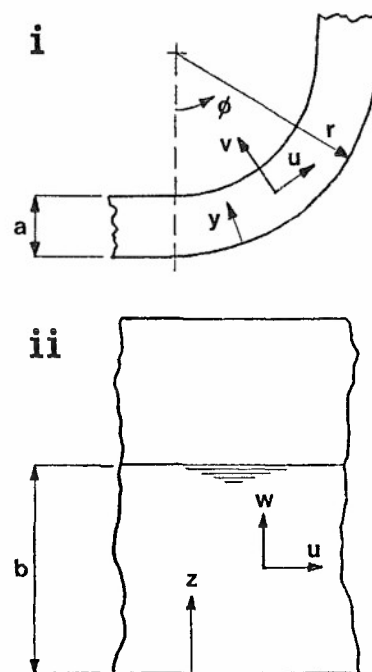


Fig. 1(c) Coordinate and velocity definitions on top (i) and side (ii) views of test section.

1. Spectra-Physics 120 He-Ne laser
2. Integrated optical unit
3. EMI 9558 photomultiplier
4. Cambridge Consultants CC01 frequency tracking demodulator
5. Tektronix 5103 oscilloscope
6. DISA 55B35 r.m.s. meter
7. DISA 55B30 true integrator
8. Schlumberger-Solarton 7040 digital voltmeter

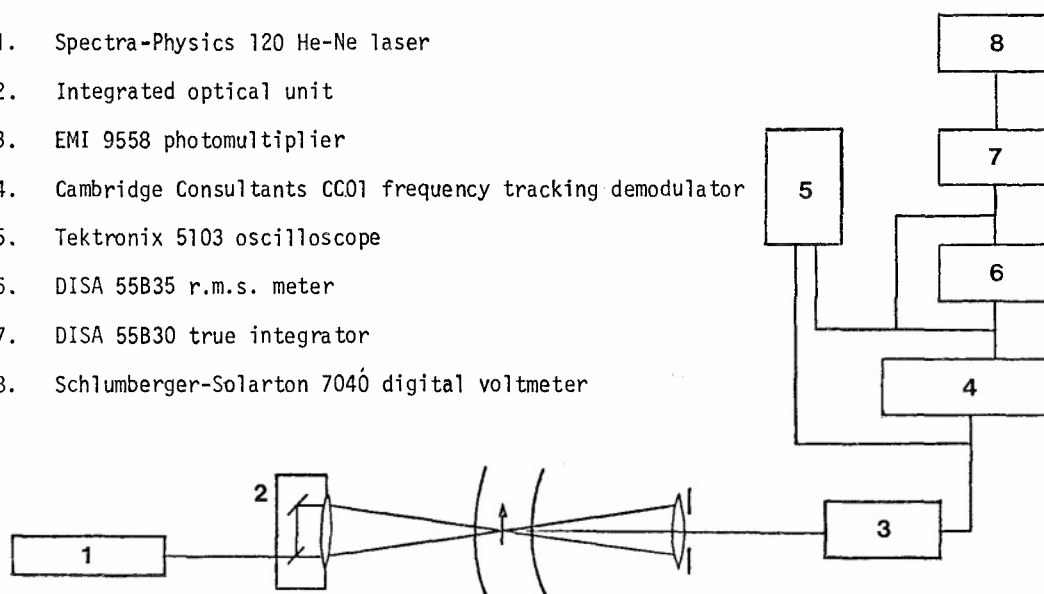


Fig. 1(b) Block diagram of laser anemometer system

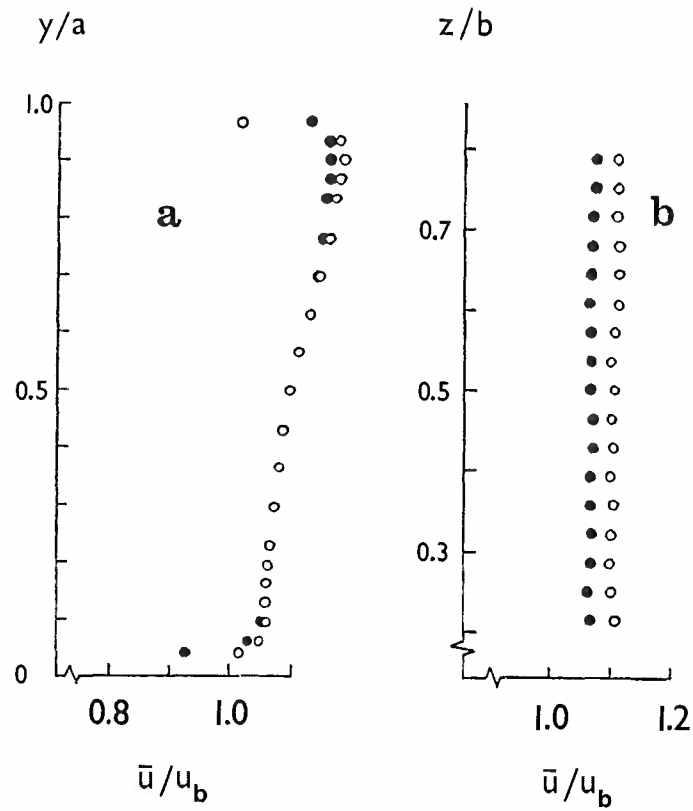


Fig. 2 Mean velocity profiles 0.08a upstream of bend entry. (a)  $z/b = 0.21$  (•) and  $0.79$  (○). (b)  $y/a = 0.13$  (•) and  $0.50$  (○).

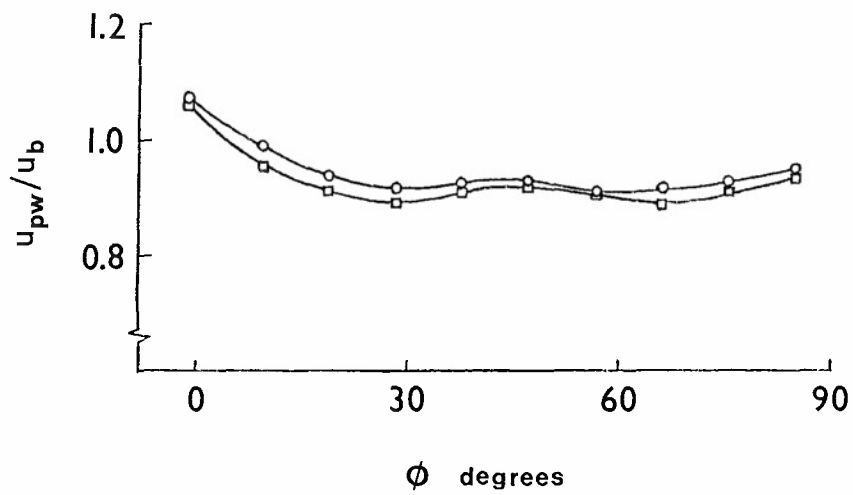


Fig. 3 Variation of potential wall velocity along concave wall.  $Re_a = 9800$  (○) and  $16000$  (□).

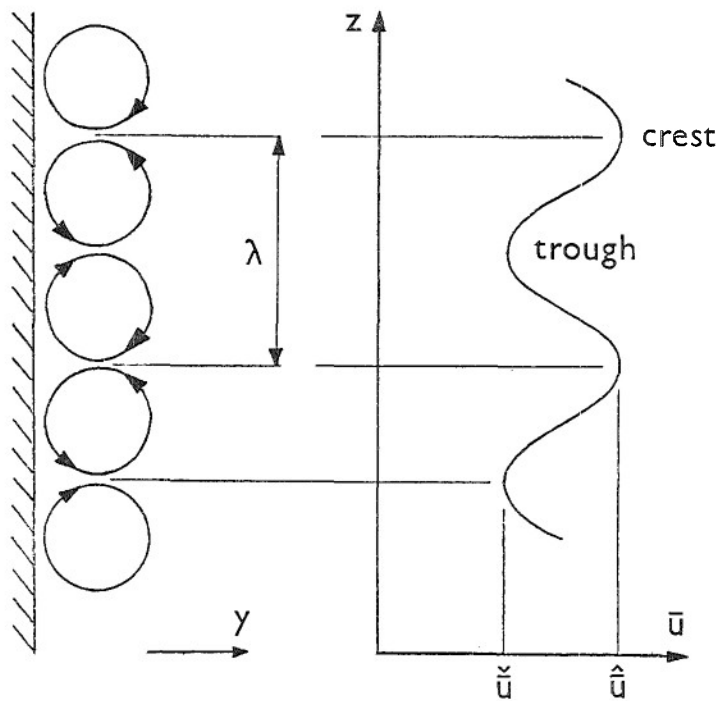


Fig. 4 Idealized vortex pattern and resulting lateral variation of longitudinal mean velocity.

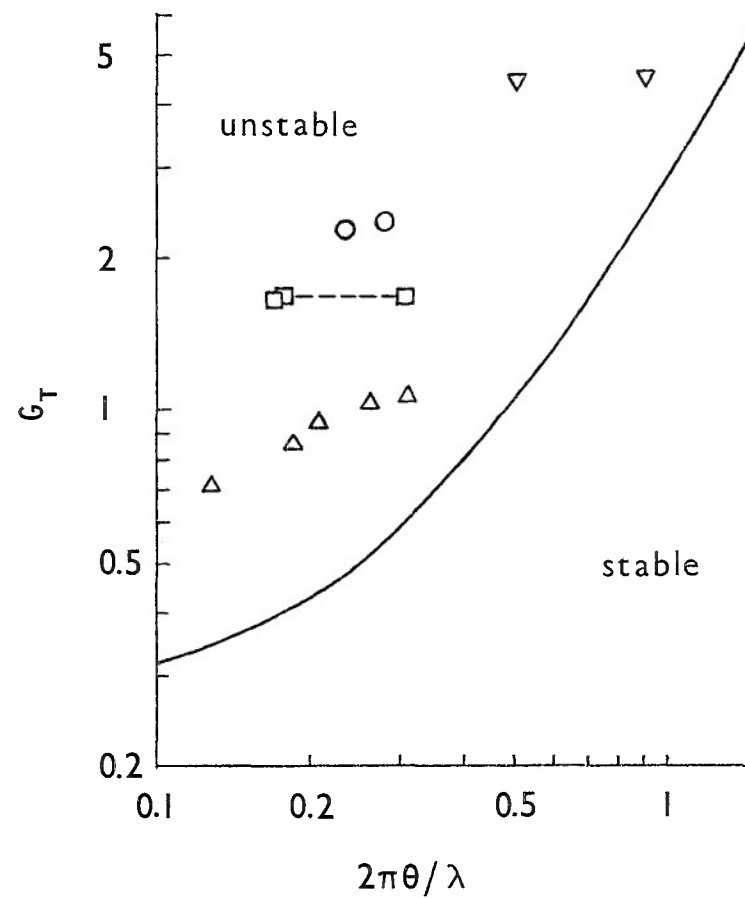


Fig. 5 Stability diagram. Present results:  $\circ$   $Re_a = 9800$ ,  $\square$   $Re_a = 16000$ .  $\nabla$  So and Mellor (2).  $\triangle$  Tani (1). — Neutral stability.

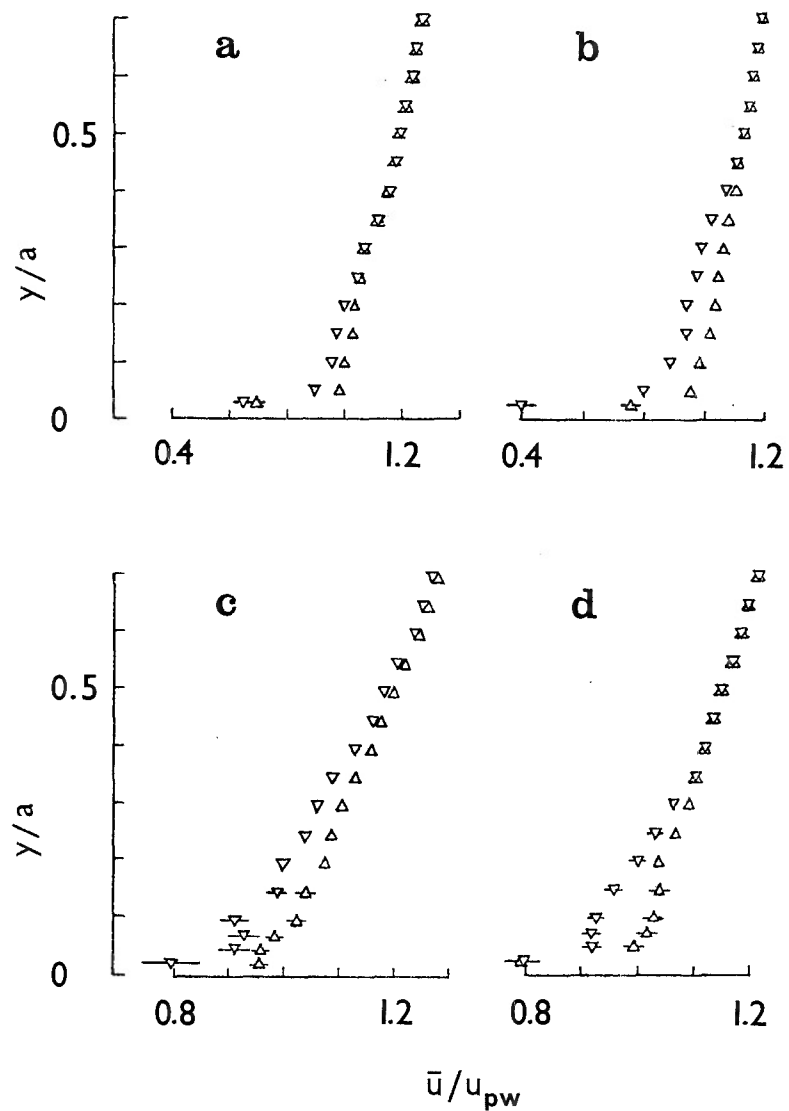


Fig. 6. Profiles of longitudinal mean velocity at crest ( $\Delta$ ) and trough ( $\nabla$ ) positions of the  $\bar{u}(z)$  distributions.  $Re_a = 9800$ :  $\phi = 57^\circ$  (a) and  $76^\circ$  (b).  $Re_a = 16000$ :  $\phi = 57^\circ$  (c) and  $76^\circ$  (d).

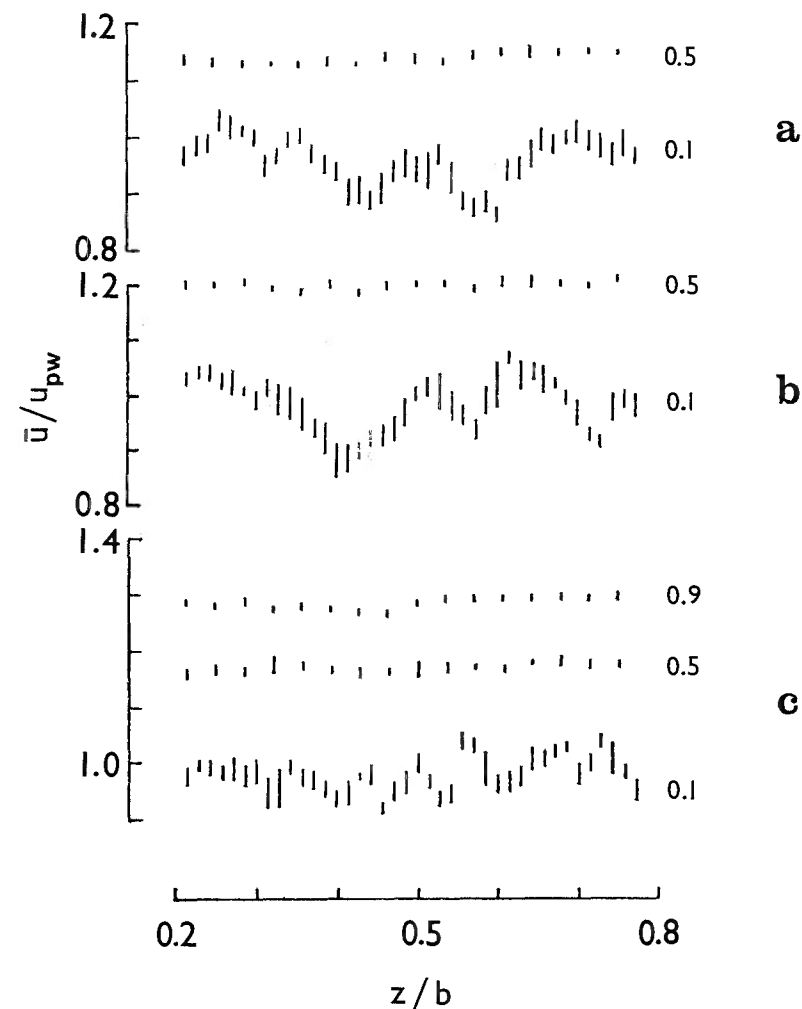


Fig. 7. Transverse distributions of longitudinal mean velocity at  $Re_a = 16000$ ,  $\phi = 38^\circ$  (a),  $57^\circ$  (b) and  $76^\circ$  (c). Numbers denote value of  $y/a$ . Vertical bars indicate scatter in 5 measurements.

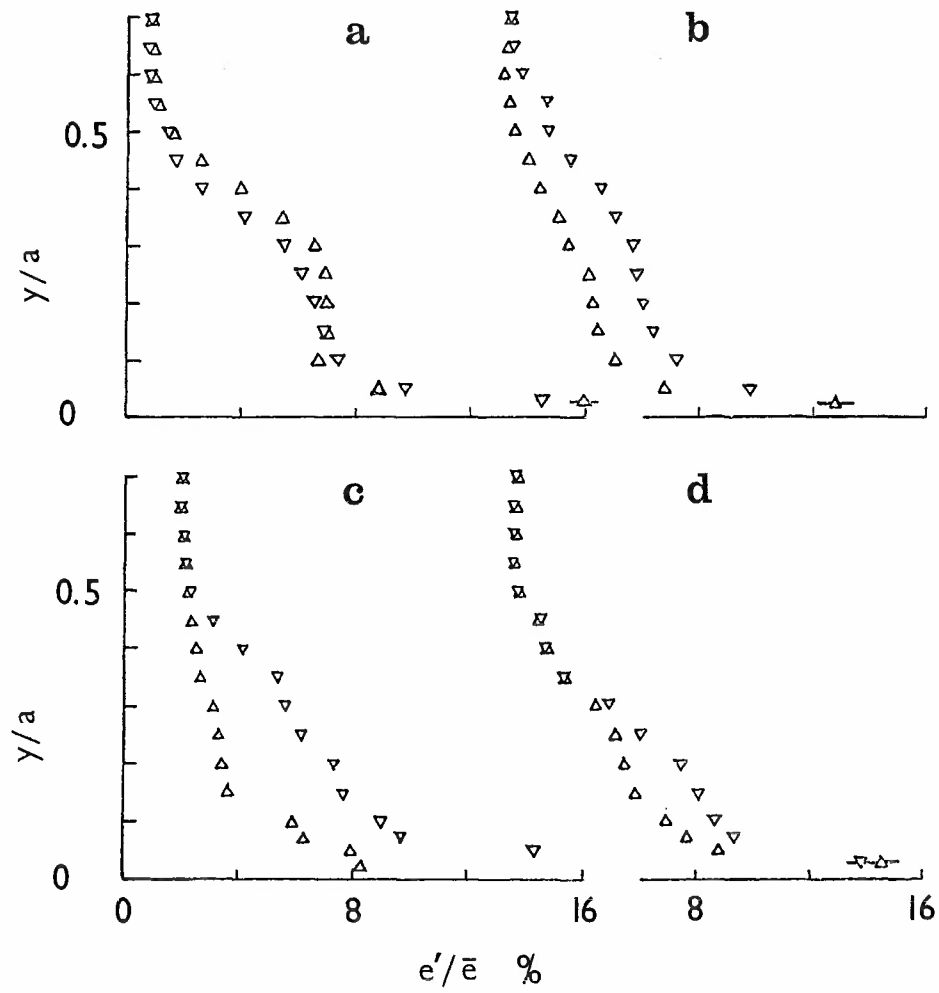


Fig. 8 Profiles of longitudinal fluctuation intensity at crest ( $\Delta$ ) and trough ( $\nabla$ ) positions of the  $\bar{u}(z)$  distributions.  $Re = 9800$ :  $\phi = 57^\circ$  (a) and  $76^\circ$  (b).  $Re_a = 16000$ :  $\phi = 57^\circ$  (c) and  $76^\circ$  (d).

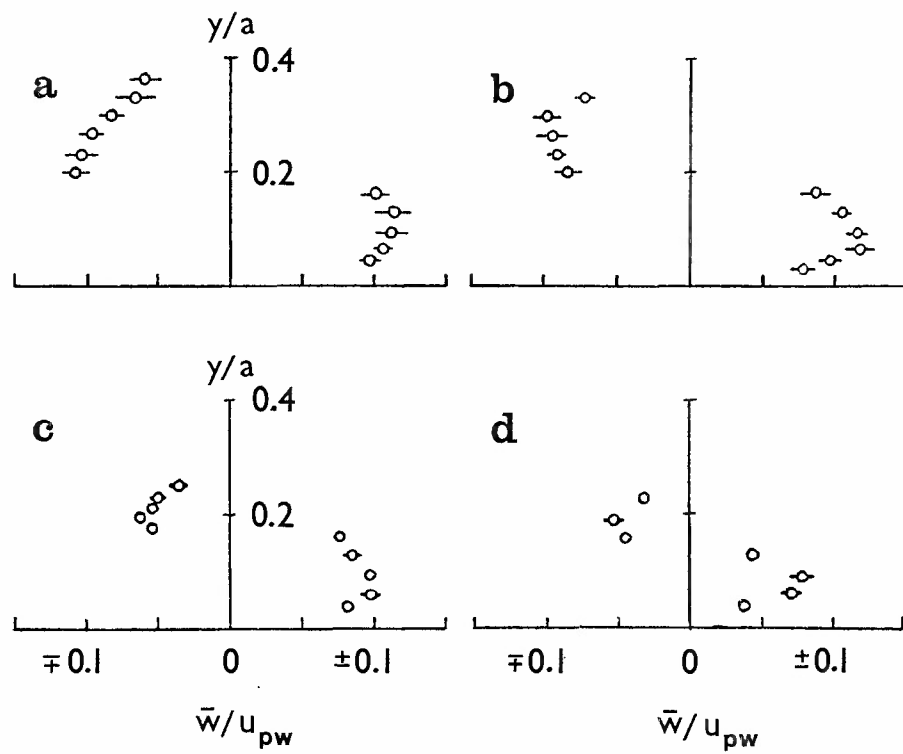


Fig. 9 Profiles of lateral mean velocity at positions of peaks in the  $\bar{w}(z)$  distributions.  $Re_a = 9800$ :  $\phi = 57^\circ$  (a) and  $76^\circ$  (b).  $Re_a = 16000$ :  $\phi = 57^\circ$  (c) and  $76^\circ$  (d).

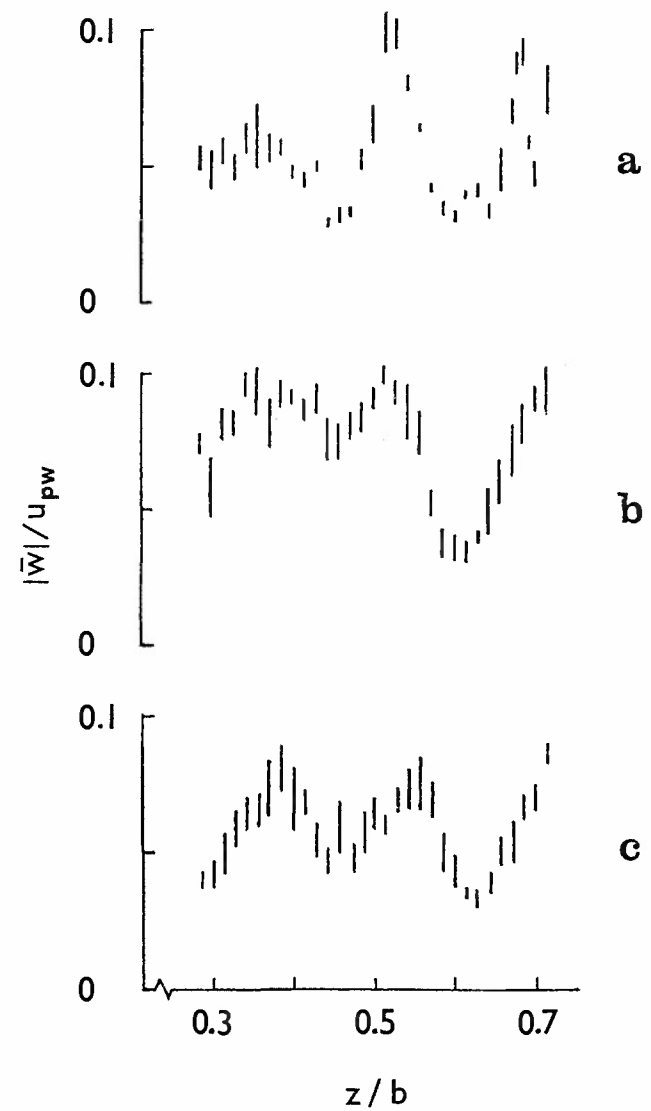


Fig. 10 Transverse distributions of lateral mean velocity at  $Re_a = 16000$ ,  $y/a = 0.10$ ,  $\phi = 38^\circ$  (a),  $57^\circ$  (b) and  $76^\circ$  (c). Vertical bars indicate scatter in 5 measurements.



A DISCUSSION OF PROBE EFFECTS AND IMPROVED  
MEASURING TECHNIQUES IN THE NEAR-WALL REGION  
OF AN INCOMPRESSIBLE THREE-DIMENSIONAL  
TURBULENT BOUNDARY LAYER

by

J.D.Vagt and H.H.Fernholz

Hermann-Föttinger-Institut für Thermo- und Fluidodynamik  
Technische Universität, 135 Strasse des 17. Juni  
D 1000 Berlin 12, Germany

## SUMMARY

Comprehensive measurements of mean and fluctuating velocities and shear stresses in three-dimensional boundary layers are urgently needed to establish turbulence models for the computation of boundary layer flows. The aim of the present investigation has been to provide such measurements and to develop or improve measuring techniques for such measurements, especially in the near-wall region of a pressure-driven three-dimensional boundary layer on a curved wall. This report describes measuring techniques and associated probe effects being due to (a) aerodynamic interference, (b) strong curvature of the streamlines in the inner region of the boundary layer, (c) wall effects on the hot-wire and the cobra probe signals, (d) low mean flow and high turbulent intensities close to separation, (e) problems related to accurate measurements of the distance between a hot wire and the wall, and (f) manufacturing problems of hot-wire probes.

## 1. INTRODUCTION

Comprehensive measurements of mean and fluctuating velocities, shear stresses and of skin friction in three-dimensional boundary layers are still rare but are urgently needed to establish turbulence models for the computation of boundary layer flows. The aim of the present investigation has been to provide such measurements in a pressure-driven three-dimensional turbulent boundary layer with special emphasis on the region close to the curved wall. Measurements have already been presented in tabulated form in Fernholz et al.(1), and a detailed discussion of the results will be published at a later date. The present report describes the measuring techniques and associated probe effects giving special attention to probe-flow interference.

Substantial aerodynamic interference effects were observed when hot-wire probes were used in a turbulent boundary layer with the stem inclined to the wall at an angle of 5 to 10 degrees. These effects could be explained, and were eliminated by developing a family of probes with single normal, slanted and crossed wires which kept disturbances of the highly curved flow to a minimum.

Flow angles were measured by means of hot-wire probes and twin-tube yawmeters, and a comparison of the results indicated severe aerodynamic interference effects when the latter probes were used in the near-wall region.

Anomalies of the mean velocity distribution in the inner layer led to the detection of errors in the determination of the absolute distance of the hot wire from the wall. Since 'in situ' measurements of the hot-wire distance from the wall could not be carried out due to access problems in the test section, an indirect measuring technique was developed to determine this distance with an accuracy of  $\pm 0.01$  mm. Finally, measuring techniques (and, where possible, their accuracy and repeatability) are discussed for the components of the Reynolds stress tensor and the skin friction.

## 2. EXPERIMENTAL ARRANGEMENT AND FLOW CONFIGURATION

A description of the wind tunnel used in this investigation was given by Vagt(2). It is a low-speed blower tunnel with a 12 KW motor and centrifugal fan, an airfilter intake and a 2 m long settling chamber with two wire-gauges (open area ratio 38 %) followed by an 11:1 axisymmetric contraction (Fig.1). A carefully organized programme of adjustment of the screens resulted in a uniform exit velocity so that local mean velocities  $U$  in the core of the flow varied at most by  $\pm 1.5$  % with a turbulence intensity  $(\overline{u'^2})^{1/2}/U$  of 0.10 % in a frequency range up to  $10^4$  Hz. All measurements were performed at a test section inlet velocity of about 18 m/s, and the Reynolds number  $U_{inlet}/\nu = 1.23 \times 10^6$  per meter was kept constant. The laboratory was airconditioned (room temperature constant at  $22 \pm 0.5$  C) in order to minimize the drift of hot wires and transducers.

The test section consisted of a sting-mounted horizontal inner cylinder (0.25 m diameter, 1.55 m long and made of Ultramid S) with an elliptical nose cone and a concentric perforated outer cylinder with 0.60 m diameter. Pitot tubes and hot-wire probes, mounted on an electrically driven traverse gear, were introduced into the test section through a slot along a generator of the wall of the outer cylinder. The traverse gear allowed precise linear (incremental resolution 0.005 mm, system Heidenhain) and angular (resolution 0.09 degree) movements. Surface fences, (5 mm diameter) protruding approximately 0.10 mm from the surface of the inner cylinder (Vagt & Fernholz(3)), alternated with static pressure tapings (0.8 mm diameter) along a generator of the inner cylinder. By turning the inner and/or the outer cylinder measurements could be made with the wall probes at fixed positions  $x$  along the circumference and with the other probes at any position in the flow field covered by a turning angle of about 30 degrees.

At the downstream end of the annulus a back plate was fitted to control the width of the flow exit and the axial pressure distribution in the test section. By inclining this back plate so that it was no longer normal to the axis of the cylinder the circumferential pressure distribution in the downstream half of the annulus could be made asymmetric, causing the originally axisymmetric boundary layer to become three-dimensional. A schematic diagram of the flow is shown in Fig.(2). The turning of the boundary layer causes flow deflections of up to 31 degrees near the wall, and the curved flow can bring about aerodynamic interference effects which substantially affect probe signals.

The flow direction outside the boundary layer is almost parallel to the axis of the cylinder, with a maximum angle of incidence in the  $xz$ -plane of about 2 degrees, and an upwash angle of about 5 degrees. It is a consequence of using a perforated outer cylinder that the flow deflection in the freestream is very small.

The test boundary layer was thickened artificially by a tripping device mounted on the circumference of the cylinder at the downstream end of the nose-cone. This consists of a strip of 'Oymo' tape with the letter V printed at intervals of 4 mm with the apices pointing upstream. The tape is 0.40 mm thick and the overall height of a printed V is 0.65 mm.

The development of the boundary layer from axisymmetric to three-dimensional is shown in Fig.(3) where we have plotted the free-stream velocity  $u_\infty$ , the skin-friction and the flow angle  $\beta$ , at a distance  $y = 0.15$  mm from the wall which is the angle measured closest to that of the limiting streamline. A description and interpretation of the mean and fluctuating flow measurements in this three-dimensional boundary layer with a strong adverse pressure gradient will be published elsewhere. The measurements can be found in tabulated form in a report by Fernholz et al.(1).

### 3. HOT-WIRE INSTRUMENTATION AND PROBES

Mean and fluctuating velocities were measured for the most part by means of probes with either a single normal wire or crossed wires. These wires were specially developed for this investigation, and operated by means of DFVLR (HDA III) constant-temperature anemometer units (Froebel (4)). The calibration curves were linearized by a polynomial linearizer (Froebel (5)) which provided a very good approximation in the velocity range investigated (3 to 30 m/s). For the measurements of flow angles the anemometers were connected to OFVLR integrators (Froebel(6)) allowing integration times up to 1000 s. These integrators have an input impedance of 10 M  $\Omega$ , and the main unit is a temperature-compensated field-effect transistor (FET) amplifier with a very high amplification and capacitive feedback. For measurements of velocity fluctuations the anemometers were used in conjunction with a turbulence-intensity measuring device (Froebel & Vagt(7)) which provided r.m.s. values, sums, differences and divisions of signals. The signals were read into a teletype unit by means of a data transfer unit (Schlumberger DTU) - connected to a digital voltmeter (Schlumberger A220) - punched on a paper tape and finally evaluated on a HP 1000 computer.

The hot wires were calibrated in the free stream of the test section at a position ( $x=531$  mm,  $\varphi = 0^\circ$ ) where the turbulence level was less than 0.003 and where the velocity was constant in a range  $20 < y < 140$  mm normal to the wall.

The flow velocity was measured in the same plane by means of a Pitot-probe (1 mm diameter) and a static pressure tapping and evaluated by an automatic micro-manometer with a resolution of 0.01 mm water column (Froebel & Vagt(8)). The hot-wire calibration curve was checked after each profile measurement. It turned out to be very stable indeed due to the air filters and the temperature control in the laboratory.

The single and cross-wire probes were designed to cause as little aerodynamic interference as possible, and their design and manufacturing process was described in detail by Oahm & Vagt(9). Figure (4) shows a sketch of a single normal, hot-wire probe. The distance between the prongs is 4 mm and their length 10 mm. The hot-wire consists of a central sensitive section of platinum-coated wolfram wire, 5  $\mu$ m in diameter and 1.3 mm long. The gold-plated end sections are approximately 30  $\mu$ m in diameter and are soldered to the prongs which have the same diameter at the tip as the plated wire. The ratio of "active" wire length to diameter is 260, the nominal wire resistance 6  $\Omega$  at 22.5 $^\circ$  C and the resistance of the prongs and the electrical leads approximately 0.5  $\Omega$ . The wires were operated at a resistance of about 1.7 times the cold resistance.

The influence of aerodynamic interference on the probe signal was investigated by using the "rotation test" described by Comte-Bellot et al.(10). If the normal-wire probe rotated through 90 $^\circ$  about the wire axis from the position in which the stem is aligned with the mean flow direction (i.e. to a position normal to the flow direction) then the mean velocity measured by the hot-wire increases by 2.3 % in the velocity range up to 30 m/s. This is slightly higher than the value given by(10) and Strohl & Comte-Bellot(11) for their reference probe A with very long prongs but lower than for their probe E which is similar to our probe. An extrapolation of the results of Comte-Bellot et al.(10) shows that the aerodynamic disturbance due to the stem increases the velocity by approximately 0.3 % while that due to the prongs (for a prong diameter at the tip <0.3 mm and a prong spacing larger than 3 mm) brings about an increase of about 2 %, the two effects adding up to the figure of 2.3 % quoted above. Bissonnette & Mellor(12) have also used a hot-wire probe with the stem normal to the wall. Our investigation confirms their suggestion "that interference effects need not be too critical", if the hot-wire probes are properly designed.

The cross-wire probe is shown in Fig.(5a). Stem and prongs have the same size as those of the normal-wire probe. The gap between the two wires is 1 mm in order to avoid effects of thermal wake interference (Guitton & Patel(13)), and the distance between the prongs is again 4 mm. The aerodynamic interference test - though not as detailed as that of(10) - agreed with their results in general and showed that the probe signals were not seriously affected in the probe positions used in the investigation.

Special care was taken during the soldering process to make sure that the wires of all probes were neither slack - which would cause changes of the calibration curve of a slanted wire - nor under tension when heated - which would cause strain gauge effects caused by a transfer of prong vibrations to the hot wire. The slanted-wire probe (Fig.5b) used for the measurement of the Reynolds stress component  $v'w'$  is discussed in section 4.1.

### 4. MEASURING TECHNIQUES

#### 4.1 MEAN AND FLUCTUATING VELOCITIES

In a three-dimensional boundary layer the velocity vector is determined by its coordinates  $x, y, z$  in the flow field, its flow angle and its magnitude. If a hot-wire probe is used to measure flow angle and magnitude of the velocity, a number of problems occur when such measurements are carried out in the immediate vicinity of the wall, say for the dimensionless wall distance  $y^+ < 40$  ( $y^+ = u_\tau \cdot y/\nu$ , where  $u_\tau$  is the skin friction velocity  $(\tau_w/\rho)^{1/2}$ ,  $\nu$  the kinematic viscosity and  $y$  the distance normal to the wall). Since our measurements were performed in a boundary layer with a severe adverse pressure gradient, the problems were aggravated by the high turbulence level in the boundary layer which reached values up to 60 %. Mean and fluctuating velocities were measured with single normal hot wires, with slanted hot wires, and with cross-wire probes.

In the case of mean flow measurements, we were worried most by the high turbulence level in the severe adverse pressure gradient. Measurements of the mean velocity  $\bar{u}$  can be corrected by taking into account higher-order terms of the so called wire-response equation (e.g. Vagt(14), eqn. 8.10). However, this contains triple correlation terms of the velocity fluctuations  $u'$  and  $w'$  which are difficult to measure.

This means that it is still rather complicated to correct hot-wire signals in highly turbulent flows and that we must be content, at least at present, if the data measured by a hot wire and by Pitot tubes, which respond in very different ways to high levels of turbulence, show satisfactory agreement. We have therefore compared mean-velocity data obtained by round and flattened Pitot tubes and a single normal hot wire in Fig.(6). These measurements were performed at  $x = 1014$  mm, well into the adverse pressure gradient region, on one of the two lines of symmetry of our flow configuration where the flow was aligned with the axis.

The local turbulence level  $(\overline{u'^2})^{1/2}/\bar{u}$  is very high, reaching the above mentioned 60 %, but agreement between the velocities measured by the various probes is surprisingly good. The open circles represent hot-wire data before the distance between the wall and the hot-wire could be determined more accurately, as described in section 4.2, and the full circles the data where the wall distance was corrected by 0.10 mm. Data obtained with the larger flattened Pitot tube lie consistently below the other data for reasons which we are unable to explain.

A further need for correction may arise from the influence of the wall acting as a heat sink for the approaching hot wire. Oka and Kostić(15) have demonstrated this effect very clearly in Fig.(7) where velocity measurements in the viscous sublayer ( $y^+ < 10$ ) lie considerably higher than they should according to the universal relationship  $u^+ = y^+$ . The upper curve is likely to be valid only for the particular wall material used in the experiments and probably for the type of hot-wire used. It must be obtained therefore for each experiment individually.

For our pairing of wall material and hot-wire probe the "heat sink effect" became noticeable at a wall distance of approximately 1.50 mm (cf. section 4.2) at zero flow velocity. But even at much smaller wall distances ( $y^+ > 4$  compare Fig.(10) and  $y > 0.15$  mm compare Fig.(6)) forced convection appears to have dominated the heat transfer from the wire, so that the "heat sink" effect is much less severe than in the case investigated by Oka & Kostić(15). For this reason it was decided not to correct the hot-wire data for wall effects.

All probes were set along the local flow direction which was determined by a hot wire as described in section 4.3, and the measurements were presented in tabulated form accordingly(1).

The normal component  $u'^2$  was measured by a single normal wire in the usual way. The  $\overline{u'w'}$  term was obtained at first by means of a cross-wire probe, the wires of which lay in xz-planes one millimeter apart to avoid interference of the thermal wakes. The effective location of the measurements is then assumed to be half-way between the two wires, which is correct for the outer region but does not hold for the inner region where shear gradients are large. We have therefore used a single normal wire set at  $+45^\circ$  to the mean flow direction. If the hot wire is calibrated in either of these two positions,  $\overline{u'w'}$  is determined from

$$\overline{u'w'} = (2K^2)^{-1} (\overline{e_1'^2} - \overline{e_2'^2}) (1-k^2)^{-1} \quad (4.1.1)$$

there  $e'$  denotes the voltage,  $K$  a calibration constant, and 1 and 2 denote the two wire inclinations. Using a single wire also avoids an incorrect alignment of the cross-wire probe with respect to the flow angle which is different for the two wires, having a large gradient in the near-wall region.

The output signal of any hot-wire probe inclined to the mean flow can be affected greatly by vibrations of the wire (strain gauge effect) caused by a periodic shedding of eddies from the prongs. Since the resonance frequency of our probes is known to be at about 8000 Hz the hot-wire signal on the oscilloscope was checked beforehand whether such a strain gauge effect occurred (see Vagt(14)). If this was the case the tension of the wire was reduced to about zero under heating conditions.

The yaw-parameter  $k$  was found to be very small for flow angles less than  $70^\circ$  and could therefore be neglected for this hot-wire probe (Dahm & Vagt(9)).

The normal stress component  $w'^2$  was determined from the single normal wire, this time in three positions (the third, normal to the flow, to obtain  $\overline{u'^2}$ ), via the relationship

$$\overline{w'^2} = [(K^2)^{-1} \cdot (\overline{e_1'^2} + \overline{e_2'^2}) - \overline{u'^2}] \frac{(1+k^2)^2}{(1-k^2)^2} \quad (4.1.2)$$

This method had again the advantage that the wire was in one plane only.

No corrections were introduced to account for the high turbulence level since the triple and quadruple correlation terms necessary for such a procedure were not measured. The data could be corrected as follows (Vagt(14)) with  $k=0$ :

$$\begin{aligned} \overline{u'^2} & \text{ by the factor } \left[ 1 + (\overline{u'w'^2} / \overline{u'^2} \bar{u}) \right]^{-1} \\ \overline{w'^2} & \text{ " } \left[ 1 - (\overline{v'^2} \overline{w'^2} / \overline{w'^2} \bar{u}^2) \right]^{-1} \end{aligned} \quad (4.1.3)$$

and

$$\overline{u'w'} \text{ by the factor } \left[ 1 + 0.5 (\overline{w'^2} \overline{u'^2} / \overline{u'w'} \bar{u}) \right]^{-1}.$$

Both the normal-stress component  $\overline{v'^2}$  and the shear-stress component  $\overline{u'v'}$  were measured by means of a cross-wire probe, now in the xy-plane, where the goose-neck lay in a plane at approximately  $90^\circ$  to the flow direction. This arrangement minimizes aerodynamic interference effects. The two wires of the probe were aligned approximately at  $+45^\circ$  to the flow direction and the probe stem was inclined at  $2.5^\circ$  to account for the average upwash angle. This angle varied across the boundary layer from zero at the wall to at most  $5^\circ$  at the boundary layer edge, but our probe-driving device could not be adapted continuously to changes in this direction. However, deviations of  $2^\circ$  from the true upwash angle caused errors of 4 % at most at the outer edge of the boundary layer. Values of  $\overline{u'v'}$  were measured by the same probe (longer integration times were necessary in this case) but here deviations of the pitch angle caused slightly larger errors, 4 % on average and 7 % maximum error. The projections of the wires on the xz plane were parallel to the projection of the mean flow vector passing through the mid point between the two wire projections. For the evaluation of  $\overline{v'^2}$  and  $\overline{u'v'}$  the following relations were used:

$$\overline{v'^2} = (1+k^2) (\overline{e_1'^2} - \overline{e_2'^2})^2 / [2K^2 (1-k^2)^2] \quad (4.1.4)$$

and

$$\overline{u'v'} = [2K^2 (1-k^2)]^{-1} (\overline{e_1'^2} - \overline{e_2'^2}), \quad (4.1.5)$$

with wires at flow angles  $\alpha = +45^\circ$ ,  $k$  as the yaw parameter and  $K$  as a calibration constant.

Corrections for high turbulence levels can again be taken into account by multiplying

$$\overline{v'^2} \text{ by the factor } \left[ 1 - (\overline{v'^2} \overline{w'^2}) / (\overline{v'^2} \bar{u}^2) \right]^{-1}$$

and

$$\overline{u^1 v^1} \text{ by the factor } [1 + 0.5 (\overline{v^1 w^1}^2 / \overline{u^1 v^1} \overline{u})]^{-1}. \quad (4.1.6)$$

k is assumed to be zero.

The measurement of the term  $\overline{v^1 w^1}$  is more difficult than that of the other components since, at first sight, the hot-wire array needs a rotatable probe stem lying in the direction of the mean velocity vector. Such a probe arrangement - as first used by Johnston (17) - may, however, cause aerodynamic interference effects in a highly curved flow (cf. Fig.12) which are probably made even worse by the probe holder. In this context attention should be drawn to the probe arrangement used by Elsenaar & Boelsma (18) where we would have expected aerodynamic interference effects to occur also.

To avoid this difficulty the slanted-wire probe shown in Fig.(5b) was developed. This could be introduced into the flow with the stem perpendicular and the plane of the gooseneck across the flow; the prongs are then parallel to the xz-plane. When the angle  $\gamma_1$  is zero the slanted wire is set at  $45^\circ$  to the flow direction in the xy-plane,  $\gamma_2$  being the angle between the projections of the wire and the mean flow velocity vector in the xz-plane. The wire had to be rotated into four different positions - determined by  $\gamma_2$  - in order to obtain the signals necessary for the evaluation of  $\overline{v^1 w^1}$ . This was done by the following relationship

$$\overline{v^1 w^1} = [\overline{e_{\gamma_2=135^\circ}^2} - \overline{e_{\gamma_2=315^\circ}^2} + (\sqrt{2})^{-1} (\overline{e_{\gamma_2=0^\circ}^2} - \overline{e_{\gamma_2=180^\circ}^2})] \cdot 4 [(1 - 0.25(1 - k^2)) \cdot [K^2(1 - k^2)^2 \sqrt{2}]^{-1}]. \quad (4.1.7)$$

Special emphasis was laid upon avoiding aerodynamic interference effects which could be confined for this probe to a range of the angle of rotation  $\gamma_2$  of about  $36^\circ$ . So the probe signals were not affected by disturbances from the prongs at the positions needed in eqn.(4.1.7).

Bissonnette & Mellor (12) also used a  $45^\circ$  slanted-wire probe, but with vertical prongs and stem which was rotated continuously with signals being recorded on an xy-plotter. For a comparison between fixed and rotating hot-wire probes and the corresponding signal evaluations the reader is referred to Pierce & Ezekwe (19).

#### 4.2 WALL DISTANCE

The measurement of the absolute distance between a measuring probe and the wall needs a certain amount of care if circular or flattened Pitot probes are used but it causes serious problems in the case of a hot-wire probe which can get closer to a wall than any other measuring device. As will be shown below, a difference in wall distance of 0.1 mm influences the interpretation of velocity measurements in the near-wall region greatly and leads easily to wrong conclusions. Therefore it is astonishing how little information is available about the determination of the wall distance. Wills (20) claims that he was able to read the distance of a hot wire to an accuracy of 0.00127 mm on a micrometer head, and obtained the zero distance by viewing the wire and its reflection in the test wall through a microscope and a  $45^\circ$  mirror, the distances between the two images being measured on a graticule in the eye-piece. Van Thinh (21) observed the distance of the wire from the wall by means of a microscope situated on the other side of the glass test wall. In the first case the wall must be reflecting, in the second transparent. If neither of these conditions is given, a method described by Orlando (22) can be used. There a "wall-stop" soldered to the probe stem prevents the wire from being accidentally damaged by the wall. The distance of the wire from the wall when the wall stop makes contact was measured by an optical comparator and set nominally to 0.127 mm with an accuracy of approximately 0.025 mm.

Finally Hebbar & Melnik (16) report on a combined optical-sighting-electrical method which is similar to the distance measuring techniques described below and used in our own investigation. Their method is, however, confined to probe arrays where the prongs emerge from the test wall and to non-conducting walls since the plated ends of the hot wire must touch the wall in the measuring process.

Our measuring technique can be applied to all cases where the probe is introduced into the boundary layer from the free stream. The calibration curve holds for our family of hot-wire probes in connection with the specific wall material but an extension of its validity to geometrically similar probes should be possible. For the application of this technique one must be sure - and we have ascertained this - that the hot-wire axis is straight and lies always parallel to the surface.

The calibration procedure ran as follows. The normal-wire probe was calibrated in the free stream for the velocity range investigated - i.e. zero voltage output for zero velocity and 10 V output for the maximum velocity - and connected to an r.m.s. meter and an oscilloscope. The oscilloscope served to detect large oscillations which gave an indication of the proximity of the wall since they occurred just before the wire touched the wall. They were due to relative movements between the wire and the test wall caused by "natural" vibrations of the laboratory building.

With the wind in the test section switched off, the output voltage was at first zero when the hot wire was moved from a fixed arbitrary, relatively large distance towards the wall. Close to the wall - in our case at about a distance of 1.5 mm - the wire feels the cooling effect of the wall. The output signal plotted against a relative value  $\Delta y$  of the wall distance increases, reaches a maximum and falls off again. Fig.(8) shows two typical output distributions in the immediate vicinity of the wall and some shapes and configurations of wires and prongs after contact with the wall. The datum points beyond the maximum are lower again because the wire is further away from the wall than at the maximum output due to probe deformation after the contact with the wall. From careful measurements of these deformed probe configurations and the wire behaviour close to the wall - some probes had to be destroyed voluntarily - we could define the position of the wire relative to the wall with an accuracy of  $\pm 0.010$  mm. Thus the output voltage measured against the relative distance could now be related to the actual distance from the wall, e.g. the effective voltage  $u_e = 1.75$  V corresponds with a wall distance of  $0.10 \pm 0.01$  mm (Fig. 9). Figure (9) shows the voltage output curves for all the hot-wire probes used. Since tight manufacturing tolerances could be maintained, the output curves are almost identical for the chosen pairing of wall material and probe type up to an output voltage of about 2 V. For higher output voltages, i.e. smaller wall distances slight inaccuracies of the probe geometry or of the probe driving mechanism can cause deviations between the individual curves.

So, once the calibration curve for a pairing of hot-wire probe and wall material has been established the determination of the absolute wall distance is straightforward: After the calibration in the free stream the probe is moved towards the wall, with the wind switched off, until the voltmeter shows some output value not far from the maximum but still on the "universal" calibration curve which is related to a certain absolute wall distance. In our case this was 1.75 V equivalent to  $0.10 \pm 0.01$  mm from the wall (Fig.9).

Measurements with an accuracy of  $\pm 0.01$  mm can only be achieved if the traversing mechanism is aligned with an accuracy better than that mentioned above and if the probe can always be traversed perpendicular to the wall. The translational motion was transferred to the probe without any backlash. It had a travel of 200 mm with a resolution of  $5 \mu\text{m}$ . The traversing mechanism was mounted externally and independent of the test section. Nevertheless, it is possible that the calibration may be changed when the wind is on but we have no reason to suspect that this is the case.

As for the angular movement, a rotation of  $360^\circ$  with a resolution of 6 minutes was possible with this arrangement.

Such accurate measurements of the wall distance were important only for velocity measurements in the region  $y^+ < 40$ , as can be seen from Fig.(10). The behaviour of the uncorrected datum points in the near-wall region which could not be explained by wall cooling effects on the hot-wire led us to suspect that we might not have given enough care to the determination of the distance between the hot-wire axis and the wall. The necessary corrections were large indeed and brought the measurements back to the linear relationship  $u^+ = y^+$  for the viscous sublayer.

#### 4.3 FLOW ANGLE

Before we discuss the problems which occur when flow angles must be measured in a turbulent boundary layer the reader's attention is drawn to the distinction between "mean direction of flow" and the "mean flow direction" which was introduced by Rose(23). Quoting from Hebbar & Melnik(16), "the mean direction of flow in any plane is the time-averaged direction of the instantaneous component of the velocity vector in that plane, whereas the mean flow direction is defined by mean-velocity components." Rose derived a relationship for the difference between the angle of the mean direction of flow and that of the mean flow direction  $\beta_m$

$$\bar{\beta} - \bar{\beta}_m = - \frac{\overline{u'w'}}{\bar{u}^2} \quad (4.3.1)$$

For our measurements this correction would have changed  $\bar{\beta}$  at most by 1 to  $2^\circ$  in the region where  $\overline{u'w'}$  reached its maximum and was therefore omitted.

Flow angles were measured by a modified version of the rotated hot-wire technique and for comparison by cobra probes which are probably the best of the nulled direction probes (Dean(24)). The tubes of the two twin-tube yawmeters (cobra probes) were chamfered at an angle of  $35^\circ$  or  $55^\circ$  in plan view and were parallel to the test wall for about 10 mm. They then rose in a "gooseneck" before entering the outer cylinder perpendicularly. The tip of each probe was on the axis formed by this perpendicular stem. The  $35^\circ$  and  $55^\circ$  ground tubes were 0.90 mm and 0.50 mm in diameter.

Unfortunately, the response time of the smaller probe was so long in this "low mean velocity", highly turbulent flow region near the wall that integration times were too long for practical measurements. All measurements with the cobra probe were recorded by means of a Statham transducer the signals of which were integrated to obtain an average value in the highly turbulent region (due to a more efficient control mechanism the transducer was superior to the micromanometer system). Near-wall measurements of the flow angle were not only hampered by probe size and response time but also because the cobra probe interfered with the curved flow. This can be seen in Fig.(11) where measurements of the mean flow angle  $\beta$  are compared. The two measuring techniques give good agreements in the outer region of the boundary layer but differ by more than 30 % in the near wall region. The cobra-probe measurements may give the impression that the alignment of the velocity vector close to the wall was constant whereas the hot-wire measurements show a monotonic increase of the flow angle towards the wall. This agrees with the momentum equation for curved flow, requiring an increase in curvature with decreasing velocity if the normal pressure in the boundary layer is constant.

It is interesting to note that interference effects even between small hot-wire probes and the flow in the near-wall region of a boundary layer can become substantial as shown in Fig.(12). The flow angle  $\beta$  was measured with a single normal hot-wire probe, the stem of which was inclined at  $5^\circ$  to the wall in one case (see Johnston(17)) and perpendicular in the other. The former probe gives flow angles which, close to the wall, show a behaviour similar to that of the cobra-probe in Fig.(11), that is the flow angle is approximately constant. The stems of both cobra probe and inclined hot-wire probe affect the near-wall flow so strongly that these measurements are not representative of the actual flow, which has a much higher deflection.

The "perpendicular" hot-wire probe shows, as in Fig.(11), a monotonic increase of the flow angle towards the wall. The assumption that the pressure  $\bar{p}$  imposed on the boundary layer is constant in the  $y$  direction is plausible, but cannot be proved satisfactorily by present experimental techniques for static pressure measurements in the near-wall region, as was shown by Vagt & Fernholz(25). Nevertheless, near-wall measurements of the flow angle by cobra probes or inclined hot-wire probes should be carefully checked for aerodynamic interference effects. They may explain the "mysterious" collateral near-wall flow, found for example by Pierce & Krommenhoek(26) and Hebbar & Melnik(16). The latter authors have used a hot-wire probe the prongs of which were introduced vertically through the test wall as was suggested by Rogers & Head(27) and also applied by Vermeulen(28).

Rogers & Head gave an indication of some aerodynamic interference in a range of about  $70^\circ$  from the original position of the wire normal to the flow, but there is no information about the behaviour of this type of probe with long thin prongs in a highly turbulent flow, especially for measurements far away from the wall. In the near-wall region the above authors(27) found a monotonic increase of the flow angle towards the wall which indicates that aerodynamic interference effects should have been negligible.

Flow angle measurements with a hot wire are usually straightforward if the flow-angle characteristic of the hot wire is symmetric so that the bisector method can be applied. At a fixed height  $y$  the wire is rotated about the probe axis until maximum output voltage gives approximately the main flow direction. From this position the hot wire is rotated until about half the maximum voltage is indicated on the voltmeter and the corresponding angle is measured by means of a protractor. The voltage output is determined very accurately by integrating up to 100 s and must then be found again on the opposite side of the hot wire flow-angle characteristic. The mean of the two protractor readings is taken as the flow direction. This technique can be applied to flows or flow regions not too close to a wall where the turbulence level is low ( $< 20\%$ ) and where temperature changes in the flow during the measurement of the flow angle can be kept small. A typical flow-angle characteristic for such "easy" flows is shown in Fig. (13a). Close to a wall, however, the flow angle characteristics become flat (Fig. 13b), and a temperature change of  $1^\circ\text{C}$  during the measuring

period can cause an error of 4 degrees for the same output voltage on both sides of the maximum. For near-wall measurements the flow temperature must therefore be kept constant within a very small temperature range in order to obtain accurate flow-angle data. Such a close temperature control ( $\pm 0.1^\circ\text{C}$ ) is difficult to achieve, and it is not surprising that the measuring time for one flow angle has been one hour in some cases.

The measuring time can be drastically reduced to about one minute by another technique which allows to perform flow-angle measurements in flow regions where velocity fluctuations are large compared to the mean velocity and/or where wall effects are severe. Here the flow angle is determined by means of the minima of the flow-angle characteristics (Fig. 14) as described below. Because of the high turbulence level, the hot-wire output had to be damped by setting a time constant in a range from 1 to 25 seconds. Damping, i.e. large time constants, causes the flow angle characteristic to become asymmetric and thus prevents the use of the bisector method.

The new technique needs a plot of the flow-angle characteristic at the measuring position over a range  $\pm 120^\circ$  so that the minima are clearly visible on the graph of an xy-plotter for example. For a fixed time constant and a given speed of rotation of the probe the distance between the minima remains constant for all flow-angle characteristics.

The measuring procedure is as follows: First, a reference flow-angle characteristic is measured in a flow region where the flow angle is known, e.g. in the free stream, and the location of this angle is determined on the graph by calculating the mid point of the distance between the minima of this reference curve (in our case this is curve a in Fig. 14). The characteristics b to e were measured at different heights  $y$  in the boundary layer and the distances between the mid points between the respective minima and the location of the reference flow angle gave the magnitude of the individual flow angle  $\beta(y)$ . The scale of the abscissa, where a unit length is related to degrees has to be determined at the outset of the experiment.

For the practical application of this method hot-wires must be inspected carefully under a microscope in order to ascertain that the wire axis is straight, parallel to the wall (in our case normal to the stem), and that the connection between the prong tips and the wire is carefully smoothed and polished after the soldering process.

A further improvement of near-wall characteristics was obtained by amplifying the output voltage by a factor 3. This is shown in Fig. (15) in which curve (1) represents the hot-wire signal as calibrated for the whole velocity range at  $y = 0.10$  mm and curve (2) the same signal with amplification. But even then it is still difficult to determine the minima of curve (2) accurately. Only when the wire was moved another 0.05 mm outwards from the wall was it easy to find the minima (curve 3). So the minimum distance from the wall for which this technique can be applied, depends apparently on the magnitude of the turbulence level and the heat conductivity of the wall. Accuracy and repeatability of this method lie within  $\pm 1^\circ$  but are better in the low turbulence outer region of a boundary layer and reach  $\pm 0.5$  degrees in the freestream (see also Delleur(37)). A similar technique of measuring flow angles suggested by Bissonnette & Mellor(12) could not be applied here since a symmetric angular-response characteristic is then necessary.

#### 4.4 SKIN FRICTION

There is no need to emphasize the importance of knowing the wall shear stress in turbulent boundary layers. Unfortunately, all the problems associated with skin friction measurements in two-dimensional flow are made even more complicated by the additional measurements of the angle of the limiting streamline which must be known in a three-dimensional boundary layer. Pierce & Krommenhoek(26) have investigated several techniques of measuring the wall shear stress which have been used successfully in two dimensional boundary layers. They showed, for example, that a Preston tube, a claw-type Preston tube and a hot wire, flush mounted into a wall, indicate wall shear stress values within 10 % of those measured by a direct force reading device, with the majority of readings within 5 % of the mechanical shear meter. A comparison between measurements made using hot-film gauges, Preston tubes and sublayer fences in a relaxing three-dimensional boundary layer was performed by Hebbar & Melnik(16, table 12). These authors found differences of  $\pm 4$  % in the skin friction values measured. Judging this excellent agreement, one should keep in mind, however, that the three-dimensional boundary layer in which these comparative measurements were made was far from separation and returning to a two-dimensional flow.

Furthermore McCroskey & Durbin(29) performed flow angle and shear stress measurements using heated films and hot-wires, especially the V-shaped hot-film probe, and Vagt & Fernholz(3) investigated the properties of a surface fence in a three-dimensional flow.

An attempt was made to show the advantages and disadvantages of the different devices to measure skin friction in Table (1). We disagree here somewhat with results of Hebbar & Melnik(16, table II) who find that the accuracy of measuring the wall flow angle hardly differs between a Preston tube, a surface fence and a hot wire mounted flush in a wall.

One of the most important distinctions between the different methods of measuring skin friction is whether they depend on the logarithmic law of the wall or not. Measuring techniques based on the log-law are usually easy to handle but there is no a priori justification for using such a two-dimensional calibration in three-dimensional flow. At present one must therefore rely on the few comparative measurements of skin friction with a Preston tube and a direct force measuring device (floating element balance) in a three-dimensional boundary layer performed by Pierce & Krommenhoek(26). These comparative measurements agree within a few percent. Additional measurements as announced by Pierce et al.(30) are, however, very welcome.

Relying on these results we have used Preston tubes to measure skin friction in the three-dimensional boundary layer. Further, though indirect, checks were made on the validity of this measuring technique by using two Preston tubes of different outer diameters  $d$  (0.434 and 0.89 mm) and by plotting the measurements in the law of the wall coordinates  $u^+$  and  $y^+$ . Measurements at the two stations in the three-dimensional region ( $x = 998$  and 1031 mm) where the comparison was made agreed within  $\pm 4$  %, the pressure difference  $\Delta p$  (Preston) being in a range  $0.06 < \Delta p < 0.55$  mm of water column. Since the measuring time for the smaller Preston tube was about an order of magnitude larger, the 0.89 mm tube was used for all measurements in the region downstream of  $x = 1014$  mm. The repeatability of the measurements then lay within a bandwidth of  $\pm 5$  %, falling to  $\pm 30$  % close to separation due to the very small pressure differences and the high fluctuations of the signal.

For the pressure measurements, which were in a range between 0.02 and 4 mm of water, a Statham transducer (PM 97 TC) and an electronically controlled micromanometer (Froebel & Vagt(8)) were used. For accurate



results special care had to be observed to keep the density of the manometer fluid constant. The Preston tube was set to an average angle determined from flow-angle measurements close to the wall. A more accurate adjustment has not been necessary since the sensitivity of circular Pitot probes to changes in flow direction is very low within a range of  $\pm 15^\circ$ . This argument contradicts East & Hoxey(31) and East(32) who suggested that a Preston tube should be aligned in the flow direction at a height  $y = 0.125$  or  $0.33 d$ , respectively.

The calibration curve of Patel(33) was used to determine the skin friction, thus assuming implicitly that the law of the wall in two-dimensional flow can be transferred to three-dimensional flow. If the magnitudes of the skin friction velocity and the mean velocity are inserted into the logarithmic law

$$(|\bar{u}|/|u_\tau|) = K^{-1} \ln(y|u_\tau|/\nu) + C \quad (4.4.1)$$

good agreement between measurements and eqn.(4.4.1) was obtained. This statement does not hold for profile 0802 which describes a velocity distribution close to separation where the uncertainties of the skin friction measurement were largest. Although these experiments were performed in a boundary layer with strong three-dimensionality, one could argue that these effects had not enough time to change the turbulence structure and with it the logarithmic law of the wall over a flow length of about four boundary layer thicknesses. Further measurements may therefore be necessary.

Patel(33) investigated the validity of the logarithmic law over a wide range of streamwise pressure gradients in two-dimensional flow and recommended to use the constants  $K = 0.42$  and  $C = 5.45$  (see also (16)). Coles gave a slightly different pair of constants,  $K = 0.40$  and  $C = 5.10$ , which was found to agree well with a large number of velocity distributions (see Fernholz & Finley(34)). We have plotted eqn.(4.4.1) with both pairs of constants for comparison.

Opinions apparently differ in what velocity should be used for the law of the wall in three-dimensional boundary layers, and a few examples are therefore given below.

East & Hoxey(31) suggested  $u = |\bar{u}| \cdot \sin \beta_w$  where  $\beta_w$  is the angle of the limiting streamline, East(32)  $u = |\bar{u}| \cos \varphi$  where  $\varphi$  is the angle of the velocity vector in the external flow, and van den Berg & Elsenäar(35)  $u_\tau$  as the component of the velocity vector in the direction of the wall shear stress. East(32) also remarked that when the cross flow is large the magnitude of the velocity vector should be used.

Finally we discuss briefly measurements performed with surface fences built into the curved wall. Calibration curves and flow angle characteristics of these fences which had a height of about 0.10 mm were described in (3). Measurements with the surface fences agreed satisfactorily with the Preston tube results over most of the boundary layer, with discrepancies ranging from +12 % to about +30 % confined to the last part of the development close to separation. These discrepancies were partly due to the small height of the fences resulting in pressure signals of a few hundredths of a millimeter of water against values ten times larger obtained with the Preston tube.

It may be useful to draw the reader's attention to the rather long response times (more than 15 minutes) which are necessary for flow measurements near the wall.

## 5. LIST OF REFERENCES

- (1) Fernholz H.H., Vagt J.-D., Dziomba B., Dengel P., Messungen in einer dreidimensionalen turbulenten Wandgrenzschicht an einer gekrümmten Wand: Tabellarische Darstellung der Meßwerte. HFI Institutsbericht 01/78.
- (2) Vagt J.D., Bemerkungen zur Auslegung eines Unterschall-Freistrahlgewindkanals. Z.f.W. 21, 159 - 162, 1973.
- (3) Vagt J.D., Fernholz H.H., Use of surface fences to measure wall shear stress in three-dimensional boundary layers. Aeronaut.Quart. XXIV, 87 - 91, 1973.
- (4) Froebel E., Beschreibung und Betriebsanleitung zum Hitzdrahtanemometer HDA III. Interner Bericht DFVLR, 1972.
- (5) Froebel E., A new linearizer unit for hot-wire anemometry. DFVLR. Inst. Turbulenzforschung. Int. Rep., 1969.
- (6) Froebel E., Integrator. Int. Rep. 2/76, DFVLR Berlin, 1976.
- (7) Froebel E., Vagt J.D., Meß- und Auswerteverfahren von Hitzdrahtsignalen mit dem Turbulenzgradmesser, TGM III der DFVLR. DLR-FB 77-61, 1977.
- (8) Froebel E., Vagt J.D., Ein automatisch abgleichendes Flüssigkeitsmanometer mit digitaler Anzeige. DLR-FB 74-40, 1974.
- (9) Dahm A., Vagt J.D., Entwicklung und Herstellung interferenzarmer Hitzdrahtsonden. Institutsbericht 01/77, Hermann-Föttinger Institut f. Thermo- u. Fluidodynamik, TU Berlin, 1977.
- (10) Comte-Bellot G., Strohl A., Alcaez E., On aerodynamic disturbances caused by single hot-wire probes. J.Appl.Mech. 38, Trans.ASME 93 Ser.E., 1971, 767 - 774.
- (11) Strohl A., Comte-Bellot G., Aerodynamic effects due to configuration of x-wise anemometers. J.Appl. Mech. Trans. ASME 95, Ser.E.1973, 661 - 666.
- (12) Bissonnette L.R., Mellor G.L., Experiments on the behaviour of an axisymmetric turbulent boundary layer with a sudden circumferential strain. J.Fluid Mech. 63, 3696 - 413, 1974.
- (13) Guitton D.E., Patel R.P., McGill Univ. MERL Rep. no. 69-7, 1969.
- (14) Vagt J.D., Hot-wire probes in low speed flow. Progr. Aerospace Sci.18, 271 - 323, 1979.
- (15) Oka S., Kostić Z., Influence of wall proximity on hot-wire velocity measurements. DISA-Inf.13, 29 - 33, 1972.
- (16) Hebbbar K.S., Melnik W.L., Measurements in the near-wall region of a relaxing three-dimensional low speed turbulent air boundary layer. Tech.Rep. AE-71-1 University of Maryland, 1976.
- (17) Johnston J.P., Measurements in a three-dimensional turbulent boundary layer induced by a swept forward-facing step. J.Fluid Mech.42, 823 - 844, 1970.

- (18) Elsenaar A., Boelsma S.H., Measurements of the Reynolds stress tensor in a three-dimensional turbulent boundary layer under infinite swept wing conditions. NLR TR 74095 U, 1974.
- (19) Pierce F.J., Ezekwe G.I., Comparison of Reynolds stress diagnostics by fixed and rotating probes. AIAA J. 14, 412 - 414, 1976.
- (20) Wills J.A.B., The correction of hot-wire readings for proximity to a solid boundary. J.Fluid Mech.12, 388 - 397, 1962.
- (21) Van Thin N., Messungen mit einem Hitzdraht in einer turbulenten Strömung in der Nähe einer Wand. DISA Inf. 7, 13 - 18, 1969.
- (22) Orlando A., Turbulent transport of heat and momentum in a boundary layer subject to deceleration, suction and variable wall temperature. Ph.D. thesis, Univ. Microfilms 74-27,073, 1974.
- (23) Rose W.G., Corrections to average measurements in unsteady flow. Proc. ASME Symp. on Measurements in Unsteady Flow. Worcester, Mass. 1962, 85 - 89.
- (24) Dean R.C.jr.(Ed.), Aerodynamic measurements, GAS TURBINE LABORATORY MIT, 1953.
- (25) Vagt J.D., Fernholz H.H., Wall interference effects of static pressure probes in an incompressible turbulent boundary layer. Aeronaut.Quart.XXVII, 1977, 176 - 184.
- (26) Pierce F.J., Krommenhoek D.H., Wall shear stress diagnostics in three-dimensional turbulent boundary layers. Virginia Polytechnic Institute, Interim Tech.Rep.2, 1968.
- (27) Rogers B.K., Head M.R., Measurement of three-dimensional boundary layers. Aeronaut.J.Roy.Aeronaut. Soc.73, 796 - 798, 1969.
- (28) Vermeulen A.J., Measurements of three-dimensional turbulent boundary layers. Ph.D.Dissertation, Univ. Cambridge, 1971.
- (29) McCroskey W.J., Durbin E.J., Flow angle and shear stress measurements using heated films and wires. Trans.ASME J. Basic Eng. 94, 46 - 52, 1972.
- (30) Pierce F.J., Tennant M.H., Rule J.A., Near wall similarity in three-dimensional turbulent flows - experimental systems. Virginia Polytech.College of Eng., Interim Rep. VPI-E-76-16, 1976.
- (31) East L.F., Hoxey R.P., Low speed three-dimensional boundary layer data Pt.1 RAE TR 69047, 1969.
- (32) East L.F., Measurements of the three-dimensional incompressible turbulent boundary layer induced on the surface of a slender delta wing by the leading edge vortex. RAE TR 73141, 1974.
- (33) Patel V.C., Calibration of the Preston tube and limitations on its use in pressure gradients. J.Fluid Mech.23, 185 - 208, 1965.
- (34) Fernholz H.H., Finley P.J., Mean flow data in compressible turbulent boundary layers: a critical survey. To be published by AGARD as AGARDograph 1979/80.
- (35) van den Berg B., Elsenaar A., Measurements in a three-dimensional incompressible turbulent boundary layer in an adverse pressure gradient under infinite swept wing conditions. NLR TR 72092 U, 1972.
- (36) Delleur J.W., Flow direction measurement by hot-wire anemometry. J.Eng.Mech.Div.Proc.Amer.Soc. Civil Engrs.92, 45 - 70, 1966.

## 6. ACKNOWLEDGEMENTS

We acknowledge the assistance of R.Kinns in the design and testing of the slanted-wire probe (Fig.5b) during his stay at the Hermann-Föttinger-Institute of the Technical University while on leave from the University of Cambridge in 1973. Thanks are further due to P.Dengel for his patience and for the suggestions made while measuring some of the data. Financial support was provided by the Deutsche Forschungsgemeinschaft and the Technical University Berlin.

## 7. FIGURES

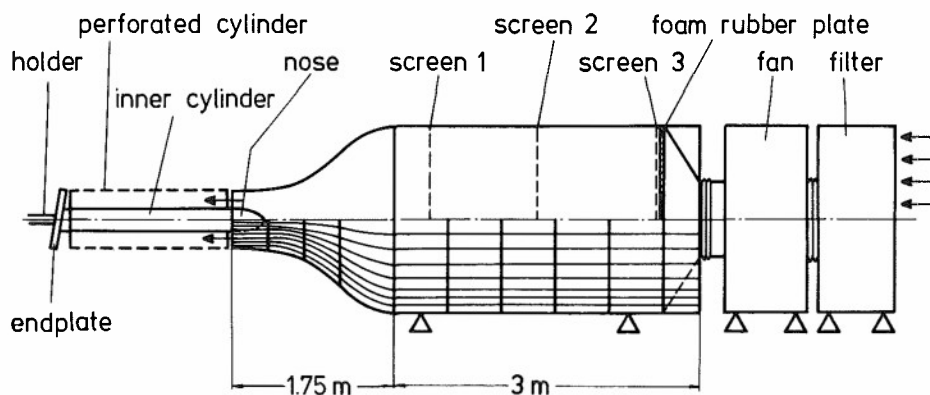


Fig. 1 Test facility



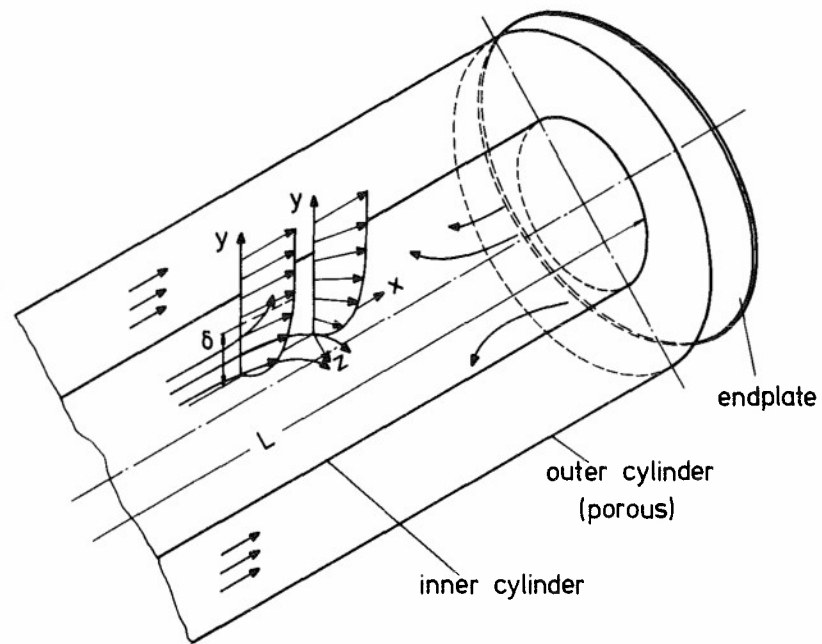
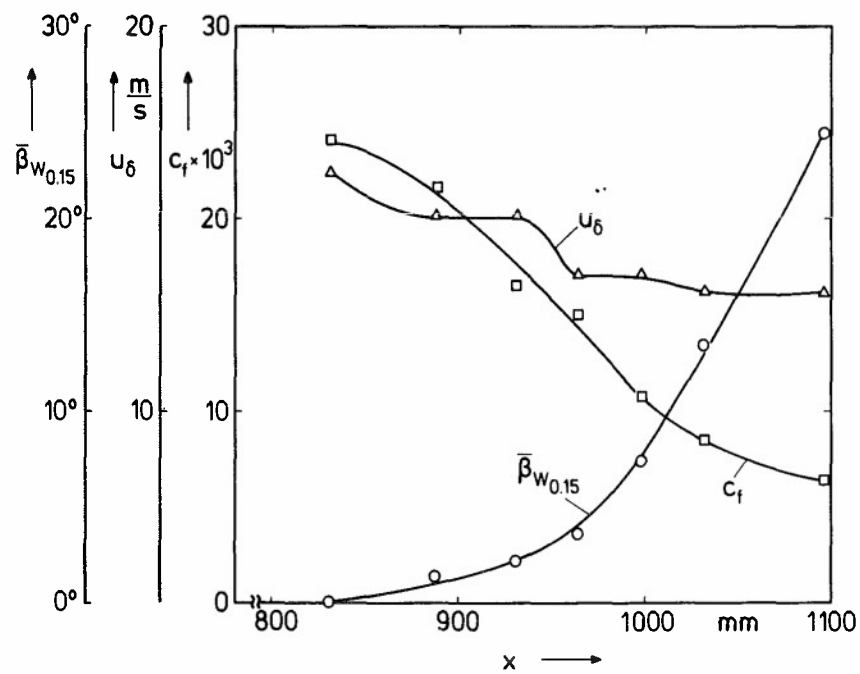


Fig. 2 Flow situation

Fig. 3 Near-wall angle  $\bar{\beta}_{w0.15}$ , skin friction and free-stream velocity  $\bar{u}_\delta$  along one generator of the axisymmetric cylinder in a three-dimensional turbulent boundary layer



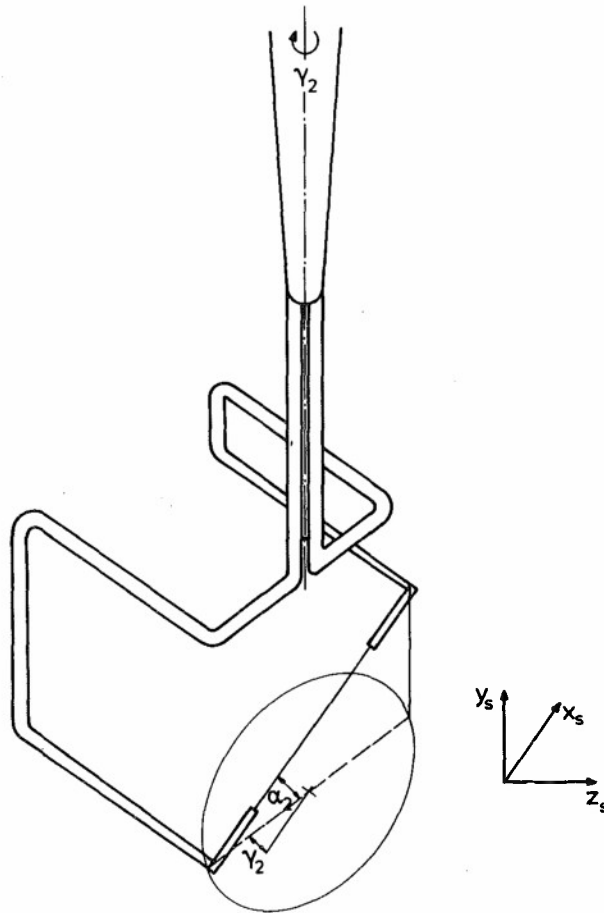


Fig. 5b Rotatable slanted wire for  $\overline{v'w'}$ -measurements

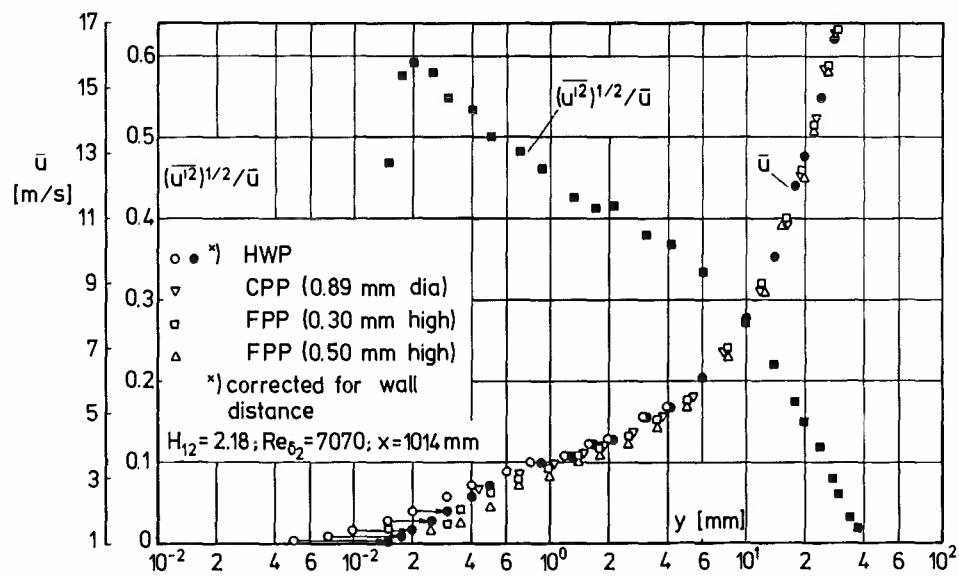


Fig. 6 A comparison between mean velocity measurements obtained by circular (CPP) and flattened (FPP) Pitot probes and a single normal hot-wire probe (HWP) in a boundary layer with a high level of turbulence

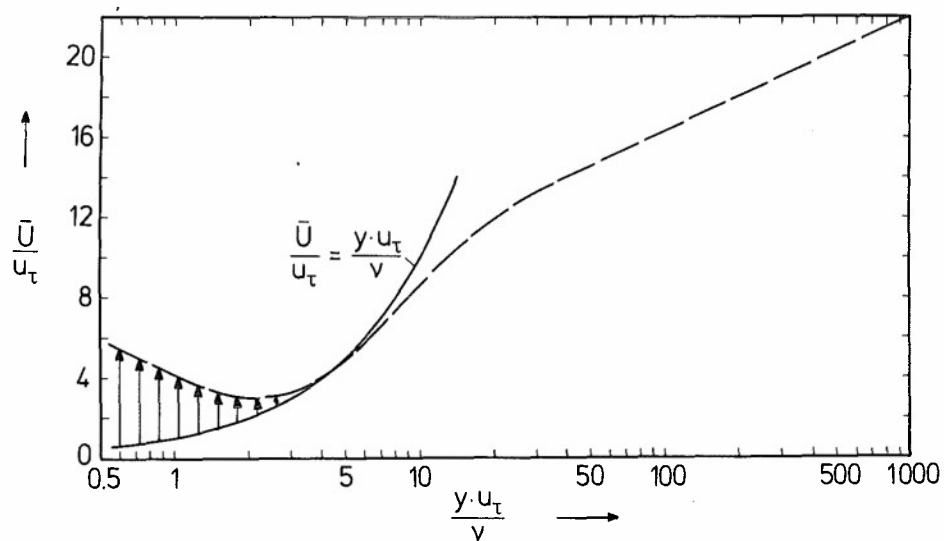


Fig. 7 Dimensionless velocity profiles with cooling effect of the wall (after Oka and Kostić)

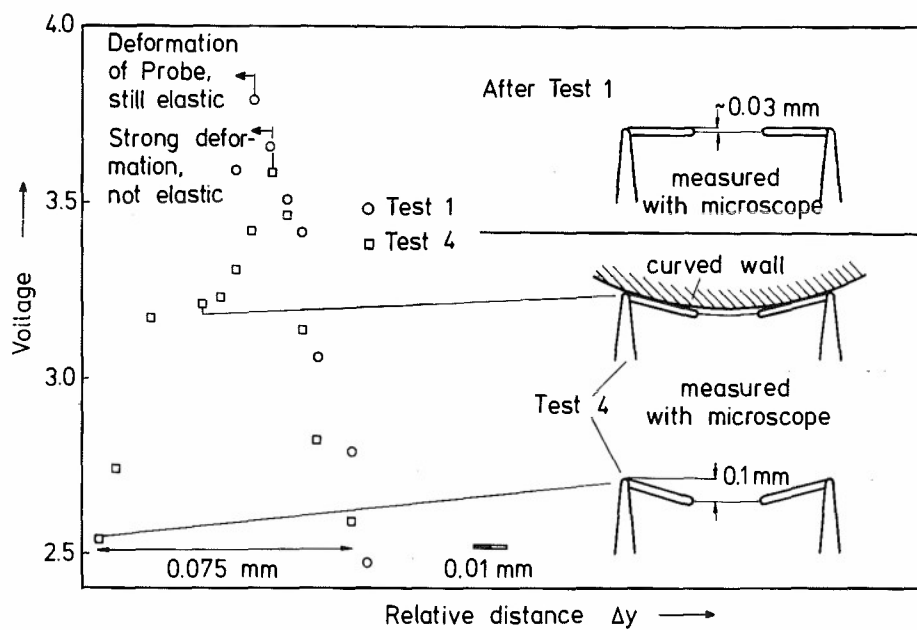


Fig. 8 Hot-wire signal versus relative distance  $\Delta y$  in the near-wall region

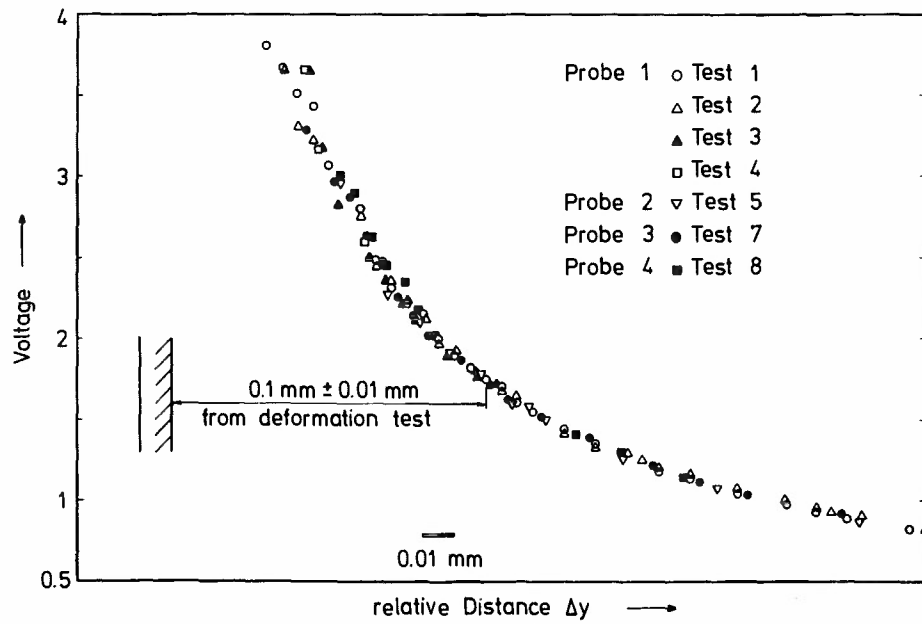


Fig. 9 Hot-wire signal versus relative distance for determination of "absolute" wall distance

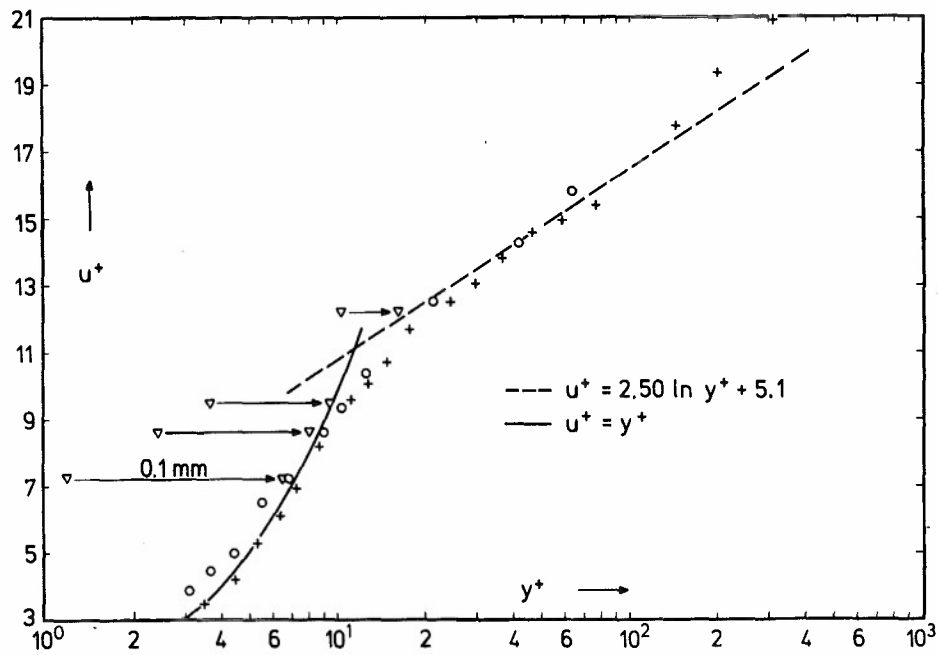


Fig. 10 Comparison between velocity measurements with and without the new wall-distance measuring technique. (Difference in wall-distance  $0.1 \text{ mm}$ !)

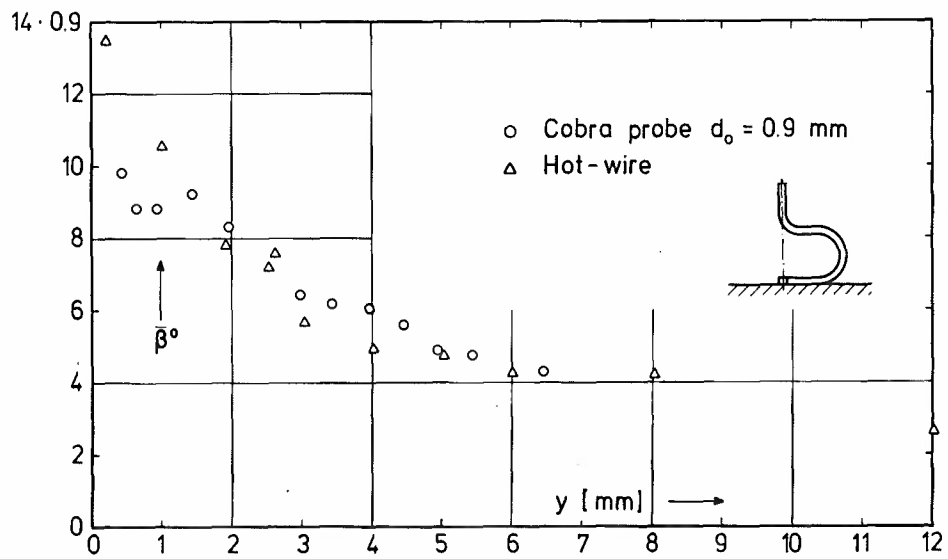


Fig. 11 Flow-angle measurements with a hot-wire and a Cobra probe in a three-dimensional boundary layer (station  $x = 998$  mm)

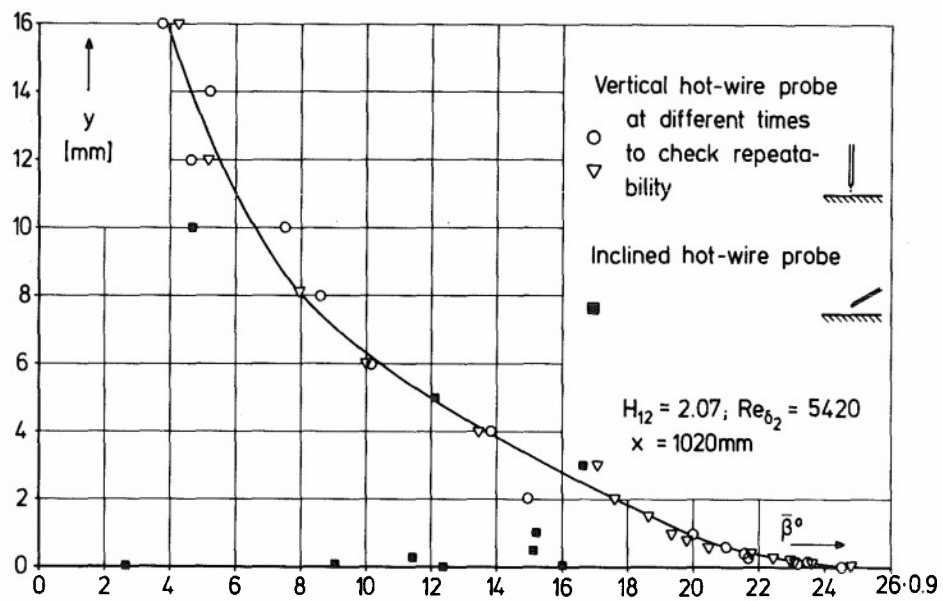


Fig. 12 Flow-angle measurements with a normal and an inclined hot-wire probe in a three-dimensional boundary layer

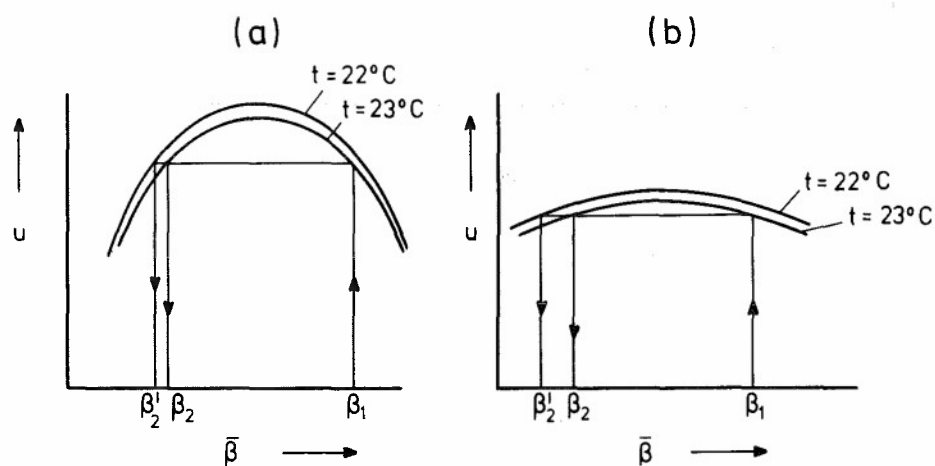


Fig. 13 Flow-angle response characteristic of a hot-wire in the outer region (a) and the near-wall region (b) of a turbulent three-dimensional boundary layer

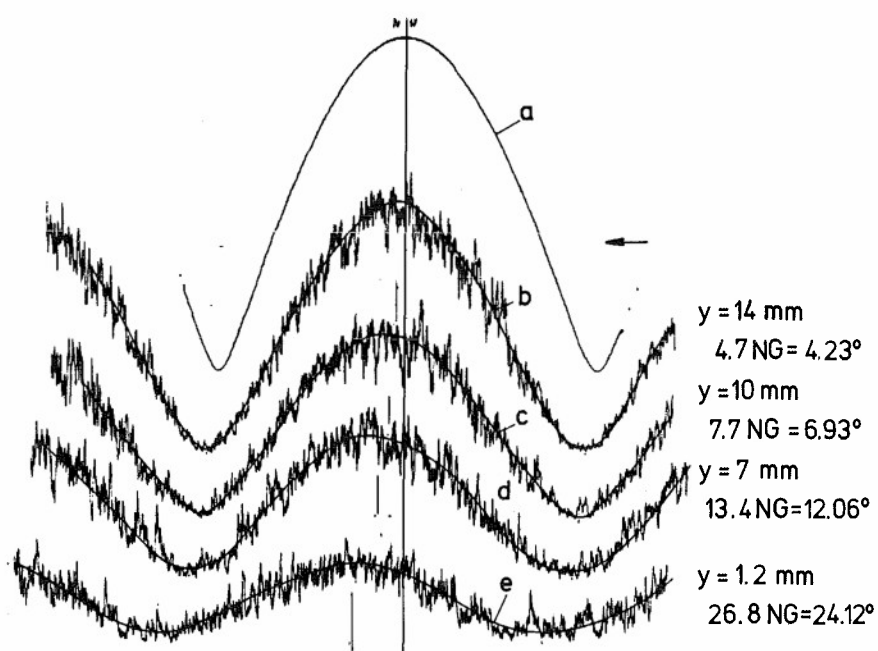


Fig. 14 Flow angle response characteristic in the outer region to demonstrate the minima method

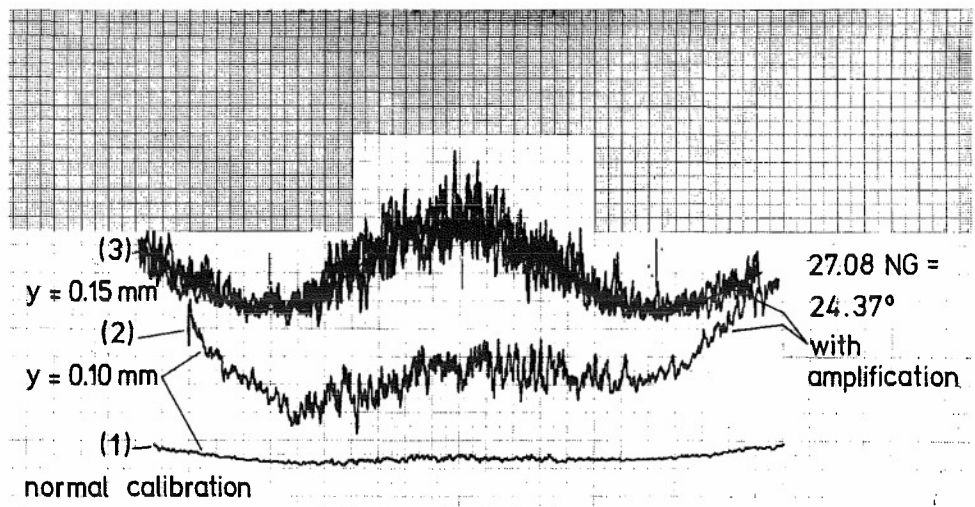


Fig. 15 Flow-angle response characteristic in the near-wall region to demonstrate the minima method

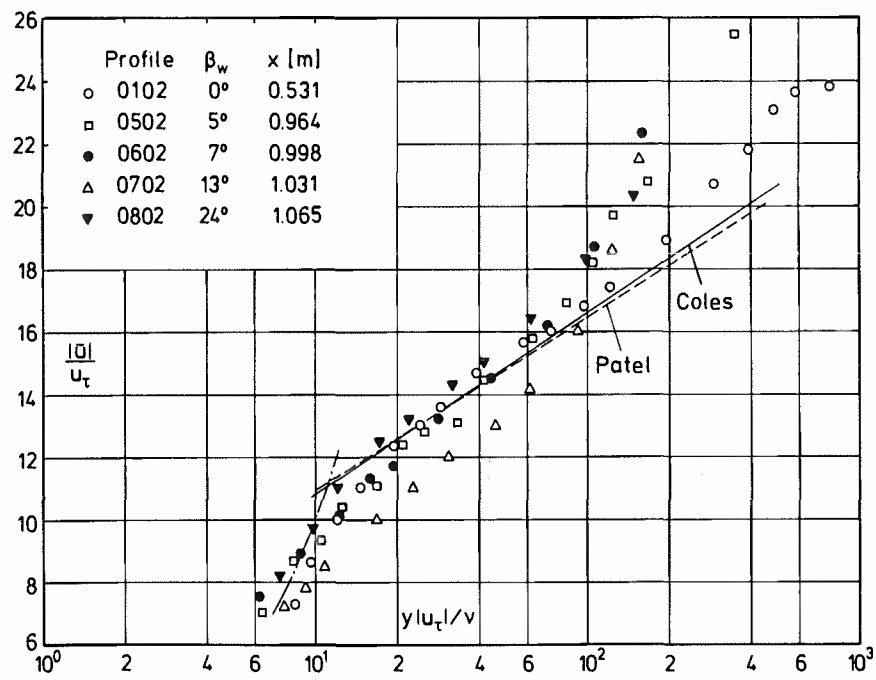


Fig. 16 Logarithmic law for an incompressible three-dimensional turbulent boundary layer with adverse pressure gradient



Measuring device	Dependence on log-law	Measurement of flow direction	Aerodynamic interference effects	Ease of application	"Point" measurement	Calibration
Preston probe	yes	no	included in calibration	good, but static pressure measurements necessary	good ++	universal calibration curve
Combined Preston and Cobra-probe	yes	yes	included in calibration	good	good +-	special calibration curve necessary
Floating element balance	no	yes	no	difficult and expensive	depends on size of element and on sensitivity of balance: +-	calibration necessary
Surface fence	basically no	yes	included in calibration, distance of two fences in flow direction must be $\approx 100$ fence heights	good to difficult	depends on size of element, usually less good than Preston-probe usually: +-	necessary
Hot-film or wire flush-mounted	no	yes	depends on overheat ratio usually: no	good to difficult	depends on size usually: +-	necessary

Table 1 Comparison of methods measuring wall shear stress

## DEVELOPMENTS IN THE COMPUTATION OF TURBULENT BOUNDARY LAYERS

Morris W. Rubesin  
Ames Research Center, NASA, Moffett Field, California 94035, U.S.A.

## SUMMARY

Computational techniques applicable to turbulent boundary layers are classified into solutions of Reynolds-averaged equations, in which all the effects of the turbulence are modelled, and solutions of three-dimensional, time-dependent Navier-Stokes equations, in which the large eddies are calculated and only the turbulence at scales smaller than the computational mesh spacings has to be modelled. Current computation costs place engineering computations in the first of these categories; large eddy simulations are appropriate currently for special studies of the dynamical processes of turbulence in idealized flow fields. It is shown that the two methods are interrelated and that each can gain from advances in the other. The degree of success of a pair of increasingly complex Reynolds stress models to broaden their range of applicability is examined through comparisons with experimental data for a variety of flow conditions. An example of a large-eddy simulation is presented, compared with experimental results, and used to evaluate the models for pressure rate-of-strain correlations and dissipation in the Reynolds-averaged equations.

## NOMENCLATURE

$a$	transverse body radius	$u_i'$	subgrid fluctuating velocity component in $i$ th direction
$C_1$	modelling coefficient in pressure rate-of-strain correlation, turbulence-turbulence interaction (Rotta term)	$u''$	fluctuating velocity in mass-weighted variables
$C_f$	skin-friction coefficient	$v_w$	surface mass-transfer normal velocity
$D_{ij}$	turbulence production tensor, Eq. (37)	$v'$	fluctuating velocity normal to surface
$e$	turbulence kinetic energy	$y$	distance normal to surface
$h$	static enthalpy	$\alpha$	scaling factor in turbulence simulation
$h''$	fluctuating enthalpy in mass-weighted variables	$\hat{\alpha}$	modelling coefficient in pressure rate of strain correlation turbulence mean-flow interaction
$\ell$	length scale	$\beta$	modelling coefficient, Eq. (31), or scaling factor in turbulence simulation
$\ell_m$	mixing length	$\beta^*$	modelling coefficient, Eq. (31)
$P_{ij}$	turbulence production tensor, Eq. (37)	$\hat{\beta}$	modelling coefficient in pressure rate of strain correlation - turbulence mean-flow interaction
$Pr_L$	Prandtl number for molecular motions	$\gamma$	modelling coefficient, Eq. (31)
$p^*$	mean specific static pressure	$\gamma^*$	modelling coefficient, Eq. (31)
$p$	static pressure	$\hat{\gamma}$	modelling coefficient in pressure rate of strain correlation - turbulence mean-flow interaction
$p^*$	specific static pressure, $p/\rho$	$\delta$	boundary-layer thickness
$\tilde{p}^*$	resolvable fluctuating specific static pressure	$\delta_{ij}$	Kronecker delta
$p^{*'}_i$	subgrid fluctuating specific static pressure	$\epsilon$	eddy viscosity (turbulence kinematic viscosity)
$Q_j$	heat flux vector	$\epsilon$	turbulence kinetic energy dissipation rate
$q$	turbulence speed	$\epsilon_{ij}$	dissipation rates of Reynolds stress component $\tau_{ij}$
$Re$	modelling coefficient, near-wall modification, Eq. (31)	$\iota$	boundary-layer edge turbulence intensity factor
$Re_T$	turbulence Reynolds number, Eq. (32)	$\lambda$	low Reynolds number modelling coefficient, Eq. (31)
$R_w$	modelling coefficient, near wall modification, Eq. (31)	$\mu$	fluid viscosity
$S_{ij}$	rate of strain tensor	$\nu$	fluid kinematic viscosity
$U_i$	mean velocity component in $i$ th direction	$\nu_{eff}$	effective eddy viscosity in subgrid model
$u_i$	velocity component in the $i$ th direction, mass-weighted in compressible flows	$\rho$	fluid density
$\tilde{u}_i$	resolvable fluctuating velocity component in $i$ th direction	$\tilde{\rho}$	instantaneous fluid density
		$\sigma$	modelling coefficient, Eq. (31)

$\sigma^*$	modelling coefficient, Eq. (31)	$( )_{,i}$	a partial derivative with respect to the $i$ th coordinate
$\tau_{ij}$	Reynolds stress component		
$\Omega_{ij}$	vorticity tensor	Superscripts:	
$\omega$	turbulence specific dissipation rate	T	total quantity, turbulent plus molecular process
Subscripts:		$(\dot{\phantom{x}})$	partial derivative with respect to time
e	boundary-layer edge condition or experimental value	Other:	
w	surface quantity	$\langle \phantom{x} \rangle$	filtered average
1,2,3	Cartesian axes direction	$(\bar{\phantom{x}})$	time averaged

## INTRODUCTION

Advances in computer technology and numerical analysis during the past decade have made it possible to compute the characteristics of turbulent flow fields with a degree of detail that was impossible in the past. This computational power has been applied to problems both in engineering and in basic fluid mechanics. Engineering methods have been confined largely to the solution of statistical equations of turbulence, usually for steady-state conditions. The increased computational power has permitted the use of second-order closure methods wherein partial differential equations are used to describe the scales, intensity, and even the individual components of Reynolds stresses distributed throughout the flow field. It is becoming quite standard in advanced engineering problems to use two-equation models representing the transport of turbulence kinetic energy and a measure of the turbulence scale to establish the local eddy viscosity. The underlying impetus to this work has been the premise that the increased complexity of a model tends to broaden its range of applicability, thereby making it a predictive tool. The past simple models of statistical turbulence, such as the mixing-length models, largely were used to explain flow-field behavior after the experimental results were obtained; they could be used only to interpolate between or moderately extrapolate conditions of a particular experiment. New situations required new experiments to guide modelling changes. With the more detailed second-order closure models, however, the rather large number of experimental coefficients employed requires drawing upon experiments of different kinds of flow fields for evaluating the modelling coefficients of the different mechanisms. For example, the coefficient for the dissipation of turbulence kinetic energy is determined in part from experiments dealing with the decay of isotropic turbulence. Coefficients for terms representing the exchange between individual components of Reynolds stress by the correlation of fluctuations in pressure and the instantaneous rate of strain come largely from experiments in homogeneous turbulence created by either uniform shearing or normal strains. Thus, when these models are used in boundary-layer flows, many of their terms reflect the behavior of turbulence under other conditions, thereby possibly broadening the model's range of applicability. On the other hand, this reliance on a group of different kinds of experiments to establish the modelling coefficients often results in a somewhat less accurate representation of a particular flow field than is provided by a fine-tuned, simple empirical model. Engineers working continuously with certain kinds of flow fields tend to fine-tune the second-order models as well, without (it is hoped) losing too much of the generality potential within the model.

Perhaps an even more important application of the powerful computation tools available today has been in the rather new field of the numerical simulation of the large eddies of turbulence. In these calculations, the three-dimensional and time-dependent character of the turbulent flow fields is retained. The principal approximations involved in these methods is in the manner of accounting for the scales of turbulence that are too small to be resolved, even in the largest of the computers, for the time-dependent and spatially-dependent boundary conditions, and for the initial field of the turbulence. Because the initial and boundary conditions involve so many degrees of freedom, it cannot be expected that individual computational realizations will be significant or even realistic. What can be expected or at least hoped for is that the results of the computations viewed statistically will accurately reflect the highly nonlinear mechanisms that govern the dynamics of the flows.

The computations, to date, have shown much promise but they need considerable development; moreover, they are much too costly to be considered as engineering tools. They are invaluable, however, as a technique for the study of fluid mechanics in that they yield a mass of information about a flow field that experiments involving discrete numbers of probes cannot possibly provide. The numerical analyst — when faced with making the choices necessary for starting his problem, the ranges of scales he is to examine, and the techniques of accounting for the subgrid scales — is forced to consider the details of turbulence that modelers of statistical turbulence have had to ignore. The apparent turbulence that numerical instabilities or bifurcations can create forces the serious worker in turbulence simulation to continually compare his numerical results with experimental data for similar flow fields. Because of the mass of detail contained within the calculations, where for example any statistical moment can be generated, it is often found that even the classic experiments lack data that unambiguously define the turbulence that was present.

The purpose of this paper is to demonstrate that both methods of turbulence computation have much in common and that they are distinguished primarily by the fraction of the turbulence that is chosen to be modelled. The statistical methods model all of the turbulence, ignoring most of the scale and all of the phase character of the actual turbulence. The large eddy simulations compute the actual physical character of the larger scales of the turbulence and model only those scales of turbulence smaller than the computational mesh dimensions. The fraction of turbulence the subgrid model represents depends largely on the local turbulence Reynolds number and on the number of mesh points that the computer can handle.

In the present discussion, the two methods are interrelated; a review is given of the success or failure of a pair of second-order closure methods to model the statistical properties of a variety of turbulent flow

fields, without adjustment of modelling constants; and some examples of large eddy simulations for simply strained homogeneous turbulent flow fields are presented and compared with data. Examples of statistical model information that can be gained from these computations is shown. Finally, a plea is made for coordinated experiments and large eddy simulations, which together should prove to be most valuable in explaining the physics of turbulence under a variety of flow conditions.

## TURBULENT FLOW EQUATIONS

In the analysis of turbulent motions, it is generally believed that the basic physics of the fluid flow is contained within the Navier Stokes equations. Since these same equations apply at a point in space and time for both laminar and turbulent motions, the distinction between these types of flows arises from the initial and boundary conditions the flows experience and from their response to small disturbances that are always present in real flow fields. This response is largely dependent on the Reynolds number of the flow. The properties of turbulence, then, are the consequence of the fluid instabilities that occur at high Reynolds number and the subsequent nonlinear, apparently chaotic, mixing processes that take place. It is these nonlinear processes that produce a broad range of length scales of motion within the turbulent flow and this, in turn, affects finite difference computations greatly.

The length scales range from those comparable to the characteristic dimensions of the apparatus down to those where the turbulent motions have largely been dissipated by viscosity into heat. Even the largest available computers fall far short of being able to resolve such a broad range of scales for flow fields of technological interest. Although the prospects of increasing the resolution of the turbulence scale with future computers is good (Ref. 1), it is not expected that it will be possible to compute the smallest dissipation scales, at Reynolds numbers of interest, in the reasonably near future.

A variety of turbulence models has been developed to account for these small irresolvable subgrid scales. These models have a great deal in common with the models for Reynolds stresses in statistical turbulence theory. This is demonstrated in this section through the equations for an incompressible fluid that describe the small scales of turbulence and their effect on the larger scales and the mean flow.

The instantaneous motion of an incompressible, viscous fluid is described by the continuity and Navier-Stokes equations

$$u_{j,j} = 0 \quad (1)$$

and

$$\dot{u}_i + (u_i u_j + \delta_{ij} p^* - \nu u_{i,j}),j = 0 \quad (2)$$

where

$$p^* = p/\rho \quad (3)$$

The instantaneous, local velocity can be expressed as the sum of three components: the time mean velocity; the sum of the fluctuating turbulence components whose length scales can be resolved by the finite-difference computational scheme; and the sum of those fluctuations too small to be resolved, namely

$$u_i = U_i + \tilde{u}_i + u_i' \quad (4)$$

The other dependent variable, the pressure, can also be resolved in a similar manner

$$p^* = P^* + \tilde{p}^* + p^{*'} \quad (5)$$

To convert Eqs. (1) and (2) to contain only resolvable dependent variables, it is necessary to average them or filter them in some manner. For the purposes at hand, it is not necessary to define the filtering process precisely. It can represent a weighted average over a line in space, a surface, a volume, or even a characteristic time comparable to the time scales of the small length scales of turbulence. The filtering process, represented by the symbol  $\langle \rangle$ , will be defined in such a way as to accomplish the following:

$$\left. \begin{aligned} \langle u_i' \rangle &= 0 \\ \langle \tilde{u}_i \rangle &= \tilde{u}_i \\ \langle U_i \rangle &= U_i \\ \langle u_i' U_j \rangle &= 0 \\ \langle u_i' \tilde{u}_j \rangle &= 0 \\ \langle u_{i,j} \rangle &= \langle u_i \rangle_{,j} \end{aligned} \right\} \quad (6)$$

Note that the fourth and fifth definitions in (6) imply that the two scales of turbulence are uncorrelated over the filter domain and that the domain is small compared to the scales of the mean motion. Leonard (Ref. 2) has demonstrated the limitations of these assumptions, but the simplicity resulting from them is attractive for the present development.

With Eq. (4), Eq. (1) becomes

$$U_{j,j} + \tilde{u}_{j,j} + u_{j,j}' = 0 \quad (7)$$

When filtered according to Eq. (6), Eq. (7) reduces to

$$U_{j,j} + \tilde{u}_{j,j} = 0 \quad (8)$$

When Eq. (8) is time-averaged in the Reynolds sense, that is,

$$\bar{f} = \lim_{T \rightarrow \infty} \frac{1}{T} \int_0^T f(t) dt \quad (9)$$

there results

$$U_{j,j} = 0 \quad (10)$$

Of course, subtracting Eq. (10) from Eq. (8), and Eq. (8) from Eq. (7) yields

$$\tilde{u}_{j,j} = 0 \quad (11)$$

and

$$u'_{j,j} = 0 \quad (12)$$

Similar operations of filtering and time-averaging on the Navier-Stokes equations (Eq. (2)) yield the following forms of the momentum equation. The mean-momentum equations are

$$U_j U_{i,j} = -\delta_{ij} p^*_{,j} + \nu U_{i,j,j} - (\bar{u}_i \bar{u}_j + \overline{u'_i u'_j})_{,j} \quad (13)$$

The momentum equations for the resolvable turbulence scales needed to evaluate the  $\tilde{u}_i$  in Eq. (13) are

$$\dot{\tilde{u}}_i + U_j \tilde{u}_{i,j} = -\delta_{ij} \tilde{p}^*_{,j} + \nu \tilde{u}_{i,j,j} - \tilde{u}_j U_{i,j} - (\tilde{u}_i \tilde{u}_j - \overline{\tilde{u}_i \tilde{u}_j})_{,j} - (\langle u'_i u'_j \rangle - \overline{\langle u'_i u'_j \rangle})_{,j} \quad (14)$$

The equations for the instantaneous values of the filtered moments of the subgrid scales, themselves at resolvable scales, can be expressed as

$$\begin{aligned} \langle u'_i u'_k \rangle + (U_j + \tilde{u}_j) \langle u'_i u'_k \rangle_{,j} = & -\langle u'_k u'_j \rangle (U_i + \tilde{u}_i)_{,j} - \langle u'_i u'_j \rangle (U_k + \tilde{u}_k)_{,j} \\ & - \langle u'_i u'_k u'_j \rangle_{,j} - \langle u'_k p^*_{,i} \rangle - \langle u'_i p^*_{,k} \rangle \\ & + \nu \langle u'_i u'_k \rangle_{,j,j} - 2\nu \langle u'_i u'_{k,j} u'_{i,j} \rangle \end{aligned} \quad (15)$$

An equation for the subgrid turbulence kinetic energy, defined as

$$\langle q^2 \rangle = \langle u'_i u'_i \rangle \quad (16)$$

follows from the trace of Eq. (15):

$$\begin{aligned} \langle \dot{q}^2 \rangle + (U_j + \tilde{u}_j) \langle q^2 \rangle_{,j} = & -2\langle u'_i u'_j \rangle (U_i + \tilde{u}_i)_{,j} - \langle u'_j (2p^*_{,i} + q^2) \rangle_{,j} \\ & + \nu \langle q^2 \rangle_{,j,j} - 2\nu \langle u'_i u'_{i,j} u'_{i,j} \rangle \end{aligned} \quad (17)$$

Equation (13) shows that the influence on the mean motion of the two scales of turbulence is through the sum of two Reynolds stresses, each associated with the different scales. In statistical turbulence theory, the different scales of turbulence are ignored by summing these Reynolds stresses into a single stress which is then modelled. Thus, all the effects of the turbulence on the mean motion are modelled. In large eddy simulations, however, the  $\tilde{u}_i$  are calculated as functions of time and in three dimensions and the corresponding large eddy Reynolds stresses are then computed through time averaging. (Actually, most large eddy simulations compute the sum of  $U_i$  and  $\tilde{u}_i$ , but in principle the mean flow is affected as stated.) Only the small scales are modelled and their influence is felt on the mean flow through the Reynolds stresses they contribute and in their effect on the larger scales of the turbulence. As the larger fraction of the turbulence spectrum is computed, less reliance has to be placed on contributions of the turbulence model. A mechanism exists, then, for converging on the correct statistical description of turbulence through a systematic increase in the fraction of the resolved turbulence scales. It is not clear, to date, how the quality of the subgrid turbulence model affects this convergence rate and actually how many scales of the large eddies require computation to provide a good description of the turbulence transport mechanism in a variety of flow fields. Another apparent advantage of the method of large eddy simulations is based on the optimism regarding the generation of a universal subgrid model. This optimism reflects the experimental evidence that the small scales of turbulence in a variety of flow fields exhibit similar spectral characteristics when scaled in the Kolmogorov sense.

Equation (14) illustrates the influence of the mean flow and the subgrid turbulence scales on the resolvable scales of the turbulence. It shows that the growth of the resolvable turbulence along a mean streamline is acted on by the turbulence pressure and viscous diffusion in the same manner that the corresponding terms act in the mean flow. The additional last three terms represent the interactions between the resolvable turbulence and the mean flow, the components of the resolvable turbulence, and the subgrid scales of the turbulence. It is the latter terms that must be modelled to close the calculation of the resolvable scales.

Incidentally, these calculations must be performed in three dimensions and in time for each component of the resolvable turbulence; it is a rather costly process on today's computers.

Equations (15) and (17) provide insight into the modelling of the subgrid turbulence scales needed to "close" Eqs. (13) and (14). When either Eq. (15) or Eq. (17) for the subgrid scale moments is compared with the equations representing the Reynolds stresses or kinetic energy in a statistical turbulence formulation, it is noted that they have essentially the same form except that the mean flow in the statistical equations has been replaced by the instantaneous large-scale motions, and the subgrid-scale moments have a time dependence. This strong similarity between the subgrid-moment equations and the Reynolds stress equations suggests that much of the experience gained with statistical modelling procedures eventually will be able to be applied to subgrid modelling. At present, the limitations of computer storage encourage use of the simplest of subgrid models, analogous to the first-order closure methods, such as constant eddy diffusivities or mixing-length models in statistical Reynolds stress methods. Equations (15) and (16), however, suggest that second-order closure methods applied in statistical methods over the past decade will have a role in subgrid closure as well. Computer limitations and costs, also, will restrict large-eddy simulation in the near future to simple flow fields. The results, however, will provide considerable insight into the physics of turbulence and will contribute to modelling of the statistical equations. Some preliminary studies of the latter are given later in this paper.

## STATISTICAL TURBULENCE MODELLING

Since the 1968 Stanford conference on the computation of turbulent boundary layers (Ref. 3), statistical turbulence modelling for engineering applications has gone in two directions. The first has been the fine tuning of first-order closure methods, involving algebraic mixing-length models. This was accomplished by fitting the models to well-defined experiments with attached boundary layers experiencing pressure gradients and/or surface mass transfer. References 4 and 5 are examples of this approach. Although these methods yield excellent representations of the data within their range of application, their abilities to extrapolate beyond the ranges of the experiments that form their basis is questionable. Any introduction of additional length scales into the boundary-layer characteristics, such as a transverse radius of curvature comparable to the boundary-layer thickness or an injection slot dimension, requires considerable remodelling of the length scales. In the absence of experimental guidance, this remodelling has to be based on ad hoc assumptions. Further, in flow fields where changes in the mean flow are rapid, the assumption inherent in most first-order closure methods, that the turbulence remains in equilibrium with the mean flow, may not be true. The recognition of these limitations of first-order closure methods has led to considerable work in the second direction, namely second-order closure methods, where one or more of the characteristics of turbulence is represented by a partial differential transport equation. These methods are based largely on the concepts presented in the pioneering papers by Kolmogorov (Ref. 6), Chou (Ref. 7), and Rotta (Refs. 8,9). As explained in the Introduction, the impetus behind the development of second-order closure methods was the belief that they have the potential of a broad range of applicability and may, with further development, become predictive tools in engineering computations.

An ideal predictive turbulence model would be one that could remain unaltered in form and in its empirical coefficients for all flow fields. It is questionable, however, that such an ideal universal model can be achieved within the framework of statistical models, even when allowance is made for acceptable engineering error. Such models inherently ignore spectral and phase relationships between eddies of different sizes. The larger eddies in a turbulent flow are known to reflect the particular nature of the flow and this alone is sufficient to raise doubts regarding the potential universality of statistical models. Of course, zonal turbulence models that differ from flow to flow but can be related to some particular mean flow feature are also of value to the design engineer; they may be the best that can be expected of statistical models. Such zonal models, however, introduce mathematical difficulties in the identification of the bounds of different zones of applicability of the individual models, and the means of coupling the interaction between these zones. It is much easier to deal with the same model throughout the flow. In view of this, it would be illuminating to learn how well or how poorly a fixed model could work on a variety of boundary-layer flows. To demonstrate this, calculations based on a pair of fixed second-order closure models will be compared here with data from a variety of experiments.

The particular models chosen for this comparison have been developed for the most part by Wilcox and Traci (Ref. 10) with some collaboration by the present author (Ref. 11), and were an outgrowth of the early work of Saffman (Ref. 12). One model uses an eddy viscosity, which is dependent on the kinetic energy of turbulence and the dissipation rate per unit of kinetic energy (a specific dissipation rate or Saffman's "pseudovorticity"). The other model closes the Reynolds stress equations directly, with the scale of turbulence again being defined with the specific dissipation rate. In choosing these models for comparison here, the author does not wish to imply that he believes them to be the best of the second-order closure methods available today to represent boundary-layer flows. In some respects, the models developed by Launder and his colleagues (Refs. 13,14) are more general and represent the mean flow very close to a surface in a more realistic manner (Refs. 14,15). On the other hand, computations of some compressible flow fields with two-equation models favor the Wilcox-Rubesin model (Ref. 11). It is not clear at present which, if any, existing model will be most uniformly valid for all applications. The primary reason for presenting models in which the author was involved was his access to computer codes containing them; as a result, the codes could be used to generate the examples that follow. Also, since both of these models and those identified with Launder utilize essentially the same data to establish their modelling coefficients, it should not make much difference in the examination of the universality of second-order closure modelling of boundary-layer flows which family of models is employed.

## Mean Flow Equations and Boundary Conditions

The mean flow equations used in computing the examples that will be treated later are written for a compressible fluid in mass-weighted-average dependent variables (Ref. 16). The conservation equations for mass, momentum, and energy are as follows:

$$\dot{\rho} + (\rho u_j)_{,j} = 0 \quad (18)$$

$$(\rho \dot{u}_i) + (\rho u_j u_i)_{,j} = -p_{,i} + (\rho \tau_{ij}^T)_{,j} \quad (19)$$

$$(\rho \dot{h}) + (\rho u_j h)_{,j} = \dot{p} + u_j p_{,j} + \rho \tau_{ij}^T u_{i,j} - (\rho Q_j^T)_{,j} \quad (20)$$

Here, the symbols  $\tau_{ij}^T$  and  $Q_j^T$  denote the specific mass-weighted-average total shear stress and heat flux that include the contributions of both the molecular and turbulent transport. These quantities are defined as

$$\tau_{ij}^T = 2\nu S_{ij} - \frac{1}{3} u_{k,k} \delta_{ij} + \tau_{ij} \quad (21)$$

and

$$Q_j^T = -\frac{\nu}{Pr_L} h_{,j} + Q_j \quad (22)$$

the mean rate of strain tensor in Eq. (21) is

$$S_{ij} = \frac{1}{2} (u_{i,j} + u_{j,i}) \quad (23)$$

Finally,  $\tau_{ij}$  and  $Q_j$  are the mass-weighted-averaged Reynolds stress tensor and heat flux vector defined by

$$\left. \begin{aligned} \tau_{ij} &= -\frac{\langle \tilde{\rho} u_i'' u_j'' \rangle}{\rho} \\ Q_j &= \frac{\langle \tilde{\rho} u_j'' h'' \rangle}{\rho} \end{aligned} \right\} \quad (24)$$

where  $\tilde{\rho}$  is the instantaneous density,  $\langle \theta \rangle$  denotes the time average of  $\theta$ , and  $\theta''$  is the fluctuating part of  $\theta$  in mass-weighted-average formulation. The surface boundary conditions for Eqs. (18) to (20) are:

at  $x_2 = 0$

$$\left. \begin{aligned} u_1 &= 0 \\ u_2 &= 0 \text{ or } v_w(x_1) \\ h &= h_w(x_1) \text{ or } (\partial h / \partial x_2) = (\partial h / \partial x_2)_w \end{aligned} \right\} \quad (25)$$

All flow variables approach free-stream flow conditions in general flow-field computations. For the special case of two-dimensional boundary layers, boundary conditions at the boundary-layer edge are

at  $x_2 = \delta(x_1)$

$$\left. \begin{aligned} u_1 &= U_e(x_1) \\ h &= h_e(x_1) \end{aligned} \right\} \quad (26)$$

The two models used to close these equations are given in the following sections.

#### Two-Equation Eddy-Diffusivity Model

The two-equation model considered here utilizes an eddy diffusivity defined as

$$\epsilon = \gamma^* e / \omega \quad (27)$$

where the turbulence kinetic energy  $e$  and specific dissipation rate  $\omega$  are given by the turbulence modeling equations:

$$(\rho \dot{e}) + (\rho u_j e)_{,j} = \rho \tau_{ij} u_{i,j} - \beta^* \rho \omega e + [(\mu + \sigma^* \rho \epsilon) e k_j]_{,j} \quad (28)$$

and

$$(\rho \dot{\omega}^2) + (\rho u_j \omega^2)_{,j} = \gamma \frac{\omega^2}{e} \rho \tau_{ij} u_{i,j} - [\beta + 2\sigma(\ell_k \ell_k)] \rho \omega^3 + [(\mu + \sigma \rho \epsilon) (\omega^2)_{,j}]_{,j} \quad (29)$$

To account for compressibility, all the dependent variables are expressed as mass-weighted averages (Ref. 16). The length scale is represented by

$$\ell = \frac{e^{1/2}}{\omega} \quad (30)$$

The modelling closure coefficients employed are as follows

$$\left. \begin{aligned} \beta &= 3/20, \beta^* = 9/100, \sigma = \sigma^* = 1/2 \\ \gamma^* &= [1 - (1 - \lambda^2)\exp(-Re_T/R_e)] \\ \gamma\gamma^* &= \gamma_\infty [1 - (1 - \lambda^2)\exp(-Re_T/R_\omega)] \\ \gamma_\infty &= 10/9, \lambda = 1/11, R_e = 1, R_\omega = 2 \end{aligned} \right\} \quad (31)$$

The Reynolds number of turbulence is given by

$$Re_T = \frac{e^{1/2} \ell}{\nu} \quad (32)$$

The boundary conditions appropriate to these modelling equations, when they are applied to boundary layers, have been guided by asymptotic analysis and reference to other models. The surface boundary conditions for Eqs. (19) and (20) are as follows:

at  $x_2 = 0$

$$\left. \begin{aligned} e &= 0 \\ \omega &\rightarrow \frac{20 \nu_W}{\beta x_2^2} \end{aligned} \right\} \quad (33a)$$

at  $x_2 = \delta(x_1)$

$$\left. \begin{aligned} e &= \nu e^2(x_1) \\ \ell &= 0.09 \beta^{*1/4} \delta(x_1) \end{aligned} \right\} \quad (33b)$$

As the quantity  $\ell/\beta^{*1/4}$  behaves much like the classical mixing length, the proportionality coefficient of 0.09 in Eq. (19) is readily seen to be consistent with the Escudier eddy-viscosity model (Ref. 17).

Since it was desired to model Reynolds stresses that do not necessarily align with the mean rates of strain, the constitutive relationship relating these quantities was written as

$$\tau_{ij} = \frac{2}{3} e \delta_{ij} + 2\epsilon \left( S_{ij} - \frac{1}{3} u_{k,k} \delta_{ij} \right) + \frac{8}{9} \frac{e}{(\beta^* \omega^2 + 2S_{mn}S_{nm})} (S_{im}\Omega_{mj} + S_{jm}\Omega_{mi}) \quad (34)$$

where the third term on the right was guided by the work of Saffman (Ref. 18). The vorticity tensor used here is defined as

$$\Omega_{ij} = \frac{1}{2} (u_{i,j} - u_{j,i}) \quad (35)$$

and the mean rate of strain is given by Eq. (23).

#### Reynolds Stress Equation Model

The modelling in the Reynolds stress equations (RSE) presented here utilizes (1) a particular version of the pressure rate-of-strain correlation presented by Launder et al. in Ref. 14, (2) gradient diffusion for third-order correlations involving velocity and pressure, and (3) isotropic dissipation. Following Launder et al., the pressure rate-of-strain correlation is represented as

$$\overline{p(u_{i,j} + u_{j,i})} = C_1 \beta^* \omega \left( \tau_{ij} + \frac{2}{3} \delta_{ij} e \right) - \hat{\alpha} \left( p_{ij} - \frac{2}{3} p \delta_{ij} \right) - \hat{\beta} \left( D_{ij} - \frac{2}{3} p \delta_{ij} \right) - \hat{\gamma} e S_{ij} \quad (36)$$

where the first term on the right, called the Rotta term, is proportional to the anisotropy of the turbulence. The terms preceded by the modelling coefficients  $\hat{\alpha}$ ,  $\hat{\beta}$ , and  $\hat{\gamma}$  are contributed by the interaction of turbulence and mean flow expressed in terms of

$$\left. \begin{aligned} p_{ij} &= \tau_{ik} u_{j,k} + \tau_{jk} u_{i,k} \\ D_{ij} &= \tau_{ik} u_{k,j} + \tau_{jk} u_{k,i} \\ p &= \frac{1}{2} p_{ij} = \frac{1}{2} D_{ii} = \tau_{mn} S_{nm} \end{aligned} \right\} \quad (37)$$

In choosing the values of  $\hat{\alpha}$ ,  $\hat{\beta}$ ,  $\hat{\gamma}$ , Wilcox and the author opted to rely on experimental data rather than the symmetry arguments recommended by Rotta (Ref. 8) and carried out by Launder et al. (Ref. 14). The first experimental observation employed was that

$$\tau_{33} \approx \frac{1}{2} (\tau_{11} + \tau_{22}) \quad (38)$$



when a homogeneous turbulent flow is equally stretched in the  $x_1$  direction and compressed in the  $x_2$  direction, which by continuity in an incompressible fluid leaves the  $x_3$  direction unstrained (Ref. 19). The second observation was that a field of homogeneous turbulence in rigid body rotation decays without developing anisotropy (Ref. 20). The latter data forces  $\hat{\alpha} = \hat{\beta}$ . The remaining constants are evaluated, after representative values of  $\tau_{22}/\tau_{11}$  and  $\tau_{12}/e$  are established from data in a homogeneous shear flow or in the law-of-the-wall region of a flat-plate boundary layer. The model used here was based on the approximate relationships  $\tau_{22}/\tau_{11} \approx 1/2$  and  $\tau_{12}/e = 0.3$ , both of which are consistent with the form of the two-equation model in shear flow. Further remarks regarding the modelling constants found in this way will be made in the section on large eddy simulations.

With the modelling described, the Reynolds stress equations expressed in terms of the components of Reynolds stress are

$$(\rho \dot{\tau}_{ij}) + (\rho u_k \tau_{ij})_{,k} = -\rho \tau_{im} u_{j,m} - \rho \tau_{jm} u_{i,m} + \frac{2}{3} \beta^* \rho \omega e \delta_{ij} - C_1 \beta^* \rho \omega \left( \tau_{ij} + \frac{2}{3} e \delta_{ij} \right) + \rho \left( \tau_{jm} S_{mi} + \tau_{im} S_{mj} - \frac{2}{3} \tau_{mn} S_{nm} \delta_{ij} \right) + \frac{4}{3} \rho e \left( S_{ij} - \frac{1}{3} u_{k,k} \delta_{ij} \right) + [(\mu + \sigma^* \rho e) \tau_{ij,k}]_{,k} \quad (39)$$

The components of the Reynolds heat flux are modelled with

$$(\rho \dot{Q}_i) + (\rho u_j Q_i)_{,j} = \rho \tau_{ij} h_{,j} - \rho Q_j u_{i,j} - \beta^{**} \rho \omega Q_i + \left[ \left( \frac{\mu}{\rho r_L} + \sigma^{**} \rho e \right) Q_{i,j} \right]_{,j} \quad (40)$$

The specific dissipation rate used to provide the scale of the turbulence is again given by Eq. (20). In these equations

$$\begin{aligned} \epsilon &= e/\omega \\ e &= -\frac{1}{2} \tau_{ii} \end{aligned} \quad (41)$$

and the modelling coefficients are

$$\left. \begin{aligned} \beta &= \frac{3}{20}, \quad \beta^* = \frac{9}{100}, \quad \beta^{**} = \frac{9}{25}, \quad \sigma = \sigma^* = \frac{1}{2}, \quad \sigma^{**} = 2 \\ C_1 &= C_{1\infty} \left[ 1 - (1 - \lambda^2) \exp\left(\frac{-Re_T}{Re}\right) \right]^{-1} \\ \frac{\gamma}{C_1} &= \frac{\gamma_\infty}{C_{1\infty}} \left[ 1 - (1 - \lambda^2) \exp\left(\frac{-Re_T}{Re}\right) \right] \\ C_{1\infty} &= \left[ \frac{9}{2} - \frac{5}{2} \exp(-5\chi) \right] \\ \gamma_\infty &= \frac{13}{11}, \quad \lambda = \frac{1}{14}, \quad Re = 1, \quad Re_\omega = 3 \end{aligned} \right\} \quad (42)$$

where

$$\chi = \sqrt{\frac{2S_{mn}S_{nm}}{\beta^* \omega^2}}$$

Again, the Reynolds number of turbulence  $Re_T$  is given by Eqs. (30) and (32). At the solid surface, Eqs. (24) again apply and, in addition

$$\text{at } x_2 = 0$$

$$\left. \begin{aligned} Q_j &= 0 \\ \tau_{ij} &= 0 \end{aligned} \right\} \quad (43)$$

At the boundary-layer edge, in addition to Eqs. (24), it is required that

$$\text{at } x_2 = \delta$$

$$\left. \begin{aligned} Q_j &= 0 \\ \tau_{ij} &= \frac{2}{3} \rho U_e^2(x_1) \delta_{ij} \end{aligned} \right\} \quad (44)$$

#### Examples of Turbulence Model Application

As an initial example of the use of the turbulence models presented here, consideration is given to the distortion of a field of fully developed, homogeneous turbulence by application of plane or normal strains. This case acts as a test of the models when near-surface effects are absent. The particular case treated

corresponds to the flow in the experiment by Tucker and Reynolds (Ref. 19). Figure 1 shows a schematic diagram of the test channel. The fluid enters at the left, is conditioned through screens, and passes toward the right in parallel flow until it reaches the station where the constant rate of strain is applied. The constant strain is achieved by exponentially expanding the channel in the  $x$  direction and contracting it in the  $y$  direction so as to maintain a constant cross-sectional area. The straining causes the initially nearly isotropic turbulence to become anisotropic, a measure of which is the straining parameter plotted as the ordinate in the lower portion of the figure. After the fluid is strained, it is returned to a parallel flow. Here the fluid tends to return to isotropy.

Use of the RSE model in computing this flow is noted to yield reasonably good agreement with the data. At the initiation of straining, the computed growth of anisotropy is somewhat faster than the data, but this trend reverses toward the end of the straining region and downstream. These trends were influenced by the assumed form of  $C_{1\infty}$  in Eq. (42) which was adjusted to fit an aggregate of homogeneous flow experiments, not just that of Tucker and Reynolds. Use of the two-equation model in the computations suffers in two respects. First, the model shows the difficulties of all eddy viscosity models when a sudden application or removal of mean strain occurs. Although the elements making up the eddy viscosity ( $\epsilon$  and  $\omega$ ) vary continuously where the discontinuities in strain occur, the corresponding Reynolds stresses are still discontinuous. Second, the rate of generation of anisotropy, by the two-equation model away from the stations where the discontinuities occurred, was too slow. Thus, although the RSE model has been shown to yield rather good agreement with the data, this example illustrates that two-equation models are limited to flow conditions with more gradual application of mean strain.

An example of the application of the turbulence models to a boundary-layer flow of an incompressible fluid is demonstrated in Figs. 2 through 4. The data are from the experiment conducted by Bradshaw in which a turbulent boundary layer was exposed to a sudden application of an adverse pressure gradient (Ref. 21). The data points designated with open symbols result from a reinterpretation of the basic data by an independent analysis (Ref. 22) and provide an indication of the uncertainty inherent in the data. Figure 2 shows the distribution of skin friction and boundary-layer shape factor along the test zone. The computations were started by matching the momentum-thickness Reynolds number from a flat-plate calculation to the Reynolds number measured at the upstream station. Beyond this station, the experimental pressure distributions were imposed on the boundary-layer calculations. It is observed that the two-equation model and the Reynolds-stress model both yield skin friction and shape factor results that are nearly the same, and that both agree well with the data. It should be noted that no adjustments were made to the modelling to account for the pressure gradient.

The measured and computed mean-velocity profiles at the farthest downstream station are shown in Fig. 3, which is expressed in wall-law coordinates. The computations based on both models yield results in good agreement with the data. In the "law-of-the-wall" region, the computed results agree with the standard logarithmic formula. In that region, also, there is a little better agreement with Coles' reinterpretation of the data (Ref. 22). Neither of these observations is surprising, as the use of the logarithmic law with the constants shown played a major role in the data reinterpretation and in establishing some of the modelling coefficients used in both models. Perhaps more significant is that the computed results based on both models show the enhanced contribution of the "wake" region that is characteristic of boundary-layer flows in adverse pressure gradients.

Figure 4 compares the Reynolds stress, turbulence energy, and mean-velocity profiles, computed from the two models, with Bradshaw's data. In these figures, the distance normal to the surface has been normalized by the boundary-layer thickness. Generally, the Reynolds stress components and the turbulent kinetic energy given by the two models differ less from each other than from the data. The normal components of Reynolds stress— $\langle u'^2 \rangle$ ,  $\langle w'^2 \rangle$  and, to a lesser degree, the kinetic energy—are evaluated rather poorly in the inner half of the boundary layer. On the other hand, the normal Reynolds stress  $\langle v'^2 \rangle$  and the shear stress  $\langle -u'v' \rangle$  fit the data much better. This reflects the adjustment of some of the modelling coefficients to provide good mean-velocity profiles in a flat-plate boundary layer, where a good evaluation of the Reynolds shear stress is paramount. In the coordinates of this figure, the two-equation model shows a little advantage over the RSE model; however, both models yield results that reflect the "flattening" of the velocity profile introduced by the adverse pressure gradient.

The results that have been shown here are representative of comparisons of many other sets of data with computed results based on the two models. For attached, subsonic boundary layers on flat plates, with or without pressure gradients, there seems to be no advantage to the Reynolds stress model. Under these flow conditions, the departure of the turbulence from being in equilibrium with the mean flow is apparently too small to cause the two-equation model difficulties that were indicated earlier with suddenly distorted homogeneous flows.

The growth of a turbulent boundary layer on a small-radius circular cylinder with its axis parallel to the free stream is an example of a flow where the mixing-length formulation required considerable change, from that on a flat plate, to make computations conform with the experimental results. Generally, the data showed that as the ratio of the boundary-layer thickness to the transverse radius increased, the "wake" region of the boundary layer diminished (as occurs on a flat plate in a favorable pressure gradient). Also the skin-friction coefficient at a given Reynolds number based on boundary-layer thickness increased with diminishing body radius. When Rao (Ref. 23) examined this flow field, he concluded that conformance with his data could be achieved if he employed a wall-region law equivalent to setting the mixing length in the inner region of the boundary layer to

$$\ell_m = ky \left[ \frac{\ln(1 + y/a)\sqrt{1 + y/a}}{(y/a)} \right] \quad (45)$$

In studying the same problem, Richmond (Ref. 24) deduced a formulation equivalent to

$$\ell_m = ky \left[ \frac{(1 + y/2a)}{(1 + y/a)^{3/2}} \right] \quad (46)$$

For values of  $y \approx a$ , Eq. (45) remains within a few percent of  $\ell_m = ky$ , whereas Eq. (46) shows a reduction of about 50%. These differences result in adjusting the position of data in opposite directions, in terms of  $y^+$ , relative to the universal "law of the wall" and demonstrates vividly how arbitrary the extensions of mixing-length closure can be.

The RSE second-order closure model given here was applied without change to this type of flow to see if the experimental data could be represented. Figure 5 compares the computed results and measured data in terms of the effect on skin friction of the ratio of  $\delta/a$ . Four sets of data are utilized (Refs. 24-27) to cover a sizable  $\delta/a$  range. The computational results are shown as a band because the ordinate employed does not collapse all of the Reynolds number dependence. The computations with the unchanged RSE model represent the trends of the data well up to a value of  $\delta/a = 10$ , where the  $C_f$  is 30% higher than that on a flat plate. Beyond this, a significant departure occurs from the data of Willmarth et al. (Ref. 27) where the measured  $C_f$  is increased to more than twice that of a flat plate. Apparently, the RSE model in its present form fails to fully account for changes in the wake character of the boundary layer over a body with an extremely small transverse radius.

The next example to be treated deals with the topic of streamwise curvature, the importance of which was first recognized by Bradshaw (Ref. 28). The Reynolds-stress equations were applied to this problem directly through the conversion of the coordinates from Cartesian to curvilinear, with one axis tangent to the surface,  $s$ , and the other normal to the surface,  $n$ . The two-equation model, however, required reinterpretation of the meaning of the symbol  $\epsilon$ , treated as the kinetic energy earlier. Details of these transformations are given in Ref. 11.

For flow over a streamwise curved surface, the  $s$ , or curvilinear coordinate system, introduces terms in the Reynolds stress equations analogous to centrifugal and Coriolis forces in the momentum equations. When the normal stresses are added together, however, most of these additional terms cancel, resulting in an energy equation that is essentially the same as on a flat surface; the only change is in the production term where the mean-velocity gradient  $\partial u/\partial y$  is replaced by  $(\partial u/\partial r) - (u/R)$ . The specific energy-dissipation-rate equation is also changed in the same way. Thus, a direct application of the two-equation model as given earlier would not show streamline curvature effects of the magnitude indicated by a Reynolds stress model or by the experimental data (e.g., Ref. 29). This deficiency was corrected by (1) observing that the Reynolds shear stress and  $v'^2$  equations in the RSE model in  $s, n$  coordinates added similar terms because of the streamwise curvature and (2) identifying  $\epsilon$  with a "mixing energy" rather than a "kinetic energy." The symbol  $\epsilon$  then is redefined as

$$\epsilon = + \frac{9}{4} \overline{v'^2} = - \frac{9}{4} \tau_{nn} \quad (47)$$

which follows from the basic model in a homogeneous shear flow where the turbulence production and dissipation are in balance. With Eq. (47) and the Reynolds stress equation for  $\overline{v'^2}$  and  $\overline{u'v'}$  as guides, the  $\epsilon$  equation for use with the two-equation model only is written in an ad hoc manner as

$$u\epsilon_{,s} + v\epsilon_{,n} + \frac{9}{2} \frac{u}{R} \tau = \tau \left( u_{,n} - \frac{u}{R} \right) - \beta^* \epsilon_w + [v + \sigma^* \epsilon] \epsilon_{,n}, \quad (48)$$

with

$$\tau = \epsilon \left( u_{,n} - \frac{u}{R} \right) \quad (49)$$

and, where  $\epsilon$  follows from Eq. (27); all the modelling coefficients and relationships employed in the two-equation model introduced earlier are retained. The third term on the left side of Eq. (48) represents the principal extra rate of turbulence production introduced by the longitudinal surface curvature.

Calculations based on these model modifications for streamline surface curvature are compared in Fig. 6 with data obtained by So and Mellor (Ref. 29) for a boundary layer on a convex wall with an adverse pressure gradient. The data represent the surface skin-friction coefficient and shape factor along the surface. The computations include the RSE and two-equation models, both with and without the corrections for longitudinal surface curvature. The computed results were matched to the first station by assuming the flow upstream of the station to be on a flat plate of a length to yield the correct skin friction there. The calculations with the RSE or two-equation model unmodified for streamwise curvature show little of the drop in skin-friction coefficient experienced in the experiment. The modified models, on the other hand, give an excellent representation of the skin-friction behavior. This is rather remarkable for the two-equation model, when its ad hoc formulation is considered. Finally, both modified models represent the form factor data also quite well.

It may seem to be illogical in the test of the universality of a turbulence model to make the modifications indicated for introducing the effects of streamwise curvature. For the RSE model, the modifications were purely geometric and were introduced by selecting the appropriate coordinates for the problem considered. No physical modelling changes were made. The original two-equation model, on the other hand, was insensitive to changes in the coordinate system and an extra production term had to be added to the  $\epsilon$  equation. One can view the need for the change as an indication of the inherent weakness of the original two-equation model, or the view of the final  $\epsilon$  equation as the basic boundary-layer model that then is simplified geometrically for planar surfaces.

The remainder of the two-dimensional boundary layers considered here involve compressible flows. As noted earlier, the extension to compressible flows is achieved by adopting dependent variables that are Favre mass-weighted averages. In these variables, the conservation equations take forms that avoid terms that are explicitly dependent on the turbulent density fluctuations. Term-by-term, the equations are comparable to their incompressible counterparts, with the compressibility entering only through the mean density variations. Although Favre averaged-model equations are, in the main, parallel term-by-term to their incompressible counterparts, they have additional terms explicitly dependent on density fluctuations that require additional

modelling (Refs. 30,31). In practice, however, it was found that these additional terms could be ignored, even under conditions involving large pressure gradients where the terms are their largest (Ref. 32). Reflecting this, the models presented here neglect these additional terms.

These models were applied to the calculation of skin friction on a cooled flat plate in airflow at a Mach number of 5. The results of these calculations based on the two models are compared with values given by the van Driest II formulas in Fig. 7. These formulas have been shown (Ref. 33) to represent the bulk of existing data under these conditions to about  $\pm 10\%$ . The agreement between all the methods is excellent, but this is not surprising in view of the similarity of the density scaling in Favre averaging (Ref. 11) and that which is inherent in the van Driest formulation.

Compressible turbulent boundary layers experiencing severe pressure gradients are cases where the models are tested more severely. The first example of such a flow is the experiment conducted by Lewis et al. (Ref. 34) at a Mach number of four. In that experiment, an axisymmetric turbulent boundary layer on the adiabatic interior wall of a circular cylinder was subjected to an adverse pressure gradient followed by a favorable pressure gradient. The pressure gradients were achieved by means of a shaped center-body; a pressure rise of 9 times the upstream pressure was attained before pressure relaxation occurred. Figure 8 shows the distribution of the surface skin-friction coefficient within the test zone. The coefficient shown is defined in terms of the upstream boundary-layer edge conditions, not the local, and is therefore proportional to the surface shear. The Reynolds number at the initial station was about  $7 \times 10^6$ . Along with the computed results based on the models presented here, computations based on the Marvin Shaeffer code (Ref. 35), which has been extended to contain a classic mixing-length model essentially identical to that of Cebeci (Ref. 4), are given for comparison. The mixing-length model fails to capture the full rise of the skin friction caused by the adverse pressure gradient. On the other hand, it follows the data in the region of favorable pressure gradient quite well. The second-order closure models demonstrate a much better prediction of the rise in skin friction in the adverse pressure gradient region; however, in the following favorable pressure gradient region they show somewhat too large a drop in the skin friction. The two second-order models yield essentially equivalent results.

Figure 9 shows data from a similar experiment conducted by Horstman et al. (Ref. 36) at an initial Mach number of 2.3 and over a large range of Reynolds numbers. In addition to computations based on the two models considered here, computed results from two versions of a mixing-length model and another two-equation model are also shown here. At this Mach number,  $M_\infty = 2.3$ , the onset of an adverse pressure gradient first reduces the skin friction before a rise similar to that which occurred in Fig. 8 also occurs. Generally, the computed values of skin friction from all the models conform to the trends in the data caused by the change in Reynolds number and the effective pressure gradient. One exception is the behavior of the mixing-length model unmodified for pressure gradient which indicates separation at the lowest Reynolds number. At the higher Reynolds numbers, the difference between the modified and unmodified mixing-length model become very small. From this figure, conclusions regarding the relative merits of the different models would be indecisive. In Fig. 10, when the adverse pressure gradient is applied over a greater distance, the models behave in a somewhat different manner. At the lowest Reynolds number, the unmodified mixing-length model no longer indicates separation. Also, at the lower Reynolds numbers, the second-order closure models are in much better agreement with the data. Omission of the explicit density fluctuation terms resulting in the model equations after Favre averaging is justified by these examples. Incidentally, the computed results labeled Aeronautical Research Associates of Princeton (ARAP) are based on a Reynolds stress model utilizing primitive dependent variables including the whole gamut of fluctuating density terms (Ref. 37).

The remaining examples of two-dimensional boundary layer and near-wake flows were computed with the compressible Navier-Stokes equations to account for strong interactions between the shear layers and the inviscid flow. Because these codes are costly to operate they have been limited, at least to date, to contain models of turbulence of the two-equation kind or simpler. Therefore, the RSE model will not appear in these examples.

Figure 11 shows calculations of the surface pressure and skin-friction distributions compared with data in the region of the interaction of a normal shock wave with a fully established turbulent boundary layer (Ref. 38). The schematic diagram shows that the flow field was developed on the surface of a tube within a slightly supersonic main flow. A normal shock wave was generated and positioned along the test section with a variable blockage device at the downstream end of the test section. The figure at the left shows that the computational results based on the two-equation model generally agree well with the measured surface pressure distributions at the five Mach numbers tested. The departures that exist from the data are small and inconsistent enough to hide any systematic deficiencies in the computational model. The computed skin-friction coefficients again conform to the main features of the data. The calculations show a downstream movement of the minimum in skin-friction coefficient with increasing Mach number. If the extreme Mach number cases are emphasized, a similar movement is seen in the data, although of larger extent. The inaccuracies inherent in skin-friction measurements can possibly exaggerate the movement of the minimum skin-friction coefficient and could be the source of these differences.

An example of a strong interaction between a boundary layer and a shock wave at higher Mach number is the experiment of Settles et al. (Ref. 39) with a turbulent boundary layer traversing a compression corner. The computations used for comparison with the data are from Ref. 40. Figure 12 shows computations and measurements of surface pressure and surface skin friction for two deflection angles of the compression corner,  $\alpha = 20^\circ$  and  $24^\circ$ . Besides the two-equation model under consideration, three other models have been used in these computations. Models not shown in any of the earlier examples are a kinetic energy model with an algebraic length scale (Ref. 31) and the Jones-Launder two-equation model (Ref. 13). A general observation is that both two-equation models yield essentially the same results, except for the level of skin friction in the reversed region. This suggests the kinds of measurement needed to distinguish between models. Comparison of the experimental data with the computations reveals that the two-equation models permitted the location of the onset of the increased surface pressure ahead of the compression corner to be computed quite well. For  $\alpha = 20^\circ$ , these models yield excellent pressure distributions over the separated zone and on the deflected surface beyond reattachment. For  $\alpha = 24^\circ$ , the calculated pressure in the separated zone is somewhat high, although ahead of separation and after reattachment the pressure is again evaluated quite well.

The zero-equation and one-equation models show late onsets of pressure rise, then overshoot the data, and then blend with the data far downstream. The comparison with the skin-friction data do not show all the same trends in the computations with the different models. The two-equation models define the position of the onset of the fall-off of skin friction, and the other models again lag this. The fall-off of the skin friction given by the two-equation models is faster than the data show, so that the points of separation are predicted upstream of where they actually are. The two-equation models also yield too long a separated region so that reattachment is calculated to be downstream of the experimental results. The comparison is inconclusive, regarding which of the models best fits the downstream data, except that the algebraic model yields results that consistently fall lower than the data.

Figure 13 compares the computations and measurements of the effect of Reynolds number on the extent of the upstream pressure influence ahead of the compression corner. The distances considered are shown schematically in the left-hand sketch in Fig. 13. Two deflection angles are considered:  $\alpha = 16^\circ$  and  $\alpha = 20^\circ$ . It is seen that the observation made earlier that the two-equation models evaluate the position of the onset of the pressure rise best is borne out in the figure over the entire range of Reynolds number covered in the experiment.

Another example in which computations with the two-equation model have been compared with experimental data is the work by Viswanath et al. (Ref. 40). The experiment was conducted at the trailing edge of a flat-plate test model that terminated with a  $12.5^\circ$  total included angle wedge. In the example cited here, the model and wedge trailing edge were both kept at zero angle of attack to an airstream at  $M = 0.7$ . Figure 14 compares measurements of the mean-velocity profiles just upstream and downstream of the trailing edge with computations employing the two-equation model and an algebraic model (Ref. 4) in both Navier-Stokes and boundary-layer equation. The high chord Reynolds number of  $40 \times 10^6$  ensured a fully turbulent boundary layer well ahead of the trailing edge. In this figure,  $\theta_0$  represents the momentum thickness of the boundary layer 0.4 cm upstream of the trailing edge; it is equal to 0.2 cm. The computations employing either model in the Navier-Stokes equations agree better with the data than the same models in the boundary-layer computations. Under these conditions, either on the wedge or just beyond the trailing edge, the flow is more sensitive to the interaction between the shear flow and the inviscid flow regions than to the particular turbulence model. Apparently the rate of change of the mean motion, even this close to the trailing edge, is sufficiently slow for either an equilibrium-model or a two-equation model to still apply. Farther downstream in the wake, both models and both computation techniques yield essentially the same results. It is important to note that the sudden removal of a surface downstream of the trailing edge did not cause any difficulties with the near-wall modifications represented by Eqs. (31), as they blended smoothly toward their asymptotic values farther in the wake.

The final example cited here is the response of a turbulent boundary layer to a sudden application of transverse shear, as studied experimentally on an axisymmetric rotating body in Refs. 25 and 26. A sketch of the model configuration is given in Fig. 15. The free-stream velocities in these experiments ranged from 10 to 19 m/sec. A comparison of the data from the two experiments with a mixing-length model (Ref. 42) modified with Eq. (45), the two-equation and RSE models, and the ARAP model (Ref. 37) has been represented in Ref. 43. In the computations with either of the eddy-viscosity models, it was necessary to introduce an additional assumption regarding the ratio of the eddy diffusivity corresponding to the transverse flow to that of the longitudinal flow. The need for assuming some value for the ratio is an inherent problem in the application of any scalar eddy-viscosity model to a three-dimensional boundary layer. In the computations with the two-equation model, this ratio was set equal to unity, as it was for the mixing-length model in Ref. 42. It was found in Ref. 43 that computations based on the simple mixing-length model yielded results in general agreement with the measurements of the mean flow. The two-equation and RSE models showed comparisons that were only somewhat better than the simpler model. The improvement achieved by the second-order closure models seemed to be limited by too rapid a response to the transverse shear. The relative agreement between the RSE model and the scalar eddy-viscosity models can be explained by reference to Fig. 15 where the ratio of the eddy viscosities calculated from the RSE model are compared to the data from the two experiments. First, it is observed that the two similar experiments result in data in serious disagreement. The appropriate ratio cannot be established experimentally. The RSE model, with or without the effects introduced by transverse curvature, shows that the ratio of eddy viscosities remains within  $\pm 10\%$  of unity over most of the transverse boundary layer, as assumed in the eddy-viscosity models. Near the outermost edge of the transverse boundary layer, in the vicinity of the onset of the transverse shear, the ratio drops to a smaller number. As there is little momentum change near the boundary-layer edge, differences in eddy viscosity such as these have negligible effect on the transverse-velocity profiles. Thus, the choice of the eddy viscosity ratio of unity in the simpler models is not inconsistent with the evaluation of the RSE model.

#### Concluding Remarks Regarding Statistical Modelling

From the foregoing set of comparisons of experimental data and computations employing a pair of fixed second-order closure models, and with other models as well, it is observed that the second-order closure models generally have a broader range of application than do the algebraic closure models. The two-equation eddy-viscosity model is accurate over a large range of Reynolds numbers for attached two-dimensional incompressible or compressible boundary layers on impervious surfaces, even those with small zones of separation. The Reynolds stress model, in addition, has advantages when sudden changes in the mean flow occur, for surfaces with streamwise curvature, and in three-dimensional boundary layers. Both models show the Favre mass-weighted dependent variables account well for compressibility, even with rather large  $\partial p / \partial x$ , and also can account for modest effects of transverse curvature.

These models still require adjustments to increase their breadth of application. For example, the two-equation model needs an extra rate of strain added to the mixing-energy equation to account for the effect of streamwise curvature on a boundary layer. This ad hoc correction is very successful, practically, for boundary-layer calculations. In the Navier-Stokes form of the model, however, it has not yet been made to account for rapid turning within a flow. Nevertheless, the trailing-edge example cited did not seem to need this correction. Both models are unable to completely relaminarize an incompressible boundary layer in strong favorable pressure gradient. This is not a general failure of second-order models; another second-order closure model (Ref. 13) has been somewhat more successful in accounting for relaminarization than the models given here. Both models also require major changes in their surface boundary conditions to account for surface mass transfer or roughness. Finally, second-order models still require special treatment in regions

approaching irrotational flow. In conclusion, then, although the second-order closure models have shown a broader range of application than simple mixing-length methods, they are not universal and need further development to broaden their range of application, especially for boundary-layer flows that interact strongly with the surrounding irrotational flow.

#### LARGE EDDY SIMULATION OF HOMOGENEOUS TURBULENCE

The background and status of the techniques of large eddy simulation were recently reviewed by Ferziger and Leslie (Ref. 44). They gave particular attention to the methods for modelling the subgrid stresses expressed as  $\langle u_i u_j \rangle$  in Eq. (14). To demonstrate the realism attained with the technique, the results of channel-flow computations were compared with data for mean-velocity profiles,  $U_j$  in Eq. (13), and mean moments, such as the pressure strain correlations. A more complete analysis of the simulation of channel flow appears in the Kim and Moin paper of this conference (Ref. 45). To supplement those papers and to demonstrate the value of turbulence simulation to statistical turbulence modelling, this author will examine what can be learned regarding statistical Reynolds stress modelling from large eddy simulations of localized flow situations.

The author is indebted to his colleague Dr. Robert Rogallo, who generously provided the results of computations he is performing on homogeneous turbulence that is experiencing decay, normal straining, or uniform shear straining. The Rogallo code has been described in Ref. 46, but has since been modified to accept uniform shearing. The code has certain unique features. The turbulence is computed in a volume of fluid that is followed in time and is defined by coordinates that move with the assigned mean velocity. In this moving frame of reference, the turbulence is spatially homogeneous. The boundary conditions on the computational volume are treated as periodic in space, which permits use of full spectral methods in the computations. The code is efficient and accurate because particular care has been exercised to conserve energy and minimize aliasing. All variables are expressed in dimensionless form and related to physical quantities (subscript e) with scaling coefficients  $\alpha$  and  $\beta$  as follows:

$$\left. \begin{array}{ll} \text{Wave number or length} & k_e = \beta k, \quad L_e = \beta^{-1} L \\ \text{Energy} & E_e = \alpha^{-1} E \\ \text{Kinematic viscosity} & \nu_e = \alpha^{-1/2} \beta^{-1} \nu \\ \text{Time} & t_e = \alpha^{1/2} \beta^{-1} t \end{array} \right\} \quad (50)$$

It should be noted that the kinematic viscosity is treated as constant.

In operating the Rogallo code, the turbulence is initially assigned an overall intensity with an arbitrarily assigned three-dimensional spectral distribution. In addition, the mean strain rate and kinematic viscosity are also assigned. The turbulence is then oriented in phase space randomly while conserving mass. Because of the use of random phase, the components of turbulence velocity in each direction are uncorrelated so that no shear stress exists at time = 0. In the presence of a mean shear, the shear stresses develop in a short time and the computed results become independent of the particular random phase distribution that was used to start the calculations. The initially assigned spectrum also readjusts to be consistent with the assigned strain rate and kinematic viscosity, and the instantaneous turbulence intensity.

The spectral range used in the calculations shown here has a ratio of the maximum to minimum wave number equal to 31. This ratio is established by (1) the storage capacity of the ILLIAC IV computer, which permits computations over volumes in phase space having 64 mesh points in each of three directions; and (2) the need for using two mesh spacings to define the minimum resolvable wavelength. Although this represents a very large number of computational mesh points, this spectral range is still inadequate to capture the range of wave numbers that is significant in a real turbulent flow, except for one at very small turbulence Reynolds numbers. Capturing the bulk of the significant eddy sizes and avoiding the use of a subgrid model is called an "honest" calculation. The Reynolds number appropriate to an "honest" calculation is an order of magnitude or more smaller than exists even in small scale laboratory experiments. If an "honest" calculation was to be compared with a low Reynolds number experiment, the physical output of the computations would be found from the calculations through Eqs. (50) after establishing  $\alpha$  and  $\beta$  from the values of  $\nu$  and  $E$  used in the calculations and the  $\nu_e$  and  $E_e$  of the experiment. An alternative interpretation of these "honest" calculations is to consider  $\nu$  used in the computations as an effective viscosity, which from Eqs. (13) and (14) is equivalent to the use of a constant eddy-viscosity subgrid model

$$\langle u_i' u_j' \rangle = (\nu_{\text{eff}} - \nu)(U_{i,j} + \tilde{u}_{i,j}) \quad (51)$$

Emphasis is placed on the computation of the largest eddies in the flow, with the larger effective viscosity and a higher than real spectrum at the upper end of the wave numbers used to account for the dissipation that actually takes place at the wave numbers well beyond those in the computation. This approach presumes that the distorted spectrum at the upper end of computed wave numbers does not significantly alter the cascade of energy out of the energy-containing eddies at the low-wave-number end of the spectrum. In this approach, the scaling parameters  $\alpha$  and  $\beta$  in Eqs. (5) can be established from comparing the calculated large eddy characteristics and corresponding quantities found in an experiment.

To test the validity of this alternative interpretation of Rogallo's calculations, the computed results from several cases were compared with data obtained in the experiment by Harris et al. (Ref. 47) in which a rather complete set of turbulence measurements was made in a nearly homogeneous shear flow. When the computed macroscales and turbulence kinetic energy were matched to the corresponding experimental quantities in the region where the experiment reached an asymptotic behavior, the  $\alpha$  and  $\beta$  needed to utilize Eqs. (50) were established.

It was found that the best agreement between computation and experiment occurred when the effective viscosity in the computation was 15 times the molecular kinematic viscosity. A comparison of several computed



and measured statistical properties is presented in Table 1. The computations show a kinetic energy dissipation rate that is about 20% higher than the rate inferred from the measurements. This difference may not be significant however, because the energy dissipation rate is difficult to measure accurately. It is made up of direct measurements plus inferences regarding local isotropy of the small dissipative wave numbers. The excellent agreement of the mean velocity gradients indicates the large turbulence structure is properly related to the mean flow in the computation. The remaining excellent comparisons between the Reynolds stress quantities is strong evidence that the computation is capturing the larger eddy structure that is principally responsible for these quantities. This conclusion is further supported by the comparison of the computed and measured two-point correlation coefficients for  $u$ , in the three Cartesian directions that are shown in Fig. 16. The general character of the experimental curves in each direction is represented very well by the calculations. Some of the weaknesses of the calculations are also demonstrated in this figure. The curve of  $R_{11}(r,0,0)$  is higher than that plotted from the data for the smaller separation distances. This is an indication that the smaller eddies or high-wave-number eddies in the experiment are not well represented by the computations. This was expected in a computation with limited resolution, and one in which emphasis is on accurately computing the larger eddies. In addition, it is noted that  $R_{11}(r,0,0)$  has not vanished at  $r_1/L_1 = 4.9$ , which corresponds to  $1/2$  the length of each side of the computational volume. This suggests the computational volume used may have been too small and that the largest eddies could be sensitive to the periodic boundary conditions that were imposed. Even with these shortcomings, the remarkably good agreement between the experimental data and the computations encouraged the author to utilize the computations as a data base to examine some of the assumptions employed in statistical Reynolds stress modelling.

For a uniform homogeneous turbulent shear flow, the Reynolds stresses are given by

$$\frac{Du_1^2}{Dt} = -2\overline{u_1 u_2} U_{1,2} + 2\overline{p u_{1,1}} - 2\nu[(\overline{u_{1,1}})^2 + (\overline{u_{1,2}})^2 + (\overline{u_{1,3}})^2] \quad (52)$$

$$\frac{Du_2^2}{Dt} = + 2\overline{p u_{2,2}} - 2\nu[(\overline{u_{2,1}})^2 + (\overline{u_{2,2}})^2 + (\overline{u_{2,3}})^2] \quad (53)$$

$$\frac{Du_3^2}{Dt} = + 2\overline{p u_{3,3}} - 2\nu[(\overline{u_{3,1}})^2 + (\overline{u_{3,2}})^2 + (\overline{u_{3,3}})^2] \quad (54)$$

and

$$\frac{Du_1 u_2}{Dt} = -\overline{u_1 u_2} U_{1,2} + \overline{p(u_{1,2} + u_{2,1})} - 2\nu[\overline{u_{1,1} u_{2,1}} + \overline{u_{1,2} u_{2,2}} + \overline{u_{1,3} u_{2,3}}] \quad (55)$$

Closure of these equations requires expressing the correlation of pressure and rate of strain and the dissipation terms containing  $\nu$  in terms of the Reynolds stresses, themselves, and the mean flow. The pressure rate-of-strain model to be evaluated here is represented by Eqs. (36) and (37). The dissipation terms in Eqs. (51) through (54) are usually replaced by the symbols  $\epsilon_{11}$ ,  $\epsilon_{22}$ ,  $\epsilon_{33}$ , and  $\epsilon_{12}$ . In terms of these quantities, the dissipation of the turbulence kinetic energy is given by

$$\epsilon = \frac{1}{2} (\epsilon_{11} + \epsilon_{22} + \epsilon_{33}) \quad (56)$$

It is usually assumed in modelling that the dissipation takes place at the smallest eddies and is, therefore, an isotropic phenomenon represented mathematically as

$$\epsilon_{ij} = \frac{2}{3} \epsilon \delta_{ij} \quad (57)$$

To learn if the computations are consistent with the assumption of isotropic dissipation in a shear flow, the computed values of  $\epsilon_{ij}$  corresponding to each Reynolds stress are plotted against a measure of the anisotropy,  $u_{ij}/e - 2/3 \delta_{ij}$ , in Fig 17. The values corresponding to the different Reynolds stresses for a range of turbulence Reynolds numbers generally lie along a straight line with a slope of about 0.7. If the dissipation had been isotropic, in the coordinates of the figure, these points would have been located on the axis or at an ordinate equal to zero. The computations show the dissipation to be anisotropic and require that Eq. (57) be modified to

$$\epsilon_{ij} = \frac{2}{3} \epsilon \delta_{ij} + 0.7 \left( \frac{\overline{u_i u_j}}{e} - \frac{2}{3} \delta_{ij} \right) \epsilon \quad (58)$$

for the shear flow. What is normally termed dissipation in a large eddy simulation actually represents the component energies that are cascaded toward the high wave number end of the calculation to be then drained from the calculation by the subgrid model. It is no surprise then that the cascade process reflects the anisotropy of the larger eddies. The emphasis on the behavior of the large eddies possibly is an advantage: it may be just what is required in Reynolds stress modelling, which also addresses the behavior of the larger eddies.

Figure 18 shows the components of dissipation as functions of anisotropy for the case of a turbulent flow relaxing after it had been instantaneously distorted with normal strains in the  $x_2$  and  $x_3$  directions. In this case, the computed results generally lie along the coordinate axis and the dissipation is approximately isotropic even though the flow itself is still anisotropic.

The homogeneous flow relaxing after instantaneous distortion by normal strains is also an excellent case for examining the first term in the pressure rate of strain relationship represented by Eq. (36). The terms in Eq. (36) preceded by  $\hat{\alpha}$ ,  $\hat{\beta}$ , and  $\hat{\gamma}$  are identically zero in the absence of continuing mean strain. The  $C_1$  were evaluated from the computed turbulence moments for a case distorted in all three directions. It was found that  $C_1$  was reasonably insensitive to the direction of the component considered. The  $C_1$  (based on  $U^2$ ) is plotted as a function of the turbulence Reynolds number  $e^2/\epsilon\nu_{eff}$  in Fig. 19. The numbers adjacent to the symbols represent the magnitude of the largest anisotropy in the three components. Three

different values of  $\nu_{\text{eff}}$  were used in the calculations to extend the range of the turbulent Reynolds number. It is observed that if the largest component of anisotropy is less than 0.25, that is, if

$$\frac{u_2^2}{e} - \frac{2}{3} \delta_{ij} < 0.25 \quad (59)$$

the values of  $C_1$  collapse onto a single curve. For those values of isotropy where the points depart from a single curve, the linear form of the Rotta term expressed in anisotropy can be considered to have failed. It is also noted that for values of anisotropy satisfying (59), the so-called "constant"  $C_1$  still has a strong Reynolds number dependence.

The value of  $C_1$  was also evaluated from the homogeneous shear flow computation of the pressure rate-of-strain correlation and Eqs. (36) and (37). To do this most simply, the interrelationships between  $\hat{\alpha}$ ,  $\hat{\beta}$ , and  $\hat{\gamma}$  derived by Launder et al. (Ref. 14) following Rotta's suggestion (Ref. 8) were utilized. The  $C_1$  formed from these computations is plotted as a function of turbulence Reynolds number in Fig. 20. Again, the maximum anisotropy is indicated at the plotted points. For comparison, the  $C_1$  from the normally strained flow, with the value of maximum anisotropy characteristic of shear flow, are also plotted on the figure. Shearing the flow tends to increase the turbulence Reynolds number so that the regions of the two flows do not overlap. The same magnitude of anisotropy is used for both flows to account for a similar departure from the linear Rotta form in each. It is observed that the line segments associated with the different types of flow fields do not appear to form a common curve. This would imply that the pressure rate-of-strain model represented by Eqs. (36) and (37) is not as universal as is suggested by its tensor form. It is most interesting, however, to note that if the  $C_1$  is considered to be the coefficient of the sum of the pressure rate-of-strain correlation and the anisotropic dissipation, the dashed curves on Fig. 20, the two flow fields tend to produce a common curve. It appears that only the sum of the dissipation and pressure rate-of-strain can be modelled universally. This observation is consistent with the theoretical approach adopted by Lumley and Newman (Ref. 48). It should be noted, again, that the anisotropy on the figure is outside the region of applicability of the Rotta relationship and that shear flows with lesser anisotropy would require larger values of  $C_1$  for the pressure rate of strain contribution.

The values of  $C_1$ ,  $\hat{\alpha}$ ,  $\hat{\beta}$ , and  $\hat{\gamma}$  that conform to the high end of the turbulence Reynolds number in these calculations are shown in Table 2 along with those used in the Launder et al. (Ref. 14) model and the RSE model described here. The agreement between the computations of Launder et al. and those of Rogallo is excellent and is primarily due to the ability of the computations to yield good values of the Reynolds stresses in equilibrium shear flow (Table 1). The requirement of  $\hat{\alpha} = \hat{\beta}$  in the RSE model apparently requires considerable compensation in all the other terms to result in the proper Reynolds stress ratios for uniform shear flows.

#### Concluding Remarks Regarding Large Eddy Simulations

Although this demonstration of the use of large-eddy simulations for guiding Reynolds stress modelling has been limited to homogeneous flows, its utility as a research tool shows great promise. Although the procedure is quite costly in terms of computer time (the calculations shown here require about 1.5 hr ILLIAC IV time per test case), the potential gains in computer technology (Ref. 1) should make large eddy simulations a research tool that will be available to most research laboratories in a decade or so. It is this author's belief that research activities involving coordinated theory, experimentation, and computer simulations will in the reasonably near future not only bring about a much clearer understanding of the physics of turbulence, but may even permit the development of predictive engineering methods for flow fields of technological interest.

#### REFERENCES

1. Chapman, D. R.: Computational Aerodynamics Development and Outlook. AIAA Dryden Lectureship in Research, AIAA Paper 79-0129, Jan. 15-17, 1979.
2. Leonard, A.: On the Energy Cascade in Large-Eddy Simulations of Turbulent Fluid Flows. Adv. in Geophysics, vol. 18A, 1974, p. 237.
3. Kline, S. J., Morkovin, M. V., Sovran, G., and Cockrell, D. J.: Proc. Computation of Turbulent Boundary Layers, vol. 1, Methods, Predictions, Evaluation and Flow Structure, 1968 AFOSR-IFP-Stanford Conference, Stanford U., Stanford, Calif., Aug. 18-25, 1968.
4. Cebeci, T. and Smith, A. M. O.: Analysis of Turbulent Boundary Layers. Academic Press, New York, 1974.
5. Kays, W. M.: Heat Transfer to the Transpired Turbulent Boundary Layer. Report No. HMT-14, Thermosciences Division, Dept. of Mechanical Engineering, Stanford U., Stanford Calif., June 1971.
6. Kolmogorov, A. N.: Equations of a Turbulent Motion of an Incompressible Fluid. Izv. Akad. Nauk, SSR Ser. fiz. VI, no. 1-2, 1942, pp. 56-58.
7. Chou, P. Y.: On Velocity Correlations and the Solutions of the Equations of Turbulent Fluctuation. Quart. Appl. Math., vol. 3, no. 1, 1945.
8. Rotta, J.: Statistische Theorie nicht-homogener Turbulenz, 1. Mitteilung, Zeitschrift fuer Physik, vol. 129, 1951, pp. 547-572.
9. Rotta, J.: Statistische Theorie nicht-homogener Turbulenz, 2 Mitteilung, Zeitschrift fuer Physik, vol. 131, 1951, pp. 51-77.
10. Wilcox, D. C. and Traci, R. M.: A Complete Model of Turbulence. AIAA Paper 76-351, July 1976.



11. Wilcox, D. C. and Rubesin, M. W.: Progress in Turbulence Modeling for Complex Flow Fields, Including Effects of Compressibility. NASA TP-1517, 1979.
12. Saffman, P. G.: A Model for Inhomogeneous Turbulent Flow. Proc. Roy. Soc. Lond. A 317, 1970, pp. 417-433.
13. Jones, W. P. and Launder, B. E.: The Prediction of Laminarization with the Two-Equation Model of Turbulence. Int. J. Heat Mass Transf., vol. 15, 1972, pp. 301-314.
14. Launder, B. E., Reece, G. J., and Rodi, W.: Progress in the Development of a Reynolds Stress Turbulence Closure. J. Fluid Mech., vol. 68, pt. 3, 1975, pp. 537-566.
15. Rubesin, M. W., Crisalli, A. J., Lanfranco, M. J., and Acharya, M.: A Critical Evaluation of Invariant Second-Order Closure Models for Subsonic Boundary Layers. Proc. Symposium on Turbulent Shear Flows, University Park, Penn., Apr. 18-20, 1977, pp. 4.1-4.38.
16. Favre, A.: Equations des Gaz Turbulents Compressibles. J. Mecan., vol. 4, no. 3, Sept. 1965, pp. 361-390.
17. Escudier, M. P.: The Distribution of the Mixing Length in Turbulent Flows Near Walls. Rept. TWF/TN/1, Imperial College, London, 1965.
18. Saffman, P. G.: Development of a Complete Model for the Calculation of Turbulent Shear Flows. Paper presented at meeting on "Turbulence and Dynamical Systems." Duke U., Durham, N.C., Apr. 1976.
19. Tucker, H. J. and Reynolds, A. J.: The Distortion of Turbulence by Irrotational Plane Strain. J. Fluid Mech. JFM, vol. 32, pt. 4, 1968, pp. 657-673.
20. Ibbetson, A. and Tritton, D. J.: Experiments on Turbulence in Rotating Fluid. J. Fluid Mech., vol. 68, pt. 4, 1975, pp. 639-672.
21. Bradshaw, P.: The Response of a Constant-Pressure Turbulent Boundary Layer to the Sudden Application of an Adverse Pressure Gradient. ARC R&M 3575, 1969.
22. Coles, D. E. and Hirst, E. A.: Proc. Computation of Turbulent Boundary Layers, vol. II, Compiled Data, 1968 AFOSR-IFP-Stanford Conference, Stanford U., Stanford, California, Aug. 18-25, 1968.
23. Rao, G. N. V.: The Law of the Wall in a Thick Axisymmetric Turbulent Boundary Layer. J. Appl. Mech., vol. 89, 1967, pp. 237-238.
24. Richmond, R.: Experimental Investigation of Thick Axisymmetric Boundary Layer on Cylinders in Subsonic and Hypersonic Speeds. Ph.D. Thesis, California Institute of Technology, Pasadena, Calif., 1957.
25. Lohmann, R. P.: The Response of a Developed Turbulent Boundary Layer to Local Transverse Surface Motion. Trans. ASME, J. Fluids Eng., Sept. 1976, pp. 354-363. (Also Ph.D. Thesis, University of Connecticut, Storrs, Conn., 1974.)
26. Bissonnette, L. R. and Mellor, G. L.: Experiments on the Behavior of an Axisymmetric Turbulent Boundary Layer with a Sudden Circumferential Strain. J. Fluid Mech., vol. 63, pt. 2, Apr. 1974, pp. 369-413. (Also Ph.D. Thesis by Bissonnette, L. R., Princeton University, Princeton, N.J., 1970.)
27. Willmarth, W. W., Winkel, R. E., Bogar, T. J., and Sharma, L. K.: Axially Symmetric Turbulent Boundary Layers on Cylinders: Mean Velocity Profiles and Wall Pressure Fluctuations. University of Michigan, Department of Aerospace Engineering Report 021490-3-7, June, 1975.
28. Bradshaw, P.: Effects of Streamline Curvature on Turbulent Flow. AGARD-AG-169, Aug. 1973.
29. So, R. M. C. and Mellor, G. L.: An Experimental Investigation of Turbulent Boundary Layers Along Curved Surfaces. NASA CR-1940, 1972.
30. Wilcox, D. C. and Alber, I. E.: A Turbulence Model for High-Speed Flows, Proc. 1972 Heat Transfer and Fluid Mechanics Institute, Stanford U. Press, 1972, pp. 231-252.
31. Rubesin, M. W.: A One-Equation Model of Turbulence for Use with the Compressible Navier-Stokes Equations. NASA TM X-73,128, 1976.
32. Coakely, T. J., Viegas, J. R., and Horstman, C. C.: Evaluation of Turbulence Models for Three Primary Types of Shock Separated Boundary Layers. AIAA Paper 77-672, June 1977.
33. Hopkins, E. J. and Inouye, M.: An Evaluation of Theories for Prediction of Turbulent Skin Friction and Heat Transfer on Flat Plates at Supersonic and Hypersonic Mach Numbers. AIAA J., vol. 9, no. 6, 1971, pp. 993-1003.
34. Lewis, J. E., Gran, R. L., and Kubota, T.: An Experiment on the Adiabatic Compressible Turbulent Boundary Layer in Adverse and Favorable Pressure-Gradients. J. Fluid Mech., vol. 51, pt. 4, 1972, pp. 657-672.
35. Marvin, J. G. and Sheaffer, Y. S.: A Method for Solving the Nonsimilar Boundary-Layer Equations Including Foreign Gas Injection. NASA TN D-5516, 1969.
36. Horstman, C. C., Kussoy, M. I., and Lanfranco, M. J.: An Evaluation of Several Compressible Turbulent Boundary Layer Models: Effect of Pressure Gradient and Reynolds Number. AIAA Paper 78-1160, July 10-12, 1978.

37. Sullivan, R. D.: GYC: A Program to Compute the Turbulent Boundary Layer on a Rotating Cone. A.R.A.P. Working Paper 76-2, Aug. 1976.
38. Mateer, G. G. and Viegas, J. R.: Effect of Mach and Reynolds Numbers on a Normal Shock Wave/Turbulent Boundary Layer Interaction. AIAA Paper 79-1502, July 23-25, 1979.
39. Settles, G. S., Vas, I. E., and Bogdonoff, S. M.: Details of a Shock-Separated Turbulent Boundary Layer at a Compression Corner. AIAA J., vol. 14, 1976, pp. 1709-1715.
40. Viegas, J. R. and Horstman, C. C.: Comparison of Multiequation Turbulence Models for Several Shock Separated Boundary Layer Flows. AIAA Paper 78-1165, July 10-12, 1978.
41. Viswanath, P. R., Cleary, J. W., Seegmiller, H. L., and Horstman, C. C.: Trailing-Edge Flows at High Reynolds Number. AIAA Paper 79-1503, July 23-25, 1979.
42. Aguilar, R.: A Numerical Analysis of Turbulent Flow Along an Abruptly Rotated Cylinder. Ph.D. Thesis, Virginia Polytechnic Inst. and State U., Blacksburg, Va., 1976.
43. Higuchi, H. and Rubesin, M. W.: Behavior of a Turbulent Boundary Layer Subjected to Sudden Transverse Strain. AIAA Paper 78-201, Jan. 16-18, 1978.
44. Ferziger, J. H. and Leslie, D. C.: Large Eddy Simulation: A Predictive Approach to Turbulent Flow Computation. AIAA Paper 79-1471, July 23-25, 1979.
45. Kim, John and Moin, Parviz: Large Eddy Simulation of Turbulent Channel Flow. Paper presented at AGARD Symposium Turbulent Boundary Layer - Experiment Theory and Modelling, 24-27 Sept. 1979, at The Hague, Netherlands.
46. Rogallo, Robert S.: An ILLIAC Program for the Numerical Simulation of Homogeneous Incompressible Turbulence. NASA TM-73,203, 1977.
47. Harris, V. G., Graham, J. A. H., and Corrsin, S.: Further Experiments in Nearly Homogeneous Turbulent Shear Flow. J. Fluid Mech., vol. 81, pt. 4, 1977, pp. 657-687.
48. Lumley, J. L. and Newman, G. R.: The Return to Isotropy of Homogeneous Turbulence. J. Fluid Mech., vol. 82, pt. 1, 1977, pp. 161-178.

TABLE 1. COMPARISON OF ROGALLO'S SHEAR FLOW CALCULATIONS WITH THE EXPERIMENTAL DATA OF HARRIS, GRAHAM, AND CORRSIN<sup>a</sup>

Quantity	Experiment	Computation
Dissipation rate, $\text{cm}^2 \text{sec}^{-3}$	3.28E+04	3.92E+04
Mean-velocity gradient, $U_{1,2} \text{sec}^{-1}$	44.0	45.3
Angle of principal stresses, deg	-22.3	-22.6
Ratio of principal stresses	4.06	5.24
$u_1 u_1 / e$	1.00	1.01
$u_2 u_2 / e$	0.40	0.36
$u_3 u_3 / e$	0.60	0.63
$-u_1 u_2 / e$	0.30	0.33

<sup>a</sup>Scaling established by matching turbulence kinetic energy and streamwise macroscales. Turbulence model  $\nu_{\text{eff}}/\nu = 15$ .

TABLE 2. PRESSURE RATE OF STRAIN CORRELATION MODELLING COEFFICIENTS

	Lauder, Reece, and Rodi model	Wilcox and Rubesin model	Rogallo's computations
$C_1$	1.5 <sup>a</sup>	4.5 <sup>a</sup>	1.5 <sup>a</sup>
$\hat{\alpha}$	0.76	0.5	0.78
$\hat{\beta}$	0.11	0.5	0.23
$\hat{\gamma}$	0.36	1.33	0.55

<sup>a</sup>Includes effects of anisotropic dissipation.

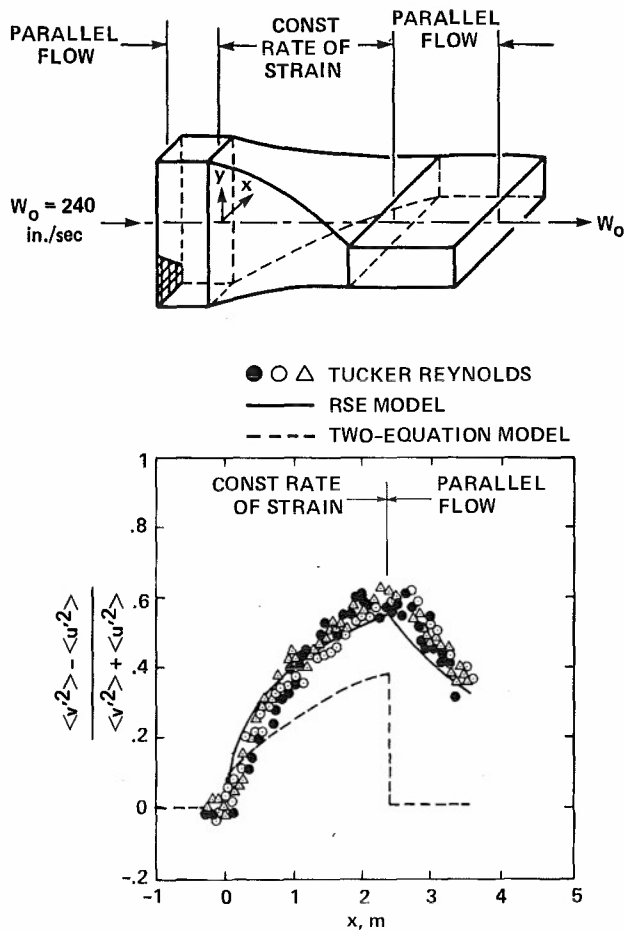
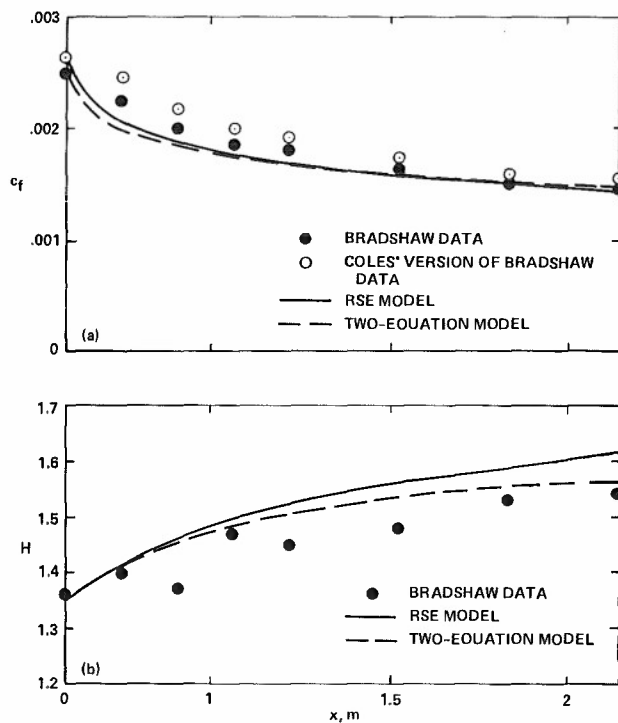


Fig. 1. Comparison of computed and measured distortion parameter for the Tucker-Reynolds plane strain flow.



(a) Skin-friction distribution.  
(b) Shape-factor distribution.

Fig. 2. Comparison of computed and measured skin friction and shape factor for the Bradshaw adverse-pressure-gradient flow.

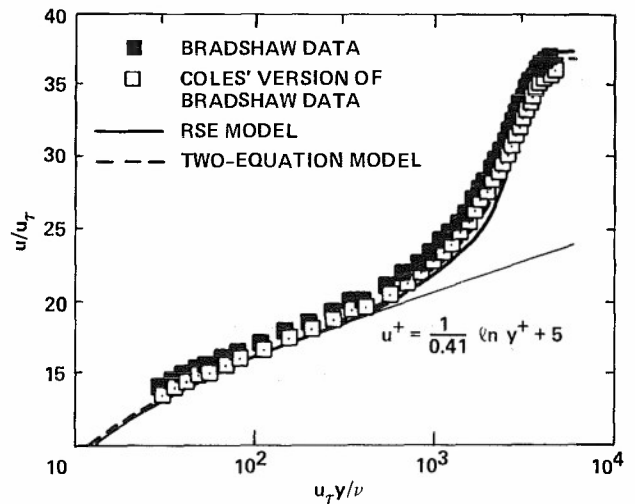


Fig. 3. Comparison of computed and measured velocity profiles for the Bradshaw adverse-pressure-gradient flow;  $x = 2.1$  m.

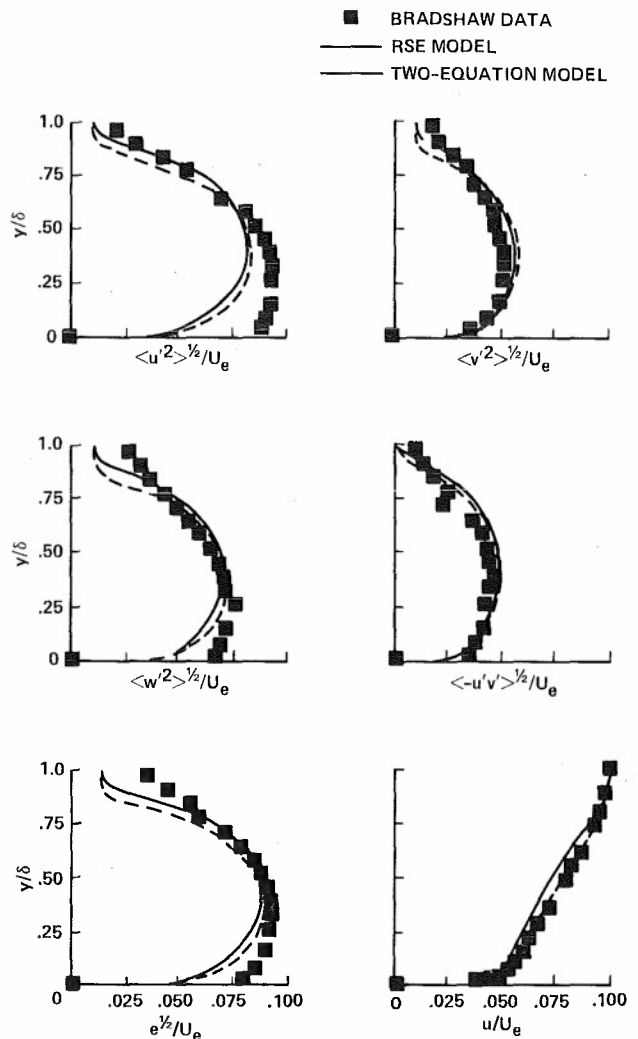


Fig. 4. Mean field profiles for the Bradshaw adverse-pressure gradient flow;  $x = 2.1$  m.

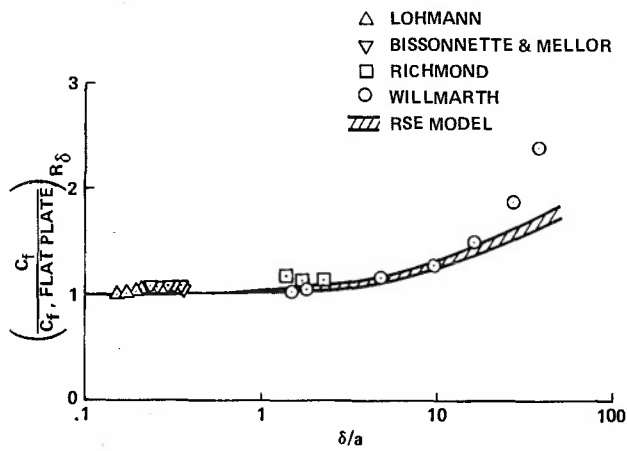


Fig. 5. Effect of transverse surface curvature on skin friction.

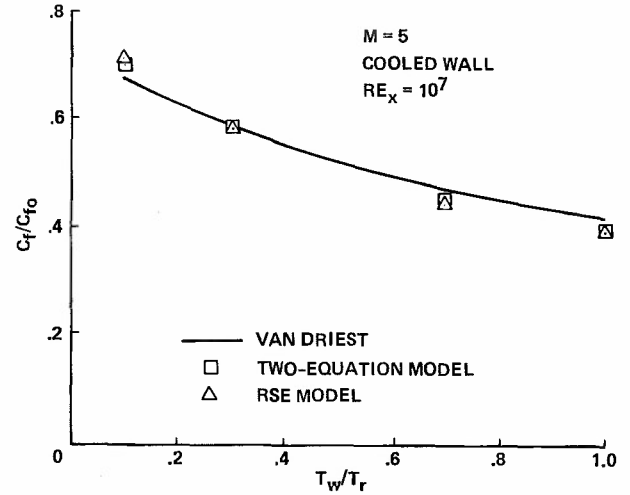
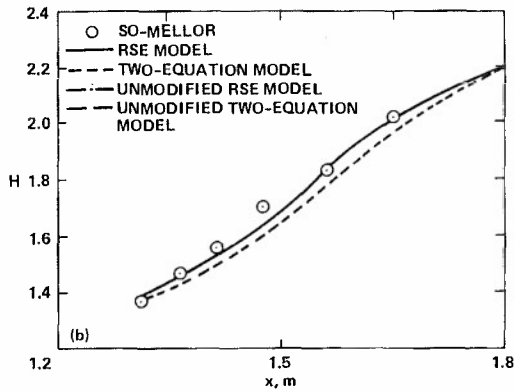
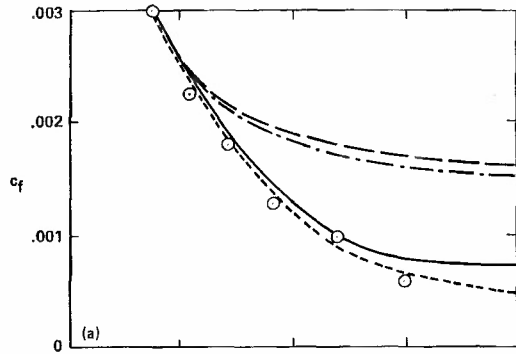


Fig. 7. Effect of surface cooling on the skin friction on a flat plate.



(a) Skin-friction distribution.  
(b) Shape-factor distribution.

Fig. 6. Comparison of computed and measured skin friction and shape factor for flow over a convex wall with adverse pressure gradient.

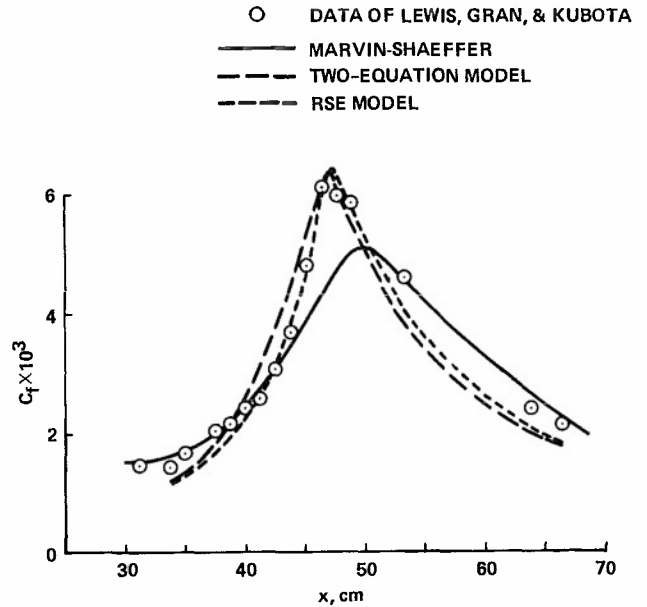


Fig. 8. Skin-friction coefficient distribution in a region of large pressure gradient at  $M_\infty = 4$ .

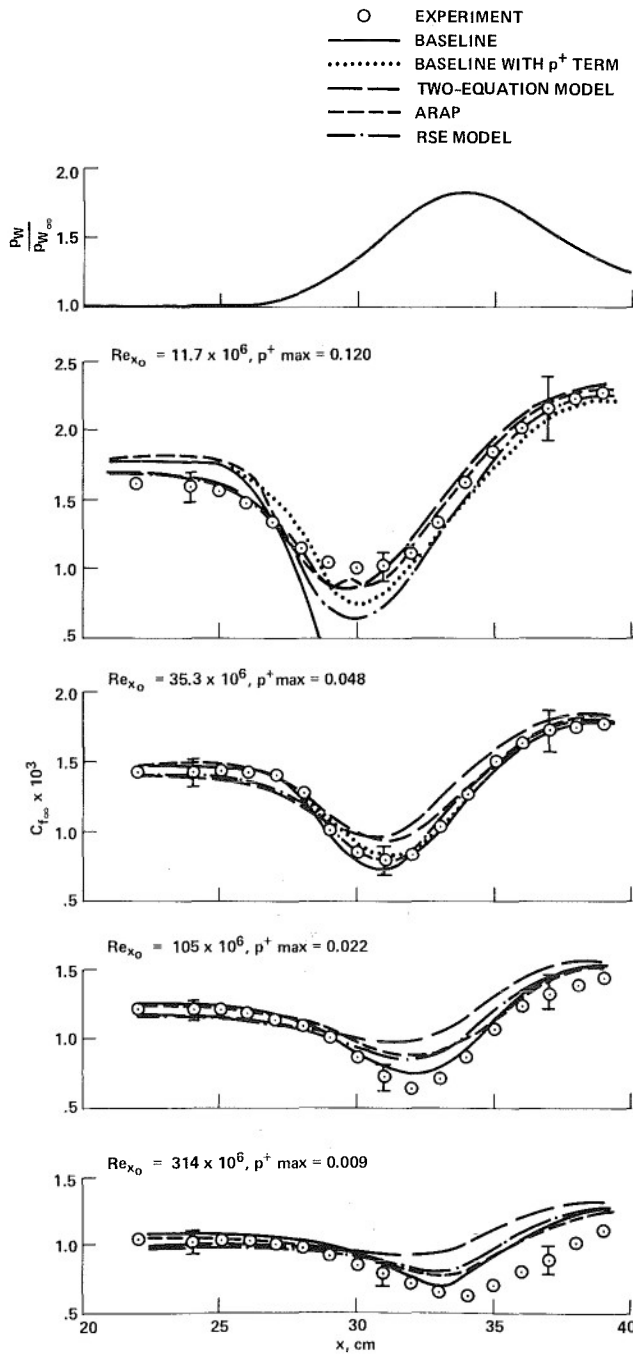


Fig. 9. Skin-friction distribution in region of large pressure gradients at high Reynolds numbers,  $M_\infty = 2.3$ .

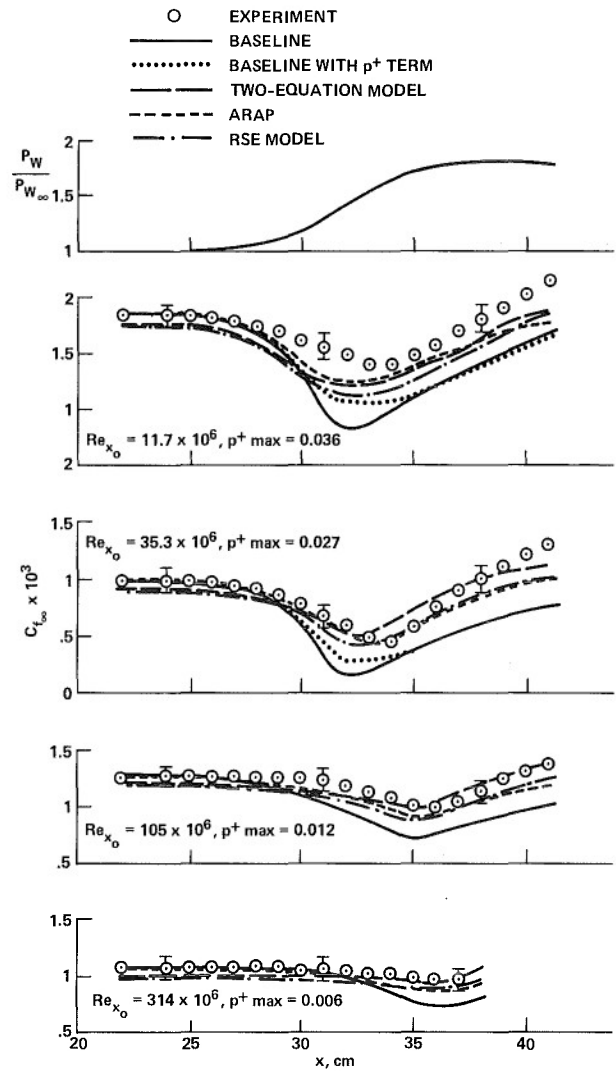


Fig. 10. Skin-friction distribution in extended region of large pressure gradient at high Reynolds numbers,  $M_\infty = 2.3$ .

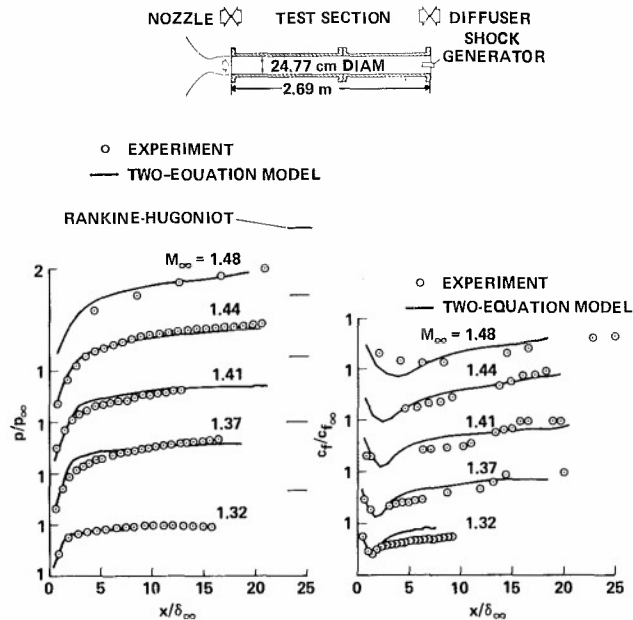


Fig. 11. Comparison of computations and surface measurements of pressure and skin friction in region of shock wave, boundary-layer interaction at low supersonic speeds.

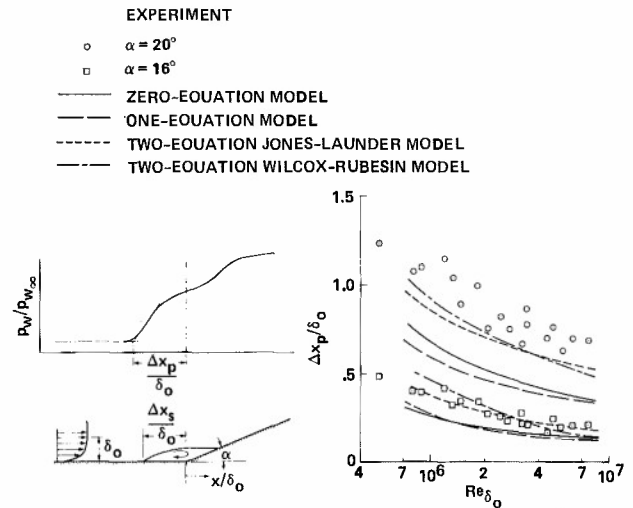


Fig. 13. Comparison of computations and measurements of the effect of Reynolds number on the extent of upstream pressure influence of a supersonic compression corner,  $M = 2.8$ .

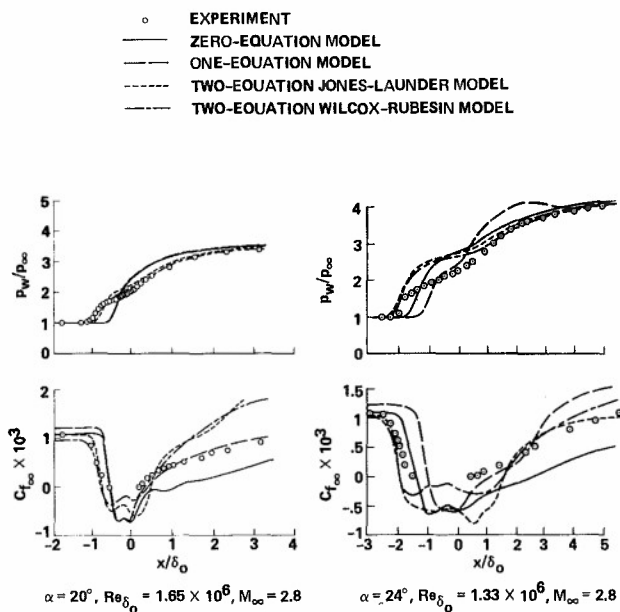


Fig. 12. Comparison of computations and surface measurements of pressure and skin friction in the region of a compression corner at supersonic speeds.

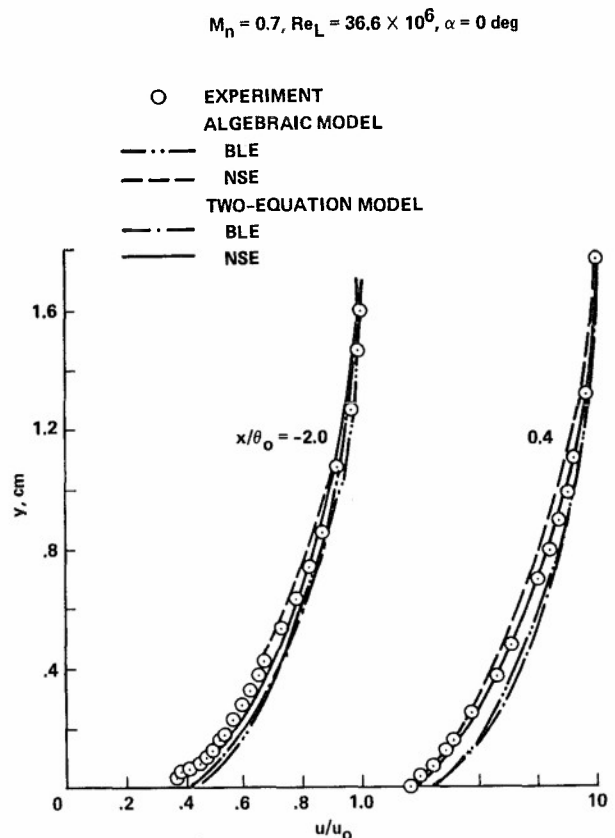


Fig. 14. Comparison of computed and measured mean-velocity profiles upstream and downstream of sharp trailing edge with a  $12.5^\circ$  wedge angle.

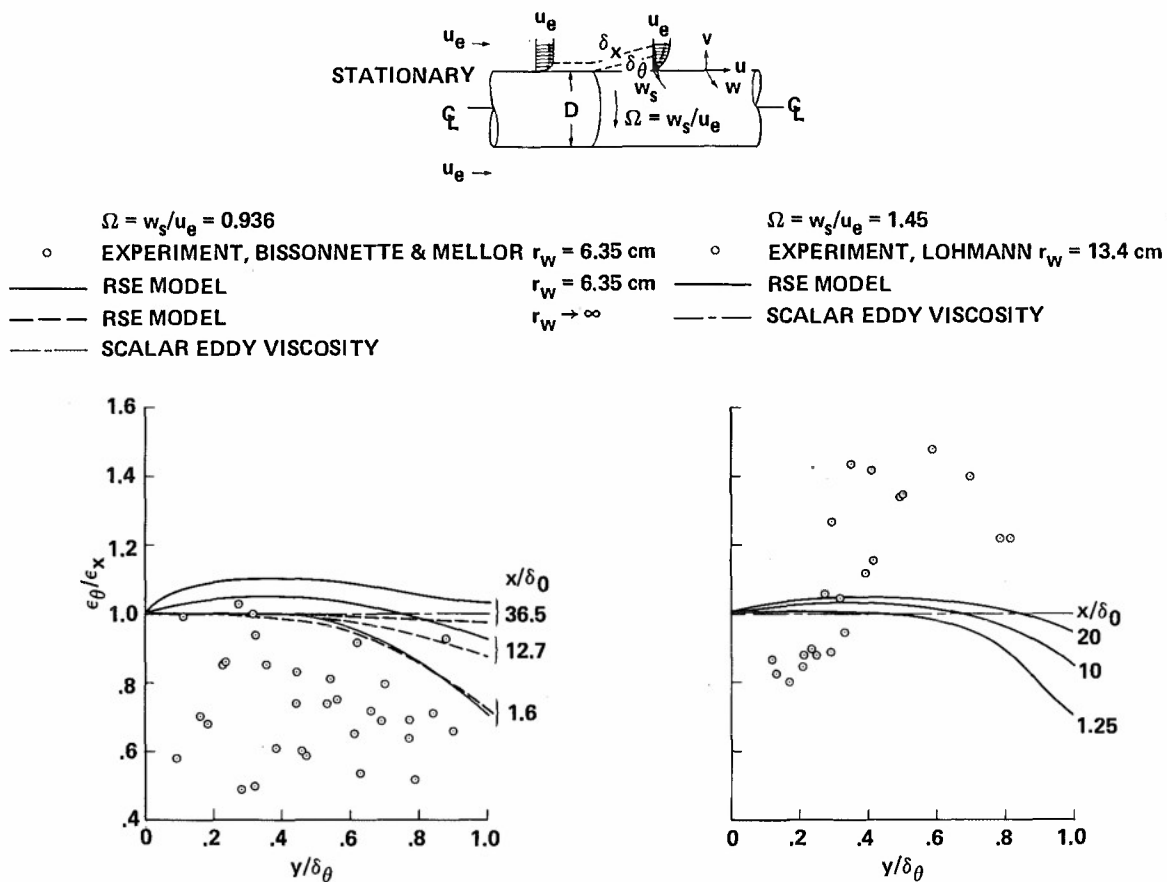


Fig. 15. Ratio of the transverse and longitudinal eddy viscosities in the region of a sudden application of transverse shear.

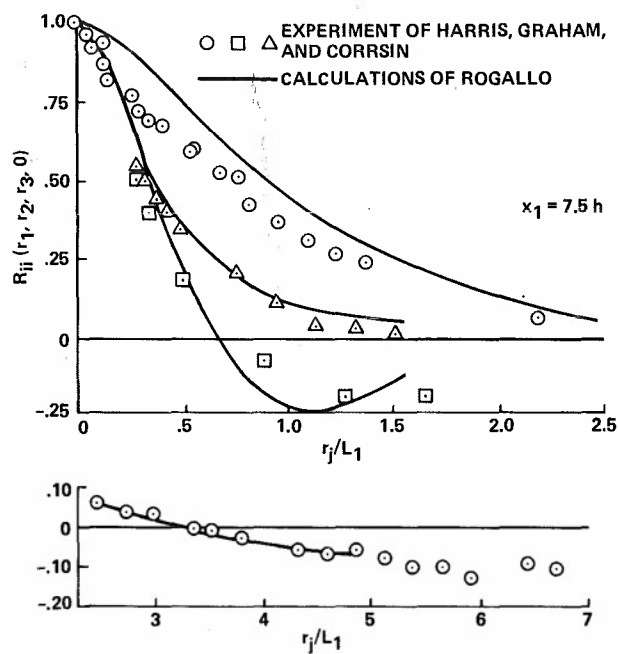


Fig. 16. Two-point correlation coefficients of  $u_1$  along the three Cartesian axes.

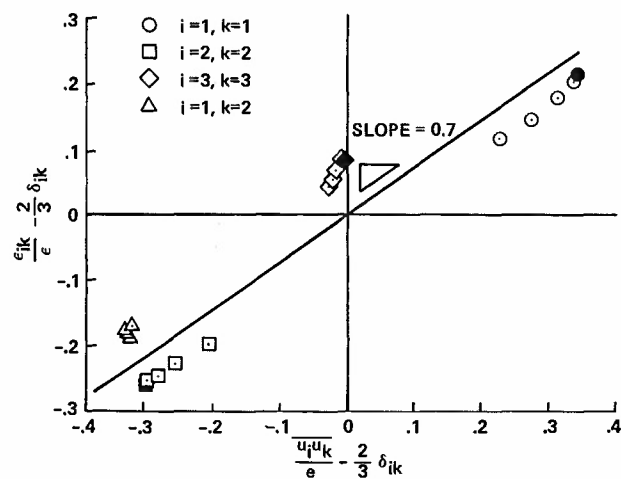


Fig. 17. Components of dissipation within a homogeneous shear flow.

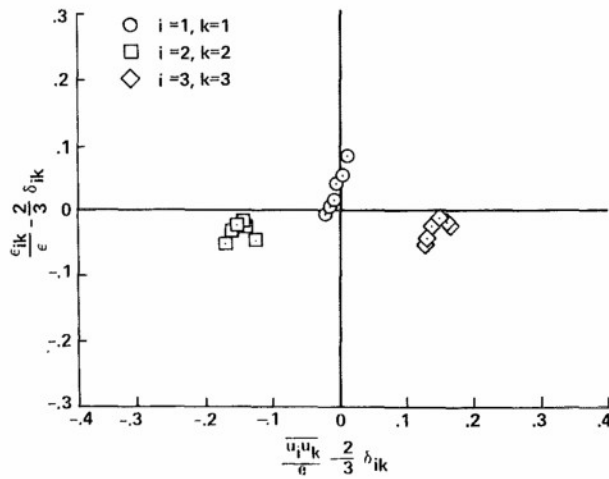


Fig. 18. Components of dissipation in a relaxing homogeneous turbulence after sudden normal distortion.

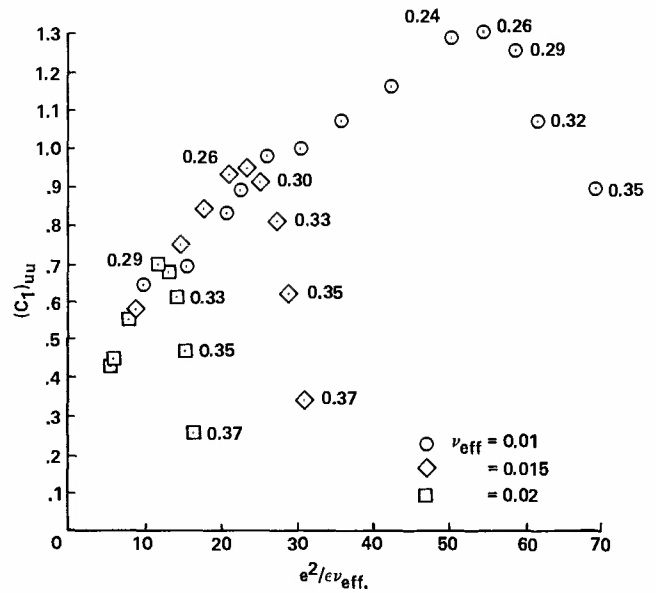


Fig. 19. Behavior of the coefficient in the Rotta pressure rate of strain correlation term in a relaxing homogeneous flow after sudden distortion by normal forces. Numbers near symbols represent the value of the largest component of anisotropy present.

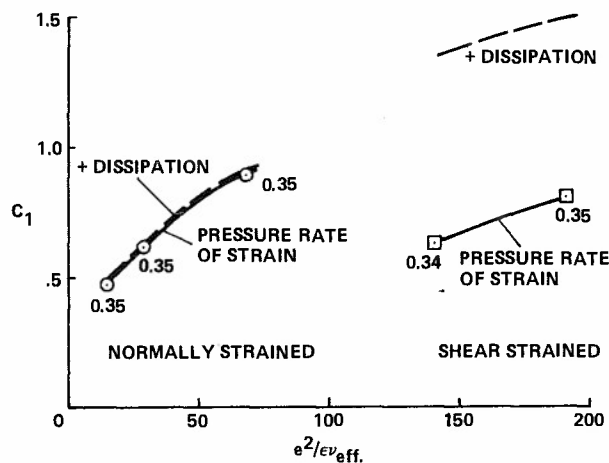


Fig. 20. Reconciliation of modeling the Rotta term in normally and shear strained flows. Numbers near the symbols represent the value of the largest component of anisotropy present.



## A NAVIER-STOKES FAST SOLVER FOR TURBULENCE MODELING APPLICATIONS

J. D. Murphy and M. W. Rubesin  
Ames Research Center, NASA, Moffett Field, California, U.S.A.

## SUMMARY

A computer program for the solution of the steady Reynolds averaged incompressible Navier-Stokes equations that can accept a variety of turbulence closure models is described. The program is sufficiently accurate and economical to permit extensive comparisons with mean moment data from experiment. Such a computer program should provide a useful tool to the turbulence modeler because of the generality of the models which can be considered and the economy with which solutions can be obtained.

In the present study 0-, 1-, and 2-equation closure models are considered and the computed results compared with experiment and with results of boundary-layer calculation using the same models. From these comparisons one may conclude that flow parameters which are sufficiently severe to provide strong tests of higher order closure models are also sufficiently severe as to cast doubt on the results based on classical boundary-layer calculations. To demonstrate the accuracy and speed of the program parametric studies are presented which show the effects of both purely numerical considerations, such as mesh size, convergence criteria, boundary location, etc., and physical consideration such as boundary conditions, etc.

It is believed that the present computer code is more general than previously available fast solvers. No near-wall equilibrium assumptions have to be made, as both the mean flow and turbulence closure relations are integrated all the way to the wall.

## INTRODUCTION

A realistic assessment of the probable advances in both computer design and algorithm development indicates that for the prediction of turbulent flows the Reynolds averaged equations of motion solved over relatively coarse grids will likely be the most sophisticated computational design tool generally available to engineers over the next decade. This places a major burden of improving our predictive capability on improved turbulence modeling. Because of the inherent empiricism of such models, this improvement requires a large data base from detailed and reliable experiments. In addition, a tool must be available that can make accurate and economical comparisons between these data and proposed models. One such tool is the subject of this paper. We propose a fast-solver for the Navier-Stokes equations capable of incorporating various first- and second-order closure models.

The so-called first-order closure models, in which the Reynolds stresses are assumed to be unique functions of the mean-velocity field, have been developed over the past 40 years to the point where they have minimal further potential and are still inadequate to treat flows undergoing rapid changes in boundary conditions. The next logical step is that of second-order closure, in which the Reynolds stresses are related to one or more properties of the turbulence itself, through differential equations. Although the second-order closure concept was proposed more than 30 years ago, it has only during the past decade been seriously considered as a predictive tool for engineering applications.

The case for second-order closure may be put in better perspective by considering its advantages and disadvantages vis-a-vis simpler modeling. First, in contrast to mixing length theory, for example, there exists a potential in second-order modeling for relatively broad application as the modeling forms themselves have been drawn from more than shear flows. Thus, they may be able to treat flow fields containing different classes of flows, for example, attached boundary layers, separation bubbles, vortex motions, and local jets. Because the models have drawn upon data from different types of flows, these models often have the disadvantage of being less accurate for a specific flow than are the more empirical first-order closure models. Second, as a result of the above, the computer logic for treating complex flows need not keep track of separate zones and need not switch either models or constants on and off. The modeling equations themselves, however, are much more complicated and due to a large range of eigenvalues, that is, stiffness, are less tolerant of breaches of mathematical etiquette, and hence are computationally more costly. Finally, second-order closure may provide a predictive capability in the sense that once confidence can be established in a model it may be reliable outside the range of experimental verification.

From the above it is clear that the potential advantages of second-order closure methods warrant their further development. In this paper we describe a computer code for the evaluation and/or optimization of the predictive potential of second-order turbulent closure models in simple two-dimensional flow configurations.

The bulk of this paper is made up of the description of a procedure for the numerical solution of the steady constant property Navier-Stokes equations together with algebraic, and one- and two-differential equation turbulence closure models. Since we consider only the steady equations, a relaxation procedure is used and a first guess of all variables over the whole field is required. This first guess is generated within the program as the solution to the boundary-layer equations. The advantages of this technique are twofold: first, boundary-layer solutions are obtained as a by-product of the Navier-Stokes solutions permitting an evaluation of boundary-layer theory for a particular flow, and second, a generally very good first guess is obtained leading to rapid convergence and hence low computation costs.

In order to illustrate the potential of the present method we present comparisons of four different turbulence models with several sets of experimental data. In addition, parametric studies of the effects of initial conditions and boundary conditions, are described. The effects of purely numerical parameters, such as mesh size, boundary locations, and convergence criteria are presented in an appendix.

Finally a table of computation time for all the results presented is provided to demonstrate the utility of the present method even under the constraint of a relatively modest computational budget.

## ANALYSIS: THE MEAN FLOW EQUATIONS

The equations of motion for a constant property steady flow in Reynolds averaged form may be written as:

$$\frac{\partial u}{\partial x} + \frac{\partial v}{\partial y} = 0 \quad (1)$$

$$u \frac{\partial u}{\partial x} + v \frac{\partial u}{\partial y} = -\frac{1}{\rho} \frac{\partial p}{\partial x} + \nu \left( \frac{\partial^2 u}{\partial x^2} + \frac{\partial^2 u}{\partial y^2} \right) + \frac{\partial \tau_{xx}}{\partial x} + \frac{\partial \tau_{xy}}{\partial y} \quad (2)$$

$$u \frac{\partial v}{\partial x} + v \frac{\partial v}{\partial y} = -\frac{1}{\rho} \frac{\partial p}{\partial y} + \nu \left( \frac{\partial^2 v}{\partial x^2} + \frac{\partial^2 v}{\partial y^2} \right) + \frac{\partial \tau_{xy}}{\partial x} + \frac{\partial \tau_{yy}}{\partial y} \quad (3)$$

which provides three equations in the six unknowns  $u$ ,  $v$ ,  $p$ ,  $\tau_{xx}$ ,  $\tau_{xy}$ , and  $\tau_{yy}$ . Here,  $\tau_{xx}$  and  $\tau_{yy}$  are the Reynolds normal stresses and  $\tau_{xy}$  is the Reynolds shear stress. In the present study the system of equations is closed by introduction of a generalized scalar eddy-viscosity via the constitutive relation.

$$\tau_{ij} = -\frac{2}{3} \epsilon \delta_{ij} + 2\epsilon \left[ \frac{1}{2} \left( \frac{\partial u_i}{\partial x_j} + \frac{\partial u_j}{\partial x_i} \right) \right] = -\overline{u_i u_j} \quad (4)$$

Evaluating the Reynolds normal stresses from (4) and substituting in (2) and (3) we obtain:

$$\frac{\partial u}{\partial x} + \frac{\partial v}{\partial y} = 0 \quad (5)$$

$$u \frac{\partial u}{\partial x} + v \frac{\partial u}{\partial y} = -\frac{1}{\rho} \frac{\partial p}{\partial x} \left( p + \frac{2}{3} \rho \epsilon \right) + \nu \left( \frac{\partial^2 u}{\partial x^2} + \frac{\partial^2 u}{\partial y^2} \right) + 2 \frac{\partial}{\partial x} \epsilon \frac{\partial u}{\partial x} + \frac{\partial \tau_{xy}}{\partial y} \quad (6)$$

$$u \frac{\partial v}{\partial x} + v \frac{\partial v}{\partial y} = -\frac{1}{\rho} \frac{\partial p}{\partial y} \left( p + \frac{2}{3} \rho \epsilon \right) + \nu \left( \frac{\partial^2 v}{\partial x^2} + \frac{\partial^2 v}{\partial y^2} \right) + \frac{\partial \tau_{xy}}{\partial x} + 2 \frac{\partial}{\partial y} \epsilon \frac{\partial v}{\partial y} \quad (7)$$

$$\tau_{xy} = \epsilon \left( \frac{\partial u}{\partial y} + \frac{\partial v}{\partial x} \right) \quad (8)$$

We note that the substitution of the Reynolds normal stress relations from (4) while the Reynolds shear stress in (6) and (7) and its defining relation (8) are retained, is somewhat arbitrary. This condition is an artifact of the development of the numerical solution procedure. It permits the imposition of continuity conditions on the Reynolds shear stress, which in turn facilitates convergence while keeping the matrix block size at  $8 \times 8$ . Equivalent treatment of the Reynolds normal stress would increase the block size to  $12 \times 12$ .

The variables are normalized as  $\bar{u} = u/U_0$ ,  $\bar{v} = v\sqrt{\text{Re}}/U_0$ ,  $\bar{x} = x/L$ , and  $\bar{y} = y\sqrt{\text{Re}}/L$  and the dimensionless stream-function and vorticity are introduced, such that

$$\frac{\partial \psi}{\partial y} = \bar{u} \quad \text{and} \quad \frac{\partial \psi}{\partial x} = -\bar{v}$$

After much manipulation we obtain

$$\omega = \frac{\partial^2 \psi}{\partial \bar{y}^2} + \frac{1}{\text{Re}} \frac{\partial^2 \psi}{\partial \bar{x}^2} \quad (9)$$

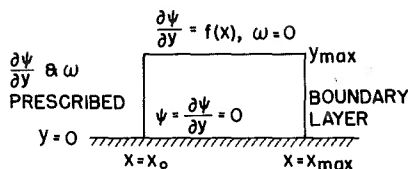
$$\frac{\partial \psi}{\partial \bar{y}} \frac{\partial \omega}{\partial \bar{x}} - \frac{\partial \psi}{\partial \bar{x}} \frac{\partial \omega}{\partial \bar{y}} = \frac{\partial^2 \omega}{\partial \bar{y}^2} + \frac{1}{\text{Re}} \frac{\partial^2 \omega}{\partial \bar{x}^2} + \frac{\partial^2 \tau_{xy}}{\partial \bar{y}^2} - \frac{1}{\text{Re}} \frac{\partial^2 \tau_{xy}}{\partial \bar{x}^2} + \frac{4}{\text{Re}} \frac{\partial^2}{\partial \bar{x} \partial \bar{y}} \epsilon \frac{\partial^2 \psi}{\partial \bar{x} \partial \bar{y}} \quad (10)$$

$$\tau_{xy} = \frac{\epsilon}{\nu} \left( \omega - \frac{2}{\text{Re}} \frac{\partial^2 \psi}{\partial \bar{x}^2} \right) \quad (11)$$

Equations (9)-(11) are solved with the boundary conditions; at

$$\left. \begin{aligned} \bar{y} = 0 & \quad \psi = \frac{\partial \psi}{\partial \bar{y}} = 0 \\ \bar{y} = \bar{y}_{\max} & \quad \frac{\partial \psi}{\partial \bar{y}} = \frac{u_e(x)}{U_0}, \quad \omega = 0 \\ \bar{x} = \bar{x}_0 & \quad \psi = \psi(x_0, y), \quad \omega = \omega(x_0, y) \\ \bar{x} = \bar{x}_{\max} & \quad \text{Eqs. (9)-(11) with } 1/\text{Re} \text{ set to zero} \end{aligned} \right\} \quad (12)$$

These relations together with one or more relations defining the eddy viscosity form the system considered here. The equations are solved on a reduced computational domain shown schematically below. Since the relation(s) used for eddy viscosity vary from model to model they will be discussed under the heading of the appropriate model.



The numerical procedure used to solve Eqs. (9)-(11) given  $\varepsilon/\nu$  is a generalized Galerkin method closely paralleling that of Ref. 1. In brief, Eqs. (9) and (10) are integrated over the interval  $\bar{y}_j$  to  $\bar{y}_{j+1}$ .

The Taylors series expansions

$$\psi'_{ij+1} = \psi'_{ij} + \psi''_{ij}\Delta\bar{y} + \psi'''_{ij}\frac{\Delta\bar{y}^2}{2!} + \psi^{IV}_{ij}\frac{\Delta\bar{y}^3}{3!} + \psi^{V}_{ij}\frac{\Delta\bar{y}^4}{4!}$$

$$\psi'_{ij+1} = \psi'_{ij} + \psi''_{ij}\Delta\bar{y} + \psi'''_{ij}\frac{\Delta\bar{y}^2}{2!} + \psi^{IV}_{ij}\frac{\Delta\bar{y}^3}{3!}$$

$$\psi''_{ij+1} = \psi''_{ij} + \psi'''_{ij}\Delta\bar{y} + \psi^{IV}_{ij}\frac{\Delta\bar{y}^2}{2}$$

where

$$\psi^{IV}_{ij} = \frac{\psi'''_{ij+1} - \psi'''_{ij}}{\Delta\bar{y}}$$

and

$$\omega_{ij+1} = \omega_{ij} + \omega'_{ij}\Delta\bar{y} + \omega''_{ij}\frac{\Delta\bar{y}^2}{2!} \quad (13)$$

where

$$\omega''_{ij} = \frac{\omega'_{ij+1} - \omega'_{ij}}{\Delta\bar{y}}$$

and

$$\bar{\tau}_{ij+1} = \bar{\tau}_{ij} + \bar{\tau}'_{ij}\Delta\bar{y} + \bar{\tau}''_{ij}\frac{\Delta\bar{y}^2}{2}$$

where

$$\bar{\tau}''_{ij} = \frac{\bar{\tau}'_{ij+1} - \bar{\tau}'_{ij}}{\Delta\bar{y}}$$

impose continuity of value and derivatives. This procedure, the integration and incorporation of Taylors series expansions, provides a system of ordinary differential equations in "x" in which the values and "y" derivatives of stream function and vorticity appear as dependent variables. Readers interested in more detail on the discretization process should consult Ref. 1.

The integrals of Eqs. (9) and (10) with Eqs. (11) and (13) provide a system of 8N-6 ordinary differential equations in the 8N unknowns for  $j = 1, N$ . The boundary conditions (10) with the additional conditions;

$$\text{at } \bar{y} = 0 \quad \omega_{i1} = \psi''_{i1}$$

$$\text{at } \bar{y} = \bar{y}_{\max} \quad \psi''_{iN} + \frac{1}{\text{Re}} \frac{\partial^2 \psi_N}{\partial \bar{x}^2} = 0$$

provide a closed mathematical system. These latter two conditions are required by the higher order differencing in  $\bar{y}$  and are simply special forms of the definition of vorticity appropriate to the boundaries. The  $\bar{x}$  dependence is treated by second-order-accurate implicit finite differences. The  $\bar{x}$  dependence of the convective terms is represented by three-point backward differences and the diffusion terms by three-point central differences. This results in a system of 8N algebraic equations in 8N unknowns at each  $\bar{x}$  station.

Although the discretization outlined above differs markedly from the usual, it is related to the compact approximation schemes that are now gaining attention. It can be shown to be fourth-order accurate in velocity and has the advantage of the direct specification of derivative boundary conditions without special treatment. Due to the high accuracy in  $\bar{y}$ , a relatively sparse nodal array may be used while retaining reasonable accuracy.

The system of algebraic equations is solved by a Newton-Raphson iteration that is equivalent, in this case, to a line relaxation method with unity relaxation factor. The resulting  $8 \times 8$  block tridiagonal matrix is solved by L-U decomposition (Ref. 2). This latter procedure for laminar flow provides about an order of magnitude speed as compared with the scheme of Ref. 1.

## TURBULENCE MODEL EQUATIONS

The above mathematical formulation has been carried out under the tacit assumption that the nondimensional eddy viscosity  $\bar{\epsilon}$  would be available as required by mean-flow calculation scheme. With the exception of Eq. (11), all of the relations describing the turbulence parameters are isolated in subroutines, each of which define a single model.

For those models that require the solution of a partial differential equation, the discretizations are carried out in both  $\bar{x}$  and  $\bar{y}$  by standard three-point second-order accurate implicit finite differences. This technique was used instead of the splined Galerkin scheme of the mean flow equations because the ease of both analysis and programming of these techniques, relative to the Galerkin procedure, permits a rapid assessment of a particular model without the investment of a great deal of effort. In addition, the demonstration that the numerics of the turbulence equation solution need not be identical with the mean flow equations would permit users unfamiliar with splined Galerkin techniques to produce alternative turbulence model subroutines using standard techniques. In order to retain a consistent level of accuracy between the fourth-order mean flow solution and the second-order turbulence model equations, the latter have been solved on a finer mesh. Typically, three or four mesh intervals of the turbulence model equations constitute one mesh interval in the mean flow equations. Although this decoupling reduces the computational speed of the overall scheme, the authors believe that the additional flexibility introduced warrants the sacrifice. The solution procedure for the turbulence equations, once discretized, parallels the iterative method of the mean flow equation. The linearization used lags the mean flow and eddy viscosity by one iteration, in the solution of the turbulence equations.

Before we consider individual models it is useful to digress for a moment to consider certain conceptual problems that arise when turbulence models, developed within the framework of a boundary-layer theory, are used in conjunction with the Navier-Stokes equations. The fundamental problem arises from the fact that  $y$  approaches  $\delta$ , to the boundary layer approximation, the strain and the vorticity are identical while for the Navier-Stokes  $\omega = (\partial u_i / \partial x_j) - (\partial u_j / \partial x_i)$ , while  $S_{ij} = (\partial u_i / \partial x_j) + (\partial u_j / \partial x_i)$ . The boundary condition of zero vorticity applied to the Navier-Stokes equations does not necessarily imply zero strain, and from this fact a whole host of problems arise. In particular we lose an unambiguous definition of the boundary-layer thickness and concomitantly of the edge velocity and boundary-layer integral parameters. This may not seem important until one realizes that the turbulence length scale for algebraic and one-equation models is generally a function of  $\delta$  or  $\delta^*$ . In addition, for the two-equation models, finite strain for  $y > \delta$  gives rise to nontrivial turbulence production in the outer flow which can, for some boundary conditions, produce completely irrational solutions.

In order to circumvent these difficulties we have adopted the following ad-hoc procedure. We define the boundary-layer thickness as the smallest value of  $y$  for which  $(u/u_e) > 0.9$  and  $\psi'' \leq 10^{-4} \psi''_{\max}$  and for  $y > \delta$  we define the eddy viscosity as  $\bar{\epsilon} = \bar{\epsilon}_0 \exp[(y - \delta)/\delta]$ . Clearly, other procedures are possible for the definition of  $\delta$ , for example, that used by Lomax and Baldwin (Ref. 3), but all of those familiar to the authors invoke some kind of equilibrium assumptions.

## Zero-Equation Model

The zero-equation model considered in the present study is the two-layer Cebeci-Smith model (ref. 4) written as:

$$\bar{\epsilon} = \min \begin{cases} \bar{\epsilon}_i \\ \bar{\epsilon}_0 \end{cases}$$

where

$$\bar{\epsilon}_i = \frac{1}{\nu} (0.4yD)^2 \left| \frac{\partial u}{\partial y} \right|$$

$$\bar{\epsilon}_0 = 0.0168 \text{ Re}_{\delta^*}$$

and

$$D = (1 - e^{-y^+/A^+})$$

$$A^+ = 26(1 - 11.8p^+)^{-1/2}$$

$$p^+ = - \frac{\nu}{\rho u_{\tau 3}} \frac{\partial p}{\partial x}$$

Although many other mixing length based models have been proposed, this model works quite well for equilibrium flows and is in reasonably general use. It can, therefore, serve as a useful standard of comparison for higher order closure models.

For attached flow, no special numerical techniques are required. Near the separation point, however, large percentage changes can occur in  $\bar{\epsilon}$  near the wall from iteration to iteration; the changes result from relatively small absolute changes in  $\partial u / \partial y$ . To surmount this difficulty, in the neighborhood of separation, we under-relax the eddy viscosity, that is,

$$\bar{\epsilon}^{m+1} = \bar{\epsilon}^m + \beta(\bar{\epsilon}^{m+1} - \bar{\epsilon}^m)$$

where  $m$  is the iteration number and  $\beta$  the relaxation factor.

Solutions have been obtained for  $\beta = 0.1, 0.2$ , and  $0.4$ , which are independent of  $\beta$ . For  $\beta = 0.6$  no convergence was obtained.

### One-Equation Model

The simplest of the second-order closure models requires the solution of an additional nonlinear partial differential equation. For this study we chose the Glushko Model (Ref. 5) as extended by Rubesin (Ref. 6). This model was selected over that of Bradshaw et al. (Ref. 7) because of mathematical convenience, because the constitutive relation for stress as a function of strain is the same as for the two-equation models, and because of a more rational extension to elliptic flows than is yet available for the Bradshaw model.

The equations describing this model for incompressible flow may be written (Ref. 6) as:

$$u \frac{\partial e}{\partial x} + v \frac{\partial e}{\partial y} = \frac{\nu \partial}{\partial y} [1 + \bar{\varepsilon}(\lambda r)] \frac{\partial e}{\partial y} + \frac{\nu \partial}{\partial x} [1 + \bar{\varepsilon}(\lambda r)] \frac{\partial e}{\partial x} + \nu \bar{\varepsilon} S_{ij} \frac{\partial u_i}{\partial x_j} - C\nu [1 + \bar{\varepsilon}(\lambda r)] \frac{e}{\ell^2}$$

where

$$e = \frac{\bar{u}'^2 + \bar{v}'^2 + \bar{w}'^2}{2} \quad \text{the turbulence kinetic energy}$$

$$\bar{\varepsilon} = \frac{\varepsilon}{\nu} \quad \text{the dimensionless turbulent viscosity}$$

$$S_{ij} = \frac{1}{2} \left( \frac{\partial u_i}{\partial x_j} + \frac{\partial u_j}{\partial x_i} \right) \quad \text{the mean strain rate}$$

and  $\ell$  is the turbulence length scale. To complete the model, the Glushko relations

$$r = \frac{\sqrt{e}\ell}{\nu}$$

$$\bar{\varepsilon} = H(r)\alpha r$$

$$H(r) = \begin{cases} \frac{r}{r_0} & 0 \leq \frac{r}{r_0} < 0.75 \\ \frac{r}{r_0} - \left(\frac{r}{r_0} - 0.75\right)^2 & 0.75 \leq \frac{r}{r_0} < 1.25 \\ 1 & 1.25 \leq \frac{r}{r_0} \end{cases}$$

$$\frac{\nu}{\delta} \quad 0 \leq \frac{\nu}{\delta} < 0.23$$

$$\frac{\ell}{\delta} = \left(\frac{\nu}{\delta} + 0.37\right)12.61 \quad 0.23 \leq \frac{\nu}{\delta} < 0.57$$

$$\left(1.48 - \frac{\nu}{\delta}\right)/2.42 \quad 0.57 \leq \frac{\nu}{\delta} < 1.48$$

and

$$\alpha = 0.2$$

$$r_0 = 110$$

$$C = 3.93$$

$$\lambda = 0.4$$

were suggested by the author (Ref. 5). He also proposed the boundary conditions

$$y = 0 \quad e = 0$$

$$y = y_{\max} \quad e = 0$$

This latter condition is required by the form of the equations for large  $y$ .

### Two-Equation Models

Two two-equation models are considered here. The first, due to Jones and Launder (Ref. 8), was chosen because it is a well-known model and is in relatively general use. The second, due to Wilcox and Rubesin (Ref. 9), was chosen because of its familiarity to the authors and because it is an extension of the promising Saffman model (Ref. 10).

The Jones-Launder model with low Reynolds number corrections may be written

$$\rho u_j \frac{\partial k}{\partial x_j} = \rho \tau_{ij} \frac{\partial u_i}{\partial x_j} + \frac{\partial}{\partial x_j} \left[ \left( \mu + \frac{\mu_T}{\sigma_k} \right) \frac{\partial k}{\partial x_j} \right] - \left[ \rho \epsilon + 2\mu \left( \frac{\partial k^{1/2}}{\partial x_{ij}} \right)^2 \right]$$

$$\rho u_j \frac{\partial \epsilon}{\partial x_j} = C_1 \frac{\epsilon}{k} \tau_{ij} \frac{\partial u_i}{\partial x_j} + \frac{\partial}{\partial x_j} \left( \mu + \frac{\mu_T}{\sigma_\epsilon} \right) \frac{\partial \epsilon}{\partial x_j} - C_2 \frac{\rho \epsilon^2}{k} + \frac{2\mu \mu_T}{\rho} \left( \frac{\partial^2 u}{\partial x_j^2} \right)^2$$

where

$$\mu_T = C_\mu \rho k^2 / \epsilon$$

$$C_\mu = 0.09 \exp[-2.5/(1 + R_T/50)]$$

$$C_1 = 1.45$$

$$C_2 = 2[1 - 0.3 \exp(-R_T^2)]$$

$$\sigma_k = 1$$

$$\sigma_\epsilon = 1.3$$

$$R_T = \frac{\rho k^2}{\mu \epsilon}$$

In the above, consistent with the notation of Ref. 8,  $k$  is the kinetic energy of turbulence,  $\epsilon$  the energy dissipation rate,  $R_T$  is a turbulence Reynolds number,  $\sigma_k$  and  $\sigma_\epsilon$  Prandtl numbers, and  $\mu_T$  the eddy viscosity.

The Wilcox-Rubesin model may be written as

$$\rho u_j \frac{\partial e}{\partial x_j} = \rho \tau_{ij} \frac{\partial u_i}{\partial x_j} + \frac{\partial}{\partial x_j} \left[ \left( \mu + \sigma_\rho^* \epsilon \right) \frac{\partial e}{\partial x_j} \right] - \beta^* \rho \omega e$$

$$\rho u_j \frac{\partial \omega^2}{\partial x_j} = \frac{\gamma \omega^2}{e} \rho \tau_{ij} \frac{\partial u_i}{\partial x_j} + \frac{\partial}{\partial x_j} \left[ \left( \mu + \sigma_\rho \epsilon \right) \frac{\partial \omega^2}{\partial x_j} \right] - \left[ \beta + 2\sigma \left( \frac{\partial \ell}{\partial x_k} \right)^2 \right] \rho \omega^3$$

where

$$\epsilon = \frac{\gamma^* \epsilon}{\omega}$$

$$\beta = \frac{3}{20}, \quad \beta^* = \frac{9}{100}, \quad \sigma = \sigma^* = \frac{1}{2}$$

$$\gamma^* = [1 - (1 - \lambda^2) \exp(Re_T/Re)]$$

$$\gamma \gamma^* = \gamma_\infty [1 - (1 - \lambda^2) \exp(-Re_T/R_\omega)]$$

$$\gamma_\infty = \frac{10}{9}, \quad \lambda = \frac{1}{11}, \quad Re = 1, \quad R_\omega = 2$$

$$Re_T = \frac{\rho e^{1/2} \ell}{\mu}, \quad \ell = e^{1/2} / \omega, \quad \gamma_\infty^* = 1$$

In the above,  $e$  is the kinetic energy of turbulence,  $\omega$  the dissipation rate per unit energy,  $Re_T$  is a Reynolds number of turbulence, and  $\sigma^*$  and  $\sigma$  are reciprocal Prandtl numbers.

The outer boundary conditions imposed on both two-equation models are that all derivatives with respect to "y" vanish. On the inner boundary, the turbulence kinetic energy is zero while, for the Jones-Launder model,  $\epsilon = 0$  at  $y = 0$  and, for the Wilcox-Rubesin model,  $\omega = 20\nu/\beta y^2$  as  $y \rightarrow 0$ .

For both two-equation models, under-relaxation of the iterative process is required. Initially, a relaxation factor of 0.1 is required; it can be increased to 0.5 as the calculation progresses. Note that all three of the second-order closure models have a mesh Reynolds number limitation,  $Re_{\Delta y} = \nu \Delta y / \nu < 2$ . Violation of this condition gives rise to large point-to-point oscillations which occur first near the boundary-layer edge.

#### PARAMETRIC STUDIES

One of the disadvantages of second-order closure from the computational viewpoint is the need to specify additional in-flow boundary conditions for the intensity and scale of turbulence. Recently, one is more likely to find that the experimenter has measured turbulence energy profiles; however, the distribution of dissipation is usually lacking, being a quantity that cannot be measured directly and that requires arguments regarding the isotropic character of dissipation to be evaluated. In order to generate these distributions the following procedure was used. Using the boundary-layer code of Wilcox (Ref. 11), for  $\partial p / \partial x = 0$  and some small level of turbulence energy, the program was run through a simulated transition until the predicted

momentum thickness corresponded to the experimental momentum thickness at the first measurement station. The values of turbulence kinetic energy and dissipation were then transformed and used as the in-flow boundary condition on the present method for the Wilcox-Rubesin model. For the Jones-Launder model the same energy profile was used and the dissipation profile was generated by assuming the eddy viscosity to be the same for the two methods, yielding the relation

$$\epsilon = C_{\mu} k w / \gamma^*$$

The utility of comparisons of second-order closure models with experiment hinges then on the sensitivity of the solution to these upstream boundary conditions and the rate at which the effects of these conditions washout in the downstream direction.

The effects of variations in the initial conditions were checked under the flow conditions of experiments chosen to be used as standards of comparison in the work that follows. These experiments are as follows: the Wieghardt flat plate case (Ref. 12), the Samuel and Joubert increasingly adverse pressure gradient case (Ref. 13), and the adverse pressure cases of Strickland and Simpson (Ref. 14), and of Simpson et al. (Refs. 14 and 15), and of Schubauer and Klebanoff (Ref. 16).

For the Wieghardt flat plate case (Ref. 12), the Glushko model was run twice with the initial energy profile multiplied by 0.9 and by 1.1, respectively. By the third streamwise station, a distance normalized by the upstream B.L. thickness of  $x/\delta_0 = 25$ , the energy profiles of both solutions had equilibrated to within about 1% of the original. Similar variations were imposed on the Wilcox-Rubesin model. With the initial dissipation profile fixed, the initial energy profiles were multiplied by 0.9 and 1.1; and with the initial energy profile fixed the dissipation profile was multiplied by 0.9 and 1.1. A comparison of these four solutions showed behavior similar to that of the Glushko model for the  $\pm 10\%$  variations in the initial energy distribution, and only a slightly stronger sensitivity to similar variations in the initial dissipation distribution. Exactly parallel calculations were carried out for the data of Samuel and Joubert (Ref. 13) with similar results.

Some difficulties with initial conditions were encountered with both the flows of Refs. 14-16. These problems will be discussed in the next section in connection with the description of calculations for the flows in question.

These experiments were chosen for comparison because, with the exception of the Wieghardt flow, they represent a class of flows, that is, flows with strong adverse pressure gradients, that severely strain our present predictive capability.

## RESULTS AND DISCUSSION

In keeping with the expressed goals of the present study, the principal result is that the computer code, satisfying the specifications of efficiency and flexibility in accepting different turbulence models, is complete and operational. The efficiency of the code is demonstrated by the execution time required, on a CDC 7600, for 15 different calculations (shown in Table 1). One should note that the times cited include solution to both the boundary-layer and Navier-Stokes equations. Typical run times can be seen to be less than 1 min, which brings the use of the present code well within the reach of all but the most stringent computational budgets. The flexibility of the code will be demonstrated by the specific results of applying four different turbulence models to four flow configurations. These results in the form of skin friction distributions, are presented in the following pages. It should be noted again that the intent of these figures is to demonstrate the performance of the basic method and not to provide definitive comparisons of the various models.

In Fig. 1 we compare the distribution of skin-friction coefficient as obtained from each of the four closure models with the data of Wieghardt (Ref. 11). This experiment was chosen to provide a baseline comparison for all the models under equilibrium flow conditions. Note that once the starting transient has damped, the Glushko model predicts a  $C_f$  about 10% too high, and the Wilcox-Rubesin model one about 5% too low; the Cebeci-Smith and Jones-Launder models are probably within the experimental error band. Modification of the modeling constants within the Glushko and Wilcox-Rubesin models could substantially improve their agreement with these data (cf. Ref. 17). In the present study, however, we have elected to use the modeling parameters proposed by the originating authors.

Figure 2 shows the streamwise distribution of free-stream velocity for the experiment of Samuel and Joubert (Ref. 13) for an increasingly adverse pressure distribution. The experiment was carried out over an extended period with the tunnel adjusted to provide  $C_p(x)$  and entry Reynolds number invariant with time. The velocities plotted in Fig. 2 are provided for reference.

Figure 3(a) compares the boundary-layer and Navier-Stokes solutions for skin-friction coefficient using the Cebeci-Smith model with the data of Samuel and Joubert. The difference between boundary-layer and Navier-Stokes calculations for this case is due to some extent to the aforementioned difficulty in defining  $\delta$  and  $\delta^*$  for the Navier-Stokes calculations. This hypothesis was verified by rerunning the calculation using the  $\delta(x)$  and  $\delta^*(x)$  computed in the boundary layer solution as the mixing length scaling factors in the Navier-Stokes solution. These results are presented in Fig. 3(b). It can be seen that roughly half the discrepancy between boundary-layer and Navier-Stokes solutions, for this case, is attributable to the uncertainties in defining  $\delta$  and  $\delta^*$  in the Navier-Stokes calculations.

Figure 3(c) presents similar results using the Glushko closure model. The behavior of the Glushko model here parallels that shown in Fig. 1. That is, the predicted skin friction rises sharply initially and then predicts values which are 15% to 20% too high compared with the data. As in the case of the Cebeci-Smith model the agreement worsens as the pressure gradient increases.

Figures 3(d) and 3(e) provide similar comparisons for the Jones-Launder and Wilcox-Rubesin closure models. The initial excursions in  $C_f$  are apparently associated with inconsistencies between the energy and dissipation profiles and the mean flow profiles at the in-flow boundary. The relatively poor performance

of the Jones-Launder model in the region  $0.84 \leq x \leq 2.4$  is almost certainly associated with the choice of in-flow boundary conditions. For  $x > 2.4$ , however, the Wilcox-Rubesin model appears to follow the trend of the experiment more closely. These latter two figures demonstrate the sensitivity of the two-equation models to in-flow boundary conditions on the turbulence properties and to the inadequacy of the present procedure for determining them in general. However, because the optimum procedure for determining these conditions will almost certainly vary from model to model, it was not considered to be fundamental to the present study; therefore, it could be deferred to a subsequent effort or left to the modelers to devise.

The next flow to be considered is that of Strickland and Simpson (Ref. 14) and of Simpson, Strickland, and Barr (Ref. 15). The most interesting point about these experiments, in addition to their complete documentation, is the fact that the imposed pressure distribution leads to separation. The free-stream velocity distribution is shown in Fig. 4. It is unfortunate that these data, insofar as they were reported in Refs. 14 and 15, were obtained at relatively large streamwise intervals in the region of adverse pressure gradient because it introduces, with the redundancy of measurement techniques (laser anemometer, pitot, and slant and normal hot films), a degree of arbitrariness into the edge velocity to be matched in the calculation. The fairing used provides the largest velocity gradient that can be inferred from the data. Figure 5(a) compares the predicted skin-friction distribution, from boundary-layer and Navier-Stokes solutions using the Cebeci-Smith model, with the data of Refs. 14 and 15. Consistent with their behavior in laminar flow (cf. Refs. 1 and 17), the boundary-layer equations tend to predict a "too early" occurrence of separation, as compared to the Navier-Stokes equations. In fact, for this case the Navier-Stokes equations do not predict separation to occur at all. Similar results are shown in Fig. 5(b) for the Glushko model. In agreement with previous results, the Glushko model predicts a  $C_f$  distribution somewhat higher in value than does the Cebeci-Smith model.

The experimental behavior of turbulent separation, noted by Simpson et al. is that the streamwise pressure distribution appears to relax immediately downstream of the intermittent separation point. This is in sharp contrast to the laminar flow cases cited above, and to the turbulent flow case to be discussed, for which we find that the strong adverse pressure gradient must be maintained well past the computed separation point in order for the flow to separate. This is apparently the result of strong streamwise ellipticity in the neighborhood of the separation point. The fact that the physical flow does not exhibit this behavior argues for some different, or at least additional, mechanism to be active in the turbulent flow case. A logical candidate for this additional mechanism, noted in Refs. 14 and 15, and consistent with the data of Ref. 18, is a strong augmentation of the Reynolds normal stresses approaching separation. In order to accommodate this behavior, it would be necessary to employ more complicated models than those considered here. The authors were recently informed that Launder is currently incorporating an augmented normal stress within a new two-equation model.

Pletcher (Ref. 19), using an inverse boundary-layer procedure specifies the experimentally observed distribution of displacement thickness, was able to predict the separation point for this flow using what might be called a half-equation model. He uses an ordinary differential equation for mixing length in the outer flow. It is interesting to note, however, that the edge-velocity distribution predicted using this method displays a velocity gradient ahead of separation that is roughly twice as large as that observed experimentally. This implies that if a method such as that proposed in Ref. 20, an inverse boundary-layer method driven to produce an imposed velocity distribution, were used the results might well be more consistent with Navier-Stokes solutions presented here.

Simpson and Collins (Ref. 21), have also predicted the separation point in this flow using a modified version of Bradshaw's model. The modification consists of the addition of Reynolds normal stress terms to both the mean flow momentum and turbulence energy equations in an ad hoc fashion. It is noteworthy that both of these techniques produce the desired results, that is, separation, but based on totally different physical hypotheses. The Simpson-Collins approach was apparently guided by the experimental measurement of Reynolds normal stresses and further emphasizes the need for good communication between the experimenter, the modeler, and the computational workers.

The in-flow boundary conditions on the mean flow, that is,  $u(x_0, y)$  and  $C_f(x_0)$ , for the calculations presented up to this point, were deduced from the experimental measurements. For the Strickland, Simpson, and Barr flows we were unable to obtain initial conditions on the energy and dissipation, using the previously described procedure, which were sufficiently consistent with the experimental mean flow conditions to permit the calculation to proceed. To circumvent this problem we used the Wilcox code (Ref. 11), starting near  $x = 0$  with a laminar flow, and allowing the flow to develop, through a simulated transition, under the effects of the experimental pressure distribution. The in-flow boundary conditions at  $x = 2.63$  m were taken entirely from this calculation. The skin-friction coefficient was about 15% higher than that observed experimentally and velocity profile was somewhat fuller in the near-wall region.

The Cebeci-Smith and Glushko models are shown in Figs. 6(a) and 6(b). The large differences between the results presented in Figs. 5(a) and 6(a) are attributable solely to the differences in mean flow conditions on the inflow boundary. Similarly, the differences between Figs. 5(b) and 6(b) can be attributed primarily to the effects of mean flow initial conditions. Although some increment of this difference is associated with differences in energy profiles at the inflow boundary, our experience cited earlier indicates that this is small and damps rapidly.

Figures 6(c) and 6(d) present similar results using the Jones-Launder and Wilcox-Rubesin models. The poor agreement of both two-equation models for this case is attributed to the inadequacy of our procedure for obtaining initial conditions.

The final flow considered in the present study was that of Schubauer and Klebanoff (Ref. 16). Because we wished to present at least one set of calculations that included a prediction of separation and reattachment, we took some liberties with the edge-velocity distribution downstream of the location  $x = 7.0$  m ( $x = 23$  ft). To demonstrate the capability of the present method to predict a region of recirculating flow, we extended the region of constant adverse velocity gradient to about 8.4 m and added a region of accelerating flow for  $8.9 \leq x \leq 9.8$  m to force reattachment within the computational domain. The experimental velocity distribution together with that used in the computation are shown in Fig. 7.



Figures 8(a) and 8(b) show the results of applying the Cebeci-Smith and Glushko closure models, respectively, to this flow using the experimental mean flow parameters as in-flow boundary conditions. The experimental skin friction is plotted only over the region for which the experimental and computational boundary conditions,  $u_e(x)$ , correspond. Again, the Glushko model produces a somewhat higher skin-friction coefficient in the attached flow region than does the Cebeci-Smith model. The separation bubble predicted using the Glushko model is somewhat larger than that predicted by the Cebeci-Smith model but in light of the uncertainty in initial conditions the authors are hesitant to interpret this as being meaningful. The mesh configuration for this flow was such that the streamwise extent of the bubble encompassed 8 nodes and the stream-normal region of negative velocity from 1 to 8 nodes.

We experienced the same difficulty with the two-equation models with this flow as was described in connection with the flows of Strickland, Simpson, and Barr. A parallel starting procedure was followed and the results for the four closure models are presented in Figs. 9(a) through 9(d).

The interesting points to be deduced from these figures, which have not already been made, are that they verify the authors' hypotheses that in order to obtain significant discrimination between turbulence models they must be used to predict flows with rapidly varying boundary conditions, and that the introduction of different turbulence models into any mean-flow-solution procedures cannot be considered a routine task, our inability to obtain a converged solution in the Navier-Stokes mode for the Wilcox-Rubesin model being a case in point. The investigator wishing to consider higher order closure models should be prepared to face substantial numerical difficulties in the development of reliable algorithms for these methods.

We turn our attention now to some observations that can be made from the collective results to date, and from the results of other studies. Viegas, Coakley, and Horstmann, in a series of studies (Refs. 22-24) have applied slightly modified versions of the models considered here to transonic, supersonic, and hypersonic shockwave boundary-layer interactions using a Navier-Stokes code based on the McCormack fast solver (Ref. 25). Although it is impossible to make rigorous comparisons of the present results with those cited above, the relative values of  $C_f$  from model to model appear to be consistent.

The difficulties faced by the present authors in the numerical solution of the two-equation models do not appear to be unique to the present study. Coakley and Viegas (Ref. 22), for example, were forced to introduce special bounding functions on the energy and length scale to prevent solution divergence.

We believe that the present method has certain advantages as a model test vehicle over that used in Refs. 22-24, despite its restriction to incompressible flow. These advantages are the economy of calculation and the innate high accuracy on a sparse mesh. Despite the fact that the restricted computational domain requires the explicit specification of the in-flow boundary conditions on turbulence properties, it is considered to provide significant advantages in a model test vehicle. First, it requires the user to be aware of the approximations involved in the generation of these conditions. Second, it permits the numerical evaluation of discrete regions of the flow field in relatively fine detail without exorbitant demands on either computer time or storage. Finally it permits the imposition of the experimentally observed free-stream velocity distribution on the calculations so that differences between the predicted and experimental values of other parameters, for example,  $C_f(x)$ , can be attributed directly to the model in use, and should facilitate rational model optimization.

Although the present algorithm is well suited to vector processing no advantage has been taken of the 7600 vector software so that the code can be used on other machines with only minor modifications.

Among the advantages of the present method relative to other incompressible Navier-Stokes solution algorithms is the fact that it is fourth-order accurate in  $y$  on an arbitrary mesh and second-order accurate in  $x$  on a uniform mesh. Since equal  $x$ -mesh size is used throughout, the lead-truncation-error term is of odd order and numerical viscosity, which frequently clouds the results of other methods, is practically nonexistent. In addition, the solution is carried out over the whole mesh  $0 \leq y \leq y_{\max}$  and no near-wall approximations are made.

#### CONCLUDING REMARKS

Substantial progress has been made toward the basic goal of the present study, which is to develop an efficient and accurate test vehicle for turbulence models that can treat flows with recirculation. In addition, we have made a substantial effort to point out some of the problems that arise when higher order models are used and particularly when they are used in conjunction with the Navier-Stokes equations.

Although the specific comparisons of the several models with each other and with experiment are not to be considered definitive, because of difficulties in obtaining consistent in-flow boundary conditions, the trends appear to agree with those of other investigations.

Finally, although the authors substantially concur with Liepman (Ref. 26) regarding the uncertainty of the meaning of the Reynolds-averaged equations and the difficulty in assessing the utility of various models, we believe that from the practical engineering point of view, modeling of turbulence within the Reynolds averaged equations constitutes an upper bound on admissible complexity for at least the next decade. It is to be hoped that methods like the present will ease the path of those engaged in modeling to the extent that the designer might ultimately have, if not a universal model, at least a family of models applicable to various types of flows and ranges of parameters.

## APPENDIX

## NUMERICAL PARAMETRIC STUDIES

In the simulation of a physical event by means of a numerical calculation scheme there are, associated with the scheme, parameters having no physical analog. As a result, the selection of values for these parameters must be based on experience with the particular calculation scheme in question and the propriety of the selection must be checked post-hoc.

The purely numerical parameters of the present method are  $\Delta X$ , the streamwise step size common to both the mean flow equations and the turbulence equations;  $\Delta Y$ , the stream-normal step size in the mean flow equations;  $\Delta Y_T$ , the stream normal step size in the turbulence equations;  $C_{ONVER}$ , the convergence criterion for the mean flow equations;  $C_{ONVERT}$ , the convergence criterion for the turbulence equations;  $Y_{MAX}$ , the upper boundary of the computational domain; and  $X_{MAX}$ , the downstream boundary of the computational domain.

EFFECTS OF  $X$  STEP SIZE

The effects of the  $X$  step size were examined by applying the present method, using the Wilcox-Rubesin model, to the flow conditions of the Wiegardt flat plate. These flow conditions were used to isolate the effects of  $\Delta X$  in the calculation from the effects of the streamwise definition of the boundary conditions.

Six sets of calculations were carried out with  $\Delta X$  ranging from  $0.5 \delta_0$  to  $16 \delta_0$ . Except for the region of the starting transient near the left-hand boundary, the skin-friction distribution changed by the order of 1% between the smallest and largest  $X$  step size.

EFFECTS OF  $Y$  STEP SIZE

The discussion of the effects of  $Y$  step size is complicated by the fact that a strongly non-uniform  $Y$ -mesh is used. In contrast to the usual finite difference procedure, the accuracy of the present method is insensitive to the rate of growth of the  $Y$ -mesh, but like finite difference methods, it is sensitive to both the size of the largest  $\Delta Y$  and to the distribution of points in  $Y$ .

Three different distributions of  $Y$  points and three different  $Y_{min}$  were considered in conjunction with the Wilcox-Rubesin model and the flow conditions of Samuel and Joubert. The array of  $Y$  points finally selected was distributed, on the basis of the initial velocity profile, as follows.

1. 5 to 6 points for  $0 \leq y^+ < 10$
2. 15 to 16 points for  $10 \leq y^+ < 200$
3. 8 to 10 points for  $200 \leq y^+ < y_{max}^+$

The use of additional points in " $y$ " produced results that were indistinguishable to three significant figures; using only every other point in the above distribution produced a change of  $C_f$  at the downstream boundary of about +6%.

The use of the mean flow mesh cited above in the turbulence equations, contrary to our expectations, provides adequate resolution. This was verified by solving the turbulence equation with 2 and 3 times the point density without significant change in the eddy-viscosity distribution. This is due, at least in part, to the fact that the eddy viscosity is the ratio of two computed parameters so that small errors of the same sign in both parameters will tend to compensate.

## EFFECT OF CONVERGENCE CRITERIA

Because of the desire for easy interchange of turbulence equations two separate iteration loops with independent convergence criteria are used. The error in each equation solved is defined as the left-hand side minus the right-hand side.

We iterate in the inner loop for the turbulence equations until the largest error, for all  $\bar{Y}$  at any  $\bar{X}$ , is less than 0.1. At that point the eddy viscosity is sent to the mean flow equations for a single iteration, and the entire cycle is repeated until the largest error in the mean flow equations is less than 0.001. This latter criterion is dominant and the inner loop is required only to prevent poor initial conditions in the turbulence properties from driving the entire solution procedure into large oscillations. For typical attached flow cases, the 0.001 convergence bound implies convergence in all variables to three significant figures. If less accuracy, and more economy, is required this value may be increased.

EFFECT OF  $Y_{MAX}$ 

The proper choice of the location of the upper computational boundary is substantially more case-dependent than are the other numerical parameters. In general, one must choose  $Y_{MAX}$  to be large enough so that  $\partial u / \partial y$  is small there. The requirement arises from the fact that the velocity along this line is specified as a boundary condition, and if  $\partial u / \partial y$  is not small, then  $u_e = u_e(x, y) \neq u_e(x)$  and the solution varies with  $Y_{MAX}$ .

For the solutions presented in the body of the paper we required that a 25% increase in  $Y_{MAX}$  must not affect the skin-friction coefficient by more than 1%.

EFFECT OF  $X_{MAX}$ 

For the majority of the cases considered here, boundary-layer-type flows, the solutions show negligible sensitivity to the downstream boundary location. For a flow with separation, the downstream boundary must be sufficiently far downstream of reattachment so that the flow has recovered its boundary layer character. This requirement is imposed by the fact that the boundary conditions at  $X_{MAX}$  are the boundary layer equations.

## REFERENCES

1. Murphy, J. D.: An Efficient Solution Procedure for the Incompressible Navier-Stokes Equations. AIAA Journal, Vol. 15, No. 9, Sept. 1977, pp. 1307-1314.
2. Isaacson, E.; and Keller, H. B.: Analysis of Numerical Methods. John Wiley and Sons, N.Y., 1966, pp. 58-61.
3. Baldwin, B. S.; and Lomax, H.: Thin Layer Approximation and Algebraic Model for Separated Turbulent Flow. AIAA Paper 78-257. Presented at AIAA 16th Aerospace Sciences Meeting, Huntsville, Ala. Jan. 16-18, 1978.
4. Cebeci, T.: Behavior of Turbulent Flow Near a Porous Wall With Pressure Gradient. AIAA Journal, Vol. 8, No. 12, Dec. 1970, pp. 2152-2156.
5. Glushko, G. S.: Turbulent Boundary Layer on a Flat Plate in an Incompressible Fluid. NASA TT F-10080, Apr. 1966.
6. Rubesin, M. W.: A One Equation Model of Turbulence for Use with the Compressible Navier-Stokes Equations. NASA TM X-73128, Apr. 1976.
7. Bradshaw, P.; Ferris, D. H.; and Atwell, N. P.: Calculation of Boundary Layer Development Using the Turbulent Energy Equation. J. Fluid Mech., Vol. 28, Pt. 3, 1967, pp. 593-616.
8. Jones, W. A.; and Launder, B. E.: The Calculation of Low Reynolds Number Phenomena With a Two Equation Model of Turbulence. Int. J. of Heat Mass Transfer, Vol. 16, 1973, pp. 1119-1130.
9. Wilcox, D. C.; and Rubesin, M. W.: Progress in Turbulence Modeling for Complex Flow Fields, Including the Effects of Compressibility. To be published as NASA TP-1517, in preparation.
10. Saffman, P. G.: A Model for Inhomogeneous Turbulent Flow. Proc. Roy. Soc. A, 317, 1970, pp. 417-433.
11. Wilcox, D. C.: User's Guide for the Incompressible Version of the EDDYBL Computer Program. Rept. No. DCW-R-16-01, Dec. 1976, DCW Industries, Inc.
12. Wieghardt, K.: Flow No. 1400. Proceedings, Computation of Turbulent Boundary Layers, 1968, AFOSR-IFP-Stanford Conference, Vol. II, Compiled Data, D. E. Coles and E. A. Hirst, eds., Thermosciences Div. Dept. of Mech. Engineering, Stanford University. Stanford, California 94305.
13. Samuel, A. E.; and Joubert, P. N.: A Boundary Layer Developing in an Increasingly Adverse Pressure Gradient. J. Fluid Mech., Vol. 66, Pt. 3, 1974, pp. 481-505.
14. Strickland, J. H.; and Simpson, R. L.: The Separating Turbulent Boundary Layer. Tech. Rept. WT-2, Southern Methodist University, Aug. 1973.
15. Simpson, R. L.; Strickland, J. H.; and Barr, P. W.: Features of a Separating Turbulent Boundary Layer in the Vicinity of Separation. J. Fluid Mech., Vol. 79, Pt. 3, 1977, pp. 553-594.
16. Schubauer, G.; and Klebanoff, P.: Flow No. 2100. Proceedings, Computation of Turbulent Boundary Layers, 1968, AFOSR-IFP-Stanford Conference, Vol. II, Compiled Data, D. E. Coles and E. A. Hirst, eds., Thermosciences Div. Dept. of Mech. Engineering, Stanford University, Stanford, California 94305.
17. Briley, W. R.: A Numerical Study of Laminar Separation Bubbles Using the Navier-Stokes Equations. J. Fluid Mech., Vol. 47, Pt. 4, 1971, pp. 713-736.
18. Newman, B. G.: Some Contributions to the Study of the Turbulent Boundary Layer Near Separation. Australian Dept. of Supply Rept. ACA 53, 1951.
19. Pletcher, R. H.: Prediction of Incompressible Turbulent Separating Flow. ASME J. Fluids Eng., Vol. 100, 1978, pp. 427-433.
20. Arieli, R.; and Murphy, J. D.: Pseudo Direct Solutions to the Boundary Layer Equations for Separated Flows. AIAA Paper 79-0139, Presented at 17th Aerospace Sciences Meeting, New Orleans, LA, Jan. 15-17, 1979. (To be published in AIAA Journal.)
21. Simpson, R. L.; and Collins, M. A.: Prediction of Turbulent Boundary Layers in the Vicinity of Separation. AIAA Journal, Vol. 16, No. 4, Apr. 1978, pp. 289-290.
22. Coakley, T. J.; and Viegas, J. R.: Turbulence Modeling of Shock-Separated Boundary Layer Flows. Symposium on Turbulent Shear Flows, Pennsylvania State University, Univ. Park, PA, Apr. 1977.
23. Coakley, T. J.; Viegas, J. R.; and Horstman, C. C.: Evaluation of Turbulence Models for Three Primary Types of Shock Separated Boundary Layers. AIAA Paper 77-692, Presented at AIAA 10th Fluid and Plasma-Dynamics Conference, Albuquerque, N.M., June 27-29, 1977.
24. Viegas, J. R.; and Horstmann, C. C.: Comparison of Multiequation Turbulence Models for Several Shock-Separated Boundary-Layer Interaction Flows. AIAA Paper 78-1165, Presented at AIAA 11th Fluid and Plasma Dynamics Conference, Seattle, Wash., July 10-12, 1978.

25. MacCormack, R. W.: An Efficient Numerical Method for Solving the Time Dependent Compressible Navier-Stokes Equations at High Reynolds Number. Computing in Applied Mechanics, AMD, Vol. 18, ASME, 1976.
26. Liepman, H. W.: The Rise and Fall of Ideas in Turbulence. American Scientist, Mar.-Apr. 1979, pp. 221-228.

Table 1. Execution Time on CDC 7600.

Flow conditions and turbulence model	MXN	Execution time, CPU-sec
Wieghardt F.P.		
Cebeci-Smith	20 x 25	4.45
Glushko	20 x 25	7.55
Jones-Launder	20 x 25	13.39
Wilcox-Rubesin	20 x 25	27.73
Samuel and Joubert		
Cebeci-Smith	22 x 31	26.3
Glushko	22 x 31	22.3
Jones-Launder	22 x 31	26.3
Wilcox-Rubesin	22 x 31	29.9
Strickland and Simpson		
Cebeci-Smith	15 x 33	19.9
Glushko	15 x 33	14.6
Jones-Launder	15 x 33	27.5
Wilcox-Rubesin	15 x 33	41.8
Modified Schubauer and Klebanoff		
Cebeci-Smith	29 x 28	69
Glushko	29 x 28	88.9
Jones-Launder	29 x 28	179
Wilcox-Rubesin	29 x 28	---

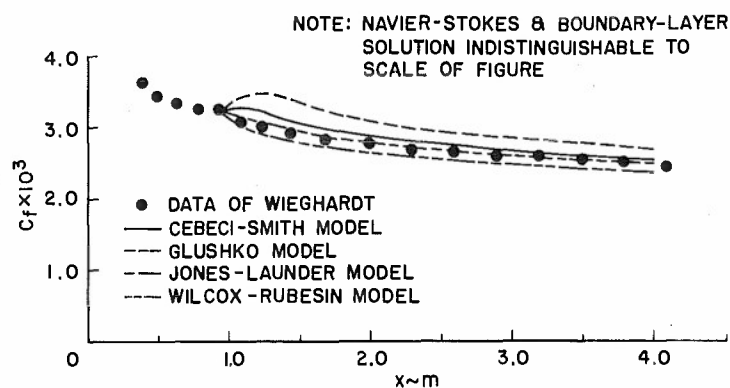


Fig. 1 Comparison of experimental skin friction on a flat plate with predictions using four closure models.

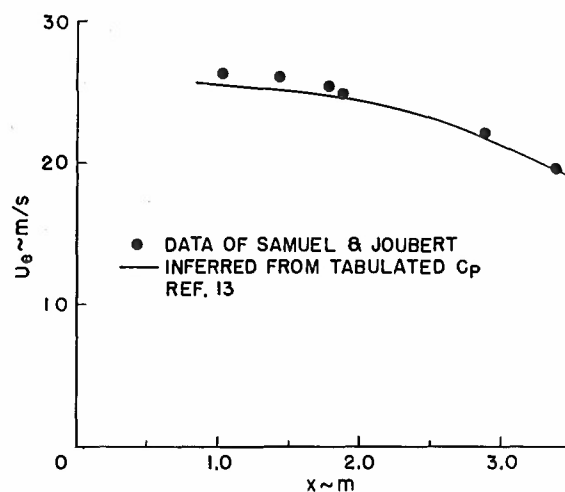
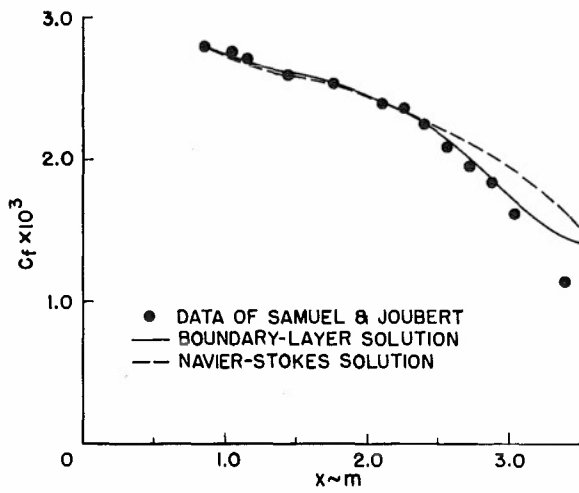
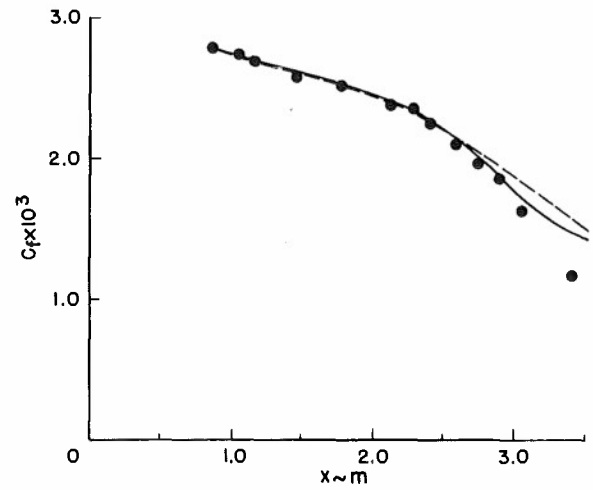
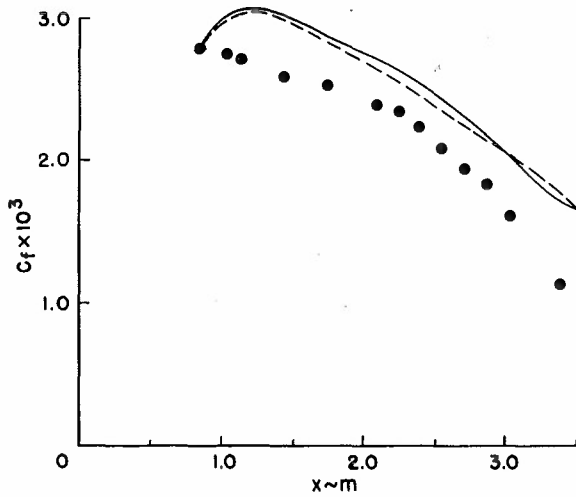


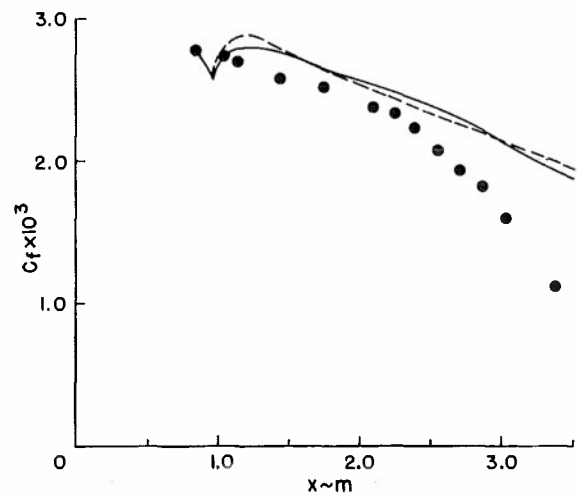
Fig. 2 Free-stream velocity distribution for Samuel and Joubert flow (ref. 13).



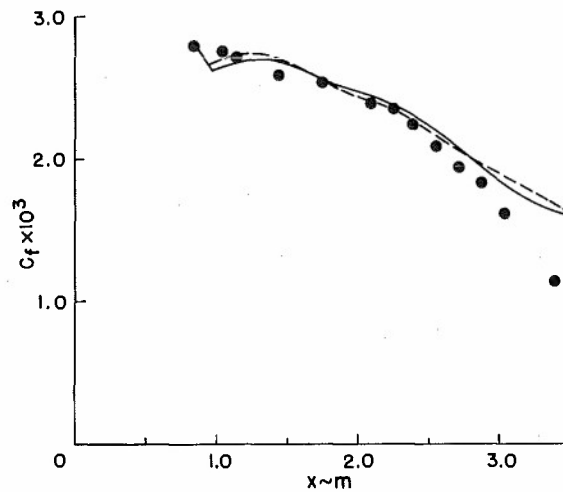
(a) Using the Cebeci-Smith closure model.

(b) Cebeci-Smith closure with B.L.  $\delta(x)$  and  $\delta^*(x)$  in N.S.

(c) Glushko closure model.



(d) Jones-Launder closure model.



(e) Wilcox-Rubesin closure model.

Fig. 3 Comparison of experimental skin friction in an increasingly adverse pressure gradient with boundary layer and Navier-Stokes solutions.

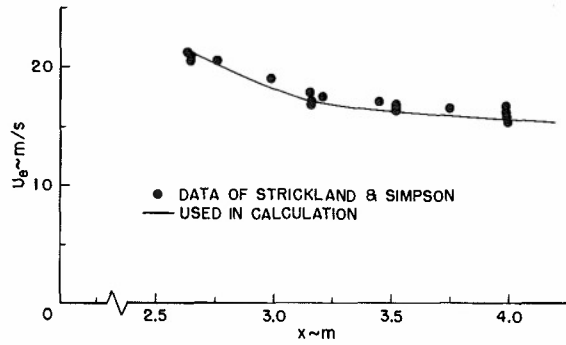
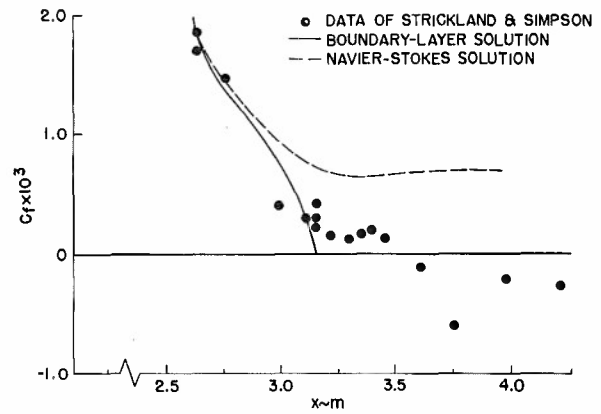
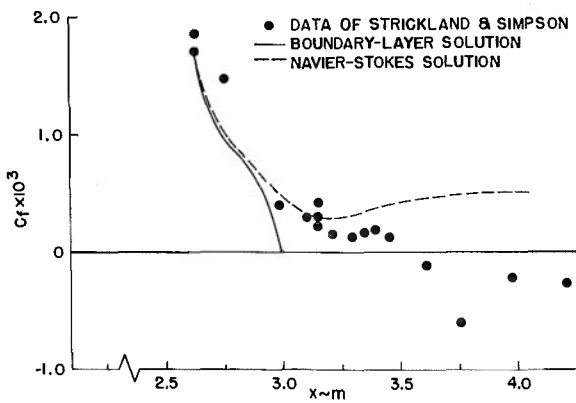


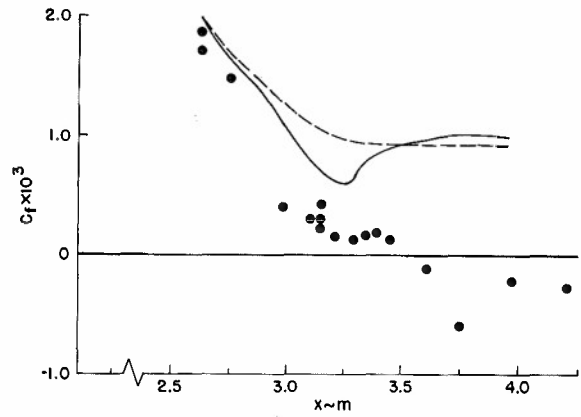
Fig. 4 Free-stream velocity distribution near separation for the experiment of Strickland and Simpson.



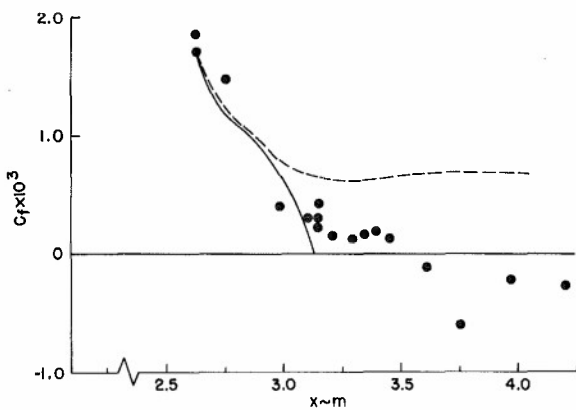
(a) Cebeci-Smith closure.



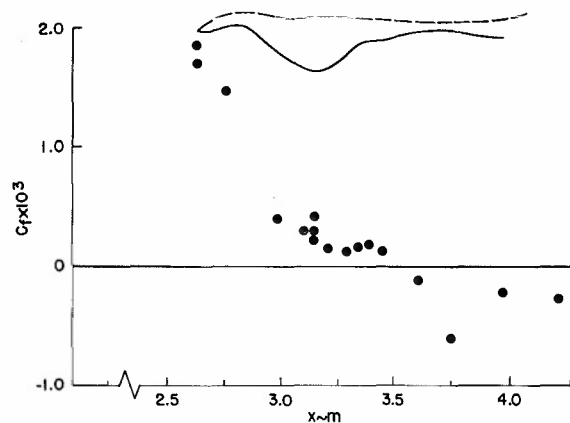
(a) The Cebeci-Smith closure model.



(b) Glushko closure.



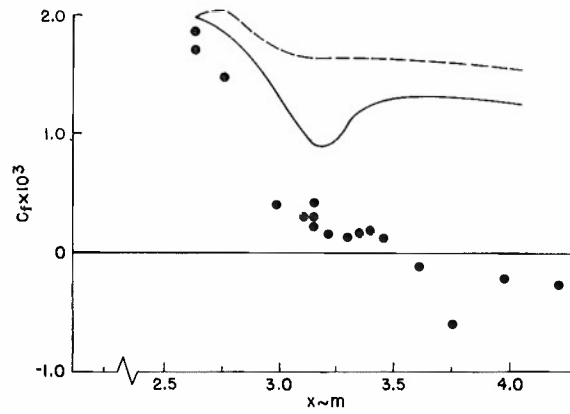
(b) The Glushko closure model.



(c) Jones-Launder closure.

Fig. 5 Comparison of experimental skin friction in an increasing adverse pressure gradient leading to separation with boundary layer and Navier-Stokes solutions.

Fig. 6 Comparison of experimental skin friction coefficient with boundary layer and Navier-Stokes solutions; all inflow boundary conditions from Wilcox code (ref. 9).



(d) Wilcox-Rubesin closure.

Fig. 6 Concluded.

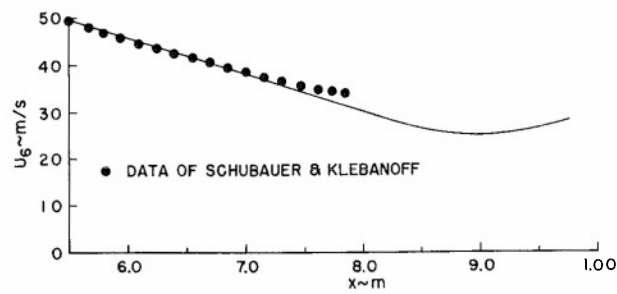
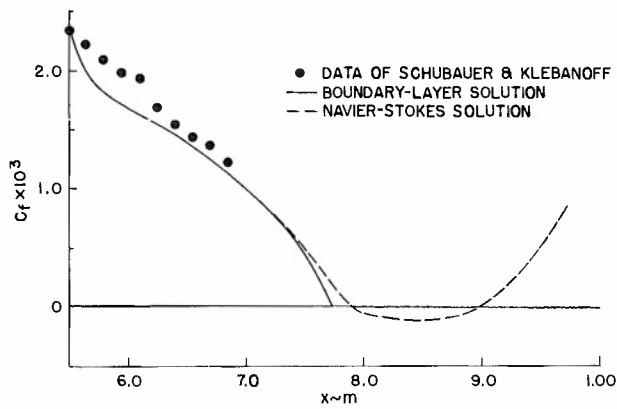
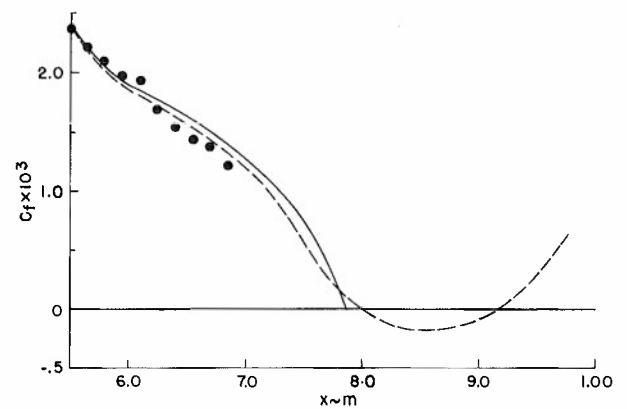


Fig. 7 Modified velocity distribution to produce separation.

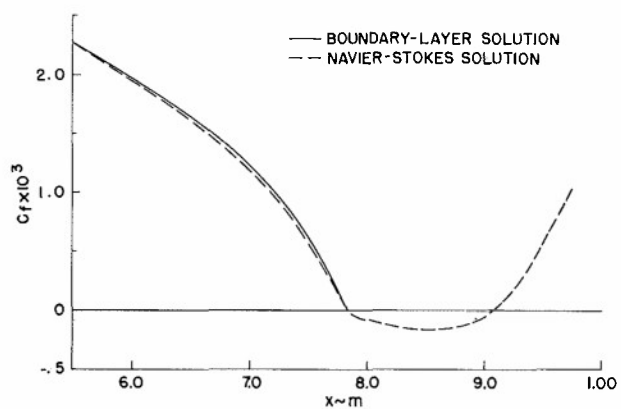


(a) Cebeci-Smith closure.

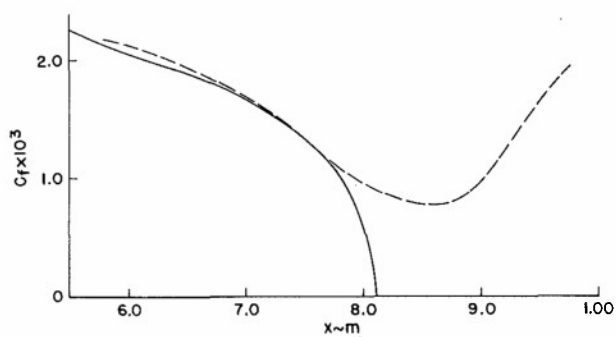


(b) Glushko closure.

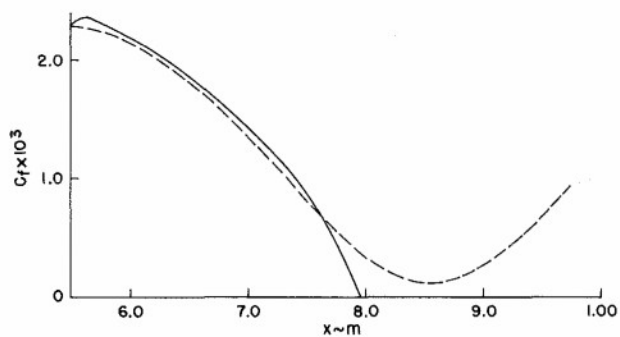
Fig. 8 Skin-friction distribution for modified Schubauer and Klebanoff velocity distribution: experimental velocity distribution at in-flow boundary.



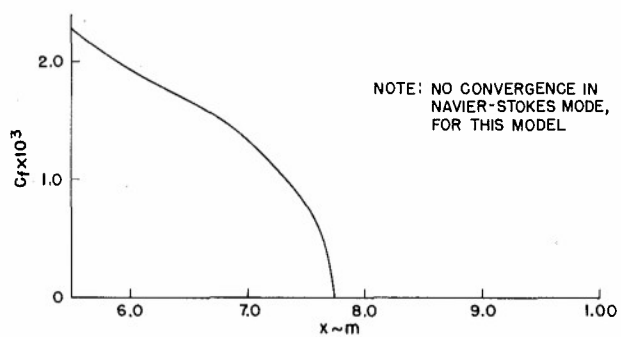
(a) Cebeci-Smith closure.



(c) Jones-Launder closure.



(b) Glushko closure.



(d) Wilcox-Rubesin closure.

Fig. 9 Skin-friction distribution for modified Schubauer and Klebanoff velocity distribution.



## REYNOLDS STRESS CLOSURES - STATUS AND PROSPECTS

by

Brian E. Launder  
 Professor of Mechanical Engineering  
 University of California  
 Davis, California 95616 USA

Summary

Although conventional single-point closures have allowed the successful calculation of many types of turbulent shear flow, there has been a steady accumulation of turbulent flow phenomena that are found to be inadequately simulated by available schemes. Partly arising from these failures a number of workers have questioned the usefulness of the statistical approach to turbulence, based upon Reynolds averaging.

The present contribution addresses two themes arising from this situation. The first is that second-order closures (those based on conventionally averaged momentum equations and a closed set of Reynolds stress transport equations) appear in principle suitable for the analysis of the vast majority of turbulent shear flows. In particular it is shown that a *single* form of the Reynolds stress transport equations has been used to predict shear flows that appear to be "dominated" by large scale structures of different types. Examples are: the "natural convection" limit in the atmospheric boundary layer, the turbulent boundary layer on a concave surface and various free turbulent shear flows. In all these cases turbulent mixing rates are appreciably higher than found, say, in a turbulent shear flow between parallel walls where large scale structures are not dominant - and in which the Reynolds stresses are also well described by the same form of rate equation.

The inference drawn is that for many purposes the large scale structures can be regarded as nature's mechanism for providing enhanced transport rates when these are demanded by the imposed strain field, force field or boundary conditions. Since the Reynolds stress transport equations contain the "signal" of influences in the stress generation terms it is reasonable that the stress levels should respond in accord with observations in the various shear flows cited.

The second theme is that, although second order closures as a class thus appear capable of achieving a wide range of applicability, current schemes contain highly simplistic ideas that can and must be removed for the closures to achieve the potential of which they are capable. Perhaps the most serious weakness is the use of just a single time scale to characterize the rates of progress of all the various turbulence interactions that need approximating. The writer and his colleagues have devised a more general approach that provides independent time scales for the large-scale and medium-scale motions. The model is developed and applications are shown to various shear flows including turbulent boundary layers close to separation. Use of the multiple time scales brings much improved predictions over an encouragingly wide range of conditions.

Introduction

Turbulence, as befits its nature, has inspired vastly different approaches towards bringing it to order. One that has appeared increasingly attractive to computationalists over the past decade is the second-order, or - as we shall term it here - the Reynolds-stress closure. For the experimentalist, in the same period, there has been perhaps even greater interest in the search for and documentation of embedded orderliness in the turbulence signal - a coherence in structure made visible by appropriate filtering of or discrimination in the measurements.

These two schools of work - the one computational, the other experimental - have so far had little, if any, impact on one another. Indeed, the posture of the groups to each other may be said to have been "stand-offish". The Organizing Committee of the present symposium, however, has made at least some attempt at dialogue by requesting that approaches to "theory and modelling" should either incorporate modern experimental knowledge of the ["organized"] structure of the turbulent boundary layer or provide a justification for its omission.

The present contribution is provided as a response to that request. It has been written chiefly for those who are not practitioners in Reynolds stress closures, though, for the turbulence modeller, at least one new suggestion has been added on how the breadth of current closures may be extended. First we summarize the basic pattern of Reynolds closures and the reason they look an attractive type of model for practical shear flow calculations. Here will be discussed, also, the writer's view of the relationship between the 'organized structures' and Reynolds stress closures. In Section 3, drawing principally on the work of the writer's group, an outline will be given of fundamental developments that are being introduced to extend the admittedly modest current reliability of Reynolds stress closures. Chief of these is the introduction of two or more independent time scales to characterize different turbulent interactions (other current schemes employ just a single scale). More far reaching, though still at the conjectural level, is the partitioning of the Reynolds stress field in wave number space with a different set of transport equations (with their attendant closure hypotheses) for each slice. Such an approach would dovetail nicely with the sub-grid-scale closures that those with unlimited computer budgets are now beginning to apply to simple shear flows. It is, however, a too complex closure level for practically interesting "difficult" flows - at any rate for the next five years or so until computer speeds and the general availability of powerful computers have advanced to the point where solving the additional sets of transport equations cease to be a significant deterrent.

## 2. Reynolds Stress Closures: Methodology and Potential

### 2.1 The Exact Stress Transport Equation and Some Inferences from the Generation Term

The 1968 Stanford Conference marked, in all probability, the first occasion at which an audience concerned with the computation of turbulent boundary layers was encouraged to obtain the unknown Reynolds stresses,  $\overline{u_i u_j}$ , by solving a set of closed transport equations for the non-zero elements of the Reynolds-stress tensor [1]. With the exception of Bradshaw [2] (who had determined the turbulent shear stress from a rate equation for kinetic energy) all those who had applied differential field methods to the calculation of the various test cases posed by the organizers of the Stanford meeting had represented the turbulent stresses by way of the relation:

$$-\overline{u_i u_j} = \nu_t \left( \frac{\partial u_i}{\partial x_j} + \frac{\partial u_j}{\partial x_i} \right) \quad (1)$$

where  $\nu_t$  is an effective (scalar) kinematic viscosity and  $(\partial u_i / \partial x_j + \partial u_j / \partial x_i)$  is the mean strain rate. At the Reynolds-stress closure level that Donaldson [1] advocated, however, the correlations between fluctuating velocities would instead be obtained from solutions to the Reynolds-stress transport equations.

An exact equation for the transport of  $\overline{u_i u_j}$  is easily obtained by multiplying the Navier-Stokes equations by the fluctuating velocity and time- or ensemble averaging. The resultant expression for a stationary, quasi-incompressible flow\* field in which molecular transport is negligible may be written:

$$\begin{aligned} \frac{D \overline{u_i u_j}}{Dt} = & - \underbrace{\left\{ \overline{u_i u_k} \frac{\partial u_j}{\partial x_k} + \overline{u_j u_k} \frac{\partial u_i}{\partial x_k} \right\}}_{P_{ij}} + \underbrace{\frac{\overline{u_i \rho'} g_j + \overline{u_j \rho'} g_i}{\rho}}_{G_{ij}} + \underbrace{\frac{p}{\rho} \left( \frac{\partial u_i}{\partial x_j} + \frac{\partial u_j}{\partial x_i} \right)}_{\Phi_{ij}} \\ & - \underbrace{2 \nu \frac{\partial \overline{u_i}}{\partial x_k} \frac{\partial \overline{u_j}}{\partial x_k}}_{\epsilon_{ij}} - \underbrace{\frac{\partial}{\partial x_k} \left( \overline{u_i u_j u_k} + \frac{p \overline{u_i}}{\rho} \delta_{jk} + \frac{p \overline{u_j}}{\rho} \delta_{ik} \right)}_{\mathcal{D}_{ij}} \end{aligned} \quad (2)$$

where  $\rho$  and  $\rho'$  denote respectively the mean density and fluctuations about this mean,  $g_i$  is the gravitational acceleration vector and  $p$  stands for the fluctuations in pressure. Although gravitational terms are hardly ever important in aeronautical fluid mechanics they have here been retained partly because of the well-known analogy between the effects of streamline curvature and buoyancy on turbulence and partly to illustrate the width of flow phenomena that may already be adequately characterized by a single set of equations. In words the equation expresses the fact that the rate of increase of  $\overline{u_i u_j}$  of a small fluid package arises from a net excess of direct rates of generation ( $P_{ij}$  and  $G_{ij}$ ) due to interaction with the mean-strain and gravitational fields over the combined loss rate due to direct viscous dissipation ( $\epsilon_{ij}$ ), pressure interactions ( $\Phi_{ij}$ ) and diffusive transport ( $\mathcal{D}_{ij}$ )<sup>+</sup>. Although expressible through tensor notation as a single equation, any use of a closed form of (2) requires, of course, solution of separate transport equations for the individual Reynolds stress elements. Equation (2), together with a clear, elementary appraisal of some of its implications, has been available in textbook form for at least 20 years [3]. The equation provides such insight into the character of the Reynolds stresses that it is hard to understand why such a small proportion of graduate majors in fluid mechanics have an familiarity with it.

The last three groups of terms in Eq. (2) are not directly knowable. To achieve closure at the Reynolds-stress level these correlations must be approximated in terms of the Reynolds stresses, the mean strain field and a characteristic time scale (or scales) of the turbulent interactions. What makes the Reynolds stress closure level a particularly interesting and effective one to work at, however, is that the generation terms in (2) may be regarded as known. Generation agencies form a major term in the Reynolds stress budget in turbulent boundary layers (except in conditions of turbulence collapse due, for example, to severe accelerations); thus, one might regard the problem of closure as being half-way dealt with without having to make approximations. One may liken the task of providing a model for the Reynolds stresses to that of assessing the wealth of an individual. With no knowledge of the individual's economics, the task is an impossible one. State specifically his income, however, and the problem of constructing an economic model begins to appear manageable. It remains, of course, to prescribe a model for his expenditures (the dissipation term), his taxes (the pressure-velocity interactions) and the checks mailed to his kids at university (diffusion). Our everyday experience tells us, however, that these other elements in a person's economic budget are strongly linked to the income itself.

\* Density fluctuations are retained only in the gravitational term - the so-called "Boussinesq approximation"

+ In this description the terms "generation" and "loss" are used rather freely: the buoyant generation may be either positive or negative according to whether the stratification is unstable or stable; the pressure interactions will produce an energy gain in some components and a loss in others (as may be inferred by noting that the trace of  $\Phi_{ij}$  is zero) while diffusive transport will act to raise  $\overline{u_i u_j}$  in some regions and to diminish it in others.

Let us proceed to some examples which emphasize the extent to which knowledge of the generative agencies allows at least qualitative inferences to be drawn about how turbulence will react to various strain and force fields. We start with the case of a plane, parallel flow,  $U_1(x_2)$  in the absence of gravitational effects cited by Hinze [3]. In this case evaluation of the generation term in Eq. (2) for each component of normal stress shows that only the streamwise fluctuations ( $u_1^2$ ) receive energy from the mean flow (at a rate equal to  $-2 \overline{u_1 u_2} dU_1/dx_2$ ); the normal stress levels in the plane perpendicular to the mean velocity owe their sustenance to pressure interactions deflecting energy from streamwise fluctuations. We may thus reasonably infer that the  $x_1$ -direction fluctuations will be larger than those in any other direction - a circumstance that experiments amply confirm. Lest we dismiss too lightly the capacity of Eq. (2) for getting such a simple feature of turbulence correct, it is well to note that Eq. (1), which is still the most widely used stress-strain relation in practical calculations, gets it lamentably wrong!

Streamline curvature is well known to have marked effects on the development of turbulent boundary layers. If we orient our axes so that  $x_1$  points in the mean flow direction, we can regard the importance of the curvature term to the flow's development as given by  $(\partial U_2/\partial x_1)/(\partial U_1/\partial x_2)$ . Bradshaw [4] was among the first to note that small amounts of  $\partial U_2/\partial x_1$  had a large effect on the boundary layer growth - indeed, inexplicably large if one's views on turbulent transport are blinkered by the effective viscosity relation, Eq. (1). The reason for the flow's sensitivity to the small additional strain due to curvature is, however, immediately apparent from the generation term in Eq. (2). The generation rate of the shear stress  $\overline{u_1 u_2}$  by mean strain is  $-(u_2^2 \partial U_1/\partial x_2 + u_1^2 \partial U_2/\partial x_1)$ . Now, in a boundary layer flow on a flat plate  $u_1^2$  is typically between two and five times larger than  $u_2^2$ , depending upon the position in the shear flow. Moreover, in the transport equation for  $u_2^2$  a direct generation due to curvature of  $-2 \overline{u_1 u_2} \partial U_2/\partial x_1$  now arises and this term further amplifies the increase or decrease of shear stress brought about by the curvature of the mean streamlines. Indeed the study of Irwin and Arnot Smith [26] suggests that when direct and indirect effects are all included the flow will be 15 times more sensitive to curvature than if turbulence acted purely as an amplified laminar viscosity as Eq. (1) implies.

Historically, nearly all approaches to calculating buoyancy-affected flows arising in engineering contexts have employed effective viscosity transport relations for the turbulent fluxes of momentum and heat. Workers have attempted to account for effects of buoyancy on the transport coefficients through empirical functions whose argument has been the local or averaged Froude, Rayleigh or Richardson numbers, (dimensionless groups involving ratios of different characteristics of the dynamic and buoyant fields). When a Reynolds-stress closure is used, however, the direct effects of buoyancy appear *exactly* in the stress transport equations. Now, of course, transport equations for the density-velocity\* correlations must be solved as well and these equations, similar in structure to Eq. (2), will require closure approximations for the different unknown correlations contained therein. Again, however the generation terms due to mean strain, mean density gradients and buoyancy can be regarded as known provided a further equation is provided for the mean square density fluctuations<sup>+</sup>. Figure 1 shows the extensive interconnections that result among the Reynolds stresses and density fluxes for the case of a thin shear flow where  $x_1$  (the flow direction) is horizontal and  $x_2$  (the direction of velocity and density gradient) is vertical. Note first that in the absence of buoyancy,  $u_2^2$  interacts with the mean strain to sustain the shear stress  $\overline{u_1 u_2}$  which, in turn, acts as the source for  $u_1^2$  some of whose energy is deflected via pressure fluctuations to maintain  $u_2^2$ . The vertical density flux,  $u_2 \rho'$ , is pivotal in the effects of buoyancy on the Reynolds stresses: it provides a direct source or sink in the  $u_2^2$  equation and acts indirectly on  $\overline{u_1 u_2}$  both through the dependence of this component on  $u_2^2$  and via the horizontal density flux,  $u_1 \rho'$ . There is direct "talk back" to the vertical density flux from both  $u_2^2$  and  $\rho'^2$  since these correlations appear in the generation terms of the  $u_2 \rho'$  equation. The inference that I suggest be drawn from this is that the interactions among the various components of the turbulent stresses and density fluxes are too numerous and intricate to hold out any hope of correlating their effects by adjoining empirical functions to expressions for the effective viscosity. As we shall see later in the section, however, the equations for the second-rank moments extrapolate well from neutral flows to account for transport effects under highly stratified situations.

## 2.2 Current Closure Methodology

In the foregoing section we have advanced the view that its exact treatment of the stress-generation agencies gives the Reynolds stress transport closure decisive potential superiority over any simpler scheme. While, however, one can extract a great deal of *qualitative* information about the character of a turbulent shear flow from analyzing the generation terms alone, Eq. (2) becomes useful for calculation purposes only if adequate closure approximations can be made of the unknown correlations appearing therein. The following paragraphs provide a brief account of current closure practices. More extensive reviews and more detailed discussion are provided in references [4-9].

For boundary layer flows, the most important of the unknown terms in (2) is the pressure redistribution term,  $\Phi_{ij}$ . Examination of the Poisson equation for  $p$  shows that pressure fluctuations are attributable to three agencies [9]: purely fluctuating velocity interactions,  $\Phi_{ij,1}$ , an additional effect due to the superposition of a fluctuating velocity field onto a mean-field deformation,  $\Phi_{ij,2}$  and thirdly, in stratified media, a contribution from perturbations in potential energy,  $\Phi_{ij,3}$ . The majority of workers now active in Reynolds stress closures devise separate approximations for each of these effects. For the contribution arising from purely turbulence interactions most workers adopt Rotta's [10] linear return-to-isotropy model:

\* If density fluctuations may be considered to arise purely from temperature fluctuations the correlations between velocity and temperature fluctuations may be solved instead.

+ The buoyant generation rate in the equation for  $\overline{\rho' u_i}$  is equal to  $\overline{\rho'^2 g_i}/\rho$ .

$$\phi_{ij,1} = -c_1 \left( \overline{u_i u_j} - \frac{2}{3} \delta_{ij} k \right) / T_\phi \quad (3)$$

where  $k$  stands for the turbulence kinetic energy,  $\overline{u_i^2}/2$  and  $T_\phi$  is a time scale of the interaction. If, as is usually the case,  $T_\phi$  is taken as the turnover time of the energy-containing motions,  $k/\epsilon$  ( $\epsilon$  being the local dissipation rate of turbulence energy) the optimum value for the coefficient  $c_1$  is about 1.8. There are some indications that  $c_1$  should in fact be an increasing function of the turbulence anisotropy, Lumley & Newman [11], though for boundary layers this effect is overshadowed by that due to the wall's proximity, to be discussed below.

Mean strain contributions to  $\Phi_{ij}$  seem likely to be particularly important for predicting three-dimensional boundary layers and other flows with complex strain fields. Overall, the most successful of current models is also one of the simplest:

$$\Phi_{ij,2} = -c_2 \left( P_{ij} - \frac{1}{3} P_{kk} \delta_{ij} \right) \quad (4)$$

The idea expressed by Eq. (4) is that pressure fluctuations will tend to isotropize the shear production: that is to say a fraction  $c_2$  of the shear stress generation (and the excess of the normal-stress production over the mean) will be obliterated. Clearly the coefficient  $c_2$  must lie between zero and unity. In isotropic turbulence ( $\overline{u_i u_j} = 2/3 \delta_{ij} k$ ) it is readily demonstrated that  $c_2 = 0.6$ ; this value seems appropriate also for many shear flows which is an encouraging result. Although more elaborate formulations have given better results for a number of test cases these may sometimes lead to serious errors when applied in complex strain fields. For example, the quasi-isotropic model of references [6] and [12] predicts that, contrary to experiment, the addition of swirl to an axisymmetric jet reduces its rate of spread, a deficiency which Launder and Morse [13] identify with the model for  $\Phi_{ij,2}$ .

Buoyant effects on  $\Phi_{ij}$  appear, to a first approximation, to be accounted for with a model identical in form to that suggested for  $\Phi_{ij,2}$ , i.e.

$$\phi_{ij,3} = -c_3 \left( G_{ij} - \frac{1}{3} G_{kk} \delta_{ij} \right) \quad (5)$$

Within the accuracy of current experimental data it appears that  $c_3$  can be taken equal to  $c_2$ .

In dealing with flows along walls one needs, unfortunately, to account for the effects of pressure reflections from the boundary which diminish the intensity of fluctuations normal to the wall. For a plane surface the strength of this effect seems to be proportional to the ratio of a local turbulent length scale to the normal distance from the wall. Specific corrections have been proposed in references [6] and [8], the latter being better adapted for use with Eq. (4). Some groups, notably those associated with Donaldson and Mellor, include no account of pressure reflections; instead the coefficients in their basic closure scheme are tuned specifically to give an adequate account of, say, the flat plate boundary layer. This approach is justified provided one confines attention *solely* to boundary layers on a plane wall. Poor predictions inevitably result, however, if one attempts to calculate, with a single set of equations, the flow around an airfoil and the wake downstream therefrom.

Diffusive transport is usually of relatively small importance in attached boundary layers in aeronautical applications. There is thus no justification for retaining transport equations for the third moments as André and his colleagues [14] do for their simulations of the atmospheric boundary layer. Some groups have attempted to model the transport by velocity and pressure fluctuations separately, the most complete studies to date being contributed by Lumley and his co-workers (e.g. Zeman and Lumley [15]). For unstratified flows, however, the simple form:

$$\mathcal{D}_{ij} = c_s \frac{\partial}{\partial x_k} \frac{k}{\epsilon} \overline{u_i u_j} \frac{\partial u_k}{\partial x_l} \quad (6)$$

has been found to give generally satisfactory behavior in a variety of free shear flows and boundary layers when the coefficient  $c_s$  is taken as 0.22, references [6] and [13].

The dissipation tensor  $\epsilon_{ij}$  is represented by most workers in terms of the dissipation rate of the turbulence energy,  $\epsilon$  by assuming isotropy of the fine scale motion:

$$\epsilon_{ij} = \frac{2}{3} \delta_{ij} \epsilon \quad (7)$$

Recently, however, Lin & Wolfshtein [16] and Mjolsness [17] have queried the basis for this assumption. There does seem to be a good deal of uncertainty as to whether Eq. (7) is justified in the inner region of the boundary layer, for  $y^+$  less than 200, say; the question can only be resolved in due course by definitive experimental data. The matter, while certainly of fundamental interest, may turn out to be somewhat academic for computational purposes since working calculation schemes will, unwittingly, have absorbed effects attributable to departures from local isotropy into their approximation of pressure interactions.

Equation (7) will be recognized as just one step towards obtaining  $\epsilon_{ij}$ ; a path is still needed for determining  $\epsilon$ . The form used by most workers may be written

$$\frac{D\varepsilon}{Dt} = \frac{\varepsilon^2}{k} \left( c_{\varepsilon 1} \frac{P_{kk}}{\varepsilon} - c_{\varepsilon 2} + c_{\varepsilon 3} A \right) \quad (8)$$

where the turbulence anisotropy is defined as:

$$A \equiv a_{ij} a_{ij} \quad \text{where} \quad a_{ij} \equiv \left( \frac{u_i u_j}{k} - \frac{2}{3} \delta_{ij} \right) / k$$

The  $c$ 's are coefficients to be determined experimentally. Table 1 gives the values recommended by two groups. We note that  $P_{kk}/\varepsilon$  varies across a shear flow in a rather similar way to  $A$ ; the absence of any effect of anisotropy in the proposal of reference [6] is accordingly accompanied by a larger value of the coefficient  $c_{\varepsilon 1}$  than that proposed in reference [15]. The diffusive transport of  $\varepsilon$  has been approximated in [6] by:

$$\mathcal{D}_\varepsilon = 0.15 \frac{\partial}{\partial x_k} \left( \frac{k}{\varepsilon} \overline{u_k u_\ell} \frac{\partial \varepsilon}{\partial x_\ell} \right)$$

Authors	$c_{\varepsilon 1}$	$c_{\varepsilon 2}$	$c_{\varepsilon 3}$
Launder, Reece, and Rodi [6]	0.72	1.90	0
Zeman and Lumley [16]	0.47	1.90	3.5

Table 1 - Coefficients in the Dissipation Rate Equation

Equation (8) should be regarded as intuitively formulated with coefficients calibrated to give tolerable agreement with experiment over a number of free and wall flows<sup>+</sup>.

The form of the equation is too simple to expect it to achieve a very wide degree of applicability. Recently Pope [18] and Hanjalić and Launder [19] have shown that, by including further terms involving the mean vorticity, the level of  $\varepsilon$  can be made rather sensitive to secondary strains. In the cases examined by these workers significant improvements were achieved in the calculated development of the axisymmetric jet - a notoriously difficult flow to predict - and, in reference [19], of several other flows as well. While these developments are encouraging and suggest that more widely valid forms of the dissipation rate equation can be devised, the proposed amendments ought for the present to be used with caution: by making the  $\varepsilon$ -equation highly sensitive to secondary strains there is the risk that a major improvement for one case may be offset by a serious worsening for some other, as yet uncalculated shear flow.

#### 2.4 Remarks on the Applicability of Reynolds Stress Closures to Flows with Organized Structures

The above remarks lead us naturally to the question of what degree of universality can ultimately be expected at the Reynolds-stress level. The question is not one that admits a precise answer - at least, not yet. Nevertheless a few general observations can perhaps usefully be made. What I should first like to emphasize is that closure at the Reynolds stress level is a *drastic* simplification from the Navier-Stokes equations which actually describe the dynamics of a turbulent flow. It would be unreasonably optimistic, therefore, to expect to devise a genuinely universal set of equations for mimicking the development of the Reynolds stresses. The best one can hope for is to evolve a system of equations and functions that give a *fairly* faithful representation over a *moderate* range of conditions. Whether that "moderate" range can be made broad enough to encompass, say, all the stationary thin shear flows encountered in aeronautics is doubtful, particularly as answers are needed to a higher degree of precision than in many other branches of engineering.

Having made these intentionally cautionary remarks, however, I wish now to underline the capabilities of this class of turbulence model for it is my impression that these are generally underestimated by fluid mechanicians not actually involved in model development. One frequently hears the view that the turbulent mixing layer, dominated by large-scale, quasi-periodic eddy structures, is unlikely to be adequately resolved by an analysis based on a purely statistical treatment. Yet, as may be seen from references [20] and [21], even a model utilizing the Boussinesq effective-viscosity relation predicts correctly the effect on the spreading rate of varying the velocity ratio of the two

<sup>+</sup> Attempts at giving the equation a more elevated status by purporting to model unknown correlations in the exact equation for  $\varepsilon$  are, in the writer's opinion, well intentioned but misguided considering that none of these correlations has yet been measured in a turbulent shear flow.

streams. The same set of empirical constants is used that serves for the calculation of the plane jet or the development of a boundary layer along a wall. The observed effect of varying Mach number in this flow is *not* well accounted for at present but here it may be said that serious consideration of compressibility effects on the fluctuating velocity field is only just beginning.

Stratification effects are likewise held not to be amenable to conventional turbulence modelling because, in highly unstable conditions, transport above a horizontal surface appears to be dominated by long funnels of less dense fluid rising up through gradually descending cooler layers. At the other extreme strongly stable stratification is sometimes regarded as unsuitable for conventional closures because the structure decomposes into disturbances, which, though random, exhibit a wave-like character.

While predictors at the Reynolds-stress closure level should certainly take note of any such structural changes between one turbulent flow and another, there is no reason to presuppose that the closure will be unable to describe the statistically averaged properties of each of them. To reiterate, a Reynolds stress model accounts for generation processes without recourse to closure approximation: no particular mechanism is postulated or implied. In a sense it is up to Nature to work out what particular kinds of mechanism it needs to produce just the right amount of transport. It appears to be the case that when large stress generation rates are demanded (referenced with respect to the local dissipation rate) large-scale coherent structures are especially likely to be present. This is the case for the plane mixing layer where the mean level of turbulence energy production is some 20% higher than the dissipation rate; for a horizontal flow under intensely unstable conditions where the principal input to the turbulence energy is from buoyant generation; and for a turbulent boundary layer developing along a concave wall where, as seen in Section 2.1, the effects of secondary-strain generation are large due mainly to the much larger turbulence intensities parallel than normal to the surface.

An impression of the state-of-the-art of Reynolds stress closures may perhaps be conveyed by the examples presented in figures 2-5. Except as noted the closure approximations are those of the (simpler) model of Launder, Reece, and Rodi [6], extended for buoyant flows in [8] and [9]. Two properties of atmospheric turbulence under unstable conditions are shown in figures 2 and 3. In figure 2 the calculated variation of the rms vertical velocity fluctuations<sup>+</sup> (normalized by the friction velocity) is compared with the measurements of Wyngaard et al. [22]. The calculated levels are about 20% below experiments due apparently to too small measured values of wall shear stress (the same study reported values of the von Karman constant of 0.35 compared with more usually reported values of about 0.41). There is excellent correspondence, however, in the trend of the variation with increasing instability ( $L$  denotes the Monin-Oboukhov length scale) including the  $1/3$ -power dependence for values of  $(-x_3/L)$  greater than 2.0 implied in the 'natural convection' limit where wind shear is negligible. The corresponding variation of the vertical heat-flux correlation coefficient is shown in figure 3. For increasing instability the vertical velocity and density fluctuations become better correlated which is generally in agreement with reported experimental data; it also conforms with the idea that the turbulence should exhibit progressively greater coherency with increasing instability.

The atmospheric boundary layer is strongly affected by pressure reflections from the ground. Such effects are absent, however, in a free shear flow considered for the case of *stable* stratification in figure 4a. As stability increases (exemplified by an increase of gradient Richardson number,  $Ri$ ) the intensity of vertical fluctuations falls substantially with respect to horizontal ones. The calculated variation reported by Gibson and Launder [8] agrees well with the measurements of Young [23] in a quasi-homogeneous horizontal free shear flow. Such a damping of vertical fluctuations will generally have a dramatic effect on the way a shear flow develops. Figure 4b shows, for example, for a case of a warm, 2-dimensional jet discharged on the surface of a body of cool, stationary water, how the stable stratification impairs entrainment of the denser fluid into the shear flow. The calculations, by Gibson and Launder [24] show a similar rate of damping to the experimental data of Ellison and Turner [25]; evidently when the mean gradient Richardson number across the jet reaches values of about 0.8 entrainment of new fluid into the jet is essentially cutoff.

Irwin and Arnot Smith [26] have made an interesting computational study of the effect of streamline curvature on the development of wall jets and boundary layers. Since, over most of a wall jet, the mean velocity decreases with distance from the wall it is the case of *convex* curvature that gives rise to augmentation in mixing where we expect strong influence of organized structures. Their turbulence model was based on the more elaborate of the two closures of reference [6] rather than the simpler version outlined here but we may expect that the latter model would lead to similar results. Figure 5 shows the computed ratio of the half width ( $y_0$ ) of a wall jet developed around a circular cylinder to the distance from discharge,  $x$ , plotted as function of  $y_0/R$ ,  $R$  being the cylinder radius. The experimental data of Fekete [27] and Guitton [28] show a strong increase of normalized half width with increasing  $y_0/R$  (corresponding to stronger influences of streamline curvature) a variation that the computations of Irwin and Arnot Smith [26] closely reproduce for values of  $(y_0/R)$  up to 0.3. (Beyond this the *mathematical* simplifications in their finite difference calculations prevent definite conclusions from being drawn.) We note that if all the secondary strain terms in the model are suppressed ( $y_0/x$ ) becomes essentially independent of curvature, which firmly identifies the success of the computations with the sensitivity of the Reynolds stress closure to small secondary strains. It may be mentioned that the same authors computed the development of Meroney's [29] study of flow in a curved channel predicting the mean levels of shear stress on the concave and convex surfaces within about 7%.

### 3. Further Development of Reynolds Stress Closures

In this section an outline is provided of some extensions in the closure schemes discussed in Section 2 that are either under development or in the planning stages.

<sup>+</sup> In conformity with meteorological terminology  $x_3$  here denotes the vertical direction.

Perhaps the most serious defect of the closure approaches discussed in Section 2 is their reliance on a single turbulence time scale to characterize rate processes in high Reynolds number turbulence. Because the response mechanisms of the large-scale and small-scale motions are so very different, we must expect that any tolerably general model would need independently calculated time scales for these different parts of the spectrum. Preliminary work on developing a scheme of this kind has been undertaken by Dr. K. Hanjalić, Dr. R. Schiestel and the writer (references [30]-[32]); the present discussion, which is abridged from reference [32] is based upon two independent (though intricately coupled) rates of energy transfer across different parts of the energy spectrum as indicated in Figure 6. The quantity  $K_1$  denotes the wave number above which no significant mean-strain production occurs while  $K_2$  is the largest wave number at which viscous dissipation of turbulence energy is unimportant. Energy leaves the first region (the "production" region) at a rate  $\epsilon_p$  and enters the high-wave-number or "dissipation" region at a rate  $\epsilon$ . Between these two zones, occupying an intermediate range of wave numbers is the "transfer" region, across which we imagine a representative spectral energy transfer rate to be  $\epsilon_T$ .

The total turbulent energy,  $k$ , is assumed to be divided between the production range ( $k_p$ ) and the transfer range ( $k_T$ ). At high Reynolds numbers there is negligible kinetic energy in the dissipation range. In a homogeneous flow the levels of  $k_p$  and  $k_T$  are controlled by the transport equations:

$$\frac{D k_p}{Dt} = - \underbrace{\overline{u_i u_j} \frac{\partial u_i}{\partial x_j}}_{P_k} - \epsilon_p \quad (9)$$

$$\frac{D k_T}{Dt} = \epsilon_p - \epsilon \quad (10)$$

where  $P_k$  denotes the production rate of turbulence energy by mean shear which, as remarked above, is assumed to be entirely contained in wave numbers less than  $K_1$ .

The dynamic response of (9) and (10) depends on the levels of the energy transfer rates  $\epsilon_p$  and  $\epsilon_T$ . The main task is thus to devise a pair of transport equations which adequately characterize the evolution of these transfer rates. We are guided in this by the "dissipation rate" equation (Eq. (8)) presented in Section 2.

Now, despite its nominal role as a *dissipation* rate equation, Eq. (8) does not make sense as such; for it makes the local rate of change of  $\epsilon$  dependent on the local mean strain rate and the anisotropy of the stress field, neither of which, under conditions of local isotropy, can directly affect the dissipation rate. Several workers have remarked that the subject of (8) should correctly be regarded as a spectral energy transfer rate associated with large-scale interactions; that is, in terms of our multiple-time-scale formulation,  $\epsilon_p$ . Accordingly, the initial form chosen for the  $\epsilon_p$  equation was:

$$\frac{D \epsilon_p}{Dt} = C_{p1} P_k \frac{\epsilon_p}{k_p} - C_{p2} \frac{\epsilon_p^2}{k_p} + \mathcal{D}_{\epsilon p} \quad (11)$$

where the partitioned energy  $k_p$  replaces the total energy giving, as characteristic time scale, the energy turnover time of the large-scale motions.

In choosing the form of the corresponding equation for  $\epsilon_T$  certain basic requirements were evident. First, the equation should contain both source and sink terms since, in the decay of grid turbulence, the level of  $\epsilon_T$  must decrease downstream while, if the turbulence energy is raised,  $\epsilon_T$  must, in due course, rise as a precursor to an increase in dissipation rate. It would, however, be contrary to established views of the spectrum to make  $\epsilon_T$  respond directly to an applied mean strain. Now, the factor that is instrumental in raising  $\epsilon_T$  is an increase in the energy flow rate from the production range into the transfer range. Accordingly, being guided by Eq. (11), the form adopted for the  $\epsilon_T$  transport equation is:

$$\frac{D \epsilon_T}{Dt} = C_{T1} \frac{\epsilon_p \epsilon_T}{k_T} - C_{T2} \frac{\epsilon_T^2}{k_T} + \mathcal{D}_{\epsilon T} \quad (12)$$

In a flow where the turbulence energy generation is suddenly switched off, there is no necessity for  $\epsilon_T$  (or  $\epsilon$ ) immediately to decrease since  $\epsilon_p$  does not fall to zero. Thus the energy dissipation rate now responds only slowly to the applied mean strain. This feature makes the present form better able to represent rapidly changing turbulence fields than Eq. (8).

Initially it was planned to provide a transport equation for  $\epsilon$  which, in structure, was similar to (but simpler than) Eqs. (11) and (12). To keep the mathematical framework as simple as possible, however, spectral equilibrium between the transfer and the dissipation regions is assumed:

$$\epsilon = \epsilon_T \quad (13)$$

This assumption can of course be relaxed later.

In making preliminary predictions of variously strained flows, it became clear that the generation term in (11) did not possess much width of applicability. For example, to reproduce the development of turbulence in an axisymmetric contraction a coefficient nearly twice as large was needed as for a simple shear flow. In the former flows energy generation is by *irrotational* straining. The implication seemed



to be that this kind of deformation proved more effective in transferring energy across the spectrum than rotational shears. Such a preferential transfer may be introduced to the mathematical model by the addition to (5) of the following term containing the mean vorticity:

$$C'_{p1} k_p \frac{\partial u_\ell}{\partial x_m} \frac{\partial u_i}{\partial x_j} \varepsilon_{lmk} \varepsilon_{ijk} \quad (14)$$

where  $\varepsilon_{lmk}$  is the alternating third order tensor. The term vanishes in an irrotational flow and (apart from the sign of the coefficient) is non-negative in a rotational strain. The coefficient  $C'_{p1}$  thus needs to be *negative* to produce higher overall energy transfer rates in an irrotational strain.

It remains to assign the various coefficients in Eqs. (11), (12), and (14). The coefficients in Eq. (8), the single-scale  $\varepsilon$  equation have usually been set to constant values and the initial impulse is to do likewise in the multiple-scale model. There are, however, two reasons for not doing so. First, research on the much more elaborate spectral or "two-point" closures has shown the necessity of letting the middle range eddies "talk back" to the larger scales. If both  $C_{1p}$  and  $C_{2p}$  are taken as constants the equation for  $\varepsilon_p$  is virtually independent of the medium scale motion since neither  $k_T$  nor  $\varepsilon_T$  appear in Eq. (11). Secondly, the adoption of constant coefficients in Eq. (8) was at least partly due to the absence of a suitable parameter of which to make them arguments. Now that the energy spectrum is divided into two parts, two parameters are available,  $k_p/k_T$  and  $\varepsilon_p/\varepsilon_T$ . The first characterizes the shape of the energy spectrum, the second the degree of spectral imbalance. Reference [32] argues that  $\varepsilon_p$  should be independent of  $\varepsilon_T$  while  $\varepsilon_T$  should in turn not be directly affected by  $k_p$ . At present only one term in each of the transfer equations has been allowed to depend on these energy or transfer-rate ratios; this limitation was imposed to keep the task of optimization within bounds.

The following is the form for the coefficients, that led to best overall agreement with the test flows considered in [32]:

$$C_{T1} = 1.08 \varepsilon_p / \varepsilon_T ; C_{T2} = 1.15 ; C_{p1} = 2.2$$

$$C'_{p1} = -1.0 ; C_{p2} = 1.8 - 0.3 \left( \frac{k_p}{k_T} - 1 \right) / \left( \frac{k_p}{k_T} + 1 \right)$$

The suggested dependence of  $C_{p2}$  on  $k_p/k_T$  ensures that the energy transfer rate from the large scale motion will be larger in a shear flow than in grid turbulence. The influence of  $(k_p/k_T)$  is more significant than may be supposed for, while  $C_{p2}$  is rarely altered by more than 10% from its asymptotic value, this is of itself sufficient to change the rate of spread of a jet by some 40%.

A fundamental question in fixing the above coefficients is where the division between the production and transfer region should be placed. If the partition is moved to too high wave numbers, such a small proportion of the total energy will be contained in  $k_T$  that the time for energy to cross the transfer region will be negligible. In this case  $\varepsilon_T \approx \varepsilon_p$  and the calculated flow behavior would be negligibly different from that of a single scale model. If, however, the division is made at too low a wave number, the assumption of zero energy production in the  $k_T$  equation becomes untenable. Provided due recognition is taken of these two limiting constraints, our experience is that the precise partitioning point does not significantly affect the predictions, provided coefficients have been appropriately tuned. The above coefficients are chosen so that in turbulence decay behind a grid the energy is divided equally between the two regions.

In [32] the diffusion terms in both the partitioned energy and transfer-rate equations have been uniformly represented as:

$$D_\phi = 0.22 \frac{\partial}{\partial x_k} \left( \frac{k_p}{k_T} \frac{\partial \phi}{\partial x_\ell} \right) \quad (15)$$

where  $\phi$  stands for  $k_p$ ,  $k_T$ ,  $\varepsilon_p$ ,  $\varepsilon_T$ .

The multiple-time-scale approach outlined above can be used in conjunction with different levels of closure. When a Reynolds-stress model is adopted the closure discussed in Section 2 may be applied except that  $(k_p/\varepsilon_p)$  would replace  $(k/\varepsilon)$  in both the return-to-isotropy and diffusion models, i.e., Eqs. (3) and (6), with minor adjustments to the coefficients. Reference [32] presents computations for a number of free shear flows and boundary layers which exhibit uniformly better agreement with experiment than with the corresponding single scale model. The potential of the approach is, however, best illustrated from the calculations of grid turbulence passed through a 4:1 axisymmetric contraction in cross-sectional area. In the calculations, Eqs. (9), (10), (11) (with (14)) and (12) have been solved for homogeneous conditions by forward integration, supplying from experiment values of the mean velocity and  $P_k$ . In this way the development of the turbulence energies could be calculated without recourse to any closure relationship between stress and strain. The initial partitioning of energy between production and transfer ranges was taken as the equilibrium levels for decaying grid turbulence. The energy levels in figure 7 show that much better agreement with measurements is obtained with the multiple-scale treatment than with the single-scale  $\varepsilon$  equation of reference [6]. The latter displays a too weak rise in energy through the contraction and a too slow decay downstream therefrom, in contrast to the virtually complete agreement shown with the present formulation. The reason for the differing behaviour may be inferred from the distributions of energy transfer rates in figure 8. The quantity  $\varepsilon_p$  exhibits a sharp rise on entering the contraction due to the action of the source term containing  $P_k$ . The dissipation rate of the single-scale scheme does likewise. The inertial transfer rate,  $\varepsilon_T$ , responds only sluggishly to the acceleration and, in fact, does not reach its maximum value until some distance *downstream* of the end of the acceleration. This is why, with the multiple-scale approximation, the calculated energy grows more rapidly through the acceleration yet falls off more steeply once the pressure gradient becomes zero.



The multi-scale approach outlined in the preceding paragraphs already shows promise of extending the width of applicability of Reynolds-stress closures. There is, however, still plenty of scope for model refinement. Here we mention the currently unpublished work led by D. Jeandel at the Laboratoire des Mécanique des Fluides of the ECL, Ecully. His group is evolving, for homogeneous flow, a complete spectral closure. It is recognized that such a formulation is too elaborate for practical calculations, however, so he plans to integrate the spectral equations to some intermediate point in the spectrum thereby simplifying the calculation to essentially the form of the multi-scale treatment discussed above. This path may well contribute significantly to improving the modelling of the  $\epsilon_p$  and  $\epsilon_T$  equations.

A major question that several groups around the world are currently pondering is whether sufficient information about the tensorial character of turbulence is carried by the Reynolds stresses themselves. Granted, it is only the Reynolds stresses one needs as an *output* from one's turbulence model; possibly, however, there may be decisive advantages to computing some other second-rank tensor that could appear in the transport equations for the Reynolds stresses. Such a closure would need to carry a dozen or so turbulent transport equations and this is an inconveniently large number at present. It *might* be a practical closure level in five years time, however, if one could rely on the computations. It is thus perhaps not too soon to precipitate a debate on what looks the best way to add a further second-rank tensor to the equation set. Donaldson and his group, in work which remains for the present undocumented, have been experimenting with tensorial length scales. At present, however, the length scales are uniquely linked via an *algebraic* equation to the Reynolds-stress tensor (thus, like other Reynolds stress closures, all the tensorial information is carried in the  $\overline{u_i u_j}$ ). The different length scales are used to provide non-isotropic transport coefficients in modelling diffusive processes. A different approach has been recommended by Lin and Wolfshtein [16] who outline the form of a set of equations for a variable proportional to  $\epsilon_{ij}$ , the viscous dissipation rate of  $\overline{u_i u_j}$ . Use of such a system of equations allows the assumption of local isotropy (Eq. (7)) to be abandoned.

The writer's current view is that provision of a set of individual length scale equations *may* be an effective way of extending the applicability of Reynolds stress closures. It is, however, chiefly through its ability to improve the modelling of the pressure-interaction terms (rather than the stress-diffusion processes) that I believe its potential strength lies; approximation of wall-reflection effects may especially benefit from such a treatment. The addition of transport equations for the components of  $\epsilon_{ij}$  seems, in contrast, an unwarranted step to take at present since, on the one hand, local isotropy appears an adequate approximation in most high-Reynolds-number, self-sustaining shear flows and on the other, no experimental data are available on the processes to be approximated.

Concerning the writer's personal explorations in introducing a second second-rank tensor to the system of turbulence transport equations, his inclination is to generalize the multi-scale approach outlined earlier. Implicit in that closure is the assumption that the Reynolds-stresses of the medium scale motion are isotropic, i.e.,  $\overline{u_i u_j}_T = 2/3 \delta_{ij} k_T$ . The validity of this assumption is much narrower than that of local isotropy and it may turn out to be the main limitation on the multi-scale scheme. The next degree of elaboration is straightforward, however. In place of a *single* set of equations for  $\overline{u_i u_j}$  and  $k_T$  (or  $k_p$ ) one would provide transport equations for  $\overline{u_i u_j}_p$  and  $\overline{u_i u_j}_T$ . The former would, in practice, be similar to the current  $\overline{u_i u_j}$  equations except that spectral transfer terms will replace dissipative ones. The equations for  $\overline{u_i u_j}_T$  could probably be of fairly simple form since departures of the transfer range from isotropy will be fairly small. For example, mean-strain contributions to pressure-interactions might be represented by the isotropic form:  $\phi_{ij,2} = 0.4 k_T (\partial u_i / \partial x_j + \partial u_j / \partial x_i)$ . One outcome of the *closure* at this level would be that it facilitated a linkage with sub-grid-scale closures, the  $\overline{u_i u_j}_T$  being roughly equivalent to the sub-grid-scale stresses for which current schemes make very rudimentary approximations.

The above paragraphs have provided a few suggestions for how current Reynolds stress closures may evolve in the 1980's. No one can be sure at present just what will prove to be the most fruitful line of attack. One thing that is sure, however, is that progress in computational modelling can only be made with a strong supporting program of measurements. Moreover, the experimental data that will be needed are of a different kind from those which most experiments are currently providing. Experimentalists are naturally sensitive to the suggestion that their role should be (merely) that of advancing, or discriminating between, current closure ideas. Nevertheless, stronger interactions than at present between computationalists and experimentalists are surely desirable.

## References

1. C. du P. Donaldson, Proceedings AFOSR-Stanford Conference on Turbulent Boundary Layers, Stanford 1968.
2. P. Bradshaw, Proceedings AFOSR-Stanford Conference on Turbulent Boundary Layers, Stanford 1968.
3. J. O. Hinze, *Turbulence*, McGraw Hill, 1959.
4. P. Bradshaw, "Effects of streamline curvature on turbulent flow", AGARDograph No. 169, 1973.
5. P. Bradshaw (editor), Chapter 6, "Heat and mass transport" in *Turbulence - Topics in Applied Physics*, vol. 12, Springer-Verlag, 1976.
6. B. E. Launder, G. J. Reece, and W. Rodi, "Progress in the development of a Reynolds stress turbulence closure", *J. Fluid Mechanics* **68**, 537, 1975.
7. J. L. Lumley, "Computational modeling of turbulent flows", *Advances in Applied Mechanics*, **124**, 1978.

8. M. M. Gibson and B. E. Launder, "Ground effects on pressure fluctuations in the atmospheric boundary layer", *J. Fluid Mechanics* 86, 491, 1978.
9. B. E. Launder, "On the effects of a gravitational field on the turbulent transport on heat and momentum", *J. Fluid Mechanics* 67 (3), 569, 1975.
10. J. C. Rotta, "Statistische theorie nichthomogener turbulenz I", *Z. Phys.* 129, 547, 1951a.
11. J. L. Lumley and G. R. Newman, "The return to isotropy of homogeneous turbulence", *J. Fluid Mechanics* 82, 161, 1977.
12. D. Naot, A. Shavit, and M. Wolfshtein, "Two-point correlation model and the redistribution of Reynolds stresses", *Phys. Fluids* 16, 6, 738, 1973.
13. B. E. Launder and A. Morse, "Numerical prediction of axisymmetric free shear flows with a Reynolds stress closure" in *Turbulent Shear Flows - I*, Springer Verlag, 279, 1979.
14. J. C. André et al., "The clipping approximation and inhomogeneous turbulence simulations" in *Turbulent Shear Flows - I*, Springer Verlag, 307, 1979.
15. O. Zeman and J. L. Lumley, "Buoyancy effects in entraining turbulent boundary layers: a second-order closure study" in *Turbulent Shear Flows - I*, Springer Verlag, 295, 1979.
16. A. Lin and M. Wolfshtein, "Theoretical study of the Reynolds stress equations" in *Turbulent Shear Flows - I*, Springer Verlag, 327, 1979.
17. R. Mjolsness, "Possible departures from local isotropy in the small scale structure of turbulent velocity fields", *Proc. 2<sup>nd</sup> Turbulent Shear Flow Symposium*, London, 1979.
18. S. B. Pope, "An explanation of the turbulent round-jet/plane-jet anomaly", *AIAA Journal* 16, 279, 1978.
19. K. Hanjalic and B. E. Launder, "Sensitizing the dissipation equation to irrotational strains", *Proceedings ASME Symposium on Turbulent Boundary Layers*, Niagara Falls, 1979.
20. W. Rodi and D. B. Spalding, *Wärme-und-Stoffübertragung*, 1972.
21. B. E. Launder, A. Morse, W. Rodi, and D. B. Spalding, "Prediction of free shear flows - a comparison of the performance of six turbulence models", in *Proceedings of NASA Free Shear Flows Symposium*, vol. 1, NASA SP-121, 361, 1973.
22. J. C. Wyngaard, O. R. Coté, and Y. Izumi, "Local free convection, similarity and the budgets of shear stress and heat flux", *J. Atmos. Sci.* 28, 1171, 1971.
23. S. T. B. Young, "Turbulence measurements in a stratified shear flow", Queen Mary College, London, Rep. QMC-EP-6018.
24. M. M. Gibson and B. E. Launder, "On the calculation of horizontal, turbulent free shear flows under gravitational influence", *J. Heat Transfer* 98C, 80, 1976.
25. T. H. Ellison and J. S. Turner, "Turbulent entrainment in stratified flows", *J. Fluid Mech* 6, 423, 1959.
26. H. P. A. H. Irwin and P. A. Arnot Smith, "Prediction of the effect of streamline curvature on turbulence", *Phys. Fluids* 18, 624, 1975.
27. G. I. Fekete, M. Sc. Thesis, McGill University, 1963.
28. D. E. Guitton, Ph.D. Thesis, McGill University, 1970.
29. R. N. Meroney, Imperial College Aeronautical Engineering Department Report 74-05, 1974.
30. B. E. Launder and R. Schiestel, "Sur l'utilisation d'échelles temporelles multiples en modélisation des écoulements turbulents", *C. R. Acad. Sci. Paris Ser. A*, 286A, 709, 1978.
31. B. E. Launder and R. Schiestel, "Application d'un modèle de turbulence à échelles multiples au calcul d'écoulements libres turbulents", *C. R. Acad. Sci. Paris Ser. B*, 288, 127, 1979.
32. K. Hanjalic, B. E. Launder, and R. Schiestel, "Multiple-time scale concepts in turbulent transport modelling", *Proc. 2<sup>nd</sup> Turbulent Shear Flows Symposium*, London, 1979.
33. M. S. Uberoi, "Equipartition of energy and local isotropy in turbulent flows", *J. Appl. Phys.* 28, 1165, 1957.

#### Acknowledgements

The work reported herein has been partially supported by the National Aeronautics and Space Administration (Ames Research Center) through grant NSG 2256.

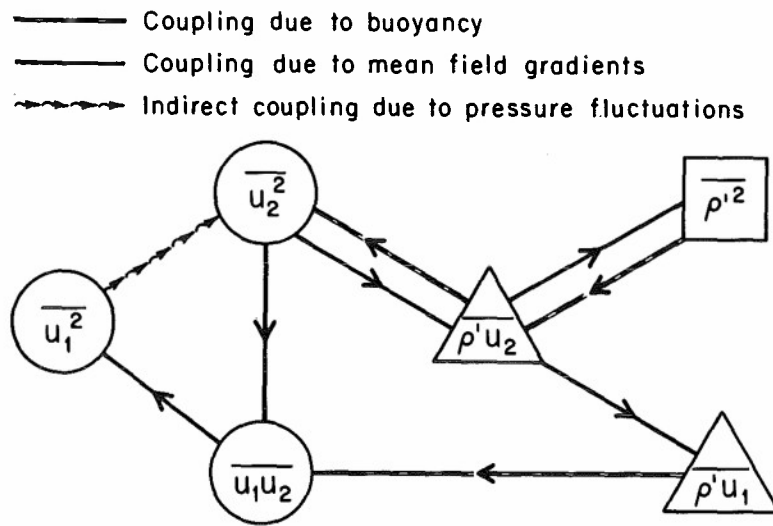


Figure 1 - Intercoupling among second-moment equations in density stratified flows.

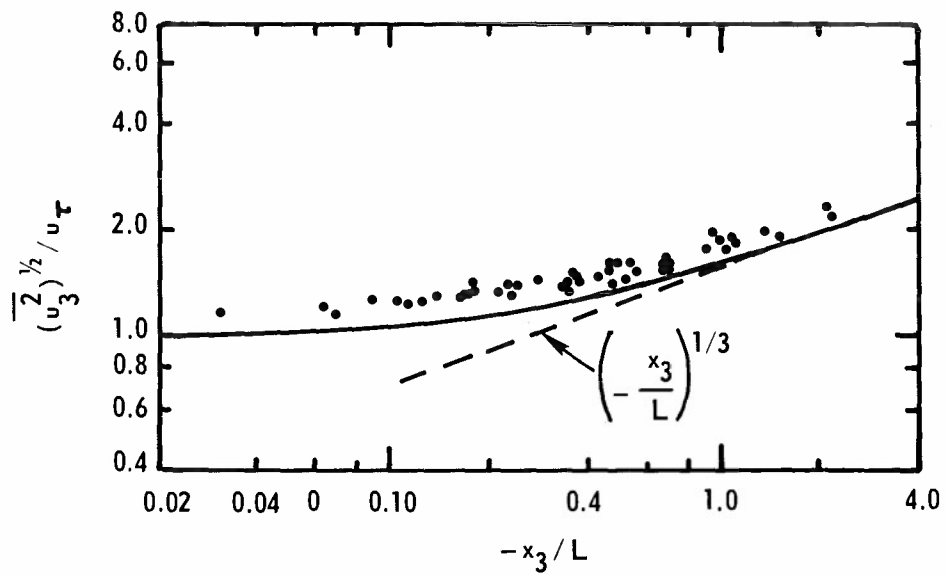


Figure 2 - Measured and predicted rms vertical velocity fluctuations under unstable conditions. Atmospheric-boundary-layer data from Wyngaard et al. [22].

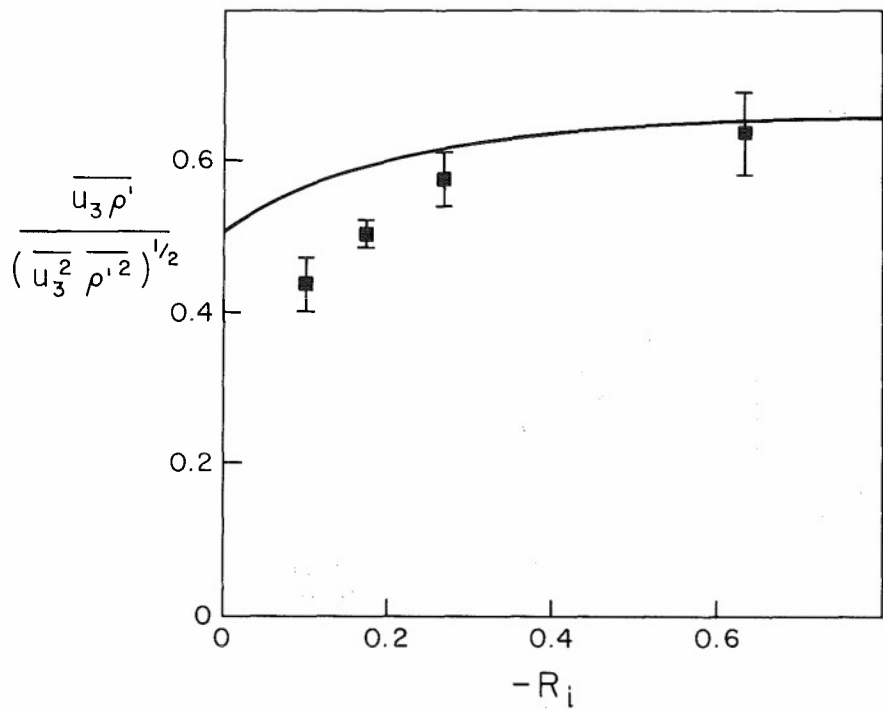


Figure 3  
Vertical density-flux correlation coefficient in atmospheric boundary layer under unstable stratification. Symbols denote experimental data, the line predictions.

Figure 4a - Ratio of vertical streamwise normal stresses in horizontal, nominally homogeneous full shear flow. From Gibson and Launder [8].

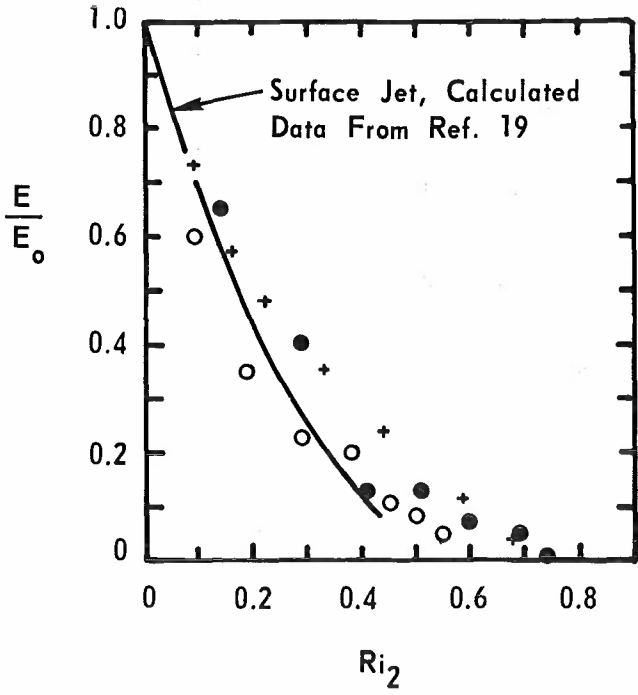
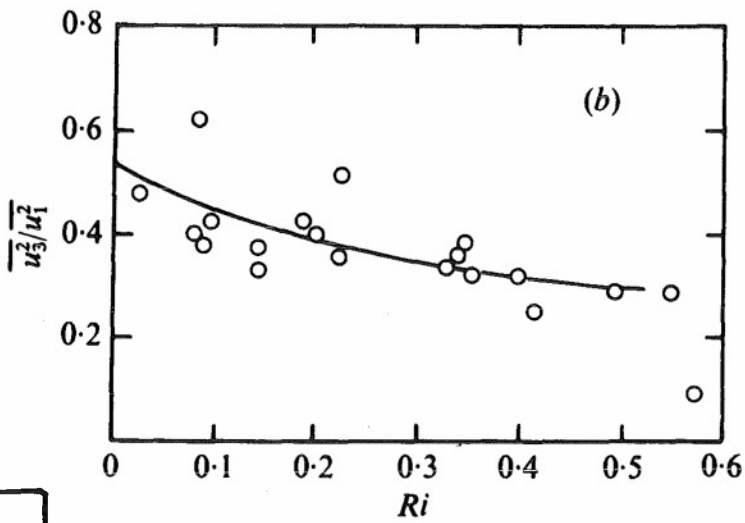


Figure 4b - Entrainment in plane surface jet

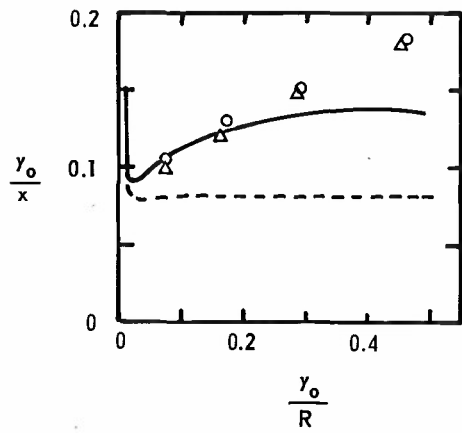


Figure 5 - Predicted and measured development of a wall jet developing on the outside of a curved cylinder (from Irwin & Arnot Smith [26])

— computed behavior ;  
 --- computed behavior with curvature terms omitted  
 o Fekete [27]  
 Δ Guitton [28] } experiment

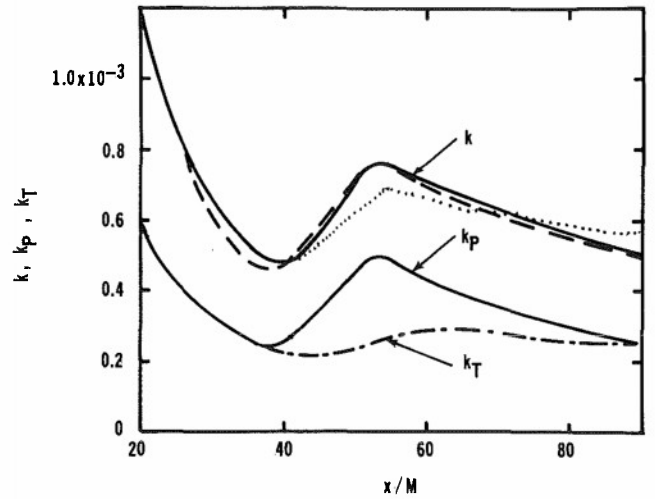


Figure 7 - Development of kinetic energies in 4:1 contraction:

--- experiment ; ... single-scale ;  
 — double scale

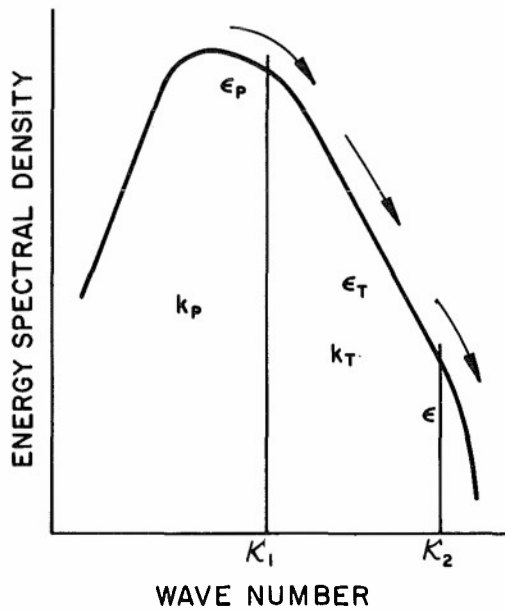


Figure 6 - The spectral division adopted in the multi-scale formulation

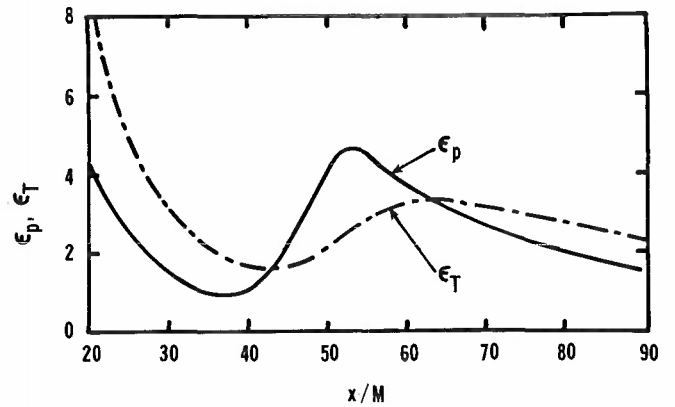


Figure 8 - Development of energy transfer rates through 4:1 contraction

LARGE EDDY SIMULATION OF TURBULENT CHANNEL FLOW —  
ILLIAC IV CALCULATION

John Kim\* and Parviz Moin\*  
Ames Research Center, NASA, Moffett Field, California 94035, U.S.A.

### SUMMARY

The three-dimensional time-dependent equations of motion have been numerically integrated for fully-developed turbulent channel flow. The large-scale flow field is obtained directly from the solution of these equations, and the small-scale field motions are simulated through an eddy viscosity model. The calculations are carried out on the ILLIAC IV computer with  $64 \times 64 \times 64$  grid points.

The computed flow patterns show that the wall layer consists of coherent structures of low-speed and high-speed streaks alternating in the spanwise direction. These structures were absent in the regions away from the wall. Hot spots, small localized regions of very large turbulent shear stress, are frequently observed. Very close to the wall, these hot spots are associated with  $\bar{u}'' > 0$  and  $\bar{v} < 0$  (sweep); away from the wall, they are due to  $\bar{u}'' < 0$  and  $\bar{v} > 0$  (burst). The profiles of the pressure velocity-gradient correlations show a significant transfer of energy from the normal to the spanwise component of turbulent kinetic energy in the immediate neighborhood of the wall ("the splatting effect").

### NOMENCLATURE

The overbar ( $\bar{\phantom{x}}$ ) denotes the filtered component and the prime ( $'$ ) denotes subgrid scale (SGS) component.

$C_s$	Smagorinsky's constant	$\bar{u}''$	$\equiv \bar{u} - \langle \bar{u} \rangle$
$G(\underline{x} - \underline{x}')$	filter function	$u_i$	velocity in the i-direction
$h_i$	mesh size in the i-direction	$\hat{u}_i$	Fourier transform of $\bar{u}_i$
$h_i^+$	$\equiv \frac{h_i u_\tau}{\nu}$	$u_\tau$	shear velocity $= \sqrt{\tau/\rho}$
$k$	wave number $\equiv \sqrt{k_1^2 + k_3^2}$	$v$	velocity in the vertical direction
$k_i$	wave number in the i-direction	$w$	velocity in the spanwise direction
$L_x$	length of the computational box in the x-direction	$x, x_1$	streamwise coordinate
$L_z$	length of the computational box in the z-direction	$x_i$	coordinate in the i-direction
$\ell$	SGS length scale	$\underline{x}, \underline{x}'$	coordinate vector
$N$	number of mesh points in the y-direction	$y, x_2$	coordinate in the direction normal to the walls
$p$	pressure	$y_w$	distance to the nearest wall
$\bar{p}$	$\equiv \frac{\bar{p}}{\rho} + \frac{R_{kk}}{3}$	$y^+$	$\frac{y_w u_\tau}{\nu}$
$p^*$	$\equiv \frac{\bar{p}}{\rho} + \frac{1}{2} \overline{\bar{u}_j \bar{u}_j} + \frac{R_{kk}}{3}$	$z, x_3$	spanwise coordinate
$\hat{p}$	Fourier transform of $\bar{p}$	$\epsilon_{ijk}$	the completely antisymmetric tensor of rank 3
$q$	root-mean-square velocity	$\lambda$	mean streak spacing
$Re$	Reynolds number based on channel half-width and the centerline velocity	$\lambda_i$	mean spacing of the turbulent structures in the i-direction
$Re_\tau$	Reynolds number based on channel half-width and shear velocity	$\lambda_i^+$	$\equiv \frac{\lambda_i u_\tau}{\nu}$
$R_{ij}$	$\equiv \overline{u_i' u_j'} + \overline{u_j' \bar{u}_i} + \overline{\bar{u}_j u_i'}$	$\lambda^+$	$\equiv \frac{\lambda u_\tau}{\nu}$
$S_{ij}$	$\equiv \frac{1}{2} \left( \frac{\partial \bar{u}_i}{\partial x_j} + \frac{\partial \bar{u}_j}{\partial x_i} \right)$ strain rate tensor	$\epsilon_j$	jth meshpoint in the vertical direction of the transformed (uniform mesh) space
$t$	dimensionless time	$\rho$	density
$u$	streamwise velocity	$\tau_{ij}$	$R_{ij} - \frac{R_{kk} \delta_{ij}}{3}$
		$\tau_w$	mean wall shear stress
		$\Delta t$	dimensionless time step

\*NRC Research Associate

$\nu$	kinematic viscosity	$\langle \rangle$	horizontal average (x-z plane)
$\nu_T$	eddy viscosity	$\langle \rangle^t$	time average
$\omega_i$	vorticity in the i-direction	Subscripts	
$\omega_x$	vorticity in the x-direction	w	wall value
$\delta_{ij} \equiv \begin{cases} 1 & i=j \\ 0 & i \neq j \end{cases}$		SGS	subgrid scale
		Superscript	
		n	time step

## 1. INTRODUCTION

The technique of large eddy simulation (LES) is a relatively new method for computing turbulent flows. The primary motivation for its undertaking is that the large eddy turbulence structures are clearly flow-dependent (e.g., jets vs boundary layers) and hence they are difficult if not impossible to model. On the other hand, there is experimental evidence (e.g., Ref. 1) that small eddies are universal in character, and consequently much more amenable to general modeling.

In LES, the large-scale motions are computed directly using three-dimensional time-dependent computation, and the small-scale motions are modeled. The dynamical equations for the large-scale field are derived by averaging the Navier-Stokes equations over volumes in space that are small compared to the overall dimensions of the flow field. This averaging is to provide sufficient smoothing of the flow variables, so they can be represented on a relatively coarse mesh. The resulting equations for the large eddies contain terms that involve small-scale turbulence. These terms are replaced by models that are to represent the interaction between the resolved and unresolved (subgrid scale, SGS) field motions.

One of the most extensive applications of LES has been to the problem of decay of homogeneous isotropic turbulence (see Refs. 2-4). A variety of numerical methods and subgrid-scale turbulence models was incorporated to compute this flow. Both the pressure-velocity and the vorticity-stream function formulations of the dynamical equations were used. These studies have shown that homogeneous turbulent flows can be reasonably simulated using simple eddy-viscosity models.

The first application of LES was made by Deardorff (Ref. 5), who simulated a fully developed turbulent channel flow at a very large Reynolds number. Utilizing a modest number of grid points (6,720), he showed that three-dimensional numerical simulation of turbulence (at least for simple flows) is feasible. His calculations predicted some of the features of turbulent channel flow with reasonable success and demonstrated the potential of LES for prediction and analysis of turbulent flows.

Schumann (Ref. 6) has also performed numerical simulation of turbulent channel flow. In addition, he has applied LES to cylindrical geometries (annuli). He used up to 10 times more grid points than Deardorff and a much more complex subgrid-scale model. In that model, an additional equation for SGS turbulent kinetic energy was integrated. However, the results showed no significant improvement over the case in which eddy-viscosity models were used (Ref. 6).

In the calculations of channel flow described above, no attempt was made to compute the flow in the vicinity of the walls. A great portion of turbulent kinetic energy production takes place in this region (see Ref. 7). Therefore, by using artificial velocity boundary conditions well beyond the viscous sublayer and buffer layer, a significant fraction of the dynamics of turbulence in the entire flow was effectively modeled. In addition, it should be noted that the boundary conditions used in the latter calculations assume that in the log layer, the velocity fluctuations are in phase with the wall shear stress fluctuations. This assumption is not supported by experimental measurements (Ref. 8).

Moin et al. (Ref. 9) simulated the channel flow, including the viscous region near the wall. The exact no-slip boundary conditions were used at the walls. In their computations, only 16 uniformly spaced grid points were used in each of the streamwise (x) and spanwise (z) directions and 65 nonuniformly spaced mesh points were used in the y-direction. The grid resolution was especially inadequate in the z-direction to resolve the now well-known streaky structures in the vicinity of the wall. In spite of this, computations did display some of the well-established features of the wall region. In particular, the results showed coherent structures of low-speed and high-speed fluid alternating in the viscous region near the wall, though not at their proper scale. The overall agreement of the computed mean-velocity profile and turbulent statistics with experimental data was satisfactory.

Encouraged by the results of the above coarse calculation, the present numerical simulation of channel flow with 262,144 grid points ( $64 \times 64 \times 64$ ) was undertaken. The ILLIAC IV computer, a parallel processor, was chosen for this purpose. Although the grid resolution in the spanwise direction is still not sufficient for an adequate representation of the wall-layer streaks, it is a significant improvement over the earlier calculation. This, in turn, allows a more realistic and comprehensive study of the structure and mechanics of this flow.

This paper is the result of a work that is now in progress and is essentially intended to demonstrate some of the capabilities of LES in the prediction and analyses of wall-bounded turbulent shear flows. In Sec. 2, the dynamical equations for large-scale field motions are derived. The subgrid model that was used is described in Sec. 3; Section 4 describes the computational grid network and its relation to the observed physical length scales in the flow. The numerical method is briefly outlined in Sec. 5; the data management process is taken up in Sec. 6; and in Sec. 7, we examine some aspects of the mechanics and structure of the flow, both in the vicinity of the wall and in regions away from the wall, and an attempt is made to correlate numerical results with laboratory observations. In Sec. 8, we present the computed flow statistics, which

include the mean-velocity profile, turbulent intensities, and turbulence shear stress. In that section, we will point out some of the deficiencies of the subgrid-scale model used and suggest improvements. Finally, conclusions are presented in Sec. 9.

## 2. GOVERNING EQUATIONS FOR THE LARGE-SCALE FIELD

The first step in LES is the definition of the large-scale field. Each flow variable  $f$  is decomposed as follows:

$$f = \bar{f} + f' \quad (1)$$

Here, the overbar denotes the large-scale or "filtered" field and the prime indicates the residual or "sub-grid" field. Following Leonard (Ref. 10) we define the large-scale field as:

$$\bar{f}(x) = \int_D G(\underline{x}, \underline{x}') f(\underline{x}') d\underline{x}' \quad (2)$$

where  $G$  is the filter function and the integral is extended over the whole flow field. In the horizontal planes ( $x$ - $z$ ), several possible choices for the filter function are available. Unless otherwise stated, most of the calculations reported here were carried out using a Gaussian filter,  $G(x-x', z-z')$ . The width of the Gaussian function characterizes the smallest scales of motion retained in the filtered field (the largest scales in the residual field). We assume that the filtering in the planes parallel to the walls provides sufficient smoothing in the vertical directions as well; our computations support this assumption. In addition, it should be noted that we use second-order finite difference schemes to approximate partial derivatives in the  $x_2$ -direction and such schemes have an implicit filtering effect associated with them. For further details see Moin et al. (Ref. 9).

After applying the filtering operation (Eq. (2)) to the incompressible Navier-Stokes and the continuity equations, the governing equations for the filtered field may be written

$$\frac{\partial \bar{u}_i}{\partial t} - \epsilon_{ijk} \bar{\omega}_j \bar{\omega}_k = - \frac{\partial \bar{p}^*}{\partial x_i} + \delta_{i1} - \frac{\partial}{\partial x_j} \tau_{ij} + \frac{1}{Re_\tau} \frac{\partial^2 \bar{u}_i}{\partial x_j \partial x_j} \quad (3)$$

$$\frac{\partial \bar{u}_i}{\partial x_i} = 0 \quad (4)$$

where we have decomposed  $u_i$  as in (1) and

$$\bar{\omega}_k = \epsilon_{pqk} \frac{\partial \bar{u}_q}{\partial x_p}$$

$$\tau_{ij} = R_{ij} - \frac{R_{kk} \delta_{ij}}{3}$$

$$R_{ij} = \overline{u_i' u_j'} + \overline{u_j' \bar{u}_i} + \overline{\bar{u}_j u_i'}$$

$$p^* = \frac{\bar{p}}{\rho} + \frac{1}{2} \overline{\bar{u}_j \bar{u}_j} + \frac{R_{kk}}{3} = \bar{p} + \frac{1}{2} \overline{\bar{u}_j \bar{u}_j}$$

Here, the variables are nondimensional using the channel half-width  $\delta$  and the shear velocity  $u_\tau = \sqrt{\tau_w/\rho}$ . The calculations will be carried out for a fixed streamwise mean-pressure gradient which is accounted for by the  $\delta_{i1}$  term in the momentum Eq. (3).

## 3. RESIDUAL STRESS MODEL

The remaining unknown quantity in Eq. (3) is  $\tau_{ij}$ . This term represents the subgrid-scale stresses and must be modeled. In the present calculations we have used an eddy viscosity model,

$$\tau_{ij} = -2\nu_T S_{ij} \quad (5a)$$

where

$$S_{ij} = \frac{1}{2} \left( \frac{\partial \bar{u}_i}{\partial x_j} + \frac{\partial \bar{u}_j}{\partial x_i} \right) \quad (5b)$$

The small-scale eddy viscosity  $\nu_T$  represents the action of the unresolved scales of motion on the resolved scales. Hence, as the resolution gets better,  $\nu_T$  should get smaller. This suggests that  $\nu_T$  should scale on a length scale  $\ell$  which is directly related to the computational resolution. The model most commonly used for  $\nu_T$  and the one we use here is the Smagorinsky model,

$$\nu_T = (C_s \ell)^2 \sqrt{S_{ij} S_{ij}} \quad (6)$$

where  $C_s = 0.1$  (Ref. 5) is a dimensionless constant and  $\ell$  is a dimensionless representative of the grid resolution, here assumed to be (Ref. 5):

$$\ell = (h_1 \cdot h_2(y) \cdot h_3)^{1/3} \quad (7)$$



This expression for  $\lambda$  is probably appropriate only for cases in which there is no significant grid anisotropy (Ref. 6). In the present calculation, the computational grid is very elongated ( $h_1, h_3 \gg h_2$ ) in the vicinity of the walls, and hence use of Eq. (7) is not strictly justified. However, to gain a better insight into the role of  $\lambda$  and to help guide its selection in future calculations, we have used Eq. (7) with a modification described below.

Near the walls, the subgrid-scale turbulence Reynolds number, defined as

$$R_{SGS} = \frac{q_{SGS} \cdot \lambda}{\nu} \quad (8)$$

is very small, and hence one expects the value of the eddy viscosity coefficient to be very small. In our calculations, we have found that the damping provided by the presence of  $(h_2(y))^{1/3}$  in Eq. (7) is not sufficient, and excessively large subgrid-scale stresses are formed near the wall. Therefore, in the present calculations we have multiplied  $\lambda$  (Eq. (7)) by an exponential damping function  $1 - \exp(-y^+/50)$ .

The eddy-viscosity model used here is best rationalized for isotropic turbulence at the scale of the computational grid. The fundamental assumption behind this model is that the resolution scale lies within an inertial range with the -5/3 power spectrum (Ref. 11). It is clear that for the moderate Reynolds number ( $Re_\tau \approx 640$ ) that we are considering and the nature of the grid volumes used, the above assumptions are not satisfied. This is particularly true in the highly viscous region in the vicinity of the walls. Thus, the present simulation is viewed as a challenge to the eddy-viscosity model used.

A critical test for the large eddy simulation technique is the prediction of the logarithmic layer and the von Karman "constant." This is one of the reasons for not utilizing the mixing-length model in the present calculations to account for inhomogeneity due to the mean shear (Ref. 6). Such a model is known to "postdict" the correct mean-velocity profile.

#### 4. THE COMPUTATIONAL GRID

The availability of computer resources restricts the size of calculations possible. For a given number of grid points  $N$ , we have to choose the grid size(s) based on the known physical properties of turbulent channel flow under consideration.

In the vertical direction ( $-1 \leq y \leq 1$ ), a nonuniform grid spacing is used. The following transformation gives the location of grid points in the vertical direction (Ref. 9):

$$y_j = \frac{1}{a} \tanh [\xi_j \tanh^{-1}(a)] \quad (9)$$

where

$$\xi_j = 1 + 2(j - 1)/(N - 2) \quad (10)$$

$$j = 1, 2, \dots, N$$

$N$  is the total number of grid points in the  $y$  direction, and the adjustable parameter of transformation is  $a$  ( $0 < a < 1$ ). We used  $a = 0.98346$ ,  $N = 64$ . This value of  $a$  was selected so that the above grid distribution in the  $y$ -direction is sufficient to resolve the viscous sublayer ( $y^+ < 5$ ).

The length  $L_x$  and  $L_z$  of the computational box in the streamwise ( $x$ ) and spanwise ( $z$ ) direction, in which periodic boundary conditions are used, should be long enough to include the important large eddies (Refs. 6, 12). Based on the two-point correlation measurements of Comte-Bellot (Ref. 13), we used  $L_x = 2\pi$ , and  $L_z = 4\pi/3$ . We have used 64 uniformly spaced grid points in each of the streamwise and spanwise directions. With the above choices for  $L_x$  and  $L_z$ , the nondimensional grid spacings in the horizontal directions expressed in the wall units are:

$$h_1^+ = 63$$

$$h_3^+ = 42$$

In the wall region, the important large eddies are the "streaks" (Ref. 14). These have a mean spanwise spacing corresponding to  $\lambda_3^+ \approx 100$ . It is clear that our grid resolution in the spanwise direction is not quite sufficient to resolve the streaks. This is especially true when we note that the above value for  $\lambda_3^+$  is based on an ensemble of measurements, and at a given instant streaks with a finer spacing than  $\lambda_3^+$  can be formed. As we shall see, however, calculations did reveal these structures, though not at their proper scale.

With relatively minor modifications to the present computer program, we are able to perform calculations with  $64 \times 64 \times 128$  grid points in the  $x$ ,  $y$ , and  $z$  directions, respectively. It is expected that in this simulation the spacing of the wall-layer streaks will be more in line with the laboratory observations.

#### 5. NUMERICAL METHOD

A complete description of the numerical method used is given in Ref. 15. Here, we give a brief outline of the method and minor modifications that were made to enhance the data management process. The partial derivatives in the  $x_2$  direction were approximated by second-order central difference formulae. In the  $x_1$  and  $x_3$  directions, partial derivatives were evaluated pseudospectrally (Ref. 16). With a given number of grid points, the use of the pseudospectral method in any given direction gives us the best possible resolution in that direction. This is particularly useful in the  $x_3$  direction where we face a lack of grid resolution (Sec. 4).

Time advancement is made using a semi-implicit method. Pressure, viscous terms, and part of the subgrid-scale model are treated implicitly, whereas explicit time advancement is used for the remaining nonlinear terms. The equation of continuity is solved directly. Second-order Adams Bashforth (Ref. 17) and Crank-Nicolson (Ref. 18) methods are used for explicit and implicit time advancement, respectively.

Next, we Fourier transform the resulting equations in  $x_1$  and  $x_3$  directions. This converts the above set of partial differential equations to the following set of ordinary differential equations for the variables at time step  $n + 1$ , for every pair of Fourier wave-numbers  $k_1$  and  $k_3$ , with  $y = x_2$  as the independent variable.

$$\frac{\partial^2 \hat{u}_1^{n+1}}{\partial y^2} + (\beta_1 - k^2) \hat{u}_1^{n+1} + ik_1 \beta_1 \frac{\Delta t}{2} \hat{p}^{n+1} = \hat{Q}_1^n \quad (11a)$$

$$\frac{\partial^2 \hat{u}_2^{n+1}}{\partial y^2} + (\beta_2 - k^2) \hat{u}_2^{n+1} + \beta_2 \frac{\Delta t}{2} \frac{\partial \hat{p}^{n+1}}{\partial y} = \hat{Q}_2^n \quad (11b)$$

$$\frac{\partial^2 \hat{u}_3^{n+1}}{\partial y^2} + (\beta_3 - k^2) \hat{u}_3^{n+1} + ik_3 \beta_3 \frac{\Delta t}{2} \hat{p}^{n+1} = \hat{Q}_3^n \quad (11c)$$

$$ik_1 \hat{u}_1^{n+1} + \frac{\partial \hat{u}_2^{n+1}}{\partial y} + ik_3 \hat{u}_3^{n+1} = 0 \quad (11d)$$

Here,  $\beta_i$  ( $i = 1, 2, 3$ ) are known functions of  $Re_\tau$  and  $\langle v_T^n \rangle$ , and  $\hat{Q}_i^n$  represent the terms involving the velocity and pressure field at time-step  $n$  and  $n - 1$  (see Ref. 15).

In addition to the use of implicit time advancement for all the viscous terms, the algorithm used in the present study is different in one other respect from the one described in Ref. 15. For reasons that will be explained in the next section, Eqs. (11a) and (11c) were multiplied by  $ik_1$  and  $ik_3$ , respectively. Thus, the dependent variables for the time-advancement equations are  $ik_1 \hat{u}$ ,  $\hat{v}$ , and  $ik_3 \hat{w}$  rather than  $\hat{u}$ ,  $\hat{v}$ , and  $\hat{w}$ .

The remaining steps in the solution procedure are as follows. Finite difference operators (described above) are used to approximate  $\partial/\partial y$  and  $\partial^2/\partial y^2$ . This gives a set of linear algebraic equations for the Fourier transform of dependent variables. This system is of block tridiagonal form and can be solved very efficiently. No-slip boundary conditions are used at the solid boundaries. Finally, inversion of the Fourier transform gives the velocity and pressure field at time-step  $n + 1$ .

The initial velocity field was the same as the one used in Ref. 9 interpolated on the finer grid used here.

## 6. DATA MANAGEMENT

In large simulations, the high-speed random-access memory of the computer on hand may not hold the entire data base of the problem being considered. In the present case, the core memory of the ILLIAC IV is large enough to hold only a few planes of velocity pressure field. Therefore, it is essential to manage the flow of data efficiently between the core memory and the disk memory where the entire data base resides. In general, separate passes over the data base are required for each time step and the task is to minimize the required number of such passes. The following describes a data management process employed in the present simulation.

The system of Eq. (11) must be solved for both real and imaginary parts of the dependent variables. This necessarily means that two passes through the data base are required: one for real parts of  $\hat{u}_1$  and  $\hat{u}_3$  and imaginary parts of  $\hat{u}_2$  and  $\hat{p}$ , and the other for imaginary parts of  $\hat{u}_1$  and  $\hat{u}_3$  and real parts of  $\hat{u}_2$  and  $\hat{p}$ .

To avoid an extra pass through the data base, we multiply Eqs. (11a) and (11c) by  $ik_1$  and  $ik_3$ , respectively (Ref. 19). (These multiplications in Fourier space amount to differentiations in real space.)

$$\frac{\partial^2 \tilde{u}_1^{n+1}}{\partial y^2} + (\beta_1 - k^2) \tilde{u}_1^{n+1} - k_1^2 \beta_1 \frac{\Delta t}{2} \hat{p}^{n+1} = \tilde{Q}_1^n \quad (12a)$$

$$\frac{\partial^2 \tilde{u}_2^{n+1}}{\partial y^2} + (\beta_2 - k^2) \tilde{u}_2^{n+1} + \beta_2 \frac{\Delta t}{2} \frac{\partial \hat{p}^{n+1}}{\partial y} = \tilde{Q}_2^n \quad (12b)$$

$$\frac{\partial^2 \tilde{u}_3^{n+1}}{\partial y^2} + (\beta_3 - k^2) \tilde{u}_3^{n+1} - k_3^2 \beta_3 \frac{\Delta t}{2} \hat{p}^{n+1} = \tilde{Q}_3^n \quad (12c)$$

$$\tilde{u}_1^{n+1} + \frac{\partial \tilde{u}_2^{n+1}}{\partial y} + \tilde{u}_3^{n+1} = 0 \quad (12d)$$

where  $\tilde{u}_1 = ik_1 \hat{u}_1$ ;  $\tilde{u}_2 = \hat{u}_2$ ;  $\tilde{u}_3 = ik_3 \hat{u}_3$ ;  $\tilde{Q}_1^n = ik_1 \hat{Q}_1^n$ ;  $\tilde{Q}_2^n = \hat{Q}_2^n$ ; and  $\tilde{Q}_3^n = ik_3 \hat{Q}_3^n$ . The above system of

equations can be solved with one pass through the data base, but two extra integrations in the Fourier space are required to obtain  $u_1$  and  $u_3$  in physical space. It should be noted, however, that such integrations cost far less than an I/O pass. In addition, to avoid the loss of information, upon differentiation, the Fourier mode associated with a null wave number is simply not multiplied by its wave number (i.e., zero) and, similarly, it is not divided by its wave number upon integration. This implies that  $\hat{u}_1$ ,  $\hat{u}_2$ , and  $\hat{u}_3$  in Eqs. 12 should be understood as

$$\hat{u}_1(0, y, k_3); ik_1 \hat{u}_1(k_1, y, k_3), k_1 \neq 0$$

$$\hat{u}_2(k_1, y, k_3)$$

$$\hat{u}_3(k_1, y, 0); ik_3 \hat{u}_3(k_1, y, k_3), k_3 \neq 0$$

The system of Eqs. (12) is solved by two separate passes through the data base. In PASS 1, the right-hand sides of these equations,  $Q_i$  ( $i = 1, 2, 3$ ), are evaluated and in PASS 2, the block tridiagonal system is solved. To compute the right-hand side vector in PASS 1, differentiations in all spatial directions are required. Since the pseudospectral method is used in the horizontal directions ( $x$  and  $z$ ) and a finite-difference scheme is used in the normal direction (central difference), all the data in an ( $x - z$ ) plane are needed for operators in these directions and the data for at least three adjacent planes are needed for finite difference operators in the  $y$  direction. Therefore, in PASS 1, two ( $x - z$ ) planes are brought into the core to be handled by a double buffer scheme. One complete pass through the data base is required to complete PASS 1.

In PASS 2, the block tridiagonal system must be solved for each  $k_1$  and  $k_3$ . In this pass, two ( $y - k_3$ ) planes are brought into the core. A special algorithm had to be developed to solve the block tridiagonal matrix because of the limitation on the core size. In a conventional block tridiagonal solver, all the results of forward sweep are stored to be used in backward sweep. For the present simulation, this would require half of the total core size (i.e.,  $16 \times 64 \times 64$ ) which is not feasible. Hence, a special algorithm\* was developed so that only a part of the results of the forward sweep is stored in the memory and the rest is recomputed as necessary in the backward sweep. Although this requires extra computations in the backward sweep, this method is much more efficient than performing the extra I/O passes that would otherwise have been necessary.

The computation described here was carried out on the ILLIAC IV computer at Ames Research Center. The dimensionless time step, during most of the calculations, was set at  $\Delta t = 0.001$ . The computer time per time-step (CPU and I/O time) was about 22 sec. This computational speed has been achieved with a full use of the parallel processing capabilities of the ILLIAC IV and the data management process just described.

## 7. DETAILED FLOW STRUCTURES

In this section, we investigate the detailed flow patterns by examining contour plots of typical instantaneous velocity and vorticity fields in  $x-z$ ,  $x-y$ , and  $y-z$  planes. In all these plots positive values are contoured by solid lines and negative values are contoured by dashed lines. In addition, all the plots are obtained at a given dimensionless time ( $t = 1.4$ ).

Figure 1 shows patterns of  $\bar{u}''$  in an  $x-z$  plane very close to the lower wall ( $y^+ = 16.1$ ). The striking feature of this figure is the existence of highly elongated (in the  $x$ -direction) regions of high-speed fluid located adjacent to low-speed ones. This picture of the flow pattern in the vicinity of the wall is in agreement with experimental observations (Refs. 20, 21) that the wall layer consists of relatively coherent structures of low-speed and high-speed streaks alternating in the spanwise direction. Examination of the typical spanwise spacing of these structures shows significant improvement over the earlier simulation (Ref. 9) where only 16 uniform grid points were used in each of the spanwise and streamwise directions. However, the typical spacing of these streaks is still about 3 times larger than the experimentally observed mean value of  $\lambda_3^+ \approx 100$ . This is expected, since our computational grid size in the spanwise direction is too large to resolve the wall layer streaks in their proper scale (Sec. 4).

Figure 2 shows patterns of  $\bar{u}''$  in an  $x-z$  plane far away from the wall ( $y/\delta = 0.73$ ). It is clear that the  $\bar{u}''$  patterns in the regions away from the wall do not show the coherent streaky structures that are characteristic of wall-layer turbulence. This is also in agreement with the experimental observations (Ref. 20). In fact, it is difficult to associate a definite structural pattern to  $\bar{u}''$  in the regions away from the wall.

Since turbulent energy production is directly proportional to  $-\langle uv \rangle^t$ , it is important to study the instantaneous map of  $\bar{u}''\bar{v}''$ . Figure 3 shows the patterns of  $\bar{u}''\bar{v}''$  in the same  $x-z$  plane as in Fig. 1; that is, very close to the wall ( $y^+ = 16.1$ ). Examination of this figure reveals several points related to the dynamics of wall-layer turbulence that deserve attention. First, it can be seen that the regions with negative  $\bar{u}''\bar{v}''$ , which have a positive contribution to the production of average turbulent kinetic energy, constitute the overwhelming majority of the entire plane. Second, pronounced streamwise elongation, the characteristic of the wall layer  $\bar{u}''$  eddies, is absent in  $\bar{u}''\bar{v}''$  patterns. This indicates that in contrast to  $\bar{u}''$  eddies,  $\bar{v}''$  eddies are not significantly elongated in the  $x$ -direction. Third, there are several small regions (hot spots), that are associated with very large values (large concentrations of dashed lines) of  $-\bar{u}''\bar{v}''$ . These regions are highly localized in space. Overlaying Fig. 3 on Fig. 1 reveals that the great majority of the "hot spots" are associated with  $\bar{u}'' > 0$  (hence,  $\bar{v}'' < 0$ ). Thus, it appears that in the close vicinity of the wall most of the regions with very large values of  $(-\bar{u}''\bar{v}'')$  are associated with high-speed fluid approaching the wall (sweeps) rather than low-speed fluid being ejected from the wall (bursts). With combined visual and hot-wire measurements, Falco (Ref. 22) has identified a new flow module in the vicinity of the wall. These relatively small but energetic structures (called pockets) appear to be footprints of high-speed fluid moving toward the wall. It is possible that the hot spots identified here may be related

\*The original concept was suggested to us by Marshall Merriam, Ames Research Center.

to pockets. Figure 4 shows the contour plots of  $\bar{u}''\bar{v}$  in the  $x$ - $z$  plane located at  $y^+ = 90$ . Examination of this figure and the corresponding  $\bar{u}''$  plot (not shown here) shows that in contrast to the near-wall region most of the hot spots that can be identified in this plane are associated with  $\bar{u}'' < 0$  and  $\bar{v} > 0$ , that is, with bursts. With quadrant analysis of  $uv$ , Brodkey et al. (Ref. 23) have found that most of the contribution to  $-\langle uv \rangle^+$  in the wall region comes from sweeps, and that in the regions away from the wall it comes from ejections. This is consistent with what is observed here in relation to Figs. 3 and 4. There are two other features in Fig. 4 that deserve attention. First, similar to Fig. 1, the regions with negative  $\bar{u}''\bar{v}$  constitute the overwhelming majority of the entire plane. Although there are regions with very large positive  $\bar{u}''\bar{v}$ , they are highly localized in space. Second, the maximum value of  $(-\bar{u}''\bar{v})$  in this plane is 17.81. This is about 20 times the expected  $-\langle uv \rangle^+$  at this plane. Such large excursions of  $\bar{u}''\bar{v}$  from its expected mean value have been a frequent observation in the laboratory (e.g., see Ref. 24).

Figure 5 shows contour plots of  $\bar{u}''\bar{v}$  in an  $x$ - $z$  plane far away from the lower wall ( $y/\delta = 0.73$ ). In contrast to planes located close to the lower wall (Figs. 3, 4), where the regions with negative  $\bar{u}''\bar{v}$  dominated the entire planes, a significant portion of this plane is associated with large positive  $\bar{u}''\bar{v}$  as well as negative  $\bar{u}''\bar{v}$ . The regions with the largest positive  $\bar{u}''\bar{v}$  are associated with high-speed fluid moving toward the upper wall, and the regions with the largest  $-\bar{u}''\bar{v}$  seem to be evenly distributed among high-speed fluid moving toward the lower wall or low-speed fluid moving away from the lower wall. Finally, examination of the  $\bar{u}''\bar{v}$  patterns in the midplane (not shown here) reveals that in contrast to the plane just described ( $y/\delta = 0.73$ ), the regions with the largest  $\bar{u}''\bar{v}$  are associated with bursts originating in the upper half of the channel, whereas the regions with the largest  $-\bar{u}''\bar{v}$  correspond to bursts originating in the lower half of the channel.

Among the conceptual models of the inner region of turbulent boundary layers is the streamwise vorticity model. This model portrays the inner region as being composed of pairs of long counter-rotating streamwise vortices located adjacent to each other. These long vortical structures, in turn, create low-speed and high-speed streaks alternating in the spanwise direction. Figure 6 shows the streamwise vorticity patterns in the same  $x$ - $z$  plane as in Fig. 1 ( $y^+ = 16$ ). These patterns do not show elongated regions of positive and negative  $\bar{\omega}_x$  alternating in the spanwise direction. Moreover, no definite relationship appears to exist between the streak patterns shown in Fig. 1 and  $\bar{\omega}_x$  patterns shown in Fig. 6. Therefore, the present simulation tends to dispute the validity of the vorticity model.

Figures 7 and 8 show patterns of  $\bar{u}''$  and  $\bar{\omega}_z$  in an  $x$ - $y$  plane,  $z = 15h_3$ . For clarity, we have expanded the region  $0 \leq y/\delta \leq 0.5$ . A pronounced feature of Fig. 7 is the two regions of high-speed fluid (with respect to the local mean velocity) that are inclined at oblique angles with respect to the wall. These structures are apparently associated with intense shear layers that are also inclined with respect to the wall (Fig. 8). Similar large-scale structures have also been observed in the laboratory. From measurements of space-time correlation of wall shear stress and velocity fluctuations in a turbulent duct flow, Rajagopalan and Antonia (Ref. 8) have identified large-scale structures that are inclined at a mean angle of about  $13^\circ$  to the wall. At this time, we have not scanned a sufficient number of  $x$ - $y$  planes at widely spaced times to obtain the mean inclination angle of these structures.

In Figs. 9 through 14, contour plots of the velocities and the streamwise vorticity in a  $y$ - $z$  plane ( $x = 0$ ) are shown. The contour plots in this plane reveal the existence of surprisingly well-organized structures in the wall region. Figure 9 shows a contour plot of the streamwise velocity  $\bar{u}''$ . Note that the figure is stretched 4 times in the vertical direction and that the contour line patterns are thus distorted in that direction. Two important features can be observed in this figure. First, away from the wall — for example,  $y/\delta > 0.4$  — no definite structure is discernible. Near the wall, however, an alternating array of low-speed and high-speed fluid is noticeable. This array has a long streaky structure in the streamwise direction, as was shown in Fig. 1. Second, as we approach the wall, the size of the eddies decreases gradually. Figure 10 is a magnified version of Fig. 9 close to the wall,  $0 < y^+ < 46$ . Again, the figure is highly stretched in the  $y$  direction so that the shapes of the flow structures are distorted. The array of low-speed and high-speed fluid is clearly discernible in this figure. This strikingly well-organized flow structure in the wall region is consistent with the previous experimental observations (Ref. 20), although the typical spacing between the streaks is not correct because of the insufficient spanwise grid spacings mentioned earlier. In addition to the well-organized structure in the wall region, there exists a very intense shear layer in the vertical plane where the low-speed and high-speed fluids come close together. This could cause free-shear-layer-type instabilities in this plane; such instabilities might be related to the experimental observations that the lifted streaks oscillate not only in the vertical direction but also in the horizontal planes.

Figure 11 shows a contour plot of the normal velocity  $\bar{v}$  in the same plane as in Fig. 10. Here, a positive  $\bar{v}$  (the solid lines) represents fluid moving away from the wall, and a negative  $\bar{v}$  (the dashed lines) represents fluid moving toward the wall. In this figure we notice an array of fluid moving away and toward the wall. If we align Fig. 10 with Fig. 11, we notice that, generally, there exists a negative correlation between  $\bar{u}''$  and  $\bar{v}$ . Note that in the vicinity of the wall, the low-speed fluid elements ( $\bar{u}'' < 0$ ) are generally being ejected away from the wall ( $\bar{v} > 0$ ), while high-speed fluid elements are moving toward the wall. Clearly, the fluid motions just described have a positive contribution to the production of averaged turbulent kinetic energy.

Figure 12 shows a contour plot of the spanwise velocity  $\bar{w}$ . A positive  $\bar{w}$  (solid lines) represents fluid moving to the right and a negative  $\bar{w}$  (dashed line) represents fluid moving to the left. Note also that a significantly large spanwise velocity gradient in  $y$  — that is,  $\partial \bar{w} / \partial y$  — exists due to the no-slip boundary conditions at the wall. This results in substantial streamwise vorticity near the wall, although flow is not actually revolving in this region. We will come back to this later. If we now align the contour plot of  $\bar{w}$  with that of  $\bar{v}$ , we can identify a definite flow pattern that exists in the wall region. A schematic illustration of this flow pattern is given in Fig. 15. This simplified illustration shows how low-speed streaks are being formed and lifted away from the wall. It is interesting to note that the rotation of the streamwise vorticity is in the opposite direction to the conventional vorticity model (Ref. 25) (see also Fig. 15b).

Figure 13 shows a contour plot of  $\bar{\omega}_x$  in the  $y$ - $z$  plane at  $x = 0$ . It can be seen that  $\bar{\omega}_x$  is concentrated only in the wall region. Away from the wall, the strength of the vorticity becomes very weak and no organized structure is discernible. Near the wall, highly localized concentrations of  $\bar{\omega}_x$  appear, sometimes in pairs of opposite sign. Figure 14 is a close-up of the wall region for  $y^+ \leq 46$ . Again, the figure is highly stretched in the vertical direction so that the patterns are distorted. By comparing these contour plots with those of  $\bar{v}$  and  $\bar{w}$ , we can distinguish the streamwise vorticity associated with the revolving fluid motion from the one associated with the velocity gradients. Recall that the existence of  $\bar{\omega}_x$  does not guarantee large-scale revolving fluid motion. In fact, most  $\bar{\omega}_x$  very close to the wall, say  $y^+ < 10$ , is due to  $\partial \bar{w} / \partial y$  and is not related to the revolving motion. Some of  $\bar{\omega}_x$  away from the wall, however, (e.g., the one in the center in Fig. 14) is associated with a large-scale revolving motion. This is in agreement with the experimental observations by flow visualization techniques (Ref. 7) where strong revolving motions are observed away from the wall ( $y^+ > 10$ ) and not very close to it. It should also be noted that although the strong vortical revolving fluid motion appears outside the sublayer, in the present simulation, the root-mean-square value of  $\bar{\omega}_x$ ,  $\langle \bar{\omega}_x^2 \rangle^{1/2}$  always attains its maximum at the wall [note that  $\bar{\omega}_x|_{\text{wall}} = (\partial \bar{w} / \partial y)|_{\text{wall}}$ ].

## 8. MEAN VELOCITY PROFILE AND TURBULENCE STATISTICS

Figure 16 shows the mean-velocity profile  $\langle \bar{u} \rangle$  that has developed after two dimensionless time units. (One nondimensional time unit corresponds approximately to the time in which a particle moving with center-line velocity travels  $22\delta$ .) Note that in the present study horizontal-average values are approximately ergodic. The calculated velocity profile shows a distinct logarithmic region over an appreciable portion of the channel width. For comparison, we have also included some of the available experimental data in this figure. The agreement of the computed mean-velocity profile with experimental data in most of the channel is satisfactory. In the vicinity of the wall, however, the values of the computed mean-velocity profile are rather low. This is due to the presence of an excessively large eddy viscosity coefficient near the wall. To verify this observation, we carried out a set of calculations (starting from  $t = 1.0$ ) where instead of the eddy viscosity model, we used a subgrid scale model similar to the one used by Fornberg (Ref. 26; in our numerical experiment, small-scale turbulence is removed by a sharp cutoff filter at each time step). Although this model is rather inadequate for proper representation of the interaction between the subgrid-scale and resolvable scale motions, it suffices for our present purpose, especially if the total time of integration is not large. Figure 17 shows the resulting  $\langle \bar{u} \rangle$  profile at  $t = 1.5$ . It is clear that the profile of  $\langle \bar{u} \rangle$  has attained the proper values in the vicinity of the wall. In addition, the logarithmic layer is once again evident. Figure 18 shows the profiles of resolvable normal turbulent intensities,  $\langle \bar{u}^2 \rangle^{1/2}$ ,  $\langle \bar{v}^2 \rangle^{1/2}$ , and  $\langle \bar{w}^2 \rangle^{1/2}$  at the same time as in Fig. 16. It can be seen that in agreement with experimental measurements, generally,  $\langle \bar{u}^2 \rangle^{1/2} > \langle \bar{w}^2 \rangle^{1/2} > \langle \bar{v}^2 \rangle^{1/2}$  throughout the channel. In addition,  $\langle \bar{u}^2 \rangle^{1/2}$  and  $\langle \bar{w}^2 \rangle^{1/2}$  attain their maximum values near the wall. Figure 19 shows the profile of the resolvable turbulent shear stress,  $\langle \bar{uv} \rangle$ . It can be seen that in the regions away from the walls the profile of  $\langle \bar{uv} \rangle$  does not follow the theoretical line. This indicates that the statistically stationary state has not been reached completely. Note that near the wall viscous stresses are important, and the total shear stress must balance the gross pressure gradient. Moreover, in the present calculations, the subgrid-scale shear stresses are significant only very near the wall ( $y^+ < 10$ ). In Fig. 20, profiles of the intensities are compared with some of the available experimental data in the vicinity of the wall. The agreement of the computed  $\langle \bar{u}^2 \rangle^{1/2}$  and  $\langle \bar{w}^2 \rangle^{1/2}$  with the data is satisfactory. However, as was also the case in Ref. 9, near the wall, a significant portion of  $\langle \bar{v}^2 \rangle^{1/2}$  seems to reside in subgrid-scale motions. This is consistent with our previous observation that  $v_T$  is still excessively large near the walls.

Figure 21 shows the resolvable portions of the pressure velocity-gradient correlations,  $\langle \bar{p}(\partial \bar{u} / \partial x) \rangle$ ,  $\langle \bar{p}(\partial \bar{v} / \partial y) \rangle$ , and  $\langle \bar{p}(\partial \bar{w} / \partial z) \rangle$  in the vicinity of the wall ( $y^+ < 100$ ,  $t = 2.0$ ). These terms are responsible for the exchange of energy between the three components of resolvable turbulence kinetic energy; they are of particular interest to turbulence modelers. Examination of these profiles reveals that except in the immediate neighborhood of the wall ( $y^+ < 20$ ), as expected, energy is transferred from  $\langle \bar{u}^2 \rangle$  to  $\langle \bar{v}^2 \rangle$  and  $\langle \bar{w}^2 \rangle$ ; that is,  $\langle \bar{p}(\partial \bar{u} / \partial x) \rangle < 0$ , and  $\langle \bar{p}(\partial \bar{v} / \partial y) \rangle$ ,  $\langle \bar{p}(\partial \bar{w} / \partial z) \rangle > 0$ . On the other hand, as we approach the wall, a significantly different behavior can be noticed. Specifically, there is a relatively large rate of energy transfer from  $\langle \bar{v}^2 \rangle$ , whereas there is a large energy transfer to  $\langle \bar{w}^2 \rangle$ . This rather unexpected result is consistent nonetheless with our previous discussions of the fluid motions very close to the wall (Sec. 7). For example, Fig. 15a shows high-speed fluid approaching the wall and spreading laterally, resulting in relatively large energy transfer from  $\langle \bar{v}^2 \rangle$  to  $\langle \bar{w}^2 \rangle$ . On the other hand, the momentum transfer from the lateral to the normal directions, which results in ejection of fluid elements away from the wall, involves the nonenergetic (slow moving) fluid in the immediate neighborhood of the wall. Thus, there is a net energy transfer from  $\langle \bar{v}^2 \rangle$  to  $\langle \bar{w}^2 \rangle$ , as shown in Fig. 21.

It should be mentioned that, in general, the values of the pressure velocity-gradient correlations computed in the present study are significantly higher than the earlier results using a much coarser grid (Ref. 9). This may indicate that a substantial portion of the pressure-strain correlation is due to small-to-medium turbulence scales. To confirm this observation, several computations were carried out with different filter widths. The results of the calculations tend to support this observation. Thus, at present, and in the absence of a better subgrid-scale turbulence theory, the computed pressure-strain correlations should be interpreted qualitatively. It should be mentioned, however, that the large-scale flow structures presented in the previous section are rather insensitive (qualitatively) to the different filter widths and subgrid-scale models used.

Before concluding this section, we turn our attention again to the subgrid-scale model used in the present study. To better resolve the relatively small turbulence scales in the vicinity of the walls, the present calculations were carried out for the case of a relatively low Reynolds number turbulent channel flow ( $Re_\tau = 640$ ,  $Re \approx 13,800$ ). Therefore, the subgrid-scale turbulence Reynolds number defined in Sec. 3 is considered to be low in the regions away from the wall and very low in the vicinity of the walls. As was mentioned in Sec. 3, the arguments used in constructing this model are valid only at a very high Reynolds number. Numerical results of McMillan and Ferziger (Ref. 30) also show that Smagorinsky's model is more appropriate at high Reynolds numbers. Thus, a low Reynolds number correction seems to be necessary. Note that because of the use of a much finer grid in this simulation than that used in Ref. 9, the effective subgrid-scale turbulence Reynolds number is lower than that in Ref. 9. In addition, because of the quasi-cyclic nature of turbulent channel flow (bursts, sweeps, etc.) the present calculations seem to indicate

that a subgrid-scale model that has a better response to the time history of the flow (a dynamic model) than the simple eddy viscosity model used here may be necessary. This is necessary for a proper long-time integration of the governing equations. Integrating an additional equation for subgrid-scale turbulence energy is an attractive possibility. In the interim, however, we have found that selective filtering of the excess small-scale turbulence may be adequate.

## 9. CONCLUSIONS

In this study, the three-dimensional time-dependent equations of motion have been numerically integrated for the case of fully-developed turbulent channel flow. The calculations were carried out on the ILLIAC IV computer with 64 mesh points in each of the spatial directions. Detailed flow patterns were studied by examining contour plots of typical instantaneous velocity and vorticity fields. In summary:

1. The wall layer consisted of coherent structures of low-speed and high-speed streaks alternating in the spanwise direction. These structures are absent in the regions away from the wall. In addition, contour plots of velocities in a typical  $y$ - $z$  plane revealed the existence of well-organized flow patterns in the wall region.
2. Hot spots, small localized regions of very large values of turbulent shear stress,  $\bar{u}''\bar{v}''$ , were frequently observed. Very close to the wall, these hot spots were associated with  $\bar{u}'' > 0$  and  $\bar{v}'' < 0$  (sweep); away from the wall, they were due to  $\bar{u}'' < 0$  and  $\bar{v}'' > 0$  (burst). In the central regions of the channel, bursts from both halves of the channel were the sources of the hot spots.
3. No evidence of a direct relationship between streaks and streamwise vorticity  $\bar{\omega}_x$  was observed in the present simulation; very close to the wall,  $\bar{\omega}_x$  was not the result of large-scale revolving fluid motions but was rather due to the spanwise velocity gradient,  $(\partial w / \partial y)$ . Though strong vortical regions were observed away from the wall ( $y^+ \sim 30$ ),  $\langle \bar{\omega}_x^2 \rangle^{1/2}$  attained its maximum value at the wall.
4. The profiles of the pressure velocity-gradient correlation showed a significant transfer of energy from the normal to the spanwise component of turbulent kinetic energy in the immediate neighborhood of the wall (the "splatting" effect). A large portion of the pressure-strain correlations appears to be due to small to medium scales of turbulent motions.

The work presented here is still in progress and much more remains to be done. In particular, a more refined model that depicts the dynamic nature of the subgrid-scale motion may become necessary. Also, more mesh points, especially in the spanwise direction, are required in order to resolve the streaks at their proper scale. A computation with twice as many grid points as in the present calculation ( $64 \times 64 \times 128$ ) will be carried out in the near future.

It is hoped that this paper has demonstrated some of the capabilities of LES as a research tool for studying the mechanics and structure of turbulent boundary layers. The authors believe that LES will make important contributions to the study of turbulent flows by supplementing the experimental data.

## REFERENCES

1. Chapman, D. R.: Computational Aerodynamics Development and Outlook, AIAA Dryden Lectureship in Research. AIAA Paper 79-0129, January 1979.
2. Kwak, D., Reynolds, W. C., and Ferziger, J. H.: Three-Dimensional, Time-Dependent Computation of Turbulent Flows. Report No. TF-5, Mech. Eng. Dept., Stanford Univ., 1975.
3. Shaanan, S., Ferziger, J. H., and Reynolds, W. C.: Numerical Simulation of Turbulence in the Presence of Shears. Report No. TF-6, Mech. Eng. Dept., Stanford Univ., 1975.
4. Mansour, N. N., Moin, P., Reynolds, W. C., and Ferziger, J. H.: Improved Methods for Large Eddy Simulation of Turbulence. Proc. Symp. on Turbulent Shear Flows, Pennsylvania State Univ., 1977.
5. Deardorff, J. W.: A Numerical Study of Three-Dimensional Turbulent Channel Flow at Large Reynolds Number. J. Fluid Mech., vol. 41, 1970, p. 283.
6. Schumann, U.: Subgrid Scale Model for Finite Difference Simulations of Turbulent Flows in Plane Channels and Annuli. J. Comp. Phys., vol. 18, 1975, p. 376.
7. Kim, H. T., Kline, S. J., and Reynolds, W. C.: The Production of Turbulence Near a Smooth Wall in a Turbulent Boundary Layer. J. Fluid Mech., vol. 50, 1971, p. 133.
8. Rajagopalan, S., and Antonia, R. A.: Some Properties of the Large Structure in a Fully Developed Turbulent Duct Flow. Phys. Fluids, vol. 22, 1979, p. 614.
9. Moin, P., Reynolds, W. C., and Ferziger, J. H.: Large Eddy Simulation of Incompressible Channel Flow. Report No. TF-12, Mech. Eng. Dept., Stanford Univ., 1978.
10. Leonard, A.: On the Energy Cascade in Large-Eddy Simulations of Turbulent Fluid Flows. Adv. In Geophysics, vol. 18A, 1974, p. 237.
11. Lilly, D. K.: The Representation of Small-Scale Turbulence in Numerical Simulation Experiments. Proc. IBM Sci. Comp. Symp. on Env. Sciences, IBM Form No. 320-1951, 1967.
12. Ferziger, J. H., Mehta, U. B., and Reynolds, W. C.: Large Eddy Simulation of Homogeneous Isotropic Turbulence. Proc. Symp. on Turbulent Shear Flows, Pennsylvania State Univ., 1977.

13. Comte-Bellot, G.: Contribution a l'etude de la Turbulence de Conduite, Doctoral Thesis, University of Grenoble, 1963.
14. Kline, S. J., Reynolds, W. C., Schraub, F. A., and Runstadler, P. W.: The Structure of Turbulent Boundary Layers. *J. Fluid Mech.*, vol. 30, 1967, p. 741.
15. Moin, P., Mansour, N. N., Reynolds, W. C., and Ferziger, J. H.: Large Eddy Simulation of Turbulent Shear Flows. *Proc. Sixth International Conference on Numerical Methods in Fluid Dynamics*, Cabannes, H., Holt, M., and Rusanov, V., eds., Springer-Verlag, Berlin, Heidelberg, New York, 1979.
16. Orszag, S. A.: Comparison of Pseudospectral and Spectral Approximation. *Studies in Appl. Math.*, vol. LI, no. 3, 1972, p. 253.
17. Lilly, D. K.: On the Computational Stability of Numerical Solutions of Time-Dependent Nonlinear Geophysical Fluid Dynamic Problems. *Monthly Weather Rev.*, vol. 93, no. 1, 1965.
18. Richtmyer, R. D., and Morton, K. W.: *Difference Methods for Initial Value Problems*, Second ed. Interscience, New York, 1967.
19. Rogallo, R. S.: An ILLIAC Program for the Numerical Simulation of Homogeneous Incompressible Turbulence. NASA TM-73203, 1977.
20. Runstadler, P. W., Kline, S. J., and Reynolds, W. C.: An Investigation of the Flow Structure of the Turbulent Boundary Layer. Report No. MD-8, Mech. Eng. Dept., Stanford Univ., 1963.
21. Kline, S. J., and Runstadler, P. W.: Some Preliminary Results of Visual Studies of Wall Layers of the Turbulent Boundary Layer. *J. Appl. Mech.*, vol. 2, 1959, p. 166.
22. Falco, R. E.: The Role of Outer Flow Coherent Motions in the Production of Turbulence Near a Wall. *Coherent Structure of Turbulent Boundary Layers*, Smith, C. R., and Abbott, D. E., eds., AFOSR/Lehigh, 1978.
23. Brodkey, R. S., Wallace, J. M., and Eckelmann, H.: Some Properties of Truncated Turbulence Signals in Bounded Shear Flows. *J. Fluid Mech.*, vol. 63, 1974, p. 209.
24. Sabot, J. and Comte-Bellot, G.: Intermittency of Coherent Structures in the Core Region of Fully Developed Turbulent Pipe Flow. *J. Fluid Mech.*, vol. 74, 1976, p. 767.
25. Blackwelder, R. F.: The Bursting Process in Turbulent Boundary Layers. *Coherent Structure of Turbulent Boundary Layers*, C. R. Smith and D. E. Abbott, eds., AFOSR/Lehigh, 1978.
26. Fornberg, B.: A Numerical Study of 2-D Turbulence. *J. Comp. Phys.*, vol. 25, 1977, p. 1.
27. Hussain, A. K. M. F. and Reynolds, W. C.: Measurements in Fully Developed Channel Flow. *J. Fluid Eng.*, vol. 97, 1975, p. 568.
28. Laufer, J.: Investigation of Turbulent Flow in a Two-Dimensional Channel. NACA Report 1053, 1951.
29. Clark, J. A.: A Study of Incompressible Turbulent Boundary Layers in Channel Flow. *J. Basic Engrg.*, vol. 90, 1968, p. 455.
30. McMillan, O. J. and Ferziger, J. H.: Direct Testing of Subgrid-Scale Models, NEAR TR 174. Nielsen Engineering and Research, Inc., 1978.

#### ACKNOWLEDGMENT

This work was carried out while the authors held NRC Research Associateships at Ames Research Center. The authors would like to express their gratitude to Dr. R. S. Rogallo for his assistance in writing the present program for the ILLIAC IV computer. Helpful discussions with Drs. A. Leonard, M. W. Rubesin, and A. W. Wray are gratefully acknowledged.



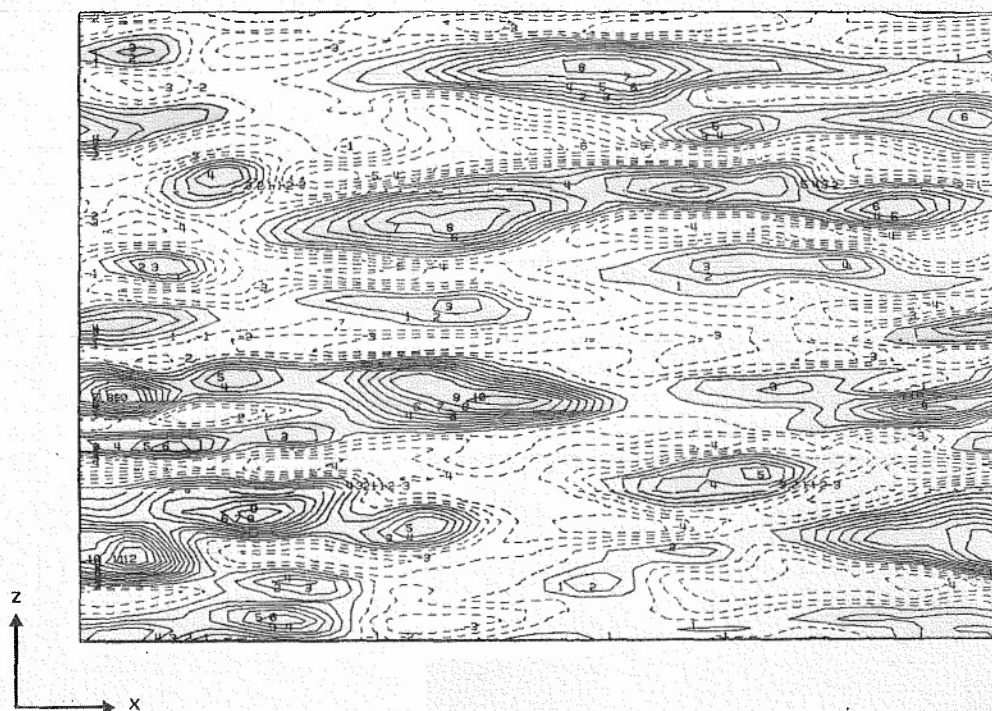


Fig. 1. Contours of  $\bar{u}''$  in the  $x$ - $z$  plane at  $y^+ = 16$ .

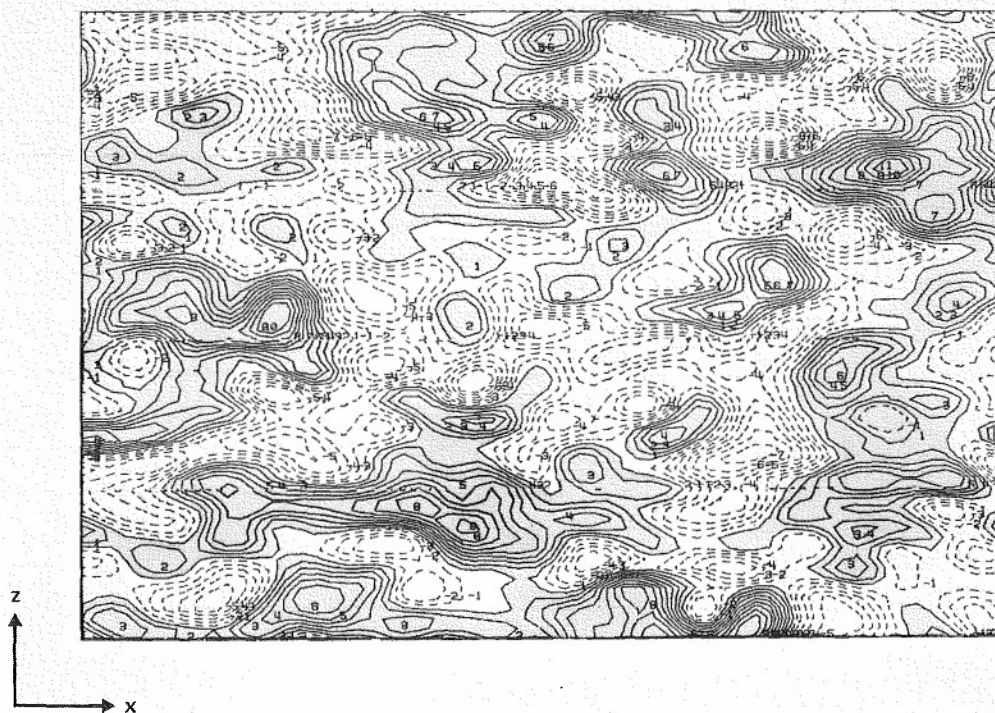


Fig. 2. Contours of  $\bar{u}''$  in the  $x$ - $z$  plane at  $y/\delta = 0.73$ .



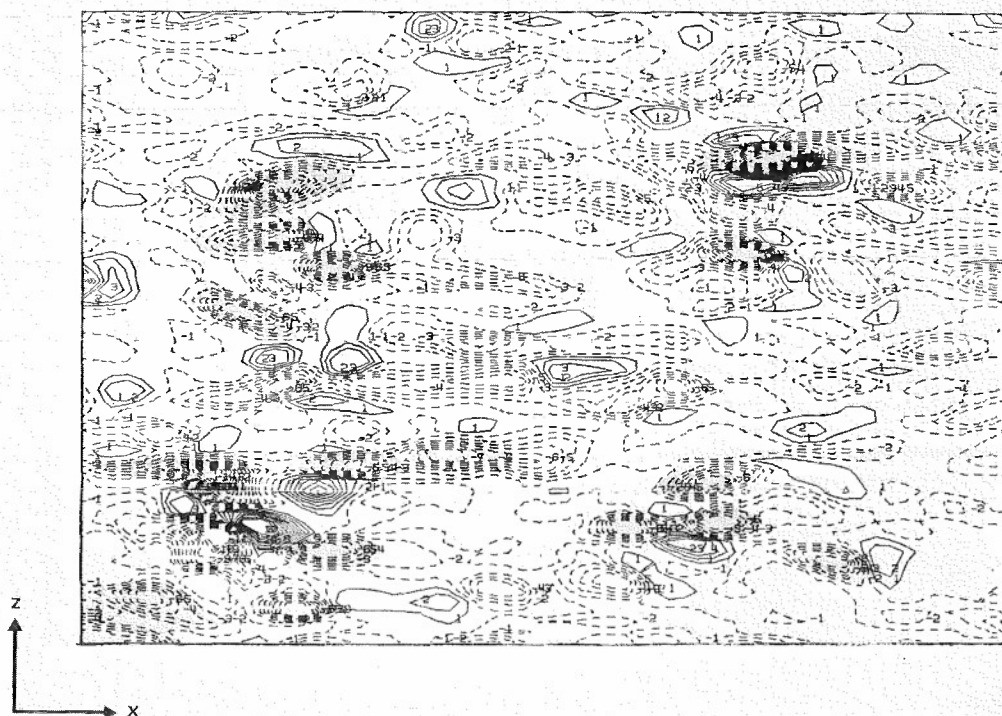


Fig. 3. Contour plot of  $\bar{u}''\bar{v}$  in the  $x$ - $z$  plane at  $y^+ = 16$ .

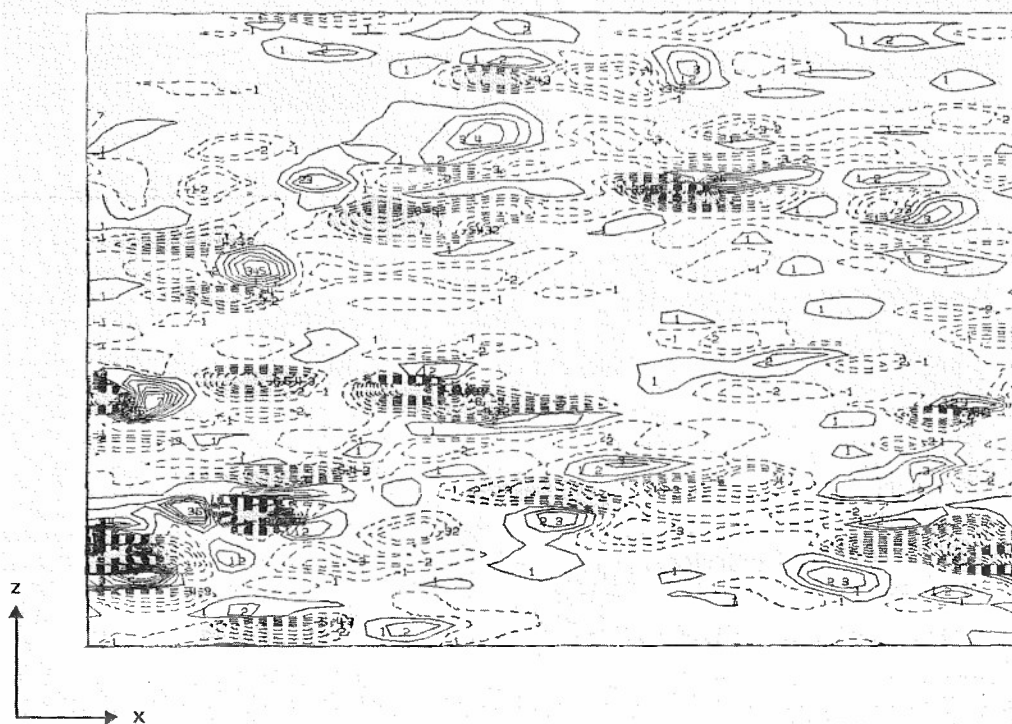


Fig. 4. Contour plot of  $\bar{u}''\bar{v}$  in the  $x$ - $z$  plane at  $y^+ = 90$ .

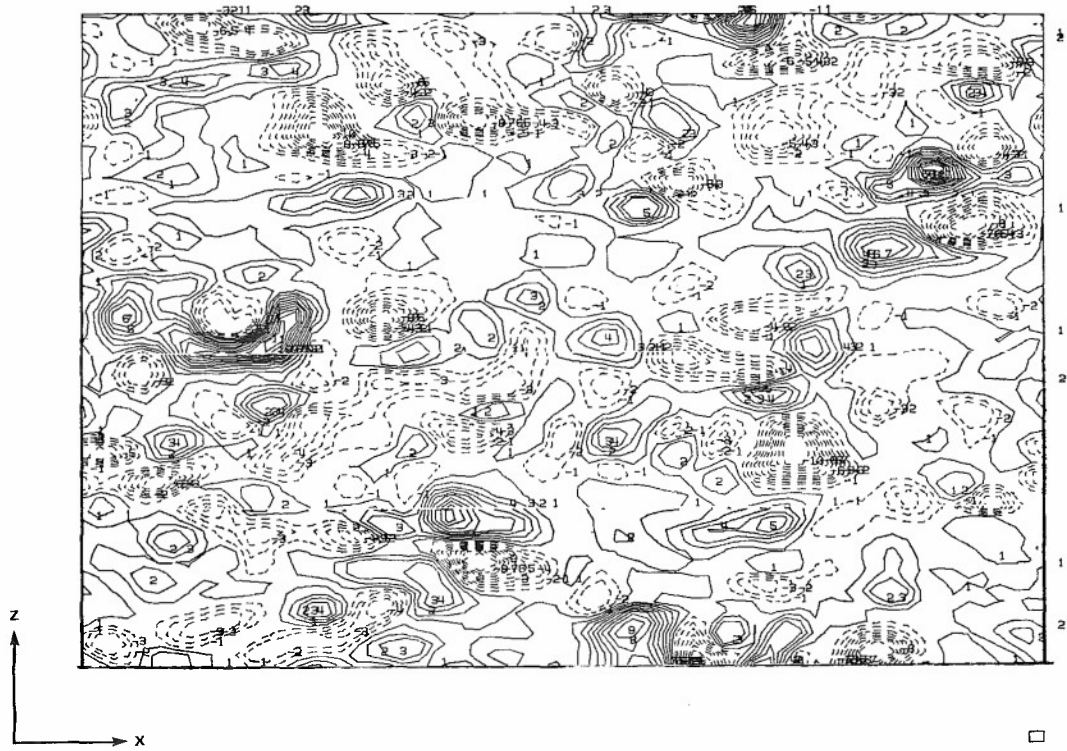


Fig. 5. Contour plot of  $\bar{u}''\bar{v}$  in the  $x$ - $z$  plane at  $y/\delta = 0.73$ .

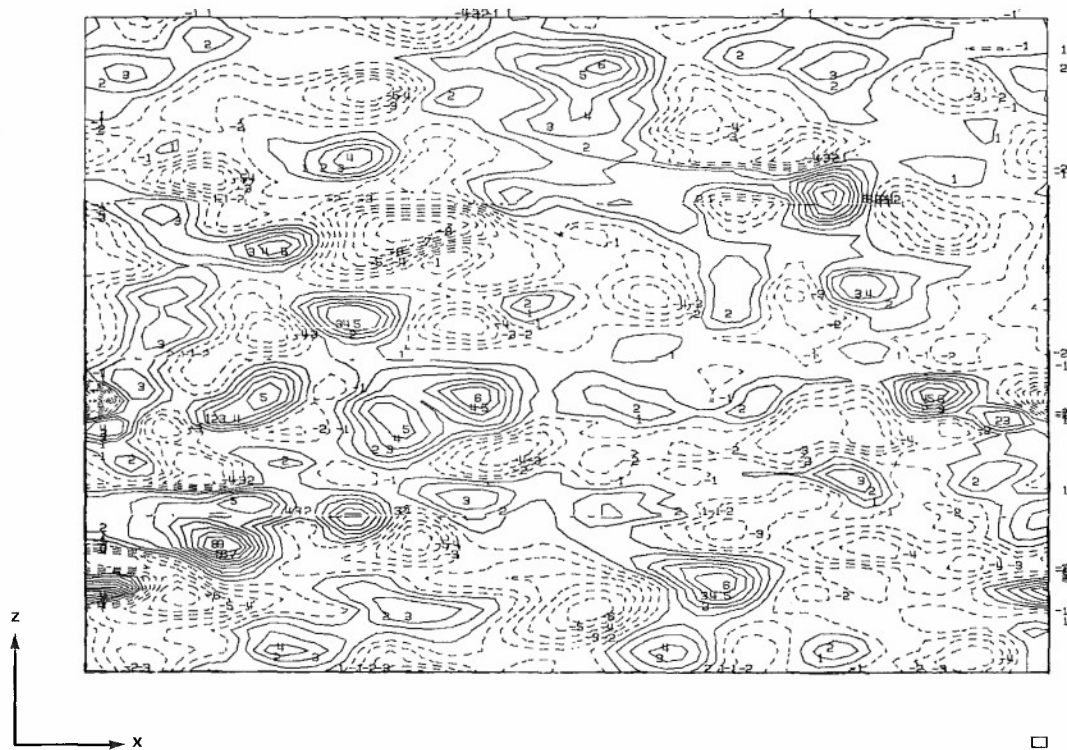


Fig. 6. Contours of the streamwise vorticity  $\bar{\omega}_x$  in the  $x$ - $z$  plane at  $y^+ = 16$ . Note that the  $\bar{\omega}_x$  patterns do not exhibit elongated structures in the  $x$ -direction.



Fig. 7. Contours of  $\bar{u}''$  in the  $x$ - $y$  plane ( $0 \leq y/\delta \leq 0.5$ ) at  $z = 15h_3$ .

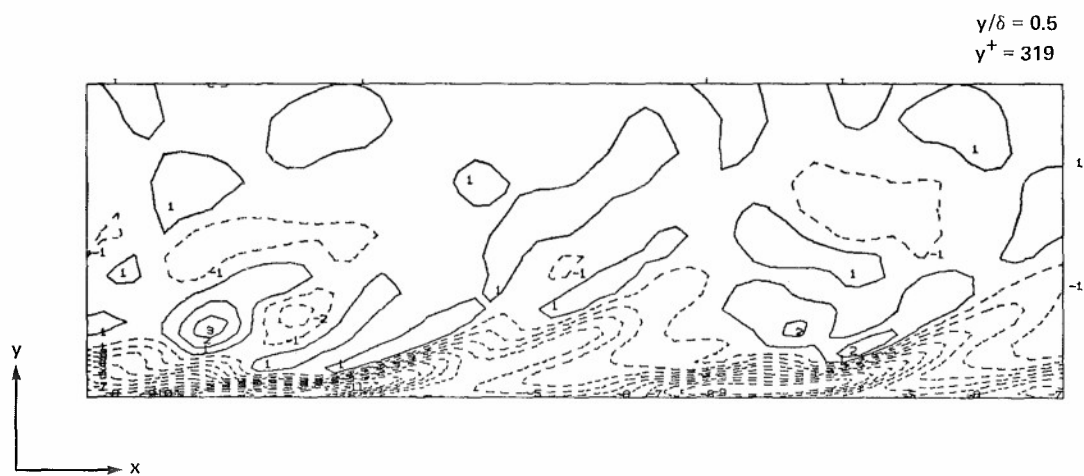


Fig. 8. Contours of spanwise vorticity  $\bar{\omega}_z$  in the  $x$ - $y$  ( $0 \leq y/\delta \leq 0.5$ ) plane at  $z = 15h_3$ .

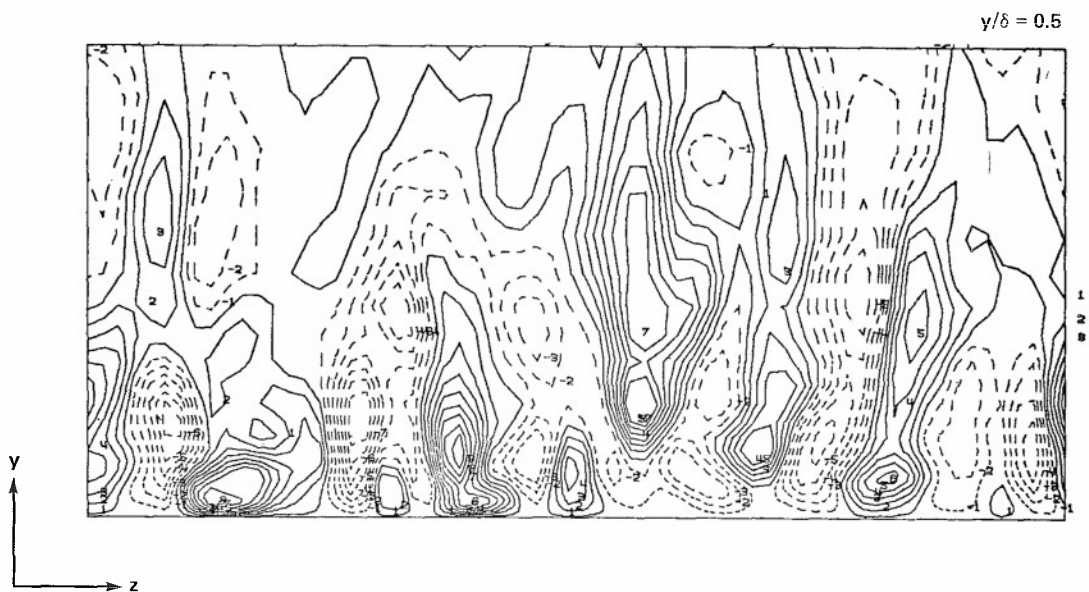
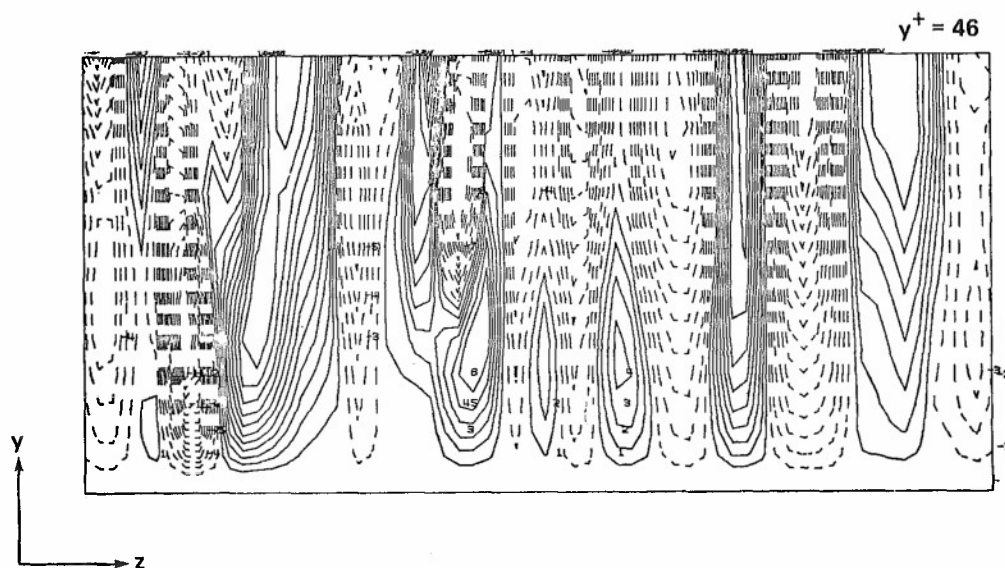
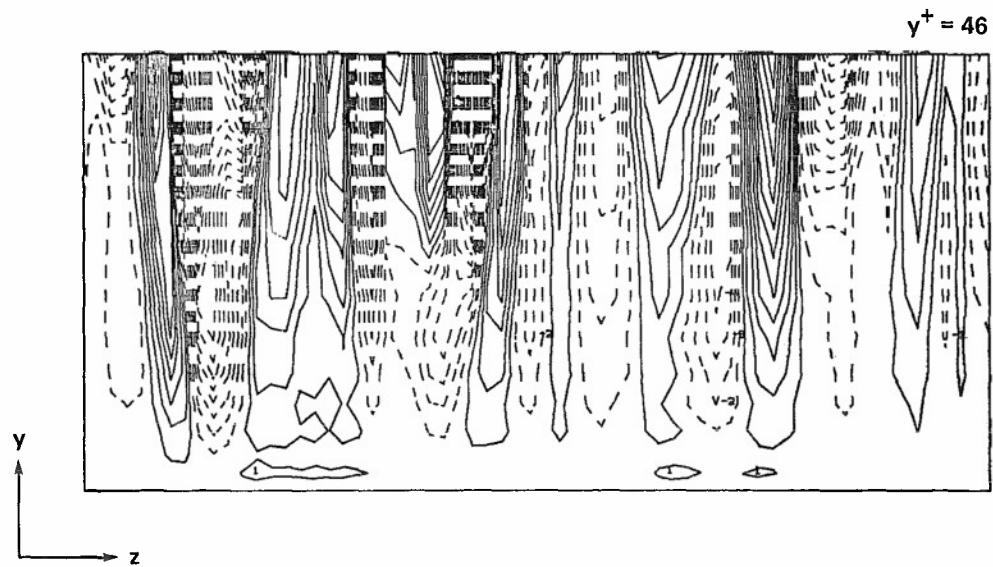
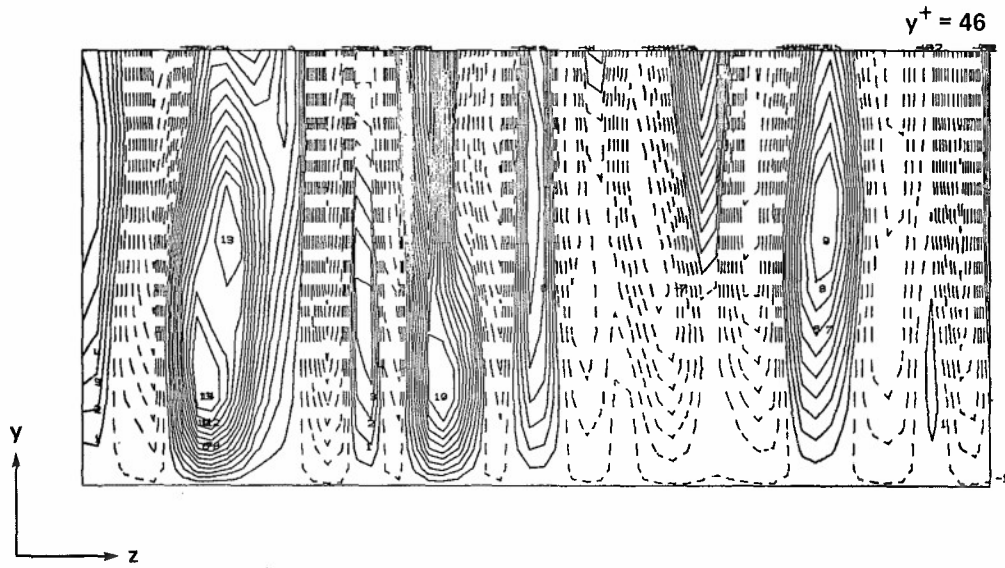


Fig. 9. Contour plot of  $\bar{u}''$  in the  $y$ - $z$  plane ( $0 \leq y/\delta \leq 0.5$ ) at  $x = 0$ .



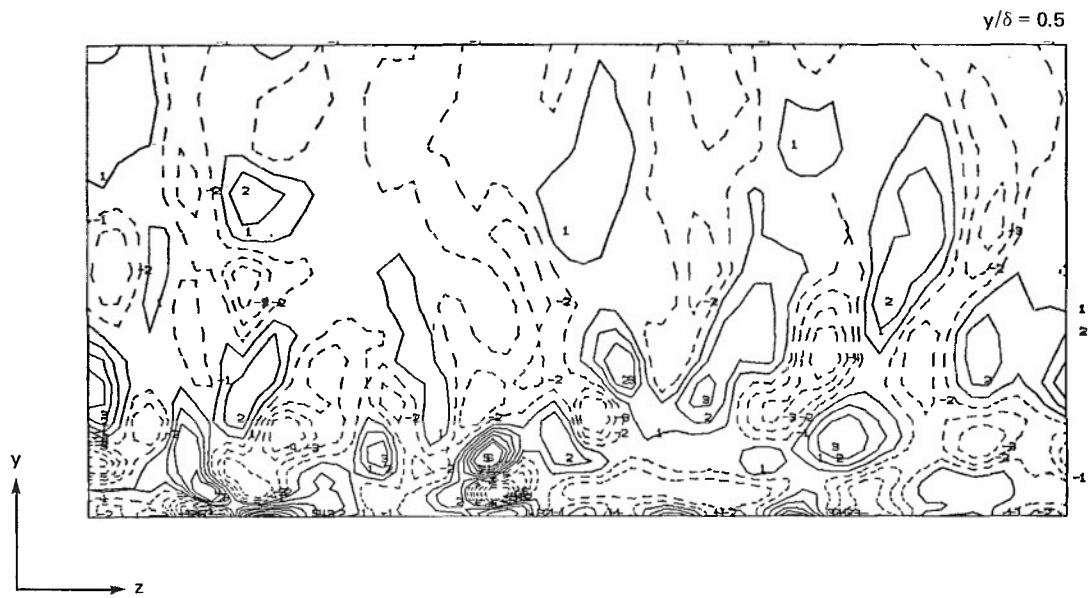


Fig. 13. Contour plot of the streamwise vorticity in the  $y$ - $z$  plane ( $0 \leq y/\delta \leq 0.5$ ) at  $x = 0$ .

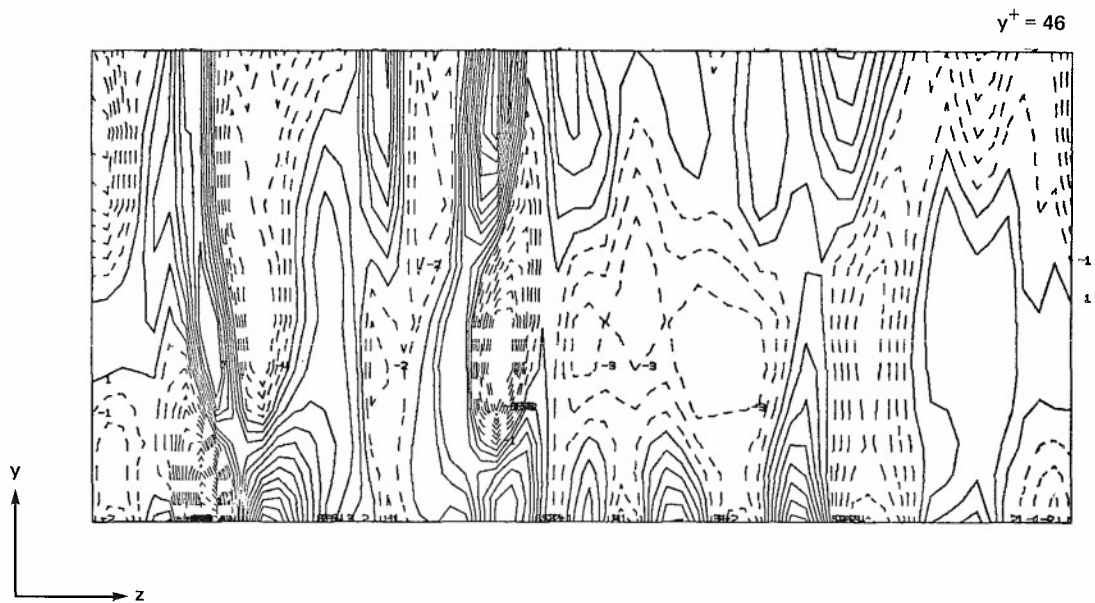
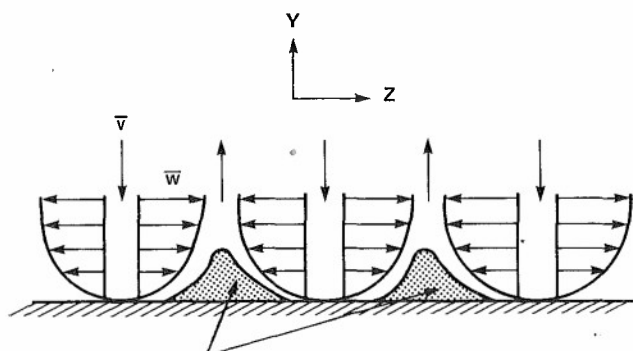
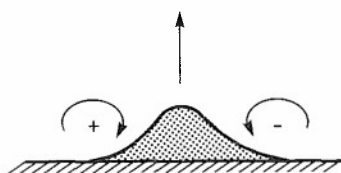


Fig. 14. Contours of the streamwise vorticity in the  $y$ - $z$  plane ( $0 \leq y^+ \leq 46$ ) at  $x = 0$ .



DYE INJECTED AT THE WALL WILL BE COLLECTED HERE AND LIFTED UPWARD

(a) Cross-sectional view of spanwise velocity in  $y$ - $z$  plane.



(b) Streamwise vorticity according to (a).

Fig. 15. Schematic diagram of the flow patterns in the immediate neighborhood of the wall.

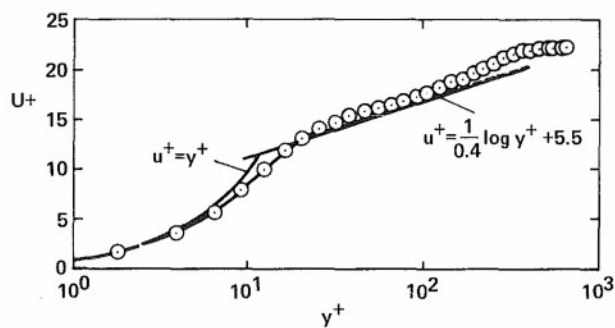


Fig. 17. Mean-velocity profile obtained with the sharp cutoff model (Ref. 26).

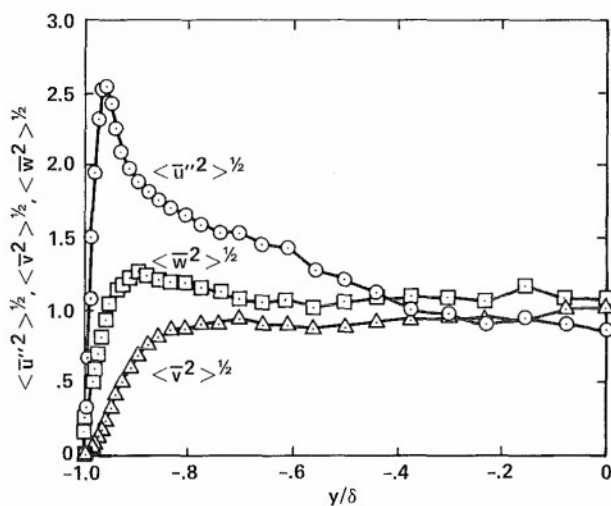


Fig. 18. Profiles of horizontally averaged resolvable turbulence intensities.

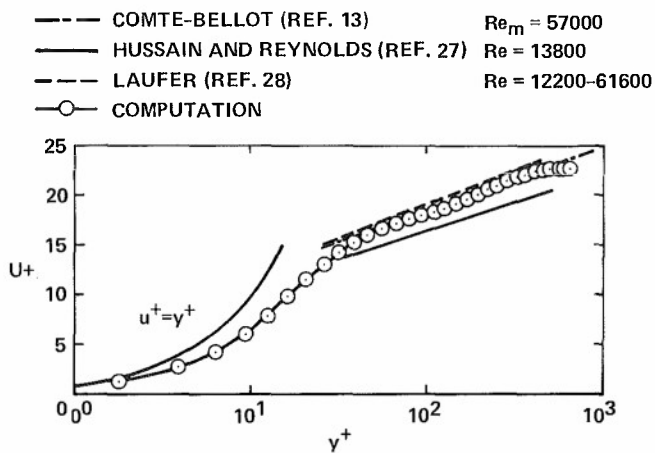


Fig. 16. Mean-velocity profile.

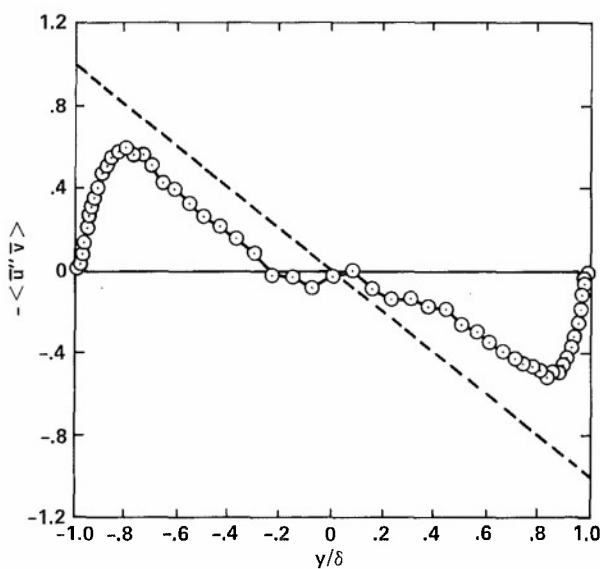


Fig. 19. Vertical profile of horizontally averaged resolvable turbulent shear stress.



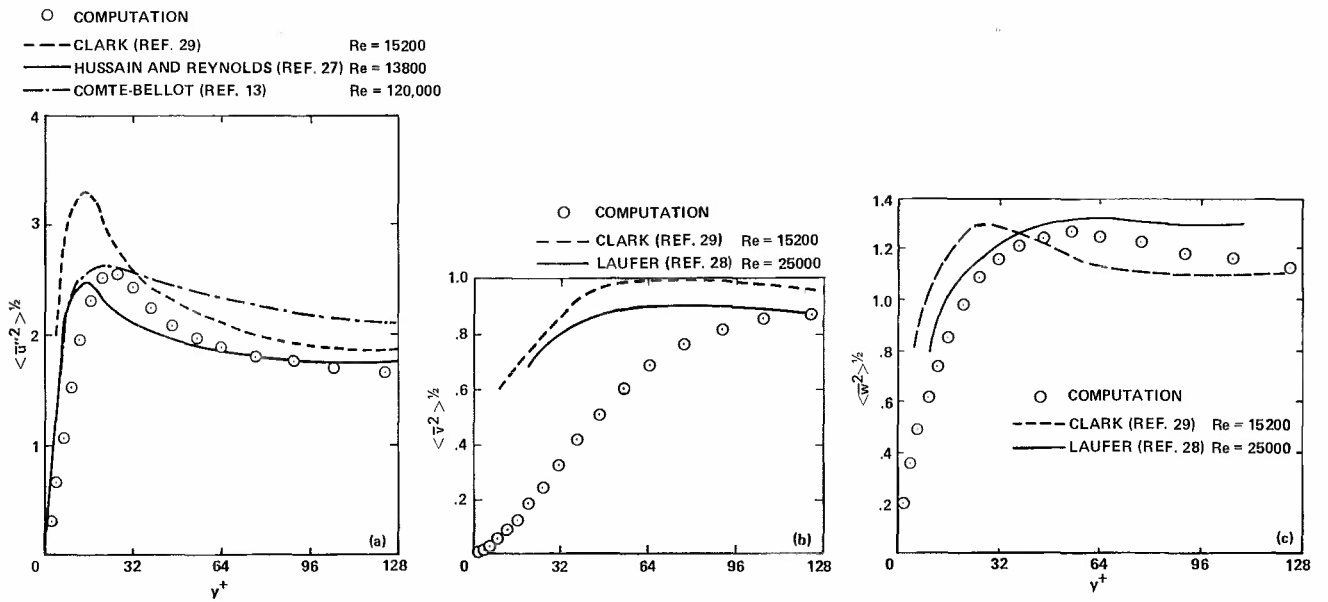


Fig. 20. Comparison of the horizontally averaged resolvable turbulence intensities with experimental data.

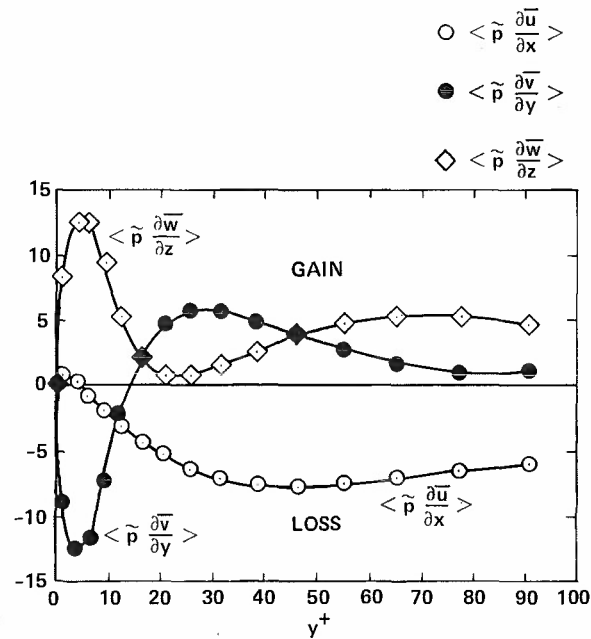


Fig. 21. Vertical profiles of horizontally averaged resolvable pressure velocity gradient correlations in the vicinity of the wall ( $y^+ \leq 100$ ).

# A TURBULENCE CLOSURE OF THE TRANSPORT EQUATION FOR THE PROBABILITY DENSITY OF VELOCITY

by

M. M. RIBEIRO  
Ph.D, Prof. Aux.  
CTAMFUL - DTA, Pav. Máquinas  
Instituto Superior Técnico  
1096 Lisboa Codex, Portugal

This paper presents a proposal for a first-order closure of the hierarchy of transport equations for the probability density of velocity in a turbulent field. The fluid is assumed to be incompressible and Newtonian. The effects of the pressure deviations on the probability density are modelled based on the assumption of homogeneous behaviour of the flow field. The closure is shown to be compatible with a well-known Reynolds stresses closure. Particular attention is given to the physical implications of the assumptions embodied in the modelling of the unknown terms that occur in the exact equation.

## 1. Introduction

A transport equation for the probability density of velocity may be obtained for the flow field of an incompressible Newtonian fluid. This is done by Lundgren /1/ and Monin /2/, who start by eliminating the pressure from the Navier-Stokes equations through the use of continuity and the Poisson equation for pressure. This is followed by the use of the definition of a probability density of velocity as an ensemble average of the instantaneous probability density of velocity,  $\delta(\underline{u}(\underline{x},t) - \underline{v})$ , which is zero everywhere except at  $\underline{v} = \underline{u}(\underline{x},t)$ ;  $\underline{u}(\underline{x},t)$  is the value of velocity at location  $\underline{x}$  and time  $t$ , and  $\underline{v}$  is the coordinate in velocity space.

Further examination of the probability density equation can assist understanding of turbulent flow and also lead to improved methods of representing turbulent flows. Thus the present paper proposes a closure for the one point probability density equation and demonstrates that it is compatible and more general than a recently proposed Reynolds stress closure. The advantages of this new closure are made clear, and the implications that the return of isotropy, in the absence of mean velocity gradient, stems from anisotropic dissipation, rather than energy exchanges at lower wave numbers, are argued and justified.

The equation for the transport of probability density of velocity reads:

$$\begin{aligned} \frac{\partial f(\underline{v}, \underline{x}, t)}{\partial t} + v_j \frac{\partial f(\underline{v}, \underline{x}, t)}{\partial x_j} = \\ = \frac{1}{4\pi} \frac{\partial}{\partial v_i} \left\{ \int_{\underline{x}', \underline{v}'} \left[ \frac{\partial}{\partial x_i} \frac{1}{|\underline{x}' - \underline{x}|} \right] \frac{\partial}{\partial x'_m} \frac{\partial}{\partial x'_n} (v'_m v'_n f(\underline{v}, \underline{x}, \underline{v}', \underline{x}', t)) d\underline{x}' d\underline{v}' \right\} - \\ - v \frac{\partial}{\partial v_i} \left[ \lim_{|\underline{x}' - \underline{x}| \rightarrow 0} \frac{\partial}{\partial x_j^2} \int_{\underline{v}'} v'_i f(\underline{v}, \underline{x}, \underline{v}', \underline{x}', t) d\underline{v}' \right] \end{aligned} \quad (1)$$

In the above equation,  $f(\underline{v}, \underline{x}, t)$  represents the probability density of occurrence of velocity  $\underline{v}$  at location  $\underline{x}$  and time  $t$ ;  $f(\underline{v}, \underline{x}, \underline{v}', \underline{x}', t)$  represents the probability density of simultaneous occurrence of velocities  $\underline{v}$  and  $\underline{v}'$  at locations  $\underline{x}$  and  $\underline{x}'$  respectively.

Eq.(1) represents the conditions implied by continuity and Navier-Stokes equations over the one-point probability density of velocity. The first term on the LHS represents the time dependence of the one-point probability density; for a steady flow (in the sense that the statistical properties are not time-dependent), it will be zero. The second term on the LHS is a result of a convective term in the Navier-Stokes equations, where the velocity appears substituted by the independent variable  $\underline{v}$ . The first term on the RHS represents the influence of the pressure field over the one-point probability density of velocity; it involves the two-point density function, therefore the pressure links the local behaviour with a finite region surrounding the point. The second term on the RHS represents the effect of the viscous field; its influence is determined by the behaviour of the two-point joint probability density,  $f(\underline{v}, \underline{x}, \underline{v}', \underline{x}', t)$  in the immediate neighbourhood of the point.

The equation involves two unknowns:  $f(\underline{v}, \underline{x}, t)$  and  $f(\underline{v}, \underline{x}, \underline{v}', \underline{x}', t)$ ; there is one more unknown than the number of equations. An equation for  $f(\underline{v}, \underline{x}, \underline{v}', \underline{x}', t)$  is therefore necessary, and it can be derived in a similar way as for  $f(\underline{v}, \underline{x}, t)$  (see Lundgren /1/). However, this equation will introduce the three-point joint probability density of velocity



through the pressure and viscous terms, and no matter how many transport equations are written, each equation will introduce a new unknown. The set is, therefore, not closed.

Some of the properties of the probability density functions, which will be used in the subsequent text, are listed below; their derivation can be found in Lundgren /1/.

a) Reduction property

$$\int_{\underline{v}} f(\underline{v}, \underline{x}, t) d\underline{v} = 1 \quad (2)$$

$$\int_{\underline{v}'} f(\underline{v}, \underline{x}, \underline{v}', \underline{x}'; t) d\underline{v}' = f(\underline{v}, \underline{x}, t) \quad (3)$$

b) Separation property

$$\lim_{|\underline{x}' - \underline{x}| \rightarrow \infty} f(\underline{v}, \underline{x}, \underline{v}', \underline{x}'; t) = f(\underline{v}, \underline{x}, t) \times f(\underline{v}', \underline{x}', t) \quad (4)$$

c) Coincidence property

$$\lim_{|\underline{x}' - \underline{x}| \rightarrow 0} f(\underline{v}, \underline{x}, \underline{v}', \underline{x}'; t) = f(\underline{v}, \underline{x}, t) \times \delta(\underline{v}' - \underline{v}) \quad (5)$$

The quantity  $\delta(\underline{v}' - \underline{v})$  is the three-dimensional Dirac delta function defined as:

$$\delta(\underline{v}' - \underline{v}) = 0 \quad \text{for } \underline{v}' \neq \underline{v}$$

$$\int_{\underline{v}'} F(\underline{v}') \times \delta(\underline{v}' - \underline{v}) d\underline{v}' = F(\underline{v})$$

d) Divergence property

For an incompressible fluid, it is:

$$\frac{\partial}{\partial x_i} \int_{\underline{v}} v_i f(\underline{v}, \underline{x}, t) d\underline{v} = 0 \quad (6)$$

and

$$\frac{\partial}{\partial x_i} \int_{\underline{v}} v_i f(\underline{v}, \underline{x}, \underline{v}', \underline{x}'; t) d\underline{v} = 0 \quad (7)$$

The first three properties are formal, and the last is a result implied by the continuity equation.

## 2. A proposal for a closure on the transport equation for the one-point probability density of velocity

The relative spread and success of one-point closures, together with the tendency to bring the level of closure to higher orders, suggests that a one-point closure on the transport equation for the probability density of velocity should be attempted. Such a closure will contain any closure based on the one-point velocity correlations. Alternatively it allows a different type of approach to solving the equations for the time-averaged one-point correlations: the one-point probability density of velocity can be represented to any order of its moments ( $\equiv$  velocity correlations) by its Gram-Charlier approximation and this allows that an equation in velocity space can be transformed into a number of transport equations for the coefficients of the approximation.

Eq.(1) can be rewritten in the form:

$$\begin{aligned}
& \frac{\partial f(\underline{v}, \underline{x}, t)}{\partial t} + v_j \frac{\partial f(\underline{v}, \underline{x}, t)}{\partial x_j} = \\
& = \frac{1}{4\pi} \frac{\partial}{\partial v_i} \left\{ \int \underline{x}' \left[ \frac{\partial}{\partial x_i} \frac{1}{|\underline{x}' - \underline{x}|} \right] \frac{\partial}{\partial x'_m} \frac{\partial}{\partial x'_n} \left[ \int \underline{v}' v'_m v'_n f(\underline{v}, \underline{x}, \underline{v}', \underline{x}', t) d\underline{v}' \quad d\underline{x}' \right] \right\} \\
& - \frac{\partial}{\partial v_i} \left[ \lim_{|\underline{x}' - \underline{x}| \rightarrow 0} \frac{\partial^2}{\partial x_j^2} \int \underline{v}'_i f(\underline{v}, \underline{x}, \underline{v}', \underline{x}', t) d\underline{v}' \right]
\end{aligned} \quad (8)$$

The analysis of the above equation shows that the two-point probability function only appears in integral forms of the type:

$$I_n = \int \underline{v}'_n f(\underline{v}, \underline{x}, \underline{v}', \underline{x}', t) d\underline{v}' \quad (9)$$

$$J_{mn} = \int \underline{v}'_m \underline{v}'_n f(\underline{v}, \underline{x}, \underline{v}', \underline{x}', t) d\underline{v}' \quad (10)$$

Since a one-point closure is to be used, these two integrals will be assumed to be locally determined, i.e., their local values are supposed not to be affected by their own transport. This will always be the case for homogeneous flow fields. In the present modelling, this assumption will be retained: the flow field is assumed to be homogeneous in a region where the integrals (9) and (10) affect the transport Eq.(8). Homogeneity is intended here to imply a linear behaviour for the mean velocities and a zero gradient for all the one-point velocity correlations. The existence of a unique relationship between the characteristic function and the probability density (see, for example, Ribeiro /3/), implies that the one-point probability density of the fluctuating velocity is, under this hypothesis, independent on  $\underline{x}$ . For the two-point joint density of fluctuating velocity, it reduces the spatial dependence to the separation vector  $\underline{r} \equiv \underline{x}' - \underline{x}$ . Another immediate implication of homogeneity is that the two-point probability density of the fluctuating velocity has reflexional symmetry:

$$f(\underline{v}^*, \underline{v}'^*, \underline{r}) = f(\underline{v}^*, \underline{v}'^*, -\underline{r}) \quad (11)$$

where  $\underline{v}^* \equiv \underline{v} - \underline{\bar{U}}$ , and  $\underline{\bar{U}}$  is the mean velocity vector, defined as  $\underline{\bar{U}}_i = \int \underline{v}_i f(\underline{v}, \underline{x}) d\underline{v}$

In the remainder of this section, a closure based on a multilinear form for the unknown quantities is presented. The implications of homogeneity are examined with respect to the pressure and viscous terms, followed by an analysis of the restrictions imposed by the same condition on the applicability of the model in 2.1. In 2.2 a multilinear relationship of known local quantities, linked with the unknown quantities, is formulated; this relationship is then made to satisfy the boundary conditions, continuity and homogeneity. The resulting expression is input to the pressure and viscous terms, yielding their final modelled forms. This is followed by a physical interpretation of the results which includes the version of the model for the Reynolds stress transport equations.

## 2.1 Implications and validity of the homogeneity assumption

In order to examine the implications of the homogeneity over the pressure and viscous contributions to the transport of the probability density of velocity, it is convenient to express these contributions (on the RHS of Eq.(8)) in terms of the joint probability density of fluctuating velocity at locations  $\underline{x}$  and  $\underline{x}'$ ,  $f(\underline{v}^*, \underline{v}'^*)$ .

The following identities will be used:

$$\begin{aligned}
i) \quad & \frac{\partial}{\partial v_i} \int \underline{v}'_m \underline{v}'_n f(\underline{v}, \underline{x}, \underline{v}', \underline{x}') d\underline{v}' = \frac{\partial}{\partial v_i^*} \int \underline{v}'_m^* + \underline{\bar{U}}'_m (\underline{v}'_n^* + \underline{\bar{U}}'_n) f(\underline{v}^*, \underline{v}'^*) d\underline{v}'^* \\
& = \underline{\bar{U}}'_m \underline{\bar{U}}'_n \frac{\partial f(\underline{v}^*)}{\partial v_i^*} + \underline{\bar{U}}'_m \frac{\partial}{\partial v_i^*} \int \underline{v}'_n^* f(\underline{v}^*, \underline{v}'^*) d\underline{v}'^* + \\
& + \underline{\bar{U}}'_n \frac{\partial}{\partial v_i^*} \int \underline{v}'_m^* f(\underline{v}^*, \underline{v}'^*) d\underline{v}'^* + \frac{\partial}{\partial v_i^*} \int \underline{v}'_m^* \underline{v}'_n^* f(\underline{v}^*, \underline{v}'^*) d\underline{v}'^*
\end{aligned} \quad (12)$$

$$\text{ii) } \frac{\partial}{\partial v_i} \int \underline{v}'_i f(\underline{v}, \underline{x}, \underline{v}', \underline{x}') d\underline{v}' = \overline{U}'_i \frac{\partial f(\underline{v}^*)}{\partial v_i^*} + \frac{\partial}{\partial v_i^*} \int \underline{v}'_i^* f(\underline{v}^*, \underline{v}'^*) d\underline{v}'^* \quad (13)$$

$$\text{iii) } \frac{\partial f(\underline{v}^*)}{\partial v_i^*} = \frac{\partial f(\underline{v})}{\partial v_i} \quad (14)$$

In addition, the contribution by the pressure forces will be split into the contribution by the mean and fluctuating pressure. It may be noticed that the mean pressure,  $\overline{P}$ , is related to the spatial distribution of mean velocity and Reynolds stresses through the following equation (e.g., Townsend /8/, p.43+44):

$$\text{iv) } \overline{P}(\underline{x}) = \frac{1}{4\pi} \int \frac{1}{|\underline{x}' - \underline{x}|} \left[ \frac{\partial \overline{U}'_m}{\partial x'_n} \frac{\partial \overline{U}'_n}{\partial x'_m} + \frac{\partial^2 \overline{U}'_m \overline{U}'_n}{\partial x'_m \partial x'_n} \right] d\underline{x}' \quad (15)$$

The preceeding four relationships are next used to analyse the implications of homogeneity on the generality of the unknown terms appearing in Eq.(8).

### 2.1.1 The viscous contribution

The contribution of the viscous forces is represented by the second term on the RHS of Eq.(8). This term will be referred to as  $T_v$ . The use of relations (13) and (14) yields:

$$\begin{aligned} T_v = & - \nu \frac{\partial}{\partial v_n^*} \left[ \lim_{\underline{r} \rightarrow 0} \frac{\partial^2}{\partial r_m^2} \int \underline{v}'_n^* f(\underline{v}^*, \underline{v}'^*, \underline{r}) d\underline{v}'^* \right] - \\ & - \nu \frac{\partial^2 \overline{U}'_n}{\partial x_m^2} \frac{\partial f(\underline{v}^*)}{\partial v_n^*} \end{aligned} \quad (16)$$

The assumption of homogeneity does not restrict the generality of this term, since it only depends on the immediate neighbourhood of  $\underline{x}$ . Obviously, the quantity

$$- \nu \frac{\partial^2 \overline{U}'_n}{\partial x_m^2} \frac{\partial f(\underline{v}^*)}{\partial v_n^*}$$

appearing on the RHS of relationship (16), is zero in a homogeneous flow. It represents the effect of mean viscous diffusion; its contribution to the transport of probability density is negligible, except in cases of severe curvature of mean velocity profiles. Since the mean viscous diffusion does not introduce any further unknowns, and therefore it does not need to be modelled, this term will be retained in the final modelled form of the transport equation.

### 2.1.2 The pressure contribution

The contribution of the pressure forces is represented by the first term on the RHS of Eq.(8). This term will be referred to as  $T_p$ . Using relations (12) and (14),  $T_p$  may be rewritten as:

$$\begin{aligned} T_p = & \frac{1}{4\pi} \frac{\partial}{\partial v_k^*} \left\{ \int \underline{X}' \left[ \frac{\partial}{\partial x_k} \frac{1}{|\underline{x}' - \underline{x}|} \right] \frac{\partial \overline{U}'_m}{\partial x'_n} \frac{\partial \overline{U}'_n}{\partial x'_m} f(\underline{v}^*) d\underline{x}' + \right. \\ & + 2 \int \underline{X}' \left[ \frac{\partial}{\partial x_k} \frac{1}{|\underline{x}' - \underline{x}|} \right] \frac{\partial \overline{U}'_m}{\partial x'_n} \frac{\partial}{\partial x'_m} \left[ \int \underline{v}'_n^* f(\underline{v}^*, \underline{v}'^*) d\underline{v}'^* \right] d\underline{x}' + \\ & \left. + \int \underline{X}' \left[ \frac{\partial}{\partial x_k} \frac{1}{|\underline{x}' - \underline{x}|} \right] \frac{\partial^2}{\partial x'_m \partial x'_n} \left[ \int \underline{v}'_m^* \underline{v}'_n^* f(\underline{v}^*, \underline{v}'^*) d\underline{v}'^* \right] d\underline{x}' \right\} \end{aligned} \quad (17)$$

Relation (15) may be used in order to separate the contributions by the mean and fluctuating pressures:

$$\begin{aligned}
 T_P = & \frac{1}{4\pi} \frac{\partial}{\partial v_K^*} \left\{ \int_{\underline{x}'} \left[ \frac{\partial}{\partial x_K} \frac{1}{|\underline{x}' - \underline{x}|} \right] \left[ \frac{\partial \bar{u}_m}{\partial x_n'} \frac{\partial \bar{u}_n'}{\partial x_m'} + \frac{\partial^2 \bar{u}_m \bar{u}_n'}{\partial x_n' \partial x_m'} \right] f(\underline{v}^*) d\underline{x}' + \right. \\
 & + 2 \int_{\underline{x}'} \left[ \frac{\partial}{\partial x_K} \frac{1}{|\underline{x}' - \underline{x}|} \right] \left[ \frac{\partial \bar{u}_m}{\partial x_n'} \frac{\partial}{\partial x_m'} \left( \int_{\underline{v}^*} v_n'^* f(\underline{v}^*, \underline{v}'^*) d\underline{v}'^* \right) \right] d\underline{x}' + \\
 & \left. + \int_{\underline{x}'} \left[ \frac{\partial}{\partial x_K} \frac{1}{|\underline{x}' - \underline{x}|} \right] \frac{\partial^2}{\partial x_m' \partial x_n'} \int_{\underline{v}^*} (v_m'^* v_n'^* - \bar{u}_m \bar{u}_n') f(\underline{v}^*, \underline{v}'^*) d\underline{v}'^* d\underline{x}' \right\} \quad (18)
 \end{aligned}$$

i) The first term on the RHS of this equation will be referred to as  $T_{p1}$  and is exactly:

$$T_{p1} = - \frac{\partial f(\underline{v}^*)}{\partial v_K^*} \frac{1}{\rho} \frac{\partial \bar{P}}{\partial x_K} = - \frac{\partial f(\underline{v})}{\partial v_K} \frac{1}{\rho} \frac{\partial \bar{P}}{\partial x_K} \quad (19)$$

Again, for homogeneous flow, there is no contribution to the mean pressure by the spatial distribution of Reynolds stresses. However, since the mean pressure does not introduce further unknowns, the quantity (19) will be retained in the final modelled form of the transport equation. In any case the contribution to the mean pressure of the second derivatives of the Reynolds stresses is much smaller than that of the derivatives of the mean velocity distribution.

ii) The last term on the RHS, that is referred to as  $T_{p3}$ , can be shown, under homogeneity, to be identically zero: homogeneity allows the dependence on  $\underline{x}$  or  $\underline{x}'$  to be expressed in terms of  $\underline{r} \equiv \underline{x}' - \underline{x}$ ; this yields:

$$T_{p3} = \frac{1}{4\pi} \frac{\partial}{\partial v_K^*} \left\{ \int_{\underline{R}} \frac{r_K}{r^3} \frac{\partial^2}{\partial r_m \partial r_n} \left[ \int_{\underline{v}^*} (v_m'^* v_n'^* - \bar{u}_m \bar{u}_n') f(\underline{v}^*, \underline{v}'^*) d\underline{v}'^* \right] d\underline{r} \right\} \quad (20)$$

Due to the reflexional property of  $f(\underline{v}^*, \underline{v}'^*)$ , the integral over  $\underline{v}'^*$  space is symmetric around  $\underline{r}$ , and so is its second derivative,  $\partial^2 / \partial r_m \partial r_n$ . Then the integrand of  $T_{p3}$  becomes the product of a symmetric and an antisymmetric function ( $r_K / r^3$ ), which is antisymmetric; the integral over  $\underline{R}$  is therefore zero.

It can be objected that the quantity

$$\frac{\partial^2}{\partial r_m \partial r_n} (\bar{u}_m \bar{u}_n'),$$

which gives no contribution in homogeneous flow, is kept inside the integrand in Eq.(20). This quantity is left there in order to emphasize that no contribution of  $T_{p3}$  is associated to the deviation of the value  $v_m'^* v_n'^*$  around its mean, rather than around zero.

iii) There remains the second term,  $T_{p2}$ , that under homogeneity becomes:

$$T_{p2} = \frac{1}{2\pi} \frac{\partial \bar{u}_m}{\partial x_n} \frac{\partial}{\partial v_K^*} \left\{ \int_{\underline{R}} \frac{r_K}{r^3} \frac{\partial}{\partial r_m} \left[ \int_{\underline{v}^*} v_n'^* f(\underline{v}^*, \underline{v}'^*) d\underline{v}'^* \right] d\underline{r} \right\} \quad (21)$$

The unknown quantity is the derivative of the integral over  $\underline{v}'^*$  of a function that involves the two-point distribution. However, by virtue of the separation and coincidence properties of the probability density, the integral over  $\underline{v}'^*$  satisfy the following conditions:

$$\int_{\underline{v}^*} v_n'^* f(\underline{v}^*, \underline{v}'^*) d\underline{v}'^* = v_n^* f(\underline{v}^*) \quad \text{for } r = 0 \quad (22)$$

$$= \bar{u}_n' f(\underline{v}^*) = 0 \quad \text{for } r = \infty \quad (23)$$

In physical terms, this quantity tends to zero with the inverse of the distance between the two points  $\underline{x}$  and  $\underline{x}'$ , at a rate that is dependent on the size of the macro-length scale associated with the two-point velocity correlations. As in Eq.(21) only its spatial derivative is used, and as it is expected a monotonic behaviour for the integral over  $\underline{v}'^*$  on  $R$ , the integrand of Eq.(21) must tend to zero at a faster rate than the RHS of Eq.(23). Therefore, the validity of homogeneity assumption is dependent on the size of the region where the spatial rate of variation of the two-point velocity correlations affects the value of Eq.(21). In flow regions remote from solid boundaries it is expected that the assumption is not too restrictive.

## 2.2 Proposal for the closure model

The analysis of the unknown viscous and pressure contributions (Eq. (16) and (21)) to the transport equation for the probability density shows the need to relate the quantity  $Q_n$ , defined as:

$$Q_n = \int_{\underline{v}^*} \underline{v}_n'^* f(\underline{v}^*, \underline{v}'^*) d\underline{v}'^* , \quad (24)$$

with the known local properties of the flow field.  $Q_n$  is obviously a function of  $\underline{r} \equiv \underline{x}' - \underline{x}$ ; and, as Eq.(22) and (23) indicate, it is also expected to depend on  $\underline{v}^*$  and  $f(\underline{v}^*)$ . Another quantity that is expected to influence the value of  $Q_n$  is the gradient of  $f(\underline{v}^*)$  in velocity space: a one-point distribution with a very narrow spread (high  $\underline{v}$ -gradient) is associated with a high rate of spatial variation of the quantity  $Q_n$ . Based on these dependencies, a tensorial expression satisfying the dimensionality of  $Q_n$  can be written:

$$Q_n = \alpha_{n\ell} \underline{v}_\ell^* f(\underline{v}^*) + \beta_{npqr} \underline{v}_q^* \underline{v}_r^* \frac{\partial f(\underline{v}^*)}{\partial \underline{v}_p^*} \quad (25)$$

In this equation,  $\alpha_{n\ell}$  and  $\beta_{npqr}$  are only functions of the separation vector  $\underline{r}$ ; furthermore, the interchangeability of  $q$  and  $r$  implies that  $\beta_{npqr} = \beta_{nprq}$ . This yields the following general form for the two tensors:

$$\alpha_{n\ell} = \frac{A_1}{r^2} r_n r_\ell + A_2 \delta_{n\ell} \quad (26)$$

and:

$$\begin{aligned} \beta_{npqr} = & \frac{A_3}{r^4} r_n r_p r_q r_r + \frac{A_4}{r^2} r_n r_p \delta_{qr} + \frac{A_5}{r^2} r_q r_r \delta_{np} + \\ & + \frac{A_6}{r^2} (r_p r_q \delta_{nr} + r_p r_r \delta_{nq}) + \frac{A_7}{r^2} (r_n r_q \delta_{pr} + r_n r_r \delta_{pq}) + \\ & + A_8 (\delta_{nr} \delta_{pq} + \delta_{nq} \delta_{pr}) + A_9 \delta_{np} \delta_{qr} , \end{aligned} \quad (27)$$

where the coefficients  $A_i$  are even functions of  $r \equiv |\underline{r}|$ . Relations (25), (26) and (27) define the general form of the model, and, so far have not been subjected to the physical constraints. This is done next:

i) Boundary conditions. These are expressed through the coincidence and separation properties of  $Q_n$ :

$$A_2 = 1; \quad A_i = 0 \quad \text{for } r = 0 \text{ and } i \neq 2 \quad (28)$$

$$A_i = 0 \quad \text{for } r \rightarrow \infty \quad (29)$$

Furthermore, as the  $A_i$ 's are even functions of  $r$ , all their odd derivatives at the origin will be zero; in particular:

$$\frac{dA_i}{dr} = 0 \quad \text{for } r = 0 \quad (30)$$

At infinity, the separation property also ensures that all the derivatives are zero:

$$\frac{d^n A_i}{dr^n} = 0 \quad \text{for } r \rightarrow \infty \text{ and for any integer } n \quad (31)$$

ii) Continuity. This condition can be applied to  $Q_n$  under the form of Eq.(7). After differentiation of Eq.(25) with respect to  $r_n$ , followed by the condition that the result is independent of the values of  $\underline{r}, \underline{v}^*, f(\underline{v}^*)$  or  $\partial f(\underline{v}^*)/\partial v_p^*$ , the following set of relations between the  $A_i$ 's emerges:

$$\begin{aligned} \frac{d}{dr} (A_1 + A_2) &= -2 \frac{A_1}{r}; \quad \frac{d}{dr} (-A_3 + A_5 + 2A_6) = \frac{2}{r} (-A_3 + A_5 - 2A_6) \\ \frac{d}{dr} (A_7 + A_8) &= -\frac{1}{r} (A_5 + A_6 + 2A_7); \quad \frac{d}{dr} (A_4 + A_9) = -\frac{2}{r} (A_4 + A_6) \end{aligned} \quad (32)$$

iii) Homogeneity. This condition is introduced through its implication over the two-point velocity correlation tensor,  $R_{ij}$ ; under this assumption:

$$R_{ij} \equiv \overline{u_i u_j(\underline{r})} = \overline{u_i(-\underline{r}) u_j} = \overline{u_i(\underline{r}) u_j} = R_{ji}$$

Using the identity:

$$R_{ij} \equiv \int_{\underline{v}^*} v_i^* Q_j d\underline{v}^*$$

to express the above results in terms of  $Q$  and substituting  $Q$  by its modelled form, the following relation between the  $A_i$ 's emerges:

$$A_1 = 2(A_3 + A_4 + A_5 + 5A_7) \quad (33)$$

Eqs.(28) to (33) represent the constraints to be satisfied by the coefficients  $A_i$  in order to obey coincidence, separation, continuity and homogeneity. These equations will be used in the algebraic manipulation as a means to obtain the final reduced forms of the pressure and viscous terms.

### 2.3 The pressure term

The modelled form of the pressure term can now be obtained; when the integral over  $\underline{v}^*$  in Eq. (21) is substituted by its approximation, represented by Eq. (25), the pressure influence becomes:

$$T_{p2} = \frac{1}{2\pi} \frac{\partial \bar{u}_m}{\partial x_n} \frac{\partial}{\partial v_n^*} \left[ f(\underline{v}^*) v_k^* \int_{\underline{R}} \frac{r_k}{r^3} \frac{\partial \alpha_{n\ell}}{\partial r_m} d\underline{r} + \frac{\partial f(\underline{v}^*)}{\partial v_p^*} v_q^* v_r^* \int_{\underline{R}} \frac{r_k}{r^3} \frac{\partial \beta_{npqr}}{\partial r_m} d\underline{r} \right] \quad (34)$$

Substitution of the tensors  $\alpha_{n\ell}$  and  $\beta_{npqr}$  by their expressions (26) and (27) followed by the use of the conditions implied by separation, coincidence, continuity and homogeneity yields:

$$\begin{aligned} T_{p2} &= \frac{\partial \bar{u}_m}{\partial x_n} \left\{ v_k^* v_k^* \frac{\partial^2 f(\underline{v}^*)}{\partial v_m^* \partial v_n^*} \left[ -\frac{24}{35} \int_{\underline{R}} \frac{A_3}{r} dr - \frac{1}{5} \right] + \right. \\ &\quad + v_k^* v_m^* \frac{\partial^2 f(\underline{v}^*)}{\partial v_k^* \partial v_n^*} \left[ \frac{64}{35} \int_{\underline{R}} \frac{A_3}{r} dr + \frac{3}{5} \right] + \\ &\quad + v_k^* v_n^* \frac{\partial^2 f(\underline{v}^*)}{\partial v_k^* \partial v_m^*} \left[ \frac{8}{35} \int_{\underline{R}} \frac{A_3}{r} dr \right] + \\ &\quad + v_m^* v_n^* \frac{\partial^2 f(\underline{v}^*)}{\partial v_k^* \partial v_k^*} \left[ -\frac{24}{35} \int_{\underline{R}} \frac{A_3}{r} dr - \frac{2}{5} \right] + \\ &\quad \left. + v_m^* \frac{\partial f(\underline{v}^*)}{\partial v_n^*} \left[ \frac{224}{35} \int_{\underline{R}} \frac{A_3}{r} dr + 2 \right] + v_n^* \frac{\partial f(\underline{v}^*)}{\partial v_m^*} \left[ -\frac{56}{35} \int_{\underline{R}} \frac{A_3}{r} dr - 2 \right] \right\} \end{aligned} \quad (35)$$

Eq.(35) represents the modelled form of the pressure term. The equation shows only one parameter, that is associated with a macro-length scale that characterizes the size of the spatial region where the velocities are correlated; the parameter is, therefore, expected to be associated with the low wave-number region of the spectrum of energy of the velocity fluctuations. For simplicity of notation, the parameter will be represented henceforward by  $C_2$ :

$$C_2 \equiv \frac{1}{35} \int_R \frac{\Lambda^3}{r} dr \quad (36)$$

It is appropriate, now, to derive the equivalent form of the result expressed through Eq.(35) for the transport equation of Reynolds stress tensor; this can be obtained by multiplying Eq.(35) by  $v_i^* v_j^*$  and integrating over  $\underline{V}$ :

$$\begin{aligned} \int_{\underline{V}} v_i^* v_j^* T_{p2} d\underline{v} = & \overline{u_\kappa u_\kappa} \left( \frac{\partial \overline{u}_i}{\partial x_j} + \frac{\partial \overline{u}_j}{\partial x_i} \right) \left( -24C_2 - \frac{1}{5} \right) + \\ & + \left( \overline{u_i u_\kappa} \frac{\partial \overline{u}}{\partial x_j} + \overline{u_j u_\kappa} \frac{\partial \overline{u}_\kappa}{\partial x_i} - \frac{2}{3} \overline{u_\kappa u_\ell} \frac{\partial \overline{u}_\kappa}{\partial x_\ell} \delta_{ij} \right) \left( 64C_2 + \frac{2}{5} \right) + \\ & + \left( \overline{u_i u_\kappa} \frac{\partial \overline{u}_j}{\partial x_\kappa} + \overline{u_j u_\kappa} \frac{\partial \overline{u}_i}{\partial x_\kappa} - \frac{2}{3} \overline{u_\kappa u_\ell} \frac{\partial \overline{u}_\kappa}{\partial x_\ell} \delta_{ij} \right) \left( 8C_2 + \frac{4}{5} \right) \end{aligned} \quad (37)$$

This equation contracts to zero and therefore its effect is purely redistributive of energy between the different components of the Reynolds stress tensor. It has the same form as proposed by Launder, Reece and Rodi /4/ and Naot, Shavit and Wolfshtein /5/. This should come as no surprise, bearing in mind that the basic assumptions in the modelling of this term are common to all these works, viz., the homogeneity of the flow field and a multilinear form for the model.

A difference between the present result and that of Launder, Reece and Rodi /4/ is that the part of the Reynolds stress redistribution attributed by Rotta /6/, solely to the turbulent interactions via the pressure term does not occur in the present situation. Since it is a widely held view that the return to isotropy which occurs in homogeneous flows in the absence of mean velocity gradients is due to turbulent interactions at wave numbers lower than those at which significant viscous dissipation occurs, it seems worthwhile to proceed this subject a little further. The convenient quantity to look at is the density of contributions (in wave number space) to the Reynolds stress tensor, known as energy tensor (cf. Batchelor /7/, p.26), and represented by  $\Phi_{ij}(\underline{\kappa})$ ; in an homogeneous flow, in the absence of mean velocity gradients,  $\Phi_{ij}$  satisfies the following relationship (Batchelor /7/, p.86):

$$\frac{\partial \Phi_{ij}(\underline{\kappa})}{\partial t} = \Gamma_{ij}(\underline{\kappa}) + \Pi_{ij}(\underline{\kappa}) - 2\nu \kappa_m \kappa_m \Phi_{ij}(\underline{\kappa}) \quad (38)$$

$\Gamma_{ij}$  and  $\Pi_{ij}$  represent the contributions to  $\Phi_{ij}$  by inertia and pressure forces;  $\nu$  is the kinematic viscosity,  $\underline{\kappa}$  is the wave number vector and  $t$  is time. It can be shown (Batchelor /7/, p.90) that  $\Gamma_{ij}$  and  $\Pi_{ij}$  must satisfy the following relationship:

$$\kappa_m \kappa_m \Pi_{ij} = -\kappa_\ell \left[ \kappa_i \Gamma_{\ell j} + \kappa_j \Gamma_{i \ell} \right] \quad (39)$$

In the inertial subrange,  $\underline{\kappa}$  is finite and  $\Gamma_{\ell j}$  is zero, therefore  $\Pi_{ij}$  is zero. Since it is difficult to imagine a physical mechanism involving only eddy interactions which is exclusive of the lower end of the wave number space, it is plausible to expect that there is no significant redistribution driven solely by eddy interactions. The weak tendency towards isotropy exhibited in the measurements of Comte-Bellot and Corrsin quoted by Townsend (/8/, p.67÷68), may be explained by a non-isotropic dissipation; in section 2.4, this subject will be discussed.

#### 2.4 The viscous term

When the unknown part of the viscous contribution (Eq.(16)) is expressed in terms of the model, Eq.(25), the following result emerges:

$$T_{v2} = -\nu \frac{\partial}{\partial v_n^*} \left\{ v_\ell^* f(\underline{v}^*) \lim_{|\underline{r}| \rightarrow 0} \frac{\partial^2 \alpha_{n\ell}}{\partial r_j^2} + v_q^* v_r^* \frac{\partial f(\underline{v}^*)}{\partial v_p^*} \lim_{|\underline{r}| \rightarrow 0} \frac{\partial^2 \beta_{npqr}}{\partial r_j^2} \right\} \quad (40)$$

After calculation of the derivatives of the two tensors,  $\alpha_{nl}$  and  $\beta_{npqr}$ , Eq. (40) can be reduced through the use of the conditions implied by separation, coincidence, continuity and homogeneity to yield:

$$\begin{aligned} T_{v2} = & 10 \nu (A_4'' + A_5'' + 5A_7'') \frac{\partial}{\partial v_K^*} \left( v_K^* f(\underline{v}^*) \right) + \\ & + \nu (5A_4'' - A_5'' + 3A_6'') \frac{\partial}{\partial v_K^*} \left( v_j^* v_j^* \frac{\partial f(\underline{v}^*)}{\partial v_K^*} \right) + \\ & + \nu (3A_5'' + A_6'' + 10A_7'') \frac{\partial}{\partial v_K^*} \left( v_j^* v_K^* \frac{\partial f(\underline{v}^*)}{\partial v_j^*} \right) \end{aligned} \quad (41)$$

where, for simplicity of notation:

$$A_i'' \equiv \lim_{r \rightarrow 0} \frac{d^2 A_i}{dr^2} \quad (42)$$

Eq.(41) shows the occurrence of three parameters, expressed as linear combinations of the second derivatives of the  $A_i$ 's at the origin.

The physical interpretation of the result expressed in Eq.(41) is considered next, by recurrence to its form in the transport equation for the Reynolds stress tensor. When that equation is multiplied by  $v_i^* v_j^*$  and integrated over the velocity space, it yields the following contribution, due to the viscous forces, in the transport equation for the Reynolds stress tensor:

$$\begin{aligned} \int_{\underline{v}} v_i^* v_j^* T_{v2} d\underline{v} = & \nu (6A_5'' + 22A_6'') (\overline{u_i u_j} - \frac{1}{3} \overline{u_K u_K} \delta_{ij}) + \\ & + \nu (30A_4'' + 40A_6'') \frac{1}{3} \overline{u_K u_K} \delta_{ij} \end{aligned} \quad (43)$$

The first term on the RHS of Eq.(43) contracts to zero: therefore the term redistributes energy between the components of the Reynolds stress tensor without altering the total level of energy. It will be shown next that the second term on the RHS of Eq.(43) represents the dissipation of the stress if the field were isotropic. This will be achieved through the use of some standard results of the theory of isotropic turbulence: In this theory, it is a well known result (e.g. Panchev, /9/) that there is a relationship between the viscous dissipation of turbulent kinetic energy,  $\epsilon$ , and the Taylor microscale,  $\lambda$ :

$$\epsilon = \frac{5\nu}{\lambda^2} \overline{u_K u_K} \quad (44)$$

The microscale  $\lambda$  is defined through the behaviour of the two-point velocity correlation tensor near the origin, as:

$$R_{ij} = \frac{1}{3} \overline{u_K u_K} \left[ \frac{1}{2\lambda^2} r_i r_j + \left( 1 - \frac{r^2}{\lambda^2} \right) \delta_{ij} \right] \quad (45)$$

On the other hand,  $R_{ij}$  can be expressed in terms of the proposed model, i.e.:

$$R_{ij} = \alpha_{jl} \int_{\underline{v}^*} v_i^* v_l^* f(\underline{v}^*) d\underline{v}^* + \beta_{ipqr} \int_{\underline{v}^*} v_j^* v_q^* v_r^* \frac{\partial f(\underline{v}^*)}{\partial v_p^*} d\underline{v}^* \quad (46)$$

After integration and upon substitution of the Reynolds stress by its isotropic value  $(\overline{u_i u_j} = \frac{1}{3} \overline{u_K u_K} \delta_{ij})$ , Eq.(46) becomes:

$$R_{ij} = \frac{1}{3} \overline{u_K u_K} \left\{ (-4A_6 - A_3 - 3A_4) \frac{r_i r_j}{r^2} + (A_2 - A_5 - 2A_6 - 10A_8 - 5A_9) \delta_{ij} \right\} \quad (47)$$

Since the region of interest is the immediate neighbourhood of the origin, the above equation can be rewritten with the help of a Taylor expansion around  $r=0$ :



$$R_{ij} = \frac{1}{3} \overline{u_k u_k} \left\{ \left( -\frac{3}{2} A_4'' - 2A_6'' \right) r_i r_j + \left[ 1 + r^2 (3A_4'' + 4A_6'') \right] \delta_{ij} \right\} \quad (48)$$

which, when identified with Eq.(45) yields:

$$3A_4'' + 4A_6'' = -\frac{1}{\lambda^2} \quad (49)$$

and, through Eq.(44)

$$3A_4'' + 4A_6'' = -\frac{\varepsilon}{5\nu} \frac{1}{\overline{u_k u_k}} \quad (50)$$

Substituting this result in Eq.(43),

$$\int_V v_i^* v_j^* T_{v2} d\underline{v} = \nu (6A_5'' + 22A_6'') (\overline{u_i u_j} - \frac{1}{3} \overline{u_k u_k} \delta_{ij}) - \frac{2}{3} \varepsilon \delta_{ij} \quad (51)$$

Before commenting upon the physical meaning of Eq.(51), an analysis of the parametric coefficient affecting its redistributive term is necessary. The second derivatives of the  $A_i$ 's at the origin are associated with the small scales of the turbulent motion, as opposed to their integrals over the  $R$  space, that are linked with macroscales; therefore, the  $A_i$ 's are expected to be the same order of magnitude:

$$\begin{aligned} o\{\nu(6A_5'' + 22A_6'')\} &= o\{\nu(30A_4'' + 40A_6'')\} \\ &= o\{-\varepsilon/k\} \end{aligned} \quad (52)$$

( $k$  represents the turbulent kinetic energy, defined as  $k = \frac{1}{2} \overline{u_k u_k}$  i.e.:

$$\nu(6A_5'' + 22A_6'') = -C_1 \frac{\varepsilon}{k} \quad (53)$$

and  $C_1$  of order 1. Therefore, Eq.(51) can now be rewritten as:

$$\int_V v_i^* v_j^* T_{v2} d\underline{v} = -C_1 \frac{\varepsilon}{k} (\overline{u_i u_j} - \frac{2}{3} k \delta_{ij}) - \frac{2}{3} \varepsilon \delta_{ij} \quad (54)$$

This equation shows two different types of viscous contributions:

i) The first part on the RHS is associated with the anisotropy of the turbulent field; its effect is to redistribute energy between the components of the Reynolds stress tensor. It is of the same formal type and magnitude as the contribution attributed by Rotta, /6/ to the pressure scrambling due solely to turbulent interactions. In section 2.1, it was concluded that such a term was not associated with pressure if the flow field were homogeneous. However, a term of this type is necessary in order to account for the measured levels of the Reynolds stresses in homogeneous flow. It seems, therefore, that this contribution is associated with the viscous term; any anisotropy present at the lower wave-number end of the inertial subrange would pass unaltered through this region as the size of the scales would be too small to be noticed by the mean flow field and too large to notice the effects of viscosity. At the upper end of the inertial subrange, the long but thin "filaments" of fluid possess a very high vorticity that will be dissipated by viscous shear.

ii) The other term on the RHS of Eq.(54) represents the contribution to the dissipation of the stress that would occur in an isotropic flow field with the same turbulent intensity.

The above comments suggest that Eq.(41) may be rewritten in terms of the dissipation of turbulent kinetic energy and of two non-dimensional coefficients,  $C_1$  and  $C_3$ ;  $C_1$  is defined by Eq.(53) and  $C_3$  is defined by:

$$C_3 = -\nu \frac{k}{\varepsilon} (30A_5'' - 40A_6'' + 150A_7'') \quad (55)$$

With these definitions, Eq.(41) becomes:

$$T_{v2} = -\frac{\varepsilon}{3k} \left\{ (1 + C_3) \frac{\partial}{\partial v_k^*} \left[ v_k^* f(\underline{v}^*) \right] + \frac{1}{2} (1 - C_1) \frac{\partial}{\partial v_k^*} \left[ v_j^* v_j^* \frac{\partial f(\underline{v}^*)}{\partial v_k^*} \right] + \right. \quad (56)$$

$$+ \left[ \frac{C_1}{2} + \frac{C_3}{5} \right] \frac{\partial}{\partial v_k^*} \left[ v_k^* v_j^* \frac{\partial f(\underline{v})}{\partial v_j^*} \right] \Bigg\}$$

The constant  $C_3$  makes its appearance for the first time. It can be seen that this constant does not appear in the transport equations for the velocity correlation tensors of order lower than the third; therefore it does not affect closures at the Reynolds stress level.

### 3. Final form of the set of equations. Determination of the constants

When, in Eq.(8), the unknown terms are substituted by their modelled forms (Eq.(35) and (56)), the following equation emerges:

$$\begin{aligned} \frac{\partial f(\underline{v})}{\partial t} + v_j \frac{\partial f(\underline{v})}{\partial x_j} &= \frac{1}{\rho} \frac{\partial \bar{P}}{\partial x_j} \frac{\partial f(\underline{v})}{\partial v_j} - v \frac{\partial^2 \bar{U}_i}{\partial x_j^2} \frac{\partial f(\underline{v})}{\partial v_i} + \\ &+ \frac{\partial \bar{U}_i}{\partial x_j} \left\{ v_k^* v_k^* \frac{\partial^2 f(\underline{v})}{\partial v_i \partial v_j} \left( -24C_2 - \frac{1}{5} \right) + v_k^* v_i^* \frac{\partial^2 f(\underline{v})}{\partial v_k \partial v_j} \left( 64C_2 + \frac{3}{5} \right) + \right. \\ &+ v_k^* v_j^* \frac{\partial^2 f(\underline{v})}{\partial v_k \partial v_i} \left( 8C_2 \right) + v_i^* v_j^* \frac{\partial^2 f(\underline{v})}{\partial v_k \partial v_k} \left( -24C_2 - \frac{2}{5} \right) + \\ &+ v_i^* \frac{\partial f(\underline{v})}{\partial v_j} \left( 224C_2 + 2 \right) + v_j^* \frac{\partial f(\underline{v})}{\partial v_i} \left( -56C_2 - 2 \right) \Bigg\} - \\ &- \frac{1}{3} \frac{\epsilon}{k} \left\{ (1 + C_3) \frac{\partial}{\partial v_k} \left[ v_k^* f(\underline{v}) \right] + \frac{1}{2} (1 - C_1) \frac{\partial}{\partial v_k} \left[ v_j^* v_j^* \frac{\partial f(\underline{v})}{\partial v_k} \right] + \right. \\ &+ \left. \left( \frac{C_1}{2} + \frac{C_3}{5} \right) \frac{\partial}{\partial v_k} \left[ v_j^* v_k^* \frac{\partial f(\underline{v})}{\partial v_j} \right] \right\} \end{aligned} \quad (57)$$

The model introduced three parameters, assumed to be constants, and the dissipation of turbulent kinetic energy; the occurrence of the latter implies that a closed set of equations can only be obtained after a constitutive relationship or a modelled transport equation is involved for the dissipation of turbulent kinetic energy. This has been done by Hanjalić and Launder /10/, who developed and used the following transport equation for  $\epsilon$ :

$$\bar{U}_j \frac{\partial \epsilon}{\partial x_j} = c_\epsilon \frac{\partial}{\partial x_j} \left[ \frac{k}{\epsilon} \bar{u}_j u_\ell \frac{\partial \epsilon}{\partial x_\ell} \right] - c_{\epsilon 1} \bar{u}_j u_k \frac{\partial \bar{U}_j}{\partial x_k} \frac{\epsilon}{k} - c_{\epsilon 2} \frac{\epsilon^2}{k} \quad (58)$$

The terms on the RHS are, respectively, modelled forms of the diffusion, generation and destruction of the dissipation of turbulent kinetic energy. Launder, Reece and Rodi /4/, used the following values for the constants appearing in Eq.(58):

$$c_\epsilon = .15; \quad c_{\epsilon 1} = 1.45; \quad c_{\epsilon 2} = 1.90$$

Analyses of Eq.(58) may be found in Pope /11/ and Ribeiro /3/.

The use of Eq.(58) in conjunction with Eq.(57) yields a closed set of equations for the transport of probability density distribution of velocity. There remains the problem of assigning values to the constants,  $C_1$ ,  $C_2$ , and  $C_3$  appearing in Eq.(57); the levels of the Reynolds stress tensor occurring in homogeneous turbulence (see Champagne, Harris and Corrsin /12/), yield a value of 1.5 for  $C_1$  and  $-.0045$  for  $C_2$ ; the determination of  $C_3$  requires the knowledge of the levels of the fourth-order velocity correlation tensor, since in homogeneous flow, the third-order tensor is identically zero; however, the formal similarity between the terms in  $C_1$  and  $C_3$  suggests that  $C_3$  might take a value around 1.5.

This concludes the objective of finding a phenomenological closure of the transport equation for the one-point probability density distributions. This was achieved by relating the behaviour of one quantity, involving the two-point probability density of velocity, to local properties of the flow field. This quantity affected the transport equation for the probability density distribution both through its rate of change in the neighbourhood of the point and through an integral behaviour; therefore, the model had to reflect these two types of effect, each of them demanding a separate physical interpretation.

#### 4. Final remarks

The proposed closure for the equation that governs the transport of the one point probability density distribution of velocity has been shown to be compatible with the Reynolds stress closure of Launder, Reece and Rodi /4/. The advantages of the proposal may be summarized: it allows any model based on the one-point velocity correlations to be obtained without further assumption thus guaranteeing the compability of the modelling of the different quantities. It must be emphasized that the model involved one unknown quantity, and that the basic assumption, homogeneity, has enough generality in flows remote from walls. The drawbacks of the model lie mainly in the increase of the number of independent variables by three. However, some economy measures can be used to avoid this disadvantage. Apart from the obvious possibility of solving for some of the lower order moments of the equation, another promising possibility is to use a series representation of the probability density of velocity: whenever the one-point probability density of velocity is unimodal, an excellent approximation can be obtained through its Gram-Charlier series (see Lumley /13/); the terms of this series are orthonormal and one of its properties is that at any order, the number of moments that are exactly satisfied is known. The influence of each term can be quantified as today's experimental techniques allow the one-point probability density of velocity to be determined with a reasonable level of accuracy (see Ribeiro and Whitelaw /14/), thus allowing the separation of the terms that best represent the probability density of velocity. When this series development is used, the one equation in velocity space reverts to a discrete number of equations for the moments of the series; thus, it is an alternative of the same formal type to the solution of the transport equation for its moments.

#### References

- /1/ Lundgren, T.S. (1967): "Distribution functions in the Statistical Theory of Turbulence". Phys. Fluids, 10, 969.
- /2/ Monin, A.S. (1967): "Equations of Turbulent Motion". Prikl. Mat. Mekh., 31, 1057.
- /3/ Ribeiro, M.M. (1976): "The Turbulence Structure of Free Jets with and without Swirl". Ph.D. Thesis, Univ. of London.
- /4/ Launder, B.E., Reece, G.J., Rodi, W. (1975): "Progress in the Development of a Reynolds Stress Turbulence Closure". J. Fluid Mech., 68, 537.
- /5/ Naot, D., Shavit, A., Wolfstein, M. (1973): "Two-point Correlation Model and the Redistribution of Reynolds Stress". Phys. Fluids, 16, 738.
- /6/ Rotta, J.C. (1951): "Statistische Theorie Nicht homogener Turbulenz". Zeitsch F. Physik, 129, 547.
- /7/ Batchelor, G.K. (1959): "The Theory of Homogeneous Turbulence". Cambridge Univ. Press.
- /8/ Townsend, A.A. (1976): "The Structure of Turbulent Shear Flow". Cambridge Univ. Press.
- /9/ Panchev, S. (1971): "Random Functions and Turbulence". Pergamon Press, p.162.
- /10/ Hanjalić, K., Launder, B.E. (1972): "A Reynolds Stress Model of Turbulence and its Application to Thin Shear Flows". J. Fluid Mech., 52, 609.
- /11/ Pope, S.B. (1975): "The Calculation of the Flow behind Bluff Bodies with and without Combustion", Ph.D. Thesis, Univ. of London.
- /12/ Champagne, F.H., Harris, V.G., Corrsin, S. (1970): "Experiments on nearly Homogeneous Shear Flow". J. Fluid Mech., 41, 81.
- /13/ Lumley, J.L. (1971): "Stochastic Tools in Turbulence". Academic Press, p.39.
- /14/ Ribeiro, M.M., Whitelaw, J.H. (1975): "Statistical Characteristics of a Turbulent Jet". J. Fluid Mech., 70, 1.

#### Acknowledgements

The present work stems from ideas developed during the author's stay at the Imperial College, London.

The author wishes to thank Prof. J.H. Whitelaw for his advice and guidance throughout the research programme; the financial support was partly provided by the University of Luanda.

# MODELLING REQUIREMENTS FOR THE CALCULATION OF THE TURBULENT FLOW AROUND AIRFOILS, WINGS AND BODIES OF REVOLUTION

by  
Tuncer Cebeci  
Aerodynamics Research  
Douglas Aircraft Company  
Long Beach, California 90846, U.S.A.  
and  
Mechanical Engineering Department  
California State University at Long Beach  
Long Beach, California 90840, U.S.A.

and  
H. U. Meier  
Deutsche Forschungs- und Versuchsanstalt  
für Luft- und Raumfahrt E.V.  
Aerodynamische Versuchsanstalt Göttingen  
Bunsenstrasse 10, 3400 Göttingen, W. Germany

## SUMMARY

The paper demonstrates, by comparison between calculations and measurements, that turbulent flows around a range of geometric configurations of relevance to aircraft and missile design can be represented by time-averaged boundary-layer equations with an algebraic eddy-viscosity hypothesis. The use of higher-order models is difficult to justify and the existence of possible "coherent" structures does not influence this conclusion.

## 1. INTRODUCTION

A major purpose of this paper is to consider and evaluate the merits of turbulence models for the calculation of the flow around geometric configurations of relevance to airplane and missile design. To achieve this, calculated results obtained with three turbulence models are compared to each other and to the boundary-layer measurements selected for use at the 1968 Stanford Conference (ref. 1); and calculations presented, and where possible compared with measurements, for several three-dimensional flows.

As can be seen from references 2 and 3, for example, considerable efforts have been devoted to the investigation of turbulence models and coherent structures in recent years. In the former case, the algebraic eddy-viscosity hypotheses have been replaced, from a research standpoint, by higher-order models ranging from eddy-viscosity models based on turbulence energy and dissipation rate obtained from differential equations, to second-order closures involving more than one length scale. In the latter, the large eddies associated with some wake flows and "bursts" observed in near-wall flows by flow visualization and conditional sampling of hot-wire signals have emphasized the need for experimental verification of calculated results for turbulent flows obtained from the solution of time-averaged equations. Of course, in many of the flows considered previously, and also in references 2 and 3, calculations based on time-averaged equations and different turbulence models have been compared with measurements and some have been shown to be within the measurement precision. It is useful, however, to determine the need for higher-order models and the need to represent possible coherent structures for the calculation of the boundary layers around aircraft-related components.

The following section presents a brief introduction to the reduced forms of the Navier-Stokes equations considered in Sections 3 and 4 and of the turbulence models used. Section 3 presents calculations obtained with time-averaged, two-dimensional, boundary-layer equations and three turbulence models corresponding to the algebraic eddy-viscosity hypothesis of Cebeci and Smith (ref. 4), the Reynolds stress method of Bradshaw Ferriss and Atwell (ref. 5) and the two-equation, eddy-viscosity approach of Jones and Launder (ref. 6). Calculations have been performed for the data of reference 1 and the sample presented corresponds to the stronger pressure-gradient cases where the algebraic assumption might be expected to be less successful. Calculations, with the model of reference 4, are then compared with measurements of a separating boundary layer and of a near wake in order to allow better assessment of the outer-region component of the model of reference 4.

Three-dimensional boundary-layer equations have been solved and the results are presented in Section 4. The infinite swept-wing of reference 7 is considered first and allows comparison between the models of references 4 and 5 for a comparatively simple flow. Calculations for a second swept wing are then presented and the more complex rectangular duct flow of Vermeulen (ref. 8) considered and used to compare the capabilities of the models of references 4 and 6. As in the case of the two-dimensional flows, the calculations with each model lead to similar results. The calculations are then extended to three-dimensional wing flows where it is shown that the Cebeci-Smith model provides results adequate for many design purposes. The limiting factor in the calculation of the flow around wings, and also around bodies of revolution, is not necessarily the turbulence model and the discussion of Section 4 and conclusions of Section 5 emphasize this important fact.

In general, it may be concluded from the comparisons of Sections 3 and 4 that, at least for the flow around aircraft components, it is difficult to justify the use of turbulence models more complicated than the algebraic eddy-viscosity formulation of reference 4. The results also suggest that the existence of "coherent structures" is of no significance. In contrast, numerical uncertainties associated with the viscous-inviscid interaction and the determination of boundary conditions and transition can introduce significant uncertainties and, together with numerical requirements, make it even more difficult to justify the use of higher-order models.

## 2. EQUATIONS, MODELS AND SOLUTION PROCEDURES

This section deals with the equations, turbulence models and the solution procedures used to obtain the results of Section 3. To conserve space, the discussion is restricted to two-dimensional forms; the reader is referred to Cebeci and Bradshaw (ref. 9) for details of three-dimensional equations, model and numerical schemes.

### 2.1 Equations for Two-Dimensional Flows

For two-dimensional steady flows, the continuity and momentum equations are:

$$\frac{\partial u}{\partial x} + \frac{\partial v}{\partial y} = 0 \quad (1)$$

$$u \frac{\partial u}{\partial x} + v \frac{\partial u}{\partial y} = u_e \frac{du_e}{dx} + \frac{\partial \tau}{\partial y} \quad (2)$$

Here

$$\tau = \nu \frac{\partial u}{\partial y} - \overline{u'v'} \quad (3)$$

and we recall that  $u', v'$  are zero in laminar flow, and  $\nu(\partial u/\partial y)$  is negligible outside the viscous sublayer in a turbulent flow. These equations are subject to the usual boundary conditions which, in the case of boundary layers, are

$$y = 0, \quad u = v = 0; \quad y \rightarrow \delta \quad u \rightarrow u_e(x) \quad (4)$$

The presence of the Reynolds stress term,  $-\rho \overline{u'v'}$ , introduces an additional unknown to the system given by Eqs. (1) to (4) and in this paper we present calculations obtained with the three turbulence models. The first is the algebraic eddy-viscosity formulation developed by Cebeci and Smith (CS), the second the transport equation model developed by Bradshaw, Ferriss and Atwell (BF) and the third the two-equation, eddy-viscosity approach of Jones and Launder (JL). In the CS model, we write Eq. (3) as

$$\tau = (\nu + \epsilon_m) \frac{\partial u}{\partial y} \quad (5)$$

with two separate formulas for  $\epsilon_m$ . In the so-called inner region of the boundary layer,  $(\epsilon_m)_i$  is defined as

$$(\epsilon_m)_i = L^2 \left| \frac{\partial u}{\partial y} \right| \quad (6)$$

where

$$L = 0.4y[1 - \exp(-y/A)], \quad A = 26\nu\tau^{-1}[1 - 11.8p^+]^{-1/2} \quad (7a)$$

$$u_\tau = \left( \frac{\tau_w}{\rho} \right)^{1/2}, \quad p^+ = \frac{\nu u_e}{u_\tau} \frac{du_e}{dx} \quad (7b)$$

In the outer region,  $\epsilon_m$  is defined by

$$(\epsilon_m)_o = 0.0168 \int_0^\infty (u_e - u) dy \quad (8)$$

The inner and outer regions are established by the continuity of the eddy-viscosity formulas.

In the BF model, which is solved only outside the viscous sublayer, we assume  $\tau = \overline{u'v'}$  and write a single first-order partial differential equation for it. The equation was originally developed from the turbulent energy equation but can be equally well regarded as an empirical closure of the exact shear-stress transport equation. It is

$$u \frac{\partial \tau}{\partial x} + v \frac{\partial \tau}{\partial y} = 2a_1 \tau \frac{\partial u}{\partial y} - \frac{\partial}{\partial y} (\tau v_\tau) - 2a_1 \frac{\tau^{3/2}}{L} \quad (9)$$

Here  $a_1$  is a dimensionless quantity,  $v_\tau$  is a velocity and  $L$  is the dissipation length parameter specified algebraically as  $L/\delta = f(\eta)$ , with  $\eta = y/\delta$  and  $f(\eta)$  given as an analytic fit to an empirical curve, by

$$f(\eta) = \begin{cases} 0.4\eta & \eta < 0.18 \\ 0.095 - 0.055(2\eta - 1)^2 & 0.18 \leq \eta < 1.1 \\ 0.016 \exp[-10(\eta - 1.1)] & \eta \geq 1.1 \end{cases} \quad (10)$$

The turbulent transport velocity  $v_\tau$ , nominally  $(\overline{p'u'} + \overline{u'v'^2})/\overline{u'v'}$  is proportional to a velocity scale of the large eddies and is chosen to be

$$v_\tau = 2a_1 \frac{\tau_{\max}}{u_e} g(\eta) \quad (11)$$

where  $g(\eta)$  is

$$g = \begin{cases} 33.3\eta^2(0.184 + 0.832\eta) & \eta < 0.5 \\ 33.3\eta^3(0.368 + 2.496\eta^3) & 0.5 \leq \eta < 1.0 \\ 18.7\eta + 14.60 & \eta \geq 1.0 \end{cases} \quad (12)$$

In the BF model equations, the inner boundary conditions for (1), (2) and (9) are applied outside the viscous sublayer, usually at  $y_1 = 50\nu/u_\tau$ . In the steady-flow study reported by Cebeci, Chang and Bradshaw (ref. 10), these boundary conditions are:

$$u_1 = u_\tau \left( \frac{1}{\kappa} \ln \frac{y_1 u_\tau}{\nu} + 5.2 \right) \quad (13)$$

$$v_1 = - \frac{u_1 y_1}{u_\tau} \frac{du_\tau}{dx} \quad (14)$$

and

$$\tau_1 = \tau_w + \frac{1}{\rho} \frac{dp}{dx} y_1 + \alpha^* \frac{d\tau_w}{dx} y_1 \quad (15)$$

Here  $\alpha^*$  is given by

$$\alpha^* = \frac{1}{2} [K_1 (\ln y_1^+)^2 + K_2 (\ln y_1^+) + K_3 + K_4 / y_1^+] \quad (16)$$

where  $y_1^+ = y_1 u_\tau / \nu$ ,  $K_1 = 5.94884$ ,  $K_2 = 13.4682$ ,  $K_3 = 15.5718$  and  $K_4 = -698.304$ . Reference 11 describes the extension of Eqs. (1), (2), (3) through (16) to unsteady flows.

In the JL model, which also assumes an eddy viscosity,  $\epsilon_m$  in Eq. (5) is defined by

$$\epsilon_m = 0.09k^2/\phi \quad (17)$$

and two partial-differential equations based on turbulent energy ( $k$ ) and dissipation rate ( $\phi$ ) are solved to determine  $\epsilon_m$ . They are:

$$u \frac{\partial k}{\partial x} + v \frac{\partial k}{\partial y} = \frac{\partial}{\partial y} \left[ (\nu + \epsilon_m) \frac{\partial k}{\partial y} \right] + \epsilon_m \left( \frac{\partial u}{\partial y} \right)^2 - \phi \quad (18)$$

$$u \frac{\partial \phi}{\partial x} + v \frac{\partial \phi}{\partial y} = \frac{\partial}{\partial y} \left[ \left( \nu + \frac{\epsilon_m}{1.3} \right) \frac{\partial \phi}{\partial y} \right] + 1.55 \frac{\phi}{k} \epsilon_m \left( \frac{\partial u}{\partial y} \right)^2 - 2 \frac{\phi^2}{k} \quad (19)$$

In this model, boundary conditions are applied at the wall  $y = 0$  (see ref. 12, for example) or outside the viscous sublayer. In our study, we have taken the second approach and used Eqs. (13), (14) for  $u_1, v_1$ . The third "wall" boundary condition was taken as

$$\left( \frac{\partial u}{\partial y} \right)_1 = 0.55 \frac{k_1^{1/2}}{\kappa y_1} \quad (20)$$

and comes from the experimentally determined relationship between the shear and turbulent energy and the definition of turbulent viscosity.

The edge boundary conditions for  $u, k$  and  $\phi$  are much easier to formulate. The most obvious of these is

$$y \rightarrow \delta \quad u \rightarrow u_e \quad (21)$$

However, the value of  $k$  and certainly  $\phi$ , are not usually measured and reported for experimental tests. Therefore, we must rely upon our model to make the edge values consistent. Writing the limiting values of Eqs. (18) and (19) at the boundary-layer edge, where all  $y$ -gradients are zero, yields

$$u_e \frac{dk_e}{dx} = -\phi_e, \quad u_e \frac{d\phi_e}{dx} = -2 \frac{\phi_e^2}{k_e} \quad (22)$$

These equations can be solved in finite-difference form along with the solutions of Eqs. (1), (2), (18) and (19), but they also have an analytic solution given by

$$k_e = k_0 \left[ 1 + \frac{\phi_0}{k_0} \int_0^x \frac{dx}{u_e} \right]^{-1}, \quad \phi_e = \phi_0 \left[ 1 + \frac{\phi_0}{k_0} \int_0^x \frac{dx}{u_e} \right]^{-2} \quad (23)$$

where the subscript zero refers to the initial data station.

## 2.2 Initial Conditions

For the parabolic problem posed by the above model equations, initial data must be provided at the first station for the solution to proceed. In most cases, the experimental data require interpolation and smoothing to provide information at finite-difference grid points and, rather than attempting this for the large number of cases considered here, we have chosen to use the measured values of boundary-layer properties as input to an empirical formula which fits measured data over a large range of flows.

Coles' law-of-the-wall/law-of-the-wake formula, modified to give a zero gradient at the edge of the boundary layer, is (ref. 3)

$$u = \frac{u_\tau}{\kappa} \left[ \ln \left( \frac{yu_\tau}{\nu} \right) + c + \pi \left( 1 - \cos \frac{\pi y}{\delta} \right) + \left( \frac{y}{\delta} \right)^2 \left( 1 - \frac{y}{\delta} \right) \right] \quad (24)$$

As shown in Cebeci and Bradshaw (ref. 9), this expression can be used along with expressions for  $\delta^*$  and  $\theta$  to form a set of three relations for the five unknowns  $c_f$ ,  $R_{\delta^*}$ ,  $R_\theta$ ,  $\delta$  and  $\pi$ . Supplying  $c_f$  and  $R_\theta$  from experiment allows the solution for the other two, and specifies the velocity profile by (24).

Since we are dealing with transport models, in addition to the velocity profiles, initial profiles are also necessary for  $\tau$ ,  $k$  and  $\phi$ . At first it would appear that one might use an algebraic eddy viscosity and a velocity profile expression to obtain the  $\tau$  (or  $k$ ) profile. Since  $\epsilon_m$  is discontinuous at the match point, an alternate method, suggested in Cebeci and Smith, is used to integrate Eq. (9), including the pressure-gradient term, to get  $\tau$ . Once  $\tau$  and  $u$  have been generated, the definition of turbulence dissipation can be used to get the initial profile for  $\phi$ , i.e.

$$\phi = \tau \frac{\partial u}{\partial y} \quad (25)$$

## 2.3 Solution Procedure

The governing equations, employing three turbulence models, are solved by using Keller's Box method, which is an efficient second-order finite-difference method extensively used by Cebeci and his associates. The application of this method to the CS model is described in detail in several references, see for example Cebeci and Bradshaw. Its application to BF model is described in Cebeci, Chang and Bradshaw (ref. 10) for two-dimensional steady flows and in Cebeci, Carr and Bradshaw (ref. 11) for unsteady flows. In each case, whether we use the CS model or the BF model, we solve a system of three first-order equations.

In the case of JL model, we solve the system given by Eqs. (1), (2), (18), (19), (13) to (16) and (20) to (23). With the Box method, this is a system of seven first-order equations with nonlinear boundary conditions. As in the solution of governing equations containing the CS model or the BF model, Newton's method is used to linearize the nonlinear finite-difference equations and the resulting system is solved by using the block elimination method described in Cebeci and Bradshaw.

## 3. COMPARISON OF TURBULENCE MODELS FOR TWO-DIMENSIONAL FLOWS

The three separate computer programs, incorporating the CS, BF and JL models and using the Box method, were tested for several wall boundary-layer flows documented in the 1968 Stanford Conference. No numerical difficulties were observed with the three models for zero and favorable pressure-gradient flows. For some adverse pressure-gradient flows, especially in those which contain flow separation, the use of the JL model involved considerable numerical difficulties even far upstream of the separation point. The CS model involved no numerical difficulties for all adverse pressure-gradient flows; the BF model had some difficulties but only in strong adverse pressure-gradient flows and allowed calculations close to the separation point. The solutions obtained with the JL model also revealed unacceptable oscillations near the edge of the boundary layer with changing pressure gradient, say from favorable to zero and then to adverse pressure gradient, as in test case 2100, which led to the breakdown of the calculation.

The results presented in Figures 1 to 7 correspond to Cases 1300, 2500 and 3500; the first has a favorable pressure gradient and the others adverse gradients of increasing severity. Before comparing the predictions of the three models with the experimental data, it is useful to discuss the sensitivity of each model to initial conditions as well as to the procedure used to perform the calculations.

Figure 1 shows predictions with the BF model for case 2500 with different initial shear stress profiles. As was discussed in Section 2, we use Eq. (24) to generate the streamwise velocity profile and Eq. (4.4.39) with pressure gradient from Cebeci and Smith to generate the initial shear stress profile  $\tau$ . Whether we include the pressure gradient term in the  $\tau$  profile strongly affects the solutions, although at some downstream location (close to where the experimental data ends!) the effect of the initial profiles vanishes. The use of Eq. (24) with a mixing length, as was done by Bradshaw, yields nearly the same results as those obtained with the  $\tau$  profile generated according to Eq. (4.4.39) with no pressure gradient effect; possibly they are slightly worse! In more than ten adverse pressure gradient flows tested with the BF model, we observed the same effect; the shear-stress profiles generated according to Eq. (4.4.39) with pressure gradient yield much better agreement with experiment than those generated with a  $\tau$ -profile which does not contain the pressure-gradient term. In some cases, like case 3500, noninclusion of the gradient term in the initial  $\tau$ -profile caused the solutions to break down after a few stations.

Figure 2 shows the effect of the initial shear-stress profile to the predictions of the JL model for case 2500. As can be seen, we observe the same effect as in the BF model.

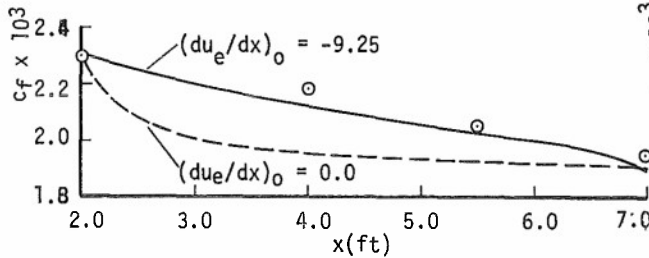


Fig. 1. Effect of initial shear-stress profile on the predictions of the BF model for case 2500.

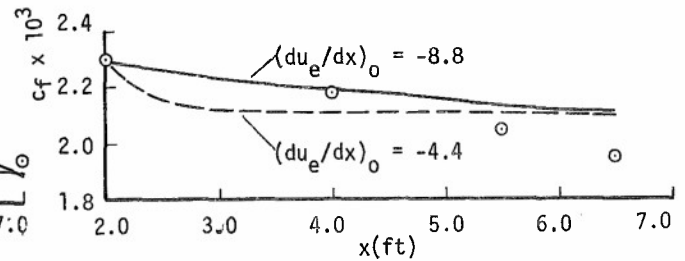


Fig. 2. Effect of initial shear-stress profile on the predictions of the JL model for case 2500.

The solution of the CS model can be obtained by solving Eqs. (1) and (2), subject to the no-slip boundary conditions given by Eqs. (13), (14), (15) and (16). The use of either one of these boundary conditions yields results in which the computed local skin-friction values differ from each other as shown in Figure 3 for case 3500.

In the solution of the governing equations for each model we need to specify the external velocity distribution  $u_e(x)$ . Since the solutions also require the velocity gradient,  $du_e/dx$ , it is useful to examine whether the procedure used to compute  $du_e/dx$  affects the solutions. Figure 4 shows the local skin-friction values for case 3500. Here the results are obtained with either the distribution of  $du_e/dx$  supplied in the Stanford Conference or by computing it from the input  $u_e(x)$  distribution, using a three-point Lagrange interpolation formula as described by Cebeci and Bradshaw (p. 261). As is seen, the results are sensitive to the procedure used to compute  $du_e/dx$ . What is even more important is that, for case 3500 and with  $du_e/dx$  computed from the  $u_e(x)$  distribution, the calculated  $c_f$ -values level off near separation rather than monotonically decreasing and going to zero as those obtained by inputting more accurate  $du_e/dx$  values.

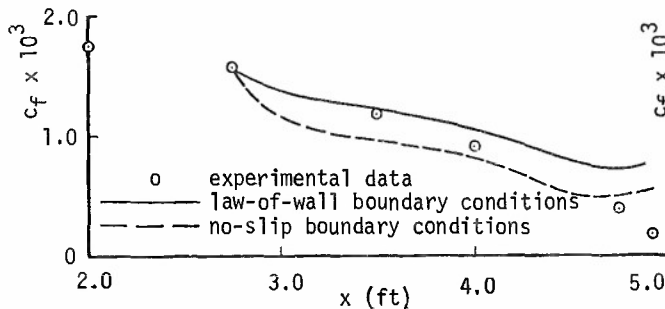


Fig. 3. Effect of different "wall" boundary conditions to the predictions of the CS model for case 3500.

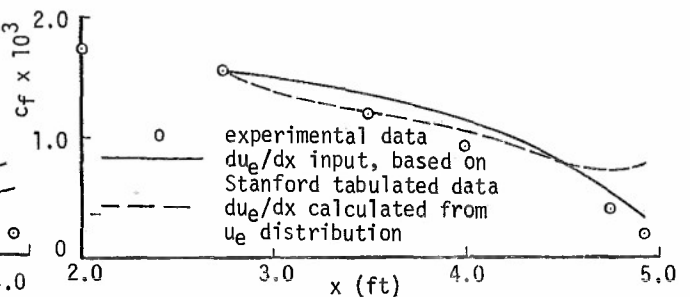


Fig. 4. Effect of  $du_e/dx$  on the computed local skin-friction values for case 3500, with the CS model.

Figures 5, 6 and 7 allow comparison between the predictions of the three turbulence models with the experimental data for cases 1300, 2500, 3500. Here the predictions of the CS model, as of the BF and JL models, are obtained by using the law-of-the-wall boundary conditions rather than the no-slip boundary conditions. The general conclusion that all models yield sensibly the same results (although the predictions of the BF model are slightly better than the CS and JL models) is inescapable and indicates that, at least for attached two-dimensional boundary layers with pressure gradients of the order of those of the test cases, the predictions of the CS model and the BF model are satisfactory and, indeed, are to be preferred since the JL model is more costly to use and requires the prescription of additional boundary conditions.

It is also relevant to ask if the same conclusion applies to two-dimensional separating boundary layers and wakes. After all, the turbulence models have been tested for flows in which the boundary-layer behavior is dominated by the inner layer (except near separation) and, therefore, the outer layer turbulence model is not too strongly tested. The turbulence model is likely to be more severely tested in free shear layers but, of course, there are far fewer data (and the data are less reliable) for free shear

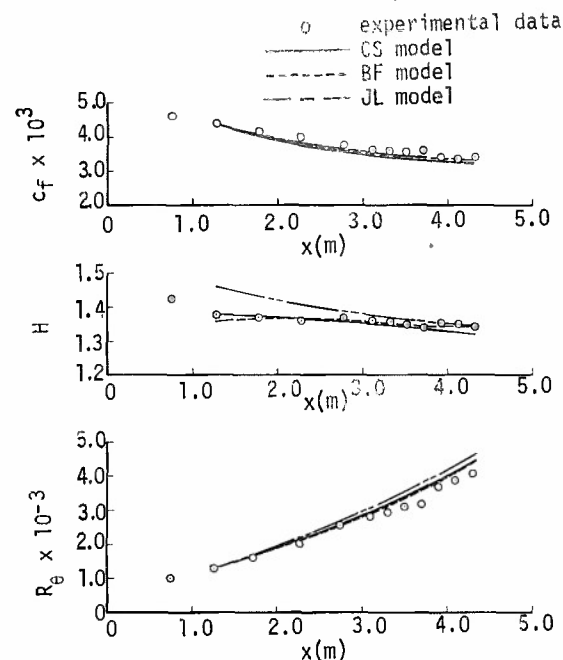


Fig. 5. Predictions with the three turbulence models for case 1300.



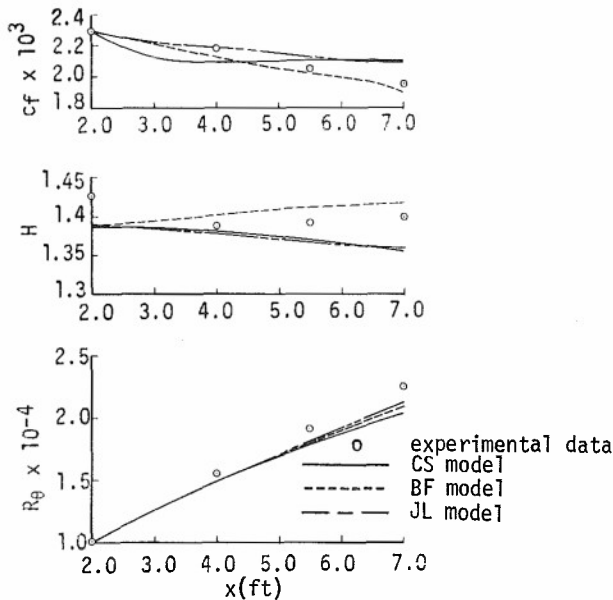


Fig. 6. Predictions with the three turbulence models for case 2500.

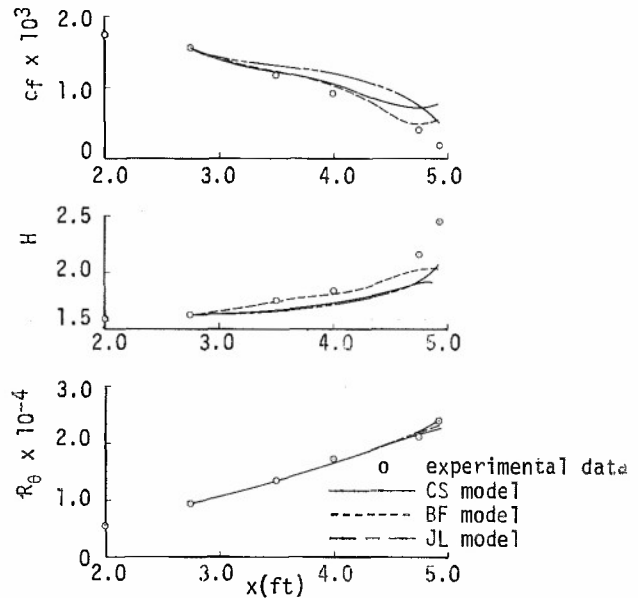


Fig. 7. Predictions with the three turbulence models for case 3500.

layers than for wall boundary layers. It should be noted that separated flows (with and without attachment) can be regarded as shear layers exposed to strong extra rates of strain and in most cases to considerable flow unsteadiness and, therefore, constitute a more serious problem.

Data in separated and reattaching flows are again rare and unreliable because the hot-wire is less precise in highly turbulent flows and laser anemometry is still relatively unquantified, although one or two groups, for example, Simpson, Strickland and Barr (ref. 13), Durão and Whitelaw (ref. 14), and Durst and Rastogi (ref. 15) have obtained very impressive results for separated flows. Therefore, progress in turbulence modelling is effectively held up for the present.

In order to investigate the predictions of the present turbulence models, Cebeci, Khalil and Whitelaw (ref. 16) considered the separating flow data of Simpson, Strickland and Barr. In their study, calculations were made by using the same boundary-layer procedure and the CS model as described above. The first calculation, with the measured distribution of freestream velocity as boundary condition, proceeded to the end of the experimental data without indicating reverse flow. The calculation was repeated using an inverse boundary-layer method; in addition to the boundary conditions given by eq.(4), the experimental displacement thickness was also specified. The calculations then indicated flow separation at the same location as the measurement. It is interesting to note that when related calculations were performed with two-dimensional elliptic equations and the JL model, separation was correctly detected but the downstream profiles, due at least in part to numerical uncertainties, were rather further from the measurements than those obtained with the parabolic equations and CS model.

Figure 8 shows the predictions of the CS model. We observe from the computed velocity profiles, Fig. 8a, that at first the agreement with experiment is quite good; it slowly deteriorates, however, as the pressure gradient becomes stronger and the flow approaches separation. The differences indicated in computed and experimental external velocity distributions shown in Fig. 8b may be due in part, to either the boundary-layer equations, the CS model, the wall functions or the measurements and it is impossible to determine which on the basis of the present evidence. The CS model, with its viscous sublayer model, is adequate only for attached flows. The inverse boundary-layer procedure is a very useful vehicle with which to examine alternative procedures, including the need to consider the influence of normal stresses as suggested by the data of Simpson et al.

Figure 9 shows the results for an asymmetric near wake behind a flat plate. The experimental data is due to Andreopoulos and Bradshaw (ref. 17). The numerical calculations were made with the CS model modified, following the ideas set forth by Bradshaw (ref. 18) and by Townsend (ref. 19). We denote the wake centerline by  $y = 0$ , and subdivide the inner region of the eddy-viscosity formula into two parts. When  $0 < y < y_2$  we define

$$\epsilon_w = 0.4(u_{\tau}^*)_{\max}^{T.E.} y_c \quad (26)$$

Here  $y_c$  is taken to be

$$y_c = \left[ \frac{0.0168 u_e^* \delta^*}{0.4(u_{\tau}^*)_{\max}^{T.E.}} \right] (x - x_{T.E.})$$

which essentially assumes that the near wake effect vanishes at  $10\delta_{T.E.}$  from the trailing edge. When  $y_2 < y < y_1$ , we use eq. (6) without the van Driest modification. In the outer region of the flow, we again use eq. (8). Note that, according to eqs. (8) and (26), the magnitude of  $\epsilon_w$  may exceed that of  $\epsilon_0$

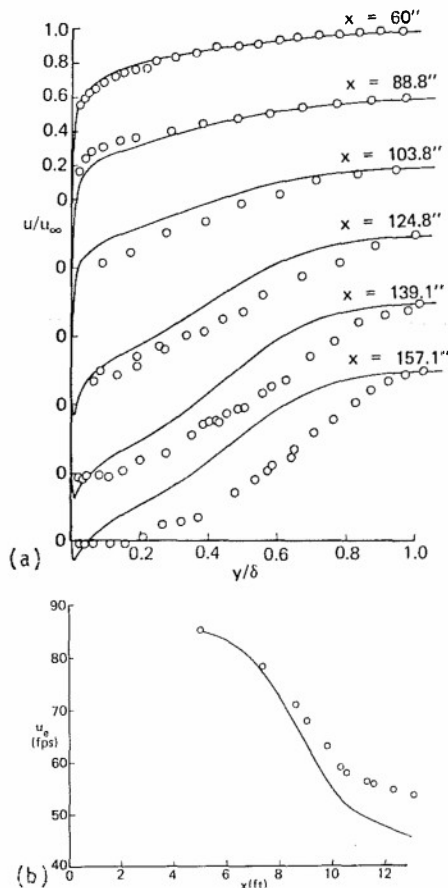


Fig. 8. Comparison between measurements of ref. 13 and the calculations with the CS model.

viously been obtained by Rastogi and Rodi (ref. 20) with the JL model and, together with present results with the CS model, allow a comparison of the two models in a three-dimensional flow. The calculations with the wing were obtained with the CS model only since, as may be surmised from the results of the previous section and confirmed by the bend flow, the use of models more complex than CS cannot easily be justified for two-dimensional flows, far less than the more complicated three-dimensional flows.

Figure 10 shows a comparison between the predictions of the CS and BF models for the 45° "infinite" swept wing measured by Bradshaw and Terrell (ref. 7). This experiment was set up especially to test the outer-layer assumptions made in extending the BF model from two dimensions to three. Measurements were made only on the rear of the wing in a region of nominally zero pressure gradient and decaying crossflow (see Fig. 10a). Spanwise and chordwise components of mean velocity and shear stress and all three components of turbulence intensity, were measured at locations corresponding to  $x' = 0, 4, 16$  and  $20$  in. from the start of the flat portion of the wing (see Fig. 10). The surface shear stress, measured with a Preston tube, was constant along a generator at the start of the flat part of the wing. In general, Figure 10 shows that the calculated results obtained with CS and BF models agree well with the experimental data and that there is little to choose between them.

A major question of particular importance to the aerospace industry concerns the structure of three-dimensional boundary layers with strong crossflow. An excellent series of experiments at the NLR (ref. 21) showed, on comparison with current calculation methods, that considerable changes in turbulent structure could occur. For example, the spanwise component of eddy viscosity in a three-dimensional boundary layer proved to be considerably less than the streamwise component, leading to the possibility of significant inaccuracy in predictions made by methods which assume an isotropic eddy viscosity. It appears that even transport equations seriously underpredict the nonisotropy of eddy viscosity in this case.

Figure 11 shows the results for the NLR data. The calculations were made by using the version of the CS model for three-dimensional flows and by using Rotta's (ref. 22) modification to mixing length to account for the nonisotropy of the eddy viscosity. For three-dimensional flows, the CS eddy-viscosity formulas for inner and outer regions are:

$$\epsilon_i = L^2 \left[ \left( \frac{\partial u}{\partial y} \right)^2 + \left( \frac{\partial w}{\partial y} \right)^2 \right]^{1/2} \quad (27)$$

$$\epsilon_o = 0.0168 \left| \int_0^\infty (u_{Re} - u_R) dy \right| \quad (28)$$

Here  $L$  is given by (7a) and (7b) except that now the friction velocity  $u_\tau$  is given by

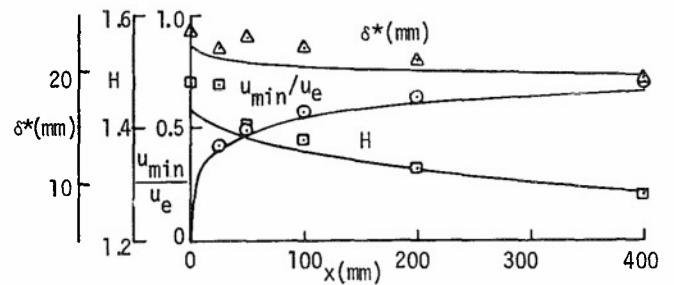


Fig. 9. Comparison between near-wake measurements of Andreopoulos and Bradshaw (ref. 17) and the calculations with the modified CS model.

at large enough distances from the trailing edge. In order to prevent this unacceptable property, we introduce the additional requirement that once  $\epsilon_o = \epsilon_w$ , the eddy viscosity for larger values of  $x$  is taken to be constant across the wake and equal to  $\epsilon_o$ .

#### 4. COMPARISON OF TURBULENCE MODELS FOR THREE-DIMENSIONAL FLOWS

The two-dimensional flows of the previous section provide information of the relative merits of the three turbulence models but the engineering problems of interest, namely those concerned with wings and bodies of revolution directly related to aircraft components are described by three-dimensional equations. After brief consideration of the swept wing of reference 7, for which calculations have been performed with the CS and BF models, and the swept wing of reference 21 which allows appraisal of Rotta's nonisotropic eddy-viscosity formulation, this section is concerned with the flow in a 60° curved duct and on a finite wing. The duct flow is considered because results have pre-

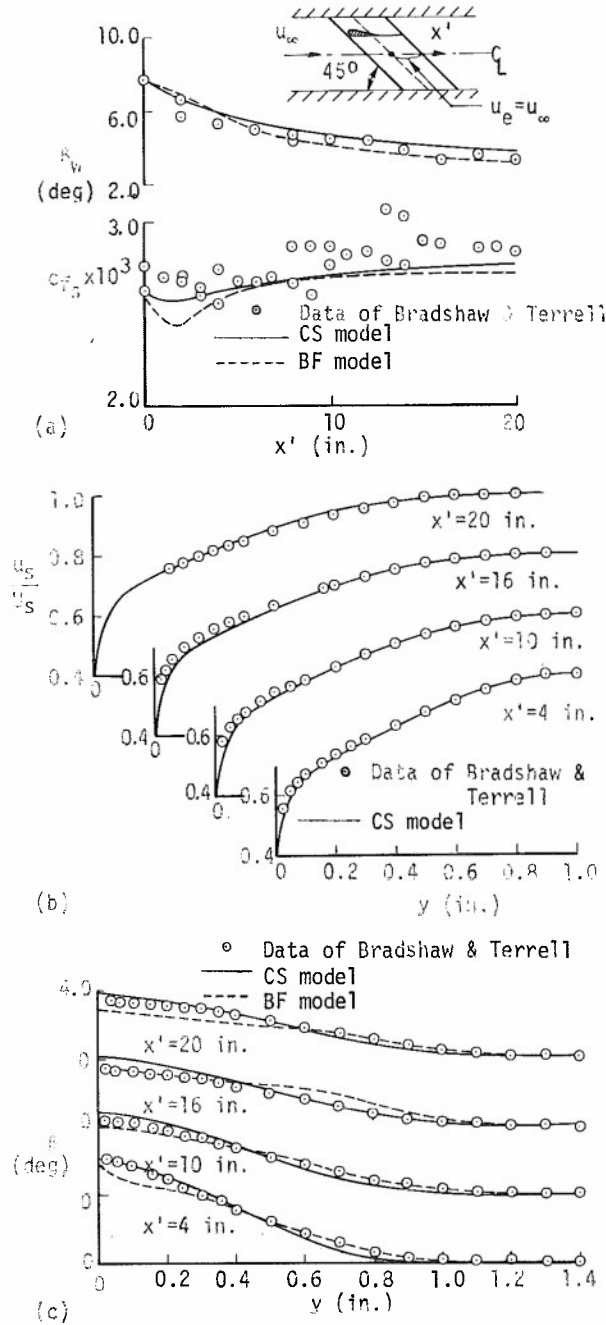


Fig. 10. Results for the relaxing flow of Bradshaw and Terrell: a) wall crossflow angle and local skin friction; b) velocity profiles; c) crossflow angle distributions.

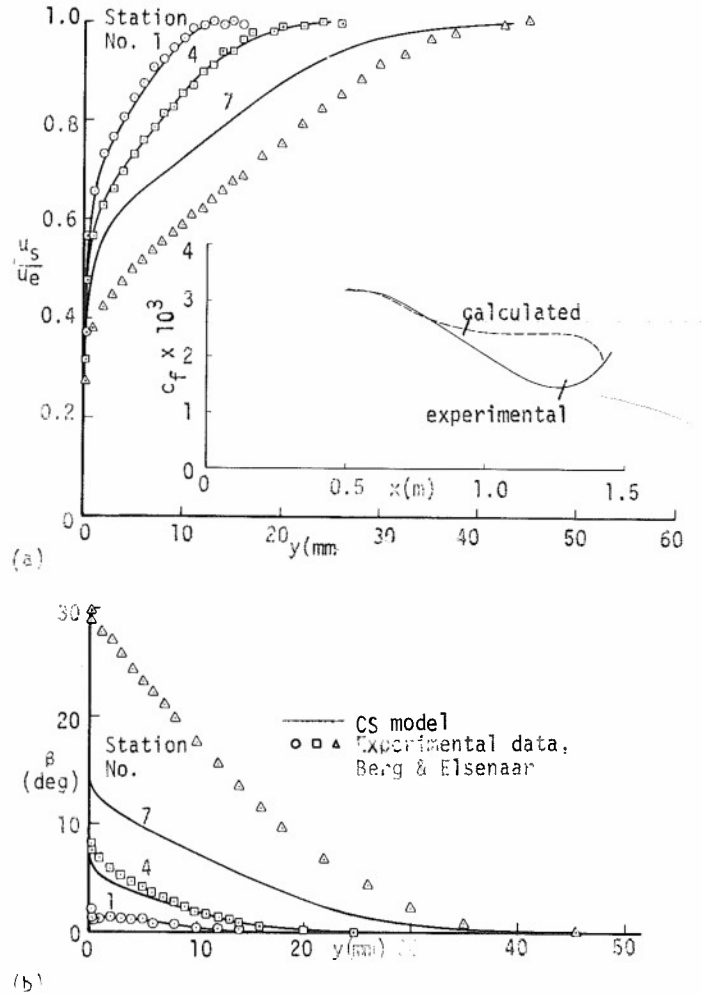


Fig. 11. Comparison of calculations and measurements for the infinite swept wing of ref. 21. (a) Total velocity profiles and total skin-friction coefficient distributions. (b) Crossflow angle distributions.

$$u_\tau = \left( \frac{\tau_s}{\rho} \right)^{1/2}, \quad (29)$$

$$\text{where } \frac{\tau_s}{\rho} = \nu \left[ \left( \frac{\partial u}{\partial y} \right)_w + \left( \frac{\partial w}{\partial y} \right)_w^2 \right]^{1/2}$$

and the dimensionless pressure-gradient parameter  $p^+$  is given by

$$p^+ = \frac{\nu u_s}{u_\tau^3} \frac{du_s}{ds}$$

Also  $u_R$  in the outer region eddy-viscosity formula is a resultant velocity defined by  $(u^2 + w^2)^{1/2}$ .

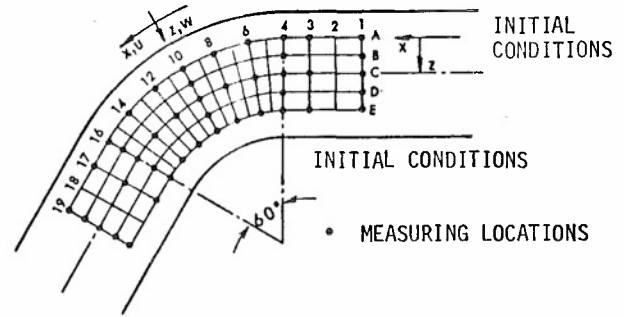
Rotta suggested that the mixing length formulation, eq.(27), be modified to

$$\epsilon_1 = L^2 \left[ \left( \frac{\partial u}{\partial y} \right)^2 + \left( \frac{\partial w}{\partial y} \right)^2 + (T - 1) \left( w \frac{\partial u}{\partial y} - u \frac{\partial w}{\partial y} \right)^2 / u_R^2 \right]^{1/2} \quad (30)$$

where  $T$  is a "constant" chosen to fit the experimental data. One can take  $L = 0.4y[1 - \exp(-y/A)]$  in the inner region and  $L = 0.085s$  in the outer region. Equation (30) can also be used for the inner region with eq. (28) for the outer region. In our study both choices were examined and produced nearly the same results.

The computed results of Figure 11 show that the predictions of both models, though initially very good (weak adverse pressure gradient), deteriorate quickly with increasing pressure gradient. The unmodified CS model does not predict flow separation and, although the modified model does predict flow separation with  $T = 0.5$ , the predicted velocity profiles and crossflow angles do not differ from those computed with the unmodified model. The modified model only affects the skin friction; by making it decrease, it causes the flow to separate.

To further test the model for "fully" three-dimensional flows, we have considered the experimental data taken in a  $60^\circ$  curved duct of rectangular cross section. Figure 12 shows a sketch of the flow geometry: the experimental data is due to Vermeulen (ref. 8). A comparison of calculated and experimental values of the streamwise momentum thickness,  $\theta_{11}$ , shape factor,  $H_{11}$ , skin-friction coefficient  $c_f$  and the limiting crossflow angle,  $\beta_w$ , is shown in Figures 13, 14, 15 and 16, respectively along the lines B, C, D, E. Figure 17 presents a comparison of calculated and experimental total velocity profile along the lines C and E. In all cases, the calculations were made by using the CS model with and without Rotta's modification. Overall the agreement with experiment is quite good and the results obtained with Rotta's modification are not too different from those obtained by the unmodified CS model. Rastogi and Rodi (ref. 20) have repeated calculations of this flow with the JL model; inspection of their results and comparison with the present results, indicates that the turbulence model has negligible influence.



In recent years several methods have been developed for computing three-dimensional laminar and turbulent boundary layers on finite wings. That of

Fig. 12. Coordinate system and notation for the curved duct.

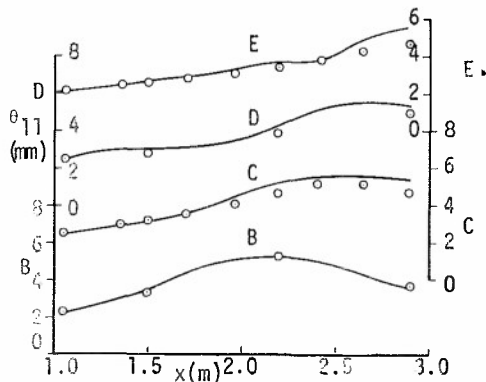


Fig. 13. Comparison of computed momentum thickness with Vermeulen's data.

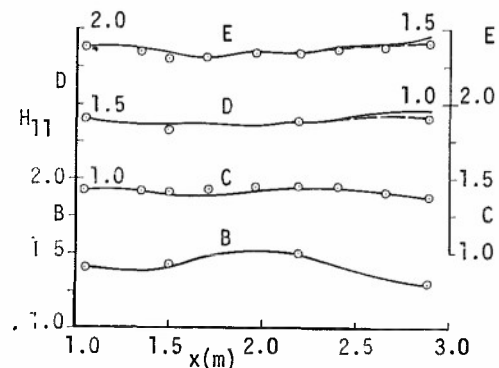


Fig. 14. Comparison of computed shape factor with Vermeulen's data.

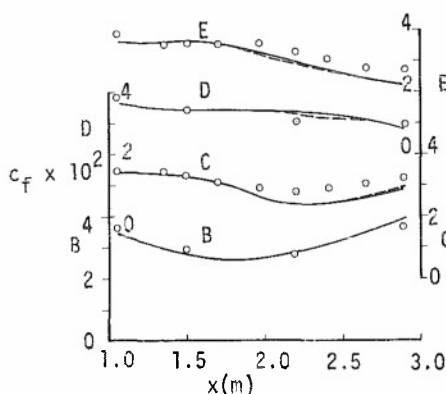


Fig. 15. Comparison of computed skin friction coefficient with Vermeulen's data.

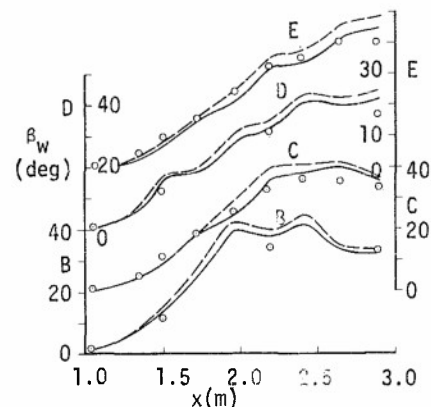


Fig. 16. Comparison of computed limiting crossflow angle with Vermeulen's data.

Cebeci, Kaups and Ramsey (ref. 23) uses a geometry package to represent the wing analytically, a novel numerical procedure to solve the governing equations for a nonorthogonal coordinate system, and an algebraic eddy-viscosity model similar to that given by eq. (27) to (29). It has recently been coupled to subsonic and transonic inviscid flow methods to account for the influence of the viscous forces on the pressure distribution. Two separate procedures were investigated. In one, the displacement surface was computed for a given inviscid pressure distribution and the potential flow computed about this modified shape; the iteration was continued until the convergence criterion was satisfied. In the other, the viscous effects were simulated by distributed sources of a blowing velocity on the body.

Figure 18 shows results for a swept wing with leading edge swept back at  $48.54^\circ$ , an aspect ratio of 3.0 and a taper ratio of 0.5. The wing has no twist and the sections conform to NACA 64A010 in planes inclined at  $45^\circ$  to the plane of symmetry. The data is due to Kolbe and Boltz (ref. 24).

The results of Figure 18 show that the "blowing" approach yields results which are in good agreement with the measurements. In contrast, the "displacement thickness" results do not agree well and it is impossible, on the basis of present evidence to isolate the reason. It should be appreciated, however, that the "marriage" of an accurate potential-flow method with an accurate boundary-layer method will not necessarily lead to accurate calculations. A major reason for this stems from the curved downstream wake which, with its viscous flow, can strongly influence the potential flow around the wing (or body of revolution). It is clear from the two-dimensional results of Section 3, that the use of incorrect boundary

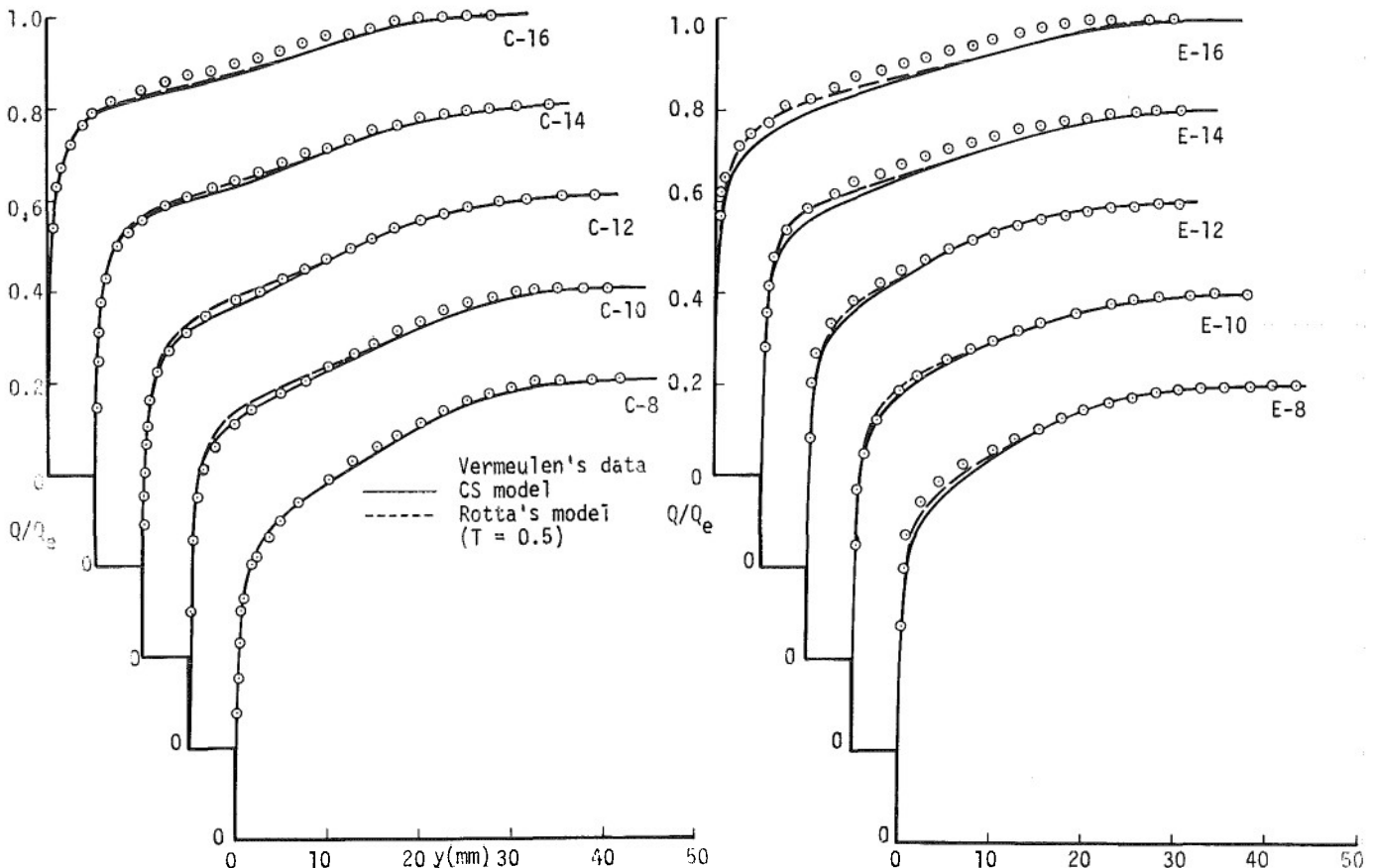


Fig. 17. Comparison of computed total velocity profiles with Vermeulen's data.

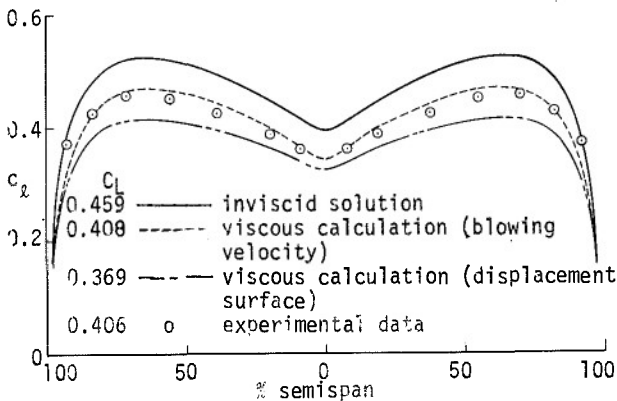


Fig. 18. Calculated and experimental results for the finite wing of ref. 24.  $Re_c = 18 \times 10^6$ .

conditions can lead to significant errors and the incorrect representation of the wake has a related effect. The calculation of the wake and its influence on the potential and boundary layers around the surface has not been carefully determined and should be incorporated into numerical calculation methods before further detailed consideration of turbulence models.

The influence of initial conditions, also demonstrated in Section 3, can also be important and can arise in two ways. First, and as in Section 2, mean-velocity measurements may be available, but with an inappropriate procedure for the determination of, for example, the shear-stress distribution, can lead to errors. Secondly, and as ably demonstrated by Meier and Kreplin (ref. 25), transition on wings and bodies of revolution can exist over a large region of a body; the details of the flow in such circumstances, are essentially unknown and cannot readily be determined. Even when a transition correlation is known, in terms

of wall measurements, appropriate details of the profiles are usually unknown with corresponding uncertainty in initial values and calculated downstream results.

## 5. DISCUSSION AND CONCLUDING REMARKS

The results of the preceeding two sections show that the three turbulence models can result in different calculated results and that the differences may not be of major significance when considered in relation to other sources of uncertainty. In particular, boundary and initial-condition effects demonstrated here in relation to two-dimensional flows, can be greater than those of the turbulence models and this situation may be expected to be at least as important in three-dimensional flows. Similarly, and although ad hoc modifications to turbulence models such as that proposed by Rotta, may work well for a limited range of flows and flow properties, they can lead to important discrepancies in other flows and properties.

An additional, and more important problem, for the calculation of the flow around the external surface of aircraft and missiles is the correct representation of the interaction between the inviscid and viscous flows from the leading edge and into the downstream wake. The calculation of important overall quantities, such as lift and drag, and of local flow properties cannot be achieved without the extension of the calculation method into the downstream flow. Thus, the three-dimensional procedure of Cebeci, Kaups and Ramsey (ref. 23) is unsatisfactory in that, as yet, it does not allow calculations downstream of the trailing-edge of a wing and is, as a result, likely to give erroneous results in the trailing-edge region which will increase in magnitude and importance as the angle of attack, and consequent wake thickness and curvature, increase. The error is also likely to be more important with asymmetric and particularly supercritical airfoil shapes. The same criticism, and others, can be levied at the wing-related calculations of others,

including those of Kordulla (ref. 26), McLean (ref. 27) and Humphreys (ref. 28), where no attempt has been made to represent the influence of the wake. The recent work of Cebeci, Thiele, Williams and Stewartson (ref. 29) provides a basis for this necessary extension which, for practical flows, is always likely to be of greater importance than the differences between the turbulence models considered here.

As a consequence of the above, it is difficult to draw positive conclusions about turbulence models and of the extent to which they represent the observed features of thin shear-layer flows including spots, bursts and other "coherent eddies." We could, for example, conclude that the present models do not represent sufficient aspects of turbulent flows and that, as a consequence, we should proceed more rapidly toward stress models, stress models with more than one dissipation equation, spectral methods, large-eddy simulation methods, etc. These might conceivably be developed to take some account of the observed structures. Alternatively, it can be concluded that two- and three-dimensional wall boundary layers are not strongly influenced by these "structures" and that the simpler models are to be preferred in their present state. Neither conclusion is satisfactory although the latter seems closer to the truth than the former.

It is clear that experimental evidence is insufficient in quantity and precision to provide tests which are completely adequate. However, even if greater quantities of data were available, it is unlikely that the precision would be adequate to prevent the uncertainties of the type shown here in connection with two-dimensional flows. Thus, the designer is unlikely to be presented with a calculation method which allows a priori predictions of flow properties with accuracy sufficient for the design of wings and bodies of revolution associated with aircraft components. Particularly with the algebraic eddy-viscosity form of turbulence models, however, he can be presented with calculation methods which are cheap to run, convenient to use and which provide precision more than adequate for comparative calculations. There is no doubt that in this way, the design function can benefit from calculations now.

## 6. REFERENCES

1. Coles, D. and Hirst, E.A.: Computation of Turbulent Boundary Layers — 1968, AF OSR-IFD-Stanford Conference, Vol. 2, Thermosciences Division, Stanford University, Stanford 1969.
2. Rubesin, M.W.: Developments in the computation of turbulent boundary layers. AGARD Conference on Turbulent Boundary Layers; Experiments, Theory and Modelling, Den Haag, the Netherlands, 24-26 Sept. 1979.
3. Second Symposium on Turbulent Shear Flow, Proceedings Volume, London, 1979.
4. Cebeci, T. and Smith, A.M.O.: Analysis of Turbulent Boundary Layers, Academic Press, N.Y. 1974.
5. Bradshaw, P., Ferriss, D.H. and Atwell, N.P.: Calculation of boundary-layer development using the turbulent energy equations. *J. Fluid Mech.*, Vol. 28, p. 593, 1967.
6. Jones, W.P. and Launder, B.E.: The prediction of laminarization with a two-equation model of turbulence. *Int. J. Heat and Mass Transfer*, Vol. 15, p. 301, 1972.
7. Bradshaw, P. and Terrell, M.G.: The response of a turbulent boundary layer on an infinite swept wing to the sudden removal of pressure gradient. Aero Rept. 1305, 1969, National Physical Lab., London, England.
8. Vermeulen, A.J.: Measurements of three-dimensional turbulent boundary layers. Ph.D. Thesis, Univ. of Cambridge, 1971.
9. Cebeci, T. and Bradshaw, P.: Momentum Transfer in Boundary Layers, McGraw-Hill/Hemisphere, Washington, D.C., 1977.
10. Cebeci, T., Chang, K.C. and Bradshaw, P.: Solution of a hyperbolic system of turbulence-model equations by the "Box" scheme. Submitted for publication.
11. Cebeci, T., Carr, W.L. and Bradshaw, P.: Prediction of unsteady turbulent boundary layers with flow reversal. 2nd Symp. on Turbulent Shear Flows, p. 14.23, July 1979, London.
12. Hirsh, R.S., Friedman, D.M. and Cebeci, T.: Solution of turbulent transport equations by an accurate numerical method. Lecture Notes in Physics. Sixth Int. Conf. on Numerical Methods in Fluid Dynamics, Springer-Verlag, p. 274, 1979.
13. Simpson, R.L., Strickland, J.M. and Barr, P.W.: Features of separating turbulent boundary layers in the vicinity of separation. *J. Fluid Mech.*, Vol. 79, p. 553, 1977.
14. Durão, D.F.G. and Whitelaw, J.H.: Velocity characteristics of the flow in the near-wake of a disc. *J. Fluid Mech.*, Vol. 85, p. 269, 1978.
15. Durst, F. and Rastogi, A.K.: Turbulent flow over two-dimensional fences. Proc. of 2nd Symp. on Turbulent Shear Flows, p. 16.30, 1979, London.
16. Cebeci, T., Khalil, E.E. and Whitelaw, J.H.: Calculation of separated boundary-layer flows. To be published in the AIAA J., 1979.
17. Andreopoulos, J. and Bradshaw, P.: Private Communication.
18. Bradshaw, P.: Prediction of the turbulent near-wake of a symmetrical airfoil. AIAA J., Vol. 8, No. 8, pp. 1507-1508, 1970.
19. Townsend, A.A.: The flow in a turbulent boundary layer after a change in surface roughness. *J. Fluid Mech.*, Vol. 26, p. 255, 1966.

20. Rastogi, A.K. and Rodi, W.: Calculation of general three-dimensional turbulent boundary layers. AIAA J., Vol. 16, No. 2, pp. 151-159, 1978.
21. Van der Berg, B. and Elsenaar, A.: Measurements in a three-dimensional incompressible turbulent boundary layer in an adverse pressure gradient under infinite swept-wing conditions, National Aerospace Laboratory, NLR TR 72092U, The Netherlands.
22. Rotta, J.C.: A family of turbulence models for three-dimensional thin shear layers. 1st Symp. on Turbulent Shear Flows, University Park, Pa., pp. 10.27-10.34, 1977.
23. Cebeci, T., Kaups, K. and Ramsey, J.A.: A general method for calculating three-dimensional compressible laminar and turbulent boundary layers on arbitrary wings, NASA, CR-2777, 1977.
24. Kolbe, C.D. and Boltz, F.W.: The forces and pressure distribution at subsonic speeds on a plane wing having  $45^\circ$  of sweepback, an aspect ratio of 3, and a taper ratio of 0.5, NACA RM A51G31, 1951.
25. Meier, H.U. and Kreplin, H.P.: Experimental investigation of the transition and separation phenomena on a body of revolution. 2nd Symp. on Turbulent Shear Flows, p. 15.1, July 1979, London.
26. Kordulla, W.: Inviscid-viscous interaction in transonic flows about finite three-dimensional wings. AIAA J., Vol. 16, No. 4, pp. 369-376, 1978.
27. McLean, J.D.: Three-dimensional turbulent boundary-layer calculations for swept wings. AIAA Paper 77-3, 1977.
28. Humphrey, D.A.: Comparison of boundary-layer calculations for a wing: The May 1978 Stockholm Workshop test cases. The Aeronautical Research Institute of Sweden, FFA TN AE-1522, Stockholm, 1979.

#### ACKNOWLEDGMENT

This work was supported by Mr. W.C. Volz under contract N00019-78-M-0466. The authors acknowledge helpful discussions with Professors Peter Bradshaw and James H. Whitelaw of Imperial College, London.

## THE TURBULENT BOUNDARY LAYER AND THE CLOSURE PROBLEM

by

Leif N. Persen  
 Full Professor  
 Institutt for mekanikk  
 Universitetet i Trondheim  
 N.T.H. 7034 Trondheim  
 Norway

Abstract.

A short review of previous attempts to establish a proper phenomenological relation for turbulent flows is followed by a suggested approach to the problem in the case of a turbulent boundary layer. An attempt is made at showing the extreme flexibility that such a relation must exhibit if it is to account for effects of outside conditions and pre-history of the flow. By selecting proper "inner variables" as parameters and properly characterizing the outer flow it is shown how a sufficiently general phenomenological relation can be established and how the closure problem may thus be considered in a different perspective.

List of symbols.

$\bar{u}$	}	mean velocity components in the
$\bar{v}$		boundary layer
$p$		pressure
$x$		independent variable along the wall
$y$		independent variable normal to the wall
$\tau$		shear stress
$\tau_w$		shear stress at the wall
$v_*$		shear velocity
$\mu$		viscosity
$\rho$		density
$u'$	}	velocity fluctuations
$v'$		
$U(x)$		outside flow velocity parallel to the wall, general case
$U_0$		outside flow velocity parallel to the wall, flat plate
$x^+$	}	non-dimensional variables in the boundary layer
$y^+$		
$u^+$		non-dimensional velocity parallel to the wall
$u_\infty^+$		constant, limiting value of $u^+$ as $y^+ \rightarrow \infty$
$u_1^+$	}	coordinates indicating the joining point between the wall- and the wake region
$y_1^+$		
$y_f^+$		value of $y^+$ at the departure from (or arrival at) the flat plate locus
$\delta$ and $y_g$		boundary layer thickness
$l$		Prandtl's mixing length



$\xi$	limiting value of $u^+$ as $y \rightarrow \delta$	} "inner variables"
$y_0^+$	limiting value of $y^+$ as $y \rightarrow \delta$	
$\xi_i$ $y_{0,i}^+$	} initial values of $\xi, y_0^+$	
$A, \kappa, \alpha$		constants
$Re_E$	entry Reynolds number	

## 1. Introduction.

Ever since REYNOLDS [1] established the equations for the mean motion in turbulent flows, major efforts have been made to relate the Reynolds apparent stresses in some way to the mean flow field. The necessary relation is of a phenomenological character, i.e. it will either have to express an experimentally established fact or it will have to be introduced as a hypothesis. Such a hypothesis will however have to render results which are reasonably well supported by experimental evidence if it is to have more than academic interest. The phenomenological relationship is thus a piece of experimental information and the well known relation between the stress field and the deformation field in an elastic medium as well as the Stokes' hypothesis for a Newtonian fluid are examples of such relations.

The earliest attempts at establishing phenomenological relations for the Reynolds' apparent stresses followed more or less as analogies to the Stokes' hypothesis for a Newtonian fluid. Boussinesque's suggestion was followed by a more sophisticated approach whereby a mixing length was introduced. The concept of a mixing length was based on assumptions on what might be the important feature of turbulent flows. L. PRANDTL [2] introduced his mixing length through "a momentum transport theory" whereas G.I. TAYLOR [3] arrived at his formulation of a mixing length through a "vorticity transport theory". In this way they left a "legacy" to their successors in the sense that they introduced the "structure of turbulence" as a key to the understanding of turbulent flows. From such a structure of turbulence the answers to problems in turbulent flow would be deducible.

The nature of the Reynolds stresses differs from that of the stresses in the Stokes' hypothesis in that they are not related to the flow field through a property (i.e. viscosity) of the fluid. Thus one is faced with the problem of identifying the proper parameters through which the phenomenological relation(s) necessary for the closure of the problem should be expressed. A great step forward was taken when KOLMOGOROV [4] introduced the energy in the turbulent fluctuations as one such parameter. In addition he also introduced a second parameter without however specifying its physical interpretation. He presented transport equations for both these parameters and gave equations whereby the Reynolds stresses could be deduced once the two parameters were known. The equations contain constants to be determined from experiments, and these are supposed to be universally valid for all flows. In this way the closure problem appears to be solved.

PRANDTL [5] improved this in the sense that he based his deductions on the mechanical energy equation for the turbulent fluctuations. He formulates this equation such that it contains two terms caused by the viscous forces; one term which expresses the total work done by these forces on an element as it moves and deforms from which he subtracts a second term which represents that part of the total work done which is converted into heat. In this way the second parameter, the dissipation of turbulent energy, is introduced. This procedure is however marred by the fact that due to the non-linearity of the basic equations the transport equations deduced from them for say the Reynolds stresses will contain the one-point trippelcorrelations. Thus one will always end up with fewer equations than unknowns. The closure of the system is achieved through a number of estimates of the different terms in the mechanical energy equation for the fluctuations. In these estimates several numerical constants appear and these are determined through information obtained from experiments. These constants should again be of universal character, but unfortunately they are not.

Most of the later theories for turbulent flow follow in the paths set by these earlier attempts, and consequently they also suffer from the necessity of forcing a closure of the problem through some type of hypothesis whereby difficult terms in the equations are estimated. The fact that a closure problem exists makes it questionable if the right parameters are found through which the necessary phenomenological relation(s) can be expressed.

BRADSHAW [6] presents a model for the turbulent boundary layer in which empirical functions are introduced instead of only empirical constants. His main point is well taken and may perhaps be expressed through the following statement: For boundary layer flow with arbitrary pressure gradients the upstream history of the boundary layer cannot be ignored and must somehow be accounted for through a proper phenomenological relation. This may mean that one must search for a relation that goes beyond whatever can be deduced from an eventual "structure of turbulence".

This rather brief and sketchy account of the development serves as a background for suggesting a somewhat different approach that seems to work well in the case of two-dimensional boundary layer flow. It can be looked upon as a continuation of the line of reasoning that may have led Bradshaw in his efforts, but it goes beyond that in the sense that contrary to the Bradshaw approach, no term in the basic equations needs to be estimated from models of a certain structure of turbulence.

## 2. The two-dimensional boundary layer.

The basic equations governing the mean flow in turbulent boundary layers are the equation of continuity:

$$\frac{\partial \bar{u}}{\partial x} + \frac{\partial \bar{v}}{\partial y} = 0 \quad (2.1)$$

and the equation of steady motion:

$$\bar{u} \frac{\partial \bar{u}}{\partial x} + \bar{v} \frac{\partial \bar{u}}{\partial y} = -\frac{1}{\rho} \frac{dp}{dx} + \frac{1}{\rho} \frac{\partial \tau}{\partial y} \quad (2.2)$$

where the total shear stress  $\tau$  is given as the sum of the Reynolds stress and the viscous shear stress due to the mean motion

$$\tau = \mu \frac{\partial \bar{u}}{\partial y} - \rho \overline{u'v'} \quad (2.3)$$

The usual notation has been used and it is stressed that the pressure gradient is given by the known outside flow  $U(x)$ :

$$-\frac{1}{\rho} \frac{dp}{dx} = U \frac{dU}{dx} \quad (2.4)$$

This set of basic equations is indeterminate in the sense that it contains one unknown more than the number of equations. The missing link is some kind of phenomenological relation which will close the system.

The specific form of (2.1), (2.2) and (2.4) is such that  $\bar{v}$  may be eliminated:

$$\bar{u} \frac{\partial \bar{u}}{\partial x} - \frac{\partial \bar{u}}{\partial y} \int_0^y \frac{\partial \bar{u}}{\partial x} dy = U \frac{dU}{dx} + \frac{1}{\rho} \frac{\partial \tau}{\partial y} \quad (2.5)$$

This equation may be formally integrated:

$$\frac{\tau_w}{\rho} \left( \frac{\tau}{\tau_w} - 1 \right) = 2 \int_0^y \bar{u} \frac{\partial \bar{u}}{\partial x} dy - \bar{u} \int_0^y \frac{\partial \bar{u}}{\partial x} dy - U \frac{dU}{dx} y \quad (2.6)$$

where  $\tau_w$  is the shear stress at the wall.

The non-dimensional variables usually introduced to describe turbulent boundary layer flow are

$$\left. \begin{aligned} u^+ &= \frac{\bar{u}}{v_*} \\ y^+ &= \frac{y v_*}{\nu} \\ x^+ &= \int_{x_0}^x \frac{v_*}{\nu} dx \end{aligned} \right\} \quad (2.7)$$

where  $x_0$  an arbitrary position along the wall and where the shear velocity  $v_*$  is defined as a function of  $x$  through

$$v_* = \sqrt{\tau_w / \rho} \quad (2.8)$$

Because of their importance in the later deductions specific attention is drawn to the limiting values of  $u^+$  and  $y^+$  at the outer edge of the boundary layer

$$\left. \begin{aligned} \bar{u} &\rightarrow U(x) \quad \text{as } y \rightarrow \delta \\ u^+ &\rightarrow \frac{U}{v_*} = \xi \quad \text{as } y^+ \rightarrow \frac{\delta v_*}{\nu} = y_0^+ \end{aligned} \right\} \quad (2.9)$$

It is seen that the assumed asymptotic character of  $u^+$  as a function of  $y^+$  at the outer edge of the boundary layer is replaced by the assumption that  $u^+ \rightarrow \xi$  for a finite value of  $y^+ = y_0^+$ . This is however a simplification of minor consequence and may even under certain circumstances be regarded as an improvement.

The velocity  $\bar{u}$  as a function of  $x$  and  $y$  is now replaced by the non-dimensional velocity  $u^+$  as a function of the independent variables  $x^+$  and  $y^+$  with no loss of generality. The basic equation of the turbulent boundary layer (2.6) will then upon some lengthy but rather straight forward algebra be brought in the form

$$\left. \begin{aligned} \frac{\tau}{\tau_w} - 1 = & 2 \int_0^{y^+} u^+ \frac{\partial u^+}{\partial x^+} dy^+ - u^+ \int_0^{y^+} \frac{\partial u^+}{\partial x^+} dy^+ - \frac{1}{\xi} \frac{d\xi}{dx^+} \int_0^{y^+} (u^+)^2 dy^+ + \\ & + \frac{1}{U} \frac{dU}{dx^+} \left[ \int_0^{y^+} (u^+)^2 dy^+ - \xi^2 y^+ \right] \end{aligned} \right\} \quad (2.10)$$

This final form of the basic equation contains three unknown functions,  $\tau, u^+$  and  $\xi$ , of which the first two depend on  $x^+$  and  $y^+$  whereas the last one depends on  $x^+$  only. Its similarity to the von Kármán's integral momentum equation is obvious but it is stressed that it is not an integral equation in the sense that one of the variables has been eliminated through integration. It must be supplemented with a proper phenomenological relation before it can be regarded as a basic equation for turbulent boundary layer flow. The subsequent presentation will be concerned with the nature of such a relation.

### 3. The nature of the phenomenological relation.

In contemplating the nature of phenomenological relation it should be realized that such a relation does not necessarily have to relate the Reynolds stresses to the flow-field directly. Any experimentally supported relation of universal character which contains sufficient information for the closure of the problem will do. KESTIN and PERSEN [7] showed how the law of the wall could be considered as such an information and this was elaborated on by BRAND and PERSEN [8]. PERSEN [9] showed how a corresponding idea solved the transfer of heat through turbulent boundary layers and what might have been considered a coherent approach to the diffusion of heat as well as momentum in turbulent boundary layers was established. Although this approach suffers both from the lack of general applicability as well as from neglected details of the non-dimensional velocity profiles, its extreme simplicity and its relevance to the subsequent deductions warrant a short recapitulation.

The law of the wall states that the non-dimensional velocity  $u^+$  is a function of  $y^+$  only, and that no explicit  $x$ -dependence is present in this relation. It can be expressed by

$$y^+ = f(u^+) \quad (3.1)$$

and SPALDING [10] gave the following empirical specification of it:

$$f(u^+) = u^+ + A[e^{\kappa u^+} - 1 - \kappa u^+ - (\kappa u^+)^2/2 - (\kappa u^+)^3/6 - (\kappa u^+)^4/24] \quad (3.2)$$

At this point a few comments on phenomenological relationships in general may be appropriate. The phenomenological relationship for a linear elastic material is expressed through two constants only. The simplicity of this relationship is extreme. For any type of nonlinearity of the phenomenological relationship a functional expression for this relationship must be given. This functional expression is experimentally established and is empirical in nature. Thus its mathematical formulation will always appear as a result of a best fit procedure. Spalding's formulation (3.2) is just that.

The formulation (3.2) is valid from the wall and satisfies the right conditions at the wall. Fig.1 shows a comparison between Spalding's function with  $A=0.1108$  and  $\kappa=0.4$  and the data obtained on a flat plate by WIEGHARDT and TILLMANN [11] as described by COLES [12]. It is noticed that the function gives a curve that goes fairly well through the data points without however describing the detailed trace of the data points from each station. If one is satisfied with such an approximate phenomenological relation as the one given in (3.1), the solution to the problem in the case of a flat plate follows immediately by realizing that (2.10) is then reduced to

$$\frac{\tau}{\tau_w} - 1 = - \frac{1}{\xi} \frac{d\xi}{dx^+} \int_0^{y^+} (u^+)^2 dy^+ \quad (3.3)$$

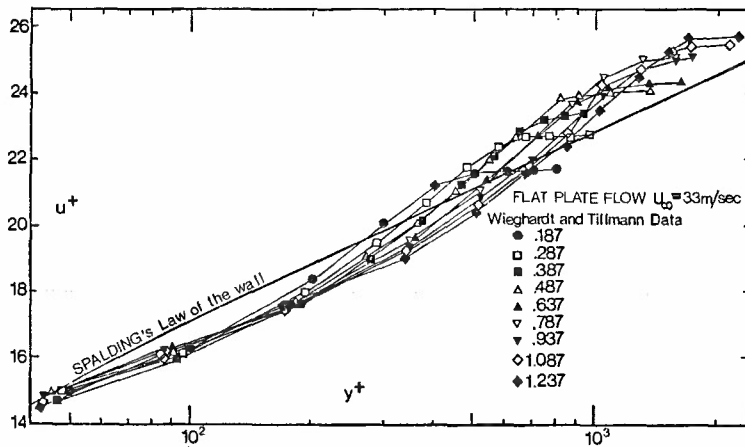


Fig.1 Comparison between experimental data obtained by WIEGHARDT/TILLMANN [11] on a flat plate and SPALDING's formulation [10] of the law of the wall

The fact that the law of the wall is assumed universally valid implies that the limiting values  $\xi, y_o^+$  at the outer edge of the boundary layer also satisfy (3.1):

$$y_o^+ = f(\xi) \quad (3.4)$$

Now, (3.3) is also valid at the outer edge of the boundary layer where presumably  $\tau=0$ , i.e.

$$\frac{1}{\xi} \frac{d\xi}{dx^+} \int_0^{y_o^+} (u^+)^2 dy^+ = 1 \quad (3.5)$$

One has here obtained a first order differential equation for  $\xi$  as a function of  $x^+$ , and all other pertinent quantities can then be found. The solution from first principles has been established, and it is realized that the phenomenological relationship used in this case lies first in the experimentally supported fact that one has a universally valid similarity law in (3.1) and secondly that the parameters  $\xi, y_o^+$  satisfy this law.

This approach works rather well when it is used to compute the shear stress at the wall for a flat plate. The reason for this is found in the fact that the end values  $\xi, y_o^+$  for each profile satisfy (3.4) rather well. Realizing this WHITE and CHRISTOPH [13] extended this procedure to incorporate a number of different cases of boundary layer flows. From a basic point of view, however, a proper phenomenological relation which accounts for details in our knowledge for turbulent boundary layer flow is not incorporated in their approach.

This survey has shown one possible type of phenomenological relation which when used to supplement the basic equation (2.10) permits a solution to be found. It is based on experimental evidence but its formulation is too simple. The main objection to it is that it neither reflects the influence of outside manipulation nor the history of the flow. A proper phenomenological relation will have to exhibit an influence of these conditions whereby the outside manipulation mainly may be taken to be caused by the pressure gradient.

#### 4. The two regions of a turbulent boundary layer.

A scrutiny of the experimental results compiled in the Proceedings of the Stanford Conference 1968 performed by PERSEN [14] reveals that the non-dimensional velocity profile  $u^+$  versus  $y^+$  exhibits a similarity type behaviour which is different in the two regions into which the boundary layer may be divided. In the inner "wall region" the profile is expressed by the law of the wall (3.1) for which Spalding's formulation (3.2) can be used with the constants  $A$  and  $\kappa$  changed as follows:

$$A = 0.015, \quad \kappa = 0.53227 \quad (4.1)$$

In agreement with COLES' [12] presentation of the Stanford data, and with PERRY, BELL and JOUBERT [15], this inner law is not influenced by any type of pressure gradient one may apply. In the outer "wake region" the profile can be expressed by:

$$\frac{u^+ - u_\infty^+}{\xi - u_\infty^+} = \exp \left[ -\frac{1}{\alpha^2} (y_o^+ - y^+)^2 \right] \quad (4.2)$$

where the constant  $\alpha$  is given by

$$\frac{1}{\alpha} = (y_0^+ - y_1^+)^{-2} \ln \left( \frac{\xi - u_\infty^+}{u_1^+ - u_\infty^+} \right) \quad (4.3)$$

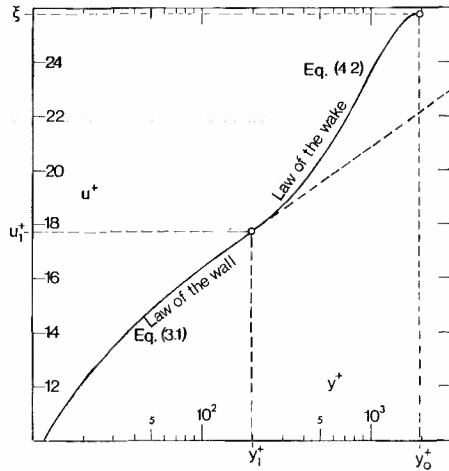


Fig. 2 Plot of the law of the wall and the law of the wake with  $(u_1^+, y_1^+)$  giving the point at which the two laws join.

The profile will then appear as shown in Fig. 2 where  $u_1^+, y_1^+$  give the point where the two regions meet. At the point  $u^+ = \xi, y^+ = y_0^+$  the profile exhibits a horizontal tangent. If this point is known, the point  $u_1^+, y_1^+$  is found by claiming that the expressions for the profile in the two regions go through this point with a common tangent. The parameter  $u_1^+$  is a constant in most cases and gives the limiting value of  $u^+$  as  $y^+ \rightarrow \infty$ . (The only cases where  $u_\infty^+$  is depending on  $x^+$  may occur in transient flows).

The profile is thus completely determined once  $\xi, y_0^+$  and  $u_\infty^+$  are specified.

##### 5. The phenomenological relation.

At this point it is possible to conceive of a phenomenological relation expressed through what may be called the "inner variables"  $\xi, y_0^+$ . It takes the form of a relation between the two which is characteristic of the situation and which may be expressed as

$$y_0^+ = K_0(\xi) \quad (5.1)$$

Such a phenomenological relation cannot be unique in the sense that it remains unchanged by whatever manipulations the boundary layer undergoes or has undergone. Brandshaw's contention that the history of the boundary layer must be accounted for by the phenomenological relation it met through specification of the initial values of this relation. The relation must reflect outside influence exerted on the boundary layer (pressure gradients etc.) but it must also exhibit some sort of uniqueness for each class of flow. Equation (5.1) represents a curve in Fig. 2 which will give the "locus of  $\xi$ ". It is realized that one should expect some explicit  $x$ -dependence to appear in the expression for the locus. This point will be taken up in the subsequent discussion. For the moment it suffices to assume that a relation like (5.1) exists.

Since the boundary layer now is divided into two regions, the basic equation (2.10) will have to be reformulated by introduction of the similarity profiles (3.1) and (4.2) in the two regions respectively.

In the wall region the function  $G(u^+)$  is defined as

$$G(u^+) = \int_0^{u^+} (u^+)^2 f'(u^+) du^+ \quad (5.2)$$

where  $f(u^+)$  is defined in (3.1). Equation (2.10) is then easily seen to simplify to:

$$\frac{\tau}{\tau_w} - 1 = - \frac{1}{\xi} \frac{d\xi}{dx^+} G(u^+) - \frac{1}{U} \frac{dU}{dx^+} \left[ \xi^2 f(u^+) - G(u^+) \right] \quad (5.3)$$

In the wake region the situation is somewhat more complicated. To simplify the expressions the following abbreviations are introduced:

$$\frac{dy_1^+}{dx^+} = f'(u_1^+) \frac{du_1^+}{dx^+} \quad (5.4)$$

$$\frac{du_1^+}{dx^+} = K_1(\xi) \frac{d\xi}{dx^+} \quad (5.5)$$

$$\frac{d}{dx^+} \left( \frac{1}{\alpha^2} \right) = K_2(\xi) \frac{d\xi}{dx^+} \quad (5.6)$$

$$\frac{\partial u^+}{\partial x^+} = K_3(\xi, y^+) \frac{d\xi}{dx^+} \quad (5.7)$$

where

$$K_1(\xi) = \frac{K'_0(\xi) - 2f'(u_1^+) \left( \frac{u_1^+ - u_\infty^+}{\xi - u_\infty^+} \right)}{\left( \frac{f''(u_1^+)}{f'(u_1^+)} + \frac{1}{u_1^+ - u_\infty^+} \right) (y_0^+ - y_1^+) - f'(u_1^+)} \quad (5.8)$$

$$K_2(\xi) = \left( \frac{1}{\xi - u_\infty^+} - \frac{K_1(\xi)}{u_1^+ - u_\infty^+} \right) (y_0^+ - y_1^+)^{-2} - \frac{2}{\alpha^2} \left\{ K'_0(\xi) - f'(u_1^+) K_1(\xi) \right\} (y_0^+ - y_1^+)^{-1} \quad (5.9)$$

$$K_3(\xi, y^+) = \frac{u^+ - u_\infty^+}{\xi - u_\infty^+} - (u^+ - u_\infty^+) \left\{ K_2(\xi) (y_0^+ - y^+)^2 + \frac{2}{\alpha^2} (y_0^+ - y^+) K'_0(\xi) \right\} \quad (5.10)$$

Finally then (2.10) transforms into:

$$\left. \begin{aligned} \frac{\tau}{\tau_w} = 1 + \frac{1}{\xi} \frac{d\xi}{dx^+} & \left\{ 2\xi \int_{y_1^+}^{y^+} u^+ K_3(\xi, y^+) dy^+ - u^+ \xi \int_{y_1^+}^{y^+} K_3(\xi, y^+) dy^+ - G(u_1^+) \right. \\ & \left. - \int_{y_1^+}^{y^+} (u^+)^2 dy^+ \right\} - \frac{1}{U} \frac{dU}{dx^+} \left[ \xi^2 y^+ - G(u_1^+) - \int_{y_1^+}^{y^+} (u^+)^2 dy^+ \right] \end{aligned} \right\} \quad (5.11)$$

In this equation  $\tau$  appears as a function of  $\xi, x^+$  and  $y^+$ . One may thus conclude that in addition to the specified universal profile  $u^+$  versus  $y^+$  a functional relationship between  $\xi$  and  $y_0^+$  (the locus of  $\xi$ ) is all that is needed as a proper phenomenological relation that neither gives redundant information nor leaves a closure problem. First the influence of the outer conditions on the locus of  $\xi$  will be nearer explored.

## 6. Characterization of the outside flow. The locus of $\xi$ .

It has been emphasized that the phenomenological relation must be expected to be influenced by the outside conditions, and as a main source of such influence the pressure gradient enters the picture. It is however not sufficient to characterize this gradient verbally as "mild, moderate or strong". One must find a way to characterize the outside flow quantitatively whereby the approach should be kept as general as possible.

First the flat plate situation ( $\partial p / \partial x = 0$ ) is considered. This simple case does not impose any explicit  $x$ -dependence from the outside flow, and a dimensional analysis then indicates that the locus of  $\xi$  expressed through (5.1) is adequate. Experimental evidence is used to establish the following flat plate locus: [PERSEN (16)].

$$\xi = 2.83649 \ln(y_0^+ / 0.216) \quad (6.1)$$

The locus is shown in Fig. 3 as a straight dashed line, and is in complete agreement with the result obtained by MILLIKAN [17]. It represents the only input necessary for solving the case of a turbulent boundary layer on a flat plate with none of the flaws in it which characterize the approach in Sec. 3.

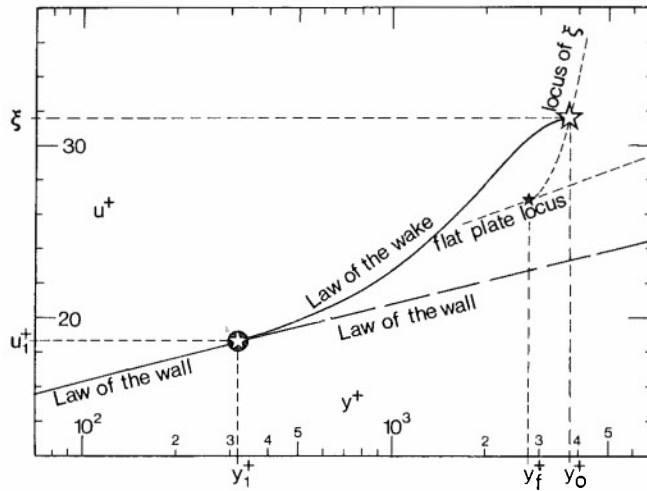


Fig. 3 Plot of an arbitrary profile  $u^+$  versus  $y^+$  with the flat plate locus and the locus of  $\xi$ , case I, indicated.

When the boundary layer is subjected to an *adverse pressure gradient*, the outside flow can usually with good accuracy be approximated in either of two ways:

$$\text{Case I, } dp/dx > 0, \quad d^2p/dx^2 < 0:$$

$$U/U_E = (1 + x/x_o)^{-1} \quad (6.2)$$

$$\text{Case II, } dp/dx > 0, \quad d^2p/dx^2 > 0:$$

$$U/U_E = 1 - \zeta^2 \quad (6.3)$$

$$\text{where } \zeta = (1 + \frac{x}{x_o})\beta \quad (6.4)$$

In these expressions  $x_o, \beta$  and  $U_E$  are constants determined through a best fit procedure to the outside velocity which must be known. It should be mentioned that all cases with adverse pressure gradients gathered in the Proceedings of the Stanford Conference, COLES [12], can be represented in either of the two ways. The way in which the outside flow varies will determine a length scale  $x_o$  (Case I) and  $x_o/\beta$  (Case II) and an "entry" velocity  $U_E$ , thus permitting an "entry" Reynolds number  $Re_E$  to be formed:

$$\left. \begin{aligned} \text{Case I: } Re_E &= \frac{U_E x_o}{\nu} \\ \text{Case II: } Re_E &= \frac{U_E x_o / \beta}{\nu} \end{aligned} \right\} \quad (6.5)$$

The two cases of adverse pressure gradients will both lead to separation. However, Case I starts out with a large gradient that decreases downstream whereas Case II starts out with a small gradient that steadily increases downstream. In the latter case the tendency towards separation becomes stronger as one proceeds downstream and separation usually takes place before the pressure gradient has reached its maximum value. In the first case one might say that the tendency towards separation diminishes downstream. One may therefore perhaps expect the locus of  $\xi$  to be influenced by this fact as will be shown subsequently.

Contemplating the variables that might possibly influence the locus of  $\xi$ , one will find it natural that (5.1) be replaced by a relation like:

$$y_o^+ = F(\xi, \xi_i, y_o^+, x) \quad (6.6)$$

where  $\xi_i, y_o^+$  represent the initial condition for the locus of  $\xi$  and thus account for the influence of the history of the boundary layer. Experimental evidence seems however to indicate that no explicit  $x$ -dependence occur in either of the two cases considered here. The expected  $x$ -dependence may be replaced by a dependence on the Reynolds number  $Re_E$  characterizing the outside flow. If the history of the boundary layer is such that it starts out from a flat plate situation,  $\xi_i$  and  $y_o^+$  can also be expressed through  $Re_E$ . Thus (6.6) will under those conditions reduce to

$$y_o^+ = F(\xi, Re_E) \quad (6.7)$$

which corresponds to (5.1). The actual formulation of the locus of  $\xi$  in Case I is as follows:

$$y_f^+ = 0.00534 Re_E^{0.8099} \quad (6.8)$$

$$\xi = 2.8365 \ln y_o^+ + 4.347 + 47.236 [\ln(y_o^+/y_f^+)]^2 \quad (6.9)$$

Here  $y_f^+$  is the point on the flat plate locus from which the locus of  $\xi$  departs as shown in Fig. 3. The locus itself is modelled as a parabola of the same shape irrespective of its position and is thus a similarity curve. Experimental results indicate that this is true also when the situation is such that the locus does not start out from the flat plate situation but experimental evidence is insufficient to be conclusive in this case.

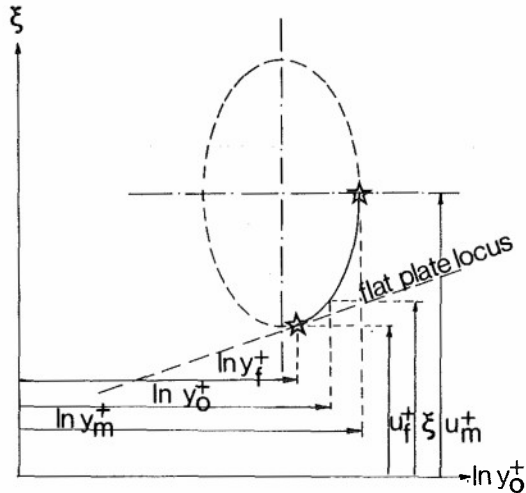


Fig. 4 Sketch of the locus of  $\xi$  for Case II of flow with an adverse pressure gradient.

Separation occurs when the locus of  $\xi$  in Fig. 3 exhibits a vertical tangent. Because of the parabolic shape chosen for the locus of  $\xi$  in Case I, separation will not be predicted. This is done deliberately because experimental evidence is vague on when separation occurs. In Case II, however, separation most definitely will occur very rapidly and the locus will have to exhibit this. Fig. 4 shows how an ellipse is used to model the locus of  $\xi$  in this case. The separation point is given by  $(u_m^+, y_m^+)$  and the point of departure from the flat plate locus is given through  $y_f^+$ . These three parameters are all given through the entry Reynolds number  $Re_E$ :

$$y_f^+ = 200.98 \ln(Re_E) - 1765$$

$$\ln(y_m^+/y_f^+) = 0.300 \ln(Re_E) - 4.21 \quad (6.10)$$

$$u_m^+ - u_f^+ = 9.374 \ln(Re_E) - 139.78$$

The locus of  $\xi$  is given as

$$\xi = 2.8365 \ln(y_0^+/0.216) + (u_m^+ - u_f^+) \left[ 1 - \sqrt{1 - \left[ \frac{\ln(y_0^+/y_f^+)}{\ln(y_m^+/y_f^+)} \right]^2} \right] \quad (6.11)$$

Perhaps the most striking example on how the history of the boundary layer influences the locus of  $\xi$  is given by the so-called *relaxing flow*. In this case the boundary layer is manipulated in such a way that it is brought close to separation and is then relaxed with zero pressure gradient. The locus of  $\xi$  will then be a curve that starts out at  $(\xi_i, y_{0,i}^+)$  and joins the flat plate locus at  $y_f^+$  as shown in Fig. 5. The curve will be given by:

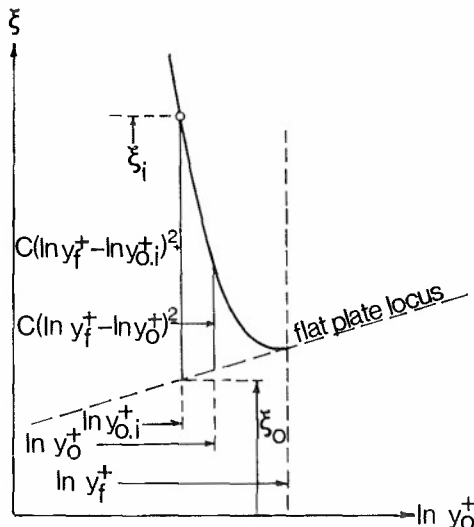


Fig. 5 The locus of  $\xi$  for relaxing flows.

$$\xi = 2.8365 \ln y_0^+ + 4.347 + 17.0 [\ln(y_f^+/y_0^+)]^2 \quad (6.12)$$

where

$$y_f^+ = y_{0,i}^+ \exp \left[ \sqrt{(\xi_i \xi_0)/17} \right] \quad (6.13)$$

The locus of  $\xi$  for cases with a *favourable pressure gradient* is not given explicitly here. The locus will be found in the region in Fig. 3 bounded by the flat plate locus and the extension beyond  $y_1^+$  of the law of the wall. All data points available from the Stanford Conference 1968 for this case fall in this region and seem to indicate a straight line locus falling within this region. This case as well as the case of *equilibrium flows* fall



within the framework of the present investigation but will be excluded here. The main point has been made plausible: The locus of  $\xi$  has been shown to exhibit a general character for each type of flow considered. It reflects the history as well as the influence of the outside pressure gradient. It thus serves well as the additional piece of experimental information necessary in addition to the universal profile to form the phenomenological relation.

## 7. The solution.

The final solution to the problem of turbulent boundary layer flow follows immediately from the basic equation (5.11) once the idea of the locus of  $\xi$  has been substantiated. One observes that this equation must be valid also at the outer edge of the boundary layer ( $u = \xi, y^+ = y_o^+$ ) where presumably  $\tau = 0$ , i.e.

$$0 = 1 + \frac{1}{\xi} \frac{d\xi}{dx^+} \left\{ 2\xi \int_{y_1^+}^{y_o^+} u^+(y^+) K_3(\xi, y^+) dy^+ - \xi^2 \int_{y_1^+}^{y_o^+} K_3(\xi, y^+) dy^+ \right. \\ \left. - G(u_1^+) - \int_{y_1^+}^{y_o^+} (u^+)^2 dy^+ \right\} - \frac{1}{U} \frac{dU}{dx^+} \left[ \xi^2 y_o^+ - G(u_1^+) - \int_{y_1^+}^{y_o^+} (u^+)^2 dy^+ \right] \quad (7.1)$$

In this equation  $dU/U dx^+$  appears as a known function. For the different cases the following expressions are obtained:

Flat plate:  $dU/dx^+ = 0$ ,

$$\frac{1}{\xi} \frac{d\xi}{dx^+} = \frac{v}{U} \frac{d\xi}{dx} = d\xi/d(Re_x) \quad , \quad Re_x = \frac{U_o x}{v} \quad (7.2)$$

Adverse pressure gradient, Case I:

$$\frac{1}{U} \frac{dU}{dx^+} = \frac{\xi}{Re_E} \quad , \quad \frac{1}{\xi} \frac{d\xi}{dx^+} = \frac{1}{Re_E} \frac{d\xi}{d\zeta} (1+\zeta) \\ \zeta = x/x_o \quad (7.3)$$

Adverse pressure gradient, Case II:

$$\frac{1}{U} \frac{dU}{dx^+} = -\frac{\xi}{Re_E} \cdot \frac{2\zeta}{(1-\zeta^2)^2} \quad , \quad \frac{1}{\xi} \frac{d\xi}{dx^+} = \frac{1}{Re_E} \cdot \frac{d\xi}{d\zeta} (1-\zeta^2)^{-1} \\ \zeta = (1 + \frac{x}{x_o}) \beta \quad (7.4)$$

Favourable pressure gradient:  $U = U_E (1 + \frac{x}{x_o})$

$$\frac{1}{U} \frac{dU}{dx^+} = \frac{\xi}{Re_E} (1+\zeta)^{-2} \quad , \quad \frac{1}{\xi} \frac{d\xi}{dx^+} = \frac{1}{Re_E} \cdot \frac{d\xi}{d\zeta} (1+\zeta)^{-1} \\ \zeta = \frac{x}{x_o} \quad (7.5)$$

In this survey also the case of a favourable pressure gradient has been listed under the assumption that most such cases can be approximated by a linear increase in the outside velocity  $U(x)$  with increasing distance  $x$  along the wall.

For the sake of brevity the following notation is introduced:

$$K_4(\xi, y^+) = 2\xi \int_{y_1^+}^{y^+} u^+ K_3(\xi, y^+) dy^+ - u^+ \xi \int_{y_1^+}^{y^+} K_3(\xi, y^+) dy^+ \\ - G(u_1^+) - \int_{y_1^+}^{y^+} (u^+)^2 dy^+ \quad (7.6)$$

$$K_5(\xi, y^+) = \frac{\xi}{Re_E} \left[ \xi^2 y^+ - G(u_1^+) - \int_{y_1^+}^{y^+} (u^+)^2 dy^+ \right] \quad (7.6)$$

Thus one will find that in the different cases the differential equation for  $\xi$  as a function of the non-dimensional distance along the wall may be expressed as follows:

The flat plate:

$$-d(Re_x) = d\xi K_4(\xi, y_0^+) \quad (7.7)$$

Adverse pressure gradient; Case I:

$$\frac{d\xi}{1+\zeta} = \frac{-K_4(\xi, y_0^+) d\xi}{[1+K_5(\xi, y_0^+)] Re_E} \quad (7.8)$$

Adverse pressure gradient; Case II:

$$\frac{d\xi}{d\zeta} = - \frac{(1-\zeta^2) + \frac{2\zeta}{1-\zeta^2} K_5(\xi, y_0^+)}{K_4(\xi, y_0^+) / Re_E} \quad (7.9)$$

Favourable pressure gradient:

$$\frac{d\xi}{d\zeta} = - \frac{(1+\zeta) - (1+\zeta)^{-1} K_5(\xi, y_0^+)}{K_4(\xi, y_0^+) / Re_E} \quad (7.10)$$

The differential equations in this list are easily solved once the locus of  $\xi$  is known (whereby  $y_0^+$  as a function of  $\xi$  is given). One may then proceed to calculate measured quantities for comparison. This has been done by PERSEN [14] and only a few additional remarks will be made here.

## 8. Some numerical results.

Previous attempts at establishing a proper phenomenological relationship may now be examined in view of the present approach. Formost among those is Prandtl's mixing length theory. The mixing length  $l$  is defined through the shear stress

$$\tau = \rho l^2 \left( \frac{\partial u}{\partial y} \right)^2 \quad (8.1)$$

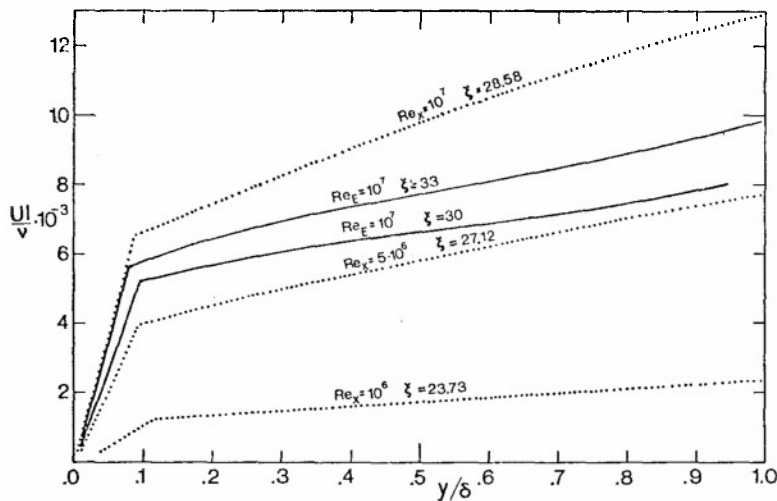


Fig. 6 Prandtl's mixing length  $l$  plotted as a function of  $y/\delta$ .  
 ..... flat plate at different locations  $R$   
 ——— adverse pressure gradient, case I,  $\infty$  at different locations (given by  $\xi$ )

In the present notation this equation may easily be reformulated as

$$\frac{\tau}{\tau_w} = \zeta^2 \xi^2 \left( \frac{\partial u^+}{\partial y^+} \right)^2 \cdot \frac{U^2}{v^2} \quad (8.2)$$

or

$$\frac{U\zeta}{v} = \xi \sqrt{\frac{\tau}{\tau_w} \frac{\partial u^+}{\partial y^+}} \quad (8.3)$$

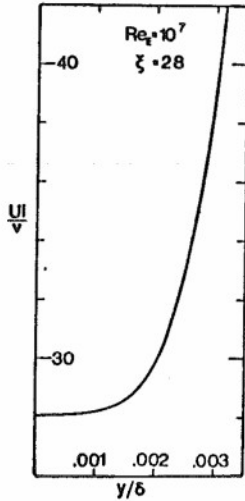


Fig. 7 Detail of Fig. 6 for small values of  $u/\delta$ .

BAKER and LAUNDER [18] measured the mixing length  $l$  over the boundary layer thickness  $y_g$  on a flat plate and using  $y_g$  to non-dimensionalize the results, they obtained data which are replotted in Fig. 8. Irrespective of the position along the plate these data are seen to coalesce into one straight line within the wall region. This straight line is given as  $l \approx 0.425y$ . One may use the present approach to put this result in perspective. Fig. 9 shows computed points for both a flat plate and for a special case of adverse pressure gradient. These points do indeed coalesce, but the straight line is influenced by the pressure gradient. Thus the straight line for the flat plate is given as  $l \approx 0.61y$ .

The result obtained for the flat plate seems to indicate a connection with the von Kármán's constant  $\kappa$ . This constant is given as

$$\kappa = \left( \frac{\partial^2 u^+}{\partial y^{+2}} \right) \sqrt{\frac{\tau}{\tau_w} \frac{\partial u^+}{\partial y^+}} \quad (8.4)$$

and is easily computed using the present approach. The result is exhibited in Fig. 10 for the inner region.

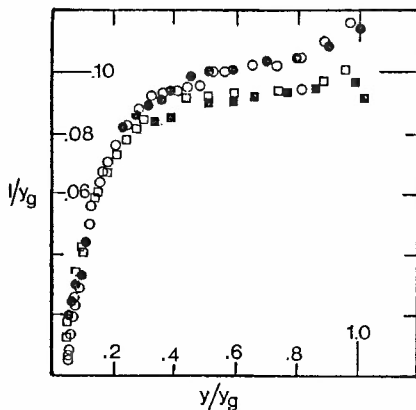


Fig. 8 Replot of the results of BAKER and LAUNDER [18].

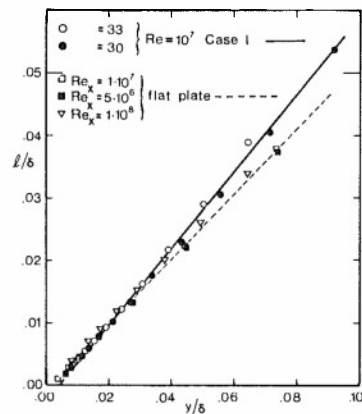


Fig. 9  $l/\delta$  plotted as function of  $y/\delta$ . Points are computed and straight lines are fitted to these data.

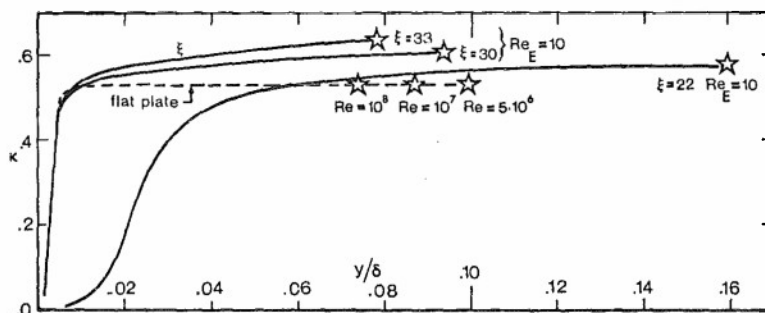


Fig. 10 Distribution of von Kármán's constant  $\kappa$  over the inner (wall) region. (☆ denotes the outer edge of the inner region).

The von Kármán's constant is defined through the second derivative of the curve  $u^+$  versus  $y^+$ . Since this curve exhibits an inflection point in the outer region, the value of  $\kappa$  is not computed in this region.

Fig. 10 shows that  $\kappa$  is indeed constant over the major portion of the inner region (the laminar sublayer excluded), but that the value of this constant change with the pressure gradient, and to some extent also with position. In general the results seem to indicate that both the concept of a mixing length and the concepts of local similarity underlying the von Kármán's concept are too simple to account for the rather complex behaviour of a turbulent boundary layer being encompassed by the present approach.

## 9. Summary.

This investigation may be summed up as follows:

1. The non-dimensional profile  $u^+$  versus  $y^+$  in a turbulent boundary layer is usually assumed to exhibit an asymptotic behaviour at the outer edge of the boundary layer where  $u^+ \rightarrow \xi$  as  $y^+ \rightarrow \infty$ . No error of partial importance is involved in replacing this assumption by assuming this value to be reached at a finite value of  $y^+$ , say  $y_0^+$ . Thus the two inner variables  $\xi$  and  $y_0^+$  are defined.
2. It has been demonstrated for different types of boundary layer flow that the non-dimensional profile can be considered built up of two parts; the inner region governed by the law of the wall and the outer region governed by the law of the wake. Improved mathematical expressions for the profile in these two regions are given, and as far as can be judged from available experimental evidence a "universal" validity of these may be assumed.
3. The investigation reveals that the point  $\xi, y_0^+$  of the non-dimensional profile is located on a curve called "the locus of  $\xi$ " which can be considered as the only additional piece of information to conclude the phenomenological relation necessary for the solution of the problem. The locus of  $\xi$  characterizes the flow. It will be influenced by the initial- and boundary conditions thus representing the influence of the immediate history of the flow as well as of the pressure gradient. However, the contention is that although the shape of the locus is defined through characteristic parameters of the outside flow, the locus exhibits a "universal" character for each type of flow.
4. Such "universal" loci are given for cases with adverse pressure gradients (Case I and II), for the flat plate and for relaxing flow. In the last case the pre-history of the flow is specified through the initial values  $\xi_i, y_{0,i}^+$ . In the first cases the pre-history of the flow is supposed to be a flat plate situation. For favourable gradients as well as for equilibrium flows the proper loci are presently being investigated.
5. The mathematical deductions are carried out to a point where the fundamental equation becomes a first order differential equation for  $\xi$  as a function of the non-dimensional distance along the wall. Since a number of numerical schemes are available for a numerical solution of such equations, this is considered to be the solution to the problem. The author will upon request supply information on the computer programs built upon this approach whereby separation among several other features in the case of adverse pressure gradients will be predictable.

6. In this investigation the closure problem of turbulent flow was intended illuminated by a direct approach to the problem in the simple case of boundary layer flow. By selecting  $\xi, y_0^+$  as the key "inner variables" and expressing the necessary phenomenological relation through these, it is possible to show how outside conditions like prehistory of the flow and the pressure gradient influence this relation. Such an influence is an expected one and it is difficult to perceive how it could be deduced from a concept of a local "structure of turbulence" alone. It is also stressed that the suggested phenomenological relation is based exclusively on experimental evidence and that no estimate of any kind based on concepts on the importance of any term is needed. No claim is made that the chosen expressions for the loci of  $\xi$  (including the numerical values of the constants) are the best possible. The many digits of the constants reflect the accuracy of the scheme used to compare experimental evidence and is not indicative of the accuracy of the results. The experimental evidence used for this investigation is almost exclusively taken from the Stanford Conference Data, COLES and HIRST [12].
7. Finally it may be mentioned that quantities such as the production of turbulent energy etc. may be computed as functions of space in all cases mentioned and that the famous measurements of KLEBANOFF [19] are reproduced with astonishing accuracy. It should perhaps also be mentioned that separation, which is predicted in Case II, can by means of a slight adjustment of the locus of  $\xi$  also be predicted in Case I, however a lesser degree of accuracy may then be expected due to lack of conclusive experimental evidence.

## BIBLIOGRAPHY

- [1] REYNOLDS, O., "On the Dynamical Theory of Incompressible Viscous Fluids and the Determination of the Criterion", (1895, Phil. Trans. of the Royal Soc. of London, A, vol. 186, p. 123.
- [2] PRANDTL, L., "Über ein neues Formelsystem für die ausgebildete Turbulenz", Nachr. Akad. Wiss. Göttingen Math.-phys. 1945, pp. 6 - 19. (see also "Collected Works", vol. II, pp. 874 - 887).
- [3] TAYLOR, G.I. "Diffusion by Continuous Movements", Proc. London Math. Soc. Ser. 2, vol. 20, 1921, pp. 196 - 211.
- [4] KOLMOGOROV, A.N., "Equations of Turbulent Motion of an Incompressible Fluid", Izv. Akad. Nauk. SSR Seria fizichiska VI, 1942, p.56.
- [5] PRANDTL, L., "Bereicht über Untersuchungen zur ausgebildeten Turbulenz", Z. Angew. Math. Mech., vol.5, 1925, pp. 136 - 139 [see also "Collected Works" (Luewig Prandtl Gesammelte Abhandlungen, Springer, Berlin, 1961) vol. II, pp. 714 - 718].
- [6] BRADSHAW, P., FERRIS, D.H. and ATWELL, N.P., "Calculation of Boundary Layer Development Using the Turbulent Energy Equation", J. Fluid Mech., vol. 28, part 3, 1967, pp. 593 - 616.
- [7] KESTIN J. and PERSEN L.N., (Unpublished report)
- [8] BRAND, R.S. and PERSEN, L.N., "Implications of "the Law of the Wall" for Turbulent Boundary Layers", Act. Pol. Scan., Ph 30, Trondheim 1964.
- [9] PERSEN, L.N., "Über die Grundlage der Theorie für Wärmeübertragung durch turbulente Grenzschichten", Act. Pol. Scan., Ph 30, Trondheim 1966.
- [10] SPALING, D.B., "A single Formula for the Law of the Wall", J. Appl. Mech., Vol. 28, Ser. E, pp. 455 - 458, Sept. 1961.
- [11] WIEGHARDT, K. and TILLMANN, W., U & M 6617 (1944), translated as "On the Turbulent Friction Layer for Rising Pressure", NACA TM 1314 (1951).
- [12] COLES, D.E. and HIRST, E.A., "Proceedings Computation of Turbulent Boundary Layers - 1968, AFOSR-IFP-Standford Conference", Vol. II, (1969), Stanford University.
- [13] WHITE, F.M. and CHRISTOPH, G.H., "A simple Analysis of Two-Dimensional Turbulent Skin Friction with Arbitrary Wall and Freestream Conditions", AGARD-CP-93-71, AGARD Conference preprint No. 93.
- [14] PERSEN, L.N., "Turbulent Boundary Layers" Institutt for mekanikk, NTH, Universitetet i Trondheim, Norway, Febr. 1978, Techn. Report 78:1.
- [15] PERRY, A.E., BELL, J.B. and JOUBERT, P.N., "Velocity and Temperature Profiles in Adverse Pressure Gradient Turbulent Boundary Layers", J. Fluid Mech. (1966) vol. 25, part 2. pp. 299 - 320.
- [16] PERSEN, L.N., "An Examination of the Law of the Wake in a turbulent boundary Layer", Proceedings of the Theodorsen Colloquium, 1976, Trondheim

- [17] MILLIKAN, C.B., "A Critical Discussion of Turbulent Flow in Channels and Circular Tubes", Proc. of 5th Int. Congr. of Appl. Mechanics, Cambridge Mass., 1938, pp. 386 - 392, Wiley New York.
- [18] BAKER R.J. and LAUNDER B.E., " The Turbulent Boundary Layer with Foreign Gas Injection - I. Measurements in Zero Pressure Gradient", Int. J. Heat transfer. Vol.17, pp. 275 - 291. Pergamon Press 1974.
- [19] KLEBANOFF, P.S., "Characteristics of Turbulence in Boundary Layer with Zero Pressure Gradient", NACA Report 1247, 1955

# BOUNDARY LAYER MEASUREMENTS ON A TWO-DIMENSIONAL WING WITH FLAP AND A COMPARISON WITH CALCULATIONS

BY

B. van den Berg and B. Oskam  
NATIONAL AEROSPACE LABORATORY NLR  
THE NETHERLANDS

## SUMMARY

Measurements were performed on a wing flap configuration, which was so designed that flow separations occur nowhere, apart from a small laminar separation bubble on the wing nose. The measurements comprise surface pressure measurements, boundary layer and wake traverses at 16 stations, and flow visualization tests to establish the presence of separation bubbles and boundary layer transition regions. The data resolve the various flow phenomena sufficiently well to provide a significant test case for calculation methods for the flow around multi-element airfoils. Comparison with such a calculation method showed satisfactory agreement in many respects. A need for improved modelling was found to exist in some regions, particularly for the wing wake above the flap.

The investigation has been performed under contract with the National Agency for Aerospace Programs (NIVR, contract numbers 1738 and 1812).

## LIST OF SYMBOLS

$c$	basic-airfoil chord
$C_D$	drag coefficient
$C_f$	local wall shear stress coefficient
$C_L$	lift coefficient
$C_p$	pressure coefficient
$H$	boundary layer shape parameter
$n$	distance from surface
$s$	streamwise distance along wing contour, measured from stagnation point
$U$	velocity magnitude
$U_p$	potential flow velocity at measured local static pressure
$x$	chordwise distance, measured from leading edge
$\alpha$	angle of attack
$\theta$	boundary layer momentum thickness

## SUBSCRIPTS

$w$	value at the wall
$\infty$	free-stream value

## 1. INTRODUCTION

Extensive boundary layer measurements have been carried out on a two-dimensional wing with flap in a low-speed wind tunnel. A practical wing flap configuration was chosen with a highly loaded wing and flap. In such a case the boundary layers and the wing wake are subjected to severe pressure gradients, resulting in a significant interaction between these shear layers and the inviscid flow. The principle aim of the experiment is to provide a test case for calculation methods for the viscous/inviscid flow around multi-element airfoils.

Boundary layer studies on multi-element airfoils have been reported earlier (ref. 1 to 5). These

earlier data are affected by flow separation near the wing shroud, however. With such a separation region the calculation of the viscous/inviscid flow interaction becomes much more difficult. Although local separation in the shroud region occurs on most practical wing flap configurations, it should be avoided preferably in a simple test case. In the present experiment a wing flap configuration has been chosen with a shroud designed in such a way, that no flow separation occurs.

In the experiment care was taken to ensure that the test data resolve the various viscous flow phenomena sufficiently well to make detail comparison possible with calculation results. Extensive measurements have been done at three angles of attack, the largest angle being just below the stalling angle. Two widths of the gap between wing and flap were applied. With the larger gap no merging of the wing wake and the flap upper surface boundary layer takes place; with the smaller gap merging does occur. In the present paper only the results of the configuration with the larger gap at two angles of attack will be presented. Full data, including those on wake boundary layer merging, are given in ref. 6.

Comparisons with calculation results have been made mainly with a calculation method developed at NLR (ref. 8), which computes the full flow, using iteratively coupled potential flow and viscous shear layer analyses. These viscous/inviscid flow calculations are supplemented by turbulent boundary layer calculations, based on the measured surface pressure distribution. In these calculations empirical assumptions have to be made about the turbulence characteristics of the shear layers and on the transition from laminar to turbulent shear flow. From the comparisons with the test data conclusions will be drawn about the areas, where improved modelling is most needed.

## 2. EXPERIMENT

### 2.1. Model and experimental techniques

A sketch of the wing with flap is given in Figure 1. The basic airfoil section is an early supercritical section: NLR 7301. The shape of the wing shroud, between 60% chord and the trailing edge, was designed on the basis of preliminary wind tunnel tests such that no flow separations occur. It should be noted that the resultant shroud shape does not permit the flap to be actually retracted. A flap of 32% chord was used at a deflection angle  $\delta_f = 20^\circ$ . This angle is near the highest angle possible without incurring boundary layer separation on the flap or flow reversal in the wing wake above the flap. The width of the gap between the wing and the flap has been varied, but only the results obtained with a flap gap of 2.6% chord will be considered here.

In Figure 1 the positions of the static pressure holes in the model and of the boundary layer measuring stations are indicated. Figure 2 shows a photograph of the model in the NLR 3x2m low speed wind tunnel. The rig used for the boundary layer traverses is also visible on the photograph. It may be noted that the boundary layer measuring plane is not at mid-span, but closer to the tunnel floor. This has been done to achieve large stiffness of the rig and yet little aerodynamic interference. Check measurements were performed to assure that the flow was two-dimensional. To achieve two-dimensional flow up to maximum lift, boundary layer control by blowing was applied at the model tunnel wall junctions. Without boundary layer control early flow separations occur at these junctions, severely affecting the test results even at mid-span, as will be illustrated later (see also ref. 9).

For the boundary layer and wake traverses a total-head tube of 0.3mm outer diameter and a static pressure tube of 1.1mm diameter were used as a rule. A 0.2mm total-head tube and a hot wire have been used as well at some stations. Wake traverses have also been made with a total-head tube rake located at about one chord behind the trailing edge. The latter wake traverses were used to derive the total drag of wing and flap.

Wall shear stress data were obtained with the razor-blade technique as introduced by East (ref. 10). This technique is based on the assumption that the law of the wall holds in a flow region near the wall. The height of the razor-blade cutting edge above the surface is 0.125mm. In the present test conditions this means that the reliability of the razor-blade technique depends on the validity of the law of the wall in the viscous sub-layer and the so-called buffer layer. Additional data may be obtained from the boundary layer traverses made with the total-head tube. When the total-head tube touches the surface, it may be regarded as a Preston tube, which can also be used for a wall shear stress determination (ref. 12). The Preston tube extends into the log law region in some of the present cases. From the velocity data in the log law region, wall shear stress data may be derived as well by making so-called Clauser plots



(ref. 13).

Oil flow and sublimation technique were applied to determine the position and extent of separation bubbles and transition regions. All measurements were carried out at a Reynolds number, based on the basic-airfoil chord  $c = 0.57\text{m}$ ,  $Re_c = 2.51 \times 10^6$  and a free stream Mach number of  $Ma_\infty = 0.185$ .

## 2.2. Experimental results

The lift, obtained from an integration of the measured model surface pressures, is plotted versus angle of attack in Figure 3. The graph also contains three data points of the drag, derived from wake traverses far downstream of the model. The two angles of attack,  $\alpha = 6.0^\circ$  and  $13.1^\circ$ , which have been selected for detail comparisons between boundary layer measurements and calculations, are indicated in the figure. The test data given here, and further in the paper, were all obtained with boundary layer control applied at the model tunnel wall junctions to keep the flow two-dimensional. To illustrate the importance of it, the measured lift curve without boundary layer control is shown also. It is evident that at the larger angles of attack the lift is low without boundary layer control due to early flow separations near the walls.

The measured surface pressure distributions on the wing and the flap at  $\alpha = 6.0^\circ$  and  $13.1^\circ$  have been plotted in Figure 4. Relatively high suction peaks are seen to occur on the wing nose upper surface. Shortly downstream of the suction peak transition from laminar to turbulent boundary layer flow occurs via a small separation bubble. The position and extent of this bubble, as observed with the oil flow technique, is indicated in the graph. On the wing lower surface and the flap upper surface transition to turbulent boundary layer flow occurs much more downstream without laminar separation. Transition was observed with the sublimation technique. A transition region is indicated, which is defined here as the region between the first visible transition line and the line observed just before full sublimation took place. The boundary layer on the flap lower surface was laminar up to the trailing edge.

Some typical boundary layer velocity profiles are shown in Figure 5. Figure 5a gives some experimental results obtained on the wing upper surface at  $\alpha = 6.0^\circ$ . At station 1, close behind the laminar separation bubble, the boundary layer is only about 1mm thick. Consequently the data, which were obtained with a 0.3mm diameter probe, will not be very accurate at this station. The boundary layer is seen to grow fast up to a thickness of more than 15mm at the wing trailing edge. Some results obtained on the wing lower surface are shown in Figure 5b. Station 9 is situated upstream of the observed transition region, the velocity profile being typical for a laminar boundary layer. At station 10, downstream of the transition region, a typical turbulent boundary layer velocity profile is found. The shape of the velocity profile at station 11 is rather unusual. Before discussing the results at station 11, attention should be drawn to the dashed line shown in the graph. This dashed line represents the variation of the potential velocity,  $U_p$ , which is derived from the measured local static pressure, while assuming the total pressure to be equal to the value in the outer potential flow. If there is no static pressure variation, this velocity will be constant across the shear layer. If the static pressure in the shear layer is not constant, as at station 11,  $U_p$  will vary with distance from the wall. From the distance between the dashed line and the full line in the graph one obtains an impression of the velocity defect in the boundary layer. The graph shows that at station 11 there is an extensive outer region with a small velocity defect and a thin region close to the wall, where the velocity decreases to zero at the wall. At this station, which is situated in the gap between wing and flap, a very large negative pressure gradient exists. Laminarization of a turbulent boundary layer may occur in these circumstances. The parameter most often used to deduce the likelihood of laminarization is  $K = (v_w/U_p^2) (dU_p/ds)$ . On the basis of the surface static pressure measurements (see Fig. 4) only a crude guess of the pressure gradient, and consequently of the velocity gradient, can be made for station 11. On this basis it was found that  $K \approx 3 \times 10^{-6}$ . According to Launder and Jones (ref. 11) laminarization begins when  $K$  exceeds about  $2 \times 10^{-6}$ . The shape of the velocity profile at station 11 suggests that the small velocity defect in the outer region represents the remains of the upstream turbulent boundary layer and that below that region a new laminar boundary layer is developing.

In Figure 5c the measured velocity variation in the wing wake above the flap is depicted. The static pressure varies considerably across the wing wake and so does the velocity  $U_p$ , as indicated by the dashed lines. The velocity defect in the wake is seen to be large at station 12 and to remain large further downstream. The effect of such a large wake on the flow over the flap may be expected to be substantial. This subject will be emphasized later. Figure 5c further shows that up to station 14, i.e.

up to the flap trailing edge, no merging of wing wake and flap boundary layer has taken place for this wing flap configuration. At station 16 at 10% chord behind the flap trailing edge the wing wake and the flap wake just merge.

Figure 6 gives some wall shear stress data obtained on the wing upper surface. Besides the data obtained with the razor-blade technique, the graph contains also the Preston tube and Clauser plot data derived from the total-head tube measurements in the boundary layer. It appears, that a satisfactory agreement exists between the wall shear stress data obtained with the various techniques, especially in view of the fact that the scatter is generally rather large with this type of measurements. The data obtained with the razor-blade technique are considered to be the more reliable, and will be employed for comparisons with calculation results. The test results show that the wall shear stress is large close behind the laminar separation bubble, decreases downstream of the bubble, is approximately constant over the centre part of the wing, and decreases further over the rearward part. The wall shear stress is close to zero near the trailing edge at  $\alpha = 13.1^\circ$ .

A full set of test data is given in ref. 6. Ref. 7 contains the results of some additional measurements, which were carried out after comparisons with calculation results were made. These include hot-wire data, which will be discussed in section 4.3. The data given in ref. 6 and 7 define the wing and flap and the flow around them in detail, so that comparisons with calculation results can readily be made.

### 3. CALCULATION METHOD

#### 3.1. General

The present calculation method handles the viscous flow around multi-component airfoils by solving incompressible potential flow and shear layer problems iteratively. The incompressible potential flow problem is solved by a revised version of the 2-D NLR panel method, being a direct extension of earlier work on multi-component airfoils by Labrujère et.al. (Ref. 14). This revised version has the capability of providing incompressible potential flow solutions with sufficient accuracy to justify the incorporation of viscous effects. The presence of these viscous shear layers is modelled in the inviscid flow by an outflow boundary condition on the airfoil surface and the wake centre-line as discussed in detail by Oskam (ref. 8).

The various viscous flow calculation procedures have been chosen with the aim of balancing the total effort required against the overall accuracy obtained. For the present purposes we will list the shear layer methods used in the present calculations.

- Laminar boundary layer is calculated by Thwaites' integral method (ref. 15).
- Natural transition is predicted by the Granville method (ref. 16).
- The calculation of laminar separation bubbles is based on the work of Van Ingen (ref. 17).
- Turbulent shear layer analysis is based on the shear stress transport equation of Bradshaw, Ferriss and Atwell (ref. 18).

Since comparisons with experimental data will be focussed on the turbulent shear layers, the physical content of the analysis will be described in some detail.

#### 3.2. Turbulent shear layer analysis

The model transport equation of Reynolds stress,  $\tau$ , may be written as

$$\frac{D}{Dt} \left( \frac{\tau}{\rho} \right) = 2a \left[ \frac{\tau}{\rho} \frac{\partial U}{\partial n} - \frac{1}{L} \left( \frac{\tau}{\rho} \right)^{3/2} \right] - \frac{\partial}{\partial n} (v_t \frac{\tau}{\rho})$$

where the constant  $a$ , and the functions  $L$  and  $v_t$  have been determined by data correlation procedures, see Bradshaw et.al. (ref. 18).

This turbulence model, which has been applied to a large variety of boundary layer problems, may be regarded as a one-transport-equation model for the turbulent velocity scale,  $(\tau/\rho)^{1/2}$ , combined with an algebraic equation for the dissipation length scale  $L$ , relating this length scale directly to the local shear layer thickness. An improvement of this universal-length-scale concept is the allowance for the effect of extra rates of strain or body forces on the turbulence structure. One such effect considered here is streamline curvature. Bradshaw (ref. 19) proposed to allow for this effect by modifying the length scale  $L$  according to

$$L/L_{\text{mod}} = 1 + \beta Ri, \text{ for convex walls. } Ri > 0$$

where  $Ri = 2 \frac{U}{(\tau/\rho)^{1/2}} \frac{L}{R}$ ,  $\beta \approx 7$ , and  $R$  = radius of curvature.

Bradshaw's model transport equation is not valid near the wall (or in the neighbourhood of laminarization). Consequently the wall boundary conditions are applied by fitting the turbulent flow computations to asymptotic relationships known to apply at some distance from the wall, such as the law of the wall. At NLR considerable attention has been paid to these boundary treatments (see ref. 8).

The basic calculation method has been extended to treat symmetric half wakes. Replacing the wall boundary conditions by symmetry conditions on the wake centre-line and taking the dissipation length  $L$  to be constant across the wake, one may calculate a turbulent symmetric half wake in a pressure gradient, see also Bradshaw (ref. 20) and Morel & Torda (ref. 21).

To start the turbulent shear layer calculation method it is necessary to initialize  $U$  and  $\tau$  profiles in the turbulent flow region. The Coles wall-wake law is employed as a two parameter family of velocity profiles. One parameter follows from the continuity of the momentum thickness, being known from the laminar boundary layer or laminar separation bubble calculation. The second parameter is obtained by assuming that the turbulent boundary layer at the initial station is in equilibrium (ref. 22). The initial stress profile follows from the mixing length formula.

#### 4. COMPARISON OF COMPUTED AND EXPERIMENTAL DATA

##### 4.1. General

Comparisons have been made chiefly with the viscous/inviscid flow calculation method, described in the preceding section. The main goal of this calculation method is to predict quantities like resultant lift and drag of the wing flap configuration. The agreement obtained was satisfactorily with some exceptions. These results are discussed in ref. 8. In the present paper comparisons will be focussed on the viscous shear layer development.

##### 4.2. Wing upper surface

Figure 7 shows some test data on the wing upper surface for  $\alpha = 6.0^\circ$  and calculation results obtained with the viscous/inviscid flow calculation method. The data have been plotted against the streamwise distance along the wing contour,  $s$ , measured from the calculated stagnation point. The experimental velocity data,  $U_p$ , plotted in Figure 7a, were derived from the measured surface static pressures and the potential flow total pressure. The agreement with the corresponding calculated surface velocity distribution is seen to be good. The slight deviations apparent near the suction peak are very probably due to compressibility effects, which are not accounted for in the calculations. Compressibility effects may be significant particularly in the wing nose region, where the local Mach number exceeds  $Ma = 0.5$ . The laminar separation bubble is computed to be situated slightly more downstream than found in the experiment. The development of the momentum thickness,  $\theta$ , of the turbulent boundary layer downstream of the bubble is shown also. The agreement between the calculations using Bradshaw's turbulence model and the test data is good. However, when looking in more detail, see Figure 7b, deviations become apparent. The turbulent boundary layer shape parameter,  $H$ , is underpredicted over the full wing length. The calculated wall shear stress coefficient,  $C_f$ , appears to be small initially and large further downstream. The initial wall shear stress has been taken equal to the value for an equilibrium turbulent boundary layer in the calculations (see section 3.2). Figure 7b suggests that this value is low. Calculations were also performed with an increased initial wall shear stress, but the effect on the calculation results appeared to be negligible shortly downstream of the initial station.

Further comparisons between boundary layer calculations and measurements on the wing upper surface have been made using a compressible flow version of Bradshaw's turbulent boundary layer calculation method and the measured surface pressure distribution. The results are shown in Figure 8 (see ref. 23 for detail results of these calculations). The momentum thickness and the wall shear stress coefficient for  $\alpha = 6.0^\circ$  are plotted in Figure 8a against chordwise distance,  $x$ . The calculations have been started at measurement station 1 with the measured momentum thickness and wall shear stress. The deviations between measured and calculated wall shear stresses are distinctly smaller than they were in the earlier calculations. The figure also shows the results of a calculation, which takes into account the effect of curvature on the turbulent shear stress. Although surface curvature radii are large in the region considered, the effect may not be negligible because of the relatively large boundary layer thickness.

Allowance for curvature effects on the turbulent shear stress was made as proposed by Bradshaw (see section 3.2). Good agreement with test data is seen to exist downstream of station 3 now.

The wall shear stress development between station 1 and 3 deserves further discussion. At station 1 the wall shear stress has been taken equal in calculation and experiment. In the calculation, however, the wall shear stress value falls down fast and levels off at a much lower value, while in experiment the wall shear stress approaches that lower value only slowly. The measured values exceed the calculated ones with 25% or more at station 2 and station 2a (between station 2 and 3). The present razor-blade measurements fall within the 3% accuracy limits for pressure gradient and probe size given by Patel (ref. 12). The difference found is believed, therefore, to be too large to be attributable to experimental uncertainties only. Generally speaking the wall shear stress measurements are invalidated when the law of wall does not hold in a region close to the wall (see section 2.1). This would, however, simultaneously invalidate the present turbulent boundary layer calculation method, since it employs the law of the wall. Apparent discrepancies should be attributed then to both theory and experiment.

One possible reason for the found discrepancy is the low Reynolds number of the boundary layer, which varies from  $Re_0 = 720$  to 4000 between station 1 and 3. Low Reynolds number effects have not been taken into account in the calculations made. It is known the effect may be appreciable in this Reynolds number range (see e.g. ref. 16). Turbulence history effects may well play a rôle also. Station 1 is situated closely behind the laminar separation bubble. This means that transition to turbulence and reattachment has taken place slightly upstream of the region considered here. Consequently the turbulence structure may be very different from that in a turbulent boundary layer in near-equilibrium condition. Return to the equilibrium condition covers a considerable streamwise distance (see e.g. ref. 30). It seems likely that both low Reynolds number and history effects play a rôle in this region downstream of the laminar separation bubble.

In Figure 8b the results of the turbulent boundary layer calculations and experiment are compared for  $\alpha = 13.1^\circ$ . The calculations have been started again with the test data at station 1. Curvature effects were taken into account. Agreement with measurements is seen to be not very satisfactory in this case. The momentum thickness growth seems to be overestimated and the wall shear stress underestimated. In the calculation boundary layer separation near the wing trailing edge is predicted in contrast with experimental observations. Calculations have been repeated with the initial momentum thickness reduced with 25%. Agreement with experiment appears to be much improved then and no separation is predicted. From this result the important conclusion must be drawn, that the turbulent boundary layer development on the wing upper surface depends strongly on the initial conditions. The initial conditions for the turbulent boundary layer calculation have to be supplied by a laminar separation bubble calculation. Consequently high demands on the reliability of the laminar separation bubble calculation method are made. One may further conclude that the accuracy of the measured momentum thickness at station 1 is poor. It has been mentioned in section 2 that this may be indeed the case, as the boundary layer is very thin there. Though agreement between experiment and calculations is much improved by reducing the initial momentum thickness, a distinct discrepancy still exists for the wall shear stress between station 1 and 3, as at  $\alpha = 6.0^\circ$ . It should be noted that consequently the calculated momentum thickness growth between station 1 and 3 may be in error as well.

#### 4.3. Wing lower and flap upper surface

Figure 9 shows the calculated velocity and momentum thickness variation on the wing lower surface for  $\alpha = 6.0^\circ$ , employing the viscous/inviscid flow calculation method. The calculated and measured velocity variation are seen to correspond well. The calculation gives laminar separation at  $s/c = 59.2\%$ . A laminar separation bubble of 4.4% chord is predicted. Downstream of reattachment the boundary layer grows fast. In the slot between wing and flap the pressure gradient changes from mildly positive to large negative and the boundary layer thickness decreases again. The boundary layer is laminarizing there, as discussed in section 2.2. Laminarization is not considered in Bradshaw's turbulence model. Yet the momentum thickness decrease found in experiment is predicted for a large part by the calculations. This is not surprising as accurate turbulence modelling is not very important in regions with large negative pressure gradients.

The calculations predict laminar separation at  $s/c = 59.2\%$ , while experiment indicates no separation, but transition to turbulent flow between  $s/c = 62.2\%$  and  $65.2\%$ , which is a substantial distance downstream of the calculated separation position. Thwaites' integral method was used for the laminar boundary layer

calculations. Supplementary laminar boundary layer calculations were made with a finite difference method, which solves the exact laminar boundary layer equations (ref. 24). No significant difference in separation position was found. It must be noted that slight differences in pressure distribution do lead to large differences in predicted separation position and that only by suitable interactive calculation methods (e.g. ref. 25) accurate predictions can be obtained. However, further measurements, which will be discussed hereafter, yielded a more likely reason for the found discrepancy between calculation results and experiments.

Detail measurements were carried out with a hot wire at station 9, which is situated just upstream of the calculated separation point and well upstream of the observed transition region. The results are depicted in Figure 10. The shape of the measured velocity profile is typical for a laminar flow. Simultaneously velocity fluctuations of the order of magnitude typical for turbulent boundary layers appear to occur. Figure 10 includes some hot-wire signal traces. These show that, though the fluctuations are not really regular, a dominant frequency is evident. This frequency (about 1000 Hz) corresponds well with the frequency of the most unstable Tollmien-Schlichting waves, predicted by linear stability theory for this boundary layer (ref. 26). Apparently the boundary layer at station 9 is in an advanced state of the transition process. A significant additional shear stress may be expected to occur, when velocity fluctuations of the order of 5% exist. Probably separation does not occur downstream of station 9 due to these additional shear stresses. The fluctuation level near the wall is small, so that the sublimation technique, which was used for transition detection in experiment, will indicate transition only further downstream.

Figure 11 shows calculated and measured velocities and momentum thicknesses on the flap upper surface for  $\alpha = 6.0^\circ$ . Agreement is seen to be satisfactory in general, but again laminar separation is predicted well upstream of the transition region found in experiment. It is believed that also in this case there is an extensive region, where the boundary layer is in a transitional state as described before. Laminar separation upstream of the observed transition position was calculated earlier at NLR on the lower surface of a swept wing (ref. 27). Cousteix et.al. of ONERA recently published similar results (ref. 28). Apparently transitional boundary layers of the type discussed here occur rather frequently.

#### 4.4. Wing wake

A typical characteristic of multi-element airfoils is the presence of a wake from an upstream element near a downstream element. If the upstream element is highly loaded, which is the case here, a thick boundary layer is created and consequently the wake is wide and its effect on the flow over the downstream element is substantial. This is illustrated in Figure 12, which shows the measured surface pressure distribution on the flap at  $\alpha = 6.0^\circ$  and  $13.1^\circ$  and the calculated inviscid flow pressure distribution. The difference is seen to be large, particularly at  $\alpha = 13.1^\circ$ . In the viscous/inviscid flow calculation method described in section 3, the wake is calculated with an extension of Bradshaw's turbulent boundary layer calculation method. The wake originating from the upper surface boundary layer and from the lower surface boundary layer are treated there separately, however, neglecting mixing of both wake parts. Good results were yet obtained for  $\alpha = 6.0^\circ$  as shown in Figure 12, but at  $\alpha = 13.1^\circ$  reverse flow in the wing wake was computed in contrast with experimental findings. It is probable that reverse flow was computed because mixing of the thick wake from the wing upper surface with the thin wake of the wing lower surface was neglected. It may be concluded that an accurate calculation of asymmetric wakes in strong adverse pressure gradients is a necessary part of a viscous/inviscid flow calculation method for multi-element airfoils.

An accurate prediction of the total drag is best obtained from a calculation of the flow momentum defect far downstream (see e.g. ref. 29). For this reason also it is necessary to predict with sufficient accuracy the viscous wake development. A complicating factor in the computation of these wakes is that the thin shear layer approximation is generally not valid, since the static pressure variation across the wake is not negligible (as demonstrated by the  $U_p$ -variation shown in Figure 5c). Further problems to be anticipated are merging of the wing wake with the flap boundary layer and/or wake.

#### 5. CONCLUDING REMARKS

The experimental data, obtained on a wing flap configuration with a highly loaded wing and flap,





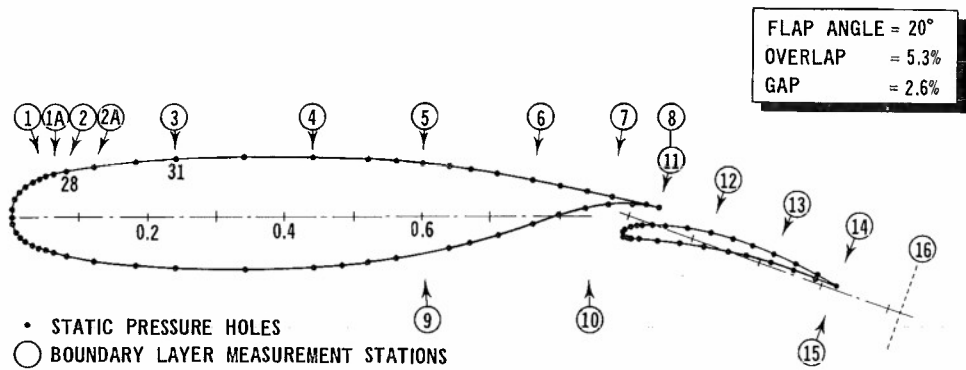


Fig. 1 Airfoil and flap section with the positions of the static pressure holes in the surface and the boundary layer measurement stations

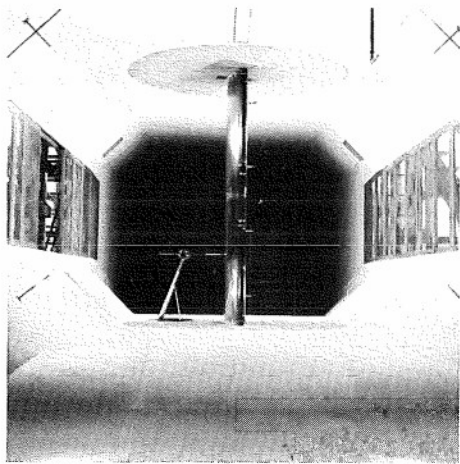


Fig. 2 Photograph of the model with boundary layer survey apparatus in the wind tunnel

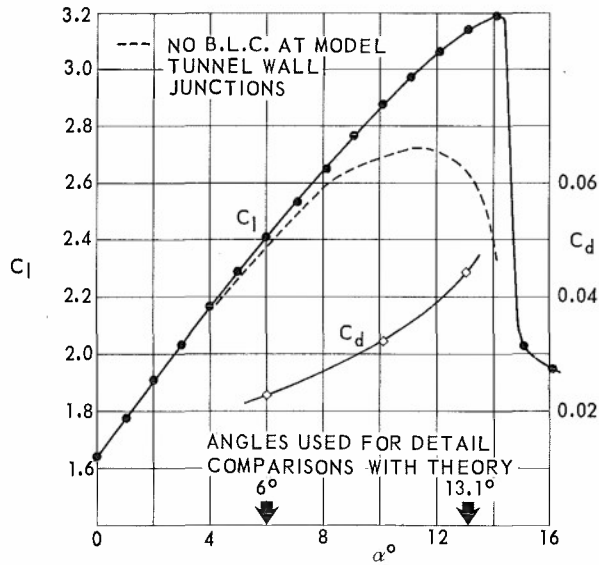


Fig. 3 Measured lift and drag versus angle of attack

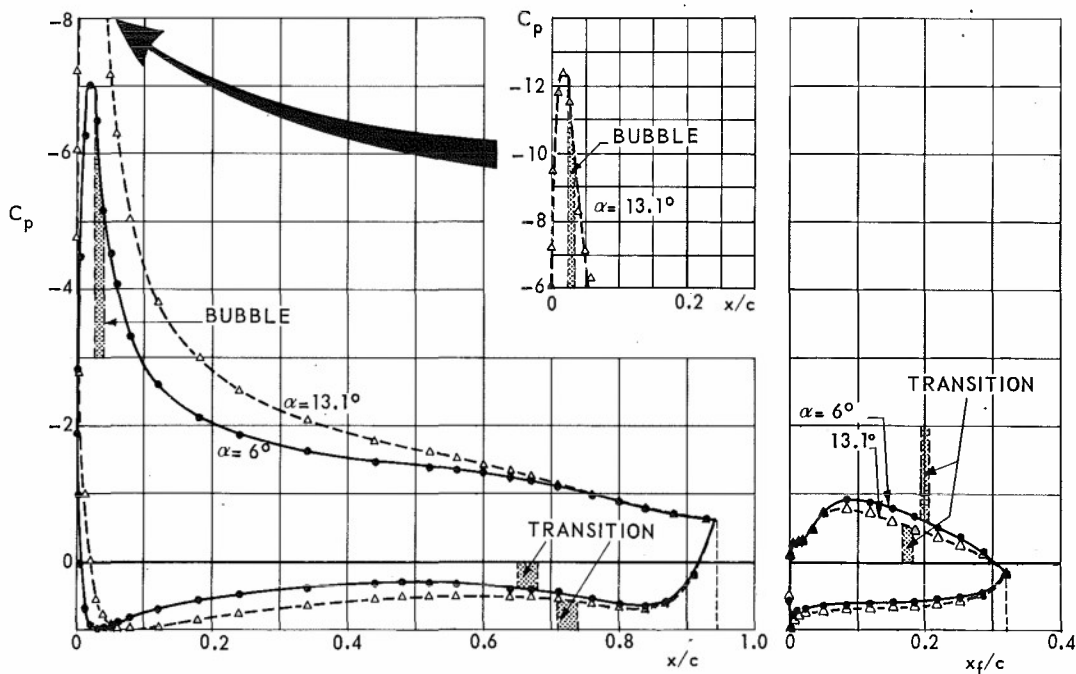


Fig. 4 Measured surface pressure distribution and position of laminar separation bubbles and transition regions.  $\alpha = 6^\circ$  and  $13.1^\circ$



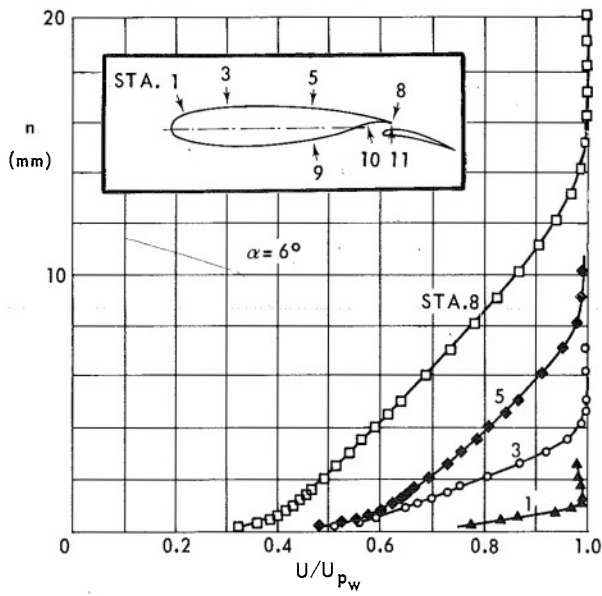


Fig. 5a Typical measured velocity profiles of boundary layer on wing upper surface.  $\alpha = 6^\circ$

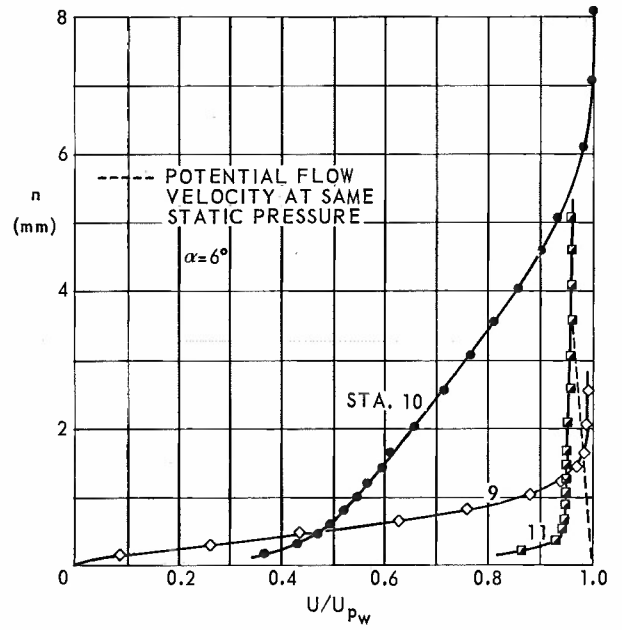


Fig. 5b Typical measured velocity profiles of boundary layer on wing lower surface.  $\alpha = 6^\circ$

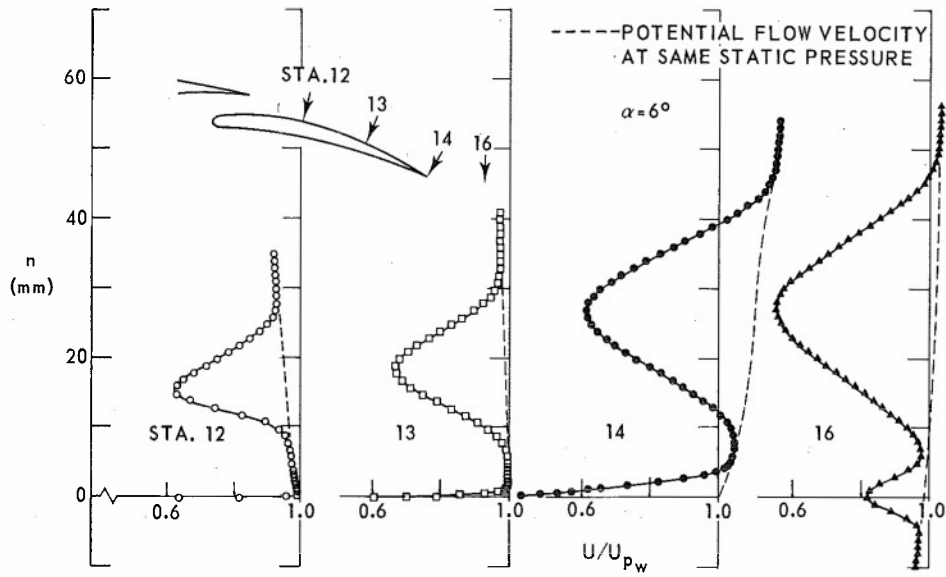


Fig. 5c Typical measured velocity profiles of shear layer above flap.

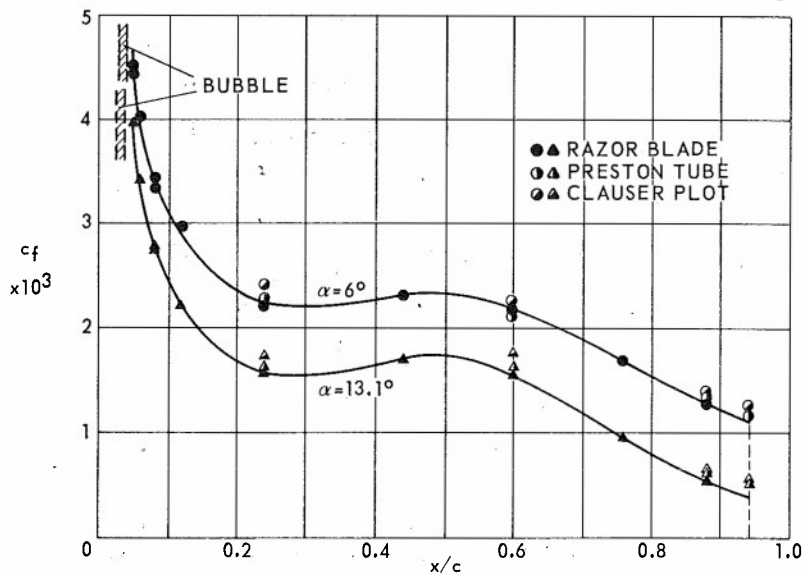


Fig. 6 Measured wall shear stress variation on wing surface.  $\alpha = 6^\circ$  and  $13.1^\circ$

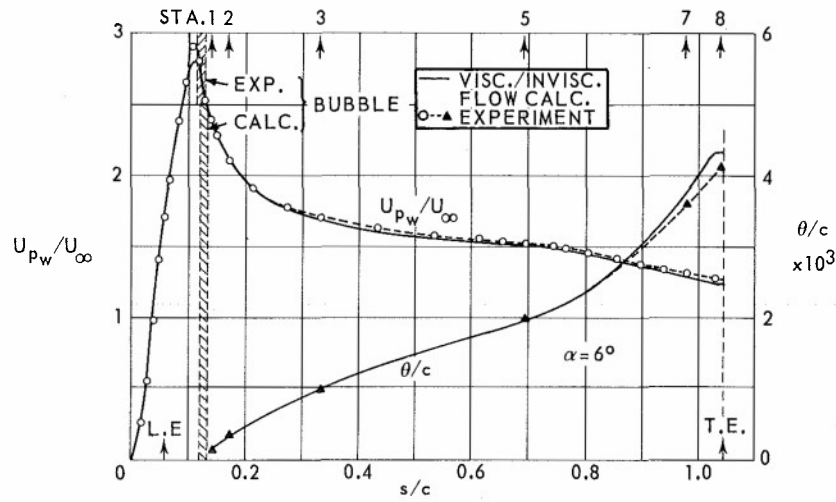


Fig. 7a Comparison between calculated and measured velocity and momentum thickness variation on the wing upper surface.  $\alpha = 6^\circ$

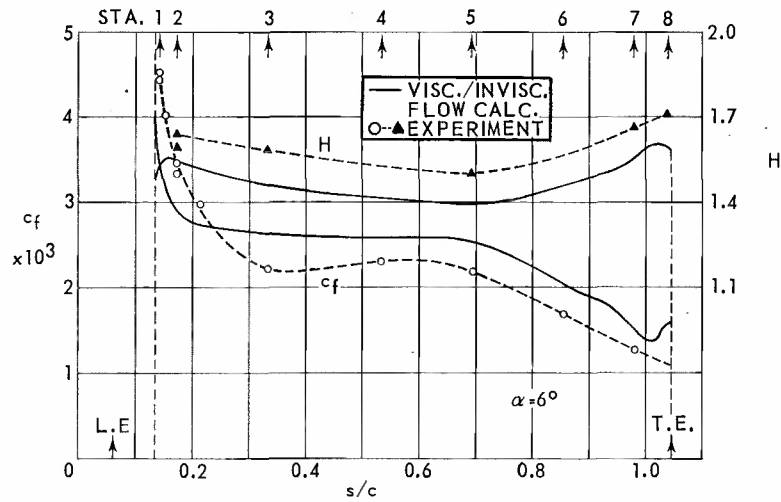


Fig. 7b Comparison between calculated and measured wall shear stress and shape factor variation on the wing upper surface.  $\alpha = 6^\circ$

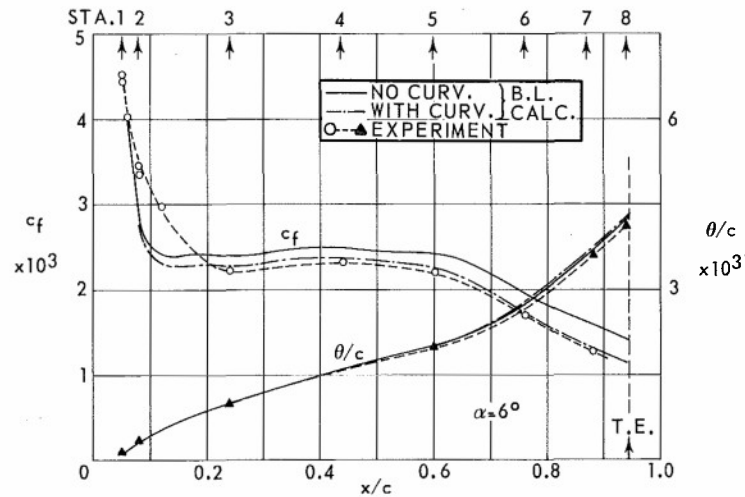


Fig. 8a Comparison with compressible turbulent boundary layer calculations, using the measured pressure distribution on the wing upper surface and the initial data at station 1.  $\alpha = 6^\circ$

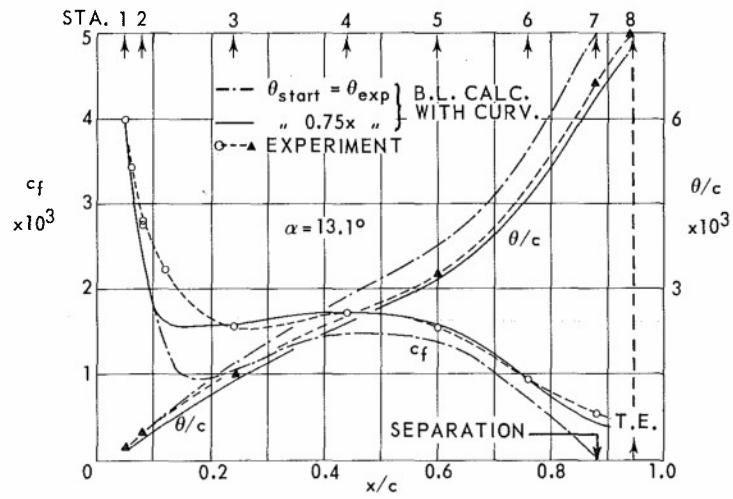


Fig. 8b Comparison with compressible turbulent boundary layer calculations, using the measured pressure distribution on the wing upper surface and the initial data at station 1.  $\alpha = 13.1^\circ$

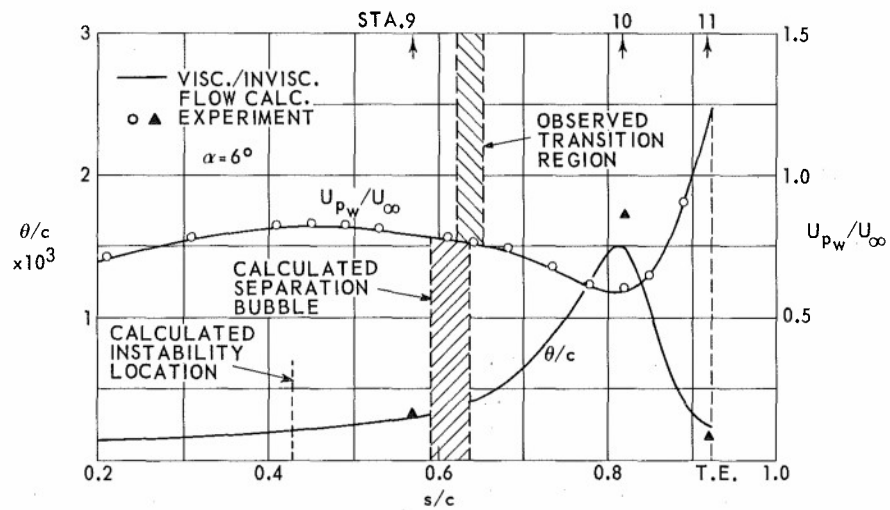


Fig. 9 Comparison between calculated and measured velocity and momentum thickness variation on the wing lower surface.  $\alpha = 6^\circ$

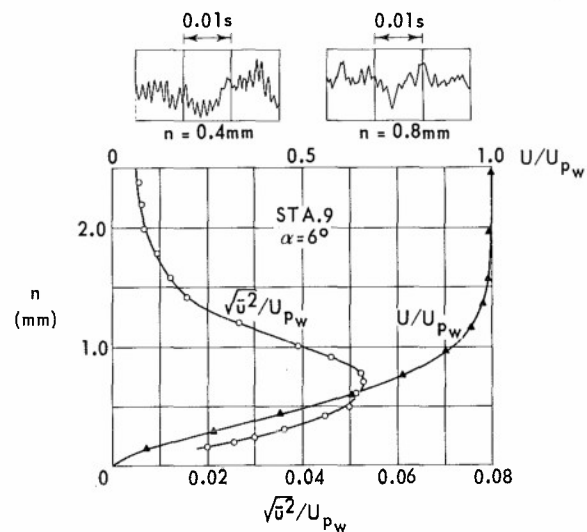


Fig. 10 Measured velocity fluctuations at station 9.  $\alpha = 6^\circ$

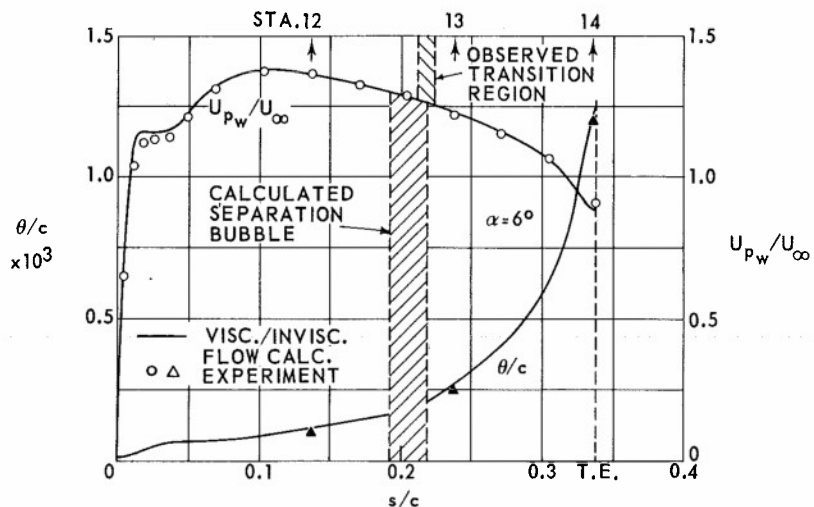


Fig. 11 Comparison between calculated and measured velocity and momentum thickness variation on the flap upper surface,  $\alpha = 6^\circ$

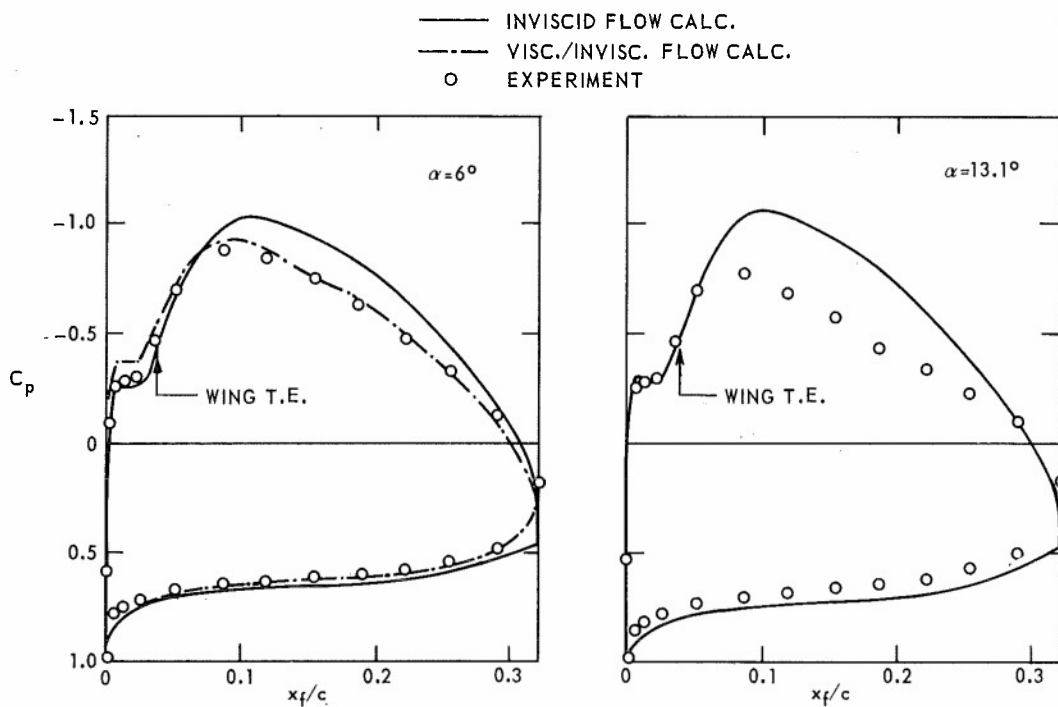


Fig. 12 Comparison between calculated and measured pressure distribution on the flap

## COUCHE LIMITE TURBULENTE TRIDIMENSIONNELLE: RESTRUCTURATION D'UN ECOULEMENT

AXISYMETRIQUE SOUMIS A UNE DISCONTINUITÉ DE LA VITESSE DE PAROI.

par

E. ARZOUMANIAN et L. FULACHIER

Institut de Mécanique Statistique de la Turbulence (IMST)

13003 Marseille, France

Jean COUSTEIX et Bertrand AUPOIX

Office National d'Etudes et de Recherches Aéronautiques (ONERA)

CERT, Toulouse, France.

## RESUME

Une couche limite turbulente bidimensionnelle se développe sur un cylindre circulaire d'axe parallèle à l'écoulement. Dans la partie aval où la couche limite est pleinement développée, le cylindre est mis en rotation autour de son axe. On se place dans un cas où la vitesse périphérique à la paroi est pratiquement égale à la vitesse extérieure. On étudie l'influence de cette rotation sur la restructuration de la couche limite tridimensionnelle qui a pris naissance, en s'appuyant principalement ici sur l'analyse du champ de vitesse moyenne.

Cette investigation a été menée parallèlement des points de vue expérimental et numérique. En ce qui concerne le calcul, on a utilisé un modèle de type  $k-\varepsilon$  dans lequel on peut tenir compte éventuellement d'une déviation de la direction de la force de cisaillement turbulent par rapport à celle du gradient de vitesse. En ce qui concerne les mesures, l'effort a été axé notamment sur l'étude de la région tampon ("buffer layer") jusque dans la sous-couche visqueuse. Elles révèlent que la collatéralité de l'écoulement s'établit d'abord dans une région très limitée près de la paroi et il semblerait qu'elles s'étendent progressivement dans la couche limite. Le calcul en revanche indique que l'hodographe possède une partie linéaire beaucoup plus étendue.

THREEDIMENSIONAL TURBULENT BOUNDARY LAYER : RESTRUCTURATION OF AN AXISYMETRIC FLOW SUBJECTED TO A DISCONTINUITY OF THE WALL PERIPHERAL VELOCITY.

## SUMMARY

A three-dimensional turbulent boundary layer is developing on a circular cylinder the axis of which is parallel to the flow. In the downstream region the boundary layer is fully developed and the rear part of the cylinder rotates about its axis.

The peripheral velocity at the wall is practically equal to the external velocity. We study the influence of the rotation on the restructuration of the developing three-dimensional boundary layer essentially by using the analysis of the mean velocity field.

This investigation has been carried out experimentally and numerically. As concerns the calculations, we have used a model of  $k-\varepsilon$  type in which we can account for the inequality of the turbulent shear stress direction and the velocity gradient direction. As concerns the measurements, emphasis has been placed on the study of the buffer layer down to the viscous sublayer. They reveal that the collaterality of the flow is first obtained in a very thin region near the wall and then seems to extend progressively in the boundary layer. In contrast, the calculations indicate a more extended linear portion of the hodograph.

## NOTATIONS

a	rayon du cylindre
$C_{fx}$	coefficient de frottement suivant x $C_{fx} = \frac{2\nu}{u_e^2} \left( \frac{\partial u}{\partial y} \right)_{y=0}$
$C_{fz}$	coefficient de frottement suivant z $C_{fz} = \frac{2\nu}{u_e^2} \left  \left( \frac{\partial w}{\partial y} \right)_{y=0} \right $
H	paramètre de forme $H = \delta_x^* / \theta_x$
k	énergie cinétique de turbulence $k = (\overline{u'^2} + \overline{v'^2} + \overline{w'^2})/2$
p	pression statique
$\vec{q}$	vecteur vitesse moyenne $\vec{q}(u, w)$
r	distance à l'axe du cylindre
$Re$	nombre de Reynolds $Re = u_e l / \nu$
u, v, w,	composantes suivant x, y, z de la vitesse moyenne absolue
$U_r, V_r, W_r$	composantes de la vitesse moyenne relative (repère lié au cylindre tournant) $U_r = U \quad V_r = V \quad W_r = W - W_0 \frac{z}{a}$
$U_e$	vitesse axiale extérieure
$U_*$	vitesse de frottement $U_* = (\tau_p / \rho)^{1/2}$
$W_0$	vitesse périphérique de la paroi.
u', v', w'	fluctuations de vitesses $u' = u \text{ instantané} - U$ $v' = v \text{ instantané} - V$ $w' = w \text{ instantané} - W$
X	distance axiale, comptée à partir de la partie tournante
x, z	coordonnées axiale et périphérique
y	distance normale à la paroi
$\beta$	angle de la vitesse absolue par rapport à l'axe du cylindre (fig. 9)
$\gamma, \psi_0$	angles définis par la figure 9
$\varepsilon$	taux de dissipation de l'énergie cinétique de turbulence
$\gamma$	viscosité cinématique

$\tau_p$	frottement de paroi
$\varphi$	angle de la vitesse absolue par rapport à la sonde
$\delta$	épaisseur de couche limite à $U/U_e = 0,99$

$$\delta_x^* = \int_0^\infty \frac{a+y}{a} \left(1 - \frac{v}{U_e}\right) dy$$

$$\delta_z^* = \int_0^\infty \left(\frac{a+y}{a}\right)^2 \frac{w}{w_0} dy$$

$$\theta_x = \int_0^\infty \frac{a+y}{a} \frac{v}{U_e} \left(1 - \frac{v}{U_e}\right) dy$$

$$\theta_{xz} = \int_0^\infty \left(\frac{a+y}{a}\right)^2 \frac{v}{U_e} \frac{w}{w_0} dy$$

## Indices

0	relatif à $X = 0$
e	à l'extérieur de la couche limite

## 1 - INTRODUCTION

La plupart des méthodes de prévision des couches limites tridimensionnelles sont des extensions souvent très directes de celles mises au point et appliquées en bidimensionnel. Or, il apparaît qu'un facteur nouveau est introduit par la tridimensionalité de l'écoulement. En effet, la torsion du profil des vitesses implique que les directions de la vitesse et de sa dérivée suivant la normale à la paroi ne sont pas confondues. Il en résulte une situation a priori plus complexe qu'en bidimensionnel, pour laquelle il peut devenir important de tenir compte d'une différence d'orientation tension/gradient très significative. (Dans toute la suite nous utiliserons un langage abusif : le mot "tension" est utilisé pour représenter un vecteur de composantes  $(-\rho u'v', -\rho w'v')$  et le mot "gradient" pour le vecteur de composantes  $(\frac{\partial u}{\partial y}, \frac{\partial w}{\partial y})$ ).

Il convient donc d'approfondir l'analyse de tels écoulements. Dans l'étude envisagée, qui est menée à la fois expérimentalement et numériquement, nous avons choisi de créer une couche limite tridimensionnelle en imposant une discontinuité de condition limite. Une couche limite turbulente bidimensionnelle se développe sur un cylindre circulaire d'axe parallèle à l'écoulement, et dans la partie aval où elle est pleinement développée, le cylindre est mis en rotation autour de son axe. On peut penser qu'au bout d'une distance suffisante, en l'absence de gradient de pression, la couche limite deviendrait collatérale ; on obtiendrait alors une couche limite bidimensionnelle dans le système d'axes relatif lié à la paroi du cylindre en rotation. Mais il est certain que dans la phase initiale où la rotation impose une réorganisation de la zone interne de la couche limite, celle-ci présente une structure tridimensionnelle en rapide évolution. Afin de créer un frottement périphérique de l'ordre du frottement longitudinal, la vitesse de la paroi a été choisie voisine de la vitesse extérieure.

Les documents expérimentaux disponibles concernent les régions externes de la couche limite /REF. 1, 2/. Nous avons donc porté plus particulièrement notre effort sur l'étude de la région tampon ("buffer layer") jusque dans la sous-couche visqueuse /REF. 3, 4, 5/.

Parallèlement, des méthodes de calcul des couches limites turbulentes tridimensionnelles ont été étudiées. Elles utilisent des équations de transport destinées à calculer l'évolution de quan-

tités turbulentes. Bien qu'une hiérarchie de modèles de turbulence, allant d'un modèle de longueur de mélange à un modèle à quatre équations de transport, ait été testée sur d'autres cas expérimentaux /REF. 6/, nous n'avons retenu ici qu'un modèle à deux équations de type  $k-\varepsilon$ . Dans une telle méthode, la force de cisaillement turbulent est reliée au gradient de vitesse par une viscosité tourbillonnaire et dans les modèles "classiques" on suppose que celle-ci est isotrope. En fait, des calculs antérieurs /REF. 6/ ont montré que même dans les modèles où la tension est calculée à l'aide d'équations de transport, on atteint rapidement un état d'équilibre pour lequel les forces de cisaillement turbulent et visqueux sont alignées. Pour tenir compte du non-alignement de ces forces, nous avons repris une idée développée par ROTTA /REF. 7/ et nous avons réexaminé le terme de corrélation pression-vitesse qui joue un rôle majeur dans l'équation aux tensions de Reynolds.

Les hypothèses introduites dans cette méthode de calcul sont testées en comparant les résultats obtenus à ceux de l'expérience. En particulier, on analyse comment se développe l'effet de la rotation à l'intérieur de la couche limite initialement bidimensionnelle.

## 2 - DISPOSITIF EXPERIMENTAL. METHODES DE MESURES

## 2.1. - Dispositif expérimental

Les mesures ont été effectuées dans la veine d'expérience de la soufflerie S1 de l'IMST, dont les caractéristiques géométriques ont déjà été données par GAVIGLIO /REF. 8/. Il s'agit d'une veine de section carrée (800 mm x 800 mm) dont les angles sont munis de pans coupés ajustés de telle sorte que, en l'absence de maquette, le gradient longitudinal de pression statique soit nul. Les paramètres aérodynamiques de l'écoulement sont étudiés de manière à minimiser les effets parasites notamment en ce qui concerne les perturbations en envergure des vitesses moyennes. Ces perturbations induiraient dans la présente expérience des défauts d'axisymétrie. L'intensité de pré-turbulence relative à la composante longitudinale de la vitesse à l'entrée de la veine est très faible  $((u')^2)^{1/2}/U_e \approx 5 \cdot 10^{-4}$ .

La maquette /REF. 3/ est représentée schématiquement sur la figure 1. Elle est constituée d'un corps cylindrique de révolution de diamètre  $2a = 197$  mm, dont une partie (c) peut être mise en rotation. La section droite de ce cylindre ne représente que 5% de celle de la veine d'expérience. La précision imposée à l'usinage et à l'installation de cette maquette a permis de réduire au minimum les défauts géométriques (faux rond inférieur à 0,01 mm) et les vibrations mécaniques en régime de rotation ; ainsi dans les mesures au fil chaud on a pu s'approcher jusqu'à 0,06 mm de la paroi, dans la gamme des vitesses utilisées. Une étude particulière du bord d'attaque a été effectuée pour obtenir notamment une axisymétrie optimale de l'écoulement et éviter les décollements. A cet effet, le profil de l'ogive a été ajusté à une ligne de courant déterminée en considérant la superposition d'une source ponctuelle et d'un écoulement uniforme à l'infini amont /REF. 5/. L'allongement  $l/a$  choisi est 3; dans ces conditions, l'effet de perturbation introduit par cette ogive devient négligeable dans la zone de mesure. Dans le but de déclencher la turbulence et de fixer la transition, des stries (St) ont été gravées, un fil de transition (f) et des rugosités (r) ont été disposés comme l'indique la figure 1. Le carénage et la géométrie des supports ont été également étudiés pour réduire au minimum les effets de sillage sur le phénomène étudié. Dans ce même but des filins en acier (e) (diamètre 0,5 mm) ont été utilisés pour

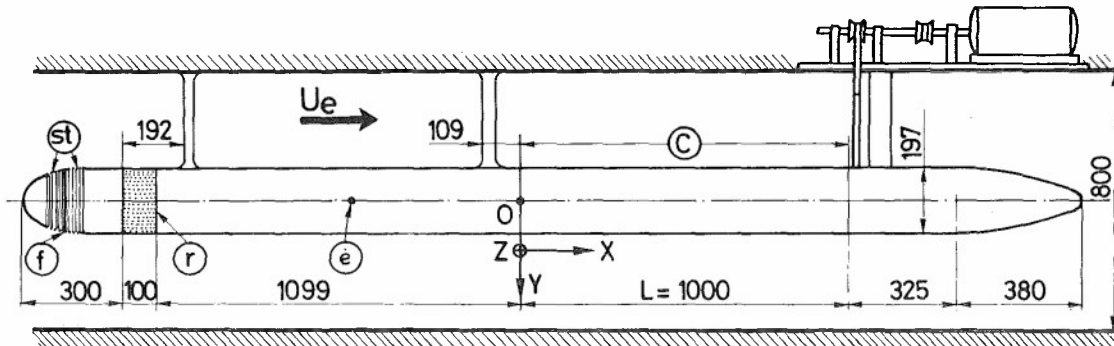


FIG. 1 : Dispositif expérimental.

St : stries  
f : fil de transition  
r : rugosités  
e : filin support  
C : cylindre tournant  
L : dimension du cylindre tournant,  
les dimensions sont en mm.

maintenir latéralement le cylindre. Le bord de fuite a été également convenablement profilé.

En définitive, les dimensions de la maquette ont été choisies de telle sorte que d'une part la couche limite turbulente soit pleinement développée au début de la paroi tournante et que d'autre part, à la fin de celle-ci, la restructuration soit dans une phase bien avancée.

## 2.2. - Conditions expérimentales.

Juste en amont de la partie tournante ( $X/\delta_o = -1,1$ ) les conditions expérimentales, avec et sans rotation, sont les suivantes :

$$U_e = 12,34 \text{ m s}^{-1}$$

$$\delta_o (U/U_e = 0,99) = 22,5 \text{ mm} \quad (\delta_o \approx 28 \text{ mm pour } U/U_e = 1)$$

$$Re_{\delta_o} = 19\,000$$

A la station de mesure généralement adoptée ( $X/\delta_o = 28$ ), avec ou sans rotation on a :

$$U_e = 12,38 \text{ m s}^{-1}$$

$$\delta (U/U_e = 0,99) = 28,3 \text{ mm} \quad (\delta \approx 34 \text{ mm pour } U/U_e = 1)$$

Le gradient longitudinal de pression statique est faiblement négatif (Avec ou sans rotation on a :

$$\frac{1}{\rho U_e^2} \frac{d p_e}{d x} = -0,0165 \text{ m}^{-1}$$

et la valeur absolue du paramètre de CLAUSER est petite ( $\pi = \frac{\delta^*}{\rho U_e^2} \frac{d p_e}{d x} = -0,026$ ).

Lorsque  $W_o = 0$  la vitesse de frottement est :

$$U_* = (\tau_p / \rho)^{1/2} = 0,47 \text{ m s}^{-1}$$

La vitesse périphérique de la paroi a été choisie pratiquement égale à la vitesse extérieure

$$W_o = 10,92 \text{ m s}^{-1}$$

En  $X/\delta_o = 28$  on a ainsi  $W_o/U_e \approx 0,887$

Par ailleurs, la distribution azimuthale de la vitesse moyenne longitudinale a été contrôlée tout au long de la partie tournante. La figure 2 donne un exemple des profils obtenus à  $X/\delta_o = 18,8$  pour différentes distances à la paroi. On vérifie ainsi que l'axisymétrie de la couche limite turbulente est satisfaisante, particulièrement dans la zone comprise entre  $\omega = -30^\circ$  et  $\omega = +30^\circ$  située autour de la position de mesure  $\omega = 0$ .

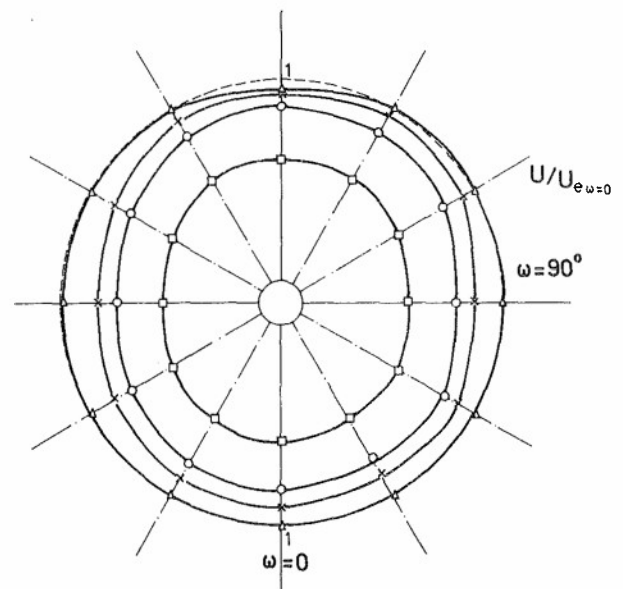


FIG. 2 : Distribution azimuthale de la vitesse moyenne longitudinale.

$X/\delta_o = 18,8$  -  $\square y = 1,1 \text{ mm}$   $\circ y = 7,3 \text{ mm}$   
 $\times y = 17,7 \text{ mm}$   $\Delta y = 40 \text{ mm}$

## 2.3. - Méthodes de mesures.

Les mesures de vitesse moyenne ont été effectuées à l'aide de sondes de pression et de fil chaud. Divers types de difficultés ont dû être surmontées notamment pour l'exploration des régions très proches de la paroi ( $y U_* / \nu \approx 2$ ).

### 2.3.1. Sondes de pression.

En ce qui concerne la mesure de la pression totale, un tube aplati de  $0,34 \text{ mm} \times 1,2 \text{ mm}$  a été utilisé. Ceci a permis de mesurer la vitesse moyenne jusqu'à une distance de  $0,17 \text{ mm}$  de la paroi ( $y U_* / \nu \approx 6$ ).

Quant à la mesure de la pression statique, une sonde a été placée à l'extérieur de la couche limite dans la section de mesure.

En l'absence de rotation, une correction due au gradient de vitesse et à la proximité de paroi a été introduite à partir des abaques de Mac MILLAN / REF. 9/ ; de plus, une correction de l'effet de turbulence a été prise en compte / REF. 10/.

Avec rotation, à proximité immédiate de la paroi, les vitesses sont fortes et aucune correc-

tion n'a été appliquée, ce qui a conduit à des résultats cohérents avec les conditions aux limites (fig. 6, 7, 8).

Pour ce qui est de la pression statique, on a montré, à partir de l'équation de quantité de mouvement relative à la composante de la vitesse normale à la paroi, que si l'on prend la valeur à l'extérieur de la couche limite on ne commet qu'une erreur de 0,7% au maximum pour le point le plus proche de la paroi

$$(1) \quad \frac{P_t - P}{\frac{1}{2} \rho U_e^2} = \frac{\Delta P_{mes}}{\frac{1}{2} \rho U_e^2} + 2 \int_y^{h \gg \delta} \left( \frac{w}{U_e} \right)^2 \frac{dy}{a+y}$$

où  $P_t$  est la pression totale et  $\Delta P_{mes} = P_t - P_e$

En fait, avec rotation, la mesure de la vitesse est effectuée après la détermination de la direction  $\beta$  du vecteur vitesse. Pour cela, la prise de pression totale elle-même est utilisée comme clinomètre : la différence de pression  $\Delta P_{mes}$  est traduite sous forme de tension électrique  $e$  qui est une fonction de l'angle  $\psi$  ( $\psi$  est l'angle de la vitesse absolue par rapport à la sonde). Cette fonction  $e(\psi)$  passe par un maximum lorsque la sonde est dans la direction du vecteur vitesse moyenne. L'angle  $\beta$  est alors déterminé par l'écart entre les angles correspondant aux maxima de  $e(\psi)$  obtenus respectivement à l'extérieur et dans la couche limite. Les résultats ainsi obtenus sont en bon accord (fig. 5 à 10) avec ceux donnés par le fil chaud.

### 2.3.2. Sondes à fil chaud.

Les fils chauds utilisés sont en Pt - Rh. Ils ont 5  $\mu m$  de diamètre et un allongement  $l/d$  de 320. Les mesures ont été effectuées à température constante et sans linéarisation. Avec ces sondes, les mesures ont pu être effectuées jusqu'à 0,06 mm de la paroi, même lorsque le cylindre est en rotation.

En l'absence de rotation, dans les régions de très proche paroi ( $y \leq 1$  mm), la vitesse étant relativement faible, les effets de conduction moléculaire dus à la présence de la paroi modifient fortement le régime de convection autour du fil.

Ces effets ont été pris en compte selon une correction due à CHAUVÉ /REF. 11/. Les résultats ainsi obtenus sont très voisins de ceux donnés par la méthode de WEISSBERG /REF. 12/.

Lorsque le cylindre est en rotation, à proximité immédiate de la paroi, l'effet relatif de conduction moléculaire (dû à la présence de la paroi) à la convection autour du fil est très faible du fait des fortes vitesses qui règnent dans cette région. Aussi, aucune correction n'a été apportée dans ce cas. Les résultats obtenus sont, là encore, cohérents avec les conditions aux limites (fig. 5 à 10).

Avec rotation, on détermine d'abord l'angle  $\beta$  : la variation de la tension moyenne aux bornes du fil chaud en fonction de l'angle  $\psi$  étant analogue à celle de la caractéristique  $e(\psi)$  du tube de pression totale, une méthode identique est utilisée (voir § 2.3.1.) avec le fil chaud tournant.

### 3 - CALCUL DE LA COUCHE LIMITE.

Afin de calculer de manière détaillée un écoulement turbulent, les techniques les plus répandues actuellement consistent en une modélisation de la turbulence dans le but essentiel de déterminer l'évolution des tensions de Reynolds.

Appliquées aux couches limites bidimensionnel-

les ces techniques conduisent en général à des résultats tout à fait corrects. En couche limite tridimensionnelle, un problème spécifique est dû à la différence d'orientation entre le vecteur vitesse moyenne  $\bar{V}$  et le vecteur dérivée  $\frac{\partial \bar{V}}{\partial y}$ . Si l'on

admet que les structures turbulentes de grande échelle ont tendance à être orientées suivant l'axe principal du tenseur de déformation de manière à être plus aptes à extraire de l'énergie au mouvement moyen /REF. 13/, et si l'on admet aussi qu'elles sont approximativement convectées dans la direction de la vitesse moyenne, on conçoit qu'il s'agit a priori d'une situation très complexe. Il en ressort en particulier, comme cela a été mis en évidence expérimentalement par quelques auteurs /REF. 14/, que la force de cisaillement turbulent n'est pas alignée avec le vecteur  $\frac{\partial \bar{V}}{\partial y}$  ; il faut cependant noter qu'on manque d'informations permettant de préciser les mécanismes qui régissent ce phénomène : ceci est l'un des objectifs futurs de l'expérience précédemment décrite.

La plupart des modèles développés jusqu'à maintenant ne tiennent pas compte de ces effets purement tridimensionnels. Dans les modèles de type viscosité tourbillonnaire la colinéarité tension/gradient est explicitement supposée dès que l'on écrit :

$$(2) \quad \begin{aligned} -\overline{v'v'} &= \nu_t \frac{\partial v}{\partial y} \\ -\overline{w'v'} &= \nu_t \frac{\partial w}{\partial y} \end{aligned}$$

Dans les modèles où les tensions sont calculées à l'aide d'équations de transport, on constate que pour de nombreuses situations d'écoulement une telle hypothèse est en fait implicitement retenue. En effet, en utilisant un modèle développé par LAUNDER et al. /REF. 15/, le calcul nous a montré qu'il s'établit très rapidement un état pour lequel les termes de convection et de diffusion sont petits /REF. 6/ ; la modélisation adoptée pour les termes de corrélation pression-vitesse impose alors la colinéarité tension/gradient.

Masqué en écoulement bidimensionnel où ces directions sont obligatoirement confondues, ce problème met donc clairement en évidence un certain nombre de défauts des modélisations classiques.

FANNELP-HUMPHREYS /REF. 16/ ont montré par une expérience numérique, que les résultats du calcul sont modifiés sensiblement en imposant une viscosité tourbillonnaire dont la valeur n'est pas la même dans la direction de l'écoulement extérieur et dans la direction qui lui est orthogonale. Signalons aussi que des remèdes peu justifiés ont été proposés par ELSENAAR et al. /REF. 17/ pour pallier ces difficultés.

En fait, il semble que le problème réside dans la modélisation des termes de corrélation pression-vitesse. ROTTA /REF. 7/ a repris la modélisation de ces termes en se limitant au cas d'une couche limite et il a montré que des hypothèses nouvelles doivent être introduites pour prendre en compte les effets tridimensionnels. Nous avons reconsidéré la modélisation de ces termes en utilisant une méthode d'analyse différente qui aboutit dans le cas des couches minces aux mêmes résultats que ceux établis par ROTTA /REF. 7/.

Après avoir décrit la modélisation proposée et les schémas de turbulence qui en résultent, nous présenterons les résultats auxquels on est conduit dans l'application au cas expérimental précédemment décrit.



### 3.1. - Equations de transport aux tensions de Reynolds : modélisation des corrélations pression-vitesse.

Les équations aux valeurs moyennes de continuité et de quantité de mouvement seront écrites dans le repère relatif lié au cylindre en rotation, en coordonnées cylindriques. Pour un écoulement axisymétrique, avec les hypothèses de couche limite, on a :

$$(3) \quad \frac{\partial U}{\partial x} + \frac{\partial V}{\partial y} + \frac{V}{r} = 0$$

$$(4) \quad U \frac{\partial U}{\partial x} + V \frac{\partial U}{\partial y} = -\frac{1}{\rho} \frac{\partial p}{\partial x} - \frac{\overline{U'V'}}{r} - \frac{\partial \overline{U'V'}}{\partial y} + \nu \left( \frac{\partial^2 U}{\partial y^2} + \frac{1}{r} \frac{\partial U}{\partial y} \right)$$

$$(5) \quad U \frac{\partial W_r}{\partial x} + V \left( \frac{\partial W_r}{\partial y} + \frac{W_r}{r} \right) + 2V \frac{W_\theta}{r} = -\frac{2}{r} \frac{\overline{V'W_\theta'}}{\partial y} - \frac{\partial \overline{V'W_\theta'}}{\partial y} + \nu \left( \frac{\partial^2 W_r}{\partial y^2} + \frac{1}{r} \frac{\partial W_r}{\partial y} - \frac{W_\theta}{r} \right)$$

On peut remarquer que le terme d'accélération de CORIOLIS doit en fait être négligé dans l'approximation de couche limite. Notons aussi que la dérivée  $\frac{\partial p}{\partial y}$  est supposée nulle ; ce problème a déjà été discuté au paragraphe 2.3.1..

En ce qui concerne le schéma de turbulence, on devrait en toute rigueur tenir compte des effets de courbure. Cependant, pour une première approche, nous les avons négligés.

Le schéma de turbulence proposé repose sur la modélisation des équations aux tensions de Reynolds qui, en négligeant tout effet de courbure, s'écrivent :

$$(6) \quad \frac{\partial}{\partial t} \overline{U_i' U_j'} = - \left( \overline{U_k' U_j'} \frac{\partial U_i}{\partial x_k} + \overline{U_k' U_i'} \frac{\partial U_j}{\partial x_k} \right) - 2\nu \frac{\partial \overline{U_i' U_j'}}{\partial x_k} \frac{\partial U_k}{\partial x_k} + \frac{\rho}{\rho} \left( \frac{\partial \overline{U_i' U_j'}}{\partial x_k} + \frac{\partial \overline{U_j' U_i'}}{\partial x_k} \right) - \frac{\partial}{\partial x_k} \left( \overline{U_i' U_j' U_k'} - \nu \frac{\partial \overline{U_i' U_j' U_k'}}{\partial x_k} + \frac{\rho}{\rho} \left( \overline{U_i' U_j' U_k'} + \overline{U_j' U_i' U_k'} \right) \right)$$

Le terme de corrélation pression-vitesse est exprimé de façon classique /REF. 7 / : on écrit d'abord l'équation de POISSON pour la pression, obtenue en prenant la divergence des équations de NAVIER-STOKES ; ensuite, par résolution de cette équation on peut déduire la formulation suivante du terme de corrélation pression-vitesse, valable loin des parois :

$$(7) \quad \left( \frac{\rho}{\rho} \frac{\partial \overline{U_i' U_j'}}{\partial x_k} \right)_{x_0} = \frac{1}{2\pi} \int_V \frac{\partial U_k(x')}{\partial x'_m} \frac{\partial \overline{U_m(x') U_i' U_j'}}{\partial x'_e} \left( \frac{\partial U_j'}{\partial x_j} \right)_{x_0} \frac{dV}{|\xi|} \\ \phi_{ij,2} \\ + \frac{1}{4\pi} \int_V \frac{\partial^2 U_k(x')}{\partial x'_e \partial x'_m} \frac{\partial \overline{U_m(x') U_i' U_j'}}{\partial x'_j} \left( \frac{\partial U_j'}{\partial x_j} \right)_{x_0} \frac{dV}{|\xi|} \\ \phi_{ij,1}$$

avec  $x'_i = x_{0i} + \xi_i$

Les intégrales sont étendues à tout l'espace.

$\phi_{ij}$  a été séparé en deux termes qui agissent séparément dans deux types d'écoulements simples différents :  $\phi_{ij,1}$  est seul présent dans le cas d'un écoulement homogène, sans gradient de vitesse moyenne, initialement anisotrope et qui tend vers l'état isotrope ;  $\phi_{ij,2}$  est prépondérant dans les premières phase de l'évolution d'un écoulement homogène, initialement isotrope soumis brutalement à l'influence d'un gradient de vitesse.

Les termes  $\phi_{ij,1}$  et  $\phi_{ij,2}$  sont étudiés séparément et l'on suppose que la modélisation de

chacun d'entre eux reste valable quel que soit l'écoulement considéré. En fait, nous examinerons simplement ici le terme  $\phi_{ij,2}$ . Quant à  $\phi_{ij,1}$  nous avons conservé une modélisation classique /REF. 7 et 15/.

Une première approximation introduite déjà par Rotta /REF. 7/ consiste à négliger l'inhomogénéité du champ de vitesses moyennes. On peut alors évaluer  $\phi_{ij,2}$  sous la forme.

$$(8) \quad \phi_{ij,2} = a_{ij}^{mi} \frac{\partial U_e}{\partial x_m} \\ a_{ij}^{mi} = -\frac{1}{2\pi} \int_V \frac{\partial^2 \overline{U_m(x_0 + \xi) U_i' U_j'}}{\partial \xi_e \partial \xi_j} \frac{dV}{|\xi|}$$

Le problème consiste ainsi à chercher un modèle pour exprimer le tenseur  $a_{ij}^{mi}$ . Quel que soit le modèle adopté,  $a_{ij}^{mi}$  doit satisfaire trois conditions /REF. 15 et 18/.

$$(9a) \text{ condition de symétrie } a_{ij}^{mi} = a_{ji}^{im} = a_{je}^{mi}$$

$$(9b) \text{ l'équation de continuité } \frac{\partial U_i'}{\partial x_i} \text{ impose } a_{ii}^{mi} = 0$$

$$(9c) \text{ de l'identité } \overline{U_m' U_i'} = -\frac{1}{4\pi} \int_V \frac{\partial^2 \overline{U_m(x') U_i'}}{\partial \xi_e^2} \frac{dV}{|\xi|}$$

$$\text{on déduit } a_{ii}^{mi} = 2 \overline{U_m' U_i'}$$

L'hypothèse de modélisation la plus simple consiste à supposer que  $a_{ij}^{mi}$  est une forme tensorielle isotrope dépendant des corrélations  $\overline{U_i' U_j'}$ . Cependant une telle hypothèse, équivalente à celle utilisée par LAUNDER et al. /REF. 15/, conduit aux schémas de turbulence classique pour lesquels on retrouve l'alignement tension/gradient si l'on néglige les termes de convection et de diffusion.

Nous avons donc cherché à introduire une hypothèse moins restrictive. Nous avons supposé que  $a_{ij}^{mi}$  est une forme tensorielle axisymétrique autour de la vitesse moyenne, dépendant des corrélations  $\overline{U_i' U_j'}$ . Il est équivalent de dire que  $a_{ij}^{mi}$  est une forme tensorielle isotrope dépendant des tensions de Reynolds et de la vitesse moyenne. L'idée physique sous-jacente est que le champ turbulent est convecté par la vitesse moyenne /REF. 19/. L'inconvénient majeur d'une telle hypothèse est, comme l'a fait remarquer Rotta /REF. 20/, la nécessité de préciser le système d'axes dans lequel on travaille : en effet, la direction de la vitesse n'est pas la même dans un repère en translation uniforme et dans un repère fixe. Tant que l'on s'intéresse aux couches limites, il semble naturel d'utiliser un système d'axes lié à la paroi de l'obstacle sur lequel se développe la couche limite.

Le tenseur  $a_{ij}^{mi}$  est donc de la forme :

$$(10) \quad a_{ij}^{mi} = \mathcal{F}(\overline{U_i' U_j'}, U_i)$$

où  $U_i$  sont les composantes de la vitesse dans un repère lié à la paroi.

Pour simplifier la modélisation, il est intéressant, comme l'a proposé LUMLEY /REF. 21/, de supposer que le champ turbulent est faiblement anisotrope, c'est à dire que la quantité :

$$(11) \quad a_{ij} = \frac{\overline{U_i' U_j'}}{k} - \frac{2}{3} \delta_{ij}$$

est petite devant l'unité.

En remplaçant  $\overline{U_i' U_j'}$  par  $a_{ij}$ , on peut

écrire que  $a_{ij}^{mi}$  est de la forme :

$$(12) \quad a_{ij}^{mi} = \mathcal{F}(a_{ij}, k, U_i)$$

et comme  $a_{ij}$  est petit devant l'unité on peut effectuer un développement de  $\mathcal{F}$  par rapport à  $a_{ij}$ . On se limitera en fait ici à l'expression de  $\mathcal{F}$  à l'ordre zéro par rapport à  $a_{ij}$ .

En s'appuyant sur les théorèmes de représentation invariante des fonctions tensorielles, utilisées de façon systématique par LUMLEY /REF. 21/ on trouve que la forme la plus générale de  $a_{ij}^{mi}$  est :

$$(13) \quad a_{ij}^{mi} = a \delta_{mi} \delta_{ij} + b \delta_{mj} \delta_{il} + b_1 \delta_{ml} \delta_{ij} + c \delta_{il} U_m U_j + c_1 \delta_{ml} U_i U_j + c_2 \delta_{ij} U_m U_l + c_3 \delta_{mj} U_i U_l + d \delta_{ij} U_i U_m + e \delta_{im} U_l U_j + f U_i U_j U_m U_l + \text{termes } O(a_{ij}) + \dots$$

où les a, b, c, d, e, f sont des coefficients.

En appliquant à l'équation (13) les conditions (9a) (9b) (9c), le nombre de coefficients indépendants est réduit à deux. D'après l'équation (8) on en déduit la forme de  $\phi_{ij,2}$  ; l'expression du terme  $\phi_{ij,2} + \phi_{ji,2}$  qui intervient dans l'équation (6) pour  $u_i' u_j'$  devient alors :

$$(14) \quad \phi_{ij,2} + \phi_{ji,2} = \left\{ \left( \frac{2}{5} - \frac{C+3E}{10} \right) (\delta_{mi} \delta_{lj} + \delta_{mj} \delta_{il}) + \left( -\frac{4}{15} + \frac{E-3C}{5} \right) \delta_{ml} \delta_{ij} + 2C (\delta_{ml} U_i U_j + \delta_{ij} U_m U_l) / U_p U_p + \frac{3C+E}{2} (\delta_{ij} U_i U_m + \delta_{il} U_m U_j) / U_p U_p + (C+E) (\delta_{im} U_j U_l + \delta_{jm} U_i U_l) / U_p U_p - (11C+3E) U_i U_j U_m U_l / (U_p U_p)^2 \right\} k \frac{\partial U_l}{\partial x_m}$$

Dans cette expression (14), C et E peuvent éventuellement être fonctions de k et  $U_p U_p$ .

### 3.2. - Modèles résultant pour le calcul d'une couche limite.

Dans le cadre des approximations usuelles de couche limite, l'expression (14) de  $\phi_{ij,2} + \phi_{ji,2}$  se simplifie. En fait, on s'intéresse seulement aux équations pour  $-u_i' v_j'$  et  $-w_i' v_j'$  dans lesquelles apparaissent les quantités :

$$(15a) \quad \phi_{12,2} + \phi_{21,2} = k \left[ \left( \frac{2}{5} - \frac{C}{10} - \frac{3E}{10} + \frac{(C+E)U^2}{U^2 + W_r^2} \right) \frac{\partial U}{\partial y} + \frac{(C+E)U W_r}{U^2 + W_r^2} \frac{\partial W_r}{\partial y} \right]$$

$$(15b) \quad \phi_{32,2} + \phi_{23,2} = k \left[ \left( \frac{2}{5} - \frac{C}{10} - \frac{3E}{10} + \frac{(C+E)W_r^2}{U^2 + W_r^2} \right) \frac{\partial W_r}{\partial y} + \frac{(C+E)U W_r}{U^2 + W_r^2} \frac{\partial U}{\partial y} \right]$$

On peut encore regrouper ces termes avec les termes de production dans les équations pour  $-u_i' v_j'$  et  $-w_i' v_j'$ , respectivement  $\bar{v}^2 \frac{\partial U}{\partial y}$  et  $\bar{v}^2 \frac{\partial W_r}{\partial y}$ .

En supposant  $\bar{v}^2 = 2k/3$  les termes sources des équations pour  $-u_i' v_j'$  et  $-w_i' v_j'$  sont :

$$(16a) \quad S_{\bar{u}v} = k \left( a_{pxx} \frac{\partial U}{\partial y} + a_{pxz} \frac{\partial W_r}{\partial y} \right)$$

$$(16b) \quad S_{\bar{w}v} = k \left( a_{pzx} \frac{\partial U}{\partial y} + a_{pzz} \frac{\partial W_r}{\partial y} \right)$$

avec :

$$(17) \quad a_{pxx} = C_{\epsilon_1} \frac{U^2 + T W_r^2}{U^2 + W_r^2}$$

$$a_{pxz} = a_{pzx} = C_{\epsilon_1} (1-T) \frac{U W_r}{U^2 + W_r^2}$$

$$a_{pzz} = C_{\epsilon_1} \frac{T U^2 + W_r^2}{U^2 + W_r^2}$$

où  $C_{\epsilon_1}$  et T sont des coefficients fonctions de C et E.

$$(18a) \quad C_{\epsilon_1} = -\frac{4}{15} + \frac{9}{10} C + \frac{7}{10} E$$

$$(18b) \quad T = \frac{8 + 3C + 9E}{8 - 27C - 24E}$$

Ainsi dans le cas des couches limites, on obtient une expression (16) des termes sources identique à celle obtenus par ROTTA /REF. 7/ en suivant une analyse différente.

Remarquons que le terme source (16a) de l'équation pour  $u_i' v_j'$  (resp. 16b pour  $w_i' v_j'$ ) fait intervenir une combinaison linéaire des dérivées  $\frac{\partial U}{\partial y}$  et  $\frac{\partial W_r}{\partial y}$

et non pas seulement la dérivée  $\frac{\partial U}{\partial y}$  (resp.  $\frac{\partial W_r}{\partial y}$ ) comme les modèles "classiques" que l'on retrouve en faisant T = 1.

Pour compléter l'expression des équations pour  $-u_i' v_j'$  et  $-w_i' v_j'$ , nous avons utilisé les modèles classiques de  $\phi_{ij,1} + \phi_{ji,1}$  et des termes de dissipation et de diffusion /REF. 7 et 15/. On aboutit ainsi à :

$$(19a) \quad \frac{D}{Dt} (-\bar{u}v) = k(a_{pxx} \frac{\partial U}{\partial y} + a_{pxz} \frac{\partial W_r}{\partial y}) + C_{\epsilon_2} \frac{\epsilon}{k} \bar{u}v + \frac{\partial}{\partial y} \left( \left( \nu + \frac{\nu_t}{\sigma_\epsilon} \right) \frac{\partial (-\bar{u}v)}{\partial y} \right)$$

$$(19b) \quad \frac{D}{Dt} (-\bar{w}v) = k(a_{pzx} \frac{\partial U}{\partial y} + a_{pzz} \frac{\partial W_r}{\partial y}) + C_{\epsilon_2} \frac{\epsilon}{k} \bar{w}v + \frac{\partial}{\partial y} \left( \left( \nu + \frac{\nu_t}{\sigma_\epsilon} \right) \frac{\partial (-\bar{w}v)}{\partial y} \right)$$

où  $C_{\epsilon_2}$  et  $\sigma_\epsilon$  sont des constantes et  $a_{pxx}$ ,  $a_{pzz}$  sont donnés par les formules (17).

Pour les applications au calcul d'une couche limite, ce jeu d'équations doit être complété d'une équation de transport pour l'évolution de l'énergie cinétique de turbulence k et d'une équation pour son taux de dissipation  $\epsilon$ .

Cependant, un modèle plus simple peut être obtenu en considérant que les termes de convection et de diffusion sont négligeables. On aboutit alors à une expression analytique de  $-\overline{u'v'}$  et  $-\overline{w'v'}$  :

$$(20a) \quad -\overline{u'v'} = \nu_t \left( \frac{a_{px}}{C_{\epsilon_1}} \frac{\partial U}{\partial y} + \frac{a_{pxz}}{C_{\epsilon_1}} \frac{\partial W_r}{\partial y} \right)$$

$$(20b) \quad -\overline{w'v'} = \nu_t \left( \frac{a_{pzx}}{C_{\epsilon_1}} \frac{\partial U}{\partial y} + \frac{a_{pzz}}{C_{\epsilon_1}} \frac{\partial W_r}{\partial y} \right)$$

$$\text{avec} \quad \nu_t = C_\mu \frac{k^2}{\varepsilon} \quad C_\mu = \frac{C_{\epsilon_1}}{C_{\epsilon_2}}$$

Ces expressions font apparaître que la force de cisaillement turbulente n'est pas alignée avec  $\frac{\partial \mathbf{v}}{\partial y}$ . On peut d'ailleurs vérifier que les formules (20a) et (20b) conduisent à /REF. 7/ :

$$(21) \quad T = \frac{\lg(\gamma_0 - \gamma)}{\lg(\gamma_g - \gamma)}$$

où  $\gamma$ ,  $\gamma_g$ ,  $\gamma_0$  représentent respectivement les directions de la vitesse, de  $\frac{\partial \mathbf{v}}{\partial y}$  et de la force de cisaillement turbulente.

Ce schéma est complété par les équations pour  $k$  et  $\varepsilon$  qui sont en fait une extension de celles proposées par JONES-LAUDER /REF. 22/ en bidimensionnel :

$$(22) \quad \frac{Dk}{Dt} = -\overline{u'v'} \frac{\partial U}{\partial y} - \overline{w'v'} \frac{\partial W_r}{\partial y} - \varepsilon - 2\gamma \left( \frac{\partial k^{1/2}}{\partial y} \right)^2 + \frac{\partial}{\partial y} \left( \left( \gamma + \frac{\gamma_t}{\epsilon_k} \right) \frac{\partial k}{\partial y} \right)$$

$$(23) \quad \frac{D\varepsilon}{Dt} = \frac{\varepsilon}{k} \left[ C_{\epsilon_1} \left( -\overline{u'v'} \frac{\partial U}{\partial y} - \overline{w'v'} \frac{\partial W_r}{\partial y} \right) + \frac{1}{2} C_{\epsilon_2} \varepsilon \right] + 2\gamma \nu_t \left[ \left( \frac{\partial^2 U}{\partial y^2} \right)^2 + \left( \frac{\partial^2 W_r}{\partial y^2} \right)^2 \right] + \frac{\partial}{\partial y} \left( \left( \gamma + \frac{\gamma_t}{\epsilon_k} \right) \frac{\partial \varepsilon}{\partial y} \right)$$

où l'on a gardé les mêmes valeurs qu'en bidimensionnel pour les différentes constantes :

$$C_\mu = 0,09 \quad C_{\epsilon_1} = 1,57 \quad C_{\epsilon_2} = 2 \quad \epsilon_k = 1 \quad \epsilon_\varepsilon = 1,3$$

les fonctions correctrices de faible nombre de Reynolds sont aussi les mêmes qu'en bidimensionnel :

$$\nu_t = f_\mu C_\mu \frac{k^2}{\varepsilon} \quad f_\mu = e^{-2,5/(1+R_t/50)} \quad R_t = \frac{k^2}{\nu \varepsilon} \\ f_2 = 1 - 0,3 e^{-R_t^2}$$

#### 4 - RESULTATS-COMPARAISONS CALCUL-EXPERIENCE.

Dans le cas où le cylindre est en rotation, deux valeurs du paramètre  $T$  ont été considérées dans le calcul :  $T = 1$  correspondant au modèle classique et  $T = 0,5$ . En l'absence de rotation, le même modèle a été mis en oeuvre mais le paramètre  $T$  n'intervient pas.

Les évolutions longitudinales des épaisseurs intégrales de couche limite  $\delta_x^*$ ,  $\theta_x$ ,  $\delta_z^*$ ,  $\theta_{xz}$  ainsi que celles du paramètre de forme  $H$  et des coefficients de frottement  $C_{fx}$  et  $C_{fz}$  sont données sur les figures 3 et 4. Les valeurs expérimentales

des coefficients de frottement sont déduites des équations intégrées de quantité de mouvement /REF. 3/; dans le cas présent, ces relations se réduisent à /REF. 5/ :

$$(24) \quad C_{fx} = 2 \frac{d\theta_x}{dx} - \frac{2(H+2)\theta_x}{\rho U_e^2} \frac{d\rho_e}{dx}$$

$$(25) \quad C_{fz} = 2 \frac{W_0}{U_e} \frac{d\theta_{xz}}{dx} - \frac{\theta_{xz}}{\rho U_e^2} \frac{d\rho_e}{dx}$$

A la station adoptée,  $X/\delta_0 = 28$ , l'expérience donne :

$$C_{fx} = 44,1 \cdot 10^{-4} \quad C_{fz} = 39,7 \cdot 10^{-4}$$

La comparaison calcul-expérience (Fig. 3 et 4) indique un bon accord général ; cependant le calcul semble sous-estimer  $C_{fx}$  et sur-estimer  $C_{fz}$ . Il est à noter aussi que les paramètres intégraux ne paraissent pas être sensibles à  $T$ .

Les résultats détaillés présentés sur les figures 5 à 11 ont été obtenus à la station  $X = 28 \delta_0 = 630$  mm ; à cette station l'effet de la rotation de la paroi sur l'angle  $\beta$  se fait sentir jusqu'aux trois quarts environ de l'épaisseur de la couche limite.

Sur chacune de ces figures ont été portées les pentes ( $K$ ) à l'origine calculées à partir des valeurs expérimentales des frottements obtenus par les équations globales (24) et (25). Ces pentes sont en bon accord avec les points de mesure les plus proches de la paroi.

On peut montrer que l'on a :

$$(26) \quad \left( \frac{\partial \eta}{\partial y} \right)_0 = \left( \frac{\partial W}{\partial y} \right)_0 = C_{fz} \frac{U_e^2}{2\nu}$$

D'autre part les approximations de sous-couche visqueuse permettent d'écrire :

$$(27) \quad \cotg \beta = \frac{(U_e^2 / 2\nu W_0) C_{fx}}{1 - (U_e^2 / 2\nu W_0) C_{fz} y} y$$

Dans la proximité immédiate de la paroi ( $y U_* / \nu < 2$ ) cette relation se ramène à /REF.5/ :

$$(28) \quad \cotg \beta = \frac{U_e^2}{2\nu W_0} C_{fx} y$$

La pente et la courbure à l'origine de la courbe  $\beta(y)$  déduites de l'équation (26) s'écrivent alors :

$$(29) \quad \left( \frac{d\beta}{dy} \right)_0 = -\frac{U_e^2}{2\nu W_0} C_{fx} \quad \left( \frac{d^2\beta}{dy^2} \right)_0 = -\frac{1}{2} \left( \frac{U_e^2}{\nu W_0} \right)^2 C_{fx} C_{fz}$$

Les valeurs et les signes obtenus sont en accord avec les résultats expérimentaux et numériques (fig. 5). Il est à noter que le calcul semble sur-estimer l'angle  $\beta$  au voisinage de la paroi.

On remarque que la majeure partie de l'influence de la rotation se manifeste dans une zone très restreinte au voisinage de la paroi. On peut estimer que celle-ci s'étend jusqu'à la position correspondante au maximum de courbure du profil  $\beta(y)$  ; l'angle  $\beta$  a alors déjà varié d'environ 60 degrés. L'épaisseur de cette zone, d'environ 0,02  $\delta$  (soit  $y U_* / \nu \approx 15$ ), est très faible par rapport à la distance 0,85  $\delta$  où  $\beta$  est pratiquement nul.

En ce qui concerne le profil du module de vitesse  $q$  (figure 6), le calcul est en très bon accord avec l'expérience. Quant aux profils de  $w$  et  $u$  (figures 7 et 8) une différence assez notable est observée près de la paroi surtout pour le profil de  $w$  : ces différences sont les conséquences de celles déjà observées pour le profil de  $\beta$ .

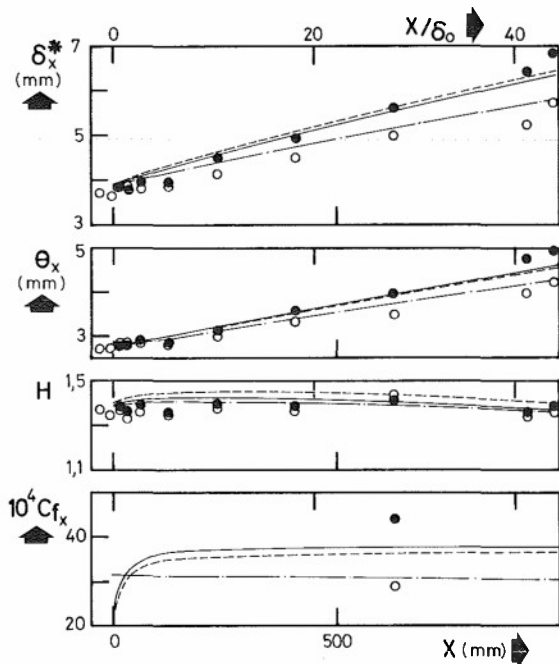


FIG. 3 :

Caractéristiques axiales de la couche limite.

Mesures :  $\circ W_0 = 0$   $\bullet W_0 = 10,98 \text{ ms}^{-1}$

Calcul :  $---$   $W_0 = 0$   $---$   $T = 1$   $---$   $W_0 = 10,98 \text{ ms}^{-1}$   $---$   $T = 0,5$

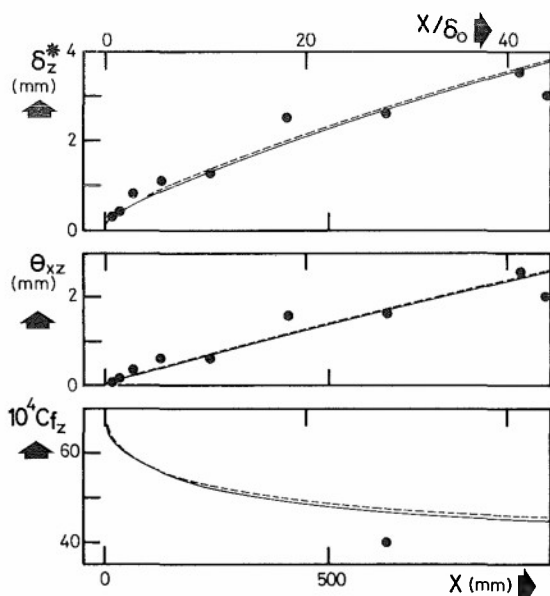


FIG. 4 :

Caractéristiques périphériques de la couche limite.

Mesures :  $\bullet W_0 = 10,98 \text{ ms}^{-1}$

Calcul :  $---$   $T = 1$   $---$   $T = 0,5$

En fait, pour rendre compte notamment de l'effet de tridimensionnalité de manière plus significative, un repère relatif lié à la paroi en rotation doit

être adopté. Les directions et les modules de vitesses dans les repères absolu et relatif sont particulièrement bien mis en évidence dans le plan de l'hodographe (figure 9). Dans cette représentation, la vitesse extérieure fait un angle  $\psi_0$  avec la direction axiale.

La figure 10 fait apparaître une différence entre les résultats numériques et expérimentaux dans les régions très voisines de la paroi ( $y u_* / \nu < 10$   $u/u_e < 0,4$ ) correspondant à une rapide variation de l'angle  $\beta$  d'environ 40 degrés. Notons que les mesures de BISSONNETTE-MELLOR /REF. 1/, no-

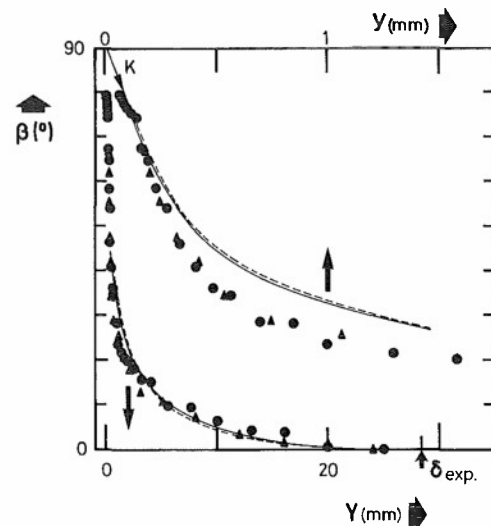


FIG. 5 :

Profil de déviation du vecteur vitesse absolue.

$X/\delta_0 = 28$  ( $X = 630 \text{ mm}$ )  $W_0/U_e = 0,887$

Mesures :  $\bullet$  Fil chaud  $\blacktriangle$  sonde de pression

$K$  : pente à l'origine (formule 29 et valeur expérimentale de  $C_{fx}$  d'après l'équation 24).

Calcul :  $---$   $T = 1$   $---$   $T = 0,5$

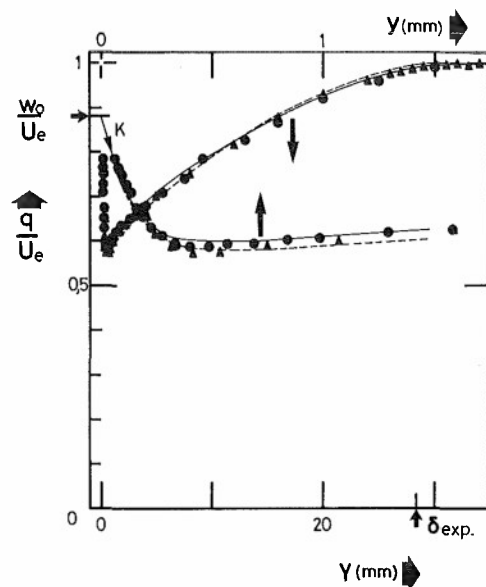


FIG. 6 :

Module de la vitesse absolue.

$X/\delta_0 = 28$  ( $X = 630 \text{ mm}$ )  $W_0/U_e = 0,887$

Mesures :  $\bullet$  Fil chaud  $\blacktriangle$  sonde de pression

$K$  : pente à l'origine (formule 26 et valeur expérimentale de  $C_{fz}$  d'après l'équation 25).

Calcul :  $---$   $T = 1$   $---$   $T = 0,5$

tamment, n'intéressaient pas ces régions et ne permettent pas une telle comparaison. Pour que les points obtenus par l'expérience et le calcul coïncident dans ces régions il faudrait supposer que  $\beta$  soit entaché d'une erreur d'environ 5 degrés.

L'évolution de ces profils polaires en fonction de la distance longitudinale est donnée sur la figure 11. Cette figure met en évidence de quelle manière l'épaisseur de la zone où  $\bar{W}$  est différent de zéro tend asymptotiquement vers l'épaisseur de

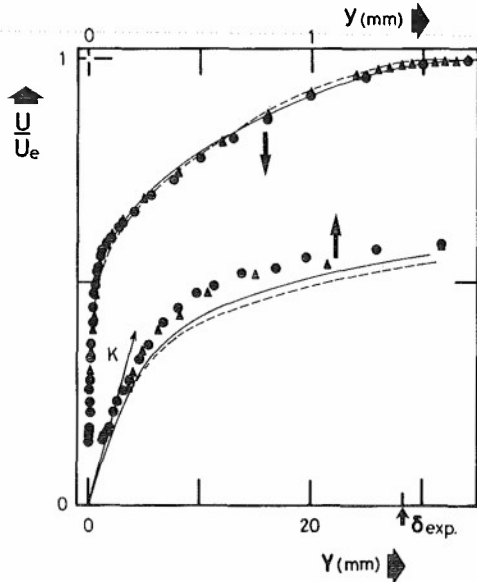


FIG. 7 :

Composante axiale de la vitesse.  
 $X/\delta_o = 28$  ( $X = 630$  mm)  $W_o/U_e = 0,887$   
 Mesures : ● Fil chaud ▲ sonde de pression  
 K : pente à l'origine (valeur expérimentale de  $C_{fx}$  d'après l'équation 24).  
 Calcul : —  $T = 1$  ---  $T = 0,5$

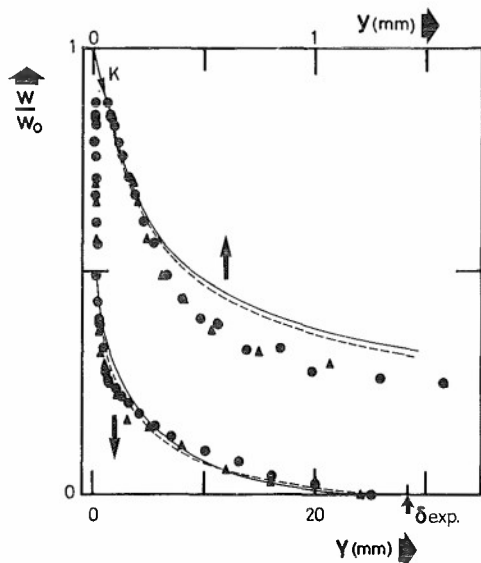


FIG. 8 :

Composante périphérique de la vitesse absolue.  
 $X/\delta_o = 28$  ( $X = 630$  mm)  $W_o/U_e = 0,887$   
 Mesures : ● fil chaud ▲ sonde de pression  
 K : pente à l'origine (valeur expérimentale de  $C_{pz}$  d'après l'équation 25).  
 Calcul : —  $T = 1$  ---  $T = 0,5$

la couche limite. Par ailleurs, si l'on considère les régions très voisines de la paroi, il semble que le calcul et l'expérience sont d'autant mieux en accord que l'on se rapproche de la restructuration, c'est à dire que l'on s'éloigne du début de la paroi mobile.

L'angle  $\gamma$  qui est représentatif de la distorsion du profil de vitesse dans la couche limite atteint une valeur maximale de l'ordre de 8 degrés à la position de mesure  $X/\delta_o = 28$  (figure 12). En fait l'effet tridimensionnel est d'autant plus marqué que l'on est près du début du cylindre tournant (figure 11) : à  $X/\delta_o = 0,67$  la valeur maximale de  $\gamma$  est de 20 degrés environ. En ce qui concerne le calcul, on constate (figure 12) que  $\gamma$  est sensible au paramètre  $T$  : une valeur de  $T$  de l'ordre de 0,7 ou 0,8 conduirait à un bon accord calcul-expérience à la station  $X/\delta_o = 28$ , tout au moins dans toute la région extérieure de la couche limite.

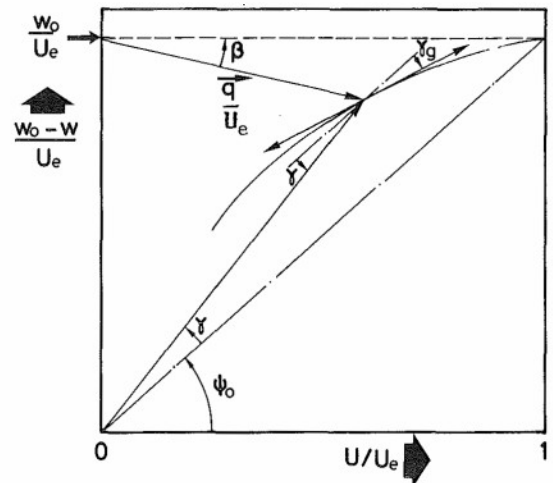


FIG. 9 :

Définition des vitesses et des angles dans le plan de l'hodographe.

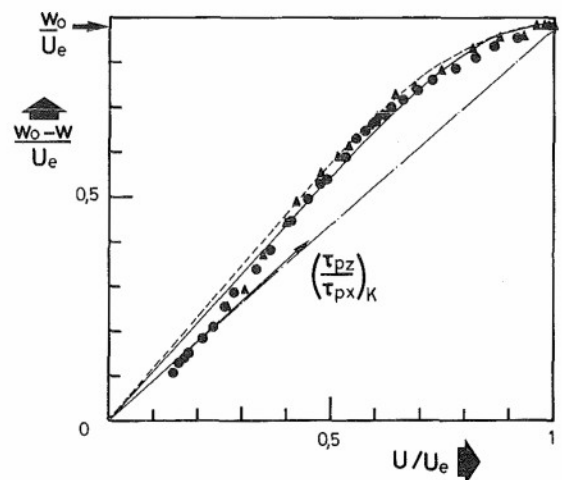


FIG. 10 :

Profil polaire.  
 $X/\delta_o = 28$  ( $X = 630$  mm)  $W_o/U_e = 0,887$   
 Mesures : ● fil chaud ▲ sonde de pression  
 $(\partial p_z / \partial p_x)_K$  : pente à l'origine (valeurs expérimentales de  $C_{fx}$  et  $C_{pz}$  d'après les équations 24 et 25).  
 Calcul : —  $T = 1$  ----  $T = 0,5$

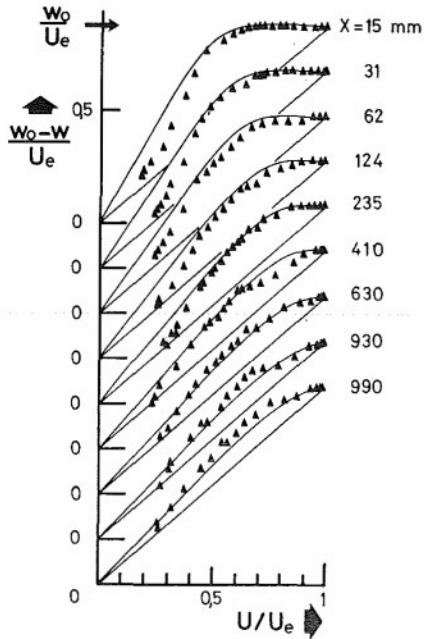


FIG. 11 :

Evolution des profils polaires.  
Mesures : ▲ sonde de pression  
Calcul : — T = 1

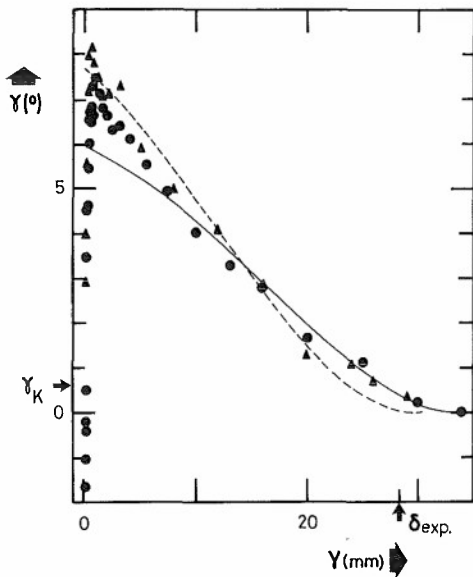


FIG. 12 :

Profil de l'angle  $\gamma$  ( $\gamma$  est défini fig. 9).  
 $X/\delta_0 = 28$  ( $X = 630$  mm)  $W_0/U_e = 0,887$   
Mesures : ● fil chaud ▲ sonde de pression  
 $\gamma_K$  : valeur à l'origine  
(valeurs expérimentales de  $C_{fx}$  et  $C_{fa}$  d'après les équations 24 et 25).  
Calcul : — T = 1 --- T = 0,5

## 5 - DISCUSSION - CONCLUSION.

Les différentes comparaisons entre le calcul et l'expérience tendent à montrer que l'accord général est correct. Cependant il faut remarquer une nette différence dans l'allure des profils polaires (figures 10 et 11) dans les régions très voisines de la paroi. En particulier, l'expérience indique que l'écoulement ne peut être collatéral que dans une région très mince, dans la sous-couche

visqueuse ( $u/u_e < 0,2$  et  $U_* / \nu \lesssim 5$ ) ; de plus la détermination expérimentale des composantes du coefficient de frottement pariétal montre que la pente à l'origine des profils polaires est pratiquement égale à  $\frac{W_0}{U_e}$  ( $\gamma_0 = 0,6$  degrés) ce qui correspond à peu près à la pente limite qu'on obtiendrait si la restructuration de la couche limite était achevée. Ceci implique d'ailleurs l'existence d'un point d'inflexion qui interdit d'extrapoler les profils polaires depuis des valeurs trop fortes de  $U/U_e$  (de l'ordre de 0,4 ou 0,5) jusqu'à l'origine pour déterminer le rapport  $C_{fx}/C_{fa}$  comme le préconisaient BISSONNETTE et MELLOR /REF. 1/. Cette situation est cohérente avec le sens de la faible courbure que l'on calcule à partir des équations de la sous-couche lorsque l'on tient compte du faible gradient de pression négatif :

$$(30) \quad \left( \frac{d^2 W}{dU^2} \right)_p = \frac{\mu^2}{a^2} \frac{W_0}{\tau_{px}^2} - \mu \frac{\tau_{p2}}{\tau_{px}^3} \frac{dp_e}{dx}$$

Cette formule généralise au cas d'une paroi convexe l'expression donnée par NASH-PATEL /REF. 23/ dans le cas d'une paroi plane. En fait, dans notre configuration le premier terme, lié à la courbure de la paroi, est négligeable devant le terme de pression. Bien que très faible ( $U_* \frac{d^2 W}{dU^2} \approx 10^{-4}$ ) cette courbure a un sens qui n'est pas en contradiction avec l'existence d'un point d'inflexion plus loin dans l'hodographe.

Notons encore que la forme du profil polaire expérimental est liée à une diminution extrêmement rapide de  $\gamma$  très près de la paroi (figure 12).

Par opposition on observe que le calcul n'indique pas un tel comportement. L'hodographe calculé reste pratiquement linéaire jusque  $U/U_e = 0,5$  c'est à dire bien au-delà de la sous-couche visqueuse. Les calculs effectués pour  $T = 1$  et  $T = 0,5$  conduisent à des formes analogues des profils polaires.

De plus, l'analyse de l'évolution des profils polaires conduit à une interprétation différente du processus de restructuration de la couche limite dans le calcul et dans l'expérience tout au moins dans sa phase initiale. Il semblerait en effet, d'après l'expérience, que le retour vers une couche limite collatérale s'établisse d'abord beaucoup plus rapidement près de la paroi et s'étende ensuite progressivement dans la couche limite. En revanche, le calcul n'indique pas une tendance privilégiée de la région voisine de la paroi à atteindre son état limite : on constate en effet que le profil polaire tend vers sa forme linéaire limite dans son ensemble.

Les calculs effectués avec différentes valeurs du paramètre  $T$  conduisent à des résultats très voisins. La quantité la plus sensible est la déviation  $\gamma$  subie par le vecteur vitesse relative, à l'intérieur de la couche limite. Cependant, les écarts obtenus pour  $T = 1$  et  $T = 0,5$  paraissent trop faibles pour que l'expérience permette de fixer plus précisément la valeur de  $T$  à choisir. Il faudrait pour cela pousser encore plus loin la comparaison entre le calcul et l'expérience et la faire porter sur les profils des tensions de Reynolds.

La faible sensibilité des résultats de calcul au paramètre  $T$  confirme des observations déjà faites lors de comparaisons à d'autres cas expérimentaux /REF. 6/. D'une façon générale, on peut dire que la déviation de la direction de la force de cisaillement turbulent par rapport au vecteur  $\frac{dV}{dy}$  peut jouer un rôle important lorsque la couche limite est soumise à de forts gradients de pression conduisant à son décollement.

Néanmoins, il est bon de préciser que le modèle de turbulence présente a priori plusieurs défauts. En particulier, la modélisation adoptée pour les régions voisines de la paroi paraît grossière. On peut penser aussi qu'une variation du paramètre  $T$  dans l'épaisseur de la couche limite modifierait la forme de l'hodographe. Remarquons encore finalement que le schéma de turbulence utilisé ne tient pas compte du tout des effets de courbure alors qu'en fin de la zone d'étude le rapport  $\delta_{0,99}/a$  est de l'ordre de 35%.

#### Remerciements

Les auteurs tiennent à remercier plus particulièrement Monsieur R. DUMAS pour tous les conseils qu'il leur a prodigués dans cette recherche. Sur le plan technique leurs remerciements vont aussi à Monsieur ASTIER.

#### REFERENCES

- /1/ BISSONNETTE L.R., MELLOR G.L., "Experiments on the behaviour of an axisymmetric turbulent boundary layer with a sudden circumferential strain" J.F.M., Vol. 63, 1974, pp 369-413.
- /2/ LOHMANN R.P. "The response of developed turbulent boundary layer to local transverse surface motion" Ph. D. Thesis, Univ. Connecticut, 1973.
- /3/ ARSLANIAN G. "Champ de vitesse moyenne d'une couche limite turbulente sur un cylindre en rotation dans un écoulement axial" Thèse, Sept. 1978, IMST Université Aix-Marseille II.
- /4/ ARSLANIAN G., DUMAS R. "Couche limite turbulente sur un cylindre en rotation dans un écoulement axial. Champ de vitesse moyenne". Note interne IMST; Univ. Aix-Marseille II, Janvier 1979.
- /5/ ARZOUMANIAN E., FULACHIER L., DUMAS R., "Experimental investigation of three-dimensional turbulent boundary layer on an axially rotated cylinder". 2nd International Symposium on Turbulent Shear Flows, London, July 2-4, 1979.
- /6/ COUSTEIX J., AUPOIX B., "Comparison of various calculation methods for three-dimensional turbulent boundary layer". 2nd Symposium on Turbulent Shear Flows, London, July 2-4, 1979.
- /7/ ROTTA J.C., "A family of turbulence models for three-dimensional thin shear layers". Symposium on Turbulent Shear Flows, Pennsylvania, April 18-20, 1977.
- /8/ GAVIGLIO J. "Les caractéristiques des souffleries subsoniques de l'IMST" ONERA, Division Aérodynamique, Problème 522-10 (1962).
- /9/ Mac MILLAN F.A. "Experiments on Pitot tubes in Shear Flows". Aero Res. Council, R.M. n° 3028, 1956.
- /10/ MARCILLAT J. "Fonction de répartition des vitesses turbulentes dans une couche limite ; effets de la réponse de l'anémomètre à fil chaud" Thèse, IMST, Univ. Aix-Marseille, 1964.
- /11/ CHAUVÉ M.P. "Détermination directe du frottement sur une paroi poreuse à l'aide d'un anémomètre". Proceedings of Euromech Colloquium 70, Nancy, July 1977.
- /12/ WEISSBERG H.L. "Velocity profiles and friction factors for turbulent pipe flow with uniform wall suction". Physics Report K-1264 OAK Ridge Tennessee (1956).
- /13/ TENNEKES H., LUMLEY J.L. "A first course in turbulence". The MIT Press 1972.
- /14/ COUSTEIX J., "Progrès dans les méthodes de calcul des couches limites bi et tridimensionnelles" ONERA, N.T. n° 1976-15, (translated in English ESA TT-385).
- /15/ LAUNDER B.E., REECE G.J., RODI W. "Progress in the development of a Reynolds stress turbulence closure". J.F.M. Vol. 8, Part. 3, pp. 537-566 (1975).
- /16/ FANNELØP T.K., HUMPHREYS D.A. "The solution of the laminar and turbulent three-dimensional boundary layer equations with a simple finite difference technique". FFA, Rep. 126 (1975).
- /17/ ELSENAAR A., Van den BERG B., LINDHOUT J.P.F., "Three-dimensional separation of an incompressible turbulent boundary layer on an infinite swept wing". AGARD CP-168 "Flow Separation" (1975).
- /18/ ROTTA J.C. "Statistische Theorie Nicht homogener Turbulenz". Z. Phys. 129 (1951).
- /19/ BATCHELOR G.K. "The theory of homogeneous turbulence". Cambridge University Press (1953).
- /20/ ROTTA J.C., "Eine theoretische Untersuchung über den Einfluss der Druckscher korrelationen auf die Entwicklung dreidimensionaler turbulenter Grenzschichten". DFVLR, FB 79-05 (1979).
- /21/ LUMLEY J.L. "Prediction methods for turbulent flows" Introduction - VKI Lecture Series 76, March 3-7 (1975).
- /22/ JONES W.P., LAUNDER B.E., "The prediction of laminarization with a two equation model of turbulence". Int. Journal of Heat and Mass Transfer, Vol. 15, n° 2 (1972).
- /23/ HEBBAR K., MELNIK W.L., "Wall region of a relaxing three-dimensional incompressible turbulent boundary layers" Journal of Fluid Mechanics, Vol. 85, part. 1, 1978, pp. 33-56.

# Evidence for instability-waves in the velocity-field of a fully developed turbulent channel-flow

by

Michael Hofbauer  
Max-Planck-Institut für Strömungsforschung  
Bunsenstraße 10  
D - 3400 Göttingen

Hot-film measurements and quantitative visual investigations were performed in the turbulent flow of the Göttingen Oil-Channel. This channel provides a fully developed turbulent flow at such a low Reynolds-number as  $Re = 8000$  (based on the mean centreline velocity and the whole channel width). Because of the low Reynolds-number we get a high spatial resolution, which enables us to study coherent structures in the near-wall region.

The apparatus used for the visual studies can be seen in figure 1. The left part of figure 1 shows a cut through the Oil-Channel in the  $y$ - $z$ -plane (plane perpendicular to the mean flow direction). A thin volume of the flow medium is illuminated through the transparent wall II of the channel using a 2 KW halogen light-source. The motion picture camera (Locam 16 mm High Speed Motion Picture Camera Model 50 - 0002), which records the paths of neutrally buoyant tracer-particles, is positioned above the free surface of the oil. The film speed was mostly 51 and in some runs 32 frames per second. The dimensions (in millimetres) of the illuminated volume are shown in the right part of figure 1. The extension of the volume into the  $z$ -direction is very small compared with the extensions into the  $x$ - and  $y$ -direction and this means, that we practically study turbulence in a plane. For hot-film measurements an  $x$ -probe (TSI Model 1241 - 20 W combined with a Constant-Temperature-Anemometer TSI Model 1050 and a Linearizer DISA Model 55 D10), which measures the time-functions of both the  $u$ - and the  $v$ -component of the velocity, was placed in the middle of the channel (half-way between the bottom and the free surface of the oil); the distance from the wall was variable. From the measured time functions statistical properties of turbulence were calculated by using a digital computer (DEC PDP-15).

The main result of the hot-film measurements is the power-spectrum of the  $v$ -component of the fluctuating-velocity. Figure 2 shows such a spectrum with high frequency-resolution. It should be noted, that the coordinates are linear. As can be seen from figure 2, the power-spectrum has regular maxima and minima. In contrast to this result it was believed up to now, that turbulence-spectra do not exhibit any characteristic peaks. In figure 3 the frequencies corresponding to the maxima of the power-spectrum are plotted as a function of the order  $n$  of the maxima. All points fall on a straight line through the origin. This means, that the frequencies of the maxima are the harmonics of a fundamental frequency, which from the slope of the straight line can be determined to be about 0.15 Hz. This frequency was determined for different distances  $y^+$  from the wall ( $12 \leq y^+ \leq 50$ ) and was found to be independent from  $y^+$ . The peaks, however, of the power-spectrum could be observed best at about  $y^+ = 12$ , where there is the maximum of the turbulence-production, and became smaller with increasing distance from the wall. An estimation shows, that the fundamental frequency is of the same order of magnitude as the roughly calculated unstable Tollmien-Schlichting frequencies of the mean turbulent velocity-profile. We therefore interpret this fundamental frequency as the most excited frequency of Tollmien-Schlichting-like instability-waves. The harmonics we believe to be due to a nonlinear amplification of the primarily excited instability-waves.

The main result of the visual studies in the evidence of regular oscillations in the near-wall region of the fully developed turbulent flow. A nice example of these oscillations can be seen in figure 4, which is showing the path of one single tracer-particle in the  $x$ - $y$ -plane. (The motion usually is three-dimensional, but the camera records only the  $x$ - and  $y$ -component. In spite of the three-dimensionality the oscillations seem to be no vortices.) The drawn points mark the positions of the particle at different times. They are equidistant with respect to time and the time interval between two consecutive points is 0.64 in dimensionless units. The particle-path strongly reminds of a damped oscillation. The amplitude and the frequency of these regular oscillations seem to be simple functions of the distance from the wall, as can be seen from figure 5. Figure 5a shows, that the dimensionless amplitude  $a^+$  is approximately one half of the dimensionless distance from the wall  $y^+$ , where we define the wall-distance of an oscillating structure to be the arithmetic mean value of the maximum and the minimum distance of the particle-path. Figure 5b shows the dimensionless angular frequency as a function of  $y^+$ . The solid curve is the derivative of the mean turbulent velocity-profile  $\partial u^+ / \partial y^+$ , which is a locally defined frequency. Within a certain scatter, which is due to errors in determining the distance from the wall, the measured points fall on the solid curve. This last result provides a relation of the statistical properties of turbulence - in this case the mean turbulent velocity-profile - and the properties of the elementary structures, which constitute turbulence. The oscillating structures described above correspond to the second phase of the burst-cycle reported by Kim, Kline and Reynolds [1]. Further investigation lead to the result, that the oscillations occur after low-speed fluid has migrated away from the wall (lifted up), but this lift-up occurs after the momentaneous velocity-profile has had an inflection-point, whereas it is usually believed, that the lift-up itself generates an inflection-point. It should be noted, that the oscillating structures detected by visual means have nothing to do with the peaks of the power-spectrum. In the near-wall region their frequencies are roughly one order of magnitude above the fundamental frequency determined from the power-spectrum.



We therefore think, that the oscillations are due to a new three-dimensional instability.

From the results of the spectral measurements it can be assumed, that there exist Tollmien-Schlichting-like instability-waves in fully developed turbulence. On the other hand the visual studies show, that there are also three-dimensional instability waves of much higher frequency. These results are in agreement with Landahl's theory [2], who considers turbulence as a superposition of permanently existing Tollmien-Schlichting wave-groups and intermittently occurring secondary instability-waves (small-scale turbulence).

### References

- [1] H.T. Kim, S.J. Kline and W.C. Reynolds  
J. Fluid Mech. (1971), vol. 50, part 1, pp. 133-160
- [2] M.T. Landahl  
Siam J. Appl. Math., vol. 28, No. 4, June 1975
- [3] M. Hofbauer  
Mitteilungen aus dem Max-Planck-Institut für Strömungsforschung und der Aerodynamischen Versuchsanstalt, Bericht Nr. 66, Göttingen 1978

### List of symbols

$a$	:	amplitude
$f$	:	frequency
$n$	:	order of the maxima of the power-spectrum
$t$	:	time
$\bar{u}$	:	local mean-value of the velocity
$u_\tau$	:	friction-velocity;
$v$	:	velocity-component normal to the wall
$x$	:	direction of the mean flow
$y$	:	direction normal to the wall
$z$	:	direction normal to $x$ and $y$ ( $x$ , $y$ and $z$ form a right-handed coordinate-system)
$Re$	:	Reynolds-number
$R_{vv}(t')$	:	normalized correlation-function;
$\Phi(f)$	:	power-spectral density;
$\nu$	:	kinematic viscosity
$\omega$	:	angular frequency;
$a^+$	:	$a^+ = a \frac{u_\tau}{\nu}$
$t^+$	:	$t^+ = t \frac{u_\tau^2}{\nu}$
$x^+$	:	$x^+ = x \frac{u_\tau}{\nu}$
$y^+$	:	$y^+ = y \frac{u_\tau}{\nu}$
$z^+$	:	$z^+ = z \frac{u_\tau}{\nu}$
$\omega^+$	:	$\omega^+ = \omega \frac{\nu}{u_\tau^2}$

$$R_{vv}(t') = \lim_{T \rightarrow \infty} \frac{\int_{-T}^T v(t) v(t-t') dt}{\int_{-T}^T v^2(t) dt}$$

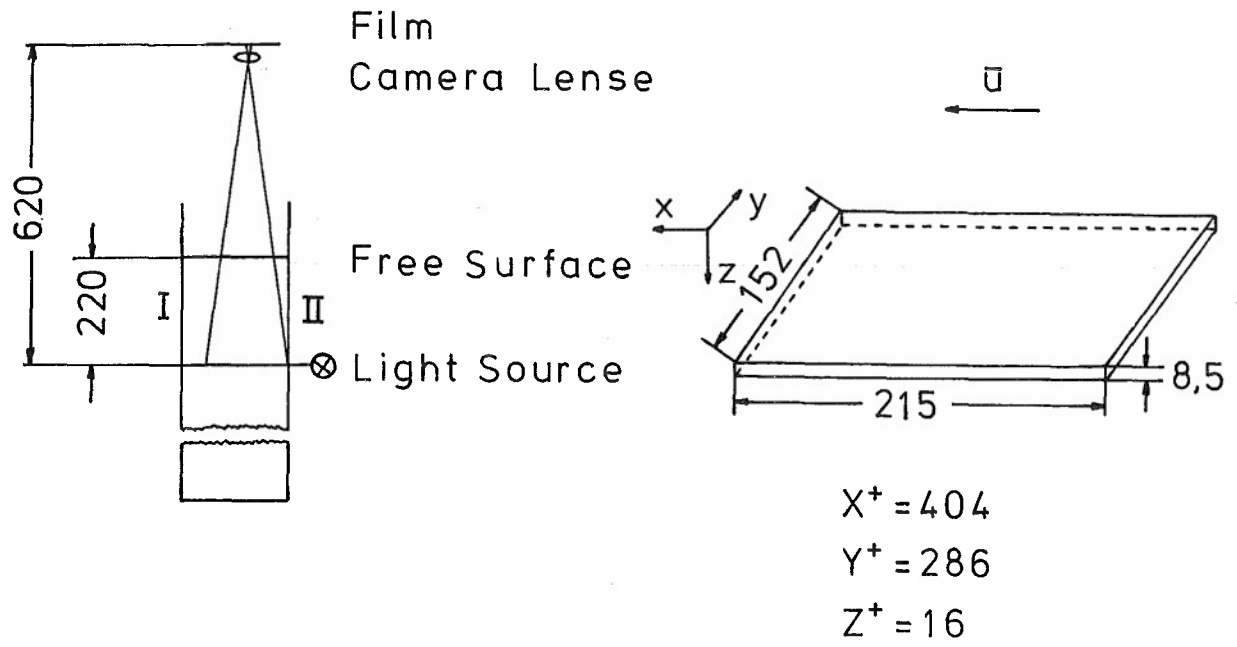
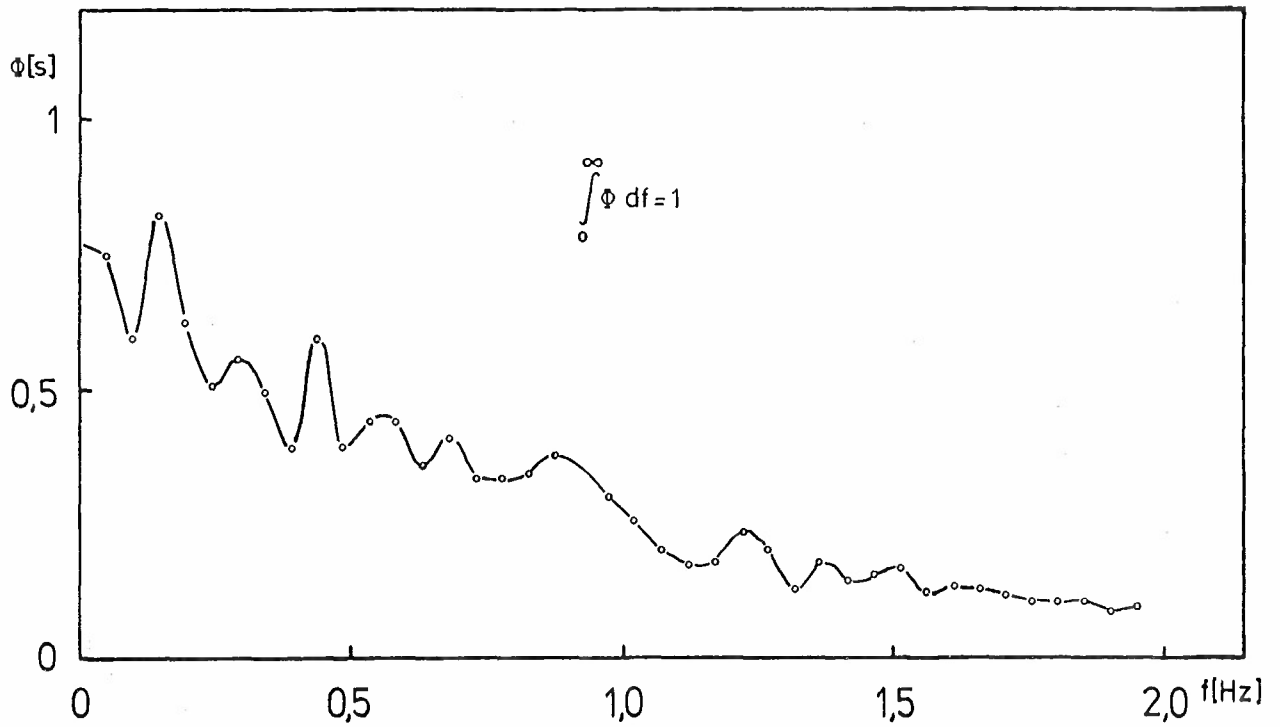


Fig.1 Apparatus

Fig.2 Power-spectrum of velocity-component normal to the wall at  $y^+$ -position 12.1

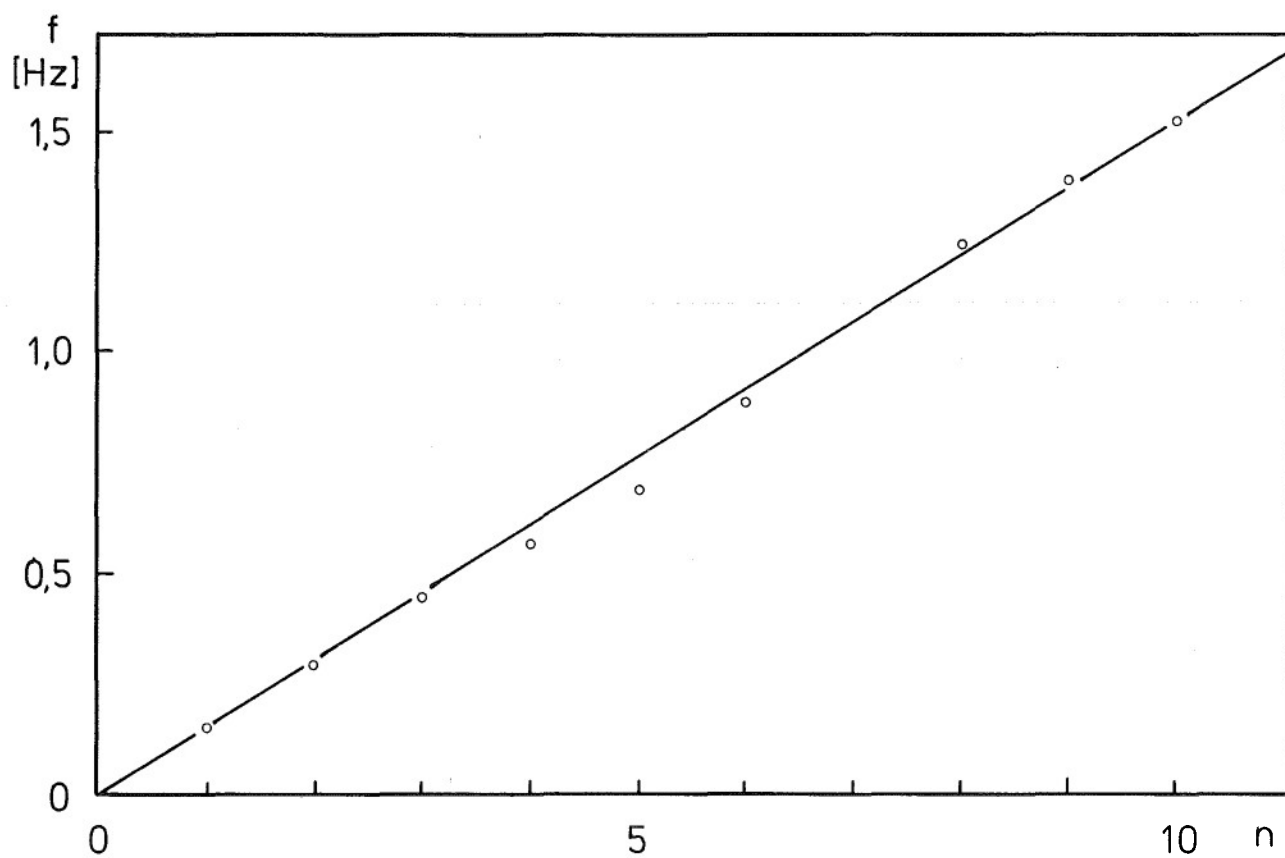


Fig.3 Frequencies of maxima of the power-spectrum

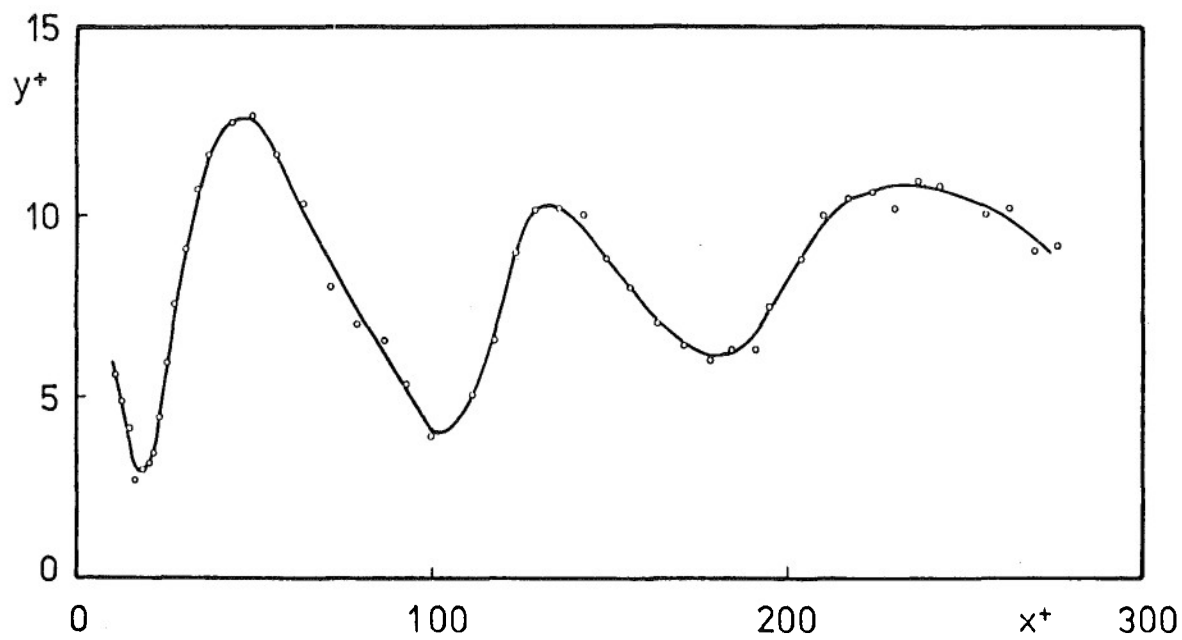


Fig.4 Oscillating particle path

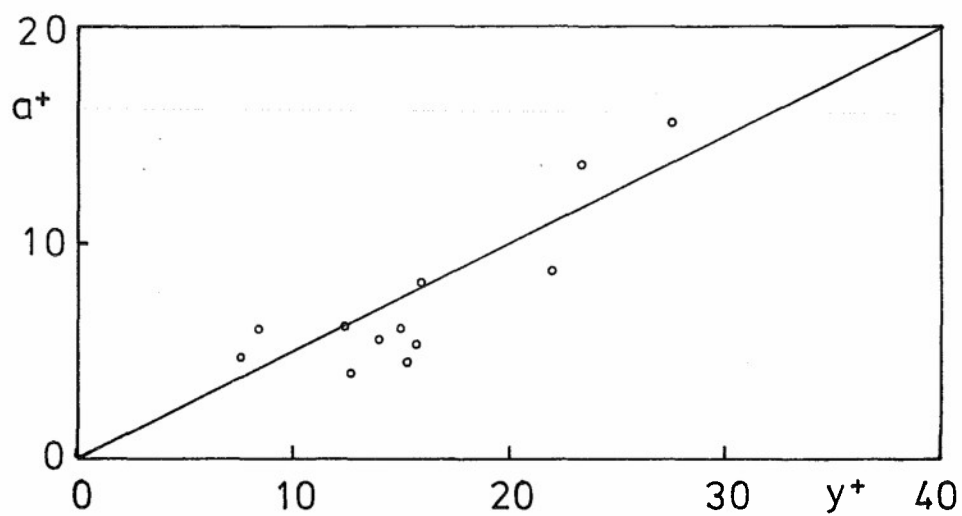


Fig.5(a) Amplitude of the regular oscillations as a function of the distance from the wall

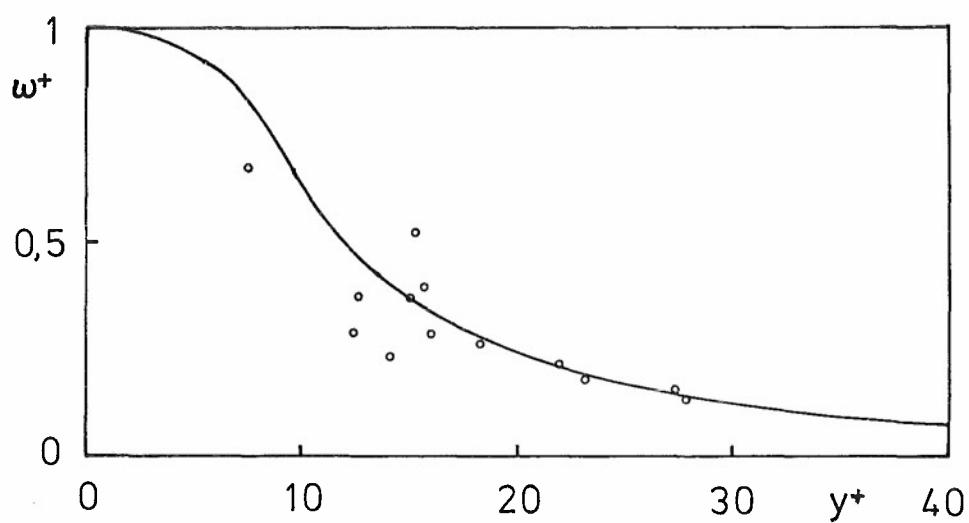


Fig.5(b) Angular frequency of the regular oscillations as a function of the distance from the wall

# RÉSULTATS EXPÉRIMENTAUX RELATIFS A L'INFLUENCE DES PROCESSUS DE TRANSITION SUR LA STRUCTURE INITIALE D'UNE COUCHE LIMITE TURBULENTE

par Daniel ARNAL et Jean-Claude JUILLEN

Office National d'Etudes et de Recherches Aéronautiques (ONERA)  
CERT, Toulouse, France.

EXPERIMENTAL RESULTS CONCERNING THE INFLUENCE OF  
TRANSITION PROCESSES ON THE INITIAL STRUCTURE OF  
A TURBULENT BOUNDARY LAYER

## RESUME

On étudie dans quelle mesure la structure initiale de la couche limite turbulente peut être influencée par les processus de transition. Dans le cas d'un écoulement extérieur uniforme, le passage du régime laminaire au régime turbulent est caractérisé par le phénomène d'intermittence ; l'analyse conditionnelle du signal fil chaud montre que les spots turbulents ont une structure analogue à celle d'une couche limite turbulente classique. Avec un faible gradient de pression positif, il devient difficile de qualifier l'intermittence. Lorsque la transition se produit en aval d'un décollement laminaire, le paramètre de forme décroît, mais l'intermittence n'apparaît plus. On observe seulement une déformation des ondes d'instabilité ; à la fin de la transition, le spectre de l'énergie turbulente est constitué de pointes correspondant aux harmoniques des ondes d'instabilité.

## SUMMARY

The purpose of this study is to specify how the initial structure of the turbulent boundary layer can be influenced by the transition mechanism. In the case of zero pressure gradient the evolution from the laminar to the turbulent regime is characterized by the intermittency phenomenon ; the conditional sampling of the hot wire signal shows that the turbulent spots exhibit a structure similar to the classical turbulent boundary layer structure. With a mild positive pressure gradient, it becomes difficult to describe the intermittency. When the transition is beginning downstream the laminar separation point, the shape parameter is decreasing, but the intermittency appears no longer. We only observe a progressive deformation of the instability waves ; at the end of the transition, the spectrum of the turbulent energy is composed by a series of peaks corresponding to harmonics of the instability waves.

## NOTATIONS

$x$  abscisse  
 $y$  ordonnée comptée à partir de la paroi  
 $t$  temps  
 $u(t)$  vitesse longitudinale instantanée  
 $U$  vitesse moyenne longitudinale  
 $U_{ref}$  vitesse de référence (expériences sur cylindre)  
 $U_{\infty}$  vitesse à l'infini amont (expériences sur profils)  
 $\langle U \rangle$  moyenne d'ensemble  
 $w, v'$  fluctuations longitudinale et verticale  
 $\overline{w'^2}, \overline{v'^2}$  moyennes quadratiques de  $w'$  et  $v'$   
 $-\overline{u'v'}$  tension de Reynolds  
 $\alpha$  demi-angle de divergence de la veine (expériences sur cylindre)  
 $\nu$  viscosité cinématique  
 $\delta$  épaisseur physique de la couche limite  
 $\delta_1$  épaisseur de déplacement  $\delta_1 = \int_0^{\delta} (1 - \frac{u}{U_e}) dy$

$\theta$  épaisseur de quantité de mouvement

$$\theta = \int_0^{\delta} \frac{u}{U_e} (1 - \frac{u}{U_e}) dy$$

$H$  paramètre de forme  $H = \delta_1/\theta$

$R_x, R_{\theta}$  nombres de Reynolds formés avec  $x$  et  $\theta$

$\Delta R_x$  nombre de Reynolds d'étendue de transition

$c$  corde du profil

$D$  facteur de dissymétrie

$F$  facteur d'aplatissement

$p$  pression statique

$\tau_t$  durée d'un spot turbulent

## Indices

$T$  début de transition.

$t$  turbulent.

$e$  extérieur à la couche limite.

## 1 - INTRODUCTION

La majorité des méthodes de calcul des écoulements cisailés turbulents reposent sur la résolution de schémas de turbulence dont la modélisation fait appel à des propriétés bien connues d'écoulements classiques (c'est ainsi que l'on suppose généralement un équilibre du spectre de turbulence). On peut cependant se demander si ces propriétés sont valables lorsque l'on considère une couche limite turbulente immédiatement en aval de la transition qui lui a donné naissance.

Des études expérimentales systématiques effectuées au Département d'Aérothermodynamique de l'ONERA/CERT sur la transition de la couche limite ont montré que les processus de transformation de l'écoulement laminaire en écoulement turbulent sont en fait très sensibles à l'intensité du gradient de pression longitudinal et que la turbulence n'apparaît pas du tout de la même façon selon que la transition s'effectue en écoulement uniforme ou après un décollement laminaire.

Le but de cet article est de décrire ces divers mécanismes d'apparition de la turbulence, mécanismes dont on peut parfois retrouver la trace lorsque la transition est terminée (ou paraît terminée si l'on considère seulement certains paramètres globaux).

## 2 - CONFIGURATIONS ETUDIÉES.

## 2.1. Transition dans un gradient de pression nul.

La transition de la couche limite est étudiée sur un corps cylindrique de 6 cm de diamètre, précédé d'une ogive et placé dans l'axe d'une veine de révolution, dont la conicité détermine la distribution de pression dans l'écoulement potentiel ; le demi-angle  $\alpha$  de divergence de la veine est ici voisin de  $0,2^\circ$  (compensation de l'effet de déplacement des couches limites).

La distribution de vitesse extérieure est tracée sur la figure 1 sous la forme  $\frac{U}{U_{\text{réf}}}(\alpha)$ , où  $U_{\text{réf}}$  est une vitesse de référence mesurée au raccordement de l'ogive et du cylindre. On a ici  $U_{\text{réf}} \approx 33$  m/s. Pour  $\alpha > 0,2$  m, cette configuration correspond sensiblement au cas de l'écoulement uniforme ; en fait, la divergence de la veine a été quelque peu surestimée, si bien que l'on observe une petite décélération vers l'aval. Le gradient de pression longitudinal reste cependant négligeable, puisque, comme on le verra au § 4, les valeurs du paramètre de forme  $H$  en régime laminaire sont très voisines de la valeur théorique du profil de Blasius.

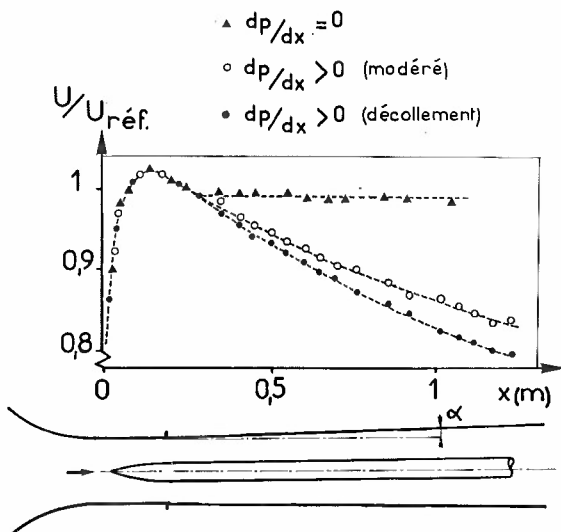


FIG. 1 : Distributions de vitesses (Expériences sur cylindre).

## 2.2. Transition dans un gradient de pression positif modéré.

On a conservé le même montage expérimental que dans la configuration précédente, mais en modifiant  $\alpha$  et  $U_{\text{réf}}$  : le demi-angle  $\alpha$  vaut maintenant  $0,7^\circ$  et la vitesse  $U_{\text{réf}}$  est égale à 28 m/s. On a également tracé sur la figure 1 la distribution de vitesse extérieure, qui correspond bien, sur la majeure partie de la zone d'étude, à un écoulement décéléré.

## 2.3. Transitions au voisinage d'un décollement laminaire.

Trois cas de ce type ont été considérés ; pour chacun d'eux, le début de la transition (au sens de début de la décroissance du paramètre de forme) s'effectue aussitôt après le point de décollement laminaire.

Le premier de ces cas a encore été étudié dans la soufflerie de révolution précédemment décrite, avec  $\alpha = 0,9^\circ$  et  $U_{\text{réf}} = 12$  m/s. La répartition de vitesse (figure 1) indique bien un gradient de pression plus intense que dans les deux premières configurations.

Les résultats expérimentaux relatifs au second cas de transition avec décollement sont empruntés aux travaux réalisés à l'ONERA/CERT par COUSTEIX et PAILHAS [1], qui ont étudié le développement de la couche limite sur un profil peaky (profil ONERA D) de 200 mm de corde, placé à incidence nulle dans une veine de section rectangulaire ( $300 \times 400$  mm<sup>2</sup>) et de 1,5 m de long. On a tracé sur la figure 2 la distribution de vitesse extérieure ; avec la valeur de  $U_\infty$  choisie (24 m/s), le nombre de Reynolds  $U_\infty c/\nu$  est voisin de 300 000.

Le troisième et dernier cas de transition avec décollement a été obtenu sur un profil laminaire de 90 mm de corde (profil NACA 64A 010). Ce profil a été étudié à incidence nulle, dans une petite veine de section rectangulaire ( $80 \times 100$  mm<sup>2</sup>) et de 380 mm de long. La répartition de vitesse, représentée figure 2, montre une zone accélérée jusqu'à 40 pour cent de corde environ, puis une zone très décélérée jusqu'au bord de fuite. La vitesse  $U_\infty$  est ici égale à 56 m/s, ce qui donne un nombre de Reynolds de corde très proche de celui des expériences réalisées sur le profil ONERA D (330 000).

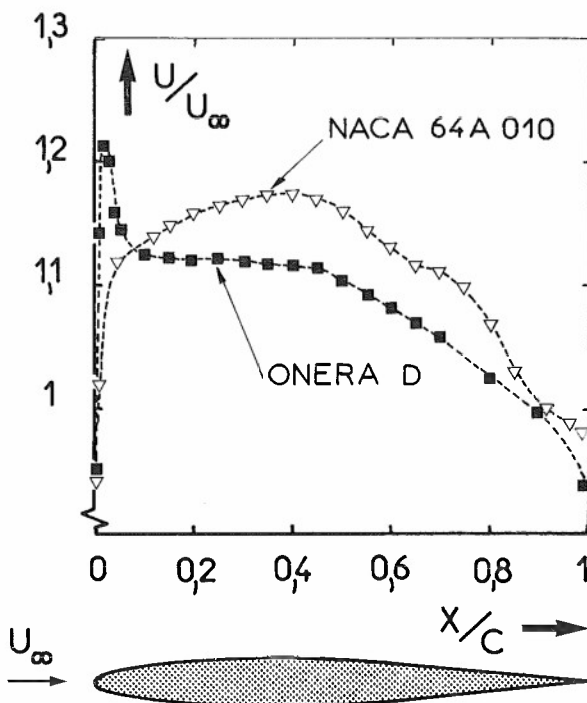


FIG. 2 : Distributions de vitesse (Expériences sur profils).

## 3 - MOYENS DE MESURE.

Les mesures sont effectuées à l'aide d'anémomètres à fil chaud à température constante. Dans certains cas, on a entrepris une étude plus approfondie de la fluctuation longitudinale  $u'$  par traitement sur ordinateur du signal instantané numérisé. La plus grande partie des résultats ainsi obtenus provient de numérisations effectuées pendant 6 secondes à la cadence de 10 000 points par seconde.

De cette façon on a pu calculer les moments d'ordre 3 (facteur de dissymétrie) et de l'ordre 4 (facteur d'aplatissement) de la fluctuation, et obtenir des spectres numériques grâce à un programme de transformée de FOURIER rapide. Enfin, l'étude du phénomène d'intermittence a fait appel à une analyse conditionnelle de la vitesse instantanée. On trouvera dans /2/ et /3/ des détails complémentaires relatifs à la chaîne d'acquisition et à la technique d'échantillonnage conditionnel.

## 4 - PASSAGE DU REGIME LAMINAIRE AU REGIME TURBULENT.

On a tracé sur la figure 3 l'évolution du paramètre de forme en fonction de  $x$  (expériences sur cylindre) ou de  $x/c$  (expériences sur profils). En première analyse, on peut considérer que la transition se déclenche lorsque  $H$  commence à décroître, et qu'elle s'achève lorsque  $H$  atteint un niveau à peu près constant. On remarquera donc en premier lieu que la fin de transition n'est pas réellement atteinte dans le cas de l'écoulement uniforme et dans les expériences sur profil ONERA D.

L'appellation "gradient de pression positif modéré" trouve ici sa justification dans la mesure où le  $H$  en début de transition est voisin de 2,8, valeur peu supérieure à celle d'un profil laminaire de plaque plane. Les trois cas de transition avec décollement laminaire montrent bien entendu des valeurs de  $H$  beaucoup plus élevées, entre 3,6 et 4,8 ; les traits verticaux portés sur les courbes expérimentales indiquent la position du décollement laminaire, obtenue par un calcul de couche limite.

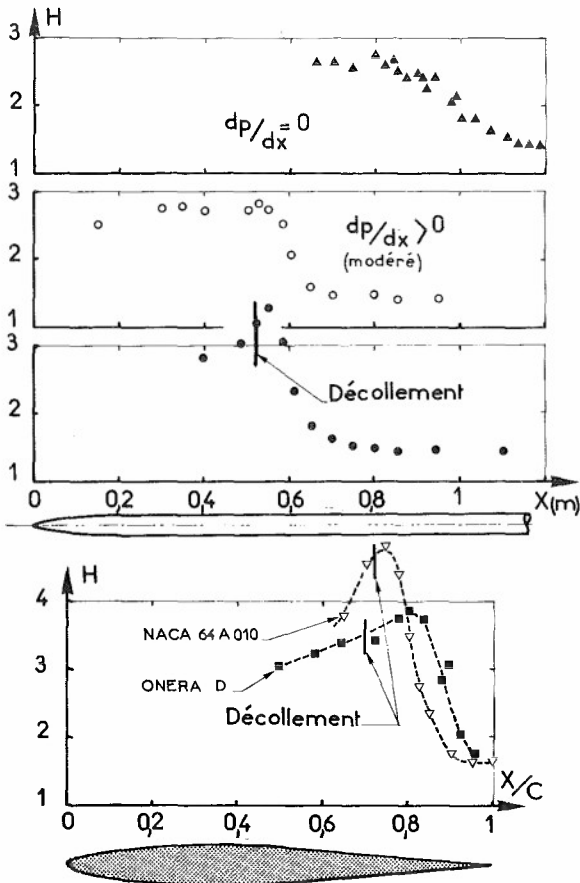


FIG. 3 : Distributions du paramètre de forme.

Il faut enfin observer que, dans tous les cas, les valeurs du paramètre de forme de la couche limite turbulente qui se développe en aval de la transition restent voisines de 1,5, valeur classique en turbulent pour un écoulement uniforme ; en d'autres termes, les gradients de pression mis en jeu sont importants pour le régime laminaire, mais très faibles pour le régime turbulent.

Les figures 4 et 5 portent les évolutions du nombre de Reynolds  $R_\theta$  en fonction du nombre de Reynolds  $R_x$  pour les divers cas étudiés. Des flèches indiquent les points de début et de fin de transition, définis comme on vient de le dire à partir de l'évolution du  $H$ . Le nombre de Reynolds  $\Delta R_x$  caractérisant l'étendue de la transition est également indiqué sur ces figures ; il diminue très rapidement lorsque  $H_T$  augmente.

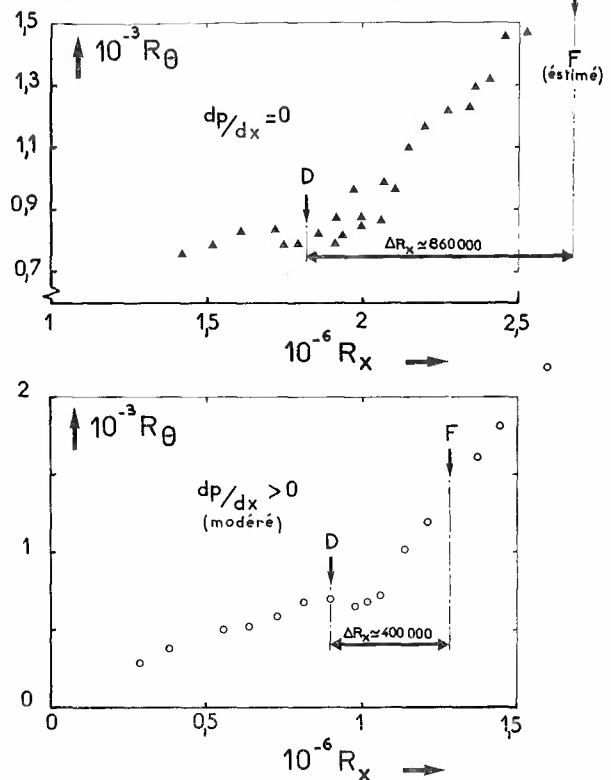


FIG. 4 : Nombres de Reynolds caractéristiques de la couche limite (a).

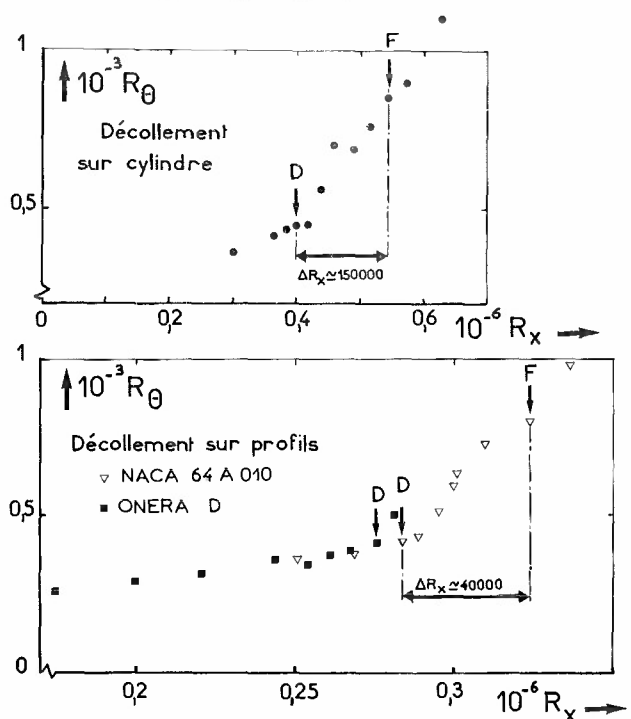


FIG. 5 : Nombres de Reynolds caractéristiques de la couche limite (b).

## 5 - ETUDE DES SPOTS TURBULENTS : CAS DE L'ECOULEMENT UNIFORME.

L'étude des spots turbulents et du phénomène d'intermittence a fait l'objet de précédentes publications ( /2/ et /3/ ) ; c'est pourquoi nous nous bornerons, dans ce paragraphe, à en rappeler les résultats essentiels.

### 5.1. Etude qualitative.

La figure 6 montre quelques exemples typiques d'enregistrement du signal  $u(t)$  à proximité de la paroi, pour trois stations situées au début, au milieu et à la fin de la région de transition. Il apparaît que le fil chaud est plongé successivement dans des zones turbulentes, caractérisées par des fluctuations à haute fréquence ("spots") et dans des régions laminaires plus ou moins rectilignes : c'est le phénomène d'intermittence. Entre  $x = 0,87$  m et  $x = 0,94$  m, le nombre des spots turbulents s'est considérablement accru, alors qu'entre  $x = 0,94$  m et  $x = 1,07$  m, c'est surtout la durée de ces spots qui a augmenté. Dans les zones laminaires, on observe des oscillations de faible amplitude, mais assez régulières, correspondant aux ondes d'instabilité, ou ondes de Tollmien-Schlichting. Sans entrer dans les détails, on peut dire que ces ondes apparaissent dans le régime laminaire, s'amplifient et finissent par déstabiliser la couche limite laminaire, donnant naissance aux spots turbulents.

Dans nos expériences, où la transition est naturelle, la naissance des bouffées turbulentes est un phénomène aléatoire, ainsi qu'il a été suggéré par EMMONS /4/. Plusieurs auteurs, tels SCHUBAUER - KLEBANOFF /5/, ELDER /6/, WYGNAŃSKI-SOKOLOV-FRIEDMAN /7/, CANTWELL-COLES-DIMOTAKIS /8/, ont étudié la structure des spots turbulents en les créant artificiellement à l'aide de décharges électriques.

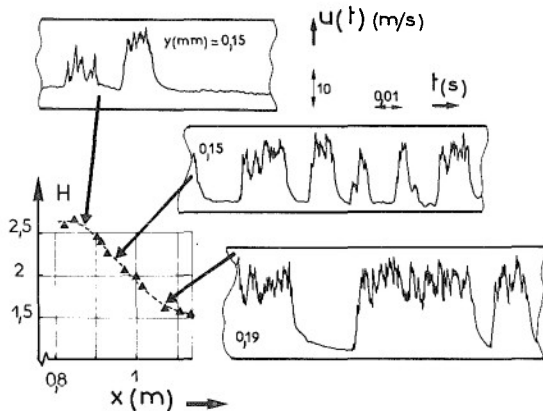


FIG. 6 : Exemples d'enregistrement près de la paroi ( $dp/dx = 0$ ).

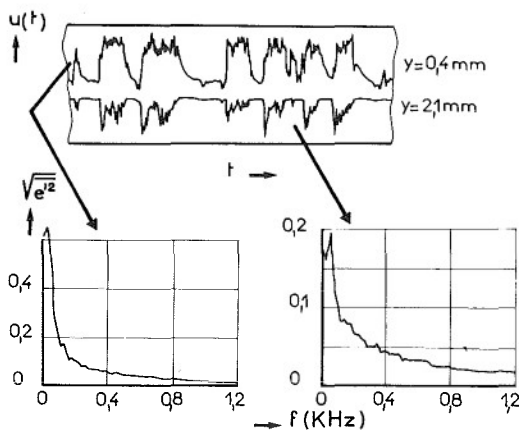


FIG. 7 : Exemples d'enregistrement en milieu de transition ( $dp/dx = 0$ ).

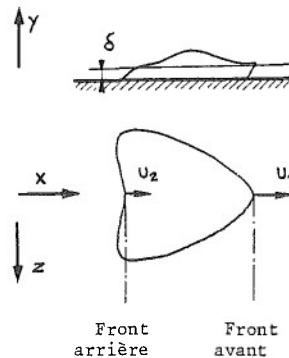
On présente sur la figure 7 deux enregistrements simultanés de la vitesse  $u(t)$ , réalisés près de la paroi ( $y = 0,4$  mm) et vers le milieu de l'épaisseur de la couche limite, ainsi que les spectres correspondants. On s'est placé à l'abscisse  $x = 0,94$  m, c'est-à-dire en milieu de transition. Cette figure appelle les remarques suivantes :

. près de la paroi, la vitesse moyenne dans les spots turbulents est supérieure à la vitesse laminaire. Lorsque  $y$  croît, le phénomène s'inverse,

. la forme des spots évolue depuis une forme quasi-rectangulaire près de la paroi à une forme en dent de scie, très dissymétrique, aux altitudes supérieures,

. aucun pic, aucune fréquence privilégiée n'apparaît sur les spectres.

Nous avons représenté ci-dessous la forme schématique d'un spot telle que l'on peut la déduire des visualisations effectuées par divers auteurs. Le front avant est convecté à une vitesse  $U_1 \approx 0,9 U_e$ , le front arrière à une vitesse  $U_2 \approx 0,5 U_e$ . La différence des vitesses de propagation des fronts avant et arrière explique le développement des spots et leur coalescence progressive en spots de plus en plus étendus, mais de moins en moins nombreux.



### 5.2. Etude quantitative.

L'analyse conditionnelle du phénomène d'intermittence nécessite avant tout le choix d'un signal de détection, permettant de distinguer avec le moins d'ambiguïté possible les régions laminaires et turbulentes.

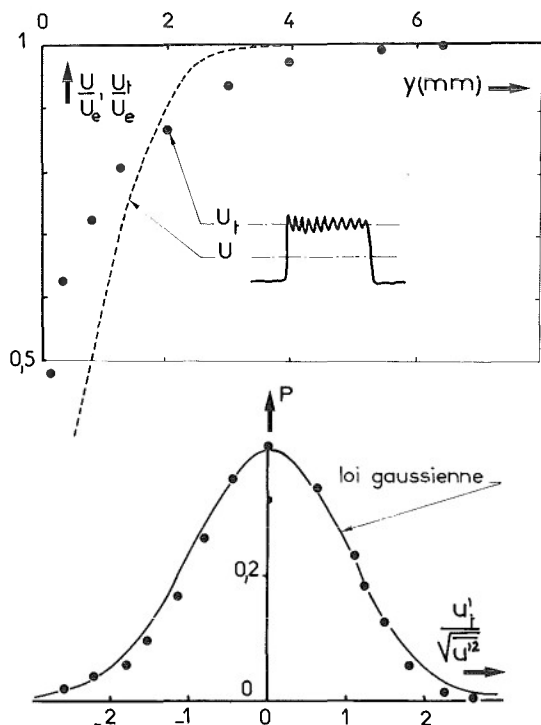


FIG. 8 : Etude des spots turbulents ( $dp/dx = 0$ ). (a).



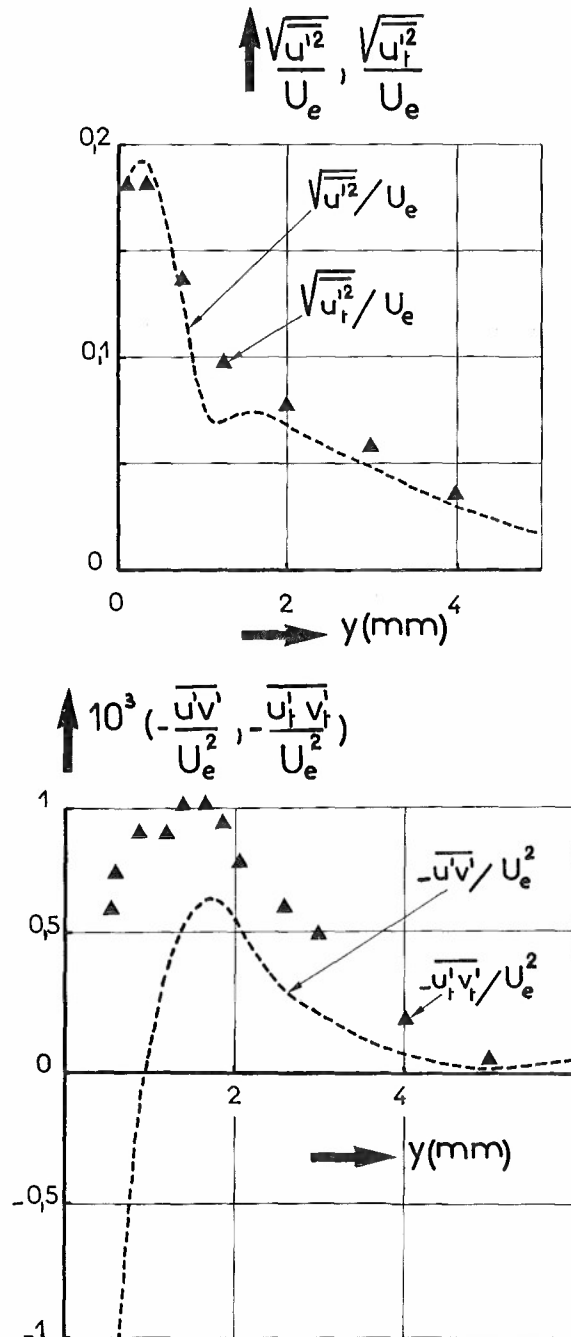


FIG. 9 : Etude des spots turbulents ( $dp/dx=0$ ). (b).

Le signal de détection adopté est  $\left| \frac{\partial^2 U}{\partial t^2} \right|$ , qui favorise les hautes fréquences des structures turbulentes. On présente sur la figure 8 le profil de vitesse moyenne turbulente  $U_t/U_e$ , que l'on compare au profil de vitesse moyenne "brut" obtenue de façon classique par une mesure sur un temps théoriquement infini, pratiquement très long. A la station considérée ( $x = 0,94$  m, milieu de la transition), le profil brut a un paramètre de forme voisin de 2, alors que le  $H$  du profil turbulent est égal à 1,47, valeur classique pour une couche limite turbulente établie.

Si l'on considère maintenant la fluctuation turbulente  $u'_t = U(t) - U_t$  on s'aperçoit qu'au voisinage de la paroi, la densité de probabilité de  $u'_t$  est voisine de la loi gaussienne (figure 8).

Nous avons également déterminé, toujours pour l'abscisse  $x = 0,94$  m, les profils de turbulence  $\omega^2$  et de tension de Reynolds  $-\overline{u'_t v'_t}$ ; ces profils sont tracés sur la figure 9 et comparés aux profils "bruts" de  $\omega^2$  et  $-\overline{u'v'}$ . La forme de ces profils bruts offre quelques particularités; c'est ainsi que le profil de  $\omega^2$  a deux maxima, l'un près de la

paroi, l'autre vers le milieu de l'épaisseur de la couche limite, et que le profil de  $-\overline{u'v'}$  présente aux faibles altitudes des valeurs négatives. Par contre, les profils de fluctuation et de tension de Reynolds mesurés dans les spots turbulents ont des formes correspondant sensiblement à celles que l'on peut rencontrer dans une couche limite turbulente pleinement établie.

Il s'avère ainsi que que l'on retrouve dans les spots turbulents un certain nombre de propriétés classiques des couches limites turbulentes. Ces spots apparaissent dans la couche limite dès le début de la transition, et la couche limite turbulente qui s'établit en aval résulte de la coalescence de ces grosses structures.

#### 6 - INFLUENCE D'UN GRADIENT DE PRESSION POSITIF MODERE. COMPARAISON AU CAS SANS GRADIENT.

Il comporte avant tout de se souvenir que le gradient de pression dit "modéré" est d'une intensité assez faible en ce sens qu'au début de la transition la paramètre de forme laminaire a une valeur très voisine de celle d'un profil de plaque plane. Cette intensité est cependant assez importante pour donner un  $R_x$  de début de transition deux fois plus faible que celui du cas sans gradient, et pour conduire dans la zone de transition à d'importantes différences qualitatives et quantitatives. Ce sont ces différences que nous allons examiner, en restreignant cette étude à des stations situées en milieu de transition.

##### 6.1. Etude qualitative.

On compare sur la figure 10 des enregistrements du signal  $u(t)$  obtenus dans le cas du gradient de pression positif modéré et dans le cas de l'écoulement uniforme. Les stations de sondage sont situées en milieu de transition, les paramètres de forme ayant dans les deux cas des valeurs très voisines: les profils de vitesse "globale" tracés dans les coordonnées  $U/U_e$  et  $y/\theta$  sont d'ailleurs confondus. On compare pour chaque cas un enregistrement réalisé près de la paroi ( $y/\theta \approx 0,4$ ) et un enregistrement réalisé au milieu de l'épaisseur de la couche limite ( $y/\theta = 6$ ).

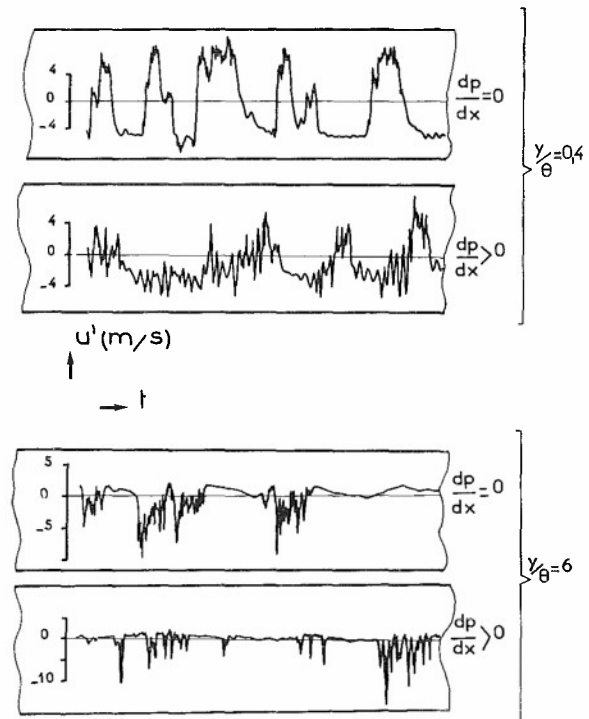


FIG. 10 : Influence d'un gradient de pression positif modéré sur la forme du signal.

Dans le cas sans gradient de pression, on retrouve bien entendu le phénomène d'intermittence, tel que l'on vient de le décrire. Ce phénomène apparaît encore avec  $dp/dx > 0$ , mais de façon beaucoup

moins nette : près de la paroi les spots turbulents se distinguent assez difficilement des zones laminaires, dans lesquelles les ondes de Tollmien-Schlichting ont des amplitudes considérables. L'influence d'un gradient de pression positif se manifeste donc par une amplification des ondes d'instabilité bien plus importante que dans le cas d'un écoulement uniforme. En  $y/\theta = 6$ , les signaux sont apparemment plus ressemblants. Il semble toutefois que la forme en dent de scie soit moins marquée avec  $dp/dx > 0$  qu'avec  $dp/dx = 0$ .

## 6.2. Etude quantitative.

Ces observations sont confirmées par l'analyse conditionnelle du signal  $u(t)$ , qui a été effectuée dans le cas du gradient de pression modéré en conservant le même signal de détection que pour le cas sans gradient. On doit cependant signaler qu'au voisinage de la paroi, la distinction entre zones laminaires et turbulentes devient beaucoup plus délicate qu'en écoulement uniforme, puisque les fluctuations laminaires (ondes d'instabilité) ont ici des amplitudes comparables à celles des régions turbulentes.

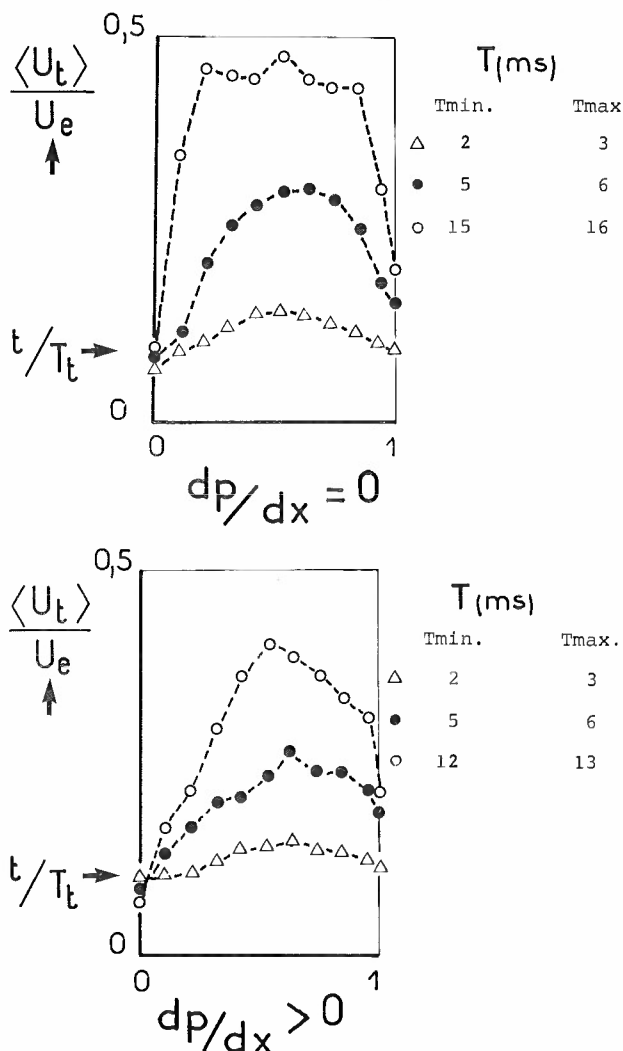


FIG. 11 : Moyennes d'ensemble des spots turbulents (près de la paroi).

On présente sur les figures 11 et 12 des moyennes d'ensemble des zones turbulentes, avec et sans gradient. Ces moyennes d'ensemble sont calculées de la façon suivante : si  $T_t$  représente la durée d'une région turbulente et  $t$  le temps mesuré depuis le début de cette région, on calcule pour une valeur donnée de  $t/T_t$  la moyenne de  $u(t)$  sur un grand nombre de zones turbulentes, dont la durée est comprise entre une valeur minimale  $T_{min}$  et une valeur

maximale  $T_{max}$ . Une telle moyenne sera notée  $\langle U_t \rangle$ . En faisant varier  $t/T_t$ , on obtient un "portrait type" des structures turbulentes.

Les résultats de la figure 11 sont relatifs à des points voisins de la paroi (correspondant aux signaux enregistrés à  $y/\theta = 0,4$  sur la figure 10).

Chaque courbe est paramétrée par le couple de valeurs  $T_{min}$  et  $T_{max}$ . Il apparaît essentiellement que l'amplitude des zones turbulentes, c'est-à-dire  $\langle U_t \rangle_{max}$ , est une fonction croissante de  $T_t$ . De plus, les régions turbulentes de grande durée ont avec  $dp/dx > 0$  des fronts avant et arrière beaucoup moins raides qu'en écoulement uniforme.

En  $y/\theta = 6$  (figure 12, correspondant aux signaux présentés au bas de la figure 10), l'influence du gradient de pression est assez nette. Dans le cas sans gradient, les spots dont la durée est comprise entre 7 et 8 millisecondes présentent la forme en dent de scie déjà signalée au § 5 ; avec  $dp/dx > 0$ , les régions turbulentes de durée comparable ont cette même forme générale, mais il apparaît trois ou quatre pointes assez nettes, d'amplitude décroissante avec le temps. Ces pointes correspondent à des ondes de Tollmien-Schlichting (de période  $\approx 2$  ms) très déformées, qui ont cependant conservé leur individualité, contrairement à ce qui se passe avec  $dp/dx = 0$ . Concernant toujours le cas avec gradient, les spots tels que  $3 \text{ ms} < T_t < 4 \text{ ms}$  présentent bien entendu deux pointes, correspondant à deux périodes des ondes d'instabilité.

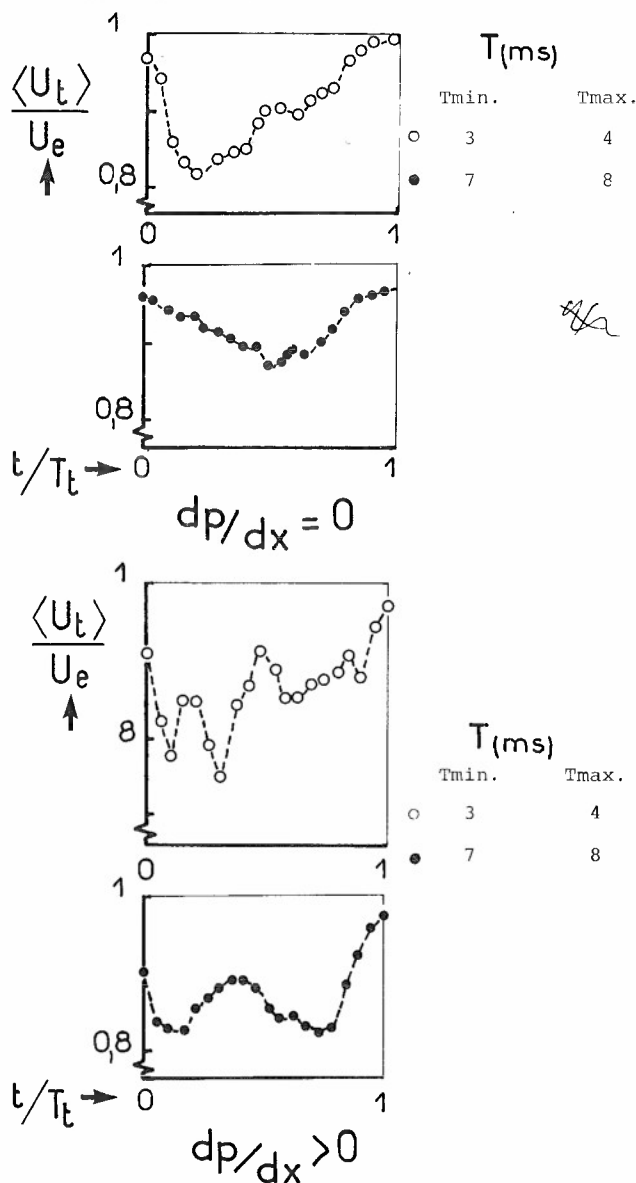


FIG. 12 : Moyennes d'ensemble des spots turbulents (milieu de la couche limite).

## 7 - TRANSITION AU VOISINAGE D'UN DECOLLEMENT LAMINAIRE.

## 7.1. Etude de la région de transition.

Nous présentons sur la figure 13 deux enregistrements du signal instantané, réalisés sur le cylindre au milieu de la région de transition, ainsi que les spectres de puissance correspondants. D'importantes différences sont à signaler par rapport au cas de l'écoulement uniforme : on ne voit plus apparaître de grosses structures turbulentes bien individualisées (spots turbulents), mais plutôt des séries de pics dirigés vers les vitesses supérieures au voisinage de la paroi, vers les vitesses inférieures aux plus grandes altitudes. La caractéristique la plus remarquable des spectres est l'existence d'un maximum pour une fréquence voisine de 200 Hz, c'est-à-dire pour la fréquence des ondes de Tollmien-Schlichting. Sur certains pics se superposent des fluctuations à plus haute fréquence, indiquant un début d'apparition de turbulence.

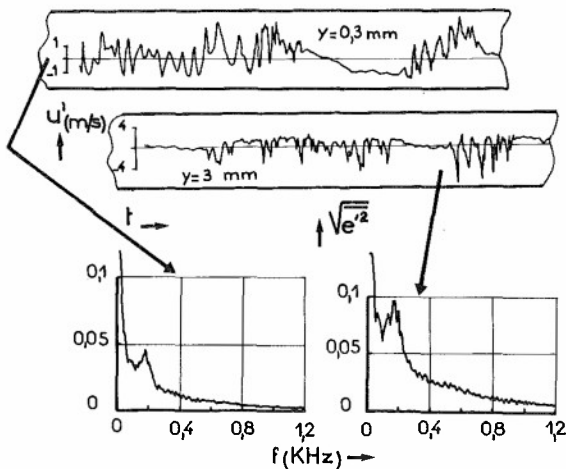


FIG. 13 : Exemples d'enregistrements en milieu de transition.  
(expériences sur cylindre ; décollement).

L'absence de spots turbulents dans la zone de transition devient encore plus évidente dans les expériences de COUSTEIX et PAILHAS sur profil ONERA D ; on montre sur la figure 14 quelques exemples de signaux  $u(t)$ , enregistrés vers le milieu de la couche limite, à divers stades du processus de transition. Les spectres de puissance correspondants sont donnés sur la figure 15. En  $x/c = 0,825$  et  $x/c = 0,875$ , on observe les ondes d'instabilité, de fréquence voisine de 1000 Hz ; leur intensité est très importante, puisqu'en  $x/c = 0,875$ , elle atteint 11 pour cent de la vitesse extérieure. Des phénomènes non linéaires entrent alors en jeu et se traduisent sur les spectres par l'apparition d'harmoniques. En  $x/c = 0,925$ , le signal fondamental à 1000 Hz reste encore visible, mais il est perturbé par une fluctuation de fréquence plus élevée : son allure est assez comparable à celle du signal obtenue sur la cylindre en  $y/\theta \approx 3,8$  (figure 13). Plus en aval, le signal s'enrichit en harmoniques supplémentaires, mais on distingue une certaine régularité dans sa forme.

Des remarques analogues peuvent être tirées de l'examen des enregistrements réalisés sur le profil NACA 64 A 010 dans la région de transition (figure 16) : on y retrouve les ondes de Tollmien-Schlichting (leur fréquence est voisine de 6000 Hz) qui se déforment et commencent à se "hérisser" de fluctuations turbulentes en fin de transition. Il n'apparaît jamais de spots turbulents, structures caractéristiques d'une transition sur plaque plane, mais dont on a vu au § 6 qu'un gradient de pression positif, même modéré, suffisait pour commencer à les estomper. Des visualisations réalisées au tunnel hydrodynamique par H. WERLE [9] dans le cas d'un bulbe de décollement de bord d'attaque montrent des "rouleaux" transversaux, d'abord très réguliers,

qui se désorganisent progressivement pour conduire à un écoulement turbulent : de telles observations sont bien cohérentes avec l'interprétation que l'on peut donner des signaux pratiquement périodiques délivrés par le fil chaud.

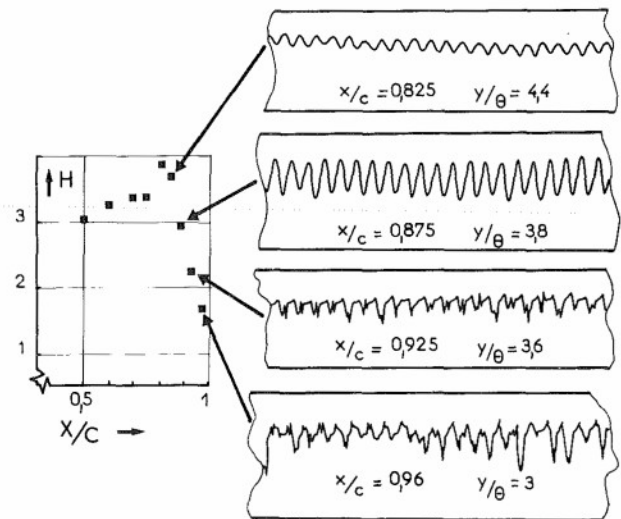


FIG. 14 : Exemples d'enregistrements (profil ONERA D)

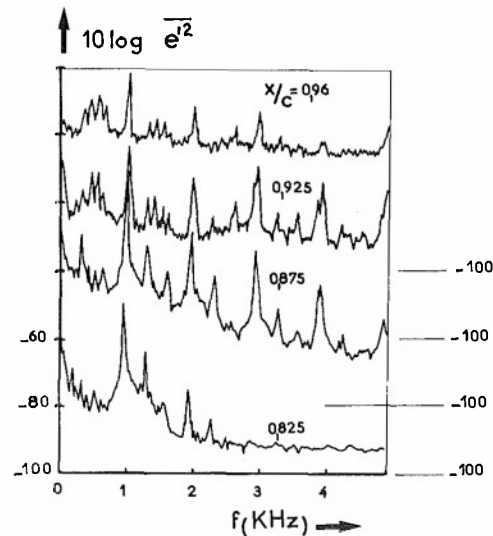


FIG. 15 : Spectre de la fluctuation longitudinale (profil ONERA D).

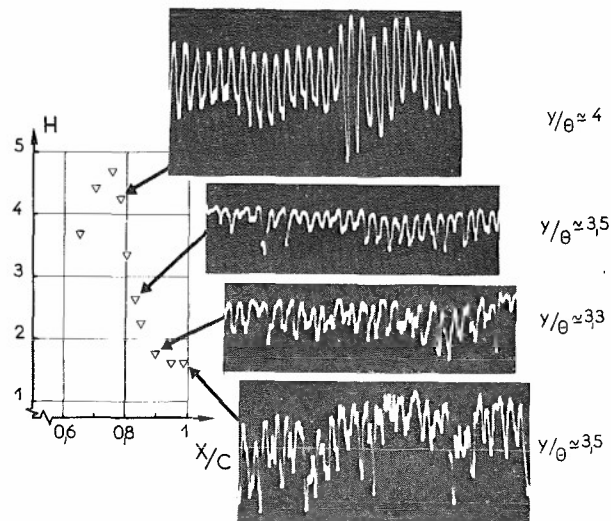


FIG. 16 : Exemples d'enregistrements (profil NACA 64 A 010).

## 7.2. Etablissement du régime turbulent.

L'établissement de la structure turbulente "classique" a d'abord été étudiée dans les expériences réalisées sur cylindre. On montre sur la figure 17 l'évolution des profils de vitesse moyenne pour cinq stations choisies à la fin de la transition et en aval de celle-ci. Tous ces profils ayant des paramètres de forme voisins (excepté celui mesuré en  $x = 0,7$  m où la transition n'est pas tout à fait achevée), il n'est pas étonnant que leur représentation dans les coordonnées  $U/U_e$  et  $y/\theta$  donne une courbe unique.

L'obtention de l'état turbulent "asymptotique" semble beaucoup moins rapide si l'on considère maintenant les profils d'intensité de turbulence longitudinale (figure 17). Leur forme évolue sensiblement avec l'abscisse, surtout dans la région extérieure de la couche limite. Aux premières stations considérées, une sorte de renflement apparaît pour  $y/\theta$  compris entre 3 et 8 environ, puis s'efface peu à peu : c'est seulement aux deux dernières stations de sondage que l'on retrouve un profil de turbulence classique. Il semble donc que la turbulence soit plus lente à atteindre son état "asymptotique" que la vitesse moyenne.

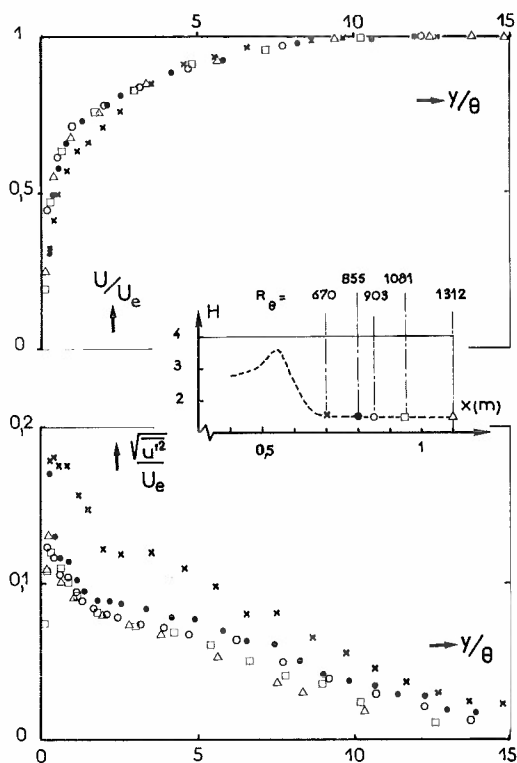


FIG. 17 : Etablissement du régime turbulent : vitesse moyenne et turbulence (expérience sur cylindre ; décollement).

Cette remarque reste bien entendu valable si l'on considère maintenant les moments d'ordre 3 et 4 de la fluctuation  $u'$ . On montre sur la figure 18 l'évolution dans la couche limite de la quantité  $3/F$ , pour les mêmes stations que précédemment.  $F$  représente le facteur d'aplatissement  $u'^4/(\overline{u'^2})^2$ ;

sa valeur est 3 pour un signal aléatoire de probabilité gaussienne. Rappelons que sous certaines hypothèses, le rapport  $3/F$  représente le facteur d'intermittence, rapport du temps où l'écoulement est turbulent au temps total. On observe qu'en

$x = 0,7$  m,  $3/F$  plafonne à 0,7 au voisinage la paroi ; à partir de  $x = 0,8$  m, la valeur unité est à peu près atteinte aux faibles valeurs de  $y/\theta$  et une décroissance de  $3/F$  vers l'extérieur de la couche limite s'amorce à une valeur de  $y/\theta$  d'autant plus élevée que l'abscisse est importante. On a également porté sur la figure 18 l'évolution de  $3/F$  mesurée par KLEBANOFF [10] dans une couche limite turbulente de plaque plane pleinement établie ; il faut aller en  $x = 1,1$  m pour obtenir dans nos expériences une évolution voisine de

celle-ci, c'est-à-dire un rapport  $3/F$  voisin de 1 jusqu'à  $y/\theta = 6$  (soit  $y/\delta \approx 0,5$ ), puis une décroissance (intermittence dite de "frontière") conduisant à une annulation dans l'écoulement extérieur.

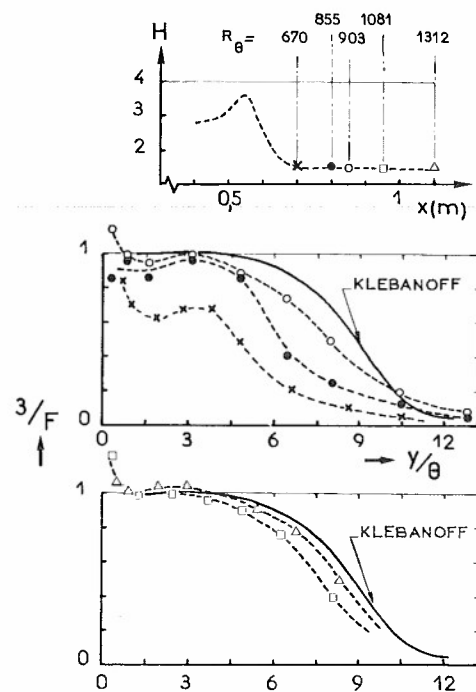


FIG. 18 : Facteur d'aplatissement (Expérience sur cylindre ; décollement).

L'étude du facteur de dissymétrie  $D = \overline{u'^3}/(\overline{u'^2})^{1.5}$

(figure 19) permet d'avoir une idée de la forme du signal instantané.  $D$  est nul pour une fluctuation gaussienne, négatif pour un signal présentant des pointes vers les vitesses supérieures. On voit sur la figure 19 que  $D$  est peu différent de zéro au voisinage de la paroi, plus exactement dans les régions où  $3/F$  est peu différent de 1, puis qu'il prend des valeurs franchement négatives vers l'extérieur de la couche limite ; à  $y/\theta$  donné, la valeur absolue de  $D$  décroît cependant lorsque  $x$  augmente. L'exemple d'enregistrement présenté sur cette même figure indique bien des pointes de  $u'$  dirigées vers les vitesses inférieures. Ces pointes sont à rapprocher de celles observées dans la zone de transition elle-même : dans le signal présenté leur fréquence est encore voisine de celle des ondes d'instabilité. Plus en aval, elles perdent peu à peu leur régularité et sont responsables de l'intermittence de frontière de la couche limite turbulente.

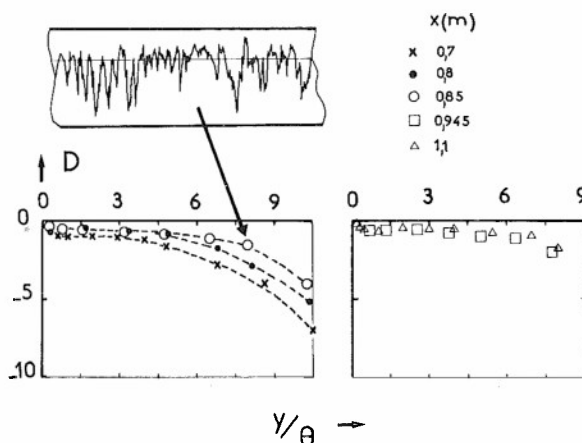


FIG. 19 : Facteur de dissymétrie (Expérience sur cylindre ; décollement).

La persistance de la régularité des pointes, quelque distance après la fin de la transition est illustrée sur la figure 20. On y montre trois spectres obtenus sur le profil NACA 64 A 010 à  $x/c = 0,99$ .

On n'observe rien de particulier près de la paroi, mais aux deux altitudes supérieures, le maximum pour la fréquence 6000 Hz, fréquence des ondes de TOLLMIEN-SCHLICHTING, apparaît nettement.

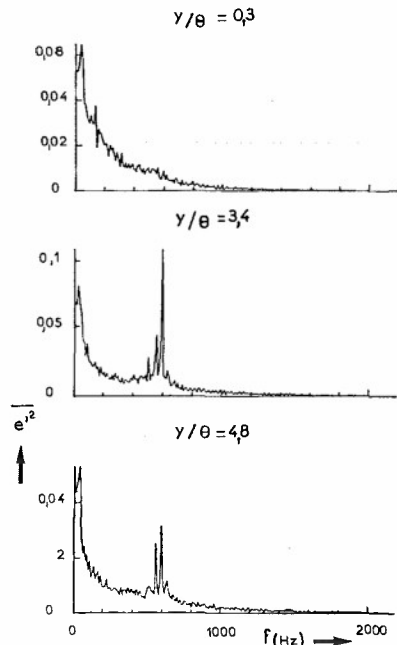


FIG. 20 : Spectres de la fluctuation longitudinale (profil NACA 64 A 010 ;  $x/c = 0,99$ )

## 8 - CONCLUSION.

Ces diverses études, essentiellement qualitatives, permettent de tirer un certain nombre de conclusions quant aux divers modes d'apparition de la turbulence en région de transition.

Dans le cas de l'écoulement uniforme, des spots turbulents apparaissent de façon aléatoire dans le temps et dans l'espace, dès le début de la transition; ces grosses structures, essentiellement tridimensionnelles, possèdent déjà un certain nombre de propriétés caractéristiques de la couche limite turbulente que leur coalescence finira par former en aval. Ce mécanisme ne garde aucune trace des processus d'instabilité (ondes de Tollmien-Schlichting) qui ont conduit à la déstabilisation de la couche limite laminaire.

La mise en jeu d'un léger gradient de pression positif conduit rapidement à des observations différentes, et ceci en raison de l'amplitude considérable que prennent les ondes de Tollmien-Schlichting. Il devient délicat de qualifier l'intermittence, et les moyennes d'ensemble des régions turbulentes font apparaître une persistance des ondes d'instabilité.

Lorsque le gradient de pression positif est suffisamment intense pour provoquer un décollement de la couche limite laminaire, la transition semble bien avoir lieu, en ce sens que le paramètre de forme décroît depuis une valeur laminaire jusqu'à une valeur turbulente, mais sans qu'apparaisse aucun phénomène d'intermittence : on enregistre seulement une amplification considérable des ondes d'instabilité, puis leur déformation progressive. Au début de la couche limite "turbulente", le spectre de  $u'^2$  indique que l'énergie de turbulence est transportée en grande partie par une suite de pointes correspondant aux harmoniques des ondes d'instabilité. Les visualisations montrent des rouleaux bidimensionnels, espacés régulièrement, très différents des spots tridimensionnels, au caractère aléatoire, rencontrés avec un écoulement uniforme. On pourrait attribuer ces différences de processus à un effet de nombre de Reynolds : dans le cas sans gradient, on a  $Re_{\theta} = 900$  et avec décollement  $Re_{\theta} \approx 400$ . Nous pensons en fait qu'il n'en est rien ; en effet, des expériences

réalisées à l'ONERA/CERT /11/ ont permis d'obtenir en écoulement uniforme des  $Re_{\theta}$  voisins de 400 par augmentation du taux de turbulence extérieure : on a retrouvé dans ce cas une intermittence avec spots tout à fait semblable à celle décrite au § 4. Le paramètre gradient de pression semble donc prépondérant. Il faut se souvenir que les transitions sans intermittence sont observées dans certains écoulements libres, du type jets ou sillages /12/ qui présentent, comme dans le cas d'un décollement, des profils de vitesse moyenne avec un point d'inflexion très marqué.

En ce qui concerne l'établissement du régime turbulent "classique" en aval de la transition, nous pouvons formuler les observations suivantes : le profil de vitesse moyenne se stabilise très rapidement ; il n'en est pas de même pour les profils des moments d'ordre 2, 3 et 4 de la fluctuation  $u'$ , qui continuent à évoluer alors que le paramètre de forme reste sensiblement constant ; la couche limite turbulente garde assez longtemps, dans sa partie extérieure, le souvenir de la fréquence des ondes d'instabilité qui ont provoqué la transition, alors qu'au voisinage de la paroi la structure turbulente s'établit assez vite ( $3/f = 1$ ,  $D = 0$ ).

## REFERENCES

- /1/ COUSTEIX J. PAILHAS G.  
"Etude exploratoire d'un processus de transition laminaire-turbulent au voisinage du décollement d'une couche limite laminaire". La Recherche Aérospatiale n° 1979-3.
- /2/ ARNAL D., JUILLEN J.C.  
"Etude de l'intermittence dans une région de transition" La Recherche Aérospatiale n° 1977-3.
- /3/ ARNAL D., JUILLEN J.C., MICHEL R.  
"Analyse expérimentale et calcul de l'apparition et du développement de la transition de la couche limite". AGARD Conf. Proc. n° 224 - Laminar-Turbulent Transition, Copenhagen, May 2-4, 1977.
- /4/ EMMONS H.W.  
"The laminar-turbulent transition in boundary layer. Part. 1". J. Aer. Sc., Vol. 18, 1951, pp. 290-298.
- /5/ SCHUBAUER G.B., KLEBANOFF P.S.  
"Contribution on the mechanics of boundary layer transition". Rept. 1289, 1956, NACA.
- /6/ ELDER J.W.  
"An experimental investigation of turbulent spots and breakdown to turbulence". J. Fluid. Mech., Vol. 9, Part. 2 (1950).
- /7/ WYGNANSKI I., SOKOLOV M., FRIEDMAN D.  
"On a turbulent spot in a laminar boundary layer". J. Fluid. Mech., Vol. 78, Part 4, 1976.
- /8/ CANTWELL B., COLES D., DIMOTAKIS P.  
"Structure and entrainment in the plane of symmetry of a turbulent spot". J. Fluid Mech., Vol. 87, Part. 4, 1978.
- /9/ WERLE H., LAVERRE J., SOULIER C.  
"Techniques de visualisations d'écoulements pariétaux". Communication présentée au Colloque Euromech 90, Nancy, Juillet 1977. ONERA T.P. n° 1977-86.
- /10/ KLEBANOFF P.S.  
"Characteristics of turbulence in a boundary layer with zero pressure gradient". NACA Report 1-247 (1955).
- /11/ ARNAL D., JUILLEN J.C.  
"Contribution expérimentale à l'étude de la réceptivité d'une couche limite laminaire, à la turbulence de l'écoulement général". Document CERT non publié.
- /12/ SATO H.  
"The stability and transition of a two-dimensional jet". J. Fluid Mech., Vol. 7, Part 1 (1960).

## SOME MEASUREMENTS IN SYNTHETIC TURBULENT BOUNDARY LAYERS

by

Ömer Savaş

Scientific and Technical Research Council of Turkey, Ankara, Turkey;  
 formerly graduate student, California Institute of Technology, Pasadena, California, U.S.A.

## SUMMARY

Synthetic turbulent boundary layers were constructed on a flat plate by generating systematic moving patterns of turbulent spots in a laminar flow. The experiments were carried out in a wind tunnel at a Reynolds number based on plate length of  $1.7 \times 10^6$ . Spots were generated periodically in space and time near the leading edge to form a regular hexagonal pattern. The disturbance mechanism was a camshaft which displaced small pins momentarily into the laminar flow at frequencies up to 80 Hz. The main instrumentation was a rake of 24 hot wires placed across the flow in a line parallel to the surface. The main measured variable was local intermittency; i.e., the probability of observing turbulent flow at a particular point in space and time. The results are reported in  $x$ - $t$  diagrams showing the evolution of various synthetic flows along the plate. The dimensionless celerity or phase velocity of the large eddies was found to be 0.88, independent of eddy scale. All patterns with sufficiently small scales eventually showed loss of coherence as they moved downstream. A novel phenomenon called eddy transposition was observed in several flows which contained appreciable laminar regions. The large eddies shifted in formation to new positions, intermediate to their original ones, while preserving their hexagonal pattern. The present results, together with some empirical properties of a turbulent spot, were used to estimate the best choice of scales for constructing a synthetic boundary layer suitable for detailed study. The values recommended are: spanwise scale/thickness  $\approx 2.5$ , streamwise scale/thickness  $\approx 8$ .

## I INTRODUCTION

The contemporary view of turbulent fluid motion is that turbulent shear flows are not as random as was once thought, but contain coherent eddy structures which represent characteristic concentrations of vorticity at the largest scale of the flow. In any attempt to find and study such coherent motions in the turbulent boundary layer, it is a serious difficulty that the eddies occur in various stages of development at random places and times. Presumably the eddies have a typical signature in terms (say) of surface pressure, surface friction, local turbulence intensity, interface geometry, large-scale vorticity, and the like. However, this signature cannot be determined until the eddy has been found, and the eddy cannot readily be found unless its signature is known.

As a possible means for bypassing this difficulty, Coles and Barker [1] proposed the concept of a synthetic turbulent boundary layer and made a few preliminary measurements in one such flow. Their point of departure was the fact that transition from laminar to turbulent flow in a boundary layer is characterized by the appearance of turbulent spots. The turbulent spot, first discovered by Emmons [2] and first documented experimentally by Schubauer and Klebanoff [3], is an arrowhead-shaped region of turbulence which appears in a laminar boundary layer (when there is a suitable natural or artificial disturbance) and moves downstream, growing in size nearly linearly in all directions. The spot has been identified as essentially a large, flat horseshoe vortex by the work of Coles and Barker [1], Wygnanski, Sokolov, and Friedman [4], and Cantwell, Coles and Dimotakis [5]. Consequently, in the context of the coherent-structure formulation, the spot suggests itself as a possible prototype large eddy for the turbulent boundary layer. Cantwell et al. [5] take the position that the spot is not so much a prototype large eddy as an alternative flow to the boundary layer, in view of the inevitable discrepancy in scale. Nevertheless, they expect the isolated spot to have important structural features in common with characteristic large-scale vorticity concentrations in the turbulent boundary layer. Zilberman, Wygnanski, and Kaplan [6] and Haritonidis, Kaplan, and Wygnanski [7] have recently followed an artificially generated spot into a turbulent boundary layer for very large distances. They find that the growth of the spot is severely inhibited in the streamwise and spanwise directions, but not in the normal direction. The characteristic celerity of the spot in the boundary layer is found to be  $c = 0.9 u_\infty$ ,  $u_\infty$  being the free-stream velocity. On the basis of these experiments, Wygnanski [8] takes the position that the turbulent spot may be viewed as the basic module for the turbulent boundary layer.

The first major investigation of outer structure in the turbulent boundary layer was carried out by Kovasznay, Kibens, and Blackwelder [9] and by Blackwelder and Kovasznay [10]. Their results of greatest interest for the present research include space-time correlations which suggest a celerity of  $0.93 u_\infty$  for the outer turbulent regions. There is strong persistence of the large eddies over distances  $\Delta x/\delta$  of 15 or more, where  $\delta$  is the boundary-layer thickness. A set of correlation maps in  $(z, t)$  have zero-correlation contours indicating a streamwise scale  $u_\infty \Delta t/\delta$  of about 2.5 and a spanwise scale  $\Delta z/\delta$  of about 1.2 for the typical large eddy at the half-intermittency level. Later triple-correlation measurements by Fulachier, Arzoumanian, and Dumas [11], using heat as a passive contaminant, support these estimates of scale. Blackwelder and Kovasznay [10] infer a qualitative picture of the mean motion in a moving reference frame which shows large-scale rotation in the same sense as the general vorticity in the flow. These authors approach, but do not quite reach, the conclusion that the large-scale mean motion is a transverse vortex. Praturi and Brodkey [12], using a combination of dye and tracer particles and a moving camera for flow visualization, frequently observe large, persistent transverse vortices, but do not observe the swept-back structure which would be characteristic of the main vortex in a turbulent spot.

The experiment carried out by Coles and Barker [1] was to generate a regular hexagonal pattern of

turbulent spots in the laminar boundary layer near the leading edge of a flat plate and to sample the flow farther downstream at times locked to the phase of the disturbance generator. They found that periodicity in space and time persisted downstream, and that the average velocity profile was close to that which would be expected in a natural turbulent boundary layer at the same Reynolds number. Figure 1 (courtesy of D. Coles) shows a photograph of a single spot in water, using surface dye for flow visualization, together with a photograph of a synthetic turbulent boundary layer under the same conditions in the same channel.

The present research continues the work begun by Coles and Barker [1]. Their measurements were made in water, using momentary jets to create the turbulent spots and using a single-channel laser-Doppler velocimeter as main instrumentation. Because of insufficient width for the channel and insufficient flow rate for the pump, the Reynolds number was relatively low, and the useful region of the plate surface was severely limited by transverse contamination from the side walls. There was also a substantial acceleration of the free stream along the plate.

The present experiments were carried out under conditions which avoid these problems, particularly the problem of transverse contamination. The main difference is that the present measurements were made in a wind tunnel, requiring a shift to the hot-wire anemometer as main instrumentation, and requiring also a shift to a disturbance mechanism capable of operating at much higher frequencies. A relatively large range of scales in space and time is explored, in an attempt to determine which patterns are most coherent at certain stations in the flow. The emphasis is on pattern and scale, as revealed by measurements of intermittency in the outer part of the layer. There are as yet no measurements of velocity, surface stress, turbulence intensity, or other variables involved in the problem of signatures and eventually in the problem of dynamics. The task of the present exploratory research is to define one or more synthetic flows which are suitable for more detailed study.

This paper is derived from the Ph. D. thesis by Savaş [13], in which a more detailed description of the experiment and of the experimental results can be found.

## II MODEL AND INSTRUMENTATION

The experiments were carried out in the Merrill wind tunnel at GALTIT (Graduate Aeronautical Laboratories, California Institute of Technology). The measurements reported here were made at a nominal free-stream speed  $U = 10$  m/s to obtain a maximum region of laminar flow. The flat-plate model was made from two sections of aluminum-alloy plate, as indicated in Figure 2. The streamwise coordinate  $x$  is measured from the leading edge of the plate; the spanwise coordinate  $z$  is measured from the plate centerline; and the normal coordinate  $y$  is measured from the plate surface. The leading edge was a 10:1 ellipse, chosen to prevent large positive pressure gradients which could cause separation and/or premature transition. The pressure coefficient was constant within  $\pm 0.01$  over most of the working surface. With no artificial disturbances, the boundary layer on the plate centerline was laminar along the total length of the plate (streamwise Reynolds number  $Re_x = 1.7 \times 10^6$  at the trailing edge).

The objectives of the present research required a disturbance generator capable of operating reliably over a range of frequencies from a few Hz to 100 Hz or more. Multiple spark gaps were not considered suitable because of probable severe electrical interference with the data-acquisition system. Fluidic methods were not considered suitable because of unavoidable frequency limitations for solenoid devices. A mechanical method was therefore adopted.

The disturbances were generated by momentarily displacing small cylindrical pins into the laminar boundary layer. Figure 3 shows some geometrical details of the mechanism. The basic element is a nylon pin which is embedded in the front section of the plate. Normally, a compression spring keeps the pin retracted and in contact with a retaining plate, as shown at the left, so that the plate surface is uninterrupted. The pin is displaced into the boundary layer, as shown at the right, by a rotating nylon cam (impregnated with molybdenum disulfide to reduce friction). A beryllium-copper leaf spring between each pin and the associated cam guarantees smooth and non-destructive contact between the two moving elements and also removes heat generated during operation.

The camshaft is mounted on the lower side of the front section of the plate. It is supported at seven locations in needle bearings. The camshaft assembly is shielded from the air flow by a curved shield which extends from side wall to side wall. Cooling air introduced into the camshaft cavity is discharged through the clearance gap around the shaft at the motor end. The life of the cam-pin assembly was found to be critically dependent on the amount of cooling provided.

The cam mechanism has an individual four-lobe cam corresponding to each pin in the plate. Any cam lobes which were not wanted were machined away. Normally two lobes, 180 degrees apart, were retained at each pin location. Alternate cams along the length of the camshaft were displaced by 90 degrees. Thus, the disturbance generator produced a close-packed hexagonal pattern in a  $(z, t)$  plane when the shaft was rotating, as shown in Figure 4. The period  $\zeta$  in the  $z$  direction was fixed by the cam in use. The period  $\tau$  in time was half the period of shaft rotation. The ostensible variable of the experiment was actually neither the period  $\tau$  nor the frequency  $f = 1/\tau$ ; it was an integer  $N = 20\,000\tau$ . For example, if  $N = 800$  then  $\tau = 0.040$  second and  $f = 25$  Hz.

Pins are installed in the model at a station 22.9 cm from the leading edge. The pins are spaced 0.508 cm (0.2 in) apart. Because room must be provided for the bearings used to support the camshaft, the minimum uniform pin spacing is 1.524 cm (0.6 in). With a hexagonal disturbance pattern, the minimum spanwise pitch or wave length  $\zeta$  is therefore 3.048 cm (1.2 in). The three values actually used in the present tests were 6.10, 9.14, and 12.19 cm (2.4, 3.6, and 4.8 in).

During bench tests, the thickness of the leaf spring and the clearances of the cam-spring-pin



geometry were varied, and strobe lighting was used to observe the motion of the various elements. Satisfactory smooth, bounce-free operation on the bench was achieved at pin frequencies up to 200 Hz. A life test was discontinued after about seventy million cycles (270 hours at 70 Hz) when no problems were encountered except for slight wear of the pins and cam lobes.

Figure 5 shows typical records of static pin displacement plotted against camshaft angle (measured from the encoder index pulse; see below). There were slight inadvertent variations in cam radius and pin length, amounting to  $\pm 0.005$  cm; these variations were sometimes detectable in the data as variations in size and strength of the turbulent spots. The figure also shows pin position at maximum displacement relative to the estimated (not measured) laminar boundary-layer profile at the pin station.

Twenty four hot-wire probes were mounted in a rake configuration transverse to the flow and parallel to the plate surface. The rake was suspended from a full-span bridge, as shown in the photograph in Figure 6. All electrical wiring except for connections at the probes was contained within the rake, struts and bridge. The probes had no common electrical connection.

The 24 hot-wire probes were located symmetrically about the plate center and were spaced 0.762 cm (0.3 in) apart. The span of the rake was therefore 17.5 cm (6.9 in). The hot-wire sensors were parallel to the plate surface and hence responded mainly to the streamwise component of velocity. The sensors were 2.5  $\mu$ m in diameter and about 0.15 cm in length. They were made of platinum-plated tungsten wire and were operated at a constant temperature of 250°C.

Intermittency  $\gamma$ , interpreted as the probability of observing turbulent flow, was the primary measured variable in the present research. Turbulent flow was distinguished from laminar flow in terms of energy content at high frequencies. Each hot-wire circuit included an intermittency meter consisting of a single-pole bandpass filter, a rectifier, a level detector, and a retriggerable monostable multivibrator, or one-shot. After some preliminary measurements, the cut-off frequencies of the band-pass filter were set at 2.7 kHz and 7.0 kHz and were left fixed throughout the course of the experiments. The threshold levels on individual channels varied slightly with differences in the particular wires and circuit components. The pulse lengths of the one-shots were set to 1 ms; no attempt was made to correct the data for the associated time lag at the end of a turbulent region.

Adjustment of the intermittency meters was essentially a subjective process. All twenty four circuits were tuned in a turbulent boundary layer flow generated by taping a tripping device onto the plate surface at  $x \approx 23$  cm. The trip extended from wall to wall. The rake was placed well downstream at a suitable distance from the plate surface. After considerable adjustment of probe height and circuit parameters, the average intermittency factor seen by the 24 wires at  $x = 118$  cm,  $y = 2.02$  cm,  $U = 10$  m/s was 0.50. Extreme individual readings were 0.48 and 0.53.

Figure 7 shows typical analog and digital signals in a typical synthetic flow for two hot wires which are spaced a half period apart in the spanwise direction.

During the main experiments, the 24 bits of intermittency information were read at regular intervals and written on magnetic tape. A 200-line encoder on the camshaft controlled the data-transfer rate, and an index pulse from the same encoder guaranteed synchronization.

### III DATA PROCESSING AND PRESENTATION

For the synthetic flows, a systematic method was wanted for setting the hot-wire rake at a suitable distance from the plate surface. During some preliminary runs with the 12.2-cm cam, it became apparent that a disturbance frequency of 25 Hz ( $N = 800$ ; the frequency is  $20\,000/N$ ) produced a very regular, coherent flow over the full length of the plate (see Figure 10). Some experimenting showed that a good rake position for this flow was one where the overall intermittency (averaged over all 24 wires) was about 0.4. This value was therefore adopted as a standard to be set at each station for the particular cam speed  $N = 800$  for each cam, and the probe position was left unchanged for all other runs with the same cam. Because of variations in spot size and density with frequency, and also changes in apparent origin for spot growth, one consequence of the method just described was that the global intermittency changed significantly but systematically with  $x$  for fixed  $N$  (for  $N \neq 800$ ), and also changed with  $N$  for fixed  $x$ .

A filtering operation was applied to the intermittency data before ensemble averages at constant phase were computed. There were two reasons. One was to sharpen the classification of the flow into laminar and turbulent regimes. The other was to provide a means for communication between adjacent wires, which sometimes had slightly different responses in the same flow.

Figure 8 shows several examples of unfiltered and filtered intermittency data. After some experimenting, the filtering method chosen was to center a rectangular window, 3 wires wide and 5 samples long, over each bit of the pattern. If the sum of the 15 bits was 8 or more, the center bit was replaced by a one; if the sum of the 15 bits was 7 or less, the center bit was replaced by a zero. The data from wires 1 and 24, at the ends of the rake, retained their original values. Because the same  $3 \times 5$  filter window was used for all of the data processing, the effect of filtering was uniform for different probe stations but not for different cam speeds.

For each run, the filtered data were ensemble averaged over 4000 cycles of the disturbance pattern as a  $24 \times 200$  array, covering one camshaft revolution. In principle, the two cycles of a revolution should be identical and could be combined. In practice, however, slight variations in maximum pin displacement were sometimes detectable as variations in peak intermittency within a turbulent region. For this reason, the fundamental period of the experiments was usually taken as one revolution rather than one cycle.

Two characteristic values for overall intermittency were eventually calculated. One is the global



mean intermittency; i.e., the value obtained by averaging over one revolution and over the number of wires corresponding to one spanwise period of the pin disturbance. This value is usually a little different from the global mean value chosen during the experiment to set the probe height (the target value was a global mean of 0.40 for  $N = 800$ ). The reason is that the probe was set with the aid of a quick-look program which did not filter the intermittency data. The second characteristic overall intermittency was the value midway between the largest and smallest values occurring in the filtered  $24 \times 200$  array. This value, called the median value, identifies the contour which is shaded to indicate regions of turbulence in Figures 9 - 11 below. The median was preferable to the mean for this purpose because it did not decrease toward zero in flows with low inherent intermittency.

During the study of synthetic boundary layers, the two main parameters, pin spacing and cam speed, were varied over a range which it was hoped would include one or more synthetic flows giving good cause for eventual closer study. This hope was realized in full. Figures 9, 10, and 11 are three typical samples from the results of the present research. In each of these figures the ensemble-averaged intermittency  $\langle \gamma \rangle$  is presented as a function of the three independent variables  $x$ ,  $z$ , and  $t$  (streamwise distance, spanwise distance, and time, or more properly phase). The main coordinates in each figure define the  $(x, t)$  plane. The origin in time is the index pulse. At each  $x$  corresponding to one of the six probe stations, a centered strip of data shows contours of constant ensemble-averaged intermittency in coordinates  $(z, t)$ ; i.e., in coordinates representing a plan view of activity in a narrow strip symmetrical about the plate centerline. These are filtered data, so that the two end wires are not used directly. The effective width of the rake is 16.0 cm (6.3 in). The contour interval in  $\langle \gamma \rangle$  is 0.1. The pattern in each strip is periodic with period  $Ut = 2U\tau$ , where  $2\tau$  is the time required for one camshaft revolution. The figures therefore depict the downstream evolution of an average disturbance pattern. To assist in visualization, the region inside the median contour is shaded for the particular pattern which was generated approximately at  $t = 0$  at the pin station. The solid horizontal lines and the small circles at the pin station indicate the time during which the flow is disturbed and the moment when the pins are at top dead center. Note that the coordinates  $x$ ,  $z$ , and  $Ut$  are all in cm and have the same scales, so that the intermittency data show the various flow patterns without distortion except for the small difference between celerity  $c$  and reference velocity  $U$ , or more precisely free-stream velocity  $u_\infty = 1.013 U$ .

#### IV RESULTS, DISCUSSION, AND CONCLUSIONS

The results of the present research, taken as a whole, establish the important conclusion that the downstream large-eddy structure always develops directly from the original disturbance pattern, with an explicit correspondence between spots and large eddies. In this sense, at least, the turbulent spot can certainly serve as a prototype large eddy. The data also confirm a related finding by Zilberman et al [6]. There is an enormous reduction in the growth rate of each spot, in both the spanwise and streamwise directions, as it moves downstream in a crowd of neighboring spots. The growth rate normal to the surface, however, is almost unaffected. The data do not support the conclusion by Elder [14] that spots grow independently of each other and can be treated by superposition. Elder studied only the case of two spots side by side, and then only at an  $x$ -Reynolds number of about  $0.4 \times 10^6$ . The present data deal with large arrays of spots and with the range of  $x$ -Reynolds numbers from  $0.4 \times 10^6$  to  $1.3 \times 10^6$ .

Another important result, apparently new, concerns an interaction phenomenon which we propose to call eddy transposition. This phenomenon is depicted in Figure 9. It involves the appearance and rapid growth of regions of new turbulence to the rear of the original spots and in the gaps between them. The original spots then decay and disappear. In the middle of the transposition process the number of large eddies is twice the normal value, and these eddies form a honeycomb pattern of hexagons with empty centers. When the transposition process is complete, the original hexagonal pattern is restored with a substantial phase shift.

It seems likely that eddy transposition in the synthetic boundary layer is connected with the appearance of wave packets and new breakdowns to turbulence at the wings of a single spot, as observed by Wygnanski, Haritonidis, and Kaplan [15]. At least the early stages of the transposition process seem to involve configurations with substantial regions of laminar flow. If so, transposition should properly be classified as part of the transition process. There is no reason at present to suppose that the transposition phenomenon cannot occur more than once in a given flow.

An important question is raised by the disappearance of the original eddies in the late stages of transposition. One conjecture can be based on the position taken by Cantwell et al. [5] regarding the process which supplies energy to a turbulent spot. In their view, freestream fluid overtakes the spot and is entrained and slowed by friction on the wall at the rear of the spot, where the surface friction is large (the large friction may be thought of as either a cause or an effect of the deceleration). It may be that during transposition the rear eddies shield the front ones and reduce their energy supply to such a level that they are obliged to decay and disappear. This conjecture, if it is correct, implies that a configuration with large eddies following in line, one behind the other, might be quite unstable. Hence a rectangular pattern would be a poor choice for a synthetic flow, whereas a hexagonal pattern would be a good one. It should be admitted that the reason for choosing a hexagonal pattern for the present experiments, following Coles and Barker [1], was aesthetic rather than scientific. In any event, an experimental test of the conjecture in these terms is clearly feasible.

Figure 10 displays a synthetic boundary-layer flow in which the original disturbance pattern preserves its identity with little loss of coherence over the full length of the plate. As the spots are packed closer together in space and time, the resulting pattern tends to lose its coherence more or less rapidly, as shown by one example in Figure 11.

In any flow configuration where the large eddies remain reasonably intact as they move downstream, their celerity can be easily measured as the slope  $Udx/dUt$  in  $x$ - $t$  diagrams like Figures 9-11. Such a measurement, corrected for the small difference between  $U = 1000$  cm/s and  $u_\infty = 1013$  cm/s, and with

emphasis on the data at the more downstream stations, gives a constant celerity  $c = 0.88 (\pm 0.02) u_\infty$ . The dispersion in this value is a measure of experimental scatter rather than of any systematic dependence of celerity on either of the two scales of the hexagonal eddy pattern over a very large range. The phenomenon of eddy transposition, in particular, affects the position but not the celerity of the large eddies.

An attempt has been made to collapse the results for different cams, different cam speeds, and different stations into a map or diagram showing the kinds of interactions and evolutions which can occur in the synthetic boundary layer. On the reasonable assumption that the flow is not much affected by viscosity, variables which suggest themselves for this purpose are the spanwise and streamwise periods normalized by the local layer thickness. Because the patterns vary from open and highly regular (Figure 10) to closed and nearly incoherent (Figure 11), it is not a simple matter to define a layer thickness consistently. The nearest available variable is the rake height, which was adjusted at each of the six stations to obtain a global unfiltered intermittency  $\langle \gamma \rangle$  close to 0.40 for the particular cam speed  $N = 800$ , and was left unchanged for other cam speeds. At each rake station, an experimental value was available for the derivative  $d\langle \gamma \rangle/dy$ , as a byproduct of the adjustment process just described. For each run, therefore, the rake height  $\Delta$  could be corrected to find a height corresponding to  $\langle \gamma \rangle = 0.40$  for any other cam speed. The correction to  $\Delta$  was appreciable only for the highest cam speeds and then only for the first one or two rake stations. On the basis of intermittency measurements by Klebanoff [16] in a tripped boundary layer, it is reasonable for synthetic flows with cam speeds which are not too low to make the tentative association  $\Delta = 0.8\delta$ , where  $\Delta$  is the probe height at which  $\langle \gamma \rangle = 0.40$  and  $\delta$  is the boundary-layer thickness according to some conventional definition.

The corrected data are displayed in Figure 12; this figure is the main product of the present research. The coordinates are proportional to the two basic scales, which are  $U_T$  in the streamwise direction and  $\zeta$  in the spanwise direction. Each of the 39 flows studied experimentally is represented by a straight line, with the local operating point moving downward and to the left as the pattern proceeds downstream and  $\Delta$  increases. Data for the three cams are denoted by three different symbols. The number attached to each flow trajectory is the value of the experimental parameter  $N$ , which by coincidence is very nearly the distance in mm travelled by the free stream during one camshaft revolution (two cycles of the disturbance pattern).

The solid symbols and the shaded area in the lower left part of Figure 12 define a region where there is substantial loss of coherence. It was first necessary to define a quantitative measure for dispersion in the intermittency maps in Figures 9-11 (and 36 similar figures). After some experimenting, the measure adopted was that a symbol in Figure 12 should be solid if the maximum value of the derivative  $|\partial \langle \gamma \rangle / \partial (z/\zeta)|$  in the corresponding map was less than unity. Roughly speaking, a larger value (near 2.5) already guarantees that full modulation between the limits 0 and 1 can no longer be expected for the surface  $\langle \gamma \rangle(z, t)$ .

Another shaded area in Figure 12 defines the region where transposition is observed to occur. This region was defined in part by a subjective classification of the intermittency maps. A more objective criterion, met by the flows represented by solid italic symbols, was that the number of distinct turbulent islands or eddies should be locally larger than the number originally generated upstream. The transposition region is shown extending indefinitely to the right, where the disturbance frequencies become very low. However, it is likely that the presence of laminar flow and the existence of a viscous length scale are decisive in this region, and this part of the figure should therefore not be taken very seriously. Note that near the center of the figure several flows pass through the transposition region and emerge as displaced but still coherent patterns, as already illustrated by the example in Figure 9.

The original synthetic flow studied by Coles and Barker [1] can be placed in Figure 12 once an estimate is made for the boundary-layer thickness. The flow apparently falls in the late transposition region, as indicated by the star at the point  $\zeta/\Delta = 3.8$ ,  $U_T/\Delta = 24$ . The present indication of transposition in this flow may account for the observation by Coles and Barker that the region of ensemble-averaged velocity defect passed the probe with its blunt end forward, rather than its narrow end.

It is now possible to reconsider the question of scales raised in the Introduction. The correlation measurements by Kovaszny et al. [9] revealed an average large eddy about  $1.2 \delta$  wide and  $2.5 \delta$  long at the half-intermittency level. Other investigators have used counting methods, measuring the frequency of various events which are believed to be related to the large-scale motion. For example, Kovaszny et al. [9] counted interface crossings and found a maximum frequency  $u_\infty/f\delta$  of about 1.3 at the half-intermittency level. This value was later confirmed by Chen and Blackwelder [17], who used heat as a passive contaminant and counted temperature-interface crossings. Various results obtained from the position of zero crossings in time correlations have been summarized, with new data at higher Reynolds numbers, by Badri Narayanan and Marvin [18]. They recommend the value  $u_\infty\tau/\delta = 5$  to 6.

These experimental estimates of scale give values which are at variance with each other and are all appreciably smaller than the scales which characterize the coherent region in Figure 12. We now propose a conceptual estimate based on a return to the idea, discussed at some length in the Introduction, that the large eddy can be explicitly identified with the turbulent spot.

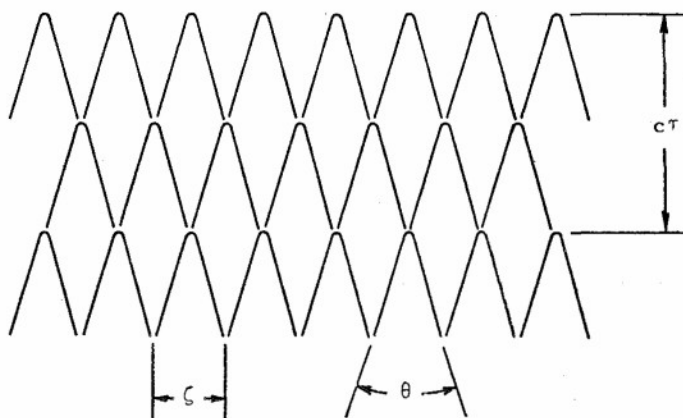
In dye photographs of spots (see Figure 4 of Cantwell et al. [5]), the vortex position is usually quite well defined by a strong concentration of dye. The included angle between the two legs of the vortex in a plan view is close to 40 degrees. The same angle can be inferred from the angle of the dye concentrations in the regions of transverse contamination, as well as from the aluminum photographs in the same paper. Consider therefore the hexagonal cross-hatched pattern shown in the sketch, in which the diagonal lines represent vortex cores aligned in a regular way. The geometry of the sketch implies  $\tan \theta/2 = \zeta/c\tau$ . For  $\theta = 40$  degrees and  $c = 0.88u_\infty$ , it follows that  $\zeta/u_\infty\tau = 0.32$ . This condition is shown in Figure 12 by the dashed line. For  $u_\infty = 1013$  cm/s and for  $\zeta = 12.2, 9.1$ , and  $6.1$  cm, the appropriate values for

$\tau$  are 0.038, 0.028, and 0.019 seconds. The corresponding flows show loss of coherence in Figure 12 at about  $\zeta/\Delta = 3.2$ ,  $U\tau/\Delta = 10$ . If  $\Delta/\delta = 0.8$ , therefore, the flow in the sketch should be marginally stable when

$$\frac{\zeta}{\delta} \approx 2.5, \quad \frac{u_{\infty}\tau}{\delta} \approx 8$$

Both values are close to the scales reported by Zilberman et al. [6] and Haritonidis et al. [7] for a spot immersed in a natural (i. e., tripped) turbulent boundary layer.

At this point, a combination of scales can be specified for constructing a synthetic boundary layer suitable for work on the signature problem discussed in the Introduction. To operate in a marginal state at a given station and a given speed, it is only necessary to know (or guess) the layer thickness. The required cam spacing and cam speed then follow from the numerical estimates just derived. Because the boundary of the loss-of-coherence region in the left center of Figure 12 has a negative slope, slightly different combinations of cam spacing and cam speed might also serve, within limits, as long as an increase in one is compensated by a decrease in the other.



What is missing from the measurements so far is any real information about the dispersion or loss of coherence which is observed to occur as the synthetic flows move downstream. It is reasonable to suppose that this loss of coherence is associated with an insupportable geometrical distortion of the three-dimensional large-eddy structure. As a synthetic flow develops in the coherent region, the spanwise and streamwise scales do not change, but the thickness increases almost linearly with time or distance. Eventually, a phenomenon like the vortex pairing or coalescence first observed in the plane mixing layer by Brown and Roshko [19] and Winant and Browand [20] must occur. To fix the ideas, suppose that eddies in the boundary layer normally coalesce in pairs, and coalesce rapidly enough so that the volume of turbulent fluid does not change (that the volume of turbulent fluid is almost constant during pairing in the mixing layer has been established by computer analysis of high-speed shadowgraph movies taken by L. Bernal in the Brown-Roshko apparatus at GALCIT; J. Jimenez, private communication). During the pairing process, the spanwise and streamwise scales must then increase by a factor  $\sqrt{2}$ , while the thickness remains unchanged. The main effect of the pairing process will therefore be to reduce the relative thickness of the large eddies, and the situation should remain stable until the thickness has again grown by a factor  $\sqrt{2}$ . This argument implies that the most comfortable synthetic eddy for a given combination of spanwise and streamwise scales is one for which the thickness  $\delta$  is about 20 percent less than the value at which loss of coherence becomes apparent in Figure 12. This conclusion should be taken into account in any selection of scales for a synthetic boundary layer, as should the likely proposition that coalescence might occur more naturally for vortex fours than for vortex pairs.

The present data have not yet been examined in detail on the question of eddy coalescence. Whatever the results may be, it is interesting to speculate about the properties of a hypothetical synthetic flow so perfectly constructed that loss of coherence is itself a deterministic process. What should happen, once the flow reaches the boundary of the shaded region in Figure 12, might facetiously be called planned coalescence. The trajectory should reverse direction and then resume its normal evolution with new scales. Since there is considerable design freedom in the method used for generating disturbances during the present research, such an experiment is probably within reach.

## REFERENCES

1. Coles, D. and Barker, S. J. Some remarks on a synthetic turbulent boundary layer. In "Turbulent Mixing in Nonreactive and Reactive Flows" (S. N. B. Murthy, ed.), Plenum, 1975, pp. 285-292.
2. Emmons, W. H. The laminar-turbulent transition in a boundary layer. Part I. 1951, J. Aeron. Sci. **18**, pp. 490-498.
3. Schubauer, G. B. and Klebanoff, P. S. Contributions on the mechanics of boundary-layer transition. 1955, NACA Tech. Note 3489; also NACA Tech. Rep. 1289, 1956.
4. Wygnanski, I., Sokolov, N., and Friedman, D. On the turbulent 'spot' in a boundary layer undergoing transition. 1976, J. Fluid Mech. **78**, pp. 785-819.
5. Cantwell, B., Coles, D., and Dimotakis, P. Structure and entrainment in the plane of symmetry of a turbulent spot. 1978, J. Fluid Mech. **87**, pp. 641-672.
6. Zilberman, M., Wygnanski, I., and Kaplan, R. E. Transitional boundary layer spot in a fully turbulent environment. 1977, Phys. Fluids **20**, No. 10, Part II, pp. S258-S271.
7. Haritonidis, J. H., Kaplan, R. E., and Wygnanski, I. Interaction of a turbulent spot with a turbulent boundary layer. In "Structure and Mechanisms of Turbulence I" (H. Fiedler, ed.), Lecture Notes in Physics No. 75, Springer-Verlag, 1977, pp. 234-247.

8. Wygnanski, I. On the possible relationship between the transition process and the large coherent structures in turbulent boundary layers. In "Coherent Structure of Turbulent Boundary Layers" (C.R. Smith and D.E. Abbott, eds.), AFOSR/Lehigh Workshop, 1978, pp. 168-193.
9. Kovasznay, L.S.G., Kibens, V., and Blackwelder, R.F. Large-scale motion in the intermittent region of a turbulent boundary layer. 1970, J. Fluid Mech. 41, pp. 283-325.
10. Blackwelder, R.F. and Kovasznay, L.S.G. Time scales and correlations in a turbulent boundary layer. 1972, Phys. Fluids 15, pp. 1545-1554.
11. Fulachier, L., Arzoumanian, E., and Dumas, R. Experimental investigation of a turbulent field from temperature fluctuations. In "Structure and Mechanisms of Turbulence II" (H. Fiedler, ed.), Lecture Notes in Physics No. 76, Springer-Verlag, 1977, pp. 46-57.
12. Praturi, A.K. and Brodkey, R.S. A stereoscopic visual study of coherent structures in turbulent shear flow. 1978, J. Fluid Mech. 89, pp. 251-272.
13. Savaş, Ö. Some measurements in synthetic turbulent boundary layers. 1979, Ph.D. Thesis, California Institute of Technology, Pasadena, California.
14. Elder, J.W. An experimental investigation of turbulent spots and breakdown to turbulence. 1960, J. Fluid Mech. 9, pp. 235-246.
15. Wygnanski, I., Haritonidis, J.H., and Kaplan, R.E. On a Tollmien-Schlichting wave packet produced by a turbulent spot. 1979 (Submitted to J. Fluid Mech.; see Wygnanski [8]).
16. Klebanoff, P.S. Characteristics of turbulence in a boundary layer with zero pressure gradient. 1954, NACA Tech. Note 3178; also NACA Tech. Rep. 1247, 1955.
17. Chen, C.-H.P. and Blackwelder, R.F. Large-scale motion in a turbulent boundary layer: a study using temperature contamination. 1978, J. Fluid Mech. 89, pp. 1-31.
18. Badri Narayanan, M.A. and Marvin, J.G. On the period of the coherent structure in boundary layers at large Reynolds numbers. In "Coherent Structure of Turbulent Boundary Layers" (C.R. Smith and D.E. Abbott, eds.), AFOSR/Lehigh Workshop, 1978, pp. 380-385.
19. Brown, G.L. and Roshko, A. On density effects and large structure in turbulent mixing layers. 1974, J. Fluid Mech. 64, pp. 775-816.
20. Winant, C.D. and Browand, F.K. Vortex pairing: the mechanism of turbulent mixing-layer growth at moderate Reynolds number. 1974, J. Fluid Mech. 63, pp. 237-255.

#### ACKNOWLEDGEMENTS

The research described in this paper was supported by the National Science Foundation under Grants ENG 75-03694 and ENG 77-23541. During the period from September, 1974 to September, 1978, the author was the recipient of a NATO Fellowship through the Scientific and Technical Research Council of Turkey. The author wishes to express his gratitude to his thesis advisor, Professor Donald Coles, for constant guidance and support throughout the research.

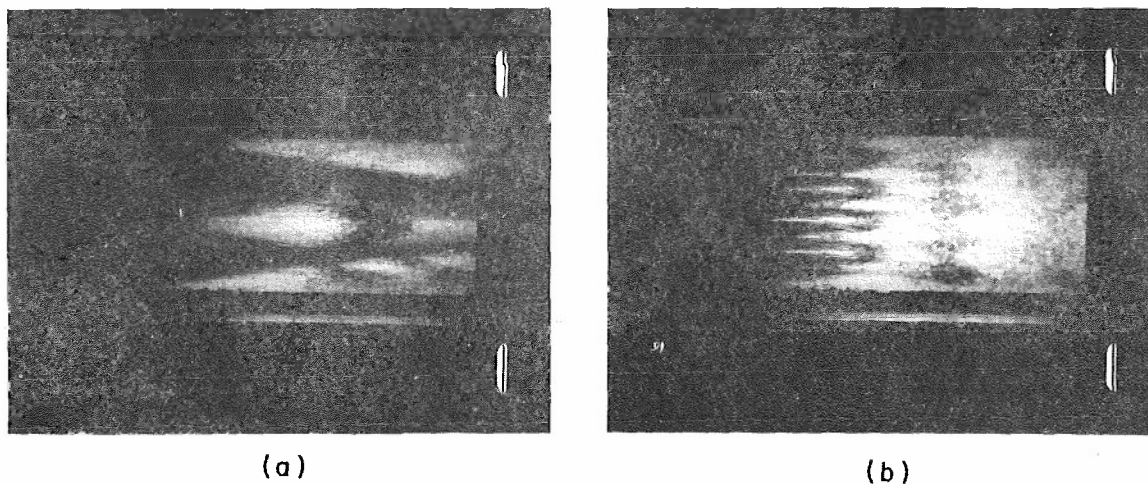


Figure 1. Dye visualization in water channel, from flow studies by Coles and Barker (Coles, private communication).

- (a) turbulent spot;  
(b) synthetic turbulent boundary layer.

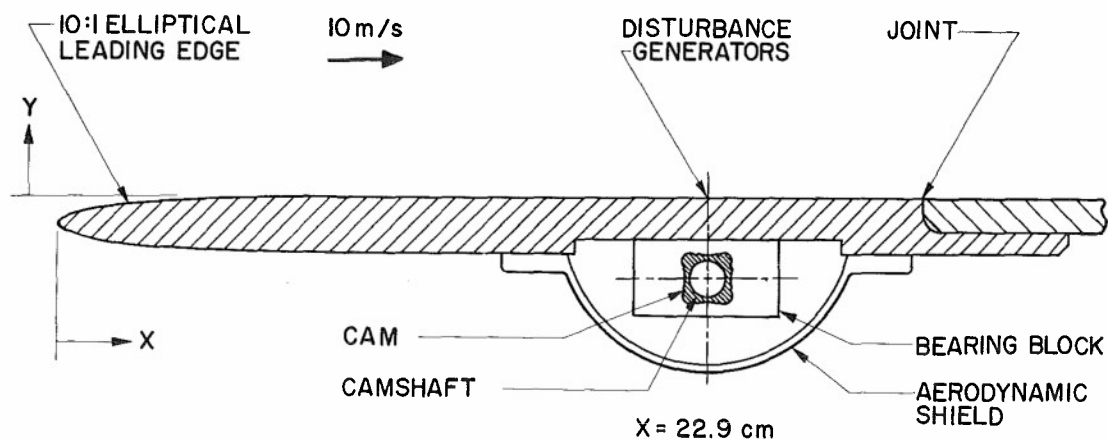


Figure 2. Detail of front section of plate, showing location of camshaft and windshield. Major and minor axes of ellipse are 19 cm and 1.9 cm.

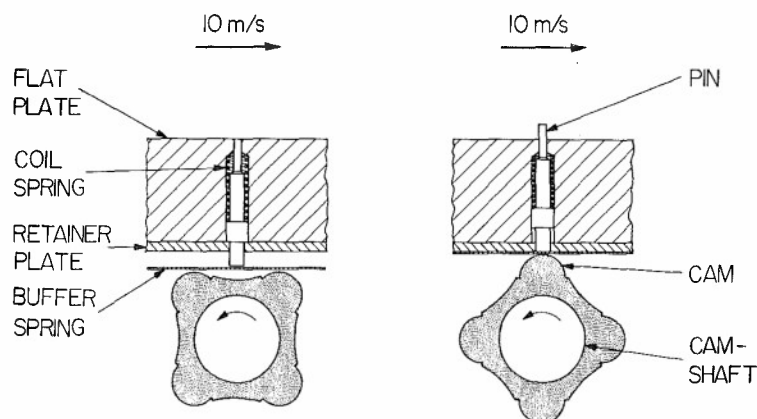


Figure 3. Detail of disturbance-generating mechanism. Left: pin retracted. Right: pin displaced into boundary layer.

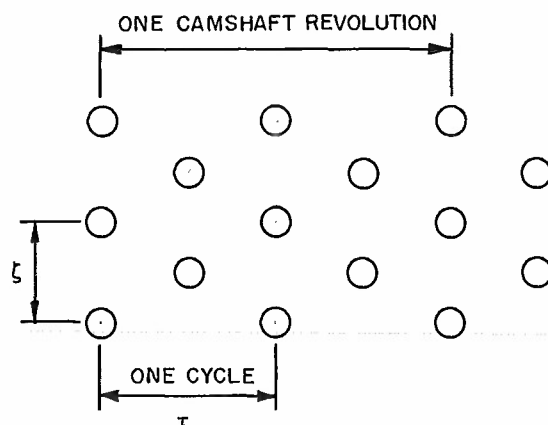


Figure 4. Close-packed hexagonal disturbance pattern in  $(z,t)$  plane. Periods  $\zeta$  and  $\tau$  in  $z$  and  $t$  directions are defined as shown.

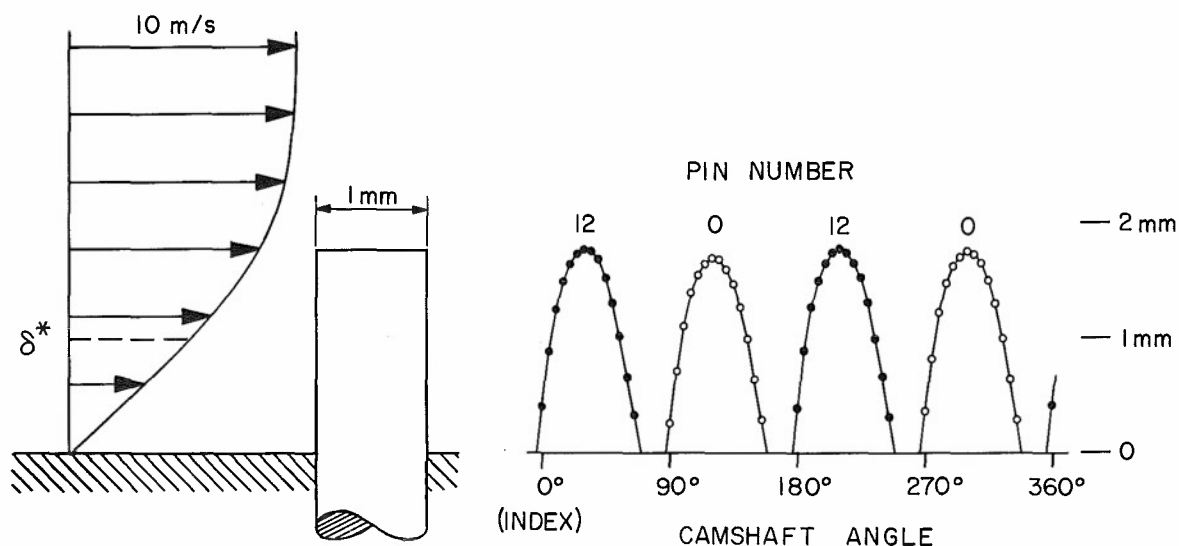


Figure 5. Pin displacement against camshaft angle for 12.2-cm cam. Open symbols: center pin. Solid symbols: pin at  $z = 6.1$  cm. At left, maximum pin displacement is compared with estimated profile in Blasius boundary layer at pin station ( $\delta^*$  is displacement thickness).

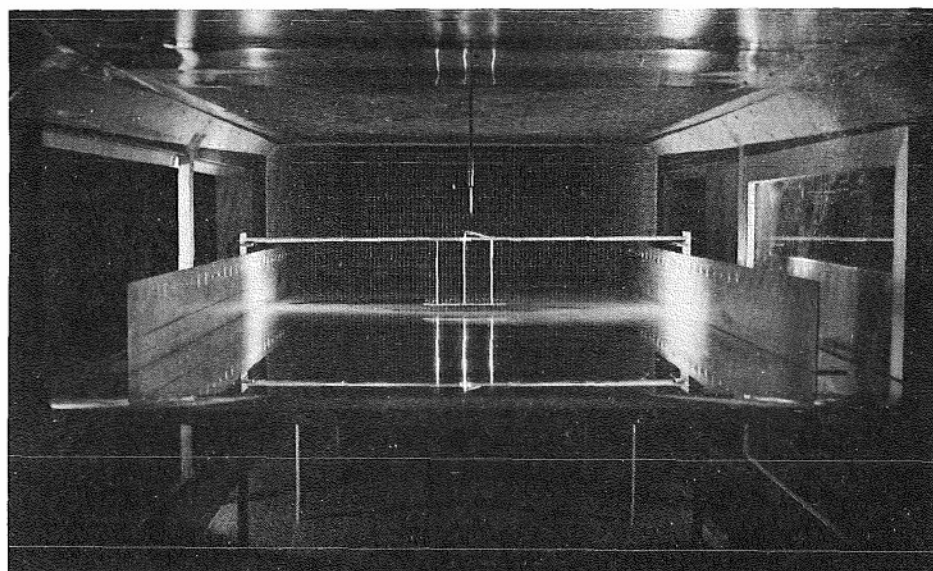


Figure 6. Photograph of model in tunnel, looking downstream. Note pitot-static probe in foreground, screen in background, and hot-wire rake supported from bridge structure attached to flow shields. Plate length is 264 cm. Plate width between shields is 97 cm.



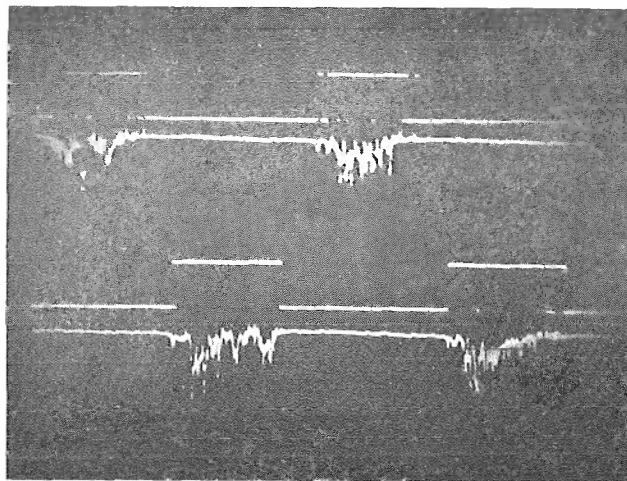


Figure 7. Examples of hot-wire analog outputs and associated intermittency signals in synthetic turbulent boundary layer. Flow is for 12.2-cm cam,  $N = 1991$ ,  $x = 56.9$  cm,  $y = 0.63$  cm. Oscilloscope is triggered at index pulse. Upper traces: hot-wire 13 ( $z = 0.38$  cm). Lower traces: hot-wire 21 ( $z = 6.48$  cm). One camshaft revolution is shown.

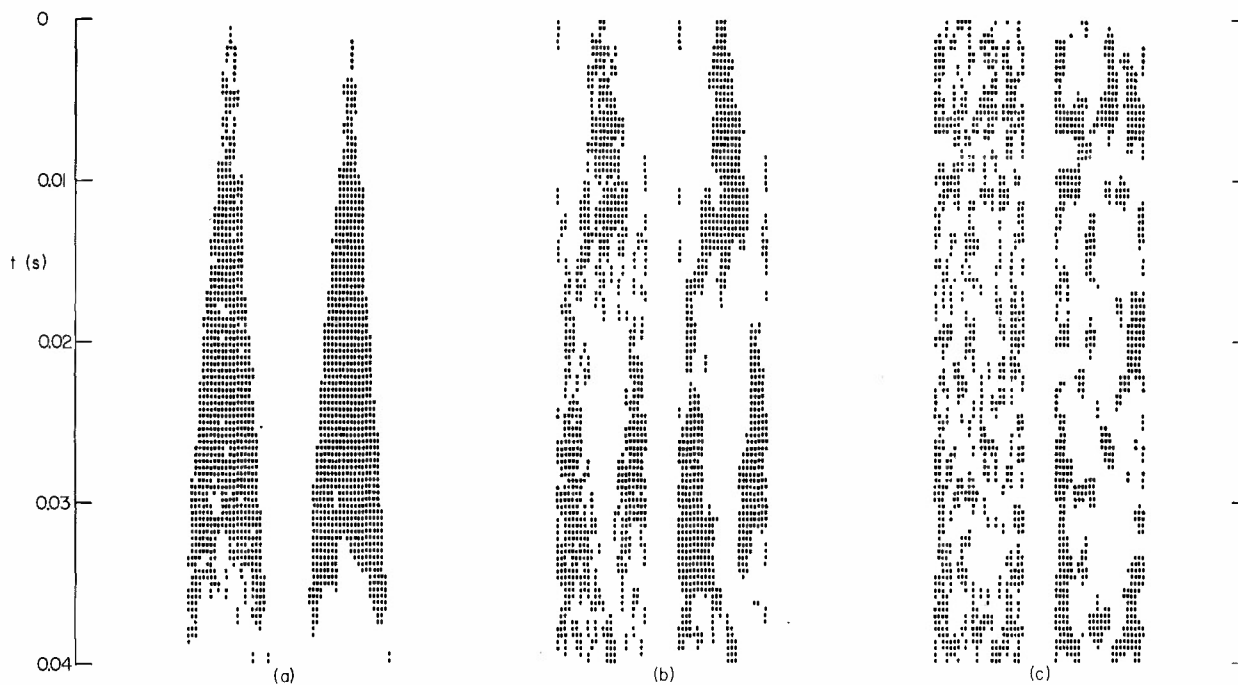


Figure 8. Typical unfiltered and filtered intermittency data for  $U = 10$  m/s,  $x = 87.3$  cm.

- (a) spot;  $y = 1.02$  cm,  $N = 800$  (Run 538);
- (b) synthetic boundary layer;  $y = 1.36$  cm, 12.2-cm cam,  $N = 800$  (Run 117);
- (c) tripped boundary layer;  $y = 1.70$  cm (Run 225).

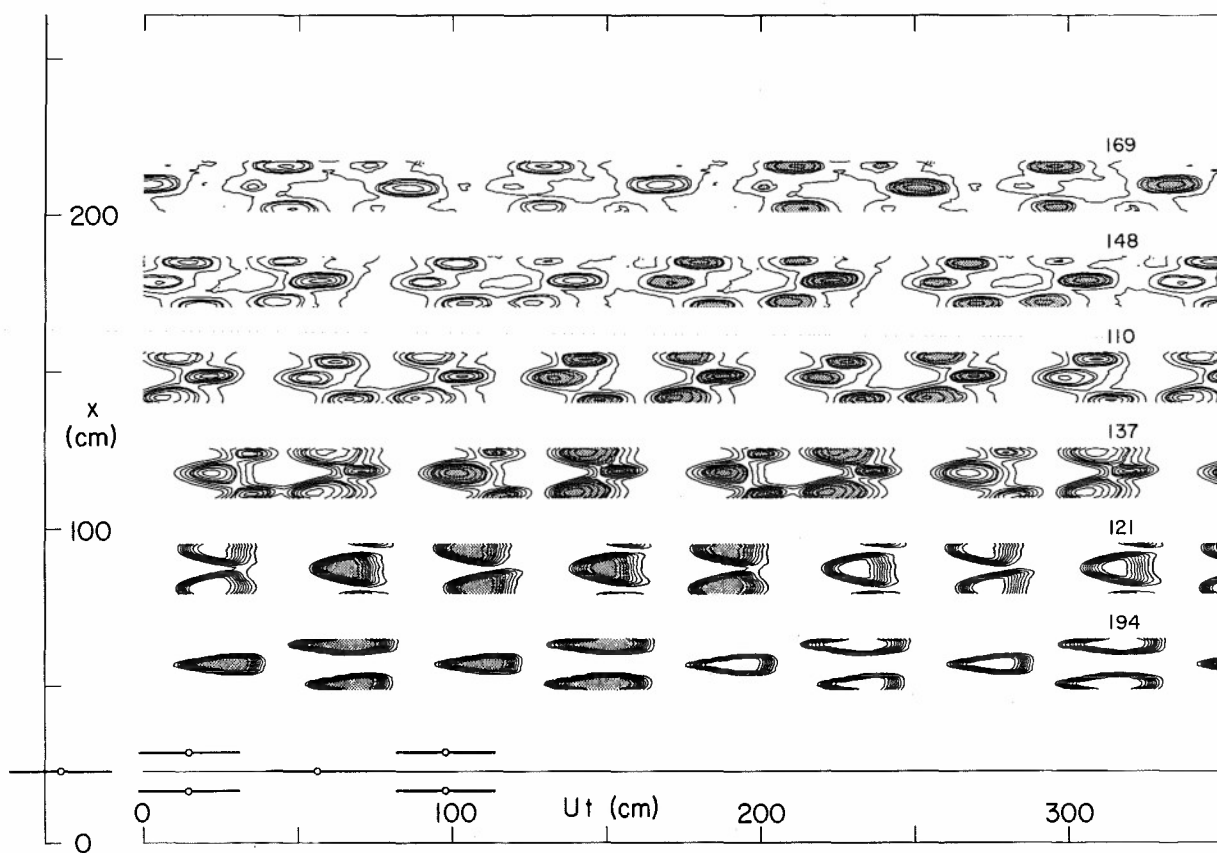


Figure 9. Synthetic turbulent boundary layer, 12.2-cm cam,  $N = 1659$  ( $\tau = 0.083$  s).

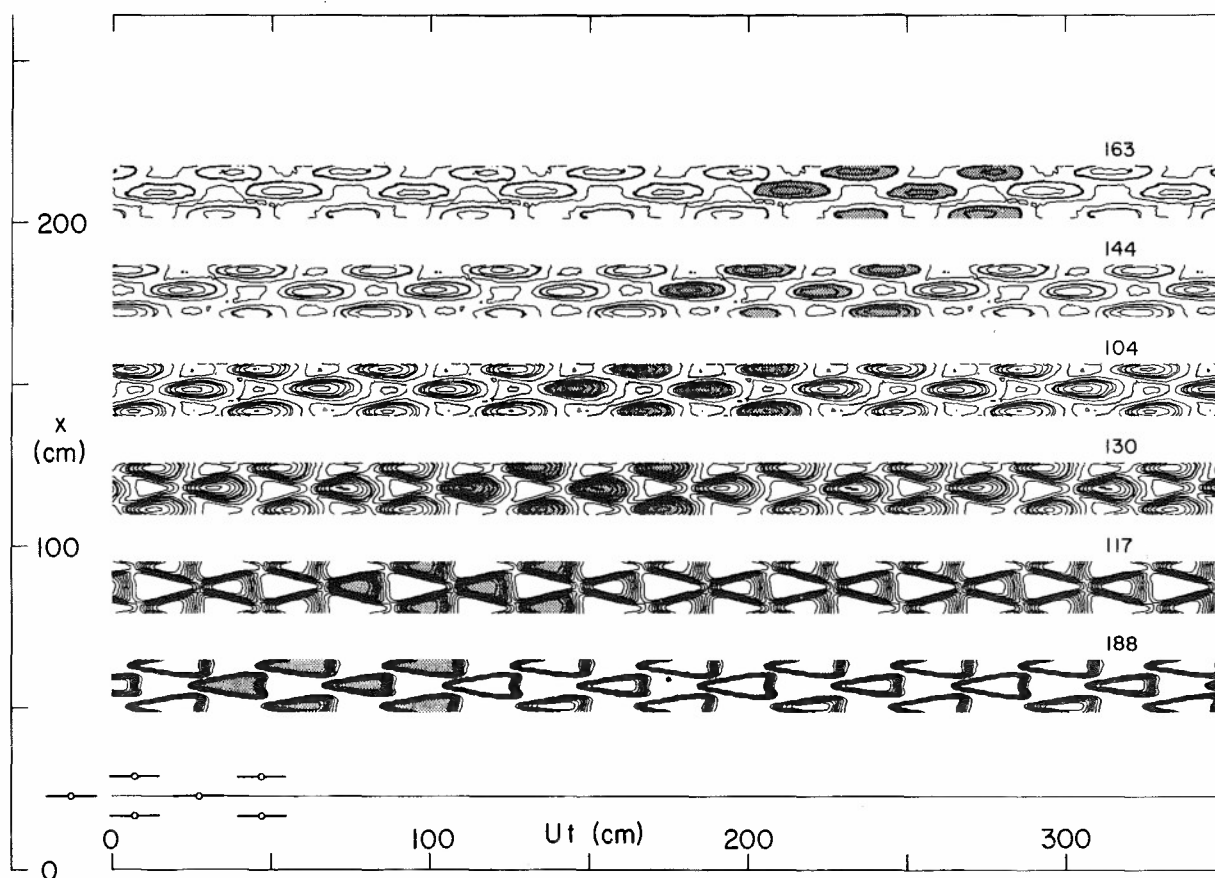


Figure 10. Synthetic turbulent boundary layer, 12.2-cm cam,  $N = 800$  ( $\tau = 0.040$  s).



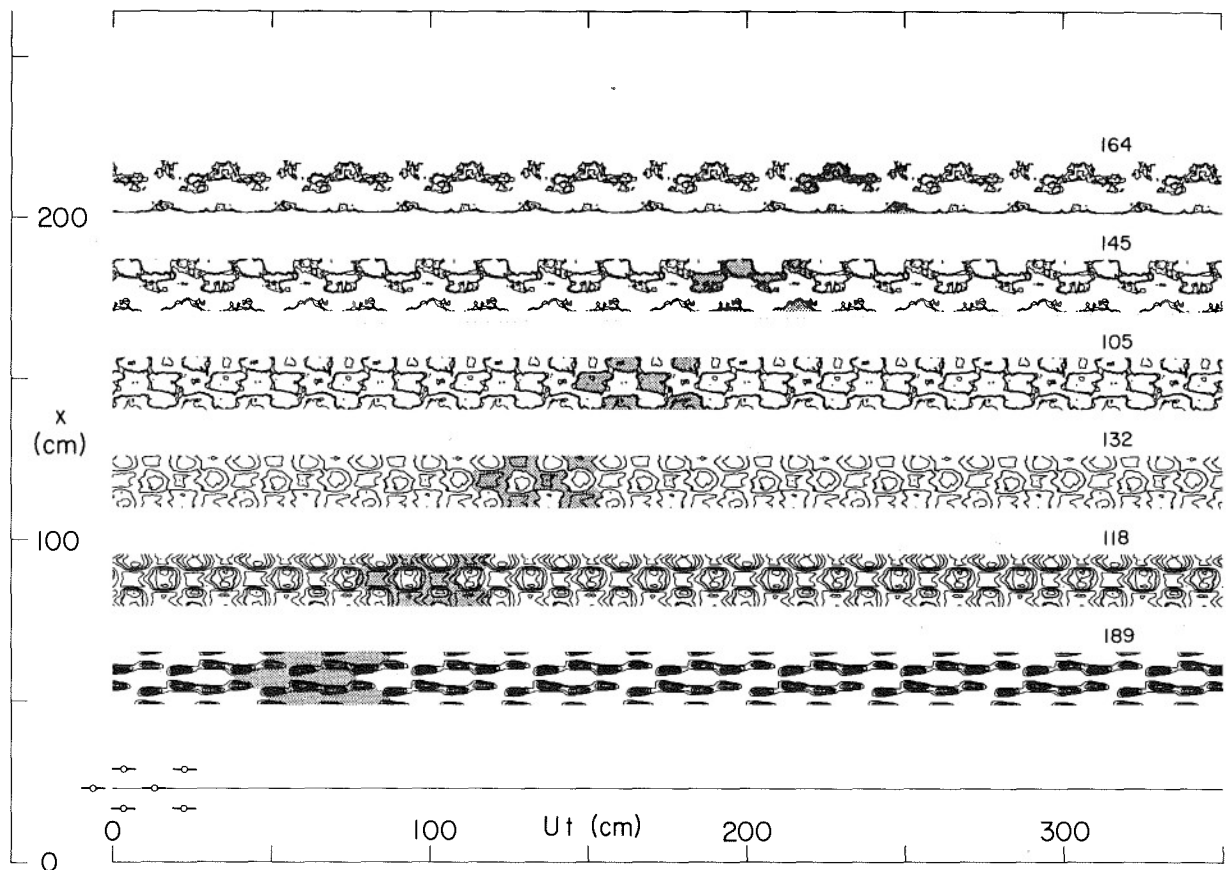


Figure 11. Synthetic turbulent boundary layer, 12.2-cm cam,  $N = 386$  ( $\tau = 0.019$  s).

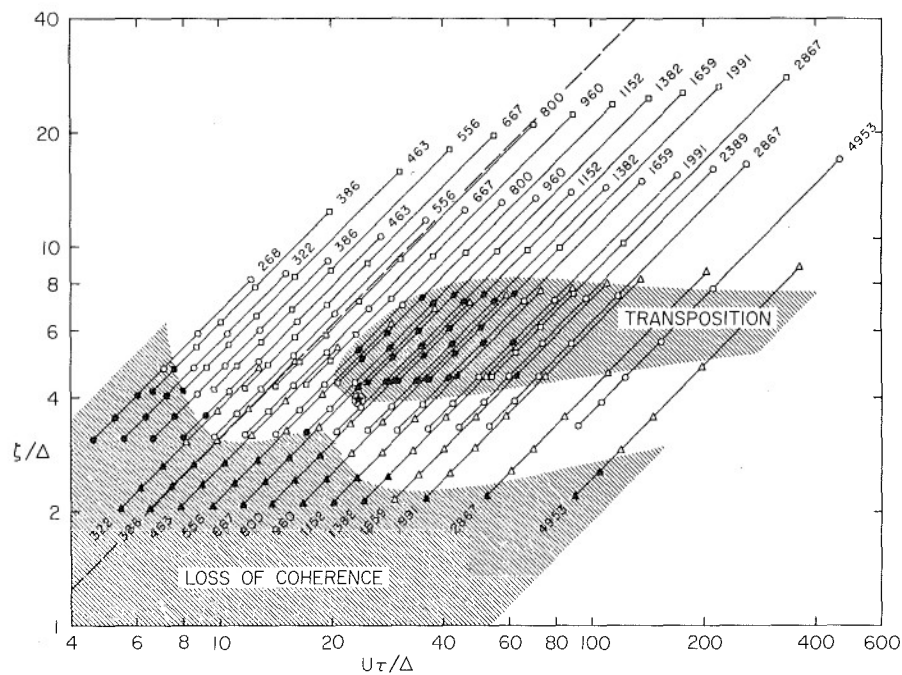


Figure 12. Coherence diagram for synthetic turbulent boundary layer. Open symbols: coherent pattern. Solid italic symbols: transposition. Solid symbols: disintegration or loss of coherence. Squares: 12.2-cm cam. Circles: 9.1-cm cam. Triangles: 6.1-cm cam. Dashed line:  $\zeta/u_{\infty}\tau = 0.32$ . Star: flow studied by Coles and Barker [1].

## COHERENT STRUCTURES IN TURBULENT BOUNDARY LAYERS

by  
R.F. Blackwelder  
Department of Aerospace Engineering  
University of Southern California  
Los Angeles, California 90007  
U.S.A.

## SUMMARY

The dynamics of turbulent boundary layers are controlled by two different eddy structures. In the intermittent region, the large scale outer structure dominates the flow field and controls the entrainment of nonturbulent fluid. Near the wall, counter-rotating streamwise vortices, with resulting elongated streaks of low speed fluid lying between them, are the predominate eddies. The interaction between these two different eddy structures seems to be the primary means by which turbulent energy is produced. The main features of these characteristic eddies are reviewed and some remaining problems are outlined.

## NOMENCLATURE

$P(\lambda_z^+)$	probability density of distance between streaks
$R_\theta$	Reynolds number based on free stream velocity and momentum thickness
$u, v, w$	velocity components in the streamwise normal and lateral directions
$U_\infty$	free stream velocity
$u_\tau$	friction velocity
$x, y, z$	coordinates in the streamwise, normal and lateral directions
$\delta$	boundary layer thickness
$\lambda_x, \lambda_z$	wavelengths in the streamwise and lateral directions
$\nu$	kinematic viscosity
$\theta$	momentum thickness
$\omega_x$	streamwise component of vorticity
$( )^+$	non-dimensional length normalized with respect to sublayer scale $\nu/u_\tau$

## 1. INTRODUCTION

A coherent eddy structure can be defined as a parcel of vortical fluid which occupies a confined spatial region and evolves in time such that a distinct phase relationship is maintained between the flow variables associated with the eddy's constituent components. Most vortices thus qualify as coherent eddies. One of the most frequently referenced eddy structures are the transverse vortices of the Karman vortex sheet behind a circular cylinder. The amplitude of the eddy structure may vary with time; for example the Karman vortices decay as they evolve downstream. On the other hand, if the eddies are the result of an instability, their strength may increase when followed downstream; e.g. Gortler vortices in a boundary layer on a concave wall. More importantly though, the phase relationship between the vorticity, velocity, etc. remains essentially constant independent of the amplitude. Indeed, the spatial phase relationship is the most recognizable characteristics of all eddies.

Coherent eddy structures are most readily identified in laminar flow because the eddies are usually periodic in space and/or time so that a regular pattern is observed throughout the entire field. The earlier definition is equally valid for defining coherent structures embedded in turbulent flow fields; however in this environment, they appear randomly in space and time. One of the most striking examples of this is the large eddy structure which dominates the free shear layer as shown by Brown and Roshko (1971) and Winant and Browand (1974). Since the eddies in turbulent flows are surrounded by background random fluctuations, they are much more difficult to identify, detect and study.

## 2. LARGE SCALE OUTER STRUCTURE

In the intermittent region of turbulent boundary layers, the large scale outer structure dominates the flow. Following Laufer (1975), their typical cross section is shown in Figure 1. These eddies scale with the boundary layer thickness,  $\delta$ , and the free stream velocity,  $U_\infty$ , and are responsible for the entrainment of the nonturbulent fluid into the boundary layer. They are separated from the irrotational fluid by a thin interface explored by Corrsin and Kistler (1955). With the advent of conditional sampling in the

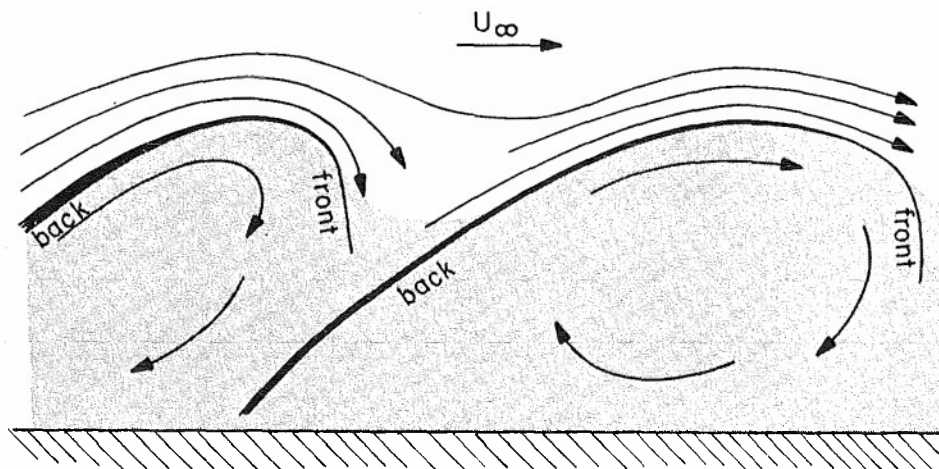


Figure 1. Sketch of the cross section of the large scale outer structure and the resulting flow field. The entrainment occurs on the back sides and/or deep in the valley between two structures. The turbulent region is denoted by the shaded area.

late 1960's, Kaplan and Laufer (1969) and Kovasznay et al. (1970) determined that these eddies had a velocity defect relative to their environment and contained a large scale vortical motion.

More detailed investigations, such as those of Antonia (1972), Falco (1977) and others, have studied the distribution of the fluctuation quantities within the large outer structures. Chen (1975) and Thomas (1977) used multiple probes to study the spatial extent of the coherent eddies. A synthesis of the existing data on the large scale outer structure clearly shows that the most active part of these eddies are the back sides, i.e., the upstream interface. Most of the entrainment occurs through this interface and/or deep in the valley between the eddies. The velocity gradients are sharper and have a greater magnitude across the upstream interface than those across the leading edge of the eddy. The small amount of turbulent production which occurs in the outer region is also concentrated near the upstream interface.

### 3. COHERENT STRUCTURE IN THE WALL REGION

Turbulent boundary layers also have another set of eddies near the wall which scale with  $u_\tau$  and  $v$ . The most readily identifiable eddy structures in this region are elongated streamwise streaks of low speed fluid. Hama (see Corrsin 1957) observed them by injecting dye at the wall; however, the first detailed study was by Kline et al. (1967) using hydrogen bubbles. They found that the bubbles coagulated into streaks which appeared randomly in space and time and moved more slowly than the surrounding fluid. Kim et al. (1971) found that the width of the streaks decreased with increasing distance from the wall

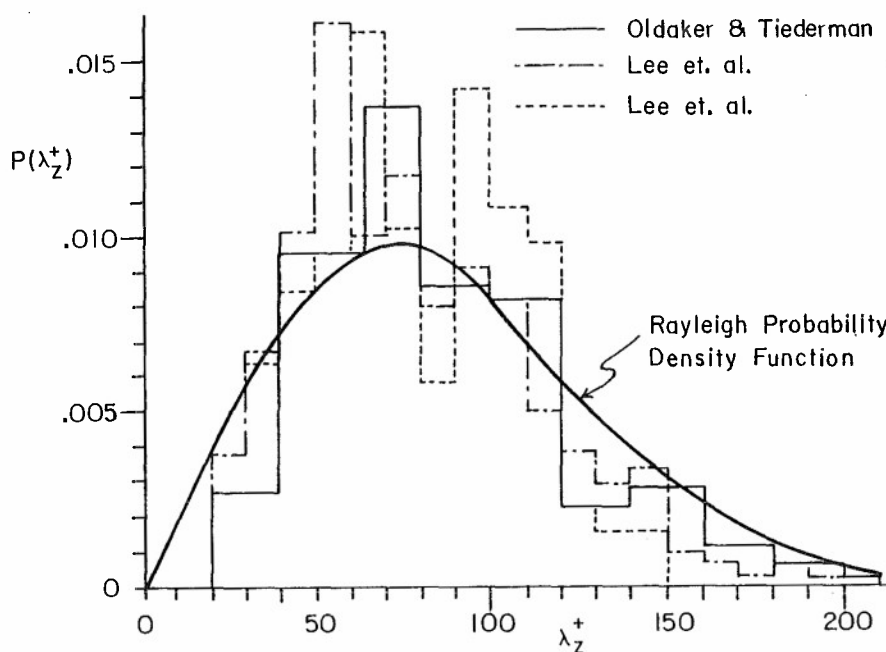


Figure 2. The probability density of the streak spacing in the wall region.

and was approximated  $10-30\nu/u_\tau$ . The probability density of the distance between the streaks was measured by Lee et al. (1974) and Oldaker and Tiedemann (1977). Their results are shown in Figure 2. The density is skewed and can be approximated by a Rayleigh probability density function. The average spanwise spacing is typically  $\lambda_z^+ = 100$ , however, the most probable spacing is significantly less. Short time correlations in the spanwise direction by Gupta et al. (1971) yielded similar results. The length of the streaks seen in the visualization studies are often greater than  $1000\nu/u_\tau$ . Space-time correlations of velocity signals obtained in the wall region by Gupta et al. (1971), Kreplin and Eckelmann (1979) and others yield similar length scales. The streaks meander slightly as they move downstream which degrades the correlations. Consequently the measured streamwise length scale is less than that observed visually.

Several authors have conjectured that the low speed streaks are the result of counter-rotating vortices in the wall region. No direct vorticity measurements of these eddies are presently available due to their small scale and the lack of a suitable sensor. However, several different investigators have measured the velocity components associated with these structures. Bakewell and Lumley (1967) used measurements of the streamwise velocity component in the wall region of a pipe flow together with an orthonormal decomposition of space-time correlations and deduced an eddy structure consistent with the  $\omega_x$  vortices. Blackwelder and Eckelmann (1979) measured the streamwise,  $u$ , and spanwise  $w$ , velocity components and used conditional averaging to study the vortex structures. Their detection probe, located at  $y^+ = 15$  and  $\Delta z^+ = 0$  in Figure 3a, essentially triggered on the abrupt ending of the low speed streaks and their sampling probe measured  $u$  and  $w$  at two  $\Delta z^+$  locations as shown. Two typical conditionally averaged  $\langle w(y^+, \Delta z^+) \rangle$  profiles are

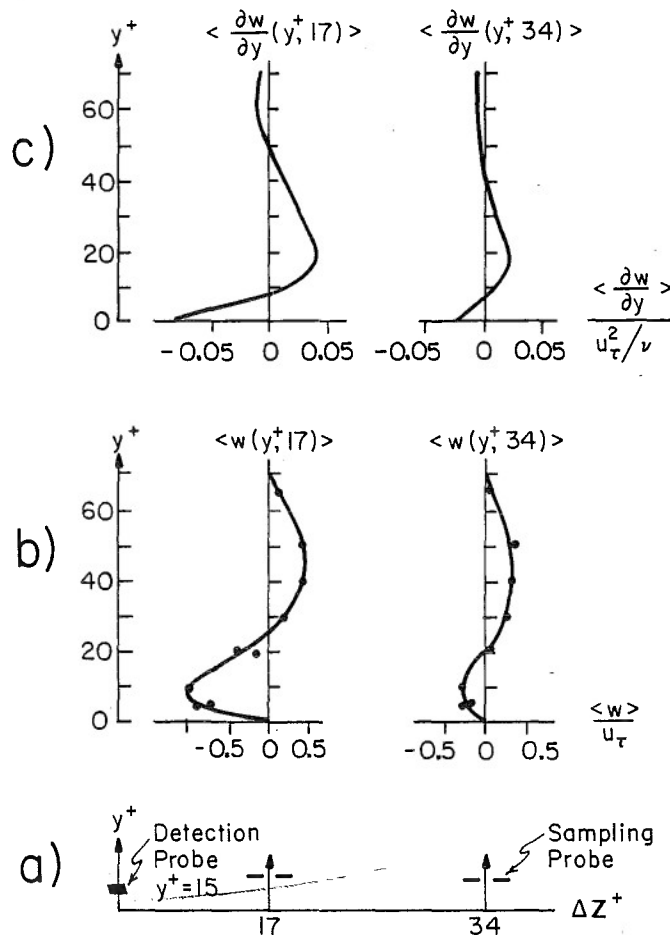


Figure 3. Conditionally averaged spanwise velocity profiles from Blackwelder and Eckelmann (1979). a) the detection probe was located at  $\Delta z^+ = 0$  and the sampling sensors were at  $\Delta z^+ = 17$  and  $34$ . b) Spanwise velocity profiles obtained at  $5\nu/u_\tau^2$  before the end of the low speed streaks were detected. c) spanwise gradient profiles obtained from 3b.

found in Figure 3b. These and other  $\langle w(y^+) \rangle$  profiles plotted by Blackwelder (1978) bear a striking resemblance to those attained by Klebanoff, et al. (1962), suggesting a similarity between the eddies in transition and turbulent boundary layers. The gradient of the spanwise velocity obtained from the curves in 3b is plotted in 3c. Coles' (1978) heuristic model for the vortices indicates  $|\partial v / \partial z| \ll |\partial w / \partial y|$ , so the gradients in Figure 3c are essentially equivalent to  $\omega_x$  vorticity. The vortices in Figure 3 extend up to  $y^+ \approx 50$ . Lee et al. (1974) indicates that the spanwise spacing between them is  $\lambda_z^+ / 2 \approx 50$ . Even though the vorticity in Figure 3 is primarily positive as expected, a

significant region near the wall is negative, illustrating the distinction between vorticity and vortices as discussed by Saffman and Baker (1979). Note that the streamwise vorticity is quite weak, i.e., an order of magnitude smaller than the spanwise vorticity at the wall,  $u^2_{\tau}/\nu$ . Nevertheless, since the vortices exist in a region of strong mean velocity gradient, they are very effective in moving high and low speed fluid toward and away from the wall respectively. As a result, they are instrumental in the subsequent dynamics.

The spatial relationship between the streaks and the streamwise vortices is sketched in Figure 4. The coordinate system in the figure is chosen to convect with the low speed streak and the streamwise scale is greatly compressed with respect to the other two axes.

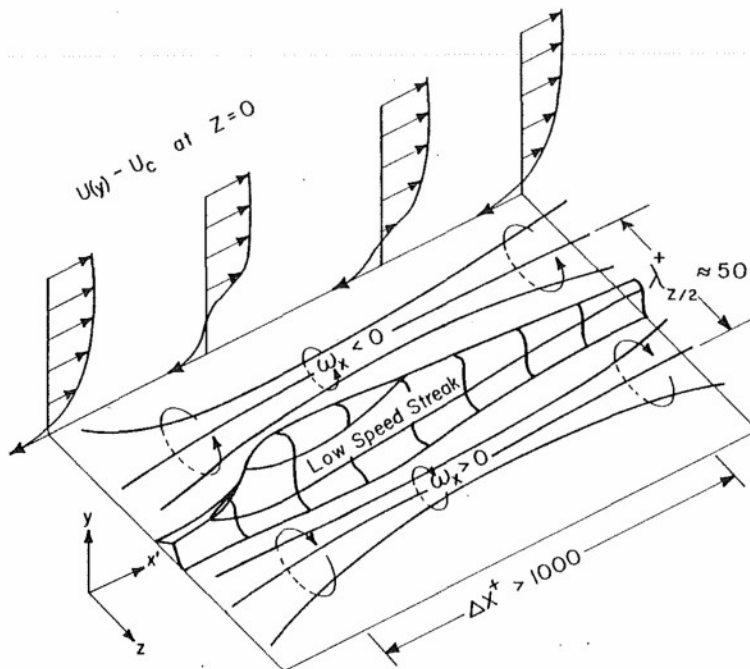


Figure 4. Model of the counter-rotating streamwise vortices which occur randomly in space and time. They remove low speed fluid from the wall into elongated low speed streaks. The conditionally averaged velocity profiles are from Blackwelder and Kaplan (1976).

As the vortices continue to add low momentum fluid to the streak, it grows in time. The vortices, represented by vortex lines, also bring higher momentum fluid toward the wall at  $z^+ = \pm 50$  resulting in a velocity profile there with greater stability.

#### 4. THE BURSTING PHENOMENON

The term "bursting" has been used by various authors to describe events which have small time scales and considerable mixing of fluid. It has been used to denote different aspects of the wall eddies and even the large scale outer structure. It is suggested that "bursting" is not a single event, but is rather a characteristic interaction between the eddy structures in the outer and wall regions. The relationship between these eddy structures was noted by Laufer and Badri Narayanan (1971) who observed that the frequency of occurrence of events in the wall region was approximately the same as the passage frequency of the large scale outer structure.

The bursting phenomenon has several features. Kline et al. (1967) and Kim et al. (1971) found that as the low speed streaks evolved downstream, they moved away from the wall and began to oscillate. These oscillations were observed in both the x-y and x-z planes and continued to grow until parts of the streak were violently flung outward into the logarithmic region. To observe the entire flow field, Corino and Brodkey (1969) used neutrally buoyant particles and observed that the wall region was randomly perturbed by large disturbances of high speed fluid called "sweeps" which entered their field of view from upstream. Parcels of low speed fluid were ejected from the wall region downstream of the sweep and were often overtaken by the higher momentum fluid. Using hot-wire anemometers, Blackwelder and Kaplan (1976) found that this interaction is most easily distinguishable by the sharp acceleration experienced when the low speed streak is displaced by the intruding high speed fluid. This characteristic acceleration has also been identified with the bursting phenomenon by Wallace et al. (1977), Brown and Thomas (1978) and others using different techniques. The acceleration is associated with an inflexional velocity profile as sketched in Figure 4.

To further explore the relationship between the bursting phenomenon and the large scale outer structure, Chen and Blackwelder (1978) slightly heated the entire wall beneath the turbulent boundary layer. They found a distinct temperature front existed throughout

the entire boundary layer from the wall to the outermost region. At each position above the wall, the temperature on the upstream side of the front was characteristically warmer than the average and that on the downstream side was cooler. In the outer region, the fronts were coincident with the backs of the large scale structures and near the wall it was related to the strong acceleration. A lower streamwise velocity existed downstream of the front and a higher velocity upstream, suggesting that it is the leading edge of the sweep found in the wall region. Nychas et al. (1973) observed a similar shear layer associated with large vortical structures in the outer region and also suggested it was related to the ejections of low speed fluid in the wall region.

The inflexional velocity profile in the wall region suggests that an instability mechanism may be related to the subsequent events. Using the results from a quasi-steady two-dimensional shear layer stability analysis, Blackwelder (1978) observed that the instability would manifest itself in an oscillation having a streamwise wavelength of  $\lambda_x^+ \approx 150$ . This compares favorably with the observed oscillations from several investigators listed in Table 1.

	$R_\theta$	$\lambda_x^+$
Blackwelder and Kaplan	2550	200
Emmerling	1800	200
Kim, et al.	660	175
Oldaker and Tiederman*	500	120
Blackwelder and Eckelmann	400	160

TABLE 1

As discussed earlier, the experimental evidence reveals that shortly after the onset of the observed oscillations, parcels of fluid are violently ejected from the wall region. Corino and Brodkey (1969) found that the ejections were narrow in the spanwise extent, i.e.  $\Delta z^+ < 20$ . Other evidence also implies that the spanwise extent of the suggested instability is small compared to its wavelength, as found by Klebanoff et al. (1962) in the "spike" formation in a transitioning boundary layer. If the observed oscillations do indeed result from an instability, one could further speculate that the ejection of low speed fluid into the logarithmic region is a result of the nonlinear and/or three dimensional aspects of that mechanism.

The visualization and probe data find the ejections are quite violent and hence should have a strong pressure field. Emmerling (1973) found strong wave-like pressure patterns impressed upon the wall and convected downstream at velocities typical of those in the buffer and logarithmic regions. These pressure disturbances had a wavelength of  $\lambda_x^+ = 200$  and were nominally  $\Delta z^+ < 50$  in spanwise extent suggesting that they were related to the ejection process.

Although a measureable Reynolds stress exists throughout the entire boundary layer, Klebanoff (1954) has shown that most all of the turbulent energy production occurs at  $y^+ < 50$ . Several aspects of the eddies contribute to this. The streamwise vortices obviously transport momentum by moving lower momentum fluid away from the wall and high speed fluid toward the wall. However, Willmarth and Lu (1972), Lu and Willmarth (1973), and others have found that the strong ejection of low speed fluid away from the wall and the following sweep of high momentum fluid toward the wall provide the largest contribution to the uv signal.

## 5. REMAINING PROBLEMS

Several aspects of the coherent eddies in boundary layers need further investigation. One of the foremost problems is the need for an adequate explanation of the formation of streamwise vortices in the wall region. Understanding this aspect of the bursting phenomenon is especially important for modelling the flow field and attempting to control it. Brown and Thomas (1977) and Coles (1978) have suggested that the  $\omega_x$  vortices are the result of a Taylor-Gortler-instability due to centrifugal forces imposed by the outer structure. It is not difficult to show that the velocity fluctuation easily yield instantaneous values of the Gortler parameter large enough to trigger that instability. Even conservative estimates of the average motion of the fluid implies it may be unstable. For example, the maximum maximum of the correlation curves near the wall from Favre et al. (1958) give a radius of curvature of 80 $\delta$ . Using the sublayer thickness as a length scale yields an unstable Gortler number and a wavelength of  $\lambda_z^+ \approx 150$ . However, the unsteady flow field near the wall hardly satisfies the steady state stability analysis of Gortler and Taylor for flows homogeneous in the streamwise direction.

The low speed fluid ejected from the wall region causes considerable mixing and production of turbulent energy. However it is not clear what happens to this fluid after it leaves the buffer layer. Kovaszny (1970) and others have suggested that this fluid may pass through the logarithmic layer and grow to ultimately form a new large scale outer structure. Falco (1977) observed eddies with a scale of  $100\nu/u_\tau$  moving outward along the backs of the large outer structure suggesting that they may have originated as an ejection.

\*Obtained from their accompanying 8mm movie film.

Support for this idea is also obtained from the triple correlations of temperature measured by Fulachier et al. (1974) on a heated wall. Although further study of this problem is imperative, it may require new data processing techniques, possibly combining Eulerian and Lagrangian data.

The frequency of occurrence of the bursting phenomenon is difficult to measure and the various techniques used to study it have found a large variation in its value. Black (1966) originally suggested that it should scale with the wall parameters. Using a crude detection scheme; Narahari Rao et al. (1971), found that when scaled with the outer variables, the frequency was independent of Reynolds number. One of their critical data points, obtained from Willmarth and Wooldridge (1962), was later shown to be incorrect by Lu and Willmarth (1973). Other evidence suggests that the frequency depends upon either the Reynolds number or, in the Eulerian measurements, possibly upon the spatial scale of the detection probe.

Most all of the experimental data have been accumulated at low Reynolds number. It remains to be seen if the dynamics change as the ratio of scales between the outer and inner structure, i.e.  $\delta u_T/v$ , increases. Zakkay et al. (1978) have explored the boundary layer structure at  $Re = 10^5$  and find that the dynamical layer associated with the backs of the outer structure is similar to those studied at lower Reynolds numbers; however because of the small scales, they were not able to make measurements in the wall region.

#### REFERENCES

- Antonia, R.A. J. Fluid Mech., Vol. 56, 1972, p.1.
- Bakewell, H.P. and Lumley, J.L. Phys. Fluids, Vol. 10, 1967, p. 1880.
- Black, T.J. Proc. Heat Trans. and Fluid Mech., Inst., Stanford Univ. Press, 1966, p. 336.
- Blackwelder, R.F. Coherent Structure of Turbulent Boundary Layers. Ed., D. Abbott and C. Smith, Lehigh University, 1979, p. 211.
- Blackwelder, R.F. and Eckelmann, H. J. Fluid Mech., Vol. 94, 1979, p. 577.
- Blackwelder, R.F. and Kaplan, R.E. J. Fluid Mech., Vol. 76, 1976, p. 89.
- Brown, G. and Roshko, A. AGARD CP93, 23:1, 1971.
- Brown, G.L. and Thomas, A.S.W. Phys. Fluids, Vol. 20, S243, 1977.
- Chen, C.H.P.: The Large Scale Motion in Turbulent Boundary Layer: A Study Using Temperature Contamination. Ph.D Thesis, University of Southern California, Los Angeles, California, 1975.
- Chen, C.H.P. and Blackwelder, R.F. J. Fluid Mech., Vol. 89, 1978, p.1.
- Coles, D.: Coherent Structures of Turbulent Boundary Layers. Ed., D. Abbott and C. Smith, Lehigh University, 1978, p. 462.
- Corino, E.R. and Brodkey, R.S. J. Fluid Mech., Vol. 37, 1969, p. 1.
- Corrsin, S. Symp. on Naval Hydrodyn, Publ. 515, NAS-NRC 373, 1957.
- Corrsin, S. and Kistler, A.L. NACA Report 1244, 1955.
- Emmerling, R.: Die momentane Struktur des Wanddruckes einer turbulenten Grenzschichtströmung. Mitt. MPI Strömungsforsch U. Aerodyn. Versuchsanst., Göttingen, no. 56, 1973.
- Falco, R.E. Phys. Fluids, Vol. 20, S124, 1977.
- Favre, A.J., Gaviglio, J.J. and Dumas, R. J. Fluid Mech., Vol. 3, 1958, p. 344.
- Fulachier, L., Giovanangeli, J.P., Dumas, R., Kovasznay, L.S.G. and Favre, A. C.R. Acad. Sci., Vol. 278, 1974, pp. 683 and 999.
- Gupta, A.K., Laufer, J. and Kaplan, R.E. J. Fluid Mech., Vol. 50, 1971, p. 493.
- Kaplan, R.E. and Laufer, J. Proc. IUTAM, Cong., Stanford, Springer, 1969, p. 236.
- Kim, H.T., Kline, S.J. and Reynolds, W.C. J. Fluid Mech., Vol. 50, 1971, p. 133.
- Kline, S.J., Reynolds, W.C., Schraub, F.A. and Runstadler, P.W. J. Fluid Mech., Vol. 30, 1967, p. 741.
- Klebanoff, P.S. NACA T.N.3178, 1954.
- Klebanoff, P.S., Tidstrom, K.D. and Sargent, L.M. J. Fluid Mech., Vol. 12, 1962, p.1.

- Kovasznyai, L.S.G.K. Ann. Review Fluid Mech., Ed., M. Van Dyke and W. Vincenti, Vol. 2, 1970, p. 95.
- Kovasznyai, L.S.G., Kibens, V. and Blackwelder, R.F. J. Fluid Mech., Vol. 41, 1970, p. 283.
- Kreplin, H.-P. and Eckelmann, H., to appear, 1979.
- Laufer, J. Ann. Reviews Fluid Mech., Vol. 7, 1975, p. 307.
- Laufer, J. and Badri Narayanan, M.A. Phys. Fluids, Vol. 14, 1971, p. 182.
- Lee, M.K., Eckelman, L.D. and Hanratty, T.J. J. Fluid Mech., Vol. 66, 1974, p. 17.
- Lu, S.S. and Willmarth, W.W. J. Fluid Mech., Vol. 60, 1973, p. 481.
- Narahari Rao, K., Narasimha, R. and Badri Narayanan, M.A. J. Fluid Mech., Vol. 54, 1971, p. 39.
- Nychas, S.G., Hershey, H.C. and Brodkey, R.S. J. Fluid Mech., Vol. 61, 1973, p. 513.
- Oldaker, K.D. and Tiederman, W.G. Phys. Fluids, Vol. 20, S133, 1977.
- Saffman, P.G. and Baker, G.R. Ann. Reviews Fluid Mech., Vol. 11, 1979, p. 95.
- Thomas, A.S.W.: Organized Structures in the Turbulent Boundary Layer. Ph.D. Thesis, U. of Adelaide, Adelaide, So. Australia, 1977.
- Wallace, J.M., Brodkey, R.S. and Eckelmann, H. J. Fluid Mech., Vol. 83, 1977, p. 673.
- Willmarth, W.W. and Lu, S.S. J. Fluid Mech., Vol. 55, 1972, p. 65.
- Willmarth, W.W. and Wooldridge, C.E. J. Fluid Mech., Vol. 11, 1962, p. 187.
- Winnant, C. and Browand, F.K. J. Fluid Mech., Vol. 63, 1974, p. 237.
- Zakkay, V., Barra, V. and Wang, C.R. AIAA Journal, Vol. 17, 1978, p. 356.

#### ACKNOWLEDGMENT

The continuing interest and critical discussions with Professor J. Laufer are gratefully acknowledged. This research was supported by the U.S. Army Research Office - Durham under Grant DA-ARO-DAAG29-76-G-0297.



## FLOW VISUALISATION OF TURBULENT BOUNDARY LAYER STRUCTURE

by  
M.R. Head and P. Bandyopadhyay  
Cambridge University Engineering Department  
Trumpington Street  
Cambridge CB2 1PZ  
England

## SUMMARY

Flow visualisation experiments have been performed using an argon-ion laser to illuminate longitudinal and transverse sections of the smoke-filled boundary layer in zero pressure gradient. Most of the experiments have been confined to the range  $600 < Re_\theta < 10,000$ .

The main finding of the investigation is that the boundary layer consists almost exclusively of vortex loops or hairpins, some of which may extend through the complete boundary layer thickness and all of which are inclined at a more or less constant characteristic angle of approximately  $45^\circ$  to the wall.

Since the cross-stream dimensions of the hairpins appear to scale roughly with the wall variables  $U_\tau$  and  $\nu$ , while their length is limited only by the boundary layer thickness, there are very large scale effects on the turbulence structure. At high Reynolds numbers ( $Re_\theta \approx 10,000$ ) there is little evidence of large-scale coherent motions, other than a slow overturning of random agglomerations of the hairpins just mentioned.

## 1. INTRODUCTION

Considering the effort that has gone into the use of hot wires for exploring turbulent boundary layer structure, it is somewhat disappointing that no final picture has emerged which describes in a physically satisfying way the basic structure of the layer and the way in which it is affected by Reynolds number.

Certainly the simple physical concepts and dimensional reasoning that were originally responsible for much of our practically useful knowledge of the boundary layer (law of the wall, velocity defect law etc.) did little to suggest that the boundary layer should consist of more than an assemblage of purely random motions, with scales that are simply related to distance from the wall or position in the boundary layer. Later work, by Townsend and others, has done much to refine these ideas and put them on a sounder basis, but the concept of at least the smaller scales of turbulence as purely random motions is retained.

The generally accepted view of turbulent boundary layer structure may perhaps be described briefly as follows. The boundary layer at reasonably high Reynolds numbers consists of two regions: first, an inner region in which turbulence production and dissipation are both large and of similar magnitudes, so that this part of the flow can be considered in a state of approximate energy equilibrium; second, an outer region where the turbulence is maintained by the relatively small excess of turbulence energy produced in the inner region, convected through the layer by large-scale motions, or large eddies. These latter, which occur on scales comparable with the boundary layer thickness are responsible for the contortions of the outer interface of the turbulent flow and the phenomenon of intermittency. Most of the turbulence energy is contained in motions that are small compared with the large eddies but still sufficiently large to be substantially unaffected by the direct effects of viscosity. There is a continuous flow of turbulence energy from larger to smaller scales, with the energy spectrum, possibly over only a very small part of its range, following Kolmogoroff's  $-3/3$  law. It is against this background of general understanding that experimental work may be said to have proceeded.

During recent years, Falco<sup>1</sup> has identified certain small-scale motions (which he terms "typical eddies") with the Taylor microscale of turbulence, and has explored their properties in detail using a combination of flow visualisation and hot-wire anemometry. He has shown that these typical eddies represent concentrations of high shear stress and has further identified them with the "bursts" of high shear stress measured in the outer part of the layer by Antonia<sup>2</sup>.

Over a rather longer period, the flow in the immediate wall region has been extensively explored by Kline and others (see, for example, the review article by Kline<sup>3</sup>) and successive events have been observed which are characterised as "bursts" and "sweeps", occurring alternately, and both contributing to the high levels of turbulent shear stress observed in the wall region. Willmarth<sup>4</sup> and Smith<sup>5</sup> suggest that the "burst" represents the lifting of a vortex loop from the wall, although it is not altogether clear whether the loop arises from pre-existing streamwise concentrations of vorticity in the sublayer or from the warping of transverse concentrations of vorticity, as Willmarth<sup>4</sup> suggests.

We have thus arrived at the situation where events in the wall region have been reasonably well documented and where concentrations of Reynolds shear stress in the outer

part of the layer have been identified with a particular type of vortex structure. What is required to fill in the outlines of the conventional picture is to establish the nature of the large-scale motions, the origin of Falco's typical eddies, and (hopefully) the mechanism connecting these with observed events in the wall region.

To a large extent, it is believed that the results presented here provide an answer to these outstanding problems, but at the cost of substantially redrawing the original picture, so that the concept of random turbulent motions, at least over the range of Reynolds numbers considered here, is largely replaced by one which involves a much more ordered structure of stretched vortex loops or hairpins arrayed at a characteristic angle to the wall. Of course a large measure of randomness is still present, but the turbulence in the layer can no longer be seen as the purely random motion of small parcels of fluid, and it now seems unnecessary to postulate the existence of large-scale eddies which convect the energetic small-scale motions from one part of the layer to another.

We shall first discuss the experiments that have led to the present conclusions and then look briefly at some of the implications. It will be recognised that the present picture has much in common with the earlier proposals of Theodorsen<sup>6</sup> and Black<sup>7</sup>, which will be referred to later.

Some of the earlier results have already been presented in References 8 and 9 and will not be described in detail here.

## 2. EXPERIMENTAL INVESTIGATION

### 2.1 Apparatus and Techniques

Experiments were performed in one or other of the tunnels shown in Figure 1, the adapted laboratory tunnel being used for values of  $Re_\theta$  greater than 2,200.

The boundary layer on the floor was filled with smoke injected either just upstream or just downstream of the trip. In the low-speed smoke tunnel this consisted simply of a serrated strip normal to the wall, with serrations 10 mm high, while in the laboratory tunnel it took the form of two staggered rows of spheres 2.5 mm in diameter at a spacing of 6 mm. In all cases transition occurred directly at the trip. Smoke, in the form of condensed oil vapour, was supplied by a C.F. Taylor Ltd. smoke generator.

The smoke-filled layer was illuminated by a plane of light formed by using a glass rod or bi-convex cylindrical lens to fan-out the beam from a 4W or 5W argon-ion laser (different lasers were used at different times).

Photography was performed using a 16 mm Fastax camera with Ilford Mk V film, and the photographs presented here are mainly enlargements of single frames from the cine films.

In the initial stages hot-wire measurements were made using two or three single wires in a staggered array or (for the first few experiments only) the combination of a crossed wire in the outer part of the layer and a single wire very close to the wall. Hot-wire signals were displayed on a storage oscilloscope in the field of view of the camera and also recorded on magnetic tape for subsequent digitisation and storage on floppy discs. To synchronise the film and the stored hot-wire signals a timing signal was used. This operated a counter in the field of view of the camera and was stored along with the hot-wire signals so that the number of waves could be counted during digitisation and checked against counter readings. Further information is given in the paper by Bandyopadhyay<sup>8</sup>.

### 2.2 Initial Experiments

Preliminary experiments were made with a single hot wire very close to the surface and a crossed wire vertically above it. From the crossed-wire signals, vectors could be plotted representing disturbance velocities, and these could be superimposed upon tracings of the instantaneous boundary layer edge as defined by the smoke. Thus, disturbance velocities associated with specific features could readily be seen. Part of a particular record is shown to a small scale in Figure 2. Perhaps the most obvious feature of this record is simply the occurrence of smoke-filled features and smoke-free fissures at a preferred angle of something like  $45^\circ$  to the surface. Inspection of the film itself suggests a similar result.

To check whether this angle was in fact significant, the hot wire next the wall was moved out to about 10 mm and the crossed wire was replaced by a second single wire staggered behind the first so that the line joining the two wires made an angle of approximately  $40^\circ$  to the surface.

With this arrangement a film was made with simultaneous hot-wire records for an  $Re_\theta$  of 2,200. As related by Bandyopadhyay<sup>8</sup>, the record showed up numerous patches about  $2.5\delta$  long where the two hot-wire signals were remarkably similar, and the suggestion was made that these represented the passage of extended arrays of vortices being convected downstream with their axes inclined at about  $40^\circ$  to the wall.

Various checks were applied to show that the similar patches were not simply due to the random coincidence of signals that covered much the same frequency range (see Head and Bandyopadhyay<sup>9</sup>).

Further evidence was then sought to support the hypothesis that the similar patches were due to arrays of hairpin vortices being convected past the hot wires. First, there was the evidence from an earlier film made for the 1969 Boeing Symposium on Turbulence that vortex loops were a common feature of the turbulent boundary layer at low Reynolds numbers (see, for example, Figure 3), and then there was the evidence from current films at higher Reynolds numbers where the longitudinal light plane showed up numerous instances of vortex loops that had been skewed into the plane of illumination (see, for example, Figure 4).

The tentative conclusion was reached at this stage that the turbulent boundary layer at all times consisted of extended vortex loops or hairpins; and that, occasionally, these were sufficiently regular and closely aligned to produce the observed similar patches in the hot-wire records.

Films taken at high Reynolds numbers (of the order of  $Re_\theta = 10,000$ ) showed no evidence of large-scale coherent motions beyond a slow toppling or overturning, and large-scale structures appeared (in most cases) simply as random arrays of very much narrower  $45^\circ$  features, as will be evident from Figure 5.

On the other hand coherent large-scale motions did appear at sufficiently low Reynolds numbers, and these are perhaps best shown by a sequence in the Boeing Symposium film where a thick smoke filament in the free stream was positioned so as to first impinge upon the boundary layer at some distance upstream of the point of observation. Thus, the frames reproduced in Figure 6 show the boundary layer after entrainment has proceeded for some appreciable time, and the details of the internal structure have become clearly visible. From this figure it seems quite plausible that, at this low Reynolds number ( $Re_\theta \approx 500$ ), the large-scale motions we see in the film are simply the result of photographing longitudinal sections of one or more vortex loops.

In fact we can account for the large differences in structure between high and low Reynolds number boundary layers if we simply assume that the vortex loops become progressively more elongated as the Reynolds number increases, somewhat as shown in Figure 7.

### 2.3 Experiments with Transverse Light Planes

With the evidence from the use of longitudinal light planes strongly suggesting the existence of vortex loops and hairpins arrayed at a characteristic angle to the surface, it seemed possible that more decisive evidence might be obtained from the use of transverse light planes inclined to the wall at something like the characteristic angle. After a delay of more than a year due to absence of a laser, experiments were resumed with this in mind, but it was in fact found that the most convincing evidence came from the use of light planes inclined at both  $45^\circ$  downstream (the characteristic angle) and  $45^\circ$  upstream. Figures 8 and 9 indicate the directions of the light planes and the views we might expect to see as inclined features are convected across them.

With light plane inclined downstream we should expect to see rapidly changing views of extended vortex loops, while with it inclined upstream we should expect to see numerous examples of vortex pairs, apparently in continuous motion towards the wall.

Further, if Figure 7 is anything like correct, we should expect to see the loops or hairpins becoming increasingly extended as the Reynolds number is increased.

With some allowance made for general randomness and the presence of a variety of scales, and for some mutual interaction between vortex pairs, this is in fact what the films actually showed.

Experiments were performed with both upstream and downstream inclinations of the light planes at three Reynolds numbers ( $Re_\theta = 600, 1,700$  and  $9,400$ ), and selected frames, which may be taken as quite reasonably representative, are shown in Figure 10 with approximate scales of  $100 \frac{v}{U_\tau}$  indicated.

Comparing the views with downstream and upstream inclinations of the light plane, we note that they exhibit characteristic differences at all three Reynolds numbers. With the  $45^\circ$  downstream inclination, the general appearance is that of continuous filaments with an overwhelming preponderance of extended loop-like structures. By contrast, the  $45^\circ$  upstream light plane shows the typically knotted type of structure we should expect, with cross sections of the loop-like structures or hairpins appearing as vortex pairs. In the outer part of the layer these may be isolated, but over a considerable distance from the surface they appear sufficiently close for some measure of interference or mutual induction to be inevitable. Both views show the presence of a variety of scales, with the upstream light plane also showing a variety of orientations of the vortex pairs where these can be distinguished.

Comparing the results for different Reynolds numbers we see that there is a consistent reduction in the scales of the hairpins with increasing  $Re_\theta$ . We also note that, at the two lower Reynolds numbers, the scales of the larger hairpins are also the dominant scales of the large-scale features, whereas at  $Re_\theta = 9,400$  the hairpins (which are now very narrow) appear to have combined to form much larger structures, although in the very outermost part of the layer they again appear as individual entities. It should be pointed out that the boundary layer on the wind tunnel floor at  $Re_\theta = 9,400$  was noticeably thicker on the centreline than on either side, and this is reflected in most frames of the cine film.

A result which shows up very clearly in the film for  $Re_\theta = 1,700$ , with the light plane inclined downstream, is the appearance of a smoke-filled "island" as the last trace of a particular feature as it passes the plane of illumination. All features that extend beyond the edge of the boundary layer, as determined from the measured mean velocity profile, disappear in this way, as well as a large number of features that do not extend quite so far. In no case have we observed the appearance of an island preceding the appearance of the remainder of the structure, and we must conclude that the tips of the hairpins are inclined forward into the flow. This has important implications, which we shall return to later (in section 4.4).

Velocity profiles and skin-friction coefficients were measured over the full range of Reynolds numbers but are not shown here.

Figure 10, and (much more convincingly, we believe) the films from which these frames were taken, seemed to provide the decisive evidence we were seeking for the basic validity of the hairpin-vortex hypothesis.

### 3. COMPARISON WITH OBSERVATIONS MADE ELSEWHERE

It is of interest to see how other authors' results fit in to the present picture.

First, it appears that the lateral dimensions of the hairpins is in the region of  $100 \frac{v}{U_\tau}$ , which is just the sort of spacing that has been observed for the sublayer streaks which are commonly accepted as representing the presence of longitudinal vortex pairs very close to the wall. (See, for example, Blackwelder<sup>10</sup>).

Already several authors have suggested (see, for example, Smith<sup>5</sup>) that bursts occurring in the wall region represent the lift-off of vortex loops from the wall, so the present results would seem in no way to contradict the extensive observations of Kline and others regarding the occurrence of bursts and sweeps in the immediate wall region.

Further out in the layer as already remarked, Falco<sup>1</sup> has identified vortical structures which he has termed "typical eddies". These are precisely the features one would expect to observe with a longitudinal light plane intersecting vortex loops or hairpins close to the plane of symmetry. Moreover, the present results would seem to provide an adequate explanation (which would otherwise be lacking) for the approximate scaling of these features with the wall variables  $v$  and  $U_\tau$ . In fact, the actual dimensions of the typical eddies as determined by Falco<sup>1</sup> ( $100 - 200 \frac{v}{U_\tau}$ ) are quite similar to the cross-stream dimensions of the hairpins, and there is at least the suggestion in the present results of a similar increase in these dimensions as  $Re_\theta$  is increased. As mentioned earlier, Falco<sup>1</sup> has identified his typical eddies with the bursts of high shear stress measured by Antonia<sup>2</sup> which he (Antonia) suggests originate in the wall region, and this result also would seem to fit into the present picture.

The observations of Chen and Blackwelder<sup>11</sup> where a vertical array of hot wires gave very nearly identical signals but with an increasing time shift with distance from the wall would seem to be in excellent accord with our suggestion of long narrow features originating close to the wall.

The results of Praturi and Brodkey<sup>12</sup>, which include sketches of both transverse vortex motions and vortex motions inclined to the wall, would seem to conform in all important respects to the present picture at a low Reynolds number.

Only one set of results, those of Brown and Thomas<sup>13</sup>, would seem seriously to conflict with the present observations. These authors showed that the highest correlations occurred along lines at  $18^\circ$  to the surface, whereas present results might suggest that the figure should be  $45^\circ$ . This, however, is not necessarily the case, and a regular sequence of hairpins with their tips lying along a line at a smaller angle to the wall will define an interface across which there must be a very substantial velocity jump, and along which changes in hot-wire signals will be very highly correlated. Such well defined interfaces are not a common feature of the present results but, where they do occur, it is very often at an angle which is similar to Brown and Thomas's value, in the vicinity of  $20^\circ$ . Figure 11 shows typical examples. Thus there may be no real conflict with present results.

In closing this section we must draw attention to the similarities between the present picture and the earlier proposals of Theodorsen<sup>6</sup> and Black<sup>7</sup>. The former clearly envisaged the key role played by horseshoe vortices in turbulence production and even predicted the  $45^\circ$  angle at which they should occur, while the latter equally clearly envisaged that the lateral dimensions and streamwise spacings of the horseshoes should be determined by the wall variables  $U_\tau$  and  $v$ , while their largest dimension should scale with the boundary layer thickness. Although their results have scarcely influenced the course of the present investigation, there can be no doubt concerning the remarkable degree of physical insight these authors have shown.

## 4. SOME IMPLICATIONS OF PRESENT RESULTS

### 4.1 General Remarks

Although in certain respects the present picture is radically different from the one that is generally accepted, it must nevertheless be compatible with hot-wire measurements that have been made in the past and with universal features of the layer that are well established (e.g. law of the wall, velocity defect law etc.) We have already seen that most of the more or less direct observations that have been made of boundary layer structure would seem to fit satisfactorily into the picture we propose, but that is very different from showing how this picture can account for all the observed features of the layer. To do so would obviously be a major task and all we can do here is to make some rather disconnected observations that may help to reconcile the present results with established concepts.

### 4.2 Inner Region

At high Reynolds numbers, it would seem likely that, in the wall region at least, a variety of scales should be present and a variety of orientations of vortex pairs, and that there may be considerable mutual interaction between adjacent hairpins. In these circumstances it would seem quite likely that, due to mutual entanglement and limited lifetimes, the majority of the hairpins should not survive into the outer region of the layer. Thus, there would seem to be nothing to contradict the idea that the flow in the inner region should be in a state of substantial energy equilibrium, with turbulence production and dissipation both very high and with all quantities scaling with  $U_\tau$  and  $v$ .

### 4.3 Hairpin Growth

There would seem to be three possible (perhaps complementary) mechanisms by which a hairpin vortex may grow. First, by simple stretching, with the hairpin axis coinciding, at least approximately, with the direction of maximum strain; second, by each limb of the hairpin inducing in the other a velocity normal to the plane of the hairpin and away from the wall; and third, by the "peeling-up" of a vortex pair from the viscous sublayer. The second would seem to be the most powerful mechanism, incidentally involving the third, while the first would seem to provide a means of maintaining the induced velocities in the face of dissipation.

### 4.4 Limits of Hairpin Growth

If we accept that hairpin growth is essentially due to induced velocities, then it is reasonable to ask why the maximum lengths of the hairpins should be set by the boundary layer edge and why they should not proceed substantially beyond it. The answer we would tentatively propose is that the hairpin can grow, approximately straight, only so long as it remains in a pre-existing region of shear; once it enters into a region of zero shear, the tip curls over and inhibits further growth. Two cases illustrating the behaviour of hairpins in zero shear are shown in Figure 12. (The second case has been taken from Reference 14). The significance of the observation made in section 2.3 that "the tips of the hairpins are inclined forward into the flow" will now be clear; growth is continuing only so long as the hairpin remains within a region of mean shear.

### 4.5 Significance of $45^\circ$ Angle to Wall

In a parallel shear flow the principal axes, along which the rates of strain are a maximum, are inclined at  $45^\circ$  to the wall, and it follows that the rate of increase of vorticity in the cross-section of a vortex element will be greatest (for a given shear flow) if the element is inclined downstream at this angle. But this by itself would not seem to explain why hairpins should set themselves at just this angle and grow out in this direction. A single vortex element for example, like a line marked in the fluid with a passive contaminant, would be rotated towards the wall by the shear flow (as well as stretched) as it is swept downstream, even if originally set at  $45^\circ$ . The presence of a vortex pair and the resulting induced velocities are evidently essential if a fixed  $45^\circ$  angle is to be maintained. However, it is still not obvious why the hairpin (or vortex pair) should set itself at this angle. The following may be a possible explanation.

If we assume that the stretching of a hairpin vortex brings the legs closer together, then such stretching will increase the induced velocities and the hairpin will tend to be rotated away from the wall, counteracting the direct effect of the shear. If we have a hairpin that initially makes an angle greater than  $45^\circ$  to the wall, dissipation will at some stage reduce the induced velocities and the hairpin will be rotated by the shear flow back towards the  $45^\circ$  angle. At the same time, the rate of stretching will be increased, increasing the induced velocities and opposing the effect of dissipation so that the status quo will tend to be maintained.

On the other hand, if the hairpin initially makes an angle that is less than  $45^\circ$  to the wall, dissipation, as it proceeds, will reduce the induced velocities and the consequent rotation towards the wall will result in a decreased rate of stretching and a further decrease in the induced velocities, so that the situation is unstable.

On the basis of the foregoing, we might expect to see the majority of hairpins making an angle of  $45^\circ$  or more to the wall, but only a small minority at lesser angles.

While the present tentative explanation may not appear altogether satisfactory it is believed that it reflects the importance of dissipation and vortex stretching as opposing effects.

#### 4.6 Lifetime of Hairpins

Since the lateral dimensions of hairpins appear to scale roughly with  $\frac{v}{U_\tau}$ , we might expect that  $v$  and  $U_\tau$  are the relevant variables defining, on average, the characteristics of the vortex pairs representing hairpin cross-sections. Thus we might expect the lifetime of an average vortex pair to be measured by  $v/U_\tau^2$ . The induced velocities associated with the vortex pair will similarly be related to  $U_\tau$ , and the time for a hairpin to grow through the layer will be measured by  $\frac{\delta}{U_\tau}$ .

The ratio (time to grow across boundary layer)/(lifetime) we should then expect to be measured by

$$\frac{\delta}{U_\tau} \frac{U_\tau^2}{v} = \frac{\delta U_\tau}{v} = \frac{U_\tau \delta}{v} \sqrt{\frac{c_f}{2}}.$$

At high Reynolds numbers, this quantity will become very large, and ultimately we might expect that a stage will be reached where hairpins will no longer survive to penetrate the outermost regions of the layer. Even taking into account the possible effects of vortex stretching in prolonging the active lifetime of the hairpins, it seems not unlikely that some change in structure should take place at Reynolds numbers above those covered in the present investigation.

Two facts may be worth noting here. First is the observation that, despite the slow overturning motion that large-scale structures appear to undergo at values of  $Re_\theta$  in the region of 10,000, they seem, nevertheless, always to be composed of very narrow features making an angle of approximately  $45^\circ$  to the wall. This suggests that these narrow features (hairpins) may have a very limited lifetime and may be in process of being continually renewed; but, of course, alternative explanations for these observations may exist.

The second fact to be noted is that, while the vorticities of opposite sign from the two legs of the hairpins may diffuse into each other and cancel, there is no similar mechanism by which the transverse vorticity in the hairpin tips can be destroyed. Thus, at really high Reynolds numbers, it may be only the tips of the hairpins that survive and remain active in the outermost regions of the layer.

#### 4.7 Transfer of Momentum

It will be obvious that the transfer of momentum by a hairpin vortex may take place in two ways, by the circulatory flow fields around each limb of the hairpin, and by the direct transport of low-momentum fluid as the hairpin grows out through the layer, impelled by the induced velocity that each limb of the hairpin imposes on the other. In the outer regions of the layer at high Reynolds numbers, it would seem that the latter must be the dominant mechanism of momentum transport since transverse scales will be very small, the hairpins comparatively widely spaced, and the probable lifetimes of the hairpins relatively short.

#### 5. CONCLUSIONS

Leaving on one side the more speculative aspects of the preceding discussion we may list the conclusions of the present investigation as follows.

(i) The turbulent boundary layer at Reynolds numbers up to  $Re_\theta \approx 10,000$  consists very largely, if not exclusively, of vortex loops, horseshoes or hairpins arrayed at a characteristic angle of approximately  $45^\circ$  to the wall.

(ii) The cross-stream dimensions of these loops, horseshoes or hairpins scale (at least approximately) with the wall variables  $U$  and  $v$ , while their length appears to be limited only by the thickness of the layer.

(iii) As a consequence of (ii) there is a very large scale effect on the structure of the layer.

(a) At very low Reynolds numbers ( $Re_\theta < 500$ , say) no very clear distinction can be made between large and small-scale motions, and the large eddies appear to consist of individual vortex loops or relatively small numbers of such loops. The eddies appear quite rounded and exhibit a relatively brisk rate of rotation.

(b) As the Reynolds number increases, at least a proportion of the loops become increasingly elongated, so that they may be better described as horseshoes or hairpins. At  $Re_\theta > 2,000$  (say) large-scale structures appear to be made up of random agglomerations of such hairpins, and it is, perhaps, misleading to refer to them as large eddies since they do not appear to exhibit any particular coherent motion beyond a relatively slow overturning or toppling due to shear.

- (c) At high Reynolds numbers ( $Re_\theta = 10,000$ ) a small proportion of the loops appear to have become almost incredibly elongated, and in the outermost part of the layer are widely separated in relation to their cross-stream dimensions.
- (iv) At the higher Reynolds numbers there is occasional evidence of hairpins being formed in a regular sequence so that their tips lie on a line which makes a smaller angle to the surface than the  $45^\circ$  angle characteristic of the individual hairpins.
- (v) There is substantial evidence that the tips of the hairpins are inclined forward into the flow, and this leads to the speculation (for reasons described in the text) that the outward growth of the hairpins continues only so long as they lie in a region of pre-existing shear.
- (vi) It is a general conclusion of the investigation that the use of smoke, with light-plane illumination by laser, provides a very satisfactory means of exploring turbulent boundary layer structure. The full potentialities of the technique remain to be exploited, and it is suggested that much of the present work should be repeated more carefully and in greater detail and extended to higher Reynolds numbers and to flows with pressure gradient.

#### REFERENCES

1. R.E. Falco. Coherent motions in the outer region of turbulent boundary layers. *Phys. Fluids*, 20, S124 (1977)
2. R.A. Antonia. Conditionally sampled measurements near the outer edge of a turbulent boundary layer. *JFM* 56, 1 (1972)
3. S.J. Kline. The role of visualisation in the study of the structure of the turbulent boundary layer. Workshop on Coherent Structure of Turbulent Boundary Layers, p1; Lehigh University (1978)
4. W.W. Willmarth. Survey of multiple sensor measurements and correlations in boundary layers. Workshop on Coherent Structure of Turbulent Boundary Layers, p130; Lehigh University (1978)
5. C.R. Smith. Visualisation of turbulent boundary layer structure using a moving hydrogen bubble wire probe. Workshop on Coherent Structure of Turbulent Boundary Layers, p48; Lehigh University (1978)
6. T. Theodorsen. Mechanism of turbulence. Proc. 2nd Midwestern Conference on Fluid Mechanics, Ohio State University (1952)
7. T.J. Black. An analytical study of the measured wall pressure field under supersonic turbulent boundary layers. NASA CR-888 (1968)
8. P. Bandyopadhyay. Combined flow visualisation and hot-wire anemometry in turbulent boundary layers. Lecture Notes in Physics No. 75, p205, Springer-Verlag (1977)
9. M.R. Head and P. Bandyopadhyay. Combined flow visualisation and hot-wire measurements in turbulent boundary layers. Workshop on Coherent Structure of Turbulent Boundary Layers, p89; Lehigh University (1978)
10. R.F. Blackwelder. The bursting process in turbulent boundary layer. Workshop on Coherent Structure of Turbulent Boundary Layers, p211; Lehigh University (1978)
11. C.H.P. Chen and R.F. Blackwelder. Large-scale motion in a turbulent boundary layer: a study using temperature contamination. *JFM* 89, 1 (1978)
12. A.K. Praturi and R.S. Brodkey. A stereoscopic visual study of coherent structures in turbulent shear flow. *JFM* 89, 251 (1979)
13. G.L. Brown and A.S.W. Thomas. Large structure in a turbulent boundary layer. *Phys. Fluids*, 20, S243 (1977)
14. H. Bergh. A method of visualising periodic boundary layer phenomena. IUTAM Symposium on Boundary Layer Research. Springer-Verlag (1957)

#### ACKNOWLEDGEMENTS

Both authors are indebted to the Science Research Council for financial assistance in the later stages of the work (GR/A/4827.3) and the second author to the Indian Government for earlier support. They are also grateful for the interest shown by Dr. A.A. Townsend and Prof. A.D. Young in the work and to Dr. D.J. Maull for helpful discussions.



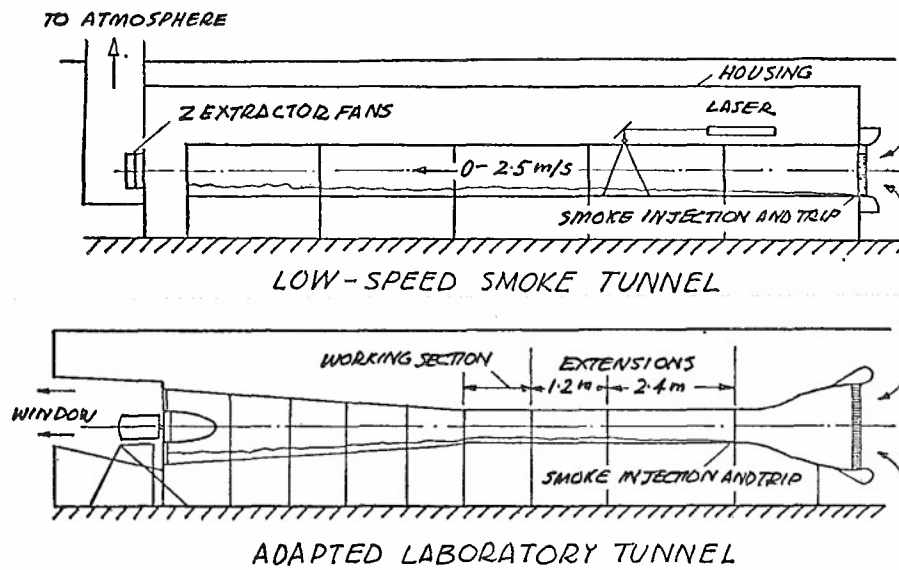
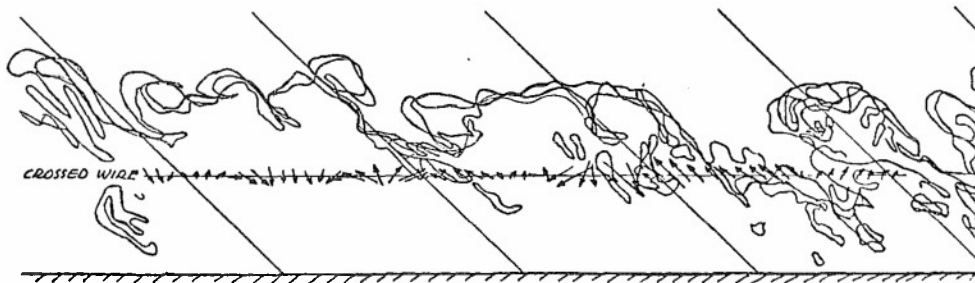
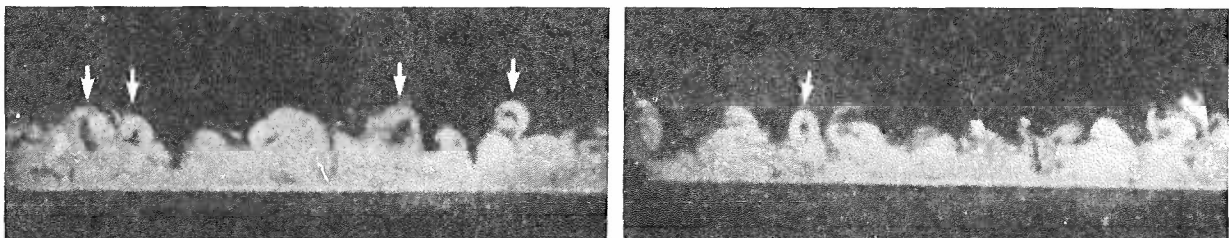


FIGURE 1 WIND TUNNELS USED IN INVESTIGATION

FIGURE 2 VECTOR PLOT OF DISTURBANCE VELOCITIES ( $Re_\theta = 1100$ )FIGURE 3 VORTEX LOOPS IN TURBULENT BOUNDARY LAYER AT  $Re_\theta \approx 500$



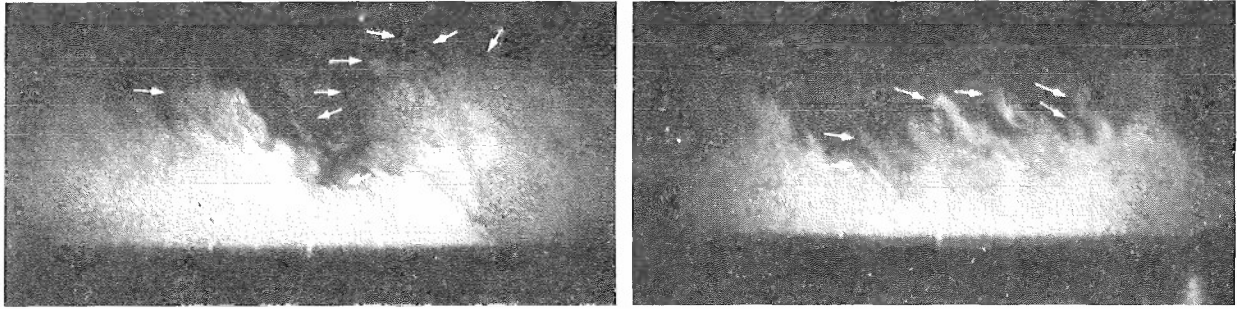


FIGURE 4 EVIDENCE OF SKEWED VORTEX LOOPS AT  $Re_{\theta} \approx 7,000$

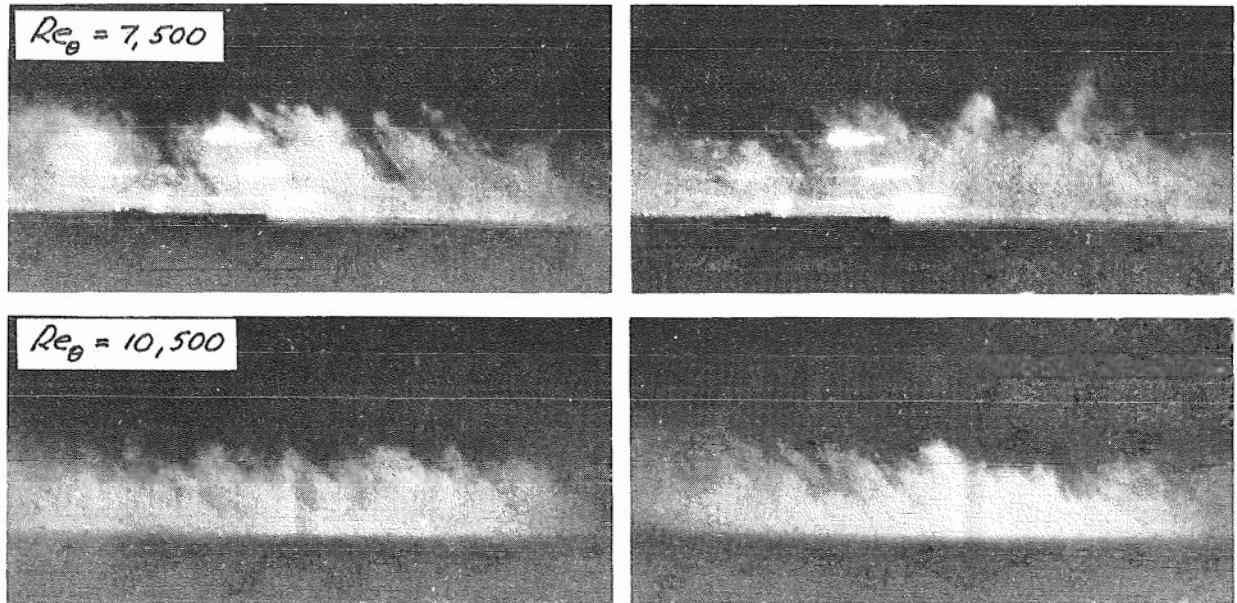


FIGURE 5 BOUNDARY LAYER STRUCTURE AT HIGH REYNOLDS NUMBERS

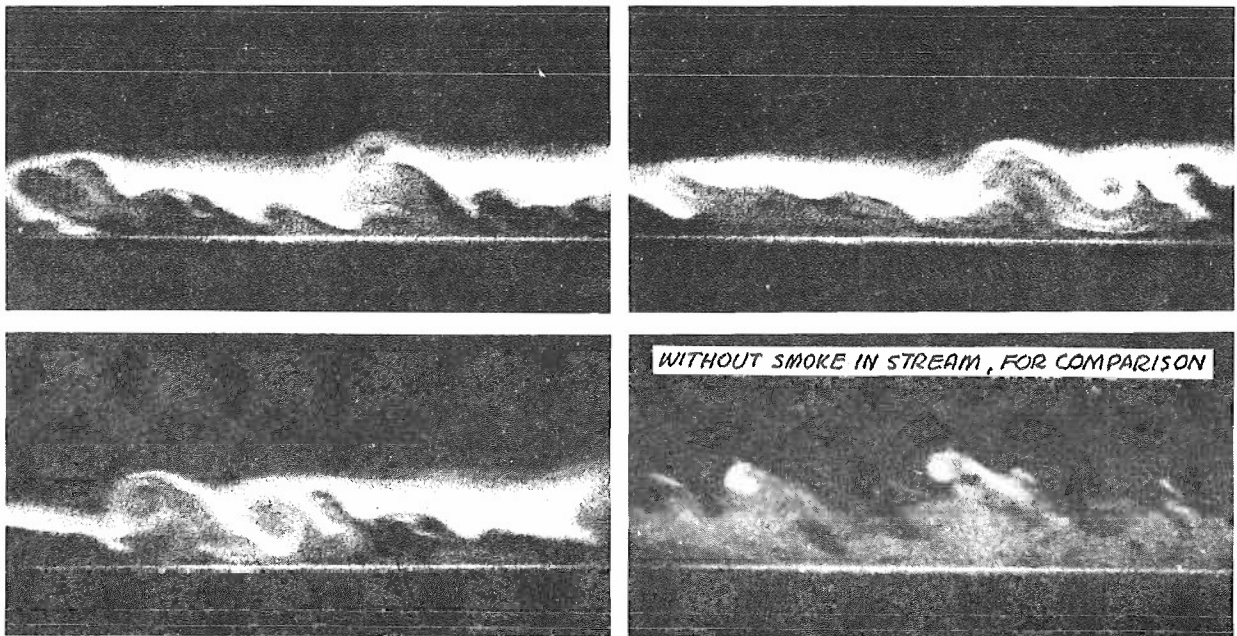


FIGURE 6 BOUNDARY LAYER STRUCTURE AT LOW REYNOLDS NUMBER ( $Re_{\theta} \approx 500$ )

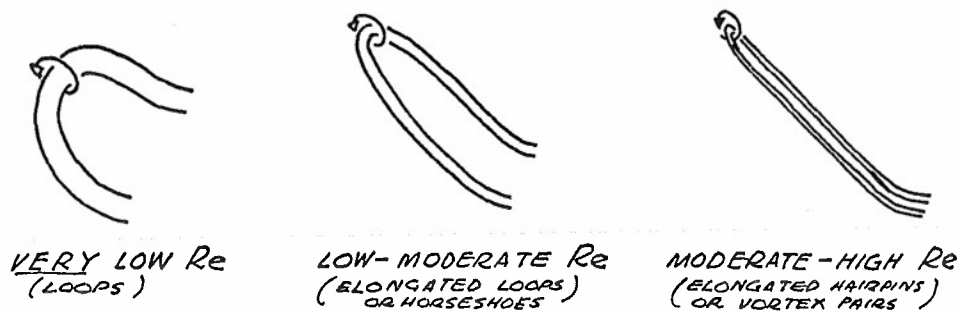


FIGURE 7 VORTEX LOOPS, HORSESHOES AND HAIRPINS

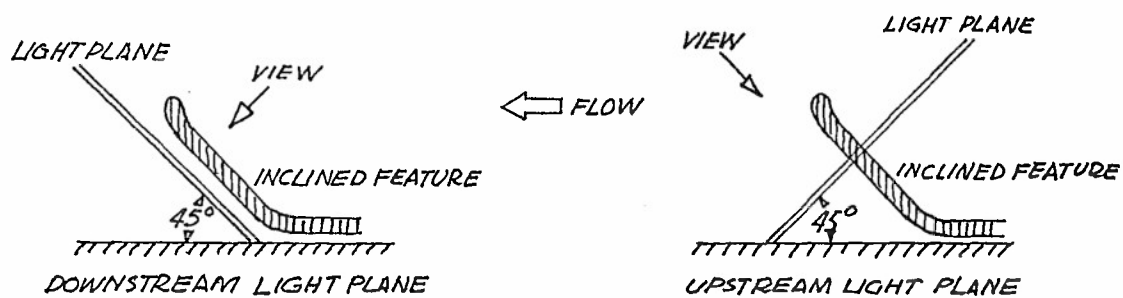


FIGURE 8 INCLINED FEATURES BEING CONVECTED PAST LIGHT PLANES



FIGURE 9 VIEWS SEEN BY CAMERA AS FEATURE CONVECTED PAST LIGHT PLANES

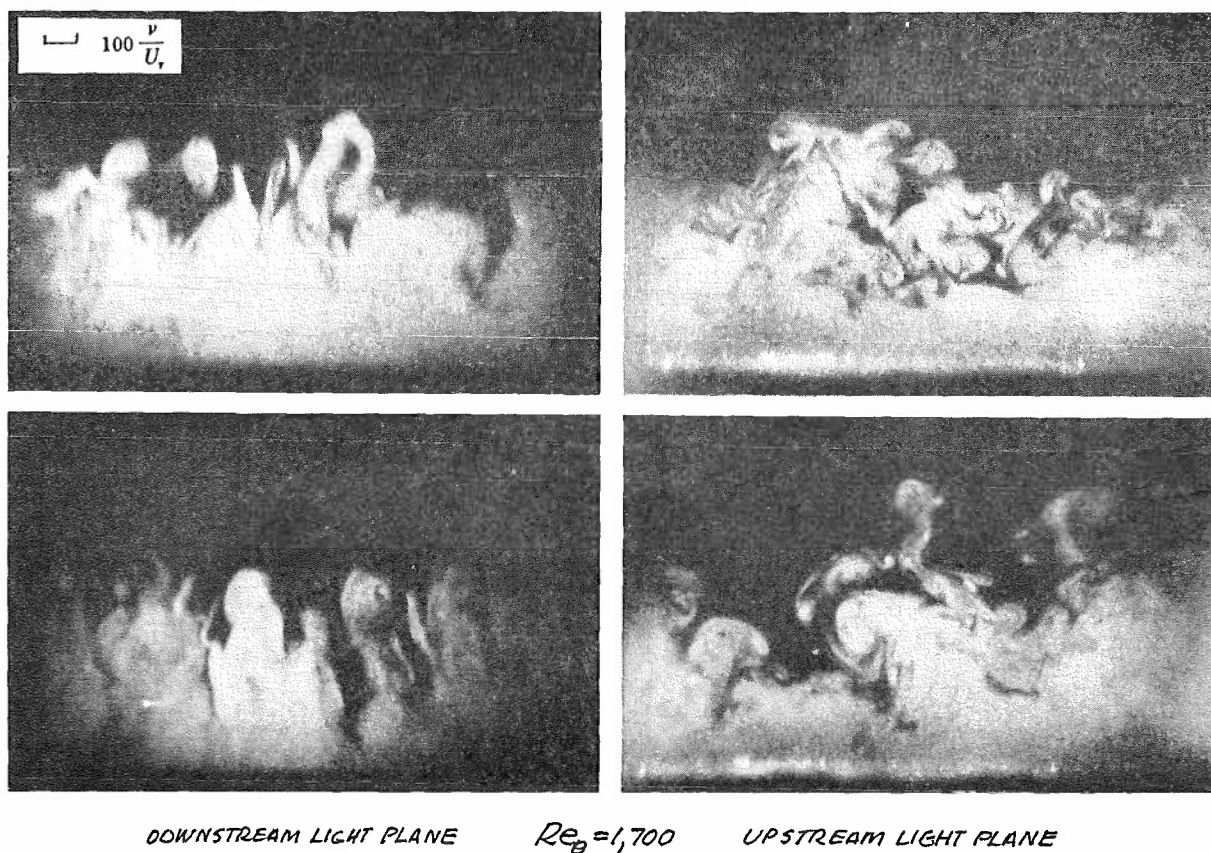
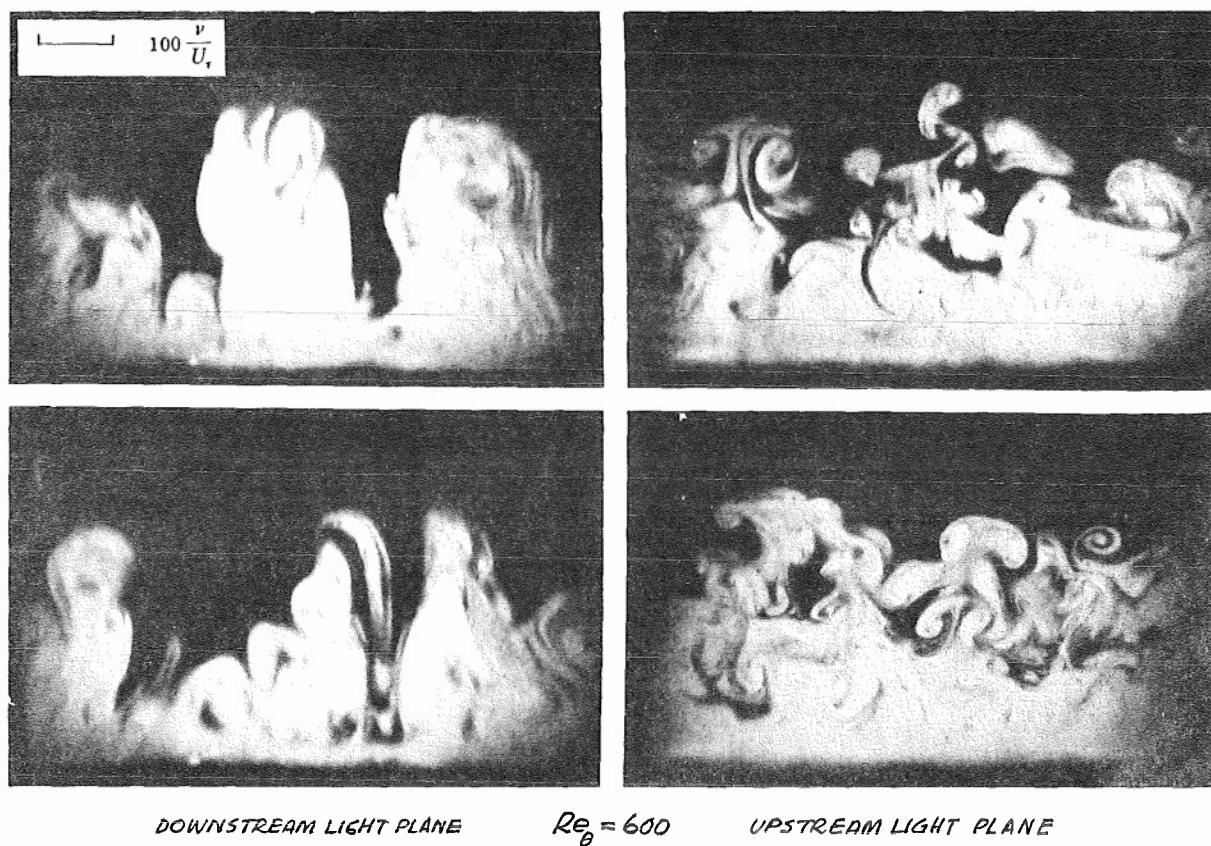
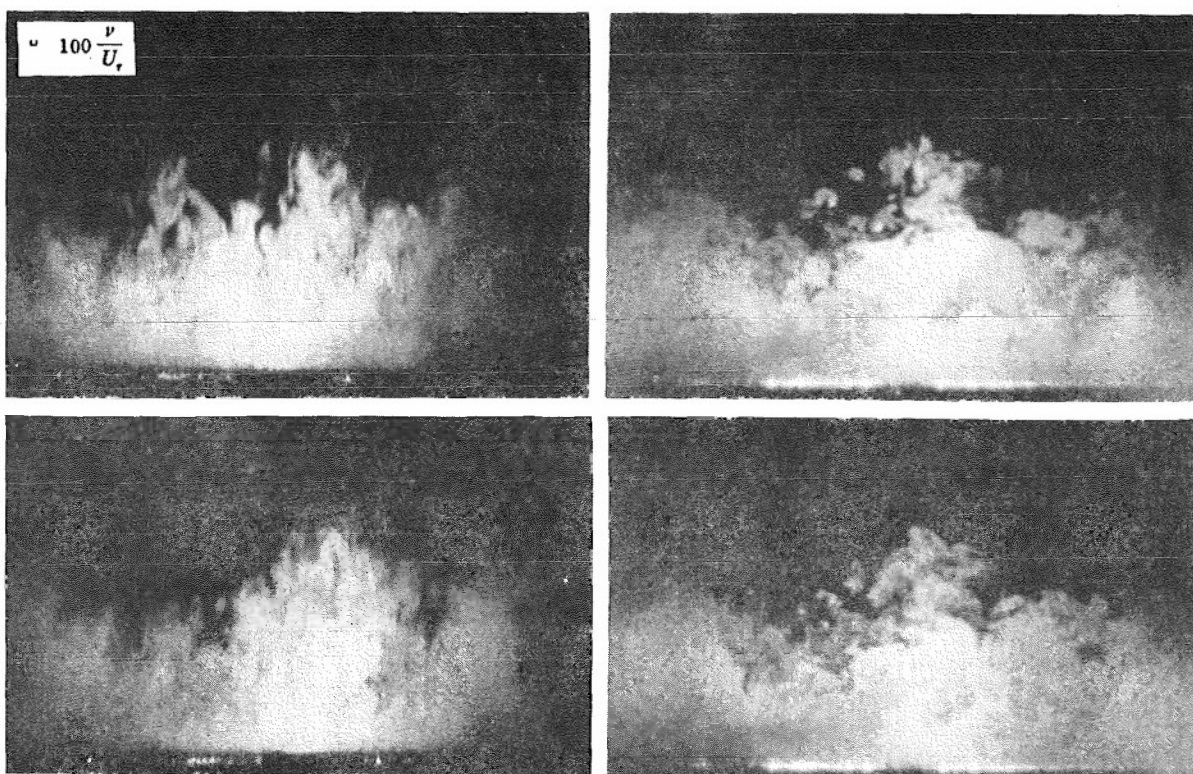


FIGURE 10 VIEWS WITH  $45^\circ$  DOWNSTREAM AND  $45^\circ$  UPSTREAM LIGHT PLANES AT  $Re_\theta = 600$  and  $1,700$





DOWNSTREAM LIGHT PLANE  $Re_\theta = 9,400$  UPSTREAM LIGHT PLANE

FIGURE 10 (CONT.) VIEWS WITH  $45^\circ$  DOWNSTREAM AND  $45^\circ$  UPSTREAM LIGHT PLANES AT  $Re_\theta = 9,400$

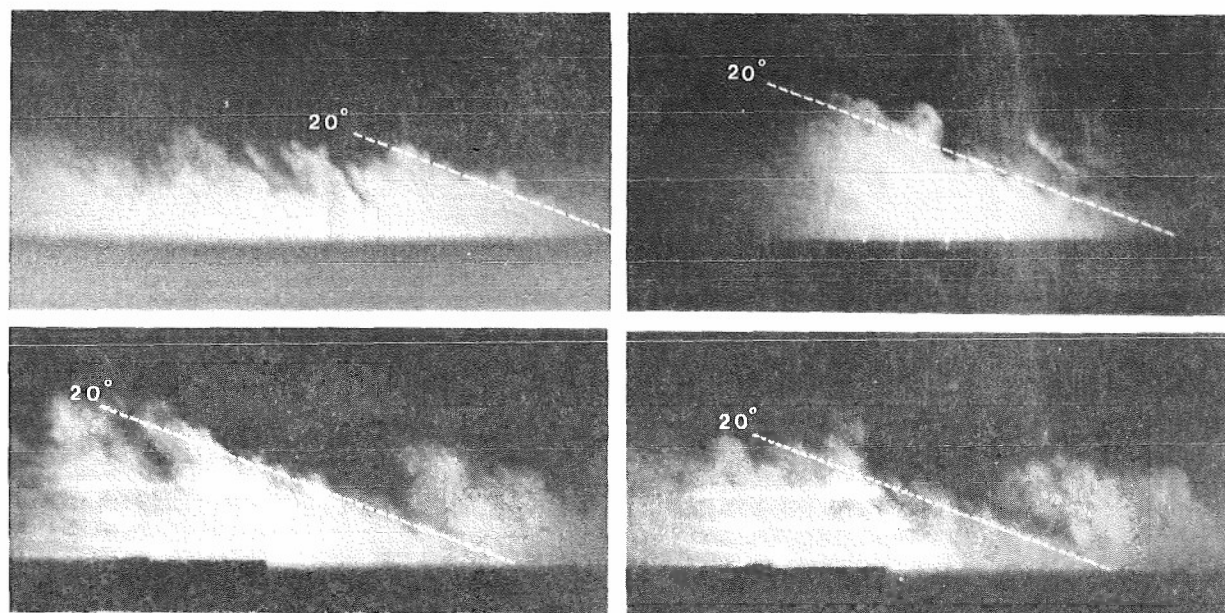


FIGURE 11 EXAMPLES OF INCLINED INTERFACES

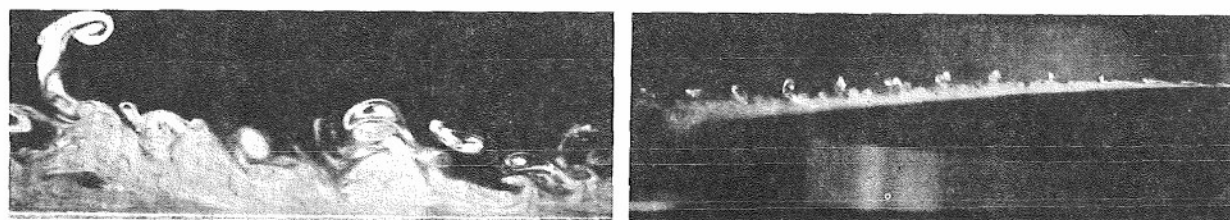


FIGURE 12 EXAMPLES OF HAIRPINS CURLING OVER INTO STREAM

# SOME OBSERVATIONS OF THE STRUCTURE OF THE TURBULENT BOUNDARY LAYER

by

Andrew S. W. Thomas\*

Department of Mechanical Engineering  
University of Adelaide  
South Australia

## SUMMARY

Results are presented to describe some measured features of the organized large structure of a turbulent boundary layer. The spanwise correlation scale, the conditional Reynolds stress contribution and the experimentally determined streamline pattern of the large structure are discussed. Correlation and conditional sampling techniques are employed to examine the influence of this structure at the wall. It is found that increased activity at the wall is associated with curved streamlines. This is to be expected if it is a rotational instability that couples the turbulent bursts to the large structure.

## 1. INTRODUCTION

It is of some interest to contemplate the techniques currently being applied to the study of boundary layer turbulence. In the past heavy use was made of long time-averaged statistics such as correlation and spectral techniques. A well-established trend is now to supplement these methods with conditional data analyses, such as conditional sampling and conditional correlations. This is, in part, indicative of the deeper understanding of the flow achieved through the important finding that the flow consists of structures possessing a considerable degree of organization and repetitivity. Since any measurement at one point will record the passage of an ensemble of structures, each originating randomly from different upstream positions at different times, a long time-averaged statistic may not show the presence of any organized component in the flow. Alternatively, a conditional approach, provided it is carefully implemented, may bring out these organized motions.

In the case of the boundary layer, these techniques, coupled with flow visualization studies, have indicated the presence of two important types of organized structure in the layer. Near the wall the flow is known to be dominated by the low speed streaks and the turbulent burst-sweep cycle of events. Kim, Kline and Reynolds<sup>1</sup>; Offen and Kline<sup>2</sup>; Nychas, Hershey and Brodkey<sup>3</sup> and others have made many contributions that have clarified aspects of this phenomenon. In the outer part of the layer, the flow is dominated instead by the large structure whose presence has been inferred from correlation and conditional sampling measurements (Kovaszny, Kibens and Blackwelder<sup>4</sup>; Antonia<sup>5</sup>). A crucial step in our understanding of the flow lies in the knowledge that these two types of motion are, in some way, intimately related together. The scaling trends of Rao, Narasimha and Narayanan<sup>6</sup> and Lu and Willmarth<sup>7</sup> suggest this to be so.

In the earlier part of the present work, Brown and Thomas<sup>8</sup> examined this critical relationship directly. Correlations were computed between the fluctuating wall shear stress and velocity fluctuations measured in the outer part of the layer. The important conclusion of the work is that the large structure gives rise to a slowly varying component in the wall shear and that intense small scale fluctuations, indicative of the bursts and sweeps, occur most often when this component is high. A hypothesis was examined suggesting that a warping of streamlines by the large structure causes a rotational instability near the wall giving rise to the streaks of longitudinal vorticity and small scale activity that have been observed in that region.

Offen and Kline suggested an alternative model for the coupling between the bursts and the large structures. They contend that the flow arising from the repeated pairing of bursting fluid near the wall gives rise to momentary adverse pressure gradients at the wall. These streamwise gradients in turn stimulate the lift up and bursting of new fluid.

In either of these two models, there is a direct coupling between the flow at the wall and the flow further from the wall. However, it is important to note that Brown and Thomas place emphasis on the role of the large structure in the dynamics of the flow, whereas it is the bursts and sweeps that are emphasized in the work of Offen and Kline. It is clear, therefore, that further study is needed to examine the problem.

Thinking such as this motivated the work described in this paper. It represents a continuation of the work of Brown and Thomas<sup>8</sup> and is aimed at studying certain features of the boundary layer structure leading, hopefully, to clarification of the mechanism that couples the bursts and sweeps to the large structure. To do this, some interesting large scale correlation features of the structure in the outer part of the layer will be presented. It will then be shown that similar correlation scales can be detected at the wall. The flow field existing within the structure responsible for these correlations, and its contributions to the Reynolds stress will then be examined in detail. These data will be shown to support the emphasis Brown and Thomas place on the role of the large structure in the dynamics of the flow. Finally, their contention that a rotational instability may be occurring near the wall will also be examined. Evidence will be presented to show that necessary (although not sufficient) conditions do exist at the wall for such a mechanism to occur. The role of the pressure field of the large structure will also be briefly discussed in relation to the alternative mechanism for this phenomenon proposed by Offen and Kline.

## 2. THE EXPERIMENTAL APPARATUS

The wind tunnel used in this investigation is of the open circuit type with aluminum test section 5m long and 230mm square. The lower floor of the tunnel consists of a thin flexible steel sheet which was adjusted to account for boundary layer growth and to give a zero pressure gradient condition. The boundary layer developing on the upper surface is used in this investigation, and the properties of the mean flow are summarized in Table 1 below.

---

\* Present address: Lockheed-Georgia Company, Marietta, Georgia, U.S.A.

Table 1

$U_0$	36.3 m/sec
$U_\tau$	1.28 m/sec
$\delta$	40.3 mm
$\delta^*$	5.5 mm
$\theta$	4.2 mm
$Re_\theta$	10,200
$x$	3.5 m

The behavior of the data observed for this high Reynolds number condition was also observed at a lower Reynolds number condition ( $Re_\theta = 4,920$ ), with no apparent Reynolds number dependency. Therefore, only the high Reynolds number results have been presented.

Wall shear stress fluctuations were measured with small (0.25 mm  $\times$  0.5 mm) hot films manufactured by the vacuum deposition of nickel onto glass. A shock tube test for these devices showed a step response time of about 50  $\mu$ secs which was well within the desired range. Calibration was achieved using the rotating disk apparatus of Brown and Davey<sup>9</sup> and in all cases the measured mean wall shear was within 5% of the value given by Preston tube measurements. A dynamic calibration was inferred from the steady calibration by assuming quasi-steady heat transfer with the appropriate correction being applied to account for the reduced spread of heat flux into the substrate at higher frequencies. For full details, the reader is referred to Thomas<sup>10</sup>.

Streamwise velocity fluctuations were measured using tungsten wires of 5  $\mu$ m diameter with copper plated ends to give an active length of 1 mm. Constant temperature operation was used.

All data analysis for this work was performed on a CDC 6400 digital computer and the data were recorded on line with a small data acquisition system and written onto computer tape. The analog to digital converters of this system operate with an 8-bit precision and each typical record of data consisted of 2560 data points. Typically, 16 such records were acquired to achieve stationarity of the averages that were computed. A sampling rate of 12.5 KHz was used which corresponds to a Nyquist folding frequency of 6.25 KHz or, in nondimensional terms,  $\omega\delta^*/U_0 = 6.0$  or  $\omega\nu/U_\tau^2 = 0.36$ . Spectral estimations showed that only 1% of the mean square signal energy existed above this frequency so that little frequency folding should be expected. Subsequent analysis showed that, indeed, there was no apparent distortion due to this phenomenon.

### 3. SPANWISE CORRELATION DATA

This report is concerned with describing measured features of the large structure and examining the way the structure influences the wall region. If, as Brown and Thomas suggest, this large structure gives rise to a slowly varying component in the wall shear, then it is reasonable to expect that the flow near the wall should indicate some spanwise correlation over scales typical of the large structure. Now the spanwise correlation data of Kovaszny, Kibens, and Blackwelder<sup>4</sup> indicate a lateral scale for the structure which is of the order of  $\delta$  in the outer part of the layer. However, data recorded much nearer the wall<sup>11</sup> have indicated a spatial lateral scale that is much smaller ( $\sim 100\nu/U_\tau$ ). This apparent inconsistency with the preceding arguments probably arises because the wall region is dominated by the smaller scale intense bursting phenomenon and this in turn dominates the correlations.

Nonetheless, it is perhaps curious that despite the documented influence of the large structure at the wall, there is no evidence of some weak but large scale spanwise correlation being present superimposed on the smaller scale correlation. It seemed important to examine this in more detail by computing a series of spanwise correlations for both the flow in the outer part of the layer and also for the flow at the wall.

#### 3.1 Spanwise Velocity Correlations

For the first experiment to be reported, time correlations have been computed between the velocity signals recorded at two adjacent spanwise positions in the layer, i.e.

$$R_{uu} = \frac{\langle u(x, y, z=0, t) \cdot u(x, y, z=\Delta z, t+\tau) \rangle}{u'^2}$$

Here, a conventional long time average is implied and, for the present purposes  $\Delta z$ , the spanwise separation, is restricted to values of  $0.15\delta$ ,  $0.3\delta$ ,  $0.45\delta$  and  $0.6\delta$ . The results for three different positions in the outer part of the boundary layer are shown in figure 1. The correlations are symmetrical about  $\tau=0$ , a necessary consequence of spanwise homogeneity. At small spanwise separations, the correlation is positive, but as the separation increases, the zero time delay value of the correlation reduces, passes through zero and then becomes negative. At  $y/\delta = 0.75$  this zero crossing occurs somewhere between separation of  $0.3$  and  $0.45\delta$ . Nearer the wall, however, it occurs sooner, being somewhere between  $0.15$  and  $0.3\delta$ . A reduction in the perception of the spanwise scale nearer the wall is already becoming apparent. The temporal extent of the correlations is quite large, being of the order of  $20\delta^*/U_0$  or about  $3\delta/U_0$ . This compares favorably with the values that can be inferred from the curves of Kovaszny, et al.<sup>4</sup>, and their interpretation of the correlations is, no doubt, correct.

A very significant feature, however, which cannot be seen in their data is that, in the outermost part of the layer, the correlations corresponding to a separation of  $\Delta z = 0.3\delta$  show a clear indication of twin

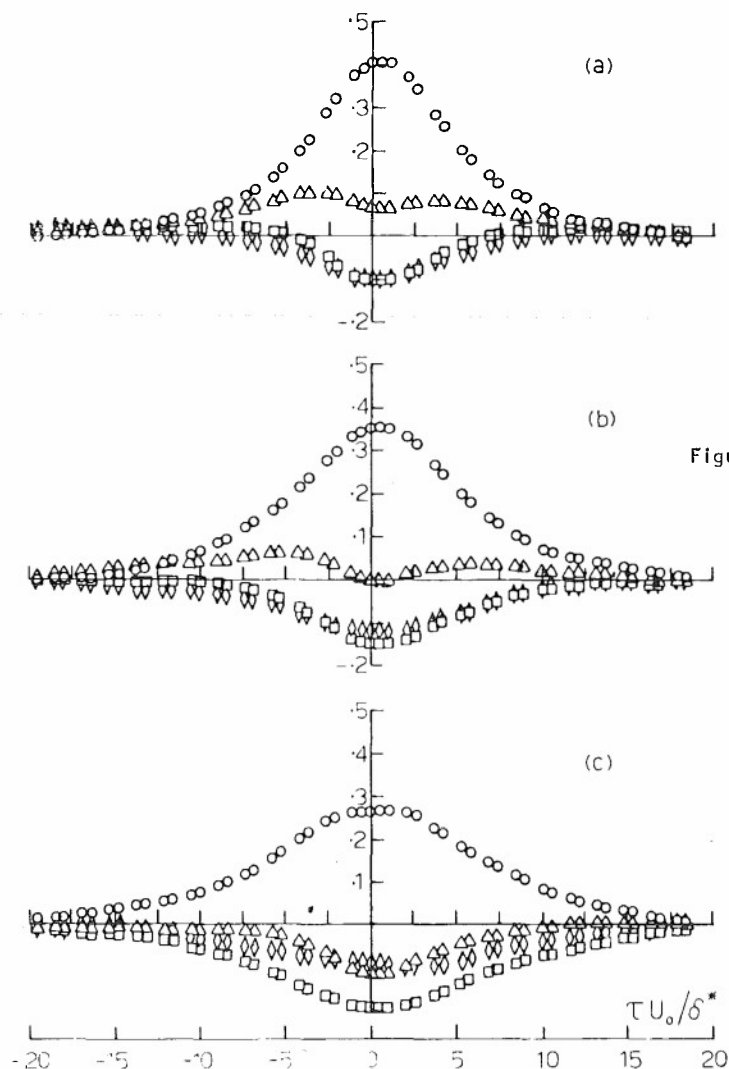


Figure 1. Time correlations of the streamwise component of velocity at adjacent points separated only in the spanwise direction. Three different heights from the wall have been presented. (a)  $y/\delta = 0.75$ , (b)  $y/\delta = 0.5\delta$ , (c)  $y/\delta = 0.25\delta$ .

Symbols are:

○	$\Delta z = 0.15\delta$
△	$\Delta z = 0.30\delta$
□	$\Delta z = 0.45\delta$
◇	$\Delta z = 0.60\delta$

maxima with symmetry about the  $\tau = 0$  axis. This correlation effect, although of small amplitude, seems unmistakable in these data, but as it was not evident in previously reported work, special studies were undertaken to prove that it was not spurious. It is noted that the same results were obtained at other flow speeds and in thinner and thicker regions of the boundary layers occurring in the wind tunnel. The mean flow was checked for spanwise homogeneity and found to be closely two dimensional. The same effect was found when any pair of wires separated by  $0.3\delta$  were used either on or off the tunnel centerline. The various tests undertaken all indicated that the twin maxima in the correlations are certainly real.

A set of correlations such as these could arise from structures that have a characteristic periodicity within them. However, no such behavior has been observed previously and none is evident in a visual examination of the signals. An alternative implication of these twin maxima is that they result from significant correlation at positive time delay for half the time and at negative time delay for the other half of the time. That is, the structure has a characteristic angle in the transverse direction. This conclusion is supported directly by a visual examination of the velocity signals where phase lead and lag can be observed between recordings from adjacent wires. The characteristic angle is quite acute, and the included angle between the structures and the flow direction appears to be about  $25^\circ$  at  $y/\delta = 0.75$  and  $0.50$ , if it is assumed that the structures responsible for the generation of these curves are convected at about the local mean velocity.

The important question is what this obliqueness really means in terms of the geometry of the structures. Another turbulent structure that displays oblique regions is the turbulent spot whose leading edges lie at a comparable acute angle to the mean flow. Coles and Barker<sup>12</sup> used the spot as a model for a synthetic boundary layer and the present results appear to be consistent with the idea that there may be a similarity between the structural element of the boundary layer and the turbulent spot. While this may indeed be the case, such a conclusion should not be drawn on a basis of the present data alone and the obliqueness may not be representative of the leading fronts of the structures. It is necessary to consider in more detail the way the correlations are generated. For example, consider the correlations that would be generated by a large structure that was basically a symmetrical "blob" of uniform velocity perturbation as shown in figure 2(a). The velocity excursions recorded on a rake of closely spaced hot wires, each separated only in the spanwise direction, would not correlate to maxima at non-zero time delays. The correlations, determined by taking slices through the structure, would be symmetrical and the same would be true if the rake was on or off of the structure centerline. If, alternatively, the blob was triangular in plan view (i.e. like a spot) as shown in figure 2(b), but still of uniform velocity defect, then the possibility arises for twin maxima to occur in the correlations. However, the same effect could arise by another means. The third example shown in figure 2(c) shows a turbulent blob that is spatially symmetrical, but whose velocity defect is nonuniform. It is possible for such a structure to also indicate twin maxima at non-zero time delays because of its streamwise asymmetry.

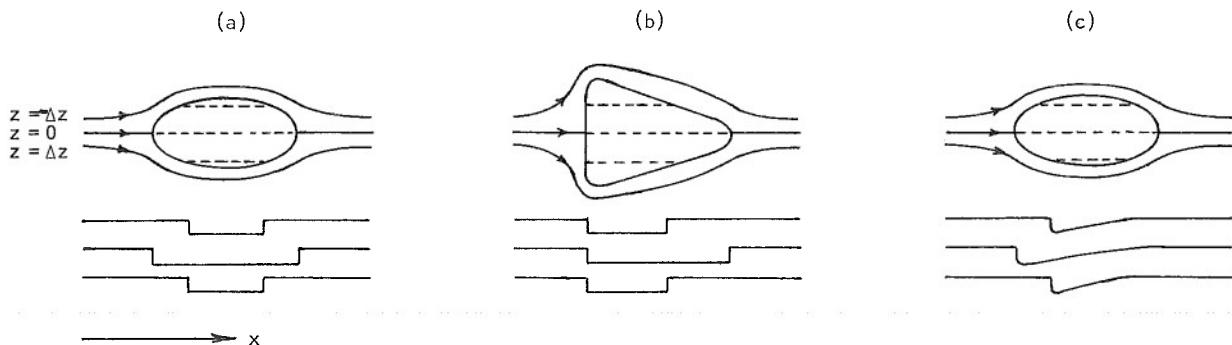


Figure 2. Plan views of a series of hypothetical turbulent structures and their velocity signatures at three adjacent spanwise locations:

- (a) A symmetrical "blob" of turbulence with uniform velocity defect.
- (b) A triangular patch of turbulence with uniform velocity defect.
- (c) A geometrically symmetrical structure, but with nonuniform velocity defect.

The conditional velocity time histories to be presented in a later section will show that the case in figure 2(c) is in fact closer to the real situation. Under these circumstances, any correlations will be dominated by the intense fluctuations occurring at the back of the structure. The apparent obliqueness implied by the correlations is most likely associated with the backs of the structures as opposed to the fronts.

### 3.2 Spanwise Wall Shear Correlations

Brown and Thomas demonstrated that the same velocity fluctuations used to generate the correlations in figure 1 are also correlated with fluctuations in the shear stress at the wall. It is reasonable then to expect the shear stress to display similar correlation extent. Since the correlation scale near the wall, as reported by others, is very much smaller than the scale implied by the data in figure 1, a careful examination of the flow near the wall is necessary. A series of long time-averaged spanwise wall shear correlations have been computed and the results are presented in figure 3(a).

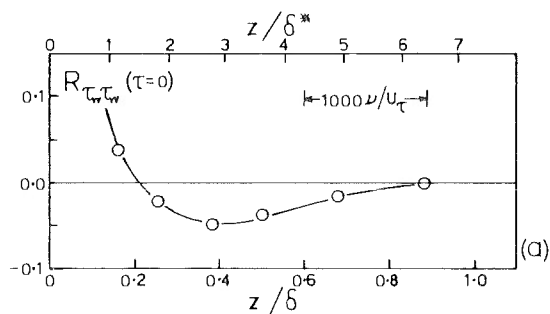


Figure 3(a). Long time-averaged correlation of the wall shear at points separated only in the spanwise direction.

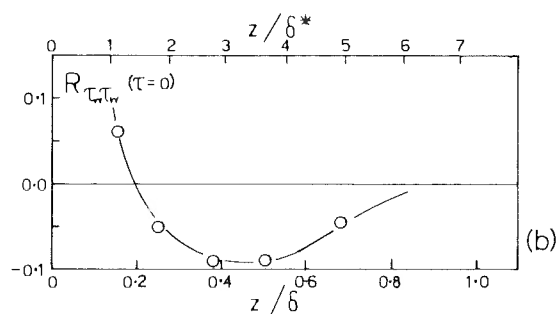


Figure 3(b). Ensemble average of short time correlations of the wall shear. The conditional approach used to obtain this curve is described in the text.

It can be seen that the general behavior is of these correlations similar to that of the velocity correlations although the level of correlation is reduced. The most significant and surprising finding is that the shear stress can be correlated, albeit weakly, over a scale of the order of  $\delta$ . Since this represents about  $2400 \nu / U_\tau$ , it is a huge scale in relation to the scales typical of the wall and clearly demonstrates that the large structure is influencing the flow at the wall.

The question now arises as to why this behavior is not evident in previously reported measurements. For example, the data of Gupta, Laufer and Kaplan<sup>11</sup> show nearly zero correlation in the velocity near the wall beyond a spanwise separation of  $300 \nu / U_\tau$ . There is no evidence of the small negative correlation values found here. The apparent inconsistency with the present data is presumably a consequence of the dramatic and violent activity occurring just outside the sublayer. This could swamp any weak large scale correlation effect, but because these fluctuations do not easily penetrate the highly viscous sublayer, it is probable they do not dominate the wall shear correlations so significantly. Consequently, the shear stress data show a weak, but detectable, large-scale presence.

It is possible to obtain what might be viewed as a more realistic measure of the presence of the large structure at the wall. The correlation data are an ensemble of all times, including those times when the structure of interest may not be present. If it were possible to discriminate upon those times when the structure was present, as opposed to those times when it was not, a more meaningful correlation might be generated.

Brown and Thomas addressed the same problem with wall shear-velocity correlations and showed that discrimination of the presence of the large structure could be based upon the correlation between the wall shear and velocity at  $y/\delta = 0.25$ . To do this, the data are first broken up into a series of short time records of length  $TU_0/\delta^* = 50$ , that is, a length somewhat larger than the scale of the structure. A series



of short time correlations are then computed between the wall shear and velocity at  $y = .25\delta$  and a search made to flag those occasions when each correlation is twice the long time average. By determining a conditional ensemble average correlation for this subset of times, Brown and Thomas found that the correlation between the wall shear and the velocity at all points in the layer was enlarged. They interpreted this as evidence of the presence of the large structure, and if this is so, then it is logical to expect that, for a similar subset of times, the spanwise wall shear correlations should also be enlarged.

To examine this possibility, an identical procedure has been applied to the data used to generate figure 3(a). The resulting conditional ensemble averaged correlations that correspond to figure 3(a) are shown in figure 3(b). The discrimination process was successful 26% of the time, and it is very reassuring to see that, without exception, all the correlations have been enlarged and are nearly double their long time average. This is true even at spanwise separations as large as  $0.7\delta$ . These data clearly demonstrate the strong influence of the large structure at the wall and support the conclusions of Brown and Thomas. The nature of this influence will be discussed in more detail in Section 5.

#### 4. CONDITIONALLY SAMPLED DATA

Having established the influence of the large structure at the wall, attention is now directed toward the structure itself. In order to extract more details of the large structure, it is now necessary to employ a conditional sampling procedure. As mentioned in the Introduction, the interpretation of long time-averaged statistics can be greatly supplemented using a conditional analysis. The results of the last section clearly demonstrate this and even the data of figure 2 are, in some sense, special cases of conditional data. They aid greatly in understanding the generation of the unusual spanwise velocity correlations. However, extraction of further details of the structure, such as its Reynolds stress contribution and streamline pattern can only be achieved with a more rigorous and objective conditional procedure.

Conditional data analysis is based upon the recognition and detection of an identifiable event in one time signal and, in some cases, its relationship to some characteristic pattern in another. These patterns or events must be repeated in time since an isolated occurrence would be meaningless to the dynamics of the flow. Having established that this is the case, it is then possible to characterize the events or patterns by ensemble averaging the time histories of all the different realizations of the pattern. The resulting average time history can then be regarded as a typical time history of all such patterns.

This procedure appears to be very straightforward, but the simplicity is notoriously deceptive and there are a number of factors which can lead to misleading results. For example, successful detection requires *a priori* knowledge of the character of the structure. The initial definition of the structure can, in turn, affect the outcome of the process. Furthermore, any detection algorithm will inevitably be satisfied by fluctuations which, fortuitously, have the character of the pattern of interest but are unrelated to the structures of interest. Likewise, random fluctuations can distort a pattern to the point where it is no longer recognizable. As a consequence events will be included when they should be omitted (false detections) and vice versa. Finally, any successful detection scheme should always identify the corresponding point in time on each successive pattern. Otherwise, the ensemble average of samples centered upon what are assumed to be corresponding times will be a distorted representation of the average pattern. Other problems may also arise with the technique and Thomas and Bull<sup>13</sup> present results which show one example where they can be quite severe. Despite this, the use of conditional sampling should not be rejected since it can provide an abundance of useful information and detail which would otherwise be unknown. Therefore, in what follows, the philosophy of the technique will not be discussed or defended in rigorous detail. Instead, results will be presented that will define some of the problems of the technique and the methods by which some of these problems can be overcome.

##### 4.1 Choice of Detection Scheme

The first problem in the present case lies in trying to detect and discriminate upon the presence of the organized structure in some unbiased manner. Various schemes have been suggested in the literature but most suffer from various shortcomings. In particular, they assume prior knowledge of the character of the structures of interest, i.e. they assume that the structures whose presence is being detected do have large excursions in vorticity or Reynolds stress, etc. In the present context, however, the amplitude and character of the excursions is unknown and it seems inappropriate to consider only large excursions in Reynolds stress or velocity as the characteristic feature of the large structure.

In considering alternatives, attention was turned to the earlier work<sup>8</sup> which highlighted two important characteristics of the large structure in the boundary layer. Firstly, a visual inspection of velocity records at various points in the layer indicated that the structure was characterized by a steep change in velocity on its back or upstream surface. Secondly, it was demonstrated that an intimate relation exists between the large scale and small scale features of a velocity signal. To demonstrate this, a correlation was computed between the low frequency component of a signal and a signal synthesized by smoothing the rectified high frequency component of the signal. That these correlations are large and maximize at a non-zero time delay is a means of quantifying the fact that steep velocity changes occur on the upstream surface of the structures. Since this behavior is a unique character of these particular signals, this suggests that the smoothed rectified high frequency component of a signal should be used as a basis for the detection of the large structure in the layer. By using the rectified high frequency signal there is evidently no bias toward either positive or negative going disturbances. Therefore, any ensemble averages obtained should reflect genuine features of a signal rather than a distortion due to the detection scheme.

In what follows a low pass digital summing filter was used to split each streamwise velocity signal into its low frequency and, by subtraction, its high frequency component. The latter was then rectified and smoothed and those points flagged that were a local maximum exceeding some certain discrimination level. Both the streamwise and normal components of fluctuating velocity were sampled and averaged at these points.

Decisions must be made as to which filter cutoff and which discrimination level should be used. These problems are discussed in detail in Appendix A where it is demonstrated that any filter-discriminator combi-

nation cannot be objectively favored over any other combination. This problem is fundamental to work of this kind but it is not as serious as it may first seem. This is because the results that are obtained depend only weakly on the filter cutoff and discrimination levels.

Therefore, in some sense the conditional average does reflect a characteristic feature of the flow and the precise settings of these variables become less important. The values of the parameters that were finally settled upon were a filter cutoff of  $\omega\delta^*/U_0 = 0.43$  (450 Hz) being used to generate the smoothed rectified high frequency detection signal, and a discrimination level of 1.5 times the rms level of the smoothed rectified high frequency signal.

#### 4.2 Enhancing the Conditional Averages

As mentioned previously, any successful detection scheme should identify the same point in the phase of each structure that satisfies the scheme. Because of the random fluctuations that are inevitably present, however, this may not always be the case. Likewise, random influences can give rise to the possibility of a number of false detections. A technique has been developed to minimize these problems.

Initially the ensemble-averaged time history is formed from those points where the detection criterion is satisfied. A series of time correlations are then computed between this average time history and each individual realization which contributes to the average. These correlations are computed at various time delays with a short averaging time and are normalized by the relevant local short time estimate of the rms value. This avoids the possibility of large correlations resulting from large signal amplitudes as opposed to genuine correlation in the statistical sense.

Now, if any one such correlation is negative, then that particular detection point may be regarded as being false and may be rejected. Usually about 30% of the initially detected points were rejected on this basis. Next, each correlation is examined to find the local maximum level nearest the zero time delay point. The largest value occurring anywhere in the time delay aperture is not used because that may be associated with some adjacent structure rather than the particular realization of interest. If the maximum occurs at a non-zero time delay, then the detection point is moved by an amount corresponding to this time. This will minimize the problem of phase uncertainty.

With the detection points redefined in this way, a new ensemble average may now be generated and, furthermore, the entire correlation process may be repeated until such time as no significant changes occur in either the average itself or the definition of the points at which the average is formed. In practice this was usually found to occur after the first two or three iterations although five were generally used.

The mechanics of this technique and the selection of an appropriate averaging time are discussed in detail in Appendix B. It is a kind of bootstrap operation in the sense that every iteration sharpens the definition of the detection criterion and reduces the set of events which now satisfy the more stringent condition.

#### 4.3 Sampling of the Velocity Field and Reynolds Stress

The techniques described in the last section have been applied to the signals recorded by a cross-wire probe placed at various positions within the boundary layer. The cross-wire probe was oriented within the flow so as to record the normal and streamwise components of velocity. The high frequency detection scheme has been applied to the streamwise component to generate the array of detection points which have then been used as a basis in the sampling scheme.

The enhancing technique has been based upon the averaged time history of the streamwise component alone, but has been used to redefine the detection points and obtain the enhanced averaged time histories of both  $u$  and  $v$  as shown in figure 4.

Consider first the averaged time histories of the streamwise component  $u$ . In most cases (except perhaps at far from the wall) the most striking feature is a region of sudden acceleration. From the data at  $y = 0.5\delta$  and  $0.7\delta$ , it appears also that this occurs on the back or upstream surface of the structure. This is consistent with the earlier visual observations and correlation data of Brown and Thomas<sup>8</sup>. The important contribution of the present data lies in the observation that these regions of acceleration are a signature of the large structure and can be observed across the entire layer. Also, they must be steeper than the corresponding regions of deceleration on the front, for were this not so, the detection scheme would not be so successful. The structure appears, therefore, to have streamwise asymmetry and the flow at the front is apparently a rather diffuse flow in relation to the flow at the back. This point was raised previously in Section 3.1 and was used in the interpretation of the correlation results.

The data near the wall are quite like those of Blackwelder and Kaplan<sup>14</sup> who used a similar detection algorithm. They argue that because the region of low velocity followed by a sudden acceleration is similar to the cycle of events observed by Corino and Brodkey<sup>15</sup> and Kline et al.<sup>16</sup> then such averages may represent the bursting phenomenon near the wall. However, the present work demonstrates that similar signal features can be identified across the entire layer. It is probably more correct to say that these features represent a signature of the large structure and that the occurrence of bursts is related to the passage of this structure.

Consider now the averages of the  $v$  or normal component of velocity. Their behavior is very similar to the average of  $u$  except for an inversion. This immediately suggests a large contribution to the Reynolds stress. A significant feature of the averages is the change in their character across the layer. Near the wall they show a predominantly positive region with a rather weaker negative region occurring at positive times. At the time when the strong acceleration occurs on the streamwise velocity, there is, correspondingly, a sudden fall in the normal component of velocity. This finding is also consistent with the results of Blackwelder and Kaplan<sup>14</sup>. However, as the point of measurement is moved farther from the wall, the

region of negative velocity becomes reduced, until at about  $y/\delta = 0.5$  the averages show mostly only a positive going region. Then at still larger  $y/\delta$  values, the averages show a negative region once again, except that now it occurs at a negative time corresponding to the downstream side of the structure. This implies the structure has a rotation and the very interesting streamline pattern which can be drawn from these results will be discussed shortly.

The ensemble-averaged time histories of the instantaneous  $uv$  product corresponding to these data are shown in figure 5. It is clear from figure 5 that significant contributions are made to the Reynolds stress; the averaged values are typically an order of magnitude greater than the mean value near the outer edge of the layer and two to three times greater than the local mean near the wall. Indeed, estimations based upon these average contributions and their measured frequency of occurrence suggest that as much as 90% of the total Reynolds stress may be carried by these structures alone.

An important feature of the present Reynolds stress data and a feature that may be observed in the data of Blackwelder and Kaplan, is that, particularly at  $y = 0.05\delta$ , the averages show two maxima, one on either side of a low value at the time of detection. Such an effect is clearly a result of the steep negative to positive jump of the streamwise velocity component and the corresponding sudden fall in the normal component of velocity. The same effect cannot be discerned in the data of Lu and Willmarth<sup>7</sup> and this is a reflection of the different sampling criterion that they used. It is based on detection of a fixed level of the streamwise component of velocity, and because of intensity variations, the detected points will not always bear the same phase relationship to the structure of interest from one realization to the next. Therefore, the rather subtle effect that may be discerned in the present averages could become lost.

Despite this, the averages are not inconsistent with the detailed and extensive set of data presented by Lu and Willmarth<sup>7</sup>. It can be concluded that large contributions to the Reynolds stress are made by slow moving disturbances lifting away from the wall (bursts in their terminology) and faster structures moving towards the wall (sweeps). The present data show, however, that these disturbances are not part of the burst-sweep cycle since they can be detected so far from the wall. They arise from the large structure itself. This explains the finding of Lu and Willmarth<sup>7</sup> who showed that the mean periods of these disturbances scale on outer flow variables and are the same across the entire layer.

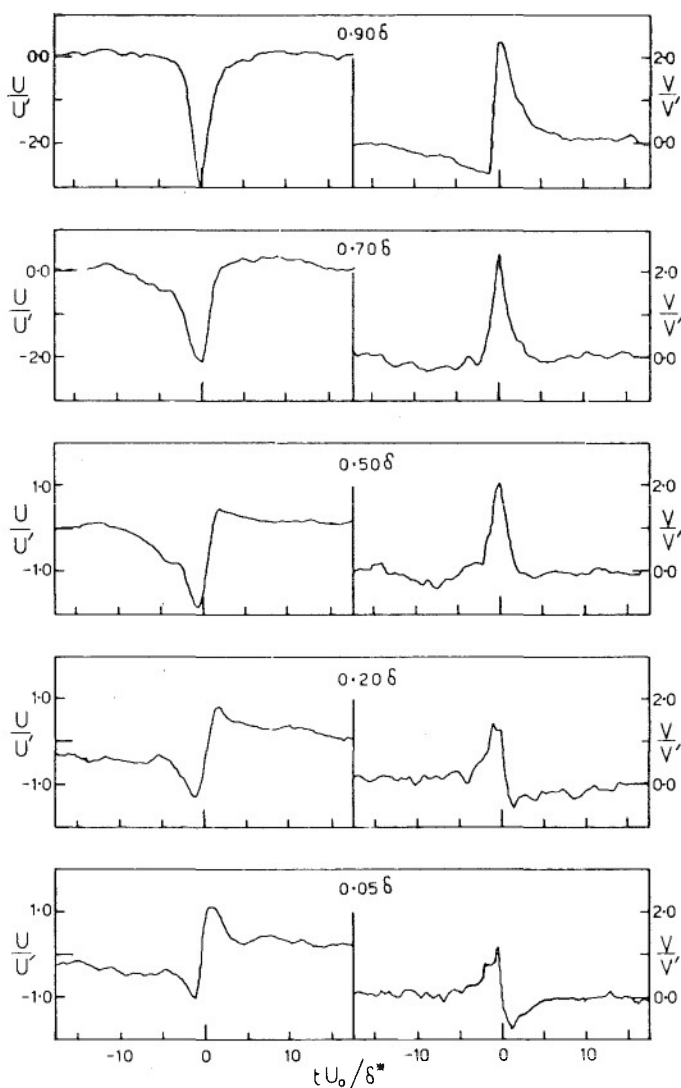


Figure 4. Ensemble-averaged time histories of the streamwise component ( $u$ ) and normal component ( $v$ ) of fluctuating velocity at different points in the boundary layer.

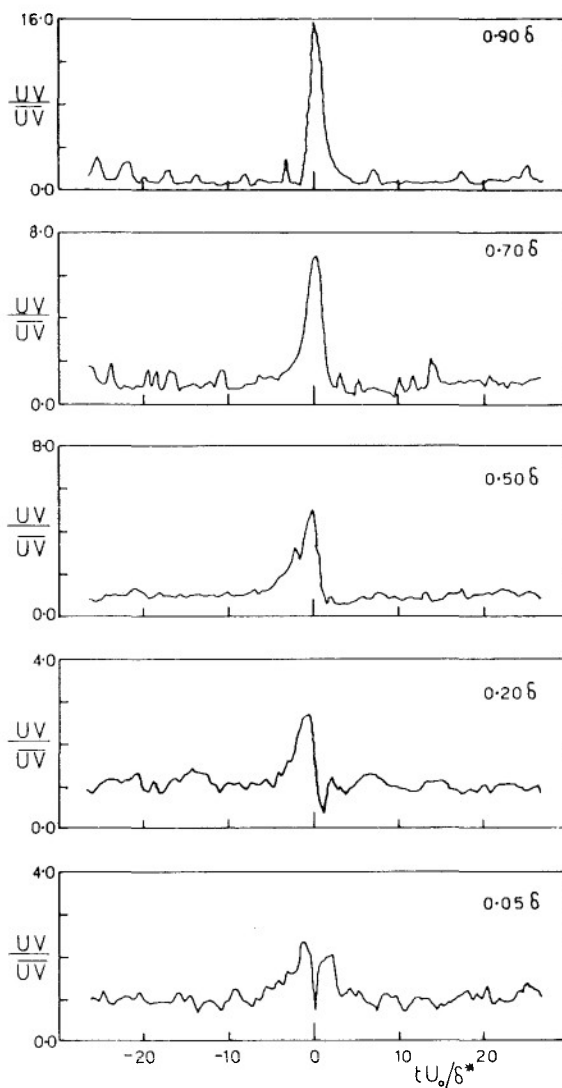


Figure 5. Ensemble-averaged time histories of the large structure contribution to the Reynolds stress.

#### 4.4 The Streamline Pattern of the Large Structure

Although the results of the previous section have served to provide a quantitative measure of some of the large structure characteristics, they have not yet provided a clear physical picture of the structure. A much clearer interpretation of the conditional velocity data can be obtained by using the ensemble averages to create a streamline pattern of the large structure.

By positioning each average time history, for a particular  $y/\delta$ , at the value of time (relative to zero at the wall) where Brown and Thomas found the wall shear-velocity correlations to peak, the streamline pattern of figure 6 is obtained. Here time has effectively been replaced by  $x$ , and the result is shown in a frame of reference moving with the large structure, that is a frame of reference moving at a speed of  $0.8 U_0$  (changing this speed has little effect on the picture, and a speed of  $0.8 U_0$  has been chosen since wall pressure correlation data suggest this to be the convective speed of the large scale motions). The arrows shown in figure 6 are, in fact, velocity vectors whose lengths are given by  $(\bar{U} + \langle u \rangle - U_c)^2 + \langle v \rangle^2)^{1/2}$  and direction by  $\arctan(\langle v \rangle / (\bar{U} + \langle u \rangle - U_c))$ , where  $\langle \rangle$  refers to the ensemble average. The solid lines are not streamlines but are presented to serve as a visual guide only.

It is quite remarkable that the independently measured sets of data from different positions in the layer form such a coherent picture of a single large structure. The dominant feature does appear to be the rear or upstream surface where the rapid changes in velocity occur. This region, which triggers the detection algorithm, is most accurately represented by the ensemble averages. Further from this region, the cumulative effects of the random variations in amplitude and time scale between different realizations cause a degradation to both the averages and the streamline pattern. Despite this the pattern is very similar to the flow field sketched by Brown and Thomas.

It is to be noted, also, that near the wall the streamlines display a region of convex curvature. The existence of such a region was suggested by Brown and Thomas and is necessary if a rotational instability is the source of the streaks of longitudinal velocity that have been observed in that region.

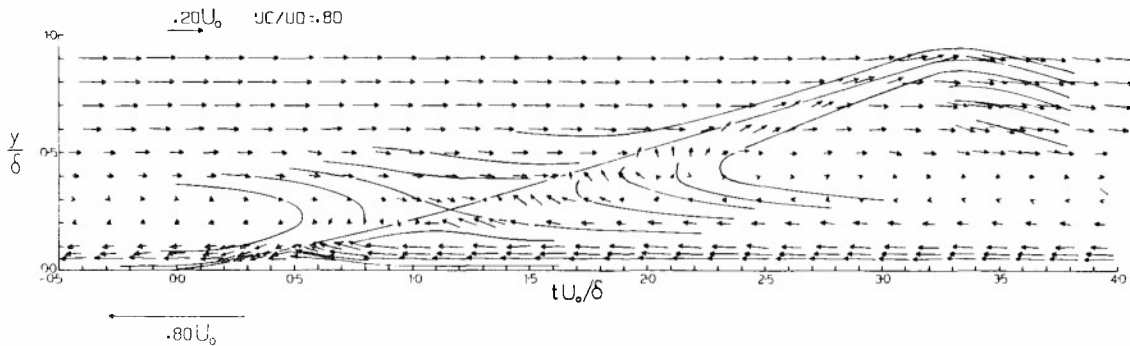


Figure 6. The experimentally determined streamline pattern of the large structure.

#### 5. THE RELATION BETWEEN THE LARGE SCALE STRUCTURE AND THE SMALLER SCALE WALL MOTIONS

Thus far, the discussion has been concerned with features of the large structure in the boundary layer. However, this report is also concerned with the burst-sweep cycle of events near the wall and its relationship to the large structure. The existence of such a relationship is undeniable and the crucial question is what is the mechanism behind this relationship. In 1978, Coles<sup>17</sup> presented some data showing that the flow in the sublayer is very like that which would be expected if the mechanism was a rotational instability occurring near the wall. Likewise, Brown and Thomas<sup>8</sup> present some estimates based upon known properties of the wall region suggesting that the wall streaks may be a consequence of a Taylor-Görtler type instability. The streamline curvature necessary for this mechanism, they suggest, arises from the large structure and the streamline pattern in figure 6 appears to support the idea. It will now be demonstrated that not only do these curved streamlines exist, but that they are associated with an increase in small scale activity near the wall.

The structure in figure 6 is presented in a convected frame of reference, that is, one in which the structure is quasi-steady (clearly it would be absurd not to view the structure in this way). As the curved streamlines near the wall are convected past a fixed cross wire, the curvature will induce fluctuations in  $u$  and  $v$ . Thus, time records of  $u$  and  $v$  can be interpreted as fluctuations in the streamline radius of curvature. Curvature is given approximately by

$$\frac{1}{R} = - \frac{d^2 y}{dx^2} \bigg|_{\psi = \text{const}},$$

and by definition, along a streamline

$$\frac{dy}{dx} = \frac{v_s}{u_s},$$

where  $v_s$  and  $u_s$  are the velocity fluctuations in the convected frame of reference. Combining these yields:

$$\begin{aligned} \frac{1}{R} &= - \frac{d}{dx} \left[ \frac{v_s}{u_s} \right] \bigg|_{\psi = \text{const}} \\ &\approx \frac{1}{U_c} \frac{d}{dt} \left[ \frac{v_s}{u_s} \right] \bigg|_{y = \text{const}} \end{aligned}$$

It is possible, therefore, to use a cross-wire pair to synthesize a time history of  $1/R(t)$  ( $R$  itself is not used since it can be numerically large when the flow is parallel to the wall). As before, the presence of small scale fluctuations near the wall has been characterized by the excursions in the smoothed rectified high frequency component of wall shear. Shown in figure 7 is the correlation between  $1/R$ , measured at  $y^+ = 170$  assuming  $U_c = 0.8 U_0$ , and the smoothed rectified high frequency component of wall shear. The time delay at which the correlation peaks arises because the hot-wire pair was directly above the hot film and the structures are inclined to the wall. The positive correlation shows that the small scale fluctuations are correlated with streamlines having convex curvature. While not proving the existence of a rotational instability, this result is certainly a necessary condition for such an instability to occur.

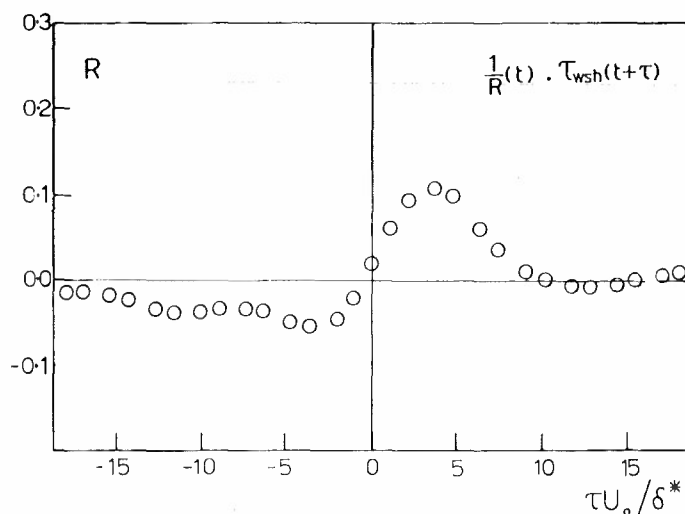


Figure 7. The correlation between the smoothed rectified high frequency component of wall shear and the synthesized curvature signal measured at  $y^+ = 170$  (see text).

As mentioned in Section 1, it has been suggested by Offen and Kline<sup>2</sup> that it is the pressure field of fluid arising from the repeated pairing of bursts at the wall that drives and maintains the wall flow. In this model momentary adverse streamwise pressure gradients give rise to inflexional velocity profiles near the wall and a phenomenon that Offen and Kline view as a convected separation of the wall flow. Willmarth<sup>18</sup> extended the ideas of the model to a larger scale effect viewed from a convected frame of reference. In this model it is the adverse pressure gradients of the large structure itself which, through convection, may act for a long time on the wall flow and lead to regions of deceleration and a loss in instability of the flow.

During the course of the present work, measurements of the wall pressure have been made using miniature transducers. To examine the two models discussed above, the same conditional approach discussed in Section 4 has been used to analyze the data. Because of the nature of the distribution of pressure sources, the full interpretation of the data is complex and beyond the necessary scope of this report. The material will instead be presented elsewhere<sup>13</sup>. It is to be noted, however, that large scale characteristic pressure fluctuations can be observed in the data and these are indeed associated with small scale fluctuations at the wall. Because these signatures are of large scale, it is difficult to view them as being generated by fluid arising from the bursting process at the wall. This is particularly true at high Reynolds numbers where there is considerable disparity between the scale of the bursts and the large structure.

It appears, instead, that these signatures are produced by the inclined near surface of the large structure where steep velocity gradients occur. These gradients tend to give rise to overpressures at the rear surface of the large structure. This places the pressure higher upstream of the burst region so that the pressure gradients are actually favorable when viewed in a frame of reference fixed on the wall.

However, this alone does not necessarily invalidate the model proposed by Willmarth. If instead the structure is viewed in the frame of reference moving with the structure, that is the convected frame of reference of figure 6, where the wall flow is perceived as being in an upstream direction, then it can be seen that the gradients felt by the flow at the wall are adverse. In the absence of more detailed measurements of this phenomenon, it is difficult to discuss the effect such gradients might have on the stability of the wall flow. Simple estimates do suggest, however, that they would be unlikely to perturb the stability of the wall flow as dramatically as would be necessary in the models discussed above.

## 6. CONCLUDING REMARKS

This paper has described a number of measurements and observations of the structure of boundary layer turbulence both near the wall and in the outer part of the layer. A summary of the important findings now follows:

- (1) The large structure appears to play a critical role in the dynamics of the flow. Its measured correlation features in the outer part of the layer suggest that its rear surface is a dominant feature.
- (2) The large structure influences the flow at the wall directly, and the wall shear displays a weak non-zero spanwise correlation even over scales as large as  $v/U_\tau$ . A conditional procedure has been used that ties the generation of this correlation to the flow further from the wall and to the large structure.
- (3) A conditional sampling procedure has been defined that identifies the large structure in the layer with a minimal bias. An enhancing procedure is described that redefines the detection points and minimizes the effects of false detections and random phase mismatch.

(4) These procedures have been used to generate ensemble averaged time histories of  $u$  and  $v$  for the large structure. They show that throughout the layer sudden changes in velocity are associated with the upstream surface of the structure. The same region also makes very large contributions to Reynolds stress and typical values may be an order of magnitude greater than the mean. Simple estimations suggest as much as 90% of the total Reynolds stress may be carried by this structure.

(5) The conditional data has been used to present a remarkably coherent view of the streamline pattern within the structure. This shows a large inclined structure with a strong outward flow along its rear surface and a more diffuse return flow at the front. Near the wall the streamlines display convex curvature below the large structure. This view is very similar to an earlier postulation of the form of the structure.

(6) By using a correlation technique and a synthesized curvature signal, it has been demonstrated that intense small scale wall shear fluctuations occur when the streamlines at the wall have convex curvature. This is a necessary condition for a rotational instability to be the source of the longitudinal vorticity observed in that region, and may provide the coupling between the large scale structures and the smaller organized structures near the wall.

#### REFERENCES

1. Kim, H. T., Kline, S. J., and Reynolds, W. C.: *J. Fluid Mech.*, Vol. 50, 1971, p. 133.
2. Offen, G. R., and Kline, S. J.: Dept. Mech. Eng., Stanford University, Report No. MD-31, 1973.
3. Nychas, S. G., Hershey, H. C., and Brodkey, R. S.: *J. Fluid Mech.*, Vol. 61, 1973, p. 573.
4. Kovaszny, L. S. G., Kibens, V., and Blackwelder, R. F.: *J. Fluid Mech.*, Vol. 41, 1970, p. 283.
5. Antonia, R. A.: *J. Fluid Mech.*, Vol. 56, 1972, p. 1.
6. Rao, K. N., Narasimha, R., and Badri Narayanan, M. A.: *J. Fluid Mech.*, Vol. 48, 1971, p. 339.
7. Lu, S. S., and Willmarth, W. W.: *J. Fluid Mech.*, Vol. 60, 1973, p. 481.
8. Brown, G. L., and Thomas, A. S. W.: *Phys. Fluids Suppl.*, Vol. 20, 1977, p. S243.
9. Brown, G. L., and Davey, R. F.: *Rev. Sci. Instr., Notes*, Vol. 42, 1971, p. 1729.
10. Thomas, A. S. W.: Ph.D. Thesis, University of Adelaide, South Australia, 1977.
11. Gupta, A. K., Laufer, J., and Kaplan, R. E.: *J. Fluid Mech.*, Vol. 50, 1971, p. 493.
12. Coles, D. E., and Barker, S. J.: *Project Squid Workshop, Turbulent Mixing in Non-reactive and Reactive Flows* (S. N. B. Murthy, Editor), Plenum Press, 1975, p. 285.
13. Thomas, A. S. W., and Bull, M. K.: To be published.
14. Blackwelder, R. F., and Kaplan, R. E.: *J. Fluid Mech.*, Vol. 76, 1976, p. 89.
15. Corino, E. R., and Brodkey, R. S.: *J. Fluid Mech.*, Vol. 37, 1969, p. 1.
16. Kline, S. J., Reynolds, W. C., Schraub, F. A., and Rundstadler, P. W.: *J. Fluid Mech.*, Vol. 30, 1967, p. 741.
17. Coles, D. E.: *Workshop on Coherent Structure of Turbulent Boundary Layers* (C. R. Smith and D. E. Abbot, Editors), Lehigh, Pennsylvania, May 1978, p. 462.
18. Willmarth, W. W.: *Adv. Appl. Mech.*, Vol. 15, 1975, p. 159.

#### APPENDIX A. THE DETECTION SCHEME

The detection scheme used in the conditional analysis of Section 4 is based upon the generation of the smoothed rectified high frequency component of a signal. This signal is then searched to find those times when it is a maximum greater than some discriminator level  $D$ . It is necessary to decide upon what combination of filter cutoff and discriminator should be used and this in turn requires an examination of the average time histories of the turbulent signals themselves. Shown in figure A1 is a series of averages of the velocity recorded at  $y/\delta = 0.05$ . Various discriminator levels and filter cutoffs have been used and in all cases it can be seen that both the amplitude and the ensemble average as well as its general shape are independent of variations in these quantities. Naturally, the steepness of the acceleration evident on the averaged time history, i.e. its frequency content, is to some extent dependent on the filter cutoff used, but the overall character is the same. Figure A2 shows the number of detections that occurred in 3.3 seconds of data for each filter setting - discriminator level combination. Clearly each curve shows a monotonic decrease as the discriminator level is increased with no indication of a plateau or region where the detection rate becomes independent of the discriminator level.

From these results, which were also checked for various other signals, any filter-discriminator combination cannot be objectively favored over any other combination. This seems to be a basic to the nature of the turbulent signals. The important point, however, is that the character of the results depend only very weakly on the filter cutoff and discrimination level. Therefore, the precise values of these parameters become unimportant.

The values that were finally chosen were a filter cutoff of 450 Hz and a discrimination level 1.5 times the rms level of the smoothed rectified signal. By visually comparing detection points obtained using this choice with the original signals, it did appear qualitatively to be more successful than other combinations.

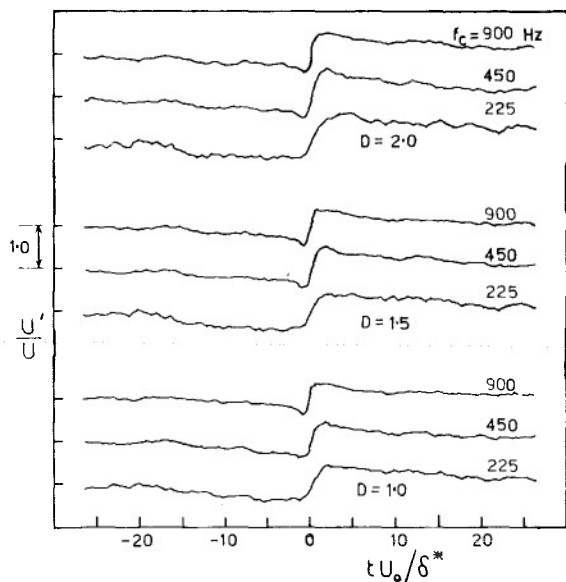


Figure A1. The different average time histories obtained by varying the filter cutoff and discrimination level of the detection scheme. The signal used in this example is the velocity component at  $y = 0.05\delta$ .

This detection technique has also been applied to a synthetic signal created by filtering white noise to yield a signal with the same power spectrum as a typical turbulent signal. The corresponding conditional average has been generated and, except for some statistical scatter, an essentially zero average is the result. This demonstrates that the detection and averaging technique does not lead to the identification of a signal pattern if none exists within a given signal.

#### APPENDIX B. THE ENHANCING TECHNIQUE

In order to demonstrate the way the conditional average time histories are enhanced, typical results are shown in figure B1 using, as before, the streamwise fluctuating velocity at  $y/\delta = 0.05$ . To obtain these data, a series of short averaging time correlations have been computed between the first ensemble-averaged time history and each realization that contributes to this average. The detection points have then been refined upon a basis of the sign of the correlation and the time delays at which each peak occurs in the correlations. Figure B1 also shows a histogram distribution of these time delays after five iterations of the process. The averaging time is  $T_{AV} U_o/\delta^* = 25$  in each case.

There is a dramatic effect associated with this enhancing technique and the amplitude of the averages is nearly doubled. The general character of the averages is still the same but the increased amplitude is now more typical of actual signal levels. Furthermore, the histogram demonstrates that only very small time adjustments are required to minimize the problem of phase uncertainty at the time of detection. The results will therefore be independent of the range of time delays used when generating the short averaging time correlations, provided, of course, the range is sufficiently large. Shown in figure B2 are the results obtained from the same data using four different averaging times. They clearly demonstrate that the effect, if any, of varying the averaging time is indeed small; the precise value is, therefore, somewhat arbitrary. In the present work a value of  $T_{AV} U_o/\delta^* = 25$  was used. Higher values were not used because of the penalizing increase in computing time associated with the process.

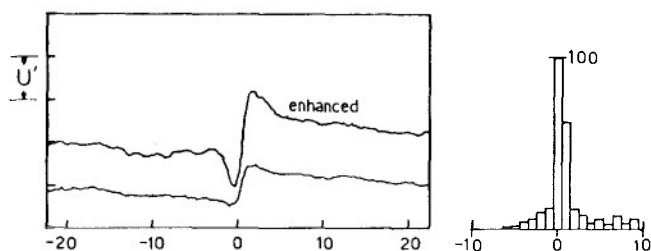


Figure B1. The effect of applying the enhancing technique to the velocity recorded at  $y = 0.05\delta$ . The histogram represents the distribution of the time shifts, inferred from each short averaging time correlation, used to redefine the detection points.

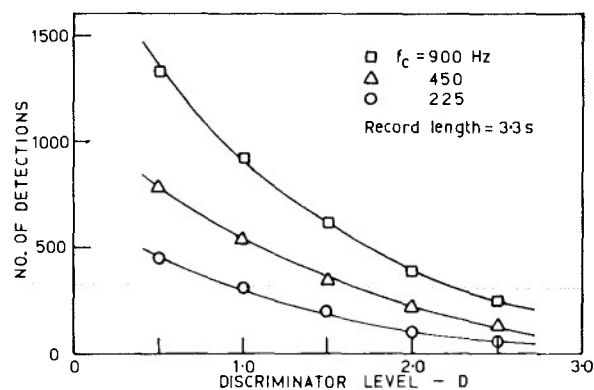


Figure A2. The number of detections obtained in 3.3 seconds of data for each of the filter cutoff discriminator level combinations used to obtain figure A1.

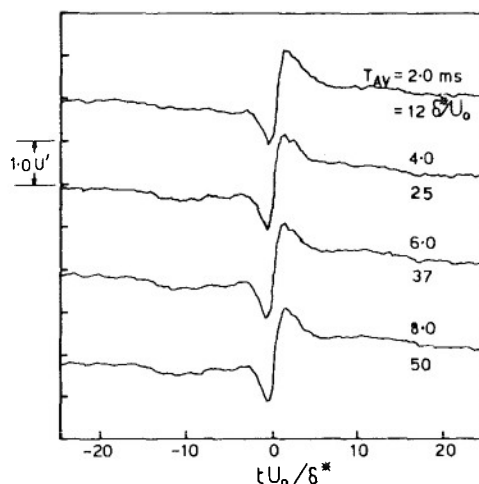


Figure B2. The effect of varying the averaging time of the correlations used to enhance the ensemble-averaged time history of the velocity at  $y/\delta = 0.05$ .

## ROUND TABLE DISCUSSION

Prof. Liepmann

To open the general discussion: sometimes it is the practice to get a number of people up on the platform and to have them discuss their views. Because of the late hour, I would prefer to make the discussion open from the floor. To start it out, I want to make a few remarks to explain why the meeting was done the way it was.

As you know, at my urging and with the support of the Committee, a great emphasis was placed on large-scale coherent structures. That was done intentionally, to balance out the meeting a little, because computational methods have had a lot of attention already. I believed, and I think a number of Committee members agreed with me, that the time had come when we should also take stock of the physical basis for what we are doing and map out future possibilities, both computational, and in particular, experimental.

It has often been remarked during the meeting that one couldn't really see what coherent structures have to do with computations, since the equations are usually averaged. I happen to be a professor, so I think in terms of classes. If you have a class in which you have two guys with an A and two guys with F, then you have an average which is about a C. This is o.k. when you discuss it with the authorities, but if you want to recommend one guy, you don't say he is a member of the C class. This is precisely what can happen with a large-scale motion. For example, if you deal with combustion, in which one part of the large-scale motion is much more important than another, the mean value may have very little meaning. For that reason, I feel strongly that the use of Reynolds averaging has to be questioned.

In the discussion we ought to keep in mind that there are several aspects of the problem. First, there is the need for the computation of turbulent boundary layers. In particular, you want to have computational methods which permit you, rather rapidly, to assess turbulent boundary layers on wings, in ducts, and so on. There is industrial and technical pressure to produce methods which are reasonably accurate, reasonably fast, and which reproduce at least the major aspects of a flow. I don't mean that anybody who doesn't use coherent structures is immediately to be omitted from further reading. I don't believe that. But, this is one aspect which is important and which should be discussed.

There is also an experimental aspect, which in my opinion and experience, is much too little supported. This is a real need for absolutely first-rate standard measurements, measurements which have an accuracy comparable to some of the work at the Bureau of Standards. Once the measurements have been done, they do not need to be questioned, and people have data with which they can compare their computations. It strikes me as slightly ridiculous that whenever anybody computes turbulent separation he goes back to the paper by Schubauer and Klebanoff, who had to do their experiments in anything but good conditions, in fact, in what amounted to a birdcage. Their tunnel was outside and had to be wrapped in chickenwire or birds would fly into the diffuser. I think there is a very urgent and important need to support work which is done with the utmost dedication and with sufficient support. We need a few standard cases that people can use to check their computations without worrying about the accuracy and reliability of the data. Producing such data is not a very thankful job, but a thing you get much credit for. It doesn't count for many brownie points in a university, and I doubt that many administrators in government labs like to have a guy measure a relatively simple case for a year at a time, but it seems to me absolutely necessary. Otherwise we will fall flat on our faces in the next computation contest. There should be some experiments which are really done to get fixed points, like you do the fixed points in the temperature scale in physics.

Another aspect is the attempt to come to grips with the discoveries by the experimenters. In recent years there have been quite a few experiments which have been made and are being made to find new physical phenomena. I am thinking of the shear layer experiments by Brown and Roshko, the boundary layer experiments by Klebanoff and Blackwelder, the channel experiments by Eckelmann, and others, which have shown that our early concepts have been at least faulty.

New approaches have been found to transition. In particular, there are the discovery of turbulent spots and the beautiful recent contribution by Gaster. All of that has to be eventually digested and put into a theoretical framework. It must effect the modelling, even if negatively. Even if you can come to the conclusion that for this case and that case you can average, there are definitely cases where you cannot. Examples are the chemical laser or the combustion problem, in which averaging in the Reynolds sense is completely inadequate. I am quite sure that we will find more of this. Understanding of coherent structure should eventually penetrate into the theory and numerics.

To my great pleasure, we have had in this meeting for the first time a real attempt by numerical experts to come to grips with this problem in one way or another. This should continue, of course, but there must also be support and encouragement of fundamental research which aims at discovery rather than at precision results. I believe that we have by no means yet exhausted the possibilities.



Just to have a certain carrot dangling before us, I would like to comment that the discovery of coherent structures - the fact that at least some features of turbulent flow are partly deterministic rather than completely stochastic - for the first time opens the possibility of turbulence control by means other than brute force. By brute force, I mean for example removal of the boundary layer by suction or attempts to control the mean profile. Phasing and interference between eddies must affect the skin friction on the one side and the acoustics on the other. We have for the first time come to a point where control may be possible. The future here I think is startling, and I can only enter a plea for an expansion of such research.

I hope that we will have more meetings in which all of these points of view can be brought forward. There should be fights, because they are absolutely essential, but people should leave the meeting with the intention of doing something, whether it is something new or more and better work on what they are doing. I am somewhat relieved, because I was worried when we started, I was less worried yesterday, and today I feel that we have succeeded in having a meeting which will contribute to this general scheme of interchange, of turbulent mixing, in a very coherent way. Let me stop here and ask for short contributions or questions from the audience. Please identify yourself and speak loudly and clearly, as this discussion will be taped.

Dr. Klebanoff

I would like to make two comments just to complement what Prof. Liepmann has said, and if they appear naive, perhaps you could excuse them because they come from a non-modeller. I have been observing and listening to the accounts of what has been accomplished and, in view of the difficulties that have been revealed relative to the handling of the very strong pressure gradients, and the difficulties in calculating separation, I believe I am permitted the observation that not much substantive progress has been made in the last 30 years. Perhaps not since we were trying to calculate separation by estimating critical shape parameters. Now, if this observation is only partly true, then I think it emphasizes the point that Prof. Liepmann made and which Prof. Gaster referred to, and that is, perhaps the equations should reflect the physical reality. By that I mean, for example, at low Reynolds numbers, where the frequency range is markedly decreased, and the flow is dominated by a large-scale structure, it does not appear feasible that a gradient diffusion-type model can be satisfactory. It then would appear that the more complicated methods with five or six empirical constants are in a sense fictitious representations. We cannot, for example, know at this stage - or I don't think evidence has been presented that can - for even a given flow geometry, handle a very wide range of Reynolds numbers, let alone a universality from geometry to geometry. I would therefore tend to emphasize the need for some very basic research experiments, experiments which keep pace with the computations as much as the computations have kept pace with the computer. Such experiments as evaluating the filter cut-off in the G functions in the large eddy simulation methods. How universal is small-scale modelling? How well can low Reynolds number flows be documented by large eddy simulation or statistical turbulence modelling?

Dr. Murphy,

I am going, since we are all agreeing, to agree with everybody else at this point; agree, but with a couple of provisos. I think that the experiments that are needed are ones with very rapidly varying boundary conditions, very severe pressure gradients, because for equilibrium conditions we really can predict very well - with about the same accuracy as the experiment. For a mild pressure gradient, favorable or adverse, I don't think that there is any problem with prediction. The second thing is that with regard to incorporating the concept of coherent structures into a calculation, we really don't know how to do it. I think that we are probably in the same situation that the particle physicists and astrophysicists were just before the turn of the century. It took an Einstein to come along and develop the mathematics in order to incorporate whatever was required to explain the experimental anomalies. In addition, it isn't clear at this point that the structure observed needs to be incorporated to provide adequate predictions.

Prof. Liepmann

I hope that is too pessimistic an attitude. I think you guys ought to be smarter than that.

Prof. Lilley

Just a small comment, Mr. Chairman, I think on the first day you mentioned the possible control of some features of the coherent structures in turbulent boundary layer flow, by grooving of the surface.

Prof. Liepmann

That is attributed to me, but it isn't right, I never said it.

Prof. Lilley

I don't say that this work is attributed to you, but I noted you mentioned it, or at least referred to the possible control of coherent structures. At any rate, I think that one or two other people have mentioned it, and I wonder whether we could have a little bit more information on whether indeed this is possible, if it has been achieved, and what are the results that have come out of this work.

Prof. Liepmann

I do not know anything myself about grooving. The only control scheme which we are playing around with is an attempt to develop some kind of active feedback control. I can imagine that it is possible, for example, to control large-scale shedding from a jet by feedback from a noise pickup, in such a way that you get minimum noise output. I think this is within the possibility of today's technology and today's understanding.

Whether you can do similar things to suppress the large-scale structures in boundary layers, I don't know. We are going to try, but I wouldn't bet on it. We know that polymers are effective in very small amounts. My conclusion is that it must be phase rather than energy which is affected because the amount of polymer is not sufficiently large.

Maybe we will be smart enough to act like a polymer and apply active control to phase. This is, of course, wild talk, but before the coherent structure was discovered, it was completely out of the question. It would have been the same as controlling Brownian motion by feedback and ending up with Maxwell's demon, which unfortunately was shown several times over not to work.

Dr. Eckelmann,

I want to come back to the second question you raised about a flow which can be used as a standard. In the oil channel, we are working now more than 10 years, and many generations of students and experienced fluid dynamicists have worked with it. Also recently Dr. Hofbauer made flow visualizations, so a second method in addition to the hot-film technique has been used. Thus, we can say that we know the flow field quite well. Anyone who is interested is welcome to make a computation and try to get what we measured, i.e., the fluctuating components, the Reynolds stress, etc.

Prof. Liepmann

Yes, but I am afraid what you are asking for may be very detailed computations on a relatively simple geometry. What the applications people want are very simple computations for a very complicated geometry. Don't misunderstand me; I am all for it, but I think we also ought to have experiments, for example, for a separated airfoil, for a swept-back airfoil, for the corner flow, and other flows which are geometrically complicated. If one thing can be handled well on a computer, it is usually the geometry. If you understand the physics, the geometry can be handled better than by the experimentalists. There should be measurements with which the computers, or rather the modellers, can at least verify their codes. But your offer is very welcome. I hope you have a large set of computers. You shouldn't always tell people the results beforehand, by the way. I even talked to Klebanoff and a few others about the proposition that we really ought to publish some utterly wrong measurements. Then we wait until they have been checked by modelling, and these models can be removed from further reading.

Prof. Coles,

In my own mind I elevate, to a fifth item on the agenda, the development of calculation methods which are specifically based on the idea of coherent structures. If I knew how to do that, of course, I would be at home doing it and not here. I think the situation where that would be easiest would be the mixing layer, but the mixing layer has not yet been observed in sufficient detail so that we know where the entrainment occurs, what the internal energy and dynamical processes are, and in particular, what the interactions are between these structures. We know there is a very violent interaction which may or may not be the major source of aerodynamic sound. That is one of the questions to be answered. But as the boundary layer has received about 80% of the effort, the boundary layer is so much more complicated, being three-dimensional in any representation, that I don't hold out too much hope.

I hope somewhere, somebody has a gleam in his eye about how to get at this problem. I think if you understood a single coherent structure you could assemble these statistically, you would have a much better chance of synthesizing the effects of roughness, pressure gradient, three-dimensionality, eventually into a common body of knowledge. I hope that I live long enough to see something happen in this field. I haven't seen any signs of it yet, and it bothers me very much.

Prof. Liepmann

You should quit smoking.

Dr. McCroskey

Could I mention something about unsteady effects for just a moment or two, and perhaps this could be in the vein of challenges for the developers of engineering methods. There are questions that interest some of us about what happens to boundary layers when the outer inviscid flow has some time-varying characteristics. First, what happens to the flow structure in some overall sense or in some engineering sense; secondly, in more detail, what happens inside the boundary layer; thirdly, what happens to your computation method; and fourthly, what happens in the turbulence modelling?

If I could just show very briefly a couple of slides, I will illustrate a simple problem. One of the simplest problems to look at unsteady effects is a flat plate that has an oscillating flow outside it - an average velocity plus some sinusoidal variation. One might expect the boundary layer throughout to respond in some sinusoidal fashion, there would be some amplitude and phase relationships inside the boundary layer, and shown schematically in Fig. 1 are the phase angle for the wall shear and for the displacement thickness. The most important parameter for this type of problem is some kind of a reduced frequency. The laminar case is well understood and well documented for low frequency behavior and high frequency behavior and shown by the dotted lines there.

The turbulent case typically shows a phase angle much smaller than the laminar one for the wall shear. That is to say, it seems to indicate that unsteady effects may be confined to a thin layer near the wall. On the other hand, the displacement thickness of the turbulent boundary layer shows normally a much larger change in phase angle with increasing reduced frequency. Those are schematics there that would be approximately correct for a flat plate.

Fig. 2 shows some comparisons of calculations for this flat plate problem with sinusoidal variations in the outer velocity. The wall shear then responds sinusoidally with some amplitude change and phase angle, and I have shown here the phase angle as calculated by a few people who have already attacked this problem.

There is one limited set of experimental data with hot wire velocity profiles from which it is very difficult to extract with any precision the phase angle of the wall shear, but nevertheless, one worker has attempted to do that, and it is shown by the dot there. I would say that there is probably a plus or minus 10 degree error band around the experimental data. These are the results by various people. I used a simple integral method, Nash-McDonald, a very old one. I also tried an eddy viscosity model of Cebeci-Smith. Telionis used the Cebeci-Smith viscosity model, the Nash calculations used Bradshaw's turbulent kinetic energy model, and the Kuhn and Nielson method is some integral method. I don't know the type, but it is obviously not correct. However, you see quite a wide discrepancy there in the calculated results for this simple problem. We don't really know for sure what the answer is. My own feeling is probably the Cebeci-Smith results are the closest to the correct value. Nonetheless, that's the situation.

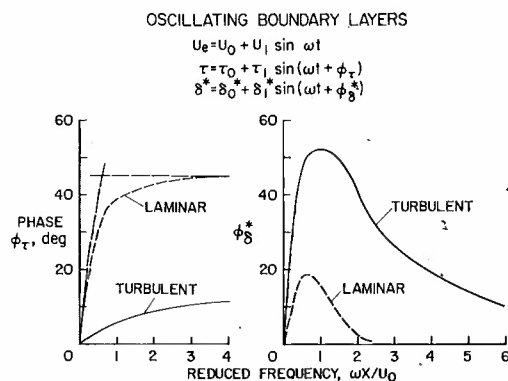


Fig. 1. Skin friction and displacement thickness characteristics on a flat plate with an oscillating free stream.

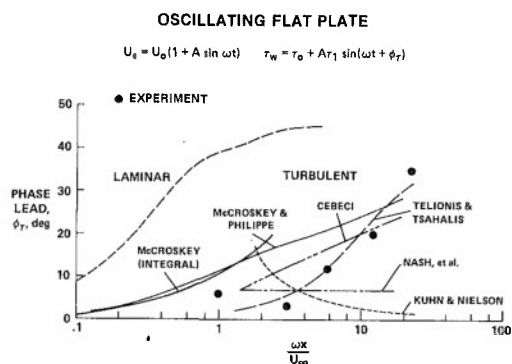


Fig. 2. Calculations of the phase angle of the wall shear on a flat plate with an oscillating free stream

I think that this perhaps represents a challenge for someone who would like to try their new engineering method, and see where they can put a curve on this. Perhaps we already have some contributions here. Basically, what we are interested in here is, if you had some flow that you thought you more or less understood in an engineering sense in a steady case, what would happen when you applied unsteady fluctuations in the outer velocity. Right now I don't think we really have satisfactory calculation methods for engineering purposes that address this question.

Prof. Liepmann

I would say that this is one particularly case where I feel you should get the experiment certified. These are not trivial experiments.

Prof. McCroskey

These are not trivial experiments, and there are some efforts underway.

Prof. Liepmann

I remember when it was still an issue to predict whether how turbulent skin friction was influenced by the mach number. There were 22 theories which covered the plane completely. The issue was only eventually resolved by one set of first-rate experiments. Therefore, my point is important, because otherwise you might give the poor modellers a bum steer. I think I would make sure that the experiments are absolutely first-rate.

Dr. Klebanoff

I just wanted to add to what Don Coles said. That is, to change the perspective in terms of what the large-scale structure is. The large-scale structure is the mean flow and the theoreticians should think of the large-scale structure from this point of view. Some recent experiments that we have made at boundary layer Reynolds numbers based on momentum thickness ranging from 400 to 5000 have shown that the logarithmic region which varies considerably in  $y^+$  units doesn't disappear, but always remains a constant percentage of the boundary layer thickness. We know that the large-scale structures do scale with the thickness. This would imply then that the log law is intrinsic to the large-scale structure. It is a property of the shape, its convective speed and its vorticity and mutual interaction, so I think that the point that Don Coles made about synthesizing and understanding large-scale structure can play a very important part in changing our attitude towards the modelling.

Prof. Liepmann

What I think you mean, and I agree completely, is that the idea of a mean-velocity profile plus fluctuations is not adequate for the large-scale structure. It is a sequence of the large-scale structures together, in average, that makes the mean velocity; that's what you mean. I can add to what Don said also, that vortex computations have, of course, been made for the mixing layer. Namely, interacting point vortices have been used as a model - and quite successfully. In a farfetched sense, these are attempts to deal with the large-scale motion and to get the mean velocity from superposition of vortex elements.

Dr. Murphy

The comments about incorporating the large-scale structure as part of a mean flow in a calculation scheme raise some difficulties in that apparently one must in order to do that, use a three-dimensional time dependent calculation. When you incorporate that kind of complexity into the mean flow, you have effectively ruled out engineering calculations for a substantial majority of the world. There simply are not enough fast machines nor enough money to support them to do that sort of thing on a routine basis.

Prof. Liepmann

Of course, we have to deal with engineering computations for which this may not be necessary. But occasionally a computation ought to be done specifically to understand the problem and put a better foundation under the engineering method. I agree fully that not everybody will compute every wing using large-scale motion. I think that is completely out of the question.

Dr. Kim

I agree with Dr. Murphy that not many people can afford a fully three-dimensional time-dependent calculation. However, we can learn a lot about turbulence from this type of simulation, and this information, in turn, can be used to improve the Reynolds average-type modelling. For example, one of the findings in our computational work is what we call the "splatting effect" near the wall. Although some people may not agree, this effect might be very significant near the wall. One could try to include this splatting effect in his model and see how it behaves. This kind of information can help, not only the large-eddy-chaser, but also for the Reynolds-average modellers with engineering applications in mind.

Prof. Blackwelder

From an experimental standpoint, a lot of us have seen, and it has been discussed this week, very close similarities between structures in turbulent shear flows and stability problems that exist in free-shear layers and in boundary layers, etc. In the stability cases, one doesn't model a fully three-dimensional time-dependent problem. One tries to capture the important physics and then model that to obtain reasonable agreement with the problem. I feel that there is some hope for using that same type of idea in modelling the turbulent structure that we are studying near the wall, the mixing layer, the outer structure, etc. The full three-dimensional time-dependent problem is out of the question. But if you capture the physics, and in particular I am thinking in terms of stability-type arguments, I think you could simplify the set of equations of Kim and Moin to a workable engineering-type approximation.

Prof. Orlandi

Most people model the turbulent pressure diffusion term as the turbulent energy diffusion one. Both Laufer's experiments and the results of the large eddy simulation show that the turbulent pressure diffusion is a production term in the viscous layer. Thus, using the one equation turbulence model to calculate the turbulent boundary layer, I modelled it in a different way than usual and I found better results; for example, the maximum  $Q^+$  reached a value of nine, closer to the Klebanoff results; on the contrary the value obtained with the usual model was eight. Thus, I think the results obtained with the expensive large eddy simulation can give a valid contribution to the cheaper time-averaged models used to solve engineering problems.

I can add one comment to the experimentalists about the pressure-strain correlation. I think the pressure in an incompressible fluid is not very well defined. It is much better to work with vorticity, which is really going closer to the physics. The only trouble is that nobody so far has come up with a decent vorticity meter. The laser-Doppler anemometer might do it. If you measure three points simultaneously, then with a reasonable digital setup you must be able to get the vorticity. I think it would be a tremendous advance if you could measure vorticity, because that is really what we are talking about in turbulence.

Dr. Cebeci

I have one simple question to raise while we are talking about engineering problems. Maybe someone should define what are some typical engineering problems and what are the problems that are associated with them.

Prof. Leipmann

Who would like to volunteer?

Dr. Yoshihara

Unfortunately, on our airplanes we have shock waves, and we have turbulent boundary layers hitting shock waves. What then happens to the coherent large scale turbulence after passage through a shock?

Prof. Liepmann

I think that is an easier problem than turbulent separation from a cylinder.

Dr. Forest

Could I add a few other nasty complications. On our turbine blades, we have flows which are partly transitional, highly curved, highly cooled, transonic mach number range, and also perhaps with shock boundary layer interaction.

Prof. Liepmann

And with an upstream boundary layer which in many cases you don't know. And then of course, there are all the problems of mixing. Nobody can predict the performance of a chemical laser because it involves mixing with chemical reactions. On the other hand, you can make absolutely astronomical gains by improving combustion efficiency by one percent. We won't run out of technical problems, even if we stick to aeronautics.

Dr. McCroskey

I think a lot of us would be interested in having a good method for  $C_{L,max}$  on a two dimensional airfoil in steady flow.

Prof. Liepmann

I think that we can only say, like the old cartoons, back to the old drawing board. I hope everybody returns being somewhat wiser, somewhat more cautious, and on the other hand, somewhat more adventurous, because you can combine the two.

Mr. Jones

I can't add very much at this time in a technical vein to the discussion that has just taken place. I would however, like to thank some of the people who have helped to make this meeting possible. First of all, the National Delegates to AGARD from the Netherlands, who have been our hosts. We are very grateful to them for that, and to Mr. Bleeker, who is the Deputy Coordinator for the Netherlands to AGARD, without whom we couldn't possibly have arranged such a fine meeting.

There are some others whom you should recognize. Following a group of technical people when they begin to describe the technical programs in which they are interested, is a very difficult job for interpreters who have to keep up with that very rapid discussion. Our interpreters for the meeting have been Mlle Malot and M. de Liffian, and I want to give them a hand. We have had further assistance from two gentlemen from SHAPE, Mr. Wauters and Mr. Grovenlock. They have handled the sound and the projection equipment. I want also to thank Mrs. Faddegon, who assisted Mlle Rivault with the registration and all of the problems that we have encountered at the registration desk in front.

I would like to thank Prof. Liepmann and his Committee for organizing this meeting, which has been a very interesting, and somewhat provocative meeting; the authors and the speakers for their efforts in putting together the papers that you have heard here; but most important, all of you for the contributions made in your discussion, because it occurs to me that one of the major contributions of this meeting has been to emphasize the communications between the theoreticians, the experimentalists and the modellers. I think that communication has to continue, if we are indeed to make progress in this total field. Thank you very much. I hope you all go home with new questions and new ideas and have found the meeting to have been quite worthwhile.

REPORT DOCUMENTATION PAGE			
1. Recipient's Reference	2. Originator's Reference	3. Further Reference	4. Security Classification of Document
	AGARD-CP-271	ISBN 92-835-0257-4	UNCLASSIFIED
5. Originator	Advisory Group for Aerospace Research and Development North Atlantic Treaty Organization 7 rue Ancelle, 92200 Neuilly sur Seine, France		
6. Title	TURBULENT BOUNDARY LAYERS – EXPERIMENTS, THEORY AND MODELLING		
7. Presented at	the Fluid Dynamics Panel Symposium held at the Europa Hotel, The Hague, Netherlands, 24–26 September 1979.		
8. Author(s)/Editor(s)	Various		9. Date January 1980
10. Author's/Editor's Address	Various		11. Pages 398
12. Distribution Statement	This document is distributed in accordance with AGARD policies and regulations, which are outlined on the Outside Back Covers of all AGARD publications.		
13. Keywords/Descriptors	<div style="display: flex; justify-content: space-between;"> <div> Turbulent boundary layer Compressible flow Incompressible flow Vortices </div> <div> Flow visualization Turbulence Computerized simulation Mathematical models </div> </div>		
14. Abstract	<p>The Symposium brought together experimental and theoretical research directed toward understanding the turbulent boundary layer, in both incompressible and compressible fluid flow. The development of computer modelling techniques taking experimental and theoretical results into account was also emphasized.</p> <p>Descriptions of coherent vortex structures utilizing new methods of flow visualization and hot-wire anemometry were presented. Developments leading to a satisfactory theoretical understanding of nonlinear vortex interactions and the decomposition of fluctuating flow fields were also discussed at the meeting. Several papers treated the early development of turbulence during, or immediately following, transition.</p> <p>Twenty-six papers and a summary discussion of the subject are included in the Proceedings of the meeting sponsored by the Fluid Dynamics Panel of AGARD in the Hague, Netherlands, 24–26 September 1979.</p>		

AGARD Conference Proceedings No.271 Advisory Group for Aerospace Research and Development, NATO <b>TURBULENT BOUNDARY LAYERS — EXPERIMENTS, THEORY AND MODELLING</b> Published January 1980 398 pages  The Symposium brought together experimental and theoretical research directed toward understanding the turbulent boundary layer, in both incompressible and compressible fluid flow. The development of computer modelling techniques taking experimental and theoretical results into account was also emphasized.  Descriptions of coherent vortex structures utilizing new methods of flow visualization and hot-wire anemometry  P.T.O.	AGARD-CP-271  Turbulent boundary layer Compressible flow Incompressible flow Vortices Flow visualization Turbulence Computerized simulation Mathematical models	AGARD Conference Proceedings No.271 Advisory Group for Aerospace Research and Development, NATO <b>TURBULENT BOUNDARY LAYERS — EXPERIMENTS, THEORY AND MODELLING</b> Published January 1980 398 pages  The Symposium brought together experimental and theoretical research directed toward understanding the turbulent boundary layer, in both incompressible and compressible fluid flow. The development of computer modelling techniques taking experimental and theoretical results into account was also emphasized.  Descriptions of coherent vortex structures utilizing new methods of flow visualization and hot-wire anemometry  P.T.O.	AGARD-CP-271  Turbulent boundary layer Compressible flow Incompressible flow Vortices Flow visualization Turbulence Computerized simulation Mathematical models
AGARD Conference Proceedings No.271 Advisory Group for Aerospace Research and Development, NATO <b>TURBULENT BOUNDARY LAYERS — EXPERIMENTS, THEORY AND MODELLING</b> Published January 1980 398 pages  The Symposium brought together experimental and theoretical research directed toward understanding the turbulent boundary layer, in both incompressible and compressible fluid flow. The development of computer modelling techniques taking experimental and theoretical results into account was also emphasized.  Descriptions of coherent vortex structures utilizing new methods of flow visualization and hot-wire anemometry  P.T.O.	AGARD-CP-271  Turbulent boundary layer Compressible flow Incompressible flow Vortices Flow visualization Turbulence Computerized simulation Mathematical models	AGARD Conference Proceedings No.271 Advisory Group for Aerospace Research and Development, NATO <b>TURBULENT BOUNDARY LAYERS — EXPERIMENTS, THEORY AND MODELLING</b> Published January 1980 398 pages  The Symposium brought together experimental and theoretical research directed toward understanding the turbulent boundary layer, in both incompressible and compressible fluid flow. The development of computer modelling techniques taking experimental and theoretical results into account was also emphasized.  Descriptions of coherent vortex structures utilizing new methods of flow visualization and hot-wire anemometry  P.T.O.	AGARD-CP-271  Turbulent boundary layer Compressible flow Incompressible flow Vortices Flow visualization Turbulence Computerized simulation Mathematical models



<p>were presented. Developments leading to a satisfactory theoretical understanding of nonlinear vortex interactions and the decomposition of fluctuating flow fields were also discussed at the meeting. Several papers treated the early development of turbulence during, or immediately following, transition.</p> <p>Twenty-six papers and a summary discussion of the subject are included in the Proceedings of the meeting sponsored by the Fluid Dynamics Panel of AGARD in the Hague, Netherlands, 24–26 September 1979.</p> <p>ISBN 92-835-0257-4</p>	<p>were presented. Developments leading to a satisfactory theoretical understanding of nonlinear vortex interactions and the decomposition of fluctuating flow fields were also discussed at the meeting. Several papers treated the early development of turbulence during, or immediately following, transition.</p> <p>Twenty-six papers and a summary discussion of the subject are included in the Proceedings of the meeting sponsored by the Fluid Dynamics Panel of AGARD in the Hague, Netherlands, 24–26 September 1979.</p> <p>ISBN 92-835-0257-4</p>
<p>were presented. Developments leading to a satisfactory theoretical understanding of nonlinear vortex interactions and the decomposition of fluctuating flow fields were also discussed at the meeting. Several papers treated the early development of turbulence during, or immediately following, transition.</p> <p>Twenty-six papers and a summary discussion of the subject are included in the Proceedings of the meeting sponsored by the Fluid Dynamics Panel of AGARD in the Hague, Netherlands, 24–26 September 1979.</p> <p>ISBN 92-835-0257-4</p>	<p>were presented. Developments leading to a satisfactory theoretical understanding of nonlinear vortex interactions and the decomposition of fluctuating flow fields were also discussed at the meeting. Several papers treated the early development of turbulence during, or immediately following, transition.</p> <p>Twenty-six papers and a summary discussion of the subject are included in the Proceedings of the meeting sponsored by the Fluid Dynamics Panel of AGARD in the Hague, Netherlands, 24–26 September 1979.</p> <p>ISBN 92-835-0257-4</p>